UNIVERSITAT POLITÈCNICA DE CATALUNYA

DOCTORAL THESIS

High-fidelity numerical simulations of reacting flows with tabulated chemistry

Author:
Ambrus BOTH

Supervisors:
Dr. Daniel MIRA
Dr. Oriol LEHMKUHL

A thesis submitted in fulfillment of the requirements for the degree of Doctor of Philosophy

in the

Doctoral Programme in Aerospace Science and Technology

Barcelona, March 2023

UNIVERSITAT POLITÈCNICA
DE CATALUNYA
BARCELONATECH

Barcelona
Supercomputing
Center
Centro Nacional de Supercomputación

無近勝利

"Mukin shôri"

TANAKA Masahiko

Abstract

In the transition to net-zero carbon emission technologies, turbulent combustion is expected to retain an important role in various applications. In particular, the aviation industry is projected to widely adapt the usage of biofuels and hydrogen-based fuels in the coming decades, while the regulations concerning non-CO_2 pollutant emissions are becoming more stringent. This transition entails both the gradual evolution of existing burner technologies, and the exploration of revolutionary new concepts. Large-eddy simulation of these combustion systems provides valuable insight into complex dynamic phenomena, such as flame stability and pollutant formation, thus it is an increasingly more important component of the engine development process. Such high-fidelity simulation approaches need to be further developed, gaining confidence in their applicability and exploring their limitations, while keeping in mind the complexity of available high-performance computing resources. This dissertation presents the development of computational tools for the study of multiphase reacting flows, and their application on model aero-engine combustors.

Specifically, the present work applies tabulated chemistry methods for combustion modeling, which allow for the representation of complex chemical phenomena while keeping the computational cost feasible. Furthermore, liquid fuel droplets are modeled in a Lagrangian manner, giving an intuitive representation of sprays. Stand-alone computational tools are created to facilitate the user friendly flamelet calculation and tabulation in a unified framework, and to increase confidence in droplet evaporation models through single droplet simulations. Meanwhile, a high-fidelity simulation method is implemented in the multi-physics simulation code: Alya, utilizing the various preexisting code elements, and exploiting the ongoing development efforts of a large team. In particular, the low-dissipation Navier-Stokes solver of Alya is extended here to variable density flows under low Mach number conditions. This Navier-Stokes solver is coupled with arbitrarily complex thermochemical tables in a new framework.

The developed stand-alone tools are used in this work to analyze the single droplet behavior, and to explore steady and temporally evolving laminar flamelets, and their applicability to chemistry tabulation. Subsequently the new framework of Alya is validated extensively and it is used in the analysis of tabulated chemistry methods. The turbulent combustion process in model aero-engines is studied with the developed method at atmospheric pressure. The flame stabilization phenomenon is analyzed in a swirl stabilized technically premixed hydrogen burner approaching flashback conditions. This turbulent hydrogen flame is studied using a perfectly premixed assumption and considering mixture fraction stratifications as well. Subsequently, the Cambridge swirl bluff-body burner is studied under different conditions. A non-premixed gaseous methane flame and two spray flames using n-heptane and n-dodecane fuels are simulated close to the lean blow-out limit, studying the shear induced localized extinction in detail. The prediction of this finite rate chemistry effect is a challenging task for the applied tabulated chemistry methods, however valuable insight is gained on the applicability of different thermochemical manifolds, and on the effect of the liquid fuel behavior.

Overall, the implemented low-dissipation finite element method is capable of predicting complex unsteady combustion phenomena, despite the simplicity of the tabulated chemistry methods. The work presented herein has been published in two peer reviewed journal articles and several conference contributions. The developed simulation framework enables the further study of industrially relevant combustion systems using high-performance computing resources.

Resum

En la transició cap a tecnologies de zero emissions de carboni, es preveu que la combustió turbulenta mantingui un paper important en diverses aplicacions. En el cas de la indústria de l'aviació, s'espera un ús ampli de biocombustibles i combustibles basats en l'hidrogen en les properes dècades, mentre que les regulacions relatives a les emissions de contaminants no CO_2 es tornen més estrictes. Aquesta transició implica tant l'evolució gradual de les tecnologies de combustió existents com l'exploració de nous conceptes revolucionaris. L'aplicació de la tècnica de 'large-eddy simulation' per simular aquests sistemes de combustió proporciona informació valuosa dels fenòmens dinàmics complexos, com l'estabilitat de la flama i la formació de contaminants, convertint-se cada vegada en una part més important del procés de desenvolupament del motor. Aquest tipus de simulacions d'alta fidelitat segueixen encara en desenvolupament, buscant millorar la seva fiabilitat i explorant les seves limitacions, tenint en compte la complexitat dels recursos de computació d'alt rendiment disponibles. Aquesta tesi presenta el desenvolupament d'eines computacionals per l'estudi de fluxos reactius multifàsica i la seva aplicació en models de combustors de motors d'aviació.

En concret, aquest estudi aplica mètodes de química tabulada per a la modelització de la combustió, que permeten la representació de fenòmens químics complexos, al mateix temps que mantenen un cost computacional factible. Les gotes de combustible líquid són modelades de manera Lagrangiana, donant una representació intuïtiva dels esprais. Eines computacionals són creades per facilitar el càlcul i la tabulació de 'flamelets' d'una manera senzilla, i per augmentar la confiança en els models d'evaporació de gotes. Al mateix temps, un mètode de simulació de alta fidelitat s'implementa en el codi de simulació multifísica Alya, utilitzant els diversos elements de codi preexistents i aprofitant els esforços d'un gran equip de programadors. En concret, el mòdul de Navier-Stokes de baixa dissipació d'Alya s'adapta aquí a fluxos de densitat variable en condicions de baix número de Mach. Aquest codi està acoblat amb taules termoquímiques en un nou marc de treball.

Els codis desenvolupades en aquest treball s'utilitzen per analitzar el comportament de gotes, i per explorar 'flamelets' estables i evolutius, així com la seva aplicabilitat a la tabulació química. El nou marc de treball d'Alya s'ha validat àmpliament i s'ha utilitzat en l'anàlisi de mètodes de tabulació química. El procés de combustió turbulent en motors d'aviació ha estat estudiat amb el mètode desenvolupat a pressió atmosfèrica. El fenomen d'estabilització de la flama s'ha analitzat en un cremador pre-mesclat d'hidrogen que s'apropa a les condicions de retrocés de flama. Aquesta flama d'hidrogen turbulent s'ha estudiat tan assumint una pre-mescla perfecta com considerant estratificacions de fracció de mescla. Posteriorment, s'ha estudiat el cremador de Cambridge tipus 'swirl bluff-body', en diferents condicions. S'han simulat una flama de metà no pre-mesclat i dues flames de pulverització utilitzant combustibles de n-heptà i n-dodecà, estudiant l'extinció localitzada amb detall. La predicció d'aquest efecte de química de taxa finita és una tasca difícil per als mètodes de tabulació química aplicats, però s'obté una idea sobre l'aplicabilitat de diferents mètodes i sobre l'efecte del comportament del combustible líquid.

En general, el mètode d'elements finits de baixa dissipació implementat és capaç de predir fenòmens de combustió complexos, malgrat la simplicitat dels mètodes de tabulació química. El treball presentat s'ha publicat en dos articles de revistes revisades per experts i en diverses contribucions a conferències. El marc de simulació desenvolupat permetrà ampliar l'estudi de sistemes de combustió industrialment rellevants utilitzant recursos de computació d'alt rendiment.

Acknowledgements

I would like to express my gratitude to the following individuals, without whom this work would have not been possible.

Firstly, I am deeply grateful to my two supervisors, Dr. Daniel Mira and Dr. Oriol Lehmkuhl, for their guidance, support, and optimism throughout my research. They were always available for discussions and they were open to my ideas, approaching them with patience and constructive criticism. Both of these are rare qualities as I learned from my fellow researchers in the La Caixa scholarship program. Their supervision and insightful feedback shaped both this work and my growth as a researcher.

I am likewise in dept to my past supervisors who motivated me to engage in research. Firstly, to Dr. Axel Groniewsky who helped me form research integrity, showed me a great example throughout our work during my bachelor's, and encouraged me to continue my studies abroad. And to Prof. Dirk Roekaerts, who ignited my interest in spray combustion during my master's studies, and mentored me ever since. They built the foundation of my research career.

I would also like to extend my sincere appreciation to the colleagues who helped me integrate in the beginning of the PhD: Dr. Enric Illana Mahiques, Dr. Georgios Chrysokentis, Dr. Alfonso Santiago, Daniel Pastrana, and Samuel Gómez González. They welcomed me with friendship, and showed me the ropes at BSC, especially in terms of using Alya. Special thanks are due to Samuel, who created the best meshes I have ever had the luck to use. Later, as I became more familiar with Alya, I spent a lot of time developing and debugging with Dr. Guillaume Houzeaux, who turned this sometime frustrating activity into a fun and rewarding one.

I am grateful to the researchers who collaborated with us on both the topics of this thesis and on other studies not included here. It has been a pleasure to work on hydrogen combustion with the group of Prof. Christian Oliver Paschereit at TU Berlin including Dr. Panagiotis Stathopoulos, Dr. Tom Tanneberger, and Dr. Thoralf Reichel. Likewise, I am thankful for the help and discussions on the behavior of the Cambridge swirl flames both with Prof. Epaminondas Mastorakos and Dr. Andrea Giusti. Their expertise and insights on both these challenging configurations had greatly enhanced the quality of this work.

The friendships I formed in Barcelona were essential in staying positive and carrying on with the work. I will be forever grateful for the teaching and guidance of Sensei Daniela Erminy and all my fellow karatekas at Shotokan Barcelona JKA. They helped me focus on what is really important and develop through practice. The network of la Caixa fellows of the 2017 call also played a key role in my life. I am especially grateful for the friendship of Dr. José Jurado, who always supported me throughout the past years, and helped me with some practical applications of chemical engineering. I would also like to acknowledge my dear colleagues who became close friends, Anurag Surapaneni and Lucas Gasparino. We worry all day about mass, energy, and momentum conservation, but something more important is to be sanity-conserving. Anurag and Lucas were a great help in achieving this.

I would like to also express my deepest gratitude to my family. They accept my decisions and provide unconditional love, always encouraging me to not just walk on the path but also enjoy the journey. Finally, I cannot overstate how grateful I am for the support of Alícia throughout the past years. You always had my back and accepted the challenges of this work with exceptional amounts of patience.
Thank you!

The project that gave rise to these results received support through the INPhINIT Fellowship Grant for Doctoral Studies at Spanish Research Centers of Excellence from the "la Caixa" Foundation (ID **100010434**).
The fellowship code is **LCF/BQ/DI17/11620032**.

The project has received funding from the European Union's Horizon 2020 research and innovation program under the Marie Skłodowska-Curie grant agreement No. **713673**.

The research leading to these results has received funding from the Clean Sky 2 JU under European Union's Horizon 2020 research and innovation program under the ESTiMatE project, grant agreement No. 821418.

The research leading to these results has received funding from the European Union's Horizon 2020 Programme under the CoEC project, grant agreement No. 952181.

Contents

List of Figures

List of Tables

List of Abbreviations

ACARE	**A**dvisory **C**ouncil of **A**eronautic **R**esearch in **E**urope
ANN	**A**rtificial **N**eural **N**etwork
ATAG	**A**ir **T**ransport **A**ction **G**roup
CAEP	**C**ommittee on **A**viation **E**nvironmental **P**rotection
CCUS	**C**arbon **C**apture, **U**tilization, and **S**torage
CFD	**C**omputational **F**luid **D**ynamics
CFDF	**C**umulative **F**ilter **D**ensity **F**unction
CFL	**C**ourant-**F**riedrichs-**L**ewy condition
CMC	**C**onditional **M**oment **C**losure
CPU	**C**entral **P**rocessing **U**nit
CRSB	CORIA **R**ouen **S**pray **B**urner
CRZ	**C**entral **R**ecirculation **Z**one
CSP	**C**omputational **S**ingular **P**erturbation
DCG	**D**eflated **C**onjugate **G**radient
DNS	**D**irect **N**umerical **S**imulation
EMAC	**E**nergy, **M**omentum, and **A**ngular momentum **C**onserving
FDF	**F**ilter **D**ensity **F**unction
FFT	**F**ast **F**ourier **T**ransform
FGM	**F**lamelet **G**enerated **M**anifold
FPDF	**F**ilter **P**robability **D**ensity **F**unction
FPI	**F**lamelet **P**rolongation of **I**ntrinsically Low Dimensional Manifold
FPV	**F**lamelet **P**rogress **V**ariable model
HPC	**H**igh-**P**erformance **C**omputing
ICAO	**I**nternational **C**ivil **A**viation **O**rganization
IEA	**I**nternational **E**nergy **A**gency
LBO	**L**ean **B**low-**O**ut
LDA	**L**aser **D**oppler **A**nemometry
LDV	**L**aser **D**oppler **V**elocimetry
LES	**L**arge-**E**ddy **S**imulation
LOL	**L**ift-**O**ff **L**ength
LPT	**L**agrangian **P**article **T**racking
LTC	**L**anding and **T**ake-off **C**ycle
NSRDS	**N**ational **S**tandard **R**eference **D**ata **S**eries
ODE	**O**rdinary **D**ifferential **E**quation
PDA	**P**hase **D**oppler **A**nemometry
PDE	**P**artial **D**ifferential **E**quation
PDF	**P**robability **D**ensity **F**unction
PIV	**P**article **I**mage **V**elocimetry
PLIF	**P**lanar **L**aser **I**nduced **F**luorescence
POD	**P**roper **O**rthogonal **D**ecomposition
PSD	**P**ower **S**pectral **D**ensity
PVC	**P**recessing **V**ortex **C**ore
RANS	**R**eynolds-**A**veraged **N**avier **S**tokes

REDIM	**Re**action–**Di**ffusion **M**anifold
RMS	**R**oot **M**ean **S**quare
SAF	**S**ustainable **A**viation **F**uel
SGS	**S**ub-**G**rid **S**cale
SMD	**S**auter **M**ean **D**iameter
TARES	**T**abulated **A**verage **R**epresentative **E**vaporation **S**tate
TPES	**T**otal **P**rimary **E**nergy **S**upply
TRL	**T**echnology **R**eadiness **L**evel
UFPV	**U**nsteady **F**lamelet **P**rogress **V**ariable model

Physical Constants

Gravitational acceleration	$\mathbf{g} = 9.81\,\mathrm{m\,s^{-2}}$
Universal gas constant	$R_u = 8.3145\,\mathrm{J\,mol^{-1}\,K^{-1}}$
Stefan–Boltzmann constant	$\sigma_{SB} = 5.669 \times 10^{-8}\,\mathrm{Wm^{-2}K^{-4}}$

List of Symbols

a	Strain rate	s^{-1}
AFR	Air-fuel ratio	1
a_k	Progress variable coefficient of species k	1
Bi	Biot number	1
B_M, B_T	Spalding transfer numbers	1
C	Scaled progress variable	1
C	Molar concentration	$\mathrm{mol\,m}^{-3}$
C_p	Molar isobaric specific heat	$\mathrm{J\,mol}^{-1}\,\mathrm{K}^{-1}$
c_p	Isobaric specific heat	$\mathrm{J\,kg}^{-1}\,\mathrm{K}^{-1}$
d	Diameter	m
$\mathcal{D}$	Diffusion coefficient	$\mathrm{m}^2\,\mathrm{s}^{-1}$
Da	Damköhler number	1
e_K	Kinetic energy	$\mathrm{J\,kg}^{-1}$
$\mathbf{F}$	Force	N
Fo	Fourier number	1
G	Stretch rate	s^{-1}
H	Molar specific enthalpy	$\mathrm{J\,mol}^{-1}$
h	Specific enthalpy	$\mathrm{J\,kg}^{-1}$
i	Scaled enthalpy	1
k	Turbulent kinetic energy	$\mathrm{J\,kg}^{-1}$
K	Vaporization rate constant	$\mathrm{m}^2\,\mathrm{s}^{-1}$
Ka	Karlovitz number	1
ℓ	Length scale	m
Le_k	Lewis number of species k	1
L_v	Latent heat of evaporation	$\mathrm{J\,kg}^{-1}$
m	Mass	kg
Ma	Mach number	1
Nu	Nusselt number	1
P,p	Pressure	Pa
Pr	Prandtl number	1
$\dot{Q}$	Heat flow rate	$\mathrm{J\,s}^{-1}$
Re	Reynolds number	1
S	Source term	$\square\mathrm{m}^{-3}\mathrm{s}^{-1}$
$\mathbf{S}$	Strain rate tensor	s^{-1}
Sc	Schmidt number	1
Sh	Sherwood number	1
S_L	Laminar flame speed	$\mathrm{m\,s}^{-1}$
Sr	Strouhal number	1
St	Stokes number	1
T	Temperature	K
t	Time	s
$\mathbf{u}$	Velocity	$\mathrm{m\,s}^{-1}$

$\mathbf{V}$	Diffusion velocity	$\mathrm{m\,s^{-1}}$
W	Molar weight	$\mathrm{kg\,mol^{-1}}$
We	Weber number	1
X	Mole fraction	1
$\mathbf{x}$	Location	m
Y_c	Progress variable	1
$Y_{c,v}$	Sub-grid progress variable variance	1
Y_k	Mass fraction of species k	1
Z	Mixture fraction	1
Z_k	Elemental mass fraction of element k	1
Z_v	Sub-grid mixture fraction variance	1
δ	Flame thickness	m
ε	Turbulent kinetic energy dissipation rate	$\mathrm{m^2\,s^{-3}}$
η	Kolmogorov length scale	m
κ	Specific heat ratio	1
κ	Wave number	$\mathrm{m^{-1}}$
λ	Excess air ratio	1
λ	Thermal conductivity	$\mathrm{W\,m^{-1}\,K^{-1}}$
μ	Dynamic viscosity	$\mathrm{kg\,m^{-1}\,s^{-1}}$
ν	Kinematic viscosity	$\mathrm{m^2\,s^{-1}}$
ρ	Density	$\mathrm{kg\,m^{-3}}$
σ	Surface tension	$\mathrm{N\,m^{-1}}$
$\boldsymbol{\tau}$	Stress tensor	Pa
τ	Time scale	s
$\mathbf{\Phi}$	Flux	$\square\mathrm{m^{-2}s^{-1}}$
ϕ	Equivalence ratio	1
χ	Scalar dissipation rate	$\mathrm{s^{-1}}$
$\dot{\omega}_k$	Mass source term of species k	$\mathrm{kg\,m^{-3}\,s^{-1}}$
$\dot{\omega}_T$	Heat release rate	$\mathrm{J\,m^{-3}\,s^{-1}}$
Ω_T	Integral heat release rate	$\mathrm{J\,s^{-1}}$

Chapter 1

Introduction

This dissertation presents the development and application of a numerical simulation framework for the analysis of practical combustion systems. This chapter details the rationale of engaging in such work, and the approach of executing it, setting up the context of the subsequent technical discussion.

1.1 Motivation

Combustion has been the default way of energy conversion in the usage of fossil and traditional biomass energy carriers throughout history. Currently combustion is involved in various technologies as the method of converting the chemically stored energy of fuels into thermal energy. The resulting hot flue gases may be used to fulfill heating demands such as the domestic space heating and hot water supply in buildings, the direct heating with flames in the high temperature applications of the steel, cement, and glass industries, or the heat requirements of other industrial processes in the form of steam and hot gas. Meanwhile, combustion may be used in other systems with the end goal of electricity generation in the electric power sector or propulsion in the aerospace, maritime, road, and rail transportation sectors.

In light of the anthropogenetic nature of the ongoing climate crisis, most industrial sectors must undergo a rapid technological transition in the coming decades to reduce carbon dioxide emissions. (Sanderson and O'Neill, 2020) In many fields this equates to changing the consumer behavior, increasing the energy efficiency, and electrifying the applications, however combustion based technologies are projected to stay relevant in various fields where other alternatives are hard to implement.

The global net-zero emissions scenario of the International Energy Agency (IEA, 2021a) envisions a plan of such a rapid adaptation of new technologies, with net-zero carbon dioxide emissions achieved by 2050. In particular, the global energy consumption of the aviation sector is expected to transition towards the usage of sustainable aviation fuels (SAF) as in this application the high energy density of fuels is crucial. By 2050 this scenario projects, that 45% of the consumption will be covered by biofuels, and 30% by hydrogen-based fuels, together forming a 75% share of SAF. The maritime shipping sector is likewise expected to keep using combustion technologies, with large shares of ammonia (46%), biofuels (21%), and hydrogen (17%) in the maritime energy consumption reached by 2050. In the net-zero emission scenario, the high-temperature heating demand of the heavy industry retains certain combustion technologies as well, with the CO_2 emissions mitigated by the application of hydrogen and carbon capture, utilization, and storage (CCUS). In the electricity generation sector, natural gas power plants without CCUS are forecast to have a rising share till 2030, delaying their phase-out compared to other fossil-based power generation. This is favorable, as natural gas entails comparatively less carbon dioxide emissions than other fossil-based systems. Co-firing with hydrogen and

ammonia is also seen as a short term mitigation strategy, using the existing power generation infrastructure with minor retrofitting. By 2050, stationary gas turbines are expected to only retain their role in supporting the stability and flexibility of the power systems, alas this is possible with a relatively low share in the total electricity production.

Less ambitious emission reduction scenarios are given by the "stated policies scenario" and the "announced pledges case" of the IEA, which consider the current measures enforced by policies and all currently pledged actions respectively. Nevertheless, there is room for optimism. For instance, the 2000 edition of the World Energy Outlook (IEA, 2000) projected a renewable share of merely 3% in the total primary energy supply (TPES) by 2020, despite the rapid growth of renewables expected at that time. In contrast, the real share of renewables was 12% in 2020 (IEA, 2021b), as the technologies matured and became economically competitive. With the further economic maturing of the technologies necessary for the net-zero scenario, the future may deviate from the current projections of the IEA (2022).

The envisioned technological transformation is to be executed in the coming 27 years. This is a very demanding task, as some of the necessary technologies are still characterized by a low technology readiness level (TRL). (Héder, 2017) Consequently, the development cycle of new technologies shall receive all possible support, including high-fidelity numerical simulations in addition to more traditional design approaches. The increasing diversity of fuels brings new concerns associated to their different burning characteristics. Furthermore, the new low-carbon burner concepts also face long standing technological challenges of combustion, such as the safety, operability and flexibility of the combustion system, and non-CO_2 emissions. The latter includes gaseous pollutants such as carbon monoxide and nitrogen oxides (NO_x), more complex chemical pollutants like unburnt hydrocarbons and non-volatile particulate matter (soot), and other effects such as noise.

The large thermal power of individual combustion devices means, that the flows are typically turbulent, as sustaining laminar flow at the expected flow rates would require very large systems allowing low velocities. (Peters, 2001) Indeed, turbulence enhances the mixing of reactants, and allows for relatively compact flames contained in manageable equipment sizes. The presence of turbulence makes the description of reacting flows a demanding task. Turbulence alone is readily a very complex phenomenon, as the fluctuating nature of the flow is unpredictable in detail, and complex mathematical tools are necessary to obtain useful quantitative information for engineering design. (Kundu, Cohen, and Dowling, 2015, §12) Combustion on its own is likewise a formidable topic, with the reaction of fuel and oxidizer being influenced by many interacting effects. The interaction of turbulence and chemical reactions brings new dimensions to the problem, an further complexities are introduced by other physical phenomena, such as multiphase flow or radiation.

The present work focuses on turbulent combustion for aeronautical applications, however the developed tools are aimed to be transferable to other turbulent reacting flow applications aiding the efforts of decarbonization. The "Waypoint 2050" study of the Air Transport Action Group (ATAG, 2023) highlights the need for accelerated research on technologies of hydrogen and SAF, in order to meet climate goals of the aerospace industry. In detail, the "Fly the green deal" report of the Advisory Council of Aeronautic Research in Europe (ACARE, 2023) sets out ambitious goals not only in terms of carbon dioxide, but also regarding other emissions. Among the short-term goals (by 2030) they mention demonstrators of hydrogen-powered regional flights, and a greater than 20% efficiency improvement in the last generation aircraft compared to 2020. Meanwhile, by 2050 a 90% reduction is targeted in

both NO_x and non-volatile particulate matter emissions with a baseline of 2020, and over 80% of the conventional fuel shall be replaced by SAF. In line with these goals, the current regulations of aero-engine emissions readily provide increasingly more stringent limits, such as the recently introduced standard on non-volatile particulate matter emissions in the landing and take-off cycle (LTO) devised by the International Civil Aviation Organization in the 11^{th} meeting of the Committee on Aviation Environmental Protection (CAEP/11). (ICAO, 2023) As Jacob and Rindlisbacher (2019) detail, the CAEP/11 controls not only limit the total emitted mass of non-volatile particulate matter, but also the number of emitted particles. The regulations regarding NO_x emissions are likewise increasingly more stringent. The challenge of reducing such non-CO_2 emissions has to be solved alongside the introduction of sustainable aviation fuels. The performance of a fuel, including the associated emissions, is influenced by various factors. (Braun-Unkhoff, Riedel, and Wahl, 2017) Physical properties affect the atomization, evaporation, and mixing, which crucially influence the flame characteristics. Furthermore, the molecular structure of the fuel profoundly affects the chemical reaction pathways leading to pollutant formation. (Kathrotia et al., 2018) The interactions of all these phenomena with the turbulent flow, heat losses, and radiation can lead to vastly different emission characteristics.

Numerical simulations provide a valuable tool in the design of such turbulent combustion systems, complementing the theoretical considerations, the vast know-how of the experts, and empirical tests of the developed components and systems. The numerical studies are not only able to reveal the details of flame stabilization and pollutant formation, but they can be competitive addition to experimental tests regarding the economic and temporal constraints of the development cycle of an aero-engine. (Slotnick et al., 2014) The commonly used simulation approaches differ in their computational cost, and their accuracy to predict physical phenomena. The methods to reproduce the turbulent flow show a trade-off between these qualities. For instance, the Reynolds-averaged Navier-Stokes (RANS) approach intends to resolve the average flow field directly, and needs extensive theoretical and empirical modeling efforts to achieve good predictions. However, it tends to be computationally cheap. Conversely, direct numerical simulations (DNS) resolve the turbulent flow entirely at a great computational expense, as turbulence involves a broad spectrum of length and time scales. The DNS has to represent the smallest of these scales with sufficient resolution, leading to fine computational grids with a high number of degrees of freedom and small time steps. RANS simulations are burdened with the uncertainty of the models, and the great effort of calibrating these models in the specific application cases. (Xiao and Cinnella, 2019) Meanwhile DNS is unaffordable in practical applications, and thus far it is restricted to canonical configurations for the study of combustion physics. (Chen, 2011) The subject of the present work is a third option: large-eddy simulation (LES). (Piomelli, 1997) LES means a trade-off between the described physical details and the computational expense compared to DNS, as in LES only the larger energy-carrying turbulent scales are resolved, and closure models are introduced only to represent the effect of un-resolved length scales. The turbulent motion on these small length scales is expected to behave more universally, thus general models can be devised without the necessity of tuning them for the specific application. This balanced trade-off between accuracy and computational cost, makes LES apt for studying the sensitive phenomena of burner operability and pollutant formation in realistic systems.

Besides the flow field, the simulation methods also have to represent chemical reactions and their interaction with turbulence. The accurate resolution of this phenomenon is likewise computationally expensive, since chemical reactions occur on

a broad spectrum of time scales, leading to so called "stiff" problems. I.e.: the time scale of the fastest evolving reactions sets a limitation to the numerical solution, while the flame propagation and pollutant formation happens on a comparatively longer time scale. Furthermore, the evolution of the reactions responds non-linearly to the local conditions of temperature, pressure, and composition, making the simplification of the problem challenging. (Lu and Law, 2009) Different techniques are available, that aim to alleviate these restrictions. As Fiorina, Veynante, and Candel (2015) summarizes, these stiff detailed chemical mechanism, which perform well in a wide range of conditions, are typically reduced to *skeletal* mechanisms, which only contain a subset of the reactions, sufficient to capture the specific operating conditions of the burner and the targeted chemical phenomena. Further optimization yields reduced chemical mechanisms, which minimize the computational expense associated to chemistry, but entail more restrictions on the range of applicability and the reproduced physics. Alternatively, the computational expense of detailed and skeletal mechanism may be mitigated by using these in *a priori* calculations and pre-tabulating the chemistry. As various reviews detail, due to the non-linear dependence of chemistry on the local state of the gas mixture, the coupling of chemistry models with large-eddy simulation needs dedicated care, since the unresolved details in LES fundamentally affect the flame propagation. (Janicka and Sadiki, 2005; Pitsch, 2006; Knudsen and Pitsch, 2010; Fiorina, Veynante, and Candel, 2015) In particular, the size of the reaction zone tends to be comparable to the LES grid spacing, prompting the need for sub-grid turbulence/chemistry interaction models. The various LES combustion models may be classified based on the targeted combustion phenomena: premixed, partially premixed, and non-premixed models. Models of perfectly premixed turbulent combustion tend to focus on predicting the turbulent flame propagation speed, as the reaction rate in practical combustion applications is enhanced by the turbulent flow. Meanwhile in non-premixed turbulent combustion the rate of molecular mixing between fuel and oxidizer is critical, as mixing is a prerequisite of reactions. (Pitsch, 2006) Predicting partially premixed combustion tends to be a more complex task than the above two limiting cases, since both mixing and flame propagation in readily mixed gases have substantial influence on the behavior of the burner. (Knudsen and Pitsch, 2010) Finally, in case of combustion of liquid fuels additional models are necessary to represent the breakup, transport, and evaporation of the liquid phase. (Jenny, Roekaerts, and Beishuizen, 2012) In most simulations this is achieved by a Lagrangian representation of individual droplets, introduced into the computational domain by a model mimicking at least a part of the spray breakup. Nevertheless, Eulerian models are also being developed, which represent the spray cloud statistically by the local mass of liquid phase and the associated interfacial surface. (Vié et al., 2013)

High-fidelity combustion LES entails a high computational cost, thus it shall be applied to problems which benefit from the increased precision compared to RANS models. Such an application is the assessment of the operational envelope of combustion devices, as the operability is limited by the onset of unsteady phenomena. These include the propagation of the flame into the mixing elements of the combustor (flashback), or the global extinction of the flame as it is convected out of the combustion chamber (blow-out). Both of these conditions are hazardous in an aero-engine as leading to damage of the equipment and loss of thrust. Other periodic combustion instabilities can also lead to unsafe conditions. LES can predict such unsteady phenomena at an affordable cost. (Tangermann et al., 2010; Noh et al., 2019; Foale, Giusti, and Mastorakos, 2021) Besides the prediction of unsteady flame propagation, LES is also highly suitable for the study of pollutant formation. The

mechanisms of pollutant production are highly sensitive to local variations of the thermo-chemical state, which is reproduced with adequate accuracy in LES. Thus, combustion LES is suitable for the assessment of CO, NO_x, and soot formation. (Ihme and Pitsch, 2008a; Pecquery et al., 2014; Gkantonas et al., 2020) In conclusion, it is of interest to further advance combustion LES approaches, which aid the development of new technologies in the transition towards net-zero emissions.

1.2 Strategy

The parallel multi-physics finite-element code Alya (Vázquez et al., 2016) is used in this study to build a simulation framework for turbulent reacting flows of gaseous and liquid fuels. At the start of the present work Alya readily contained various useful elements, forming the base of the development described here. For instance, Gövert (2016) implemented tabulated chemistry methods for combustion modeling in low Mach number gaseous flows, Chrysokentis (2019) developed a low-dissipation LES solver for incompressible flows, and Olivares Mañas (2018) started the work on Lagrangian particle transport for inert particles that do not affect the flow. These models are revised, extended, or repurposed here, bringing Alay to the state of the art in simulation of multiphase turbulent reacting flows, and enabling further development to go beyond. Furthermore, Alya readily provides an extensive infrastructure for high-performance computing (HPC), which is necessary in light of the increasingly more available HPC resources. (Mira et al., 2022) The code is continuously optimized, keeping in mind the intricacies of the HPC architecture, as showcased by many recent studies. (Borrell et al., 2018; Banchelli et al., 2020; Borrell et al., 2020; Oyarzun, Mira, and Houzeaux, 2021; Banchelli et al., 2022; Houzeaux et al., 2022)

Tabulated chemistry methods are developed and applied here, as they are able to represent complex chemical phenomena at a limited computational cost. (Van Oijen, Lammers, and De Goey, 2001) Detailed chemical mechanisms are used to compute canonical one dimensional flames (flamelets) and the thermo-chemical state of these flames is mapped onto a table parameterized by a reduced set of control variables. The control variables shall be sufficient to uniquely identify any state among the original set of 1D solutions. The main assumption of the applied tabulated chemistry methods, is that these 1D flamelets are representative of the actual phenomena in complex combustion devices. This can be justified in cases, where the time scales of chemical reactions are significantly shorter, than the time scales of turbulent motion, thus the local states relax towards the 1D solution significantly faster than the turbulent flow can disturb them. In such a situation the turbulent flame front is an ensemble of 1D flamelet structures along the wrinkled flame front, convected by the turbulent flow. Tabulated chemistry methods have been applied successfully in various turbulent flames, as an array of recent studied illustrates. (El-Asrag, Braun, and Masri, 2016; Langella, Swaminathan, and Pitz, 2016; Avdić et al., 2017; Franzelli et al., 2017; Hu, Olguin, and Gutheil, 2017; Ma and Roekaerts, 2017; Vascellari et al., 2017; Ventosa Molina et al., 2017; Gövert et al., 2018; Rieth et al., 2019; Fossi et al., 2020; Hansinger, Ge, and Pfitzner, 2020; Benajes et al., 2022; Huang et al., 2022b) Within this work the tabulated chemistry capabilities of Alya are extended. The *a priori* solution and processing of 1D flamelets is refactored in order to accommodate a broader variety of reference flamelets and arbitrarily complex table structures in terms of the tabulated quantities and the number of control variables (table dimensions). The framework to treat such tables and calculate the necessary control

variables is likewise implemented in Alya in a flexible way. The details of the tabulation algorithm are revised thoroughly, examining the ability of control variables to represent the flamelet states uniquely. Dedicated attention is given to the modeling of heat loss, and post-processing tools are developed to evaluate if applying tabulated chemistry methods is appropriate.

The dispersion and evaporation of the liquid fuel sprays is modeled in an Eulerain-Lagrangian manner here, corresponding to treating the gas phase in the Eulerian frame of reference, and the liquid phase in the Lagrangian one. (Kronenburg, 2007; Jenny, Roekaerts, and Beishuizen, 2012) Such an approach is widely used in spray combustion LES, as the Lagrangian tracking of the individual particles allows for the straightforward and intuitive modeling of various phenomena. (Ma and Roekaerts, 2016; Giusti and Mastorakos, 2017; Shum-Kivan et al., 2017; Elasrag and Li, 2018; Noh et al., 2018; Sitte and Mastorakos, 2019; Chatelier et al., 2020; Paulhiac et al., 2020; Zhang et al., 2020b; Dressler et al., 2021; Benajes et al., 2022) For instance, the Lagrangian treatment represents easily the velocity difference between the liquid and gas phases and the broad spectrum of various particle sizes. The individual droplets are treated as a lumped point of mass, energy, and momentum. Thus the interaction of the gas phase with the liquid droplets relies on a large set of coupled empirical models. In Alya, the Lagrangian particle tracking approach of Houzeaux et al. (2016) is extended to model evaporating droplets with two-way coupling between the Eulerian gas phase and Lagrangian liquid phase. The necessary empirical models are adapted to interface with the tabulated chemistry approach of the gas phase. The conservation of mass, energy, and momentum is enforced between the two phases. Attention is dedicated to the analysis of the droplet evaporation models, as these have a direct effect on the availability of fuel in the gas phase, profoundly influencing the combustion.

The chemistry and liquid phase models are integrated into Alya for the application on combustion LES. In this context, the accurate simulation of the flow field is imperative. Here the low-dissipation incompressible flow solver of Lehmkuhl et al. (2019b), based on a non-incremental fractional step algorithm, is extended to variable density flows. To achieve this, the low Mach number approximation of the Navier-Stokes equations is applied. This development is tested on various laminar flame configurations, isothermal and anisothermal turbulent channel flows, and well known turbulent flame configurations, without the tuning of modeling constants. Finally, the developed tools are applied for the LES study of two laboratory-scale aero-engine combustors under atmospheric pressure conditions. These cases correspond to a turbulent swirl stabilized hydrogen flame developed in TU Berlin (Reichel, Goeckeler, and Paschereit, 2015), and gaseous and spray flames in the Cambridge swirl-bluff-body burner (Cavaliere, Kariuki, and Mastorakos, 2013; Yuan, Kariuki, and Mastorakos, 2018). On one hand, these simulations further challenge the developed low-dissipation finite element algorithm, demonstrating its potential. While on the other hand, valuable insights can be synthesized regarding the flame stabilization mechanism. Overall, the developed capabilities are in line with the needs of the aerospace industry, considering the role of hydrogen and liquid sustainable aviation fuels in the decarbonization of air travel. Besides the application on flame stabilization explored in this work, the flexibility of the framework also allows for the straightforward integration of pollutant formation models, as demonstrated by the recent work of Kalbhor and Van Oijen (2023). Note however, that exploring such applications is out of the scope of the present study.

1.3 Objectives

The present work concerns a substantial development effort on the well established multi-physics simulation code: Alya. (Vázquez et al., 2016) An extensive pre- and post-processing framework has to be established to support the numerical analysis of multiphase turbulent combustion. Furthermore, the developed simulation approach is applied on relevant model burners. The objectives of the study are summarized as:

1. extend the low-dissipation Navier-Stokes solver of Alya to variable density flows;
2. implement a flexible tabulated chemistry framework, for the automated generation and processing of 1D premixed and diffusion flamelets;
3. incorporate heat-loss effects into the tabulated chemistry framework;
4. extend the Lagrangian particle transport capabilities of Alya to model evaporating droplets with two-way coupling to Eulerian tabulated chemistry models;
5. explain the performance and underlying *modus operandi* of the state of the art droplet evaporation models;
6. integrate the developed models into a combustion LES framework, without the *ad hoc* tuning of model constants;
7. establish a practice of assessing the validity of the applied models in Alya, by estimating the scales of turbulent motion and the turbulent combustion regime *a posteriori*;
8. provide insight to the flame stabilization mechanism of a turbulent technically premixed hydrogen flame approaching the onset of flashback;
9. evaluate the performance of tabulated chemistry models in predicting localized extinction in the Cambridge swirl bluff-body burner.

1.4 Outline of the dissertation

The rest of this dissertation describes the developed models and presents the analysis of laminar and turbulent flames. The structure of the thesis is as follows:

Chapter 2 provides a background in the modeling of the gas phase. The focus is on the low Mach number approximation of the Navier-Stokes equations for ideal gas mixtures, and the simple description of the thermo-chemical gas state used in tabulated chemistry methods.

Chapter 3 presents the behavior of canonical flamelet solutions under various conditions, including premixed and counterflow diffusion flame configurations. Subsequently, these flamelets are used to create thermo-chemical manifolds parameterized by a small set of controlling variables. This mapping procedure is assessed in detail, with special attention on evaluating the quality of reaction progress variable definitions, and gauging the effect of sub-optimal definitions on the thermo-chemical manifold.

Chapter 4 discusses the Lagrangian modeling of evaporating droplets. The kinematic droplet transport is described briefly. Meanwhile, the heat and mass transfer

is studied extensively providing insight to the Reynolds number and Stefan flow effects on evaporation. The equilibrium (wet-bulb) conditions of the droplets are identified in case of different models, and the time scales of droplet heat-up, evaporation, and motion are discussed.

Chapter 5 introduces the key aspects of large-eddy simulation of multiphase reacting flows. The applied LES models are discussed, such as the eddy-viscosity model, and the sub-grid turbulence/chemistry interaction model. Special attention is taken in the application of the latter in relation to the presently used tabulated chemistry approach. Furthermore, a method is derived to estimate the scales of turbulent motion from the present variable density LES results. These are contextualized by discussing the regimes of turbulent combustion.

Chapter 6 presents the details of the numerical solution of gas phase flows and the Eulerian-Lagrangian coupled problem. Subsequently, the method is applied on various well know benchmark cases. A channel flow is studied in the incompressible limit and under anisothermal conditions with gas-like material properties. The canonical flamelet configurations of chapter 3 are simulated with Alya, evaluating the extension of the fractional step algorithm to low Mach number variable density flows. The performance of the tabulated chemistry methods combined with the developed Navier-Stoked solvers is also evaluated in turbulent flames. The PRECCINSTA technically premixed swirl flame, and the DLR-A non-premixed jet flame are studied under stable burning conditions. Subsequently, these turbulent cases are used to showcase the developed post-processing tools.

Chapter 7 elaborates on the CFD analysis of the swirl stabilized hydrogen flame developed at TU Berlin. The flame stabilization mechanism is discussed broadly, introducing the typical phenomena of this burner. The flow is analyzed under inert conditions, highlighting the dynamic effects of a typical flow instability in swirl stabilized flames: the precessing vortex core. The reacting conditions are evaluated under two steady operating conditions, one far from the stability limits and one near the onset of flashback. By applying different tabulated chemistry models, the case is analyzed both using the perfectly premixed assumption, and considering the mixture stratification effects.

Chapter 8 presents the study of the Cambridge swirl bluff-body burner under various conditions near the limit of lean blow-out. The combined effect of the swirling air inlet and the bluff-body are discussed in the context of the inert flow. A non-premixed methane case of the burner is studied using tabulated chemistry methods based on counterflow diffusion flamelets. Subsequently, two spray flames of the configuration are evaluated using n-heptane and n-dodecane fuels. The n-heptane case is used to demonstrate the spray flame behavior in detail, with a focus on the local extinction process of the outer reaction zone. This case is also used to evaluate various modeling decisions, especially regarding the effect of different approaches in tabulated chemistry. Finally, the n-heptane and n-dodecane flames are compared under the same flow conditions, revealing the differences between these alkane fuels.

Chapter 9 summarizes the main outcomes of this work, concludes the findings, and recommends future research topics and areas of improvement in the Alya code.

Chapter 2

Gas phase modeling

In computational fluid dynamics (CFD) the simulated systems are represented by a set of partial differential equations (PDEs), that are assumed to characterize the underlying physical phenomena. These PDEs may correspond to fundamental conservation laws of physics, such as conservation of mass, momentum, energy, or chemical elements. Furthermore, additional PDEs may be formulated based on these laws, that describe the evolution of specific derived properties. These latter equations not only accentuate the behavior of the flow, but they may be advantageous for the numerical solution of quantities of interest, especially in the context of large-eddy simulation (LES) further detailed in chapter 5. The PDEs are coupled to one another through the material property laws.

A comprehensive overview is given by Kundu, Cohen, and Dowling (2015, §4) on the conservation laws governing fluid motion. Furthermore, the specificities of applying these laws in combustion systems is extensively discussed by Kuo (1986, §3) and more recently by Poinsot and Veynante (2005, §1). The present chapter summarizes the governing equations in the context of this study, keeping in mind the spray models of chapter 4 in the context of tabulated chemistry described in chapter 3.

The rest of this chapter is structured as follows. The laws applied for the evaluation of material properties are introduced in section 2.1. These material properties are necessary for the closure of the governing equations. Subsequently, foreshadowing the usage of tabulated chemistry models, section 2.2 describes a reduced set of derived quantities, that may be applied for the identification of the gas state under the assumptions of the tabulated chemistry models. The partial differential equations representing mass and momentum conservation are presented in section 2.3. Section 2.4 extends the set of equations to the description of the thermal state of the gas. Finally, the transport of chemical species is described in section 2.5, including the behavior of chemical reactions. Governing equations are introduced for species mass fractions, and other quantities suitable for tabulated chemistry models.

Credit

While this chapter, does not contain novel methods, it sets the framework for the rest of the study introducing the relevant material properties and governing equations. Numerical examples are prepared by the author with the hope of illustrating some of the key concepts in gas phase combustion. Furthermore, the effect of volumetric source terms and the unity Lewis number assumption is discussed in detail, deriving the equations from first principles. The former is an important aspect in the point-like treatment of fuel droplets, while the latter is a significant simplification enabling the straightforward application of tabulated chemistry. Parts of this chapter are published in: Both et al. (2020).

2.1 Material properties of gas mixtures

The partial differential equations introduced in this chapter describe the continuum behavior of the modeled fluid. As such, the equations are dependent on the local continuum properties of the fluid such as the mass density, the thermal conductivity, or the viscosity. This section details the laws, that facilitate the calculation of such continuum properties for ideal gas mixtures, which are assumed to represent the gas phase fluid in the targeted spray combustion applications.

2.1.1 Mixture composition

Throughout this work different mixtures are modeled. In the field of combustion simulation, the composition of such a fluid is predominantly described in terms of mole fractions X_k, or mass fractions Y_k. As the name suggests, the former describes the moles of species k in one mole of mixture, while the latter the kilograms of species k in one kilogram of mixture. By definition, the sum of all X_k and the sum of all Y_k are both unity, thus, with this constraint, the composition of a mixture of N_C different species can be described by $N_C - 1$ mass or mole fractions.

Once the composition is known, the gas mixture may be described by its average molar mass (W), expressed as:

$$W = \sum_{k=1}^{N_C} X_k W_k \quad \text{or} \quad \frac{1}{W} = \sum_{k=1}^{N_C} \frac{Y_k}{W_k}, \tag{2.1}$$

where W_k is the molar mass of species k. The molar masses facilitate the conversion between the mole and mass based representation of the composition:

$$Y_k = \frac{W_k}{W} X_k. \tag{2.2}$$

There are various other definitions for properties describing the mixture composition. One such quantity is the molar concentration C_k of species k. This property describes the moles of species k per unit volume of mixture, thus:

$$C_k = X_k C = X_k \frac{\rho}{W} = \frac{Y_k}{W_k} \rho, \tag{2.3}$$

where $C = \frac{\rho}{W}$ is the molar concentration of the entire mixture, i.e.: the moles of mixture per unit volume, and ρ is the mass density of the mixture. Note, that above relations are a consequence of the definition of these properties, without any assumption on the behavior of the mixture, thus they hold even for real gases and liquids. However, additional assumptions are necessary to link the molar concentrations to the other two mixing quantities, providing the molar concentration or the density of the mixture.

In the field of combustion, mole fractions (X_k) are typically used to describe the composition of gas phase fuels in an experimental setting. This practice is ultimately linked to Amagat's law stating, that the volume fractions of species in ideal gas mixtures are additive, and they are equivalent to the mole fractions. (Bejan, 2006, §4.7) Thus, when gas mixtures are prepared at a constant pressure and temperature, it is sufficient to measure their volumes or volume flow rates, to obtain their mole fractions. (Meier et al., 2000) Molar concentrations (C_k) are used traditionally in the description of chemical kinetics, determining the net production rate of individual

species as described in section 2.5.1. Finally, mass fractions (Y_k) are convenient in the formulation of species conservation equations presented in section 2.5.2.

2.1.2 Ideal gas mixtures

In general, if a mixture is in local thermodynamic equilibrium within a control volume, its state may be described by $N_C - N_P + 2$ degrees of freedom where N_C is the number of components, and N_P is the number of phases. (Gibbs, 1879) For the single phase mixtures discussed in this chapter, Gibbs' law states, that the local state of the fluid can be described as a function of $N_C - 1$ variables identifying the composition, and two other state variables. For instance:

$$\psi = \psi(h, P, Y_k) \quad \text{with} \quad k = 1..(N_C - 1)\,, \tag{2.4}$$

where ψ is a material property of interest, h is the specific enthalpy of the mixture, and P is the pressure. In chapter 4 liquid droplets are introduced, however in the present approach the droplet-gas interface is never enclosed in a control volume, thus the average continuum properties of such a multiphase system are not of interest in this work.

In the gas phase calculations of this chapter the material properties of interest are: the mean molar mass (W), the density (ρ), the isobaric specific heat (c_p), the dynamic viscosity(μ), the thermal conductivity (λ), and the mass diffusivity $(\mathcal{D}_k)$ of individual species. Locally the gas is assumed to be in internal thermal and mechanical equilibria (Green and Maloney, 1999, §4). Phase equilibrium is not of interest in this section, as the the gas and liquid phases are treated as separate thermodynamic systems. The local phase equilibrium on the interface of liquid droplets and the gas phase is discussed in chapter 4. Finally, chemical equilibrium is not imposed. In this context, in infinitesimal control volumes of the studied domain, the local values of the above defined material properties may be obtained as Eq. (2.4).

The mean molar mass only depends on the composition as presented in Eq. (2.1). In general the other properties are described as a function of temperature and pressure, rather than a function of enthalpy and pressure. This change of state variables is possible in the context of this work with the above local equilibria assumptions, as in a locally homogeneous gas mixture the enthalpy and temperature are injective functions of one another at constant pressure.

More specifically, ideal gas mixtures are used throughout this work to represent the gas phase. In this case the equation of state is:

$$\frac{P}{\rho} = \frac{R_u}{W} T, \tag{2.5}$$

meaning that the density ρ is proportional to the pressure P and the mean molar mass of the mixture W, and it is inversely proportional to the temperature T. Furthermore the isobaric specific heat, and the specific enthalpy only depend on temperature, and are independent of the pressure. This dependence is commonly described using the so called NASA polynomials. (Gordon and McBride, 1994) The polynomials describe the molar isobaric specific heat of a species $\left(C_{p,k}\right)$ as:

$$C_{p,k} = R_u \left(a_{k,1} + a_{k,2}T + a_{k,3}T^2 + a_{k,4}T^3 + a_{k,5}T^4\right) = R_u \sum_{i=1}^{5} a_{k,i} T^{i-1}, \tag{2.6}$$

where $a_{k,i}$ is the i^{th} coefficient of the NASA polynomial of species k. The isobaric specific heat is calculated by dividing its molar counterpart by the molar mass of the species: $c_{p,k} = \frac{C_{p,k}}{W_k}$. The specific heat of the mixture is a weighted average of the specific heat values of the components:

$$c_p = \frac{\sum_{k=1}^{N_C} X_k C_{p,k}}{W} = \sum_{k=1}^{N_C} Y_k c_{p,k}. \tag{2.7}$$

Considering this, one may define a different polynomial, that gives the (mass based) specific heat directly at a given gas composition:

$$c_p = \sum_{i=1}^{5} b_i T^{i-1}, \tag{2.8}$$

where b_i is a weighted average of the coefficients based on molar quantities:

$$b_i = \sum_{k=1}^{N_C} \frac{R_u}{W_k} Y_k a_{k,i}. \tag{2.9}$$

In case of ideal gas mixtures, the enthalpy is related to the specific heat, as:

$$\mathrm{d}H_k = C_{p,k}\mathrm{d}T, \tag{2.10}$$

where H_k is the molar specific enthalpy of species k. Thus, by integration, the NASA polynomials only have to be complemented with a reference enthalpy level to calculate the specific molar enthalpy as:

$$H_k = R_u \left(a_{k,6} + \sum_{i=1}^{5} \frac{a_{k,i}}{i} T^i \right), \tag{2.11}$$

where the additional coefficient $a_{k,6}$ provides this reference. The mass based counterpart of the specific enthalpy associated with a species is denoted as $h_k = \frac{H_k}{W_k}$. By a similar derivation as above, Eq. (2.9) is valid for this additional coefficient as well, thus the temperature dependence of the specific enthalpy $h = \sum_{k=1}^{N_C} Y_k h_k$ of a given gas mixture can be expressed directly as a function of the temperature as:

$$h = b_6 + \sum_{i=1}^{5} \frac{b_i}{i} T^i. \tag{2.12}$$

The temperature corresponding to a given enthalpy is easily found using the Newton–Raphson method as the derivative of the enthalpy h with respect to temperature is the specific heat itself. The process is descried in algorithm 2.1, where the tolerance $tol_H = 10^{-6}$ J/kg is used throughout this work. This ensures high accuracy, as the specific heat of the studied gas mixtures is $c_p = \mathcal{O}\left(1000\,\mathrm{J/kgK}\right)$, thus this value of tolerance represents an error in the temperature of $e_T = \mathcal{O}\left(10^{-9}\,\mathrm{K}\right)$.

The last detail that has to be mentioned about the NASA polynomials and their usage in this work is, that the usual way to cover a large range of temperatures is to have two set of coefficients for the polynomials corresponding to a high and a low temperature range, ensuring continuity for the enthalpy and the specific heat at the common boundary of the two temperature ranges. This intermediate temperature is most commonly set as 1000 K, however it might be different for some species.

Algorithm 2.1: Newton–Raphson method to calculate the temperature corresponding to the specific enthalpy (h). The variable e_H is the error between the currently estimated enthalpy (h^*) and the real enthalpy. The temperature is initialized to a reasonable value (T_0), and the loop is evaluated until the error is below a given tolerance tol_H.

$T = T_0$;
$e_H = 10^{10}$;
$tol_H = 10^{-6}$;
while $|e_H| > tol_H$ **do**
  Evaluate $c_p^* = c_p(T, b_i)$ as in Eq. (2.8);
  Evaluate $h^* = h(T, b_i)$ as in Eq. (2.12);
  $e_H = h^* - h$;
  $T = T - e_H / c_p^*$;

These differences are neglected in the weighted averaging of Eq. (2.9), as in this work the intermediate temperature is always kept as 1000 K where the precomputed coefficients b_i are used. However this introduces only a minimal error, as the main species are continuous at 1000 K. Lanzafame and Messina (2000) compared various specific heat functions with experimental data, including the NASA polynomials. While their work advocates for other c_p functions, they also show, that the error of the present method is quite limited.

The remaining 3 properties $(\mu, \lambda, \mathcal{D}_k)$ are transport properties related to the diffusion of conserved quantities. These are calculated the way commonly used in chemical kinetic software, e.g.: Chemkin (Kee et al., 1999), Chem1D (Somers, 1994), or Cantera (Goodwin, 2002). The properties of pure components are determined based on kinetic theory. Subsequently mixing laws are applied to determine the transport properties of the gas mixtures.

The dynamic viscosity μ_k, and the thermal conductivity λ_k of a pure species k are a function of the temperature only, they does not depend on pressure. The binary diffusion coefficients between species are inversely proportional to pressure, thus, using the ideal gas law, the pressure dependence is canceled for $\rho\mathcal{D}_{kj}$ for species k and j. (Kee et al., 1999) Note, that in many applications of the present study the unity Lewis number assumption is used, eliminating the problem of obtaining species diffusion coefficients, however this property is particularly important in the evaporation model introduced in chapter 4.

Finally, mixing laws are applied to obtain the mixture properties. The dynamic viscosity of a mixture is evaluated following Wilke (1950):

$$\mu = \sum_{k=1}^{N_C} \frac{X_k \mu_k}{\sum_{j=1}^{N_C} X_j \Phi_{kj}}, \tag{2.13}$$

where μ_k is the viscosity of pure component k evaluated at the mixture temperature, and the factor Φ_{kj} is:

$$\Phi_{kj} = \frac{1}{\sqrt{8}} \left(1 + \frac{W_k}{W_j}\right)^{-\frac{1}{2}} \left(1 + \left(\frac{\mu_k}{\mu_j}\right)^{\frac{1}{2}} \left(\frac{W_j}{W_k}\right)^{\frac{1}{4}}\right)^2. \tag{2.14}$$

To evaluate the mixture's thermal conductivity, a combination of arithmetic and harmonic averaging is used:

$$\lambda = \frac{1}{2}\left(\sum_{k=1}^{N_C} X_k \lambda_k + \frac{1}{\sum_{k=1}^{N_C} \frac{X_k}{\lambda_k}}\right), \tag{2.15}$$

where λ_k is the thermal conductivity of the pure component k evaluated at the mixture temperature. The so called *mixture-averaged* molar diffusion coefficient of species k is given by:

$$\mathcal{D}_k^{mol} = \frac{1 - Y_k}{\sum_{j=1, j\neq k}^{N_C} \frac{X_j}{\mathcal{D}_{kj}}} = \frac{\sum_{j=1, j\neq k}^{N_C} X_j W_j}{W \sum_{j=1, j\neq k}^{N_C} \frac{X_j}{\mathcal{D}_{kj}}}, \tag{2.16}$$

where $\mathcal{D}_{kj}$ is the binary diffusion coefficient of species k and j evaluated at the mixture temperature and pressure. Note, that the expression is undefined at $Y_k = 1$. In this case the limiting value is used: $\mathcal{D}_k^{mol}(Y_k = 1) = \lim_{Y_k \to 1} \mathcal{D}_k^{mol}$.

In the context of species diffusion, it is widely assumed, that a Fickian (Fick, 1855) diffusion law may be applied, neglecting the Soret and Dufour effects of interactions between diffusion of species and heat. (Poinsot and Veynante, 2005, §1.1.4) One such model is Hirschfelder's law (Hirschfelder et al., 1964), stating that the diffusion velocity of species k: $\mathbf{V}_k$ can be computed in a Fickian way, from the mole fraction gradients:

$$X_k \mathbf{V}_k = -\mathcal{D}_k^{mol} \nabla X_k. \tag{2.17}$$

Ebrahimian and Habchi (2011) points out, that if the calculations are based on mass fractions, then Hirschfelder's law may be rewritten, converting the mass fractions to mole fractions:

$$Y_k \mathbf{V}_k = -\mathcal{D}_k^{mol} \left(1 - X_k + Y_k \sum_{j=1, j\neq k} \frac{X_j}{Y_j}\right) \nabla Y_k. \tag{2.18}$$

In this case, the mixture-averaged *mass* diffusion coefficient may be defined as:

$$\mathcal{D}_k = \mathcal{D}_k^{mol} \left(1 - X_k + Y_k \sum_{j=1, j\neq k} \frac{X_j}{Y_j}\right). \tag{2.19}$$

For binary mixtures, the mass diffusion coefficient of both species is equal to their binary diffusion coefficient, since:

$$\mathcal{D}_1^{mol} = \frac{1 - Y_1}{X_2 / \mathcal{D}_{12}} = \frac{Y_2}{X_2} \mathcal{D}_{12}, \tag{2.20}$$

$$\begin{aligned} \mathcal{D}_1 &= \mathcal{D}_1^{mol} \left(1 - X_1 + Y_1 \frac{X_2}{Y_2}\right) = \mathcal{D}_1^{mol} \left(X_2 + Y_1 \frac{X_2}{Y_2}\right) \\ &= \mathcal{D}_1^{mol} \frac{X_2}{Y_2} (Y_2 + Y_1) = \mathcal{D}_1^{mol} \frac{X_2}{Y_2}. \end{aligned} \tag{2.21}$$

Note, that the diffusion velocities defined by Hirschfelder's law in Eq. (2.17) do not strictly impose mass conservation, which necessitates $\sum_{k=1}^{N_C} Y_k \mathbf{V}_k = 0$. Instead, a

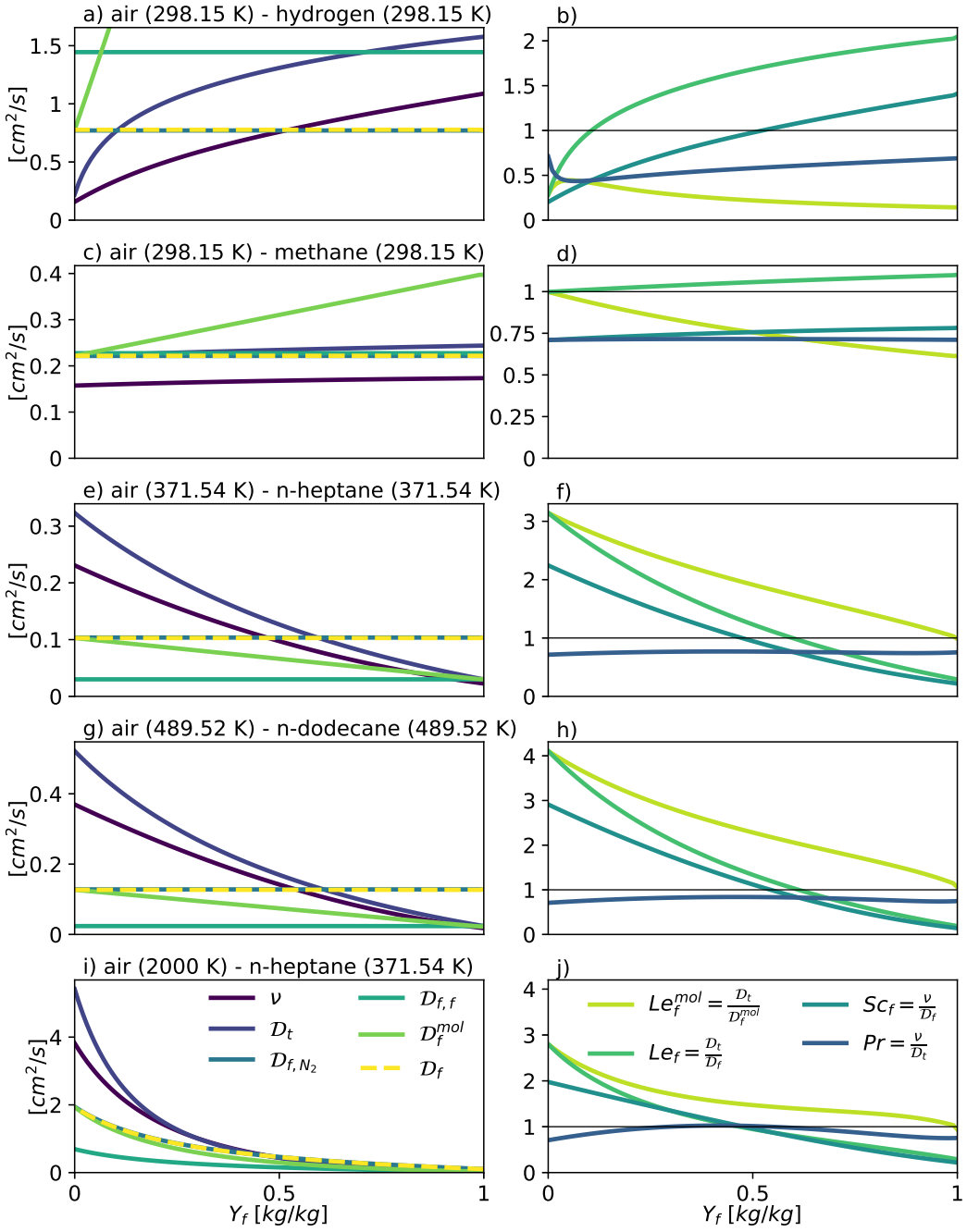

FIGURE 2.1: Transport properties in various air-fuel mixtures at atmospheric pressure as function of the fuel mass fraction. a,c,e,g,i): kinematic viscosity $\nu = \frac{\mu}{\rho}$, thermal diffusivity $\mathcal{D}_t = \frac{\lambda}{\rho c_p}$, binary diffusion coefficient of fuels with nitrogen gas $\mathcal{D}_{f,N_2}$, self diffusion coefficient of fuels $\mathcal{D}_{f,f}$, mixture-averaged molar diffusion coefficient of fuels according to Eq. (2.16) $\mathcal{D}_f^{mol}$, and mixture-averaged mass diffusion coefficient of fuels according to Eq. (2.19) $\mathcal{D}_f$; b,d,f,h,j): Lewis number of fuel Le_f^{mol} based on molar diffusion coefficient, Lewis number of fuel Le_f based on mass diffusion coefficient, Schmidt number of the fuel Sc_f, Prandtl number of the mixture Pr.

corrected diffusion velocity may be defined as:

$$\mathbf{V}_k = -\frac{\mathcal{D}_k}{Y_k}\nabla Y_k + \mathbf{V}^c, \tag{2.22}$$

where $\mathbf{V}^c = \sum_{k=1}^{N_C} \mathcal{D}_k \nabla Y_k$ is the correction velocity.

2.1.3 Example of mixture transport properties

Figure 2.1 illustrates the mixing laws of transport properties for various air-fuel mixtures, with the air modeled as a mixture of $X_{N_2} = 0.79$ and $X_{O_2} = 0.21$. Four fuels are presented corresponding to typical cases of interest: molecular hydrogen gas (H_2: a,b), methane (CH_4: c,d), n-heptane (C_7H_{16}: e,f,i,j), and n-dodecane ($C_{12}H_{26}$: g,h). The figure shows transport properties in the left column of plots, and non-dimensional numbers based on these transport properties in the right column of plots:

$$Pr = \frac{\nu}{\mathcal{D}_t}, \quad Sc_f = \frac{\nu}{\mathcal{D}_f}, \quad Le_f^{mol} = \frac{\mathcal{D}_t}{\mathcal{D}_f^{mol}}, \quad Le_f = \frac{\mathcal{D}_t}{\mathcal{D}_f}, \tag{2.23}$$

where Pr is the Prandtl number, Sc_f is the Schmidt number of the fuel, and Le_f^{mol} and Le_f are the Lewis numbers of the fuel based on the molar and mass diffusivity respectively. Here $\nu = \mu/\rho$ is the kinematic viscosity, while $\mathcal{D}_t = \lambda/\left(\rho c_p\right)$ is the thermal diffusivity of the mixture. Note the difference between the two definitions of the Lewis number. Some works, where the Lewis number is explicitly defined, use the one based on mass diffusivity: Le_k. (Ramaekers, 2011; Doost et al., 2015; Mukundakumar et al., 2021) However, in other cases the definition may be less meticulous. This difference makes little impact on flames of fuels and atmospheric air, since the flame is only sustainable in very dilute regions of the mixture. (See section 3.1.1.) Under such conditions, the molar and mass diffusivities are approximately equal, and so are the two Lewis numbers. The rigorous definition of the Lewis number is more important where significant fuel mass fractions are observed, such as in the spray combustion models presented in chapter 4 where the mass based Le_f is used.

Figures 2.1a-h show the constant temperature mixing of fuel and air. In case of hydrogen and methane, the mixture is at room temperature, while for the n-heptane and n-dodecane the temperature is chosen as the boiling point of the volatile fuels corresponding to cases of saturated fuel vapor mixing with air at the same temperature. The temperature dependence is illustrated only for n-heptane in Fig. 2.1i-j by considering n-heptane at its boiling point, and air at 2000 K.

The kinematic viscosity $\nu = \mu/\rho$ and the thermal diffusivity $\mathcal{D}_t = \lambda/\left(\rho c_p\right)$ show similar trends as a function of the fuel mass fraction since Wilke's rule for μ and the combination averaging for λ are comparable in these examples. As a result, the Prandtl number $Pr = \nu/\mathcal{D}_t$ varies only moderately as a function of the fuel mass fraction even when variations in temperature are considered. In general, light molecules like H_2 have higher transport rates than air, CH_4 is rather comparable to air, and the large hydrocarbons display much lower values.

The two shown binary diffusion coefficients ($\mathcal{D}_{f,N_2}$ and $\mathcal{D}_{f,f}$) are constant in the isothermal cases, since these are not a property of the mixture, and they only depend on temperature and pressure. In these examples the mixture-averaged mass diffusion coefficient ($\mathcal{D}_f$) is practically indistinguishable from the binary diffusion

coefficient of fuel and nitrogen ($\mathcal{D}_{f,N_2}$) due to the abundance of nitrogen and the similarity of diffusion in oxygen and nitrogen. (See Eq.(2.20) and Eq.(2.21).)

Furthermore, as also shown in Fig. 2.1, in the dilute limit ($Y_f \to 0$), the mass and molar diffusion coefficients are equal. The latter is a linear function of the fuel mass fraction in the isothermal cases, and its slope is controlled by the molar weight difference between the oxidizer and the fuel, i.e.: large positive slope for H_2, negative slopes for large hydrocarbons. While the former, as said before, follows closely the binary diffusion coefficient of the fuel and nitrogen, that is constant in isothermal cases. A Lewis number may be defined based on either the molar or mass diffusion coefficients. Subsequently in Chapter 4 the mass-based Lewis number $Le_f = \mathcal{D}_t/\mathcal{D}_f$ is used. An often overlooked detail in this context, is that below-unity Lewis numbers can be observed in rich mixtures of large hydrocarbons.

2.2 Identification of gas state

As discussed above, the material properties of a gas mixture are uniquely determined by its composition given by Y_k or X_k, and two additional state variables, such as pressure: P and enthalpy: h in accordance with Gibbs' law. In combustion applications the local gas composition varies in space and time due to mixing and reactions. Even though the full local composition determines the gas state, other useful variables may be derived that represent the gas phase in a simplified way. These quantities are applied, yielding a more intuitive characterization of the gas state, especially in the context of tabulated chemistry models.

Below, these properties are introduced and discussed in the context of characterizing a homogeneous gas mixture, while in sections 2.4 and 2.5 conservation equations are formulated for some of these quantities. Three distinct aspects of the mixture are studied:

1. the elemental composition
   (mixture fraction, equivalence ratio, excess air ratio),
2. the evolution of the chemical reactions (reaction progress),
3. and the thermal condition.

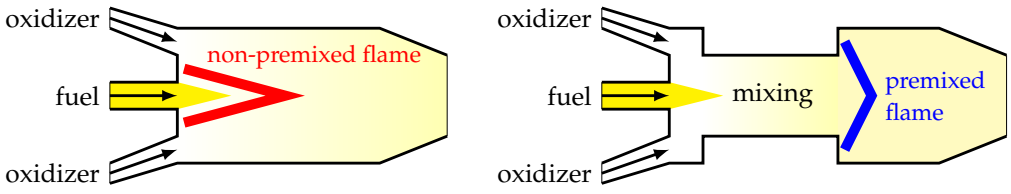

(A) Non-premixed combustion system.

(B) Premixed combustion system.

FIGURE 2.2: Illustration of non-premixed and premixed combustion of fuel and oxidizer streams.

2.2.1 Mixture fraction

Many combustion systems are characterized by the mixing of inlet streams of exactly two different kinds: oxidizer and fuel. As illustrated in Fig. 2.2, the material

originating from these two kind of inlets is mixed together, and they react with each other either simultaneously with the mixing (non-premixed combustion), or in a subsequent step (premixed combustion), or most often between these two extreme situations (partially premixed combustion). (Knudsen and Pitsch, 2010) The mixture fraction is a quantity describing this mixing process. The concept of distinguishing the two streams holds whether the oxidizer and fuel are in solid, liquid or gas phase. However, in this work, mixture fraction is used in only two contexts:

1. to describe the local *gas phase* composition,
2. to describe the global ratio of mass flow rates of fuel and oxidizer *irrespective* of the phase of inlets.

The former serves to characterize the mixture in a continuum approach, while the letter provides an understanding on the general behavior of the system. The global mixture fraction of a continuously operated combustion system at steady state is simply defined by the mass flow rates as:

$$Z_{glob} = \frac{\dot{m}_f}{\dot{m}_f + \dot{m}_{ox}}, \tag{2.24}$$

where $\dot{m}_f$ and $\dot{m}_{ox}$ are the inlet mass flow rates of fuel and oxidizer respectively.

Since reactions may occur while the two streams mix, it is not sufficient to know the local mass fractions of the fuel and oxidizer species to describe the progress of mixing. Bilger, Stårner, and Kee (1990) introduced a definition for a local mixture fraction, that is able to describe mixing despite the reactions. This quantity is based on the mass fractions of elements composing each stream. The basis of this metric is, that elements are not destroyed nor created by chemical reactions, thus knowing the local elemental composition one may calculate the fractions of oxidizer and fuel that results in the same elemental composition.

TABLE 2.1: Simple mixture fraction example.

	Mixture 1	Mixture 2
N_{H_2} [kmol]	0.5	0.3
N_{O_2} [kmol]	0.5	0.4
N_{H_2O} [kmol]	0.0	0.2
m_{H_2} [kg]	~ 1.0	~ 0.6
m_{O_2} [kg]	~ 16.0	~ 12.8
m_{H_2O} [kg]	0.0	~ 3.6
m_H [kg]	~ 1.0	$\sim 0.6 + 3.6\frac{2\ \frac{\text{kg}}{\text{kmol}}}{18\ \frac{\text{kg}}{\text{kmol}}} = 1.0$
m_O [kg]	~ 16.0	$\sim 12.8 + 3.6\frac{16\ \frac{\text{kg}}{\text{kmol}}}{18\ \frac{\text{kg}}{\text{kmol}}} = 16.0$

To provide a rudimentary example let us take a system of pure molecular hydrogen fuel and pure molecular oxygen oxidizer, which defines the two inlets. Furthermore, let us take two different mixtures defined in Tab. 2.1. Mixture 1 is an unreacted gas mixture of 0.5 kmol H_2 and 0.5 kmol O_2, while Mixture 2 originates from Mixture 1 after undergoing partial reaction. In the latter mixture 0.2 kmol of hydrogen,

and 0.1 kmol oxygen have reacted perfectly and formed 0.2 kmol of water. Approximating the molar weights of H and O as 1 kg/kmol and 16 kg/kmol respectively, Tab. 2.1 demonstrates, that the fresh Mixture 1 contains $\frac{1}{17}$ H_2 by mass, while the partially reacted Mixture 2 contains only $\frac{0.6}{17}$ H_2. Nevertheless, taking into account the hydrogen content of H_2O in the second mixture, both mixtures are composed of $\frac{1}{17}$ H atoms by mass. Thus, the elemental mass fraction reveals, that $\frac{1}{17}$ of the mass of both mixtures presented in Tab. 2.1 originates from the fuel stream. Note, that for the sake of this simple example the molar weights are rounded to the nearest integer.

Bilger's mixture fraction definition exploits this property of element conservation, and generalizes it for arbitrary hydrocarbon fuel and oxidizer. A given gas mixture is characterized by a factor defined as:

$$b = 2\frac{Z_C}{W_C} + 0.5\frac{Z_H}{W_H} - \frac{Z_O}{W_O}, \tag{2.25}$$

where Z_C, Z_H, and Z_O, and W_C, W_H, and W_O are the elemental mass fractions and molar weights off carbon, oxygen and hydrogen atoms in the gas mixture. Then a scaling is applied, to achieve a value bounded to the [0,1] interval, yielding the mixture fraction:

$$Z = \frac{b - b_o}{b_f - b_o}, \tag{2.26}$$

where b_o and b_f are evaluated at the conditions of pure oxidizer and fuel. If species k is represented by the generic molecular formula: $H_{\alpha_k}C_{\beta_k}N_{\gamma_k}O_{\delta_k}$, then the elemental mass fractions of this single species are constants depending on the species composition only:

$$Z_{C,k} = \frac{\beta_k W_C}{W_k}; \quad Z_{H,k} = \frac{\alpha_k W_H}{W_k}; \quad Z_{O,k} = \frac{\delta_k W_O}{W_k}, \tag{2.27}$$

where the species molecular mass is $W_k = \alpha_k W_H + \beta_k W_C + \gamma_k W_N + \delta_k W_O$. The elemental mass fractions of the gas mixture, are the weighted averages of species elemental mass fractions:

$$Z_C = \sum_{k=1}^{N_C} \frac{\beta_k W_C}{W_k} Y_k; \quad Z_H = \sum_{k=1}^{N_C} \frac{\alpha_k W_H}{W_k} Y_k; \quad Z_O = \sum_{k=1}^{N_C} \frac{\delta_k W_O}{W_k} Y_k, \tag{2.28}$$

thus the factor b can be expressed simply as a linear combination of the species mass fractions:

$$b = \sum_{k=1}^{N_C} \left(2\frac{\beta_k}{W_k} + 0.5\frac{\alpha_k}{W_k} - \frac{\delta_k}{W_k} \right) Y_k = \sum_{k=1}^{N_C} b_k Y_k, \tag{2.29}$$

where $b_k = 2\frac{\beta_k}{W_k} + 0.5\frac{\alpha_k}{W_k} - \frac{\delta_k}{W_k}$ is a constant, solely depending on the structure of species k. Thus the mixture fraction formula of Bilger may also be expressed as a linear combination of the species mass fractions with a shift corresponding to the stoichiometric mixture fraction $Z_{st} = -b_o / \left(b_f - b_o\right)$:

$$Z = Z_{st} + \frac{1}{b_f - b_o} \sum_{k=1}^{N_C} b_k Y_k = Z_{st} + \sum_{k=1}^{N_C} b_k^* Y_k, \tag{2.30}$$

with $b_k^* = \frac{b_k}{b_f - b_o}$ is a case dependent constant characterizing species k, that is only a function of the molecular composition of the oxidizer and fuel streams. The shifting value: Z_{st} is further detailed in Eq. (2.39).

Continuing the example of Tab. 2.1 the elemental mass fractions of fuel and oxidizer are trivial: with $Z_{H,f} = 1$ and $Z_{O,o} = 1$, and all other elemental mass fractions in the fuel and oxidizer being zero. Furthermore, the b_k values of individual species may be calculated: $b_{O_2} = -\frac{2}{32} = -\frac{1}{16}$, $b_{H_2} = 0.5\frac{2}{2} = 0.5$, and $b_{H_2O} = 0.5\frac{2}{18} - \frac{1}{18} = 0$. Thus the b values of the fuel and oxidizer based on Eq. (2.25) or Eq. (2.29) are: $b_f = 0.5$ and $b_o = -\frac{1}{16}$. The b values of both mixtures are: $b = 0.5\frac{1/17}{1} - \frac{16/17}{16} = -\frac{1}{34}$, thus applying the scaling gives a mixture fraction of: $Z = \frac{-1/34+1/16}{0.5+1/16} = \frac{1}{17}$, which is exactly the fraction of mass originating from the fuel stream.

The key difference between the non-premixed and premixed combustion modes illustrated on Fig. 2.2, is the location of the flame with relation of the location of mixing. In non-premixed combustion the flame is situated on the boundary of oxidizer and fuel streams, thus the chemical reactions take place across various mixture fractions. In premixed combustion the mixing is entirely completed prior to the flame front, hence the gas in the flame region is characterized by a single mixture fraction. The intermediate option: partially premixed combustion can arise for various reasons. Combustion systems that are intended to be premixed, but there is no sufficient room for the completion of mixing, are often called stratified or technically-premixed to express, that there are local variations in Z around Z_{glob} in the flame region, and they are not "perfectly-premixed". (Gövert et al., 2018) Another example is spray flames, where the liquid droplets act as localized moving sources of fuel, creating an non-homogeneous mixture. (Franzelli, Fiorina, and Darabiha, 2013) The aim of the local mixture fraction Z is exactly to create a property, that is insensitive to the flame location, thus allowing the separated characterization of mixing and chemical reactions.

2.2.2 Equivalence ratio and excess air ratio

The equivalence ratio (ϕ) and excess air ratio (λ) are different transformations of the mixture fraction, associating the level of mixedness with the chemistry. These quantities relate le mixture composition to the stoichiometric mixture, i.e.: the mixture in which exactly as many oxygen atoms are present, as it is required to fully oxidize all hydrogen, carbon, and other oxidizable elements in the mixture.

In this work, fuels and oxidizers are limited to mixtures containing only H, C, N, and O atoms, thus below only these 4 elements are considered. In a generic approach, both fuels and oxidizers may be described with an average molecular formula: $H_{\alpha_f}C_{\beta_f}N_{\gamma_f}O_{\delta_f}$ and $H_{\alpha_{ox}}C_{\beta_{ox}}N_{\gamma_{ox}}O_{\delta_{ox}}$ respectively, where α, β, γ, and δ are the weighted average number of atoms in the fuel and oxidizer molecules, in case of mixtures, weighted by the mole fraction of species. E.g. a mixture of 0.5 moles of O_2 and 0.5 moles of H_2O may be described as 1 mol of "$H_{1.0}O_{1.5}$".

In this context the molar stoichiometric mixture is found, by solving for X_f with the condition that the right hand side of the following global reaction equation shall

contain zero oxygen gas ($\theta = 0$):

$$X_f \cdot H_{\alpha_f} C_{\beta_f} N_{\gamma_f} O_{\delta_f} + (1 - X_f) \cdot H_{\alpha_{ox}} C_{\beta_{ox}} N_{\gamma_{ox}} O_{\delta_{ox}} \rightarrow \epsilon H_2O + \zeta CO_2 + \eta N_2 + \theta O_2, \tag{2.31}$$

$$\epsilon = \frac{X_f \alpha_f + (1 - X_f)\alpha_{ox}}{2}, \tag{2.32}$$

$$\zeta = X_f \beta_f + (1 - X_f)\beta_{ox}, \tag{2.33}$$

$$\eta = \frac{X_f \gamma_f + (1 - X_f)\gamma_{ox}}{2}, \tag{2.34}$$

$$\theta = \frac{X_f \delta_f + (1 - X_f)\delta_{ox}}{2} - \frac{\epsilon}{2} - \zeta, \tag{2.35}$$

$$\tag{2.36}$$

thus the stoichiometric mole fraction of fuel is:

$$X_{f,st} = \frac{-2\beta_{ox} - 0.5\alpha_{ox} + \delta_{ox}}{2(\beta_f - \beta_{ox}) + 0.5(\alpha_f - \alpha_{ox}) - (\delta_f - \delta_{ox})}. \tag{2.37}$$

Note the similarity between Eq. (2.25), and the terms of Eq. (2.37). Indeed, the elemental mass fractions may be expressed as: $Z_{H,f} = \frac{\alpha_f W_H}{W_f}$, etc., thus the b parameter of Bilger may be used for stoichiometry calculations directly as:

$$X_{f,st} = \frac{-b_o W_{ox}}{b_f W_f - b_o W_{ox}}, \tag{2.38}$$

where W_{ox} and W_f are the mean molar weights of fuel and oxidizer respectively. In the example of Tab. 2.1, the stoichiometric mole fraction of the H_2 fuel may be expressed according to Eq. (2.37): $X_{f,st} = \frac{-2\cdot 0 - 0.5\cdot 0 + 2}{2\cdot(0-0)+0.5\cdot(2-0)-(0-2)} = \frac{2}{3}$, or according to Eq. (2.38): $X_{f,st} = \frac{32/16}{2/2+32/16} = \frac{2}{3}$ demonstrating the equivalence. Converting to mass fractions, one may reach the stoichiometric mixture fraction:

$$Y_{f,st} = Z_{st} = \frac{W_f X_{f,st}}{W_f X_{f,st} + W_{ox}(1 - X_{f,st})} = \frac{-b_o}{b_f - b_o}. \tag{2.39}$$

Consequently, b is zero for a stoichiometric mixture. This holds even in systems of more that two different inlet streams, without a definition for b_o and b_f.

An open combustion system may be characterized by the global mixture fraction, calculated from the two inlet streams $\left(Z_{glob}\right)$, however a more practical metric is provided by simply relating the oxidizer mass flow to the fuel mass flow. This property is called the Air-Fuel Ratio $\left(AFR_{glob} = \frac{\dot{m}_{ox}}{\dot{m}_f}\right)$, as historically most combustion systems ingest atmospheric air. Two properties are related as:

$$Z_{glob} = \frac{1}{1 + AFR_{glob}}; \quad AFR_{glob} = \frac{1 - Z_{glob}}{Z_{glob}}. \tag{2.40}$$

The AFR may be extended to define the mixture locally, however its numerical treatment is problematic, as it diverges when the mixture approaches the pure oxidizer. The local value may be calculated as:

$$AFR = \frac{1 - Z}{Z} = -\frac{b - b_f}{b - b_o}, \tag{2.41}$$

while the stoichiometric air-fuel ratio can be simply related to the b parameters of oxidizer and fuel, since in the stoichiometric mixture b is zero:

$$AFR_{st} = \frac{-b_f}{b_o}, \tag{2.42}$$

A scaling of the air-fuel ratio with the stoichiometric value yields the equivalence ratio (ϕ) and excess air ratio (λ) as:

$$\phi = \frac{AFR_{st}}{AFR} = \frac{\frac{b}{b_o} - 1}{\frac{b}{b_f} - 1} = AFR_{st}\frac{Z}{1-Z}, \tag{2.43}$$

$$\lambda = \frac{AFR}{AFR_{st}} = \frac{\frac{b}{b_f} - 1}{\frac{b}{b_o} - 1}. \tag{2.44}$$

where both terms can be interpreted locally or globally as well. By definition both quantities are unity for a stoichiometric mixture. The former has a singularity approaching pure fuel, while the latter diverges at pure oxidizer, however they provide the advantage of instantly identifying rich (excess fuel, $\phi > 1$) and lean (excess oxidizer, $\phi < 1$) mixtures. The distinction of lean and rich conditions is useful for characterizing the mixing field and identifying which gas mixtures are likely to react, as too rich or too lean conditions may inhibit the reaction.

In the examples of Tab. 2.1, the stoichiometric air-fuel ratio is $AFR_{st} = \frac{-0.5}{-1/16} = 8$, while the AFR of the two examples is: $AFR = 16$, thus they correspond to a lean mixture with an equivalence ratio of $\phi = 0.5$ and an excess "air" ratio of $\lambda = 2$. The combustion systems studied in this work use atmospheric air as oxidizer. This increases the typical values of AFR_{st} compared to the above example, since air contains high amounts of N_2, consequently the b factor in air: $b_o \approx -0.0146\frac{kmol}{kg}$ is considerably low. The stoichiometric quantities of various fuels are presented in Tab. 2.2 for reference. The table contains four alkanes: methane (CH_4), n-heptane (C_7H_{16}), n-decane ($C_{10}H_{22}$), and n-deodecane ($C_{12}H_{26}$), furthermore molecular hydrogen (H_2) and an oxygenated fuel: dimethoxy-methane (OME1, $C_3H_8O_2$) are also presented that behave significantly different from the alkanes. (Pastor et al., 2020)

TABLE 2.2: Typical stoichiometric quantities of various fuels in atmospheric air.

	$b_f \left[\frac{\text{kmol}}{\text{kg}}\right]$	$AFR_{st} \left[\frac{\text{kg}_{\text{air}}}{\text{kg}_{\text{fuel}}}\right]$	$Z_{st} \left[\frac{\text{kg}_{\text{fuel}}}{\text{kg}_{\text{mixture}}}\right]$	$X_{f,st} \left[\frac{\text{kmol}_{\text{fuel}}}{\text{kmol}_{\text{mixture}}}\right]$
molecular hydrogen	~ 0.496	~ 34.1	~ 0.0285	~ 0.2958
methane	~ 0.249	~ 17.1	~ 0.0552	~ 0.0950
OME1	~ 0.105	~ 7.2	~ 0.1216	~ 0.0499
n-heptane	~ 0.220	~ 15.1	~ 0.0621	~ 0.0187
n-decane	~ 0.218	~ 15.0	~ 0.0626	~ 0.0134
n-dodecane	~ 0.217	~ 14.9	~ 0.0628	~ 0.0112

Concentrating first on the alkanes, their b_f factor decreases as the carbon chain becomes longer, and the fraction of hydrogen atoms within the molecule decreases. In fact, for alkanes of size β_f, the factor is $b_f = \frac{3\beta_f+1}{\beta_f(W_C+2W_H)+2W_H}$, which asymptotically approaches 0.214 $\frac{\text{kmol}}{\text{kg}}$ as the alkane's size increases. The stoichiometric air-fuel

ratio decreases linearly with b_f according to Eq. (2.42), while Z_{st} slightly increases. The stoichiometric mole fraction of fuel $X_{f,st}$, that also expresses the volume fraction of fuel in the mixture assuming ideal gases, decreases sharply with the increase of the alkane molecules according to Eq. (2.38), since b_f approaches a constant while W_f increases unbounded.

In comparison each mole of H_2 needs less air to fully oxidize, thus the stoichiometric mole fraction of fuel is significantly larger, approximately 3 times larger than in the case of methane. This high mole fraction corresponds to large volume fractions of molecular hydrogen, and high volume flow rates of fuel, that are recognized as one of the main sources of difficulties in hydrogen combustion. (Taamallah et al., 2015b) Because of the low density of hydrogen, this high volume fraction is hidden in the other mass based quantities of Tab. 2.2, that indicate a low mass fraction of H_2.

Finally, comparing the hydrocarbons to the oxygenated example: OME1, the b factor of the fuel is particularly low, since oxygen is readily present in the fuel. This availability of fuel-bound oxygen decreases the amount of air necessary for complete oxidation, thus the fraction of fuel in stoichiometric mixtures in considerably high both in terms of mass and volume.

2.2.3 Reaction progress

By definition, the quantities introduced above (Z, AFR, ϕ, λ) intentionally do not distinguish between unreacted and reacted mixtures. The two mixtures of Tab. 2.1 are identical in terms of mixture fraction, but mixture 2 is partially reacted. One may capture this feature by defining a progress variable that changes with the advancement of chemical reactions. This concept has been introduced for premixed combustion (Bray and Moss, 1977), where the mixture fraction is constant, and hence the reaction progress is the primary factor distinguishing between gas states. Subsequently, it has been extended to non-premixed combustion, where mixture fraction and reaction progress determine the state together. (Bilger, 1980) The progress variable is extensively used in various tabulated chemistry methods (Fiorina et al., 2003; Pierce and Moin, 2004; Pitsch and Ihme, 2005), and recently in the doubly conditional moment closure (DCMC). (Sitte, 2019) Various options are available for tracking the change from unburnt to burnt state. In the context of adiabatic lean perfectly-premixed combustion, a linear transformation of the temperature can assume this role. However in this work a more generally applicable concept is used. The progress variable Y_c is defined as a linear combination of various species mass fractions:

$$Y_c = \sum_{k=1}^{N_C} a_k Y_k, \tag{2.45}$$

where the a_k weights have to be different from the weights used in the mixture fraction: b_k, to yield a representation different form the mixture fraction. The selection of the a_k coefficients is crucial for creating a well defined progress variable. Typically a_k is only non-zero for the major products of the combustion (CO_2, H_2O) and other intermediate species that are present in relatively high mass fractions (CO, H_2). For example in Tab. 2.1, the water mass fraction is sufficient to distinguish between the two states, as $Y_c = Y_{H_2O}$ is 0 and $\frac{3.6}{17}$ for the two mixtures respectively.

The main dilemma is defining the coefficients such, that the level of mixedness

(Z, AFR, ϕ, or λ) and the progress variable can distinctly characterize any gas mixture occurring in the combustion system. This topic is further examined in section 3.2 in the context of tabulated chemistry.

2.2.4 Thermal state

Above some tools were introduced to distinguish different gas mixtures based on their elemental and species composition. Different thermal states introduce an additional degree of freedom, since a mixture characterized by a certain mixture fraction and an appropriately defined progress variable may exist at different temperatures.

Primarily the specific enthalpy h is used to distinguish different thermal states in the presented framework, as by definition h stays constant during adiabatic isobaric processes, such as the isobaric reaction of a homogeneous gas mixture. The interchangeability of specific enthalpy and temperature is managed through Eq. (2.12) and algorithm 2.1.

Since the specific enthalpy is conserved during the isobaric advancement of reactions, under adiabatic conditions it may be described as a function of the composition only. For example in case of combustion systems of two inlet streams, the enthalpy is a linear function of mixture fraction under the unity Lewis number assumption. (See section 2.4.) In such conditions, the enthalpy is redundant, and it can simply be calculated as:

$$h = h_{ad}(Z) = h_{ox} + (h_f - h_{ox})Z, \tag{2.46}$$

where h_{ox} and h_f are the enthalpy of oxidizer and fuel evaluated at the temperatures of the inlet streams.

In specific applications the present study departs from the adiabatic assumption for two possible reasons:

- heat exchange between the gas phase and the boundary walls,
- heat exchange between the gas phase and the liquid phase.

The flame-wall interactions are not examined exhaustively in this work, although the developed models are capable of capturing the wall heat loss effects, and this phenomenon is included in certain simulations. Furthermore, modeling the heat exchange between the gas and liquid phase is indispensable for the simulation of spray flames, as the latent heat of droplet evaporation has a significant effect on the gas phase. I.e.: a system of liquid fuel droplets immersed in a gas atmosphere at the same temperature is bound to cool down as the liquid droplets evaporate. In both of these cases the thermal state may be described by the enthalpy difference:

$$\Delta h = h - h_{ad}(Z). \tag{2.47}$$

where h_{ad} is given by Eq. (2.46). Assuming Δh is always negative, its magnitude $|\Delta h| = -\Delta h$ is the *enthalpy deficit*. The enthalpy associated with the fuel inlet h_f needs to be defined in case of spray flames. In the present work, h_f is fixed as the enthalpy of pure gaseous fuel at its boiling point. Note, that this is an arbitrary choice of reference point.

2.3 Low Mach number approximation of the Navier-Stokes equations

The Navier-Stokes equations describe the coupled mass and momentum conservation in a continuum fluid. Solving this non-linear system of partial differential equations poses a great challenge. In this work the low Mach number approximation, a modification of the PDE system, is used that enables higher computational performance, while it still resolves the key phenomena in the targeted combustion systems. Note, that acoustics, supersonic flows, and detonations, which would necessitate a different approach, are out of the scope of the present work.

2.3.1 Pressure treatment

The Mach number characterizing a problem is defined as the ratio of a velocity scale of the problem: u and the speed of sound: v_{sound} evaluated at characteristic thermochemical conditions of the problem:

$$Ma = \frac{u}{v_{sound}}, \tag{2.48}$$

where in general the speed of sound is:

$$v_{sound} = \sqrt{\left(\frac{\partial P}{\partial \rho}\right)_{|s}}, \tag{2.49}$$

and specifically for the ideal gases applied in this work $v_{sound} = \sqrt{\kappa \frac{R_u}{W} T}$, with the specific heat ratio of the gas: $\kappa = \frac{c_p}{c_v} = \frac{c_p}{c_p - R_u/W}$, where c_v is the isochoric specific heat. (Goodwin, Sangers, and Peters, 2010) Compressibility effects tend to become significant over a certain Mach number, the limit of $Ma < 0.3$ is a typical rule of thumb estimate. (Keshtiban, Belblidia, and Webster, 2004)

In the low Mach number limit, the compressible Navier-Stokes equations can be reformulated to decouple the thermochemical state of the flow from the momentum equation. This splitting technique removes the acoustic modes, thus the flow is forced to behave as incompressible in terms of pressure variations, however the density may change due to temperature and composition variations. This is realized by a decomposition of the pressure into a spatially homogeneous thermodynamic pressure P_0, and a hydrodynamic pressure p as:

$$P(x, y, z, t) = P_0(t) + p(x, y, z, t). \tag{2.50}$$

Only the hydrodynamic pressure p appears in the momentum equation, since the spatial gradients of the thermodynamic component are zero. As detailed in chapter 5, the hydrodynamic pressure is determined such, that a mass conserving velocity field arises in the numerical solution of the equations. Meanwhile, only the first term: the thermodynamic pressure, is retained in the equation of state of the material, which in this work is the ideal gas law (Eq. (2.5)):

$$\rho \approx \frac{P_0 W}{R_u T}. \tag{2.51}$$

Density variation due to temperature change are directly considered in this equation, while changes in the gas composition also affect the density through the mean

molecular mass: Eq. (2.1), the two effects together achieve the dilatation of the gas flow through reacting fronts. As Tab. 2.2 illustrates, in practical flames the mixture is predominantly composed by air ($AFR_{st} \gg 1$), thus within the flame W suffers only small variations, and the density is predominantly determined by the temperature. However, during the isothermal mixing of reactants local variations of ρ are induced by the varying molar mass in the different gas mixtures.

The decomposition of the pressure according to Eq. (2.50) and the substitution of the hydrodynamic pressure in the Navier-Stokes equations is always valid, since P_0 is defied as the spatial average of the pressure. The important change of the low Mach number approximation is calculating the gas density according to Eq. (2.51) instead of considering the total pressure. The density errors (e_ρ) introduced by this approximation are the same order of magnitude as the adiabatic stagnation density (Ames, 1953) in a compressible flow of ideal gas:

$$\frac{\rho + e_\rho}{\rho} = \mathcal{O}\left(\left[1 + \frac{\kappa - 1}{2} Ma^2\right]^{\frac{-1}{\kappa - 1}}\right). \tag{2.52}$$

In the limiting case of $Ma = 0.3$, with a representative specific heat ratio for diatomic gases of $\kappa = 1.3 \,..\, 1.4$, the density error can be approximated as 4.4%, and it drops sharply for lower Mach numbers. For example at $Ma = 0.1$, this error is only 0.5%.

In open domains, the thermodynamic pressure is taken as a constant, matching the total pressure of quiescent fluid in the simulated case. In many of the cases presented in this work, this means atmospheric pressure: $P_0 = 1$ atm $= 101325$ Pa. However, in closed domains or domains where all inlet and outlet mass flows are known the thermodynamic pressure is time dependent such, that global mass conservation is ensured. In the case of the ideal gas law, the temporal evolution of thermodynamic pressure is calculated as:

$$P_0(t) = \frac{MR_u}{\int_\Omega \frac{W}{T} \mathrm{d}V}, \tag{2.53}$$

where $\int_\Omega \mathrm{d}V$ signifies a volumetric integral in the domain, and M is the total gaseous mass contained in the domain. In case of closed domains, this is simply a constant, calculated from the initial mass: $M = M_{t_0} = \int_\Omega \rho \mathrm{d}V$. In case of known inlet and outlet flows, the total mass M is tracked in time with the initial condition given by M_{t_0} as: $M(t) = M_{t_0} + \int_{t_0}^{t} \sum \dot{m}_{in/out} \mathrm{d}t$, with $\sum \dot{m}_{in/out}$ being the net mas flow through the boundaries. (Avila, Principe, and Codina, 2011)

2.3.2 Conservation equations

Considering a gas phase flow in the low Mach number regime with variable composition, the problem consists of finding a velocity $\mathbf{u}$, a hydrodynamic pressure p, and a set of scalars ξ_k in domain Ω with boundary Γ for the time interval (t_0, t_f). In conservative form using the vector notation the PDE system is:

$$\partial_t \rho + \nabla \cdot (\rho \mathbf{u}) = S_\rho \qquad \text{on } \Omega \times (t_0, t_f), \tag{2.54}$$

$$\partial_t (\rho \mathbf{u}) + \nabla \cdot (\rho \mathbf{u} \otimes \mathbf{u}) + \nabla p - \nabla \cdot \boldsymbol{\tau}(\mathbf{u}) = S_\mathbf{u} \qquad \text{on } \Omega \times (t_0, t_f), \tag{2.55}$$

$$\partial_t (\rho \xi_k) + \nabla \cdot (\rho \xi_k \mathbf{u}) + \nabla \cdot \boldsymbol{\Phi}_k = S_k \qquad \text{on } \Omega \times (t_0, t_f), \tag{2.56}$$

where the operator: $\otimes$ marks the outer product, $\boldsymbol{\tau}(\mathbf{u}) = 2\mu\mathbf{S}^{\mathbf{D}}(\mathbf{u})$ is the viscous stress tensor with the strain rate tensor defined as: $\mathbf{S}(\mathbf{u}) = \frac{1}{2}\left(\nabla\mathbf{u} + \nabla^{\mathrm{T}}\mathbf{u}\right)$, and its deviatoric part as: $\mathbf{S}^{\mathbf{D}}(\mathbf{u}) = \frac{1}{2}\left(\nabla\mathbf{u} + \nabla^{\mathrm{T}}\mathbf{u}\right) - \frac{1}{3}(\nabla\cdot\mathbf{u})\mathbf{I}$. Note, that the Stokes assumption is used here, neglecting the bulk viscosity effects. (Kundu, Cohen, and Dowling, 2015, §4.5) The diffusive flux of scalar k is denoted: $\boldsymbol{\Phi}_k = -\rho\mathcal{D}_k\nabla\xi_k$. The right hand side of each equation contains a volumetric source term. The volumetric source of mass: S_ρ is zero for single phase flows, the one of momentum: $S_{\mathbf{u}}$ can represent body forces like gravity, and the one of the scalar equations: S_k is used for representing chemical reactions and other volumetric scalar sources. All of these source terms are used for modeling the effect of evaporating droplets as point-like sources, hence even S_ρ is retained here for generality.

The system is closed using the equation of state Eq. (2.51). The scalars ξ_k are such, that they uniquely define the temperature T, the molecular weight W, the dynamic viscosity μ, and the diffusivity $\mathcal{D}_k$, thus coupling the mass and momentum equations to this set of of scalar equations. The selection of transported scalars depends on the physics of the problem. One could transport the enthalpy h and the mass fractions of species Y_k, yielding the complete gas state. Another possibility, is to consider a reduced set of transported scalars, that is still suitable for identifying the gas state, such as the scalars introduced in section 2.2. The density only depends on this set of scalars and the thermodynamic pressure, and it is independent of the hydrodynamic pressure. Consequently, using the low Mach number approximation, the apparent speed of sound is infinity $\left(\frac{\partial p}{\partial\rho} \to \infty\right)$, and the acoustic coupling is removed. As a result, changes in the flow field in one part of the domain Ω are affecting other parts infinitely fast.

The problem has to be appended with appropriate initial and boundary conditions. The initial conditions are:

$$\mathbf{u} = \mathbf{u}_0, \quad \xi_k = \xi_{k,0} \qquad \text{on } \Omega \times \{t_0\} \tag{2.57}$$

and

$$P_0 = P_0^0 \qquad (\text{for closed systems}). \tag{2.58}$$

Dirichlet and Neumann boundary conditions are defined for the velocity $\mathbf{u}$ on $\Gamma_{\mathbf{u},D}$ and $\Gamma_{\mathbf{u},N}$, and for the k^{th} scalar ξ_k on $\Gamma_{\xi_k,D}$ and $\Gamma_{\xi_k,N}$ respectively. These subsets of the total boundary cover the total boundary without any intersection: $\Gamma_{\mathbf{u},D} \cup \Gamma_{\mathbf{u},N} = \Gamma$, $\Gamma_{\xi_k,D} \cup \Gamma_{\xi_k,N} = \Gamma$, $\Gamma_{\mathbf{u},D} \cap \Gamma_{\mathbf{u},N} = \emptyset$, and $\Gamma_{\xi_k,D} \cap \Gamma_{\xi_k,N} = \emptyset$. The boundary conditions are defined as:

$$\mathbf{u} = \mathbf{u}_D \qquad \text{on } \Gamma_{\mathbf{u},D} \times (t_0, t_f), \tag{2.59}$$

$$(-p\mathbf{I} + \boldsymbol{\tau}(\mathbf{u}))\cdot\mathbf{n} = 0 \qquad \text{on } \Gamma_{\mathbf{u},N} \times (t_0, t_f), \tag{2.60}$$

$$\xi_k = \xi_{k,D} \qquad \text{on } \Gamma_{\xi_k,D} \times (t_0, t_f), \tag{2.61}$$

$$\nabla\xi_k \cdot \mathbf{n} = 0 \qquad \text{on } \Gamma_{\xi_k,N} \times (t_0, t_f), \tag{2.62}$$

where $\mathbf{n}$ is the local normal vector of Γ.

Weak form

In the context of the finite element method, the PDE system shall be expressed in the weak form in place of the conservative form used above. (Lehmkuhl et al., 2019b) The following definitions are needed to obtain the weak form of the governing equations. $\mathbf{V}_D = \mathbf{H}_D^1(\Omega)$, $\mathbf{V}_0 = \mathbf{H}_0^1(\Omega)$, $Q = L^2(\Omega)/\Re$, $E_{D,k} = H_D^1(\Omega)$, and

$E_{0,k} = H_0^1(\Omega)$ are introduced, where $L^2(\Omega)$ is the square integrable function space. $H^1(\Omega)$ is a subspace of $L^2(\Omega)$, such that the derivatives of functions in $H^1(\Omega)$ are elements of $L^2(\Omega)$. Finally the 0 and D subscripts mark the subspace of $H^1(\Omega)$ that is constant 0 on the boundary Γ, or satisfy the Dirichlet conditions on boundary Γ respectively. $\mathbf{H}_0^1(\Omega)$ and $\mathbf{H}_D^1(\Omega)$ are their 2 or 3 dimensional vector counterparts. Parentheses are used to denote the L^2 inner product operator as: $(\mathbf{a}, \mathbf{b}) = \int_\Omega \mathbf{a} \cdot \mathbf{b} \mathrm{d}V$, where $\mathbf{a}$ and $\mathbf{b}$ are arbitrary vectors.

For temporally evolving problems, the above mentioned function spaces are extended with a temporal component: $\mathbf{V}_t \equiv L^2(t_0, t_f; \mathbf{V}_D)$, $Q_t \equiv \mathcal{D}'(t_0, t_f; Q)$, and $E_{t,k} \equiv L^2(t_0, t_f; E_{D,k})$, where $L^p(t_0, t_f; X)$ is the space of time dependent functions in a normed space X such that $\int_{t_0}^{t_f} \|f\|_X^p \, \mathrm{d}t < \infty$, $1 \leq p \leq \infty$, and Q_t consists of mappings whose Q-norm is a distribution in time.

The weak form of equations (2.54), (2.55), and (2.56) is defined as: find $\mathbf{u} \in \mathbf{V}_t$, $p \in Q_t$, and $\xi_k \in E_{t,k}$ such that:

$$(\partial_t \rho, q) + (\nabla \cdot (\rho \mathbf{u}), q) = (S_\rho, q), \tag{2.63}$$

$$(\mathcal{T}(\rho, \mathbf{u}), \mathbf{v}) + (C(\rho, \mathbf{u}), \mathbf{v}) - (P_0 + p, \nabla \cdot \mathbf{v}) + (\boldsymbol{\tau}(\mathbf{u}), \nabla \mathbf{v}) = (S_\mathbf{u}, \mathbf{v}), \tag{2.64}$$

$$(\partial_t (\rho \xi_k), \eta_k) + (\nabla \cdot (\rho \xi_k \mathbf{u}), \eta_k) + (\rho \mathcal{D}_k \nabla \xi_k, \nabla \eta_k) = (S_k, \eta_k), \tag{2.65}$$

for arbitrary test functions: $(q, \mathbf{v}, \eta_k) \in Q_0 \times \mathbf{V}_0 \times E_{0,k}$, where $\mathcal{T}(\rho, \mathbf{u})$ and $C(\rho, \mathbf{u})$ are the temporal and convective terms of the momentum equation. The weak form of expressing the conservation equations is directly used in chapter 5 in the context of the finite element discretization of the problem.

2.3.3 Conservation of higher moments

The partial differential equations of section 2.3.2 uniquely define the problem. However, it is possible to define various conservation laws, representing other physical quantities of interest. Below such equations are described.

Square of scalars

As demonstrated below, it is of interest to describe the transport of the square of scalars. Such equations are used for the description of the unresolved scales of scalar fields in large-eddy simulations as described in chapter 5. However, they can readily provide valuable insight on the behavior of fields. The derivation involves multiplying Eq. (2.56) by $2\xi_k$, and taking advantage of the continuity equation. The temporal term is transformed as:

$$\begin{aligned} 2\xi_k \partial_t (\rho \xi_k) &= \tfrac{1}{\rho} 2\rho \xi_k \partial_t (\rho \xi_k) = \tfrac{1}{\rho} \partial_t (\rho \xi_k)^2 = \tfrac{1}{\rho} \partial_t \left[\rho (\rho \xi_k^2)\right] \\ &= \tfrac{1}{\rho} \left[\rho \partial_t (\rho \xi_k^2) + \rho \xi_k^2 \partial_t \rho\right] = \partial_t (\rho \xi_k^2) + \xi_k^2 \partial_t \rho. \end{aligned} \tag{2.66}$$

Similar steps are taken to transform the convective term, yielding:

$$2\xi_k \nabla \cdot (\rho \xi_k \mathbf{u}) = \nabla \cdot (\rho \xi_k^2 \mathbf{u}) + \xi_k^2 \nabla \cdot (\rho \mathbf{u}). \tag{2.67}$$

Finally, the diffusive term is treated as:

$$\begin{aligned} 2\xi_k \nabla \cdot \boldsymbol{\Phi}_k &= -2\xi_k \nabla \cdot (\rho \mathcal{D}_k \nabla \xi_k) = -\nabla \cdot (2\xi_k \rho \mathcal{D}_k \nabla \xi_k) + 2\rho \mathcal{D}_k \nabla \xi_k \cdot \nabla \xi_k \\ &= -\nabla \cdot (\rho \mathcal{D}_k \nabla \xi_k^2) + 2\rho \mathcal{D}_k \nabla \xi_k \cdot \nabla \xi_k = \nabla \cdot \boldsymbol{\Phi}_{k^2} + \rho \chi_{\xi_k}, \end{aligned} \tag{2.68}$$

where $\mathbf{\Phi}_{k^2} = -\rho \mathcal{D}_k \nabla \xi_k^2$ is the diffusive flux of ξ_k^2, and $\chi_{\xi_k} = 2\mathcal{D}_k \nabla \xi_k \cdot \nabla \xi_k$ is the scalar dissipation rate of ξ_k. Thus, by using the continuity equation, the transport equation of ξ_k^2 takes the form:

$$\partial_t \left(\rho \xi_k^2\right) + \nabla \cdot \left(\rho \xi_k^2 \mathbf{u}\right) + \nabla \cdot \mathbf{\Phi}_{k^2} = \underbrace{2\xi_k S_k}_{\text{I}} \underbrace{-\rho \chi_{\xi_k}}_{\text{II}} \underbrace{-\xi_k^2 S_\rho}_{\text{III}}. \tag{2.69}$$

The three terms on the right hand side of Eq. (2.69) shows, that I: ξ_k^2 is generated together with ξ_k, II: it is dissipated in the presence of ξ_k gradients, and III: it is "diluted" if volumetric mass source terms are present. (Pera et al., 2006)

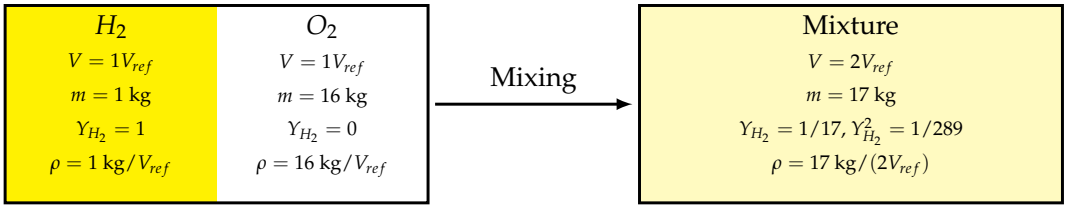

FIGURE 2.3: Mixing of two reactants of Mixture 1 of Tab. 2.1.

The scalar dissipation rate χ_{ξ_k} is always non-negative as only non-negative diffusivities are physical, and the magnitude of $\nabla \xi_k$ is non-negative as well. Consequently, in the absence of source terms, the right hand side of Eq. (2.69) is strictly non-positive. I.e.: the square of the scalar unknowns is bound to decrease if they are mixed on the molecular level. To illustrate this dissipation, take 1 kmol of Mixture 1 of Tab. 2.1. Assume further, that at the initial state of this system, the hydrogen and oxygen are completely separated. The mixing process is illustrated in Fig. 2.3. The density weighted integral of $Y_{H_2}^2$: $\int_\Omega \rho Y_{H_2}^2 \mathrm{d}V$ in the two states of Fig. 2.3 are: 1 kg before the mixing, and $1/17$ kg after the mixing. The rate of this transition is governed by Eq. (2.69), which gives the following relation in a closed domain without volumetric source terms:

$$\int_\Omega \partial_t \left(\rho \xi_k^2\right) \mathrm{d}V = \frac{\mathrm{d}}{\mathrm{d}t} \int_\Omega \rho \xi_k^2 \mathrm{d}V = -\int_\Omega \rho \chi_{\xi_k} \mathrm{d}V. \tag{2.70}$$

This is consistent with the mixing time scale estimate: $\tau_m = \frac{\xi_k^2}{\chi_{\xi_k}}$ of Ihme and Pitsch (2008a), where it is assumed, that the local values of ξ_k and χ_{ξ_k} evaluated at a relevant point provide a good measure for the mixing time scale.

An interesting side note is, that similar concepts arise in the analysis of numerical discretization schemes, where ξ_k^2 is identified as a suitable *entropy function* of ξ_k, since it is bound to have a non-positive volumetric source term. (Guermond, Pasquetti, and Popov, 2011; Lehmkuhl et al., 2019a) This aspect is then utilized, to identify the minimum necessary numerical diffusion, that results in the correct $\frac{\mathrm{d}}{\mathrm{d}t} \int_\Omega \rho \xi_k^2 \mathrm{d}V \leq 0$ behavior. This constraint corresponds to not producing spurious numerical oscillations that would increase the integral of $\rho \xi_k^2$.

Kinetic energy

The above analysis is executed for a transported scalar field, however a similar derivation can be executed for the momentum equation, yielding the governing equation of specific kinetic energy: $e_K = \frac{1}{2}\mathbf{u} \cdot \mathbf{u} = \frac{1}{2}|\mathbf{u}|^2$. This is done, by taking

the scalar product of $\mathbf{u}$ and Eq. (2.55). The transport equation of kinetic energy (Kuo, 1986, §3.6) takes the form:

$$\partial_t \left(\rho e_K\right) + \nabla \cdot \left(\rho e_K \mathbf{u}\right) = \underbrace{\mathbf{u} \cdot S_{\mathbf{u}}}_{\text{I}} \underbrace{-\mathbf{u} \cdot \nabla p}_{\text{II}} \underbrace{+\mathbf{u} \cdot \nabla \cdot \boldsymbol{\tau}\left(\mathbf{u}\right)}_{\text{III}} \underbrace{-e_K S_\rho}_{\text{IV}}, \tag{2.71}$$

where the right had side terms are: I: rate of work of volumetric forces, II: rate of work of pressure forces, III: rate of work of viscous forces, and IV: dilution of kinetic energy due to mass sources. Similarly to Eq. (2.68), it is possible to rearrange the pressure and viscous terms (II and III) into terms, that redistribute the kinetic energy, and terms that act as volumetric sources:

$$\mathbf{u} \cdot \nabla p = \nabla \cdot \left(p\mathbf{u}\right) - P \nabla \cdot \mathbf{u}, \tag{2.72}$$

$$\mathbf{u} \cdot \nabla \cdot \boldsymbol{\tau}\left(\mathbf{u}\right) = \nabla \cdot \left(\mathbf{u} \cdot \boldsymbol{\tau}\left(\mathbf{u}\right)\right) - \nabla \mathbf{u} : \boldsymbol{\tau}\left(\mathbf{u}\right). \tag{2.73}$$

Note, that the complete pressure: P is used in the rearrangement of the pressure term, since in the momentum equation (Eq. (2.55)) the thermodynamic component is only absent because P_0 is homogeneous in space. Since $\boldsymbol{\tau}\left(\mathbf{u}\right)$ is symmetric, the last term of Eq. 2.73 can be taken using only the symmetric part of the velocity gradient, which is the strain rate tensor: $\nabla \mathbf{u} : \boldsymbol{\tau}\left(\mathbf{u}\right) = \mathbf{S} : \boldsymbol{\tau}\left(\mathbf{u}\right)$. (Kundu, Cohen, and Dowling, 2015, §4.8) Consequently, the kinetic energy equation may be written as:

$$\partial_t \left(\rho e_K\right) + \nabla \cdot \left(\rho e_K \mathbf{u}\right) + \nabla \cdot \left(p\mathbf{u}\right) - \nabla \cdot \left(\mathbf{u} \cdot \boldsymbol{\tau}\left(\mathbf{u}\right)\right) = \mathbf{u} \cdot S_{\mathbf{u}} + P \nabla \cdot \mathbf{u} \underbrace{-\mathbf{S} : \boldsymbol{\tau}\left(\mathbf{u}\right)}_{-\rho\varepsilon^{tot}} - e_K S_\rho, \tag{2.74}$$

where the terms on the right hand side may produce or dissipate kinetic energy. The total kinetic energy dissipation rate due to viscous forces is denoted as:

$$\varepsilon^{tot} = \frac{1}{\rho} \mathbf{S} : \boldsymbol{\tau}\left(\mathbf{u}\right), \tag{2.75}$$

with the ":" operator marking the double inner product. The term: $P \nabla \cdot \mathbf{u}$ corresponds to kinetic energy sources due to the dilation of the flow. This is an important kinetic energy production mechanism in combustion systems, since $\nabla \cdot \mathbf{u}$ is typically positive in the reaction fronts due to thermal dilatation. Similarly to the ξ_k^2 equation, the kinetic energy equation is used in chapter 5 in the context of large-eddy simulation, in the analysis of unresolved scales.

2.4 Energy transport

As mentioned in section 2.3, the resolved scalars (ξ_k) together with the thermodynamic pressure must uniquely determine the material properties necessary for the closure of the PDE system: T, W, μ, $\mathcal{D}_k$, and indirectly ρ. Here possible candidates are described that express energy conservation, solving part of this closure problem.

As introduced in section 2.2, the thermal state of the modeled gas mixtures may be described with an adiabatic approach, where there is no heat transfer between the gas phase domain and other entities. Otherwise the local thermal state of the gas mixture is given by either using the temperature or the specific enthalpy. Using these quantities, one can represent the heat transfer effects within the domain and between the gas phase domain and other objects. Overall, in this work the energy

conservation is described in three different ways, which are listed below in order of decreasing complexity:

1. using a governing equation for enthalpy,
2. formulating a governing equation in terms of temperature for constant composition flows,
3. not using a dedicated PDE by assuming adiabatic conditions.

Note, that the thermal effects of viscous kinetic energy dissipation are neglected on the basis, that these scale with the Mach number as $\propto Ma^2$, thus they are negligible in the low Mach number regime. (Ventosa-Molina et al., 2017) Furthermore, the work of body forces (gravity) is also neglected in the energy conservation.

2.4.1 Enthalpy equation

The first and most generic alternative is formulating a PDE for the specific enthalpy $h = \sum_{k=1}^{N_C} Y_k h_k$. Since advection affects all species equally, the temporal and advective terms may be written in terms of h, considering the enthalpy of the mixture directly. Furthermore, the specific enthalpy has a source term associated to the work of changing thermodynamic pressure. Thus the governing equation can be formulated as:

$$\partial_t (\rho h) + \nabla \cdot (\rho h \mathbf{u}) + \nabla \cdot \mathbf{\Phi}_h = \frac{\mathrm{d}P_0}{\mathrm{d}t} + S_h^e, \tag{2.76}$$

where $\frac{\mathrm{d}P_0}{\mathrm{d}t}$ is the work of thermodynamic pressure changes per unit volume, and S_h^e marks the enthalpy source term associated with evaporation of sprays further discussed in section 5.5.3, thus the overall source term of this equation is: $S_h = \frac{\mathrm{d}P_0}{\mathrm{d}t} + S_h^e$.

The net diffusive enthalpy flux $\mathbf{\Phi}_h$ is a complex expression, since different species may have different mass diffusivities and thus diffuse at different rates, as discussed in section 2.1. In general the net diffusive enthalpy flux is the sum of diffusive transport due to enthalpy gradients of a specific species (∇h_k) associated with temperature gradients, and diffusive transport due to species diffusion (∇Y_k) where different species being characterized by different enthalpies. The net diffusive enthalpy flux may be formulated as:

$$\mathbf{\Phi}_h = \rho \sum_{k=1}^{N_C} \left(-\mathcal{D}_t Y_k \nabla h_k + h_k Y_k \mathbf{V}_k \right), \tag{2.77}$$

where the enthalpy variation of a single species is diffused using the thermal diffusivity $\mathcal{D}_t$, while species are diffused according to Eq. (2.18) or Eq. (2.22) using the diffusion velocity $\mathbf{V}_k$. This flux simultaneously captures enthalpy transfer due to temperature differences, and due to species transport. Note, that the Dufour effect is neglected. By applying the chain rule to the enthalpy gradient: $\nabla h_k = c_{p,k} \nabla T$, the diffusion flux may be written in its usual form:

$$\mathbf{\Phi}_h = \rho \sum_{k=1}^{N_C} \left(-\mathcal{D}_t Y_k c_{p,k} \nabla T + h_k Y_k \mathbf{V}_k \right), \tag{2.78}$$

$$= -\rho \mathcal{D}_t \sum_{k=1}^{N_C} \left(Y_k c_{p,k} \right) \nabla T + \rho \sum_{k=1}^{N_C} h_k Y_k \mathbf{V}_k = -\lambda \nabla T + \rho \sum_{k=1}^{N_C} h_k Y_k \mathbf{V}_k. \tag{2.79}$$

As mentioned in section 2.1.2, the gas phase species transport is primarily treated using the unity Lewis number assumption. In this case the mass diffusivity of the species is approximated as the thermal diffusivity $\left(\mathcal{D}_k = \mathcal{D}_t = \frac{\lambda}{\rho c_p}\right)$, and the species diffusion can be expressed as: $Y_k \mathbf{V}_k = -\mathcal{D}_t \nabla Y_k$. Consequently, the net diffusive enthalpy flux of Eq. (2.77) simplifies to:

$$\mathbf{\Phi}_h^{Le=1} = -\rho \mathcal{D}_t \sum_{k=1}^{N_C} \nabla \left(Y_k h_k\right) = -\rho \mathcal{D}_t \nabla \left(\sum_{k=1}^{N_C} Y_k h_k \right) = -\rho \mathcal{D}_t \nabla h, \tag{2.80}$$

and the enthalpy equation takes the form:

$$\partial_t \left(\rho h\right) + \nabla \cdot \left(\rho h \mathbf{u}\right) - \nabla \cdot \left(\rho \mathcal{D}_t \nabla h\right) = \frac{\mathrm{d}P_0}{\mathrm{d}t} + S_h^e. \tag{2.81}$$

While many formulations of the energy conservation are theoretically correct, selecting a specific treatment is governed by the pragmatic reasons. For instance, one may formulate an energy conservation equation based on temperature as well for reacting flows, however the chemical heat release can be hard to manage numerically. The conservation equation of specific enthalpy is significantly easier to handle, as it has no volumetric source term in case of open domains, and in the absence of Lagrangian spray models. And it is even simpler in the case of the unity Lewis number assumption, since the equation is closed by simply obtaining the density and thermal diffusivity based on the gas state, without the evaluation of the temperature or species mass fraction gradients.

2.4.2 Temperature equation

In the present work, in case of constant mixture composition, the enthalpy is a simple polynomial function of the temperature, in accordance with Eq. (2.12). One may formulate a simple transport equation of the temperature directly, and avoid the potentially costly evaluation of algorithm 2.1. This form can be easily achieved based on Eq. (2.76), since in case of constant composition the partial derivatives of mass fractions are zero $\nabla Y_k = 0$, and the partial derivatives of the specific enthalpy may be expressed using the definition of the specific heat as $\partial h_k = c_{p,k} \partial T$. Furthermore, the mass conservation (Eq. (2.54)) is used, to transform the advective and temporal terms into the non-conservative form:

$$\begin{aligned} \partial_t \left(\rho h\right) + \nabla \cdot \left(\rho h \mathbf{u}\right) &= h \partial_t \rho + \rho \partial_t h + \rho \mathbf{u} \nabla \cdot h + h \nabla \cdot \left(\rho \mathbf{u}\right) && (2.82) \\ &= \rho \partial_t h + \rho \mathbf{u} \nabla \cdot h + h S_\rho. && (2.83) \end{aligned}$$

where the last term is a consequence of the non-conservative formulation, and it is disregarded hereafter, since the consideration of evaporating sprays is generally inconsistent with the assumption of constant composition applied here. Thus the left hand side of the enthalpy equation, at constant composition and without mass source terms, can be transformed as:

$$\begin{aligned} \partial_t \left(\rho h\right) + \nabla \cdot \left(\rho h \mathbf{u}\right) + \nabla \cdot \mathbf{\Phi}_h &= \rho \partial_t h + \rho \mathbf{u} \nabla \cdot h + \nabla \cdot \left(-\lambda \nabla T\right), && (2.84) \\ &= c_p \rho \partial_t T + c_p \rho \mathbf{u} \nabla \cdot T + \nabla \cdot \left(-\lambda \nabla T\right). && (2.85) \end{aligned}$$

So, for constant composition flows, energy conservation may be expressed using the temperature as:

$$c_p \rho \partial_t T + c_p \rho \mathbf{u} \cdot \nabla T - \nabla \cdot (\lambda \nabla T) = \frac{\mathrm{d}P_0}{\mathrm{d}t}, \tag{2.86}$$

which is as simplistic as the enthalpy equation under the unity Lewis number assumption, with the added benefit of yielding the temperature directly, thus the evaluation of algorithm 2.1 is avoided.

2.4.3 Adiabatic flows

One may formulate a transport equation for mixture fraction Z similar to the PDE of h in Eq. (2.76), since the mixture fraction can be expressed as a weighted average using the species mass fractions as in Eq. (2.30). The diffusive mixture fraction flux can be defined analogously to the flux of enthalpy as: $\mathbf{\Phi}_Z = -\rho \sum_{k=1}^{N_C} \left(\mathcal{D}_k b_k^* \nabla Y_k \right)$. Further details are given in section 2.5.3, but for the sake of the adiabatic treatment of the energy conservation, it is enough to know, that this diffusive flux simplifies in the same way as the enthalpy flux in Eq. (2.80) for $Le = 1$:

$$\mathbf{\Phi}_Z^{Le=1} = -\rho \mathcal{D}_t \sum_{k=1}^{N_C} \left(b_k^* \nabla Y_k \right) = -\rho \mathcal{D}_t \left(\nabla \sum_{k=1}^{N_C} b_k^* Y_k \right) = -\rho \mathcal{D}_t \nabla Z. \tag{2.87}$$

Thus under the unity Lewis number assumption, the transport equations of enthalpy (Eq. (2.81)) and that of mixture fraction are analogous, if they are characterized by analogous Dirichlet and Neumann boundary conditions, and the source terms are zero. Under these conditions there is a linear relationship between the two quantities:

$$h = h_{ox} + (h_f - h_{ox}) Z, \tag{2.88}$$

where h_{ox} is the value of the Dirichlet boundary conditions of enthalpy on the boundaries where $Z = 0$, and h_f is the corresponding boundary condition for $Z = 1$. The relationship only holds if $\Gamma_{h,D} = \Gamma_{Z,D}$ and $\Gamma_{h,N} = \Gamma_{Z,N}$, i.e.: there are no boundaries where mixture fraction is characterized by a zero gradient boundary condition and enthalpy by a fixed value. The physical meaning of such an initial and boundary condition problem is a system without heat transfer through the walls (adiabatic) and with only two kinds of inlet not just in terms of composition, but also in terms of thermal state.

2.5 Species transport

Knowing the thermal state and the thermodynamic pressure is not enough to find a closure for the material properties: T, W, μ, D_k, and ρ. The set of scalars ξ_k shall also include information on the composition of the gas mixture, so the local gas state based on (h, P, Y_k) or (T, P, Y_k) may be fully determined. Partial differential equations may be defined to capture different aspects of gas composition Y_k.

2.5.1 Chemical reactions

The number of chemical species involved in the oxidation process of a complex hydrocarbon fuel is very high, since a chemical species is a unique arrangement of

atoms connected with chemical bonds, and in the case of carbon these arrangements may become arbitrarily complex. Nevertheless, considering a limited set of species is sufficient to model the reacting gas mixture with a high accuracy, thus the number of modeled species N_C is finite. (Law, 2007) This model is the *chemical mechanism*, that defines the set of species involved in the characterization of the reacting mixture, and it also defines the chemical reactions that transform *reactant* species into *product* species. The mechanism has to be accompanied with thermodynamic and transport constants for each of the species, allowing for the description of the material properties as in section 2.1.

In this work, detailed and skeletal chemical mechanisms are used, which contain a set of chemical reactions. The reactions can be loosely classified as elementary reactions, that involves the collision of two reactants, and three-body reactions, that involve the simultaneous collision of two reactants and a third molecule that only participates in the kinetic energy exchange but its structure stays unchanged. An example of elementary reactions is the reaction between an oxygen radical and a hydrogen molecule forming a hydrogen radical and a hydroxyl radical: $O + H_2 \rightarrow H + OH$, while three-body reactions may be illustrated by the reaction combining oxygen and hydrogen radicals into hydroxyl radical in the presence of a third molecule: $O + H + M \rightarrow OH + M$, where M may be any other species of the gas mixture. The importance of this third body may vary depending on its abundance, that is predominantly controlled by the pressure of the system. A sub-class of the three-body reactions, the fall-off reactions, behaves as third body reactions at low pressures, where the low availability of a third reaction partner is a limiting factor, but it behaves as an elementary reaction at high pressure where third-bodies are abundant. The simultaneous collision of more than three molecules in an ideal gas is highly improbable, thus there are no reactions describing such events. (Kuo, 1986, §2.2)

Such simple reactions represent the actual processes happening in chemically reacting flows, opposed to global reactions such as the generic form of Eq. (2.31), that is used in stoichiometric calculations. The elementary and three-body reactions may be expressed in a generic form:

$$\sum_{k=1}^{N_C} \nu_{rk}^{(r)} A_k \,(+M) \xrightarrow{k_r} \sum_{k=1}^{N_C} \nu_{rk}^{(p)} A_k \,(+M) \tag{2.89}$$

where, $\nu_{rk}^{(r)}$ and $\nu_{rk}^{(p)}$ are the stoichiometric coefficients of species k on the reactant and product side respectively in reaction r . Furthermore k_r is the rate constant of this reaction r and A_k stand for species k. E.g.: in the above simple example of the elementary reactions, $\nu_{rO}^{(r)} = 1$, $\nu_{rH_2}^{(r)} = 1$, $\nu_{rH}^{(p)} = 1$, and $\nu_{rOH}^{(p)} = 1$, and all other coefficients of any other species is zero. Note, that in case of elementary reactions, the stoichiometric coefficients may be zero, one, or two, the latter corresponding to reactions involving two molecules of the same species in the reactant or product side.

The reactions defined by the mechanism must conserve the elements on the reactant and product side, thus the involved species cannot be arbitrary. The stoichiometric coefficients $\nu_{rk}^{(r)}$ and $\nu_{rk}^{(p)}$ are such, that, for a species k represented by the

generic molecular formula: $H_{\alpha_k} C_{\beta_k} N_{\gamma_k} O_{\delta_k}$, the following holds:

$$\sum_{k=1}^{N_C} \alpha_k \nu_{rk}^{(r)} = \sum_{k=1}^{N_C} \alpha_k \nu_{rk}^{(p)}; \qquad \sum_{k=1}^{N_C} \beta_k \nu_{rk}^{(r)} = \sum_{k=1}^{N_C} \beta_k \nu_{rk}^{(p)}; \tag{2.90}$$

$$\sum_{k=1}^{N_C} \gamma_k \nu_{rk}^{(r)} = \sum_{k=1}^{N_C} \gamma_k \nu_{rk}^{(p)}; \qquad \sum_{k=1}^{N_C} \delta_k \nu_{rk}^{(r)} = \sum_{k=1}^{N_C} \delta_k \nu_{rk}^{(p)}. \tag{2.91}$$

The goal of the reaction mechanism is to determine the rate at which the defined reactions occur. Continuing the simple example of the elementary reaction: $O + H_2 \rightarrow H + OH$, according to the kinetic theory of gases, the rate of this reaction depends on two factors: the probability of collision of an O radical with an H_2 molecule, and the probability that these molecules carry sufficient kinetic energy to break the initial energy barrier. (Kuo, 1986, §2.1) The former probability is proportional to the product of the species concentrations: $C_O C_{H_2}$, while the latter may be inferred from the Maxwell–Boltzmann distribution (Rowlinson, 2005) that gives the probability of a certain molecule being characterized by a given kinetic energy. In case of the example, the rate of change of the concentration of the involved species due to the occurrence of this one reaction r is:

$$\left(\frac{\partial C_O}{\partial t}\right)_r = -1 \cdot k_r C_O C_{H_2}; \qquad \left(\frac{\partial C_{H_2}}{\partial t}\right)_r = -1 \cdot k_r C_O C_{H_2};$$

$$\left(\frac{\partial C_H}{\partial t}\right)_r = 1 \cdot k_r C_O C_{H_2}; \qquad \left(\frac{\partial C_{OH}}{\partial t}\right)_r = 1 \cdot k_r C_O C_{H_2},$$

where the reaction rate constant k_r is independent of the concentrations, and it expresses the probability that O and H_2 are having sufficient kinetic energy to facilitate the reaction. A generalization of the net rates of elementary reactions can be expressed as:

$$\left(\frac{\partial C_k}{\partial t}\right)_r = k_r \left(\nu_{rk}^{(p)} - \nu_{rk}^{(r)}\right) \prod_{i=1}^{N_C} C_i^{\nu_{ri}^{(r)}}. \tag{2.92}$$

The calculation of reaction rate is slightly different in case of three-body reactions, where the probability of collision is not only influenced by the availability of the reactants, but also by the availability of the third molecule that participates in the collision. In the example three-body reaction, the probability of this collision taking place is proportional to the concentration of the reactants: $C_O C_H$, but also proportional to the concentration of all available third-body candidates: $C = \sum_{i=1}^{N_C} C_i$. Furthermore, different third-bodies may have different effects on the reaction, as they are characterized by different mass, thus the total pool of possible third-body candidates is usually expressed as a modified concentration depending on reaction r: $C_{M,r} = \sum_{i=1}^{N_C} \epsilon_{i,r} C_i$, where $\epsilon_{i,r}$ is the so called collision efficiency of species i in the context of reaction r. (Jasper, Oana, and Miller, 2015) Thus the reaction rate may be further generalized, by considering the third body reactions as:

$$\left(\frac{\partial C_k}{\partial t}\right)_r = k_r \left(\nu_{rk}^{(p)} - \nu_{rk}^{(r)}\right) C_{M,r}^{\nu_{rM}} \prod_{i=1}^{N_C} C_i^{\nu_{ri}^{(r)}}, \tag{2.93}$$

where $\nu_{rM} = 0$ is applied for elementary reactions and $\nu_{rM} = 1$ for three-body reactions. Note, that another type of reaction behavior is the so called fall-off reaction, that represents a smooth transition between considering and ignoring the effect of

third-bodies depending on the pressure of the reacting gas mixture. This effect can also be described in the same framework, by including such effects in the reaction constant.

The net formation rate of species k considering all reactions is:

$$\left(\frac{\partial C_k}{\partial t}\right)_{reac} = \sum_{r=1}^{N_R} \left(\frac{\partial C_k}{\partial t}\right)_r, \tag{2.94}$$

where N_R is the number of reactions considered in the chemical mechanism. Optionally it can be numerically beneficial, to separate the production and consumption rates into different terms. (Ihme and Pitsch, 2008a) In this case, the consumption rates are composed of the contribution where the species k is on the reactant side:

$$\left(\frac{\partial C_k}{\partial t}\right)^- = \sum_{r=1}^{N_R} \left[-k_r \nu_{rk}^{(r)} C_{M,r}^{\nu_{rM}} \prod_{i=1}^{N_C} C_i^{\nu_{ri}^{(r)}} \right], \tag{2.95}$$

while production rates are the contribution of reactions where k is on the product side:

$$\left(\frac{\partial C_k}{\partial t}\right)^+ = \sum_{r=1}^{N_R} \left[k_r \nu_{rk}^{(p)} C_{M,r}^{\nu_{rM}} \prod_{i=1}^{N_C} C_i^{\nu_{ri}^{(r)}} \right]. \tag{2.96}$$

To use in the context of mass fractions, the net formation rate, and the production and consumption rates, have to be scaled by the molar weight of the species according to Eq. (2.3) as:

$$\left(\frac{\partial \rho Y_k}{\partial t}\right)_{reac} = W_k \left(\frac{\partial C_k}{\partial t}\right)_{reac} = \dot{\omega}_k, \tag{2.97}$$

$$= W_k \left[\left(\frac{\partial C_k}{\partial t}\right)^+ + \left(\frac{\partial C_k}{\partial t}\right)^- \right] = \dot{\omega}_k^+ + \dot{\omega}_k^-, \tag{2.98}$$

where $\dot{\omega}_k$ is the mass source term of species k with units of $\mathrm{kg}/\left(\mathrm{m}^3\mathrm{s}\right)$, that can be decomposed to production and consumption rates as: $\dot{\omega}_k = \dot{\omega}_k^+ + \dot{\omega}_k^-$.

For elementary reactions, the rate constant k_r is given by the Arrhenius law:

$$k_r = A_r T^{b_r} e^{-\frac{E_{ar}}{R_u T}} \tag{2.99}$$

where b_r is a dimensionless constant, E_{ar} is the activation energy associated with the reaction, and A_r is the pre-exponential constant with a unit such that Eq.(2.94) is dimensionally correct, considering the type of reaction, and the value of b_r. This expresses the fraction of collision events that have sufficient energy to overcome the barrier of activation energy. The rate constant takes a similar form for three-body reactions, while for fall-off reactions it is modified to consider the pressure dependence.

The evolution of chemical species concentrations in a homogeneous constant pressure reactor, can readily be modeled by using the ordinary differential equation (ODE) system based on Eq.(2.97): $\frac{\mathrm{d}\rho Y_k}{\mathrm{d}t} = \dot{\omega}_k$ and considering a constant pressure and enthalpy. In a reacting mixture, this ODE system becomes very computationally stiff due to the different time scales characterizing different reactions, and the strong coupling between the unknowns Y_k. (Lu and Law, 2009) Nevertheless, the equilibrium

conditions of this homogeneous constant pressure reactor can be found relatively easily. Hereafter this gas composition is denoted *chemical equilibrium* or simply equilibrium. It is a function of the chemical mechanism, the pressure, the enthalpy, and the initial reactant mixture composition. Note that this ODE system tends towards equilibrium if the chain branching reactions are able to overcome the chain breaking reactions, i.e. the gas mixture undergoes *autoignition*. (Buckmaster et al., 2005) Under ambient temperature and pressure conditions autoignition typically does not happen, as the chain breaking reactions create a metastable equilibrium practically identical to the fresh mixture state. Even if chain branching occurs, the speed of the reactions can be infinitesimal under ambient temperature conditions due to the $\exp\left(-\frac{E_{ar}}{R_u T}\right)$ term, thus it would take extremely long time to reach equilibrium.

The different strategies of solving such problems efficiently are not discussed in detail in this work. However different tools are used, to characterize the reaction process such as the general combustion library: Cantera (Goodwin, 2002), or the one dimensional flame solver: Chem1D (Somers, 1994). These tools use various strategies to solve the stiff system, by either treating the stiff partial differential equation system directly, or by splitting the advection-diffusion problem from the above stiff ODE system.

To characterize the overall evolution of such a system, one may use a compound quantity expressing the intensity of the exothermic process: the heat release rate $\dot{\omega}_T$. The heat release rate may be computed using the species source terms as:

$$\dot{\omega}_T = -\sum_{k=1}^{N_C} \Delta h^0_{f,k} \dot{\omega}_k, \tag{2.100}$$

where $\Delta h^0_{f,k}$ is the enthalpy of formation of species k. In practice this enthalpy can be taken by evaluating the NASA polynomials at the standard temperature: 298.15 K. The heat release rate is positive if species with high enthalpy of formation are consumed and species with low enthalpy of formation are created. The former corresponds to complex molecules that are destabilized easily, such as fuels, while the latter group is characterized by very stable molecules such as combustion products. One may formulate the temperature equation for reacting flows as in section 2.4, where the heat release rate would appear as a reactive source term. Such an expression of the energy conservation is out of the scope of this work, however the heat release rate is used for identifying gas mixtures with intense exothermic reactions.

2.5.2 Species mass fraction equations

To completely characterize the state of the gas mixture in the modeled domain, the scalar PDEs: Eq (2.56) must uniquely determine the enthalpy h and the species mass fractions Y_k. The most straightforward approach, is to formulate a transport equation for the species mass fraction directly:

$$\partial_t \left(\rho Y_k\right) + \nabla \cdot \left(\rho Y_k \mathbf{u}\right) + \nabla \cdot \mathbf{\Phi}_{Y_k} = \dot{\omega}_k + S^e_{Y_k}, \tag{2.101}$$

where $\mathbf{\Phi}_{Y_k} = \rho Y_k \mathbf{V}_k$ is the diffusive flux of species k, and $S^e_{Y_k}$ marks the species source term associated with evaporation further discussed in section 5.5.3. Here the diffusive flux is either calculated using the mixture-averaged mass diffusivity of the

species ($\mathbf{\Phi}_{Y_k}^{mix}$) or by the unity Lewis number assumption ($\mathbf{\Phi}_{Y_k}^{Le=1}$) as:

$$\mathbf{\Phi}_{Y_k}^{mix} = -\rho \mathcal{D}_k \nabla Y_k + \rho Y_k \mathbf{V}^c; \quad \mathbf{\Phi}_{Y_k}^{Le=1} = -\rho \mathcal{D}_t \nabla Y_k, \tag{2.102}$$

where $\mathbf{V}^c = \sum_{k=1}^{N_C} \mathcal{D}_k \nabla Y_k$ is the correction velocity as used in Eq. (2.22). In this work, such equations are solved by Cantera (Goodwin, 2002) and Chem1D (Somers, 1994) in 1D configurations, where $\dot{\omega}_k$ is evaluated using detailed or skeletal chemical mechanisms, as defined by Eq. (2.97). Such a solution of the gas composition is often called a *finite rate chemistry* approach, thus distinguishing it from other approaches that assume infinitely fast relaxation to the chemical equilibrium. Although, scalar equations like these may also be solved in the developed finite element framework with the finite rate chemistry approach, this is not discussed here in detail. (Surapaneni, 2019; Surapaneni and Mira, 2021; Surapaneni and Mira, 2023)

2.5.3 Mixture fraction equation

One may derive a partial differential equation representing the mixture fraction Z of the gas mixture. Departing from the definition of Eq. (2.30), the equation for Z is a linear combination of the Y_k equations for the full composition (Eq. (2.101)). Exploiting the linear nature of the differential operators, the left hand side of the mixture fraction equation reads:

$$\sum_{k=1}^{N_C} b_k^* \left[\partial_t \left(\rho Y_k\right) + \nabla \cdot \left(\rho Y_k \mathbf{u}\right) + \nabla \cdot \mathbf{\Phi}_{Y_k}\right] \tag{2.103}$$

$$= \partial_t \left(\rho \sum_{k=1}^{N_C} b_k^* Y_k\right) + \nabla \cdot \left(\rho \sum_{k=1}^{N_C} b_k^* Y_k \mathbf{u}\right) + \nabla \cdot \sum_{k=1}^{N_C} b_k^* \mathbf{\Phi}_{Y_k}, \tag{2.104}$$

$$= \partial_t \left(\rho \left(Z - Z_{st}\right)\right) + \nabla \cdot \left(\rho \left(Z - Z_{st}\right) \mathbf{u}\right) + \nabla \cdot \sum_{k=1}^{N_C} b_k^* \mathbf{\Phi}_{Y_k}, \tag{2.105}$$

$$= \partial_t \left(\rho Z\right) + \nabla \cdot \left(\rho Z \mathbf{u}\right) + \nabla \cdot \sum_{k=1}^{N_C} b_k^* \mathbf{\Phi}_{Y_k} - Z_{st} \left[\partial_t \rho + \nabla \cdot \left(\rho \mathbf{u}\right)\right], \tag{2.106}$$

where the continuity equation is used to express the last term as: $-Z_{st} S_\rho$. The diffusive flux of mixture fraction is a linear combination of the diffusive flux of species mass fractions. Thus, in case of mixture averaged transport, it is:

$$\mathbf{\Phi}_Z^{mix} = \sum_{k=1}^{N_C} b_k^* \mathbf{\Phi}_{Y_k}^{mix} = \rho \sum_{k=1}^{N_C} \left(-\mathcal{D}_k b_k^* \nabla Y_k + \mathbf{V}^c b_k^* Y_k\right), \tag{2.107}$$

$$= -\rho \sum_{k=1}^{N_C} \left[\mathcal{D}_k \nabla \left(b_k^* Y_k\right)\right] + \rho \mathbf{V}^c \left(Z - Z_{st}\right). \tag{2.108}$$

Under the unity Lewis number assumption this flux may be written simply in terms of the gradient of Z:

$$\mathbf{\Phi}_Z^{Le=1} = -\rho \sum_{k=1}^{N_C} \left[\mathcal{D}_t \nabla \left(b_k^* Y_k\right)\right] = -\rho \mathcal{D}_t \nabla \left(\sum_{k=1}^{N_C} b_k^* Y_k\right) \tag{2.109}$$

$$= -\rho \mathcal{D}_t \nabla \left(Z_{st} + \sum_{k=1}^{N_C} b_k^* Y_k\right) = -\rho \mathcal{D}_t \nabla Z. \tag{2.110}$$

The effect of chemical reactions on the right hand side of the Z equation is ultimately trivial, as the mixture fraction represents elemental mass fractions, that are conserved throughout the reactions, thus the reactive source term of Z is zero. Nevertheless, this is less straightforward to derive. The reactive term of this linear combination of the Y_k equations can be expressed as:

$$\sum_{k=1}^{N_C} b_k^* \dot{\omega}_k = \sum_{k=1}^{N_C} \frac{b_k}{b_f - b_o} W_k \left(\frac{\partial C_k}{\partial t}\right)_{reac} \tag{2.111}$$

$$= \frac{1}{b_f - b_o} \sum_{k=1}^{N_C} \left(2\beta_k + 0.5\alpha_k - \delta_k\right) \left(\frac{\partial C_k}{\partial t}\right)_{reac}, \tag{2.112}$$

where $b_k = \left(2\beta_k + 0.5\alpha_k - \delta_k\right)/W_k$ is the b value of a single species k. Further expanding this equation, one can reach:

$$\sum_{k=1}^{N_C} b_k^* \dot{\omega}_k = \frac{1}{b_f - b_o} \sum_{k=1}^{N_C} \left(2\beta_k + 0.5\alpha_k - \delta_k\right) \sum_{r=1}^{N_R} k_r \left(\nu_{rk}^{(p)} - \nu_{rk}^{(r)}\right) C_{M,r}^{\nu_{rM}} \prod_{i=1}^{N_C} C_i^{\nu_{ri}^{(r)}}, \tag{2.113}$$

where the factor $\left(2\beta_k + 0.5\alpha_k - \delta_k\right)$ is independent of the reactions, and the other factors $f_r = k_r C_{M,r}^{\nu_{rM}} \prod_{i=1}^{N_C} C_i^{\nu_{ri}^{(r)}}$ are independent of the individual species k, thus:

$$\sum_{k=1}^{N_C} b_k^* \dot{\omega}_k = \frac{1}{b_f - b_o} \sum_{r=1}^{N_R} f_r \sum_{k=1}^{N_C} \left(2\beta_k + 0.5\alpha_k - \delta_k\right) \left(\nu_{rk}^{(p)} - \nu_{rk}^{(r)}\right), \tag{2.114}$$

where Eq. (2.90) and Eq. (2.91) imply, that the sum: $\sum_{k=1}^{N_C} \left(2\beta_k + 0.5\alpha_k - \delta_k\right) \left(\nu_{rk}^{(p)} - \nu_{rk}^{(r)}\right)$ is constant zero irrespective of the reaction. Consequently, the mixture fraction equation indeed does not have a reactive source term:

$$\sum_{k=1}^{N_C} b_k^* \dot{\omega}_k = 0. \tag{2.115}$$

Meanwhile, the linear combination operation is simply executed on the evaporative source term of the Y_k equations. Overall, a generic transport equation for the mixture fraction may be written as:

$$\partial_t \left(\rho Z\right) + \nabla \cdot \left(\rho Z \mathbf{u}\right) - \nabla \cdot \rho \sum_{k=1}^{N_C} \left(\mathcal{D}_k b_k^* \nabla Y_k\right) + \nabla \cdot \left(\rho \mathbf{V}^c \left(Z - Z_{st}\right)\right) = Z_{st} S_\rho + \sum_{k=1}^{N_C} b_k^* S_{Y_k}^e. \tag{2.116}$$

This PDE is simplified under the unity Lewis number assumption:

$$\partial_t (\rho Z) + \nabla \cdot (\rho Z \mathbf{u}) - \nabla \cdot (\rho \mathcal{D}_t \nabla Z) = Z_{st} S_\rho + \sum_{k=1}^{N_C} b_k^* S_{Y_k}^e, \tag{2.117}$$

which is independent of the Y_k fields. Such a quantity can be transported independently of the Y_k equations, provided, that the Dirichlet and Neumann boundary conditions of Z correspond to those of Y_k. This property of the unity Lewis number mixture fraction transport is used in tabulated chemistry methods, to avoid solving the transport equations of all individual species.

In case of gas phase combustion the right hand side of Eq. (2.117) is zero and the mixture fraction behaves as a passive scalar. Meanwhile, in case of spray combustion calculations the right hand side is more complex. A mayor simplification may be attained, by constraining the problem to the evaporation of single component droplets, where these droplets contain the single species of fuel: f. In this case all $k \neq f$ source terms are zero: $S_{Y_k|k\neq f}^e = 0$, and the source therm of fuel is the same as the source term of total mass exchange between the phases: $S_{Y_f}^e = S_\rho$. Finally, in this case the fuel is composed of the single species characterized by a b value of: $b_f^* = \frac{b_f}{b_f - b_o}$. Consequently, using Eq. (2.39), the right hand side of Eq. (2.116) and Eq. (2.117) are simplified as:

$$S_Z = S_Z^e = Z_{st} S_\rho + \sum_{k=1}^{N_C} b_k^* S_{Y_k}^e = S_\rho \left(Z_{st} + b_f^* \right) = S_\rho. \tag{2.118}$$

The evaporative source terms are further discussed in section 5.5.3.

2.5.4 Progress variable equation

As discussed in section 2.2.3, the progress variable serves for the distinction of reacted gas mixtures from fresh reactants. The progress variable is a linear combination of species just like the mixture fraction. Thus similar arguments can be made, to derive the transport equation of Y_c as above. The key difference is, that a well defined progress variable has a non-zero reactive source term. Thus the transport equation, in the generic case takes the form:

$$\partial_t (\rho Y_c) + \nabla \cdot (\rho Y_c \mathbf{u}) - \nabla \cdot \rho \sum_{k=1}^{N_C} (\mathcal{D}_k a_k \nabla Y_k) + \nabla \cdot (\rho Y_c \mathbf{V}^c) = \dot{\omega}_{Y_c} + \sum_{k=1}^{N_C} a_k S_{Y_k}^e, \tag{2.119}$$

where the reactive source term of the progress variable is: $\dot{\omega}_{Y_c} = \sum_{k=1}^{N_C} a_k \dot{\omega}_k$. Similarly to the mixture fraction, the progress variable diffusion also becomes independent of the local species mass fraction gradients under the unity Lewis number assumption:

$$\partial_t (\rho Y_c) + \nabla \cdot (\rho Y_c \mathbf{u}) - \nabla \cdot \rho \mathcal{D}_t \nabla Y_c = \dot{\omega}_{Y_c} + \sum_{k=1}^{N_C} a_k S_{Y_k}^e. \tag{2.120}$$

The equation may be further simplified, by constraining the progress variable definition to species not present in the Lagrangian droplets. In this case, the right hand

side is solely composed of the reactive source term. I.e.: for the single component fuels of this work $a_f = 0$.

2.6 Summary of gas phase modeling

The assumptions of gas phase modeling are set in this chapter. As discussed, the present framework is capable of describing flows of ideal gas mixtures. Furthermore, the introduced governing equations are constrained to low Mach numbers, where compressibility effects are negligible, and the material properties such as density, viscosity, or thermal conductivity are a function of the spatially homogeneous thermodynamic pressure and scalar fields describing the local thermal and chemical state of the gas mixture.

A diverse set of scalar properties and the corresponding transport equations are introduced, that can describe the thermo-chemical gas state. Different combinations of these equations are possible, resulting in physical problems of various degrees of freedom. These options are further used in the context of the so called *finite rate* and *tabulated* chemistry. The former describes the gas phase composition using the full set of species mass transfer equations of section 2.5.2, while the latter uses only mixture fraction and progress variable to capture the gas state under the unity Lewis number assumption. All equations are derived retaining the source terms that model the effects of point-like Lagrangian droplets.

Chapter 3

Tabulated chemistry methods

This chapter describes tabulated chemistry methods, the modeling strategy of gas phase combustion in the present work. Such methods are widely used in the numerical simulation of complex geometries and realistic engine conditions, as they present a significantly lower computational cost than using detailed reaction mechanisms in finite rate chemistry, yet they are capable of capturing complex combustion physics. In this work, the method is applied using the following steps:

1. a set of one dimensional flamelets is computed using detailed chemistry;
2. these flamelets are uniquely characterized by *control variables*;
3. the flamelets are mapped onto a discretization of these control variables;
4. a *lookup table* of properties is created on this rectilinear discretization;
5. the control variables are attained in the complex geometry by solving PDEs;
6. the lookup properties are mapped onto the domain using the control variables.

The advantage of the method lies in executing steps 1.-4. *a priori*, and only repeating steps: 5. and 6. during the run-time of the simulation of the complex domain, thus placing the costly detailed chemistry calculations in a pre-processing step. This chapter discusses the selection of flamelet set, the control variable definition, and the details of the mapping procedure. Furthermore, the tabulated physical and chemical properties are introduced.

Various reviews have discussed the different aspects of tabulated chemistry. Van Oijen and De Goey (2000) summarized the early steps in tabulating premixed flamelets. A more current view of the field is provided by Fiorina, Veynante, and Candel (2015) detailing both premixed and diffusion flamelet tabulation. Recently, Van Oijen et al. (2016) revisited the novel developments, concentrating on topical issues of premixed flamelet tables, such as curvature and non-unity Lewis number effects, and pollutant formation. This chapter summarizes a number of well known phenomena, with the aim to present the utilized tabulated chemistry methods in a unified framework.

The chapter is structured as follows. The 1D flamelet configurations are presented in section 3.1. These flamelets are solved using detailed chemical mechanisms with the finite rate chemistry approach, and their structure is briefly analyzed here. Section 3.2 discusses the mapping of these flamelets onto the plane of mixture fraction and progress variable, with dedicated attention on treating non-injective behavior along progress variable. Subsequently non-adiabatic effects are discussed in section 3.3. Finally, the resulting tables are analyzed in section 3.4, pointing out the differences between various manifolds.

Credit

This chapter introduces some novel analysis of well established models. The presented analysis is entirely the work of the author. Novel details are introduced in the creation of the thermo-chemical tables, including the methods applied to represent heat loss, and the identification of injective behavior along progress variable. The former involves the incorporation of a minimal enthalpy level in the manifold corresponding to cold products. Furthermore, the usage of artificially scaled radiative heat loss in the counterflow diffusion flames is extended to various flamelet states beyond just the stable branch. The numerical results are obtained using third-party software, which are indicated throughout the chapter. Parts of this analysis is published in: Both, Mira, and Lehmkuhl (2021b), Benajes et al. (2022), and Both, Mira, and Lehmkuhl (2022a). The software used in this chapter is partially published in open source repositories at: `https://gitlab.com/BothAmbrus/LectIO` and `https://gitlab.com/BothAmbrus/AlyaTab`.

3.1 Canonical flamelet configurations

The PDE system of mass, momentum, and species transport can be solved in simplified one-dimensional, steady or unsteady cases. In this work, these configurations are studied by *finite rate chemistry solvers*, i.e.: computational tools, that model the transport of individual species mass fractions and evaluate the species source terms based on the (detailed) chemical mechanisms. One-dimensional flamelet solvers, such as Cantera (Goodwin, 2002) and Chem1D (Somers, 1994), are used for this purpose, as the solution of finite rate chemistry problems with Alya (Vázquez et al., 2016) is out of the scope of the present work. Below three canonical flamelet problems are described: premixed free flamelets, burner-stabilized flamelets, and counterflow diffusion flamelets. The latter describes the simultaneous mixing and burning of the fuel and oxidizer, while the former two deals with the reaction process of premixed reactants in adiabatic and reduced enthalpy conditions.

The configurations are illustrated with the numerical solution given by the flamelet solvers. For this purpose, the GRI3.0 (Smith et al., 2011) chemical mechanism is used, and pure methane (CH_4) and a simple approximation of air: $X_{O_2} = 0.21$, $X_{N_2} = 0.79$ are selected as fuel and oxidizer (reactants.) Both reactants are taken at room temperature: $T_f = T_o = 298.15$ K. The configurations are studied at atmospheric pressure: $P = 101325$ Pa.

3.1.1 Premixed free flamelets

Premixed free flamelets describe the propagation of a planar flame in homogeneous reactants. Figure 3.1 illustrates the steady state conditions in this configuration: the unburnt reactants are characterized by the composition and temperature of the mixture. Heat, reaction products, and radicals diffuse towards this unburnt mixture on the left side of the domain. Through this diffusive process, at a certain location, the temperature becomes sufficiently high and radicals sufficiently abundant, that strong reactions may be sustained, consuming the fuel and oxidizer. The velocity of the unburnt gases at steady state defines the laminar flame speed S_L, which is a characteristic value of the problem that only depends on the state of the inlet mixture.

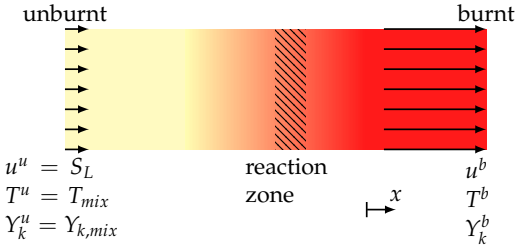

FIGURE 3.1: Illustration of steady 1D premixed free flamelet, with u^u, T^u, and Y_k^u being the velocity, temperature, and species mass fractions of the unburnt mixture.

The one-dimensionality of the configuration and the assumption of steady state simplifies the problem significantly. The continuity equation alone provides a restriction for the velocity as: $\frac{\mathrm{d}\rho u}{\mathrm{d}x} = 0$, thus the mass flux throughout the flame is constant: $\rho u = \rho^u S_L = const.$, where u is the velocity component in the x direction. The PDEs of the transported scalars take the form:

$$\frac{\mathrm{d}}{\mathrm{d}x}\left(\rho u Y_k\right) - \frac{\mathrm{d}}{\mathrm{d}x}\left(\rho \mathcal{D}_k \frac{\mathrm{d}Y_k}{\mathrm{d}x}\right) = \dot{\omega}_k, \tag{3.1}$$

$$\frac{\mathrm{d}}{\mathrm{d}x}\left(\rho u h\right) - \sum_{k=1}^{N_C} \frac{\mathrm{d}}{\mathrm{d}x}\left(\rho \mathcal{D}_t Y_k \frac{\mathrm{d}h_k}{\mathrm{d}x} + \rho \mathcal{D}_k h_k \frac{\mathrm{d}Y_k}{\mathrm{d}x}\right) = 0, \tag{3.2}$$

with Dirichlet boundary conditions on the left of the 1D domain, and Neumann boundary conditions on the right in the case of both species and enthalpy. The PDE system can be further simplified under the unity Lewis number assumption, where the enthalpy and mixture fraction become constant throughout the 1D domain. Solving for the steady state of this configuration needs dedicated care, since under cold inlet conditions the reactions are sustained by the diffusion of heat and radicals towards the unburnt gases. If the domain size is limited in such a case, then the residence time of the reactants is finite and the problem has a trivial solution: cold flow, where the species mass fractions are practically constant throughout the domain. The applied 1D solvers take dedicated measures to force the reacting solution if possible.

The problem may be solved using the full unsteady equations as well. In this case the inlet velocity of the unburnt mixture u^u is not an unknown of the problem as in the steady case, but it is a boundary condition. Thus the reaction zone may move, if $u^u \neq S_L$. Nevertheless, after the initial transients subside, the steady equations presented above are valid in a moving frame of reference fixed to the flame front, if the reacting zone is sufficiently far from the boundaries. This reference frame can be represented by replacing u by $u^* = u - (u^u - S_L)$ in the governing equations: Eq. (3.1) and Eq. (3.2) where continuity can be expressed in its steady state form: $\rho u^* = const.$. Consequently, the laminar flame speed may be expressed from mass conservation $\rho^u u^{*u} = \rho^b u^{*b}$ as:

$$S_L = \frac{u^b - u^u}{\frac{\rho^u}{\rho^b} - 1}, \tag{3.3}$$

where ρ^u and ρ^b are the densities of the unburnt and burnt gas mixture respectively.

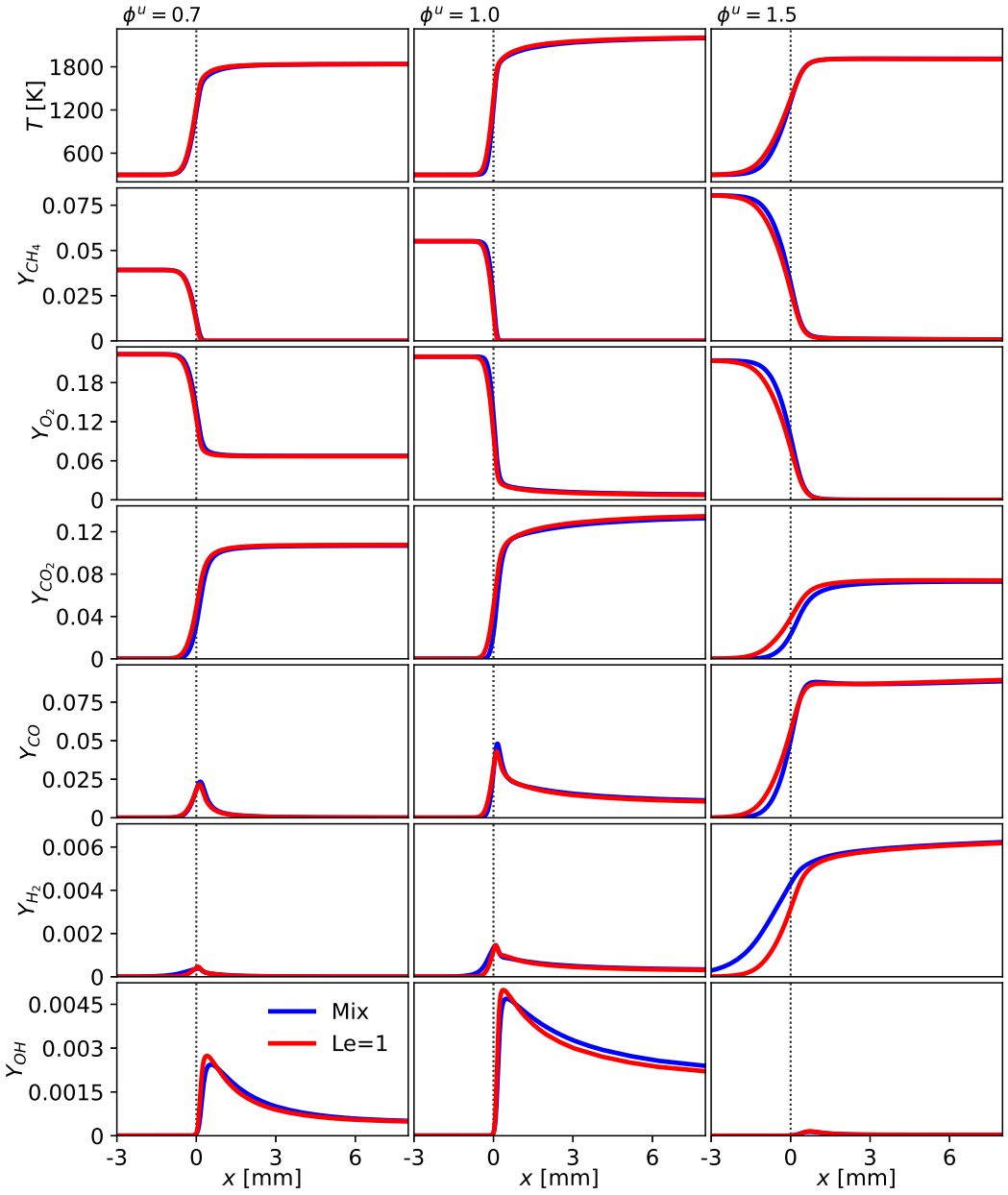

FIGURE 3.2: Typical temperature and species mass fraction profiles of 1D premixed free flamelets of methane-air mixtures computed with Cantera using the GRI3.0 (Smith et al., 2011) chemical mechanism and mixture-averaged transport properties. The columns correspond to different equivalence ratios in the unburnt mixture. The different rows show temperature, and the mass fractions of methane, molecular oxygen, carbon dioxide, carbon monoxide, molecular hydrogen, and hydroxyl radical respectively. The colors correspond to the two transport models: mixture-averaged transport properties ("Mix") and the unity Lewis number assumption ("Le=1").

Typical profiles of temperature and species mass fractions in 1D premixed free flamelets are shown in Fig. 3.2. The flamelets are solved using Cantera on a domain of $x \in [-40, 40]$ mm. The profiles shown are shifted in the x direction, such that

the maximum temperature gradient is located at $x = 0$, this location is shown with the gray dotted line for better comparison. In general the temperature and the gas composition approaches chemical equilibrium towards the right of the domain. The three shown equivalence ratios correspond to a lean ($\phi^u = 0.7$), a stoichiometric ($\phi^u = 1.0$), and a rich ($\phi^u = 1.5$) mixture from left to right, and the figure shows solutions with both the unity Lewis number assumption and mixture-averaged transport.

The first row of plots indicate the temperature along the flame. Note, that the rich flame has a local maxima in temperature around $x = 1$ mm, but the difference between the maximum temperature and the outlet temperature is within 20 K, that is too small to display here. In the lean and stoichiometric flamelets the temperature raises injectively throughout the domain. The stoichiometric flame (middle column) is characterized by the steepest temperature gradient among these examples, i.e.: the zone of intense reactions is completed in the shortest distance among the examples. However, after this initial sharp rise of temperature, there is a rather smooth relaxation to the final outlet value at $\phi = 1$. The lean and rich flamelets conclude this second part in a shorter distance than the stoichiometric flame. This phenomenon is better understood through the analysis of the availability of fuel and molecular oxygen. The second and third rows indicate these mass fractions respectively. In the lean flame fuel is consumed almost entirely before the $x = 0$ reference location, while molecular oxygen is present throughout the domain, thus the consumption of hydrocarbon species is not limited by the availability of oxygen. In case of the rich flamelet the roles are reversed: the oxidizer is consumed rapidly leading to the quick termination of the reactions. However, under stoichiometric conditions both fuel and oxidizer suffer a rapid drop around $x = 0$, after which still a significant part of the initial carbon and hydrogen content is contained in intermediate species, yet the oxygen concentration is very low. Under such condition, the rate of oxidation of said intermediate species is limited by low availability of O_2, hence the profiles shown in Fig. 3.2 continue developing with a modest slope behind the flame.

The fourth row of plots in Fig. 3.2 shows one of the final combustion products: carbon dioxide. These profiles behave fairly similar to temperature as both indicate the evolution of the oxidation process. The remaining three rows illustrate the mass fractions of intermediate combustion products: carbon monoxide, molecular hydrogen, and hydroxyl radical respectively. These species further highlight the behavior outlined above. In the lean flamelet, CO and H_2 is completely oxidized close to the flame front as O_2 is abundant at any point. Meanwhile the OH radical rises sharply in the reaction zone then converges to its equilibrium value towards the outlet. In the rich flamelet, the oxidation of CO and H_2 is interrupted shortly after the flame due to the lack of oxygen and these relatively stable unburnt intermediate species leave the domain. The concentration of the hydroxyl radical is low throughout the domain, related to the scarcity of oxygen, i.e.: any oxygen atom, that could be present in the form of OH is rather used in other reactions to oxidize the unburnt species. In the stoichiometric case the carbon monoxide and molecular hydrogen profiles are characterized by a peak at the $x = 0$ reference location, behind which they are partially consumed again, however, at a slow rate.

The difference between the mixture-averaged transport and unity Lewis number assumptions is the most significant in case of the rich flamelet. In the former case, molecular hydrogen is transported upstream at a higher rate than heat and other species. This phenomena has the highest effect on the rich flamelet, since in this case H_2 is more abundant on the rich side. Nevertheless, the upstream hydrogen transport affects all cases. The phenomenon is further discussed below.

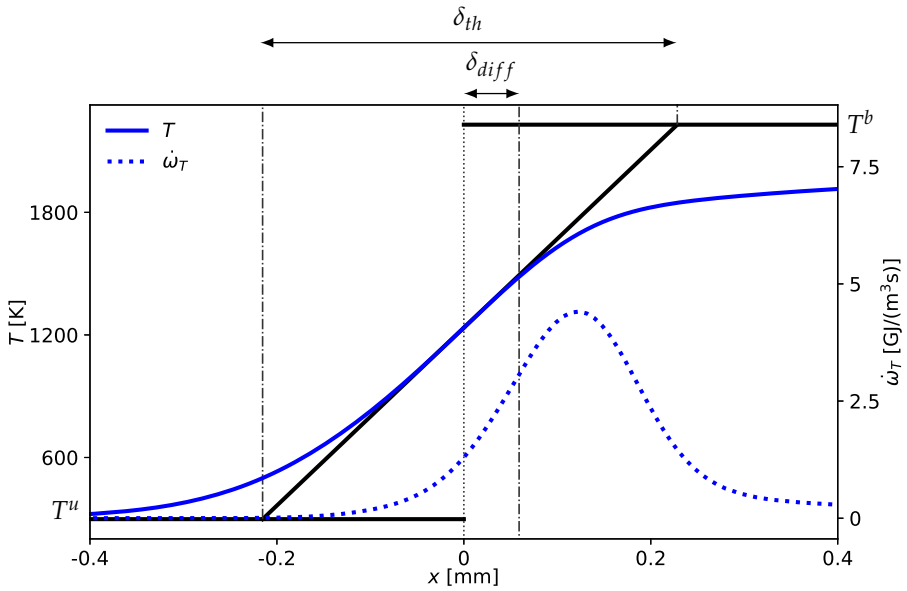

FIGURE 3.3: Illustration of thickness definitions of 1D premixed free flamelets. The temperature profile is marked by the solid curve, while the dotted curve shows the heat release rate indicating the reacting zone.

The combustion of a premixed mixture is completed in different distances depending on the equivalence ratio as Fig. 3.2 shows. This distance may be measured with various methods. The thermal flame thickness δ_{th} is defined based on the inlet and equilibrium temperatures, and the highest observed temperature gradient as:

$$\delta_{th} = \frac{T^b - T^u}{\max\left(\frac{\mathrm{d}T}{\mathrm{d}x}\right)}. \tag{3.4}$$

Furthermore, since the diffusion of heat and radicals plays an important role in the ignition of the fresh reactants, a diffusive thickness δ_{diff} can be defined as well:

$$\delta_{diff} = \frac{\mathcal{D}_t^u}{S_L}, \tag{3.5}$$

where $\mathcal{D}_t^u$ is the thermal diffusivity in the unburnt mixture. The two thicknesses are illustrated on the stoichiometric free flamelet of the above example in Fig. 3.3. As shown, the thermal flame thickness is significantly higher than the diffusive one. Hereafter, the thermal flame thickness is used as a reference of the length scales, as this distance provides a good upper estimate of the size of the reaction zone.

In the premixed free flamelets the unburnt and fully burnt states are characterized by the same mixture fraction and enthalpy due to the conservation laws. However local variations in Z and h may happen due to preferential diffusion of different species if the mixture-averaged transport model is applied. Thus, this configuration is ideal for the demonstration of the non-unity Lewis number effects in isolation. These effects are illustrated in Fig. 3.4, that shows the local variations of mixture fraction and enthalpy compared to the value at the unburnt mixture. Furthermore

the flux of Z and h are shown as well using dashed lines. The contribution of hydrogen gas diffusion on the mixture fraction is indicated separately using dotted lines.

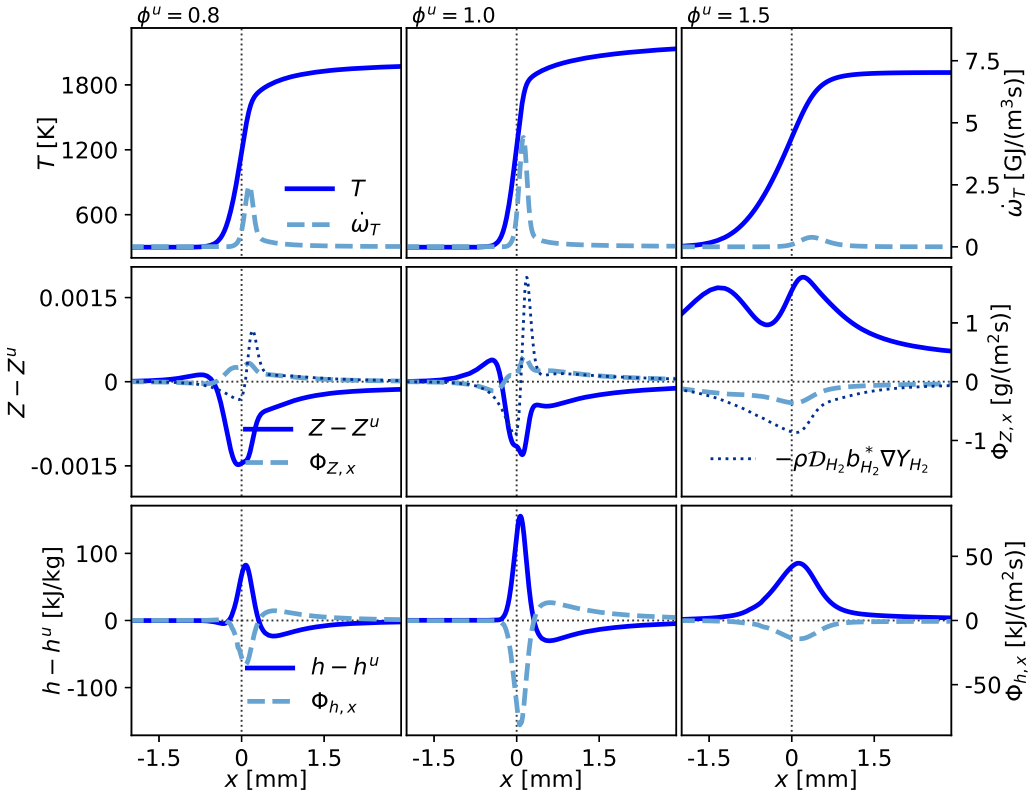

FIGURE 3.4: Preferential diffusion effects in 1D premixed free flamelets of methane-air mixtures using mixture-averaged transport properties. The columns correspond to different equivalence ratios in the unburnt mixture. The different rows show the temperature and heat release rate, the mixture fraction variations and diffusive mixture fraction flux according to Eq. (2.107), and enthalpy and diffusive enthalpy flux according to Eq. (2.77).

In the lean flamelet the mixture fraction predominantly shows a deficit in the flame region, that is associated to a positive mixture fraction flux. I.e.: mixture fraction is transported from the flame region towards the burnt gases due to diffusion of species. In the case of the stoichiometric flamelet the mixture fraction shows a pronounced maximum and minimum. The maximum is located in the unburnt side, and it is clearly linked to H_2 diffusion into the unburnt mixture as indicated by the dotted curve. Furthermore, the higher H_2 mass fraction is also visible in Fig. 3.2. This effect is further magnified in the rich flamelet, as it is characterized by high molecular hydrogen concentration on the burnt side. Thus for $\phi^u = 1.5$ the mixture fraction flux is uniformly negative, partly due to the upstream diffusion of H_2, consequently the mixture fraction is consistently higher than Z^u in the flame region.

The enthalpy variations show a different trend than the mixture fraction. The non-unity Lewis number effects consistently create a higher enthalpy region at the location of the peak temperature gradient ($x = 0$), associated to a negative enthalpy flux meaning that the preheating of the reactants happens at a higher rate than the

unity Lewis number assumption would predict. In case of the lean and stoichiometric mixture, a smaller negative peak is also present behind the flame, however this is absent in the rich flamelet.

Overall, the premixed flamelets are often represented by their macroscopic properties: the adiabatic flame temperature T^b, the laminar flame speed S_L, and the flame thickness δ_{th} or δ_{diff}. Note, that here the displayed adiabatic flame temperature is taken as the outlet temperature of the 1D domain, since mixture approaches the adiabatic equilibrium conditions towards the outlet. Minor differences from the true adiabatic equilibrium may occur, as the residence time of the gas mixture is finite in the simulation domain. These properties are shown in Fig. 3.5 at different equivalence ratios calculated using Cantera with mixture-averaged transport properties ("Mix") and the unity Lewis number assumption ("Le=1").

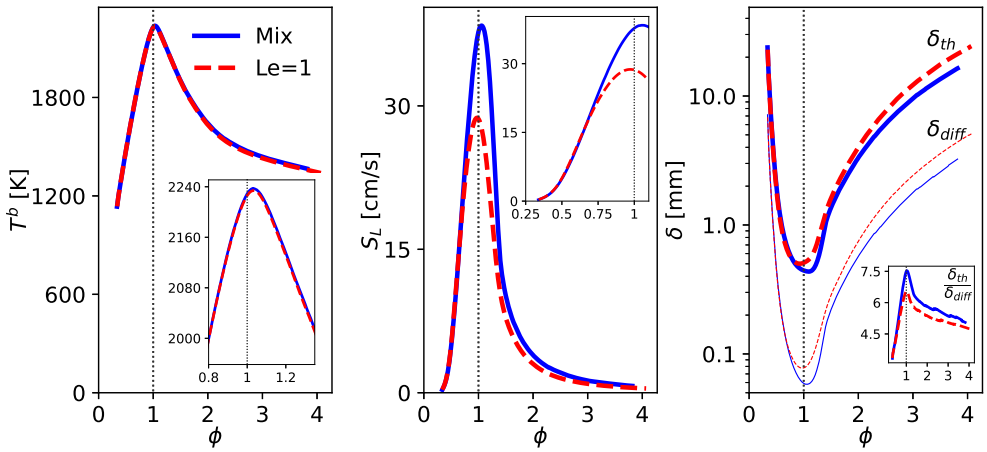

FIGURE 3.5: Properties of 1D premixed free flamelets of methane-air mixtures as function of equivalence ratio at atmospheric pressure. The fresh reactant temperature is $T^u = 298.15$ K. From left to right: adiabatic flame temperature T^b, laminar flame speed S_L, flame thickness δ. Magnified plots are included for clarity.

The adiabatic flame temperature reaches its maximum slightly above the stoichiometric point, and it drops sharply on both sides. At some point the flame becomes too lean or too rich to sustain the steady state reaction, these conditions give the lean and rich flammability limits. Here these limits are taken as the last condition where the numerical solution method of Cantera converges. Specifically, for unity Lewis number the limits identified are: $0.0206 \leq Z \leq 0.1920$, $0.35 \leq \phi \leq 4.07$. Given that the studied domain is sufficiently long, the outlet temperature T^b corresponds to chemical equilibrium, since in a freely propagating premixed flame there is sufficient time to complete all reactions, undisturbed by diffusive or convective effects. The equilibrium state is a function of the species in the chemical mechanism and the NASA polynomials only, and it is independent of the transport properties. Thus, the adiabatic flame temperature is the same irrespective of the transport model.

The laminar flame speed reaches its maximum near stoichiometric conditions as well, and it drops to almost zero near the flammability limits, indicating very low reaction rates. This highlights the behavior of these limits: even though the equilibrium conditions are still at a higher temperature than the fresh gases, the

flame cannot produce a positive propagation speed, because diffusion dissipates the radical species faster than they are created by reactions. In the case of laminar flame speed, non-unity Lewis number effects have barely any effect on the lean side, up to an equivalence ratio of $\phi \approx 0.7$. Above this equivalence ratio the two transport models start to deviate, as the flame speed becomes significantly higher in the case of mixture-averaged transport properties. The increased flame speed is partly related to the upstream transport of hydrogen from the reaction zone towards the unburnt mixture shown on Fig. 3.4. This upstream transport of hydrogen is significant at higher equivalence ratios only, since leaner flamelets have less H_2 in the flame as illustrated on Fig. 3.2. Furthermore, the consistent enthalpy surplus in the reacting zone also promotes faster reactions.

The flame thickness is approximately inversely proportional to the flame speed as Eq. (3.5) suggests. Hence, it takes its minimum at stoichiometry and grows towards the flammability limits showing more than an order of magnitude variation. The diffusive and thermal thicknesses show a similar trend but their ratio is variable. The difference between the two thicknesses is the highest near stoichiometry, where the thermal flame thickness is approximately 7 times higher than the diffusive flame thickness. These two length scales are more similar for lean and rich flamelets.

3.1.2 Burner-stabilized flamelets

Burner-stabilized flamelets (Van Oijen and De Goey, 2000; Fiorina et al., 2003; Gubernov, Bykov, and Maas, 2017) also represent premixed combustion but in a different approach. In this case, the mass flow rate through the system: m is not an unknown of the problem, but defined by a Dirichlet boundary condition on the left hand side. If this mass flow rate is lower than the mass flow rate corresponding to the laminar flame speed $\rho^u S_L$, the flamelet would propagate towards the left boundary. Boundary conditions are defined on the left side, such that this propagation is halted right at the boundary. These boundary conditions model the effect of a porous burner plate. In case the mass flow rate is higher than $\rho^u S_L$, the flame is propagated towards the outlet and the problem has no stable solution. Theoretically the problem is equivalent to a free premixed flamelet if the mass fluxes are exactly equal, although the stability of the numerical solution is not guaranteed.

The PDEs describing the burner-stabilized flamelet are the same as the ones of premixed free flamelets: Eq. (3.1) and Eq. (3.2). And the mass flux $m = \rho u$ is still conserved across the domain in steady state conditions. The only differences are the boundary conditions on the left side of the domain that imitate the presence of a porous cold burner plate. This effect is imposed by assuming a constant burner temperature equal to the temperature of the unburnt mixture, and by imposing the conservation of species across the burner, i.e.: no reactions take place in the burner. Thus the mass flux of species entering the burner is solely convective: $mY_{k,mix}$, since it is assumed that the burner is long enough for all diffusive transport to take place. Meanwhile the mass flux of species leaving the burner and entering the simulation domain through the left boundary is composed of a convective and a diffusive flux: $mY_k^{in} + \Phi_{Y_k,x}^{in}$, since the species may have a non-zero gradient here. From the equality of the two fluxes across the burner one gets the boundary condition:

$$Y_k^{in} = Y_{k,mix} - \frac{\Phi_{Y_k,x}^{in}}{m}. \tag{3.6}$$

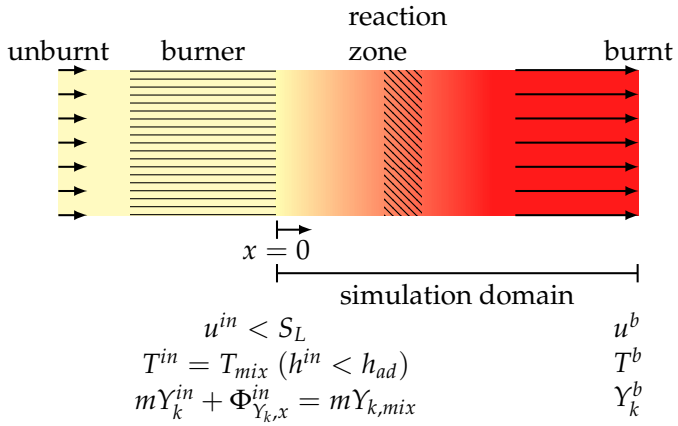

FIGURE 3.6: Illustration of 1D burner-stabilized flamelet, with u^{in}, T^{in}, and Y_k^{in} being the velocity, temperature, and species mass fractions at the inlet of the domain. The thermal state of the unburnt mixture is given by T_{mix} and $Y_{k,mix}$. The mass flux throughout the domain is denoted by m, while $\Phi^{in}_{Y_k,x} = -\rho \mathcal{D}_k \frac{\mathrm{d}Y_k}{\mathrm{d}x}$ is the diffusive flux of species at the inlet.

The species that are absent in the fuel-oxidizer mixture but present in the flame are diffused towards the burner ($\Phi^{in}_{Y_k,x} < 0$), thus they are characterized by a non-zero mass fraction at the inlet. The fuel and oxidizer species are diffused towards the reacting zone ($\Phi^{in}_{Y_k,x} > 0$) where they are consumed, so they are characterized by lower mass fractions at the inlet than in the unburnt mixture. Cold reaction products and intermediate species are present on the boundary at T^{in}, consequently the boundary enthalpy is lower than the enthalpy of the adiabatic reactant mixture. This enthalpy deficit decreases the reaction rates, affecting the flame propagation. Note, that after the inlet boundary, which models the presence of the burner, subsequently the enthalpy is constant within the simulation domain.

The temperature, heat release rate, and species mass fraction profiles of some burner-stabilized flamelets are presented in Fig. 3.7, following the same structure as Fig. 3.2. For reference the profiles of free flames are plotted along the burner-stabilized profiles, that are shifted along the physical coordinate such, that the temperature change at $x = 0$ is 0.5% of the total temperature change between T^u and T^b. Note, that this shift in x is arbitrary, so point-to-point comparisons are not necessarily meaningful, the free flame profiles only illustrate the trends and the magnitudes. The burner-stabilized flames are solved using Cantera on a domain of $x \in [0, 40]$ mm with the same fuel and oxidizer properties as the free flames. The different columns show cases of different mass fluxes: 75%, 50%, and 10% of free flame mass flux ($\rho^u S_L$) respectively.

At $m/(\rho^u S_L) = 0.75$ the temperature and reactant profiles are fairly similar to the free flame. The carbon dioxide mass fraction is similar as well, as discussed in case of the free flamelets, this mass fraction follows closely the temperature. The intermediate species CO, H_2, and OH show more notable differences, in particular the hydroxyl radical profile downstream of the flame is significantly lower than the free flame values. Even at this moderate reduction of the mass flux, the intermediate species start to appear at the inlet of the domain according to Eq. (3.6). The decrease in heat release rate is similar to the decrease in hydroxyl radical.

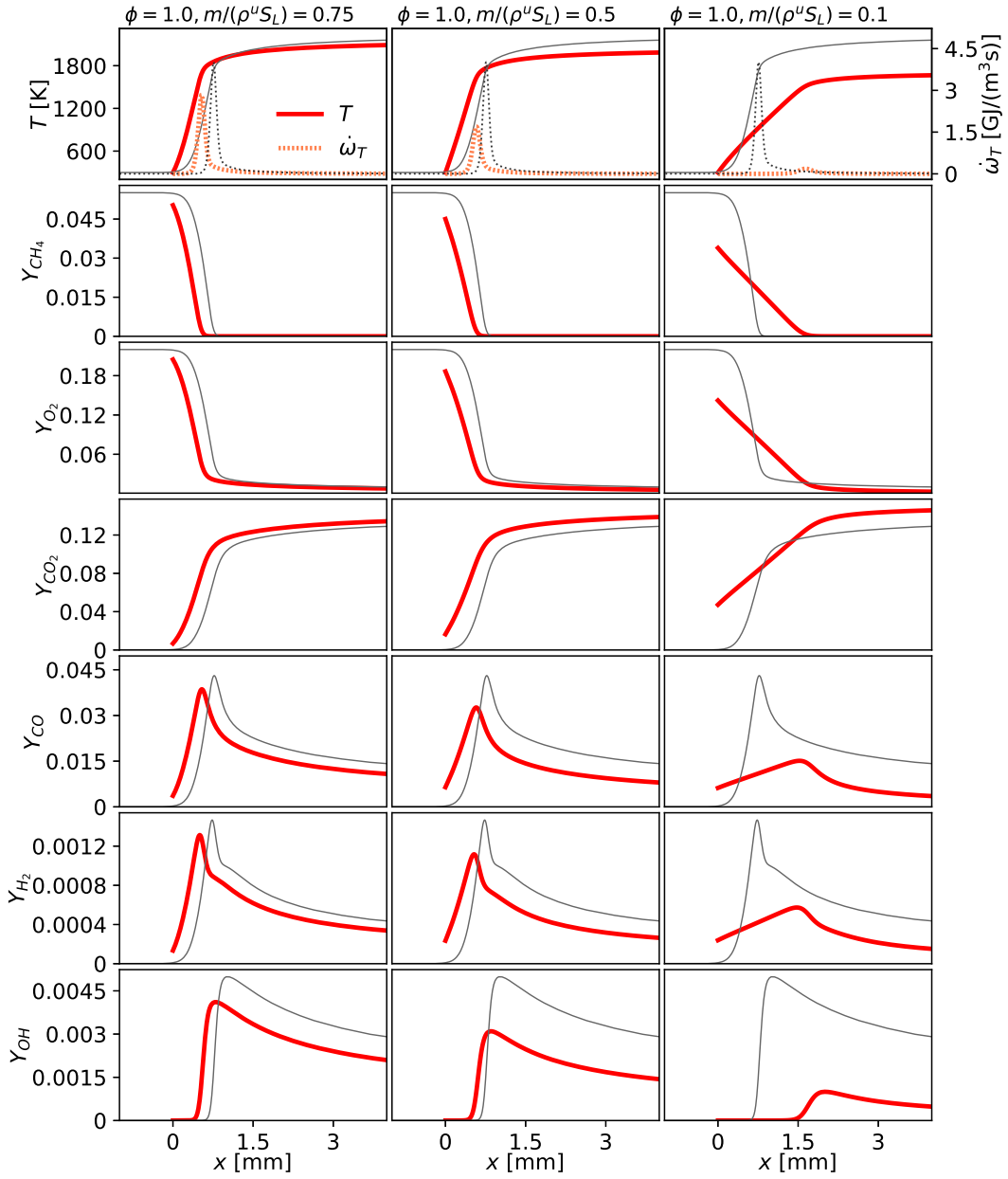

FIGURE 3.7: Typical temperature, heat release rate, and species mass fraction profiles of stoichiometric 1D premixed burner-stabilized flamelets of methane-air mixtures computed with Cantera using the GRI3.0 (Smith et al., 2011) chemical mechanism and the unity Lewis number assumption. The columns correspond to different mass fluxes. The different rows show temperature, and the mass fractions of methane, oxygen gas, carbon dioxide, carbon monoxide, hydrogen gas, and hydroxyl radical respectively. Additionally, the first row shows the heat release rate too. The profiles of the free flamelet are shown by the thin gray lines, shifted such, that the temperature change at $x = 0$ is 0.5% of the total temperature change.

At $m/(\rho^u S_L) = 0.5$ the effects are more pronounced. The burnt gas temperature is significantly lower than the adiabatic one, and the mass fractions of methane

and oxygen at the inlet are notably lower than in the fresh mixture. Carbon dioxide appears at the inlet, and there is a significant amount of carbon monoxide and molecular hydrogen too. The trend of the hydroxyl radical and heat release rate is continued as it keeps decreasing with the decrease of the mass flux. With further reduction of the mass flux to $m/(\rho^u S_L) = 0.1$, the observed behavior is continued. In this case the flamelet becomes significantly thicker, and the reaction zone is shifted downstream as indicated by the heat release rate curve.

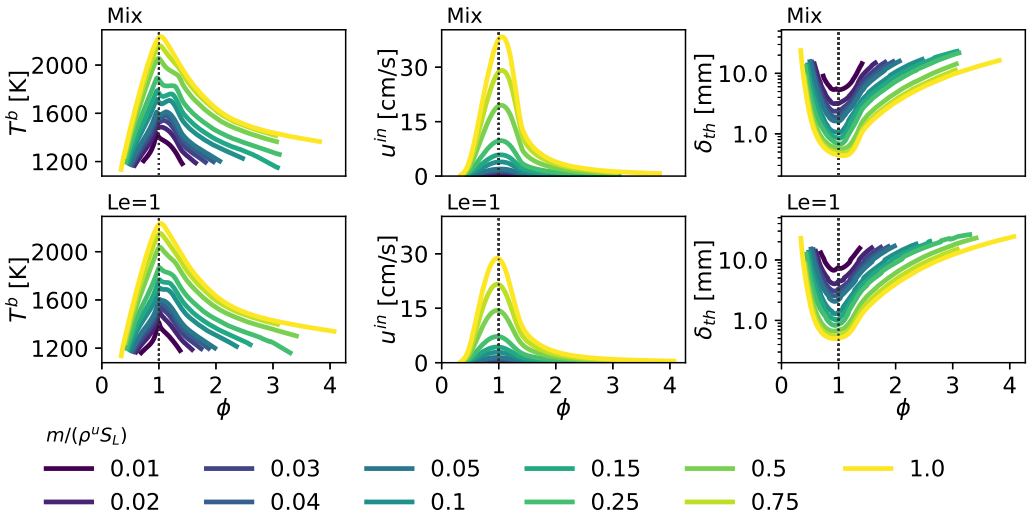

FIGURE 3.8: Properties of 1D premixed burner-stabilized flamelets of methane-air mixtures as function of equivalence ratio. From left to right: adiabatic flame temperature T^b, laminar flame speed S_L, flame thickness δ. The two rows correspond to mixture-average transport, and the unity Lewis number assumption respectively. Different line correspond to different mass fluxes defined by $m/(\rho^u S_L)$ as indicated by the legend.

The variation of outlet temperature T^b, inlet velocity u^{in}, and thermal flame thickness δ_{th} as a function of the mass flux is illustrated on Fig. 3.8 comparing the results with mixture-average transport ("Mix") and with the unity Lewis number assumption ("Le=1"). Note that the mass flux is decreased in a non-linear manner, as smaller reductions (e.g.: $m/(\rho^u S_L) = 0.75$) have very little effect on the outlet temperature. This effect is also shown on Fig. 3.7.

Of course, as the mass flux decreases, the inlet velocity decreases as well since the relation between the two is almost linear, except for the effects of small density variations due to the changing inlet composition. The outlet temperature decreases with the mass flux, since the inlet gas mixture contains more and more intermediate species and combustion products but its temperature is kept equal to the temperature of the unburnt mixture. This corresponds to a decreased enthalpy level. As already demonstrated in Fig. 3.7, the thickness of the flamelets increases with decreasing flame speed. Finally, the flammability limit gets reduced severely at very low mass flux values, as it is linked to a minimum outlet temperature $T^b \approx 1200$ K below which reactions cannot be sustained. This is related to the *crossover temperature* above which chain branching reactions overcome the chain breaking reactions. (Peters, 2001; Buckmaster et al., 2005)

The limiting case of $m \to 0$ is peculiar in the sense, that the boundary conditions

TABLE 3.1: Examples of isothermal equilibrium mass fractions of methane-air mixtures, given by the constraints: $\dot{\omega}_k = 0$ and $T = T_{mix}$, computed with Cantera using the GRI3.0 (Smith et al., 2011) chemical mechanism.

	$\phi = 0.7$	$\phi = 1.0$	$\phi = 1.5$
Y_{N_2} [%]	73.7	72.5	70.5
Y_{O_2} [%]	6.7	0.0	0.0
Y_{CH_4} [%]	0.0	0.0	2.7
Y_{H_2O} [%]	8.8	12.4	12.1
Y_{CO_2} [%]	10.8	15.1	14.7
$\sum Y$ [%]	100.0	100.0	100.0

become undefined. In this work, a natural extension of the method is applied on this limit, where not just the convective terms but the entire left hand sides are set to 0 in Eq.(3.1) and Eq.(3.2). By still imposing the fresh gas temperature as a constraint, the problem consists of finding the equilibrium ($\dot{\omega}_k = 0$) composition corresponding to the given inlet composition $Y_{k,mix}$ and inlet temperature T_{mix}. If T_{mix} is near room temperature, the thermal dissociation of final combustion products into intermediate species is negligible. Thus Y_k is a mixture of final combustion products (H_2O and CO_2) mixed with part of the fresh gases that were not utilized in the reactions. Using the general example of methane combustion used in this chapter, the major mass fractions of the aforementioned species given by this process for the equivalence ratios $\phi \in \{0.7, 1.0, 1.5\}$ are presented in Tab. 3.1. As the examples demonstrate, the mixture consists of the 5 indicated species. Remaining molecular oxygen or methane are present under lean and rich conditions respectively.

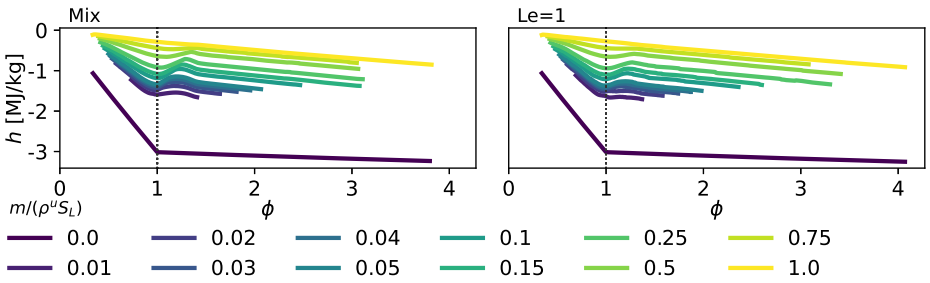

FIGURE 3.9: Enthalpy of 1D premixed burner-stabilized flamelets of methane-air mixtures as function of equivalence ratio. The two columns correspond to mixture-average transport, and the unity Lewis number assumption respectively. Different line correspond to different mass fluxes defined by $m/(\rho^u S_L)$ as indicated by the legend.

The enthalpy of burner stabilized flamelets is illustrated in Fig. 3.9, compared to the adiabatic enthalpy of free flamelets ($m/(\rho^u S_L) = 1$), and the enthalpy of the isothermal equilibrium state ($m/(\rho^u S_L) = 0$). The latter corresponds to the maximum attainable enthalpy enthalpy deficit considered for premixed flamelets. The maximum enthalpy deficit according to Eq (2.47) is attained at the stoichiometric

point:

$$\max\left(|\Delta h_{st}|\right) = Z_{st} \cdot Q, \tag{3.7}$$

where Q is the heat of combustion of the fuel. For the present case of methane the maximum enthalpy deficit is: $\max\left(|\Delta h_{st}|\right) = 2.85\ \frac{\mathrm{MJ}}{\mathrm{kg}}$, corresponding to a heat of combustion of $Q = 2.85/0.0552\ \frac{\mathrm{MJ}}{\mathrm{kg}} = 51.61\ \frac{\mathrm{MJ}}{\mathrm{kg}}$. Note, that according to the framework presented in chapter 4, the dew point of water is $T^{dew} \approx 336$ K in the isothermal equilibrium composition at stoichiometry. (Gatley, 2005, §12) Thus the NASA polynomials are used in a situation, where the assumption of ideal gas is not valid. Consequently Q is between the commonly reported lower and higher heating values of methane. In general, the maximum attainable heat loss at a given mixture fraction is:

$$\max\left(|\Delta h|\right) = \begin{cases} Z \cdot \max\left(|\Delta h_{st}|\right), & Z \leq Z_{st}, \\ Z_{st} \cdot \max\left(|\Delta h_{st}|\right) \dfrac{1-Z}{1-Z_{st}}, & Z > Z_{st}. \end{cases} \tag{3.8}$$

Such a relation is only valid, if the inlet temperatures are relatively low, thus the species of the isothermal equilibrium do not undergo dissociation.

3.1.3 Counterflow diffusion flamelets

Counterflow diffusion flamelets (Tsuji, 1982) are symmetric 2D configurations, which can be treated in a 1D manner along the symmetry axis. The problem is illustrated in Fig. 3.10. It corresponds to the simultaneous mixing and burning of oxidizer and fuel in a purely straining flow, so both oxidizer and fuel are advected towards the reaction zone situated in the middle of the domain. In such a configuration heat and reaction products diffuse from the reaction zone outwards into the oxidizer and fuel streams. In the far field of the fuel and oxidizer streams the composition and temperature is practically constant, and the flow behaves as an incompressible potential flow. The case is characterized by the inlet conditions of the pure streams (T_{ox}, T_f, $Y_{k,ox}$, $Y_{k,f}$) , and the strain rate in the far field of the oxidizer flow (a). In this work, such flamelets are solved using a finite rate chemistry approach with Chem1D (Somers, 1994). Note, that in Fig. 3.10 and in the description below the oxidizer inlet is located on the left boundary (L) and the fuel on the right (R) so the mixture fraction increases from left to right. This is the other way around in the framework of Chem1D, but the mirrored problem was chosen here, for a more intuitive correspondence with mixture fraction.

At a constant far field oxidizer strain rate a, the one dimensional problem along the symmetry plane of the planar strained flame is described by the following PDE system according to Ramaekers (2011):

$$\frac{\partial \rho}{\partial t} + \frac{\partial \rho u}{\partial x} = -\rho G, \tag{3.9}$$

$$\frac{\partial \rho Y_k}{\partial t} + \frac{\partial \rho u Y_k}{\partial x} - \frac{\partial}{\partial x}\left(\rho \mathcal{D}_k \frac{\partial Y_k}{\partial x}\right) = \dot{\omega}_k - \rho G Y_k, \tag{3.10}$$

$$\frac{\partial \rho h}{\partial t} + \frac{\partial \rho u h}{\partial x} - \frac{\partial}{\partial x}\left[\rho \sum_{k=1}^{N_C}\left(\mathcal{D}_t Y_k \frac{\partial h_k}{\partial x} + \mathcal{D}_k h_k \frac{\partial Y_k}{\partial x}\right)\right] = -\rho G h, \tag{3.11}$$

$$\rho\frac{\partial G}{\partial t}+\rho u\frac{\partial G}{\partial x}-\frac{\partial}{\partial x}\left(\mu\frac{\partial G}{\partial x}\right)=\rho_{ox}a^2-\rho G^2, \tag{3.12}$$

where G is the local flame stretch rate defined as: $G=\frac{\partial v}{\partial y}$, with v being the velocity component in y. The equations may be derived from the generic conservation equations: Eq. (2.54), Eq. (2.55), Eq. (2.76), and Eq. (2.101), by assuming that the gradients of scalars are zero in the y direction (planar flame). In this case $\frac{\partial \rho}{\partial y}=0$, thus the 2D continuity equation Eq. (3.9) is indeed equivalent to the generic case, since: $\frac{\partial \rho u}{\partial x}+\frac{\partial \rho v}{\partial y}=\frac{\partial \rho u}{\partial x}+\rho\frac{\partial v}{\partial y}=\frac{\partial \rho u}{\partial x}+\rho G$. The scalar transport equations are transformed similarly by using $\frac{\partial \xi_k}{\partial y}=0$, so $\frac{\partial \rho u\xi_k}{\partial x}+\frac{\partial \rho v\xi_k}{\partial y}=\frac{\partial \rho u\xi_k}{\partial x}+\rho G\xi_k$, proving the equivalence of Eq. (3.10) and Eq. (3.11) to Eq. (2.101) and Eq. (2.76) respectively. The transformation of the momentum equation into the stretch transport equation is less straightforward. The momentum equation in the y direction is used, together with the assumption, that the far-field flow in $x\rightarrow-\infty$ is a potential flow. For further details see the work of Ramaekers (2011).

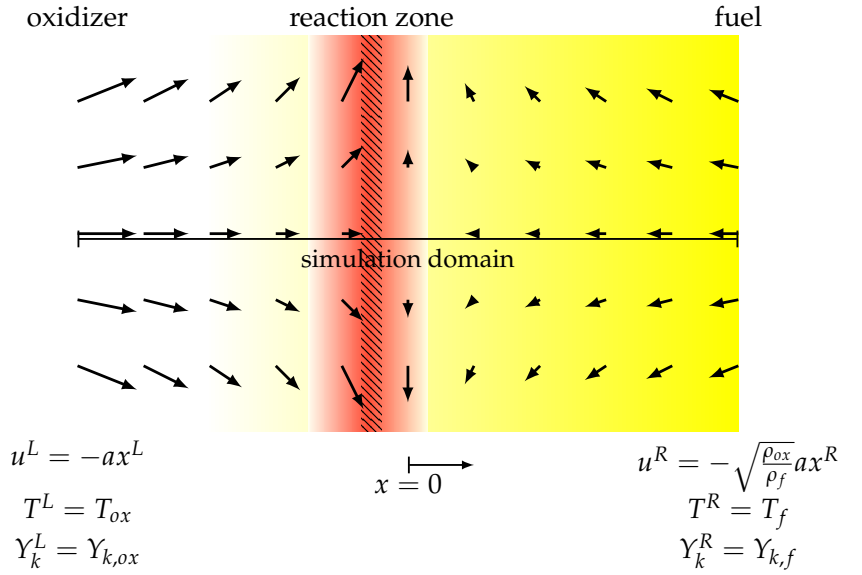

FIGURE 3.10: Illustration of counterflow diffusion flamelet.

The problem is closed by Dirichlet boundary conditions for the enthalpy and species mass fractions, and a combination of Dirichlet and Neumann boundary conditions for stretch rate or the left (L) and right (R) boundaries corresponding to the oxidizer and fuel respectively:

$$Y_k^L=Y_{k,ox};\qquad h^L=h_{ox}(Y_{k,ox},T_{ox});\qquad G^L=a, \tag{3.13}$$

$$Y_k^R=Y_{k,f};\qquad h^R=h_f(Y_{k,ox},T_{ox});\qquad \left(\frac{\partial G}{\partial x}\right)^R=0. \tag{3.14}$$

Furthermore, appropriate initial conditions have to be introduced as well for the unknowns: Y_k, h, and G.

Solving the problem in two dimensions necessitates different boundary treatment. Dirichlet boundary conditions can be prescribed on the left and right boundary, as shown on Fig. 3.10. The prescribed velocities are: $u^L = -ax^L$, $v^L = ay$ on the oxidizer side, and $u^R = -\sqrt{\rho_{ox}/\rho_f}ax^R$, $v^R = \sqrt{\rho_{ox}/\rho_f}ay$ on the fuel side. In this case the top and bottom boundaries would have a Neumann boundary condition for the velocity representing the outlets of the domain. In this work such 2D problems are solved using tabulated chemistry for benchmarking purposes in section 6.3.

Another alternative approach is solving the problem in *mixture fraction space*. This means, that first the mixture fraction distribution is solved under some assumptions, thus providing mixture fraction as a function of the spacial coordinate. Subsequently all other transport equations are formulated as a function of Z instead of a function of x, by applying the chain rule: $\frac{\partial}{\partial x} = \frac{\partial Z}{\partial x}\frac{\partial}{\partial Z}$. This concept is mainly used under the unity Lewis number assumption, where the species transport equations take the form:

$$\rho\frac{\partial Y_k}{\partial t} - \rho\frac{\chi}{2}\frac{\partial^2 Y_k}{\partial Z^2} = \dot{\omega}_k, \tag{3.15}$$

with χ being the scalar dissipation rate of mixture fraction, defined using the thermal diffusivity $\left(\mathcal{D}_t = \frac{\lambda}{\rho c_p}\right)$:

$$\chi = 2\mathcal{D}_t \left|\nabla Z\right|^2. \tag{3.16}$$

If the mixture fraction is know, then the profile of χ is known as well, given that the material properties are calculated. Thus Eq. (3.15) may be solved on its own in mixture fraction space.

The scalar dissipation rate is already discussed in section 2.3.3 in the context of the mixing of arbitrary conserved scalars. It expresses the local speed at which a conserved scalar field approaches the perfectly mixed solution. I.e.: regions with higher gradients in the scalar are mixed faster by diffusion. In Eq. (3.15) the transport of species is expressed relative to the mixture fraction. Both Z and Y_k are advected with the same velocity fields, thus in mixture fraction space the species are modified by diffusion and chemical sources only. Furthermore with the unity Lewis number assumption all species are diffused with the same diffusivity. In this context χ expresses the rate of mixing of the mixture fraction coordinate Z itself.

As χ approaches zero, Eq. (3.15) behaves as the homogeneous reactor equation discussed in section 2.5.1. In this case the local gas composition evolves towards an equilibrium state in time at each point of the domain because gradients between different mixtures are infinitesimal, thus the interaction between them is negligible. However, at non-negligible values of χ, diffusion between gas mixtures of different mixture fractions becomes more important, and the steady-state reactive solution shifts towards states, where high chemical source terms are balanced by high diffusive transport. In case of very high scalar dissipation rates, $\dot{\omega}_k$ cannot balance the diffusive dissipation, thus steady reactive solutions are not possible, and the only existing solution of the problem is non-reactive mixing of the oxidizer and fuel. The limiting case with the highest scalar dissipation rate values, where a steady reactive solution is still possible marks the *extinction point*.

Note, that with similar arguments, there is a highest scalar dissipation rate profile below which autoignition is able to drive the counterflow diffusion flame towards chemical equilibrium. Above this limit, the diffusive dissipation of the radical pool is

high enough to counter the effect of non-zero $\dot{\omega}_k$, and the unsteady counterflow diffusion flame does not ignite spontaneously. In this work, the mixture temperatures are close to the temperature of the ambient, thus chain branching reaction cannot overcome the chain breaking reactions, and autoignition does not occur. Note, that at low temperatures even if the fresh reactants would not be in a metastable state, the ignition process would be extremely slow, and a very small scalar dissipation could prevent autoignition. In practice, even at zero scalar dissipation rate it would take unreasonably long time for autoignition to start making a difference in the gas composition, thus one may consider, that cold mixtures simply do not auto-ignite.

The scalar dissipation rate and the strain rate of the problem describe different aspects of opposing diffusion flames, the former being a measure of mixture fraction gradients, while the latter a scale of flame stretching. However, they are strongly related, as more stretched flames are characterized by sharper mixture fraction profiles. For example, under the assumption of constant density and diffusivity, the analytical solution of the steady state mixture fraction equation is:

$$Z = \tfrac{1}{2}\left[1 - \mathrm{erf}\left(\zeta\right)\right], \tag{3.17}$$

with $\zeta = x\sqrt{a/\left(2\mathcal{D}_t\right)}$ being a scaled coordinate along the flame, where $\mathcal{D}_t$ is the constant diffusivity. In this case the scalar dissipation rate profile is: $\chi = \frac{a}{\pi}\exp\left(-\frac{a}{\mathcal{D}_t}x^2\right)$, or in mixture fraction space: $\chi = \dfrac{a}{\pi}\exp\left(-2\left[\mathrm{erf}^{-1}\left(1-2Z\right)\right]^2\right)$. (Peters, 1983; Poinsot and Veynante, 2005) Thus, under these assumptions, the scalar dissipation rate is a known function of the mixture fraction, and it scales linearly with the strain rate. In this case, the scalar dissipation rate profile may be described by a single value of itself taken at the location of the stoichiometric mixture: χ_{st} which is a linear function of the strain at constant density and diffusivity. Further details on the validity of this analytical solution are provided in Appendix A.

As introduced above, depending on the values of χ_{st} or analogously a, the flame may or may not have steady reacting solutions, and may or may not auto-ignite to reach a stable burning state. The extinction point can be described by the single values of χ_{st}^{ext} or a^{ext}, and similarly the lowest stoichiometric scalar dissipation and strain prevent autoignition are: χ_{st}^{ign} or a^{ign}. (The latter are practically zero in the applications of the present work.) The strain rate of extinction is always higher than the last possible strain rate of autoignition, thus, three different conditions can be distinguished based on the strain rate of the flow:

1. at $a < a^{ign}$ there is one stable solution: the stable burning flame,
2. at $a^{ign} \leq a \leq a^{ext}$ there are two stable solutions: the mixing of pure fuel and oxidizer, and the stable burning flame,
3. at $a^{ext} < a$ there is one stable solution: the mixing of pure fuel and oxidizer.

The second scenario is the most relevant in this work, since a^{ign} is negligibly small for low temperature cases, thus the mixing of pure fuel and oxidizer is always a valid steady-state solution of the problem. (Peters, 1988) Under these circumstances, two stable solutions exist, and the flamelet solver has to be started with appropriate initial conditions to find the stable burning flame, instead of finding the more trivial solution of pure mixing. Furthermore, under the conditions of $a^{ign} \leq a \leq a^{ext}$, there is an additional steady-state solution of the problem, that is unstable. Finding the unstable solution needs special numerical methods, as the time dependent solution of the problem would converge to one of the stable solutions.

Steady counterflow diffusion flamelets

Chem1D is used to find steady state solutions for the counterflow diffusion flame configuration at different strain rates. First specific strain rates are initialized with an approximate solution, assuming a mixture fraction profile of Eq. (3.17). These profiles are evolved in time to achieve a smoother initial conditions, that is used in the steady-state solver of Chem1D for finding the stable steady-state solutions. After at least one stable burning solution is found with such a method, it can be used as an initial guess for nearby strain rates using the scaling methods of Fiala and Sattelmayer (2014). I.e.: the simulation domain itself is stretched according to: $x_2 = x_1\sqrt{\frac{a_1}{a_2}}$, and the stretch rate is modified as: $G_2 = G_1\frac{a_2}{a_1}$, where the 1 subscript marks the reference solutions at a different strain, and the 2 subscript the initial guess that is used in the steady solution at a_2 strain rate. Thus, if the strain increases, then the initial condition is compressed along the physical coordinate, and the stretch is increased along the entire domain such, that the boundary conditions are satisfied (see Eq. (3.13)).

To get the unstable solutions, first the extinction point has to be found with high accuracy. The last stable flamelet at a^{ext} is used to initialize the calculation of the unstable flamelets. To find the first unstable solution, special care has to be taken to avoid converging to the stable solution. In this work, this is achieved by applying an artificial diffusion on the last stable flamelet in an unsteady manner for a time frame of $0.03/a^{ext}$, then scaling the resulting profiles with the method of Fiala and Sattelmayer (2014), so they correspond to a strain rate that is below a^{ext}. Such an initial profile is used in the steady-state solver of Chem1D to find an unstable solution. Once the first unstable solution is found, the process is repeated with the latest unstable solution, using a combination of artificial unsteady diffusion and the scaling method to prove the initial solutions at lower strain rates.

Figure 3.11 illustrates some of the characteristics of the steady-state solutions of counterflow diffusion flames. The thermal state of the flamelets is characterized by the temperature of the stoichiometric mixture T_{st} as function of the strain rate a and the stoichiometric scalar dissipation rate χ_{st}. Such plots are often referred to as the "S-curve", referring to the shape formed by the stable burning, and mixing solutions connected by the unstable solutions. (Peters, 2001; Pitsch and Ihme, 2005; Fiorina, Veynante, and Candel, 2015) Furthermore, to describe the rate of reactions at different strain rates, the maximum heat release rate is also displayed. The figure contains data from the stable and unstable solutions for the two different transport models: mixture-averaged transport ("Mix"), and the unity-Lewis number assumption ("Le=1"). The displayed properties are a smooth function of the strain rate and the scalar dissipation rate, and they are second order continuous even at the extinction point. On the stable branch the temperature of the stoichiometric mixture monotonously decreases as the strain rate increases. Then on the unstable branch the trend is reversed, as the temperature decreases from the extinction point towards lower strain rates. The maximum heat release rate of the domain $\max(\dot{\omega}_T)$ increases with the strain for both stable and unstable solutions, except for a small decrease on the stable branch near the extinction point. At any strain, the heat release rate is lower in the unstable branch than in the stable branch.

The difference between mixture-averaged transport and the unity Lewis number assumption is significant. At any strain rate, the unity Lewis number solutions are characterized by much higher heat release rates, and the strain rate and stoichiometric scalar dissipation rate of the extinction point is much larger. As further detailed below, this is related to the faster depletion of the radical species like H_2 in case of

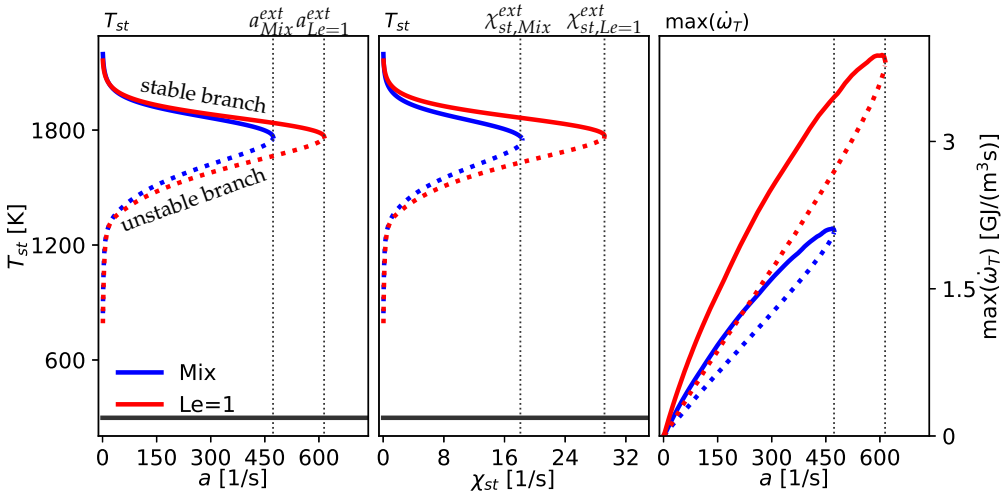

FIGURE 3.11: Properties of 1D counterflow diffusion flamelets of methane and air calculated with Chem1D (Somers, 1994) using the GRI3.0 (Smith et al., 2011) chemical mechanism. The left and middle plots show the temperature at the stoichiometric point T_{st} comparing the two parametrization of the flamelet: a and χ_{st}. The right plot shows the maximum heat release rate along the flamelet. Solid lines indicate the stable solutions, in color the stable burning flamelets, and in black the pure mixing solution. Dotted lines show the unstable solutions. The colors correspond to the two transport models: mixture-averaged transport properties ("Mix") and the unity Lewis number assumption ("Le=1").

the mixture-averaged transport model, since these low Lewis number species diffuse faster towards the fuel and oxidizer.

Besides the global flamelet properties mentioned above (a, χ_{st}, T_{st}), another key property of the counterflow flamelets is a length scale. Based on the analytical solution of mixing in a constant density flow, a mixing length scale can be established using the oxidizer diffusivity:

$$\delta_{diff} = \sqrt{\frac{2\mathcal{D}_t}{a}}. \tag{3.18}$$

As shown in Appendix A, this provides an exact length scale for constant density mixing. For example, the length between the $Z = 0.01$, and $Z = 0.99$ points of the constant density solution is: $\delta_{diff} \left| \text{erf}^{-1}(1 - 2 \cdot 0.99) - \text{erf}^{-1}(1 - 2 \cdot 0.01) \right| = \delta_{diff} \left| -1.64 - 1.64 \right| = 3.28\delta_{diff}$. However, as Fig. A.3 illustrates, considering variable material properties, the reactive mixing layer is significantly thicker than with constant properties. Nevertheless, as discussed below, this diffusive thickness still provides a reasonable length scale, as the ratio of the high temperature mixing thickness and the constant property mixing thickness does not vary significantly. For further details on the scales of non-premixed combustion see section 5.3.1.

The structure of the flamelets is illustrated on Fig. 3.12 along the physical coordinate x of the domain. The simulations are executed on domains adjusted to the selected strain rate: $x \in [-12\delta_{diff}, 8\delta_{diff}]$, however, only the central part is displayed

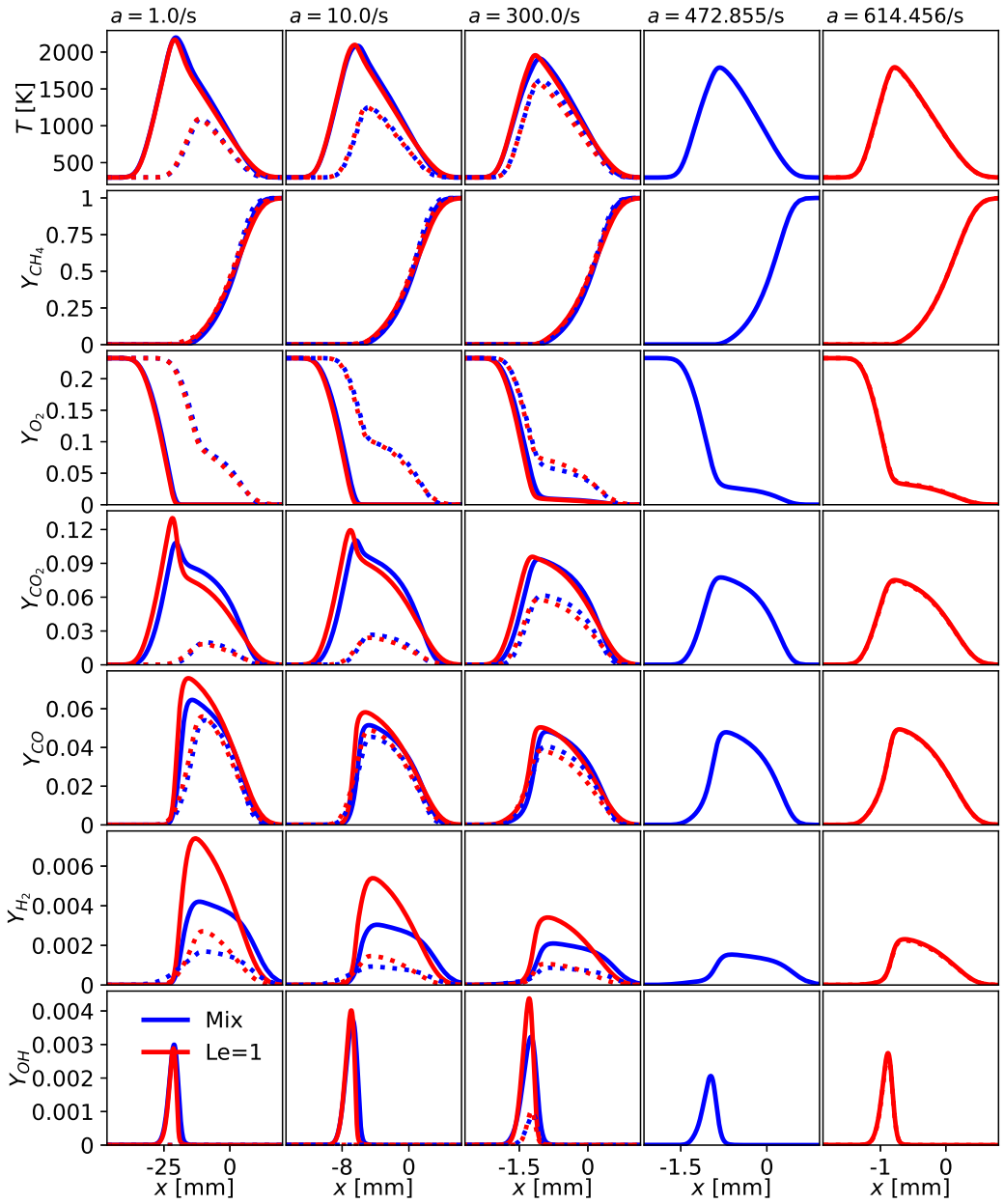

FIGURE 3.12: Typical temperature and species mass fraction profiles of 1D counterflow diffusion flamelets of methane and air computed with Chem1D using the GRI3.0 (Smith et al., 2011) chemical mechanism with mixture-averaged transport properties ("Mix") and the unity Lewis number assumption ("Le=1"). The columns correspond to different strain rates. The different rows show temperature, and the mass fractions of methane, molecular oxygen, carbon dioxide, carbon monoxide, molecular hydrogen, and hydroxyl radical respectively. The solid and dotted lines correspond to the stable and unstable solutions respectively at the given strain rate.

in the $-7\delta_{diff} \leq x \leq 3\delta_{diff}$ range in the figure. Five different strain rates are presented in the different columns of the figure: two considerably low strain rates of $a = 1/\text{s}$ and $a = 10/\text{s}$, a strain in the middle of the stable branch at $a = 300/\text{s}$,

and finally the extinction points of the two transport models $a^{ext}_{Mix} = 472.855/\text{s}$, and $a^{ext}_{Le=1} = 614.456/\text{s}$. The domain length of $10\delta_{diff}$ encompasses all stable and unstable flamelets plotted here. The structure of the stable flamelets at different strain rates shows similarities with the scaling of the x coordinate, thus the δ_{diff} length scale is still a useful measure.

The first row of plots show the temperature along the 1D domain. At a strain rate of $1/\text{s}$ the local gas state is fairly close to equilibrium, and the temperature profile has a convex bend on the rich side, resembling the same phenomena observed on the true equilibrium temperatures displayed in Fig. 3.5. In general at this low strain the flame is fairly thick ($\delta_{diff} = 6.65$ mm), thus interactions between mixtures of different mixture fraction is low. As the strain rate increases, the importance of diffusion across different mixture fraction states rises. Consequently, with higher strains, the peak temperature decreases, and the temperature profile becomes smoother. The temperature profiles of the unstable branch are consistently lower than those of the stable solution. This decreased temperature leads to more compact mixing layers in case of the unstable flamelets, for example at $a = 1/\text{s}$ the unstable flamelets are around half as thick as their stable counterparts.

The second and third rows of Fig. 3.5 show the fuel and oxidizer respectively. The fuel profile is fairly similar in all 14 flamelets, because the variable density effects are highest near the stoichiometric point ($Z_{st} = 0.0552$), as also illustrated in Fig. A.4. The oxidizer profile is the one, where the strain rate takes a bigger effect. At the stable flamelets of $a = 1/\text{s}$ the fuel and oxidizer do not coexists, as each point along the flame is near equilibrium. As the strain rate increases there is more and more oxidizer present on the rich side of the flame. In the case of the unstable flamelets the trend is reversed, and higher oxygen gas mass fractions are found at the lowest strain.

The fourth row of plots displays carbon dioxide, one of the final combustion products. As in the case of the premixed free flamelets, the CO_2 profiles have similarities with the temperature. For $a = 1/\text{s}$ and $a = 10/\text{s}$, the carbon dioxide shows the characteristic peak near the stoichiometric mixture, that is even more pronounced, than it is for temperature. This peak is absent for higher strains, that are further from equilibrium. The rest of the rows show intermediate species. Molecular hydrogen, and carbon monoxide are typically found on the rich side of the flamelets, while the hydroxyl radical is abundant on the lean side and near stoichiometry. The former two radicals are consistently decreasing with strain rate as they are depleted by diffusion more and more. However, the hydroxyl radical shows a different trend, as it is highest at intermediate strain rates. In all cases, the unstable flamelets are characterized by lower mass fractions of CO_2 and intermediate species, than their stable counterparts. The effect of non-unity Lewis numbers is the most pronounced in the H_2 mass fraction. This species diffuses more rapidly towards the oxidizer and the fuel inlets in case of mixture-averaged transport properties, thus the peak value of Y_{H_2} is consistently lower with mixture-averaged transport properties. This lower availability of H_2 is likely a key reason why the case of mixture averaged transport shows consistently lower heat release rates in Fig. 3.11, and why the extinguishing strain rate is lower in this case.

Unsteady counterflow diffusion flamelets

Above, the steady-state solutions of the counterflow diffusion flamelet problem are discussed. The two possible stable solutions (stable burning branch, pure mixing)

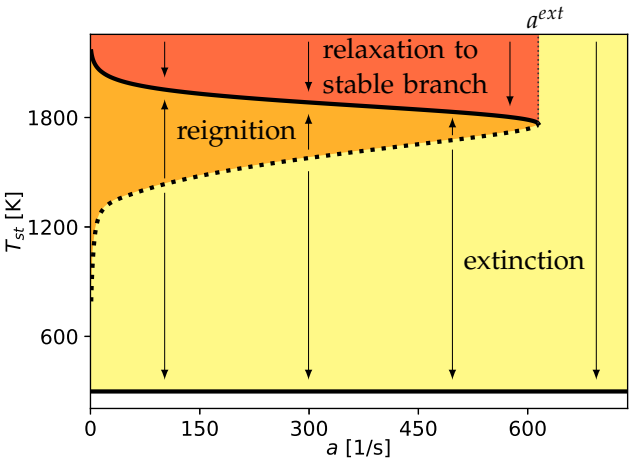

FIGURE 3.13: Illustration of the unsteady counterflow diffusion flamelet behavior on the S-curve at different strain rates.

act as attractors of unsteady solutions as illustrated in Fig. 3.13. (Pitsch and Fedotov, 2001) At low mixing temperatures the unburnt mixture does not auto-ignite, thus the unsteady flamelet can behave the following ways, depending on the initial condition:

1. at $T_{st} < T_{st}^{unstable}$ or $a^{ext} < a$ the unsteady flamelet evolves towards the mixing solution, i.e.: it *extinguishes*,

2. at $T_{st}^{unstable} < T_{st} < T_{st}^{stable}$ and $a < a^{ext}$ the unsteady flamelet evolves towards the stable burning solution, i.e.: it *reignites*,

3. at $T_{st}^{stable} < T_{st}$ and $a < a^{ext}$ the unsteady flamelet evolves towards the stable burning solution, while the peak temperature decreases.

Note, that these regimes are only valid under certain assumptions about the initial condition of the flamelet. For example, using a the flamelet equations in physical space it is found, that reignition is not guaranteed, just because the stoichiometric temperature is sufficiently high. If the stoichiometric layer is thinner than in case of the unstable steady-state flamelet, then the radicals may be depleted too fast and extinction occurs nevertheless.

The limit of extinction and reignition is especially sensitive to the initial condition, as the steady solution separating the two regimes is unstable. If a steady-state unstable flamelet at a higher strain rate is taken as initial condition, and the strain rate boundary condition is suddenly decreased, the unsteady solution may still extinguish. This happens, because the modification of the boundary conditions does not immediately modify the stretch rate and the scalar dissipation rate throughout the simulation domain. Such conditions will not be studied in detail in this work.

Instead, for the purpose of computing reignition or extinction starting from the unstable branch, the initial condition is transformed according to the strain rate ratio using the scaling methods of Fiala and Sattelmayer (2014). This is equivalent to modifying the scalar dissipation rate profile throughout the entire domain, as it is done when the problem is solved in mixture fraction space. (Pitsch and Fedotov, 2001; Naud et al., 2015) In case of extinction at a strain rate above a^{ext} the scaling of

the initial condition is not necessary, and a simple change in the strain rate boundary condition is sufficient.

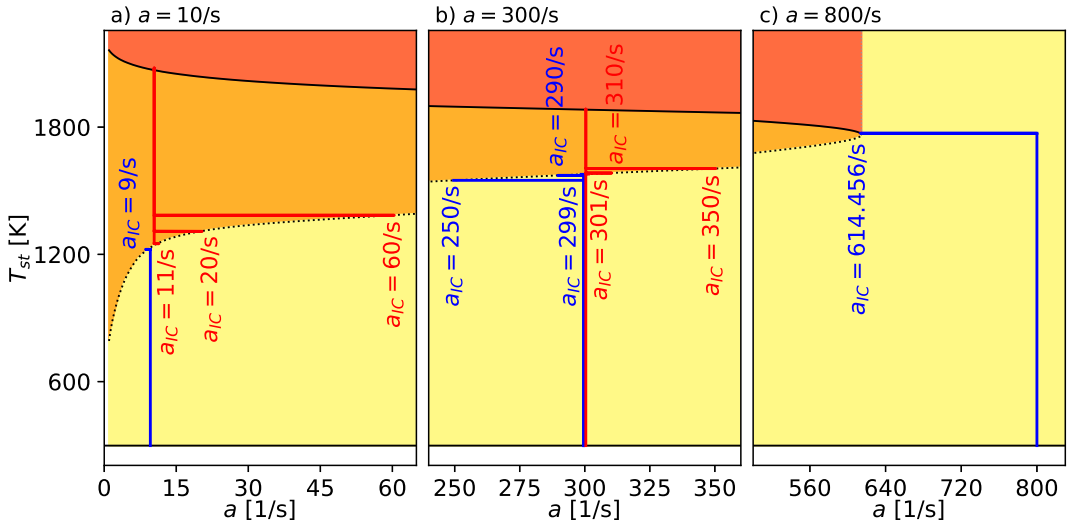

FIGURE 3.14: Behavior of a set of unsteady 1D counterflow diffusion flamelets on the S-curve. The flamelets are of methane and air, computed with Chem1D using the GRI3.0 (Smith et al., 2011) chemical mechanism with the unity Lewis number assumption ("Le=1"). The columns correspond to different strain rates: $a = 10/\text{s}$, $a = 300/\text{s}$, and $a = 800/\text{s}$ from left to right. The initial conditions are indicated on the plots.

A set of these possible unsteady processes is studied at three different strains as illustrated in Fig. 3.14. At a low strain rate of $a = 10/\text{s}$ four cases are evaluated: one extinguishing flamelet starting from the steady-state unstable solution of $a_{IC} = 9/\text{s}$, and three reigniting cases initialized from unstable solutions at strain rates of $a_{IC} \in \{11, 20, 60\}/\text{s}$. At an intermediate strain rate of $a = 300/\text{s}$ six cases are studied, four of them became extinct with initial conditions: $a_{IC} \in \{250, 290, 299, 301\}/\text{s}$, while the ones initialized with $a_{IC} \in \{310, 350\}/\text{s}$ have reignited. Finally, extinction is studied by an unsteady flamelet at $a = 800/\text{s}$ initialized from the steady solution at the extinction point. Note the uncertainty of the reignition process demonstrated by the case with $a_{IC} = 301/\text{s}$. This case is supposedly in the reignition regime, but the small difference between a and a_{IC} is insufficient to guarantee this, and the flamelet extinguishes.

The temporal evolution of these cases is illustrated by their temperature and heat release rate at the stoichiometric point in Fig. 3.15. The first two rows correspond to the reigniting cases at strain rates of $10/\text{s}$ and $300/\text{s}$ respectively. While the third, fourth, and fifth rows show extinguishing cases at strain rates of $10/\text{s}$, $300/\text{s}$ and $800/\text{s}$. The time axis is scaled by the strain rate. The igniting cases are always faster than the extinguishing ones, in terms of the $\tau_{strain} = 1/a$ time scale of the strain. Furthermore, the time scale of the ignition is different at the two studied strains in the applied non-dimensional scale. The range of the horizontal axis is chosen to incorporate most of the temporal evolution. Note the difference between the range of the horizontal axes, the heat release rate plots on the right always correspond to the first 40% of time represented in the left column.

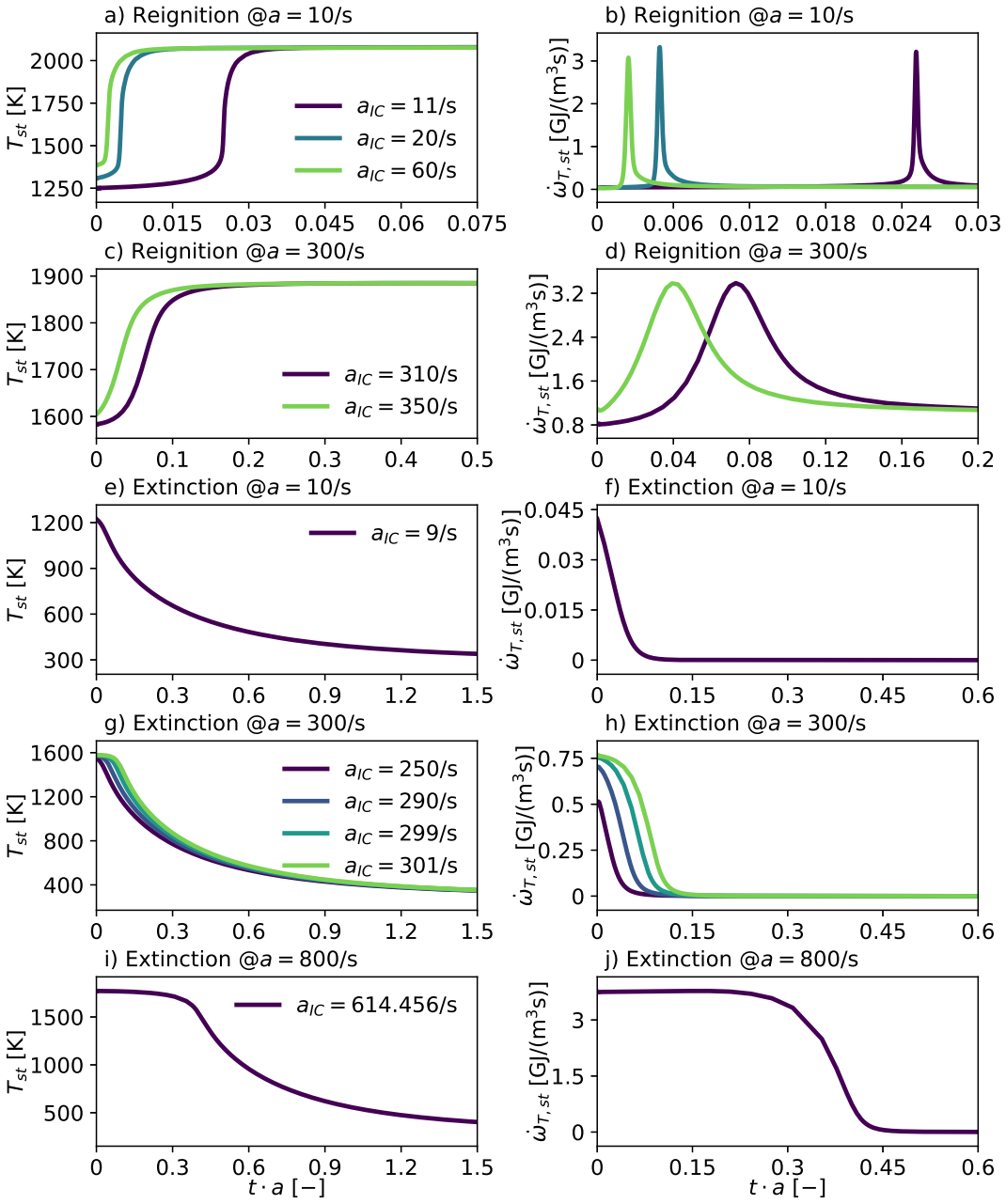

FIGURE 3.15: Behavior of a set of unsteady 1D counterflow diffusion flamelets it time. The flamelets are of methane and air, computed with Chem1D using the GRI3.0 (Smith et al., 2011) chemical mechanism with the unity Lewis number assumption ("Le=1"). The rows correspond to different strain rates. Two columns show the stoichiometric temperature and heat release rate respectively. Colors indicate the initial condition.

The reigniting cases of Fig. 3.15a-d show a lot of variation depending on the initial condition. Higher differences between the strain rate of the steady-state unstable initial condition and the strain rate of the case result in faster reignition. The time instance when the stoichiometric heat release rate reaches its maximum are: 2.51 ms, 0.49 ms, and 0.25 ms for the cases at $a = 10/\text{s}$, and 0.24 ms, and 0.13 ms for the cases at $a = 300/\text{s}$. This time scale is more sensitive to the initial condition than to the

strain rate. For instance, starting from a profile of $a_{IC} = a + 10/\mathrm{s}$ reignition happens only twice as fast at $300/\mathrm{s}$ than at $10/\mathrm{s}$.

The extinguishing cases of Fig. 3.15e-j show much more similarity between them, given the present scaling of the time axis, because τ_{strain} provides a good time scale for the extinction process. A different initialization method is used at $a = 800/\mathrm{s}$ than in the other extinguishing cases, namely at $a = 800/\mathrm{s}$ the strain rate boundary condition is simply increased to $800/\mathrm{s}$ at the start, while in all other cases the scaling methods of Fiala and Sattelmayer (2014) are used. This difference explains why in Fig. 3.15e-h the extinction seems to start instantly, while in Fig. 3.15i-j the flow field first needs to adapt to the new boundary condition before the extinction can start. At $a = 10/\mathrm{s}$ the stoichiometric heat release rate is already quite low initially, and it promptly drops to zero. After this point the solution relaxes to the mixing line. This relaxation is exponential in nature, as the flame stretch rate G does not vary significantly in Eq. (3.10), so the right hand side of the scalar equations is basically proportional to the unknown. As illustrated in Appendix A, the stretch rate is the same order of magnitude as the strain rate, thus the time scale of the extinction event is indeed $1/a$. The sensitivity to the initial conditions is demonstrated in Fig. 3.15g-h for $a = 300/\mathrm{s}$. The stoichiometric heat release rate drops to zero quite quickly in this case as well. After this initial drop in reactivity, all the cases behave rather similarly.

Finally, the flame structure of these unsteady flamelets is compared on Fig. 3.16 by plotting the local heat release rate as function of the local temperature at specific points of the flamelets. The points along the flamelet are identified by a mixture fraction value corresponding to a very lean mixture: $\phi = 0.3$, another mixture on the lean side $\phi = 0.8$, the stoichiometric mixture: $\phi = 1.0$, a rich mixture: $\phi = 1.5$, and an even richer mixture: $\phi = 3.0$. These are represented by the different rows of Fig. 3.16. This range of mixture fractions represents well the reactive part of the domain, since at the leanest (first row) and richest (last row) studied conditions the heat release rate is significantly lower than at the stoichiometric point (middle row). The three columns are corresponding to the three different studied strain rates: $a = 10/\mathrm{s}$, $a = 300/\mathrm{s}$, and $a = 800/\mathrm{s}$. For comparison the steady state stable and unstable solutions are plotted with a gray dotted line. All the flamelets depart from this line, as the unstable branch is used as initial condition. Furthermore, the reigniting flamelets also terminate on the same line, since they evolve towards the stable burning branch.

The low strain reigniting cases ($a = 10/\mathrm{s}$), represented by the first column of plots, are particularly interesting, as in these cases the initial condition have a significant effect on the trajectory of the unsteady flames on the $\dot{\omega}_T - T$ plane. As the magnified plots at $\phi = 1$ and $\phi = 1.5$ illustrate, these differences originate from the shape of the steady unstable branch. This branch exhibits a local minimum and maximum heat release rate on the $\dot{\omega}_T - T$ plane at low strain rates. The case with $a_{IC} = 60/\mathrm{s}$ is initialized near the local minimum, while the other two reigniting cases: $a_{IC} = 11/\mathrm{s}$ and $a_{IC} = 20/\mathrm{s}$, are closer to the local maximum. Thus the latter two cases start from higher initial heat release rate, and they consistently show higher $\dot{\omega}_T$ in the first half of the reignition event. At this strain rate the peak heat release rate is always below the peak observed in the steady-state cases. Near stoichiometry this is just a small difference, but at the leanest and richest points, the flame basically evolves straight towards the steady-condition without a significant increase of the heat release rate between. Overall, at this low strain rate the reignition is governed by strong reactions near stoichiometry with slower processes lagging behind on the rich and lean side.

The cases at $a = 300/\mathrm{s}$ do not show such sensitivity to the initial condition, as

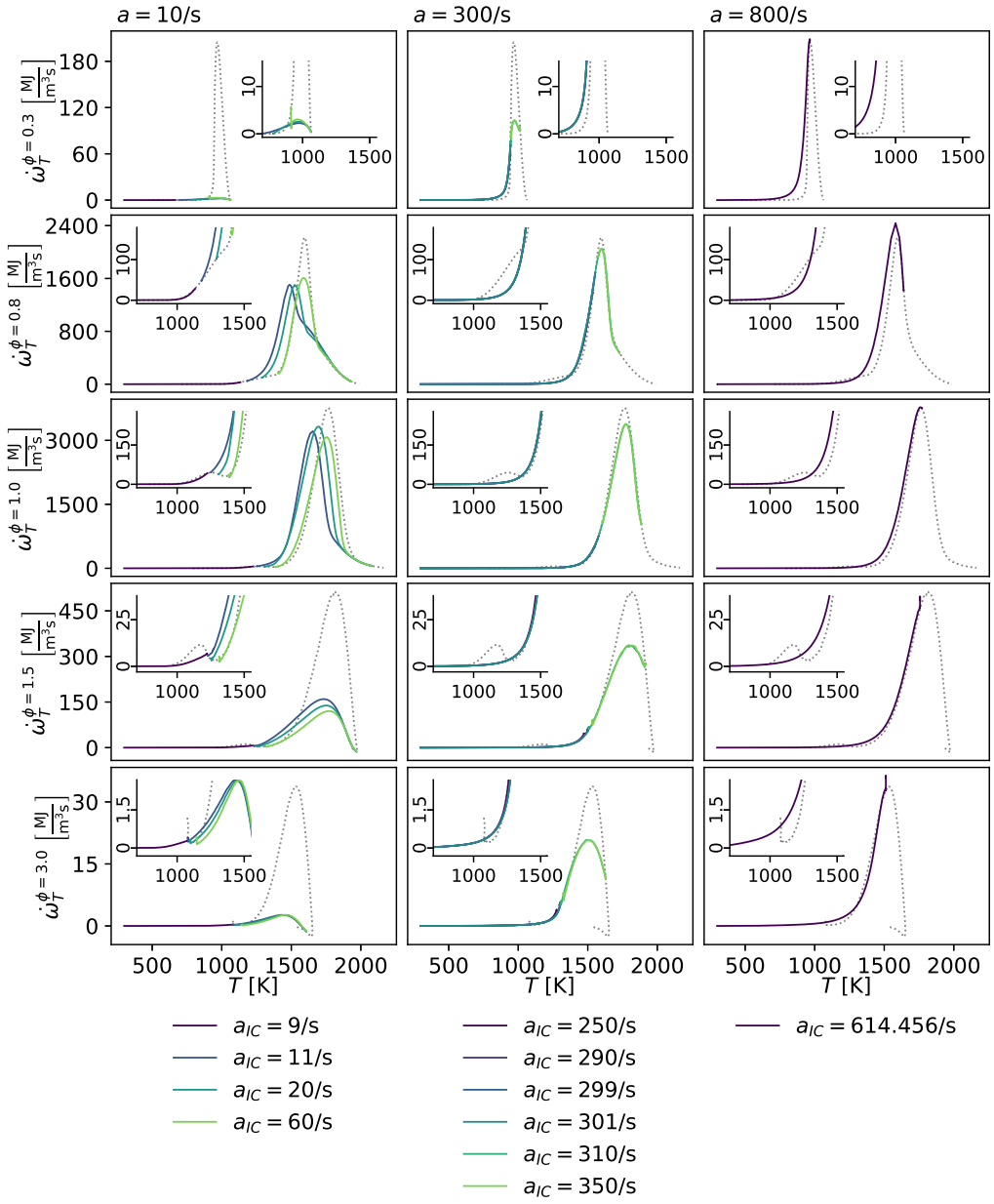

FIGURE 3.16: Flame structure of unsteady extinguishing and reigniting 1D counterflow diffusion flamelets. The flamelets are of methane and air, computed with Chem1D using the GRI3.0 (Smith et al., 2011) chemical mechanism with the unity Lewis number assumption ("Le=1"). The rows correspond to different position along the flame identified by specific equivalence ratios: $\phi \in \{0.3, 0.8, 1.0, 1.5, 3.0\}$ respectively. The columns correspond to different strain rates: $a \in \{10, 300, 800\}/\mathrm{s}$. The dotted line represent the stationary solutions of the stable and unstable branch.

at first the trajectory of the reignition follows closely the unstable solutions. Consequently all the solutions in the middle column of Fig. 3.16 overlap. This means, that the time till peak heat release (0.24 ms and 0.13 ms) only differs, because this is the time the reignition takes to move from one initial condition ($a_{IC} = 310/\mathrm{s}$) to the

next more reactive initial condition ($a_{IC} = 350/\text{s}$.) The heat release rate profile approaches the steady-state solutions more closely than at the low strain case, and the peak $\dot{\omega}_T$ occurs at a temperature fairly close to the steady state solution, although the value of the peak is notably lower. At this strain rate, the leanest and richest points exhibit significant heat release rates unlike in the low strain case, because the stronger interaction between different mixture fractions eliminates the lagging of the very rich and very lean parts.

Finally, the extinction cases are compared. At $a = 10/\text{s}$ extinction is fairly simple, since the initial condition is already quite close to the mixing solution. The unsteady extinguishing solutions only deviate significantly from the steady unstable solutions at the two rich conditions, where the local maximum of the heat release is not followed by the unsteady process. Similarly, the extinction events at $a = 300/\text{s}$ differs the most from the steady solution near this local maximum. With the further increase of the strain rate ($a = 800/\text{s}$) the heat release rate is predominantly higher at every temperature than the steady solutions.

The above demonstration provides insight to the unsteady processes of counterflow diffusion flames. The influence of the initial condition is imperative not only in determining the final state of the flamelet (reignition or extinction), but it also affects the time scales and the unsteady trajectory on the $\dot{\omega}_T - T$ plane. This highlights the importance of history effects on the flame behavior as also pointed out in the recent work of Foale (2022). Overall, the reigniting cases do not have sufficient time to relax to the steady-state solution during their evolution, thus they are characterized by lower heat release rates. Meanwhile, the high strain extinguishing cases shows the opposite trend, namely, the gas mixtures stay highly reactive even at lower temperatures.

Radiative heat loss in counterflow diffusion flamelets

A simple method to include reduced enthalpy states in the counterflow diffusion flame configuration is to include a negative source term on the right hand side of the enthalpy equation. In this work Chem1D is used with a source term, that corresponds to optically thin radiative interaction between the gas mixture and a constant temperature far-field treated as a black body. The enthalpy equation of the configuration is simply appended with this source term S_h^{rad}:

$$\frac{\partial \rho h}{\partial t} + \frac{\partial \rho u h}{\partial x} - \frac{\partial}{\partial x}\left[\rho \sum_{k=1}^{N_C}\left(\mathcal{D}_t Y_k \frac{\partial h_k}{\partial x} + \mathcal{D}_k h_k \frac{\partial Y_k}{\partial x}\right)\right] = -\rho G h + S_h^{rad}. \tag{3.19}$$

The optically thin treatment means, that the radiative energy emitted at a given point of the flame is not re-absorbed in a different point. Thus, the heat loss term takes the following form, being approximately proportional to the fourth power of the local temperature:

$$S_h^{rad} = -4 c_{rad} \kappa_P \sigma_{SB} (T^4 - T_{ff}^4), \tag{3.20}$$

where c_{rad} is a modeling constant, which is 1 in physically meaningful cases and higher than 1 in cases artificially forced to have more radiation. Furthermore, κ_P is the Planck mean absorption coefficient of the gas mixture, σ_{SB} is the Stefan–Boltzmann constant, and $T_{ff} = 300$ K is the far field temperature. (Modest and Mazumder, 2013, §11.11, §15.1, §20.3) The Planck mean absorption coefficient of the gas is calculated locally based on the gas composition, temperature, and pressure. Only four

species are considered to participate in radiation: CO_2, H_2O, CO, and CH_4, since these species are the most relevant for the thermal radiation of methane flames. (Lammers and De Goey, 2004) However, the first three species contribute to radiative heat losses in all hydrocarbon flames, thus the framework of Chem1D can be used with other fuel compositions as well. To yield the Planck mean absorption coefficient of the gas mixture, the individual absorptivity of these species is calculated using polynomials in temperature, these are multiplied by the partial pressure of the species and the contributions are summed.

The factor c_{rad} is a user input of Chem1D allowing the arbitrary scaling of this radiative source term. Using this factor different enthalpy levels can be reached. Such flamelet solutions are illustrated on Fig. 3.17, showing the stoichiometric temperature and the maximum heat release rate as function of the strain rate. Linear and logarithmic scales are both used for the strain rate axis, the former to provide a comparison with the adiabatic flamelets presented in Fig. 3.11, and the latter to emphasize the effect of radiation at low strain rates. The figure highlights how the effect of the radiative source term diminishes with increasing strain, considering the Lagrangian residence time of fluid particles, which is approximately proportional to $1/a$. At higher strain rates the residence time of the gas decreases, thus there is less time for radiative heat loss to take effect. (Ihme and Pitsch, 2008a)

Radiation affects the stable and unstable branches differently. The stable branch consistently exhibits lower and lower stoichiometric temperatures as the radiative heat loss is scaled up. Furthermore, since the heat loss effects are larger at lower strains, T_{st} has a maximum at an intermediate strain rate. Nevertheless, the higher strain rate cases are affected as well, which manifests in the decrease of the extinguishing strain rate.

The effect on the unstable branch is less straightforward. Firstly, the temperatures are quite low even in the adiabatic case ($c_{rad} = 0$), and the radiative heat loss scales with the temperature to the fourth power, so the heat loss is significantly lower on the unstable branch than on the stable one at any c_{rad} value. Secondly, these cases are unstable, thus to maintain the steady state while also dissipating energy through radiative heat loss, the heat release rate has to be higher than in the adiabatic case. In some parts of the unstable branch this evokes an inverted effect of the radiation scaling: the stoichiometric temperature increases as the radiative heat loss is scaled up. These conditions have to be reached, because the heat release rate has to be sufficiently larger to cope with the radiative heat loss, and in some cases this is only possible at higher temperatures where the mixture is more reactive. (See the Arrhenius law: Eq. (2.99).) As a result, at certain radiation scaling levels the "S-curve" is transformed into a loop, characterized by both a lowest and highest strain rate where stable burning is possible.

The behavior of these flamelets is further illustrated in Fig. 3.18. This figure present the temperature (T), the enthalpy (h), the mass fraction of molecular oxygen (Y_{O_2}), carbon dioxide (Y_{CO_2}), carbon monoxide (Y_{CO}), molecular hydrogen (Y_{H_2}), and hydroxyl radical (Y_{OH}), and the heat release rate ($\dot{\omega}_T$) along the flamelet as function of the mixture fraction (Z). Four different strain rates are shown: $a \in \{1, 10, 50, 300\}/\mathrm{s}$ with different levels of possible enthalpy deficit. Each plot includes two additional curves for reference corresponding to two equilibrium conditions: the adiabatic equilibrium illustrating the zero strain rate limit of the adiabatic case ($a \to 0/\mathrm{s}$, $c_{rad} = 0$), and the isothermal equilibrium showing the highest possible heat loss achievable at a certain mixture fraction (See Fig. 3.9). Only the stable branch with the unity Lewis number assumption is displayed for simplicity. The

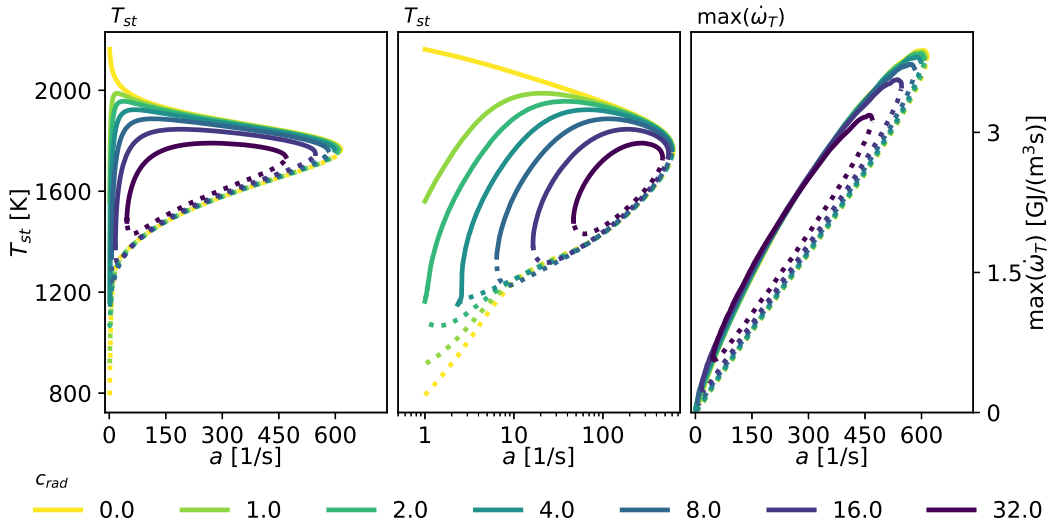

FIGURE 3.17: Properties of 1D counterflow diffusion flamelets of methane and air at different enthalpy levels calculated with Chem1D (Somers, 1994) using the GRI3.0 (Smith et al., 2011) chemical mechanism with the unity Lewis number assumption. The left and middle plots show the temperature at the stoichiometric point T_{st} as function of the strain rate a using linear and logarithmic scales on the horizontal axis. The right plot shows the maximum heat release rate along the flamelet. Solid lines indicate the stable solutions, and dotted lines show the unstable solutions. The colors correspond to the scaling of the radiative term as indicated in the legend.

mixture fraction is limited to $Z \in [0, 3Z_{st}]$ corresponding to an equivalence ratio interval of $\phi \in [0, 3.4]$ resembling the flammability range of the premixed flamelets. (See Fig. 3.8 and Fig. 3.9.) For reference the stoichiometric mixture fraction is indicated by a vertical line.

In general, as higher and higher heat loss is imposed, the flamelet solutions resemble more the isothermal equilibrium and less the adiabatic equilibrium. This is particularly visible at low strain rates, where the flamelets are closest to the respective equilibria. As the strain rate increases, the effect of the heat loss diminishes, and the solutions with different c_{rad} become more alike.

In particular the first and second row of plots in Fig. 3.18 show how the temperature monotonously decreases as the enthalpy deficit is scaled up. Meanwhile the enthalpy follows the same trend except one outlier: $a = 1/\mathrm{s}, c_{rad} = 2.0$. The trend is reversed in this single case, because it is not possible to reach the isothermal equilibrium by radiative heat loss. As explained above in relation to Tab. 3.1, the isothermal equilibrium conditions correspond to a mixture of final combustion products (H_2O and CO_2) and fresh reactants (N_2, O_2 and CH_4) at the mixture temperature. However, the counterflow configuration is characterized by a limited Lagrangian residence time of the fluid particles, which is proportional to $1/a$. Thus, reactions need to take place at a rate comparable to the scalar dissipation rate, associated to this finite residence time, to maintain a sufficient level of radicals, and keep the mixture in a reactive state. These non-zero rates are only possible at higher temperatures, thus the isothermal equilibrium cannot be reached by means of radiation. A similar limitation is observed in case of the burner-stabilized flamelets, illustrated in Fig. 3.9 where the enthalpy of the last stable flamelets at $m/\left(\rho^u S_L\right) = 0.01$ is approximately

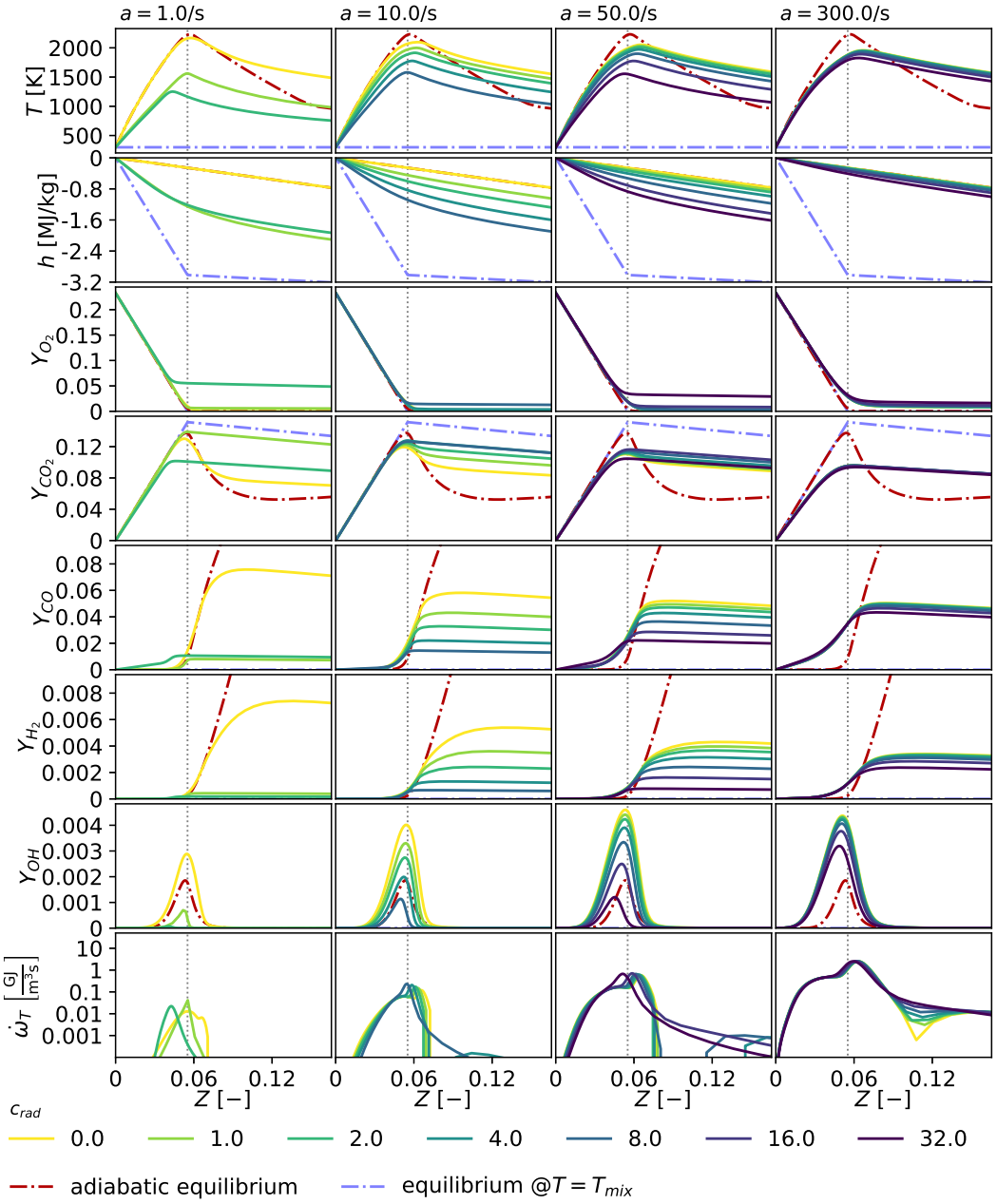

FIGURE 3.18: Typical temperature and species mass fraction profiles of stable 1D counterflow diffusion flamelets of methane and air computed with Chem1D using the GRI3.0 (Smith et al., 2011) chemical mechanism with the unity Lewis number assumption ("Le=1") including different scalings of the radiative heat loss term. The columns correspond to different strain rates. The different rows show temperature, enthalpy, the mass fractions of molecular oxygen, carbon dioxide, carbon monoxide, molecular hydrogen, and hydroxyl radical, and the heat release rate respectively.

halfway between the adiabatic and isothermal equilibrium enthalpy.

The O_2 mass fraction profiles in the third row of plots are fairly simple. The oxygen molecules are mostly consumed on the lean side of the flame, and only low quantities are present on the rich side. As the strain rate increases more and

more oxygen penetrates to the rich side. In this case, three outliers can be identified, characterized by significantly higher Y_{O_2} on the rich side than other flamelets: i) $(a = 1/\text{s}, c_{rad} = 2.0)$, ii) $(a = 10/\text{s}, c_{rad} = 8.0)$, and iii) $(a = 50/\text{s}, c_{rad} = 32.0)$. These outliers are a product of the same process as described in the case of enthalpy: at a certain c_{rad} value the flame is cooled down so much, that the consumption of O_2 is disrupted, thus it can be present on the rich side of the flame.

The transition from resembling more the adiabatic equilibrium to resembling the isothermal one is best illustrated by the fourth row of plots showing carbon dioxide mass fraction. At $a = 1/\text{s}$ the adiabatic flamelet follows closely the adiabatic equilibrium Y_{CO_2} curve, while the case with $c_{rad} = 1$ approaches the isothermal equilibrium very closely. Meanwhile switching to $c_{rad} = 2$ at this strain rate already impedes the reactions substantially, resulting in outlier i) with significantly lower amounts of CO_2. At $a = 10/\text{s}$ the cases are concentrated in a narrower band, even with the wider range of radiation scaling. The adiabatic flamelet resembles less the adiabatic equilibrium, and the higher heat-loss flamelets cannot approach the isothermal equilibrium as much. The above mentioned outlier ii) has overlapping Y_{CO_2} levels with the case of $c_{rad} = 4$. The band of possible Y_{CO_2} values further shrinks at $a = 50/\text{s}$. In this case outlier iii) is more visible, as the carbon dioxide mass fraction drops significantly transitioning from $c_{rad} = 16$ to 32.

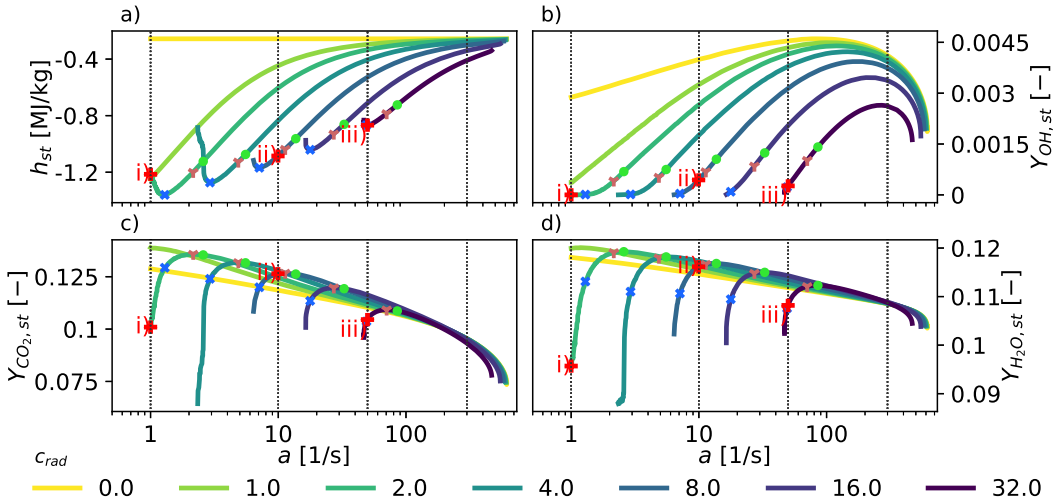

FIGURE 3.19: Stoichiometric enthalpy and species mass fractions of stable 1D counterflow diffusion flamelets of methane and air computed with Chem1D using the GRI3.0 (Smith et al., 2011) chemical mechanism with the unity Lewis number assumption ("Le=1") including different scalings of the radiative heat loss term. The different plots are: a) enthalpy, b) hydroxyl mass fraction, c) carbon dioxide mass fraction, d) water mass fraction. Grey vertical lines indicate the strain rates: $a \in \{1, 10, 50, 300\}/\text{s}$, while red crosses mark the outliers identified at these strain rates. Other symbols mark the flamelets associated to a specific local extrema along a constant c_{rad}: blue x: $\min(h_{st})$, orange triangle: $\max(Y_{CO_2,st})$, green circle: $\max(Y_{H_2O,st})$.

The intermediate species (CO, H_2, OH) behave in a similar manner, but they can be described easier, as at the isothermal equilibrium conditions these species are fully absent. Consequently their mass fraction consistently decreases as the radiative heat loss is scaled up, except of the outliers. Finally, the heat release rate $\dot{\omega}_T$ is

represented in a logarithmic scale so the different strain rate cases can be presented using the same axis. With the scale-up of the radiative heat loss, the heat release rate has to stay at similar values or even increase in order to compensate for the heat loss and maintain the stable burning.

The three outliers identified on Fig. 3.18 are further studied in Fig. 3.19. The figure indicates the outliers in relation to distinguished points corresponding to the minimum of enthalpy and the maxima of carbon-dioxide and water mass fraction at a certain c_{rad} value at the stoichiometric point. Out of these three different kind of extrema, the minimum enthalpy point is located at the lowest strain rates, and the maximum of the two reaction products is situated at strain rates above the enthalpy limit. These latter two extrema are fairly close to each other. The outliers observed above are related the local maxima of the reaction products, as this was the measure of identifying them in Fig. 3.18. The representation in Fig. 3.19 explains why outlier i) shows the peculiar behavior in enthalpy, while outliers ii) and iii) are only affected in terms of species mass fractions: outlier i) is the only one of these three cases that is located at a strain below the enthalpy minimum.

3.1.4 Summary of flamelet configurations

Free and burner-stabilized premixed flamelets and counterflow diffusion flamelets with and without radiation are described above in section 3.1. These arrangements are fundamentally different in terms of the direction of heat and species transport along the Y_c and Z spaces. In premixed flamelets the mixture fraction is constant (except if preferential diffusion is considered, where small differences arise as seen in Fig. 3.4). Thus, the prevailing difference between gas states along the premixed flamelet are in terms of the reaction progress, and the flame is fundamentally characterized by the transport of heat and radicals from the burnt gases into the fresh reactant mixture. Meanwhile in the counterflow diffusion flamelets the reaction products are located in the middle of the domain, and heat and radicals are diffused towards the fresh fuel and oxidizer. This transport is simultaneous with the net transport of mixture fraction from the fuel towards the oxidizer.

Foreshadowing the usage of tabulated chemistry models, Tab. 3.2 arranges the different adiabatic flamelets presented of this section in a structure. In premixed free flamelets, the reactions advance as the gas mixture is convected through the domain. The individual flamelet problems are characterized by the inlet mixture, and the propagation speed is a dependent quantity of the setup. Accordingly, the only degree of freedom of premixed free flamelets is the inlet state, which, in case of a predefined fuel and oxidizer composition, reduces to a single parameter: the mixture fraction (or equivalence ratio) as presented in Fig. 3.5.

The behavior of the presented counterflow diffusion flamelets is different, as the mixing happens within the domain, thus all possible mixture fractions can be found in each flamelet. Steady cases are uniquely defined by their strain rate and the branch they belong to (stable, unstable, mixing). Thus, different levels of reaction progress are reached by varying the strain rate, as Fig 3.11 illustrates. In case of the stable branch, the reactions are more advanced at low strain rates, since the higher residence times allow relaxation to the adiabatic equilibrium. Meanwhile, the behavior is inverted in case of unstable branch, that approaches pure mixing at low strain rates. This may be interpreted as lower strains allowing a higher deviation from the stable burning solutions, since at low strains a small amount of heat release and radical production is enough to maintain this unstable steady state, since these conserved quantities are depleted at a slower rate.

TABLE 3.2: Illustration of adiabatic flamelet configurations.

Premixed free flamelets	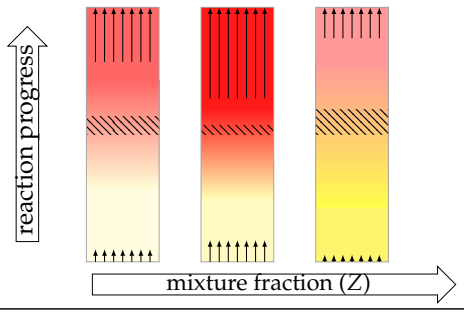
Stable counterflow diffusion flamelets at different strain rates	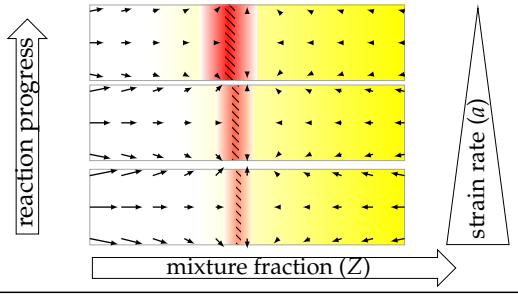
Unstable counterflow diffusion flamelets at different strain rates	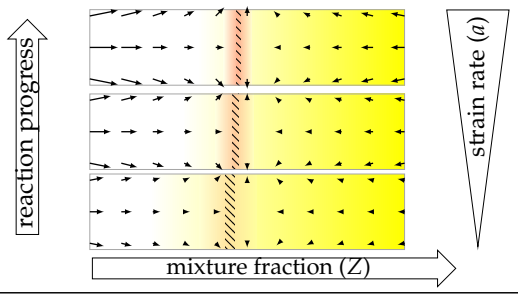
Extinguishing counterflow diffusion flamelets at constant strain rate	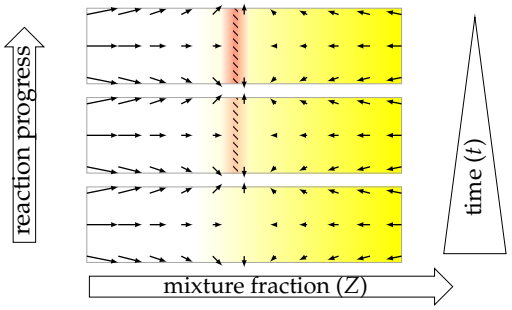
Reigniting counterflow diffusion flamelets at constant strain rate	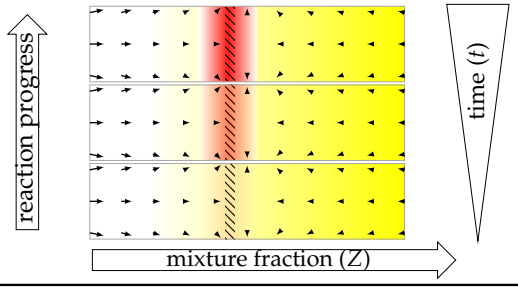

In the transient extinguishing and reigniting counterflow diffusion flamelets, the temporal evolution is not only dependent on the strain rate of the case, but there is also a strong influence associated to the initial condition. The most important aspect determined by these two constraints, is whether the flamelet will reignite or extinguish, as demonstrated in Fig. 3.14. The initial condition influences the time

scale of the unsteady process and in some cases even the underlying flame structure. This influence is especially significant in case of the reignition, where the time to peak heat release rate (ignition delay time) is very sensitive to the initial condition.

TABLE 3.3: Illustration of flamelet configurations at decreased enthalpy levels.

Premixed burner-stabilized flamelets at constant mixture fraction	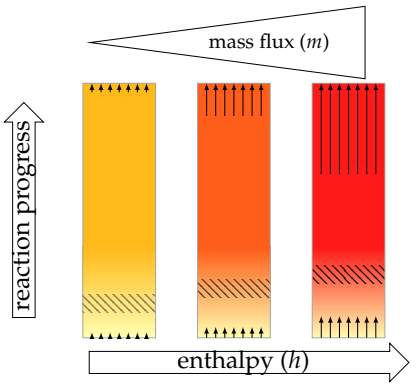
Counterflow diffusion flamelets with radiation at constant strain rate	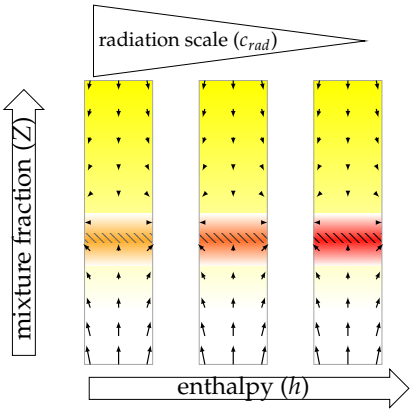

This section also introduces the concept of heat loss in premixed and counterflow diffusion flamelet configurations. The two studied methods are illustrated in Tab. 3.3: burner-stabilization for premixed flamelets, and a radiative heat loss term for the counterflow diffusion flamelets. The former modifies the enthalpy at the inlet of the premixed flamelet domain, by imposing the temperature of the inlet while allowing the presence of partially reacted gas states on this boundary. And the latter achieves reduced levels of enthalpy by including a negative term on the right hand side of the enthalpy transport equation.

Both of these enthalpy reduction methods suffer from a similar limitation, namely: stable burning becomes impossible when the mass flux decreases or the radiation scale increases beyond a certain level. The maximum attainable enthalpy deficit of valid flamelet solutions is compared to the theoretical limit of isothermal equilibrium in Fig. 3.9 and Fig. 3.18. In burner-stabilized flamelets of the examples shown in this section, approximately half of the maximum enthalpy deficit can be realized near stoichiometry. In case of the counterflow diffusion flamelets with radiative heat loss the enthalpy deficit varies along the domain, since radiation takes higher effect in the high temperature regions. Also, it is highly dependent on the strain rate. Nevertheless, at low strain rates the enthalpy limitations of feasible flamelets are quite similar to the limit observed in the burner-stabilized simulations.

Figure 3.18 also highlights an intriguing difference between the behavior of the burner-stabilized flamelets and the counterflow flamelets at decreased enthalpy levels. In burner-stabilized flamelets, the decrease of heat release is closely linked to the decrease of hydroxyl radical concentration as the mass flux m is reduced. (See Fig. 3.7) Meanwhile, as higher and higher radiative enthalpy loss is imposed on the counterflow configuration, the hydroxyl radical mass fraction decreases, but the heat release rate is maintained on similar levels. This phenomenon is further examined, by comparing the global heat release rate in the 1D domains, defined as:

$$\Omega_T = \int_{x_{min}}^{x_{max}} \dot{\omega}_T \mathrm{d}x. \tag{3.21}$$

Figure 3.20 compares the global heat release rate of the burner-stabilized and counterflow diffusion flamelet configurations as function of the equivalence ratio for the former, and the strain rate for the latter.

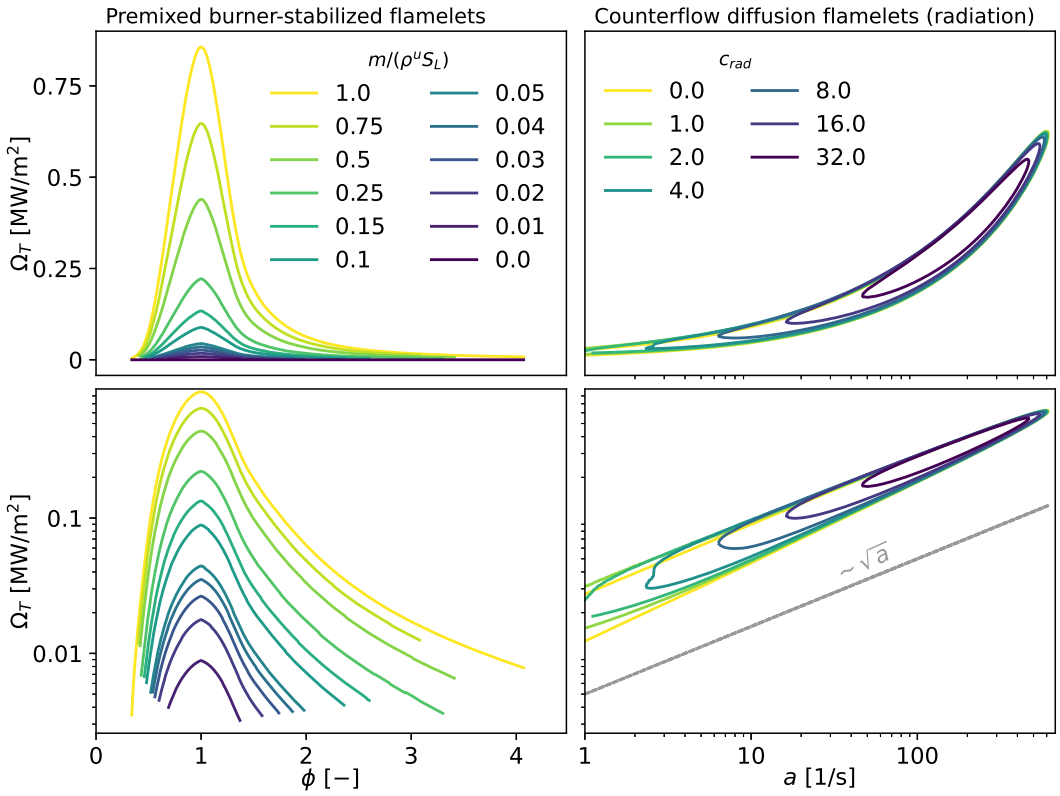

FIGURE 3.20: Global heat release rate of 1D flamelets of methane and air using the GRI3.0 (Smith et al., 2011) chemical mechanism with the unity Lewis number assumption ("Le=1"). Premixed burner-stabilized flamelets (left) are compared to counterflow diffusion flamelets (right) at various enthalpy levels indicated by the legend. Linear (top) and logarithmic (bottom) scales are used for the global heat release rate to highlight the effects at low heat release rate.

The global heat release rate of the burner-stabilized flamelets is a quasi-linear function of the mass flux m, since, in the cases where stable burning is possible, the fuel is consumed as much as possible and converted to a set of combustion products. The chemical energy supplied to the system is a linear function of m, and the global heat release rate in the domain can only deviate from this linear relation to the extent

of modest variations in the outlet composition. Meanwhile, as Fig. 3.20 illustrates the behavior of the counterflow diffusion flamelets, the stable branch solutions (higher heat release) are almost entirely overlapping in the regions where stable burning is possible. The small differences that are observed, are located near the extinction point and the lower limit of the strain rate. The unstable branch exhibits slightly higher sensitivity to c_{rad}, but the general trend is similar. The effect of radiation is relatively small on the heat release of steady burning flamelets, as long as burning solutions exists. However, it can be the determining factor between stable burning and heat loss induced extinction.

Another aspect displayed on Fig. 3.20 is the scaling of the global heat release rate with the strain rate in the steady counterflow diffusion flamelets. The apparent $\propto \sqrt{a}$ scaling stems from the simultaneous change of the flame thickness and local heat release rates. The former approximately follows a relation of $\delta_{th} \propto \delta_{diff} \propto \sqrt{1/a}$, while the latter is more close to linear scaling as suggested by Fig. 3.11. Consequently, the integral of heat release still raises with the strain rate, but following a square root relation.

Overall, the discussed adiabatic and decreased enthalpy flamelet configurations are capable of representing different gas states associated to the combustion of exactly two inlet streams: fuel and oxidizer. The structured tabulation of these gas states is discussed in the rest of this chapter.

3.2 Mapping of adiabatic flamelets to the control variable space

The variables introduced in section 2.2: mixture fraction Z, progress variable Y_c, and enthalpy deficit $|\Delta h|$ may identify a given gas mixture uniquely under certain conditions. Firstly, the unity Lewis number assumption greatly simplifies the treatment of Bilger's mixture fraction, as in this case, it is straightforward to compute it from detailed chemistry calculations (Eq. (2.30)), and it is likewise simple to formulate a transport equation for the stand-alone usage, since Eq. (2.117) only depends on material properties and solved unknowns.

Furthermore, in case of adiabatic flamelets, the enthalpy deficit is constant zero by definition, thus Z uniquely defines the value of the enthalpy (Eq (2.46)). However, the definition of the progress variable (Eq. (2.45)) is an open question. Once an appropriate definition is found, the flamelet sets of Tab. 3.2 can be mapped on the $Z - Y_c$ plane.

3.2.1 Progress variable definitions

For hydrocarbon combustion, different progress variable definitions were proposed in the literature. These mostly involve the two final reaction products of hydrocarbons: CO_2 and H_2O, and two of the most abundant intermediate species: CO and H_2. As illustrated throughout section 3.1, when the reactions advance towards equilibrium, the final products can show a local maxima under rich conditions. However, CO and H_2 may provide a monotonically increasing value at these conditions. A non-exhaustive list of progress variable definitions is presented in Tab. 3.4. Note, that this table excludes a number of conditions. Firstly, studies on hydrogen combustion are not mentioned, as in this case H_2O appears to be an adequate progress variable. (Van Oijen and De Goey, 2000; Regele et al., 2013) Secondly, many works studying autoigniting conditions are likewise excluded, as in this case it is common practice to include hydroperoxyl (HO_2) (Bekdemir et al., 2013; Egüz et al., 2014;

Naud et al., 2015; Zhang et al., 2019; Ceriello et al., 2020; Zhang et al., 2020b) or formaldehyde (CH_2O) (Bekdemir, Somers, and De Goey, 2011; Wehrfritz et al., 2016; Zhang et al., 2020b) in the progress variable definition. These intermediate species can provide an indicator for the low temperature combustion, and hence play a crucial role in correctly capturing the ignition delay time.

The diversity of definitions in Tab. 3.4 indicates, that various approaches can provide the satisfactory accuracy for the parametrization of the flamelet states. Thus, selecting an adequate linear combination of species is not an obvious task. This prompted various studies, aiming to optimize the progress variable definition. Ihme, Shunn, and Zhang (2012) introduced an optimization approach and assessed different a_k weights for the selected species of Pierce and Moin (2004): $Y_c = a_{CO_2} Y_{CO_2} + a_{H_2O} Y_{H_2O}$, for the species of Fiorina et al. (2003): $Y_c = a_{CO_2} Y_{CO_2} + a_{CO} Y_{CO}$, and for their preferred set of species: $Y_c = a_{CO_2} Y_{CO_2} + a_{CO} Y_{CO} + a_{H_2O} Y_{H_2O} + a_{H_2} Y_{H_2}$. They defined an objective function that promotes the strict monotonic growth of progress variable in counterflow flames, and found, that the optimal weights are highly dependent on the studied set of flamelets. Another effort on finding an optimal definition was performed by Najafi-Yazdi, Cuenot, and Mongeau (2012) using principal component analysis on premixed free flames. Such optimization approaches have since been executed, including an approach developed as part of the present work. (Both, Mira, and Lehmkuhl, 2021b) However, the continued popularity of the more classical definitions is evident from the more recent references listed in Tab. 3.4. The case-to-case variation of the optimized weights and the lack of explicable underlying physical meaning seem to make these approaches less desirable.

TABLE 3.4: Progress variable definitions for hydrocarbon combustion.

Progress variable definition	Reference
T	(Libby and Williams, 1980)
	(Bradley et al., 1988)
	(Bajaj, Ameen, and Abraham, 2013)
$-Y_{O_2}$	(Vreman, Bastiaans, and Geurts, 2009)
$-Y_{fuel}$	(Bray, Domingo, and Vervisch, 2005)
	(Ferraris and Wen, 2007)
	(Langella, Swaminathan, and Pitz, 2016)
Y_{H_2O}	(Langella, Swaminathan, and Pitz, 2016)
Y_{CO_2}	(Delhaye et al., 2008)
	(Kuenne, Ketelheun, and Janicka, 2011)
	(Albrecht et al., 2008)
	(Darbyshire and Swaminathan, 2012)
	(Pantangi et al., 2014)
	(Avdić et al., 2017)
	(Sitte, 2019)
$Y_{CO_2} + Y_{H_2O}$	(Pierce and Moin, 2004)
	(Ventosa Molina, 2015)
	(Hu, Olguin, and Gutheil, 2017)
$Y_{CO_2} + Y_{CO}$	(Fiorina et al., 2003)
	(Fiorina et al., 2005a)
	(Fiorina et al., 2005b)

Continued on next page

Progress variable definition	Reference
	(Domingo, Vervisch, and Veynante, 2008) (Michel et al., 2009) (Nguyen et al., 2010) (Cecere et al., 2011) (Franzelli, Fiorina, and Darabiha, 2013) (Chen, Ruan, and Swaminathan, 2015) (Locci et al., 2015) (Colin and Michel, 2016) (El-Asrag, Braun, and Masri, 2016) (Langella, Swaminathan, and Pitz, 2016) (Rieth et al., 2019) (Fossi et al., 2020) (Illana, Mira, and Mura, 2021)
$Y_{CO_2} + Y_{H_2O} + Y_{H_2}$	(Proch and Kempf, 2014) (Rittler, Proch, and Kempf, 2015)
$Y_{CO_2} + Y_{H_2O} + Y_{CO}$	(Franzelli et al., 2017)
$\frac{Y_{CO_2}}{W_{CO_2}} + \frac{Y_{H_2O}}{W_{H_2O}} + \frac{Y_{CO}}{W_{CO}}$	(Hansinger, Ge, and Pfitzner, 2020)
$\frac{Y_{CO_2}}{W_{CO_2}} + \frac{Y_{H_2O}}{W_{H_2O}} + \frac{Y_{H_2}}{W_{H_2}}$	(Van Oijen and De Goey, 2004) (Vreman et al., 2008) (Ramaekers, 2011) (Chrigui et al., 2012) (Klapdor et al., 2013) (Ma, Naud, and Roekaerts, 2016) (Ma, 2016) (Sacomano Filho et al., 2017) (Ma and Roekaerts, 2017) (Ma, Huang, and Roekaerts, 2017) (Gövert et al., 2018)
$Y_{CO_2} + Y_{CO} + Y_{H_2O} + Y_{H_2}$	(Pitsch and Ihme, 2005) (Ihme and Pitsch, 2008b) (Ihme and See, 2010) (De and Kim, 2013) (Dhuchakallaya, Rattanadecho, and Watkins, 2013) (Ventosa Molina, 2015) (Popp et al., 2015) (Proch and Kempf, 2015) (Saghafian et al., 2015) (Wu et al., 2015) (Vascellari et al., 2017) (Ventosa Molina et al., 2017) (Luo et al., 2018) (Wen et al., 2018) (Huang et al., 2022b)
$4\frac{Y_{CO_2}}{W_{CO_2}} + \frac{Y_{CO}}{W_{CO}} + 2\frac{Y_{H_2O}}{W_{H_2O}} + 0.5\frac{Y_{H_2}}{W_{H_2}}$	(Ma, 2016) (Both, 2017) (Benajes et al., 2022)

The progress variable definitions incorporating carbon monoxide and hydrogen,

aim to utilize the counteracting relation of CO_2 with CO and H_2O with H_2 respectively. It is assumed, that the non-unique behavior of carbon dioxide and water in rich mixtures near high reaction progress is related to the dissociation of these species forming carbon monoxide and molecular hydrogen. These processes may be represented by the *virtual* reactions:

$$2CO_2 \rightarrow 2CO + O_2, \tag{3.22}$$
$$2H_2O \rightarrow 2H_2 + O_2. \tag{3.23}$$

Note, that these do not correspond to actual chemical processes described by elementary reactions, they are merely a global representation of the processes.

TABLE 3.5: Normalized weights of common progress variable definitions compared to their weight used for CO_2.

	$\frac{a_{CO_2}}{a_{CO_2}}$	$\frac{a_{CO}}{a_{CO_2}}$	$\frac{a_{H_2O}}{a_{CO_2}}$	$\frac{a_{H_2}}{a_{CO_2}}$
Y_c^{PM}: Pierce and Moin (2004)	1		1.000	
Y_c^{F}: Fiorina et al. (2003)	1	1.000		
Y_c^{OG}: Van Oijen and De Goey (2004)	1		2.443	21.830
Y_c^{PI}: Pitsch and Ihme (2005)	1	1.000	1.000	1.000
Y_c^{ref}: Ma (2016)	1	0.393	1.221	2.729

This perspective also explains the usage of the reciprocal of the molecular weight: $a_k = \frac{1}{W_k}$ proposed by Van Oijen and De Goey (2004), since the dissociation of each mole of CO_2 or H_2O according to Eq. (3.22) and Eq. (3.23) produces a mole of CO or H_2 respectively. In comparison, the definitions using simple summation, put significantly larger weight on the heavier species. The last entry of Tab. 3.4 introduced by Ma (2016) departs from the approach of Van Oijen and De Goey (2004) and aims for further improvement by fine-tuning the coefficients. Interestingly, their optimal solution places more weight on the heavier species, but not as much as using unity weights. In particular, the coefficient of molecular hydrogen is significantly lower. The definition of Ma (2016) is the preferred choice in the present study, and it will be used as reference from here on:

$$Y_c^{ref} = 4\frac{Y_{CO_2}}{W_{CO_2}} + \frac{Y_{CO}}{W_{CO}} + 2\frac{Y_{H_2O}}{W_{H_2O}} + 0.5\frac{Y_{H_2}}{W_{H_2}}, \tag{3.24}$$
$$\approx 0.0909Y_{CO_2} + 0.0357Y_{CO} + 0.1110Y_{H_2O} + 0.2480Y_{H_2}. \tag{3.25}$$

The a_k coefficients of some of the most common progress variable definitions are summarized in Tab. 3.5 with respect to the weight these definitions use for carbon dioxide.

Computational singular perturbation method

Finally, in terms of the optimization of progress variable definitions, the work of Gövert et al. (2015) is highlighted here. They use the computational singular perturbation (CSP) method (Lam and Goussis, 1989) to find an optimal progress variable definition under perfectly premixed conditions. The CSP method finds N_C different basis vectors in composition space, that separate M fast and $N_C - M$ slow time scales. (Massias et al., 1999) Each one of these basis vectors form an array of weights,

like the a_k definition of the progress variable. In the application of CSP to mechanism reduction, it is assumed, that the fast bases are converging infinitely fast to their steady state at each point of time. In such a case, the possible compositions are bound to an $N_C - M$ dimensional manifold, that can be significantly simpler, than the full composition space. Consequently, $N_C - M$ degrees of freedom are sufficient for the description the composition's evolution along this manifold.

In the methodology of Gövert et al. (2015), followed in the present study, a limiting case of the above reduction process is used, where the number of fast bases is selected as: $M = N_C - 1$, thus only a single slow basis is retained. Instead of using this heavily reduced mechanism directly, the weights of this slowest basis vector are utilized to define the progress variable in the context of tabulated chemistry.

TABLE 3.6: Progress variable weights used for the perfectly premixed combustion of hydrogen as reported by Mira et al. (2020).

Weights reported by Mira et al. (2020)			
	a_k	$a_k W_k$	$b_k W_k / 2$
$N2$	0	0	0
H	−0.2480	−0.25	0.25
$O2$	0.0313	1.00	−1.00
OH	0.0147	0.25	−0.25
O	0.0313	0.50	−0.50
$H2$	−0.2480	−0.50	0.50
$H2O$	0	0	0
$HO2$	0.0227	0.75	−0.75
$H2O2$	0.0147	0.50	−0.50

For the application published by Mira et al. (2020) and further detailed in chapter 7, a single premixed free flamelet of hydrogen and preheated air is solved using Cantera (Goodwin, 2002) at an equivalence ratio of $\phi = 0.6$ using the San Diego mechanism. (UCSD, 2018) The method of Gövert et al. (2015) identifies the fastest reacting gas mixture along this flamelet, and uses CSP to form the basis vector a_k corresponding to the slowest reactions. The weight reported by Mira et al. (2020) are presented in Tab. 3.6. As the table demonstrates, these weights prove to give an equivalent representation to the mixture fraction, since $a_k = -b_k/2$. The only reason, that the present a_k weights still produce a reasonable representation for perfectly premixed conditions, is because during the tabulation process they are subjected to numerical rounding, thus strictly speaking $Z \neq Y_c$, and the resulting Y_c still shows enough variation along the flamelet to distinguish between gas states.

The applied CSP methodology is reevaluated here, giving the basis presented in Tab. 3.7. This Y_c definition is significantly different from the mixture fraction, and provides a good representation of the reaction progress along the flamelet. Nevertheless, in the rest of this work $Y_c = Y_{H_2O}$ is used in the case of H_2, as this is found to be an adequate definition, without the need for a dedicated optimization process.

3.2.2 Flamelets on the $Z - Y_c$ plane

In partially premixed and non-premixed combustion, the flame encounters various mixture fractions. Consequently, it is important to have a representative tabulated

TABLE 3.7: Optimized progress variable weights using the CSP method of Gövert et al. (2015) in the fastest reacting point of a hydrogen-air premixed free flamelet at $\phi = 0.6$.

N_C^{th} CSP basis		
	a_k	$a_k W_k$
$N2$	0	0
H	0.4960	0.5
$O2$	0.0313	1.0
OH	0.0294	0.5
O	0.0625	1.0
$H2$	0	0
$H2O$	0	0
$HO2$	0.0151	0.5
$H2O2$	0	0

flamelet state corresponding to any of the possible gas states that are encountered. This section details different methods, that aim to cover the $Z - Y_c$ plane thoroughly.

Figure 3.21 shows the behavior of different adiabatic methane-air flamelets on the $Z - Y_c^{ref}$ plane using the unity Lewis number assumption. For reference, the figure shows a few individual flamelets indicated by red curves: The two straight vertical lines are two premixed flamelets at the lean and rich flammability limits corresponding to $Z_L = 0.0206$ ($\phi_L = 0.35$) and $Z_R = 0.1920$ ($\phi_R = 4.07$) respectively. Meanwhile, the four curved lines correspond to steady counterflow diffusion flamelets. In order of increasing progress variable: unstable flamelet at $a = 1/\text{s}$, unstable flamelet at $a = 300/\text{s}$, stable flamelet at the extinction point ($a^{ext} = 614.456/\text{s}$), and finally stable flamelet at $a = 1/\text{s}$. The different plots show the different scenarios described in Tab. 3.2. The premixed free flamelets shown in plot a) are capable of representing all reaction progress states between unburnt and burnt, but they are limited to the flammability range in mixture fraction. The considered counterflow diffusion flames are more diverse, and different arrays of flamelets can cover different levels of reaction progress while they range across all mixture fractions. The stable counterflow diffusion flamelets in Fig. 3.21b can cover all states with reaction progress higher than the extinction point, while their unstable counterparts in Fig. 3.21c represent a large portion of the reaction progress below the extinction point, however, these do not reach pure mixing ($Y_c^{ref} = 0$). This can be achieved by the unsteady extinguishing flamelets of Fig. 3.21d-e that cover the lower half of possible Y_c values. Lastly, the reigniting flamelets of Fig. 3.21f cover a third type of region that reaches neither pure mixing nor equilibrium.

The different flamelet-based tabulated chemistry methods, that use the flamelets presented in Fig. 3.21, are present in the literature under various names. Premixed flamelet are used in the Flamelet Generated Manifold (FGM) model of Van Oijen and De Goey (2000), and in the Flame Prolongated Intrinsically Low Dimensional Manifold (FPI) model of Gicquel, Darabiha, and Thévenin (2000). Meanwhile counterflow diffusion flamelets are used in the model of Peters (1984), where only the stable branch is utilized, parametrized by mixture fraction and scalar dissipation rate. Pierce and Moin (2004) introduced the combination of stable and unstable branches in the Flamelet Progress Variable (FPV) model, parametrized by mixture fraction and progress variable. This model was extended by Ihme and See (2010) resulting the

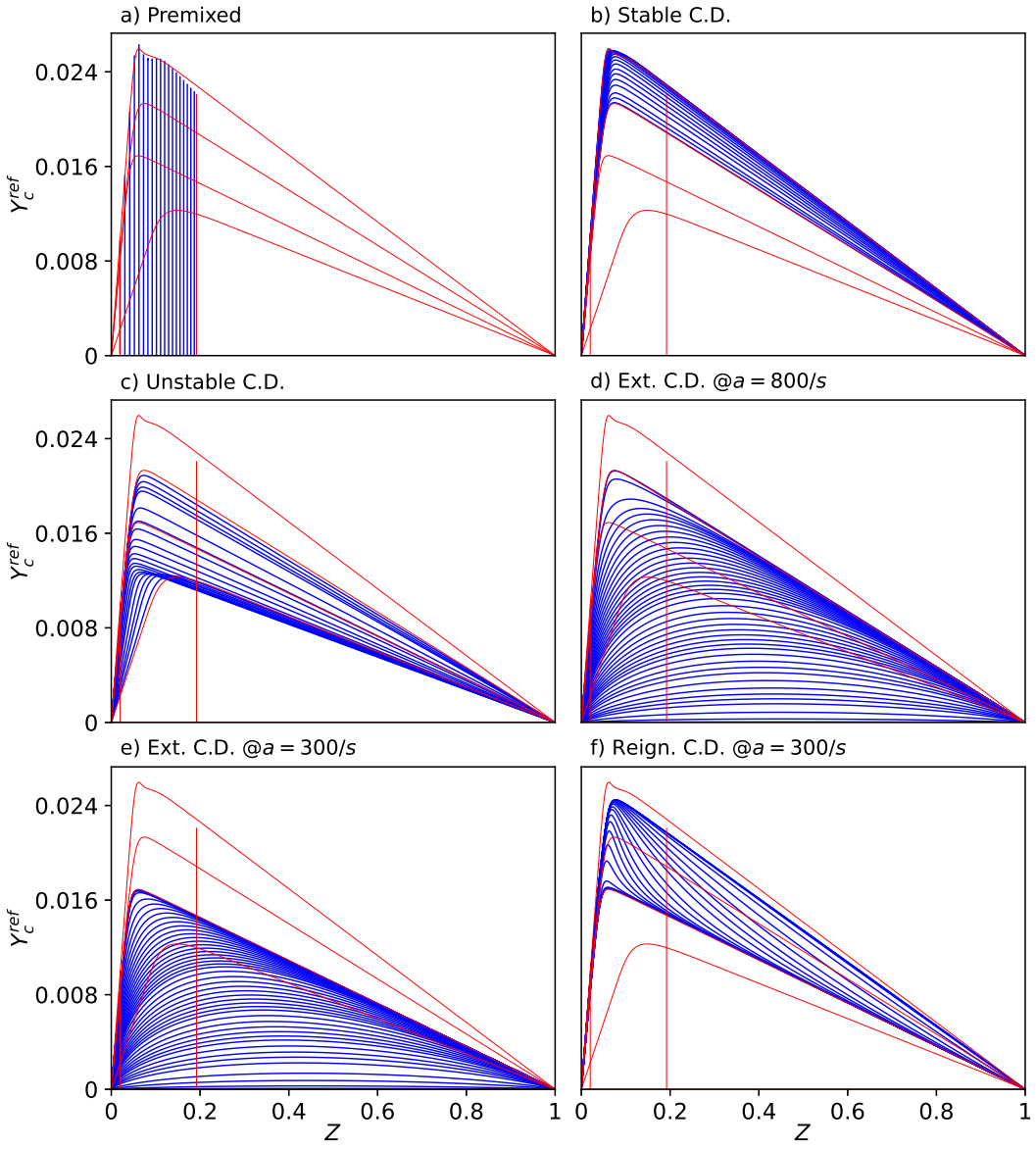

FIGURE 3.21: Location of adiabatic 1D flamelets of methane and air on the $Z - Y_c$ plane using the GRI3.0 (Smith et al., 2011) chemical mechanism with the unity Lewis number assumption ("Le=1"). a) premixed free flamelets, b) stable counterflow diffusion flamelets, c) unstable counterflow diffusion flamelets, d) unsteady extinguishing counterflow diffusion flamelets at $a = 800/\text{s}$ initialized from the extinction point, e) unsteady extinguishing counterflow diffusion flamelets at $a = 300/\text{s}$ initialized from the unstable solution at $a = 290/\text{s}$, f) unsteady reigniting counterflow diffusion flamelets at $a = 300/\text{s}$ initialized from the unstable solution at $a = 310/\text{s}$. The limits of these regions are indicated by red curves for reference.

Unsteady Flamelet Progress Variable (UFPV) model. This method captures transient phenomena like extinction and reignition by tabulating these unsteady flamelets at various strain rates (or scalar dissipation rates.) Meanwhile various studies have applied counterflow diffusion flamelets in the context of FGM. (Vreman et al., 2008;

Chrigui et al., 2012; Ma and Roekaerts, 2016) In the present study the utilized combination of flamelets are detailed case-by-case for clarity.

As Fig. 3.21 illustrates, none of the presented flamelet arrays are capable of covering all relevant points of the $Z - Y_c$ plane alone. One option to fill the missing regions, is to use linear interpolation of species and enthalpy between known gas states. (Fiorina, Veynante, and Candel, 2015) This mathematical operation corresponds to the mixing of the two gases without any reactions taking place. Such an interpolation is applied in this work in two cases: 1) between the premixed flamelets corresponding to the lean and rich flammability limits and pure oxidizer and fuel respectively, and 2) between the unstable flamelet at the lowest strain rate and the pure mixing states. Interpolation is justified in these cases, since the reactivity of the gas mixtures is very low, both in premixed flamelets at the flammability limit, and in unstable diffusion flamelets at a low strain rate. The interpolation does not generate arbitrary information about the chemical behavior, since the heat release rate is already minimal at these limiting cases as shown in Fig. 3.20. Thus, the interpolation only serves to describe the physical properties of the intermediate mixtures (ρ, μ, etc.). For example, the mixing law applied for states richer than the richest flammable solution is:

$$\forall x \in [x^R_{min}, x^R_{max}] : Y_k^{interpolated}(x) = Y_k^R(x) + \frac{Z^{interpolated} - Z^R}{1 - Z^R} Y_{k,f}, \tag{3.26}$$

$$h^{interpolated}(x) = h^R(x) + \frac{Z^{interpolated} - Z^R}{1 - Z^R} h_f, \tag{3.27}$$

were the R superscript marks the richest burning flamelet, and $Z^{interpolated}$ is the mixture fraction where the conditions are interpolated. Subsequently, laws of section 2.1 are used to obtain material properties. Furthermore, for the sake of consistency, the chemical source terms are recalculated according to Eq. (2.97), however, they are negligibly low compared to the reacting flamelets. The process is the same between the lean limit and pure oxidizer. A similar method is applied between the mixing line and the unstable flamelet at the lowest strain rate:

$$\forall Z \in [0,1] : Y_k^{interpolated}(Z) = Y_k^{mix}(Z) + \frac{Y_c^{interpolated} - Y_c^{mix}(Z)}{Y_c^{unstab}(Z) - Y_c^{mix}(Z)} Y_k^{unstab}(Z), \tag{3.28}$$

$$h^{interpolated}(Z) = h^{mix}(Z) + \frac{Y_c^{interpolated} - Y_c^{mix}(Z)}{Y_c^{unstab}(Z) - Y_c^{mix}(Z)} h^{unstab}(Z), \tag{3.29}$$

where the superscripts: *mix* and *unstab* stand for the mixing solution, and the last unstable solution respectively, and the properties are evaluated at a given progress variable: $Y_c^{interpolated}$.

The other option to cover the $Z - Y_c$ plane with flamelet solutions is to concatenate the different flamelet arrays displayed in Fig. 3.21. In the present work this is applied in the context of counterflow diffusion flamelets. Firstly, in certain cases, it is satisfactory to tabulate only steady counterflow diffusion flamelets, as they describe the stable burning conditions of non-premixed combustion sufficiently (Peters, 1984). To include lower reaction progress states, associated with extinction and reignition, more solutions of Fig. 3.21 have to be combined. The combination of the stable and unstable branches (Fig. 3.21 b+c) was proposed by Pierce and Moin (2004), that is completed by the extrapolation towards the mixing solution. Another solution, especially for the modeling of local extinction, is the combination of the stable branch with the different time instances of an unsteady extinguishing flamelet

initialized from the extinction point (Fig. 3.21 b+d). (Chrigui et al., 2012; Ma and Roekaerts, 2016; Benajes et al., 2022) Finally, a more complex modeling framework is the unsteady/flamelet progress variable model of Pitsch and Ihme (2005), that considers the extinction and reignition at various strain rates in a single model. Implementing such a model is out of the scope of the present work. However, many studies employ unsteady flamelets at a single strain rate lower than the extinguishing one. (Bekdemir, Somers, and De Goey, 2011; Wehrfritz et al., 2016; Ma and Roekaerts, 2016; Zhang et al., 2019; Mira et al., 2021a) This approach is common in the field of autoiginiting flames, where a single autoigniting flamelet at a fixed strain rate may be representative to the unsteady part of the problem, and including the stable flamelets with higher reaction progress gives a thorough coverage of the $Z - Y_c$ plane. A logical extension of this simplified approach to non-autoigniting cases, is to combine the extinguishing and reigniting flamelets at a given strain rate, and add the stable flamelets below this strain rate (Fig. 3.21 e+f+b(partly)). Note, that these modeling decisions have a significant effect on the resulting table, as Fig. 3.16 suggests and as further discussed in section 3.4.1. Namely, using the stable branch and the unsteady extinguishing flamelet beyond the extinction limit (Fig. 3.21 b+d) gives the highest heat release values, followed by using the stable and unstable branches (Fig. 3.21b+c), and finally using unsteady flamelets at a lower strain rate (Fig. 3.21 e+f+b(partly)) may give significantly lower $\dot{\omega}_T$. The possible methods of covering the full $Z - Y_c$ plane are summarized in Tab. 3.8.

TABLE 3.8: Summary of adiabatic tabulation strategies for covering the relevant parts of the $Z - Y_c$ plane.

Key	Reference
Prem.	Van Oijen and De Goey (2004)
Stab.	Peters (1984)
Stab.+Unstab.	Pierce and Moin (2004)
Stab.+Ext.	Chrigui et al. (2012)
Stab.+Reign.+Ext.	Following Bekdemir, Somers, and De Goey (2011)
Key	**Regions and Extrapolations**
Prem.	Fig. 3.21a (+ Eq. (3.26) + Eq. (3.27))
Stab.	Fig. 3.21b
Stab.+Unstab.	Fig. 3.21b+c (+ Eq. (3.28) + Eq. (3.29))
Stab.+Ext.	Fig. 3.21b+d
Stab.+Reign.+Ext.	Fig. 3.21e+f+b(partly)

3.2.3 Injectivity of progress variable definitions

Weather or not the weights of the progress variable are optimized or they are defined *ad hoc*, it is important to study the Y_c definition's capability to uniquely characterize the flamelets. Below, a preprocessing step is described, that is applied on a set of counterflow diffusion flamelets, to obtain *pseudo-premixed flamelets* composed of the thermo-chemical states that are found in the real counterflow flamelets. Subsequently, the injectivity of the a progress variable definition of these pseudo-premixed flamelets and the actual premixed free flamelets can be studied in a unified framework. (Both, Mira, and Lehmkuhl, 2021b)

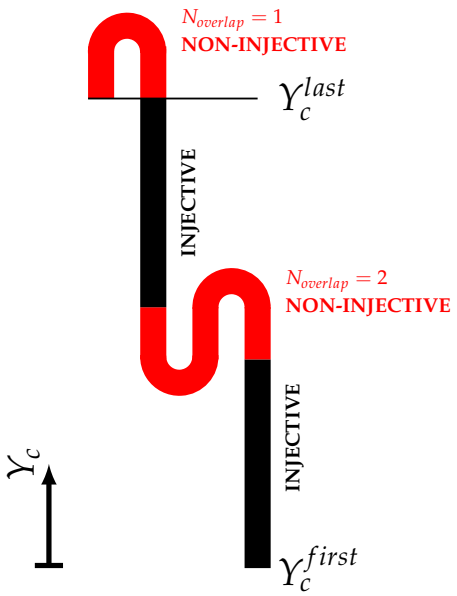

FIGURE 3.22: Injective and non-injective regions along a premixed or pseudo-premixed flamelet.

To transform the counterflow flamelets, Bilger's mixture fraction is evaluated along them, and the flamelet solution is interpolated on a predefined discretization of the mixture fraction coordinate. For simplicity this Z discretization is the same as the one applied on the complete thermo-chemical table. Pseudo-premixed flamelets are formed from the set of thermo-chemical states at each mixture fraction value by appending these states in the intrinsic order of counterflow diffusion flamelets. This ordering depends on the choice of flamelets. and it follows the structure presented in Tab. 3.2. If the pure mixing solution is included explicitly in the array of flamelets, then it is first in order. It is followed by the unsteady extinguishing flamelets in order of decreasing time, or unstable steady state flamelets in order of increasing strain rate. Next in the array are the reigniting flamelets in order of increasing time, and finally, if stable flamelets are used, these are added last in the order of decreasing strain rate. An ideal progress variable must change monotonically along each one of these pseudo-premixed flamelets and along each actual premixed free flamelets as well.

Figure 3.22 displays a possible evolution of the progress variable along a premixed or pseudo-premixed flamelet. Red parts indicate the typical examples of non-injective behavior observed in practical applications. At certain mixture fractions it is typical, that two solutions are not distinguished well by the progress variable near equilibrium (Y_c^{last}). Meanwhile, three coexisting solutions may be observed in the central part of the pseudo-premixed flamelets, typically associated to the transition between the different non-premixed sub-arrays displayed in Fig. 3.21. Note, that higher number of coexisting gas states are also possible, but these are seldom observed with reasonable progress variable definitions. In this context, the injectivity of the progress variable definition may be characterized by the number of overlapping solutions at a given value of Y_c, hereby defined as the number of coexisting solutions minus one. I.e.: injective behavior is indicated by $N_{overlap} = 0$.

Such non-injective regions are shown in Fig. 3.23 for various arrays of flamelets

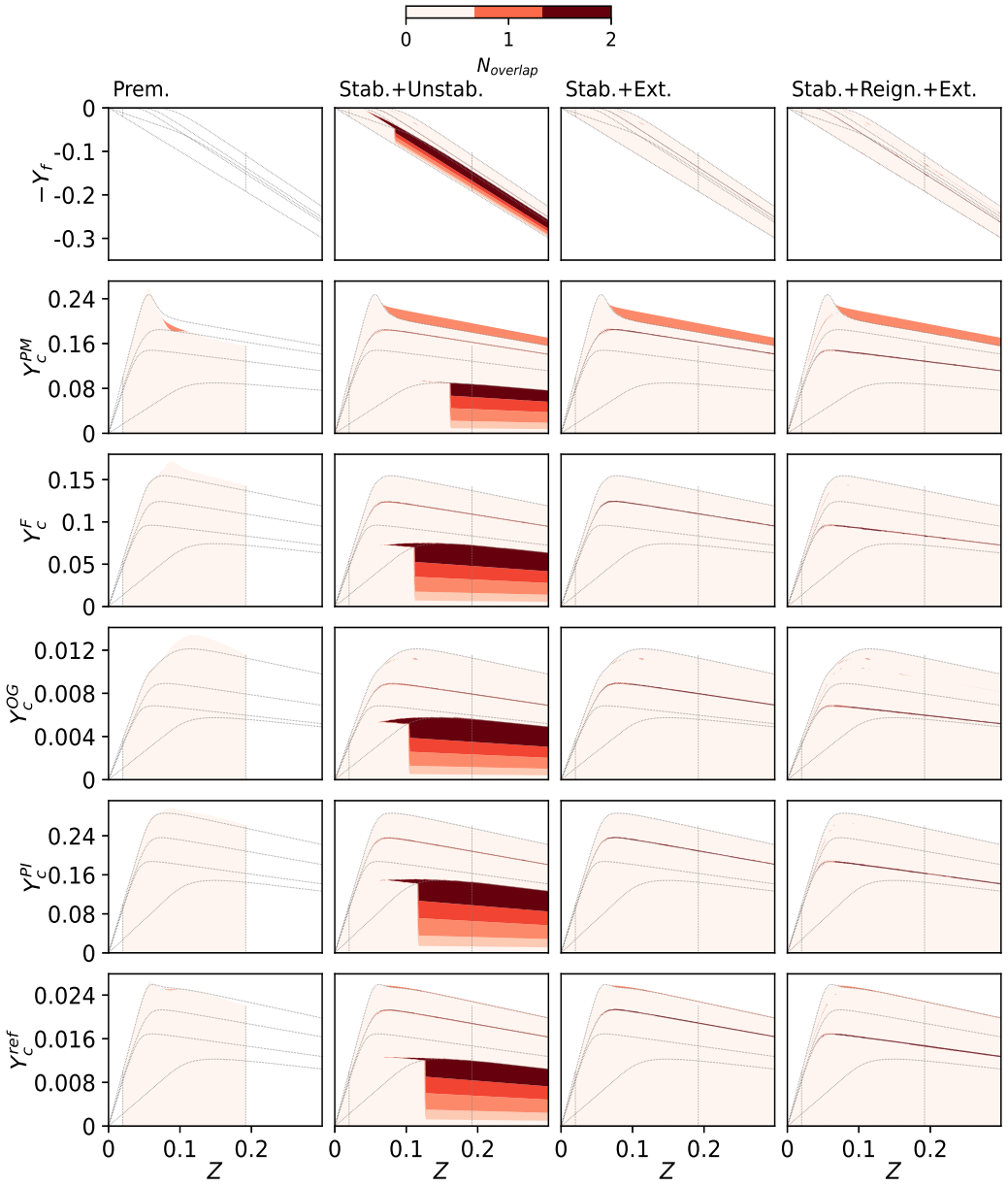

FIGURE 3.23: Non-injective regions of adiabatic 1D flamelets of methane and air on the $Z - Y_c$ plane using the GRI3.0 (Smith et al., 2011) chemical mechanism with the unity Lewis number assumption ("Le=1"). The different columns correspond to combinations of different flamelet arrays. First column: premixed flamelets, second column: stable and unstable counterflow diffusion flamelets, third column: stable and unsteady extinguishing counterflow diffusion flamelets, fourth column: reigniting and unsteady extinguishing counterflow diffusion flamelets at $a = 300/\mathrm{s}$ complemented with stable flamelets of $a < 300/\mathrm{s}$. The different rows correspond to different definitions of the progress variable. First row: $Y_c = -Y_f$, second row: definition of Pierce and Moin (2004), third row: definition of Fiorina et al. (2003), fourth row: definition of Van Oijen and De Goey (2004), fifth row: definition of Pitsch and Ihme (2005), sixth row: reference definition of this work. (Ma, 2016)

(columns), and various progress variable definitions (rows.) The linear combinations resulting in the progress variable are listed in Tab. 3.5, while the flamelet arrays are described in Tab. 3.8. In particular, the rows of plots correspond to progress variables using the fuel mass fraction, and the definitions of Pierce and Moin (2004), Fiorina et al. (2003), Van Oijen and De Goey (2004), Pitsch and Ihme (2005), and Ma (2016) respectively. Meanwhile, the different columns represent an array of premixed flamelets, a combination of stable and unstable counterflow flamelets, a combination of stable and unsteady extinguishing counterflow flamelets at a strain rate of $a = 800/\mathrm{s}$, and finally a combination of unsteady extinguishing and reigniting flamelets at a strain rate of $a = 300/\mathrm{s}$ started from unstable solutions at $a_{IC} = 290/\mathrm{s}$ and $a_{IC} = 310/\mathrm{s}$ appended with stable counterflow flamelets below this strain rate. The plots show the values of $N_{overlap}$ evaluated using premixed and pseudo-premixed flamelets on the $Z - Y_c$ plane. The reference flamelets of Fig. 3.21 are indicated by gray dotted lines.

Comparing the overall behavior of the different flamelet arrays, it can be identified, that the most challenging set of states is produced by combining stable and unstable counterflow diffusion flamelets. In case of all other combinations, the non-injective behavior is concentrated near the transition between different flamelet sets and near equilibrium. Meanwhile, in the "Stab.+Unstab." case there is a band of non-injectivity associated with unstable counterflow flamelets at low strain rates. For instance, Illana, Mira, and Mura (2021) used such a flamelet set with the $Y_c^F = Y_{CO_2} + Y_{CO}$ progress variable definition, and their thermo-chemical tables exhibit signs of this non-injective behavior. Although, this is hardly the fault of the progress variable definition of Fiorina et al. (2003), since none of these popular definitions can describe uniquely both branches. In comparison, uniquely representing premixed flamelets ("Prem.") is significantly easier task, as even using only CO_2 and H_2O (Y_c^{PM}) the overlapping is concentrated to a small region of rich flamelets near equilibrium. Moreover, the extinguishing counterflow flamelets are tracked injectively by all the presented progress variables both at $a = 800/\mathrm{s}$ and $a = 300/\mathrm{s}$, and reignition is similarly straightforward to capture. However, the stable branch is more difficult to uniquely describe, since near equilibrium (at low strain rate) the final combustion products dissociate as Fig. 3.12 illustrates.

The definition of Pierce and Moin (2004) is characterized by a one-fold overlap near equilibrium, since both carbon dioxide and water vapor are less abundant at equilibrium than at intermediate levels of reaction progress. Such non-injective behavior is restricted to rich conditions, where the scarcity of oxidizer allows for the dissociation of CO_2 and H_2O. All the other Y_c definitions aim to resolve this problem by including varied amounts of intermediate species in Y_c as summarized in Tab. 3.5. However, this improvement near equilibrium comes at the cost of worse performance on the unstable branch. This is indicated by the shift of the non-injective region towards lower values of Z.

The injectivity is further examined on Fig. 3.24. The different progress variables are compared along the pseudo-premixed flamelets for the "Stab. + Unstab." manifold at the stoichiometric mixture and 3 different rich mixtures. For reference the left column of the figure indicates the ordinal numbering of flamelets: n_{flame} along the S-curve. The focus of this depiction is the right column, where this ordinal numbering is used to identify the different states along the given mixture fraction. The injectively represented states are shown using thick dashed lines, while the states that cannot be described uniquely by the progress variable are indicated using thin solid lines. The progress variables are normalized by $Y_c^{last}(Z)$, which are the progress variable value taken from the stable counterflow flame at $a = 1/\mathrm{s}$. Thus, a direct

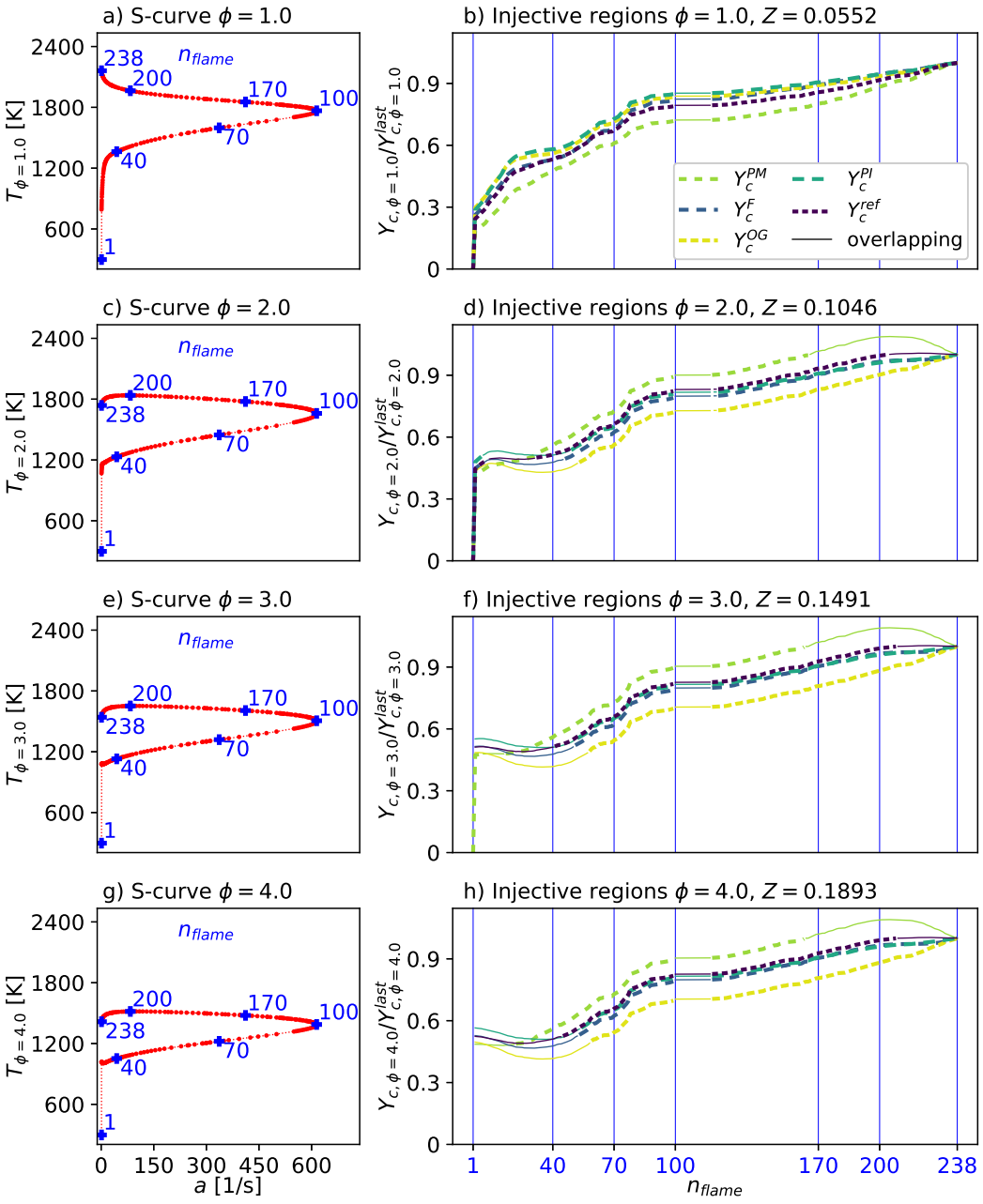

FIGURE 3.24: Injective regions of stable and unstable counterflow diffusion flamelets at selected equivalence ratios using the GRI3.0 (Smith et al., 2011) chemical mechanism with the unity Lewis number assumption ("Le=1"). The left column shows the standard S-curve using pseudo-premixed flamelets at various equivalence ratios, indicating the ordering of the flamelets: n_{flame} from pure mixing to the stable flamelet at the lowest strain rate. The right column presents the progress variable along these pseudo-premixed flamelets, as the function of n_{flame}. The dashed lines indicate various progress variable definitions including the ones proposed by Pierce and Moin (2004), Fiorina et al. (2003), Van Oijen and De Goey (2004), Pitsch and Ihme (2005), and Ma (2016). The the injective parts are marked with thick dashed lines, while the non-injective parts with thin solid lines.

comparison is possible between the different progress variables.

Throughout all the examined mixture fractions there is a common non-injective region located between the 100^{th} and $\sim 120^{\text{th}}$ flamelet. This is associated with the extinction point at $n_{falme} = 100$. The region is created in the process of finding the true extinction point, and it represent many flamelets with extremely small differences in strain rate, hence small differences in the thermo-chemical state. Consequently, the non-unique behavior for $100 < n_{flame} < 120$ is not a real concern and can be disregarded in the rest of the analysis.

Under the stoichiometric conditions, illustrated in Fig. 3.24b, all progress variable definitions describe the flamelets uniquely, and they all behave quite similarly. For the stable flamelets of $n_{falme} > 120$ the progress variable increases with varied slopes along the different flamelets. The higher slopes may be more desirable, since they correspond to a better ability to distinguish between solutions. The definition of Pierce and Moin (2004) stands out in this regard, while all other studied definitions that consider intermediate products evolve less steeply. Note, that the second steepest slope belongs to the reference definition used in this work. (Ma, 2016)

The remaining three rows: Fig. 3.24d,f,h are representing the rich conditions, where most of the non-injective behavior is found as Fig. 3.23 shows. The plots d,f,h show the flamelet conditions at equivalence ratios of $\phi \in \{2, 3, 4\}$, that correspond to $Z \in \{0.1046, 0.1491, 0.1893\}$ respectively. All three of these rich preudo-premixed flamelets show similar trends regarding the progress variable. The definitions of Fiorina et al. (2003), Pitsch and Ihme (2005), and Ma (2016) are very close to one another with the differences located near equilibrium ($n_{falme} > 200$) and near the lower-strain parts of the unstable branch ($n_{falme} < 70$). Meanwhile, the definition of Pierce and Moin (2004) produces a steeper increase of Y_c in the unstable branch, and it is characterized by generally higher progress variable, that decreases near equilibrium creating a large non-unique region. Finally, the definition of Van Oijen and De Goey (2004) behaves the opposite way. It is characterized by large non-unique parts in the unstable branch, however in return, it stays considerably steeper even near equilibrium.

Regarding the more subtle differences between Y_c^F, Y_c^{PI}, and Y_c^{ref}, they all suffer from overlapping in the low strain parts of the unstable branch. This appears to be the least limited using the Y_c definition of Ma (2016). Nevertheless, this comes at the cost of worse performance near equilibrium, where both the definitions of Fiorina et al. (2003) and Pitsch and Ihme (2005) stay injective till the least strained flamelet, while the Y_c^{ref} becomes non-unique.

Placing the tabulation method into context, Fig 3.16 demonstrates, that the heat release rate is two orders of magnitude higher at stoichiometry than at $\phi = 3$. Which also indicates their respective importance in the thermo-chemical modeling of diffusion flames. In this point of view, near-stoichiometry effects are more important. A case can be made for a compromise like Y_c^{ref}, that is considerably steep at stoichiometry, yet it can capture a significant part of the unstable branch at rich conditions.

Note, that these conclusions are conditional on the studied flamelets, including the choice of fuel, and the imposition of unity Lewis number transport. In fact, as Fig. 3.12 illustrates, the mass fraction of molecular hydrogen is greatly affected by the transport model. However, considering flamelets of mixture-averaged transport for thermo-chemical tabulation is out of the scope of this work.

Truncation of non-unique regions

To map the flamelet solutions on a rectilinear table, the non-unique regions of the (pseudo-)premixed flamelets have to be addressed. This mapping implies interpolating along these flamelets to get information on predefined levels of progress variable. Such interpolation is only possible, if the progress variable behaves monotonically across the dataset. In this work the following strategies are explored, assuming that the progress variable is expected to increase from Y_c^{first} to Y_c^{last} as illustrated in Fig. 3.22:

1. Cut out (C) the non injective parts,
2. Order (O) according to increasing Y_c along the flamelet,
3. keep the First Unique (FU) increasing parts.

The behavior of these strategies is shown in Fig. 3.25. An important distinction between the strategies, is the highest progress variable encountered in the kept parts. In case of the cut out (C) strategy the lowest and highest progress variables are determined by the endpoints of the (pseudo-)premixed flamelet: $Y_c^{start} = Y_c^{first}$ and $Y_c^{end} = Y_c^{last}$. Meanwhile, the other two strategies may capture information between $Y_c^{start} = \min(Y_c)$ and $Y_c^{end} = \max(Y_c)$.

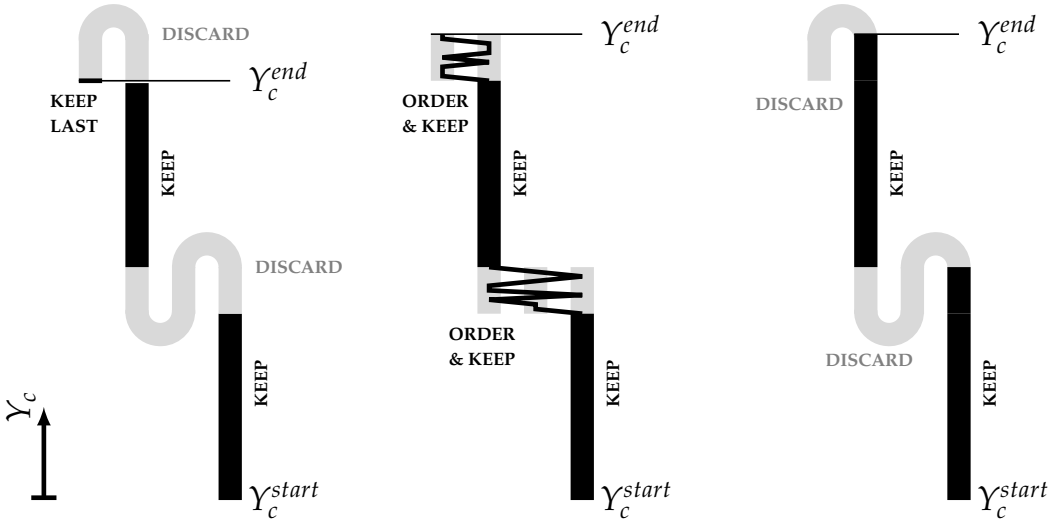

(A) Cut out (C.) (B) Ordered (O.) (C) First Unique (FU.)

FIGURE 3.25: Strategies of truncating the non-injective parts of (pseudo-)premixed flamelet.

A priori the best strategy seems to be the First Unique (FU) that utilizes as large portion of the solutions as possible, while making sure, that the solutions are as continuous as possible. In the example of Fig. 3.25c there is only one discontinuity associated to the double overlap in the center. The option of simply Ordering (O) can induce problems, as the themo-chemical states adjacent in progress variable space might behave significantly differently in other aspects. Finally, the option of Cutting (C) the non-injective solutions out removes an unnecessarily large portion of all states. However, it offers the benefit of including the real first (Y_c^{first}) and last (Y_c^{last}) points in the set of unique solutions. The latter may be important in capturing

the near-equilibrium behavior, but it can introduce a large discontinuity between the last data point and the preceding one.

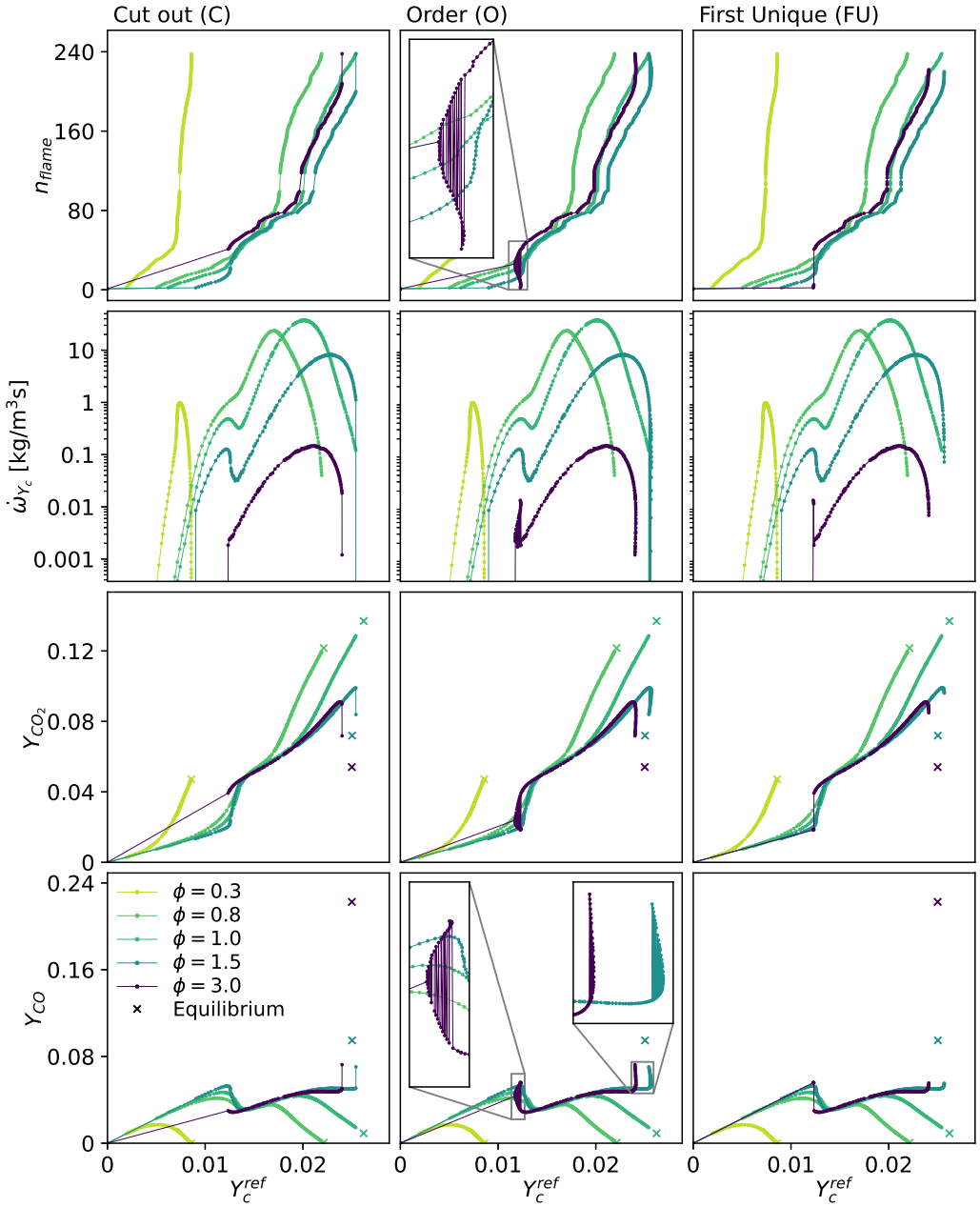

FIGURE 3.26: Effect of truncation strategies on stable and unstable counterflow diffusion flamelets at selected equivalence ratios using the GRI3.0 (Smith et al., 2011) chemical mechanism with the unity Lewis number assumption ("Le=1") and the progress variable definition of Ma (2016). The different columns show the truncation strategies. The rows show the ordinal numbering of the flamelets (n_{flame}), the source term of the progress variable ($\dot{\omega}_{Y_c}$), and the mass fractions of carbon dioxide (Y_{CO_2}) and carbon monoxide (Y_{CO}) respectively.

The actual effect of the truncation is further illustrated in Fig. 3.26 using the reference progress variable definition defined in Eq. (3.24). (Ma, 2016) The figure compares the Cut out (C), the Order (O), and the First Unique (FU) truncation strategies

introduced above. The first row of plots shows n_{flame}: the ordinal number of counterflow diffusion flamelets. In all cases, Y_c^{ref} allows the inclusion of all flamelet states at lean and stoichiometric conditions, as already indicated in Fig. 3.23. For the two presented rich conditions ($\phi \in \{1.5, 3\}$) problems of non-injectivity arise, thus truncation or ordering takes effect.

In particular, in case of the Cut out (C) strategy, many flamelets are discarded near the extinction point ($100 < n_{flame} < 120$.) Furthermore, at an equivalence ratio of 1.5 low strain stable flamelets are discarded beyond $n_{flame} = 200$ corresponding to a strain rate of $a = 83.2/\text{s}$. This limitation is less severe at $\phi = 3.0$, where the 208$^{\text{th}}$ flamelet can be retained with $a = 36.3/\text{s}$. However, at this equivalence ratio the unstable branch is affected, where the first flamelet to be included after the mixing line is the 41$^{\text{st}}$, corresponding to $a = 50.0/\text{s}$. The strategy using Ordering (O) does not discard any solutions by definition, however the ordering of the gas states no longer follows n_{flame} under rich conditions as the magnified plot illustrates. Finally, the First Unique (FU) strategy keeps considerably more flamelets than the Cut out (C) strategy, while ensuring the injectivity of both Y_c and n_{flame}. In this case, the lowermost strain rate cases of the unstable branch are kept at all assessed equivalence ratios, even though a large portion needs to be still discarded in the range: $6 < n_{flame} < 40$. This strategy's effect is more notable on the stable branch, where the 220$^{\text{th}}$ and the 222$^{\text{nd}}$ flamelets are retained at equivalence ratios of 1.5 and 3 respectively. These last flamelets correspond to strain rates of $a = 13.9/\text{s}$ and $a = 10.0/\text{s}$.

The second row of plots in Fig. 3.26 shows the source term of the progress variable as defined in section 2.5.4. This illustrates, how the truncation strategy only has a minor effect on the source term, in regions where $\dot{\omega}_{Y_c}$ is at least one order of magnitude lower than its peak value. Note, that in the final tabulation the source term is clipped to zero at the last point, thus avoiding spurious values outside the $[Y_c^{start}, Y_c^{end}]$ interval.

Finally, Fig. 3.26 also present the mass fractions of carbon dioxide and carbon monoxide in the third and fourth row of plots. Such mass fractions are of interest in the *a posteriori* lookup of species using the thermo-chemical tables. These figures also indicate the equilibrium conditions at each studied equivalence ratio. The two lean cases reach the equilibrium at the lowest considered strain rate, however at stoichiometry, this strain rate of $a = 1/\text{s}$ is already sufficiently high to prevent the complete relaxation to equilibrium. In the two rich cases the equilibrium conditions are quite far from the last flamelet, as it is already suggested by Fig. 3.18. In light of this, it is arguable, that the forceful inclusion of the last flamelet in the Cut out (C) strategy does not reach its goal. I.e.: the discrepancy between the last included state and the true equilibrium condition is quite significant irrespective of the truncation strategy, especially in case of carbon monoxide. Thus it may be advantageous to favor the continuity of neighboring flamelets and the smoothness of properties near high Y_c as the First Unique (FU) strategy does.

3.2.4 Tabulation of adiabatic flamelets

For a better utilization of the control variable space, it is advantageous to re-scale the progress variable to the $[0, 1]$ interval. This normalization is done using the limiting progress variable values: Y_c^{start} and Y_C^{end} as illustrated in Fig. 3.25. The limits are

dependent on the mixture fraction, thus the scaled progress variable is:

$$C = \frac{Y_c - Y_c^{start}(Z)}{Y_c^{end}(Z) - Y_c^{start}(Z)}, \tag{3.30}$$

that ranges from 0 to 1 from pure mixing till near equilibrium. Once the progress variable is defined, and a truncation method is selected, it is possible to calculate these limiting functions, and to evaluate the scaled progress variable along the flamelets.

Subsequently, the interpolation can be executed first along the flamelets, then across the various flamelets forming the flamelet array, to reach a rectilinear discretization on the $Z - C$ plane. In fact, the process can be understood as creating pseudo-flamelets from the actual data set, then repeating the process, as illustrated in Fig. 3.27. The figure shows the three stages of this mapping process in the columns. The first and second rows illustrate the process of mapping premixed flamelets and extrapolating to pure fuel and oxidizer, while the third and fourth rows show the same process for counterflow diffusion flames. The coloring of the real and pseudo flamelets represents the ordinal number of the used flamelets n_{flame}, thus it indicates where the information in the rectilinear table has originated. Red lines indicate a few distinguished flamelets: the leanest and richest premixed free flamelets, and the counterflow flamelets at $a = 1.0/\mathrm{s}$ on the unstable branch, at the extinction point, and at $a = 1.0/\mathrm{s}$ on the stable branch.

As Fig. 3.27a-f illustrates, the premixed free flamelets with the unity Lewis number assumption readily provide states at predetermined mixture fractions. Nevertheless, the mapping is still done in two steps, allowing the final discretization in Z to differ from the location of the original flamelets. This is especially outstanding in case of the states outside the flammability limit, that are created using Eq. (3.26) and Eq. (3.27) and marked with the lightest colors on Fig. 3.27f. The direction of the interpolation, that transforms the data from one column to the next is indicated by dashed lines on the plots of scaled progress variable.

The states present in counterflow diffusion flamelets are not aligned with neither Z nor C, as Fig. 3.27j demonstrates. Consequently, the final rectilinear discretization contains information from various strain rates along a constant value of C. This variability is further emphasized by the indicative flamelets shown over the plots. The unstable flamelet with the lowest strain rate is characterized by $C \approx 0.2$ on the lean side and $C \approx 0.5$ on the rich side. Meanwhile, the stable flamelet of the extinction point also displays non-constant scaled progress variable, with steep variations in the flammability limit. Finally, the lowest strain rate stable flamelet is characterized by $C \approx 1$, although, due to the slight non-unique behavior discussed above, C drops below one on the rich side. This is an effect of the First Unique (F) truncation strategy. Low strain stable flamelets, indicated by the lightest colors on Fig. 3.27l, are only utilized up to the stoichiometric point, as already discussed above.

These interpolations are executed on species mass fractions and the enthalpy, and subsequently the resulting thermo-chemical state is used to recompute the desired material properties according to section 2.1.2. The chemical source terms of species is likewise recomputed according to section 2.5.1. These are subsequently used as $\dot{\omega}_{Y_c} = \sum_{k=1}^{N_C} a_k \dot{\omega}_k$ to calculate the source term of the progress variable. Exceptions from this recalculation process are the properties, that need information from the original flamelets such as n_{flame} in Fig. 3.27. These include quantities related to gradients, such as the scalar dissipation rate, or quantities related to global variables of the flamelet, such as n_{flame}, the strain rate or the flame speed. If the tabulation of such quantities is required for post-processing purposes, then these properties are

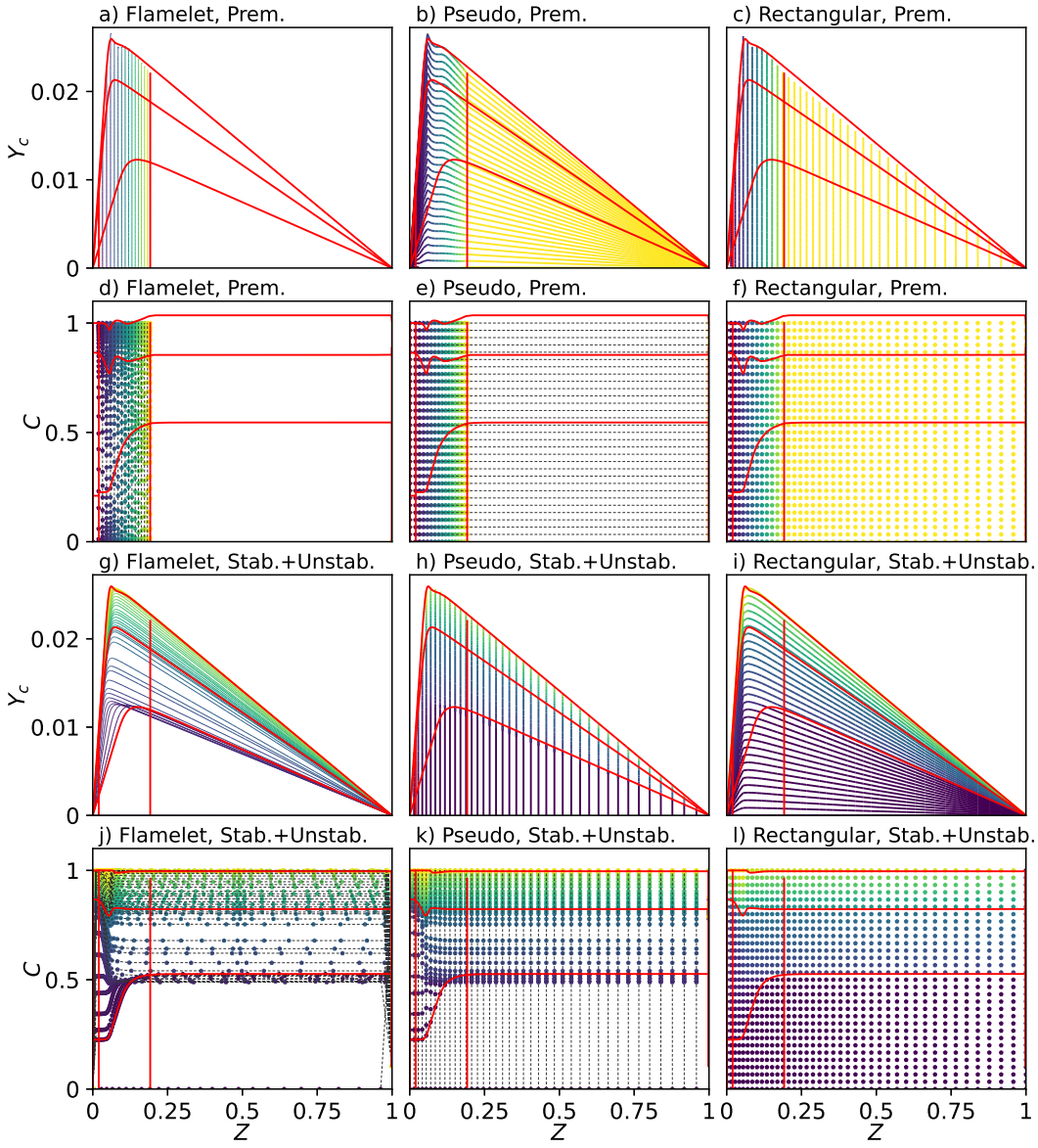

FIGURE 3.27: Process of flamelet interpolation onto a rectilinear discretization using premixed free flamelets (a-f) and counterflow diffusion flamelets (g-l.) The example uses methane-air flamelets with the unity Lewis number assumption ("Le=1") and the progress variable definition of Ma (2016). The different columns show the stages of the mapping procedure. The rows show the unscaled and scaled progress variable along the real and pseudo flamelet colored by the ordinal number of the flamelets within the array. The coloring indicates the ordinal number of the flamelet in the flamelet set ($n_{flame^\cdot}$) Selected premixed and diffusion flamelets are indicated by red lines for reference.

computed on the flamelets, and they are interpolated directly.

Discretization of control variables

As described above, the thermo-chemical states of the flamelet are mapped onto a discretization of Z and C. The progress variable, being a linear combination of species of interest, characterizes important states throughout its entire range. Although, the upper half of possible progress variable values ($C > 0.5$) may be regarded as more important since this range contains the most reactive gas states. (See Fig. 3.26.) Overall, these differences are not so severe, that any region would require additional focus on the expense of other ranges. Thus, throughout this work, a uniform discretization of C is favored. The reaction progress is described using $n_C = 101$ equidistant points in C, corresponding to a step size of $\Delta C = 0.01$.

Nonetheless, as demonstrated throughout this chapter, the mixture fraction shows more differences throughout its possible range. Most of the heat release is concentrated in the flammability limits, even in diffusion flamelets as Fig. 3.16 demonstrates. Far from stoichiometry, the gas mixtures along diffusion flamelets are not reacting and these are given simply by mixing. This is even more relevant in the tabulation of premixed flamelets, where the reacting mixtures are indeed constrained to the flammability limits, and mixing laws (Eq. (3.26), Eq. (3.27)) are used to obtain gas states outside this limit. Consequently, here a discretization is preferred, that favors the states near the stoichiometric mixture.

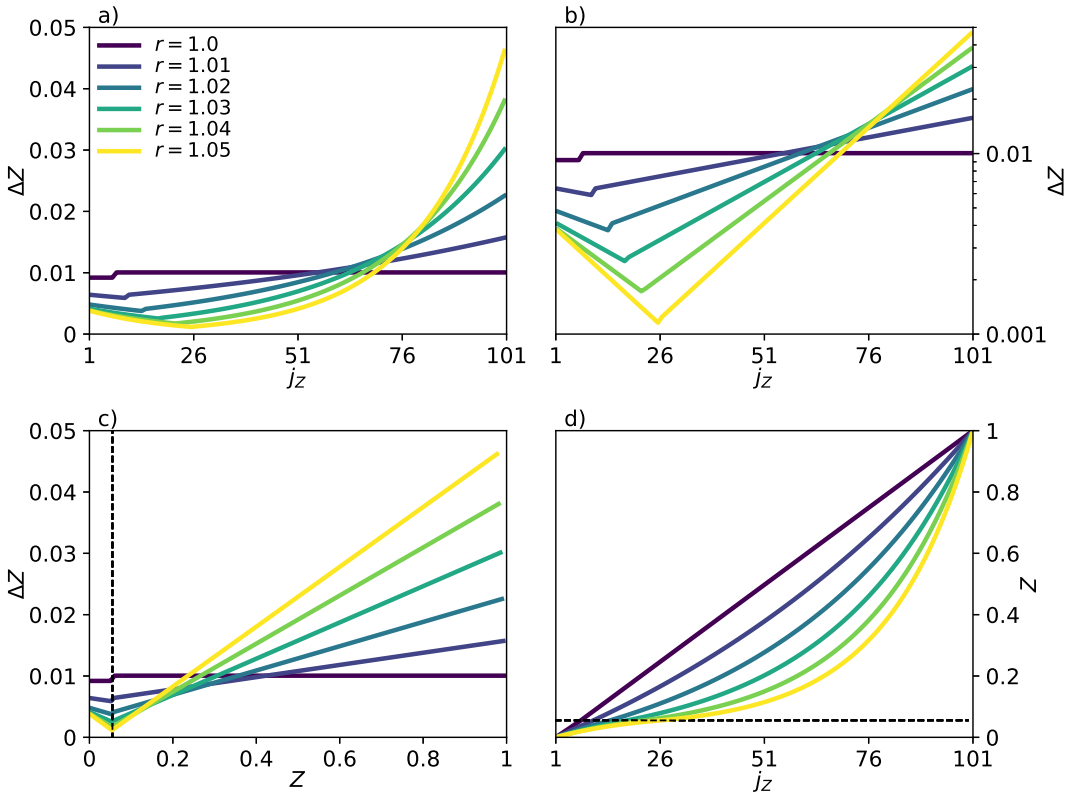

FIGURE 3.28: Mixture fraction discretization with attractor function at different r growth rates. The function creates $n_Z = 101$ points in the $Z \in [0, 1]$ interval, with a refinement around $Z_{st} = 0.0552$.

This refinement is done with an attractor function, that consists of two separate functions below and above the stoichiometric mixture fraction. These separate lean and rich discretizations are such, that the step size in mixture fraction: ΔZ follows a

geometric sequence as the function of the index in the grid:

$$\Delta Z\left(j_Z\right) = \Delta Z_{min} r^{j^*}, \tag{3.31}$$

where $\Delta Z\left(j_Z\right)$ is the step size between j_Z and $j_Z + 1$, ΔZ_{min} is the smallest step size in the vicinity of the stoichiometric point, and r is the growth rate of the step size. Furthermore j^* is the index relative to the stoichiometric point: j_{st}:

$$j^*_{lean} = j_{st} - j_Z, \qquad j^*_{rich} = j_Z - j_{st}. \tag{3.32}$$

Consequently, the actual location of a point in mixture fraction space is given by a shifted geometric series (the partial sum of the sequence), and at a predetermined total number of points: n_Z and index of the stoichiometric point: j_{st} the discretization is completely defined. In this case, ΔZ_{min} is calculated such, that the two series range from Z_{st} to $Z = 0$ and $Z = 1$ respectively. Furthermore, j_{st} is determined iteratively, such, that the difference in the step size on the left and right of the stoichiometric point is small. The python code corresponding to this process is included in the open source repository at: https://gitlab.com/BothAmbrus/LectIO.

Figure 3.28 illustrates such a discretization along mixture fraction in the case of methane, using a total of $n_Z = 101$ points, and various growth rates: $r \in \{1.0, 1.01, 1.02, 1.03, 1.04, 1.05\}$. In Fig. 3.28a-b the step size is shown along the index of the point using linear and logarithmic scaling. The limiting case of growth rate of 1.0 corresponds to uniform discretization on the rich and lean sides. In this case the step size is: $\Delta Z \approx 0.01$, with small variations at the stoichiometric point, in order to actually include the exact value of Z_{st}. As the logarithmic scale illustrates, when r is increased, the smallest step sizes decrease exponentially. This higher refinement around the point of interest also entails, that the minimum step size on the two sides of j_{st} become more and more similar. In Fig. 3.28c the step size is shown as a function of the mixture fraction itself, with the center of the attractor indicated by a dashed vertical line. The ΔZ is a linear function of Z itself, since both the geometric sequence (Eq. 3.31) and its series take the same r^j form with different constant shifts. The slope of this relation is determined by $r - 1$. All the studied non-unity growth rates result in lower step sizes in the entire flammability limit. In the $Z \in [0, Z_{st}]$ interval, the step size is throughout consistently lower at higher r values due to the off-center location of the stoichiometric mixture fraction. This refinement is possible at the expense of coarser discretization on the rich side outside the flammability limit. Finally, Fig. 3.28d presents the distribution of the points in mixture fraction space, further illustrating how the increase of the step growth rate focuses the resources on the vicinity of Z_{st}. In the six different presented cases, the indeces of stoichiometric mixture fraction are: $j_{st} \in \{7, 10, 14, 18, 22, 26\}$ respectively. This illustrates, that at $r = 1.05$ a quarter of the database is dedicated to lean flamelets. Finally, considering the lean and rich flammability limits at: $Z_L = 0.0206$ and $Z_R = 0.1920$, the indeces closest to these limits are $j_Z(Z_L) \in \{3, 4, 5, 6, 6, 7\}$ and $j_Z(Z_R) \in \{19, 28, 38, 48, 56, 63\}$ respectively, indicating, that at $r = 1.05$ more than half of the points are representing flammable mixtures. Overall, this high refinement is preferred in this work, but increasing the growth rate above $r = 1.05$ is not recommended.

3.3 Mapping non-adiabatic effects

In section 3.2 flamelets are mapped onto a discretization of the $Z - C$ plane, with the assumption, that enthalpy may be determined according to Eq. (2.46), and the

enthalpy deficit is constant zero. Such methods provide a good representation of the thermo-chemical state, when the targeted complex cases are indeed largely adiabatic, i.e.: interaction with cold walls or volumetric heat loss due to radiation or a separately modeled liquid phase are all negligible.

Non-adiabatic effects often become relevant, and these not only affect the temperature and consequently the density field, but as discussed in relation of Fig. 3.20, they also modify the reactivity of the gas mixture. The decreased enthalpy levels are characterized by lower flame speed, narrower flammability limits, and the presence of flame extinction due to heat loss. Gövert et al. (2015) and Proch and Kempf (2015) evaluated this effect, by tabulating adiabatic flamelets, but allowing for the variation of density and other properties due to heat loss. This method neglects the heat loss effect on the chemical source terms, which is the main driver behind the flame speed reduction. Both studies found, that while this simplified method captures well the temperature field, it fails in terms of predicting the flame length, due to the lack of non-adiabatic effects on the source term.

Since the importance of the phenomenon is clear, non-adiabatic effects are considered in the present work as well. This section details the tabulation strategy of two different kinds of flamelets with enthalpy deficit: premixed burner-stabilized flamelets, and counterflow diffusion flamelets with radiative heat loss.

3.3.1 Enthalpy deficit in premixed flamelet databases

Van Oijen and De Goey (2000) introduced heat loss to premixed flamelets considering a single mixture fraction, targeting perfectly premixed combustion. They use a combination of methods to decrease the inlet enthalpy. At moderate levels of enthalpy deficit the inlet temperature is decreased. This is considered feasible down to 240 K. To reach even more enthalpy deficit, product species (CO_2 and H_2O) are used for replacing part of the oxidizer and fuel stream, corresponding to mixing the isothermal equilibrium gas composition (Tab. 3.1) into the inlet at the corresponding equivalence ratio. Subsequently, Van Oijen, Lammers, and De Goey (2001) extended this method to using burner-stabilized flamelets instead of mixing in cold products. In fact, the two methods are largely equivalent as Fig. 3.7 demonstrates, since most of the new species present at the inlet boundary are the products like CO_2, due to their abundance in the flame. Fiorina et al. (2003) applied burner stabilized flamelets to model heat loss, but in this case the database was extended to various mixture fractions, with partially-premixed systems in mind. By comparing flamelets of decreased inlet temperature to the burner stabilized flamelet corresponding to the same enthalpy they show, that the points in the database identified by a Z, Y_c, and $|\Delta h|$ are indeed insensitive to the heat loss method itself. More recently Proch and Kempf (2015) assessed different heat loss methods for premixed combustion, and found, that the burner-stabilized flamelets perform reasonably well. Their preferred alternative: the artificial scaling of the heat release rate, shows very similar results with slight improvements under certain near-wall conditions.

The benefit of tabulating burner-stabilized flames for representing heat loss is highlighted by other successful LES applications as well. Cecere et al. (2011) tabulated burner-stabilized flamelets at a single equivalence ratio to simulate a turbulent bluff body stabilized premixed flame. Ketelheun, Kuenne, and Janicka (2013) studied the performance of burner-stabilized flamelets in a bluff body stabilized and a stratified configuration using information from the entire flammability limit. The study of Mercier et al. (2014) focused on the same stratified configuration, and found that the application of burner-stabilized flamelets in the tabulation method greatly

improved the lift-off characteristics of this flame. Pantangi et al. (2014) used this enthalpy reduction method in the tables, to study a turbulent premixed jet flame impinging on a cooled surface. The work of Gövert (2016) investigates the heat loss effects in a confined premixed jet flame. They found, that the usage of burner-stabilized flamelets improves the flame length predictions. Overall, all the mentioned studies find the burner-stabilized heat loss approach adequate for premixed and partially premixed applications. However, the recent work of Ganter et al. (2017) indicates, the tabulated chemistry methods may preform poorly in case of high wall heat loss, especially in terms of predicting pollutant formation. Since in the present study, flame-wall interactions are not studied in detail, the burner-stabilized heat loss approach is retained here.

Figure 3.29 presents the burner stabilized flamelets of section 3.1.2 as a function of the progress variable. The fist row of plots shows the enthalpy, which is largely constant along the flamelets, as expected using the unity Lewis number assumption. (Note, that small variations arise due to the discretization errors in the numerical methods of Cantera.) These plots illustrate well the triangular region, that can be mapped on the $Y_c - h$ plane, as the decreased enthalpy levels are only accessible if the inlet progress variable takes an elevated value. (Van Oijen and De Goey, 2000) This is taken to the limit at the isothermal equilibrium ($m = 0$) where the enthalpy is significantly lower than the enthalpy of the last burning flamelet, and the progress variable can only take one single value.

The second row of plots in Fig. 3.29 shows the source term of the progress variable in logarithmic scale. As the heat loss to the burner increases, and global heat release rate approaches zero (Fig. 3.20) and so does the source term of the progress variable. The peak of $\dot{\omega}_{Y_c}$ decreases significantly and its location shifts towards higher progress variables. Finally, the last two rows of Fig. 3.29 show the mass fractions of carbon dioxide and carbon monoxide respectively. As the mass flow of the flamelets is decreased, the amount of CO decreases as well. In case of the lean and stoichiometric flamelets the gas mixture of the outlet always reaches a similar composition of high CO_2 and relatively low CO, since the dissociation of final combustion products is less prevailing at such equivalence ratios. However, at the rich flamelet in the third column of plots, there is a large discrepancy between the outlet states of the burning flamelets and the isothermal equilibrium. The rich flamelets are characterized by high amount of carbon monoxide throughout the domain, and the peak of CO_2 is significantly lower than the isothermal equilibrium value.

Tabulation of burner-stabilized flamelets

As discussed above, the inlet composition has to change across different enthalpy levels in burner-stabilized flamelets. However, even the outlet values are significantly different, causing slight differences in the progress variable at the outlet. For instance, in the middle column of Fig. 3.29 showing stoichiometric flamelets, at $m/(\rho^u S_L) = 1.0$ the progress variable is in the range of $Y_c^{ref} \in [0, 0.026]$, while at $m/(\rho^u S_L) = 0.01$ it is contained in $Y_c^{ref} \in [0.014, 0.027]$. To manage this variability of the limiting progress variable values, the scaled progress variable is obtained by using the maximum and minimum possible start and endpoints at a certain mixture fraction across all enthalpy levels, so Eq. (3.30) is replaced by:

$$C = \frac{Y_c - \min\left(Y_c^{start}\right)(Z)}{\max\left(Y_c^{start}\right)(Z) - \min\left(Y_c^{start}\right)(Z)}. \tag{3.33}$$

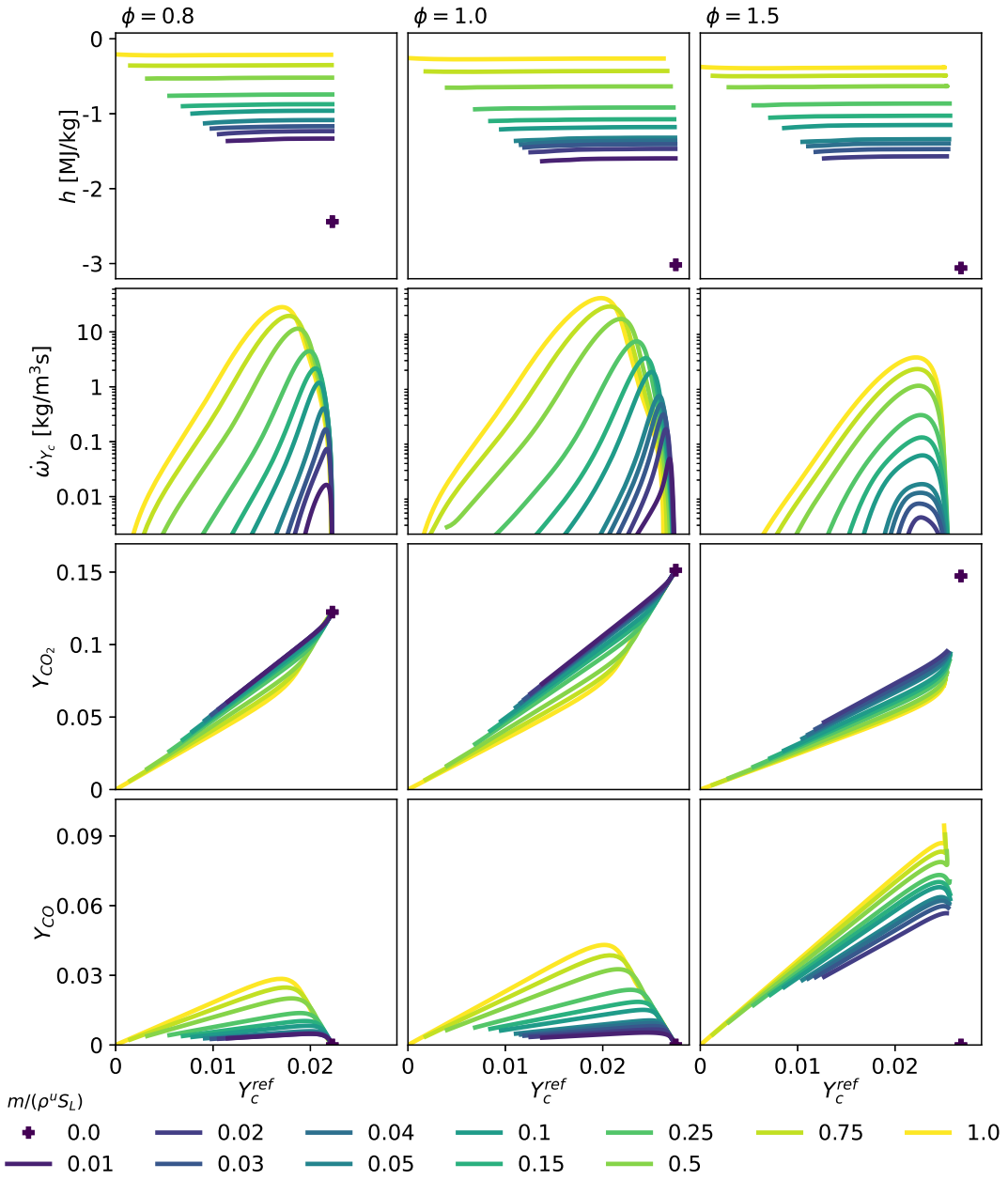

FIGURE 3.29: Burner-stabilized flamelets in progress variable space at selected equivalence ratios using the GRI3.0 (Smith et al., 2011) chemical mechanism with the unity Lewis number assumption and the progress variable definition of Ma (2016). The different columns show the equivalence ratios: $\phi \in \{0.8, 1, 1.5\}$. The rows show the enthalpy (h), the source term of the progress variable ($\dot{\omega}_{Y_c}$), and the mass fractions of carbon dioxide (Y_{CO_2}) and carbon monoxide (Y_{CO}) respectively.

Consequently, at certain flamelets not all scaled progress variable values are present. In the interpolation process this is overcame, by taking the gas state of the nearest existing solution in progress variable space.

Figure 3.30 illustrates the process of interpolation of burner-stabilized flamelets. The different columns indicate different stages of the process. The two rows show

unscaled and scaled progress variable respectively, the former indicating where each gas state of the table is taken from, while the latter showing the structure of the table. The coloring also indicates the unscaled progress variable, further clarifying the origin of each tabulated gas state. Similar to Fig. 3.27 the dashed lines indicate the direction of interpolation that is carried out for reaching the next step. Note, that in this figure only stoichiometric flamelets are shown, however, the process is the same whether or not multiple mixture fractions are included in the table.

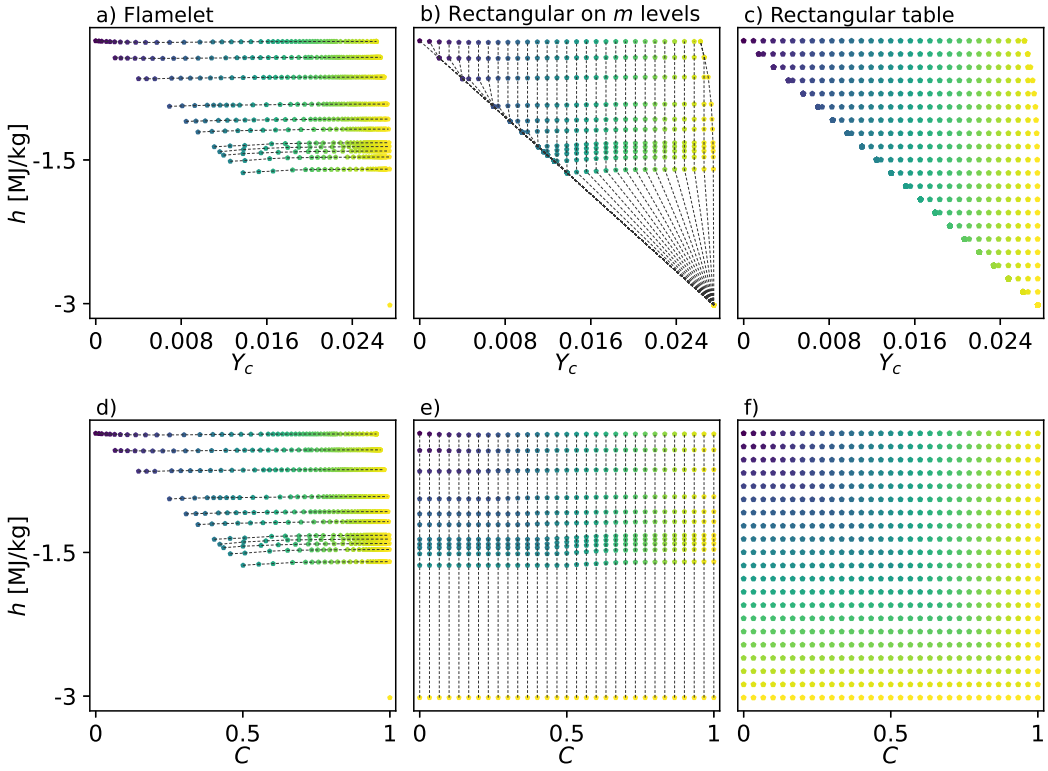

FIGURE 3.30: Process of interpolation of stoichiometric burner-stabilized flamelets onto a rectilinear discretization. The example uses methane-air flamelets with the unity Lewis number assumption ("Le=1") and the progress variable definition of Ma (2016). The different columns show the stages of the mapping procedure. The rows show the unscaled and scaled progress variable colored by the scaled progress variable of the original gas mixture used in the data point.

As Fig. 3.30 indicates, the raw flamelets indeed only cover a limited area both in h and Y_c. To reach the state of the second column of plots, the interpolation strategy of "adiabatic" flamelet arrays is executed at each scaled mass flux level, according to section 3.2.4. Since in this case the progress variable is scaled according to Eq. (3.33), all relevant gas states are contained in the $C \in [0, 1]$ interval. In some cases this results in repeating the same gas state multiple times outside the limits of physically possible conditions. This repetition of states is evident comparing Fig. 3.30b and Fig. 3.30e, where the lower left half of the $C - h$ plane is filled with the inlet states of the burner stabilized flamelets, while on the $Y_c - h$ plane these states remain unaccessible. Note, that this approach does not use Eq. (3.33) to obtain C from Y_c, rather the values of C are predetermined according to a linear discretization, and different states are obtained using either interpolation or by the repetition of the last state.

The transition from the second to the third column in Fig. 3.30 depicts the transformation to a fully rectilinear table, where the enthalpy is also obtained at predetermined levels. In case of burner-stabilized flamelets the minimum and maximum enthalpy levels are only taken as a function of mixture fraction according to Eq. (2.46) and Eq. (3.8), as depicted in Fig. 3.9. The enthalpy levels are characterized by the scaled enthalpy parameter:

$$i = \frac{h - h^{min}(Z)}{h_{ad}(Z) - h^{min}(Z)}, \tag{3.34}$$

where $h^{min}(Z) = h_{ad}(Z) - \max(|\Delta h|)(Z)$ is the lowest possible enthalpy at isothermal equilibrium. An important aspect of this last step, is the interpolation between the isothermal equilibrium and the last stable burner-stabilized flame. As Fig. 3.30b indicates with dashed lines, the interpolation is not executed along constant Y_c in this region. Consequently, the states created between this flamelet and the isothermal equilibrium need to be re-sampled at the actual target values of Y_c determined by the discretization of C.

3.3.2 Enthalpy deficit in counterflow diffusion flamelet databases

The burner-stabilized flamelets introduced above provide an excellent method to reach decreased enthalpy levels in premixed configurations where the reduction of the inlet temperatures is infeasible. Such situations in non-premixed flames received somewhat less attention in the literature in the context of tabulated chemistry. In fact, the desired levels of enthalpy deficit may be reached by simply decreasing the oxidizer temperature in some applications. (Ma and Roekaerts, 2016; Zhang et al., 2019) Nevertheless, various methods exist to obtain counterflow diffusion flamelets with adequate levels of enthalpy loss in the case of low fresh gas temperatures.

Hossain, Jones, and Malalasekera (2001) tabulated counterflow diffusion flames by reducing the inlet enthalpy at the boundaries. To achieve relevant enthalpy loss levels, they use a reduced mixture fraction interval of $Z \in [Z_L, Z_R]$, where according to Eq. (3.8) larger enthalpy deficits are feasible at the adiabatic inlet temperature conditions. Thus, in fact they are tabulating partially premixed flamelets, for the sake of enthalpy reduction. Ihme and Pitsch (2008a) used a radiative source term in the flamelet equations as the present work does, but they used this to consider the actual radiative effects on a free jet flame whereas the present study uses radiation to access higher enthalpy deficits. Ma et al. (2018) used a permeable thermal boundary condition within the counterflow flame domain to reach an enthalpy deficit, resembling the burner-stabilized method of premixed flamelets. Recently Wollny, Rogg, and Kempf (2018) compared the method of artificial radiation applied in the present study, and the method of damping the heat release term in the flamelets. They found, that the two methods behave very similarly considering the stable branch only. In the present work only the artificial scaling of the radiation term is explored as a heat loss mechanism.

Progress variable injectivity in counterflow flamelets with radiation

As illustrated in Fig. 3.19 it can be challenging to uniquely describe the flamelet sets of decreased enthalpy level, since major products like CO_2 and H_2O show a local maximum across different strain rates. Furthermore, as Fig. 3.17 demonstrates, at radiation scales of $c_{rad} \geq 4$ the temperature becomes continuous between the stable

and unstable branches on the lower end of the strain rate range, suggesting that the thermo-chemical states themselves become identical at this point, and the "S-curve" is transformed into a loop. Consequently, the progress variable cannot provide a unique discretization at any part of the stable and unstable branches, since there are always two coexisting solutions.

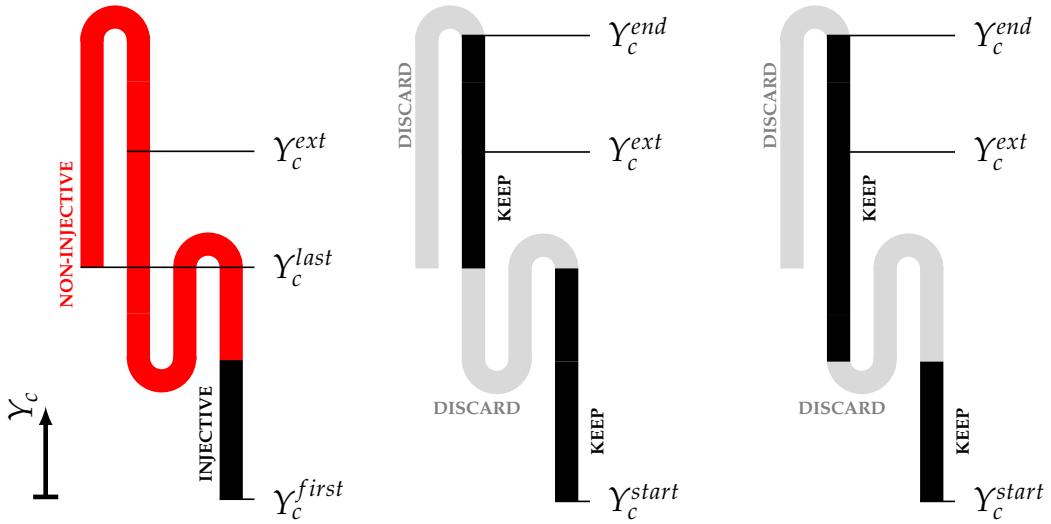

(A) Non-unique regions (B) First Unique (FU.) (C) Central Unique (CU.)

FIGURE 3.31: Non-injective parts of pseudo-premixed flamelet of a counterflow flamelet with elevated radiative heat loss.

Figure 3.31 illustrates a pseudo-premixed flamelet of the flamelet array composed of the stable and unstable branches at $c_{rad} \geq 4$. The progress variable values at the mixing line, at the extinction point, and at the stable flamelet with the lowest strain rate are indicated by Y_c^{first}, Y_c^{ext}, and Y_c^{last} respectively. As Fig. 3.31a shows, the Cut out (C) truncation strategy of section 3.2.3 would discard almost all reacting states. A new truncation method: Central Unique (CU) is introduced here, illustrated in Fig. 3.31c, which has favorable properties for tabulating the S-curve using radiative heat loss. The Central Unique (CU) strategy consists of taking the unique progress variable regions closest to the extinction point, or closest to the initial condition in case of the "Stab.+Reign.+Ext." flamelet set of Tab. 3.8. Both the FU and CU methods discard the thermo-chemical states of the stable branch at lower strain rates, which are below the maximum Y_c. The difference between the two methods lies in the location of the discontinuity in the unstable branch. It is argued, that a favorable manifold is given by keeping a larger continuous part of the S-curve indicated on Fig. 3.31c.

The Central Unique (CU) truncation strategy is further illustrated in Fig. 3.32, where it is used on pseudo-premixed flamelets of the "Stab.+Unstab." flamelet set at different c_{rad} radiation scales. For reference, an additional pseudo-premixed flamelet is included, corresponding to inert mixing between the fresh mixture and the isothermal equilibrium state. The first row of plots presents the S-curve in progress variable space, while the rest of the figure shows the flame structure the same way as Fig. 3.29. These two figures display the exact same ranges for better comparison between premixed burner-stabilized flamelets and counterflow diffusion flamelets with scaled radiative heat loss.

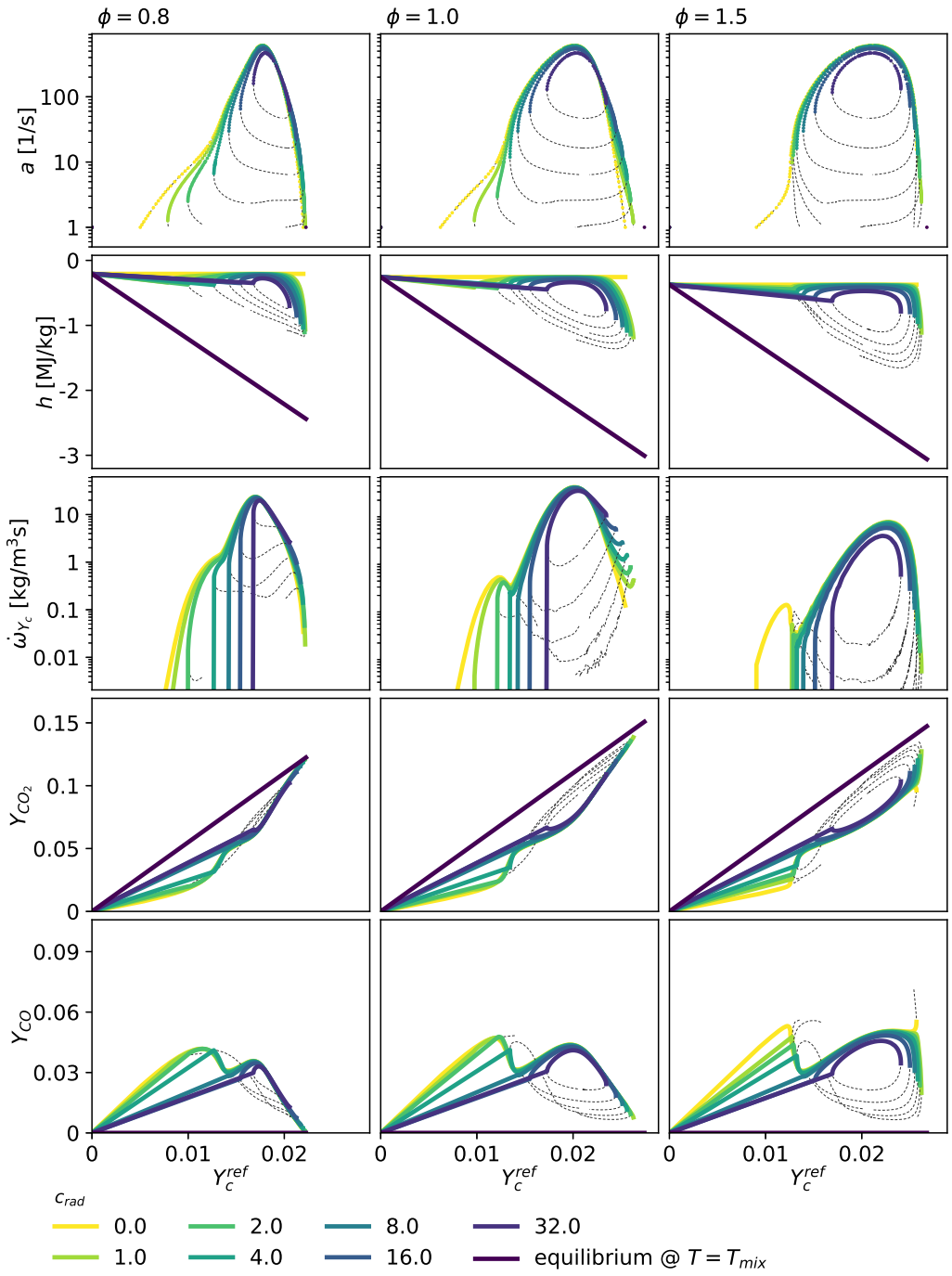

FIGURE 3.32: Counterflow diffusion flamelets with artificially scaled radiative heat loss in progress variable space at selected equivalence ratios using the GRI3.0 (Smith et al., 2011) chemical mechanism with the unity Lewis number assumption and the progress variable definition of Ma (2016). The different columns show the equivalence ratios: $\phi \in \{0.8, 1, 1.5\}$. The rows show the strain rate (a), enthalpy (h), the source term of the progress variable ($\dot{\omega}_{Y_c}$), and the mass fractions of carbon dioxide (Y_{CO_2}) and carbon monoxide (Y_{CO}) respectively. The Central Unique (CU) truncation strategy is used to obtain injective solutions on progress variable.

The effect of the CU truncation is highlighted by plotting the full set of flamelets form both the stable and unstable branches with thin dashed lines. As the first row of plots shows, indeed the retained flamelets form the largest unique interval encompassing the extinction point. Thus the discarded parts consistently correspond to low strain rates. Since, the high retained strain rates correspond to low residence times, the effect of radiative heat loss is moderate. Consequently, as the second row of Fig. 3.32 indicates, the region of enthalpy accessible by such flamelet arrays is quite limited compared to burner-stabilized flamelets. Considerable enthalpy deficits are only accessible towards higher Y_c.

The third row of Fig. 3.32 shows the source term of the progress variable in logarithmic scale. The dereferences between varied c_{rad} solutions are minor in comparison to the remarkable differences observed in burner-stabilized flamelets. The lowest strain rate states, that are characterized by reduced source terms, have to be discarded for the sake of injectivity. This highlights the importance of selecting an adequate progress variable, which can incorporate as large portion of the flamelet solutions as possible. The observed differences between various enthalpy levels are principally occurring in the discarded gas states, where the reduced enthalpy cases can no longer provide a unique solution. In this region the source term drops steeply with increasing c_{rad}. Furthermore, smaller differences are occurring under stoichiometric conditions (middle column) near the highest progress variable values. Here $\dot{\omega}_{Y_c}$ grows with the decrease of enthalpy. A similar trend is observed in Fig. 3.29, where in a similar region of Y_c higher source terms belong to the burner-stabilized flamelets of lower enthalpy.

Finally, the last two rows of Fig. 3.32 show carbon dioxide and carbon monoxide mass fraction respectively. Due to the high importance of mixing along the counterflow flamelets the different equivalence ratios show considerably more similar values than in the case of burner-stabilized flamelets. The most striking difference is observed under rich conditions ($\phi = 1.5$.) Here CO_2 approaches the isothermal equilibrium value corresponding to a more "complete" combustion, and lower Y_{CO}.

Tabulation of counterflow diffusion flamelets with radiative heat loss

In the tabulation of counterflow diffusion flamelets with radiative heat loss, the scaled control variable of enthalpy is slightly modified to approximate the dataset better. Instead of scaling the enthalpy solely as a function of mixture fraction, the limits are determined individually at each Z and C. Thus the scaled enthalpy is:

$$i = \frac{h - h^{min}\left(Z, C\right)}{h_{ad}\left(Z\right) - h^{min}\left(Z, C\right)}, \tag{3.35}$$

where $h^{min}\left(Z, C\right) = h_{ad}\left(Z\right) - C \cdot \max\left(\left|\Delta h\right|\right)\left(Z\right)$ is the lowest possible enthalpy on the inert mixing solution between fresh reactants and the isothermal equilibrium.

The interpolation process of opposing diffusion flamelets with radiative heat loss is illustrated on Fig. 3.33. The figure follows the structure of the similar figure illustrating burner-stabilized flamelets (Fig. 3.30.) The different columns show different stages of the interpolation process: pseudo-premixed flamelets at each c_{rad} level, rectilinear discretization at each c_{rad} level, fully rectilinear discretization across all dimensions of the manifold. Dashed lines indicate the direction of interpolation that is executed in order to reach the next stage.

The flamelets solutions are first interpolated at onto a predetermined discretization of the mixture fraction, as detailed in section 3.2.4. Figure 3.33 shows only the

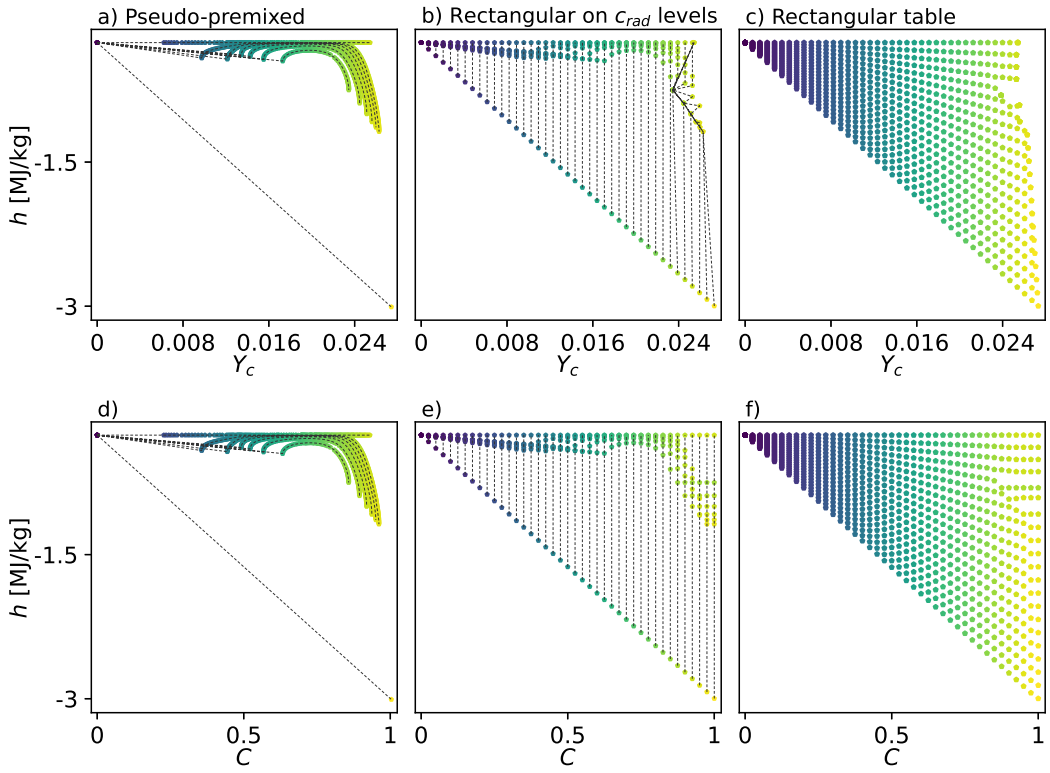

FIGURE 3.33: Process of interpolation of counterflow diffusion flamelets with radiative heat loss onto a rectilinear discretization. The example uses methane-air flamelets with the unity Lewis number assumption ("Le=1") and the progress variable definition of Ma (2016). Only the layer of stoichiometric mixture fraction is displayed. The different columns show the stages of the mapping procedure. The rows show the unscaled and scaled progress variable colored by the scaled progress variable of the original gas mixture used in the data point.

stoichiometric mixture fraction. Subsequently, flamelet states are selected from the pseudo-premixed flamelets according to the Central Unique (CU) truncation strategy such, which may be uniquely described by the progress variable at each c_{rad} scale. Next the interpolation along these pseudo-premixed flamelets is carried out according to the discretization of C. This is the state represented in the central column of Fig. 3.33, where all flamelet arrays are discretized rectilinearly, but the enthalpy levels still form an unstructured pattern. Finally, the data points are grouped according to the given Z and C values, and gas mixtures are obtained along the given values of scaled enthalpy i. Note, that the mixing solution between fresh reactants and the isothermal equilibrium is included as an additional level along the different c_{rad} values. Most of the tabulated states are reached by linear interpolation between these inert gas states and the flamelet state with the lowest enthalpy, and only a small region of modest enthalpy deficits is captured by the actual counterflow flamelet solutions.

3.4 Thermo-chemical tables

Sections 3.2 and 3.3 present methods to interpolate flamelet solutions onto a rectilinear discretization of selected control variables. The present section details how these interpolations are executed and what properties are stored in the thermo-chemical tables.

3.4.1 Tabulation process

As section 2.1.2 describes, the local properties of the gas state are uniquely identified by the pressure, the enthalpy, and the composition, where in this work the pressure is taken as constant according to the low Mach number approximation. Consequently, it is sufficient to store the enthalpy and the gas composition in the entries of the table, in order to obtain any thermodynamic and transport properties. The interpolation process of Fig. 3.27, Fig. 3.30 and Fig. 3.33 is executed for h and Y_k, applying linear interpolation between neighboring gas states on the predetermined grid of Z, C, and i. This process if followed to obtain properties listed in Tab. 3.9. The relations presented in section 2.1 give the thermodynamic and transport properties of the interpolated gas mixtures, while even the chemical source terms are recomputed following section 2.5.1.

TABLE 3.9: Quantities recomputed using the interpolated gas state.

Material or transport property	Symbol	Relation
Mean molecular weight	W	Eq. (2.1)
Density	ρ	Eq. (2.51)
Specific heat	c_p	Eq. (2.7)
Mean NASA polynomials	b_i	Eq. (2.9)
Temperature	T	Algorithm 2.1
Dynamic viscosity	μ	Eq. (2.13)
Thermal conductivity	λ	Eq. (2.15)
Mixture-averaged mass diffusion coefficient	$\mathcal{D}_k$	Eq. (2.19)
Chemical quantity	**Symbol**	**Relation**
Net formation rate of species	$\dot{\omega}_k$	Eq. (2.97)
Production rate of species	$\dot{\omega}_k^+$	Eq. (2.98)
Consumption rate of species	$\dot{\omega}_k^-$	Eq. (2.98)
Heat release rate	$\dot{\omega}_T$	Eq. (2.100)
Progress variable source term	$\dot{\omega}_{Y_c}$	Eq. (2.120)

The information stored in the adiabatic layer of the final tables is illustrated in Fig. 3.34, by plotting the iso-contours of the chemical source term of the unscaled progress variable: $\dot{\omega}_{Y_c}$ in the left column and the temperature in the right column. The latter is computed from the interpolated composition and enthalpy using Algorithm (2.1), while the chemical mechanism is utilized for the recalculation of the former. These quantities are represented on the Z-Y_c plane. All tabulation is executed using the same discretization of the control variables, the scaled progress variable is sampled uniformly using $n_C = 101$ points, while an attractor type discretization is used for the mixture fraction, centered on the stoichiometric point and using a growth rate of $r = 1.05$ with also $n_Z = 101$ points. (See Fig. 3.28.) The First Unique

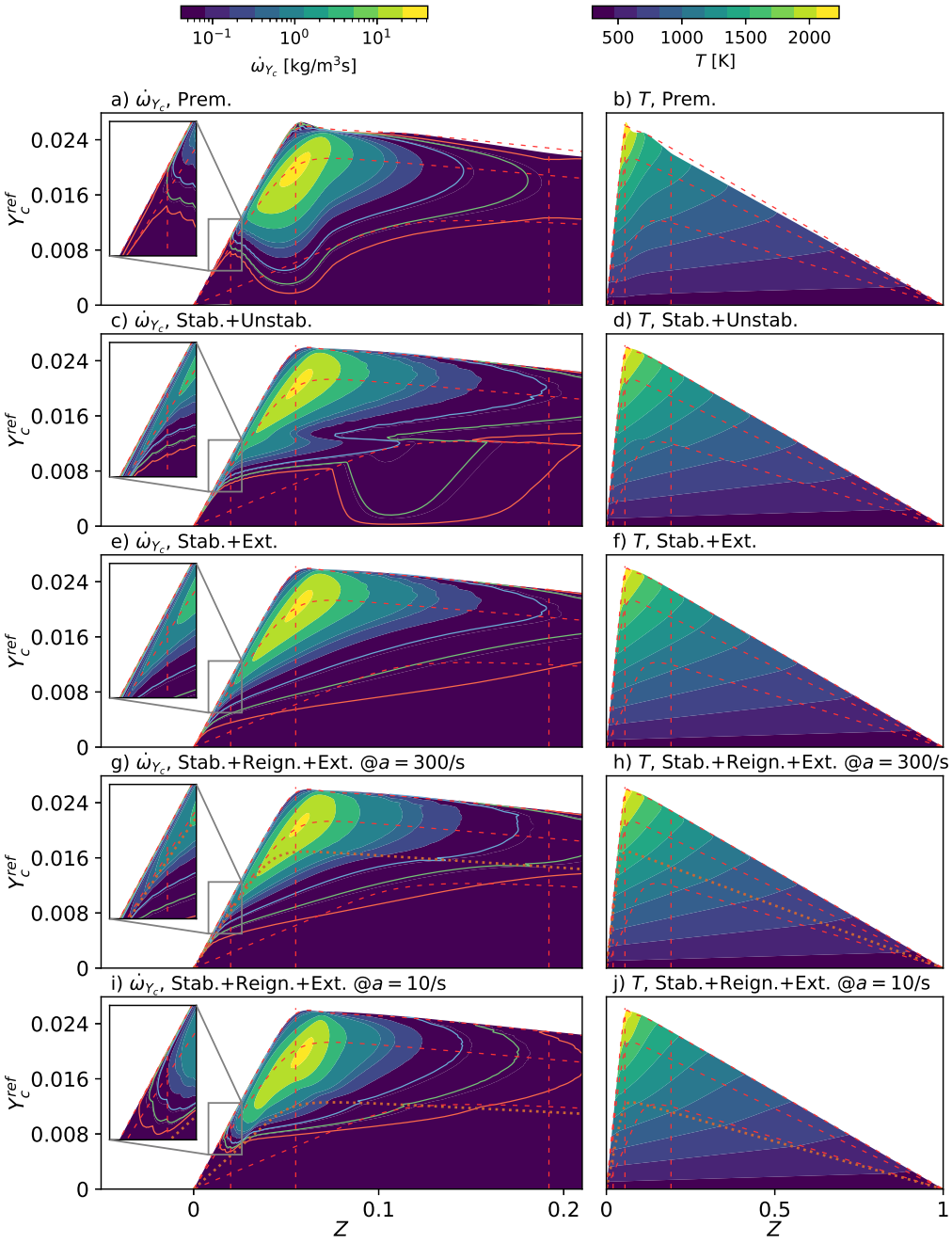

FIGURE 3.34: Illustration of tabulated progress variable source term (left) and temperature (right) using various flamelet sets (rows). Reference flamelets are indicated by dashed lines. Premixed flamelets show the lean flammability limit, the stoichiometric flamelet, and the rich flammability limit using vertical lines. Diffusion flamelets indicate the stable flamelet at $a = 1$/s, the extinction point, and the unstable flamelet at $a = 1$/s. In the last two rows, that use unsteady reigniting and extinguishing flamelets, the initial conditions are indicated by dotted lines. The contour plot of progress variable source term uses a logarithmic color map, and additional contour lines are included to indicate the low source terms of: $\dot{\omega}_{Y_c} = 0.04$ kg/m^{3}s (blue), $\dot{\omega}_{Y_c} = 0.01$ kg/m^{3}s (green), and $\dot{\omega}_{Y_c} = 0.0025$ kg/m^{3}s (red).

(FU) truncation strategy is used to ensure injective solutions across various progress variables.

Five tables are compared in the different rows of Fig. 3.34 identified by the abbreviations listed in Tab. 3.8. The first table (Prem.) uses premixed free flamelets in the flammability limit ($0.0206 \leq Z \leq 0.1920$, $0.35 \leq \phi \leq 4.07$), and interpolates between pure oxidizer and fuel, and the leanest and richest burning flamelets respectively. (Van Oijen and De Goey, 2004) The second table (Stab.+Unstab.) uses the stable and unstable steady counterflow diffusion flamelets and interpolates between the last uniquely represented point along Y_c and the mixing line. (Pierce and Moin, 2004) The third approach (Stab.+Ext.) retains the stable branch, but replaces the rest of the flamelet data by the temporally sampled solutions of an unsteady extinguishing flamelet computed at a strain rate of $a = 800/\mathrm{s}$, above the extinction point. (Chrigui et al., 2012) The fourth and fifth approaches (Stab.+Reign.+Ext.) use only the lower strain rate part of the stable branch, and the rest of the Z-Y_c plane is represented by time sampling of unsteady reigniting and extinguishing flamelets at two different strain rates: $a = 300/\mathrm{s}$ and $a = 10/\mathrm{s}$. (Bekdemir, Somers, and De Goey, 2011) In the fourth and fifth rows of the figure the unstable flamelet at $a = 300/\mathrm{s}$ and $a = 10/\mathrm{s}$ is represented by dotted lines, indicating the separation between the unsteady reigniting and extinguishing flamelets.

Concentrating first on the temperature contours of Fig. 3.34 the difference between the various manifolds is quite minor. One of the main differences between premixed and diffusion flamelets is the peak value of the progress variable $Y_c^{end}(Z)$. For most mixture fractions this limit is higher in case of diffusion flamelets, except a few flamelets near stoichiometry. In terms of temperature, the premixed flamelets are notably cooler at the same level of progress variable, as indicated by the T iso-lines occurring at higher values of Y_c. Moreover, a minor detail is illustrated in Fig. 3.34d, where the temperature iso-lines show a discontinuity near the unstable flamelet at $a = 1/\mathrm{s}$. This discontinuity is a consequence of non-injective behavior in the unstable branch at low strain rates, as illustrated in Fig. 3.24. However, this gap is rather small and does not affect significantly the source terms, thus such tables may be used without numerical issues associated with the small discontinuity in density.

The left column of Fig. 3.34 shows more pronounced differences. In all cases the progress variable source term is positive in the entire manifold, and it has a local maximum near stoichiometry at the reaction progress corresponding to the counterflow diffusion flamelet at the extinguishing strain rate. This point is indicated by the intersection of the overlaid flamelets. There are slight differences between the various flamelet sets in the behavior of this maximum point. In case of premixed flamelets the highest displayed source terms are located more toward the lean side, and towards lower progress variables. Using the stable branch of the diffusion flamelets (Fig. 3.34c,e), the peak is concentrated towards richer mixtures and towards progress variables above the extinguishing flamelet. In case of unsteady extinguishing and reigniting flamelets at $a = 300/\mathrm{s}$ the peak behavior is quite similar to above, but the region with the highest values is notably smaller, indicating a lower peak value. Meanwhile, in case of the same configuration at $a = 10/\mathrm{s}$ the peak is shifted towards richer mixtures and lower equivalence ratios.

Near stoichiometry the premixed flamelet table of Fig. 3.34a shows a more distributed profile of the source term as function of Y_c, with the lowest contour lines nearly touching the mixing line. This is explained by the exchange of matter between different progress variable states along the premixed flamelets, i.e.: radicals are present at lower progress variables, making the gas mixtures more chemically active.

In return, the lack of mixing between different mixture fraction states limits the high source terms to a rather narrow range near stoichiometry. The $\dot{\omega}_{Y_c} = 0.01$ kg/m^{3}s iso-line, indicated in green, is entirely contained within the flammability limit, while the even lower iso-line of red $\dot{\omega}_{Y_c} = 0.0025$ kg/m^{3}s can stretch beyond these limits, because the composition is linearly interpolated between the last burning flamelets and the pure reactants, and the source term is recalculated in the table from the full composition and the temperature.

The table using the stable and unstable branch of steady diffusion flamelets in Fig. 3.34c shows a double peak structure in the progress variable source term at certain mixture fractions. This behavior is also observed in case of the heat release rate in Fig. 3.16, and it is related to the high temperature reaction zone shifting to richer composition in low strain rate unstable flamelets as demonstrated in Fig. 3.12. Despite the existence of this source term peak at low progress variables, the source term iso-lines are significantly further from the mixing line than in the case of premixed flamelets near stoichiometry, since there is no material transfer between different progress variable states. Note, that this trend is broken at richer conditions, where the Firs Unique (FU) truncation strategy forces the interpolation between the mixing line and higher strain rate flamelets. In this case, the radicals of the linearly interpolated composition can sustain a non-zero source term at quite low Y_c. Due to the material exchange between different mixture fraction conditions, the source is distributed more widely along Z, and notable source terms are present well beyond the flammability limits.

The next studied table of Fig. 3.34e only differs from the "Stab.+Unstab." strategy at progress variables below the extinction point. In this case the detailed structures of the unstable branch are all absent, and there are no truncation issues as the flamelets used in the construction of this part of the manifold are correlated in time. Consequently, the solution is significantly smoother along Y_c. The red iso-contour of $\dot{\omega}_{Y_c} = 0.0025$ kg/m^{3}s is located at quite low values of progress variable. In fact, near stoichiometry it is the lowest among all diffusion flamelet tables studied here. This is caused by the history effects of unsteady extinction, as the process is quite fast and the mixture is able to stay more reactive than in the flamelets used for other manifolds. The source term contours are as extended in mixture fraction as in the case of the "Stab.+Unstab." manifold, since the two tables share the stable branch.

In case of the table using unsteady reigniting and extinguishing flamelets at $a = 300/\text{s}$ initialized from the unstable branch (Fig. 3.34g) significant differences arise. The region with significant source terms becomes narrower both along progress variable and mixture fraction. The effect is even more notable at $a = 10/\text{s}$ in Fig. 3.34i. In this case, the contour lines are just as limited in mixture fraction space as in the case of premixed flamelets. Nevertheless, a key difference between the "Prem." database, and this one, is the distribution along Y_c. The "Stab.+Reign.+Ext. @$a = 10/\text{s}$" table has low source terms at low values of progress variable near stoichiometry, similar to the "Stab.+Unstab." manifold.

Figure 3.34 pays dedicated attention on the lean flammability limit of the tables, by displaying this region in magnified plots. As discussed above, the premixed flamelets are constrained by the lean flammability limit. Diffusion flamelets are able to produce significant source terms outside this limit. The highest and most widely distributed $\dot{\omega}_{Y_c}$ profiles are associated to the extinguishing flamelet at $a = 800/\text{s}$. Both using the unstable branch or unsteady flamelets at a lower strain rate results in lower progress variable source terms in this region. In case of the "Stab.+Reign.+Ext. @$a = 10/\text{s}$" manifold this source term reduction on the lean side is so severe, that the table is almost as limited as the one using premixed flamelets. At this low strain

rate the diffusion flamelets become quite thick ($\mathcal{O}$ (1 cm) see Fig. 3.12) thus mixing between different mixture fraction states is less significant in the reigniting flamelet, and the parts below the lean flammability limit are not chemically active.

Non-adiabatic tables

Including non-adiabatic effects introduces the enthalpy h as a control variable, and the scaled enthalpy i as a dimension of the table according to Eq. (3.34) or Eq. (3.35). In this chapter $n_i = 31$ uniformly placed points are used to discretize the scaled enthalpy coordinate. The different non-adiabatic tables are illustrated in Fig. 3.35 by iso-lines of the progress variable source term on the Y_c - h plane at different equivalence ratios. The limit with the highest enthalpy on this figure forms the adiabatic layer presented above. Meanwhile the lower limit corresponds to an inert mixture of reactants and products at the inlet temperature. In case of the burner-stabilized flamelets, presented in the first row of plots, this mixture is a consequence of the boundary conditions described in section 3.1.2. Consequently, the cold mixture composition can contain radicals, as demonstrated in Fig. 3.7. In the case of the counterflow diffusion flamelets this minimal enthalpy level is added artificially, by interpolating between the pure mixing solution and the isothermal equilibrium solution, corresponding to the upper left and lower right corners of the regions presented in Fig. 3.35 respectively. In this case, the minimum enthalpy states only contain reactants, and the products of the perfect oxidation: CO_2 and H_2O.

Figure 3.35a-c presents the behavior of burner-stabilized flamelets on the Y_c - h plane at different equivalence ratios. As discussed in relation of Fig. 3.30, this manifold has finely spaced flamelet solutions at the upper half of the possible enthalpies. The other half of the plane is covered by interpolation. Non-zero source terms are observed solely at higher enthalpies, where flamelet solutions are actually present, thus the interpolation process below this limiting enthalpy only serves to calculate thermodynamic properties, and this part is not chemically active. Another interesting feature of this manifold, is the shift of peak $\dot{\omega}_{Y_c}$ to higher values of Y_c as the enthalpy is decreased. The phenomenon is better understood by observing Fig. 3.7. Indeed, despite radicals being present at the inlet of the burner-stabilized flamelets, high temperatures are required to sustain intense reactions as indicated by the downstream shift of heat release rate. Consequently, the reaction zone associated to higher and higher reaction progress as the enthalpy of the flamelets is decreasing.

The subsequent plots of Fig. 3.35 (d-l) illustrate the behavior of counterflow diffusion flamelets with radiative heat loss, appended with the mixing solution between pure reactants and the isothermal equilibrium state. This appended minimal enthalpy level naturally produces zero progress variable source term, since the temperature is the fresh reactant temperature irrespective of Y_c and there are no radicals present in the mixture. Nevertheless, the actual flamelet solutions are concentrated in a quite narrow range of the Y_c - h plane as Fig. 3.32 illustrates. Consequently, most of the decreased enthalpy states in the manifold arise from interpolation between the lowest enthalpy state flamelet and the minimal enthalpy level, as Fig. 3.33b presents. The complexity of the flamelet behavior on the presented sections of the tables causes certain irregularities, including some inaccessible states near higher progress variables, and the presence of positive source terms in a larger zone of the Y_c - h plane. Nevertheless, in the thin region, where flamelet solutions exist, the trends between the burner-stabilized premixed flamelets and the counterflow diffusion flamelets appear to be similar with signs of decreasing source terms and source term peaks shifting to higher values of Y_c as the enthalpy decreases. Such tables

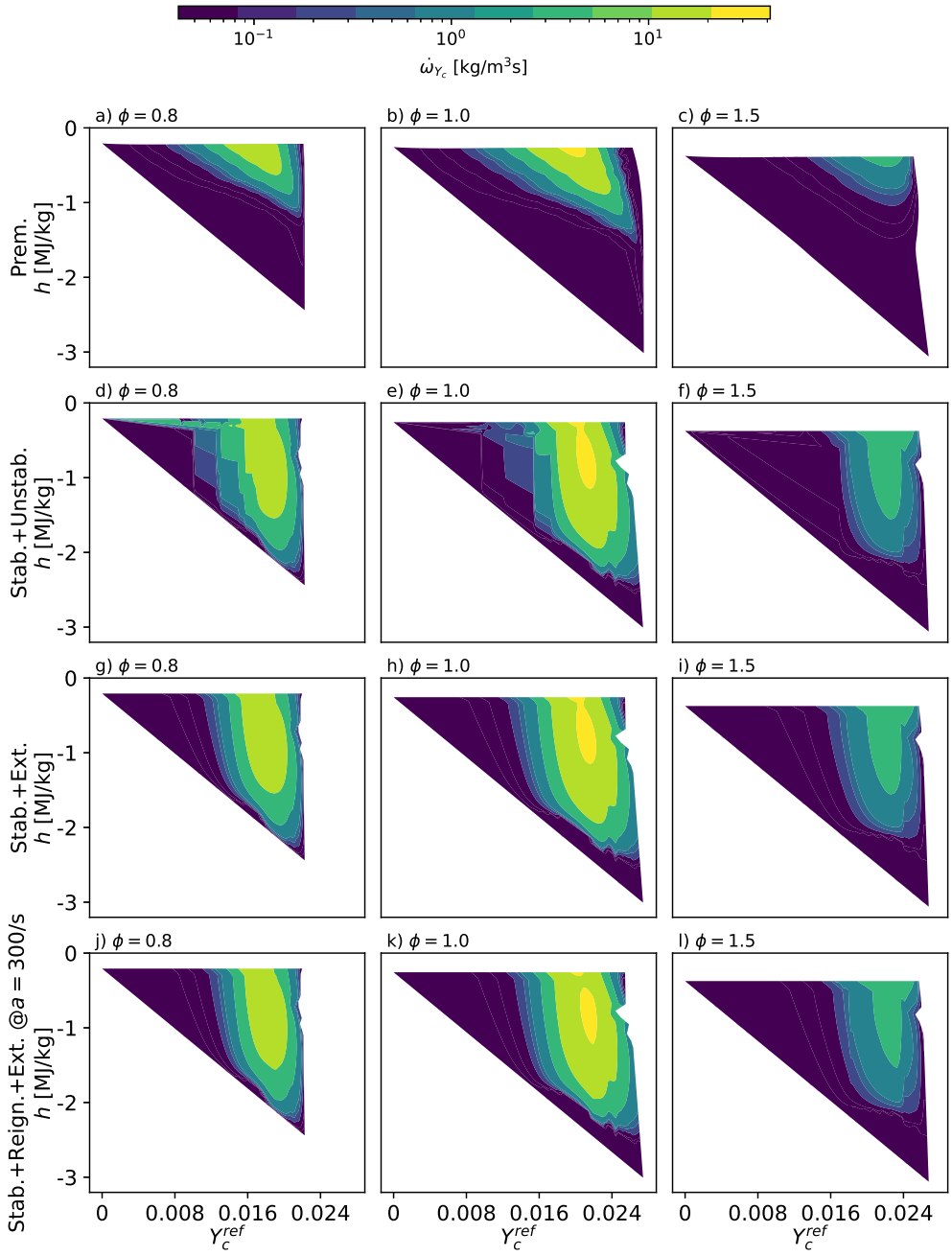

FIGURE 3.35: Illustration of tabulated progress variable source term in non-adiabatic tables using a logarithmic color map. The columns correspond to different equivalence ratios. The rows present the various manifolds using: premixed free and burner stabilized flamelets (first row), and counterflow diffusion flamelets with artificially scaled radiative heat loss including flamelets sets of the stable and unstable branch (second row), the stable branch and an unsteady extinguishing flamelet (third row), and unsteady extinguishing and reigniting flamelets at a single strain rate appended with stable flamelets below this strain rate (fourth row.) All tables use the Central Unique (CU) truncation strategy.

have to be used cautiously, with dedicated care on analyzing which parts of the thermo-chemical manifold are accessed.

3.4.2 Tabulated properties

The final goal of the tabulated chemistry method is to map relevant properties from the 1D flamelet solutions onto the more complex reacting flow problems, while assuming that the underlying flamelet structures are representative to the thermo-chemistry. One has to select which properties to lookup from the tables and which to compute run-time. In this work the approach of Gövert (2016) is followed, that intents to separate the thermodynamic consequences of non-adiabatic states from the tabulated quantities. Namely, density variations and the free linking of enthalpy and temperature are permitted even if only an adiabatic table is used. This is possible by the tabulation of the high and low temperature NASA polynomial coefficients b_i, that link the enthalpy and the temperature through Algorithm 2.1. Subsequently, by tabulating the molecular weight W, the density is calculated using the ideal gas law Eq. (2.51) considering the low Mach number approximation. Additionally, three more variables are tabulated. The source term of the progress variable $\dot{\omega}_{Y_c}$ closes the tabulated chemistry model representing all chemical effects in a single variable. The dynamic viscosity μ is used to close the momentum equation. Finally, the thermal conductivity k provides closure to all transported scalar equations using the specific heat provided by Algorithm 2.1 and the unity Lewis number assumption:

$$\mathcal{D}_k = \frac{\lambda}{\rho c_p Le_k}, \tag{3.36}$$

with assuming $Le_k = 1$ for each scalar equation: Eq. (2.56).

Using double precision floating point numbers the memory requirement of a single tabulated parameter ψ is:

$$MEM_\psi = (8\ \mathrm{B}) \prod_k n_k. \tag{3.37}$$

where $n_k \in \{n_Z, n_C, n_i\}$ are the number of discrete points along each control variable. The adiabatic and non-adiabatic tables presented in this chapter contain $\prod_k n_k = 101 \times 101 = 10201$ and $\prod_k n_k = 101 \times 101 \times 31 = 316231$ different states respectively. Which corresponds to $MEM_\psi \approx 0.08$ MB and $MEM_\psi \approx 2.41$ MB for each tabulated quantity. Considering, 12 coefficients for the NASA polynomials, and the 4 additional quantities, these tables require 1.2 MB and 38.6 MB memory at the run-time of the simulation. This is a preferable solution compared to the trivial option of tabulating the full composition, since, in case of large chemical mechanisms, both the memory cost and the computational load are reduced, because the run-time calculations of section 2.1 and section 2.5.1 are omitted. Avoiding the run-time lookup of the composition keeps the size of the tables independent of the complexity of the chemical mechanism, thus making the usage of large mechanisms possible, such as the ones used in chapter 8: the n-heptane mechanism of Lu and Law (2006) with $N_C = 188$, and the Jet A surrogate mechanism of Kathrotia et al. (2018) with $N_C = 189$. The tabulation of the full thermo-chemical state with such mechanisms could require 450 MB of RAM using the non-adiabatic table structure of the present chapter. Note, that the memory limitation becomes even graver with the increasing number of control variables, such as the dimensions introduced for the

treatment of turbulence-chemistry interaction in section 5.4. These memory requirements have to be considered in the context of modern supercomputers. For example the typical compute node of MareNostrum4, the supercomputer used in this work, has 1.88 GB memory per CPU. (BSC, 2021) Considering the current parallelization strategy that Alya utilizes, each process has a local copy of the tables. With such memory constraints, it is unreasonable to dedicate too large portion of the memory to the thermo-chemical manifolds, given that other procedures of the code are also memory-intensive.

3.5 Summary of tabulated chemistry methods

Tabulated chemistry methods are presented in this chapter, starting with the 1D canonical flamelet configurations in which finite rate chemistry calculations are computationally affordable using detailed reaction mechanisms. These flamelets are analyzed in detail, presenting their characteristic properties such as flame thickness or flame speed using methane as fuel and air as oxidizer at ambient conditions. Moreover, a short discussion is presented on the detailed flame structure and non-unity Lewis number effects. Note, that the latter only serves to illustrate which phenomena are neglected in the present study, since throughout this work the unity Lewis number assumption is used.

Subsequently the details of the actual mapping procedure are elaborated which results in rectilinear tables parametrized by a reduced set of control variables. A central theme in this part is the unique representation of reaction progress by a single definition of progress variable Y_c. Different progress variable definitions are assessed, and truncation strategies are discussed, that treat the often inevitable non-unique regions. The remaining part of the chapter presents the somewhat straightforward mapping of adiabatic flamelets onto the plane of mixture fraction and progress variable and the extension of such manifolds with an additional dimension representing enthalpy.

The section on canonical flamelet configurations contains few noteworthy outcomes, as the behavior of these flames is already well studied in the literature. An interesting aspect is the maximum attainable enthalpy deficit by premixed burner-stabilized flamelets, and counterflow diffusion flamelets with artificially scaled radiative heat loss. The largest enthalpy deficit where reacting solutions are present is similar in the two configurations. (Fig. 3.9 and Fig. 3.18) Other notable aspects are the sensitivity of unsteady reigniting counterflow flamelets to the initial condition at low strain rates (Fig. 3.16), and the approximate $\Omega_T \propto \sqrt{a}$ scaling of the integral heat release rate in counterflow diffusion flamelets. (Fig. 3.20)

In terms of tabulation, most problems are centered around the progress variable definition. A few options are compared in this chapter, with special attention to uniquely characterizing the stable and unstable branches of counterflow diffusion flamelets, that are identified as the most challenging problem to injectively describe. It is found, that the widely used definitions all show a trade-off between characterizing better either the stable or the unstable branch. (Fig. 3.24) Since in most cases non-injective regions are inevitable, truncation strategies are discussed, that allow for the selection of injective segments along progress variable. The preferred options identified here are the First Unique (FU) and Central Unique (CU) truncation strategies, that incorporate as much information from the flamelets as possible. This decision is further supported by the realization, that the gas mixtures are still considerably far from adiabatic equilibrium on the rich side of the low strain rate counterflow

diffusion flamelets. (Fig. 3.18 and Fig. 3.26) Consequently, the tables cannot possibly contain the equilibrium solution in a meaningful way, without large discontinuities.

Finally, the thermo-chemical tables are analyzed *a priori*, by comparing the progress variable source term. (Fig. 3.34 and Fig. 3.35) Important differences are identified between the source term distribution of different flamelet sets. Counterflow diffusion flamelets tend to produce a wider distribution of source terms in mixture fraction, while inversely premixed flamelets are more distributed along progress variable. In both cases this trend is related to the transport of radicals along the physical coordinate of the 1D flamelets. Furthermore, it is found, that the non-adiabatic effects are covered very well by burner-stabilized flamelets, while the counterflow diffusion flamelets with artificially scaled radiative heat loss struggle to reach all relevant conditions, and consequently the resulting tables heavily rely on interpolation.

Chapter 4

Liquid phase modeling

The combustion of fuels occurs in high temperature gas mixtures where the intensity of the reaction kinetics is sufficiently high. Nevertheless, liquid fuels provide the advantage of relatively easy storage and high volumetric energy density compared to gaseous fuels. In combustion systems of liquid fuels the fuel has to be evaporated and mixed with the gas phase environment to facilitate the oxidation. To increase the rate of mass transfer between the liquid and the gas, the interface area between the two phases is increased by atomizing the liquid into a cloud of small droplets. During the atomization process the liquid enters the combustion chamber as a continuous flow. Due to the forces acting on the liquid phase, this continuous liquid core is broken into ligaments, then larger droplets, which are further broken into smaller droplets. (Lefebvre and Ballal, 2010) The atomization process is typically completed in a much shorter distance than the length scales of the other processes in the combustion chamber. (Prakash, Gadgil, and Raghunandan, 2014) In this work, the liquid fuel behavior is studied after the atomization process is completed, where the spray cloud consists of individual droplets.

Spray combustion simulations overwhelmingly use an Eulerian-Lagrangian approach to account for the gas and liquid phases respectively. (Sazhin, 2014) In this approach, the liquid droplets are represented by point particles, that move independently in the computational domain interacting with the gas phase. This modeling strategy is known to be valid in the dilute spray regime, where the liquid volume fraction is lower than 0.001. (Jenny, Roekaerts, and Beishuizen, 2012) Below the physical phenomena related to the movement and evaporation of liquid droplets is described and corresponding models are presented.

The models are chosen with the following general constrains in mind, that are expected to be valid in the targeted spray combustion applications: i) the density of the droplets is much larger than the density of the surrounding gas; ii) the surface tension forces are much larger than other forces seeking to deform the droplets, thus the droplets are considered perfectly spherical. The first assumption is valid at an extensive range of environmental pressures, especially at atmospheric conditions, as illustrated in appendix B for common hydrocarbons. The second assumption is governed by the Weber number We_g, that expresses the ratio of inertia and surface tension forces:

$$We_g = \frac{\rho_m \left|\mathbf{u}_s\right|^2 d_p}{\sigma}, \tag{4.1}$$

where ρ_m is a representative gas phase density, $\mathbf{u}_s = \mathbf{u}_g - \mathbf{u}_p$ is the slip velocity between the gas and liquid phases, d_p is the droplet diameter, and σ is the surface tension of the liquid-gas interface.

The deformation of droplets to the point of breakup is unlikely below a critical Weber number of $We_{g,c} \approx 13$. (Green and Maloney, 1999, §6) Furthermore,

at $We_g < 1$ the deformation of the droplets is not significant. (Giusti, 2013) In this regime the assumption of spherical droplets is justified. The surface tension of typical hydrocarbon fuels is of order of magnitude $\sigma = \mathcal{O}(0.01\,\mathrm{N/m})$. (Foale, 2022) Thus, with slip velocities of $\mathbf{u}_s = \mathcal{O}(10\,\mathrm{m/s})$, and gas phase densities of $\rho_m = \mathcal{O}(1\,\mathrm{kg/s})$, the droplet diameter where deformation would become significant is: $d_{p,max}^{sphere} = \mathcal{O}(100\,\mu\mathrm{m})$. The assumption of sphericity is valid below this droplet size. Additional assumptions are introduced below in relation to the submodels.

This chapter dedicates special attention to the modeling of evaporation at subcritical pressure. Note, that the present assumptions shall be re-evaluated in case of supercritical heat and mass transfer. While this is highly relevant under engine-like conditions, it is out of the scope of the present work. Various strategies are present in the literature to account for droplet evaporation considering different aspects of heat and mass transfer. Miller, Harstad, and Bellan (1998) introduced a unified framework of different evaporation models, and conducted a comparative study. However, as the models were developed under easily measurable conditions, corresponding to rather large droplets ($\sim$ 1 mm), their direct application to spray combustion could be questionable under certain conditions, where droplet diameters are rather small ($\sim$ 1 μm..10 μm). These modeling decisions were revisited by many works. (Shashank, Knudsen, and Pitsch, 2011; Sazhin, 2017) The topic enjoys renewed interest, prompted by the recent experimental investigation of Verdier et al. (2017) using Global Rainbow Thermometry to characterize the mean droplet temperatures in a complex lab-scale n-heptane spray flame. This flame was numerically investigated in the Workshop on Measurement and Computation of Turbulent Spray Combustion by different groups using Lagrangian droplet models for the evaporating spray cloud. (Both, 2017; Noh et al., 2018; Sitte and Mastorakos, 2019; Alessandro, Stankovic, and Merci, 2019; Chatelier et al., 2020; Benajes et al., 2022) Specifically, Noh et al. (2018) compared various evaporation models following Miller, Harstad, and Bellan (1998), using large-eddy simulation (LES) to asses the droplet temperature predictions. These studies provide an overview of the state of the art of spray combustion simulations of gas turbine model combustors, however the underlying behavior of the droplet evaporation models requires further assessment.

The behavior of stand-alone Lagrangian droplets is examined using fuels characterized by different volatility, including: OME1 (dimethoxymethane, formerly methylal), and 3 alkanes: n-heptane, n-decane, and n-dodecane, that have a boiling point of 315.0 K, 371.5 K, 447.5 K, and 489.5 K respectively. In this aspect, OME1 is especially interesting, as it is a high volatility fuel showing the distinctive effects of high evaporative mass flux even in moderate temperature environments.

The rest of the chapter is structured the following way. In section 4.1 the kinematic modeling of droplet movement is described. Section 4.2 introduces the problem of heat and mass transfer around droplets, and solutions are derived under the commonly employed assumptions. The material properties, that are necessary for the closure of the evaporation and kinematic models are discussed in section 4.3. The heat and mass transfer models are combined with additional assumptions to form the evaporation models in section 4.4. The concept of the wet-bulb condition is introduced in section 4.5 shedding light on the behavior of the evaporation models. The transient behavior of the Lagrangian droplets is further analyzed in section 4.6. Finally, the fallacy of the non-equilibrium interface thermodynamics model is explained in detail in section 4.7.

Credit

The work in this chapter was executed solely by the author. The unique contributions include the clarification of the definition of evaporation models from first principles using a film theory approach, and the analysis of these evaporation models in an extensive range of flame-relevant conditions. Furthermore, a new model is presented for obtaining representative gas phase properties in the context of tabulated chemistry. Finally, it is demonstrated by the numerical examples, that the non-equilibrium model of Miller, Harstad, and Bellan (1998) is inadequate for the present spray combustion applications. The main findings of this chapter are published in: Both, Mira, and Lehmkuhl (2022b). The software used to produce these results is made available on GitLab. It may be used to reproduce the presented findings.
Access at: https://gitlab.com/BothAmbrus/DropletEvaporation

4.1 Kinematic behavior of spheres

The movement of the droplets is governed by Newton's laws of motion. As proposed above, the droplets are treated as solid spheres, whose motion may be described by a drag and other forces like gravity. The droplet deformation is neglected on the ground, that surface tension forces are sufficiently high. Furthermore, the rotation of the droplets is also assumed to be negligible.

The location and velocity of a droplet is found by solving the ODE system:

$$\frac{\mathrm{d}\mathbf{x}_p}{\mathrm{d}t} = \mathbf{u}_p, \tag{4.2}$$

$$m_p \frac{\mathrm{d}\mathbf{u}_p}{\mathrm{d}t} = \sum_i \mathbf{F}_i, \tag{4.3}$$

where $\mathbf{x}_p$ is the droplet location, $\mathbf{u}_p$ is the droplet velocity, m_p the mass of the droplet, and $\mathbf{F}_i$ are different forces acting on the droplet. This ODE system has to be appended with appropriate initial conditions:

$$\mathbf{x} = \mathbf{x}_{p,0}, \quad \mathbf{u}_p = \mathbf{u}_{p,0} \quad \text{at} \quad t_{0,p}, \tag{4.4}$$

where 0 subscripts signify initial, and the the droplet enters the domain of interest at $t_{0,p}$. These initial conditions may be referred to as *injection* conditions, since in the simulation of spray combustion systems the selection of the initial conditions of each Lagrangian particle mimics the behavior of the spray injection system.

Various forces may act on the droplet, however, in the systems studied here, the two noteworthy forces are drag: $\mathbf{F}_d$ and body forces: $\mathbf{F}_g$. Other forces that are not considered in this work may include: buoyancy, added-mass effects, and lift force near walls. Even the body forces are often neglected in spray combustion modeling, since they are generally insignificant compared to the inertia of a fast moving droplets and the effect of drag between the droplet and a the turbulent flow.

Drag is the principal force affecting the path of the droplets. This effect is best studied in terms of the droplet Reynolds number Re_p:

$$Re_p = \frac{\rho_m \left|\mathbf{u}_s\right| d_p}{\mu_m}, \tag{4.5}$$

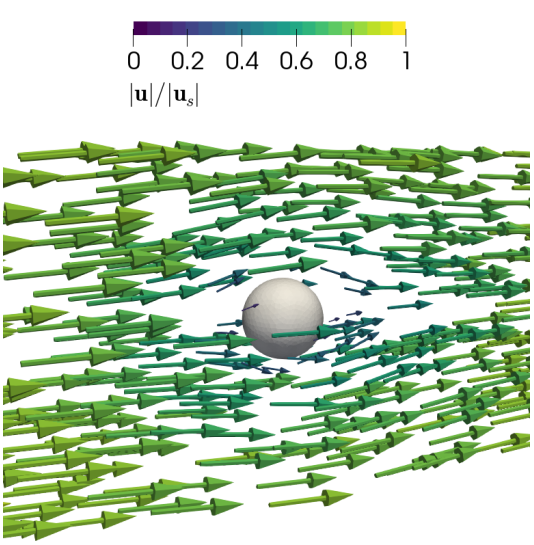

(A) Creeping flow around sphere in the Lagrangian frame of reference.

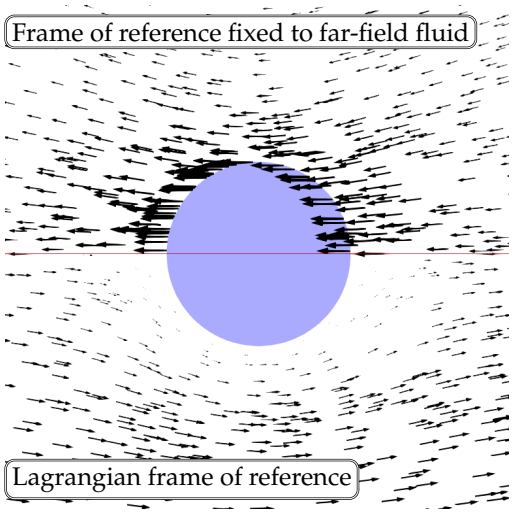

(B) Creeping flow in a frame of reference fixed to the far-field fluid and in the Lagrangian frame of reference.

FIGURE 4.1: Illustration of creeping flow around a sphere. (Stokes, 1851)

where d_p is the droplet diameter, μ_m and ρ_m are the viscosity and density of the surrounding gas evaluated at appropriate reference conditions, and $\mathbf{u}_s = \mathbf{u} - \mathbf{u}_p$ is the slip velocity between the droplet and the surroundings with $\mathbf{u}$ denoting the far-field gas phase velocity. As Stokes (1851) shows, in the low Reynolds number limit where the motion is dominated by viscous forces (creeping flow), the flow around a rigid sphere has an analytical solution illustrated in Fig. 4.1. As Fig. 4.1b shows, relative to the far-field the droplet appears to push the fluid in front of it at a speed of $|\mathbf{u}_s|$, and through viscous transport induces a flow in its vicinity. Meanwhile, relative to the droplet, in the Lagrangian frame of reference, the droplet experiences an apparent incoming flow of $|\mathbf{u}_s|$ magnitude, that is significantly affected by viscous friction in a large region around the droplet.

The surface integral of pressure and shear stress distributions of this analytical solution yields the Stokes-drag:

$$\mathbf{F}_{d,St} = 3\pi\mu_m d_p \mathbf{u}_s. \tag{4.6}$$

The drag acting on solid bodies is often described in relation of the stagnation pressure of the far-field flow, and the projected area of the body in question, yielding the non-dimensional drag coefficient. In the low Reynolds number regime the drag coefficient of the droplet is:

$$C_{d,St} = \frac{|\mathbf{F}_{d,St}|}{\frac{1}{2}\rho_m |\mathbf{u}_s|^2 \frac{\pi d_p^2}{4}} = \frac{24}{Re_p}. \tag{4.7}$$

In spray combustion the particle diameter and consequently the particle Reynolds number tend to zero as the droplets are evaporating, thus it is important that the applied drag model asymptotically approaches the Stokes-drag at low Reynolds numbers. A widely applied model is the empirical correlation introduced by Naumann

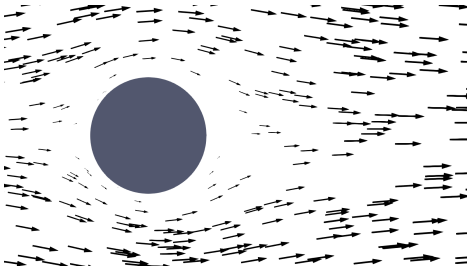

(A) In-plane velocity vectors around sphere at $Re_p = 1$.

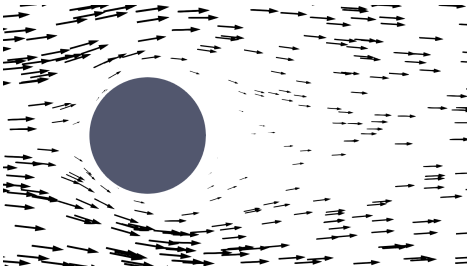

(B) In-plane velocity vectors around sphere at $Re_p = 10$.

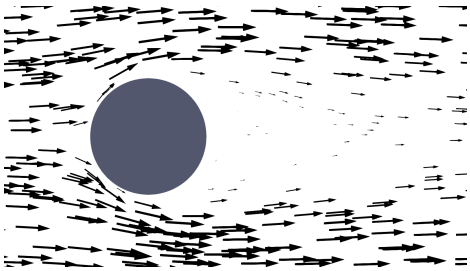

(C) In-plane velocity vectors around sphere at $Re_p = 100$.

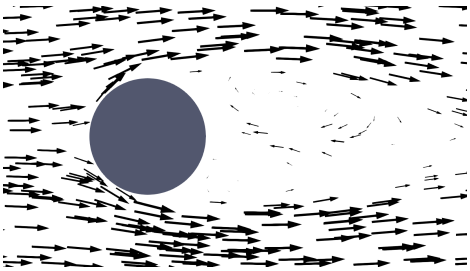

(D) In-plane velocity vectors around sphere at $Re_p = 1000$.

FIGURE 4.2: Illustration of flow around a sphere at different Reynolds numbers in the Lagrangian frame of reference.

and Schiller (1935):

$$C_d = \begin{cases} \frac{24}{Re_p} + 3.6Re_p^{-0.313}, & Re_p \leq 1000, \\ 0.44, & Re_p > 1000, \end{cases} \tag{4.8}$$

that satisfies this condition, moreover in the high Reynolds number limit it approaches a constant drag coefficient of $C_d = 0.44$. The latter limit is typical to turbulent flow. (Bird, Stewart, and Lightfoot, 1960, §6.3)

Figure 4.2 illustrates the flow around a sphere at different Reynolds numbers, highlighting behavior of the drag coefficient. At $Re_p = 1$ the flow practically behaves like the solution of Stokes, exhibiting a minor elongation of the wake of the sphere. As the Reynolds number increases to 10, the wake becomes notably elongated, and at $Re_p = 100$ is even exhibits a weak recirculation region. Finally, at a Reynolds number of 1000 the recirculation is strong, and the wake is notably unsteady. The drag coefficient values of (Naumann and Schiller, 1935) and the values corresponding to Stokes' solution are displayed on Fig. 4.3. The correlation is only first-order continuous at $Re_p = 1000$, however such high droplet Reynolds numbers are not observed in this study, thus numerical difficulties related to the discontinuity of the slope are not expected.

4.2 Heat and mass transfer around spheres

A crucial aspect besides the kinematic modeling of the computational particles, is the heat and mass transfer process resulting in the evaporation of the fuel that ultimately feeds the reacting front in combustion simulations.

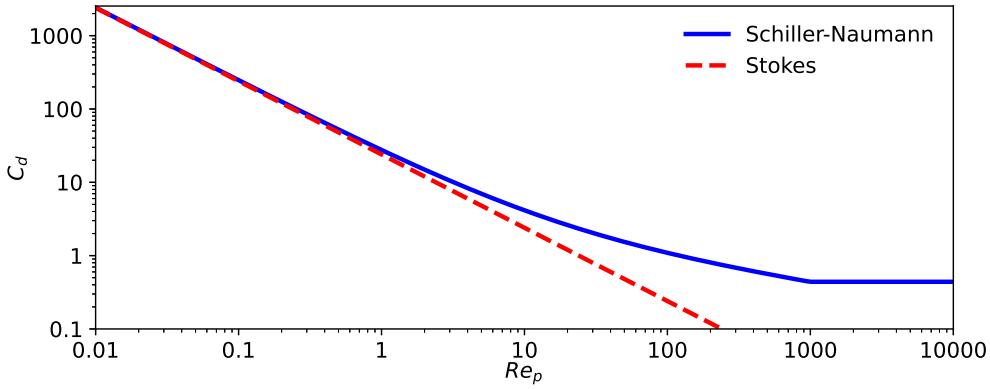

FIGURE 4.3: Drag coefficient of a sphere according to Stokes (1851), and Naumann and Schiller (1935) as function of the Reynolds number.

In the Eulerian-Lagrangian spray modeling approach, the heat and mass transfer is usually treated as an exchange, between the practically infinite gas phase, and the spherical particle. These assumptions are justified in the dilute spray regime, where the direct influence of droplet to droplet interactions is negligible. (Jenny, Roekaerts, and Beishuizen, 2012) Furthermore, the length scale of the droplets in typical spray combustion systems is of $\mathcal{O}(10\ \mu\text{m})$, that is below the smallest length scales of thermo-chemical nonhomogenities associated to the flame thickness: $\delta_{diff} = \mathcal{O}(100\ \mu\text{m})$ (Poinsot and Veynante, 2005, §5.1.2), thus the far-field behavior of the gas phase may be regarded homogeneous with respect to the droplets. For examples of δ_{diff} at atmospheric pressure in premixed 1D flamelets, see Fig. 3.5. Furthermore, a similar length scale is given for diffusion flamelet in Eq. (3.18), where the smallest length scales associated to the extinguishing of the flamelet are attained at a strain rate of $a = a^{ext} = \mathcal{O}(1000/\text{s})$, giving length scales of $\delta_{diff} = \mathcal{O}(100\ \mu\text{m})$ as well. (Benajes et al., 2022)

In this work, both heat and mass transfer are studied under the quasi-steady state assumption, postulating that the thermal and mass transfer boundary layers surrounding the droplet reach their steady conditions infinitely fast. In the case of spheres immersed in quiescent fluids ($|\mathbf{u}_s| = 0$), the relaxation towards this steady state is characterized by the dimensionless time, the Fourier number:

$$Fo = \frac{t\mathcal{D}_{t,m}}{d_p^2}, \tag{4.9}$$

where t is the time passed since an initial non-steady condition, and $\mathcal{D}_{t,m} = \frac{\lambda_m}{\rho_m c_{p,m}} = \mathcal{O}\left(10\ \text{mm}^2/\text{s}\right)$ is the thermal diffusivity in the mixture, with λ_m and $c_{p,m}$ being the thermal conductivity and specific heat of the gas phase at a reference condition. The boundary layers approach their quasi-steady form for $Fo = Fo_{QS}$, thus the quasi-steady relaxation time may be defined as:

$$\tau_{p,QS} = \frac{d_p^2 Fo_{QS}}{\mathcal{D}_{t,m}}. \tag{4.10}$$

As shown below in section 4.6, the vaporization rate constant: K gives a good estimate of the droplet lifetime, regardless the other time scales. Stationary droplets are

characterized by $K = \mathcal{O}\left(0.1\ \mathrm{mm}^2/\mathrm{s}\right)$ as Fig. 4.15 demonstrates. Consequently, the steady boundary layers of stationary droplets are expected to be established an order of magnitude faster, than the droplet lifetime, even assuming $Fo_{QS} = 10$. (Finneran, Garner, and Nadal, 2021)

The recent work of Finneran, Garner, and Nadal (2021) sheds more light on the issue of the quasi-steady assumption. They identify two distinct situations, where the this assumption significantly under-performs compared to a fully transient solution of the boundary layer evolution. The first is related to the energy and mass balances for the initial and quasi-steady states. I.e.: if the mass of vapor contained in the quasi-steady boundary layer is the same order of magnitude, than the initial droplet mass, then by the time this boundary layer state would be reached, the droplet would already be consumed. The second critical situation they identify, is near the end of the droplet lifetime, when a surroundings are formed by an already established quasi-steady state. In this case the existing cold vapor in the boundary layer insulates the droplet and slows the evaporation process. Considering such history effects is out of the scope of the present work, however, as Finneran, Garner, and Nadal (2021) show, the error introduced by the quasi-steady assumption is below 3% at atmospheric pressure, that characterizes the cases studied here.

Many widely applied models study the phenomenon of evaporation based on film theory. Film theory postulates that the differences between interface and bulk states diminish in a finite δ_M and δ_T thickness for the mass and thermal transfer respectively. Figure 4.4 summarizes four theoretical scenarios of the treatment of heat and mass transfer between a spherical particle and its surroundings. The illustrated scenarios include:

1. Mass Transfer solely due to Diffusion (MTD),
2. Thermal Transfer solely due to Diffusion (TTD),
3. Mass Transfer including the convective effect of Stefan flow (MTS),
4. Thermal Transfer including the convective effect of Stefan flow (TTS).

Stefan flow, the blowing effect of intense evaporation, is an important phenomena affecting rapidly evaporating droplets, as it obstructs heat transfer from the high temperature gas to the droplet interface. Below the steady-state solution of heat and mass transfer of these four scenarios is presented. Subsequently, these derivations are used in the definition of the evaporation models and their analysis in section 4.4. The heat and mass fluxes are derived in an isolated manner, allowing the step-by-step construction of the evaporation models, and the detailed insight in their behavior.

4.2.1 Quasi-steady heat and mass transfer in film theory

The diffusive mass flux across gas phase boundary layer surrounding the droplet is proportional to the gradient of the volatile species. For a species f with mass fraction Y_f dissolved in a bath gas b of mass fraction $Y_b = 1 - Y_f$ the Hirschfelder's law defines the diffusive mass flux as:

$$\mathbf{\Phi}_{M,f}^{diff} = -\rho_m \mathcal{D}_m \nabla Y_f, \tag{4.11}$$

where ρ_m is the density of the mixture, and $\mathcal{D}_m$ is the mass diffusion coefficient of species f in the mixture. Furthermore, in case the gas mixture has a net mass flux

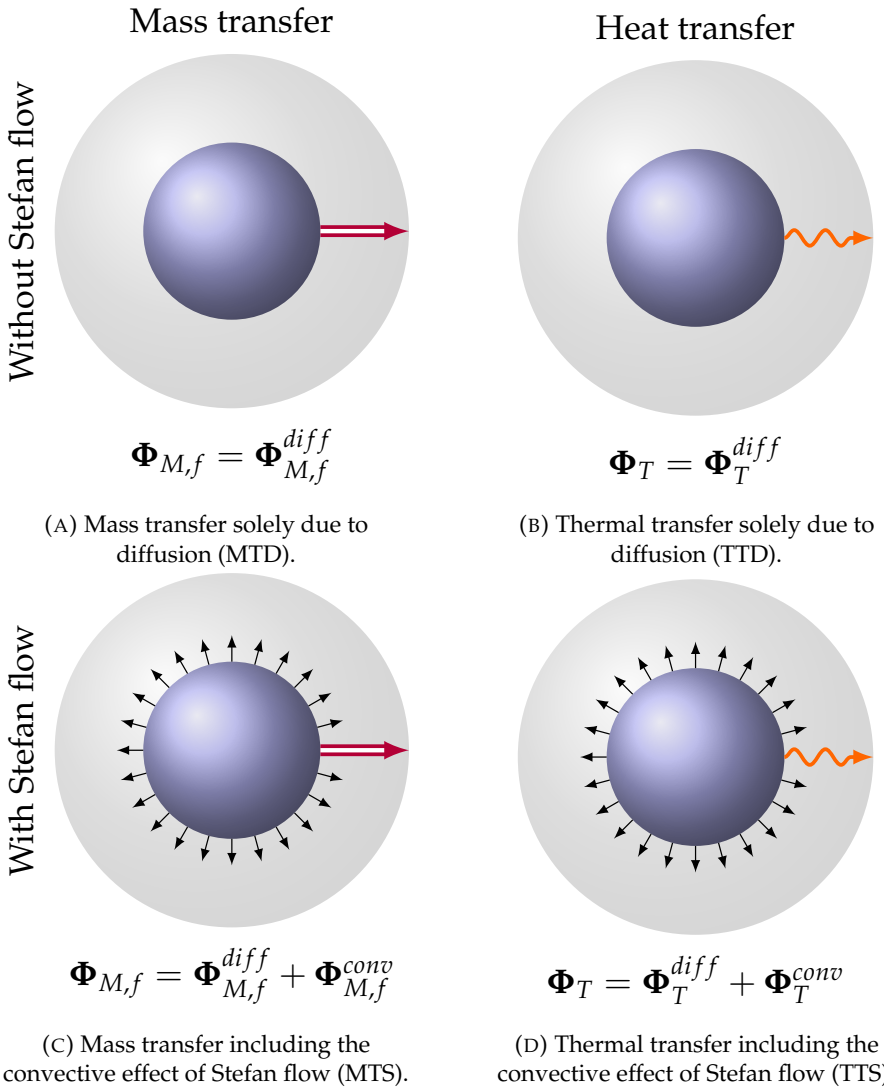

(A) Mass transfer solely due to diffusion (MTD).

(B) Thermal transfer solely due to diffusion (TTD).

(C) Mass transfer including the convective effect of Stefan flow (MTS).

(D) Thermal transfer including the convective effect of Stefan flow (TTS).

FIGURE 4.4: Summary of different droplet heat and mass transfer model problems.

$\mathbf{\Phi}_M$, species f and b are also transported by convection:

$$\mathbf{\Phi}^{conv}_{M,f} = Y_f \mathbf{\Phi}_M. \tag{4.12}$$

This latter flux is the one related to Stefan flow, i.e.: the net mass flux caused by the vapor leaving the droplet surface. The convective mass flux is negligible at low evaporation rates, but it is relevant under flame-like conditions, especially for highly volatile fuels. In the evaporation of single component droplets, the net mass flux is the mass flux of the volatile species only: $\mathbf{\Phi}_M = \mathbf{\Phi}_{M,f}$. This holds under the assumption, that the bath gas is practically insoluble in the liquid droplet, thus $\mathbf{\Phi}_{M,b} = 0$ at the quasi-steady state.

Similarly, the diffusive flux of heat is given by Fourier's law of heat conduction:

$$\mathbf{\Phi}^{diff}_{T} = -\lambda_m \nabla T, \tag{4.13}$$

where λ_m is the thermal conductivity in the gas mixture. However, to determine the

convective heat transport, the net mass flux is used again creating a coupling between the heat and mass transfer. The enthalpy of the volatile component is defined using a first order approximation using the specific heat. Thus, the convective heat flux is:

$$\mathbf{\Phi}_T^{conv} = c_{p,vap,m}\mathbf{\Phi}_{M,f}\left(T - T_0\right), \tag{4.14}$$

where $c_{p,vap,m}$ is the specific heat of the vapor of species f, and T_0 is an appropriately chosen reference temperature.

The problems illustrated in Fig.4.4 are rotationally symmetric, thus only the radial components of fluxes are non-zero. Under the quasi-steady assumption, mass and energy conservation implies that the surface integral of the radial mass and thermal fluxes $\mathbf{\Phi}_{M,f,r}$ and $\mathbf{\Phi}_{T,r}$ are constant within the film on concentric spheres:

$$\dot{m}_r = 4r^2\pi\mathbf{\Phi}_{M,f,r} = const., \tag{4.15}$$

$$\dot{Q}_r = 4r^2\pi\mathbf{\Phi}_{T,r} = const. \tag{4.16}$$

The above two equations form ODEs for the unknowns: $Y_f(r)$ and $T(r)$ respectively. In the framework of Film theory, these are appended with the corresponding boundary conditions:

$$Y_f(r_p) = Y_{f,i}, \qquad Y_f(r_{BL,M}) = Y_{f,s}, \tag{4.17}$$

$$T(r_p) = T_p, \qquad T(r_{BL,T}) = T_s, \tag{4.18}$$

where r_p is the droplet radius, $r_{BL,M} = r_p + \delta_M$ and $r_{BL,T} = r_p + \delta_T$ are the outer film radii of mass and thermal transfer, $Y_{f,i}$ is the vapor mass fraction on the droplet interface, $Y_{f,s}$ is the seen vapor mass fraction (far-field), T_p is the droplet temperature, and T_s is the seen gas temperature.

Assuming $\rho_m\mathcal{D}_m = const.$ and $\lambda_m = const.$, the solutions of Eq. (4.15)-(4.18) may be derived for the different scenarios presented in Fig. 4.4. The temperature and vapor mass fraction profiles are presented in Tab. 4.1. The MTS, TTD, and TTS solutions are derived in the appendix in section E.2, while the solution of the MTD scenario is rather straightforward and can be found in the literature. (Bird, Stewart, and Lightfoot, 1960). Additionally, the radial mass and heat fluxes of the four studied scenarios are presented in Tab. 4.2, and the total radial mass and heat transfer from the droplet to the far field in Tab. 4.3. Here the factor Ξ_1 relates the heat transfer terms of conduction and transport through Stefan flow:

$$\Xi_1 = \frac{c_{p,vap,m}}{c_{p,m}Le_m}\frac{1}{\frac{1}{r_p} - \frac{1}{r_{BL,M}}}\ln\left(\frac{1 - Y_{f,i}}{1 - Y_{f,s}}\right), \tag{4.19}$$

where $c_{p,m}$ is the specific heat of the gas mixture, and $Le_m = \frac{\lambda_m}{c_{p,m}\rho_m\mathcal{D}_m}$ is the Lewis number of the volatile species in the film.

In accordance with section E.1.2, the Stefan flow effects on heat transfer in an arbitrary system are often taken to be the same as those derived in Cartesian coordinates for a flat plate without separate derivations (Miller, Harstad, and Bellan, 1998; Bird, Stewart, and Lightfoot, 1960). It is found, as shown in section E.2.2, that the same correction factor, often known as Bird's (Bird, Stewart, and Lightfoot, 1960) correction, is indeed valid in spherical and Cartesian coordinates as well.

To evaluate the transfer rates, one needs to know the mass and heat transfer film thickness. These thicknesses are commonly inferred from the empirical heat

TABLE 4.1: Solution profiles in the four studied cases of droplet heat and mass transfer, with $\Xi_1 = \frac{c_{p,vap,m}}{c_{p,m}Le_m}\frac{1}{1/r_p - 1/r_{BL,M}}\ln\left(\frac{1-Y_{f,i}}{1-Y_{f,s}}\right)$, assuming constant gas phase properties.

MTD	$Y_f^{MTD} = Y_{f,i} + \left(Y_{f,s} - Y_{f,i}\right)\frac{\frac{1}{r} - \frac{1}{r_p}}{\frac{1}{r_{BL,M}} - \frac{1}{r_p}}$
MTS	$\frac{1 - Y_f^{MTS}}{1 - Y_{f,i}} = \left(\frac{1 - Y_{f,s}}{1 - Y_{f,i}}\right)^{\frac{\frac{1}{r_p} - \frac{1}{r}}{\frac{1}{r_p} - \frac{1}{r_{BL,M}}}}$
TTD	$T^{TTD} = T_p + \left(T_s - T_p\right)\frac{\frac{1}{r} - \frac{1}{r_p}}{\frac{1}{r_{BL,T}} - \frac{1}{r_p}}$
TTS	$T^{TTS} = T_p + \left(T_s - T_p\right)\frac{e^{\frac{\Xi_1}{r}} - e^{\frac{\Xi_1}{r_p}}}{e^{\frac{\Xi_1}{r_{BL,T}}} - e^{\frac{\Xi_1}{r_p}}}$

TABLE 4.2: Radial heat and mass fluxes with and without Stefan flow, with $\Xi_1 = \frac{c_{p,vap,m}}{c_{p,m}Le_m}\frac{1}{1/r_p - 1/r_{BL,M}}\ln\left(\frac{1-Y_{f,i}}{1-Y_{f,s}}\right)$, assuming constant gas phase properties.

MTD	$\mathbf{\Phi}_{M,f,r}^{MTD} = -\rho_m \mathcal{D}_m \frac{Y_{f,s} - Y_{f,i}}{\left(\frac{1}{r_p} - \frac{1}{r_{BL,M}}\right) r^2}$
MTS	$\mathbf{\Phi}_{M,f,r}^{MTS} = -\rho_m \mathcal{D}_m \frac{\ln\left(\frac{1 - Y_{f,i}}{1 - Y_{f,s}}\right)}{\left(\frac{1}{r_p} - \frac{1}{r_{BL,M}}\right) r^2}$
TTD	$\mathbf{\Phi}_{T,r}^{TTD} = -\lambda_m \left(T_s - T_p\right) \frac{1}{\left(\frac{1}{r_p} - \frac{1}{r_{BL,T}}\right) r^2}$
TTS	$\mathbf{\Phi}_{T,r}^{TTS} = -\lambda_m \left(T_s - T_p\right) \frac{-\Xi_1 e^{\frac{\Xi_1}{r_p}}}{\left(e^{\frac{\Xi_1}{r_{BL,T}}} - e^{\frac{\Xi_1}{r_p}}\right) r^2}$

transfer correlations of spheres, which do not include Stefan flow. The correlations are formulated to find the Nusselt number $Nu_{m,0} = 2\left(1 - \frac{r_p}{r_{BL,T}}\right)$ such, that:

$$\dot{Q}_r^{TTD} = \pi \lambda_m d_p \left(T_p - T_s\right) Nu_{m,0}. \tag{4.20}$$

Thus, the film thickness is:

$$\delta_T = \frac{d_p}{Nu_{m,0} - 2}. \tag{4.21}$$

Just as in the case of the drag coefficient, it is very important in the simulation of spray combustion systems to recover the analytical solution at the low Reynolds number limit. As shown in appendix D, this corresponds to $Nu_{m,0} \to 2$ as $Re_p \to 0$. Frössling (1938) introduced an empirical correlation adhering to this requirement,

TABLE 4.3: Radial heat and mass flow rates with and without Stefan flow, with $\Xi_1 = \frac{c_{p,vap,m}}{c_{p,m}Le_m}\frac{1}{1/r_p - 1/r_{BL,M}}\ln\left(\frac{1-Y_{f,i}}{1-Y_{f,s}}\right)$, assuming constant gas phase properties

MTD	$\dot{m}_r^{MTD} = \pi\rho_m\mathcal{D}_m d_p\left(Y_{f,i} - Y_{f,s}\right)\dfrac{2}{1-\frac{r_p}{r_{BL,M}}}$
MTS	$\dot{m}_r^{MTS} = \pi\rho_m\mathcal{D}_m d_p \ln\left(\frac{1-Y_{f,s}}{1-Y_{f,i}}\right)\dfrac{2}{1-\frac{r_p}{r_{BL,M}}}$
TTD	$\dot{Q}_r^{TTD} = \pi\lambda_m d_p\left(T_p - T_s\right)\dfrac{2}{1-\frac{r_p}{r_{BL,T}}}$
TTS	$\dot{Q}_r^{TTS} = \pi\lambda_m d_p\left(T_p - T_s\right)\dfrac{2\frac{\Xi_1}{r_p}}{1-e^{\frac{\Xi_1}{r_{BL,T}}-\frac{\Xi_1}{r_p}}}$

that assesses the Nusselt number of a sphere in forced convection in the form:

$$Nu_{m,0} = 2 + CRe_p^{1/2}Pr_m^{1/3}, \tag{4.22}$$

with $C = 0.552$, where $Pr_m = \frac{c_{p,m}\mu_m}{\lambda_m}$ is the Prandtl number in the heat transfer film. Subsequently Ranz and Marshall (1952) reported $C = 0.6$ in their empirical study. Throughout this work $C = 0.6$ is retained in accordance with the Ranz-Marshall model. The heat transfer film thickness according to this model is proportional to the droplet diameter and inversely proportional to the square root of the Reynolds number:

$$\delta_T = \frac{1}{0.6}Pr_m^{-1/3}Re_p^{-1/2}d_p. \tag{4.23}$$

Analogously, the mass transfer film thickness is given by:

$$\delta_M = \frac{1}{0.6}Sc_m^{-1/3}Re_p^{-1/2}d_p, \tag{4.24}$$

where $Sc_m = \frac{\mu_m}{\rho_m\mathcal{D}_m}$ is the Schmidt number of the vapor in the mass transfer film. Corresponding to a Sherwood number of:

$$Sh_{m,0} = \frac{2}{1-\frac{r_p}{r_{BL,M}}} = 2 + 0.6Re_p^{1/2}Sc_m^{1/3}. \tag{4.25}$$

In fact, the factor: Ξ_1 of the TTS profiles relates the β factor of Bird's correction to the droplet size and the film thickness. Consequently, the factor present in $\dot{Q}_r^{TTS}$ is indeed corresponding to Bird's correction:

$$\frac{2\frac{\Xi_1}{r_p}}{1-e^{\frac{\Xi_1}{r_{BL,T}}-\frac{\Xi_1}{r_p}}} = \frac{\beta}{e^\beta - 1}Nu_{m,0}, \tag{4.26}$$

where the β factor can be expressed in its usual form as: $\beta = \frac{c_{p,vap,m}}{c_{p,m}Le_m}\frac{Sh_{m,0}}{Nu_{m,0}}\ln\left(1+B_M\right)$, with the Spalding mass transfer number defined as $B_M = \frac{Y_{f,i}-Y_{f,s}}{1-Y_{f,i}}$.

The film thickness according to the correlation of Ranz and Marshall (1952) is illustrated in Fig. 4.5 for various Reynolds numbers. At $Re_p = 1$ the heat and mass

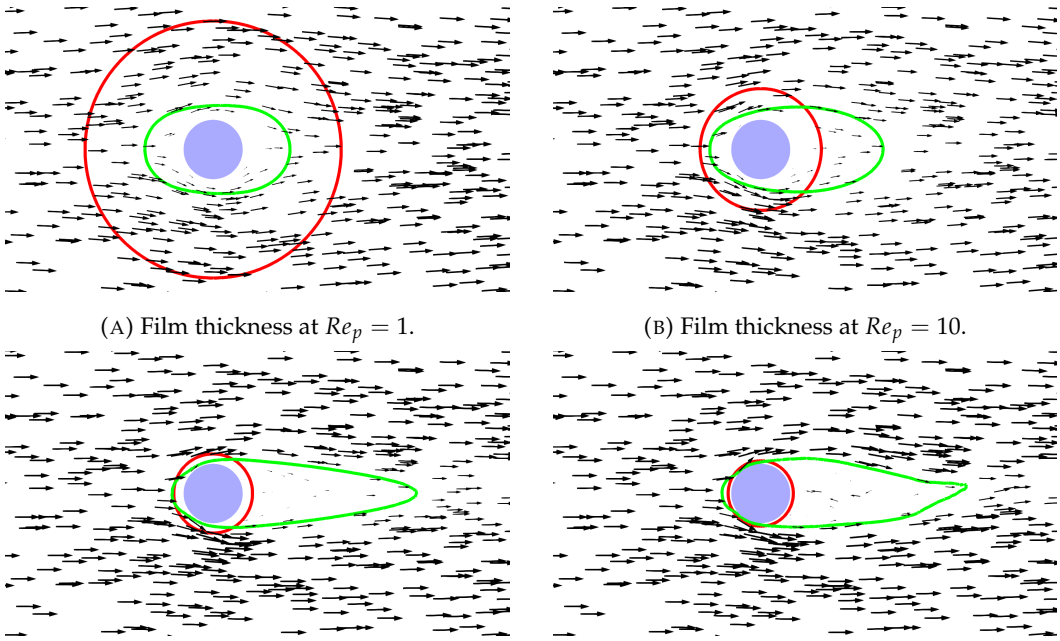

(A) Film thickness at $Re_p = 1$.

(B) Film thickness at $Re_p = 10$.

(C) Film thickness at $Re_p = 100$.

(D) Film thickness at $Re_p = 1000$.

FIGURE 4.5: Illustration of film thickness (the red circle marks $r_{BL,T}$) around a sphere at different Reynolds numbers according to the empirical correlation of Ranz and Marshall (1952) using a Prandtl number of unity. For reference a green contour line marks the region, where the streamwise component of the velocity filed in the Lagrangian frame of reference drops below 50% of the far-field value.

transfer is dominated by diffusion and the film thickness is significantly larger than the droplet diameter. As the velocity increases the flow becomes asymmetric. In the front side of the sphere the transition from free stream conditions to stagnation happens in a shorter and shorter distance, as marked by the green contour line of low streamwise velocity. Meanwhile, in the wake of the sphere the low velocity region becomes elongated. The thermal film radius follows the trend of the velocity on the front side of the sphere, marked by the red circles according to Eq. (4.23). I.e.: this empirical correlation expresses, how the higher incoming velocity compresses the thermal boundary layer on the front of the sphere hence increasing the heat transfer rate.

The scaled temperature (T^{TTS}) and vapor mass fraction (Y_f^{MTS}) profiles around a sphere considering Stefan flow are demonstrated in Fig. 4.6 for a relatively low Reynolds number case, where the film thickness and the droplet diameter are comparable. The profiles range from the imposed surface values to the likewise imposed far-field ("seen") values within the film thickness. The gradients are the steepest on the sphere's surface, as the spherical symmetry makes the steady state fluxes follow a $1/r^2$ profile. The thermal and mass transfer film thicknesses do not coincide, if the Lewis number of the volatile species differs from unity. Using the correlation of Ranz and Marshall (1952), the ratio of the film thicknesses is: $\frac{\delta_T}{\delta_M} = \frac{Pr_m^{-1/3}}{Sc_m^{-1/3}} = Le_m^{1/3}$. The case in Fig. 4.6 depicts a hypothetical situation of $Le_m = 3.4$, that is a possible value for n-heptane and n-dodecane as shown in Fig. 2.1.

The heat and mass transfer models presented in this section are used below in section 4.4 combined with the material property models described in section 4.3 to

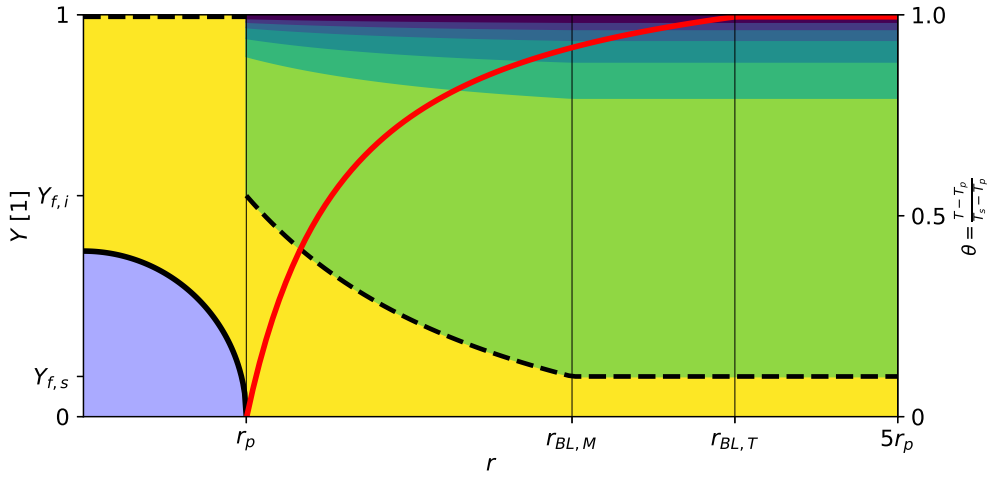

FIGURE 4.6: Thermal and mass transfer films around a sphere. The black dashed line marks the mass fraction of fuel: Y_f^{MTS}, while the solid red line is the scaled temperature profile: $\theta^{TTS} = \frac{T^{TTS}-T_p}{T_s-T_p}$.

construct droplet evaporation models.

4.3 Material property models

To evaluate the heat and mass transfer rates derived in section 4.2 one needs a representative value of various material properties of the gas phase. Furthermore, thermodynamic relations are also needed to couple the boundary conditions of temperature and vapor mass fraction on the droplet interface. (Eq. (4.17) and Eq. (4.18)) Finally, to formulate the ordinary differential equations of the droplet mass and energy conservation, more properties are required related to the liquid phase and the phase change. This section describes the closure models of each of these properties.

4.3.1 Phase change and liquid properties

An important aspect of droplet evaporation models, is the way the interface temperature and interface vapor mass fraction are linked. In the evaporation models defined below, with the exception of the non-equilibrium models, the interface vapor mass fraction is related to the droplet temperature assuming local thermodynamic equilibrium: $Y_{f,i} = Y_{f,i}^{eq}$. In accordance with Rault's law, the equilibrium vapor mole fraction on the droplet interface is given by the partial pressure of the vapor: $X_{f,i}^{eq} = P_{sat}/P$. To yield the interface vapor mass fraction, the frozen chemistry assumption is used, postulating that the bath gas composition is constant in the boundary layer around the droplet:

$$Y_{f,i} = \frac{X_{f,i}}{X_{f,i} + (1 - X_{f,i}) \frac{W_b}{W_f}} \tag{4.27}$$

where W_b is the mean molar mass of the bath gas, and W_f is the molar mass of the volatile component. The frozen chemistry assumption speculates, that the chemical reactions are inactive in the thin boundary layer surrounding the droplet, thus the bath gas species do not react with the volatile fuel in the film, and the conservation equations of fuel mass Eq. (4.15) and enthalpy Eq. (4.16) only need to consider advection and diffusion as derived in section 4.2.

Besides the temperature and fuel mass fraction profiles, Fig. 4.6 also illustrates the frozen chemistry assumption by distinguishing the vapor and the non-reacting bath gas mixture using different colors. In this view the bath gas, that may be composed of different gas phase species, is represented by different shades of green and blue in the region above the fuel mass fraction profile. According to the frozen chemistry assumption, the composition of this $(1 - Y_f)$ part of the mixture is constant. Consequently, the molar mass of this part W_b is a constant and Eq. (4.27) is a rearrangement of Eq. (2.2).

The saturation pressure P_{sat} is evaluated using the the standardized material property functions of Daubert and Danner (1985), which gives P_{sat} as a function of the liquid temperature. The remaining unknown terms of the heat and mass conservation equations are the density of the droplet ρ_p relating the droplet mass to the diameter, and the specific heat of the liquid phase $c_{p,p}$, and latent heat of evaporation L_v that play a role in the energy conservation equation of the droplet. These are also closed using the functions of Daubert and Danner (1985). The function templates and their coefficients are summarized in appendix B, where the general behavior of these correlations is examined. The appendix concludes, that the proposed functions show the expected behavior as function of the liquid temperature. Furthermore, the critical pressure of all studied volatile fluids is well above atmospheric pressure, thus their treatment as liquids is justified in this study, where the simulated cases are restricted to atmospheric pressure.

The functions of P_{sat}, ρ_p, $c_{p,p}$, and L_v are further examined in appendix C, that compares the functions of water, n-heptane, and n-dodecane to alternative sources of reference data in the temperature range of interest: between 273.15 K and the boiling point: T_{sat} of the liquid, that is such, that $P_{sat}(T_{sat}) = 101325$ Pa. The appendix shows, that the proposed functions reproduce well the reference data. Furthermore, it is also proved, that these liquid and phase-change properties show large fluctuations in hydrocarbons in the studied temperature range. This, the inclusion of such elaborate models is well justified over simplified methods such as using constant liquid properties.

4.3.2 Representative average gas phase properties

In section 4.2 it is implicitly assumed that the gas phase material properties are constant across the film around the droplet. However these properties vary in function of the temperature and composition in reality. (See. section 2.1.) To overcome this difficulty, the assumption of the existence of mean state is used, such that using the properties of this state results in minimal error in momentum, heat, and mass transfer. The subscript "m" used throughout this chapter represents this mean state.

Yuen and Chen (1976) introduced the so called "1/3 law", where the mean state is found as a weighted average between the temperature and composition on the droplet interface and in the far-field with a weight of $\alpha = 1/3$ allocated to the far-field. Ma, Naud, and Roekaerts (2016) compared this assumption with using a far field properties directly ($\alpha = 1$) in the Delft Spray-in-Hot-Coflow burner. They

found, that α has a great influence on the droplet cloud, and the weight of "1/3" produces better overall correlation with measurement data. Recently Finneran (2021) carried out an extensive evaluation of this weighting rule in the case of stationary droplet, and devised a method to dynamically choose α such that the transfer rates match the solution where variable properties are used. Realistic coefficients were found in the $\alpha \in [0.25, 0.4]$ interval, where the lower coefficients correspond to higher seen gas temperatures. Meanwhile Finneran (2021) also shows, that if the 1/3 law is used the error of the evaporation rate is within 15%. The highest errors are encountered at high seen temperatures.

Recently most Lagrangian spray combustion simulations still apply the "1/3 law". (Jenny, Roekaerts, and Beishuizen, 2012; Noh et al., 2018; Sitte and Mastorakos, 2019; Benajes et al., 2022) The adaptation of the dynamic model of Finneran (2021) is out of the scope of the present work, and the "1/3 law" of Yuen and Chen (1976) is retained. However, it is reassuring to know, that the error is bounded. Two versions of the film property model is used, the classical "1/3 law" is applied in the assessment of single droplets, while a new model is developed that mimics the "1/3 law" in the context of tabulated chemistry, where the full information of the bath gas composition is not feasible to use.

Classical 1/3 law

Yuen and Chen (1976) propose the so called "1/3 law", where the mean properties are evaluated at a virtual state characterized by a weighted average of the seen and interface composition and temperature:

$$T_m = \alpha T_s + (1-\alpha) T_p, \tag{4.28}$$

$$Y_{k,m} = \alpha Y_{k,s} + (1-\alpha) Y_{k,i}, \tag{4.29}$$

with $\alpha = 1/3$, and $k = 1..N_C$ where N_C is the number of species considered in the gas phase. To evaluate the transfer rates at a given far field and droplet surface conditions, the material properties used in the above equations ($c_{p,vap,m}$, $c_{p,m}$, λ_m, μ_m, ρ_m, $\mathcal{D}_m$) need to be calculated according to the "1/3 law".

The specific heat of the vapor and of the mean gas mixture is calculated based on the NASA polynomials widely used in reacting flow calculations. Note, that the mixture mean specific heat $c_{p,m}$ is a weighted sum of the individual specific heat of the species according to Eq. (2.7). Meanwhile, the specific heat of the vapor is simply the polynomial of the volatile species evaluated at T_m using Eq. (2.6) and the molar weight of the volatile species. The latter is typically higher than the former for the studied complex hydrocarbon fuels, meaning, that the factor $c_{p,vap,m}/c_{p,m}$ of Ξ_1 in Eq. (4.19) is above unity.

The transport properties: thermal conductivity λ_m, dynamic viscosity μ_m, and the diffusivity of the volatile species $\mathcal{D}_m$, are calculated following the transport theory of multicomponent mixtures, following Eq. (2.15), Eq. (2.13), and Eq. (2.19) respectively. As Ebrahimian and Habchi (2011) point out, it is of the utmost importance, that the diffusivity of the volatile species is evaluated using the correct relations. As in this work the mass fluxes are based on the mass fraction gradients, the *mass* diffusion coefficient is to be used. Here the conversion of molar and mass

diffusion coefficients (Eq. (2.19)) is repeated for emphasis:

$$\mathcal{D}_m = \mathcal{D}_m^{mol} \left(1 - X_{f,m} + Y_{f,m} \sum_{k=1, k\neq f}^{N_C} \frac{X_{k,m}}{Y_{k,m}} \right), \tag{4.30}$$

where $X_{k,m}$ is the molar fraction of species k in the mean mixture. As Fig. 2.1 illustrates in section 2.1, in isothermal mixtures $\mathcal{D}_m$ is practically constant when mixtures with air are considered. Meanwhile, $\mathcal{D}_m^{mol}$ according to Eq. (2.16) is a linear function of the fuel mass fraction. In the applications of the present work, where atmospheric air is used as an oxidizer, $\mathcal{D}_m$ is approximated well by the binary diffusion coefficient of the volatile species in molecular nitrogen: $\mathcal{D}_m \approx \mathcal{D}_{f,N_2}(T_m)$ as suggested by Eq. (2.21). The approximation is evaluated in Fig. 2.1 under various conditions for n-heptane.

Finally, the density is evaluated using the ideal gas law: $\rho_m = (PW_m) \,/\, (R_u T_m)$, where P is the pressure of the system, W_m is the mean molar mass in the reference gas mixture, and R_u is the universal gas constant. The fuel's mass diffusivity and mean density are crucial properties for the evaporation process, as the mass flow rates are directly proportional to $\rho_m \mathcal{D}_m$, and this term is also present in the Lewis number, influencing the Stefan flow effects through the factor Ξ_1. The less volatile hydrocarbon fuels (e.g.: n-dodecane) are generally also characterized by lower diffusivity, further impeding their evaporation.

This approach is used in section 4.5 and section 4.6 for the simulation of standalone droplets. In the context of these sections the classical "1/3 law" is chosen, in order to recreate and analyze the most standard model behavior. This ensures, that the conclusions of the present chapter are widely applicable for spray flame modeling at atmospheric pressure.

1/3 law in tabulated chemistry methods

With large chemical mechanisms the tabulation of all species and the subsequent calculation of mixture-averaged transport properties becomes infeasible. This is mainly due to the sheer amount of memory needed for the tabulation of a high number of species. (Both, 2017) For example, a table of dimensions: $n_Z \times n_{\zeta_{Z_v}} \times n_C \times n_i = 101 \times 11 \times 101 \times 11$ contains over 1.2 million unique states. Using double precision floating point numbers, this corresponds to a memory requirement per tabulated parameter:

$$MEM_\psi = (8\ \mathrm{B}) \prod_k n_k. \tag{4.31}$$

Using the above example, each table entry requires $\sim$ 9.4 MB memory. Considering a detailed chemical mechanism containing $N_C = \mathcal{O}(100)$ species, to tabulate the full thermo-chemical state with such a table size, it would be required to dedicate $MEM_\psi \times N_C = \mathcal{O}(1\ \mathrm{GB})$ of memory just to the tabulated chemistry database.

On present supercomputers, such high amount of memory may not be available. For instance in MareNostrum4, the supercomputer utilized in this study, the normal compute nodes dispose of 1.88 GB memory per CPU. (BSC, 2021) In the current parallelization strategy of Alya, each MPI process has a copy of the thermo-chemical tables. Thus, using more a table size of $\mathcal{O}(1\ \mathrm{GB})$ may indeed be prohibitive. Furthermore, the excessive usage of table lookup would also penalize the numerical performance of the code. (POP, 2021)

Various recent works recognize this limitation posed by tabulated chemistry and propose alternatives. Sacomano Filho et al. (2019) proposed to use a reduced set of species in Eq. (4.29), and evaluate the material properties based on this simplified mixture using the classical relations of chapter 2. Zhang et al. (2020b) uses artificial neural networks (ANNs) to predict the species concentrations as function of the control variables of the tabulated chemistry. In case the ANN training is not possible with sufficient accuracy, their method reverts to the usage of lookup tables. Subsequently, this representative gas mixture of all N_C species is used to evaluate the properties in the droplet film.

The above methods apply two steps to obtain the relevant gas phase properties: first, the seen gas composition and temperature is identified involving table lookup, then T_m and $Y_{k,m}$ of Eq. (4.28) and Eq. (4.29) is passed to the gas property functions to evaluate: $c_{p,vap,m}$, $c_{p,m}$, λ_m, μ_m, ρ_m, and $\mathcal{D}_m$. In the previous work of author (Both, 2017) a method is presented, where the desired material properties are obtained from the lookup tables directly. This has two potential effects on performance. Firstly, the number of lookup properties is decoupled from the complexity of the mechanism and is limited to a relatively low number. Secondly, the properties are obtained using fewer numerical operations than those involved in Eq. (2.15), Eq. (2.13), Eq. (2.19), etc. The tabulated film property models presented below are an improvement of this initial attempt, where a correction is introduced to account for first order temperature dependences.

Tabulated Average Representative Evaporation State (TARES)

The Tabulated Average Representative Evaporation State (TARES) model presented hereafter is an improvement on the original model of Both (2017). It utilizes the fact, that the thermo-chemical tables introduced in chapter 2 readily contain a large amount of information about the properties of the far-field ("seen") gas: the molecular weight ($W^\star$), dynamic viscosity (μ), thermal conductivity (λ), and the mean NASA polynomials (b_i) of the mixture. These may be evaluated, provided that the control variables of the table are known at the location of the droplet.

The TARES model works with adiabatic and non-adiabatic tables as well. In both cases the control variables of the table and the enthalpy are interpolated on the location of the droplet using the Eulerian solution of the gas phase. The variables obtained at the location of the droplet may include: the resolved mixture fraction $\widetilde{Z}_s$, the resolved progress variable: $\widetilde{Y}_{c,s}$, the resolved specific enthalpy: $\widetilde{h}_s$, and in case variance models are employed, the sub-grid variance of mixture fraction: $Z_{v,s}$, and the sub-grid variance of progress variable: $Y_{c,v,s}$. The "s" subscript stands for seen conditions. These quantities are defined in chapter 5, for the sake of the present derivation their definition is not crucial.

First the boundary conditions of the heat and mass transfer problem need to be evaluated. Using the NASA polynomials: b_i^s and the specific enthalpy: $\widetilde{h}_s$ at the location of the droplet, the seen temperature can readily be obtained using the Newton-Raphson method of algorithm 2.1. The vapor mass fraction: $\widetilde{Y_{f,s}}$ has to be added to the thermo-chemical tables, so the lookup can provide it directly. This first lookup procedure also gives the mean molecular weight of the seen gas: $W_s^\star$. With this information, the molecular weight of the bath gas can be obtained directly, that

is a constant throughout the film, according to the frozen chemistry assumption:

$$W_b = \frac{1 - \widetilde{Y_{f,s}}}{\frac{1}{W_s^\star} - \frac{\widetilde{Y_{f,s}}}{W_f}}, \tag{4.32}$$

where the molar weight of the volatile species W_f is a known constant. In most cases the droplet interface boundary conditions of the heat and mass transfer problems are linked to the droplet temperature. Once T_p is known, the mean temperature T_m may be evaluated directly. Furthermore, the equilibrium interface vapor mass fraction may be evaluated using Eq. (4.27), with the result of Eq. (4.32) and with the interface vapor mole fraction, that is given by the imposed equilibrium condition. Up to this point no specific assumptions are made, and the computed quantities are fully equivalent to the classical 1/3 law. The boundary conditions of the transfer rates in Tab. 4.3 are known.

The specific heat of pure fuel vapor at the mean temperature $c_{p,vap,m}$ can readily be evaluated using the NASA polynomials contained in the table at $Z = 1$:

$$c_{p,vap,m} = \sum_{i=1}^{5} b_i^f T_m^{i-1}. \tag{4.33}$$

Note that b_i^f is only retrieved from the table once in the beginning of the time step. Also, the choice of any other control variables is irrelevant, since the coefficients of pure fuel do not depend on temperature.

The remaining unknown terms are only the film properties of the gas mixture. These are obtained by executing the table lookup again with a representative set of control variables:

$$Z_m = \alpha \widetilde{Z}_s + (1 - \alpha) Y_{f,i}, \tag{4.34}$$

$$Y_{c,m} = \alpha \widetilde{Y}_{c,s}, \tag{4.35}$$

$$Z_{v,m} = \alpha Z_{v,s}, \tag{4.36}$$

$$Y_{c,v,m} = \alpha Y_{c,v,s}. \tag{4.37}$$

Note that in this modified 1/3 law the interface values of progress variable and the variances are assumed to be zero. Furthermore, the interface fuel mass fraction is used to attain a "mean" mixture fraction. In this instance of lookup additional variables are required including: the diffusivity of the volatile species $\mathcal{D}$, partial derivatives of the transport properties with respect to temperature $\frac{\partial \lambda_g}{\partial T}$, $\frac{\partial \mu_g}{\partial T}$, $\frac{\partial \mathcal{D}_g}{\partial T}$, and the temperature corresponding to the tabulated state $T^\star$.

In case of adiabatic tables, the lookup is simply done once. While in case of non-adiabatic tables, an iterative process in applied to minimize the difference between the mean temperature of Eq. (4.28) and the tabulated temperature: $T_m^{\star,tab}$. Note, that the manifold may not contain a low enough enthalpy level at given $(Z_m, Y_{c,m}, Z_{v,m}, Y_{c,v,m})$ to reach $\left| T_m - T_m^{*,tab} \right| = 0$. This lookup procedure yields: the NASA polynomials at the mean state: b_i^{tab}, the tabulated temperature: $T_m^{\star,tab}$, the tabulated transport properties: λ_m^{tab}, μ_m^{tab}, and $\mathcal{D}_m^{tab}$, and their partial derivatives with respect to temperature: $\left(\frac{\partial \lambda_m}{\partial T}\right)^{tab}$, $\left(\frac{\partial \mu_m}{\partial T}\right)^{tab}$, and $\left(\frac{\partial \mathcal{D}_m}{\partial T}\right)^{tab}$.

Given these properties the mean specific heat is calculated from the NASA polynomials following Eq. (2.8):

$$c_{p,m} = \sum_{i=1}^{5} b_i^{tab} T_m^{i-1}. \tag{4.38}$$

In the calculation of mean transport properties, a first order correction is applied to correct for the temperature difference between the tabulated state and T_m:

$$\Delta T = T_m - T_m^{\star,tab}, \tag{4.39}$$

thus the mean transport properties are:

$$\lambda_m = \lambda_m^{tab} + \Delta T \left(\frac{\partial \lambda_m}{\partial T} \right)^{tab}, \tag{4.40}$$

$$\mu_m = \mu_m^{tab} + \Delta T \left(\frac{\partial \mu_m}{\partial T} \right)^{tab}, \tag{4.41}$$

$$\mathcal{D}_m = \mathcal{D}_m^{tab} + \Delta T \left(\frac{\partial \mathcal{D}_m}{\partial T} \right)^{tab}. \tag{4.42}$$

The mean density can be calculated such, that it perfectly matches the results of the classical "1/3 law" using the ideal gas law (Eq. (2.5)). Here, the molar mass of the mean state is calculated as:

$$W_m = \left(\frac{\alpha}{W_s^\star} + \frac{1-\alpha}{W_i} \right)^{-1}, \tag{4.43}$$

with $W_i = X_{f,i} W_f + (1 - X_{f,i}) W_b$, thus and the mean density is:

$$\rho_m = \frac{P_0 W_m}{R_u T_m}. \tag{4.44}$$

Overall the TARES model requires six additional tabulated properties: $\widetilde{Y_f}$, $\widetilde{\mathcal{D}}$, $\frac{\partial \lambda}{\partial T}$, $\frac{\partial \mu}{\partial T}$, $\frac{\partial \mathcal{D}}{\partial T}$, and $T^\star$. Furthermore, the lookup is executed at least two times. However, the direct evaluation of gas mixture properties is avoided at runtime.

4.4 Droplet evaporation models

In this section the droplet evaporation models are constructed, by combining the heat and mass transfer models of section 4.2 with the material property models of section 4.3. The gas phase transport phenomena are linked to the conservation of droplet mass and energy.

4.4.1 Infinite conductivity assumption

In the present modeling framework, the droplets are treated as homogeneous spheres under the infinite conductivity assumption. I.e.: the heat (and mass) transfer inside the droplet is significantly faster than outside of it, thus the droplet can be characterized by a constant temperature profile.

Ma et al. studied the Delft Spray-in-Hot-Coflow burner using two different numerical codes: a Lagrangian-Lagrangian RANS code: "PDFD", where the gas phase

is solved with a transported PDF method (Ma, Naud, and Roekaerts, 2016), and an OpenFOAM based implementation of the Eulerian-Lagrangian URANS and LES approach: "sprayFGMFoam" (Ma and Roekaerts, 2016). In the former study, they show the benefit of applying a parabolic temperature profile within the droplet, compared to the infinite conductivity model. This model allows faster evaporation, since the droplet interface temperature can exceed the mean droplet temperature, leading to higher interface vapor mass fraction. They conclude, that this is an important mechanism for the removal of small droplets, and it allows the correct prediction of the Sauter mean diameter (SMD). Meanwhile the latter Eulerian-Lagrangian study employs the infinite conductivity model, and achieves reasonable fitting with the experimental SMD without the added complexity of internal droplet modeling. Sazhin (2014, §7.1) points out, that indeed the impact of the parabolic temperature is most important for breakup modeling, and it also has a notable influence on autoigniting, however in other cases its effect is small. In the present work, the infinite conductivity assumption is retained for its simplicity, since neither breakup modeling not autoignition is considered.

To assess this assumption, one may use the Biot number Bi, that provides a comparison of the time scales of heat transfer outside and inside the droplet:

$$Bi = \frac{h_T^{heat} d_p}{\lambda_p}, \tag{4.45}$$

where λ_p is the thermal conductivity in the liquid phase, and h_T^{heat} is a heat transfer coefficient in the gas phase that only considers the heat reaching the liquid droplet:

$$h_T^{heat} = \frac{-\dot{Q}_r - L_v \dot{m}_r}{\pi d_p^2 \left(T_s - T_p\right)} = \frac{\lambda_m Nu_m}{d_p} - \frac{L_v \dot{m}_r}{\pi d_p^2 \left(T_s - T_p\right)} \tag{4.46}$$

where L_v is the latent heat of evaporation, and Nu_m is an effective Nusselt number of the heat transfer problem, that may be corrected for considering Stefan flow effects. Thus, the Biot number may range between zero and $\lim_{\dot{m}_r \to 0} Bi = \frac{\lambda_m Nu_m}{\lambda_p}$. The former corresponds to the case where all the heat transferred to the droplet is consumed by the evaporation (wet-bulb condition), while the latter to the case of negligible evaporation.

Non-uniform internal temperature profiles are relevant at high Biot numbers. Based on the above discussion, this is relevant if the droplet is far from the wet-bulb conditions and the Nusselt number is high. Even with negligible mass transfer rates the Biot number can be small for slow moving droplets, since the liquid thermal conductivity is an order of magnitude higher than the mean gas phase thermal conductivity. (Daubert and Danner, 1985) It is plausible, that high Biot number conditions occur only near the droplet injection or when a droplet crosses a flame front at high speed. In a large part of the droplet lifetime the Biot number is low, and the infinite conductivity model may be applied. In this approach, the droplet is fully described by two quantities influencing the evaporation: its mass and its specific enthalpy or temperature.

4.4.2 Lumped conservation equations of the droplet

Ordinary differential equations can be formed to represent the conservation of droplet mass and enthalpy in relation to the transfer rates presented in section 4.2. This

model postulates, that while the inner droplet temperature profile relaxes to a constant temperature infinitely fast, similarly the gas phase temperature and vapor mass fraction profiles also relax to their steady state infinitely fast (quasi-steady assumption). The ODEs can be formulated using a control volume depicted in Fig. 4.7. The mass change of the droplet is simply expressed as:

$$\frac{\mathrm{d}m_p}{\mathrm{d}t} = -\dot{m}_r, \tag{4.47}$$

where m_p is the mass of the droplet.

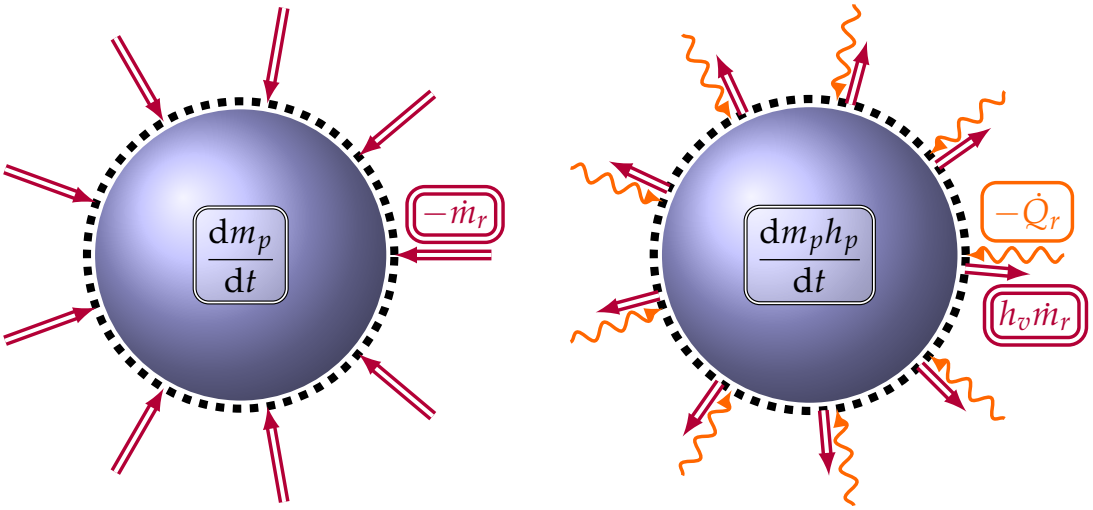

(A) Mass balance of droplet.

(B) Enthalpy balance of droplet.

FIGURE 4.7: Illustration of mass and enthalpy balance of droplet.

The enthalpy conservation of the droplet is more complex, as Fig. 4.7b illustrates, since the vapor enthalpy has to be accounted for. Using a contour volume right outside the droplet surface, the thermal balance can be expressed, by equating the heat flow reaching the droplet surface to the enthalpy change of the system inside the control volume, and the enthalpy of vapor crossing this boundary:

$$-\dot{Q}_r = \frac{\mathrm{d}m_p h_p}{\mathrm{d}t} + h_v \dot{m}_r, \tag{4.48}$$

where h_p and h_v are the liquid and vapor enthalpies respectively. The enthalpy change of the liquid droplet can be transformed using the definition of isobaric specific heat:

$$\frac{\mathrm{d}m_p h_p}{\mathrm{d}t} = m_p \frac{\partial h_p}{\partial T_p}_{|p} \frac{\mathrm{d}T_p}{\mathrm{d}t} + h_p \frac{\mathrm{d}m_p}{\mathrm{d}t} = m_p c_{p,p} \frac{\mathrm{d}T_p}{\mathrm{d}t} + h_p \frac{\mathrm{d}m_p}{\mathrm{d}t}, \tag{4.49}$$

where $c_{p,p} = \frac{\partial h_p}{\partial T_p}_{|p}$ is the isobaric specific heat of the liquid. Using the definition of the latent heat of evaporation: $L_v = h_v - h_p$, the energy conservation of a droplet can be formulated in terms of the droplet temperature as:

$$\frac{\mathrm{d}T_p}{\mathrm{d}t} = \frac{-\dot{Q}_r}{m_p c_{p,p}} + \frac{L_v}{m_p c_{p,p}} \frac{\mathrm{d}m_p}{\mathrm{d}t}, \tag{4.50}$$

The different evaporation models used in this work are summarized in Tab. 4.4 and further described below. They differ in terms of considering Stefan flow, introducing additional corrections for the film thickness, and considering non-equilibrium conditions on the liquid-vapor interface.

4.4.3 Diffusion only model (D/D: MTD + TTD)

The diffusion only model considers the diffusion based transport quantities derived in section 4.2. The mass and heat transfer rates are given by $\dot{m}_r^{MTD}$ and $\dot{Q}_r^{TTD}$, thus both rates scale linearly with the "potential differences": $\left(Y_{f,i} - Y_{f,s}\right)$ and $\left(T_p - T_s\right)$. This model is equivalent to M5 (Mass analogy IIa) of Miller, Harstad, and Bellan (1998).

4.4.4 Classical model (S/D: MTS + TTD)

The Classical model combines the mass transport considering Stefan flow ($\dot{m}_r^{MTS}$) with the thermal transport neglecting Stefan flow ($\dot{Q}_r^{TTD}$). Such a combination is quite straightforward, as it is more natural to derive the mass transfer including Stefan flow (unimolecular diffusion), while in heat transfer the Stefan flow effects are not inherent to the problem. (See the derivations in appendix E.) Nevertheless, this asymmetry makes the Classical model (S/D) open to doubt. In this case the mass transfer rate is no longer proportional to the difference between fuel mass fractions on the interface and in the far-filed, but the rate is governed by the logarithmic term: $\ln\left(\frac{1-Y_{f,s}}{1-Y_{f,i}}\right)$. This term is widely expressed as $\ln\left(1 + B_M\right)$, giving the definition of the Spalding mass transfer number:

$$B_M = \frac{Y_{f,i} - Y_{f,s}}{1 - Y_{f,i}}. \tag{4.51}$$

The transformation is preferred, since B_M expresses the mass transfer potential in a single variable. It tends to zero at low evaporation rates, and it provides a more sensitive measure near the boiling point of the droplet, since B_M can reach very high values, as the interface vapor mass fraction approaches 1. This model is equivalent to M1 (Classical rapid mixing) of Miller, Harstad, and Bellan (1998), and to EM1 of Noh et al. (2018). The mass conservation equation of the classical model is shown in Tab. 4.4.

4.4.5 Bird's correction (B: MTS + TTS)

Bird, Stewart, and Lightfoot (1960, §19.4, §22.8) noted, that high mass transfer rates distort the temperature profile around the droplet, as the energy carried by the unimolecular diffusion of vapor becomes significant. In the case of forced convection, this results in decreased heat transfer rates if the net mass transfer is away from the surface (e.g.: fast evaporation of a droplet).

Bird defined a rate factor β, as the ratio of enthalpy transported by Stefan flow to the enthalpy transported by conduction in the absence of the Stefan flow:

$$\beta = \frac{c_{p,vap,m} \mathbf{\Phi}_{M,f,r}^{MTS} \left(T_p - T_s\right)}{\mathbf{\Phi}_{T,r}^{TTD}}, \tag{4.52}$$

By substituting the expressions of Tab. 4.3 it is reviled, that the β factor of Eq. (4.52) is indeed equivalent to the β discussed in section 4.2.1:

$$\beta = \frac{c_{p,vap,m}}{c_{p,m}} \frac{Pr_m}{Sc_m} \frac{Sh_{m,0}}{Nu_{m,0}} \ln(1 + B_M) = \phi_m \ln(1 + B_M), \tag{4.53}$$

where $\phi_m = \frac{c_{p,vap,m}}{c_{p,m}} \frac{1}{Le_m} \frac{Sh_{m,0}}{Nu_{m,0}}$ expresses the β ratio's dependence on factors other than the Spalding number, and $Le_m = \frac{Sc_m}{Pr_m}$ is the Lewis number of the volatile species in the mixture based on the mass diffusivity $\mathcal{D}_m$. Note, that since the Ranz-Marshall correlation takes the same form for the Nusselt and Sherwood numbers, ϕ_m is only weakly dependent on the Reynolds number. In the limiting cases ϕ_m takes the following values:

$$\lim_{Re_m \to 0} \phi_m = \frac{c_{p,vap,m}}{c_{p,m}} \frac{1}{Le_m}, \quad \text{and} \quad \lim_{Re_m \to \infty} \phi_m = \frac{c_{p,vap,m}}{c_{p,m}} \frac{1}{Le_m^{2/3}}, \tag{4.54}$$

and ϕ_m is confined within these limits. The typical values of ϕ_m are further discussed in the context of the wet-bulb conditions in section 4.5, and they are shown in Fig. 4.14.

Based on the simultaneous heat and mass transfer of a flat plate using film theory, Bird proposes an effective Nusselt number corrected for the influence of Stefan flow on the heat transfer as:

$$Nu_m^{*,B} = \frac{\beta}{e^\beta - 1} Nu_{m,0} = \frac{\phi_m \ln(1 + B_M)}{(1 + B_M)^{\phi_m} - 1} Nu_{m,0}. \tag{4.55}$$

Note, that $Nu_m^{*,B}$ does not have direct relation to the film thickness. It is merely a factor that represents the effect of film thickness and the effect of Stefan flow together. Analogous to B_M, a Spalding *heat* transfer number can be defined as:

$$1 + B_T = (1 + B_M)^{\phi_m}, \tag{4.56}$$

that simplifies the expression of Bird's correction. In this case, the heat transfer equation of the droplet takes the form:

$$\frac{\mathrm{d}T_p}{\mathrm{d}t} = \frac{\pi d_p \lambda_{g,m} Nu_{m,0}}{m_p c_{p,p}} (T_s - T_p) \frac{\ln(1 + B_T)}{B_T} + \frac{L_v}{m_p c_{p,p}} \frac{\mathrm{d}m_p}{\mathrm{d}t}. \tag{4.57}$$

The correction factor is illustrated in Fig. 4.8. Depending on the value of ϕ_m the heat transfer rate can be reduced quite significantly.

Bird, Stewart, and Lightfoot (1960) derived the above correction for mass transfer from a flat interface. However, one may demonstrate that the same correction is to be applied in spherical coordinates as shown in appendix E. Bird's correction considers the radial heat flux with Stefan flow $\dot{Q}_r^{TTS}$ (defined in Tab. 4.3), the components of the last term of this equation are:

$$2\frac{\Xi_1}{r_p} = -\beta Nu_{m,0}; \quad \frac{\Xi_1}{r_{BL,T}} - \frac{\Xi_1}{r_p} = \beta. \tag{4.58}$$

Hence, despite the different solution, the correction proposed by Bird still holds for spheres as well: $Nu_m^{*,B} / Nu_{m,0} = 2\frac{\Xi_1}{r_p Nu_{m,0}} \Big/ \left(1 - e^{\frac{\Xi_1}{r_{BL,T}} - \frac{\Xi_1}{r_p}}\right) = \beta / \left(e^\beta - 1\right)$.

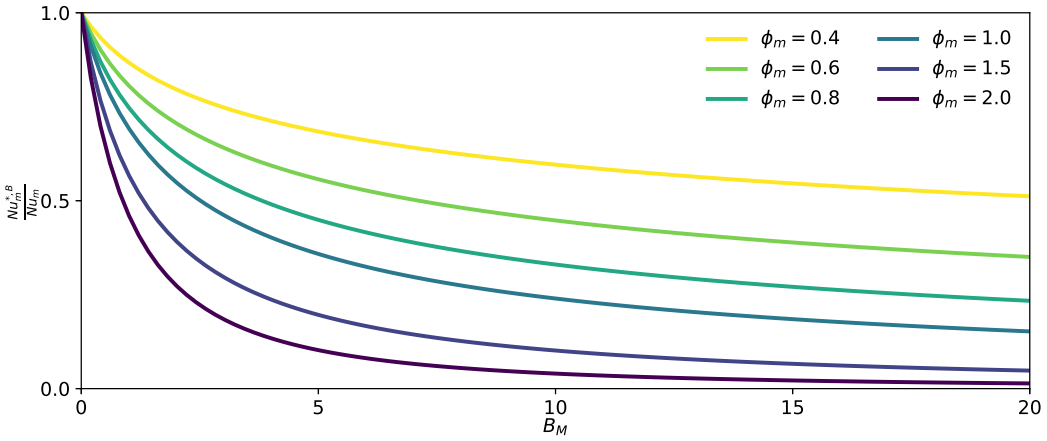

FIGURE 4.8: Effective Nusselt number correction factor of Bird, Stewart, and Lightfoot (1960, §19.4, §22.8) parametrized by $\phi_m = \frac{c_{p,vap,m}}{c_{p,m}} \frac{1}{Le_m} \frac{Sh_{m,0}}{Nu_{m,0}}$.

4.4.6 Abramzon-Sirignano model (AS)

As described in section 4.2.1, the finite film thickness is a modeling artifact, that expresses the mean effects of the advective transport by relating the film thickness to the Reynolds number. Illustrated in Fig. 4.5, there is a clear relation between the deceleration of the velocity field near the droplet (indicating the momentum boundary layer) and the empirical film thickness of Ranz and Marshall (1952). The momentum boundary layer is expected to change, if the velocity associated with the Stefan flow is significant. Abramzon and Sirignano (1989) argue, that the heat and mass transfer film thickness is likewise influenced by Stefan flow.

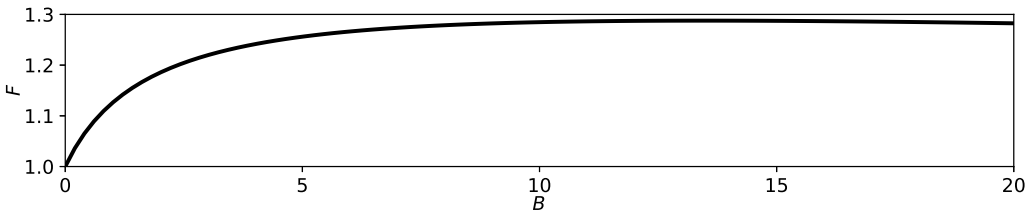

FIGURE 4.9: Thickness correction factor of Abramzon and Sirignano (1989) according to Eq. (4.59).

In the Abramzon-Sirignano model the difference between the affected and unaffected film thickness is expressed by the correction factors $F_T = \delta_T^*/\delta_T$ and $F_M = \delta_M^*/\delta_M$, where the $*$ superscript signifies the film thickness in the presence of Stefan flow. In their study of a vaporizing wedge, they concluded, that F_T and F_M are mainly influenced by the transfer numbers B_M and B_T^*. The correction factors take the form:

$$F(B) = (1+B)^{0.7} \frac{\ln(1+B)}{B}, \tag{4.59}$$

where $F(B)$ can be $F_T(B_T^*)$ or $F_M(B_M)$, with B_T^* evaluated using the modified Sherwood and Nusselt numbers as detailed below. Note, that the validity range of

Eq. (4.59) is restricted to $0 \leq B \leq 20$. As Fig. 4.9 illustrates, strong Stefan flow may thicken the boundary layers by as much as 28% according to Eq. (4.59).

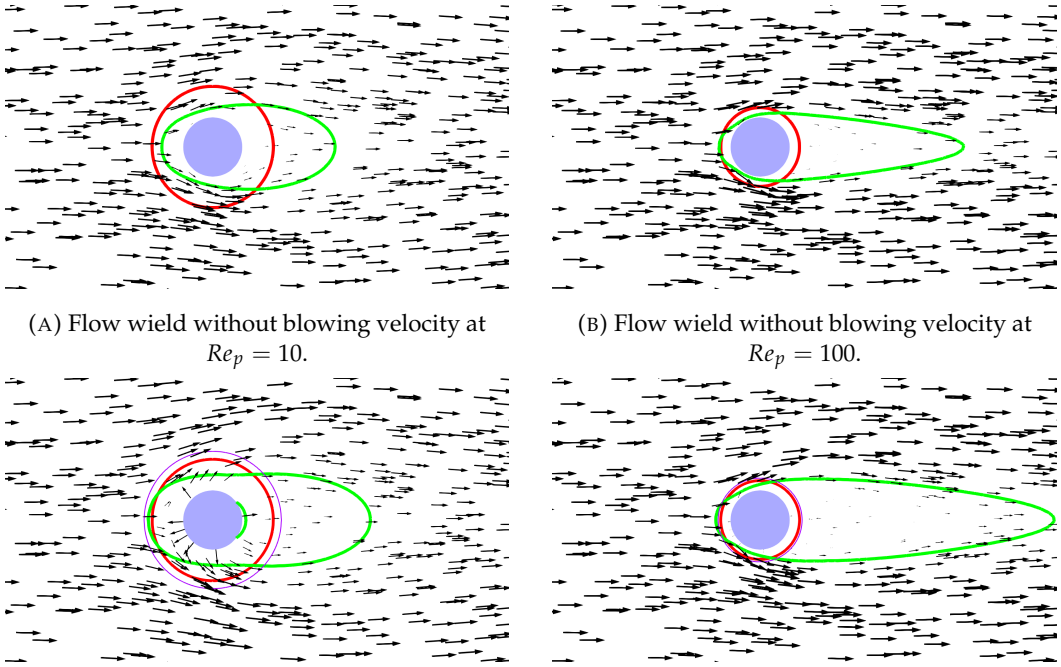

(A) Flow wield without blowing velocity at $Re_p = 10$.

(B) Flow wield without blowing velocity at $Re_p = 100$.

(C) Flow wield with blowing velocity at $Re_p = 10$ and $B_M = 5$. ($u_b/u_s = 0.629$)

(D) Flow wield with blowing velocity at $Re_p = 100$ and $B_M = 5$. ($u_b/u_s = 0.121$)

FIGURE 4.10: Illustration of film tickness augmentation by Stefan flow around a sphere at two different Reynolds numbers using the correlation of Ranz and Marshall (1952) in combination with the Abramzon-Sirignano model. For reference a green contour line marks the region, where the streamwise component of the velocity filed in the Lagrangian frame of reference drops below 50% of the far-field value. Red circles mark $r_{BL,M}$ according to the Ranz-Marshall model, while the thin purple circle indicates $r^*_{BL,M} = r_p + \delta^*_M$. These estimates are calculated assuming unity Schmidt number.

The modified Nusselt and Sherwood numbers take the form:

$$Nu_m^{*,AS} = 2 + \frac{Nu_{m,0} - 2}{F_T}; \quad Sh_m^{*,AS} = 2 + \frac{Sh_{m,0} - 2}{F_M}. \tag{4.60}$$

Finally, the model is closed, by relating the Spalding transfer numbers of mass and energy through $B_T^* = (1 + B_M)^{\phi_m^*} - 1$, where $\phi_m^* = \frac{c_{p,vap,m}}{c_{p,m}} \frac{1}{Le_m} \frac{Sh_m^{*,AS}}{Nu_m^{*,AS}}$ is the parameter introduced in Eq. (4.53), but evaluated at the modified Nusselt and Sherwood numbers. Thus, the Abramzon-Sirignano model is implicit and has to be solved iteratively, considering:

$$\phi_m^* = \phi_m \frac{Sh_m^{*,AS}}{Sh_{m,0}} \frac{Nu_{m,0}}{Nu_m^{*,AS}}. \tag{4.61}$$

The overall process of calculating $Sh_m^{*,AS}$ and $Nu_m^{*,AS}$ is summarized in Algorithm 4.1.

Algorithm 4.1: Evaluation of the Abramzon-Sirignano model with given B_M, $Sh_{m,0}$, $Nu_{m,0}$, ϕ_m.

Evalueate F_M as in Eq. (4.59);
Evalueate $Sh_m^{*,AS}$ as in Eq. (4.60);
$e_{Nu} = 10^{10}$;
$tol_{Nu} = 10^{-7}$;
$Nu_m^{*,AS} = Nu_{m,0}$;
while $|e_{Nu}| > tol_{Nu}$ **do**
  $Nu_m^{*,AS,old} = Nu_m^{*,AS}$;
  Evalueate ϕ_m^* as in Eq. (4.61);
  $B_T^* = (1 + B_M)^{\phi_m^*} - 1$;
  Evalueate F_T as in Eq. (4.59);
  Evalueate $Nu_m^{*,AS}$ as in Eq. (4.60);
  $e_{Nu} = \frac{|Nu_m^{*,AS,old} - Nu_m^{*,AS}|}{Nu_m^{*,AS}}$

The phenomena of film thickening due to Stefan flow may be characterized by the blowing velocity (Miller, Harstad, and Bellan, 1998):

$$u_b = \frac{\left(\mathbf{\Phi}_{M,f,r}^{MTS}\right)_{|r=r_p}}{\rho_m} = \mathcal{D}_m Sh_m^{*,AS} \frac{\ln\left(1 + B_M\right)}{d_p}. \tag{4.62}$$

The ratio of blowing and seen velocities may be expressed as a function of the non-dimensional numbers characterizing the mass transfer around a sphere:

$$\frac{u_b}{u_s} = \frac{Sh_m^{*,AS}}{Sc_m Re_p} \ln\left(1 + B_M\right). \tag{4.63}$$

At a given Splading mass transfer number, the u_b/u_s velocity ratio decreases with the Reynolds number. Figure 4.10 illustrates this blowing effect at $B_M = 5$, at two different Reynolds numbers. In Fig. 4.10a and Fig. 4.10b the reference fields are provided identical to the illustration in Fig. 4.5. Meanwhile in Fig. 4.10c and Fig. 4.10d the corresponding cases are shown including a normal velocity on the sphere surface, corresponding to the blowing velocities predicted by the Abramzon-Sirignano model. These latter figures indicate the corrected and uncorrected film thicknesses of mass transfer. Indeed, the region characterized by low streamwise velocity increases, when a significant blowing velocity is present. The thickening of the velocity boundary layer is expected to be accompanied by the thickening of the corresponding heat and mass transfer layers as well. At $Re_p = 10$ the two film thickness estimates are clearly distinguishable, while at the higher Reynolds number case, the two indicators are very similar in the figure. Nevertheless, as shown subsequently, the relative importance of the Abramzon-Sirignano model increases with the Reynolds number.

Sazhin (2014) points out, that the naming of modified Nusselt and Sherwood numbers is a possible source of confusion, as the work of Abramzon and Sirignano departs from a model, that already considers the Stefan flow effects in both heat and mass transfer. The correction introduced is regarding the film thicknesses only. Stefan flow effects should be considered in the heat transfer as in Eq. (4.57). Thus,

the equations solved using the Abramzon-Sirignano model take the form presented in Tab. 4.4.

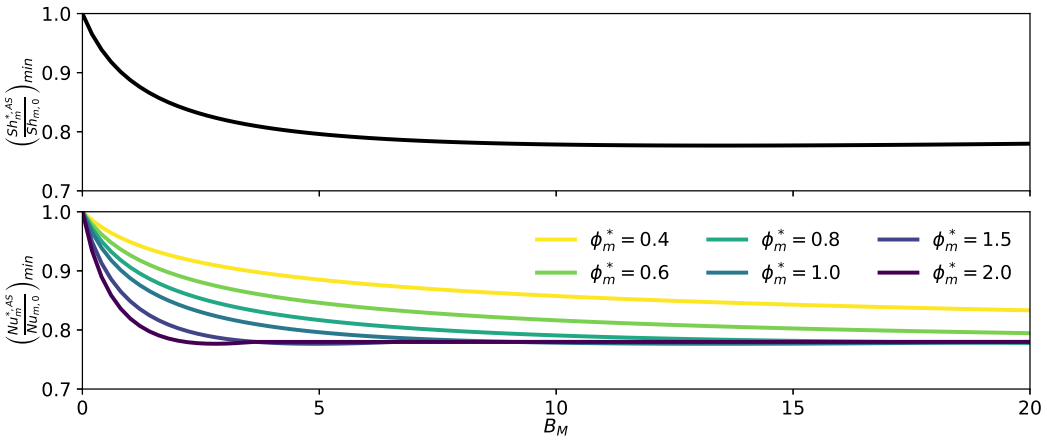

FIGURE 4.11: Minimum possible ratio of corrected and uncorrected Nusselt and Sherwood numbers of Abramzon and Sirignano (Abramzon and Sirignano, 1989) parametrized by $\phi_m^* = \frac{c_{p,vap,m}}{c_{p,m}} \frac{1}{Le_m} \frac{Sh_m^{*,AS}}{Nu_m^{*,AS}}$.

The effect of the model may be estimated, by rearranging Eq. (4.60) as:

$$\frac{Nu_m^{*,AS}}{Nu_{m,0}} = \frac{1 + 2\frac{F_T - 1}{Nu_{m,0}}}{F_T}; \quad \frac{Sh_m^{*,AS}}{Sh_{m,0}} = \frac{1 + 2\frac{F_M - 1}{Sh_{m,0}}}{F_M}, \tag{4.64}$$

one can see, that in the limiting case of $Re_m \to 0$ ($Nu_{m,0} \to 2$, $Sh_{m,0} \to 2$), there is no correction, irrespective of the transfer rates, since the "film" thickness at $Re_m \to 0$ approaches infinity. However, for high Nusselt and Sherwood numbers of fast moving droplets, the correction is limited by: $\left(\frac{Nu_m^{*,AS}}{Nu_{m,0}}\right)_{min} = \frac{1}{F_T}$, $\left(\frac{Sh_m^{*,AS}}{Sh_{m,0}}\right)_{min} = \frac{1}{F_M}$. The typical values of the correction at the high Reynolds number limit are illustrated in Fig. 4.11, showing that the Abramzon-Sirignano model can result in a maximum of 22% further reduction of Nusselt and Sherwood numbers compared to Bird's correction. Note, that here B_T is clipped at 20 according to the validity range of Eq. (4.59), affecting the curves of $\phi_m^* > 1$.

4.4.7 Langmuir-Knudsen models (LK1,LK2)

In the discussion above, the surface composition is determined using the equilibrium vapor pressure on the droplet surface, and the frozen chemistry assumption. The former means, that the partial pressure of the volatile component on the droplet interface is the saturation pressure corresponding to the interface temperature. While the latter refers to the assumed inactivity of chemical reactions in the mass transfer film. The Langmuir-Knudsen model considers an additional resistance in the mass transfer, by postulating that the vapor mole fraction on the droplet interface is not at equilibrium. The non-equilibrium mole fraction on the droplet surface may be calculated as:

$$X_{f,i}^{neq} = X_{f,i}^{eq} - \frac{2L_K}{d_p} \beta^{eq/neq}, \tag{4.65}$$

where β can be evaluated multiple ways. Miller, Harstad, and Bellan (1998) proposes, that the evaluation of β using the equilibrium Spalding mass transfer number is sufficient: $\beta^{eq} = \phi_m \ln\left(1 + B_M^{eq}\right)$. Hereafter this model is denoted LK1. In the present work, an alternative solution is proposed by the LK2 model, where β is evaluated iteratively from the non-equilibrium mass transfer rate: $\beta^{neq} = \phi_m \ln\left(1 + B_M^{neq}\right)$, where B_M^{eq} and B_M^{neq} are the Spalding mass transfer numbers evaluated using the equilibrium and non-equilibrium surface mass fractions respectively, and the Knudsen layer thickness is:

$$L_K = \rho_m \mathcal{D}_m \sqrt{2\pi T_p \frac{R_u}{W_f}} \Bigg/ \left(\alpha_e P\right), \tag{4.66}$$

with $\alpha_e = 1$ molecular accommodation coefficient.

The non-equilibrium interface vapor mass fraction $Y_{f,i}^{neq}$ is still calculated with the frozen chemistry assumption, but replacing $X_{f,i}^{eq}$ with $X_{f,i}^{neq}$. In case the Langmuir-Knudsen model is used, the Spalding number is evaluated with the non-equilibrium interface vapor mass fraction. However, the representative gas phase properties are calculated assuming equilibrium conditions, thus an additional iterative lookup of the mean properties can be avoided. (Miller, Harstad, and Bellan, 1998) However, the calculation of the surface mole fraction requires an iterative solution for model LK2. The models include Bird's correction, but using the non-equilibrium transfer numbers evaluated using the non-equilibrium surface mass fraction: $B_M^{neq} = \frac{Y_{f,i}^{neq} - Y_{f,s}}{1 - Y_{f,i}^{neq}}$, and $B_T^{neq} = \left(1 + B_M^{neq}\right)^{\phi_m} - 1$.

4.4.8 Summary of evaporation models

The ODEs of different evaporation models used in this work are summarized in Tab. 4.4. All of the cases use the following assumptions and sub-models:

1. quasi-steady heat and mass transfer in gas phase,
2. infinite thermal conductivity in liquid phase,
3. temperature dependent liquid and phase change properties,
4. "1/3 law" for representative gas phase properties.

The differences between the models originate from the omission or inclusion of Stefan flow in the film theory, the consideration of film thickening due to Stefan flow effects, and the application of non-equilibrium thermodynamics in relating the droplet temperature and the droplet interface vapor mass fraction. In the remaining part of this chapter, the behavior of these models is analyzed in detail.

4.5 Wet-bulb conditions

In psychrometry, the *thermodynamic* wet-bulb temperature is defined as the temperature of adiabatic saturation, i.e.: the temperature to which a given fuel/bath gas mixture can be adiabatically cooled by the evaporation of the fuel at the same temperature into the vapor/bath gas mixture (Gatley, 2005).

Figure 4.12 illustrates the concept of adiabatic saturation using the nomenclature of this work, where T_p^{th} is the thermodynamic wet-bulb temperature, $Y_{f,s}$ and T_s are

TABLE 4.4: Summary of the different evaporation models. D/D: diffusion only model, S/D: Classical model, B: Bird's correction, AS: Abramzon-Sirignano model, LK: Langmuir-Knudsen model.

D/D	$\frac{\mathrm{d}T_p}{\mathrm{d}t} = \frac{\pi d_p \lambda_m Nu_{m,0}}{m_p c_{p,p}} \left(T_s - T_p\right) + \frac{L_v}{m_p c_{p,p}} \frac{\mathrm{d}m_p}{\mathrm{d}t}$ $\frac{\mathrm{d}m_p}{\mathrm{d}t} = -\pi d_p \rho_m \mathcal{D}_m Sh_{m,0} \left(Y_{f,i} - Y_{f,s}\right)$
S/D	$\frac{\mathrm{d}T_p}{\mathrm{d}t} = \frac{\pi d_p \lambda_m Nu_{m,0}}{m_p c_{p,p}} \left(T_s - T_p\right) + \frac{L_v}{m_p c_{p,p}} \frac{\mathrm{d}m_p}{\mathrm{d}t}$ $\frac{\mathrm{d}m_p}{\mathrm{d}t} = -\pi d_p \rho_m \mathcal{D}_m Sh_{m,0} \ln\left(1 + B_M\right)$
B	$\frac{\mathrm{d}T_p}{\mathrm{d}t} = \frac{\pi d_p \lambda_m Nu_{m,0}}{m_p c_{p,p}} \left(T_s - T_p\right) \frac{\ln\left(1 + B_T\right)}{B_T} + \frac{L_v}{m_p c_{p,p}} \frac{\mathrm{d}m_p}{\mathrm{d}t}$ $\frac{\mathrm{d}m_p}{\mathrm{d}t} = -\pi d_p \rho_m \mathcal{D}_m Sh_{m,0} \ln\left(1 + B_M\right)$
AS	$\frac{\mathrm{d}T_p}{\mathrm{d}t} = \frac{\pi d_p \lambda_m Nu_m^{*,AS}}{m_p c_{p,p}} \left(T_s - T_p\right) \frac{\ln\left(1 + B_T\right)}{B_T} + \frac{L_v}{m_p c_{p,p}} \frac{\mathrm{d}m_p}{\mathrm{d}t}$ $\frac{\mathrm{d}m_p}{\mathrm{d}t} = -\pi d_p \rho_m \mathcal{D}_m Sh_m^{*,AS} \ln\left(1 + B_M\right)$
LK	$\frac{\mathrm{d}T_p}{\mathrm{d}t} = \frac{\pi d_p \lambda_m Nu_{m,0}}{m_p c_{p,p}} \left(T_s - T_p\right) \frac{\ln\left(1 + B_T^{neq}\right)}{B_T^{neq}} + \frac{L_v}{m_p c_{p,p}} \frac{\mathrm{d}m_p}{\mathrm{d}t}$ $\frac{\mathrm{d}m_p}{\mathrm{d}t} = -\pi d_p \rho_m \mathcal{D}_m Sh_{m,0} \ln\left(1 + B_M^{neq}\right)$

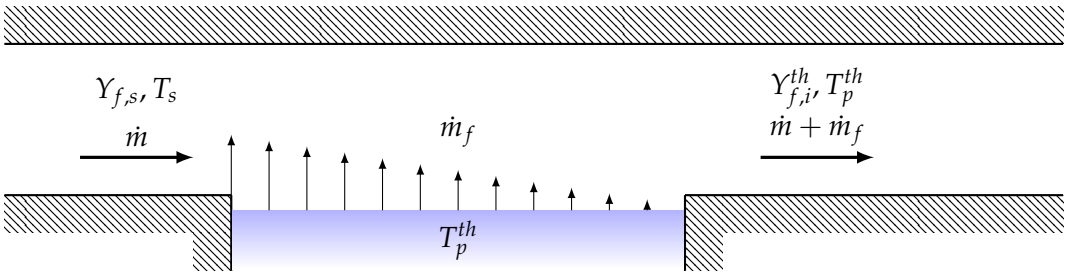

FIGURE 4.12: Illustration of the thermodynamic wet-bulb temperature definition.

the fuel mass fraction and temperature at the studied gas conditions, while $Y_{f,i}^{th}$ is the fuel mass fraction at saturated conditions. At the outlet of the control volume, the gas phase flow is in equilibrium with the liquid reservoir:

1. the liquid and the gas phase are at the same temperature T_p^{th},
2. the partial pressure of fuel in the gas is the saturation pressure at T_p^{th}.

The model problem is characterized by an inlet mass flow rate of $\dot{m}$. The mass flow rate of evaporation $\dot{m}_f$ is such, that $Y_{f,i}$ is reached at the outlet. Interestingly, this constraint gives rise to the Splalding mass transfer number, and the fuel mass flow

rate is expressed as:

$$\dot{m}_f = \frac{Y_{f,i}^{th} - Y_{f,s}}{1 - Y_{f,i}^{th}} \dot{m} = B_M^{th} \dot{m}. \tag{4.67}$$

The heat transfer to the liquid reservoir solely facilitates the evaporation, thus the energy conservation relates the cooling of the incoming gas mixture and the heat absorbed by the evaporation process:

$$\dot{m} \left(h_s \left(T_s \right) - h_s \left(T_p^{th} \right) \right) = \dot{m}_f L_v, \tag{4.68}$$

$$h_s \left(T_s \right) - h_s \left(T_p^{th} \right) = B_M^{th} L_v, \tag{4.69}$$

where $h_s(T_s)$ is the enthalpy at the inlet, and $h_s(T_p^{th})$ is the enthalpy at the inlet composition but evaluated at the thermodynamic wet-bulb temperature. Eq. (4.69) may be solved for T_p^{th} at the given inlet conditions, yielding the thermodynamic wet-bulb temperature.

Figure 4.13 shows the solutions of Eq. (4.69) at atmospheric pressure for OME1, n-heptane, n-decane, and n-dodecane. The wet-bulb temperature T_p^{th}, the corresponding wet-bulb vapor mass fraction $Y_{f,i}^{th}$, and the Spalding mass transfer number B_M^{th} are presented as function of the inlet temperature T_s, and the inlet vapor mass fraction $Y_{f,s}$ of the model problem in Fig. 4.12.

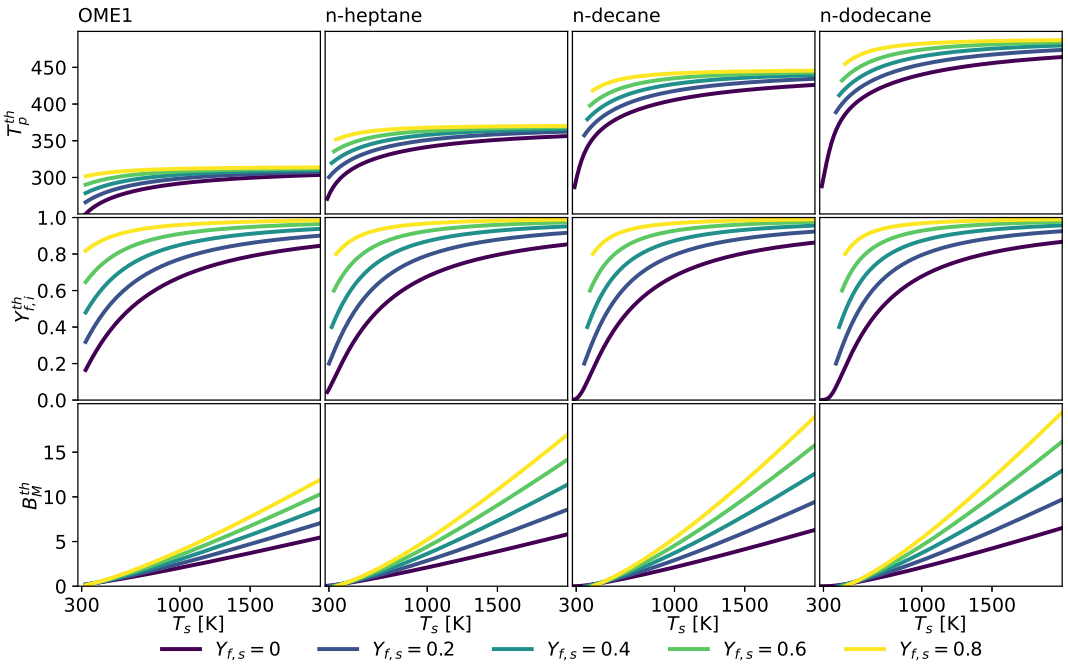

FIGURE 4.13: Thermodynamic wet-bulb conditions of OME1, n-heptane, n-decane, and n-dodecane at atmospheric pressure with air as bath gas according to Eq. (4.69).

The wet-bulb temperature asymptotically approaches the boiling point of the fluid as the inlet temperature and vapor mass fraction increase. Consequently, the wet-bulb vapor mass fraction approaches unity. The conditions are evaluated under seen gas temperatures ranging from 300 K to 2000 K. Concentrating on the $Y_{f,s} = 0$

cases, one can identify that the volatility of the different fuels has the greatest effect at low seen gas temperatures. While in case of OME1, the wet-bulb vapor mass fraction $Y_{f,i}^{th}$ is already ~ 0.18 at $T_s = 300$ K, it is closer to zero in case of the other fuels, and n-decane and n-dodecane even show an inflection point in the wet-bulb vapor mass fraction.

4.5.1 Psychrometric wet-bulb conditions

The proposed experiment of Fig. 4.12 is defined with the following hypotheses: the domain is adiabatic to the environment, the liquid surface is large enough to reach equilibrium at the outlet, and the liquid is at a constant temperature equal to the outlet temperature. A more practical point of view is given by the *psychrometric* wet-bulb temperature, that is defined by finding the equilibrium solution of a wet sphere (i.e.: a droplet) at $\frac{\mathrm{d}T_p}{\mathrm{d}t} = 0$, where the received heat is exactly the heat necessary for the phase transition. The equations yielding the wet-bulb conditions for the different models are described below and summarized in Tab. 4.5.

TABLE 4.5: Summary of the wet-bulb conditions of different evaporation models.

Thermodynamic	$h_s\left(T_s\right) - h_s\left(T_p^{th}\right) = B_M^{th} L_v$
Diffusion olny (D/D)	$c_{p,vap,m}\left(T_s - T_p^{psy,D/D}\right) = \phi_m \left(Y_{f,i} - Y_{f,s}\right) L_v$
Classical (S/D)	$c_{p,vap,m}\left(T_s - T_p^{psy,S/D}\right) = \ln\left(1 + B_T^{psy,S/D}\right) L_v$
Bird's correction (B)	$c_{p,vap,m}\left(T_s - T_p^{psy,B}\right) = B_T^{psy,B} L_v$
Abramzon-Sirignano (AS)	$c_{p,vap,m}\left(T_s - T_p^{psy,AS}\right) = \frac{\phi_m^*}{\phi_m} B_T^{psy,AS} L_v$
Langmuir-Knudsen (LK)	$c_{p,vap,m}\left(T_s - T_p^{psy,LK}\right) = B_T^{neq,psy,LK} L_v$

The diffusion only model (D/D) is only able to produce equilibrium conditions for a limited range of seen temperatures. The inadequacy of the model for combustion applications is demonstrated in appendix F. The application of the diffusion only model should be limited to low temperature, however choosing it over the other models presented here cannot be justified. The classical evaporation model (S/D) is also flawed due to the arbitrary consideration of Stefan flow in only the mass transfer. It is able to produce steady wet-bulb states at any seen temperature, as explained in appendix G, however the resulting equilibrium conditions are unrealistic. This inconsistency is masked by the low significance of Stefan flow at low temperature applications where $(B_M \approx \ln\left(1 + B_M\right))$. Nevertheless, the model is often extended to regimes where Stefan flow dominates the overall heat transfer, resulting in highly overestimated evaporation rates. These models are given less attention in the rest of the present study, as their inherent flaws are are already demonstrated in the appendices.

The heat and mass transfer corrections of Bird, Stewart, and Lightfoot (1960), the model of Abramzon and Sirignano (1989), and the Langmuir-Knudsen model are considered below. Based on the $\frac{\mathrm{d}T_p}{\mathrm{d}t} = 0$ condition, the wet-bulb conditions of Bird's correction are simply given by:

$$c_{p,vap,m}\left(T_s - T_p^{psy,B}\right) = B_T^{psy,B} L_v, \tag{4.70}$$

where $B_T = (1 + B_M)^{\phi_m} - 1$ is the Spalding heat transfer number. Meanwhile, the wet-bulb conditions for the model of Abramzon and Sirignano are determined by the equation:

$$c_{p,m}\left(T_s - T_p^{psy,AS}\right) = \frac{1}{Le_m}\frac{Sh_m^{*,AS}}{Nu_m^{*,AS}}\frac{B_T^{psy,AS}}{\ln\left(1+B_T^{psy,AS}\right)}\ln\left(1+B_M^{psy,AS}\right)L_v, \tag{4.71}$$

that can be expressed as:

$$c_{p,m}\left(T_s - T_p^{psy,AS}\right) = \frac{\phi_m^*}{\phi_m}B_T^{psy,AS}L_v, \tag{4.72}$$

using the definitions of ϕ_m^* in Eq. (4.61).

The wet-bulb conditions of Bird's correction and the Abramzon-Sirignano model are almost identical in the studied cases, since the ratio of corrected and uncorrected Sherwood and Nusselt numbers are rather similar for the two approaches. Note, that this similarity only concerns the wet-bulb conditions, the two models do differ in heat and mass transfer rate for non-zero Reynolds numbers. For the Langmuir-Knudsen model (that includes Bird's correction), the wet-bulb conditions can be defined as:

$$c_{p,vap,m}\left(T_s - T_p^{psy,LK}\right) = B_T^{neq,psy,LK}L_v, \tag{4.73}$$

considering that the Spalding heat transfer number is based on the non-equilibrium vapor mass fractions.

For simplicity, the results of the Abramzon-Sirignano model are not shown, since these are virtually the same as the results of Bird's correction displayed in Fig. 4.14. Likewise, the Langmuir-Knudsen model also produces similar equilibrium conditions to Bird's correction in case of large droplet diameters. The influence of the droplet diameter on this model is further discussed in section 4.7, showing that equilibrium conditions do not exist below a certain diameter. The wet-bulb conditions of Eq. (4.70) are compared to the thermodynamic wet-bulb state through the difference in wet-bulb temperature $\Delta T_p^B = T_p^{psy,B} - T_p^{th}$ and vapor mass fraction $\Delta Y_{f,i}^B = Y_{f,i}^{psy,B} - Y_{f,i}^{th}$.

The quantities: ΔT_p^B, $\Delta Y_{f,i}^B$, and B_M of Fig. 4.14 illustrate how the similarity between heat and mass transfer equations is restored by considering the effect of Stefan flow on both transfer rates. In comparison, the analogous figures of the diffusion only and classical models in appendix F and appendix G show much larger differences. The wet-bulb conditions of Bird's correction generally get closer to the thermodynamic ones. The remaining differences between Eq. (4.69) and Eq. (4.70) are mainly caused by the effect of Lewis number, and the disparity between the mean gas specific heat and the vapor specific heat both displayed in Fig. 4.14.

The parameter $\phi_m = \frac{c_{p,vap,m}}{c_{p,m}}\frac{1}{Le_m}\frac{Sh_{m,0}}{Nu_{m,0}}$ combines these Lewis number $\left(Le_m = \frac{\lambda_m}{c_{p,m}\rho_m\mathcal{D}_m}\right)$ and specific heat effects. The former parameter expresses the diffusivity of the volatile species relative to the thermal diffusivity, i.e.: high Lewis numbers correspond to low fuel diffusivity. While the latter provides a measure of the heat carried by the unimolecular diffusion of the fuel (Stefan flow) compared to heat carried by other advective phenomena where all species are carried by the flow equally. However, the parameter ϕ_m depends also on the Reynolds number, as $Nu_{m,0}$ and $Sh_{m,0}$ are present in this parameter. Using the Frössling-type correlations for $Nu_{m,0}$ and $Sh_{m,0}$

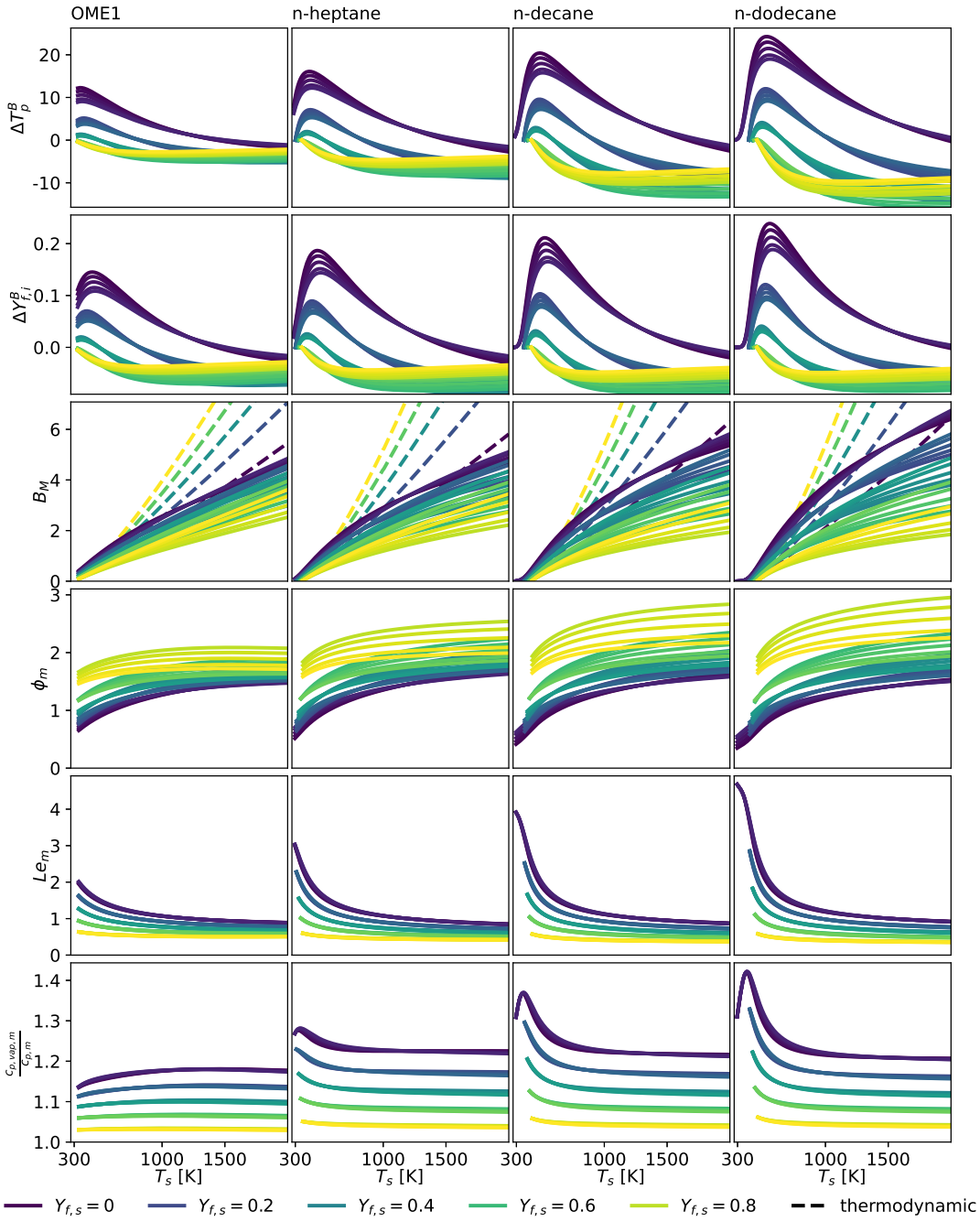

FIGURE 4.14: Comparison of psychrometric and thermodynamic wet-bulb conditions of OME1, n-heptane, n-decane, and n-dodecane at atmospheric pressure with air as bath gas considering Bird's correction according to Eq. (4.70). The difference in wet-bulb temperatures and the corresponding vapor mass fractions are $\Delta T_p^B = T_p^{psy,B} - T_p^{th}$, and $\Delta Y_{f,i}^B = Y_{f,i}^{psy,B} - Y_{f,i}^{th}$.

such as the Ranz-Marshall model, ϕ_m is limited between the $\frac{c_{p,vap,m}}{c_{p,m}} \frac{1}{Le_m}$ and $\frac{c_{p,vap,m}}{c_{p,m}} \frac{1}{Le_m^{2/3}}$ corresponding to the low and high Reynolds number limits shown in Eq. 4.54. As Fig. 4.14 illustrates, the mass-based Lewis number of the volatile component drops sharply as the seen vapor mass fraction and temperature increase, and the specific

heat ratio $\frac{c_{p,vap,m}}{c_{p,m}}$ also shows more variation at low seen temperatures, while it is almost constant otherwise. These two distinct regions are the most pronounced in case of the heavier hydrocarbons, that are characterized by near-zero wet-bulb vapor mass fractions at low seen temperatures. The change of behavior with increasing seen temperature is explained by the changes in mean composition, since for high seen temperatures the mean composition $Y_{k,m}$ is practically constant because the interface composition approaches pure volatile vapor, while the mean temperature keeps increasing according to the "1/3 law". The mass-based Lewis number drops sharply as the mass fraction of vapor increases in the mean gas mixture, since it is largest in the dilute limit as Fig. 2.1 shows. Overall the high temperature region is dominated by high specific heat ratios and low Lewis numbers resulting in ϕ_m above unity. If the far field does not contain any of the volatile species ($Y_{f,s} = 0$), the Lewis numbers and specific heat ratios show a certain similarity across the different fuels at high seen temperatures. Thus under these conditions $\phi_m \approx 1.5$ is generally true for all four studied fuels. However, as seen vapor mass fractions increases, by definition $c_{p,vap,m}/c_{p,m}$ approaches unity slowly, while Le_m decreases sharply, resulting in significantly higher ϕ_m for the heavier hydrocarbons. In any case, at these levels of $\phi_m > 1$ observed at high seen gas temperatures, the heat transfer reduction is quite pronounced as demonstrated in Fig. 4.8.

4.5.2 Evaporation at the psychrometric wet-bulb conditions

As described above, most of the presented models can yield a psychrometric wet-bulb temperature, meaning that this temperature behaves as an attractor of the dynamic system formed by Eq. (4.47) and Eq. (4.50). The diffusion only model (D/D) is limited in this sense, because it clearly does not have an equilibrium state for high seen temperatures, and the model is simply invalid for these cases. The Langmuir-Knudsen models (LK1,LK2) show signs of a similar problem, but only affecting very small droplets sizes.

Meanwhile, under the studied conditions, the mass of the droplet always approaches zero until the droplet completely evaporates. The mass conservation equation Eq. (4.47) can be rewritten in terms of the diameter as:

$$\frac{\mathrm{d}d_p^2}{\mathrm{d}t} = -\frac{4\dot{m}_r}{\pi\rho_p d_p} - \frac{2d_p^2}{3\rho_p}\frac{\mathrm{d}\rho_p}{\mathrm{d}t}. \tag{4.74}$$

Since $\dot{m}_r$ scales linearly with the diameter as summarized in Tab. 4.3, the droplet surface ($\sim d_p^2$) decreases at a constant rate, if the droplet temperature, Reynolds number, and the seen conditions are constant. The evaporation of droplets that reached their equilibrium temperature are widely described using such "d^2" relations (Godsave, 1953), simply implying that the evolution of droplet surface is linear in time:

$$\frac{\mathrm{d}d_p^2}{\mathrm{d}t} = -K, \tag{4.75}$$

where $K = -\left(\frac{\mathrm{d}m_p}{\mathrm{d}t}\right)^{psy}\frac{\pi\rho_p d_p}{4}$ is the vaporization rate constant.

Chauveau et al. (2019) show that most vaporization rate constant measurements significantly overestimate K at high temperature conditions, as additional heat is transferred to the droplet through the support fibers that hold the droplet in place and are characterized by a diameter comparable to the droplet diameter. Such an example is the work of Nomura et al. (1996), where significantly different results are

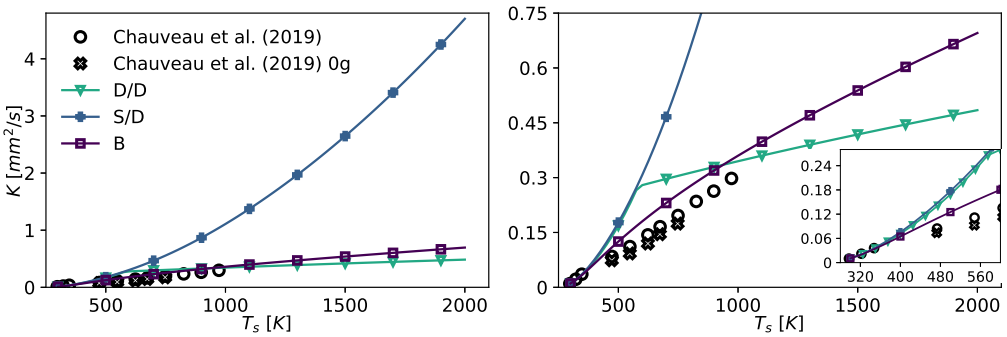

FIGURE 4.15: Comparison of the experimental evaporation rate constants of Chauveau et al. (2019) against the diffusion only model (D/D), the classical model (S/D), and Bird's correction (B) for an n-heptane droplet of $d_{p,0} = 500$ μm in nitrogen gas atmosphere. The different plots show the data at different scales. The models are evaluated between 300 K and 2000 K, with a step size of 25 K.

obtained, compared to the ones presented in Fig. 4.15. Chauveau et al. (2019) propose a measurement technique of reducing the support fiber diameter by an order of magnitude eliminating this deterministic measurement error.

Figure 4.15 shows the comparison of rate constants obtained for a stationary n-heptane droplet in molecular nitrogen gas atmosphere under psychrometric wet-bulb conditions along different seen gas temperatures for the diffusion only (D/D) and classical (S/D) models and for Bird's correction (B) along with the measurement data of Chauveau et al. (2019). The other models (AS, LK1, LK2) are omitted, since they give the same results as Bird's correction (B) for large stationary droplets. The classical "1/3" law is used to evaluate the film properties. In general, all models overestimate the experimentally determined evaporation rates at high temperature conditions.

The best agreement with the measurement is observed using Bird's correction (B), that qualitatively captures the slope of K as a function of the seen temperature. The remaining error is limited to a 20% overestimation and can be attributed to the real gas behavior of the fluid in the heat and mass transfer films, as suggested by Ebrahimian and Habchi (2011). However, addressing these effects is out of the scope of the present study. The classical model (S/D) results in particularly fast evaporation, overestimating the evaporation rate by a factor of 3.5 for the highest temperature measurement ($T_s = 973.15$ K) and producing a 6.8 higher rate than Bird's correction (B) at $T_s = 2000$ K. The diffusion only model (D/D) is assessed both in its range of applicability and outside of it. In the former regime, it follows closely the behavior of the classical model (S/D) despite the higher wet-bulb temperatures observed using the diffusion only model (D/D). The behavior of the model changes drastically, once thermal equilibrium conditions become impossible and $Y_{f,i}$ is clipped to 1. In this regime, the evaporation rates continue growing solely because $\rho_m \mathcal{D}_m$ increases with temperature due to the application of the "1/3-law". Note, that this clipping is nonphysical, and simulations applying this model would violate energy conservation, as a significant part of the heat transferred to the droplet is not spent neither on increasing the droplet temperature, nor on facilitating the phase change.

4.6 Time scale analysis of Lagrangian droplets

Different time scales related to the Lagrangian droplets are analyzed below. These time scales may be used, to estimate the expected droplet behavior *a priori*. The comparison of different time scales characterizes the relation between each phenomena.

4.6.1 Time scales of heat and mass transfer

A time scale for the droplet evaporation may be estimated, given that the droplet is already at the wet bulb conditions initially:

$$\tau_{p,evap} = \frac{d_{p,0}^2}{K}, \tag{4.76}$$

where $d_{p,0}$ is the initial droplet diameter, and the vaporization rate constant K is evaluated under the wet-bulb conditions. As discussed in section 4.5.2, K is independent of the droplet diameter, and it is the function of all influencing other quantities.

Concerning the heat-up of the droplets, Deprédurand, Castanet, and Lemoine (2010) and Castanet et al. (2016) showed experimentally, that in case the initial droplet temperature is significantly lower than the wet-bulb temperature, then the majority of heat is transferred to the liquid phase and only a fraction of it facilitates the phase change. Here a time scale is proposed for estimating the heat-up time using the initial heat-up rate:

$$\tau_{p,heat} = \frac{T_p^{psy} - T_{p,0}}{\left(\frac{\mathrm{d}T_p}{\mathrm{d}t}\right)_0} = \frac{m_{p,0} c_{p,p,0} \left(T_p^{psy} - T_{p,0}\right)}{-\dot{Q}_{r,0} - L_{v,0}\dot{m}_{r,0}}, \tag{4.77}$$

where T_p^{psy} is the wet-bulb temperature and the 0 subscript signifies the terms evaluated at the initial condition. Considering $m_{p,0} \propto d_{p,0}^3$, $\dot{Q}_{r,0} \propto d_{p,0}$, and $\dot{m}_{r,0} \propto d_{p,0}$, this heat-up time scale is proportional to the initial diameter as: $\tau_{p,heat} \propto d_{p,0}^2$ just like the evaporation time scale $\tau_{p,evap}$.

Figure 4.16 illustrates the two time scales: $\tau_{p,heat}$ and $\tau_{p,evap}$. The scales are plotted over the simulated evolution of an n-heptane droplet using Bird's correction with an initial diameter of $d_{p,0} = 50$ μm, and initial temperature difference of $T_p^{psy} - T_{p,0} = 40$ K in air. The droplet is stationary ($Re_p = 0$) and the seen conditions are $T_s = 1500$ K and $Y_{f,s} = 0$. (Note, that under these conditions the psychrometric wet-bulb temperature is: $T_p^{psy,B} = 351.4$ K.) Figure 4.16 also shows two time scales of the simulated droplet evolution using the classical "1/3 law". A heat-up time scale $\tau_{p,T90\%}$ is defined as the time when the droplet temperature has completed 90% of the change between the initial temperature $T_{p,0}$, and the psychrometric wet-bulb temperature T_p^{psy}. And the lifetime of the droplet $\tau_{p,tot}$ is defined as the time it takes to reach 0.1% of the initial droplet mass. Note, that the simulation is stopped at this point.

Such simulations are executed over a wide range of parameters to study the model behavior and compare the estimates $\tau_{p,heat}$ and $\tau_{p,evap}$ to their simulated counterparts $\tau_{p,T90\%}$ and $\tau_{p,tot}$. The four fuels: OME1, n-heptane, n-decane, and n-dodecane are studied using the proposed models: diffusion only (D/D), classical (S/D), Bird's correction (B), Abramzon-Sirignano (AS). The varied parameters are the initial droplet diameter $d_{p,0} \in \{0.5, 5, 50, 500\}$ μm, the difference between the psychrometric wet-bulb temperature and the initial temperature: $T_p^{psy} - T_{p,0} \in \{5, 10, 20, 40\}$ K the

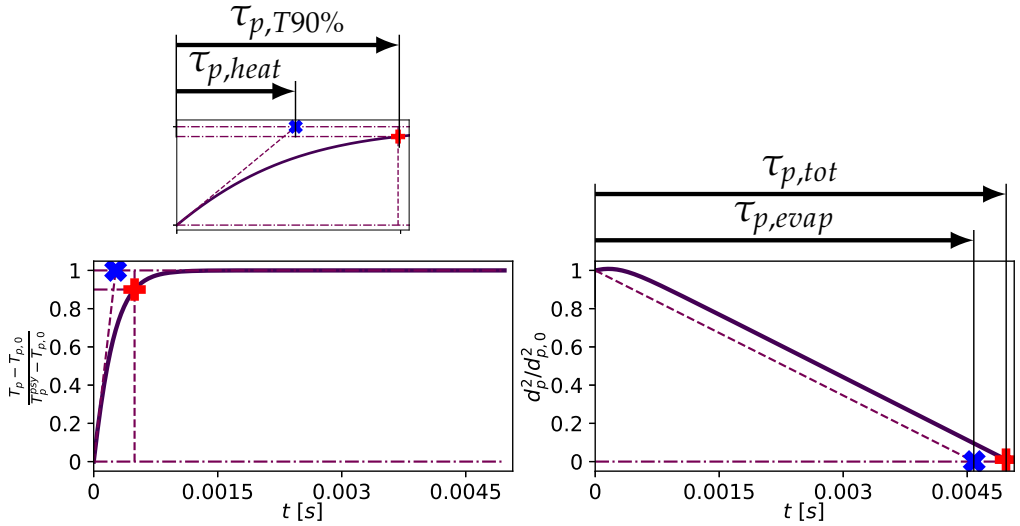

FIGURE 4.16: Illustration of the time scale estimations for the heat-up period and droplet lifetime. The blue x markers indicate the estimates, while red cross markers provide a reference based on the numerical simulation of the evaporation process. The heat up timescale is marked on a magnified plot for clarity. This reference case shows the evolution of an n-heptane droplet using Bird's correction with an initial diameter of $d_{p,0} = 50$ μm, and initial temperature difference of $T_p^{psy} - T_{p,0} = 40$ K. The droplet is stationary ($Re_p = 0$) and the seen conditions are $T_s = 1500$ K and $Y_{f,s} = 0$.

Reynolds number $Re_p \in \{0, 1, 10, 100, 1000\}$, and the seen temperature $T_s \in \{500, 750, 1000, 1250, 1500, 1750, 2000\}$ K. For simplicity the seen vapor mass fraction is kept constant zero. The classical "1/3 law" is used, evaluating film properties at the representative temperature and species mass fractions.

Evaporation time scale

Figure 4.17 illustrates the total simulation time $\tau_{p,tot}$, compared to the estimate assuming the droplet evaporates under wet-bulb conditions $\tau_{p,evap}$. The ratio $\tau_{p,tot}/\tau_{p,evap}$ is displayed as a function of the seen gas temperature T_s. The color scheme indicates the initial temperature difference $T_p^{psy} - T_{p,0}$. The effect of droplet Reynolds number Re_p on this ratio is negligible and only $Re_p = 0$ is displayed here. Likewise, the different initial droplet diameters $d_{p,0}$ are not distinguished as the symbols are completely overlapping.

As Fig. 4.16 shows, this ratio is an indication of what fraction of the droplet lifetime is spent with heat-up, since $\tau_{p,tot} - \tau_{p,evap}$ is the additional time the droplet spends with reduced evaporation rate due to temperatures lower than the wet-bulb temperature. The initial droplet diameter $d_{p,0}$ has no effect on this property, the droplet Reynolds number Re_p has limited influence in the Abramzon-Sirignano model (AS) only, however, it is too small to visualize. There is a slight dependence on the seen gas temperature T_s, and most of the variation can be attributed to the difference between the initial temperature and the wet-bulb temperature. As expected, the $\tau_{p,tot}/\tau_{p,evap}$ ratio decreases as the initial droplet temperature approaches the wet-bulb temperature, since the heat-up period diminishes.

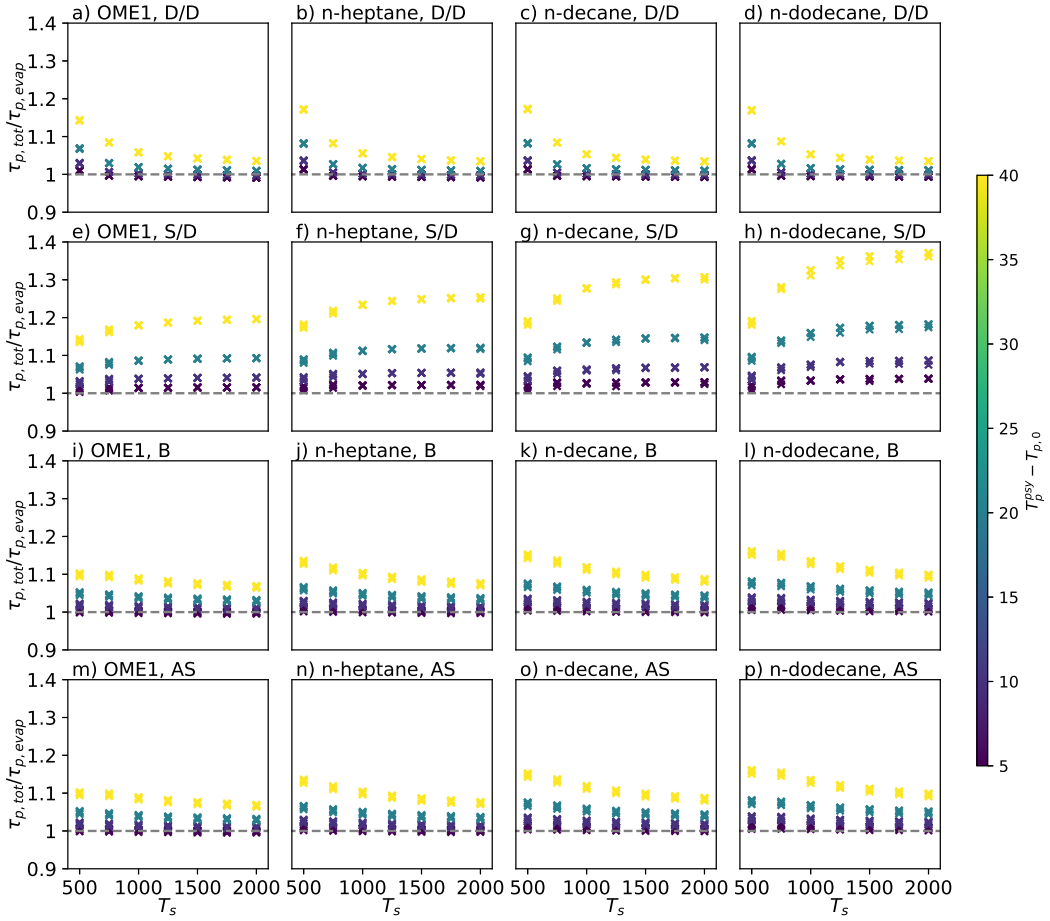

FIGURE 4.17: Comparison of the evaporation timescale estimate $\tau_{p,evap}$ and the time necessary to evaporate 99.9% of the initial droplet mass in simulations. The ratio of the two time scales is assessed as function of the seen gas temperature under different initial temperatures marked by the color scheme, under different constant Reynolds numbers, and with different initial droplet sizes. The droplet size and the Reynolds number are not indicated as there is insignificant dependence on these parameters.

Bird's correction (B) and the Ambramzon-Sirignano model (AS) show similar trends even at non-zero Reynolds numbers not shown here, as the presented ratio decreases with the increase of the seen gas temperature T_s, indicating that the relative importance of the heat-up period diminishes in high temperature environments. The classical model (S/D) shows an opposite trend, that is better understood observing the evaporation rate constants of Fig. 4.15. One may observe, that the evaporation rate constant increases faster than linear as function of the seen gas temperature. Meanwhile the heat up time scale is relatively linear as a function of T_s, thus the classical model (S/D) predicts higher and higher fractions of time spent on the heat-up.

Heat-up time scale

Figure 4.18 shows the ratio of the simulated heat-up time scale and the estimate derived from the initial temperature slope: $\tau_{p,T90\%}/\tau_{p,heat}$, for the single droplet simulation cases. This ratio is displayed in a similar manner as in Fig. 4.17. The influence of initial droplet diameter is negligible on this property, thus the symbols are overlapping. Similarly, this timescale ratio is not dependent on the Reynolds number except in the case of the Abramzon-Sirignano model (AS), thus the other models only display the $Re_p = 0$ case. Two different Reynolds numbers are shown for AS, to illustrate the small influence of the Reynolds number on the heat up estimation.

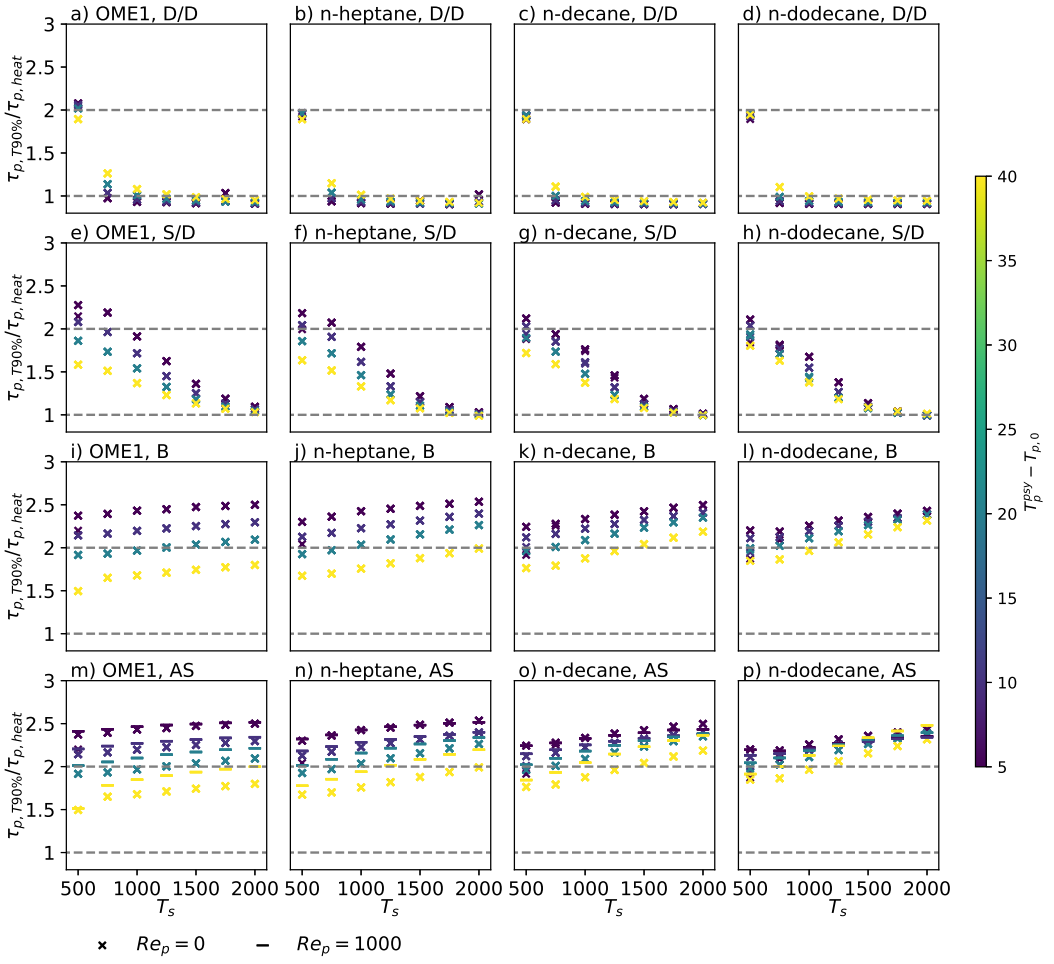

FIGURE 4.18: Comparison of the heat-up timescale estimate $\tau_{p,heat}$ and the time necessary to complete 90% of the total temperature change in simulations. The ratio of the two time scales is assessed as function of the seen gas temperature under different initial temperatures marked by the color scheme, under different constant Reynolds numbers marked by the symbols, and with different initial droplet sizes. The droplet size is not indicated as there is no dependence, and similarly the Reynolds number is only indicated for the Abramzon-Sirignano model (AS).

Taking Bird's correction (B) as reference, the $\tau_{p,T90\%}/\tau_{p,heat}$ ratio ranges between 1.5 and 2.5, indicating a behavior similar to the example shown in Fig. 4.16, where the droplet temperature smoothly transitions to the wet-bulb condition. There is no

variation in terms of $d_{p,0}$ and Re_p, and even the seen temperature only has a weak effect on this ratio. At a given fuel, the ratio is varied the most by the initial temperature difference $T_p^{psy} - T_{p,0}$, indicating, that the temperature evolution during the heat-up period is not self-similar, but depends on the initial value. The dependence on the initial temperature diminishes as the volatility of the fuels decrease, i.e.: the variation is highest for OME1, and it diminishes almost completely for n-dodecane, especially under high seen gas temperatures. The high variability of the displayed ratio indicates, that the $\tau_{p,heat}$ estimate can only be used, to determine the order of magnitude of the heat-up period, but it is not accurate enough to define an exact relation.

The different modeling strategies are also compared on Fig. 4.18. The Abramzon-Sirignano model (AS) behaves almost identically to Bird's correction (B), except that the $\tau_{p,T90\%}/\tau_{p,heat}$ ratio slightly increases with the Reynolds number, further comparison is provided below. In the case of the diffusion only model (D/D), the two regimes shown in Fig. 4.15 are clearly distinguishable. For $T_s = 500$ K, this model is able to provide a stable solution, and consequently the ratio is approximately 2, since the droplet temperature reaches wet-bulb condition smoothly. In case of the rest of the seen temperatures, the diffusion only model (D/D) is unable to find stable solutions, and the droplet reaches the boiling point in approximately one $\tau_{p,heat}$ time. The classical model (S/D) shows very similar $\tau_{p,T90\%}/\tau_{p,heat}$ ratio to Bird's correction (B) at lower seen gas temperatures, but it transitions to fast heat-up as the seen gas temperature increases. This is due to the inconsistent consideration of Stefan flow in only the mass transfer, as this model needs orders of magnitudes higher Spalding mass transfer numbers than Bird's correction (B) to maintain the energy balance (see Fig. G.1 and Fig. 4.14). Thus, in the transient cases of the present analysis, the latent heat of evaporation only starts to have a significant effect, once the droplet temperature is near the boiling point in case of high seen gas temperatures.

Summary of evaporation and heat-up time scales

Overall, according to the analytical derivations of section 4.2, the diffusion only model (D/D) neglects an important part of the physical phenomena involved in evaporation: Stefan flow, while the classical model (S/D) considers it wrongly. The validation against the experimental data of Chauveau et al. (2019) underlines this discrepancy as illustrated in Fig. 4.15. In the remaining part of the study, the diffusion only model (D/D) and the classical model (S/D) are disregarded, since their validity is limited to low temperature applications. Only the models correctly considering Stefan flow are analyzed below.

4.6.2 Reynolds number effects in the Abramzon-Sirignano model (AS)

As shown in Fig. 4.11, the Abramzon-Sirignano model (AS) introduces a modification to Bird's correction (B), that only acts in case of finite film thickness, i.e.: in case of non-zero Reynolds number. The correction is limited to a maximum of 22% reduction of the transfer rates in very high Reynolds numbers.

The ratio of time scale estimates of evaporation is shown in Fig. 4.19a-d ($\tau_{p,evap}^{AS}/\tau_{p,evap}^{B}$) and of heat-up at different initial temperatures in Fig. 4.19e-t ($\tau_{p,heat}^{AS}/\tau_{p,heat}^{B}$) for the Abramzon-Sirignano model (AS) and Bird's correction (B) respectively. As expected, the additional correction introduced by Abramzon and Sirignano (1989) increases the time scales for the combination of high Reynolds numbers with high Spalding mass transfer numbers. The degree of time scale augmentation is within 30% under

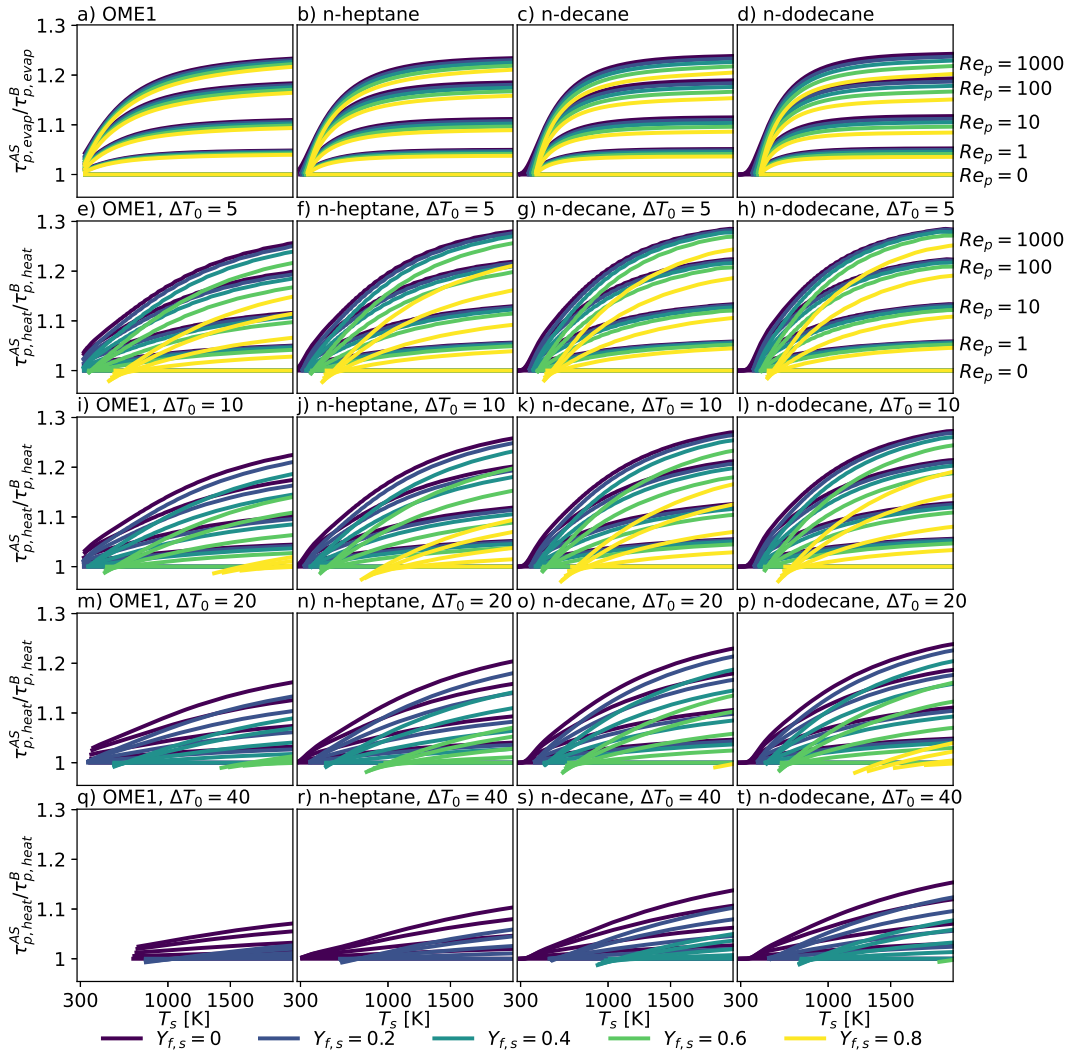

FIGURE 4.19: Comparison of the evaporation (a-d) and heat-up (e-t) timescales between the Abramzon-Sirignano model (AS) and Bird's correction (B). The evaporation time scales are compared under the wet-bulb conditions of the respective models, while the heat-up time scales are assessed using the same initial temperature:

$$T_{p,0} = T_p^{psy,B} - \Delta T_0.$$

the studied conditions, which is consistent with the factor of film thickening displayed in Fig. 4.9. These values are approached only at high seen temperatures and high Reynolds numbers. For low temperature applications, the Abramzon-Sirignano model (AS) only affects the highly volatile OME1, the rest of the studied fuels is practically unaffected at seen gas temperatures of 300 K.

The evaporation time scales displayed in Fig. 4.19a-d are evaluated under the wet-bulb conditions according to $\tau_{p,evap} = \frac{d_{p,0}^2}{K}$. This ratio shows a clear growth as function of the Reynolds number Re_p, and the seen gas temperature T_s. The correction factor of Abramzon and Sirignano (1989) saturates after a certain Spalding mass transfer numbers is reached, thus the $\tau_{p,evap}^{AS}/\tau_{p,evap}^{B}$ ratio similarly reaches a plateau with increasing seen gas temperatures. The dependence on seen vapor mass fraction is secondary compared to the Reynolds number and Spalding number dependence.

The heat-up time scales are shown for different initial temperatures in Fig. 4.19e-t where $\Delta T_0 = T_p^{psy,B} - T_{p,0}$ is the difference between the psychrometric wet-bulb temperature given by Bird's correction and the initial droplet temperature. Note, that this means that $T_{p,0}$ is the same for both Bird's correction (B) and the Abramzon-Sirignano model (AS) even though $T_p^{psy,B}$ and $T_p^{psy,AS}$ are slightly different. The effect on the heat-up timescale diminishes as ΔT_0 increases and the droplets get further from the wet-bulb conditions, since the transfer rates are low at high ΔT_0, consequently only part of the heat-up process is really affected. Comparing Fig. 4.19a-d and Fig. 4.19e-h, one can observe a difference between the behavior of mass and heat transfers. Overall, the correction of the heat transfer time scale is higher than that of the mass transfer time scale, as ϕ_m tends to be over unity at higher seen temperatures. The Spalding mass transfer number B_M is lower than 6 under the presently studied array of conditions (see Fig. 4.14), so $B_T^* > B_M$ and the correction of heat transfer can reach the maximum 28% while that of mass transfer cannot. (See Fig. 4.11 for the maximum possible Sherwood and Nusselt number corrections.)

In general, the Abramzon-Sirignano model (AS) introduces significant changes compared to Bird's correction (B) at high Reynolds numbers, and the effect is notable even at $Re_p = 1..10$. Such droplet Reynolds numbers are typically sustained in a turbulent flow field, where the variability of the gas phase velocity and the inertia of the droplets keeps up a non-zero slip velocity. Thus, the usage of the Abramzon-Sirignano model (AS) is recommended for spray combustion simulations.

4.6.3 Time scales of droplet kinematics

An alternate way of assessing the effect of drag, is to use the kinematic relaxation time: $\tau_{p,kin}$, defined by the hypothetical case when only drag affects the spherical particle. This metric originates from the linear behavior of the particle acceleration as function of the slip velocity in case of creeping flow. (Eq. (4.6)) In the low Reynolds number limit the slip velocity decays exponentially, characterized by the constant Stokes relaxation time:

$$\tau_{p,kin,St} = \frac{\mathbf{u}_s m_p}{\mathbf{F}_{d,St}} = \frac{\rho_p d_p^2}{18\mu_m}, \tag{4.78}$$

that only depends on the particle density ρ_p, the cross sectional area of the particle $\propto d_p^2$, and the viscosity in the fluid μ_m. The kinematic relaxation time may be generalized for the non-linear regime of Reynolds numbers, using the instantaneous acceleration and slip velocity:

$$\tau_{p,kin} = \frac{\mathbf{u}_s}{\left(\frac{\partial \mathbf{u}_p}{\partial t}\right)_{drag}}. \tag{4.79}$$

In case of the correlation of Naumann and Schiller (1935), the relaxation times take the form:

$$\tau_{p,kin} = \begin{cases} \tau_{p,kin,St} \Big/ \left(1 + 0.15 Re_p^{0.687}\right), & Re_p \leq 1000, \\ \tau_{p,kin,St} \Big/ \left(0.44 \frac{Re_p}{24}\right), & Re_p > 1000. \end{cases} \tag{4.80}$$

The ratio of relaxation times between the Shiller-Naumann and Stokes models is illustrated in Fig. 4.20. According to the model of Naumann and Schiller (1935),

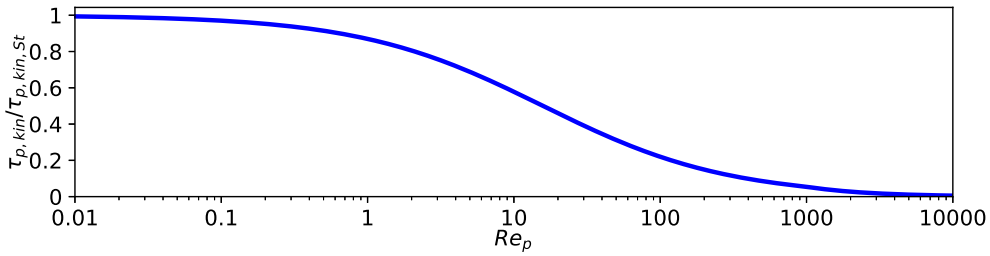

FIGURE 4.20: Ratio of kinematic relaxation times of Naumann and Schiller (1935) and Stokes (1851) as function of the Reynolds number.

the droplet relaxes towards zero slip velocity at an increased rate at higher Reynolds numbers. The effect of the corrected drag is significant even at Reynolds numbers as low as $Re_p = 1$, where this ratio is: $\tau_{p,kin}/\tau_{p,kin,St} = 0.87$. This effect is hidden by the logarithmic scale of Fig. 4.3 where the drag coefficient is presented.

4.6.4 Time scale comparison

As shown in section 4.6.1 $\tau_{p,evap} = \frac{d_{p,0}^2}{K}$ is a good estimate for the droplet lifetime. Figure 4.17 illustrates, that the initial heat-up of the droplets may enlarge the real droplet lifetime by $\sim$ 10% if an initial temperature difference of 40 K is imposed. An estimate of heat-up time: $\tau_{p,heat}$ is given in Eq. (4.77), that proves to be a good order of magnitude estimate, for the actual time necessary to approach the wet-bulb conditions. In this section, other timescales are compared to $\tau_{p,evap}$.

The kinematic relaxation time at the initial condition of the droplet $\tau_{p,kin}$ is compared to the evaporation time in Fig. 4.21 using Stokes drag and the Schiller-Naumann drag correlation. The displayed ratios are:

$$\frac{\tau_{p,kin,St}}{\tau_{p,evap}} = \frac{\rho_p K}{18\mu_m}, \tag{4.81}$$

$$\frac{\tau_{p,kin}}{\tau_{p,evap}} = \begin{cases} \frac{\rho_p K}{18\mu_m} \Big/ \left(1 + 0.15 Re_p^{0.687}\right), & Re_p \leq 1000, \\ \frac{\rho_p K}{18\mu_m} \Big/ \left(0.44 \frac{Re_p}{24}\right), & Re_p > 1000. \end{cases} \tag{4.82}$$

The first row of plots compares the $\tau_{p,kin,St}$ to the evaporation time estimate of the Abramzon-Sirignano model. This highlights how the underestimated drag of the Stokes model would cause the droplets to keep moving throughout their lifetime. The second and third row of plots compares the relaxation time of Naumann and Schiller (1935) to the evaporation time scale of the Abramzon-Sirignano model and Bird's correction respectively. The Schiller-Naumann correction brings the kinematic relaxation time, and the evaporation time closer. These ratios are below 1 in most of the studied conditions, indicating that, irrespective of the droplet size, the droplets adapt to the gas phase velocity faster than they evaporate. Naturally, at low seen gas temperature the evaporation is slow, and droplets reach the gas phase speed in a fraction of the droplet lifetime. The two timescales become almost equal at the highest assessed temperature of $T_s = 2000$ K. For low Reynolds numbers of $Re_p < 5$, the iso-lines of $\tau_{p,kin}/\tau_{p,evap}$ are approximately aligned with the ordinate

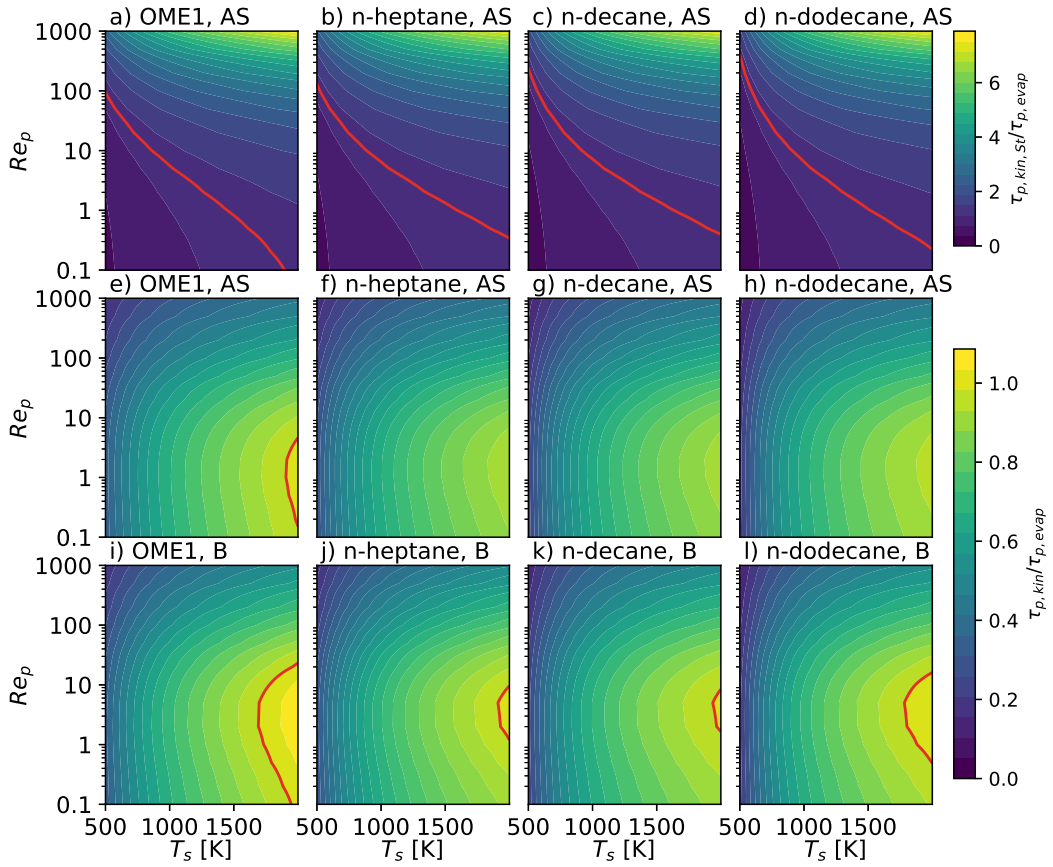

FIGURE 4.21: Ratio of kinematic relaxation time and evaporation time at wet-bulb conditions as function of the seen gas temperature and the Reynolds number with $Y_{f,s} = 0$. Plots a-d compare the kinematic relaxation time of Stokes (1851) to the evaporation time of Abramzon and Sirignano (1989). Plots e-h compare the kinematic relaxation time of Naumann and Schiller (1935) to the evaporation time of Abramzon and Sirignano (1989). And plots i-l compare the kinematic relaxation time of Naumann and Schiller (1935) to the evaporation time of Bird, Stewart, and Lightfoot (1960). The ratio of unity is marked with a red line.

axis, indicating, that in this region the ratio is independent of the Reynolds number, and it is mostly determined by the seen gas temperature.

The final goal of the droplet modeling presented in this chapter, is to apply these Lagrangian particles in the context of Eulerian-Lagrangian simulations of turbulent spray combustion systems. In this context, it is important to compare the droplet time scales to the time scales characterizing the gas phase environment. One such metric is the Stokes number, that compares the kinematic relaxation time $\tau_{p,kin}$ of the droplet to the time scales of the velocity field:

$$St = \frac{\tau_{p,kin}}{\tau_{flow}}. \tag{4.83}$$

The various flow time scales are discussed in more detail in section 5.1.6. High Stokes numbers correspond to the ballistic behavior of the particles, since they are unable to relax to the fluctuations of the flow characterized by a short time scale.

Meanwhile low Stokes numbers signify, that the particle follows the path lines of the fluid flow perfectly. In case of $St_\eta = \mathcal{O}(1)$ defined based on the smallest scales of turbulence (Kolmogorov scales), the particles immersed in the turbulent flow tend to agglomerate in regions of low vorticity. Such cases are very challenging to the large-eddy simulation technique used in the present work. (Jin, He, and Wang, 2010) Thus, it is important to assess at least *a posteriori*, whether the kinematic model of section 4.1 is capturing the targeted multi-phase phenomena well. Recently Kulkarni, Silva, and Polifke (2022) analyzed droplets of $St = \mathcal{O}(1)$ and found a strong relation between the length scales of the flow and of the produced vapor field due to the preferential clustering of the particles. This gives rise to additional coupling mechanisms between the gas phase and the droplet cloud through equivalence ratio fluctuations.

Note, that the Stokes number may be used to estimate the velocity difference between the fluctuating gas flow and the droplet. Crowe et al. (2012, §2.5) uses the "constant lag" assumption to estimate:

$$\frac{|\mathbf{u}_p|}{|\mathbf{u}|} \propto \frac{1}{1+St}. \tag{4.84}$$

Thus, knowing the gas phase flow scales and the droplet size, the slip velocity and droplet Reynolds number may be estimated, which facilitates the *a priori* assessment of the present models.

4.7 Limitations of the Langmuir-Knudsen models

In case of the Langmuir-Knudsen models (LK) described in section 4.4.7, finding the wet-bulb temperature becomes more complex, as size-dependence interferes with the results. To illustrate this, the non-equilibrium Spalding mass transfer numbers of model LK1 and LK2 are presented in Fig. 4.22 as function of the droplet temperature at different seen temperatures, and different droplet diameters. Note that a coordinate transformation is applied in the droplet temperature: $\theta = -\ln\left(1 - \frac{T_p}{T_{sat}}\right)$ to highlight the behavior near the boiling point. Also, this figure differs from the previously shown examples in the sense, that the droplet is not at its steady state temperature. The equilibrium Spalding mass transfer number B_M^{eq} is simply a function of the droplet temperature as indicated by the thin black line of the figure. The non-equilibrium counterpart varies with the droplet diameter as shown in the different rows of plots. Moreover, B_M^{neq} is also sensitive to seen gas temperature as indicated by the different colors, since the reference properties are involved in the Knudsen layer thickness calculation: Eq. (4.66) and in other factors influencing the non-equilibrium interface vapor mole fraction. Generally, the mass transfer resembles the equilibrium solution better at higher diameters and low droplet temperatures.

The model without the iterative solution of $X_{f,i}^{neq}$ (LK1) is illustrated with dashed lines. As the droplet temperature increases the LK1 model shows local maxima in the mass transfer number, and even drops below 0 with the further increase of the droplet temperature. Not shown in the graph, this results in nonphysical cases where the non-equilibrium interface vapor mass fraction is negative. In the further testing of the model, these conditions are omitted, and $X_{f,i}^{neq} \geq 0$ is imposed. For the 50 μm droplets (Fig. 4.22 a,b,c,d) this shortcoming only takes effect within 1 K of the boiling point, however as the droplets evaporate, larger and larger portions of the

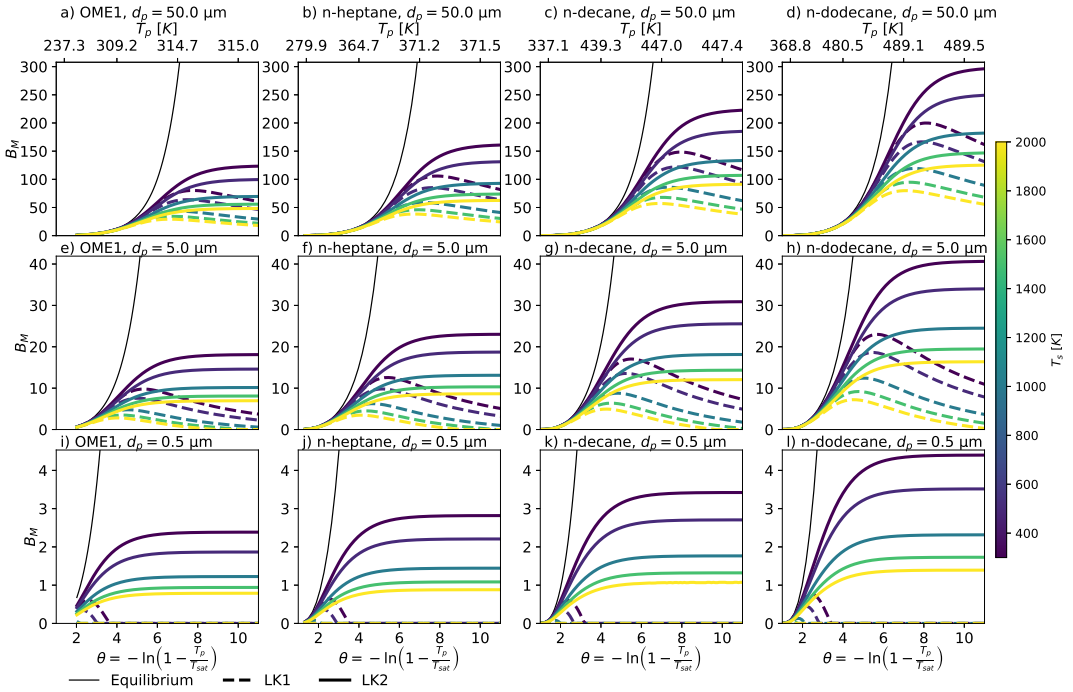

FIGURE 4.22: Non-equilibrium Spalding mass transfer numbers given by model LK1 and LK2 as function of droplet temperature for various liquids, at three different droplet diameters: a,b,c,d) 50 μm, e,f,g,h) 5 μm, and i,j,k,l) 0.5 μm, and at 5 different seen temperatures: 300 K, 500 K, 1000 K, 1500 K, and 2000 K. The seen gas is dry air at atmospheric pressure.

range of viable droplet temperatures is affected. In conclusion, the LK1 model cannot be recommended for droplets evaporating at high temperatures like combustion applications, as it completely eliminates mass transfer at high droplet temperatures.

As the solid curves of Fig. 4.22 illustrate, the LK2 model also limits the mass transfer numbers to a maximum, but B_M^{neq} stays injective respect to the droplet temperature. The maximum attainable mass transfer number is a function of droplet size, seen temperature and gas composition. B_M^{neq} decreases with the seen temperature as the "1/3 law" gives higher Knudsen layer thicknesses. Overall, the non-equilibrium mass transfer numbers still approach 0 as the droplet size decreases, but the non-physical local maxima and negative mass fractions are avoided with the iterative solution of $\beta^{neq} = \phi_m \ln\left(1 + B_M^{neq}\right)$. B_M^{neq} also decreases with increasing seen vapor mass fraction, which is not shown here for simplicity.

In conclusion, the Langmuir-Knudsen model may not provide a solution for Eq. (4.73), as $B_T^{neq,psy,LK}$ is bounded since B_M^{neq} is bounded as shown in Fig. 4.22. On the left hand side of Eq. (4.73) $T_p^{psy,LK}$ is bounded by the boiling point, but T_s is unbounded, thus the possible equilibrium states are limited just like in the case of the diffusion only model (D/D). In case a sufficiently high $B_T^{neq,psy,LK}$ cannot be provided, there is no equilibrium state, however it does not mean the model is invalid, as the temperature takes a finite time to relax towards new equilibrium states. As Fig. 4.22 illustrates, the range of feasible Spalding mass transfer numbers can accommodate the necessary values for droplets of $d_p = 50$ μm, since the mass transfer number only plateaus between 50 and 150 even for a seen temperature of 2000 K, but under these seen conditions, $B_M < 6$ is sufficient to keep a equilibrium temperature (Fig. 4.14).

The range of mass transfer number necessary for equilibrium is only unattainable for very small droplets of $d_p = \mathcal{O}(0.1\ \mu\text{m})$ ..$\mathcal{O}(1\ \mu\text{m})$. As demonstrated below, in practice the Langmuir-Knudsen model (LK2) largely behaves similarly to Bird's correction (B) for droplets that start the evaporation in the $d_p = \mathcal{O}(10\ \mu\text{m})$ range, with a small interval near the end of the droplets lifetime, where the non-equilibrium effects slow down the mass transfer and the droplet temperature can quickly rise.

4.7.1 Single droplet evaporation with non-equilibrium effects

The Langmuir-Knudsen models are rather particular in the sense, that these models introduce diameter dependence on quantities, that are independent of the diameter in all the other studied models. For this reason, the wet-bulb conditions are undefined as the droplets do not approach a specific equilibrium temperature during their lifetime as it is the case with the other studied models. Furthermore, as already illustrated in 4.7, the non-equilibrium mass transfer number B_M^{neq} is limited depending on the droplet diameter. Thus applying the Langmuir-Knudsen models, the droplets may reach a minimum diameter $d_{p,min}$ in their lifetime, where the liquid droplet temperature approaches the boiling point (thus $B_M^{eq} \to \infty$) and energy conservation cannot be satisfied because the mass transfer is limited by $\max(B_M^{neq})$, similarly to the case of the diffusion only model (D/D).

A number of single droplet simulations were executed using the two different Langmuir-Knudsen models: LK1 and LK2. The chosen parameter set is similar as before: the initial droplet diameter is: $d_{p,0} \in \{0.5, 2, 5, 20, 50, 500\}\ \mu$m, the difference between the psychrometric wet-bulb temperature calculated with Bird's correction and the initial temperature is: $\Delta T_0 = T_p^{psy,B} - T_{p,0} \in \{0, 40\}$ K the Reynolds number is: $Re_p \in \{0, 10, 1000\}$, and the seen temperature T_s is varied between 300 K and 2000 K with 100 K steps. For simplicity the seen vapor mass fraction is again kept constant zero. The simulations are run until 99.9% of the initial droplet mass is evaporated, indicating a successful application of the model. Otherwise, if at any point the equilibrium Spalding number surpasses the arbitrary limit: $B_M^{eq} > 10^5$, this is taken as an indication that the minimum possible droplet diameter: $d_{p,min}$ is reached, indicating that the non-equilibrium models are not applicable to the case.

The simulated cases are analyzed in Fig. 4.23 presenting the time necessary to reach the final possible droplet mass normalized by the time necessary to reach the same mass using Bird's correction. I.e.: in case it is possible to evaporate 99.9% of the initial droplet mass, the presented ratio is $\tau_{p,tot}^{LK}/\tau_{p,tot}^{B}$ (represented by triangles), where $\tau_{p,tot}$ is defined as shown in Fig. 4.16. Otherwise, if the droplet evaporation cannot be completed, then the denominator of the ratio is interpolated from the complete simulation using Bird's correction corresponding to the same mass (represented by dots). This figure quantifies the importance of using the Langmuir-Knudsen models, as the non-equilibrium models only deviate from Bird's correction for very small droplet sizes. Above an initial droplet size of 20 μm this deviation is completely insignificant, and is omitted here. I.e.: 99.9% of the droplet mass can evaporate, without any notable non-equilibrium effects.

As the initial droplet size decreases, the non-equilibrium models (LK1,LK2) become more important, however the diameter limitation, further discussed in section 4.7.2, restricts their applicability to low seen temperatures as at higher T_s the evaporation is terminated prematurely. In general, the non-iterative LK1 model suffers from this limitation to a greater extent. The $d_{p,0} = 20\ \mu$m droplets can complete

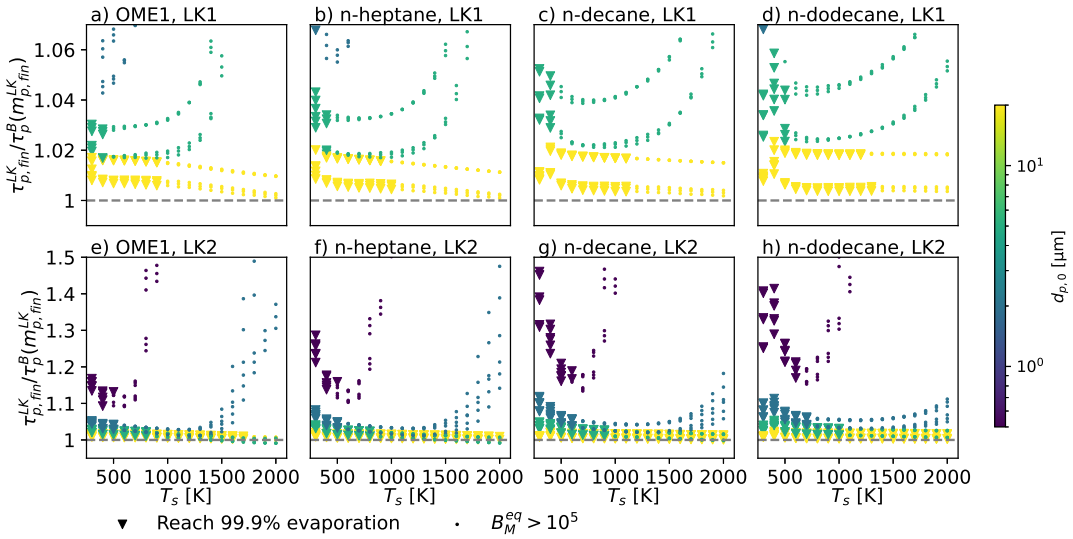

FIGURE 4.23: Ratio of time taken till the final droplet mass is reached in case of Langmuir-Knudsen models (LK1 and LK2) and Bird's correction (B) as function of the seen gas temperature. The models are assessed under various seen gas temperatures, initial temperatures, Reynolds numbers, and initial droplet diameters. The initial diameter is indicated by the color scheme, while symbols indicate the cause of termination of the Langmuir-Knudsen simulations: triangles represent successful cases, while dots show early termination.

their evaporation under most studied conditions, but smaller droplets cannot. Overall, the effects of the LK1 model are either small, because of the larger droplet size, or the effects get severe enough to impede full evaporation.

The iterative solution of the non-equilibrium conditions (LK2) is much less restricted in terms of $d_{p,min}$, thus even droplets of $d_{p,0} = 0.5$ μm can be successfully simulated under certain seen temperatures. For this reason the observed effect can be much larger in the cases that complete the evaporation (Fig. 4.23e-h triangles). In general, the effect increases with larger and less volatile hydrocarbons. In most fuels, the effect monotonously decreases with increasing seen gas temperature, except in the case of n-dodecane. This characteristic change of behavior is related to the extremely low volatility of n-dodecane at $T_s = 300$ K that can be observed in the other analysis of the present chapter.

The behavior of the Langmuir-Knudsen models is further analyzed in Fig. 4.24. The figure shows $d_p^2/d_{p,0}^2$ as function of $t/d_{p,0}^2$, for stationary droplets ($Re_p = 0$) under different seen gas temperature, and zero seen vapor mass fraction. The scaling of the coordinates, makes the plot independent of initial droplet size in case of Bird's correction, as the evaporation constant is only a function of the seen conditions and material properties. Thus, Fig. 4.24 can highlight the differences introduced by the non-equilibrium models. The figure provides examples of simulations using the non-iterative (LK1) and iterative (LK2) models for three different initial droplet diameters. In this scale, the effect appears quite insignificant even for these small droplets except for the sub-micron case of $d_{p,0} = 0.5$ μm.

The evolution of the droplet size highlights a key issue of the non iterative method (LK1) related to the phenomena shown in Fig. 4.22: the non-equilibrium mass transfer number B_M^{neq} has a local maximum in droplet temperature T_p then drops to zero

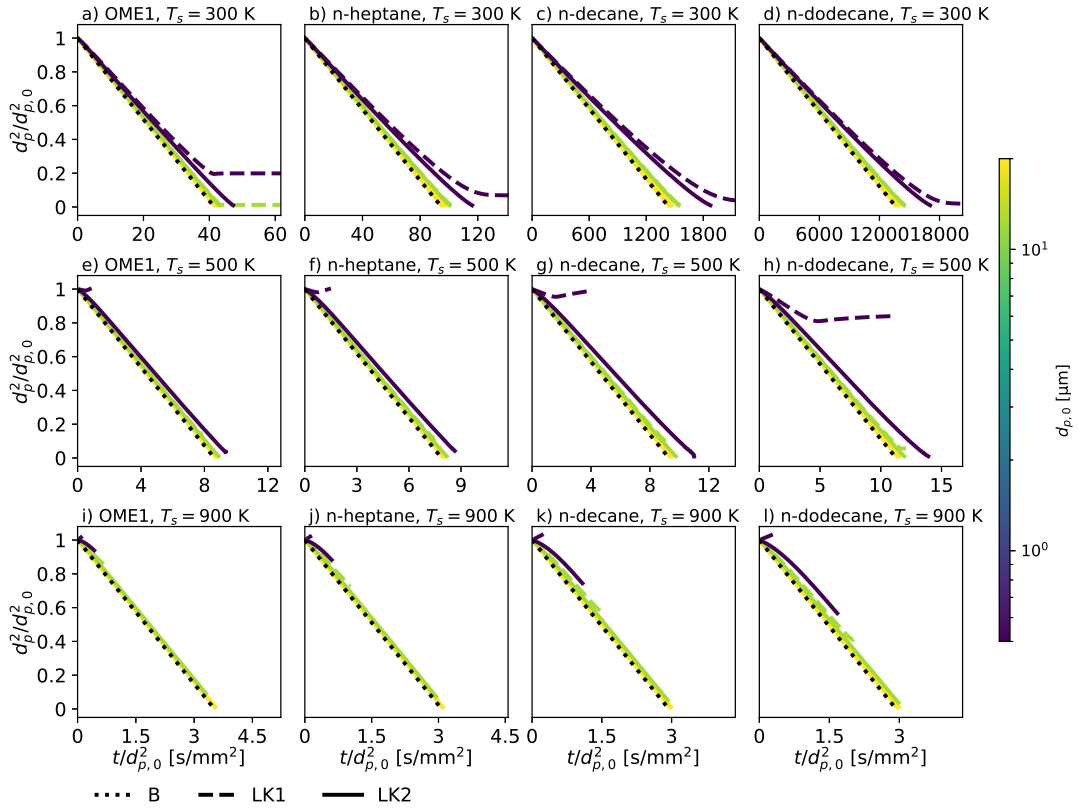

FIGURE 4.24: Evolution of droplet surface in time using the non-iterative (LK1) and iterative (LK2) Langmuir-Knudsen models under various seen gas temperatures. The Reynolds number and seen vapor mass fraction are zero. Three initial diameters are indicated by the color scheme in $d_{p,0} \in \{0.5, 2, 5\}$ μm, while the initial droplet temperature is given by the wet-bulb conditions using Bird's correction. The equilibrium solution using Bird's correction (B) is indicated for reference.

and this zero-crossing is rather far from the boiling point in case of sub-micron droplet diameters (Fig. 4.22i-l). Thus the LK1 model can completely impede the evaporation process before the highest temperatures are reached, resulting in cases like the one presented in Fig. 4.24h for $d_{p,0} = 0.5$ μm where the droplet temperature keeps increasing, causing the swelling of the droplet, even though the evaporation is terminated. The LK2 model does not show this behavior, as it asymptotically approaches a maximum B_M^{neq} as the droplet temperature increases (Fig. 4.22). Consequently, the evaporation is never completely terminated. However, this model is also limited by a minimum possible diameter.

4.7.2 Limiting droplet diameter of non-equilibrium models

The single droplet simulation data of section 4.7.1 is used below to further demonstrate the limitations of the Langmuir-Knudsen models. In these simulations the droplets may reach a minimum diameter $d_{p,min}$ in their lifetime, where the liquid droplet temperature approaches the boiling point. Figure 4.25 presents $d_{p,min}$ as the final diameter in the simulation cases where $B_M^{eq} > 10^5$ is reached, indicating an unsuccessful application o the non-equilibrium models. Such conditions are only

observed starting from the initial diameter of $d_{p,0} \in \{0.5, 2, 5, 20\}$ μm. In the studied parameter range $d_{p,min}$ appears to be independent of the initial droplet temperature $T_{p,0}$, and there is only a slight dependence on the Reynolds number Re_p. Furthermore, the initial droplet diameter $d_{p,0}$ only affects the minimum possible diameter, if the energy balance is unsatisfied almost instantly after the start of the simulation and $d_{p,min} \approx d_{p,0}$. Thus the determining factor of $d_{p,min}$ for a given fuel is the seen gas temperature T_s. The minimum diameter of the LK1 model can be estimated well, by solving for d_p assuming $B_M^{eq} = 10^5$ and $X_{f,i}^{neq} = 0$, and using material properties from the wet-bulb conditions of Bird's correction (B). This estimate takes the form:

$$d_{p,min}^{LK1} \approx 2L_K^B \phi_m^B \ln\left(1 + 10^5\right), \tag{4.85}$$

and it is indicated by the dashed lines in Fig. 4.25. Indeed, the diameter where the single droplet simulations fail is approximated well by Eq. (4.85). As expected, the iterative process of the LK2 model extends its applicability range, and produces a minimum diameter less than half of the LK1 model in the cases that fail.

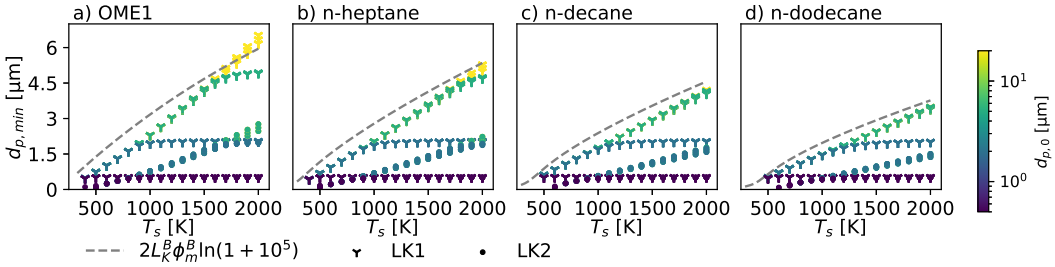

FIGURE 4.25: Minimum diameter of applicability of the Langmuir-Knudsen models (LK1 and LK2) as function of the seen gas temperature identified as the diameter where $B_M > 10^5$ is reached in single droplet simulations. The models are assessed under various seen gas temperatures, initial temperatures, Reynolds numbers, and initial droplet diameters.

Summary of non-equilibrium models

Overall, the applicability of the Langmuir-Knudsen models is limited on two fronts. On one side, if the initial droplet diameter is too large, the models have barely any effect on the major part of the evaporation process. In this case 99.9% of the initial mass can be evaporated without any significant effect. On the other side, if the initial droplet diameter is too small, the models are limited by the minimum achievable diameter: $d_{p,min}$. (See Eq. (4.85).) The latter limitation increases with the seen gas temperature, thus the Langmuir-Knudsen models can only be used in low temperature applications. Furthermore, experimental evidence is lacking for assessing the performance of these models, as sub-micron measurements are not yet possible. State of the art measurements can study droplets of $d_{p,0} = \mathcal{O}(100)$ μm. (Chauveau et al., 2019)

In light of these characteristics, the present study concludes, that the Langmuir-Knudsen models formulated following Miller, Harstad, and Bellan (1998) are not suitable for spray combustion systems at atmospheric pressure.

4.8 Summary of liquid phase modeling

This chapter sets the assumptions applied throughout this work for liquid phase modeling. An extensive parametric study of the droplet evaporation models is executed, motivated by the recent increase of interest in this topic. (Noh et al., 2018) The sub-models, that are out of the scope of this analysis are kept relatively simple, in their most widely used forms. (Schiller-Naumann drag, quasi-steady film, Ranz-Marshall film thickness, constant "1/3 law" film properties with ideal gas law, infinite conductivity assumption within the droplet.) This is done in the hopes, that the present conclusions of this work may reach a wider audience.

Apart of these classical methods, a new model is introduced for the evaluation of "1/3 law"-like film properties in the framework of tabulated chemistry. The model aims to describe the gas phase around the droplet using the data readily available in the chemistry tables, appended with only six more entries. Consequently the complexity of the model is independent of the chemical mechanism, and memory limitations are avoided.

The fundamentals of analytical heat and mass transfer sub-models have been reviewed in the context of film theory for spherical droplets using the classical "1/3 law". The combination of these two sub-models yields widely used evaporation models under the infinite conductivity assumption, that describe the evolution of droplet size and temperature at given far-field ("seen") gas phase conditions. The family of models considering Stefan flow in both heat and mass transfer stand out in terms of performance among the studied options, namely the model denoted as Bird's correction (B), the Abramzon-Sirignano model (AS) and the Langmuir-Knudsen model (LK). (Given that the latter is applied to large droplets.) The two other studied models either ignore Stefan flow as in the case of diffusion only model (D/D), or partially ignore it in case of the classical model (S/D). Both resulting in nonphysical behavior in high temperature environments. In the literature many of these models are validated at low temperature conditions where all of them behave very similarly.

It must be noted, that Bird, Stewart, and Lightfoot (1960, §19.4, §22.8) originally derived the heat transfer correction term for evaporation or condensation over a flat plate. This correction is expressed in terms of non-dimensional numbers (β) and it is applied to spherical cases such as evaporating droplets. In the present work, the correction is derived from first principles to spherical coordinates, yielding the conclusion, that Bird's correction is indeed the same for droplets and flat plates despite the fundamental differences in configuration.

The evaporation characteristics of four different pure compounds: OME1, n-heptane, n-decane, and n-dodecane are studied using the aforementioned models. These fuels differ in terms of volatility, that causes the most variation between their behavior. The difference is most striking in low temperature environment, where n-dodecane behaves radically different from the more volatile fuels. The evaporation of single droplets of these fuels is numerically investigated under an extensive range of conditions from ambient to flame-like environments. It is found, that the initial heat-up process can extend the droplet lifetime by $\sim$ 10% if the initial temperature is sufficiently far from the wet-bulb conditions.

The time scales of the problem are assessed. Good estimates are found for the calculation of evaporation and heat-up times. These scales are compared with the kinematic relaxation time, revealing, that at high temperature conditions the kinematic time scale is comparable to the droplet lifetime. Nevertheless, under the assessed conditions, the droplets are expected to relax to the flow faster than they

evaporate. The importance of relating these time scales to the Eulerian flow fields is highlighted.

The additional considerations of non-equilibrium thermodynamics (Miller, Harstad, and Bellan, 1998) is also evaluated extensively. It is found that the Langmuir-Knudsen model needs an iterative process, to correctly evaluate the non-equilibrium vapor pressures. Even with this iterative solution, the application of this model shall be limited to low temperature evaporation of sub-micron droplets, where the computation is not limited neither by the inherent instability of the model, nor by its negligible effect compared to Bird's correction. Thus, the Langmuir-Knudsen models are not suitable for combustion simulations.

In summary, the Reynolds number effects considered by the model of Abramzon and Sirignano (1989) are found to be significant even at relatively low Reynolds numbers. The model assumes, that the effective film thickness primarily determined by the Reynolds number is strongly affected by the intense blowing velocity of Stefan flow. This model may be considered the state of art in Lagrangian fuel spray modeling under the conditions of the present work, and it can be used with confidence for liquid fuel combustion applications.

Chapter 5

Large-eddy simulation of multiphase reacting flows

Many industrially relevant combustion devices are characterized by turbulent flow. This entails the existence of a range of length and velocity scales, commonly understood as *eddies* embedded in a mean flow filed, vortical structures of different size and intensity. While this enhances mixing and allows combustion devices to stay compact, it also introduces a myriad of physical phenomena which are very challenging to model. A particularly big issue in the context of numerical simulation is the size of the smallest vortical structures (Kolmogorov scales). Resolving these small structures with a discretization small enough to capture them is prohibitively expensive in practical systems. Large-eddy simulation (LES) emerges as a viable trade-off between accuracy and numerical cost, where only the larger structures are resolved, while models are introduced for the small scale behavior. Using LES for combustion is a particularly onerous task, because part of the important phenomena occurs on these unresolved scales, such as the fine mixing of reactants, the chemical reactions, and the evaporation of fuel droplets.

This chapter presents the overall modeling framework of turbulent reacting flows with or without the added complexity of evaporating droplet clouds. To facilitate the discussion, the chapter briefly outlines some relevant concepts of turbulent flow and turbulence/chemistry interaction. The building blocks of LES are also discussed, introducing the spacial *filtering* of the equations, and the closure of the arising sub-grid terms. The focus is directed to specific issues of high-fidelity reacting flow simulations using tabulated chemistry. Furthermore, a strategy is presented for the *a posteriori* confirmation of the validity of modeling assumptions. Finally the Eulerian transport equations of the gas phase are coupled to the Lagrangian representation of the droplet cloud. Thus, the concepts introduced in chapters 2, 3, and 4 are integrated into a strategy capable of describing multiphase reacting flows under well established restrictions.

The chapter is structured as follows. Section 5.1 introduces the filtering operation, and discusses its effect on the scales of turbulent motion. Then this filtering is applied on the governing equations giving rise to a PDE system describing the evolution of the filtered unknowns, and a the arising unclosed momentum transport term is treated with an eddy-viscosity model. The meaning of the filtered unknowns are discussed, putting the LES results in context. Furthermore, a method is developed for the estimation of turbulent length, time, and velocity scales in variable density flows. Section 5.2 discusses an important aspect of Navier-Stokes equations: the non-linearity of the convective momentum transport. The equations are cast into different forms, that inherently conserve different properties. The implications on numerical solutions are discussed. Section 5.3 briefly discusses the nature of turbulence/chemistry interaction, providing ways to assess the validity of the

flamelet concept, which is a prerequisite of the applied tabulated chemistry approach. Section 5.4 compiles the various sub-grid closure models of filtered transport properties and filtered scalar equations in the context of tabulated chemistry. Finally, section 5.5 introduces the coupling of the Lagrangian representation of the volatile fuel droplets with the filtered Eulerian equations of the gas phase.

Credit

This chapter discusses well established LES combustion approaches. Novelty is introduced in some aspects of the models. In section 5.1.5 the author presents a new way to estimate the effect of a commonly accepted but less studied inconsistency: taking the ensemble average of Favre-filtered quantities as the true ensemble average. In section 5.1.6, extending the methods developed by Oriol Lehmkuhl for incompressible flows, the author presents a technique to estimate the relevant scales of turbulence from single point data of LES of variable density flows. A software library is developed to obtain these estimates on temporally sampled single point data, and locate the case on combustion regime diagrams for the verification of the flamelet concept. Finally, in section 5.4.4 the author devises a consistent approach to use the equation of state in the context of presumed FPDF integrated gas properties. The software used in this chapter is partially published in open source repositories at: `https://gitlab.com/BothAmbrus/LES1DFilter`
and `https://gitlab.com/BothAmbrus/KolmogorovAtWitness`.

5.1 Large-eddy simulation

The turbulent flows studied in this work are, by nature, unsteady and they show a wide range of scales in space and time. This extensive variety of scales poses a challenge for numerical solutions, as there is a strong interaction across them, thus they cannot be decoupled in a trivial manner. Consequently, the direct numerical simulation (DNS), i.e.: the complete solution of all relevant spatial scales, would need a fine spatial resolution capable of representing even the smallest scales. This would result in a prohibitively large number of degrees of freedom in industrially relevant combustion systems. The method of large-eddy simulation (LES) approaches this physical phenomena, by making a conscious decision of which larger spatial scales to *resolve* (large eddies) and which smaller spatial scales to *model*, separated by a cut-off length scale. Such a distinction can be adequate, since the behavior of the smaller scales is thought to be rather universal, thus modeling the effect of the unresolved scales on the resolved scales may be done using universal models. (Pope, 2000, §13.1)

5.1.1 Filtering

To achieve this distinction between the resolved and unresolved length scales, the governing equations need to be modified such, that they only represent the evolution of the resolved length scales. This is done by applying spatial filters on the PDEs in a way, that the unknowns of the equations become the resolved part only. The filtering gives rise to additional terms, representing the interaction between resolved and unresolved scales. These terms need to be modeled based on the resolved quantities. As Rogallo and Moin (1984) point out, if this interaction is not modeled adequately, the solution "may have no relation to fluid physics".

The resolved length scales have to be large enough, to be represented by the computational mesh. In practice, the cut-off is typically determined by the computational grid size itself: Δ, assuming that every length scale that can be represented on the grid, will indeed be represented on the grid. (Poinsot and Veynante, 2005, §4.7) In fact, the real filtering effect of the numerical discretization is generally unknown. (Rogallo and Moin, 1984) In most LES studies (including this work) it is merely presumed, that a filtering operation exists, corresponding to the discretization effect. This filtering operation is assumed to be characterized by a filter length sale: Δ_f proportional to the grid size. This approach is often called *implicit filtering* (Germano, 1992), not to be confused with implicit time marching schemes, or with the implicit LES method. (Grinstein, Margolin, and Rider, 2007)

Even though the exact filtering effect is unknown, it can be mathematically characterized as:

$$\overline{\psi}(\mathbf{x}, t) = \int_{\Omega} \psi(\mathbf{x}^*, t) G(\Delta, \mathbf{x}, \mathbf{x}^*) \mathrm{d}\mathbf{x}^*, \tag{5.1}$$

where the bar superscript represents the filtering, $\psi(\mathbf{x}, t)$ is an arbitrary field defined on the Ω domain at time instance t, and $G(\Delta, \mathbf{x}, \mathbf{x}^*)$ is the value of the filter kernel centered at $\mathbf{x}$, and evaluated at $\mathbf{x}^*$. To illustrate the filter kernel one might take the so-called top-hat or box filter defined as:

$$G(\Delta, \mathbf{x}, \mathbf{x}^*) = \begin{cases} \dfrac{1}{\Delta_f^3}, & \max |\mathbf{x}_i^* - \mathbf{x}_i| \leq \Delta_f/2, \; i = 1..3, \\ 0, & \max |\mathbf{x}_i^* - \mathbf{x}_i| > \Delta_f/2, \; i = 1..3, \end{cases} \tag{5.2}$$

where Δ_f can be interpreted as an L^1 distance around the points where the computational grid represents the unknowns, thus Δ_f is ultimately related to the grid size Δ. Note, that this filtering operation is *not* used explicitly at any point of this work, since the unfiltered field ψ is simply not available. The large-eddy simulation may produce only the filtered quantities directly, but attaining the unfiltered fields from these filtered ones (Vreman, Bastiaans, and Geurts, 2009; Domingo and Vervisch, 2015; Grenga et al., 2022) is out of the scope of the present work. Thus, Eq. (5.2) is included here only for the illustration of the filtering concept in the examples presented below. For an extensive explanation of the filtering procedure, see the work of Sagaut (2006).

This LES filtering, and the corresponding notation $(\overline{\psi})$ resembles the notation of Reynolds-averaging in the context of RANS simulations. For pragmatic reasons, the two notations are often treated analogously. (Ma, 2016; MacArt, Grenga, and Mueller, 2018; Sitte, 2019) However, the differences are significant in the underlying meaning, since the Reynolds-averaging is primarily executed over an ensemble of statistically independent realizations of the same flow problem. Subsequently, this is extended to averaging along certain directions using symmetry arguments, and to averaging over time in case the problem is statistically steady and the ergodicity principle applies. The resulting RANS equations would be solved on a grid, that adequately represents the Reynolds-averaged fields. Meanwhile, the LES filtering may be interpreted as an instantaneous spatial average in a local control volume (Eq. (5.2)), and the filtering is a necessity enforced by the insufficient grid size. As the present work focuses on LES simulations, hereby a distinction is made between the notation of LES filtering (Eq. (5.1)), and the temporal (Reynolds-)averaging of

statistically steady cases. The latter is defined as:

$$\langle \psi \rangle (\mathbf{x}) = \frac{1}{t_f - t_0} \int_{t_0}^{t_f} \psi(\mathbf{x}, t) \mathrm{d}t. \tag{5.3}$$

This quantity is used in the statistical description of the LES results.

The above distinction of $\overline{\psi}$ and $\langle \psi \rangle$ presents the opportunity to define various decompositions of the turbulent field. One such splitting is introduced in the context of Reynolds-averaging, where the flow field is expressed as the sum of the temporal average at a given point and the corresponding fluctuations in time:

$$\psi(\mathbf{x}, t) = \langle \psi \rangle (\mathbf{x}) + \psi^{\dagger}(\mathbf{x}, t), \tag{5.4}$$

where the temporal average of the fluctuations themselves is zero: $\langle \psi^{\dagger} \rangle = 0$ because $\langle \psi \rangle$ is independent of time, thus the double execution of the time-averaging operator does not modify the mean: $\langle \langle \psi \rangle \rangle = \langle \psi \rangle$. Note, that this interpretation is constrained to temporal averaging of statistically steady processes.

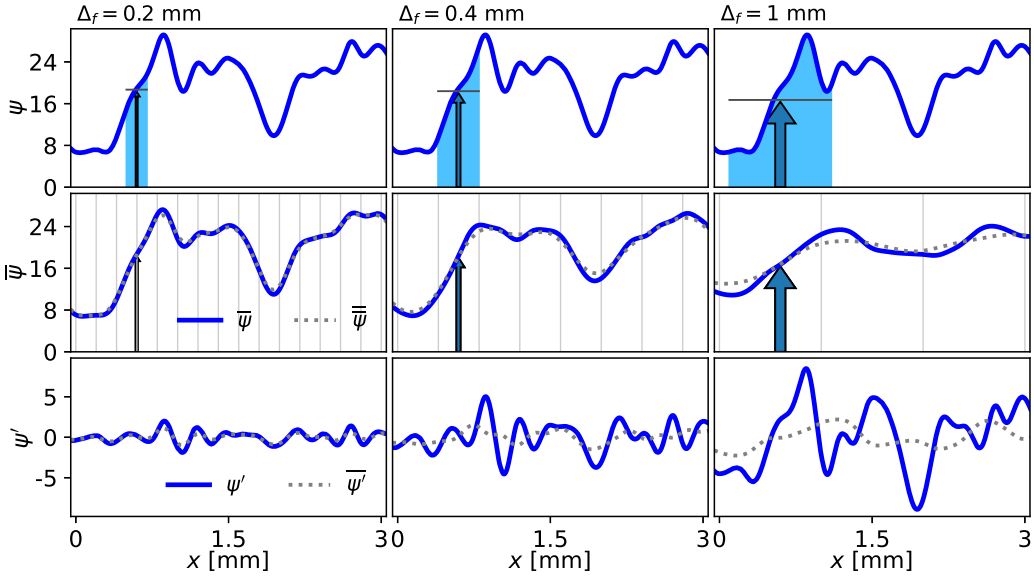

FIGURE 5.1: Illustration of filtered and sub-grid components of a 1D field using the box filter with different filter lengths. The different columns correspond to filter widths of $\Delta_f \in \{0.2, 0.4, 1.0\}$mm respectively, while the rows show the unfiltered filed, the filtered field, and the sub-grid fluctuations. The double filtered field, and filtered fluctuations are shown with dotted lines.

Similarly, the LES decomposition describes the instantaneous fields as the sum of the filtered field, and the unresolved part:

$$\psi(\mathbf{x}, t) = \overline{\psi}(\mathbf{x}, t) + \psi'(\mathbf{x}, t), \tag{5.5}$$

where ψ' denotes the sub-grid component of ψ. Even though the LES filtering operator of Eq. (5.1) has linear properties ($\overline{A + B} = \overline{A} + \overline{B}$, $\overline{cA} = c\overline{A}$), it is not guaranteed to be a so called "Reynolds operator". (Germano, 1992) I.e.: the consecutive filtering

of a field is not invariant, and the filtered sub-grid field is not necessarily zero:

$$\overline{\overline{\psi}} \neq \overline{\psi}, \qquad \overline{\psi'} \neq 0. \tag{5.6}$$

For example, the aforementioned box filter would exactly filter out harmonic fluctuations with the same wave length as the filter size $\lambda = \Delta_f$. However, as Pope (2000, §13.2) shows, smaller fluctuations such as $\lambda = \frac{2}{3}\Delta_f$ would be less attenuated. To further illustrate the meaning of filtering, Fig. 5.1 shows the application of the box filter on a one dimensional field. The first row of plots presents the fully resolved field and demonstrates the filter size, while the last two rows show the filtered and sub-grid components. Despite the imperfections of the box filter, a separation of scales is achieved, since the filtered field is significantly smoother than the original one. As the filter width is increased from right to left, less and less details are represented by the filtered quantity, and the amplitude of the sub-grid fluctuations increase.

Figure 5.1 also demonstrates, that the box filter is indeed not a Reynolds operator, since the double filtered fields do not coincide with the filtered fields, and since the filtering of the sub-grid component does not result in a constant zero signal, as indicated by the gray dashed lines. In fact, the inequalities of Eq. (5.6) only become equalities if the filtering operation is a *sharp spectral filter*, meaning, that from the spatial Fourier spectrum of the field only large wave lengths of $\lambda > 2\Delta_f$ are retained and smaller wave lengths are completely attenuated. This corresponds to the retention of small angular wave numbers of $\kappa < \frac{\pi}{\Delta_f} = \kappa_c$, where κ_c is the cut-off wave number.

Finally, the last detail represented on Fig. 5.1 is the overlay of a grid of width Δ_f in the middle row of plots. This grid illustrates, that the filtered field can indeed be captured to a good accuracy by a spatial discretization that is proportional to the filter length, although $\Delta = \Delta_f$ might seem rather coarse. Note, that in Fig. 5.1 the filter kernel is moved continuously through the domain, and the integral of Eq. (5.1) is evaluated at every $\mathbf{x}$ of the original field. In practice, this is not the case, as the discretization itself implicitly imposes a certain unknown filter, nevertheless the proportionality of the filter width and the grid sizing is illustrated here.

A general property of the filtering, given the definition of Eq. (5.1), is its commutability with temporal derivatives, because in this work the meshes are static and G is constant in time. However, commutability with spatial derivatives is also required in the derivation of conservation equations of filtered quantities. In principle this is only possible, if the filter itself is homogeneous in space ($\nabla G(\Delta, \mathbf{x}, \mathbf{x}^*) = 0$) corresponding to a uniform grid size ($\nabla\Delta = 0$). In the present study the commutability is assumed to hold even in non uniform meshes while the growth rate of the meshes is kept limited to support this assumption. (Poinsot and Veynante, 2005, §4.7.1)

Favre-filtering

The non-density-weighted LES filtering described above poses modeling challenges in variable density flows, since the governing equations Eq. (2.54)-(2.56) contain products of the density and unknowns, such as: $\rho\mathbf{u} \otimes \mathbf{u}$ and $\rho\xi_k\mathbf{u}$. The challenge is demonstrated here using the filtered convective scalar flux:

$$\overline{\rho\xi_k\mathbf{u}} = \overline{(\overline{\rho} + \rho')\left(\overline{\xi_k} + \xi_k'\right)(\overline{\mathbf{u}} + \mathbf{u}')}, \tag{5.7}$$

$$= \overline{\overline{\rho}\,\overline{\xi_k}\,\overline{\mathbf{u}}} + \overline{\overline{\rho}\,\overline{\xi_k}\mathbf{u}'} + \overline{\overline{\rho}\,{\xi_k}'\overline{\mathbf{u}}} + \overline{\rho'\overline{\xi_k}\overline{\mathbf{u}}} + \overline{\overline{\rho}\,{\xi_k}'\mathbf{u}'} + \overline{\overline{\xi_k}\,\rho'\mathbf{u}'} + \overline{\overline{\mathbf{u}}\rho'\,{\xi_k}'} + \overline{\rho'\,{\xi_k}'\mathbf{u}'}. \tag{5.8}$$

As the LES only gives information about the filtered quantities, models would be required to provide closure for the double and triple sub-grid correlations, such as $\overline{\rho' \xi_k{}' \mathbf{u}'}$.

To reduce the number of modeled terms, Favre (1965) introduced density-weighted averaging, that was subsequently extended to density-weighted LES filtering. In this context, the Favre-filtering of a field is denoted as:

$$\widetilde{\psi}(\mathbf{x}, t) = \frac{\overline{\rho\psi}}{\overline{\rho}} = \frac{\int_\Omega \rho(\mathbf{x}^*, t)\psi(\mathbf{x}^*, t)G(\Delta, \mathbf{x}, \mathbf{x}^*)\mathrm{d}\mathbf{x}^*}{\int_\Omega \rho(\mathbf{x}^*, t)G(\Delta, \mathbf{x}, \mathbf{x}^*)\mathrm{d}\mathbf{x}^*}, \tag{5.9}$$

where ρ is the unfiltered density field. It is important to stress again, that neither of the filtering operations is executed explicitly in this work, they are simply a mathematical tool to understand the underlying meaning of the resolved fields. The instantaneous field may be decomposed now in a different manner as:

$$\psi(\mathbf{x}^*, t) = \widetilde{\psi}(\mathbf{x}, t) + \psi''(\mathbf{x}^*, t), \tag{5.10}$$

where ψ'' is the Favre-filtered sub-grid fluctuation of ψ. Based on Eq. (5.9) terms in the form of $\overline{\rho\psi}$ are simply replaced by $\overline{\rho}\widetilde{\psi}$. Consequently the above example of the convective scalar flux, becomes:

$$\overline{\rho\xi_k\mathbf{u}} = \overline{\rho}\widetilde{\xi_k\mathbf{u}} = \overline{\rho}\widetilde{\xi}_k\widetilde{\mathbf{u}} + \overline{\rho}\widetilde{\xi}_k\widetilde{\mathbf{u}''} + \overline{\rho}\widetilde{\xi_k''}\widetilde{\mathbf{u}} + \overline{\rho}\widetilde{\xi_k''\mathbf{u}''} \tag{5.11}$$

where only the density-weighted double correlations need to be modeled.

Figure 5.2 shows a similar plot as the case of non-density-weighted filtering, but with applying Favre-filtering. In the second row of plots, the integrals of Eq. (5.9) are illustrated using a local plot of $\rho(\mathbf{x}^*, t)\psi(\mathbf{x}^*, t)/\overline{\rho}(\mathbf{x}, t)$. In this example problem, the two filtered fields: $\overline{\psi}$ and $\widetilde{\psi}$ are fairly similar, even though the integrated areas, shaded in Fig. 5.1 and Fig. 5.2, have radically different shapes. The difference only becomes notable in case of the largest filter size. To fully relate the two quantities, one may use the definition of the Favre-filtering:

$$\widetilde{\psi} = \overline{\psi} + \frac{\overline{\rho\psi} - \overline{\rho}\overline{\psi}}{\overline{\rho}}. \tag{5.12}$$

As the above equation suggests, if there is a strong positive sub-grid correlation between the density and the field ($\overline{\rho\psi} > \overline{\rho}\overline{\psi}$), then the Favre-filtered quantity is greater. This is exactly the case of Fig. 5.2, where on the left of the studied domain ρ and ψ rise together sharply. Meanwhile, in the rest of the domain the relation is less obvious, and the two filtered values are closer. Irrespective of the correlation, as the filter width approaches the smallest scales of the fields, both $\overline{\psi}$ and $\widetilde{\psi}$ approach the unfiltered field. The relation of these two filtering operations is further examined in appendix H, demonstrating that the difference between the two is bounded by $\sqrt{\overline{\psi^2} - \overline{\psi}^2}\sqrt{\overline{\rho^2} - \overline{\rho}^2}/\overline{\rho}$.

Analogously to the density weighted filtering, a Favre time-averaging may be defined as well, here denoted with curly brackets following Poinsot and Veynante (2005, §4.7.7):

$$\{\psi\} = \frac{\langle\rho\psi\rangle}{\langle\rho\rangle}, \tag{5.13}$$

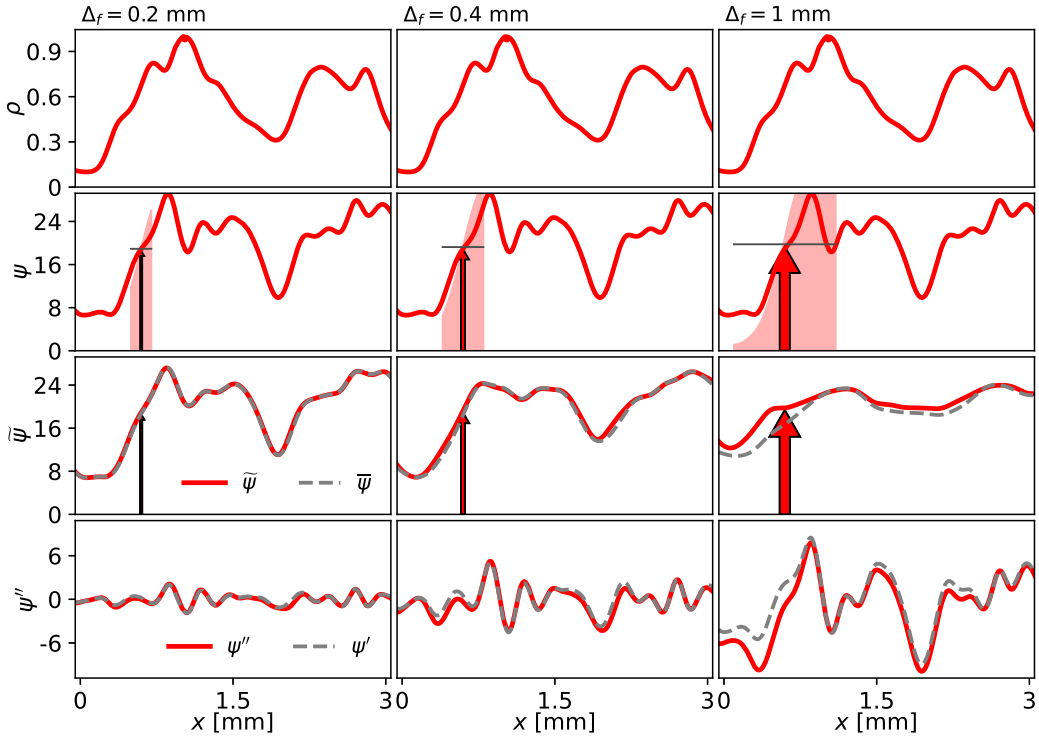

FIGURE 5.2: Illustration of Favre-filtered and sub-grid components of a 1D field using the box filter with different filter lengths. The different columns correspond to filter widths of $\Delta_f \in \{0.2, 0.4, 1.0\}$mm respectively, while the rows show the density, the unfiltered filed, the filtered field, and the sub-grid fluctuations. The non-density-weighted filtered field, and corresponding filtered fluctuations are shown with dashed lines.

with the corresponding decomposition:

$$\psi(\mathbf{x}, t) = \{\psi\}(\mathbf{x}) + \psi^{\dagger\dagger}(\mathbf{x}, t), \tag{5.14}$$

where $\psi^{\dagger\dagger}$ represents the density weighted fluctuations in time. Similarly to Reynolds-averaging, the double execution of the Favre-averaging operator does not modify the mean: $\{\{\psi\}\} = \{\psi\}$, and the Favre-average of the density weighted fluctuations is zero: $\{\psi^{\dagger\dagger}\} = 0$. However, as Bilger (1975) points out, to relate Favre-averaged quantities to the standard time averages, one needs information on the temporal cross correlation of density fluctuations and the fluctuation of the quantity itself:

$$\langle\psi\rangle = \{\psi\} - \frac{\langle\rho^{\dagger}\psi^{\dagger}\rangle}{\langle\rho\rangle}, \tag{5.15}$$

and this term is non-zero, since density and the transported scalars are not statistically independent. For example, when molecular hydrogen is mixed into an oxidizer, the lower densities are constantly associated with higher hydrogen mass fractions, thus $\langle Y_{H_2}\rangle$ would differ from $\{Y_{H_2}\}$ significantly.

Statistical description of the filtering

Relating the standard LES filter and the density-weighted filter is frequently done in a statistical manner. A major concept in this regard, is the filter density function (FDF) that describes the instantaneous sub-grid state. FDFs and joint FDFs are powerful tools for relating the resolved and filtered fields without the need of completely resolving the unknowns. (Colucci et al., 1998; Mustata et al., 2006; Raman, Pitsch, and Fox, 2006) The direct application of this concept is out of the scope of the present work. However, appendix H uses the joint filter density functions of density and an unknown to provide additional explanation on the difference between $\overline{\psi}$ and $\widetilde{\psi}$ observed in the example of Fig. 5.2. Furthermore, an upper bound is given for the difference of the two filtered quantities $|\widetilde{\psi} - \overline{\psi}| \leq \sqrt{\overline{\psi^2} - \overline{\psi}^2}\sqrt{\overline{\rho^2} - \overline{\rho}^2}/\overline{\rho}$.

Pitsch (2006) points out, that many of the probabilistic methods are adapted directly from RANS models, but these need to be re-evaluated in the LES context as sub-grid statistics can behave quite differently from the ensemble or temporal statistics of RANS. It is important to clarify, that the filter density functions discussed in appendix H are in fact *random variables* in the sense, that the FDF values depend directly on the particular realization of the flow field. (Fox, 2003, §4.2.2) To achieve a true statistical description of the sub-grid scales, one would need to perform an ensemble averaging of various FDFs, that result in the same filtered field *in all parts of the domain*. This averaging would result in the filter probability density function (FPDF) of the field at a single point and time instance that is an actual statistical quantity. Since this ensemble averaging is conditioned on having the same filtered field in different realizations, the FPDF can be used like the FDF to obtain the mean values:

$$\overline{\psi}(\mathbf{x}, t) = \int_{-\infty}^{\infty} \psi^* P_\psi(\psi^*; \mathbf{x}, t) \mathrm{d}\psi^*, \tag{5.16}$$

where P_ψ is the marginal FPDF of field ψ. In the context of using the box filter, $P_\psi(\psi^*)\mathrm{d}\psi^*$ may be interpreted as the probability of encountering a value of the unfiltered field in the $[\psi^* - \frac{1}{2}\mathrm{d}\psi^*, \psi^* + \frac{1}{2}\mathrm{d}\psi^*]$ interval within the filter volume, by selecting among equal infinitesimal control volumes within the filter. Note, that this interpretation becomes more complex in case of other filter types.

The validity of Eq. (5.16) follows from the definition of the FPDF, however, it is not guaranteed that at a certain time instance the FPDF can give the filtered value of higher modes of ψ as Eq. (H.5) does. These higher filtered modes evaluated using the FPDF in place of the FDF are simply the statistically most likely values. The same is true of non-linear functions of the field ψ. Given the FPDF, the filtered value of such non-linear functions (f) may be estimated with their expected filtered value:

$$\overline{f(\psi)}(\mathbf{x}, t) \approx \int_{-\infty}^{\infty} f(\psi^*) P_\psi(\psi^*; \mathbf{x}, t) \mathrm{d}\psi^*. \tag{5.17}$$

Furthermore, one may define joint filter probability density functions of more fields. The joint FPDF is an ensemble average of the corresponding joint FDFs, now conditioned on having the same filtered field of all variables in the entire domain. Here the joint PFDF is denoted: $P_{\psi_1\psi_2\ldots\psi_N}$. In particular, the joint PFDF of density and an unknown ψ: $P_{\psi\rho}$ is relevant in the computation of Favre-filtered quantities. For this purpose the marginal density-weighted filter probability density function

(Pitsch, 2006) of ψ is possible to express as:

$$\overline{\rho}\widetilde{P}_{\psi}(\psi^*) = \int_{-\infty}^{\infty} P_{\psi\rho}(\psi^*, \rho^\bullet; \mathbf{x}, t)\mathrm{d}\rho^\bullet. \tag{5.18}$$

Continuing the analogy of the box filter, $\widetilde{P}_{\psi}(\psi^*)\mathrm{d}\psi^*$ would still express the probability of finding a value of the unfiltered field in the $[\psi^* - \frac{1}{2}\mathrm{d}\psi^*, \psi^* + \frac{1}{2}\mathrm{d}\psi^*]$ interval, however the location is selected from infinitesimal control volumes containing equal mass. In the context of the present work, the density-weighted FPDF of the control variables of tabulated chemistry models is further discussed in section 5.4.

5.1.2 Scales of turbulent motion in LES

Section 5.1.1 demonstrates the effect of filtering on 1D profiles, and shows how these example signals become smoother as the consequence of the filtering. This gives a feeling of the behavior of filtered scalar fields, however, the case of vector fields is better illustrated by Fig. 5.3. In this representation, the turbulent flow is understood as a superposition of eddies of various size and speed. As Fig. 5.3b shows, in LES only the larger of these eddies will be captured by the computational mesh, and the smaller ones are forming the unresolved sub-grid field.

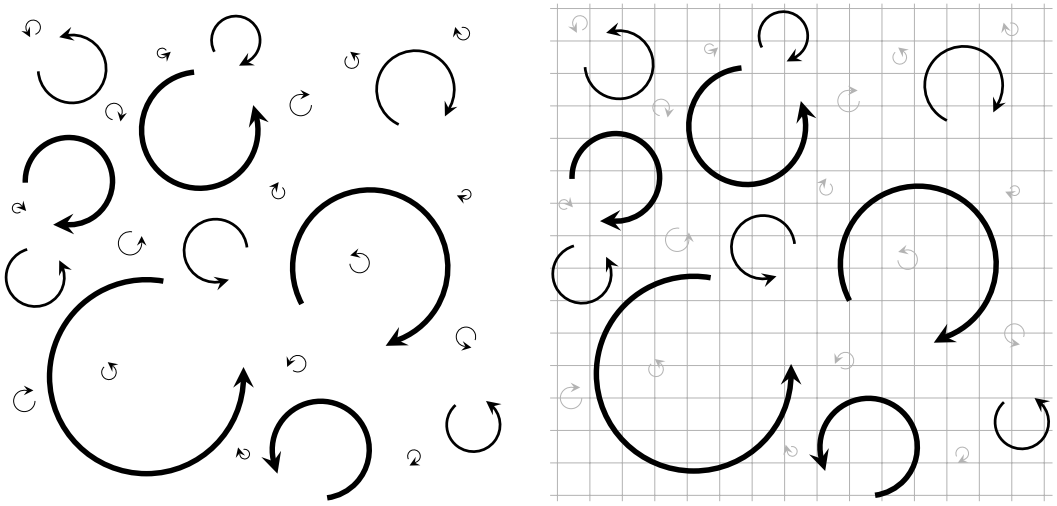

(A) True flow. (B) Resolved and sub-grid components.

FIGURE 5.3: Illustration of turbulent eddies and their resolved and sub-grid scales.

In fluid flow problems the range of length scales naturally has an upper limit associated to the geometrical length scales of the case. In internal flows of combustion devices an eddy cannot be larger than the combustion chamber itself. Nevertheless these largest geometric length scales are seldom reached by a single coherent eddy. Instead, as Peters (2001, §1.4) summarizes, the *integral length scale* can be referred from the two-point spacial correlation of a turbulent velocity component (e.g.: $u^\dagger$.) This length scale expresses the mean distance that may separate two points such, that the instantaneous turbulent motion in these points is still significantly related, thus it provides a length scale of the large turbulent structures. Nevertheless, the integral length scale is indeed comparable to specific geometrical scales of the flow (Pope, 2000, §6.1.1), such as the width of a narrow channel, or the diameter of a jet.

The mean flow suffers hydrodynamic instabilities and forms the largest eddies. Or in an alternate point of view: the largest eddies interact with the mean flow, and extract kinetic energy from it. In return, similar processes occur between the largest eddies and somewhat smaller ones, as the largest eddies themselves are unstable as well. These large eddies deform the others and transfer kinetic energy to them. The kinetic energy transfer is the strongest at neighboring eddy sizes. If there is a large disparity between the two vortical structures, then the smaller eddy is simply advected around the larger one. The process of energy exchange predominantly occurs between neighboring scales, thus creating the so called *turbulent energy cascade*. (Kundu, Cohen, and Dowling, 2015, §12.7) The cascade terminates with the smallest occurring eddies, where, with the decrease of the eddy Reynolds number, the viscous effects become dominant and the kinetic energy is dissipated into heat. Since this dissipation occurs predominantly on the smallest sales, the energy transfer between larger scales is mostly constant, determined by the average kinetic energy dissipation rate of the turbulent motion.

The smallest turbulent scales are named in honor of Kolmogorov (1941), who suggested the theory of determining their size in incompressible flow. Accordingly, in locally homogeneous and isotropic turbulence, the smallest turbulent scales are solely a function of the viscosity, and the average turbulent kinetic energy dissipation rate. This readily provides appropriate length, time and velocity scales for incompressible flow, respectively:

$$\eta_{inco} = \left(\frac{\langle \nu \rangle^3}{\langle \varepsilon \rangle} \right)^{1/4}, \qquad \tau_{\eta,inco} = \left(\frac{\langle \nu \rangle}{\langle \varepsilon \rangle} \right)^{1/2}, \qquad v_{\eta,inco} = \left(\langle \nu \rangle \langle \varepsilon \rangle \right)^{1/4}, \tag{5.19}$$

where $\langle \varepsilon \rangle$ is the Reynolds-averaged turbulent kinetic energy dissipation rate of the flow, and $\langle \nu \rangle$ is the Reynolds-averaged kinematic viscosity that is generally constant, thus the averaging does not take effect. Here, the averaging is included to define these scales in a general sense.

The extension of this hypothesis to variable density problems is not straightforward, and different solutions are proposed even in more recent works. As appendix I discusses, the turbulent kinetic energy $\{k\} = \frac{1}{2}\{\mathbf{u}'' \cdot \mathbf{u}''\}$ is indeed dissipated at a rate of $\{\varepsilon\}$, however, this has no direct insight on the energy cascade. Knaus and Pantano (2009) studied the direct numerical simulation of different non-reacting and reacting mixing layers (non-premixed combustion) with infinitely fast chemistry, and found that substituting the Favre-averaged kinematic viscosity and dissipation rate into the relations of Kolmogorov still provides a good estimate of the smallest turbulent scales. As Bilger (2004) describes the phenomenon, in turbulent non-premixed flames the turbulence dominates over thermal dilatation, since the rate of dilatation is tied to the diffusion of mixture fraction that is relatively less intense.

Contrarily, in turbulent premixed flames of industrial relevance the effects of dilatation and that of turbulent strain are comparable. (Bilger, 2004) Nevertheless, the same Favre-averaged properties are often used to describe the smallest scales. (Hawkes et al., 2012) Recently Kolla et al. (2014) revisited the phenomena using the DNS of a premixed slot-jet flame. They found large deviations compared to the incompressible behavior of the energy cascade. Namely, in this turbulent premixed flame the thermal dilation effects may generate kinetic energy on the small scales, comparable to the thermal flame thickness. Consequently, *back scatter* happens, i.e.: the energy transfer is no longer unidirectional and the image of the turbulent energy

cascade becomes questionable. A range of small scales become affected. More recently MacArt, Grenga, and Mueller (2018) found a quantitative limit, where back scatter is significant. They state, that intense back scatter happens at Karlovitz numbers of: $Ka < \frac{\rho^u}{\rho^b} - 1$ where $\frac{\rho^u}{\rho^b}$ is the density ratio between the fresh reactants and the burn gases. For the interpretation of this non-dimensional limit see section 5.3.2.

Nevertheless, using the Favre-averaged kinematic viscosity and turbulent kinetic energy dissipation rate is retained here, as they still provide a suitable approximation. The Kolmogorov scales of length, time and velocity, following Knaus and Pantano (2009) are then:

$$\eta = \left(\frac{\{\nu\}^3}{\{\varepsilon\}} \right)^{1/4}, \qquad \tau_\eta = \left(\frac{\{\nu\}}{\{\varepsilon\}} \right)^{1/2}, \qquad v_\eta = \left(\{\nu\} \{\varepsilon\} \right)^{1/4}, \tag{5.20}$$

where $\{\varepsilon\}$ and $\{\nu\}$ are the Favre-averaged turbulent kinetic energy dissipation rate and kinematic viscosity respectively.

As Fig. 5.3 illustrates, in LES the smallest length scales, including the Kolmogorov, scales are not resolved. Consequently, the resolved turbulent flow field is missing the mechanism, that is responsible for dissipating the turbulent kinetic energy. If appropriate models are not applied to dissipate the kinetic energy, the simulations would likely be impossible, since the resolved part of the energy cascade is still functional, thus kinetic energy would accumulate at the smallest resolved scales indefinitely. The method of introducing the correct amount of dissipation on the resolved scales is described in section 5.1.4.

The Kolmogorov scales provide a lower limit of the observed scales, however, the large scales can be characterized by a myriad of differently defined quantities. Fox (2003, §2) provides a comprehensive overview of the different scales. Including ones based on spacial correlations dubbed *longitudinal and transversal integral scales*, ones using temporal correlations simply referred to as *integral scales*, and ones that relate the dissipation rate to the turbulent kinetic energy: $\langle k \rangle$ labeled *turbulence integral scales*. They also define the eddy turnover time, using the longitudinal integral length scale and the velocity scale taken as the square root of $\langle k \rangle$. Note the difference compared to the velocity scale of Peters (2001, §1.4), where a $\sqrt{2/3}$ factor is introduced in the velocity scale to obtain the mean value of a single velocity component assuming isotropy. Furthermore, many of these descriptions originate from incompressible turbulence and they do not address the effect of density variations. To address this, Kolla et al. (2014) redefined the spatial correlation functions including density variations, and found valuable insight about the underlying physics. To be consistent with the Kolmogorov scales of Eq. (5.20), the present work also considers density variations in the form of Favre-averaging, however, evaluating spatial correlations is out of the scope of this study, thus the turbulence integral scales of Fox (2003) are applied without any constant factors. Thus, the turbulent kinetic energy is calculated as:

$$\{k\} = \left\{ e_K - \frac{1}{2} \{\mathbf{u}\} \cdot \{\mathbf{u}\} \right\} = \frac{1}{2} \left(\left\{ u''^2 \right\} + \left\{ v''^2 \right\} + \left\{ w''^2 \right\} \right), \tag{5.21}$$

and the turbulence integral scales of length, time, and velocity are:

$$\ell_t = \frac{\{k\}^{3/2}}{\{\varepsilon\}}, \qquad \tau_t = \frac{\{k\}}{\{\varepsilon\}}, \qquad v' = \sqrt{\{k\}}, \tag{5.22}$$

which ensures the consistency between the three scales: $v' = \ell_t/\tau_t$, and avoids the introduction of scalar factors. The Reynolds number associated to the turbulence integral scales is:

$$Re_t = \frac{\ell_t v'}{\{\nu\}} = \frac{\{k\}^2}{\{\varepsilon\}\{\nu\}}. \tag{5.23}$$

The turbulence Reynolds number determines the ratio of the integral scales and the Kolmogorov scales as:

$$\frac{\ell_t}{\eta} = \frac{\{k\}^{3/2}\{\varepsilon\}^{1/4}}{\{\varepsilon\}\{\nu\}^{3/4}} = Re_t^{3/4}, \tag{5.24}$$

$$\frac{\tau_t}{\tau_\eta} = \frac{\{k\}\{\varepsilon\}^{1/2}}{\{\varepsilon\}\{\nu\}^{1/2}} = Re_t^{1/2}, \tag{5.25}$$

$$\frac{v'}{v_\eta} = \frac{\{k\}^{1/2}}{\{\varepsilon\}^{1/4}\{\nu\}^{1/4}} = Re_t^{1/4}. \tag{5.26}$$

Here such scales are only used for order of magnitude estimates during post-processing, thus the details are of lesser importance. The Kolmogorov and turbulence integral scales are further discussed in section 5.1.6, where the scales are estimated based on LES results.

Figure 5.3 provides an idealistic view on turbulence. In practice, starting from the complete turbulent vector field the identification of such coherent structures is a complex task. Such a superposition of different length scales is typically studied using Fourier transformation. Pope (2000, §6.4) details the three-dimensional Fourier analysis of the velocity fields, while Peters (2001, §1.4) provides a more intuitive illustration based on dimensional analysis. Here the detailed description of two-point velocity correlations and the Fourier transformation is omitted. Instead, the kinetic energy spectrum function of locally isotropic and homogeneous turbulence: $E(\kappa)$ is introduced directly. This property expresses the kinetic energy associated to a wave number $\kappa = 2\pi/\ell$ such, that the total turbulent kinetic energy of the flow is:

$$\{k\} = \int_0^\infty E(\kappa)\mathrm{d}\kappa, \tag{5.27}$$

where $E(\kappa)\mathrm{d}\kappa$ is the kinetic energy contained in the $[\kappa - \frac{1}{2}\mathrm{d}\kappa, \kappa + \frac{1}{2}\mathrm{d}\kappa]$ wave number interval. The behavior of this spectrum can be well illustrated using the model function of Von Kármán (1948) and Pao (1965):

$$E^{KP}(\kappa) = C_K \frac{\{k\}^{5/2}}{\{\varepsilon\}} \underbrace{\left(\frac{\kappa}{\kappa_e}\right)^4}_{\mathrm{I}} \underbrace{\left(1 + \left(\frac{\kappa}{\kappa_e}\right)^2\right)^{-17/6}}_{\mathrm{II}} \underbrace{e^{\left(-\frac{3C_K}{2}(\kappa\eta)^{4/3}\right)}}_{\mathrm{III}}, \tag{5.28}$$

where C_K is the Kolmogorov constant, and $\kappa_e = \frac{2}{\ell_t}$ is a wave number associated to the large scales. (Bailly and Juve, 1999) Note, that κ_e does not correspond exactly to the wave number of turbulence integral scales defined in Eq. (5.22). Sreenivasan (1995) has concluded that $C_K \approx 0.5$ is a reasonable value of the Kolmogorov constant, that is also used here for demonstration.

The turbulent kinetic energy spectrum is illustrated in Fig. 5.4 using the model function of Von Kármán (1948) and Pao (1965). The example uses an integral length

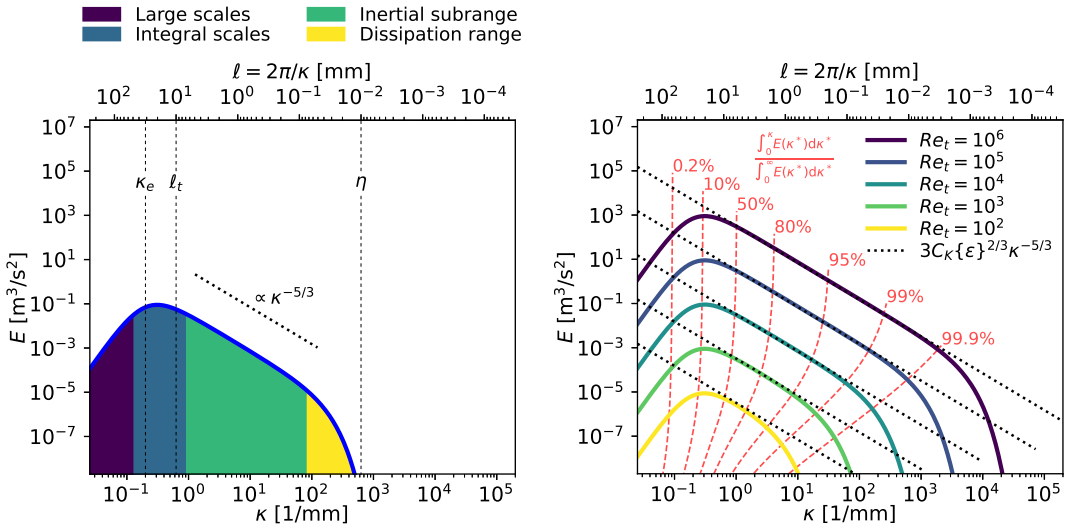

(A) Example at $Re_t = 10000$.

(B) Energy content in the spectrum.

FIGURE 5.4: Turbulent kinetic energy spectrum of homogeneous isotropic turbulence characterized by $\ell_t = 10$ mm following Von Kármán (1948) and Pao (1965). (Assuming a constant kinematic viscosity of $\nu = 10^{-5}$ m^2/s.)

scale of $\ell_t = 10$mm, that is representative to the turbulent cases studied in the present work, as ℓ_t is proportional to the typical length scales of the geometry. Moreover, a constant kinematic viscosity of $\nu = 10^{-5}$ m^2/s is imposed in this example. The figures show E as function of the wave number in double logarithmic scale. For reference, the length scales corresponding to the wave numbers are also displayed on the upper horizontal axis. The left figure (Fig. 5.4a) illustrates the regimes of the turbulent kinetic energy spectrum dominated by different physical phenomena. This example imposes $Re_t = 10000$, thus the Kolmogorov length scale is $\eta = 0.01$ mm according to Eq. (5.24). Note, that such variety of scales is impossible to illustrate on figures like Fig. 5.3. The large scales, corresponding to the smallest wave numbers, are characterized by moderate $E(\kappa)$. In fact, the logarithmic horizontal axis exaggerates their energy content, as in this particular example the shaded area of the large scales corresponds to only 1% of the turbulent kinetic energy. The behavior of this large scales is modeled by term I in Eq. (5.28). The next regime: the integral scales, is associated to the most energy content. It encompasses the characteristic wave number of the von Kármán-Pao spectrum: κ_e, the location of peak value of E: $\kappa = \sqrt{12/5}\kappa_e$, and the turbulence integral length scale: ℓ_t. The shaded area in this case corresponds to 49% of $\{k\}$, illustrating, that indeed this regime contains a large part of the total turbulent kinetic energy. The inertial subrange, characterized by higher wave numbers, is where the mechanism of the turbulent energy cascade functions. Turbulent motion is created by flow instabilities on the integral scales, and it is transported through the inertial subrange by larger structures breaking up into smaller ones. As both the turbulent kinetic energy production and the viscous dissipation are negligible in this part of the spectrum, the behavior of this regime is universal in locally homogeneous isotropic turbulence. This universal nature of turbulence is captured by the Kolmogorov spectrum, that follows an $E \propto \kappa^{-5/3}$ relationship, and describes the behavior of the inertial subrange. In the von Kármán-Pao spectrum this proportionality is captured by the product of term I and II. In the

example, the region associated with the inertial subrange contains 49.5% of $\{k\}$. Finally, viscous forces become substantial in the dissipation range, where the viscous work converts the turbulent kinetic energy into heat. The lower limit of meaningful length scales (highest wave numbers) is given by the Kolmogorov scale: η. Term III of Eq. (5.28) models this behavior. The highlighted region contains only 0.5% of the total turbulent kinetic energy.

The inertial subrange is characterized by constant energy transfer rate between scales, i.e.: the turbulent energy cascade. (Pope, 2000, §6.1.2) Under these conditions the eddy size and the turbulent kinetic energy dissipation rate: $\{\varepsilon\}$ uniquely defines the velocity and time scales, and relates them to the integral and Kolmogorov scales:

$$v_\ell = v' \left(\frac{\ell}{\ell_t}\right)^{1/3} = v_\eta \left(\frac{\ell}{\eta}\right)^{1/3}, \qquad \tau_\ell = \tau_t \left(\frac{\ell}{\ell_t}\right)^{2/3} = \tau_\eta \left(\frac{\ell}{\eta}\right)^{2/3}. \tag{5.29}$$

At all these scales the transfer rate of kinetic energy in the turbulent energy cascade is constant: $\{\varepsilon\} = v_\ell^2/\tau_\ell = v_\ell^3/\ell = \ell^2/\tau_\ell^3$. Furthermore, the relations of Eq. (5.24), Eq. (5.25), and Eq. (5.26) are generally true using the Reynolds number of the intermediate scale: $Re_\ell = \ell v_\ell / \{\nu\}$.

The regions in Fig. 5.4a are chosen arbitrarily based on the behavior of the $E(\kappa)$ curve. A more complete view is provided by Fig. 5.4b, that presents a parametric evaluation of the spectrum. Here the turbulence Reynolds number is varied in the set: $Re_t \in \{100, 1000, ..., 1000000\}$, while the integral length scale is kept constant: $\ell_t = 10$ mm. The partial energy content is indicated along the spectrum. The figure also illustrates the exact values of the Kolmogorov spectrum: $E(\kappa) = 3C_K \{\varepsilon\}^{2/3} \kappa^{-5/3}$, which captures the behavior of the inertial subrange. The largest scales of the inertial subrange in Fig. 5.4a are chosen as the point, where the definite integral of the spectrum on the $\kappa^* \in [0, \kappa]$ interval reaches 50% of the total turbulent kinetic energy. As Fig. 5.4b demonstrates, this 50% limit indeed appears to coincide with the start of the inertial subrange, given a high enough turbulence Reynolds number.

A frequently used criterion, for the assessment of grid quality in LES, is requiring, that at least 80% of the turbulent kinetic energy should be represented by the filtered velocity field. (Pope, 2000, §13.1) In the example of Fig. 5.4b this limit consistently lies in the inertial subrange, where the turbulent motion is expected to behave rather universally. Thus, the existence of case-independent models appears to be possible. The 80% isoline becomes perpendicular to the κ axis at high Reynolds numbers, suggesting, that this criterion is only a function of the integral length scale in highly turbulent flows which is dictated by the geometry. Another possible quality criterion is comparing the filter scale to the Kolmogorov scale. If Δ_f/η is required to be bounded, then the mesh has to follow the $\Delta_f \propto Re_t^{-3/4}$ scaling.

The effect of large-eddy simulation on the turbulent kinetic energy spectrum is illustrated in Fig. 5.5. The curve labeled as the "True spectrum" corresponds to the von Kármán-Pao spectrum at $Re_t = 10000$ depicted in Fig. 5.4a. Different LES modeling scenarios are illustrated, that may arise from the culmination of numerical dissipation and the explicitly introduced dissipation of the LES model. The "Ideal LES" modeling introduces just the right amount of dissipation, acting near the cut-off wave number, so in a large portion of the spectrum the solution corresponds to the fully resolved "True spectrum". Specifically, the larger scales containing 80% of $\{k\}$ are identical. A more concerning situation is depicted by the "Dissipative LES" curve, where due to different sources of dissipation the spectrum deviates significantly form ideal. This solution substantially influences even the energy containing

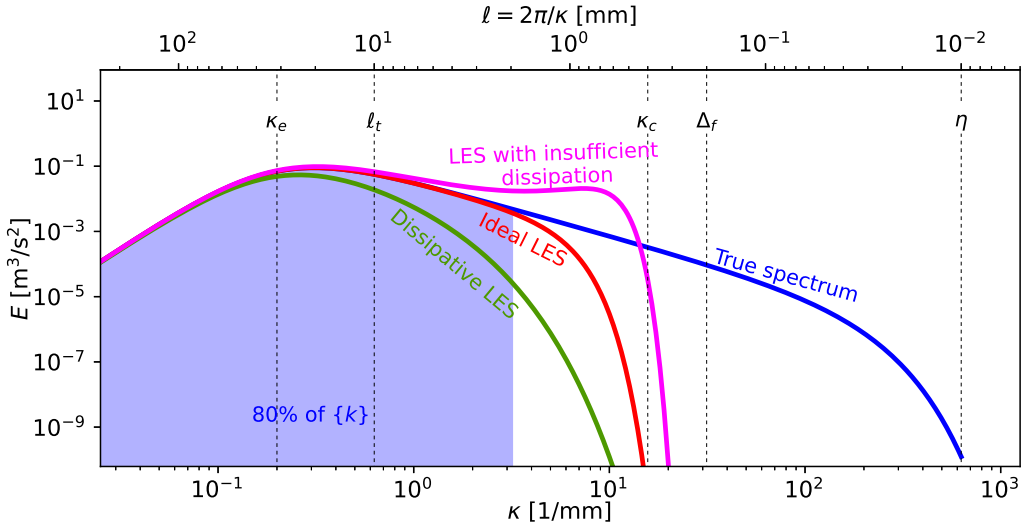

FIGURE 5.5: Illustration of turbulent kinetic energy spectrum in LES based on the von Kármán-Pao spectrum. The example is characterized by $\ell_t = 10$ mm, $Re_t = 10000$, $\nu = 10^{-5}$ m^2/s. The LES filter size is chosen as $\Delta_f = 20\eta$, corresponding to a cut-off wave number of $\kappa_c = \pi/\Delta_f$.

integral scales, thus changing the physical phenomena on all scales. Finally, another way to deviate significantly from the physical behavior is by under-predicting the dissipation, labeled as: "LES with insufficient dissipation". In this example the smallest resolved scales lack the correct mechanism of dissipation, thus kinetic energy accumulates in this regime. In the resolved fields this may manifest as spurious small-scale oscillations, however, if the model does not include any dissipation, then these oscillations may grow indefinitely and lead to divergence. In the present work, low-dissipation numerical methods are combined with explicit sub-grid models, which create the desired kinetic energy dissipation rate (ε^{tot} defined in Eq. (2.75)) on the resolved scales, thus aspiring to reach the "Ideal LES" scenario. (Lehmkuhl et al., 2019b) Note the difference compared to the implicit LES method, that uses the existing numerical dissipation to model the unresolved part of ε^{tot}. (Grinstein, Margolin, and Rider, 2007)

5.1.3 Filtered equations

In large-eddy simulation the filtering operator is not applied on the fields themselves, but on the governing equations. Through the rearrangement of the operators, new governing equations are obtained, where the unknowns are the filtered quantities. If the LES model is well designed, then these filtered quantities can be represented well on the applied computational grid, and the equations may be solved numerically. The filtered version of the generic governing equations of section 2.3.2

are then written in the following form:

$$\partial_t \overline{\rho} + \nabla \cdot (\overline{\rho}\widetilde{\mathbf{u}}) = \overline{S_\rho}, \tag{5.30}$$

$$\partial_t (\overline{\rho}\widetilde{\mathbf{u}}) + \nabla \cdot (\overline{\rho}\widetilde{\mathbf{u}} \otimes \widetilde{\mathbf{u}}) + \nabla \overline{p} - \nabla \cdot \overline{\boldsymbol{\tau}(\mathbf{u})} + \nabla \cdot \underbrace{\left(\widetilde{\overline{\rho}\mathbf{u} \otimes \mathbf{u}} - \overline{\rho}\widetilde{\mathbf{u}} \otimes \widetilde{\mathbf{u}}\right)}_{\boldsymbol{\tau}^{SGS}} = \overline{S_{\mathbf{u}}}, \tag{5.31}$$

$$\partial_t \left(\overline{\rho}\widetilde{\xi_k}\right) + \nabla \cdot \left(\overline{\rho}\widetilde{\xi_k}\widetilde{\mathbf{u}}\right) + \nabla \cdot \overline{\boldsymbol{\Phi}_k} + \nabla \cdot \underbrace{\left(\widetilde{\overline{\rho}\xi_k\mathbf{u}} - \overline{\rho}\widetilde{\xi_k}\widetilde{\mathbf{u}}\right)}_{\boldsymbol{\Phi}_k^{SGS}} = \overline{S_k}, \tag{5.32}$$

where $\boldsymbol{\tau}^{SGS}$ and $\boldsymbol{\Phi}_k^{SGS}$ are the sub-grid scale stress tensor and sub-grid scale scalar flux respectively, which are to be modeled according to section 5.1.4. The filtered form of the diffusive terms is simply expressed using the filtered quantities:

$$\overline{\boldsymbol{\tau}(\mathbf{u})} = 2\overline{\mu}\widetilde{\mathbf{S^D}(\mathbf{u})} = \overline{\mu}\left(\nabla\widetilde{\mathbf{u}} + \nabla^{\mathrm{T}}\widetilde{\mathbf{u}}\right) - \frac{2}{3}\overline{\mu}\left(\nabla \cdot \widetilde{\mathbf{u}}\right)\mathbf{I} \tag{5.33}$$

$$\overline{\boldsymbol{\Phi}_k} = -\overline{\rho}\widetilde{\mathcal{D}_t}\nabla\widetilde{\xi_k}, \tag{5.34}$$

where the bulk viscosity effects are neglected following the Stokes assumption. (Kundu, Cohen, and Dowling, 2015, §4.5) The thermal diffusivity $\mathcal{D}_t = \frac{\lambda}{\rho c_p}$ is used in the transport of all scalar fields, according to the unity Lewis-number assumption. Note, that the weak form of these equations is analogous to the weak form of the unfiltered governing equations presented in section 2.3.2, thus the transformation is not repeated here.

Higher moments

Additional governing equations may be obtained by the filtering of the PDEs presented in section 2.3.3. The transport equation of the filtered second moment of scalars takes the form:

$$\partial_t \left(\overline{\rho}\widetilde{\xi_k^2}\right) + \nabla \cdot \left(\overline{\rho}\widetilde{\xi_k^2}\widetilde{\mathbf{u}}\right) + \nabla \cdot \overline{\boldsymbol{\Phi}_{k^2}} + \nabla \cdot \underbrace{\left(\widetilde{\overline{\rho}\xi_k^2\mathbf{u}} - \overline{\rho}\widetilde{\xi_k^2}\widetilde{\mathbf{u}}\right)}_{\boldsymbol{\Phi}_{k^2}^{SGS}} = 2\overline{\xi_k S_k} - \overline{\rho}\widetilde{\chi_{\xi_k}} - \overline{\xi_k^2 S_\rho}, \tag{5.35}$$

where $\overline{\boldsymbol{\Phi}_{k^2}} = -\overline{\rho}\widetilde{D_t}\nabla\widetilde{\xi_k^2}$ is the resolved flux of ξ_k^2, while $\boldsymbol{\Phi}_{k^2}^{SGS}$ is its sub-grid scale counterpart. The latter term, and the terms on the right hand side all necessitate closure models. The filtered scalar dissipation term may be decomposed to a resolved and sub-grid component as: $\widetilde{\chi_{\xi_k}} = 2\widetilde{D_t}\nabla\widetilde{\xi_k} \cdot \nabla\widetilde{\xi_k} + \chi_{\xi_k}^{SGS}$, where the sub-grid scalar dissipation rate needs modeling. Such higher moments are used in this work, to obtain information about the sub-grid distribution of transported scalars.

Similarly to the derivations of section 2.3.3, a transport equation may be constructed for the square of the filtered unknown by multiplying Eq. (5.32) by $2\widetilde{\xi_k}$ and using the filtered continuity equation Eq. (5.30):

$$\partial_t \left(\overline{\rho}\widetilde{\xi_k}^2\right) + \nabla \cdot \left(\overline{\rho}\widetilde{\xi_k}^2\widetilde{\mathbf{u}}\right) - \nabla \cdot \left(\overline{\rho}\widetilde{D_t}\nabla\widetilde{\xi_k}^2\right) =$$
$$-2\nabla \cdot \left(\widetilde{\xi_k}\boldsymbol{\Phi}_k^{SGS}\right) + 2\boldsymbol{\Phi}_k^{SGS} \cdot \nabla\widetilde{\xi_k} + 2\widetilde{\xi_k}\overline{S_k} - 2\overline{\rho}\widetilde{D_t}\nabla\widetilde{\xi_k} \cdot \nabla\widetilde{\xi_k} - \widetilde{\xi_k}^2\overline{S_\rho}, \tag{5.36}$$

where the term: $2\widetilde{\xi}_k \nabla \cdot \mathbf{\Phi}_k^{SGS}$ is split as:

$$2\widetilde{\xi}_k \nabla \cdot \mathbf{\Phi}_k^{SGS} = 2\nabla \cdot \left(\widetilde{\xi}_k \mathbf{\Phi}_k^{SGS} \right) - 2\mathbf{\Phi}_k^{SGS} \cdot \nabla \widetilde{\xi}_k. \tag{5.37}$$

One may define the Favre-filtered sub-grid variance of a scalar ξ as:

$$\xi_{k,v} = \widetilde{\xi_k^2} - \widetilde{\xi}_k^{\,2} \tag{5.38}$$

The importance of such quantities is illustrated in Appendix H. In particular, $\xi_{k,v}$ is the variance associated to the marginal density-weighted filter probability density function of ξ defined in Eq. (5.18). A transport equation for the sub-grid variance is reached by subtracting Eq. (5.36) from Eq. (5.35):

$$\begin{aligned} &\partial_t \left(\overline{\rho} \xi_{k,v} \right) + \nabla \cdot \left(\overline{\rho} \xi_{k,v} \widetilde{\mathbf{u}} \right) - \nabla \cdot \left(\overline{\rho} \widetilde{D_t} \nabla \xi_{k,v} \right) + \nabla \cdot \underbrace{\left(\mathbf{\Phi}_{k^2}^{SGS} - 2\widetilde{\xi}_k \mathbf{\Phi}_k^{SGS} \right)}_{\mathbf{\Phi}_{k,v}^{SGS}} = \\ &\underbrace{-2\mathbf{\Phi}_k^{SGS} \cdot \nabla \widetilde{\xi}_k}_{\text{I}} + \underbrace{2\left(\overline{\xi_k S_k} - \widetilde{\xi}_k \overline{S_k} \right)}_{\text{II}} \underbrace{-\overline{\rho} \chi_{\xi_k}^{SGS}}_{\text{III}} \underbrace{- \left(\overline{\xi_k^2 S_\rho} - \widetilde{\xi}_k^{\,2} \overline{S_\rho} \right)}_{\text{IV}}, \end{aligned} \tag{5.39}$$

where $\mathbf{\Phi}_{k,v}^{SGS}$ is the sub-grid flux of $\xi_{k,v}$. The term labeled "I" is responsible for sub-grid variance production, term "II" is the source term associated to volumetric source terms of ξ_k, term "III" is the dissipation of sub-grid variance, finally term "IV" is associated to the dilution of transported quantities due to volumetric mass sources. Note, that the transport equation of the filtered square of scalars (Eq. (5.35)) contains the complete scalar dissipation rate as a sink term. Meanwhile the transport equation of the square of the filtered scalar (Eq. (5.36)) only contains the resolved part of the scalar dissipation rate. Consequently, the sub-grid variance is only dissipated by the sub-grid scalar dissipation rate: $\chi_{\xi_k}^{SGS}$, which needs a closure model.

5.1.4 Eddy-viscosity model

The filtered equations presented in section 5.1.3 contain various unclosed terms. Most notably, it is necessary to properly model the sub-grid scale stress tensor: $\boldsymbol{\tau}^{SGS} = \widetilde{\overline{\rho}\mathbf{u} \otimes \mathbf{u}} - \overline{\rho}\widetilde{\mathbf{u}} \otimes \widetilde{\mathbf{u}}$ of the filtered momentum equation (Eq. (5.31)), which needs to capture the effects of the turbulent energy cascade. As Fig. 5.5 illustrates, part of the turbulent kinetic energy is resolved and a part remains on the sub-grid scales. A distinction can be made between filtered and sub-grid kinetic energy:

$$e_K^f = \tfrac{1}{2} \widetilde{\mathbf{u}} \cdot \widetilde{\mathbf{u}}, \qquad e_K^{SGS} = \tfrac{1}{2} \left(\widetilde{\mathbf{u} \cdot \mathbf{u}} - \widetilde{\mathbf{u}} \cdot \widetilde{\mathbf{u}} \right), \tag{5.40}$$

where the the sub-grid part can be expressed using the trace of the sub-grid scale stress tensor: $\overline{\rho} e_K^{SGS} = \mathrm{tr}\left(\boldsymbol{\tau}^{SGS} \right)$. Note, that the sub-grid kinetic energy is analogous to the sub-grid turbulent kinetic energy, since the mean flow is expected to have length scales of $\mathcal{O}\left(\ell_t\right)$, which shall be well resolved in a proper LES. (Pope, 2000, §13.4) Consequently, the kinetic energy of the mean flow only contributes to e_K^f.

Piomelli (1997, §5.1) presents transport equations for e_K^f and e_K^{SGS} in incompressible flow, to illustrate turbulence modeling concepts. Note, the differences compared to the present work, where variable density effects may be significant, especially considering the production of kinetic energy in flames characterized by strong thermal dilatation. Such kinetic energy equations may be derived for the present variable

density problems as well, however this is omitted here. The derivation is partly analogous to the one of sub-grid scalar variance equation presented in section 5.1.3.

The kinetic energy of the filtered velocity field (e_K^f) is dissipated by resolved viscous forces to a limited extent characterized by the dissipation rate:

$$\overline{\rho}\varepsilon_\nu^f = 2\overline{\mu}\mathbf{S}\left(\widetilde{\mathbf{u}}\right) : \mathbf{S}^{\mathbf{D}}\left(\widetilde{\mathbf{u}}\right), \tag{5.41}$$

where the operators of strain rate and its deviatoric part are evaluated using the resolved velocity field. As the turbulent kinetic energy dissipation only becomes significant at sufficiently small scales, ε_ν^f falls short of the true dissipation rate: ε^{tot}. The goal of eddy-viscosity models is to determine $\boldsymbol{\tau}^{SGS}$ such, that the true dissipation rate is recovered: $\varepsilon^{tot} = \varepsilon_\nu^f + \varepsilon^{SGS}$, where the modeled part of the dissipation rate is:

$$\overline{\rho}\varepsilon^{SGS} = -\mathbf{S}\left(\widetilde{\mathbf{u}}\right) : \boldsymbol{\tau}^{\mathbf{D},SGS}, \tag{5.42}$$

with the **D** superscript marking the deviatoric part of the sub-grid scale stress tensor. Note, that the trace of $\boldsymbol{\tau}^{SGS}$ would only produce significant effect at high Mach numbers. In eddy-viscosity models, the sub-grid scale stress tensor is modeled by setting an analogy to the viscous stress tensor, by extending the hypothesis of Boussinesq (1877) to LES. Consequently, purely dissipative behavior: $\varepsilon^{SGS} \geq 0$ is ensured for positive sub-grid viscosities. (Piomelli, 1997, §5.3) Thus, the deviatoric part of the sub-grid scale stress: $\boldsymbol{\tau}^{\mathbf{D},SGS} = \boldsymbol{\tau}^{SGS} - \frac{1}{3}\mathrm{tr}\left(\boldsymbol{\tau}^{SGS}\right)$ is modeled as:

$$\boldsymbol{\tau}^{\mathbf{D},SGS} = 2\overline{\rho}\nu^{SGS}\mathbf{S}^{\mathbf{D}}\left(\widetilde{\mathbf{u}}\right), \tag{5.43}$$

where ν^{SGS} is the sub-grid viscosity. The trace of the sub-grid stress tensor is not included explicitly in the governing equations, rather it is absorbed in the hydrodynamic pressure term. In the present approach this is permissible without any further consideration, as p is not used in any physical relations beyond the momentum equation. Note, that ε^{SGS} shall only contribute to the kinetic energy dissipation rate of the turbulent motion defined in Eq. (I.6), since the dissipation of the mean flow is fully resolved in a well executed LES.

Vreman model

In this work, the sub-grid viscosity model of Vreman (2004) is applied to obtain ν^{SGS}. This model departs from the pioneering work of Smagorinsky (1963), who devised an eddy viscosity model appropriate for high Re_t locally homogeneous isotropic turbulence, assuming that the cut-off wave number is situated in the inertial subrange, and that the sub-grid scales relax to their equilibrium state instantaneously. As Fig. 5.4b illustrates, under these conditions the Kolmogorov spectrum models well the turbulent kinetic energy spectrum, thus an adequate model can be devised exploiting this information, using a velocity scale based on the double inner product of the resolved strain rate tensor.

In practical applications the high Reynolds number turbulence is only present is specific regions of the flow, while other parts are characterized by weakly turbulent motion or even laminar flow. The Smagorinsky model over-predicts the kinetic energy dissipation in the latter regions, as the modeled ν^{SGS} does not vanish in strained laminar flows such as the laminar part of near-wall boundary layers. Vreman (2004) devised a method, that correctly reproduces $\nu^{SGS} \to 0$ in low turbulence regions by

exploiting the mathematic properties of the velocity gradient tensor in such flows. According to this model the sub-grid scale viscosity is determined as:

$$\nu^{SGS} = c\sqrt{\frac{B_\beta}{\boldsymbol{\alpha} : \boldsymbol{\alpha}}}, \tag{5.44}$$

where c is a modeling constant, $\boldsymbol{\alpha} = \nabla \mathbf{u}$ is the velocity gradient tensor, and B_β is the second scalar invariant of a tensor $\boldsymbol{\beta}$, which is commonly defined using Einstein's summation convention:

$$\beta_{ij} = \Delta_m^2 \alpha_{mi} \alpha_{mj}, \tag{5.45}$$

where Δ_m is the filter width in dimension m. Note, that in this work the filter is kept isotropic and equal to the mean element size, thus: $\Delta_m = \Delta_f = \Delta$, where $\Delta = \sqrt[3]{V_{element}}$ is computed using the the element volume: $V_{element}$. The second scalar invariant of this tensor is:

$$\begin{aligned} B_\beta &= 0.5\left(\left(\mathrm{tr}\left(\boldsymbol{\beta}\right)\right)^2 - \left(\mathrm{tr}\left(\boldsymbol{\beta}^2\right)\right)\right) \\ &= \beta_{11}\beta_{22} + \beta_{22}\beta_{33} + \beta_{33}\beta_{11} - \beta_{12}\beta_{21} - \beta_{23}\beta_{32} - \beta_{13}\beta_{31}. \end{aligned} \tag{5.46}$$

The modeling constant c can be related to the constant of the Smagorinsky model as: $c = 2.5C_S^2$, where C_S is derived from the Kolmogorov spectrum: $C_S = \frac{1}{\pi}\left(\frac{3}{2}(3C_K)\right)^{-3/4}$. A Kolmogorov constant of $C_K \approx 0.5$ (Sreenivasan, 1995) would result in $C_S \approx 0.17$ and $c \approx 0.07$. Nevertheless, following the recommendation of Vreman (2004), in this work a more dissipative value: $c = 0.1$ is used, which is more appropriate for complex flows.

As Vreman (2004) shows, this model correctly produces a vanishing sub-grid viscosity in various laminar flow configurations. This is achieved with only using the local velocity gradient tensor and filter width, thus the model is outstandingly simple. Despite its simplicity, the model performs well in canonical cases such as a turbulent mixing layer or a turbulent channel flow. Note, that in this work the incompressible Vreman model is directly extended to variable density cases. Consequently, the filtered momentum equation takes the form:

$$\partial_t\left(\overline{\rho}\widetilde{\mathbf{u}}\right) + \nabla\cdot\left(\overline{\rho}\widetilde{\mathbf{u}}\otimes\widetilde{\mathbf{u}}\right) + \nabla\overline{p} - \nabla\cdot\left(2\left(\overline{\mu} + \overline{\rho}\nu^{SGS}\right)\widetilde{\mathbf{S^D}\left(\mathbf{u}\right)}\right) = \overline{S_{\mathbf{u}}} \tag{5.47}$$

5.1.5 Averages of LES results

Solving the filtered governing equations of section 5.1.3 produces the time-resolved Favre-filtered unknown fields: $\widetilde{\mathbf{u}}$ and $\widetilde{\xi_k}$ as the direct result of the computation. These instantaneous fields may provide valuable insight to the observer on the behavior of the large scales of the flow problem, however, these insights have to be paired with rigorous mathematical analysis in order to quantify the results. The most fundamental of these quantitative results are the temporal averages defined by Eq. (5.3). In the most general sense, the temporal average of a field is given by:

$$\langle\psi\rangle = \langle\overline{\psi}\rangle + \langle\psi'\rangle. \tag{5.48}$$

As the LES only provides the filtered fields: $\overline{\psi}$ or $\widetilde{\psi}$, evaluating the temporal average is only possible under certain circumstances. Pope (2000, §13.4) argues, that the time averaged fields $\langle\psi\rangle(\mathbf{x})$ vary in space on scales comparable to the energy-containing

motions of the turbulent flow: ℓ_t. Thus, on the condition that the filter size is significantly smaller than these length scales ($\Delta \ll \ell_t$), the filtering of the time-averaged fields does not change them significantly: $\langle\psi\rangle \approx \overline{\langle\psi\rangle}$. Furthermore, if $\frac{\partial G}{\partial t} = 0$, then the order of temporal-averaging and LES filtering is interchangeable, thus the temporal average fields can be approximated as:

$$\langle\psi\rangle \approx \overline{\langle\psi\rangle} = \langle\overline{\psi}\rangle \qquad \text{if } \Delta \ll \ell_t \text{ and } \frac{\partial G}{\partial t} = 0. \tag{5.49}$$

In this work the first condition is guaranteed by sufficiently fine meshes, while the second condition is always satisfied, since the computational grid does not change in time. Equation (5.49) provides an easy treatment of the time-averages in case the filtered quantity $\overline{\psi}$ is indeed an output of the LES simulation. However, in the present work most unknown fields are Favre-filtered. By similar arguments the Favre-averaged quantities can be approximated using the Favre-filtered fields and the filtered density (Poinsot and Veynante, 2005, §4.7.7) as:

$$\{\psi\} \approx \frac{\langle\overline{\rho}\widetilde{\psi}\rangle}{\langle\overline{\rho}\rangle} \qquad \text{if } \Delta \ll \ell_t \text{ and } \frac{\partial G}{\partial t} = 0. \tag{5.50}$$

Note, that this Favre-averaged quantities are of lesser importance in practice, especially for the validating the numerical codes against experimental data, since Favre-averaged measurements are seldom available. As Poinsot and Veynante (2005, §4.7.7) concludes, in practical simulations the temporal average of the Favre-filtered fields is used to approximate temporal averages:

$$\langle\psi\rangle \approx \langle\widetilde{\psi}\rangle\,. \tag{5.51}$$

Veynante and Knikker (2006) analyze the error of this approximation in the limit of infinitely thin flame fronts. As they show, the equivalence is only justified in the case of fine filter sizes, while in coarsely resolved flows $\langle\widetilde{\psi}\rangle$ approaches $\{\psi\}$. Additionally to the restrictions on filter size and the steady filter function, further restrictions may be formulated to support the validity of Eq. (5.51). In particular, as appendix H shows, the difference between the non-density-weighted filtered quantities and Favre-filtered quantities has an upper bound determined by the sub-grid variances. The maximum instantaneous error of this approximation: $\epsilon_{\overline{\psi}=\widetilde{\psi}} \geq |\overline{\psi} - \widetilde{\psi}|$ is given by the sub-grid variances:

$$\epsilon_{\overline{\psi}=\widetilde{\psi}} = \frac{\sqrt{\overline{\psi^2} - \overline{\psi}^2}\sqrt{\overline{\rho^2} - \overline{\rho}^2}}{\overline{\rho}}. \tag{5.52}$$

In the present modeling framework both $\overline{\rho}$ and $\overline{\rho^2}$ may be obtained from the tabulated chemistry method, as described below in section 5.4. Furthermore, the thermochemical tables may also provide the non-density-weighted filtered value of any property of the gas mixture. Thus the main dilemma of averaging is regarding the gas velocity: $\mathbf{u}$, since Eq. (5.47) gives the Favre-filtered value. The error made by the approximation: $\langle\mathbf{u}\rangle \approx \langle\widetilde{\mathbf{u}}\rangle$, may be estimated, by estimating the sub-grid kinetic energy. The formula of Yoshizawa (1986) is used for this purpose:

$$\overline{\rho}e_K^{SGS} \approx 2C_I\overline{\rho}\Delta^2\mathbf{S}\left(\widetilde{\mathbf{u}}\right) : \mathbf{S}\left(\widetilde{\mathbf{u}}\right), \tag{5.53}$$

where C_I is a model constant. Originally, Yoshizawa proposed $C_I = 0.0886$. (See the work of Vreman, Geurts, and Kuerten (1994).) More recently, Bogey and Bailly (2006) determined the constant dynamically in a jet flow, and found a mean value of $C_I = 0.01$. A sub-grid velocity scale may be obtained as: $v^{SGS} = \sqrt{2e_K^{SGS}}$, thus the instantaneous difference between $\overline{\mathbf{u}}$ and $\widetilde{\mathbf{u}}$ is of order: $\epsilon_{\overline{\mathbf{u}}=\widetilde{\mathbf{u}}} = v^{SGS}\sqrt{\overline{\rho^2}/\overline{\rho}^2 - 1}$ using Eq. (5.52). The maximum possible error after Reynolds-averaging may be estimated as:

$$|\langle\widetilde{\mathbf{u}}\rangle - \langle\overline{\mathbf{u}}\rangle| \leq \left\langle v^{SGS}\sqrt{\overline{\rho^2}/\overline{\rho}^2 - 1}\right\rangle. \tag{5.54}$$

Higher moments

Similar problems arise in the computation of the mean of second moments, that are necessary to compute variances. Poinsot and Veynante (2005, §4.7.7) analyses these throughly, highlighting the difficulties. In this work, the issue of variances is not examined in detail. However, it is noted, that a good estimate of the variance would be given by:

$$\langle\psi^2\rangle - \langle\psi\rangle^2 \approx \underbrace{\left\langle\overline{\psi}^2\right\rangle - \langle\overline{\psi}\rangle^2}_{\text{Variance of resolved field}} + \underbrace{\left\langle\overline{\psi^2} - \overline{\psi}^2\right\rangle}_{\text{Sub-grid variance}}. \tag{5.55}$$

The computation of this quantity is problematic in various ways. Firstly, the non-density weighted filtering is necessary. And secondly, the sub-grid variance needs to be modeled and averaged.

Solving these problems is out of the scope of the present work, thus the the variances, just as the mean values, are approximated by using the Favre-filtered fields. Furthermore, the average of the sub-grid variance is neglected in the comparison with experiments, in order to refrain from introducing modeling steps in the post-processing. Thus the root mean square fluctuations of a quantity is estimated by:

$$\psi_{rms} = \sqrt{\langle\psi^2\rangle - \langle\psi\rangle^2} \approx \sqrt{\left\langle\left(\widetilde{\psi}\right)^2\right\rangle - \langle\widetilde{\psi}\rangle^2}. \tag{5.56}$$

5.1.6 Estimation of turbulent scales

When LES models are used in complex geometries, it may be difficult to judge *a priori* the mesh quality. This section outlines a methodology for estimating the scales of turbulent motion presented in section 5.1.2. The Kolmogorov scales and turbulence integral scales are calculated based on the complete time history of specific resolved properties recorded in selected points of the simulation domain.

Kolmogorov scales

The Kolmogorov scales are given solely by the mean kinematic viscosity and kinetic energy dissipation rate. As Eq. (5.20) presents, both are calculated using Favre-averaging. The Favre-averaged kinematic viscosity is determined according to Eq. (5.50) as:

$$\{\nu\} \approx \frac{\langle\overline{\rho}\widetilde{\nu}\rangle}{\langle\overline{\rho}\rangle}, \tag{5.57}$$

where $\overline{\rho}$ and $\widetilde{\nu}$ are given by the tabulated chemistry model, as further discussed in section 5.4. As appendix I details, the turbulent kinetic energy dissipation rate is given by the double inner product of the fluctuating parts of the strain rate and stress tensors according to Eq. (I.6). Extending this to LES, the instantaneous turbulent kinetic energy dissipation rate may be estimated as:

$$\rho\varepsilon \approx \left(\mathbf{S}\left(\widetilde{\mathbf{u}}\right)\right)^{\dagger} : \left(2\rho\left(\nu + \nu^{SGS}\right)\mathbf{S}^{\mathbf{D}}\left(\widetilde{\mathbf{u}}\right)\right)^{\dagger}, \tag{5.58}$$

which is Reynolds-averaged to reach $\{\varepsilon\} = \frac{\langle\rho\varepsilon\rangle}{\langle\rho\rangle}$ in accordance with the definition of Knaus and Pantano (2009).

Turbulence integral scales

In this work the integral scales are computed using the Favre-average turbulent kinetic energy: $\{k\}$. As discussed in section 5.1.2, in an adequate LES simulation at least 80% of the turbulent kinetic energy is contained on the resolved scales. Furthermore, the mean velocity field is entirely resolved, thus:

$$k^f = e_K^f - \frac{1}{2}\left\{\widetilde{\mathbf{u}}\right\}\cdot\left\{\widetilde{\mathbf{u}}\right\} \geq 0.8k. \tag{5.59}$$

Consequently, ℓ_t can readily be estimated to at least 72% accuracy using the Favre-average of k^f and $\{\varepsilon\}$. One could include more detailed approximation of k in this scale estimation, based one Eq. (5.53): the sub-grid kinetic energy estimate of Yoshizawa (1986):

$$k = k^f + e_K^{SGS} \approx k^f + 2C_I\Delta^2\mathbf{S}\left(\widetilde{\mathbf{u}}\right) : \mathbf{S}\left(\widetilde{\mathbf{u}}\right). \tag{5.60}$$

with C_I being a modeling constant. Nevertheless, the value of this modeling constant is uncertain. (Vreman, Geurts, and Kuerten, 1994; Bogey and Bailly, 2006) Consequently, using only k^f is preferred in this work, along with the Favre-averaged kinetic energy dissipation rate, to calculate the turbulence integral scales according to Eq. 5.22.

An alternative method is to estimate the scales based on the velocity correlations. In this work this approach is restricted to studying the temporal behavior of velocity components, sampled at selected locations dubbed *witness points*. Specifically, the power spectral density (PSD) of a discrete signal ψ available at constant Δt sampling rate on the $t \in [0, T]$ time interval, with final time: $T = N\Delta t$ may be calculated as:

$$PSD_{\psi\psi}(f) = \frac{\Delta t^2\left|\sum_{n=0}^{N-1}\psi\left(t\right)e^{-i2\pi ft}\right|^2}{T}, \tag{5.61}$$

where the term: $\sum_{n=0}^{N-1}\psi\left(t\right)e^{-i2\pi ft}$ may be obtained using Fast Fourier Transform (FFT). Note, that the spectrum's quality may be improved by the method of Welch (1967), by computing the PSD over smaller overlapping periods and averaging the results. Furthermore, there are methods to analyze unevenly sampled signals which is useful in simulations of variable time step size. (Lomb, 1976; Scargle, 1982) The above definition of Eq. 5.61 considers both positive and negative frequencies, alas the resulting function is symmetric. The resolved kinetic energy of a velocity component

u may be obtained as:

$$e^f_{K,u} = \frac{1}{2}\int_{-\infty}^{\infty} PSD_{uu}(f)\mathrm{d}f = \int_0^{\infty} PSD_{uu}(f)\mathrm{d}f. \tag{5.62}$$

As $PSD_{uu}(0)$ is related to the kinetic energy of the mean field: $\frac{1}{2}\langle u\rangle\langle u\rangle$, the turbulent kinetic energy may be obtained by excluding the lowest frequency components from the integration. Note, that some signal processing tools may define the PSD as double of the present definition, but restricted to non-negative frequencies.

Using Taylor's hypothesis of *frozen turbulence* (Taylor, 1938) it is possible to relate the frequencies of the present analysis to the wave numbers of kinetic energy spectrum: $E(\kappa)$. The hypothesis requires the fluctuations to be significantly smaller than the mean velocity, in which case the turbulent structures are advected through the witness point location significantly faster than their own rate of change, thus an equivalence can be drawn between spacial correlation at a fixed time instance and temporal correlation at a fixed location. In this case an equivalence can be established between the length scale and the frequency:

$$\ell = \frac{|\{\mathbf{u}\}|}{2\pi f}. \tag{5.63}$$

The python code producing these scale estimates from witness point data is published through the open source repository:
https://gitlab.com/BothAmbrus/KolmogorovAtWitness.

5.2 Conservative momentum transport

As section 5.1.2 illustrates, one of the fundamental challenges of large-eddy simulation is reproducing the correct amount of sub-grid scale dissipation. The large scale motion and large structures of transported scalar fields are well resolved in an adequate LES, however the corresponding kinetic energy dissipation and scalar dissipation rate may have significant sub-grid components, as gradients are highest at the smallest scales. In the present modeling strategy the sub-grid dissipation is captured by dedicated sub-grid models, such as the Vreman model presented in section 5.1.4. Assuming this model captures the kinetic energy dissipation rate properly, it is imperative to minimize any additional sources of dissipation, to avoid the sub-optimal "Dissipative LES" scenario depicted in Fig. 5.5.

Lehmkuhl et al. (2019b) introduced a low-dissipation modeling strategy for incompressible flows in the presently used simulation code: Alya. This method is extended to the low Mach number limit in the present work, since the accurate velocity predictions are crucial for the success of reacting flow simulations. (Both et al., 2020) An essential component of this strategy is the conservative nature of the temporal (T) and convective (C) operators of the momentum equation. Equation (2.55) present momentum conservation in its *conservative* or *divergence* form. In this case the two operators are:

$$\mathcal{T}_{div}(\rho,\mathbf{u}) \equiv \partial_t(\rho\mathbf{u}), \qquad C_{div}(\rho,\mathbf{u}) \equiv \nabla\cdot(\rho\mathbf{u}\otimes\mathbf{u}). \tag{5.64}$$

Below different formulations of these operators are described.

The convective operator has been extensively studied in incompressible flows (Charnyi et al., 2017; Verstappen and Veldman, 2003; Reiss, 2015) and likewise in compressible flows. (Nicoud, 2000; Morinishi, 2010; Brouwer, Reiss, and Sesterhenn,

2014; Rozema et al., 2018; Coppola et al., 2019) The different formulations are characterized by whether they inherently adhere to the conservation of physical quantities like kinetic energy, or momentum. More specifically, in the case of finite elements, it is well established, that kinetic energy conservation can be ensured by devising the convective term of the momentum equation such, that it preserves skew-symmetry at the discrete level. (Codina, Principe, and Ávila, 2010) Below, the different formulations and their conservation properties are discussed, especially regarding the effect of volumetric mass source terms associated to the Lagrangian particles.

5.2.1 Convection of momentum in variable density flows

The discretization strategy of $\mathcal{T}(\rho, \mathbf{u})$ and $C(\rho, \mathbf{u})$ is a critical feature of flow simulation algorithms, since the convection term should not introduce spurious numerical dissipation. (Lehmkuhl et al., 2019b) The straightforward approach is to retain the conservative form of Eq. (2.55) and use the corresponding operators:

$$\partial_t(\rho\mathbf{u}) + \nabla\cdot(\rho\mathbf{u}\otimes\mathbf{u}) = \mathcal{T}_{div} + C_{div}. \tag{5.65}$$

The conservative form of the convective operator may be expressed also as: $C_{div} = (\rho\mathbf{u}\cdot\nabla)\,\mathbf{u} + (\nabla\cdot(\rho\mathbf{u}))\,\mathbf{u}$.

One of the simplest alternatives to express the temporal and convective operators, involves exploiting the mass conservation equation (Eq. (2.54)) resulting in the so called *non-conservative* or *advective* form of the operators (Piomelli, 1997, §3.4):

$$\partial_t(\rho\mathbf{u}) + \nabla\cdot(\rho\mathbf{u}\otimes\mathbf{u}) = \underbrace{\rho\partial_t\mathbf{u}}_{\mathcal{T}_{adv}} + \underbrace{(\rho\mathbf{u}\cdot\nabla)\,\mathbf{u}}_{C_{adv}} + \mathbf{u}\left(\underbrace{\overbrace{\partial_t\rho}^{\mathcal{T}_{mass}} + \overbrace{\nabla\cdot(\rho\mathbf{u})}^{C_{mass}}}_{S_\rho}\right), \tag{5.66}$$

where the last term: $\mathbf{u}S_\rho$ is a dilution term, that arises in the presence of non-zero volumetric mass sources in the non-conservative form of the momentum equations. Furthermore, $\mathcal{T}_{mass}$ and C_{mass} are the temporal and convective terms of the mass conservation equation.

Another widely used discretization form is the *skew-symmetric* formulation (Nicoud, 2000; Brouwer, Reiss, and Sesterhenn, 2014), which is preferred for its kinetic energy conserving nature. In this case, the operators are the arithmetic mean of the conservative and non-conservative terms:

$$\partial_t(\rho\mathbf{u}) + \nabla\cdot(\rho\mathbf{u}\otimes\mathbf{u}) = \frac{1}{2}\left(\mathcal{T}_{div} + C_{div}\right) + \frac{1}{2}\left(\mathcal{T}_{adv} + C_{adv} + \mathbf{u}S_\rho\right). \tag{5.67}$$

Note, that the skew-symmetric operators may be expressed using the advective forms and the mass conservation alone, as:

$$\partial_t(\rho\mathbf{u}) + \nabla\cdot(\rho\mathbf{u}\otimes\mathbf{u}) = \mathcal{T}_{adv} + C_{adv} + \frac{1}{2}\mathbf{u}S_\rho + \frac{1}{2}\mathbf{u}\left(\mathcal{T}_{mass} + C_{mass}\right) \tag{5.68}$$

Consequently, the skew-symmetric temporal and convective terms are:

$$\mathcal{T}_{skew}(\rho, \mathbf{u}) = \rho\partial_t\mathbf{u} + \frac{1}{2}\left(\partial_t\rho\right)\mathbf{u} \tag{5.69}$$

$$C_{skew}(\rho, \mathbf{u}) = (\rho\mathbf{u}\cdot\nabla)\,\mathbf{u} + \frac{1}{2}\left(\nabla\cdot(\rho\mathbf{u})\right)\mathbf{u}. \tag{5.70}$$

and the dilution term related to volumetric mass source is $\frac{1}{2}\mathbf{u}S_\rho$.

TABLE 5.1: Temporal and convective operators of the momentum equation. The less conventional notations stand for: $\mathbb{A} = \sqrt{\rho}\mathbf{u}$, and $\mathbf{D}(\mathbb{A}) = \frac{\nabla\mathbb{A}+(\nabla\mathbb{A})^T}{2}$.

	$\mathcal{T}(\rho,\mathbf{u})$	$C(\rho,\mathbf{u})$
Conservative (div)	$\partial_t(\rho\mathbf{u})$	$(\rho\mathbf{u}\cdot\nabla)\mathbf{u} + (\nabla\cdot(\rho\mathbf{u}))\mathbf{u}$
Non-conservative (adv)	$\rho\partial_t\mathbf{u}$	$(\rho\mathbf{u}\cdot\nabla)\mathbf{u}$
Skew-symmetric	$\rho\partial_t\mathbf{u} + \frac{1}{2}(\partial_t\rho)\mathbf{u}$	$(\rho\mathbf{u}\cdot\nabla)\mathbf{u} + \frac{1}{2}(\nabla\cdot(\rho\mathbf{u}))\mathbf{u}$
EMAC	$\rho\partial_t\mathbf{u} + (\partial_t\rho)\mathbf{u}$	$2\mathbf{D}(\mathbb{A})\mathbb{A} + (\nabla\cdot\mathbb{A})\mathbb{A} - \frac{1}{2}\nabla\lvert\mathbb{A}\rvert^2$
	$S_{\mathbf{u},dilution}$ (on RHS)	
Conservative (div)	0	
Non-conservative (adv)	$-\mathbf{u}S_\rho$	
Skew-symmetric	$-\frac{1}{2}\mathbf{u}S_\rho$	
EMAC	0	

Finally, the Energy, Momentum, and Angular momentum Conserving (EMAC) formulation of Charnyi et al. (2017), may also be extended to low Mach number flows, as detailed in appendix J. In general the weak form of the momentum equation can be expressed using any of the above described operators as:

$$(\mathcal{T}(\rho,\mathbf{u}),\mathbf{v}) + (C(\rho,\mathbf{u}),\mathbf{v}) - (p+P_0,\nabla\cdot\mathbf{v}) + (\boldsymbol{\tau}(\mathbf{u}),\nabla\mathbf{v}) = (S_\mathbf{u} + S_{\mathbf{u},dilution},\mathbf{v}), \tag{5.71}$$

where the temporal, convective, and dilution terms are summarized in Tab. 5.1. This extension of the EMAC formulation is a promising strategy for ensuring the simultaneous conservation of multiple properties in compressible flows. (Ortega, 2018) However, its integration into the presently used low Mach number scheme needs additional work, thus it is only discussed in appendix J. Note, that the dilution term due to the operator treatment ($S_{\mathbf{u},dilution}$) is added to the volumetric momentum source term ($S_\mathbf{u}$) which describes physical phenomena like body forces or interactions with the separately modeled Lagrangian phase.

5.2.2 Conservation properties

This section presents an analysis of the conservation properties of the convective operators described above. Equations are derived representing the conservation of kinetic energy, momentum, and angular momentum integrated over the whole domain. These equations are simplified assuming specific conditions, under which the properties are to be conserved. While all of the operators preserve these conservation laws analytically, some of them necessitates the strict imposition of mass conservation. However, local mass conservation is not imposed strictly in the discrete form of the equations. The present analysis postulates, that certain forms of the operators are superior, which intrinsically result in the conservation of kinetic energy, momentum, or angular momentum without the strict imposition of mass conservation.

Kinetic energy

Kinetic energy conservation is discussed in detail in section 2.3.3. Here, an alternative expression is explored, for the conservation of overall kinetic energy in the domain Ω. The integral of kinetic energy in the domain may be defined as: $E_K = \frac{1}{2}(\rho\mathbf{u},\mathbf{u}) = \frac{1}{2}\int_\Omega \rho\,|\mathbf{u}|^2\,\mathrm{d}\Omega$. Using the weak form of the momentum equation, the kinetic energy conservation can be expressed by testing Eq. (5.71) with $\mathbf{v}=\mathbf{u}$:

$$(\mathcal{T}(\rho,\mathbf{u}),\mathbf{u}) + (C(\rho,\mathbf{u}),\mathbf{u}) - (P_0+p,\nabla\cdot\mathbf{u}) + (\boldsymbol{\tau}(\mathbf{u}),\nabla\mathbf{u}) = (S_\mathbf{u}+S_{\mathbf{u},dilution},\mathbf{u}). \tag{5.72}$$

As already discussed in relation to Eq. (2.74), the pressure term of Eq. (5.72) expresses the volumetric work of the hydrodynamic pressure, which vanishes in the incompressible limit and corresponds to the work of dilatation otherwise. (E.g.: the flow accelerating due to heat release.) In the context of the weak form used in this section, the work of dilatation may also be approached using the continuity equation Eq. (2.63). The weak form of the continuity equation may be reformulated as:

$$\left(\frac{1}{\rho}(\partial_t\rho+\mathbf{u}\cdot\nabla\rho),q\right) - \left(\frac{S_\rho}{\rho},q\right) = -(q,\nabla\cdot\mathbf{u}). \tag{5.73}$$

Testing Eq. (5.73) with $q = P = p+P_0$ and introducing the notation of material derivative $\frac{D\rho}{Dt} = \partial_t\rho+\mathbf{u}\cdot\nabla\rho$ gives the pressure term of Eq. (5.72):

$$-(p+P_0,\nabla\cdot\mathbf{u}) = \left(\frac{1}{\rho}\frac{D\rho}{Dt},p+P_0\right) - \left(\frac{S_\rho}{\rho},p+P_0\right). \tag{5.74}$$

Using the common interpretation of the material derivative, this expression indicates, that if the density of fluid particles changes, the pressure is doing work on the fluid.

To study the effect of the discretization strategy on the kinetic energy transport, consider a constant density $\left(\frac{D\rho}{Dt}=0\right)$, inviscid ($\mu=0$) flow without volumetric forces ($S_\mathbf{u}=\mathbf{0}$) on a periodic domain. In such a problem, kinetic energy is conservation can be expressed by the remaining terms:

$$(\mathcal{T}(\rho,\mathbf{u}),\mathbf{u}) + (C(\rho,\mathbf{u}),\mathbf{u}) - (S_{\mathbf{u},dilution},\mathbf{u}) = 0. \tag{5.75}$$

Using similar arguments as in Eq. (2.66), the conservative formulation gives the temporal kinetic energy term as:

$$(\mathcal{T}_{div}(\rho,\mathbf{u}),\mathbf{u}) = \frac{1}{2}\frac{\mathrm{d}}{\mathrm{d}t}\|\rho\mathbf{u}\cdot\mathbf{u}\| + \int_\Omega \frac{1}{2}\mathbf{u}\cdot\mathbf{u}\,(\partial_t\rho)\,\mathrm{d}\Omega, \tag{5.76}$$

$$= \frac{\mathrm{d}}{\mathrm{d}t}E_K + \int_\Omega e_K\,(\partial_t\rho)\,\mathrm{d}\Omega. \tag{5.77}$$

Meanwhile, the non-conservative term gives:

$$(\mathcal{T}_{adv}(\rho,\mathbf{u}),\mathbf{u}) = \int_\Omega \rho\,(\partial_t e_K)\,\mathrm{d}\Omega = \frac{\mathrm{d}}{\mathrm{d}t}E_K - \int_\Omega e_K\,(\partial_t\rho)\,\mathrm{d}\Omega. \tag{5.78}$$

In case of the Skew-symmetric operator, either by substituting the formulation of Tab. 5.1, or by averaging Eq. (5.76) and Eq. (5.78), one may see, that the temporal

kinetic energy conservation term is exactly:

$$\left(\mathcal{T}_{skew}\left(\rho,\mathbf{u}\right),\mathbf{u}\right)=\frac{\mathrm{d}}{\mathrm{d}t}E_K. \tag{5.79}$$

Similarly, the convective term also contributes differently to the kinetic energy balance, depending on the formulation. The convective term of the conservative approach may be treated using the notation of the *trilinear* form further discussed in appendix J. Specifically, using Eq. (J.4) one gets:

$$\begin{aligned}\left(C_{div}\left(\rho,\mathbf{u}\right),\mathbf{u}\right)&=\left(\left(\rho\mathbf{u}\cdot\nabla\right)\mathbf{u},\mathbf{u}\right)+\left(\left(\nabla\cdot\left(\rho\mathbf{u}\right)\right)\mathbf{u},\mathbf{u}\right),\\&=b\left(\rho\mathbf{u},\mathbf{u},\mathbf{u}\right)-2b\left(\rho\mathbf{u},\mathbf{u},\mathbf{u}\right),\\&=\frac{1}{2}\left(\left(\nabla\cdot\left(\rho\mathbf{u}\right)\right)\mathbf{u},\mathbf{u}\right),\\&=\int_\Omega e_K\left(\nabla\cdot\left(\rho\mathbf{u}\right)\right)\mathrm{d}\Omega.\end{aligned} \tag{5.80}$$

Similarly, the contribution of the non-conservative method is analogous to the first therm in Eq. (5.80), thus:

$$\left(C_{adv}\left(\rho,\mathbf{u}\right),\mathbf{u}\right)=\left(\left(\rho\mathbf{u}\cdot\nabla\right)\mathbf{u},\mathbf{u}\right)=-\frac{1}{2}\left(\left(\nabla\cdot\left(\rho\mathbf{u}\right)\right)\mathbf{u},\mathbf{u}\right)=-\int_\Omega e_K\left(\nabla\cdot\left(\rho\mathbf{u}\right)\right)\mathrm{d}\Omega. \tag{5.81}$$

One may use again the identity of Eq. (J.4) to show, that the skew-symmetric formulation of the convective term indeed inherently does not contribute to the kinetic energy balance:

$$\begin{aligned}\left(C_{skew}\left(\rho,\mathbf{u}\right),\mathbf{u}\right)&=\left(\left(\rho\mathbf{u}\cdot\nabla\right)\mathbf{u},\mathbf{u}\right)+\left(\tfrac{1}{2}\left(\nabla\cdot\left(\rho\mathbf{u}\right)\right)\mathbf{u},\mathbf{u}\right)\\&=b\left(\rho\mathbf{u},\mathbf{u},\mathbf{u}\right)-b\left(\rho\mathbf{u},\mathbf{u},\mathbf{u}\right)=0.\end{aligned} \tag{5.82}$$

The remaining part of Eq. (5.75) is the dilution source term. In the non-conservative formulation this gives:

$$\left(S_{\mathbf{u},dilution,adv},\mathbf{u}\right)=\int_\Omega -S_\rho\mathbf{u}\cdot\mathbf{u}\mathrm{d}\Omega=\int_\Omega -2e_KS_\rho\mathrm{d}\Omega, \tag{5.83}$$

while in the skew-symmetric case, the term is exactly half of this:

$$\left(S_{\mathbf{u},dilution,adv},\mathbf{u}\right)=\int_\Omega -e_KS_\rho\mathrm{d}\Omega. \tag{5.84}$$

TABLE 5.2: Kinetic energy conservation with different operators.

	$\left(\mathcal{T}\left(\rho,\mathbf{u}\right),\mathbf{u}\right)$	$\left(C\left(\rho,\mathbf{u}\right),\mathbf{u}\right)$	$-\left(S_{\mathbf{u},dilution},\mathbf{u}\right)$
Cons. (div)	$\frac{\mathrm{d}}{\mathrm{d}t}E_K+\int_\Omega e_K\left(\partial_t\rho\right)\mathrm{d}\Omega$	$\int_\Omega e_K\left(\nabla\cdot\left(\rho\mathbf{u}\right)\right)\mathrm{d}\Omega$	0
Non-cons. (adv)	$\frac{\mathrm{d}}{\mathrm{d}t}E_K-\int_\Omega e_K\left(\partial_t\rho\right)\mathrm{d}\Omega$	$-\int_\Omega e_K\left(\nabla\cdot\left(\rho\mathbf{u}\right)\right)\mathrm{d}\Omega$	$2\int_\Omega e_KS_\rho\mathrm{d}\Omega$
Skew-sym.	$\frac{\mathrm{d}}{\mathrm{d}t}E_K$	0	$\int_\Omega e_KS_\rho\mathrm{d}\Omega$

The kinetic energy conserving nature of the studied operators is examined in

Tab. 5.2. Analytically, all the formulations recover the correct behavior of $\frac{\mathrm{d}}{\mathrm{d}t}E_K = -\int_\Omega e_K S_\rho \mathrm{d}\Omega$. (See Eq. (2.74).) However, if mass conservation is not enforced strictly in each point of the domain, then the strategies conserve kinetic energy differently. Only the skew-symmetric operator holds kinetic energy conservation independently of the strict imposition of the continuity equations. In the other cases Eq. 5.75 holds, on the condition, that mass is conserved.

Momentum

The linear momentum is defined as: $\mathbf{M} = \int_\Omega \rho \mathbf{u} \mathrm{d}\Omega$. To prove its conservation, the weak forms of the continuity (Eq. (2.63)) and momentum (Eq. (5.71)) equations are tested with $\mathbf{v} = \chi(\mathbf{e}_i)$ and $q = 0$, where $\chi(\mathbf{e}_i)$ is a function such that:

$$\chi(\mathbf{e}_i) = \begin{cases} \mathbf{e}_i & \text{on } \hat{\Omega}, \\ \mathbf{g} \in \mathbf{H}_0^1(\Omega) & \text{on } S = \Omega \backslash \hat{\Omega}, \end{cases} \tag{5.85}$$

where $\mathbf{g}$ is an arbitrary function satisfying zero boundary conditions, and $\hat{\Omega}$ is a strictly interior subdomain. Testing with this function yields,

$$(\mathcal{T}(\rho, \mathbf{u}), \mathbf{e}_i) + (C(\rho, \mathbf{u}), \mathbf{e}_i) - (P_0 + p, \nabla \cdot \mathbf{e}_i) + (\boldsymbol{\tau}(\mathbf{u}), \nabla \mathbf{e}_i) = (S_\mathbf{u} + S_{\mathbf{u},dilution}, \mathbf{e}_i). \tag{5.86}$$

The terms $(P_0 + p, \nabla \cdot \mathbf{e}_i)$ and $(\boldsymbol{\tau}(\mathbf{u}), \nabla \cdot \mathbf{e}_i)$ vanish, as $\mathbf{e}_i$ is constant. Thus Eq. (5.86) simplifies to:

$$(\mathcal{T}(\rho, \mathbf{u}), \mathbf{e}_i) + (C(\rho, \mathbf{u}), \mathbf{e}_i) - (S_\mathbf{u} + S_{\mathbf{u},dilution}, \mathbf{e}_i) = 0. \tag{5.87}$$

Linear momentum is to be conserved in the domain if there are no volumetric source terms: $(S_\mathbf{u}, \mathbf{e}_i) = 0$. The remaining terms are studied individually to assess momentum conservation.

The temporal term of the conservative formulation gives:

$$(\mathcal{T}_{div}(\rho, \mathbf{u}), \mathbf{e}_i) = \frac{\mathrm{d}}{\mathrm{d}t}(\rho \mathbf{u}, \mathbf{e}_i) = \frac{\mathrm{d}}{\mathrm{d}t}\mathbf{M}_i. \tag{5.88}$$

Meanwhile, the non-conservative formulation results in:

$$(\mathcal{T}_{adv}(\rho, \mathbf{u}), \mathbf{e}_i) = (\rho \partial_t \mathbf{u}, \mathbf{e}_i) = \int_\Omega \rho (\partial_t \mathbf{u}) \cdot \mathbf{e}_i \mathrm{d}\Omega = \frac{\mathrm{d}}{\mathrm{d}t}\mathbf{M}_i - \int_\Omega \mathbf{u}_i (\partial_t \rho) \mathrm{d}\Omega. \tag{5.89}$$

As stated before, the skew-symmetric term may be obtained by substitution of the definitions in Tab. 5.1, or simply by the arithmetic mean of the above two solutions:

$$(\mathcal{T}_{skew}(\rho, \mathbf{u}), \mathbf{e}_i) = \frac{\mathrm{d}}{\mathrm{d}t}\mathbf{M}_i - \frac{1}{2}\int_\Omega \mathbf{u}_i (\partial_t \rho) \mathrm{d}\Omega. \tag{5.90}$$

The convective terms may be evaluated similarly. In case of the conservative form, using Eq. (J.3) and the definition of the trilinear form discussed in appendix J gives:

$$\begin{aligned} (C_{div}(\rho, \mathbf{u}), \mathbf{e}_i) &= ((\rho \mathbf{u} \cdot \nabla)\mathbf{u}, \mathbf{e}_i) + ((\nabla \cdot (\rho \mathbf{u}))\mathbf{u}, \mathbf{e}_i), \\ &= b(\rho \mathbf{u}, \mathbf{u}, \mathbf{e}_i) + ((\nabla \cdot (\rho \mathbf{u}))\mathbf{u}, \mathbf{e}_i), \\ &= b(\rho \mathbf{u}, \mathbf{u}, \mathbf{e}_i) - b(\rho \mathbf{u}, \mathbf{u}, \mathbf{e}_i) - b(\rho \mathbf{u}, \mathbf{e}_i, \mathbf{u}) = 0, \end{aligned} \tag{5.91}$$

where $b\left(\rho\mathbf{u}, \mathbf{e}_i, \mathbf{u}\right)$ is zero since $\mathbf{e}_i$ is constant. Again using Eq. (J.3), the non-conservative formulation gives:

$$\begin{aligned}\left(C_{adv}\left(\rho, \mathbf{u}\right), \mathbf{e}_i\right) &= \left(\left(\rho\mathbf{u}\cdot\nabla\right)\mathbf{u}, \mathbf{e}_i\right) = b\left(\rho\mathbf{u}, \mathbf{u}, \mathbf{e}_i\right), \\ &= -\left(\left(\nabla\cdot\left(\rho\mathbf{u}\right)\right)\mathbf{u}, \mathbf{e}_i\right) = -\int_\Omega \mathbf{u}_i\left(\nabla\cdot\left(\rho\mathbf{u}\right)\right)\mathrm{d}\Omega. \end{aligned} \tag{5.92}$$

The skew-symmetric term may be obtained as the mean of the above two results:

$$\left(C_{skew}\left(\rho, \mathbf{u}\right), \mathbf{e}_i\right) = -\frac{1}{2}\int_\Omega \mathbf{u}_i\left(\nabla\cdot\left(\rho\mathbf{u}\right)\right)\mathrm{d}\Omega. \tag{5.93}$$

Finally, the dilution terms are simply integrated over the volume.

TABLE 5.3: Linear momentum conservation with different operators.

	$\left(\mathcal{T}\left(\rho, \mathbf{u}\right), \mathbf{e}_i\right)$	$\left(C\left(\rho, \mathbf{u}\right), \mathbf{e}_i\right)$	$-\left(S_{\mathbf{u},dilution}, \mathbf{e}_i\right)$
Cons. (div)	$\frac{\mathrm{d}}{\mathrm{d}t}\mathbf{M}_i$	0	0
Non-cons. (adv)	$\frac{\mathrm{d}}{\mathrm{d}t}\mathbf{M}_i - \int_\Omega \mathbf{u}_i\left(\partial_t\rho\right)\mathrm{d}\Omega$	$-\int_\Omega \mathbf{u}_i\left(\nabla\cdot\left(\rho\mathbf{u}\right)\right)\mathrm{d}\Omega$	$\int_\Omega \mathbf{u}_i S_\rho \mathrm{d}\Omega$
Skew-sym.	$\frac{\mathrm{d}}{\mathrm{d}t}\mathbf{M}_i - \frac{1}{2}\int_\Omega \mathbf{u}_i\left(\partial_t\rho\right)\mathrm{d}\Omega$	$-\frac{1}{2}\int_\Omega \mathbf{u}_i\left(\nabla\cdot\left(\rho\mathbf{u}\right)\right)\mathrm{d}\Omega$	$\frac{1}{2}\int_\Omega \mathbf{u}_i S_\rho \mathrm{d}\Omega$

The terms concerning linear momentum conservation are summarized in Tab. 5.3. It follows straightforwardly, that the conservative formulation intrinsically conserve momentum, without the strong imposition of mass conservation, while the non-conservative and skew-symmetric options do not.

Angular momentum

The study of angular momentum conservation is fairly similar to that of the linear momentum. The angular momentum is defined as: $\mathbf{M}_\mathbf{x} = \int_\Omega \rho\mathbf{u}\times\mathbf{x}\mathrm{d}\Omega$, where $\mathbf{x}$ is the position vector within the Ω domain. Conservation equations of Eq. (2.63) and Eq. (5.71) are tested with $\mathbf{v} = \chi\left(\phi_i\right)$ and $q = 0$, where $\phi_i \equiv \mathbf{x}\times\mathbf{e}_i$, with χ defined by Eq. (5.85). The equation of angular momentum conservation over the domain takes the form:

$$\left(\mathcal{T}\left(\rho, \mathbf{u}\right), \phi_i\right) + \left(C\left(\rho, \mathbf{u}\right), \phi_i\right) - \left(P_0 + p, \nabla\cdot\phi_i\right) + \left(\boldsymbol{\tau}\left(\mathbf{u}\right), \nabla\phi_i\right) = \left(S_\mathbf{u} + S_{\mathbf{u},dilution}, \phi_i\right). \tag{5.94}$$

The pressure term vanishes since $\nabla\cdot\phi_i = 0$, and in inviscid cases without source terms the requirement for angular momentum conservation is

$$\left(\mathcal{T}\left(\rho, \mathbf{u}\right), \phi_i\right) + \left(C\left(\rho, \mathbf{u}\right), \phi_i\right) - \left(S_\mathbf{u} + S_{\mathbf{u},dilution}, \phi_i\right) = 0. \tag{5.95}$$

Considering the identity: $\mathbf{u}\cdot\left(\mathbf{v}\times\mathbf{w}\right) = \mathbf{v}\cdot\left(\mathbf{w}\times\mathbf{u}\right) = \mathbf{w}\cdot\left(\mathbf{u}\times\mathbf{v}\right)$, the temporal term of the conservative formulation is:

$$\begin{aligned}\left(\mathcal{T}_{div}\left(\rho, \mathbf{u}\right), \phi_i\right) &= \int_\Omega \partial_t\left(\rho\mathbf{u}\right)\cdot\left(\mathbf{x}\times\mathbf{e}_i\right)\mathrm{d}\Omega = \int_\Omega \mathbf{e}_i\cdot\left(\partial_t\left(\rho\mathbf{u}\right)\times\mathbf{x}\right)\mathrm{d}\Omega, \\ &= \frac{\mathrm{d}}{\mathrm{d}t}\mathbf{M}_{\mathbf{x}i}. \end{aligned} \tag{5.96}$$

Similar to the case of the linear momentum, the temporal term of the non-conservative formulation gives:

$$\left(\mathcal{T}_{adv}\left(\rho,\mathbf{u}\right),\phi_i\right)=\left(\rho\partial_t\mathbf{u},\phi_i\right)=\frac{\mathrm{d}}{\mathrm{d}t}\mathbf{M}_{\mathbf{x}i}-\int_\Omega\left(\mathbf{u}\times\mathbf{x}\right)_i\left(\partial_t\rho\right)\mathrm{d}\Omega. \tag{5.97}$$

And the skew-symmetric formulation results in:

$$\left(\mathcal{T}_{skew}\left(\rho,\mathbf{u}\right),\phi_i\right)=\frac{\mathrm{d}}{\mathrm{d}t}\mathbf{M}_{\mathbf{x}i}-\frac{1}{2}\int_\Omega\left(\mathbf{u}\times\mathbf{x}\right)_i\left(\partial_t\rho\right)\mathrm{d}\Omega. \tag{5.98}$$

The convective terms interact with ϕ_i similarly as in the case of linear momentum as well, thus the derivation here is omitted.

TABLE 5.4: Angular momentum conservation with different operators.

	$\left(\mathcal{T}\left(\rho,\mathbf{u}\right),\phi_i\right)$	$\left(C\left(\rho,\mathbf{u}\right),\phi_i\right)$
Cons. (div)	$\frac{\mathrm{d}}{\mathrm{d}t}\mathbf{M}_{\mathbf{x}i}$	0
Non-cons. (adv)	$\frac{\mathrm{d}}{\mathrm{d}t}\mathbf{M}_{\mathbf{x}i}-\int_\Omega\left(\mathbf{u}\times\mathbf{x}\right)_i\left(\partial_t\rho\right)\mathrm{d}\Omega$	$-\int_\Omega\left(\mathbf{u}\times\mathbf{x}\right)_i\left(\nabla\cdot\left(\rho\mathbf{u}\right)\right)\mathrm{d}\Omega$
Skew-sym.	$\frac{\mathrm{d}}{\mathrm{d}t}\mathbf{M}_{\mathbf{x}i}-\frac{1}{2}\int_\Omega\left(\mathbf{u}\times\mathbf{x}\right)_i\left(\partial_t\rho\right)\mathrm{d}\Omega$	$-\frac{1}{2}\int_\Omega\left(\mathbf{u}\times\mathbf{x}\right)_i\left(\nabla\cdot\left(\rho\mathbf{u}\right)\right)\mathrm{d}\Omega$
	$-\left(S_{\mathbf{u},dilution},\phi_i\right)$	
Cons. (div)	0	
Non-cons. (adv)	$\int_\Omega\left(\mathbf{u}\times\mathbf{x}\right)_i S_\rho\mathrm{d}\Omega$	
Skew-sym.	$\frac{1}{2}\int_\Omega\left(\mathbf{u}\times\mathbf{x}\right)_i S_\rho\mathrm{d}\Omega$	

The angular momentum conservation properties of different operators are summarized in Tab. 5.4. Similarly to the case of linear momentum, the conservative formulation is intrinsically conserving $\mathbf{M}_\mathbf{x}$. Meanwhile the non-conservative and skew-symmetric operators rely on the mass conservative nature of the velocity field, to fulfill angular momentum conservation.

5.2.3 Summary of conservation properties of the momentum equation

Following Charnyi et al. (2017) the intrinsic conservative properties of different formulations of the low Mach number Navier-Stokes equations are examined. The non-uniform nature of density introduces substantial complexity to the problem. Firstly, the temporal term of momentum conservation is no longer as simple as in incompressible flows. Moreover, the temporal and convective operators have to be transformed together if the continuity equation is to be exploited for these conversions.

In the rest of this study, the non-conservative (adv) operator is employed unless otherwise stated. This strategy is directly compatible with the modular multiphysics strategy of Alya, where scalar equations are solved separately from the Navier-Stokes equations. (Vázquez et al., 2016) Such a modular structure makes it difficult to accurately represent the $\partial_t\rho$ terms of the temporal operator. (See Tab. 5.1.)

5.3 Turbulent combustion

The previous sections of the present chapter focus on the Navier-Stokes equations while treating the scalar transport in a general manner. Although turbulence originates from the non-linear nature of the momentum equation, it also profoundly affects scalar transport. This section provides details on turbulent combustion.

5.3.1 Relevant scales of combustion

Section 3.1 presents canonical configurations that may be considered the most rudimentary examples of premixed and non-premixed combustion: premixed free flamelets, and counterflow diffusion flamelets respectively. These model problems provide typical length, time and velocity scales, which characterize the interaction of chemical reaction and molecular diffusion, leading to the specific behavior of these laminar flames.

TABLE 5.5: Chemical scales of premixed combustion at given mixture fraction.

	Based on diffusivity (Eq. (3.5))	Based on thermal thickness (Eq. (3.4))
Length	$\delta_{diff} = \frac{\mathcal{D}_t^u}{S_L}$	$\delta_{th} = \frac{T^b - T^u}{\max\left(\frac{\mathrm{d}T}{\mathrm{d}x}\right)}$
Time	$\tau_{diff} = \frac{\mathcal{D}_t^u}{S_L^2}$	$\tau_{th} = \frac{\delta_{th}}{S_L}$
Velocity	S_L	S_L

In case of the premixed burning mode, these canonical scales are well defined and they are summarized in Tab. 5.5. The problem of premixed free flamelets may be fully characterized by the flame speed and a diffusivity, the latter taken as the thermal diffusivity in the unburnt mixture following the unity Lewis number assumption. The flame thickness may also be approached by geometrical arguments, however, as Fig. 3.5 demonstrates, δ_{diff} and δ_{th} are strongly related. The difference between the two scales tends to be within one order of magnitude. In case of perfectly premixed combustion, Tab. 5.5 provides a single length, time and velocity scale for the characterization of the chemistry. (Peters, 2001, §2.3)

There is less consensus in the literature on such reference scales in non-premixed combustion, as the chemical effects do not culminate in a well defined velocity scale, such as the flame speed in premixed flamelets. Nevertheless, the importance of a reference value of the diffusivity is recognized, here also taken as the thermal diffusivity: $\mathcal{D}_t$. Length scales are generally defined similar to δ_{diff} of Eq. (3.18). (Peters, 2001, §3.6) As appendix A demonstrates, the flame may become significantly thicker, than this value due to thermal dilatation. Here the formula may be used with the thermal diffusivity evaluated in the oxidizer or in the stoichiometric mixture:

$$\delta_{diff} = \sqrt{\frac{2\mathcal{D}_{t,ox}}{a}}, \qquad \delta_{diff,st} = \sqrt{\frac{2\mathcal{D}_{t,st}}{a}}. \tag{5.99}$$

An alternative option is to take advantage of the definition of the scalar dissipation rate (Vervisch and Poinsot, 1998), and define a length scale based on the mixture

fraction gradient evaluated at the stoichiometric point as:

$$\delta_{\chi,st} = \frac{1}{|\nabla Z|_{st}} = \sqrt{\frac{2\mathcal{D}_{t,st}}{\chi_{st}}}, \tag{5.100}$$

which is a similar approach of the thermal flame thickness of premixed flamelets (Eq. (3.4)) using a difference and a gradient. Note, that δ_χ is related to δ_{diff} approximately linearly, considering that the scalar dissipation rate and the strain rate are associated in steady state. (See Fig. A.4.)

Different time scales may be defined as well in counterflow diffusion flamelets. The rate of mixing may be characterized following Eq. (2.70). (Ihme and Pitsch, 2008a) Based on this the mixing time scale is:

$$\tau_m = \frac{Z_{st}^2}{\chi_{st}}. \tag{5.101}$$

These scales define the behavior of passive scalar transport, however, they carry no information on the chemistry. A chemical time scale is provided by the asymptotic analysis of Liñan (1974) for one step chemistry, which was subsequently used in numerical studies on diffusion flames. (Cuenot and Poinsot, 1994) It is possible to define a chemical time scale for complex chemistry, by analyzing the individual reactions. (Ihme, Bodony, and Pitsch, 2005) However, as Vervisch and Poinsot (1998) note, a chemical time scale may be provided using the extinction strain rate:

$$\tau_c^{ext,a} = \frac{1}{a^{ext}}. \tag{5.102}$$

Alternatively, the chemical scales may be provided by the definition of Peters (Oran and Boris, 1991, §6.II.B):

$$\tau_c^{ext,\chi} = \frac{Z_{st}^2\left(1 - Z_{st}^2\right)}{\chi_{st}^{ext}} \approx \tau_m^{ext}, \tag{5.103}$$

which is approximately the mixing time scale at the extinction point, if Z_{st} is low. Indeed, the extinction point marks the limit, where the production of radicals by chemical effects is overcame by the dissipation of the radical pool due to diffusive mixing. Thus the two time scales become comparable as well. Ihme and Pitsch (2008a) utilize an alternative chemical time scale, based on the concept of the progress variable in unsteady counterflow diffusion flamelets. In this approach the chemical effects may be characterized by:

$$\tau_c^{\dot{\omega}} = \frac{\rho_{st}^{end} Y_{c,st}^{end} - \rho_{st}^{start} Y_{c,st}^{start}}{\max\left(\dot{\omega}_{Y_c,st}\right)}, \tag{5.104}$$

where a characteristic source term is obtained in the stoichiometric point along the evolution of the unsteady flamelets. Note, that this time scale is not expected to be sensitive to the strain rate, since both the range of reaction progress and the peak source term are largely similar between different strain rate unsteady cases. (See Fig. 3.34.)

Independently of the length scales, one may define a chemical velocity scale analogously to the premixed case, solely based on the time scale and a diffusivity. (Buckmaster, 1985, §III.3.3) This velocity scale may be defined using the thermal diffusivity

of oxidizer, or that of the stoichiometric mixture in the extinction point:

$$v_{c,ox} = \sqrt{\frac{\mathcal{D}_{t,ox}}{\tau_c}}, \qquad v_c = \sqrt{\frac{\mathcal{D}_{t,st}}{\tau_c}}, \tag{5.105}$$

where τ_c may be taken as any of the above defined options.

TABLE 5.6: Example of chemical scales in atmospheric methane flames using the unity Lewis number assumption and the GRI3.0 (Smith et al., 2011) chemical mechanism.

Stoichiometric premixed flame	
S_L	0.286 m/s
δ_{diff}	0.078 mm
δ_{th}	0.509 mm
τ_{diff}	0.273 ms
τ_{th}	1.780 ms
Counterflow diffusion flame	
δ^{ext}_{diff}	0.268 mm
$\delta^{ext}_{diff,st}$	1.265 mm
$\delta^{ext}_{\chi,st}$	5.805 mm
$\delta^{ext}_{\chi,Z=0.5}$	0.980 mm
τ^{ext}_{m}	0.104 ms
$\tau^{ext,a}_{c}$	1.627 ms
$\tau^{ext,\chi}_{c}$	0.104 ms
$\tau^{\dot{\omega}}_{c}$	0.104 ms
$v^{ext,a}_{c,ox}$	0.117 m/s
$v^{ext,\chi}_{c,ox}$	0.461 m/s
$v^{\dot{\omega}}_{c,ox}$	0.461 m/s
$v^{ext,a}_{c}$	0.550 m/s
$v^{ext,\chi}_{c}$	2.174 m/s
$v^{\dot{\omega}}_{c}$	2.174 m/s

The scales of a stoichiometric premixed free flamelet, and a counterflow diffusion flamelet are illustrated in Tab. 5.6 for methane-air flames. In the premixed case, the example confirms what is readily illustrated in Fig. 3.5. The flamelets become very thin near stoichiometry, and the diffusive thickness is an order of magnitude lower than the thermal flame thickness. The resulting time scales are likewise separated by an order of magnitude: $\mathcal{O}\left(0.1ms\right)$ and $\mathcal{O}\left(1.0ms\right)$ respectively.

The case of the diffusion flamelet is more alluring. As the last column of Fig. 3.12 illustrates, the actual width of the flame at the extinction point is somewhat over 1 mm, which seems to be closest to $\delta^{ext}_{diff,st}$. Using the thermal diffusivity of the oxidizer (δ^{ext}_{diff}) greatly under-predicts this length scale. (See appendix A.) Meanwhile, using the length scale estimate based on the stoichiometric mixture fraction gradient ($\delta^{ext}_{\chi,st}$) results in a very large length. This is explained by the very low value of the stoichiometric mixture fraction: $Z_{st} = 0.0552$, as the mixture fraction profile is expected to be similar to the error function (Eq. (A.5)), thus the gradient at Z_{st} is not representative to the thickness of the profile. As a comparison, the gradient is also

evaluated at $Z = 0.5$, which results in a length scale ($\delta^{ext}_{\chi,Z=0.5}$) similar to the actual flame thickness.

In terms of the time scales, as expected the mixing time scale at the extinction point (τ^{ext}_m), and the chemical time scale of Peters ($\tau^{ext,\chi}_c$) are identical due to the low stoichiometric mixture fraction. However, surprisingly, the time scale of Ihme and Pitsch (2008a) also gives an identical time scale up to three significant digits. (Note, that this is a coincidence.) Contrarily, the time scale given by the strain rate ($\tau^{ext,a}_c$) is an order of magnitude larger. This time scale is already introduced in relation to Fig. 3.15, where τ^a_c of unsteady flamelets is used for scaling the time coordinate. Indeed, extinction processes seem to behave exponentially, with a time scale that is proportional to τ^a_c but lower. Meanwhile, reignition shows no apparent relation to the strain rate, and is rather connected to the chemical time scales such as $\tau^{\dot{\omega}}_c$.

Regarding the velocity scales, the present definitions show large variation. The velocity scales defined using the oxidizer diffusivity are the same order of magnitude as the stoichiometric laminar flame speed (S_L). This analogy is well known by the asymptotic analysis of Seshadri and Peters (1988), relating premixed flamelets and counterflow diffusion flamelet at the extinction point. Meanwhile, using the thermal diffusivity at the stoichiometric point one gets notably higher velocity scales.

5.3.2 Scales of turbulence/chemistry interaction

The flamelet concept postulates, that turbulent flames may be modeled as laminar flames embedded in the turbulent flow. Such a view is valid if the chemical time scales are significantly smaller than the flow time scales, thus the flame structures relax to their laminar form faster than the turbulent flow perturbs them. The relation of chemical time scales and the turbulent flow is often expressed in terms of the Damköhler and Karlovitz numbers. The former expresses the speed of the reactions compared to the flow, while the latter the reciprocal of this. Thus, flamelet concepts are thought to be valid under high Damköhler and low Karlovitz number conditions.

Validity of premixed flamelet based tabulated chemistry models

The existence of such embedded flamelet structures in perfectly premixed flames has long been a matter of discussion independently from numerical modeling. Borghi (1985) reviewed this early debate and concluded, that depending on the conditions the structure of turbulent premixed flames may be composed of an ensemble of thin flamelets, or it may be a continuous more distributed region where reactions take place. As proposed by Borghi (1985) these regimes may be distinguished by a Damköhler number defined using the turbulence integral scale of Eq. (5.22), and the chemical time scale τ_{diff} based on the diffusivity:

$$Da = \frac{\tau_t}{\tau_{diff}}. \tag{5.106}$$

Note, that the turbulent time scale is meant to characterize the incoming fresh reactants interacting with the flame. Moreover, a Karlovitz number is typically defined based on the Kolmogorov time scale of Eq. (5.20) as:

$$Ka = \frac{\tau_{diff}}{\tau_\eta}. \tag{5.107}$$

Above, the unity Lewis number assumption is already utilized in the definition of the chemical scales, hence $\mathcal{D}_t$ is used. A further assumption of $Pr \approx Sc \approx 1$ is generally employed in the analysis of chemical scales. Here the Schmidt number is retained for the time being, using $\nu = Sc\mathcal{D} = Pr\mathcal{D}_t$ with the unity Lewis number assumption. Under these conditions, the kinematic viscosity may be related to the flame scales as: $\nu = \frac{\delta_{diff} S_L}{Sc}$, resulting in the turbulence Reynolds number:

$$Re_t = \frac{\ell_t v' Sc}{\delta_{diff} S_L}. \tag{5.108}$$

Furthermore, the Damköhler number becomes:

$$Da = \frac{\ell_t S_L}{v' \delta_{diff}}. \tag{5.109}$$

Finally, the Karlovitz number may be expressed using the $\sqrt{Re_t}$ (Eq. (5.25)) relation of integral and Kolmogorov time scales.

$$Ka = \frac{\sqrt{Re_t}}{Da}. \tag{5.110}$$

Based on such scale estimates, Borghi (1985) suggested that in cases of $Ka < 1$, where the turnover time of the smallest eddies is larger than the time scales of the flame, the reacting fronts are flamelet-like and undisturbed by the turbulent flow. The different regimes proposed in this paradigm are displayed in Fig. 5.6a on the $v' - \ell_t$ plane normalized by the corresponding chemical scales. In this view undisturbed flamelets are only found below the $Ka = 1$ isoline. Meanwhile, Borghi (1985) postulates, that in the $Da > 1, Ka > 1$ regime part of the turbulent energy cascade can penetrate the flame, and significantly distribute the reaction zone, and with further increase of the turbulence intensity at $Da < 1$ the reaction layers cease to exist, and the reactions behave like well-stirred reactors.

This view was debated early on by Poinsot, Veynante, and Candel (1991), who studied the quenching of planar reaction layers by vortex pairs using direct numerical simulation. A quenching limit was established by the conditions: $Re_t > 250$ and $v'/S_L > 4Re_t^{1/4}$, where the latter limit corresponds to a Karlovitz number of $Ka = 16$. This discriminating limit is illustrated in Fig. 5.6b on the normalized $v' - \ell_t$ plane. Since below this quenching limit the vortices are unable to break the continuity of the flame front, Poinsot, Veynante, and Candel (1991) argue, that the cases below this limit are characterized by the flamelet-like behavior.

Peters (1999) reassessed the problem based on the used flame scales, and proposed a new regime diagram displayed in Fig. 5.6b. In this context a new length scale is introduced: $\delta_R = 0.1\delta_{diff}$, which is thought to represent well the thickness of the reaction zone. This gives an alternative Karlovitz number: $Ka_\delta = Ka/100$. Peters (1999) postulates, that in the range of: $Ka > 1$ and $Ka_\delta < 1$ the eddies may broaden the preheat zone of the underlying flamelet structures, but the reaction zone remains thin and flamelet-like.

Poinsot and Veynante (2005, §5.2.3) point out various uncertainties in predicting the outcome of turbulence-chemistry interactions from order of magnitude estimates of the Damköhler and Karlovitz numbers. The turbulent motion of the fresh gas has to overcome various barriers in order to perturb the flame significantly. For instance the eddies of the Kolmogorov scale are often very weak, and as the viscosity increases by an order of magnitude across the flame front, these structures may be

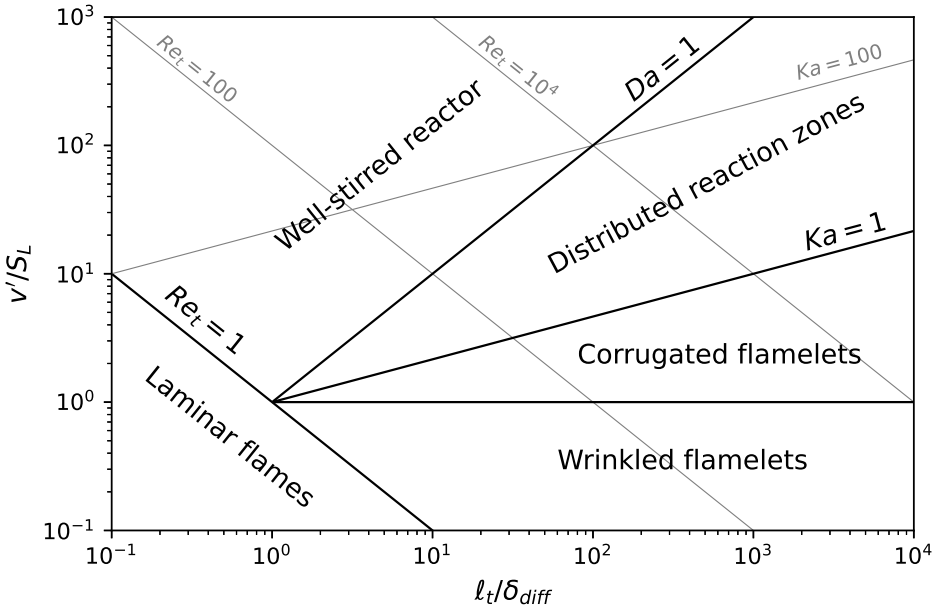

(A) Classical regime diagram.

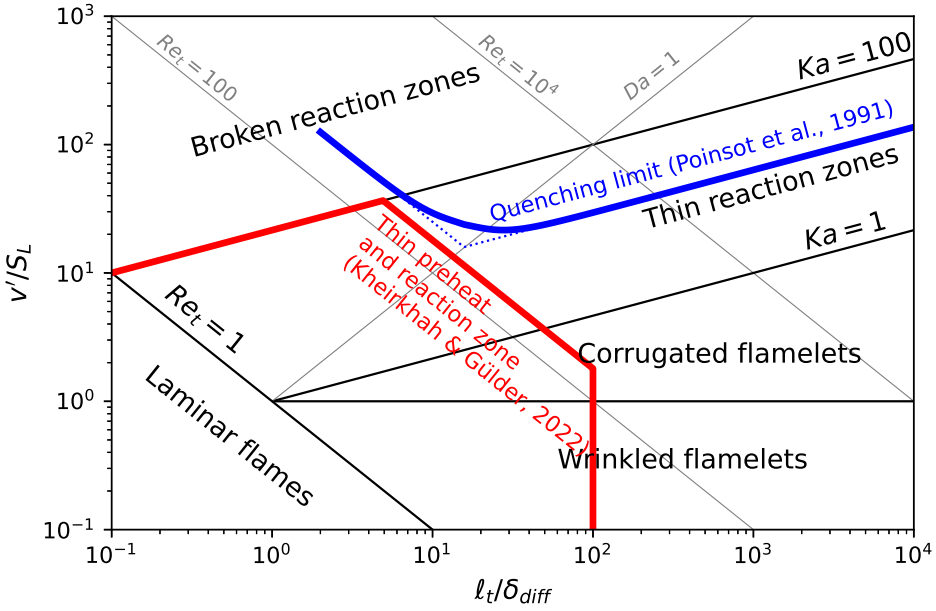

(B) Peters' regime diagram.

FIGURE 5.6: Regimes of turbulent premixed combustion with unity Schmidt number.

dissipated very fast. Recently, Kheirkhah and Gülder (2022) revisited the validity of the flamelet concept in premixed turbulent flames, reviewing the available DNS findings. Indeed, they identify a large part of the regime diagram, where the underlying flamelet structures are not disturbed neither in the preheat zone, nor in the reacting zone. This region is indicated in Fig. 5.6b, and it is enclosed by the limits of $Ka < 100$, $Re_t < 180$, and $\ell_t/\delta_{diff} < 100$. This Reynolds number limit nearly

coincides with the left branch of the quenching limit of Poinsot, Veynante, and Candel (1991). Formulating a limit in terms of Reynolds number is aligned with the aforementioned concern about the strength of the small scale eddies. As Fig. 5.4b illustrates, the increase of turbulence Reynolds number at a fixed integral length scale not only broadens the range of length scales, but also increases the kinetic energy throughout the entire spectrum. Thus, in low Reynolds number cases the flamelet-like layers are not perturbed by the weak small scale structures. Kheirkhah and Gülder (2022) note, that the remaining part of the "Thin reaction zones" regime of Peters likely features thickened preheat zones, and even the reaction zones may or may not undergo thickening due to turbulence.

The tabulated chemistry methods of the present work assume the existence of flamelet-like reaction fronts embedded in the turbulent flow. Consequently, the developed models are to be applied with caution. The developed framework allows for the *a posteriori* verification of the combustion regime, using the turbulence scale estimates of section 5.1.6. The $Ka < 100$ limit is employed for simplicity. Flamelet-based models are applied without *a priori* discrimination, as they are the only option explored in this work.

The above discussion is concerned purely about the actual turbulent flame behavior, and the possibility of representing the turbulent flame as an ensemble of laminar flamelets. As Pitsch and De Lageneste (2002) recognize, the filtering imposed by finite LES meshes adds more complexity to the problem. They argue, that a regime diagram shall represent these effects. Assuming, that the filter width falls in the inertial subrange of the turbulence spectrum, the Karlovitz number may be expressed in terms of the filter width and the sub-grid scale velocity fluctuations using Eq. (5.29) and the definition of the Kolmogorov time scale:

$$Ka^2 = \frac{\tau_{diff}^2}{\tau_\eta^2} = \frac{\tau_{diff}^2}{\{\nu\} \,/\, \{\varepsilon\}} = \frac{\tau_{diff}^2 v_\Delta^3}{\{\nu\}\,\Delta}. \tag{5.111}$$

The term may be further transformed, by using $\{\nu\} = \frac{\delta_{diff} S_L}{Sc}$, and $\tau_{diff} = \frac{\delta_{diff}}{s_L}$:

$$Ka = \sqrt{Sc \frac{\delta_{diff}}{\Delta} \frac{v_\Delta^3}{S_L^3}}. \tag{5.112}$$

Pitsch and De Lageneste (2002) use this alternative form of the Karlovitz number to construct a new regime diagram considering the resolution of the discretization: Δ. The proposed regimes are presented in Fig. 5.7 on the $Ka - \Delta$ plane, normalizing the grid size with the flame thickness and assuming unity Schmidt number. The representation departs from Peters' assumption, that in the $Ka < 100$ regime the underlying reaction-zone structure is flamelet-like. The vertical coordinate of the diagram distinguishes the level of resolution, thus in this case the identified regimes have a different meaning than those of Fig. 5.6b.

The lower half of this diagram represents different scenarios of direct numerical simulation (DNS). The $Re_\Delta = 1$ iso-line corresponds to the limit of flow DNS, i.e.: below this filter size the entire turbulent velocity spectrum is resolved. Nevertheless, this regime is separated to true DNS and a regime labeled "Resolved turbulence". In the former, the resolution is sufficient to adequately resolve all relevant scales including the reaction zone ($\Delta \leq 0.1\delta_{diff}$), while in the latter, even though the turbulent motion is fully resolved, the grid is insufficient to adequately represent the reacting layer.

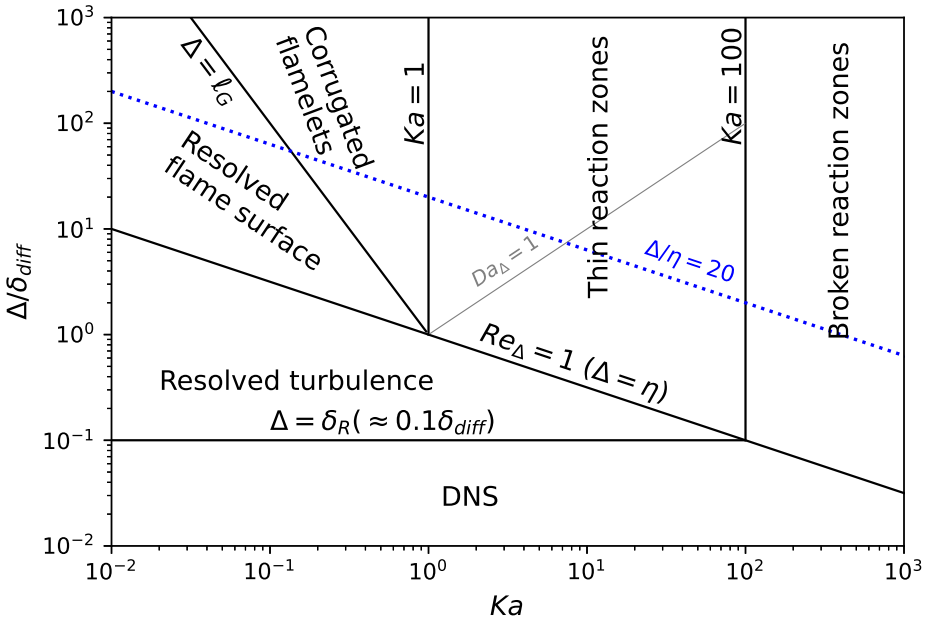

FIGURE 5.7: Regimes of LES in turbulent premixed combustion with unity Schmidt number.

The upper half ($\Delta > \eta$) of the diagram corresponds to LES. As a quality criterion, the $\Delta/\eta = 20$ limit is added to the diagram, which is regarded as a good LES resolution. Note, that such iso-lines are given by the $\Delta/\eta = \Delta/\delta_{diff}\sqrt{Ka}$ relation. Other limiting lines are given by the Karlovitz number limits, as in the regime diagram of Peters. Furthermore, the filter-scale Damköhler number Da_Δ and the Gibson length scale also play a role. The latter is defined as the length scale where the velocity scale becomes equal to the flame speed, and it marks the smallest eddies, which can effectively corrugate the flame front. (Peters, 1988) As the diagram illustrates, an important universal feature of large-eddy simulations of $Ka < 100$, is that the flame structure is bound to be unresolved. In the low Karlovitz number limit two regimes can be identified depending on the resolution of the simulation. If the filter size is larger than the Gibson length, then the corrugation of the flamelets cannot be completely resolved, and the sub-grid models have to contain the effect of the corrugation. Meanwhile, with the decrease of Δ, the "Resolved flamelet surface" regime is reached, where the flame wrinkling is completely known. (Pitsch and De Lageneste, 2002) At $Ka = 1$ the Gibson length becomes smaller than the Kolmogorov length, thus beyond this point the flame wrinkling cannot be resolved unless the turbulence is fully resolved as well. In the "Thin reaction zones" regime ($1 < Ka < 100$) the preheat zone of the flamelet structures may be thickened by turbulent transport. The $Da_\Delta = 1$ line separates a region, where the entire reaction zone is on the sub-grid scale, from another where part of this broadened turbulent preheat zone may be solved. (Pitsch, 2005) In any case, sub-grid models are necessary to correctly represent flame propagation, which are discussed in section 5.4.

Validity of diffusion flamelet based tabulated chemistry models

Similarly, it has long been established, that under certain conditions turbulent diffusion flames can be understood as an ensemble of diffusion flamelets embedded in

the turbulent flow field. (Peters, 1984) In this view the reacting layers are concentrated near the stoichiometric mixture fraction iso-surface. The reaction rate is dictated by the rate of mixing across these embedded flamelet structures, which may be characterized by the stoichiometric scalar dissipation rate. (See Fig. 3.11.) The problem is characterized using Damköhler numbers based on the turbulence integral scales, and the Kolmogorov scales following Balakrishnan and Williams (1994), respectively defined as:

$$Da_t = \frac{\tau_t}{\tau_c}, \qquad Da_\eta = \frac{\tau_\eta}{\tau_c} = \frac{1}{Ka}. \tag{5.113}$$

The latter is analogous to the reciprocal of the Karlovitz number commonly defined in premixed combustion. As demonstrated in Tab. 5.6, the chemical time scale may be defied as Eq. 5.103, using the scalar dissipation rate at the extinction point.

Regime diagrams can be formulated for non-premixed combustion, containing the same information as Fig. 5.6. One choice of coordinates is proposed by Williams using the $Da - Re_t$ plane. (Buckmaster, 1985, §III.3.4) Such representations are widely used in supersonic combustion (Balakrishnan and Williams, 1994; Ingenito and Bruno, 2010; Fureby, 2017; Mura, Techer, and Lehnasch, 2022), but the identification of regimes is similarly important in the low Mach number cases studied here.

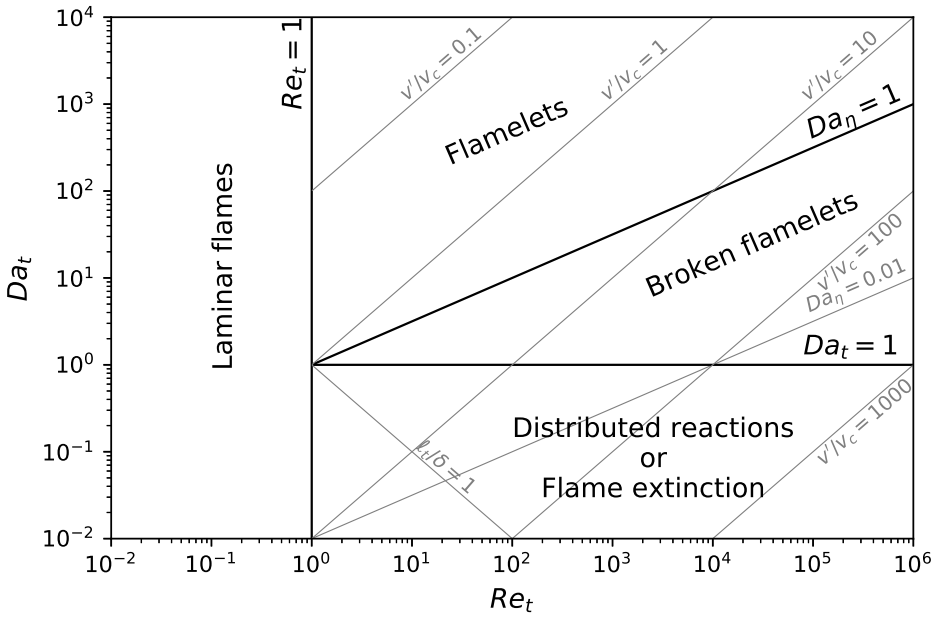

FIGURE 5.8: Regimes of turbulent non-premixed combustion with unity Schmidt number.

On this plane, under the unity Schmidt number assumption, it is possible to identify iso-lines relating the turbulence integral scales to the chemical velocity scale: v_c of Eq.5.105, and to the corresponding length scale: $\delta = v_c \tau_c$. The diagram carries equivalent information to the ones of premixed combustion in Fig. 5.6. However, since in non-premixed flames v_c is not as meaningful as S_L is in premixed flames, the $Da - Re_t$ coordinate system is preferred. Williams (2006) has revisited this regime diagram identifying the non-premixed combustion modes shown in Fig. 5.8. In the flamelet regime ($Da_\eta > 1$) the time scale of the smallest eddies is larger than the reaction time scale, thus the reaction zones are indeed sheet-like structures deformed

by the turbulent flow. In the "Broken flamelets" regime ($Da_\eta < 1,\ Da_t > 1$), part of the turbulent energy can influence the flame front significantly, thus turbulence may cause localized extinction. Finally, in the region of $Da_t < 1$ the entire turbulent energy cascade interacts with the reacting media. Under such conditions, the high rate of turbulent mixing may result in the broadening of the reaction fronts leading to the "Distributed reactions" regime. However, in practical combustion applications, the same regime may correspond to the complete extinction of the flame, if the turbulent mixing depletes radical pools too rapidly.

The strict limits of Damköhler numbers in Fig. 5.8 are challenged by various studies, just as in the case of premixed combustion. Cuenot and Poinsot (1994) used DNS to study the effect of vortex-flame interaction in diffusion flames with a given initial scalar dissipation rate, much like the work of Poinsot, Veynante, and Candel (1991) in premixed flames. Their finding supports the existence of unquenched flamelet structures at Damköhler numbers ~ 2.5 smaller than the *a priori* limits given by time scale analysis. This suggests, that the $Da_\eta = 1$ limit of Fig. 5.8 shall be shifted to lower values, as also recognized by Williams (2006).

Beyond the existence of sheet-like reaction zones embedded in the flow, it is also of interest, to assess the temporal behavior of these flamelets. In particular, whether it is adequate to model these flamelets as steady counterflow flamelets at the given stoichiometric scalar dissipation rate (laminar flamelet assumption, steady laminar flamelet model). Cuenot and Poinsot (1994) found a limiting Damköhler number, approximately twice the *a priori* extinguishing value, above which the vortex-flame interaction problem locally relaxes to the corresponding stable flamelets. Between this limit and the above mentioned local extinction limit the flamelet stays continuous, but unsteady effects are significant. I.e.: the local flame structure takes time to relax to the corresponding steady state. The importance of these unsteady effects in further underlined in the numerical study of Cuenot, Egolfopoulos, and Poinsot (2000), and the asymptotic analysis of Swaminathan (2002). To some extent such unsteady effects are considered in the modeling strategy of non-premixed flames applied here, trough transporting the progress variable instead of basing the thermochemical lookup on the scalar dissipation rate, following the Flamelet Progress Variable (FPV) model of Pierce and Moin (2004). In this approach the progress variable may lag behind the state predicted solely by the scalar dissipation rate. However, as Fig. 3.16 illustrates, the history of unsteady flamelets may have significant consequences on the reaction rates, which is not captured by the applied models. Such details may be represented by the Unsteady Flamelet Progress Variable (UFPV) model of Ihme and See (2010), nonetheless this is out of the scope of the present work.

As Peters (1984) points out, the chemical time scales and the level of turbulence are not the sole determining factors in the behavior of non-premixed combustion. In non-premixed flames, additional complexity emerges from the turbulent nature of the mixture fraction field as well. Combustion might be impossible near the fuel injection sites due to high scalar dissipation rates. If this is the case, some level of fuel-oxidizer mixing may be achieved prior to combustion, thus the combustion mode is no longer strictly non-premixed. An important role is played by the range of mixture fractions that the flame experiences, since if the mixture is homogeneous, then the combustion mode will be that of premixed flames. Furthermore, as already discussed throughout section 3.1.3, the scalar dissipation rate plays a crucial role in the behavior of the flamelets embedded in the turbulence. Recently Denker et al. (2019) used such analysis to distinguish regions with fine scale mixing from ones characterized by diffusion flamelets embedded in the turbulence.

In the framework developed by Peters (2001, §3.6) the range of mixture fractions

is characterized by the spacial variance of the local mixture fraction profiles. This is meaningfully influencing the reactions around the stoichiometric mixture fraction, thus it shall be evaluated such, that the mean mixture fraction is stoichiometric. The stoichiometric mixture fraction fluctuation is defined as:

$$Z'_{st}(\mathbf{x},t) = \sqrt{\left\{\left(Z^{\dagger\dagger}(\mathbf{x},t)\right)^2\right\}}, \qquad \text{such that } \{Z(\mathbf{x},t)\} = Z_{st}, \tag{5.114}$$

where the $\{\cdot\}$ operator is denoting spacial Favre averaging in a representative control volume, and $Z^{\dagger\dagger}(\mathbf{x},t) = Z(\mathbf{x},t) - \{Z(\mathbf{x},t)\}$. The local scalar dissipation rate is likewise characterized by a mean quantity, specifically the conditional mean of the scalar dissipation rate: $\{\chi\}_{st}(\mathbf{x},t) = \{\chi(\mathbf{x},t)|Z_{st}\}$.

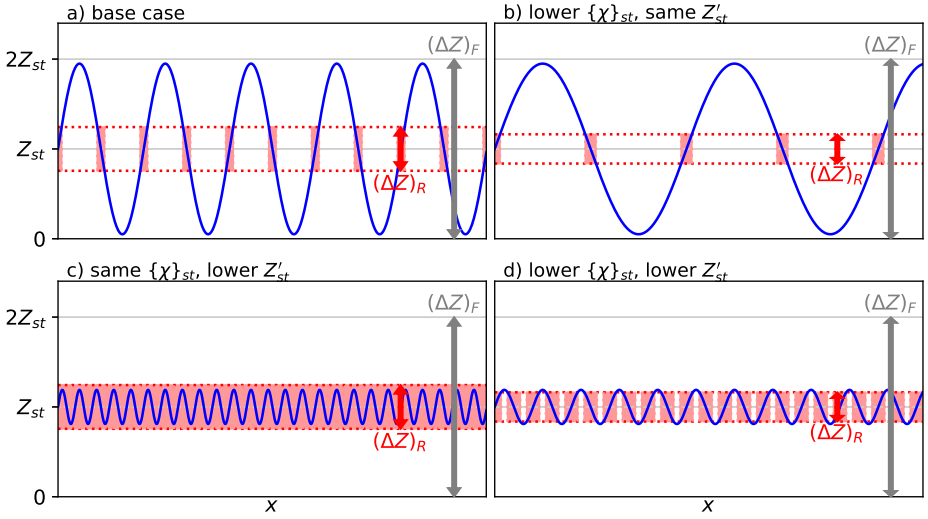

FIGURE 5.9: Model mixture fraction profiles in partially premixed mixtures neglecting the effect of property variations.

The stoichiometric mixture fraction fluctuations have to be related to the underlying structure of the flame. Peters (2001, §3.6) defines a diffusion thickness in mixture fraction space: $(\Delta Z)_F$, and smaller reaction zone thickness: $(\Delta Z)_R$ corresponding to the oxidation layer of the counterflow diffusion flamelet:

$$(\Delta Z)_F = 2Z_{st}, \qquad (\Delta Z)_R = \epsilon\,(\Delta Z)_F, \tag{5.115}$$

where ϵ is a scale of the oxidation layer thickness, which weakly grows with the scalar dissipation rate. The effect of these parameters is illustrated in Fig. 5.9. If Z'_{st} is large, then only a portion of the mixture fraction field can be located in the reaction zone. The distance of these reaction zones is determined by the scalar dissipation rate. Meanwhile, if Z'_{st} is small, then the mixture is largely homogeneous and the entire Z profile may be contained in the highly reactive zone (Fig. 5.9c). In all of the presented cases, the adjacent non-premixed flamelets may influence each other significantly. This influence is only diminished with additional separation of the flamelets in mixture fraction space, which would be signified by higher Z'_{st} values.

Peters (2001, §3.6) constructed a regime diagram for non-premixed combustion, using the $Z'_{st} - \{\chi\}_{st}^{-1}$ plane, normalizing the coordinates with the diffusion thickness in mixture fraction space, and the stoichiometric scalar dissipation rate at the

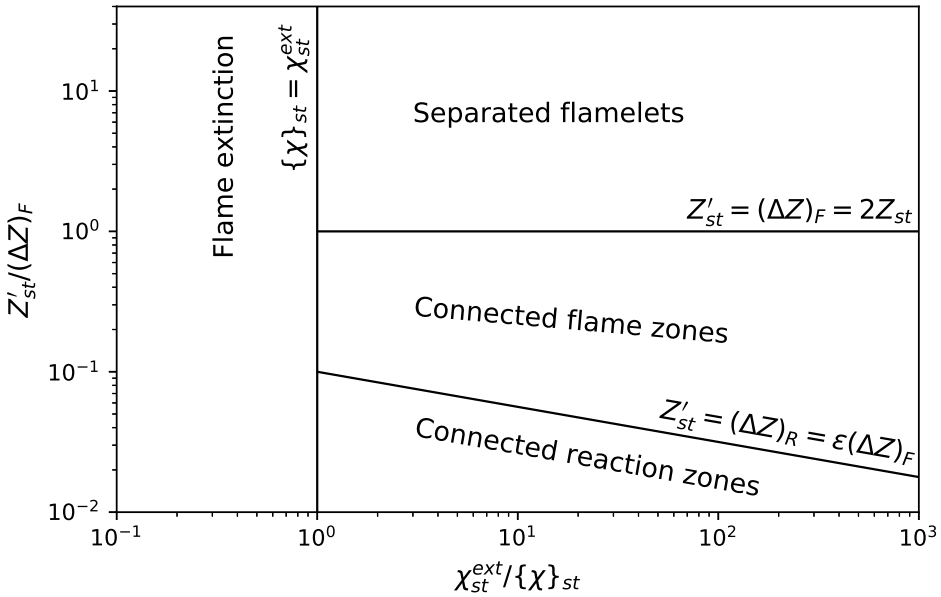

FIGURE 5.10: Regimes of turbulent non-premixed combustion based on the mixture fraction field.

extinction point of counterflow diffusion flamelets. If the conditional stoichiometric scalar dissipation rate exceeds the value at the extinction point, the flamelets are expected to undergo unsteady extinction. Otherwise different regimes are possible, principally governed by Z'_{st}. If the spacial mixture fraction fluctuations are large, then separate flamelet structures are present in the flame, which do not interact significantly. Smaller variations of Z entail, that the flamelets interact at in the diffusion zone, leading to the "Connected flame zones" regime. Such cases are depicted in Fig. 5.9a-b. If the mixture fraction variations are even smaller, then most of the gas mixture is located within the reaction zone. Such a condition is illustrated in Fig. 5.9c, while the case of Fig. 5.9d located near the limit of the two regimes.

As Williams (2006) note, the horizontal coordinate of this figure may be understood as a Damköhler number, since there is a strong relation between the mean scalar dissipation rate, and the strain rate of the flow field. Thus the top part of Fig. 5.10 corresponds to the turbulent regimes in the diagram of Williams (Fig. 5.8.) However, the vertical coordinate is an additional degree of freedom, not represented in Fig. 5.8, which underlines the complexity of non-premixed combustion. For further details on these regimes, see the work of Oran and Boris (1991, §6.III.B) and Peters (2001, §3.6). Such tools are used in this work, to assess the validity of flamelet models *a posteriori*.

Additional complexity is associated to the influence of flame curvature. Based on the DNS results of vortex-flame interaction Cuenot and Poinsot (1994) argue, that curvature is important below a certain ℓ_t/δ limit, corresponding to the lower left corner of Fig. 5.8. Recently, Scholtissek et al. (2015) revisited the curvature effects, and devised new regimes relating the curvature to the flame thickness. Their analysis of a lifted hydrogen jet flame shows an important contribution of curvature effects, note however, that this jet is characterized by moderate Reynolds numbers, thus the results may be consistent with the findings of Cuenot and Poinsot (1994). In the present work curvature effects are not studied in detail.

The discussed regime diagrams may be plotted using the open source repository: https://gitlab.com/BothAmbrus/KolmogorovAtWitness.

5.4 Turbulent combustion modeling with tabulated chemistry in LES

Section 5.1.3 introduces a set of filtered Eulerian transport equations, that define the low Mach number LES problem. These filtered equations contain various unclosed terms, which need information about the sub-grid scales in order to devise sub-grid closure models. In section 5.1.4 such a closure model is described for the sub-grid scale stress tensor. The closure models of the remaining unclosed terms constitute the turbulent combustion model. This section provides details on how the tabulated chemistry models of chapter 3 are extended to large-eddy simulation, forming such a combustion model.

The tabulated chemistry models are constrained by the limits of the flamelet assumption discussed in section 5.3.2. (E.g. $Ka < 100$ for premixed systems, $Da_t > 1$ and $Z''_{st} / (\Delta Z)_F > 1$ for non-premixed systems.) As Fig. 5.7 illustrates, the flamelets are typically entirely unresolved, which calls for dedicated combustion modeling for LES. A review of the early development of viable LES combustion models is provided by Janicka and Sadiki (2005) and Pitsch (2006). More recently Fiorina, Veynante, and Candel (2015) reviewed the advances in LES of reacting flows, with more attention on tabulated chemistry models.

Below, the remaining unclosed terms of the filtered equations are discussed in the context of tabulated chemistry. Closure models are described for the sub-grid scale scalar flux ($\mathbf{\Phi}_k^{SGS}$), the filtered gas properties ($\overline{\rho}, \overline{\mu}, \widetilde{\mathcal{D}_t}$), and the filtered source term ($\overline{S_k}$). In the present modeling strategy the Favre-filtered sub-grid variance of transported scalars is used to characterize their marginal density-weighted filter probability density function (FPDF): $\widetilde{P}_{\xi_k}(\xi_k^*)$. (See Eq. (5.18).) Thus, additional closure models are needed in the sub-grid variance transport equation: Eq. (5.39), such as the sub-grid scalar dissipation rate ($\chi_{\xi_k}^{SGS}$), or the variance production due to volumetric source terms $\left(\overline{\xi_k S_k} - \widetilde{\xi}_k \overline{S_k}\right)$.

5.4.1 Sub-grid diffusion model

The most common approach to close sub-grid scalar fluxes, is the *gradient diffusion assumption*. In this contexts, an analogy is drawn with the eddy-viscosity model, and the sub-grid scalar flux of Eq. (5.32) is expressed as:

$$\mathbf{\Phi}_k^{SGS} = \left(\widetilde{\overline{\rho}\xi_k \mathbf{u}} - \overline{\rho}\widetilde{\xi}_k \widetilde{\mathbf{u}}\right) = -\frac{\overline{\rho}\nu^{SGS}}{Sc^{SGS}} \nabla \widetilde{\xi}_k, \tag{5.116}$$

where Sc^{SGS} is the sub-grid scale Schmidt number. Consequently, the scalar transport equations take the form:

$$\partial_t \left(\overline{\rho}\widetilde{\xi}_k\right) + \nabla \cdot \left(\overline{\rho}\widetilde{\xi}_k \widetilde{\mathbf{u}}\right) - \nabla \cdot \left(\overline{\rho}\left(\widetilde{\mathcal{D}_t} + \frac{\nu^{SGS}}{Sc^{SGS}}\right) \nabla \widetilde{\xi}_k\right) = \overline{S_k}. \tag{5.117}$$

Janicka and Sadiki (2005) reviewed the sub-grid scalar flux modeling strategies used in the literature. They recognize the apparent faults of the gradient diffusion assumption, but note, that reasonable success has been achieved using this approach.

The sub-grid scale Schmidt number, (or sub-grid scale Prandtl number in case of thermal transport) is a model parameter. The constant value of: 0.7 is widely used in combustion simulations. (Cecere et al., 2011; Chrigui et al., 2012; Tyliszczak, Cavaliere, and Mastorakos, 2014; Proch and Kempf, 2015; Rittler, Proch, and Kempf, 2015; Chen, Ruan, and Swaminathan, 2016; Giusti, Kotzagianni, and Mastorakos, 2016; Aulery et al., 2017; Franzelli et al., 2017) However, it is well known, that the actual value of Pr^{SGS} and Sc^{SGS} is dependent on the local conditions. Nicoud (1998) proposes a reasonable constant of 0.9 in thermal channel flows, which is used in thermal flows and flames likewise. (Chatelain, Ducros, and Metais, 2004; Lessani and Papalexandris, 2006; Gravemeier and Wall, 2010; Colin and Michel, 2016; Ma et al., 2019) Meanwhile, Pitsch and Steiner (2000) propose a constant value of 0.4, which agrees well with a dynamically predicted Sc^{SGS} in a piloted jet flame. This value was also adapted in flame simulations. (Sitte and Mastorakos, 2019) In this work the value of $Sc^{SGS} = Pr^{SGS} = 0.7$ is retained unless otherwise stated. It is important to specify the same value in all scalar equations, in order to not create artificial preferential sub-grid transport between different scalars.

As Pitsch (2006) points out, the performance of the gradient diffusion assumption is poor in premixed flames under low Re_t conditions, where counter-gradient turbulent transport of scalars can occur due to thermal dilation across the flame. Poinsot and Veynante (2005, §5.3.8) provide an estimate of turbulence intensity where counter-gradient transport is significant as: $\frac{v'}{S_L} \leq 3$. Furthermore, they argue (Poinsot and Veynante, 2005, §5.4.6), that the mean counter-gradient diffusion is partially resolved in LES, and reasonable results may be obtained even if the sub-grid fluxes are modeled using the gradient diffusion assumption. Addressing this problem is out of the scope of the present work.

5.4.2 Sub-grid variance transport

Equation (5.39) provides a way, to solve for the sub-grid variance of different scalars, such as the mixture fraction: $Z_v = \widetilde{Z^2} - \widetilde{Z}^2$ or the progress variable: $Y_{c,v} = \widetilde{Y_c^2} - \widetilde{Y_c}^2$. As appendix H illustrates, the sub-grid variance carries valuable information on the nature of the filter density function. Such variances are used in the presumed shape FPDF approach described below, which provides closure for the filtered reaction source terms and material properties.

In case of passive scalar mixing with $\mathcal{O}(1)$ Schmidt number in homogeneous isotropic turbulence, the *scalar-energy* (ξ_k^2) behaves similarly to the kinetic energy, and shows a similar $\propto \kappa^{-5/3}$ behavior in part of its spectrum. (See Fig. 5.4.) Algebraic closures of $\xi_{k,v}$ are widely used, which assume, that the cut-off wave number lies within the inertial subrange of the scalar spectrum. These methods are similar to estimating the sub-grid kinetic energy following Yoshizawa (1986) in Eq. (5.53). Such a model was proposed by Branley and Jones (2001), and similar approaches were successfully applied in LES studies. (Pitsch and Steiner, 2000; Pierce and Moin, 2004; Pitsch and Ihme, 2005; Dianat et al., 2006; Ferraris and Wen, 2007; Ihme and Pitsch, 2008a; Vreman et al., 2008; Floyd et al., 2009; Navarro-Martinez and Kronenburg, 2009; Chrigui et al., 2012; Popp et al., 2015; Zhang et al., 2015; El-Asrag, Braun, and Masri, 2016; Wehrfritz et al., 2016) These applications sometime even extend to the variance of reactive scalars. (El-Asrag, Braun, and Masri, 2016; Ma, Huang, and Roekaerts, 2017)

In case of reactive scalars the behavior of the spectrum is not necessarily universal, as small scale structures are created at the length scale of the flame thickness.

In the variance transport this is reflected in term "II" of Eq. (5.39): $\left(2\overline{\xi_k S_k} - 2\widetilde{\xi_k}\overline{S_k}\right)$, where the S_k source contains contributions from chemical reactions. As mentioned above, algebraic closures do exist for the variance of reactive scalars, however, it is possible to solve Eq. (5.39) or variations of it with closure models for the individual terms in order to obtain the sub-grid variance. (Domingo et al., 2005; Cecere et al., 2011; Zhang et al., 2016; Gövert et al., 2018; Mira et al., 2020; Massey, Chen, and Swaminathan, 2021; Tang and Raman, 2021)

In the present work the approach of Domingo, Vervisch, and Veynante (2008) is preferred for both passive and reactive scalar variances, where Eq. (5.39) is solved. Such sub-grid variance transport equations are used for the mixture fraction (Z) and the progress variable (Y_c), in case their variance is needed by the presumed FPDF sub-grid closure. The closure methods are detailed below.

The sub-grid scale diffusion of the square of the scalar is modeled the same way as above, thus the sub-grid flux of the variance can be directly modeled using the gradient diffusion assumption:

$$\boldsymbol{\Phi}_{k,v}^{SGS} = \underbrace{\boldsymbol{\Phi}_{k^2}^{SGS}}_{-\frac{\overline{\rho}\nu^{SGS}}{Sc^{SGS}}\nabla\widetilde{\xi}_k^2} - \underbrace{2\widetilde{\xi}_k\boldsymbol{\Phi}_k^{SGS}}_{-\frac{\overline{\rho}\nu^{SGS}}{Sc^{SGS}}\nabla\widetilde{\xi}_k{}^2} = -\frac{\overline{\rho}\nu^{SGS}}{Sc^{SGS}}\nabla\widetilde{\xi_{k,v}}. \tag{5.118}$$

Term "I" of Eq. (5.39) represents the production of sub-grid variance due to the sub-grid transport of the filtered variable. This term is also readily closed by the sub-grid diffusion model:

$$-2\boldsymbol{\Phi}_k^{SGS}\cdot\nabla\widetilde{\xi}_k = 2\frac{\overline{\rho}\nu^{SGS}}{Sc^{SGS}}\nabla\widetilde{\xi}_k\cdot\nabla\widetilde{\xi}_k. \tag{5.119}$$

Term "II" describes sub-grid variance production due to volumetric sources. In case of the progress variable, the term is associated to reactive sources: $2\overline{Y_c\dot{\omega}_{Y_c}} - 2\widetilde{Y}_c\overline{\dot{\omega}_{Y_c}}$. This is closed by directly tabulating $\overline{\dot{\omega}_{Y_c}}$ and $\overline{Y_c\dot{\omega}_{Y_c}}$ computed using the presumed FPDF approach described below. In case of the mixture fraction, term "II" has no reactive sources.

If a separately modeled Lagrangian spray cloud is used to model the liquid fuel, then the transported Eulerian scalars are coupled to the fuel spray through source terms. The details are described in section 5.5. For the sake of the consequences on the variance transport, it is sufficient to know, that the evaporative source term of mixture fraction: S_Z^e is the only source term of Z. It is equal to the evaporative mass source: S_ρ^e, which is also the only volumetric mass source. Furthermore, in this work the progress variable has no volumetric source associated to the progress variable. Note, that such terms could become necessary if single droplet combustion (Paulhiac et al., 2020) would be modeled.

Since the mixture fraction has a significant volumetric source term, the sub-grid mixture fraction variance equation has a corresponding term: $2\overline{ZS_Z^e} - 2\widetilde{Z}\overline{S_Z^e}$. Reveillon and Vervisch (2000) used the DNS of dilute spray in decaying homogeneous turbulence to show, that this sub-grid spray source term is likely to be non-negligible in LES. Hollmann and Gutheil (1996) devised a closure for RANS equations, that was subsequently extended to LES by Pera et al. (2006). However, in the latter case a dynamically evaluated modeling constant is introduced, that was found to be necessary to achieve good correlation with DNS. Nevertheless, Ma and Roekaerts (2017) used the model of Pera et al. with the fixed modeling constants of Hollmann and Gutheil derived for RANS.

Tyliszczak, Cavaliere, and Mastorakos (2014) presented an algebraic sub-grid mixture fraction variance model for spray combustion. Giusti, Kotzagianni, and Mastorakos (2016) used this model and pointed out the numerical difficulties of applying algebraic models in spray combustion, due to the local spikes of Z_v associated to Lagrangian droplets. They advocate the usage of sub-grid variance transport equations, that would ensure smoother variance fields. Recently Sitte and Mastorakos (2019) applied such variance equations and neglected the spray source terms altogether, due to the uncertainty in the modeling approach. Due to the high modeling uncertainty and since dynamic closures are out of the scope of the present work, the Z_v equation is solved without spray source terms. Moreover, term "IV" of Eq. (5.39) is likewise neglected, although this decision is more justified, as this dilution term tends to be small. (Pera et al., 2006)

Finally, term "III" of Eq. (5.39) is closed by modeling the sub-grid scalar dissipation rate of the transported scalar: $\overline{\rho}\chi_{\xi_k}^{SGS} = \overline{2\rho\mathcal{D}_t\nabla\xi_k\cdot\nabla\xi_k} - 2\widetilde{\rho D_t}\nabla\widetilde{\xi}_k\cdot\nabla\widetilde{\xi}_k$. The correct closure of $\chi_{\xi_k}^{SGS}$ is of great importance, as in the present modeling this is the only sink term of the equation. Following Domingo, Vervisch, and Veynante (2008), the term is closed using the *linear relaxation hypothesis*, i.e.: the sub-grid variance is assumed to decay at a constant time scale, given that all other terms are zero. This may be expressed as:

$$\chi_{\xi_k}^{SGS} = C_\chi \frac{\xi_{k,v}}{\tau_\Delta}, \tag{5.120}$$

where $C_\chi = 2$ is a modeling constant (Kemenov, Wang, and Pope, 2012), and τ_Δ is the time scale associated to the sub-grid scales. Ventosa Molina et al. (2017) found, that τ_Δ has to be derived consistently with the eddy-viscosity model for proper variance behavior. In most works the time scale is taken as Δ^2/ν^{SGS} which is strictly true in the Smagorinsky model and dynamic versions of it. Here, the instantaneous value of the time scale is estimated using the scaling laws of Eq. (5.29), assuming that the cut-off is within the inertial subrange of the turbulent energy cascade:

$$\tau_\Delta \propto \left(\frac{\varepsilon^{SGS}}{\Delta^2}\right)^{-1/3}, \qquad \tau_\Delta = \left(\frac{C_\varepsilon^2 \nu^{SGS}\mathbf{S}\left(\widetilde{\mathbf{u}}\right):\mathbf{S}^{\mathbf{D}}\left(\widetilde{\mathbf{u}}\right)}{\Delta^2}\right)^{-1/3}, \tag{5.121}$$

where $C_\varepsilon = 1.8$ is a modeling constant.

Recently Nilsson et al. (2019) analyzed different closures of the reactive scalar variance equation with filtering DNS data of premixed flames. They found, that variance production with the gradient diffusion assumption may be inadequate at low Karlovitz numbers, where this term becomes negative in order to balance the chemical production rate. Furthermore, they note, that the sub-grid scalar dissipation rate of reactive scalars needs further study, including the reevaluation of the linear relaxation models, and the tuning of the modeling constant: C_χ. Note, that Garmory and Mastorakos (2011) proposes a modification of the modeling constant even for passive scalars ($C_\chi = 24$). Nevertheless, here the classical value of 2 is retained.

Overall, the variance equations of mixture fraction and progress variable take the form:

$$\partial_t\left(\overline{\rho}Z_v\right)+\nabla\cdot\left(\overline{\rho}Z_v\widetilde{\mathbf{u}}\right)-\nabla\cdot\left(\overline{\rho}\left(\widetilde{\mathcal{D}_t}+\frac{\nu^{SGS}}{Sc^{SGS}}\right)\nabla Z_v\right)= 2\frac{\overline{\rho}\nu^{SGS}}{Sc^{SGS}}\nabla\widetilde{Z}\cdot\nabla\widetilde{Z}-\underbrace{\overline{\rho}\,C_\chi\frac{Z_v}{\tau_\Delta}}_{\chi_Z^{SGS}}, \tag{5.122}$$

$$\partial_t\left(\overline{\rho}Y_{c,v}\right)+\nabla\cdot\left(\overline{\rho}Y_{c,v}\widetilde{\mathbf{u}}\right)-\nabla\cdot\left(\overline{\rho}\left(\widetilde{\mathcal{D}_t}+\frac{\nu^{SGS}}{Sc^{SGS}}\right)\nabla Y_{c,v}\right)= 2\frac{\overline{\rho}\nu^{SGS}}{Sc^{SGS}}\nabla\widetilde{Y}_c\cdot\nabla\widetilde{Y}_c+2\left(\overline{Y_c\dot{\omega}_{Y_c}}-\widetilde{Y}_c\overline{\dot{\omega}_{Y_c}}\right)-\underbrace{\overline{\rho}\,C_\chi\frac{Y_{c,v}}{\tau_\Delta}}_{\chi_{Y_c}^{SGS}}, \tag{5.123}$$

where $C_\chi=2$, and the sub-grid time scale is evaluated according to Eq. 5.121.

5.4.3 Presumed FPDF sub-grid chemistry model

In the presumed FPDF approach, the sub-grid distribution of the scaled control variables of chemistry tables: Z, C, and i, are characterized by a model function, which is parameterized by different moments of the transported control variable: Z, Y_c, and h. In the present work, delta and beta FPDFs are applied for this purpose. First is simply a Dirac delta function at the filtered control variable, while the second is defined by the filtered control variable and its sub-grid variance. Note, that besides the presumed FPDF approach various other sub-grid models exist, which provide closure to the sub-grid turbulence/chemistry interaction in the context of tabulated chemistry. The review of Fiorina, Veynante, and Candel (2015) provides an excellent comparison of these sub-grid models. Many of these are dedicated to overcome different limitations of the presently used FPDF approach. Namely, in this work the thickness of the resolved flame front is not controlled explicitly, but it is a consequence of the various models interacting with the finite computational grid. This is undesirable in terms of the numerical solution of the flame propagation. Furthermore, in the presumed FPDF method, under-resolved laminar flame fronts may not reproduce the correct laminar flame propagation speed.

TABLE 5.7: Thermo-chemical tabulation strategies with control variables of mixture fraction (Z), scaled progress variable (C), and scaled enthalpy (i).

System	Tabulation ($\mathcal{F}=\mathcal{F}\left(\xi_k\right)$)
Inert mixing of reactants	$\mathcal{F}=\mathcal{F}\left(Z\right)$
Adiabatic perfectly premixed combustion	$\mathcal{F}=\mathcal{F}\left(C\right)$
Non-adiabatic perfectly premixed combustion	$\mathcal{F}=\mathcal{F}\left(C,i\right)$
Adiabatic non-premixed combustion	$\mathcal{F}=\mathcal{F}\left(Z,C\right)$
Non-adiabatic non-premixed combustion	$\mathcal{F}=\mathcal{F}\left(Z,C,i\right)$

In the present tabulated chemistry approach, the thermo-chemical state is expressed as a function of the control variables. As detailed in chapter 3, such tables may be devised for various systems listed here in Tab. 5.7. In a general form, for a

tabulation: $\mathcal{F}(\xi_k)$, with N independent control variables: ξ_k, the sub-grid thermo-chemical state is fully described by the joint density-weighted filter probability density function of the control variables: $\widetilde{P}_{\xi_1\xi_2...\xi_N}$. The joint FPDF may be expressed as a product of one marginal and multiple conditional FPDFs, as Eq. (H.10) suggests:

$$\widetilde{P}_{\xi_1\xi_2...\xi_N}\left(\xi_1^*,\xi_2^*,...\xi_N^*\right)=\widetilde{P}_{\xi_1}\left(\xi_1^*\right)\widetilde{P}_{\xi_2|\xi_1}\left(\xi_2^*|\xi_1^*\right)...\,\widetilde{P}_{\xi_N|\xi_1,\xi_2,...\xi_{N-1}}\left(\xi_N^*|\xi_1^*,\xi_2^*,...,\xi_{N-1}^*\right) \tag{5.124}$$

Furthermore, it is assumed, that the control variables are statistically independent on the sub-grid scale, thus the conditional FPDFs are the marginal FPDFs, and the joint function is expressed as:

$$\widetilde{P}_{\xi_1\xi_2...\xi_N}\left(\xi_1^*,\xi_2^*,...\xi_N^*\right)=\prod_{k=1}^{N}\widetilde{P}_{\xi_k}\left(\xi_k^*\right). \tag{5.125}$$

As Massey, Chen, and Swaminathan (2021) points out, this statistical independence is much less questionable in LES than in RANS, and correction methods may be omitted.

Filtered properties in the presumed FPDF method

The joint filter probability density function of the control variables may be used to provide a sub-grid closure to any tabulated quantity. These tabulated quantities may be any of species mass fraction, and the enthalpy, or the derived properties listed in Tab. 3.9. The filtered dependent quantities are obtained, similar to Eq. (5.17) with the control variables being the independent variables. Thus the Favre-filtered tabulated quantities are:

$$\widetilde{\mathcal{F}}=\int_0^1...\int_0^1\mathcal{F}\left(\xi_1^*,\xi_2^*,...\xi_N^*\right)\widetilde{P}_{\xi_1\xi_2...\xi_N}\left(\xi_1^*,\xi_2^*,...\xi_N^*\right)\mathrm{d}\xi_1^*\mathrm{d}\xi_2^*...\mathrm{d}\xi_N^*, \tag{5.126}$$

The filtered density: $\overline{\rho}$, may be obtained by taking the Favre-filtered specific volume: $\widetilde{1/\rho}=\overline{\rho/\rho}/\overline{\rho}$, thus the filtered density is:

$$\overline{\rho}=\frac{1}{\int_0^1...\int_0^1\frac{1}{\rho\left(\xi_1^*,\xi_2^*,...\xi_N^*\right)}\widetilde{P}_{\xi_1\xi_2...\xi_N}\left(\xi_1^*,\xi_2^*,...\xi_N^*\right)\mathrm{d}\xi_1^*\mathrm{d}\xi_2^*...\mathrm{d}\xi_N^*}. \tag{5.127}$$

Finally, non-density-weighted filtered quantities are obtained from $\widetilde{\mathcal{F}/\rho}=\overline{\mathcal{F}}/\overline{\rho}$:

$$\overline{\mathcal{F}}=\overline{\rho}\int_0^1...\int_0^1\frac{\mathcal{F}\left(\xi_1^*,\xi_2^*,...\xi_N^*\right)}{\rho\left(\xi_1^*,\xi_2^*,...\xi_N^*\right)}\widetilde{P}_{\xi_1\xi_2...\xi_N}\left(\xi_1^*,\xi_2^*,...\xi_N^*\right)\mathrm{d}\xi_1^*\mathrm{d}\xi_2^*...\mathrm{d}\xi_N^*. \tag{5.128}$$

FPDF model functions

The density function of each control variable in Tab. 5.7 is either modeled by a delta or beta function. The former distribution is defined simply as:

$$\widetilde{P}_{\xi_k}^{\delta}\left(\xi_k^*;\widetilde{\xi}_k\right)=\delta\left(\widetilde{\xi}_k-\xi_k^*\right). \tag{5.129}$$

where δ is the Dirac delta function. Meanwhile the beta function is defied as:

$$\widetilde{P}^{\beta}_{\xi_k}\left(\xi^*_k;\widetilde{\xi}_k,\xi_{k,v}\right)=\frac{\Gamma\left(a+b\right)}{\Gamma\left(a\right)\Gamma\left(b\right)}\left(\xi^*_k\right)^{a-1}\left(1-\xi^*_k\right)^{b-1}, \tag{5.130}$$

with the parameters a and b depending on the filtered value and sub-grid variance of the modeled field:

$$a=\widetilde{\xi}_k\left(\frac{\widetilde{\xi}_k\left(1-\widetilde{\xi}_k\right)}{\xi_{k,v}}-1\right), \qquad b=\left(1-\widetilde{\xi}_k\right)\left(\frac{\widetilde{\xi}_k\left(1-\widetilde{\xi}_k\right)}{\xi_{k,v}}-1\right). \tag{5.131}$$

Furthermore, the gamma function in Eq. 5.130 is defined by an improper integral as:

$$\Gamma\left(a\right)\int_0^{\infty}t^{a-1}e^{-t}\mathrm{d}t. \tag{5.132}$$

The β-FPDF takes real values for $\xi^*_k\in[0,1]$, $\widetilde{\xi}_k\in[0,1]$, and $\xi_{k,v}\in\left[0,\widetilde{\xi}_k\left(1-\widetilde{\xi}_k\right)\right]$. Consequently, it is suitable for the modeling of random variables bounded in the $[0,1]$ interval such as Z or C. The maximum possible sub-grid variance varies with the filtered value, consequently, it is customary to to express the variance in a scaled form:

$$\zeta_{\xi_k}=\frac{\xi_{k,v}}{\widetilde{\xi}_k\left(1-\widetilde{\xi}_k\right)}. \tag{5.133}$$

The scaled variance ζ_{ξ_k} is often called the *segregation factor* to refer to its physical meaning. Irrespective of the presumed FPDF modeling, if the variable ξ_k is bounded to the $[0,1]$ interval, then $\zeta_{\xi_k}=0$ corresponds to constant $\xi_k=\widetilde{\xi}_k$ on the sub-grid scale. Meanwhile, $\zeta_{\xi_k}=1$ is only possible, if the sub-grid states are composed of two completely unmixed regions of $\xi_k=0$ and $\xi_k=1$. The β-FPDF correctly recovers these solutions, and smoothly transitions between the two states.

Some representative examples of the beta function are shown in Fig. 5.11. The different columns correspond to different filtered control variables: $\widetilde{\xi}_k$, while the two rows represent the FPDF, and its cumulative counterpart. Darker curves mark lower scaled variance. Indeed, the β-function recovers the two limiting situations. At $\zeta_{\xi_k}\to 0$ the function approaches a Dirac delta function at $\widetilde{\xi}_k$, as indicated by the cumulative curve approaching a Heaviside function. Meanwhile with $\zeta_{\xi_k}\to 1$, the cumulative function is composed of two Heaviside functions, corresponding to two Dirac deltas in $\widetilde{P}^{\beta}_{\xi_k}$ at locations 0 and 1, with intensities of $1-\widetilde{\xi}_k$ and $\widetilde{\xi}_k$ respectively. Interestingly, very small values of the scaled variance are causing notable deviation from the zero variance limit.

Cook and Riley (1994) proposed to use a β-FPDF model for mixture fraction in the LES of non-premixed flames. The approach was subsequently extended to reactive scalars as well. Nonetheless, several works dispute the validity of β-FPDFs for both Z and C. For instance, Floyd et al. (2009) proposed a top-hat FPDF profile for passive scalars in LES, which agrees well with assuming linear profiles of the transported quantity on the sub-grid scale. However, in an *a posteriori* assessment, they found little difference between the proposed approach and the classical β-FPDF. They argue, that the actual prediction of the variance value is more important, than the choice of the modeling function of the FPDF. More recently, Lapointe and Blanquart (2017) used DNS of perfectly premixed turbulent flames and found that the

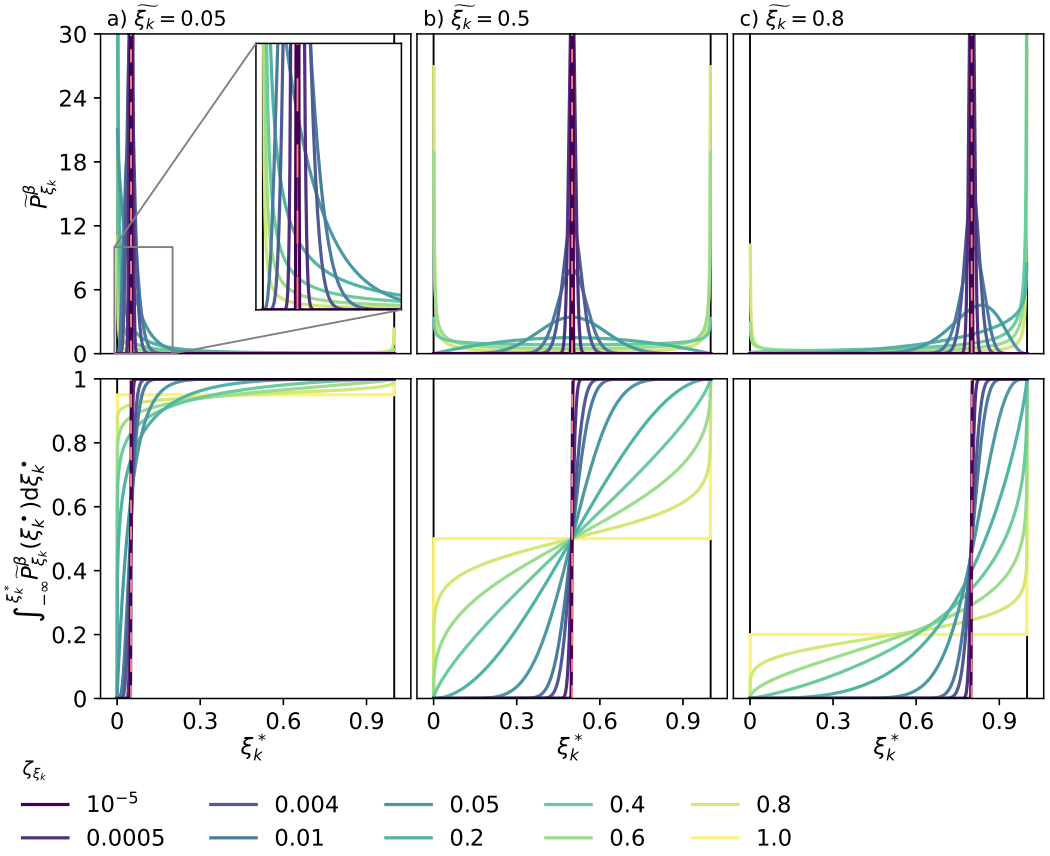

FIGURE 5.11: β-FPDF examples at different scaled variance values. The columns correspond to different filtered values with $\xi_k^* = \widetilde{\xi_k}$ indicated by the dashed line.

β-FPDF model coupled with tabulated chemistry predicts the turbulent flame speed to a satisfactory degree, despite the observed discrepancies in the actual FPDF. Note, that this study obtains the mean and variance of progress variable by filtering the DNS data, thus the adequacy of the presumed FPDF is again conditional on the appropriate modeling of the variance transport equations.

Presumed FPDFs in tabulated chemistry

If the tabulated chemistry model is characterized by a single control variable, like the case of inert mixing or adiabatic premixed combustion, then the modeling choices are simple: either beta or delta functions are applied on the sub-grid scale. (Pitsch and Steiner, 2000; Gövert et al., 2018; Mira et al., 2020) However, in case of multiple control variables the joint FPDF (Eq. (5.125)) can be constructed various ways. Delta-FPDF is widely accepted in the modeling of scaled enthalpy in non-adiabatic cases on the basis, that properties change quasi-linearly as the function of enthalpy, and that sub-grid enthalpy variations are linked to the distribution of Z rather than different sub-grid levels of i. This approach is used in premixed (Cecere et al., 2011; Tang and Raman, 2021) and non-premixed (Ihme and Pitsch, 2008a; Pantangi et al., 2014; Mercier et al., 2014; Locci et al., 2015; Ma, 2016; Wollny, Rogg, and Kempf, 2018; Massey, Chen, and Swaminathan, 2021) systems likewise.

In partially premixed or non-premixed flames both the mixture fraction and the scaled progress variable has to be considered. Two main approaches are common. Pierce and Moin (2004) proposed to model the joint FPDF in a non-premixed flame as the product of beta-function of mixture fraction and delta function of scaled progress variable. They argue, that the filter volume is dominated by a single counterflow diffusion flamelet solution, thus C shall not vary on the sub-grid scale. Meanwhile, Domingo, Vervisch, and Veynante (2008) recommends to treat Z and C as independent variables on the sub-grid scale, and model both $\widetilde{P}_Z$ and $\widetilde{P}_C$ as beta functions.

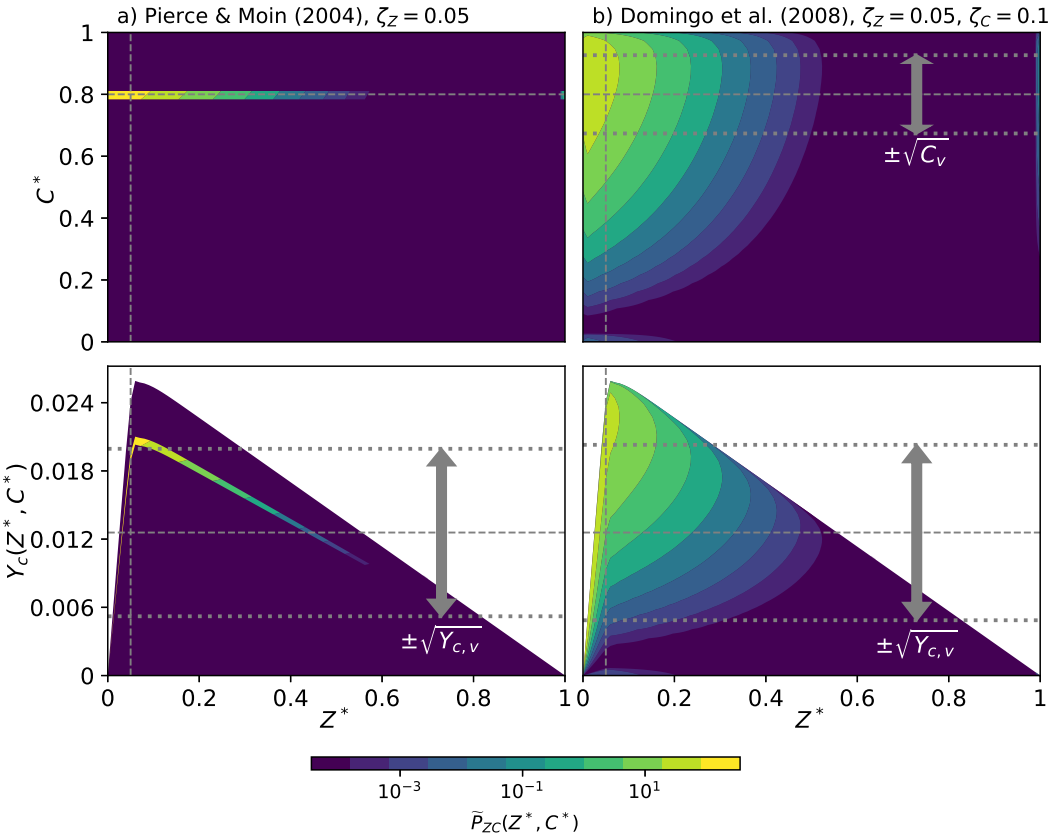

FIGURE 5.12: Illustration of presumed joint FPDF of mixture fraction and scaled progress variable. The filtered control variables are indicated with dashed lines: $\widetilde{Z} = 0.05$, $\widetilde{C} = 0.8$. The columns correspond to the approach of Pierce and Moin (2004): $\widetilde{P}_{ZC} = \widetilde{P}_Z^{\beta}\widetilde{P}_C^{\delta}$, and to the approach of Domingo, Vervisch, and Veynante (2008): $\widetilde{P}_{ZC} = \widetilde{P}_Z^{\beta}\widetilde{P}_C^{\beta}$. The square root of the sub-grid variance of the un-scaled and scaled progress variable is indicated by dotted lines. .

Both the methods of Pierce and Moin (2004) and Domingo, Vervisch, and Veynante (2008) build on the independence of Z and C, but approach the problem in a different light. In the former, a single scaled progress variable is believed to characterize the filter volume, roughly corresponding to a single counterflow diffusion flamelet. Meanwhile in the latter sub-grid variations are permitted in both control variables. Table 5.8 presents a non-exhaustive list of different LES studies using beta and delta marginal FPDFs for the convolution of flamelet solutions. Both methods are widely used in adiabatic and non-adiabatic cases likewise.

TABLE 5.8: Joint FPDF approaches in flamelet-based partially premixed or non-premixed LES studies.

Reference	$\widetilde{P}_Z$	$\widetilde{P}_C$	$\widetilde{P}_i$
(Pierce and Moin, 2004)	β	δ	–
(Pitsch and Ihme, 2005)	β	δ	–
(Olbricht et al., 2010)	β	δ	–
(Chrigui et al., 2012)	β	δ	–
(De and Kim, 2013)	β	δ	–
(Bekdemir et al., 2013)	β	δ	–
(Lamouroux et al., 2014)	β	δ	δ
(Pantangi et al., 2014)	β	δ	δ
(Locci et al., 2015)	β	δ	δ
(Popp et al., 2015)	β	δ	–
(Wehrfritz et al., 2016)	β	δ	–
(Nguyen and Sirignano, 2018)	β	δ	–
(Benajes et al., 2022)	β	δ	δ
(Domingo, Vervisch, and Veynante, 2008)	β	β	–
(Vreman et al., 2008)	β	β	–
(Ma, Huang, and Roekaerts, 2017)	β	β	–
(Gövert et al., 2018)	β	β	δ
(Hu and Kurose, 2019)	β	β	–
(Domingo-Alvarez et al., 2020)	β	β	–
(Massey, Chen, and Swaminathan, 2021)	β	β	δ
(Novoselov et al., 2021)	β	β	–
(Mira, Both, and Surapaneni, 2022)	β	β	δ

The two approaches of $\widetilde{P}_Z^{\beta}\widetilde{P}_C^{\delta}$ and $\widetilde{P}_Z^{\beta}\widetilde{P}_C^{\beta}$ are illustrated in Fig. 5.12. The figure shows the contour plot of the joint FPDF of mixture fraction and progress variable as function of the sample space $Z^* - C^*$. Furthermore, in the second row of plots, the progress variable sample space is replaced by the un-scaled progress variable: $Y_c(Z^*, C^*)$. The two columns correspond to the the two approaches: on the left, all sub-grid variations are explained by the mixture fraction, while on the right sub-grid variations of the scaled progress variable are also occurring. The dashed line in the second row of plots represents the filtered progress variable, calculated as the integral:

$$\widetilde{Y}_c = \int_0^1 \int_0^1 Y_c(Z^*, C^*)\widetilde{P}_{ZC}\left(Z^*, C^*\right) \mathrm{d}Z^* \mathrm{d}C^* \tag{5.134}$$

$$= \int_0^1 \int_0^1 Y_c^{start}(Z^*) + C^*(Y_c^{end}(Z^*) - Y_c^{start}(Z^*))\widetilde{P}_Z\left(Z^*\right)\widetilde{P}_C\left(C^*\right) \mathrm{d}Z^* \mathrm{d}C^* \tag{5.135}$$

From this, it is straightforward to express the Favre-filtered scaled progress variable as:

$$\widetilde{C} = \frac{\widetilde{Y}_c - \widetilde{Y_c^{start}}}{\widetilde{Y_c^{end}} - \widetilde{Y_c^{start}}}, \tag{5.136}$$

where the limits are only a function of mixture fraction, thus they can be integrated by the marginal FPDF of mixture fraction alone:

$$\widetilde{Y_c^{start}} = \int_0^1 Y_c^{start}(Z^*)\widetilde{P}_Z\left(Z^*\right)\mathrm{d}Z^*, \qquad \widetilde{Y_c^{end}} = \int_0^1 Y_c^{end}(Z^*)\widetilde{P}_Z\left(Z^*\right)\mathrm{d}Z^*. \tag{5.137}$$

Similarly, the filtered scalar energy of the progress variable is expressed as:

$$\begin{aligned}\widetilde{Y_c^2} &= \int_0^1\int_0^1 Y_c^2(Z^*,C^*)\widetilde{P}_{ZC}\left(Z^*,C^*\right)\mathrm{d}Z^*\mathrm{d}C^* &(5.138)\\ &= \int_0^1 Y_c^{start\,2}(Z^*)\widetilde{P}_Z\left(Z^*\right)\mathrm{d}Z^* \\ &\quad + \int_0^1\int_0^1 2C^*\left(Y_c^{start}(Z^*)Y_c^{end}(Z^*) - Y_c^{start\,2}(Z^*)\right)\widetilde{P}_Z\left(Z^*\right)\widetilde{P}_C\left(C^*\right)\mathrm{d}Z^*\mathrm{d}C^* \\ &\quad + \int_0^1\int_0^1 C^{*2}\left(Y_c^{end}(Z^*) - Y_c^{start}(Z^*)\right)^2\widetilde{P}_Z\left(Z^*\right)\widetilde{P}_C\left(C^*\right)\mathrm{d}Z^*\mathrm{d}C^* &(5.139)\end{aligned}$$

From this relation $\widetilde{C^2}$ can be expressed, and the sub-grid variance: $C_v = \widetilde{C^2} - \widetilde{C}^2$, is given by:

$$C_v = \frac{Y_{c,v} + \widetilde{Y}_c^{\,2} - \widetilde{Y_c^{start\,2}} - 2\left(\widetilde{Y_c^{start}Y_c^{end}} - \widetilde{Y_c^{start\,2}}\right)\widetilde{C}}{\widetilde{Y_c^{end\,2}} - 2\,\widetilde{Y_c^{start}Y_c^{end}} + \widetilde{Y_c^{start\,2}}} - \widetilde{C}^2. \tag{5.140}$$

Note, that this expression is commonly defined in a simplified form for the special case of $Y_c^{start} = 0$ (Domingo, Vervisch, and Veynante, 2008; Zhang et al., 2016; Gövert et al., 2018):

$$C_v = \frac{Y_{c,v} + \widetilde{Y}_c^{\,2}}{\widetilde{Y_c^{end\,2}}} - \frac{\widetilde{Y}_c^{\,2}}{\widetilde{Y_c^{end}}^2}, \qquad \text{if } Y_c^{start} = 0. \tag{5.141}$$

The terms: $\widetilde{Y_c^{start\,2}}$, $\widetilde{Y_c^{start}Y_c^{end}}$, and $\widetilde{Y_c^{end\,2}}$ are integrated with the FPDF of the mixture fraction. Similar to Eq. (5.136), the filtered value of the scaled enthalpy can be obtained as:

$$\widetilde{i} = \frac{\widetilde{h} - \widetilde{h^{min}}}{\widetilde{h_{ad}} - \widetilde{h^{min}}}, \tag{5.142}$$

where the limit: $\widetilde{h^{min}}$ is integrated with the FPDF of mixture fraction, or the joint FPDF of mixture fraction and progress variable, depending on the tabulation strategies described in section 3.3. Note, that in principle $\widetilde{h_{ad}}$ shall be integrated by the mixture fraction FPDF, but since in the present work the unity Lewis number assumption is used and h_{ad} is linear in Z, this integration does not change the value evaluated at the mean: $\widetilde{h_{ad}}\left(\widetilde{Z}, Z_v\right) = h_{ad}\left(\widetilde{Z}\right)$.

Indeed, neither of the methods presented in Fig. 5.12 imply, that the variance of the un-scaled progress variable is zero. However in the view of Pierce and Moin (2004) $Y_{c,v}$ is completely explained by the sub-grid distribution of Z. As the figure illustrates, a significant amount of sub-grid progress variable variance ($Y_{c,v}$) is present, simply because Y_c is a function of the mixture fraction at constant C. In comparison,

the progress variable variance on the bottom right plot is barely higher. Yet, it corresponds to a scaled variance of $\zeta_C = 0.1$, and to a much broader distribution of the joint PFDF. The minimum $\widetilde{Y_c^2}$ corresponding to $C_v = 0$ may be expressed from setting Eq. (5.140) to zero:

$$\widetilde{Y_c^2} \geq \widetilde{Y_c^{start2}} + 2\left(\widetilde{Y_c^{start}Y_c^{end}} - \widetilde{Y_c^{start2}}\right)\widetilde{C} + \left(\widetilde{Y_c^{end2}} - 2\,\widetilde{Y_c^{start}Y_c^{end}} + \widetilde{Y_c^{start2}}\right)\widetilde{C}^2 \tag{5.143}$$

$$\widetilde{Y_c^2} \geq \widetilde{Y_c^{end2}}\widetilde{C}^2, \qquad \text{if } Y_c^{start} = 0. \tag{5.144}$$

This lower limit of $\widetilde{Y_c^2}$ (and $Y_{c,v}$) is associated to the sub-grid variance in mixture fraction, which creates a difference between $\widetilde{Y_c^{end}}^2$ and $\widetilde{Y_c^{end2}}$. This is the variance value displayed in the lower left plot of Fig. 5.12. In this work, such limits are imposed on the solution, to avoid numerical undershoots.

5.4.4 Tabulation strategy for LES

The tabulated chemistry model is meant to provide closure for the material properties: $\overline{\rho}, \overline{\mu}, \widetilde{\mathcal{D}_t}$, which are used in the transport equations. Furthermore, filtered source terms such as $\overline{\dot{\omega}_{Y_c}}$ and $\overline{Y_c\dot{\omega}_{Y_c}}$ are also closed by the tabulated chemistry model. In case of the source terms and the dynamic viscosity the non-density-weighted filtering is executed directly using Eq. (5.128).

The filtered density and Favre-filtered thermal diffusivity could also be obtained directly using Eq. (5.127) and Eq. (5.126) respectively. However, a different approach is followed here, which builds on the pre-existing functionalities implemented within the studies of Gövert (2016) in the Alya code. In this approach the enthalpy equation is solved, irrespective of whether $\widetilde{h}$ is a control variable of the tabulation. The temperature is recalculated with algorithm 2.1 using the NASA polynomials: $T^\star = T\left(\widetilde{h}, b_i^\star\right)$. Subsequently, this temperature is used along with a tabulated molecular weight ($W^\star$) and the thermodynamic pressure (P_0) to recompute the filtered density with the ideal gas law: Eq. (2.51). The approach permits deviations from the intrinsic temperature of the thermo-chemical table, thus heat loss may affect the density field even using adiabatic tables. The key is to determine $b_i^\star$ and $W^\star$ in a reasonable way, so physical behavior is retained.

Filtering effect on the thermal state

In this work, the NASA polynomials are determined from the Favre-filtered composition using Eq. (2.9) and integrating the full composition with the joint PFDF:

$$b_i^\star = \sum_{k=1}^{N_C} \frac{R_u}{W_k} a_{k,i} \widetilde{Y}_k. \tag{5.145}$$

Note, that here the coefficient: $\frac{R_u}{W_k} a_{k,i}$ is only dependent on k and i, thus this recalculation is completely equivalent to Favre-filtering the mass based NASA polynomials

directly:

$$b_i^\star = \overbrace{\sum_{k=1}^{N_C} \frac{R_u}{W_k} a_{k,i} Y_k}^{} = \widetilde{b}_i. \tag{5.146}$$

TABLE 5.9: Possible strategies to obtain temperature in LES with presumed FPDF tabulated chemistry.

Approach	
Re-computation using $\widetilde{Y}_k$	$T^\star = T\left(\widetilde{h}, \widetilde{Y}_k\right) = T\left(\widetilde{h}, b_i^\star\right) = T\left(\widetilde{h}, \widetilde{b}_i\right)$
Favre-filtering using Eq. (5.126)	$\widetilde{T}$
Filtering using Eq. (5.128)	$\overline{T}$
Re-computation using $\overline{Y_k}$	$T\left(\widetilde{h}, \overline{Y_k}\right) = T\left(\widetilde{h}, \overline{b_i}\right)$

Table 5.9 lists four different manners of determining the temperature in LES with tabulated chemistry methods. These options are illustrated in Fig. 5.13 using inert mixing cases with a presumed β-FPDF for the mixture fraction: $\mathcal{F} = \mathcal{F}\left(\widetilde{Z}, Z_v\right)$. In the first case the reactants are pre-heated air at 600 K and molecular hydrogen at ambient temperature. While in the second case air and CH_4 are mixed at ambient temperature. The material properties are obtained from the GRI3.0 (Smith et al., 2011) chemical mechanism.

The temperatures of Fig. 5.13 on their own are not very meaningful, as temperature is not linked directly to an extensive thermodynamic quantity, thus volume or mass weighted averages of T in a filter volume do not have a direct meaning. However, the figure demonstrates, that the problem is non-trivial, and if one wants to use a temperature in the equation of state, then modeling consistency has to be assessed. In this work, the first option is preferred, i.e.: temperature is recalculated with the Favre-filtered NASA polynomials, corresponding to the Favre-filtered composition. (Fig. 5.13a) As the figure illustrates, the sub-grid variance does not affect $T^\star$ in simple cases of inert mixing. All other alternatives show variations of temperature with ζ_Z. The option of integrating the NASA polynomials with non-density-weighted filtering (Eq. (5.128)) clearly stands out as an incorrect option. In this case the misalignment of the Favre-filtered enthalpy, and the non-density-weighted NASA polynomials causes a considerable overshoot of temperature in the methane case. Note, that such outstanding erroneous behavior is not observed in the case of hydrogen, since the enthalpy of H_2 is much closer to the enthalpy of the oxidizer.

Filtering effect on the equation of state

To obtain the density using the ideal gas equation of state, a molecular weight needs to be tabulated as well. This may be obtained either using the filtering operator, or using Favre-filtering. Nevertheless, a third option is preferred in this work, that defines an artificial molecular weight: $W^\star$, which ensures that the filtered density is recovered exactly if $T^\star$ is used:

$$W^\star = \frac{\overline{\rho} R_u T^\star}{P_0}. \tag{5.147}$$

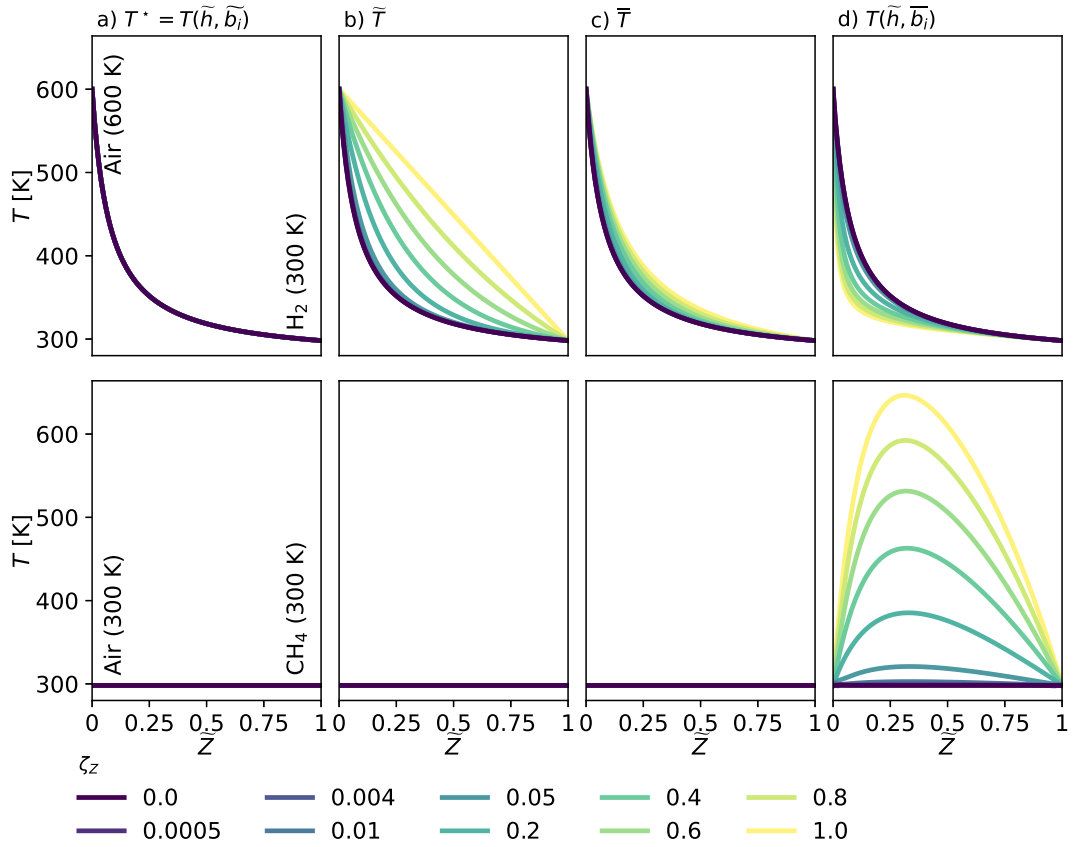

FIGURE 5.13: Different temperature evaluation options in mixing problems. Top row: pre-heated air at 600 K and ambient temperature H_2. Bottom row: ambient temperature air and methane.

The same hydrogen-air and methane-air mixing scenarios are assessed in this context as before. In mixing problems $W^\star$ stays constant irrespective of the subgrid state. The non-density-weighted filtered molecular weight is fairly close to this constant state as well, however in the hydrogen case small variations arise due to the temperature difference.

The filtered density is a very important term in the coupled governing equation system. As Eq. (5.74) demonstrates, density oscillations are associated to the creation and destruction of kinetic energy. Thus it is crucial to avoid spurious density oscillation generated by the tabulated chemistry model. Figure 5.15 illustrates the relative error between the actual filtered density calculated by Eq. (5.127), and the density obtained using the ideal gas law, with different evaluations of $T \in \left\{T^\star, \widetilde{T}, \overline{T}\right\}$ and $W \in \left\{W^\star, \widetilde{W}, \overline{W}\right\}$. Two of these combinations are unconditionally correct:

$$\overline{\rho} = \frac{P_0 W^\star}{R_u T^\star}, \quad \text{and} \quad \overline{\rho} = \frac{P_0 \overline{W}}{R_u \widetilde{T}}, \tag{5.148}$$

which correspond to Fig. 5.15a and Fig. 5.15h respectively. The first relation holds by construction, due to the definition of $W^\star$. The second relation follows from the definition of the Favre-filtering and the rearrangement and filtering of the ideal gas law as: $\overline{\rho T} = \frac{P_0}{R_u}\overline{W}$. In this work the first form of the ideal gas law is preferred,

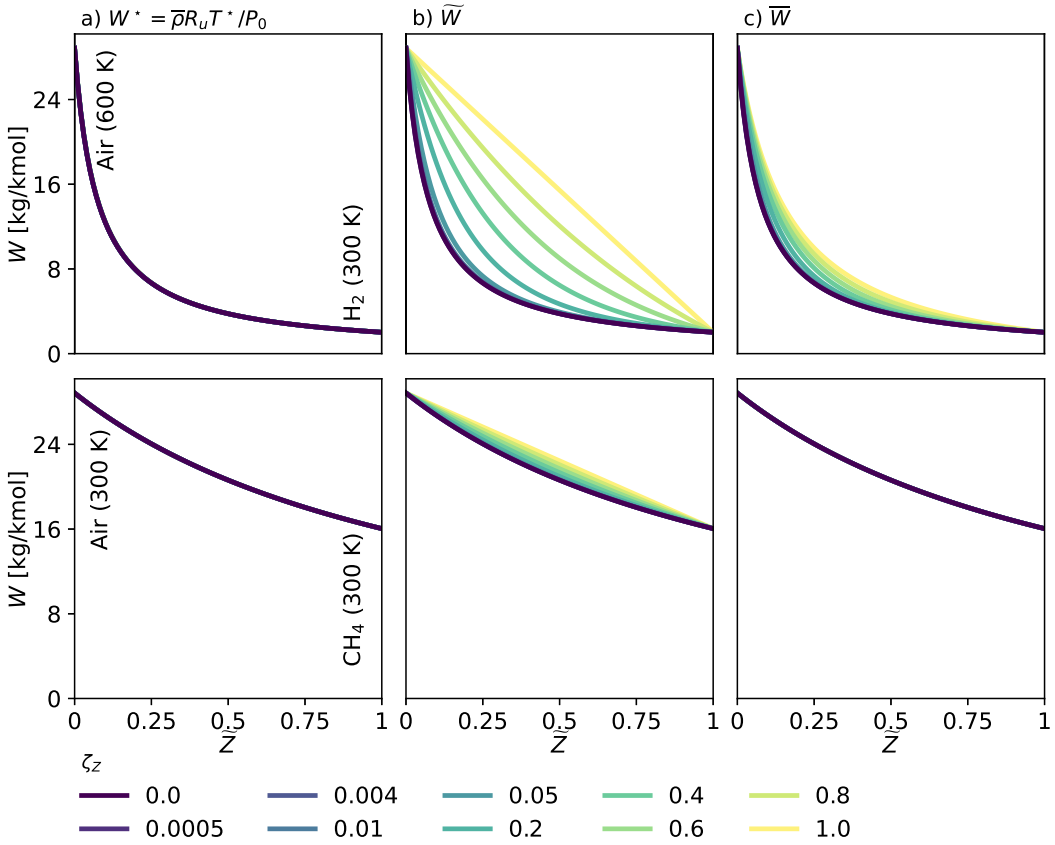

FIGURE 5.14: Different molecular weight evaluation options in mixing problems. Top row: pre-heated air at 600 K and ambient temperature H_2. Bottom row: ambient temperature air and methane.

since $T^\star$ can be easily related to the resolved enthalpy: $\widetilde{h}$. Contrarily, the Favre-filtered temperature is not straightforward to obtain from the enthalpy, and it lacks a physical meaning. The rest of the combinations shown in the figure all produce notable errors, especially where the Favre-filtered molecular weight is applied in Fig. 5.15d-f.

Filtered diffusivity

The Favre-filtered thermal diffusivity appears in the governing equations of transported scalars: Eq. (5.117). The diffusive term is dominated by the contribution of the sub-grid viscosity in the highly turbulent regions of the flow. Sub-grid variance tends to be significant in the same regions, thus the effect of non-zero variances on $\widetilde{\mathcal{D}_t}$ are less important. In this work the diffusivity is approximated using the filtered thermal conductivity as:

$$\widetilde{\mathcal{D}_t} = \frac{\overline{\lambda / c_p}}{\overline{\rho}} \approx \frac{\overline{\lambda}}{c_p(\widetilde{h}, \widetilde{b_i})\overline{\rho}}, \tag{5.149}$$

where the filtered thermal conductivity: $\overline{\lambda}$ is tabulated, and the specific heat is obtained during the evaluation of $T^\star$ with algorithm 2.1.

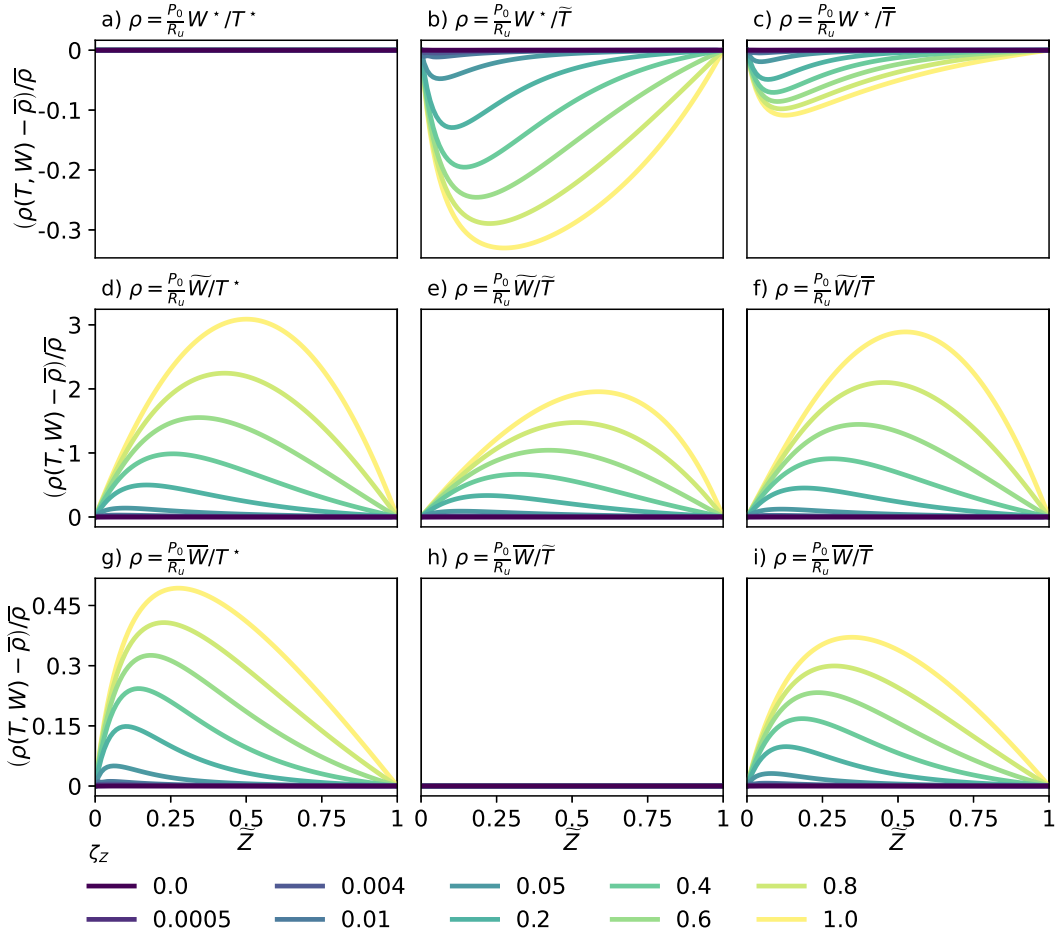

FIGURE 5.15: Relative filtered density error in different property options in a mixing problem of pre-heated air at 600 K and molecular hydrogen at ambient temperature.

Summary of tabulated properties

The final set of tabulated properties is listed in Tab. 5.10. This results in $1 + 15$ or $2 + 15$ tabulated quantities for the source terms and material properties respectively, depending on whether the sub-grid variance of the progress variable is considered. Note, that the mean NASA polynomials consist of 2×6 coefficients storing both the high and low temperature range. The FPDF integration is executed *a priori* and the properties are stored on a rectilinear discretization of the Favre-filtered control variables and their scaled variances.

The lookup is executed in each time step during the run-time of the LES. Subsequently, the NASA polynomials $\widetilde{b}_i$ and the transported enthalpy $\widetilde{h}$ are used in algorithm 2.1 to obtain $T^\star$ and $c_p(\widetilde{h}, \widetilde{b}_i)$. The Favre-filtered thermal diffusivity is calculated using the thermal conductivity in Eq. (5.149). Finally the density is calculated using the ideal gas law: Eq. (5.148) using $W^\star$ and $T^\star$.

TABLE 5.10: Tabulated quantities for LES of gas phase combustion.

Quantity	Symbol	Thermo-chemical relation	Filtering or processing
Progress variable source term	$\overline{\dot{\omega}_{Y_c}}$	Eq. (2.120)	Eq. (5.128)
$\widetilde{Y_c^2}$ source term	$\overline{Y_c \dot{\omega}_{Y_c}}$	-	Eq. (5.128)
Dynamic viscosity	$\overline{\mu}$	Eq. (2.13)	Eq. (5.128)
Thermal conductivity	$\overline{\lambda}$	Eq. (2.15)	Eq. (5.128)
Mean NASA polynomials	$\widetilde{b_i}$	Eq. (2.9)	Eq. (5.126)
Mean molecular weight	$W^\star$	Eq. (2.1)	Eq. (5.147)

The benefits of keeping the number of tabulated quantities small, cannot be overstated. As already discussed in section 3.4.2 and section 4.3.2, the memory requirement of a single tabulated quantity is:

$$MEM_\psi = (8\ \mathrm{B}) \prod_k n_k, \tag{5.150}$$

where n_k is the number of points in the k^{th} dimension of the table. Considering tables of the above mentioned 16 or 17 quantities, Tab. 5.11 contains recommendations on reasonable table sizes and the corresponding memory requirement. Taking MareNostrum4 (BSC, 2021) as a reference, 1.88 GB memory per CPU is a reasonable limit, that has to fit both the thermo-chemical tables and the rest of the data structures of the numerical method. As the table illustrates, the memory limitation of the CPU is not an issue for low dimensional tabulations. The limitations only start to show in case of non-adiabatic non-premixed problems. If only one variance is transported following Pierce and Moin (2004), then a finer discretization may be kept. However, if the non-adiabatic table is parameterized by both mixture fraction and progress variable variance following Domingo, Vervisch, and Veynante (2008), then some resolution needs to be renounced for the sake of feasibility.

TABLE 5.11: Recommended thermo-chemical table sizes and their memory requirement considering $1+15$ and $2+15$ variables depending on whether the progress variable variance is computed.

	n_Z	n_C	n_i	$n_{\zeta_{Z_v}}$	$n_{\zeta_{C_v}}$	$\sum MEM_\psi$ [MB]
Inert mixing	101			11		0.1
Adiabatic premixed		101			11	0.1
Non-adiabatic premixed		101	31		11	4.5
Adiabatic non-premixed	101	101		11		13.7
	101	101		11	11	160.1
Non-adiabatic non-premixed	101	101	21	11		287.7
	71	71	11	11	11	870.2

In case of spray combustion six additional variables are tabulated which are used in the context of the TARES model introduced in section 4.3.2. This increases the memory needs of a $71 \times 71 \times 11 \times 11 \times 11$ thermo-chemical manifold to 1.15 GB,

which is the largest table used in this work. This is close to the actual limit of feasibility in the current implementation in the Alya code. Note, that significant improvements may be achieved by using a shared memory concept between the parallel processes, by partially replacing the tables with neural networks (Zhang et al., 2020b), or by executing the PDF integration run-time. (Novoselov et al., 2021)

5.5 Lagrangian spray model in LES

Chapter 4 introduces the Lagrangian droplet modeling strategy and discusses the single droplet models extensively. Coupling such empirical droplet models with the Eulerian gas phase simulation (Eulerian-Lagrangian method) is the state of the art in the combustion LES of dilute sprays. (Jenny, Roekaerts, and Beishuizen, 2012) Nevertheless, Eulerian representation of the dilute dispersed phase is also explored by some studies. (Sanjosé et al., 2011; Vié et al., 2013) As Kronenburg (2007) points out, the standard Eulerian-Lagrangian approaches tend to ignore the sub-grid behavior of the spray cloud. This work is no exception as the Lagrangian droplets are assumed to interact with the filtered Eulerian fields. Addressing this problem is out of the scope of the present study, nevertheless the key phenomena are revised below.

5.5.1 Droplets in turbulent flow

As already discussed in section 4.6, the Stokes number indicates the nature of the interaction of the gas phase flow and the dispersed droplets. High stokes numbers signify high droplet relaxation times, where the droplet behavior is ballistic: i.e.: the droplet path is not modified significantly by the flow. Meanwhile in case of low Stokes numbers the droplet relaxation time is negligible, and the the droplet relaxes to the local flow virtually instantly. Stokes numbers may be defined based on the turbulence integral scales or the Kolmogorov scales:

$$St_t = \frac{\tau_{p,kin}}{\tau_t}, \qquad St_\eta = \frac{\tau_{p,kin}}{\tau_\eta}. \tag{5.151}$$

The kinematic droplet time scale is explained in detail in section 4.6.3, while the turbulent scales are introduced in section 5.1.2. An order of magnitude estimate of the former scale may be given in the low Reynolds number limit by the Stokes relaxation time: $\tau_{p,kin,St}$, defined in Eq. (4.78). Since the relaxation time scales quadratically with the diameter, typical values range from $\mathcal{O}\left(10^{-5}\ \mathrm{s}\right)$ in micron scale droplets, up to $\mathcal{O}\left(10^{-1}\ \mathrm{s}\right)$ for the largest stable spherical droplets: $d_p = \mathcal{O}\left(100\ \mu\mathrm{m}\right)$. As a reference, take a case of $v' = 1$ m/s, $\ell_t = 10^{-2}$ m and $Re_t \approx 1000$, where the integral time scale is $\tau_t = 10^{-2}$ s, and the Kolmogorov time scale is $\tau_\eta \approx 3 \cdot 10^{-4}$ s. In such a flow, the Stokes numbers of the large droplets are higher than unity: $St_t = \mathcal{O}\left(10\right)$, $St_\eta = \mathcal{O}\left(100\right)$. Consequently, these are barely affected by the turbulent motion. Nevertheless, the mean flow may affect them. Meanwhile the Stokes numbers of micron scale droplets are consistently below unity: $St_t = \mathcal{O}\left(10^{-3}\right)$, $St_\eta = \mathcal{O}\left(10^{-2}\right)$. Meaning, that these droplets shall be perfect racers of all turbulent motions.

The above example illustrates, that in practical cases the convolution of the turbulent spectrum and the range of different droplet sizes results in all the different possible modes of droplet/turbulence interactions being expressed in the same combustion system. Large droplets may behave completely ballistic, intermediate

droplets will be affected by some eddies and may show trends of preferential concentration, while the smallest droplets act as perfect tracers of the turbulent motion. Urzay et al. (2014) studied this phenomena with Eulerian-Lagrangian DNS, and in the corresponding LES with neglecting the sub-grid interaction between the particles and the flow. They conclude, that the lack of LES modeling manifests in under-predicted dispersion rate in particles of $St_\Delta = \frac{\tau_{p,kin}}{\tau_\Delta} \ll 1$, where τ_Δ is the eddy-turnover time scale at the filter width. While this is an important aspect for the droplet transport, form the point of view of the combustion most of the fuel is carried by the larger droplets. From this perspective the details of the small droplet motion is of lesser importance, and sub-grid dispersion modeling is not addressed here.

5.5.2 Validity of Lagrangian models

Jenny, Roekaerts, and Beishuizen (2012) define the limit of dilute spray regime by the local volume fraction of droplets in the flow: $\alpha < 0.001$. In this regime, the probability of droplet-droplet collision is negligible, which could be challenging to model in a Lagrangian approach efficiently. Moreover, the low volume fraction allows the straightforward decoupling of the gas phase form the spray cloud. Since the spray occupies negligible space in a control volume, the governing equations of Eulerian phase remain unchanged, except the source terms modeling the interaction of the two phases. The interface of this exchange is likewise infinitesimal, associated to the droplet surface, which allows to treat the droplets as point-like sources of mass, momentum, and energy.

In a numerical setting it is practical to use the computational mesh of the Eulerian phase to assess the local volume fraction, corresponding to a control volume of $V_{element} = \Delta^3$. This gives an upper limit on the droplet size, under the assumption, that only one droplet is within the element:

$$\frac{\pi d_{p,max}^3/6}{\Delta^3} = 0.001, \qquad d_{p,max} \approx 0.124\Delta. \tag{5.152}$$

TABLE 5.12: Droplet size limits considering regular elements of typical sizes with edge length: a.

a [mm]	Tetrahedron $\left(V_{element} = \sqrt{2}/12a^3\right)$		Hexahedron $\left(V_{element} = a^3\right)$	
	Δ [mm]	$d_{p,max}$ [μm]	Δ [mm]	$d_{p,max}$ [μm]
1	0.49	61	1	124
0.5	0.25	30	0.5	62
0.25	0.12	15	0.25	31

Table 5.12 presents this limit in some typically used elements. Accordingly, the LES of reacting sprays using Eulerian-Lagrangian methods is limited on two fronts. On one hand the mesh refinement is expected to improve the quality of gas phase predictions. While on the other hand the coupling with the Lagrangian spray requires the mesh elements to be significantly larger than the largest droplets. Droplets that violate such a size limit may cause inconsistencies related to their point-like treatment in the Eulerian-Lagrangian coupling through source terms. Furthermore, the assumptions made in the empirical droplet models may be broken as well. The two inconsistencies are described below.

Issues of the point-particle source term treatment

If the size of the Lagrangian particles is the same order of magnitude as the computational elements, then the point-like treatment of the source terms is incorrect, and the forces acting on the fluid have to be distributed over multiple Eulerian elements. This fallacy was recognized early on in the two-way-coupled momentum transport in particle-laden flows. Neglecting this phenomena overestimates the local source terms, and besides deteriorating the results it also poses numerical challenges.

This limitation is commonly addressed by the conservative *smoothing* of the source terms, which treat the coupling with the Lagrangian phase in a more distributed manner. (Capecelatro and Desjardins, 2013; Radl et al., 2015; Sun and Xiao, 2015) The method shows adequate results in particle transport, and it has been applied even in reacting flows involving heat and mass transfer. (Xia et al., 2013; Huang et al., 2022a) Nevertheless, implementing such models is out of the scope of the present work, and the point-particle assumption is retained here on the grounds, that such large droplets or fine meshes are not of interest here.

Issues of limited cell size on the heat and mass transfer

As section 4.2.1 details, in the Lagrangian droplet models applied in the present study, the heat and mass transfer is driven by temperature and fuel mass fraction gradients in a finite film thickness surrounding the droplets. (See Fig. 4.5.) The film thickness may range anywhere between negligibly thin films at high Reynolds number, to an infinite film in quiescent flow according to the correlation of Ranz and Marshall (1952). Thus large droplets at relatively low speed may have a sphere of influence larger than the computational grid, even if they adhere to the size limits of Tab. 5.12. I.e.: part of the droplet boundary layer is resolved in the gas phase mesh. This poses an issue, because the heat and mass transfer models assume, that the seen temperature and vapor mass fraction may be taken as the gas phase values at the droplet location. Consequently, the transfer rates are under-predicted if part of the film is resolved on the grid.

Recently Zhang et al. (2020a) explored different smoothing methods for solid biomass combustion, including the smoothing of the seen quantities. In a validation case of single particle combustion they found improved grid convergence, and they observed better representation of the physics than in the baseline point-particle method. They conclude, that applying the smoothing method on the seen temperature and the seen vapor mass fraction recovers the expected performance of the empirical Lagrangian models assuming quasi-steady heat and mass transfer.

It is not clear whether these promising results could be directly extended to systems with multiple Lagrangian particles. The limitation of the point-like particle treatment is recognized, but the smoothing of the seen properties is not addressed in this work. The large droplets, where such effects may be relevant, typically show a ballistic behavior characterized by large droplet Reynolds numbers. In such situations one may argue, that the film thickness is thin, and taking the seen properties as the gas phase properties at the droplet location is sufficient.

5.5.3 Source terms of Eulerian-Lagrangian coupling

In the Eulerian-Lagrangian approach, the evolution of the Lagrangian particles is represented by an ODE system, that is dependent on the seen conditions given by the Eulerian phase. (See section 4.3.2.) The mass, energy, and momentum of the particles evolve in time, and the source terms of the gas phase equations have to be

formulated such, that the global conservation is ensured. While this interchange is already discussed in chapter 4 form the droplet's perspective, here the balances of mass energy and momentum are assessed again, with global conservation in mind.

The flow rates of conserved quantities crossing the droplet/gas interface are summarized in Fig. 5.16. On the droplet side, the temporal change of the conserved quantities gives:

$$\frac{\mathrm{d}m_p}{\mathrm{d}t} = -\dot{m}_r, \quad \frac{\mathrm{d}m_p h_p}{\mathrm{d}t} = -\dot{m}_r h_p - \left(\dot{Q}_r + \dot{m}_r L_v\right), \quad \frac{\mathrm{d}m_p \mathbf{u}_p}{\mathrm{d}t} = -\dot{m}_r \mathbf{u}_p + \mathbf{F}_d, \quad (5.153)$$

which corresponds exactly to Eq. (4.47), Eq. (4.50), and Eq. (4.3) derived in chapter 4. On the liquid side of the interface it is more intuitive to express the energy transport as the sum of a convective flow carrying the liquid enthalpy towards the interface: $\dot{m}_r h_p$, and a radial heat flow that is modifying the droplet temperature: $\left(\dot{Q}_r + \dot{m}_r L_v\right)$. In practical cases $\dot{Q}_r$ is negative (heat is carried towards the droplet), and the liquid side heat flow: $\left(\dot{Q}_r + \dot{m}_r L_v\right)$ is approaching zero as the droplet approaches the web-bulb conditions.

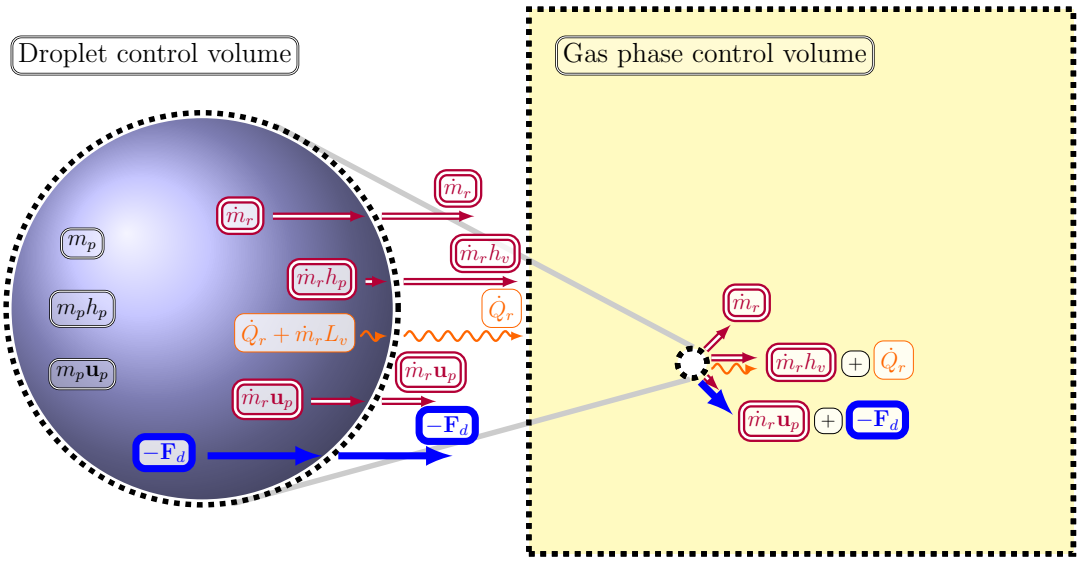

FIGURE 5.16: Mass, energy, and momentum conservation in the Eulerian-Lagrangian approach, with only drag acting on the droplet. The specific enthalpies h_p and h_v are evaluated at the droplet temperature.

On the other side of the interface the same flow rates enter the gas phase control volume. Here it is more natural to express the energy exchange as the sum of the convective enthalpy flux carried by the vapor: $\dot{m}_r h_v$, and the conductive flux: $\dot{Q}_r$. The specific enthalpy of the vapor: h_v has to be evaluated at the droplet temperature, since $\dot{Q}_r$ corresponds to purely conductive heat transfer only on the interface. (See the last remarks of appendix E.) A literal interpretation of the point-particle

assumption results in Dirac delta-like source terms in the Eulerian phase:

$$S_\rho^e = \sum_p \delta\left(\mathbf{x} - \mathbf{x}_p\right)\left(\dot{m}_r\right)_p, \tag{5.154}$$

$$S_\mathbf{u}^e = \sum_p \delta\left(\mathbf{x} - \mathbf{x}_p\right)\left(\dot{m}_r \mathbf{u}_p - \mathbf{F}_d\right)_p, \tag{5.155}$$

$$S_h^e = \sum_p \delta\left(\mathbf{x} - \mathbf{x}_p\right)\left(\dot{m}_r h_v + \dot{Q}_r\right)_p, \tag{5.156}$$

$$S_Z^e = \sum_p \delta\left(\mathbf{x} - \mathbf{x}_p\right)\left(\dot{m}_r\right)_p, \tag{5.157}$$

where the sources of individual droplet are summed in the entire domain, and δ signifies the three dimensional Dirac delta function. This gives the coupling source term fields over the domain. For the rationale of taking $S_Z^e = S_\rho^e$ see section 2.5.3.

Filtered coupling source terms

The coupling source terms consist of a collection of different intensity Dirac deltas. Fortunately, in LES the source terms need to be filtered, which gives a computationally manageable source filed illustrated in Fig. 5.17. The first row of plots show the Dirac-delta mass source terms with different $\dot{m}_r$ intensities. An intensive mass source is located on the left side of this domain, while a group of three droplets is on the right, with the middle one representing condensation. The second row presents the filtered mass source fields. The filtering makes the source terms finite, as the filter volume is finite as well. In the first column, the filter kernel is fine enough to capture each droplet individually, and the filtered source term value is $\dot{m}_r / (0.2\ \text{mm} \cdot 1\ \text{m}^2)$ due to the one dimensional nature of the problem. With the growth of the filter width the absolute value of the source terms is decreasing, and the effects of the droplet cluster on the right are merged together.

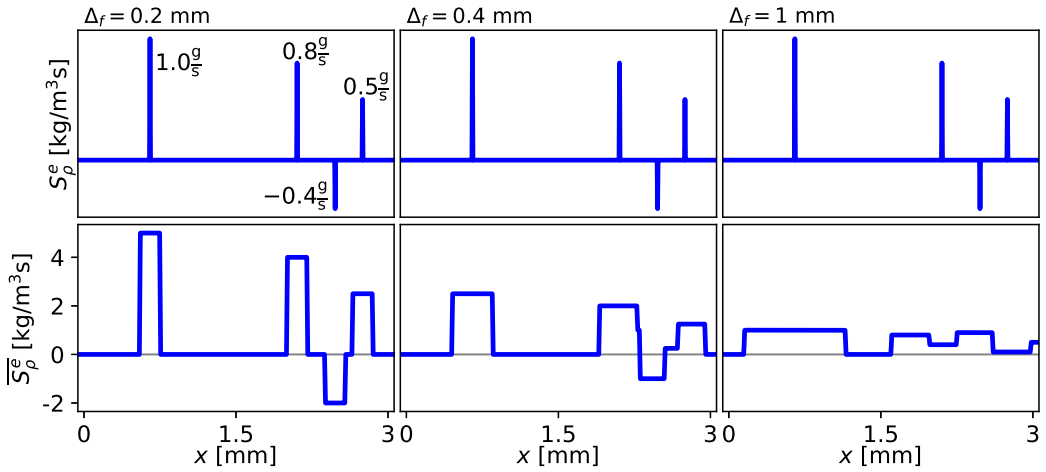

FIGURE 5.17: Example of filtered 1 dimensional Eulerian-Lagrangian coupling source terms with different filter widths.

In practice the actual value of the filtered coupling source terms is of lesser importance, since in the numerical method the transfer rates of the actual conserved quantities are used directly in the construction of the discrete equations. Hence the Eulerian-Lagrangian coupling is inherently conservative.

5.6 Summary of LES of reacting flows

The chapter presents the theoretical aspects of incorporating the tabulated chemistry methods of chapter 3 and the Lagrangian droplet models of chapter 4 in the framework of large-eddy simulation. First the concept of LES is introduced in sufficient detail for the purposes of this work. The scales of turbulence are discussed in the context of the turbulent kinetic energy spectrum, together with the effect of filtering, then governing equations are derived for the LES problem. Particular attention is given to the non-linear convective term of the momentum equation, which can be cast in different forms with different intrinsic conservation properties.

Subsequently the aspects of turbulence/chemistry interaction are revised, including the applicability of tabulated chemistry methods in premixed and non-premixed flames. The effects of LES filtering on the flame structure are discussed, and the presumed FPDF method is presented as a potential sub-grid closure for flamelet-based methods in LES. Governing equations are introduced for the controlling variables of this FPDF-integrated manifold. Finally, the Eulerian-Lagrangian method of spray combustion LES is discussed, giving the closure model of the last unclosed terms of the governing equations.

One minor modeling contribution arises from the strict requirements of the applied material property models. As section 5.4.4 demonstrates, inconsistencies in the tabulated NASA polynomials and the resolved enthalpy can result in spurious temperature errors. Furthermore, using the equation of state to calculate the filtered density from the tabulated gas state requires great care. In this work, a virtual molecular weight: $W^\star$ is proposed as a simple approach to recover the filtered density exactly. (See. Fig. 5.15.) Enthalpy variations may affect this density, if the local enthalpy differs from the tabulated state.

The overall combustion LES framework is largely based on well established concepts, which are successfully applied in the literature as outlined throughout the chapter. However, new tools and concepts are introduced, which help in the identification of the limitations of the simulation approach. As section 5.1.5 shows, a common error is introduced in the post-processing by taking the ensemble average of Favre-filtered quantities as the true ensemble average $\left(\langle\psi\rangle \approx \langle\widetilde{\psi}\rangle\right)$. In the case of velocity this error is shown to be bounded by an estimate, which can be calculated from the LES results using Eq. (5.54). Moreover, the developed Kolmogorov and integral scale estimation strategy of section 5.1.6 also contributes to assessing the quality of the LES, and to making informed decisions on the credibility of the result. This is possible through the simple analysis of temporal data sampled in specific points of interest. These estimates are further used in section 5.3.2 to locate the simulation case in the well established combustion diagrams of Broghi, Peters, Pitsch, and Williams, which helps in assessing the validity of the LES combustion model. Similarly, the limits of Lagrangian droplet models are also explored.

The studied limitations of the present LES model lead to the same conclusion: the continued refinement of the computational grid does *not* guarantee the improvement of the simulation results. From the side of the combustion modeling, this disturbing effect is illustrated on the LES combustion regime diagram of Pitsch and De Lageneste (2002) in Fig. 5.7. Under conditions, where flamelet-based tabulated chemistry methods are known to perform well ($Ka < 100$), the turbulent flow needs less resolution than the flame front. Consequently, mesh refinement can lead to conditions, where the turbulence is fully resolved and well designed eddy-viscosity models become inactive, but large part of the chemical effects remain on the sub-grid

scale. Since in this work the sub-grid chemistry modeling relies closely on the eddy-viscosity model, the sub-grid chemistry models cannot capture situations, where the turbulence is resolved but the chemistry is not. Similar limitations arise from the side of the spray modeling. The Lagrangian droplet model takes the far-field temperature and vapor mass fraction as an input from the Eulerian gas phase. In coarser grids this corresponds to the real far-field of the heat and mass transfer boundary layer of the droplet, however, with grid refinement, part of these boundary layers may become resolved, which culminates in the under-estimation of evaporation rates on fine grids. Overall, these limitations need to be evaluated at each individual LES case.

Chapter 6

Numerical aspects of the low-dissipation finite element strategy

The problem formed by the Navier-Stokes equations coupled with various scalar equations and Lagrangian particles is highly demanding, especially considering the strong non-linear dependences of material properties, and the complex geometries targeted in the present work. Analytical studies are limited to greatly simplified cases. In the present work the problem is solved numerically with the methods detailed in this chapter. The approach is developed in the framework of the Alya code (Vázquez et al., 2016), which provides an excellent platform for incorporating various physical phenomena in a well tested and highly optimized finite element environment. The present work builds on the previous developments of Alya in many areas. In the work of Gövert (2016) tabulated chemistry methods were introduced to the code, combined with a different numerical scheme based on the variational multiscale stabilization method. Olivares Mañas (2018) introduced the transport of passive Lagrangian tracers into Alya. More recently Chrysokentis (2019) implemented the presently used low-dissipation strategy for the incompressible Navier-Stokes equations.

The rest of this chapter is structured as follows. The numerical method is introduced in section 6.1, detailing Lagrangian particle evolution, the low-dissipation scheme applied on the Eulerian unknowns, the coupling of these two phases, and the overall behavior of the numerical scheme. Section 6.2 assesses the behavior of the Navier-Stokes solver in non-reacting turbulent conditions. Section 6.3 evaluates the tabulated chemistry methods under laminar conditions. In section 6.4 the Lagrangian droplet models are studied, including the evaporation modeling and the two-way coupling of the Eulerian and Lagrangian phases. Finally, in section 6.5 the developed framework is tested in turbulent reactive conditions in a confined premixed swirl flame, and a diffusion jet flame.

Credit

The work described in this chapter builds extensively on pre-existing resources and collaborative efforts. The extension of the low-dissipation incompressible flow solver to low Mach number conditions was initiated by Oriol Lehmkuhl, Matias Avila, and Daniel Mira, with the author involved in implementing certain details and verifying the overall strategy. The scalar stabilization methods were in place at the beginning of the present work, together with their application to tabulated chemistry in

Alya within the work of Simon Gövert and Daniel Mira. This initial implementation was extensively revised by Enric Illana Mahiques and the author. Subsequently, the author implemented the lookup of tabulated properties on the Gaussian integration points, taking full advantage of the integration rules implemented in Alya. The author also extended the initially hard-coded governing equation system of the tabulated chemistry method, to a flexible framework of arbitrary number of governing equations for the transport of the control variables and various other scalar equations on demand. Furthermore, the tabulated chemistry approach was also completely refactored by the author, allowing Alya to accept various tables of arbitrary data in terms of contained variables and number of dimensions. Finally, the Eulerian scalar transport was computationally optimized by Guillermo Oyarzun. The Lagrangian spray modeling developments departed from the work of Edgar Olivares Mañas. This model was extended to two-way coupled evaporating droplets by Guillaume Houzeaux, Margarida Moragues, and the author with the initial implementations concentrating on simplified physics concerning water droplets. Subsequently, the author incorporated the detailed physical models of Chapter 4 into Alya, implemented an implicit integration scheme of the evaporation model based on a numerical Jacobian, and devised a conservative coupling strategy between the two phases. The author was initially trained in the usage of Alya and post-processing by Georgios Chrysokentis, Alfonso Santiago, and Daniel Pastrana in relation to the turbulent channel flow case. However, the final turbulent channel flow simulations included below are solely the work of the author, and so are the various laminar simulations of flames and single droplets. The computational grid of the PRECCINSTA configuration created by Simon Gövert is reused in the present turbulent reacting simulations, and the two grids used in the DLR-A jet flame are created by Samuel Gómez González. In these turbulent reacting tests the author initially received the help of Enric Illana Mahiques and Daniel Mira in creating the thermo-chemical databases, however these tools were entirely refactored in the present study, to create the capabilities presented in chapter 3. Finally, the turbulent inlet database of the DLR-A jet is created using the tools originally developed by Georgios Chrysokentis. The execution and analysis of the discussed simulations is solely the work of the author. The description of the numerical method, and the turbulent simulation results are published in: Both et al. (2020). The single point analysis of the PRECCINSTA and DLR-A flames is executed using the library published at: https://gitlab.com/BothAmbrus/KolmogorovAtWitness

6.1 Numerical methods

This section presents a low-dissipation discretization strategy for variable density flows in the low Mach number limit within the finite element context. First the Lagrangian particle transport is discussed, including the numerical solution of the kinematic model responsible for tracking the droplets in space, and the evaporation model capturing the heat and mass transfer between the liquid and gas phase. Subsequently, the finite element method is applied on the Navier-Stokes and scalar equations, modeling variable density flows. Finally, the Eulerian-Lagrangian coupling is discussed, yielding the overall low dissipation scheme.

6.1.1 Lagrangian particle tracking

The motion of the particles is governed by Newton's laws according to section 4.1. The goal of the Lagrangian particle tracking (LPT) method, is to solve for the particle location in the next time step of the time-marching solution of the Eulerian-Lagrangian system: $\mathbf{x}_p^{n+1}$. The problem is determined by the state of the droplet in the previous time step: $\mathbf{x}_p^n$, $\mathbf{u}_p^n$, m_p^n, and by the gas phase velocity field: $\mathbf{u}^n$. Here a splitting technique is applied, which assumes that the droplet mass m_p remains constant for the solution of the particle location. Similarly constant kinematic properties are assumed during the heat and mass transfer described below in section 6.1.2. These assumptions are expected to be adequate, for the relevant numerical time steps and droplet sizes of the present work, i.e.: the change of the droplet size is expected to be smooth in time and well resolved with the typical time step size.

Considering the splitting of kinematic transport from the heat and mass transfer, the pre-existing particle tracking method of Alya is reused in the context of evaporating sprays. Below the most important concepts are described for the sake of completeness. For details see the work of Olivares Mañas (2018).

The kinematic equations of the individual Lagrangian particles are treated using the generic implicit scheme of Newmark (1959), leading to the discrete equations of velocity and location:

$$\mathbf{u}_p^{n+1} = \mathbf{u}_p^n + \delta t_p \underbrace{\left((1-\gamma)\, \mathbf{a}_p^n + \gamma \mathbf{a}_p^{n+1} \right)}_{\mathbf{a}_p^\gamma}, \tag{6.1}$$

$$\mathbf{x}_p^{n+1} = \mathbf{x}_p^n + \delta t_p \mathbf{u}_p^n + \frac{\delta t_p}{2} \underbrace{\left((1-2\beta)\, \mathbf{a}_p^n + 2\beta \mathbf{a}_p^{n+1} \right)}_{\mathbf{a}_p^\beta}, \tag{6.2}$$

where δt_p is the time step of the particle and $\mathbf{a}_p = \frac{\sum_i \mathbf{F}_i}{m_p}$ is its acceleration. The internal time step used in the LPT algorithm: δt_p is taken equal to the time step used in the temporal scheme of the Eulerian fields. Note, that a smaller particle time step may be used as well if necessary. The mean accelerations of the Newmark scheme: $\mathbf{a}_p^\gamma$, and $\mathbf{a}_p^\beta$ shall be chosen appropriately for the velocity and position equations respectively. In this work the two accelerations are taken equal by using the parameters: $\gamma = 0.5$ and $\beta = 0.25$, which results in a robust scheme.

The acceleration depends on the particle state in a non-linear way considering the drag correlation of Naumann and Schiller (1935). (Eq. (4.8).) Thus the acceleration in the next time step: $\mathbf{a}_p^{n+1}$ is *a priori* unknown, and the ODE system needs an iterative solution. Here, the Newton-Raphson method is used to obtain a converged particle velocity: $\mathbf{u}_p^{n+1}$, and acceleration: $\mathbf{a}_p^{n+1}$, where the Jacobian of the problem is computed analytically from the equations of the drag correlation. Subsequently, the particle location is calculated directly using Eq. (6.2).

The ODE system is appended with proper initial conditions given by the *injection model*, which aims to capture the effects of atomization. Besides the thermodynamic droplet properties (mass and temperature), the injection model gives the initial particle location and velocity. The particle is initially localized within the computational mesh of the Eulerian gas phase using a robust search algorithm. (Houzeaux and Codina, 2003) Once the first host element is found, the subsequent ones are tracked by detecting when a particle crosses the faces of an element.

This method is implemented in the Alya code, and it has been extensively tested by Olivares Mañas (2018) in case of constant mass particles. Subsequently it has been used in various applications of respiratory aerosol transport. (Houzeaux et al., 2016; Calmet et al., 2018; Calmet et al., 2019; Calmet et al., 2022) In such applications the Lagrangian phase is very dilute, and the effect of particles on the fluid flow is negligible, thus *one-way* coupling is used, i.e.: the Eulerian source terms of section 5.5.3 are neglected. In the present work, this is extended to variable droplet size and *two-way* coupling to properly represent evaporating sprays. While such a formulation may also be used in respiratory flows (Calmet et al., 2021), the main focus is on spray flames. (Mira et al., 2021b; Both, Mira, and Lehmkuhl, 2021a; Benajes et al., 2022; Both, Mira, and Lehmkuhl, 2022a)

6.1.2 Heat and mass transfer of Lagrangian particles

As explained above, the heat and mass transfer is decoupled from the kinematic transport, under the assumption that the time steps are sufficiently small to allow such splitting. The droplet evaporation is governed by the conservation equations outlined in section 4.4.2. The problem consists of finding: m_p^{n+1} and T_p^{n+1} given the current droplet state, and all the necessary gas phase properties. According to the splitting technique applied here, the droplet velocity is kept constant: $\mathbf{u}_p^n$ during the numerical solution of the evaporation.

The evaporation of Lagrangian droplets is a complex non-linear process detailed in chapter 4. The main difficulty is associated to the extremely non-linear coupling between the evaporation rate and the droplet temperature. Furthermore, for droplet temperatures equal or higher than the boiling point of the liquid, the problem is non-physical and the transfer rates are undefined. Two different approaches are explored to solve the heat and mass transfer equations of droplets: a first order explicit scheme, and a first order implicit scheme with a numerically evaluated Jacobian. To discuss these schemes, the following notation is introduced:

$$\mathcal{U} = \begin{bmatrix} m_p \\ T_p \end{bmatrix}, \quad \mathcal{R} = \begin{bmatrix} \frac{\mathrm{d}m_p}{\mathrm{d}t} \\ \frac{\mathrm{d}T_p}{\mathrm{d}t} \end{bmatrix} = \begin{bmatrix} \mathcal{R}_m \\ \mathcal{R}_T \end{bmatrix}, \quad \mathcal{J} = \frac{\partial \mathcal{R}}{\partial \mathcal{U}} = \begin{bmatrix} \frac{\partial \mathcal{R}_m}{\partial m_p} & \frac{\partial \mathcal{R}_m}{\partial T_p} \\ \frac{\partial \mathcal{R}_T}{\partial m_p} & \frac{\partial \mathcal{R}_T}{\partial T_p} \end{bmatrix}, \tag{6.3}$$

where $\mathcal{U}$ is the unknown vector, $\mathcal{R}$ is the residual vector, and $\mathcal{J}$ is the Jacobian of the coupled mass and energy transfer equations.

First order explicit scheme

A first order explicit scheme is constructed by simply evaluating the residual according to section 4.4.8 at the previous particle time step:

$$\frac{\mathcal{U}^{n+1} - \mathcal{U}^n}{\delta t_p} = \mathcal{R}^n, \tag{6.4}$$

Thus the unknowns of the evaporation model in the next step are:

$$\mathcal{U}^{n+1} = \mathcal{U}^n + \delta t_p \mathcal{R}^n. \tag{6.5}$$

In this work δt_p is taken equal to the time step of the gas phase time marching scheme, however, smaller time steps may be chosen if required.

First order implicit scheme

The explicit scheme outlined above, is expected to be inadequate for evaporating sprays interacting with high temperature gases. The main concern is regarding temperature overshoots, which would render the next solution non-physical. Indeed, as section 4.6.1 presents, the initial droplet heat-up is a rather fast process in comparison to the evaporation. Furthermore, the droplet approaches the web-bulb temperature asymptotically, which makes overshoots a usual problem.

To overcome these difficulties an implicit scheme is introduced here. In principle, the implicit scheme would necessitate knowing the residual vector in the next step:

$$\frac{\mathcal{U}^{n+1} - \mathcal{U}^n}{\delta t_p} = \mathcal{R}^{n+1}, \tag{6.6}$$

One might solve this problem iteratively, however, this could easily lead to temperature overshoots as well. Instead, the present method uses a numerical approximation of the Jacobian, that can be evaluated in a more conservative manner. The Jacobian is used to obtain a first order approximation of the residual in the next time step:

$$\mathcal{R}^{n+1} \approx \mathcal{R}^n + \mathcal{J}^n \left(\mathcal{U}^{n+1} - \mathcal{U}^n \right). \tag{6.7}$$

This approximate residual is substituted into Eq. (6.6), thus the unknown vector in the next time step can be expressed as:

$$\mathcal{U}^{n+1} = \text{inv}\left(\mathcal{A}^n\right) \left(\mathcal{R}^n + \mathcal{A}^n \mathcal{U}^n \right), \tag{6.8}$$

where the matrix: $\mathcal{A}^n = \frac{1}{\delta t_p} I - \mathcal{J}^n$ is used with I being the unit tensor. The inversion of this 2×2 matrix is simply done analytically as:

$$\text{inv}\left(\mathcal{A}^n\right) = \frac{1}{\mathcal{A}^n_{11}\mathcal{A}^n_{22} - \mathcal{A}^n_{12}\mathcal{A}^n_{21}} \begin{bmatrix} \mathcal{A}^n_{22} & -\mathcal{A}^n_{12} \\ -\mathcal{A}^n_{21} & \mathcal{A}^n_{11} \end{bmatrix}, \tag{6.9}$$

where the subscripts mark the row and column indeces respectively.

An approximation of the Jacobian is calculated numerically by evaluating the residual three times. Once in the current droplet state: $\mathcal{R}^n$, and twice with slight modification in the droplet mass: δ_m and droplet temperature: δ_T yielding the residuals: $\mathcal{R}_{\delta_m}$ and $\mathcal{R}_{\delta_T}$ respectively. The numerical Jacobian approximation is:

$$\mathcal{J}^n \approx \begin{bmatrix} \dfrac{\mathcal{R}_{m,\delta_m} - \mathcal{R}^n_m}{\delta_m} & \dfrac{\mathcal{R}_{m,\delta_T} - \mathcal{R}^n_m}{\delta_T} \\ \dfrac{\mathcal{R}_{T,\delta_m} - \mathcal{R}^n_T}{\delta_m} & \dfrac{\mathcal{R}_{T,\delta_T} - \mathcal{R}^n_T}{\delta_T} \end{bmatrix}. \tag{6.10}$$

The key is to choose δ_m and δ_T such, that the residuals are always evaluated under physical conditions. In this work, these parameters are taken as function of the current droplet state:

$$\delta_m = 0.001 m_p, \qquad \delta_T = -0.0001 T_p. \tag{6.11}$$

It is imperative to take a positive δ_m and a negative δ_T, in order to ensure that the droplet mass is always positive, and the droplet temperature is always below the boiling point of the liquid.

Note, that the implicit scheme is used throughout chapter 4 in the numerical examples with a slight modification. Under the wet-bulb conditions $\mathcal{R}_T^n$ becomes zero, however $\mathcal{J}_{22}^n$ remains large, in this case the droplet evaporation becomes very simple, as the temperature shall stay constant, and the mass should change according to a d^2 law. To simulate sub-micron particles studied in chapter 4, it is found advantageous to revert to the explicit scheme under the wet-bulb conditions, detected by $\mathcal{R}_T^n < 10$ K/s. This is simply done by setting $\mathcal{J}^n = 0$, in which case Eq. (6.8) corresponds to the explicit scheme.

These temporal schemes are implemented in the Lagrangian particle tracking of Alya without this modification, since in practical spray combustion cases the seen conditions change constantly, and the wet-bulb condition varies. However, it is the preferred method in the stand-alone python library:
https://gitlab.com/BothAmbrus/DropletEvaporation.

6.1.3 Spacial discretization of the Eulerian governing equations

In this work linear finite elements are used to construct the spacial discretization of the Eulerian equations. Note, that the developed framework allows for the straightforward extension to higher order elements, however, this possibility is not explored here. The continuous sub-spaces of section 2.3.2 are approximated by the following piece-wise linear sub-spaces: $\mathbf{V}_{D,h} \subset \mathbf{V}_D$, $\mathbf{V}_{0,h} \subset \mathbf{V}_0$, $Q_h \subset Q$, $E_{D,k,h} \subset E_{D,k}$, and $E_{0,k,h} \subset E_{0,k}$. The discretized problem consists of finding $\mathbf{u}_h^{n+1} \in \mathbf{V}_{D,h}$, $p_h^{n+1} \in Q_h$, and $\xi_{k,h}^{n+1} \in E_{D,k,h}$ given the n^{th} solution such, that this $(n+1)^{\text{th}}$ solution satisfies the discrete governing equations:

$$\left(\partial_t \rho_h, q_h\right) + \left(\nabla \cdot \left(\rho_h \mathbf{u}_h\right), q_h\right) = \left(S_{\rho,h}, q_h\right), \tag{6.12}$$

$$\left(\mathcal{T}\left(\rho_h \mathbf{u}_h\right), \mathbf{v}_h\right) + \left(C\left(\rho_h, \mathbf{u}_h\right), \mathbf{v}_h\right) - \left(p_h, \nabla \cdot \mathbf{v}_h\right) + \left(\boldsymbol{\tau}\left(\mathbf{u}_h\right), \nabla \mathbf{v}_h\right) = \left(S_{\mathbf{u},h} + S_{\mathbf{u},dilution,h}, \mathbf{v}_h\right), \tag{6.13}$$

$$\left(\rho_h \partial_t \xi_{k,h}, \eta_{k,h}\right) + \left(\rho_h \mathbf{u}_h \cdot \nabla \xi_{k,h}, \eta_{k,h}\right) + \left(\rho \mathcal{D}_k \nabla \xi_{k,h}, \nabla \eta_{k,h}\right) = \left(S_{k,h} \underbrace{-\xi_{k,h} S_{\rho,h}}_{S_{k,dilution,h}} - S_{k,stab,h}, \eta_{k,h}\right), \tag{6.14}$$

for all test functions: $(q_h, \mathbf{v}_h, \eta_{k,h}) \in Q_h \times \mathbf{V}_{0,h} \times E_{0,k,h}$. See section 5.2 for the possible definitions of the temporal ($\mathcal{T}$), convective (C), and dilution terms of the momentum equation defined as Eq. (5.71). Note, that the scalars are transported using the advective form, which results in the appearance of a dilution term: $\left(-\xi_{k,h} S_{\rho,h}\right)$ associated to the volumetric mass sources originating from the Lagrangian spray cloud. (See Eq. (5.66).) Furthermore, a stabilization term is introduced only to the scalar equations:

$$S_{k,stab,h} = \sum_{e=1}^{n_{el}} \tau_e \left(\rho_h \mathbf{u}_h \cdot \nabla \xi_{k,h} + \nabla \cdot \left(\rho \mathcal{D}_k \nabla \xi_{k,h}\right) - S_{k,h},\ \mathbf{u}_h \cdot \nabla \eta_{k,h}\right), \tag{6.15}$$

where n_{el} is the number of elements, and τ_e is a local timescale of the scalar governing equations in accordance with Avila, Principe, and Codina (2011):

$$\tau_e = \left(c_1 \frac{\mathcal{D}_k}{h^2} + c_2 \frac{|\mathbf{u}_h|}{h} + c_3 \frac{1}{\rho_h} \left| \left(\frac{S_{k,h}^-}{\xi_{k,h}} \right)^{tab} \right| \right)^{-1}, \tag{6.16}$$

where the model constants $c_1 = 4$, $c_2 = 2$, and $c_3 = 1$ are utilized, and h is a length scale of element e here taken as the smallest length scale for anisotropic elements. Note, that the last term of τ_e is only active in the special case, where the source term of ξ_k is expressed as a linear function of the unknown: $S_k = S_k^+ + \frac{S_k^-}{\xi_k}\xi_k$. Here the superscripts $(+)$ and $(-)$ signify the only usage of such linearization in the present work: splitting the chemical source term into consumption and production rates, and tabulating the corresponding terms. (See Eq. (2.98).)

Following Chrysokentis (2019), a more compact notation is applied hereafter, expressing the discretized governing equations in the matrix form:

$$\mathsf{M}\partial_t \Sigma + \mathsf{D}\left[\Sigma \mathbf{U}\right] = \mathsf{R}_\mathsf{c}, \tag{6.17}$$

$$\mathsf{M}\mathsf{I}\Sigma\partial_t \mathbf{U} + \mathsf{K}_\mathsf{m}\mathbf{U} + \mathbf{G}\mathsf{P} = \mathsf{R}_\mathsf{m}, \tag{6.18}$$

$$\mathsf{M}\Sigma\partial_t \Xi_k + \mathsf{K}_\mathsf{k}\Xi_k = \mathsf{R}_\mathsf{k}. \tag{6.19}$$

The superscripts: a, b are used for the node indices, and i, j for the space indices. The shape function of node a is N^a. Since in the present work, the continuous Galerkin approach is used with equal order finite elements for the all unknowns, the following notation is adapted in the matrix form: $\mathsf{M}^{ab} = \left(N^b, N^a\right)$ is the mass matrix of the elements, $\mathsf{D}_j^{ab} = \left(\partial_j N^b, N^a\right)$ is the discrete divergence operator, $\mathbf{G}_i^{ab} = -\left(N^b, \partial_i N^a\right)$ is the discrete gradient operator, and $\mathsf{I}_{ij} = \delta_{ij}$ is the identity tensor, with δ_{ij} being the Kronecker delta. The variables: Σ, $\mathbf{U}$, P, and Ξ_k stand for the matrices of density, velocity, pressure, and k^{th} scalar respectively.

The momentum equation is characterized by the matrix: $\mathsf{K}_\mathsf{m} = \mathsf{K}_\mathsf{m}^{\mathsf{CONV}} + \mathsf{K}_\mathsf{m}^{\mathsf{VISC}}$ which is composed of the convective and viscous matrices. The viscous term is discretized as,

$$\mathsf{K}_\mathsf{m}^{\mathsf{VISC}}{}_{ij}^{ab} = \left(\boldsymbol{\tau}\left(N^b\right), \nabla N^a\right)\delta_{ij}, \tag{6.20}$$

while the continuous form of the convective term may be expressed in various ways in accordance with Tab. 5.1. The discrete matrix counterpart of the the convective operators are:

$$\mathsf{K}_{\mathsf{m,adv}}^{\mathsf{CONV}}{}_{ij}^{ab} = \left(\Sigma\mathbf{U}\cdot\nabla N^b, N^a\right)\delta_{ij}, \tag{6.21}$$

$$\mathsf{K}_{\mathsf{m,skew}}^{\mathsf{CONV}}{}_{ij}^{ab} = \left(\Sigma\mathbf{U}\cdot\nabla N^b, N^a\right)\delta_{ij} + \tfrac{1}{2}\left(\left(\nabla\cdot\left(\Sigma\mathbf{U}\right)\right)N^b, N^a\right)\delta_{ij}, \tag{6.22}$$

$$\begin{aligned}\mathsf{K}_{\mathsf{m,emac}}^{\mathsf{CONV}}{}_{ij}^{ab} = \sqrt{\Sigma}\Big(&\left(\mathbb{A}_h\cdot\nabla N^b, N^a\right)\delta_{ij} + \left(\partial_i N^b \mathbb{A}_h^j, N^a\right)\\ &+ \left(\left(\nabla\cdot\mathbb{A}_h\right)N^b, N^a\right)\delta_{ij} - \tfrac{1}{2}\left(\partial_i\mathbb{A}_h^j N^b, N^a\right)\Big),\end{aligned} \tag{6.23}$$

for the non-conservative (advective), skew-symmetric, and EMAC operators respectively. For the scalar transport, the convective and diffusive terms are represented by $\mathsf{K}_\mathsf{k} = \mathsf{K}_\mathsf{k}^{\mathsf{CONV}} + \mathsf{K}_\mathsf{k}^{\mathsf{DIFF}}$ matrix similarly. The two terms are discretized as,

$$\begin{aligned}\mathsf{K}_\mathsf{k}^{\mathsf{DIFF}}{}^{ab} &= \Sigma\mathcal{D}_k\left(\nabla N^b, \nabla N^a\right)\\ &\quad - \left(\nabla\left(\Sigma\mathcal{D}_k\right)\cdot\nabla N^b + \Sigma\mathcal{D}_k\Delta N^b,\ \tau_e\mathbf{U}\cdot\nabla N^a\right),\end{aligned} \tag{6.24}$$

$$\mathsf{K}_\mathsf{k}^{\mathsf{CONV}}{}^{ab} = \Sigma\left(\mathbf{U}\cdot\nabla N^b, N^a\right) + \Sigma\left(\mathbf{U}\cdot\nabla N^b,\ \tau_e\mathbf{U}\cdot\nabla N^a\right). \tag{6.25}$$

Note, that the stabilization terms are included in the matrix forms.

Finally, the residuals of the governing equations are assessed. In Eq. (6.18), the temporal term of the momentum equation is readily expressed in the non-conservative form. This is necessary for the temporal treatment of the equations, detailed below in section 6.1.4. The form of the temporal term depends on the common discretization strategy of the temporal and convective terms in accordance to Tab. 5.1, thus the temporal term is split into $\mathcal{T}_{adv}$, and an additional term depending on the temporal derivative of density, which is added to the right hand side. Thus the final momentum residual vectors are:

$$\mathsf{R}_{\mathsf{m,adv}}{}_i^a = S_{\mathbf{u},h,i} N^a - \mathbf{U}_i S_{\rho,h} N^a, \tag{6.26}$$

$$\mathsf{R}_{\mathsf{m,skew}}{}_i^a = S_{\mathbf{u},h,i} N^a - \tfrac{1}{2}\mathbf{U}_i S_{\rho,h} N^a - \tfrac{1}{2}\mathbf{U}_i \left(\partial_t \Sigma\right) N^a, \tag{6.27}$$

$$\mathsf{R}_{\mathsf{m,emac}}{}_i^a = S_{\mathbf{u},h,i} N^a - \mathbf{U}_i \left(\partial_t \Sigma\right) N^a, \tag{6.28}$$

Where the temporal derivative of the density: $\partial_t \Sigma$ has to be approximated from the previous time steps to attain an explicit time marching scheme. This topic is further discussed in section 6.1.4. The residuals of the continuity and scalar equations are simply expressed as:

$$\mathsf{R}_{\mathsf{c}}{}^a = S_{\rho,h} N^a, \tag{6.29}$$

$$\mathsf{R}_{\mathsf{k}}{}^a = \left(S_{k,h} - \xi_{k,h} S_{\rho,h}\right)\left(N^a + \tau_e \mathbf{U}\cdot\nabla N^a\right), \tag{6.30}$$

where the residual of the scalar equations contains a stabilization term.

6.1.4 Temporal discretization of the Eulerian governing equations

The time integration of the discretized governing equations is done using the strong stability preserving 3rd order Runge-Kutta scheme of Shu and Osher (1988). The Butcher tableau of this scheme is presented in Tab. 6.1.

TABLE 6.1: Butcher tableau of strong stability preserving 3rd order Runge-Kutta scheme of Shu and Osher (1988).

c_ℓ		$a_{\ell m}$	
0			
1	1		
1/2	1/4	1/4	
	1/6	1/6	2/3
		b_ℓ	

Time marching of scalar equations

For scalars, the ℓ^{th} Runge-Kutta sub-step ($\ell = 2..3$) is accomplished as:

$$\Xi_k^\ell = \Xi_k^n + \delta t \left(\mathsf{M}\Sigma^n\right)^{-1} \sum_{m=1}^{\ell} a_{\ell m}\left(-\mathsf{K}_{\mathsf{k}}{}^n \Xi_k^m + \mathsf{R}_k^n\right), \tag{6.31}$$

where δt is the time step, and it is sufficient to evaluate the convective and diffusive matrix: K_{k} and the density and right hand side vectors: Σ and R_k in the previous

time step marked by the n superscript. The complete time step uses the linear combination of the sub-step terms, yielding the next unknown scalar field:

$$\Xi_k^{n+1} = \Xi_k^n + \delta t \left(\mathsf{M}\Sigma^n\right)^{-1} \sum_{\ell=1}^{s} b_\ell \left(-\mathsf{K_k}^n \Xi_k^\ell + \mathsf{R}_k^n\right). \tag{6.32}$$

Fractional step algorithm of the Navier-Stokes equations

The low Mach number approximation allows for the seamless extension of the incompressible flow solver of Chrysokentis (2019), previously implemented in Alya, to variable density flows. The fractional step algorithm of Donea et al. (1982) is adapted here, that solves the pressure and velocity fields in a mass conserving manner. For the time marching of the velocity field, the fractional step method is incorporated in the Runge-Kutta steps. First only the convective, viscous, and force terms are considered, neglecting the pressure term, to calculate an intermediate solution: $\mathbf{U}^{\ell,*}$,

$$\mathbf{U}^{\ell,*} = \mathbf{U}^n + \delta t \left(\mathsf{MI}\Sigma^n\right)^{-1} \sum_{m=1}^{\ell} a_{\ell m} \left(-\mathsf{K_m}\left(\mathbf{U}^m, \Sigma^n\right)\mathbf{U}^m + \mathsf{R}_m^n\right). \tag{6.33}$$

Then two options are possible, one may solve for the pressure in every Runge-Kutta sub-step according to the fractional step algorithm. Or following Capuano et al. (2016) the intermediate pressure solution may be approximated. In the first case, the pressure equation is formed utilizing the discrete continuity equation: Eq. (6.17), which ensures, that each $\mathbf{U}^\ell$ sub-step solution is strictly mass conserving. The resulting PDE is a Poisson equation with the pseudo-pressure Φ being the unknown:

$$\mathsf{D}\left[\left(\mathsf{MI}\right)^{-1}\mathbf{G}\Phi^\ell\right] = \frac{1}{c_\ell \delta t}\left(\mathsf{D}\left[\Sigma^n \mathbf{U}^{\ell,*}\right] + \mathsf{M}\partial_t \Sigma^\ell - \mathsf{R_c}^\ell\right), \tag{6.34}$$

where $\Phi = \mathsf{P} + \mathcal{O}(\delta t)$ is the pseudo-pressure: a first order approximation of the pressure. As Perot (1993) shows, the order of the pressure solution, does not affect the order of accuracy of the velocity solution, thus the usage of the pseudo-pressure is appropriate. This Poisson equation has to be solved numerically to yield Φ. In Alya the preferred solver for the pressure equation is the deflated conjugate gradient (DCG) method of Löhner et al. (2011). The numerical solution of this equation entails a considerable cost (POP, 2021), thus it is omitted in the Runge-Kutta sub-steps, and the approximation of Capuano et al. (2016) is the preferred option in this work. The velocity field of the next sub-step is calculated as:

$$\mathbf{U}^\ell = \mathbf{U}^{\ell,*} - c_\ell \delta t \left(\mathsf{MI}\Sigma^n\right)^{-1} \mathbf{G}\Phi^\ell, \tag{6.35}$$

where Φ^ℓ is approximated. The complete Navier-Stokes time step is calculated similarly using the linear combination of temporal changes to obtain the intermediate solution: $\mathbf{U}^{n+1,*}$ which does not hold mass conservation:

$$\mathbf{U}^{n+1,*} = \mathbf{U}^n + \delta t \left(\mathsf{MI}\Sigma^n\right)^{-1} \sum_{\ell=1}^{s} b_\ell \left(-\mathsf{K_m}\left(\mathbf{U}^\ell, \Sigma^n\right)\mathbf{U}^\ell + \mathsf{R}_m^n\right). \tag{6.36}$$

In the full time step, there are no means to avoid the solution of the pressure equation, thus a linear system has to be solved iteratively:

$$\mathsf{D}\left[\left(\mathsf{MI}\right)^{-1}\mathbf{G}\Phi^{n+1}\right] = \frac{1}{\delta t}\left(\mathsf{D}\left[\Sigma^n \mathbf{U}^{n+1,*}\right] + \mathsf{MI}\partial_t \Sigma^{n+1} - \mathsf{R_c}^{n+1}\right), \tag{6.37}$$

which yields the pseudo-pressure in the next time step: Φ^{n+1}. Finally, the intermediate velocity solution is projected onto the field of mass conserving velocity solutions according to the fractional step algorithm:

$$\mathbf{U}^{n+1} = \mathbf{U}^{n+1,*} - \delta t \left(\mathsf{M}\mathsf{I}\Sigma^{n}\right)^{-1} \mathbf{G}\Phi^{n+1}. \tag{6.38}$$

In the above equations, the Runge-Kutta coefficients are denoted: $a_{\ell m}$, b_ℓ, and $c_\ell = \sum_m a_{\ell m}$, as presented in the Butcher tableau in Tab. 6.1.

The time derivative of the density: $\partial_t \Sigma$ appears in multiple equations of the outlined discretization strategy, including the right hand side of the momentum equation using the skew-symmetric (Eq. (6.27)) or EMAC (Eq. (6.27)) operators, or the Poisson equations of the pseudo-pressure in the sub-steps (Eq. (6.34)) and the time step (Eq. (6.37)). In this work this term is expressed using a first order approximation based on the previous density fields following Vreman, Bastiaans, and Geurts (2009) as:

$$\partial_t \Sigma^{n+1} = \frac{\Sigma^n - \Sigma^{n-1}}{\delta t}. \tag{6.39}$$

6.1.5 Approximation of the discrete Laplacian

As the use of the discrete Laplacian: $\left(\mathsf{D}\left(\mathsf{M}\mathsf{I}\right)^{-1}\mathbf{G}\right)$ in Eq. (6.34) and Eq. (6.37) is a rather expensive operation, the use of an approximated Laplacian can reduce substantially the computational cost of the algorithm. Since the low Mach number solver of the present work is a direct extension of the incompressible solver of Lehmkuhl et al. (2019b), in this work the same approximation is used for the discrete Laplacian:

$$\mathsf{D}\left(\mathsf{M}\mathsf{I}\right)^{-1}\mathbf{G} = \mathsf{L}, \qquad \text{with} \quad \mathsf{L}^{ab} = -\left(\nabla N^b, \nabla N^a\right). \tag{6.40}$$

Such an approximation introduces a stabilizing effect to the pressure equation, which is the reason why equal order finite elements can be used for the pressure and velocity without explicitly introducing additional stabilization.

The stabilizing effect can be shown by applying this discrete Laplacian in the pressure equations (Eq. (6.34) and Eq. (6.37)):

$$\mathsf{L}\Phi^{\ell} = \frac{1}{c_\ell \delta t}\left(\mathsf{D}\left[\Sigma^n \mathbf{U}^{\ell,*}\right] + \mathsf{M}\partial_t \Sigma^{\ell} - \mathsf{R_c}^{\ell}\right), \tag{6.41}$$

$$\mathsf{L}\Phi^{n+1} = \frac{1}{\delta t}\left(\mathsf{D}\left[\Sigma^n \mathbf{U}^{n+1,*}\right] + \mathsf{M}\mathsf{I}\partial_t \Sigma^{n+1} - \mathsf{R_c}^{n+1}\right). \tag{6.42}$$

Furthermore the equation of the velocity sub-step: Eq. (6.35) is rearranged into:

$$\Sigma^n \mathbf{U}^{\ell,*} = \Sigma^n \mathbf{U}^{\ell} + c_\ell \delta t \left(\mathsf{M}\mathsf{I}\right)^{-1} \mathbf{G}\Phi^{\ell}. \tag{6.43}$$

Introducing this term into Eq. (6.41), and denoting the difference between the discrete and continuous operators with $\mathsf{B} = \mathsf{D}\left(\mathsf{M}\mathsf{I}\right)^{-1}\mathbf{G} - \mathsf{L}$, one obtains the term associated to the mass conservation error:

$$c_\ell \delta t \mathsf{L}\Phi^{\ell} = \mathsf{D}\left[\Sigma^n \mathbf{U}^{\ell} + c_\ell \delta t \left(\mathsf{M}\mathsf{I}\right)^{-1} \mathbf{G}\Phi^{\ell}\right] - \mathsf{R_c}^{\ell}, \tag{6.44}$$

$$\mathsf{M}\partial_t \Sigma^{\ell} + \mathsf{D}\left[\Sigma^n \mathbf{U}^{\ell}\right] + c_\ell \delta t \mathsf{B}\Phi^{\ell} = \mathsf{R_c}^{\ell}. \tag{6.45}$$

Similarly for the time step,

$$\mathsf{M}\partial_t \Sigma^{n+1} + \mathsf{D}\left[\Sigma^n \mathbf{U}^{n+1}\right] + \delta t \mathsf{B}\Phi^{n+1} = \mathsf{R_c}^{n+1}. \tag{6.46}$$

Codina and Blasco (1997) showed, that the error introduced by $\mathsf{B}\Phi^{n+1}$ is the same order as the pressure interpolation error: $\mathcal{O}\left(h^{k+1}\right)$, where k is the order of the elements. Using the stabilization term in Eq. (5.73), yields a kinetic energy dissipation term of $(\delta t \mathsf{B}\Phi, \Phi)$. Thus the stabilization term introduces an error of $\mathcal{O}(\delta t\ h^{k+1})$ in the kinetic energy conservation, which is acceptable for the purposes of the current work. Lehmkuhl et al. (2019b) tested the present method extensively in the incompressible limit, and confirmed in the Taylor-Green vortex case at $Re = 1600$, that the kinetic energy error indeed shows second order scaling with the mesh size using linear finite elements ($k = 1$).

6.1.6 Conservative coupling of Eulerian and Lagrangian phases

The evaporative source terms of the Eulerian equations are formally derived in section 5.5.3. However, computing the actual filtered source terms: $\overline{S^e_\rho}$, $\overline{S^e_{\mathbf{u}}}$, $\overline{S^e_h}$, and $\overline{S^e_Z}$, and subsequently integrating these over the elements would result in non-conservative behavior. I.e.: the mass leaving the evaporating droplet would not match the mass added to the gas phase. Such errors would have very severe effect on flames, since the chemistry is very sensitive to the local mixture fraction.

The problem is illustrated by taking the matrix form of the mixture fraction equation:

$$\mathsf{M}\Sigma\partial_t \mathsf{Z} + \mathsf{K_Z}\mathsf{Z} = \mathsf{R_Z}, \tag{6.47}$$

where the right hand side term is associated to the Lagrangian spray only, here neglecting the stabilization term:

$$\mathsf{R_Z}^a = \left(S_{Z,h} - Z_h S_{\rho,h}\right) N^a. \tag{6.48}$$

One could compute the nodal representation of $\left(S_{Z,h} - Z_h S_{\rho,h}\right)$, and treat the right hand side as all other terms are treated in the present scheme: i.e.: using a Gaussian quadrature method, to integrate the source terms over the elements. A conservative formulation would entail the computation of a finite element representation of $S_{Z,h}$ and $S_{\rho,h}$, such that their volume integral is exactly $\sum_p \left(\dot{m}_r\right)_p$, according to section 5.5.3.

Instead, to get the evaporative contribution to $\mathsf{R_Z}$ in node a, the source term is assembled directly from the Lagrangian droplets contained in the elements surrounding the node. The shape functions of the host element are used to distribute the source terms onto the element nodes in a conservative manner. The same method is used for all coupling source terms of the Eulerian-Lagrangian approach.

6.1.7 Low-dissipation scheme for multiphase reacting flows

The complete approach is summarized in algorithm 6.1. The time step is calculated as the minimum of the time step of the scalar and the momentum equations. For the scalar equations, the standard Courant-Friedrichs-Lewy (CFL) condition is applied, while the self-adaptive strategy of Trias and Lehmkuhl (2011) is used for the momentum equations. The algorithm is built in a modular way, following the multi-physics approach of the Alya code. (Vázquez et al., 2016) Accordingly, the time marching

of the Lagrangian droplets, the scalar equations, and the Navier-Stokes equations is executed in separate units.

Algorithm 6.1: Overview of the low dissipation scheme.

$t = t_0$;
while $t \leq t_f$ **do**
  Evalueate δt;
  $t = t + \delta t$;
  Evaluate Lagrangian time step according to algorithm 6.2;
  Evaluate scalar time step according to algorithm 6.3;
  Evaluate Navier-Stokes time step according to algorithm 6.4;
  Lookup tabulated properties;
  Evaluate the density: Σ^{n+1} using Eq. (5.148);

The time step of the Lagrangian particles is further detailed in algorithm 6.2. First, new droplets may be initialized by the injection model mimicking the fuel injector. Then each droplet is advanced individually, first the kinematic transport is solved, then the evaporation is tracked. The nodal source terms, which represent the source terms described in section 5.5.3, are assembled from the individual contributions of each Lagrangian particle. I.e.: the total mass change of the droplets hosted in an element are distributed among the nodes of the element as a mass source. Likewise, an enthalpy source is associated to the convective heat transfer between the gas and the droplet, and the enthalpy of the incoming matter. Finally, the drag-induced deceleration of the droplet and the momentum of the incoming fuel vapor are considered as momentum sources in the gas phase.

Algorithm 6.2: Overview of the time step of Lagrangian particles, where N_p is the number of particles in the domain.

Inject new particles and increment N_p;
$j = 1$;
while $j \leq N_p$ **do**
  Evaluate $\mathbf{u}_p^{n+1}$ using the Newmark/Newton-Raphson algorithm;
  Evaluate $\mathbf{x}_p^{n+1}$ using Eq. (6.2);
  Evaluate m_p^{n+1} and T_p^{n+1} using Eq. (6.8);
Sum contributions of individual interactions to the nodal source terms;

These source terms are computed in the ongoing time step, and are added to this same time step in the Eulerian equations. Note, that this is the only instance, where the order of the different physics modules matter, as the Eulerian phase is solved with a fully explicit scheme, meaning, that the previous (n^{th}) time step uniquely determines the evolution of the unknowns.

Next the scalars are transported using stabilized finite elements, using the 3$^{\text{rd}}$ order strong stability preserving Runge-Kutta scheme of Shu and Osher (1988). This step is a fairly straightforward application of the Runge-Kutta method, as depicted by algorithm 6.3. Then the new velocity field is calculated with the combination of the Runge-Kutta scheme with the fractional step method. For the momentum transport the convective operator is assembled according to Eq. (6.21), Eq. (6.22), or Eq. (6.23) for the non-conservative, skew-symmetric and EMAC discretizations respectively.

Algorithm 6.3: Overview of the Runge-Kutta time step of scalar equations, where s is the number of sub-steps in the Runge-Kutta method.

$\ell = 2$;
$\Xi_k^1 = \Xi_k^n$;
while $\ell \leq s$ **do**
  Evaluate Ξ_k^ℓ using Eq. (6.31) ;
  $\ell = \ell + 1$;
Evaluate Ξ_k^{n+1} using Eq. (6.32);

Algorithm 6.4: Overview of the Runge-Kutta time step of the Navier-Stokes equations with the Fractional step method, where s is the number of sub-steps in the Runge-Kutta method.

$\ell = 2$;
$\mathbf{U}^1 = \mathbf{U}^n$;
while $\ell \leq s$ **do**
  Evaluate $\mathbf{U}^{\ell,*}$ using Eq. (6.33) ;
  Evaluate Φ^ℓ solving Eq. (6.41) or approximate Φ^ℓ (Capuano et al., 2016);
  Evaluate $\mathbf{U}^\ell$ using Eq. (6.35) ;
Evaluate $\mathbf{U}^{n+1,*}$ using Eq. (6.36);
Evaluate Φ^{n+1} solving Eq. (6.42) ;
Evaluate $\mathbf{U}^{n+1}$ using Eq. (6.38) ;

Finally the overall time stepping scheme of algorithm 6.1 ends with evaluating the derived properties in the next time step. The thermo-chemical lookup is executed using the transported scalars as control variable. The temperature: $T^\star$ is evaluated using the tabulated NASA polynomials in algorithm 2.1. And finally the density is calculated using the tabulated properties. The overall scheme preserves the low-dissipation properties of the scheme developed by Lehmkuhl et al. (2019b) while extending it to low Mach number flows. The resulting method is suitable for the simulation of gas phase and multiphase reacting flows, given that the limits of applicability discussed throughout chapter 5 are respected. In the rest of the present chapter the developed scheme is tested extensively.

6.2 Benchmarking of the low Mach number solver

The developed algorithm has been extensively tested in incompressible conditions. A set of dedicated test cases has been published in the recent work of Lehmkuhl et al. (2019b). The included tests are: the inviscid and viscous Taylor-Green vortex, a turbulent channel flow, flow past a sphere, and flow around the Ahmed body. Using the Taylor-Green vortex, it has been shown, that the kinetic energy dissipation introduced by the numerical scheme is indeed scaling as $\mathcal{O}(\delta t\ h^{k+1})$. Subsequently, the same algorithm has been used in various challenging cases including engineering problems and biological flows. (Martin et al., 2019; Flammang et al., 2020; Lehmkuhl, Lozano-Durán, and Rodriguez, 2020; Rodriguez, Lehmkuhl, and Borrell, 2020; Rodriguez, Lehmkuhl, and Soria, 2021; Miró et al., 2021; Oks et al.,

2022) It is important to note, that the same code is used in the present study with the following modifications:

1. addition of scalar transport equations,
2. extension to state dependent material properties,
3. inclusion of coupling terms with the Lagrangian droplets,
4. inclusion of the $\partial_t \Sigma$ term in Eq. (6.41) and Eq. (6.42).

Thus, the results of Lehmkuhl et al. (2019b) are retained in the incompressible limit with the present formulation.

6.2.1 Channel flow problem

In this section the extension to low Mach number flows is tested, without the added complexity of reacting flows or Lagrangian particle transport. A periodic turbulent channel flow is examined, depicted in Fig. 6.1. The problem is characterized by dimensions of $L_x = 2\pi h$, $L_y = 2h$, and $L_z = \pi h$ in the streamwise, wall-normal, and spanwise directions respectively, where $h = 1$ m was chosen as the channel half-height. Toutant and Bataille (2013) used a larger domain and showed, that the two point correlations diminish over these distances, i.e.: the largest scale coherent structures fit in the selected domain, and the dimensions can be considered adequate for the problem. The domain is periodic in the spanwise and streamwise directions.

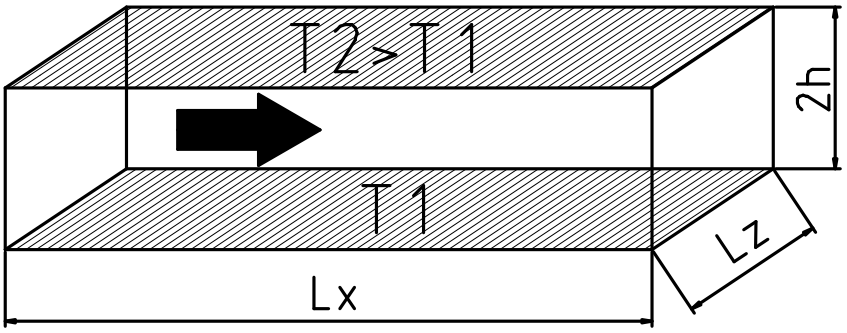

FIGURE 6.1: Channel geometry.

Herein, the problem is studied both with negligible temperature variations, and with a significant temperature difference between the walls. In any case, the mean flow is induced by applying a constant artificial pressure gradient ($\overline{S_{\mathbf{u},x}}$) in the x direction. Note, that in variable density cases this is different from applying a gravity-like force, which would affect more the denser parts of the flow. Following the convention of incompressible channel simulations the flow is characterized by the wall Reynolds number: Re_τ. However, to make this metric general, the material properties are evaluated at the corresponding wall temperature:

$$Re_\tau = \frac{\rho_w u_\tau h}{\mu_w}, \tag{6.49}$$

where "w" indicates the wall state ($\rho_w = \rho(P_0, T_w)$, $\mu_w = \mu(T_w)$). Furthermore, a velocity scale of the problem is given by u_τ, the friction velocity:

$$u_\tau = \sqrt{\frac{\langle \tau_w \rangle}{\rho_w}}, \tag{6.50}$$

with $\langle \tau_w \rangle$ being the mean wall shear stress on the wall, calculated as a temporal average over the entire wall:

$$\langle \tau_w \rangle = \frac{1}{\Delta t} \sum_{t_0}^{t_0+\Delta t} \frac{|\mathbf{F}^n_{w,x}|}{A_w} \delta t^n, \tag{6.51}$$

where $\mathbf{F}^n_{w,x}$ is the friction force exerted on the wall in the streamwise direction at time step n, A_w is the wall surface, Δt is length of the averaging interval, and δt^n is the time step size.

Governing equations

In general the problem is characterized by the low Mach number Navier-Stokes equations (Eq. (5.30) and Eq. (5.47)) appended with a single scalar equation expressing the enthalpy transport, using the Favre-filtered temperature as unknown. This set of equations is retained even in the case of negligible temperature variations, to confirm, that the present scheme is equivalent to the incompressible implementation of Lehmkuhl et al. (2019b) in this limit. For the sake of completeness, the equations are:

$$\partial_t \overline{\rho} + \nabla \cdot (\overline{\rho}\widetilde{\mathbf{u}}) = 0 \tag{6.52}$$

$$\partial_t (\overline{\rho}\widetilde{\mathbf{u}}) + \nabla \cdot (\overline{\rho}\widetilde{\mathbf{u}} \otimes \widetilde{\mathbf{u}}) + \nabla \overline{p} - \nabla \cdot \left(2 \left(\overline{\mu} + \overline{\rho} \nu^{SGS} \right) \widetilde{\mathbf{S^D}(\mathbf{u})} \right) = \overline{S_\mathbf{u}} \tag{6.53}$$

$$c_p \overline{\rho} \partial_t \widetilde{T} + c_p \overline{\rho} \widetilde{\mathbf{u}} \cdot \nabla \widetilde{T} - \nabla \cdot \left(\left(\lambda + \frac{c_p \overline{\rho} \nu^{SGS}}{Pr_t} \right) \nabla \widetilde{T} \right) = \frac{\mathrm{d}P_0}{\mathrm{d}t}, \tag{6.54}$$

where λ is the thermal conductivity, and $c_p = 1005 \, \frac{\mathrm{J}}{\mathrm{kgK}}$ is the specific heat. The material properties are representing realistic gas-like behavior. The sub-grid model of Vreman (2004) is applied with the model constant chosen $c = 0.1$. The equation of state Eq. (2.51) is used with a specific gas constant of $R = \frac{R_u}{W} = 287 \, \frac{\mathrm{J}}{\mathrm{kgK}}$, and the dynamic viscosity is set by Sutherland's law: $\mu = \frac{T^{3/2}}{T + 111 \, \mathrm{K}} 1.461 \cdot 10^{-6} \, \frac{\mathrm{Pas}}{\sqrt{\mathrm{K}}}$. Furthermore, the thermal conductivity is calculated using a constant molecular Prandtl number: $\lambda = \frac{\mu c_p}{Pr}$ with $Pr = 0.71$. Finally, in this case the turbulent Prandtl number is set to $Pr_t = 0.9$ as proposed by Nicoud (1998). The time evolution of the thermodynamic pressure is tracked by Eq. (2.53), ensuring, that the mass enclosed in the periodic domain remains constant.

Computational grid

A structured hexahedral grid is applied with homogeneous size in x and z. The grid is refined in the wall-normal direction, with the following function giving the node locations:

$$y_i = h \left(1 + \frac{1}{\alpha} \tanh \left(\operatorname{atanh}(\alpha) \left(\frac{2i}{N_{ey}} - 1 \right) \right) \right), \qquad i = 0..N_{ey}, \tag{6.55}$$

where N_{ey} is the number of elements in y, and α is a parameter expressing the level of refinement. A coarse and a fine mesh are considered to evaluate the effects of resolution on the discretization strategy.

TABLE 6.2: Channel flow mesh size and corresponding non-dimensional mesh sizes evaluated suing $Re_\tau = 395$.

	N_{ex}	N_{ey}	N_{ez}	α	Δ_x^+	$\Delta_{y,min}^+$	$\Delta_{y,max}^+$	Δ_z^+	DoF
Coarse	70	66	39	0.9933	35.5	0.50	34.2	31.8	180k
Fine	165	123	82	0.9830	15.0	0.54	15.5	15.1	1.66M

Table 6.2 presents the parameters chosen for the coarse and fine channel grids. The two meshes result in 180k and 1.66M degrees of freedom respectively corresponding to the number of nodes. The element sizes are expressed in the *wall units* typically employed in wall-bounded flows:

$$\Delta^+ = \frac{\rho_w u_\tau \Delta}{\mu_w} = \frac{Re_\tau \Delta}{h}, \tag{6.56}$$

where Δ is the element size in any of the directions, and h/Re_τ is the viscous length scale: a typical length scale of the boundary layer. In wall bounded turbulence, the typical size of the eddies decreases near the wall, as they cannot cross this boundary. Consequently, different regions are characterized by different physical phenomena. For a detailed discussion of near-wall turbulent flows see Pope (2000, §7) and Kundu, Cohen, and Dowling (2015, §12.9).

In this work the near-wall flow has to be well resolved in the LES applications, hence the need for the boundary layer refinement of Eq. (6.55). Such an approach is called *wall-resolved LES*. Note, that the smallest element size in the wall-normal direction is approximately half of the viscous length scale in both meshes. The location where the unknowns are represented closest to the wall is on the nodes of the first element. Thus the present meshes are equivalent to ones applied in cell-centered finite volume methods using a $\Delta_{y,min}^+$ of 1, where the degree of freedom is located within the cell. As Fig. 6.2 illustrates, the center of the flow is discretized with roughly regular hexahedra with edge length of ~ 30 and ~ 15 wall units in the coarse and fine meshes respectively. To achieve the same near-wall refinement but use twice as fine mesh in the core of the flow, the α parameter is tuned.

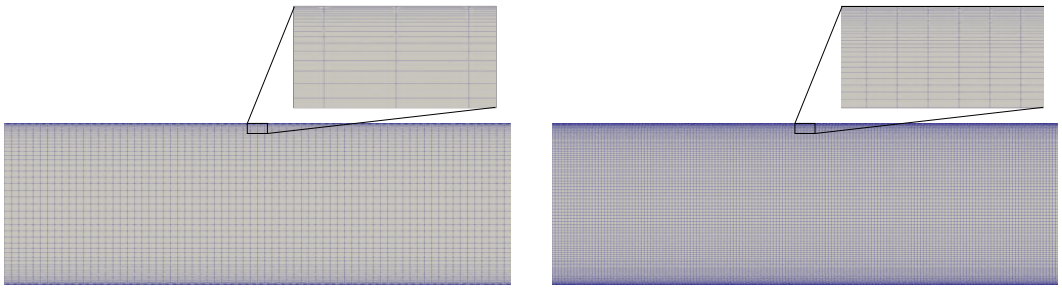

(A) Coarse grid. (B) Fine grid.

FIGURE 6.2: Coarse and fine channel grids.

Note, that boundary layer refinement is specially important in cases governed by a known pressure drop. The channel flow is such a case, where the balance of the

imposed $\overline{S_{\mathbf{u},x}}$ pressure gradient and the wall shear stress determines the flow rate through the domain. This is not always the case in combustion systems, where the flow rate is often an input of the simulation. Nevertheless, the correct prediction of the pressure drop throughout different parts of the system necessitates a good representation of the shear stresses. This affects the turbulence, and flow rates through different passages of the complex combustion systems.

While in this work the near-wall flow has to be fully resolved, it is also a possibility to devise *wall-models*, which represent the shear stress correctly even on poorly resolved boundary layers. For the wall-modeling capabilities of Alya in incompressible flows, see the recent work of (Owen et al., 2020). The extension of such models to heat transfer and variable density flows is out of the scope of the present work, thus all simulations presented are considered wall-resolved.

6.2.2 Quasi-incompressible channel flow

The problem outlined above in section 6.2.1 is first simulated using essentially equal temperatures on the two walls. The lower wall is taken as the cold wall with constant temperature: $T_1 = 293$ K. The thermal state of the problem is expressed as the ratio of the wall temperatures: $Tr = \frac{T_2}{T_1}$, which is $Tr = 1.01$ is this case, corresponding to $T_2 = 295.93$ K. For the sake of setting the forcing term, the material properties are evaluated at T_1 only: $\mu_w \approx 1.81 \cdot 10^{-5}$ Pas and $\rho_w \approx 1.20$ kg/m^3. Here the thermodynamic pressure is initialized as atmospheric, and its subsequent change is negligible. The rest of the conditions correspond to the DNS of Moser, Kim, and Mansour (1999) at $Re_\tau = 392.24$. At a given Re_τ the mean wall sheer stress: $\langle \tau_w \rangle$ is defined by Eq. (6.49) and Eq. (6.50). The imposed pressure gradient can be obtained from the mean balance of forces acting on the entire fluid volume:

$$2\langle \tau_w \rangle A_w = \underbrace{2hA_w}_{\text{volume}} \overline{S_{\mathbf{u},x}}. \tag{6.57}$$

Thus the pressure gradient term (or momentum source term) is:

$$\overline{S_{\mathbf{u},x}} = \frac{\langle \tau_w \rangle}{h} = \frac{Re_\tau^2 \mu_w^2}{\rho_w h^3} = 4.26 \cdot 10^{-5} \text{ N/m}^3. \tag{6.58}$$

This case has been simulated on the fine grid described in Tab. 6.2, using the low-dissipation strategy outlined in section 6.1 with the non-conservative (advective) discretization scheme of the Navier-Stokes equations. The results are presented in Fig. 6.3, with the mean velocity components normalized by the friction velocity, using the assumptions of time averaging outlined in section 5.1.5. The displayed mean velocity is:

$$U^+ = \frac{\langle \widetilde{u} \rangle}{u_\tau}. \tag{6.59}$$

Meanwhile the fluctuations are:

$$u^+_{rms} = \frac{\sqrt{\left\langle (\widetilde{u})^2 \right\rangle - \langle \widetilde{u} \rangle^2}}{u_\tau}, \; v^+_{rms} = \frac{\sqrt{\left\langle (\widetilde{v})^2 \right\rangle - \langle \widetilde{v} \rangle^2}}{u_\tau}, \; w^+_{rms} = \frac{\sqrt{\left\langle (\widetilde{w})^2 \right\rangle - \langle \widetilde{w} \rangle^2}}{u_\tau}, \tag{6.60}$$

with the wall-normal location also normalized following Eq. (6.56): $y^+ = Re_\tau y/h$.

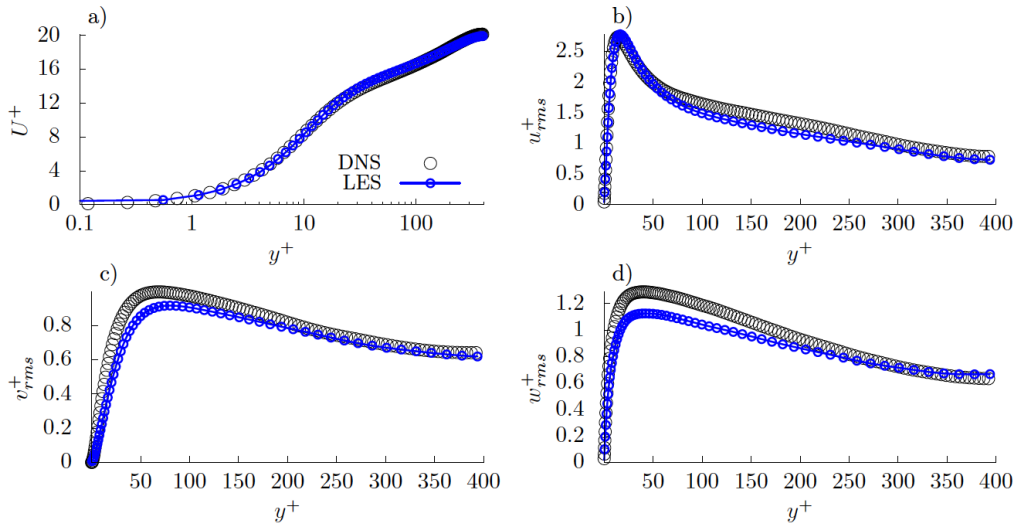

FIGURE 6.3: Channel flow LES at wall Reynolds number of $Re_\tau = 392.24$ in the incompressible limit ($Tr = 1.01$), compared with the DNS data of Moser, Kim, and Mansour (1999). The symbols in the LES results represent the location of the grid nodes. The figure present the mean streamwise velocity (a), and the RMS velocity fluctuation in the streamwise (b), wall-normal (c), and spanwise (d) directions normalized with the wall units.

The results show an excellent match with the DNS of Moser, Kim, and Mansour (1999). The mean streamwise velocity practically overlaps with the DNS data, while the RMS velocity components show minor differences, which are expected considering, that the sub-grid variance is not included in these RMS values. In conclusion, this quasi-incompressible case are comparable to those of Lehmkuhl et al. (2019b), which confirms, that the extension of the low-dissipation finite element scheme to variable density flows does not deteriorate the quality of the scheme in incompressible cases, even using the non-conservative form of the Navier-Stokes equations.

6.2.3 Anisothermal channel flow

Increasing the complexity of the problem, the same channel geometry is studied using a temperature ratio of $Tr = 2$. This flow is characterized by significant density fluctuations, making the temporal derivative of the density ($\partial_t \Sigma^{n+1}$) a significant term in the pressure's Poisson-equation: Eq. (6.37). Such a case allows for testing the effect of density gradients in an isolated manner.

The two walls have different wall Reynolds numbers in case of non-unity temperature ratios. The usual approach to reach different temperature ratios is keeping the cold wall at ambient temperature ($T_1 = 293$ K), while increasing the temperature of the hot wall ($T_2 = 586$ K). If Sutherland's law is applied, the viscosity at the hot wall increases, and the wall Reynolds number decreases. However, the cases can be characterized by the average wall Reynolds number:

$$Re_\tau = \frac{Re_{\tau,c} + Re_{\tau,h}}{2}, \tag{6.61}$$

where "c" and "h" indicates the cold and hot walls respectively.

There are numerous approaches in the literature for comparing different temperature ratios. In this work, the anisothermal channel flow DNS study of Toutant and Bataille (2013) is followed, in which they impose a volumetric force term such, that the average wall Reynolds number is prescribed. In the present case $Re_\tau = 395$ is used. The mean force balance of the channel does not take the form presented in Eq. (6.57), since the two walls may exert different shear forces on the fluid. In this case the forcing pressure gradient term is expressed as:

$$\overline{S_{\mathbf{u},x}} = \frac{\tau_c + \tau_h}{2h} = \frac{\frac{Re_{\tau,c}^2 \mu_c^2}{\rho_c} + \frac{Re_{\tau,h}^2 \mu_h^2}{\rho_h}}{2h^3}. \tag{6.62}$$

To calculate the force term in the $Tr = 2$ case, the two wall Reynolds numbers are taken *a priori* from the DNS of Toutant and Bataille (2013) as: $Re_{\tau,c} = Re_{\tau,c}^{DNS} = 235$ and $Re_{\tau,h} = Re_{\tau,h}^{DNS} = 565$. Furthermore, assuming a near atmospheric thermodynamic pressure, the material properties on the hot wall are: $\mu_h \approx 2.97 \cdot 10^{-5}$ Pas and $\rho_h \approx 0.60$ kg/m^3, resulting in a volumetric force term of: $\overline{S_{\mathbf{u},x}} = 8.41 \cdot 10^{-5}$ N/m^3, which is approximately the double of the quasi-incompressible case. I.e.: to maintain the average wall Reynolds number while increasing the temperature of one wall, the forcing pressure gradient has to increase. Note, that there is very little difference between the shear force exerted on the fluid by the two walls, on the cold side: $\tau_c = 8.72 \cdot 10^{-5}$ Pa, while on the hot side: $\tau_h = 8.10 \cdot 10^{-5}$ Pa.

The case is simulated with both the coarse and fine grids of Tab. 6.2. The same numerical method is maintained, using the non-conservative (advective) form of the Navier-Stokes equations. The case is initialized with a constant temperature profile and an initial thermodynamic pressure of $P_0 = 101325$ Pa. After a statistically steady state is obtained, the case is restarted with preserving the unknowns: $\widetilde{u}$, and $\widetilde{T}$, while resetting the initial thermodynamic pressure to $P_0 = 101325$ Pa. After some initial transients, the case is time averaged, During the averaging period the total change of the thermodynamic pressure is within 1%. This procedure is necessary to ensure, that the thermodynamic pressure is nearly atmospheric, as the forcing term is calculated *a priori* assuming atmospheric conditions.

The fully developed flow is illustrated by iso-contours of the streamwise velocity and temperature on the fine grid in Fig. 6.4. The instantaneous velocity field does not show signs of any outstanding effect related to the density fluctuations. Meanwhile, the temperature contours suggest, that the bulk flow is characterized by moderate temperature gradients, and steep changes are concentrated near the top and bottom wall. Observing the instantaneous fields, there is an apparent correlation between the temperature and streamwise velocity. For instance, near the top wall higher velocity regions carry colder fluid to the wall from the bulk, while lower velocity regions appear to be hotter.

The nature of the coupled heat and momentum transfer is further illustrated in Fig. 6.5, comparing the mean and RMS profiles of the streamwise velocity and temperature in the coarse and fine grids. The RMS values are calculated as:

$$u_{rms} = \sqrt{\left\langle (\widetilde{u})^2 \right\rangle - \langle \widetilde{u} \rangle^2}, \qquad T_{rms} = \sqrt{\left\langle \left(\widetilde{T}\right)^2 \right\rangle - \left\langle \widetilde{T} \right\rangle^2}. \tag{6.63}$$

Indeed, all the profiles stay fairly symmetric, despite the strong temperature gradient. The velocity profile is only affected to a small extent, as the boundary layer on the hot side ($y/h = 2$) becomes slightly thicker. Nevertheless, the magnitude of

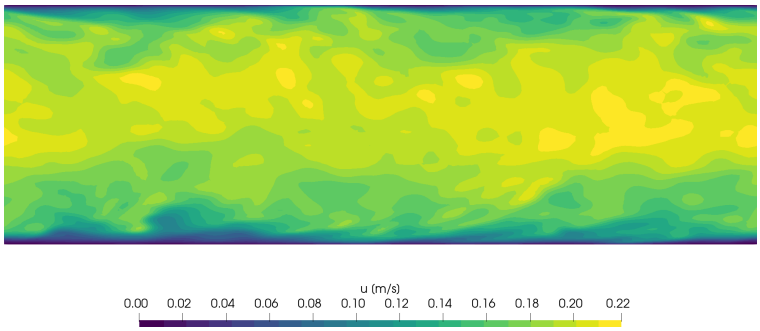

(A) Streamwise velocity.

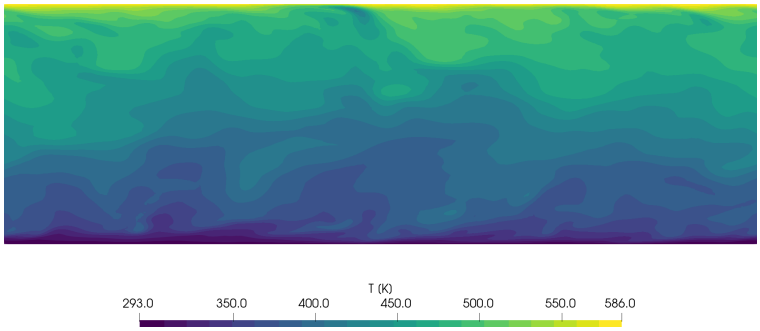

(B) Temperature.

FIGURE 6.4: Illustration of anisothermal channel flow on the fine grid with temperature ratio of $Tr = 2$.

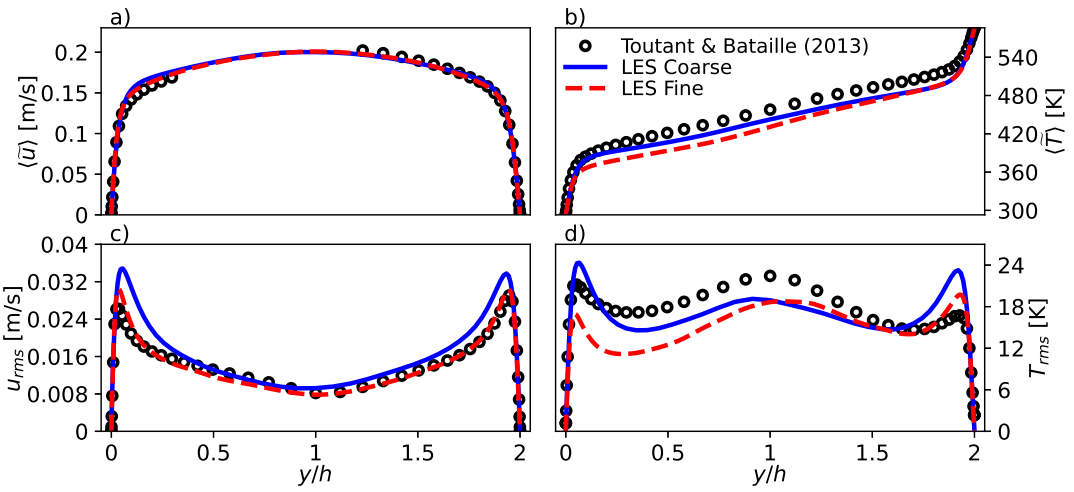

FIGURE 6.5: Anisothermal channel flow LES profiles in natural coordinates at mean wall Reynolds number of $Re_\tau = 395$ with a temperature ratio of $Tr = 2.0$, compared with the DNS data of Toutant and Bataille (2013). The figure present the mean streamwise velocity (a), the mean temperature (b), the RMS of the velocity fluctuations (c), and the RMS of the temperature fluctuations (d).

the velocity fluctuations stays similar on the cold and hot sides. The mean temperature profile is characterized by high gradients in the boundary layer, and a rather

modest slope in the center of the channel. The temperature RMS shows three peaks, two associated to the boundary layers coinciding with the local maxima of u_{rms}, and an additional local maximum in the center of the channel. Comparing to the DNS of Toutant and Bataille (2013), the mesh refinement clearly shows an improvement in the streamwise velocity fluctuations. Larger discrepancies are observed in temperature profiles, possibly related to the numerical schemes of the scalar transport. Nonetheless, the trends are reproduced well.

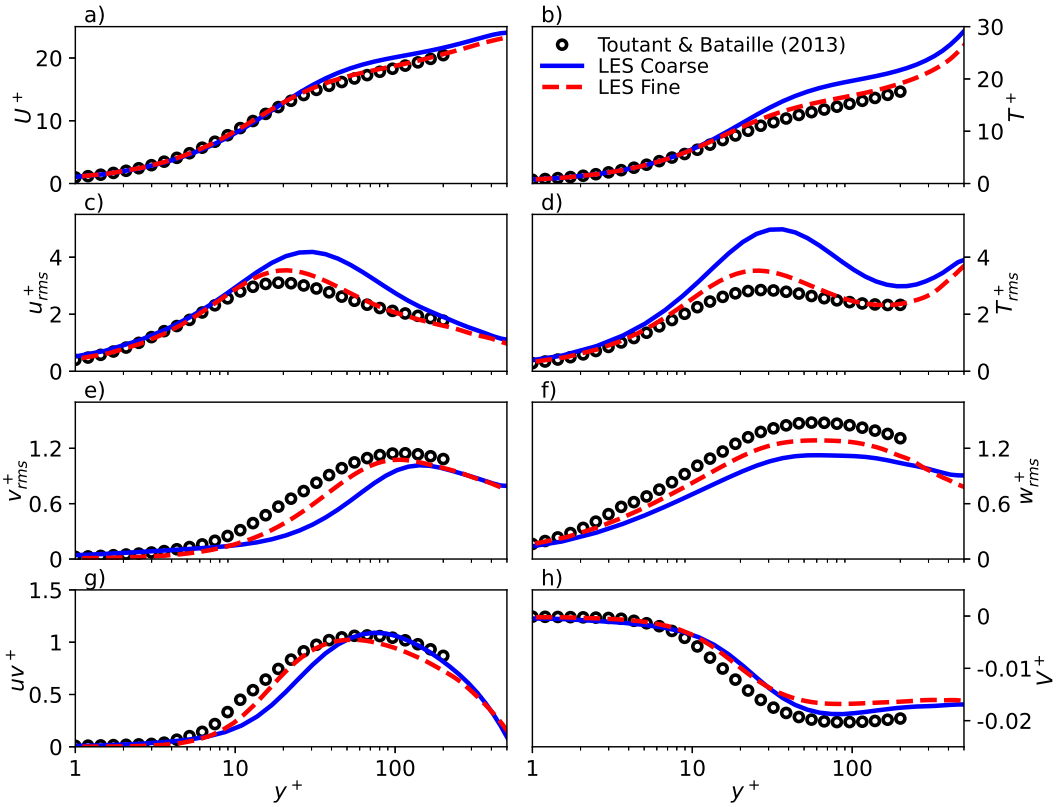

FIGURE 6.6: Anisothermal channel flow profiles on the *cold* side in wall units at a mean wall Reynolds number of $Re_\tau = 395$ with a temperature ratio of $Tr = 2.0$. The LES results are compared with the DNS data of Toutant and Bataille (2013). The figure presents the mean streamwise velocity (a), the mean temperature (b), the RMS of streamwise (c) velocity fluctuations, the RMS of the temperature fluctuations (d), the RMS of wall-normal (e) and spanwise (f) velocity fluctuations, the cross-correlation of streamwise and wall-normal velocity fluctuations (g), and the mean wall-normal velocity (h).

The quality of the LES simulations is better quantified by assessing the macroscopic properties of the flow. In case of the momentum transport, the wall Reynolds number fills this role, as this property is a normalization of the mean wall shear stress with known material properties. Similarly, the friction temperature is a normalized heat flux characterizing the heat transfer:

$$T_\tau = \frac{\langle \dot{q}_w \rangle}{\rho_w c_p u_\tau}, \tag{6.64}$$

where $\langle \dot{q}_w \rangle$ is the time averaged heat flux normal to the wall surface, with positive

TABLE 6.3: Macroscopic parameters of anisothermal channel flow at a mean wall Reynolds number of: $Re_\tau = 395$ and temperature ratio of $Tr = 2$ compared to the DNS of Toutant and Bataille (2013).

	DNS	LES Coarse	LES Fine
Re_τ	400	396 (−1.0%)	404.5 (+1.1%)
$Re_{\tau,c}$	565	553 (−2.1%)	571 (+1.1%)
$Re_{\tau,h}$	235	239 (+1.7%)	238 (+1.3%)
$u_{\tau,c}$ [m/s]		0.0083	0.0086
$u_{\tau,h}$ [m/s]		0.0118	0.0118
$T_{\tau,c}$ [K]		−4.89	−4.80
$T_{\tau,h}$ [K]		6.97	7.63

values corresponding to inward heat flux. These macroscopic properties are summarized in Tab. 6.3. The wall Reynolds numbers are rather close to the DNS value, indicating, that the shear forces are predicted well. The friction velocity and temperature are reported for completeness. Following Kader (1981), the friction temperature may be used for scaling the temperature as:

$$T^+ = \frac{T_w - \left\langle \widetilde{T} \right\rangle}{T_\tau}, \qquad T^+_{rms} = \frac{T_{rms}}{T_\tau}. \tag{6.65}$$

Results for the mean and RMS profiles of the present LES simulations are shown in Fig. 6.6 on the cold side of the channel, and in Fig. 6.7 on the hot side. The classical wall unit based scaling is applied for the velocities, while the scaling of Kader (1981) is used for the mean and RMS temperature. The cross-correlation of the streamwise and wall-normal velocity is likewise scaled as:

$$uv^+ = \frac{\langle \widetilde{u}\widetilde{v} \rangle - \langle \widetilde{u} \rangle \langle \widetilde{v} \rangle}{u_\tau^2}. \tag{6.66}$$

As Toutant and Bataille (2013) explains, the mean streamwise velocity retains the logarithmic scaling in the log-law region ($y^+ > 30$ and $y/h > 0.3$ (Pope, 2000, §7.1)). However, the nature of the scaling changes due to the variable density effects. The mean temperature profile shows similar behavior in the log-law region, however in the core of the flow it becomes linear as Fig. 6.5 shows, thus the nature of the U^+ and T^+ profiles differ in this region. The mean density gradient induces a mean wall-normal velocity in the bulk flow, as a consequence of mass conservation. Hot fluid particles generally moving downwards are less dense than the cold fluid particles moving upwards, thus the former ones need to have a higher velocity to satisfy mass conservation. This manifest in a slight downward velocity displayed in Fig. 6.6h and Fig. 6.7h. Overall, the LES simulations show a good level of correlation with the reference DNS data using the scaled quantities. The correspondence is improved compared to the unscaled thermal quantities of Fig. 6.5. This suggests, that the main difference between the DNS and the present results originate from discrepancies in T_τ, since after scaling both the DNS and LES with the corresponding T_τ the differences diminish.

The results in the cold side shown in Fig. 6.6 are in good agreement for the first-order statistics (mean streamwise velocity and temperature), while the second-order statistics show a higher dependency with the mesh resolution. Meanwhile on the

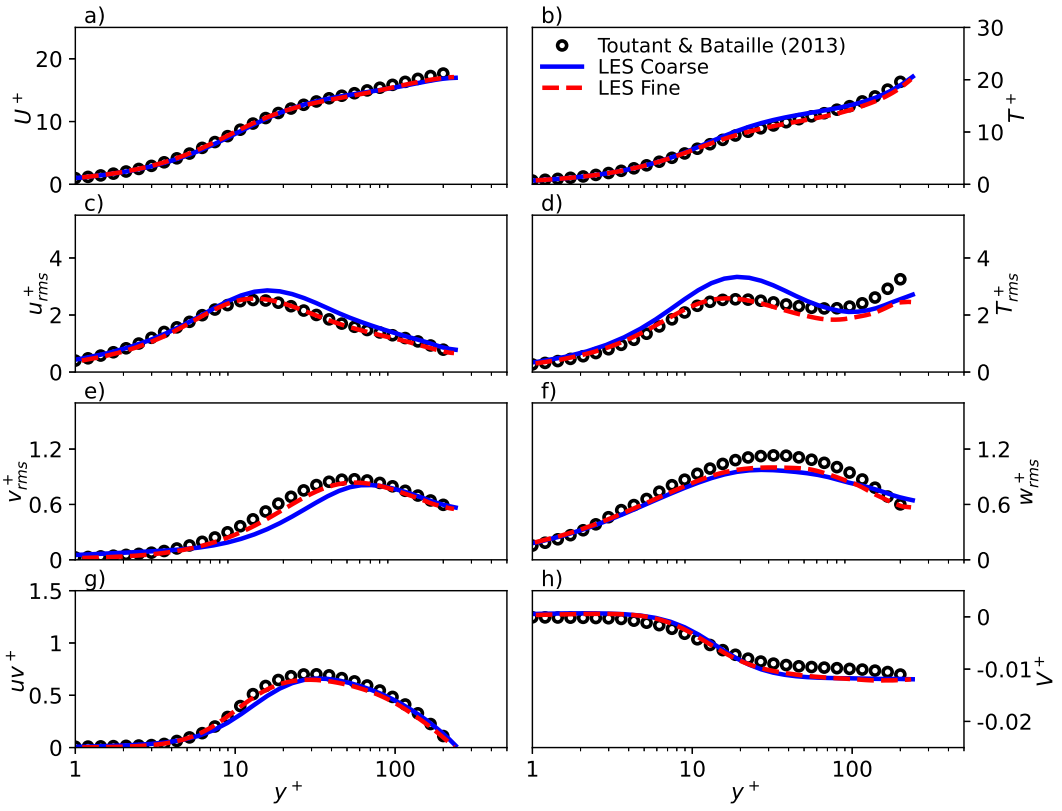

FIGURE 6.7: Anisothermal channel flow profiles on the *hot* side in wall units at a mean wall Reynolds number of $Re_\tau = 395$ with a temperature ratio of $Tr = 2.0$. The LES results are compared with the DNS data of Toutant and Bataille (2013). The figure presents the mean streamwise velocity (a), the mean temperature (b), the RMS of streamwise (c) velocity fluctuations, the RMS of the temperature fluctuations (d), the RMS of wall-normal (e) and spanwise (f) velocity fluctuations, the cross-correlation of streamwise and wall-normal velocity fluctuations (g), and the mean wall-normal velocity (h).

hot side in Fig. 6.7, the correlation with the reference data is substantially better when compared to the cold side, and show less dependency on the resolution. This difference is explained by the different wall Reynolds numbers on the two sides. As the mesh was constructed with the same refinement law along the wall-normal direction, the momentum and thermal boundary layer thicknesses are not as well resolved on the cold side as on the hot one.

Overall, the proposed low Mach number scheme performs well in both quasi-incompressible conditions of the channel flow, and conditions characterized by a density ratio of 2. While this falls short from the density ratios observed in combustion systems, it is a good indication of the capabilities of the low-dissipation finite element method. The scalar fields show larger discrepancies compared to DNS, than the velocity field. While scalar transport is identified as a possible area of improvement, this is left for future work.

6.3 Assessment of the tabulated chemistry model under laminar conditions

While the focus of the present work is on the LES of turbulent combustion systems, it is imperative to validate the chemistry model is isolated conditions. In this section laminar flames as simulated with adequate resolution using the tabulated chemistry models of chapter 3. Thus the thermo-chemical lookup procedure outlined in section 5.4.4 is followed without the prior FPDF integration of the properties.

6.3.1 Validation with premixed free flame

The premixed freely propagating planar flame configuration of section 3.1.1 is simulated using the low-dissipation scheme of the present work with tabulated chemistry to assess the performance of the approach. This case mainly tests the correct implementation of the tabulated chemistry method in Alya. Nevertheless other numerical effects also impact the results, such as the numerical diffusion introduced by the scalar stabilization scheme, or the ability of the fractional step algorithm to conserve mass in flows with high density variations.

The thermo-chemical table is based on the same premixed flamelet configuration, which is to be simulated. In principle it would be sufficient to tabulate a single premixed flamelet at the given equivalence ratio, which corresponds to the case exactly. However, for the sake of generality a two-dimensional table is applied here, parameterized by mixture fraction Z and progress variable Y_c. Both control variables are discretized by 101 point, applying a uniform discretization in scaled progress variable, and a discretization refined around stoichiometry in mixture fraction. The latter has a step growth rate of $r = 1.05$ as illustrated in Fig. 3.28. The thermo-chemical states contained in the table are presented in Fig. 3.34a-b. Note, that the GRI3.0 (Smith et al., 2011) chemical mechanism is used, and the flamelets are computed with the unity Lewis number assumption, which is also used in the tabulated chemistry simulation.

As detailed in section 5.4.4, the present tabulated chemistry strategy requires the transport of enthalpy, even in adiabatic cases. Thus the solved governing equations are: Eq. (2.54), Eq. (2.55), Eq. (2.81), Eq. (2.117), and Eq. (2.120), here repeated for the sake of completeness:

$$\partial_t \rho + \nabla \cdot (\rho \mathbf{u}) = 0, \tag{6.67}$$

$$\partial_t (\rho \mathbf{u}) + \nabla \cdot (\rho \mathbf{u} \otimes \mathbf{u}) + \nabla p - \nabla \cdot \boldsymbol{\tau}(\mathbf{u}) = 0, \tag{6.68}$$

$$\partial_t (\rho h) + \nabla \cdot (\rho h \mathbf{u}) - \nabla \cdot (\rho \mathcal{D}_t \nabla h) = 0, \tag{6.69}$$

$$\partial_t (\rho Z) + \nabla \cdot (\rho Z \mathbf{u}) - \nabla \cdot \rho \mathcal{D}_t \nabla Z = 0, \tag{6.70}$$

$$\partial_t (\rho Y_c) + \nabla \cdot (\rho Y_c \mathbf{u}) - \nabla \cdot \rho \mathcal{D}_t \nabla Y_c = \dot{\omega}_{Y_c}, \tag{6.71}$$

where the unity Lewis number assumption is used, and the evaporative source terms and body forces are zero. This case corresponds to an open system, thus the thermodynamic pressure is constant 101325 Pa.

The simulation domain is composed of a single row of quadrilateral elements, since the Navier-Stokes solver is implemented for domains of at least two dimensions. The edge size of the elements is determined in function of the case, such that $\Delta_x = \Delta_y = 0.1\delta_{diff}$, i.e.: the grid size is one tenth of the diffusive flame thickness. For instance at stoichiometry $\Delta_x = \Delta_y = 7.8$ μm. (See Tab. 5.5.) The domain covers a large range, to avoid interactions with the boundaries: $x \in [-200\delta_{diff}, 400\delta_{diff}]$ m,

thus it is composed of 6000 elements in each case. On the left of the domain, Dirichlet boundary conditions are prescribed for the velocity, temperature, mixture fraction, and progress variable. Here the flame speed of the Cantera simulation is given as the inlet velocity of the fresh mixture. A similar flame speed is expected to be recovered, however the exact match is not guaranteed, thus the case is inherently unsteady and the flame may move slightly within the domain. In such conditions the flame speed is calculated using the unburnt and burnt velocities and densities according to Eq. (3.3). The initial conditions are likewise given by the finite rate Cantera simulations translated in space, such that $T(x = 0, t = 0) = 1000$ K. The simulations are run for a physical time of at least τ_{diff}, which is sufficient for removing the effects of the initialization.

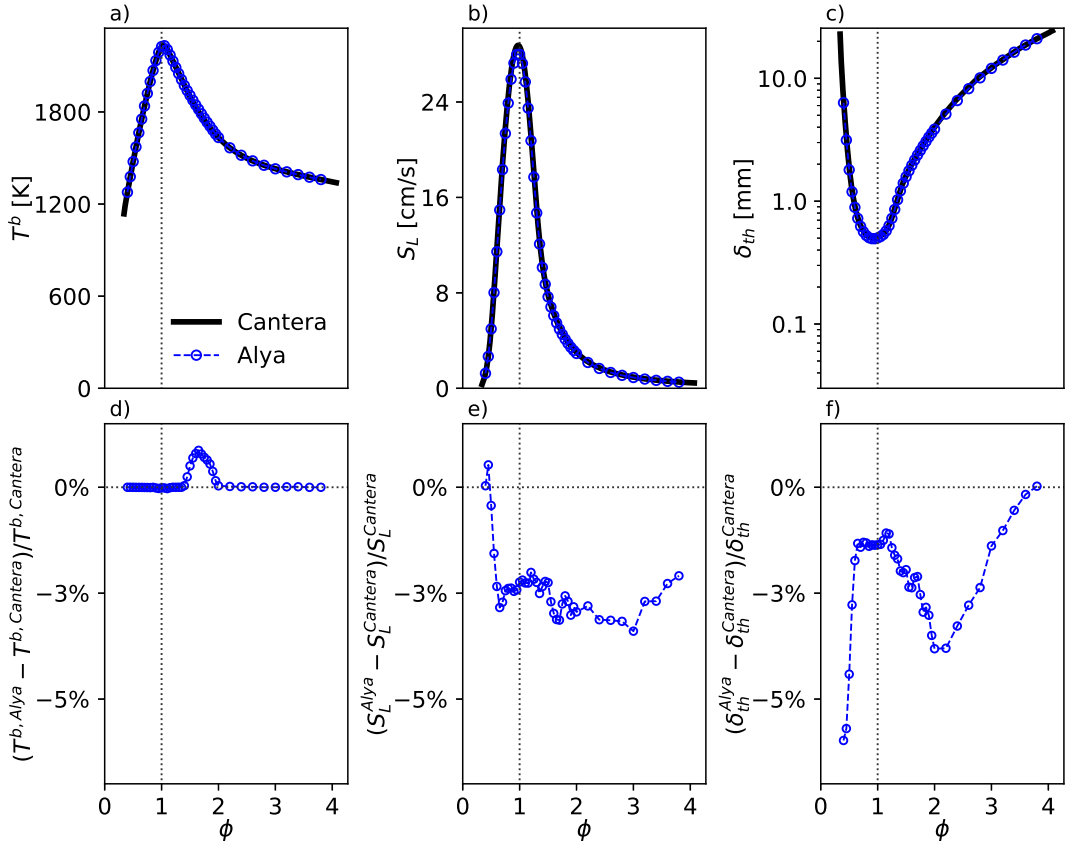

FIGURE 6.8: Properties of planar premixed free flames using tabulated chemistry in Alya compared with the finite rate chemistry calculations of Cantera. The top row of plots shows the adiabatic flame temperature, the flame speed calculated by Eq. (3.3), and the thermal flame thickness calculated by Eq. (3.4). The bottom row shows the relative error between the two methods.

Figure 6.8 presents the results of Alya simulations using the outlined setup at various equivalence ratios within the flammability limits. Using such a fine mesh, the results are hard to distinguish from the reference Cantera solutions. Hence, the differences are better studied using the relative errors between the tabulated chemistry and finite rate chemistry solutions. As Fig. 6.8d indicates, in a large part of the studied equivalence ratios the adiabatic flame temperature is reproduced perfectly. This is not a surprising outcome, as the progress variable has non-negative

source terms, thus $C = 1$ is attained at the outlet if the domain is sufficiently large. Notable discrepancies are found only in the $\phi \in [1.5, 2]$ interval where the $C = 1$ state differs from the adiabatic equilibrium. As discussed in section 3.2.3, this is the only region where premixed flamelets suffer the effects of non-injective progress variable definitions. The observed over-prediction of T^b is related to the minor non-injectivity introduced by the Y_c^{ref} definition of Ma (2016). Furthermore, applying the First Unique (FU) truncation strategy (see Fig. 3.25), the thermo-chemical table does not contain the outlet conditions of the premixed flamelets. Nevertheless, the difference is minor, and the error in adiabatic flame temperature is below 1%.

The flame speed is slightly under-predicted at most of the studied equivalence ratios as Fig. 6.8e shows. The discrepancy is generally around -3% except for the leanest studied flamelets ($\phi \in \{0.4, 0.45, 0.5, 0.55\}$). As the flame speed is an overall consequence of the balance of diffusive transport and chemical reactions, it is affected by all modeling decisions made here. Finally, Fig. 6.8f shows the error in the *thermal* flame thickness, which is around -1.5% near stoichiometry, and becomes larger further away. The relation of the diffusive and thermal flame thicknesses vary at different equivalence ratios, as Fig. 3.5 illustrates. Thus, the applied grid size corresponds to $\sim$ 70 elements in the flame near stoichiometry, while only $\sim$ 40 near the flammability limits. This may explain the deterioration of the thermal flame thickness. In conclusions, neither the flame speed nor the flame thickness error is alarming, although further studies are necessary to uncover the source of the discrepancy. Overall, these results confirm the correct implementation of the tabulated chemistry model, and its coupling with the Navier-Stokes solver.

6.3.2 Grid sensitivity of premixed free flame propagation

The simulations of section 6.3.1 show a good performance on a computational grid, that is sufficient to resolve even the fastest evolving radicals, as the grid size is set to $\Delta_x = 0.1\delta_{diff}$. Nevertheless, such fine grids are not necessarily required for the solution of laminar flame propagation using tabulated chemistry. Below, the same case is studied with varying grid size.

In this array of simulations the grid size is varied in function of the diffusive thickness at the given equivalence ratio. Seven different grid sizes are assessed at each inlet condition: $\Delta_x/\delta_{diff}\,(\phi) \in \{0.1, 0.2, 0.5, 1, 2, 5, 10\}$, with the finest grid corresponding to the one used in section 6.3.1. All other aspects of the simulations are identical to the cases of section 6.3.1.

The results of this sensitivity study are shown in Fig. 6.9 using the values of the adiabatic flame temperature, the flame speed, and the thermal flame thickness. The absolute value of the relative errors between the tabulated chemistry cases and the reference finite rate chemistry solution of Cantera are also displayed. The errors of adiabatic flame temperature are identical in all the meshes. As discussed above, this is a consequence of the Firs Unique (FU) truncation strategy, and it is related to the thermo-chemical states stored in the $C = 1$ layer of the table. Consequently this error is independent of the discretization.

The errors of flame speed and thermal thickness are displayed in Fig. 6.9e and f respectively. The finest mesh, produces the expected errors both in S_L and δ_{th}. With increasing the grid size to $0.2\delta_{diff}$ and to $0.5\delta_{diff}$, the error of both properties stay roughly constant. By further increasing the element size to $\Delta_x = \delta_{diff}$, the flame speed correlation is still preserved, while the thermal flame thickness is over-predicted by $\sim$ 10%. This case corresponds to only 4 to 7 elements in the thermal thickness of the flame. (See the inset plot in Fig. 3.5.) The discrepancy in δ_{th} is caused

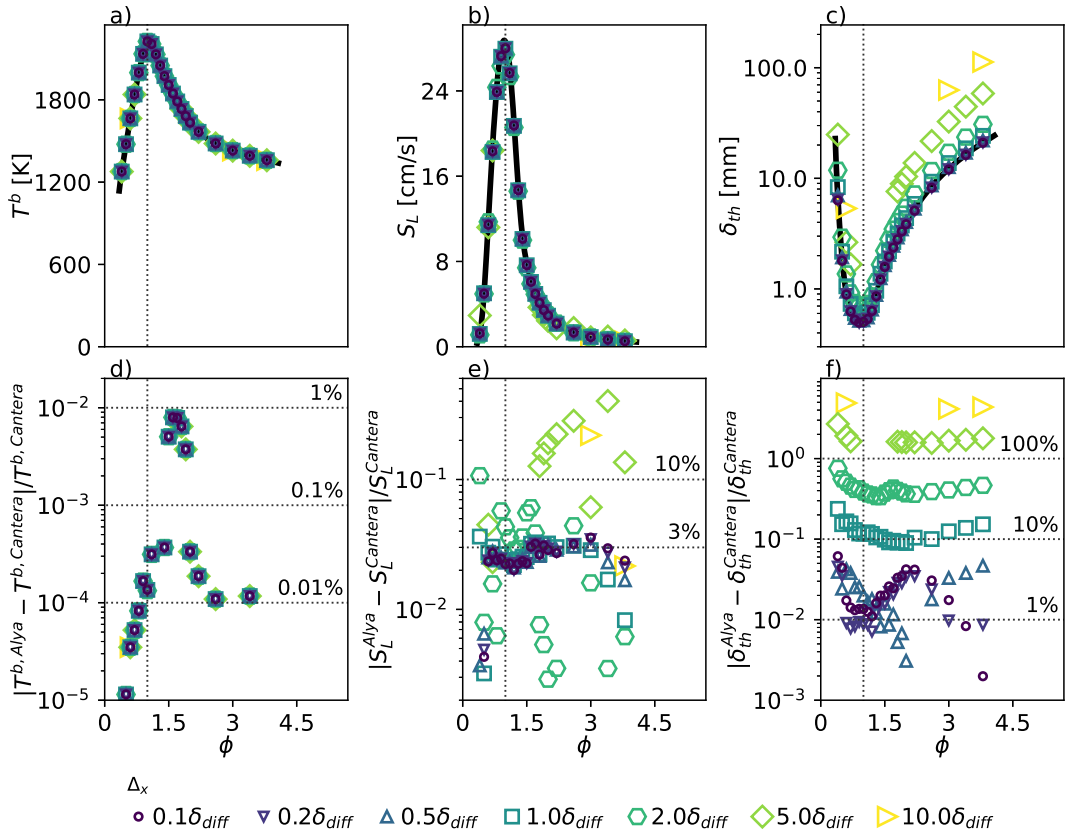

FIGURE 6.9: Mesh sensitivity of laminar premixed flame propagation using tabulated chemistry in Alya compared with the finite rate chemistry calculations of Cantera. The top row of plots shows the adiabatic flame temperature, the flame speed calculated by Eq. (3.3), and the thermal flame thickness calculated by Eq. (3.4). The bottom row shows the magnitude of the relative error between the two methods in logarithmic scale.

by the under-predicted temperature gradient on this rather coarse grid, it does not mean an actual thickening of the flame.

At $\Delta_x = \delta_{diff}$ the flame speed is still remarkably well reproduced, despite the slightly thicker flame front. This good performance is explained by the integration method of the finite element framework applied here. To integrate the terms of the governing equations over the domain, such as the chemical source term: $\dot{\omega}_{Y_c}$, a Gaussian quadrature method is applied. I.e.: the control variables: Z and Y_c, which are stored on the element nodes, are interpolated onto the integration points of the Gaussian quadrature using the shape functions of the elements. In the present case this means linear interpolation. Here these interpolated control variables are used for the lookup of $\dot{\omega}_{Y_c}(Z, Y_c)$, and subsequently the source term is integrated using the Gaussian quadrature method. The applied integration rule is exact up to the integration of 3$^{\text{rd}}$ order polynomials, thus if the source term would be a third order function of Y_c, then the integration would be exact irrespective of the mesh size. This is not the case, since $\dot{\omega}_{Y_c}$ is a more elaborate function, however, the source therm is integrated well on remarkably coarse meshes.

By further increasing the mesh size to $\Delta_x = 2\delta_{diff}$, the trends in the flame speed error become unpredictable. The flame speed may be reproduced better or worse

than on fine meshes, depending on the alignment of the Gaussian quadrature with the flame profile. However, the error rarely exceeds 10%. Meanwhile the over-prediction of flame thickness becomes consistently higher than 30%. This extreme case corresponds to only 2 or 3 elements within the thermal flame thickness. By further increasing the element size, the transition from unburnt to burnt conditions is within one element. In such cases the stability of the coupled PDE system is no longer guaranteed. At $\Delta_x = 5\delta_{diff}$ the cases near stoichiometry diverge, while at $\Delta_x = 10\delta_{diff}$ only three cases produce a converged solution accidentally. In both cases the flame speed is significantly over-predicted. Note, that on the lean side the errors are beyond the displayed range of Fig. 6.9e.

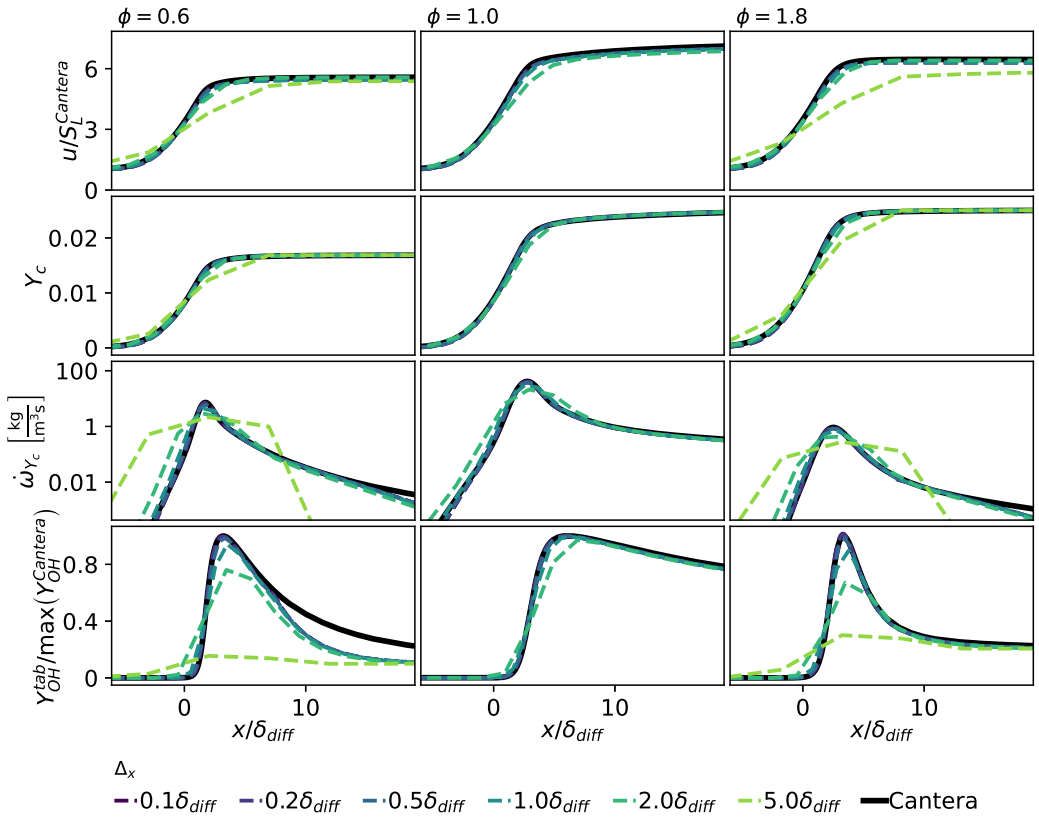

FIGURE 6.10: Laminar premixed flame profiles with different meshes using tabulated chemistry in Alya compared with the finite rate chemistry calculations of Cantera. The columns correspond to three different inlet mixtures of equivalence ratio: $\phi \in 0.6, 1.0, 1.8$, while the rows show the velocity, the progress variable, the source term of the progress variable, and the hydroxyl radical mass fraction retrieved from the table: $Y_{OH}^{tab} = \mathcal{F}(Z, Y_c)$.

The deterioration of the simulated profiles with the coarsening of the grid is further studied in Fig. 6.10 by comparing the profiles of velocity, progress variable, progress variable source term, any hydroxyl radical mass fraction along the flame. Note, that the latter two quantities are retrieved from the table on the Gaussian integration points, but the displayed quantities are a nodal projection of these fields. Consequently, the nodal values are not necessarily in the manifold. In the stoichiometric case (middle column) converged solutions are possible for $\Delta_x \in \{0.1\delta_{diff}, 0.2\delta_{diff}, 0.5\delta_{diff}, \delta_{diff}, 2\delta_{diff}\}$ only. Up to $\Delta_x = \delta_{diff}$ the profiles follow closely the

reference finite-rate solution. Deviations are only observed with an element size of $2\delta_{diff}$. In this case the flame is discretized by only three elements, yet the flame propagation is recovered adequately along with all the studied quantities.

Meanwhile in the lean and rich examples of Fig. 6.10 convergence is possible even for $\Delta_x = 5\delta_{diff}$. The finer grids perform well under these conditions similar to the stoichiometric case. Discrepancies are observed in $\dot{\omega}_{Y_c}$ and Y_{OH} even at $\Delta_x = \delta_{diff}$, however, this is a consequence of the aforementioned nodal projection. Interestingly, the coarsest mesh is also capable of capturing the flame propagation to some extent. Although, the hydroxyl radical profile is severely under-predicted. Note, that at $\phi = 0.6$ there is a discrepancy in the Y_{OH} profile associated to the tabulation. In the post-flame region the progress variable becomes constant, and cannot parameterize this radical well.

Species retrieval strategies

As discussed above, species mass fractions may be retrieved from the thermo-chemical tables for post-processing. In this work, two other methods are assessed for obtaining species mass fractions both involving the transport of an additional scalar. In the first method the source term of the species is tabulated, and the species mass fraction is obtained by solving:

$$\partial_t \left(\rho Y_k\right) + \nabla \cdot \left(\rho Y_k \mathbf{u}\right) - \nabla \cdot \left(\rho \mathcal{D}_t \nabla Y_k\right) = \dot{\omega}_k^{tab}, \tag{6.72}$$

where $\dot{\omega}_k^{tab}$ is the tabulated source term, retrieved the same way as the source term of the progress variable. In the second method following Ihme and Pitsch (2008a), the source term is split into production and consumption terms, and the governing equation of the species is formulated as:

$$\partial_t \left(\rho Y_k\right) + \nabla \cdot \left(\rho Y_k \mathbf{u}\right) - \nabla \cdot \left(\rho \mathcal{D}_t \nabla Y_k\right) = \dot{\omega}_k^{+,tab} + \left(\frac{\dot{\omega}_k^-}{Y_k}\right)^{tab} Y_k, \tag{6.73}$$

where the production term: $\dot{\omega}_k^{+,tab}$ is tabulated directly, while the consumption term is tabulated in the form: $\left(\frac{\dot{\omega}_k^-}{Y_k}\right)^{tab}$ thus it has to be multiplied by the resolved unknown to retrieve the consumption rate. This latter method naturally avoids numerical undershoots related to the reactive terms, as consumption is only possible Y_k is non-zero.

While such a method is primarily applied for pollutant transport as in the work of Ihme and Pitsch (2008a), here it is applied for the transport of the hydroxyl radical, to test the numerical performance of these approaches. The simulation results are compared in Fig. 6.11, where Y_{OH}^{tab} is retrieved directly from the table, Y_{OH}^{transp} is transported with a single tabulated source term according to Eq. (6.72), and $Y_{OH}^{transp\pm}$ is transported with the split production and consumption terms according to Eq. (6.73). The first row of plots is identical to the results presented in Fig. 6.10, repeated here for the sake of comparison.

The direct lookup of the OH mass fraction already captures well most of the cases, except at $\phi = 0.6$, where the table cannot characterize the near-equilibrium behavior. Meanwhile, solving for Y_{OH} with a single tabulated source term is characterized by the highest errors among all three methods. This method appears satisfactory only in the case of fine meshes, and it is characterized by large errors associated to the non-unique behavior at $\phi = 0.6$, where even the $\Delta_x = 0.1\delta_{diff}$ mesh deviates

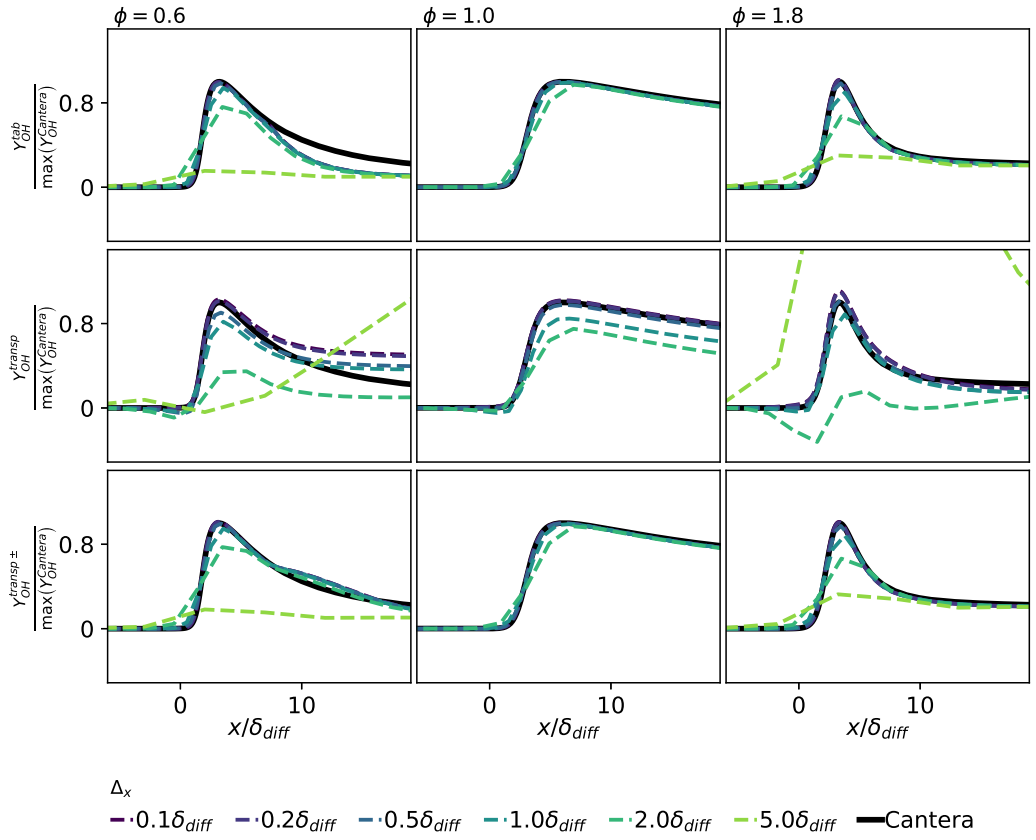

FIGURE 6.11: Hydroxyl radical profiles in laminar premixed flames with different meshes and retrieval strategies using tabulated chemistry in Alya compared with the finite rate chemistry calculations of Cantera. The columns correspond to three different inlet mixtures of equivalence ratio: $\phi \in 0.6, 1.0, 1.8$, while the rows show the direct lookup value: Y_{OH}^{tab}, the transported value: Y_{OH}^{transp} with a single tabulated source term, and the transported value of $Y_{OH}^{transp\pm}$ with tabulated production and consumption rates following Ihme and Pitsch (2008a).

significantly from the finite-rate solution. As the mesh is coarsened, undershoots appear on the unburnt side and the correlation diminishes quickly. Finally, solving for OH with the split source terms gives the best results, showing a slight improvement compared to the direct tabulation of the radical. In most instances Y_{OH}^{tab} and $Y_{OH}^{transp\pm}$ are virtually identical. An exception is formed where the tabulated mass fraction cannot reproduce the profile at $\phi = 0.6$. Here, $Y_{OH}^{transp\pm}$ shows a smoother transition towards the outlet value, thus it approximates the finite-rate chemistry solution better.

In the source term splitting strategy of Ihme and Pitsch (2008a) the final outlet value of the transported species is solely determined by the production and consumption terms at the $C = 1$ point of the table, since the right hand side of Eq. (6.73)

becomes zero precisely at:

$$Y_{k,out}^{transp\pm} = -\dot{\omega}_{k,C=1}^{+,tab} \Big/ \left(\frac{\dot{\omega}_k^-}{Y_k} \right)_{C=1}^{tab}. \tag{6.74}$$

In fact, if the species mass fraction deviates from this equilibrium value when $C = 1$ is reached already, then it is driven towards $Y_{k,out}^{transp\pm}$, with a time scale of:

$$\tau_k = \frac{\rho_{C=1}}{\left(\frac{\dot{\omega}_k^-}{Y_k} \right)_{C=1}^{tab}}. \tag{6.75}$$

This further explains the behavior of the $\phi = 0.6$ flame in Fig. 6.11, as in the case of Y_{OH}^{tab} the relaxation to the outlet value is driven by the reactive term of Y_c, while in the case of $Y_{OH}^{transp\pm}$ an additional delay is introduced by τ_{OH}.

Overall, as the present assessment shows, the tabulated chemistry method can handle remarkably coarse grids, which would be unable to correctly represent the flame propagation in finite-rate chemistry simulations. An element size of $\Delta_x = \delta_{diff}$ can be considered adequate for the study of laminar flame propagation, while even the case of $\Delta_x = 2\delta_{diff}$ performs satisfactorily with notable but controlled errors. This is partly possible due to the applied Gaussian quadrature integration method.

6.3.3 Effect of different manifolds on premixed flame propagation

Practical combustion systems are typically partially premixed, in which case the flame propagates in a stratified mixture. Under such conditions, it is *a priori* unclear whether a manifold of premixed flamelets or one of diffusion flamelets shall be applied. In any case, it is of interest to assess the performance of diffusion flamelet tables under perfectly premixed conditions. In this section, the premixed laminar flame propagation case of section 6.3.1 is repeated with the different tabulation strategies.

Figure 6.12 shows the outlet temperature and the flame velocity using the different tabulated chemistry models applied in this work. The tables correspond to the ones analyzed in section 3.4.1: one using premixed flamelets, which is extensively discussed in the preceding sections, and four different strategies involving counterflow diffusion flamelets. As Fig. 3.34 illustrates, all the tables show different behavior in terms of the progress variable source term, which is aligned with the findings of the analysis presented below.

The final outlet temperature only depends on the $C = 1$ states in the tables, thus the manifolds of diffusion flamelets all produce the same outlet conditions, since at least a part of the stable branch is included in all of the tested cases. The difference from the Cantera solutions in Fig. 6.12c indicates, that the equilibrium conditions are only included in a very limited part of these manifolds at lean conditions. Near stoichiometry the temperature is lower than adiabatic, since the last stable flamelet at a strain rate of $a = 1/\mathrm{s}$ is still notably different from equilibrium. (See Fig. 3.18.) Meanwhile on the rich side, the outlet temperature is significantly higher than equilibrium. While this is also partly related to the distance between the lowest strain flamelet and equilibrium, it is also affected by the First Unique (FU) truncation strategy, as some of the lowest strain flamelets are not included on the rich side of the manifold. (See Fig. 3.26.)

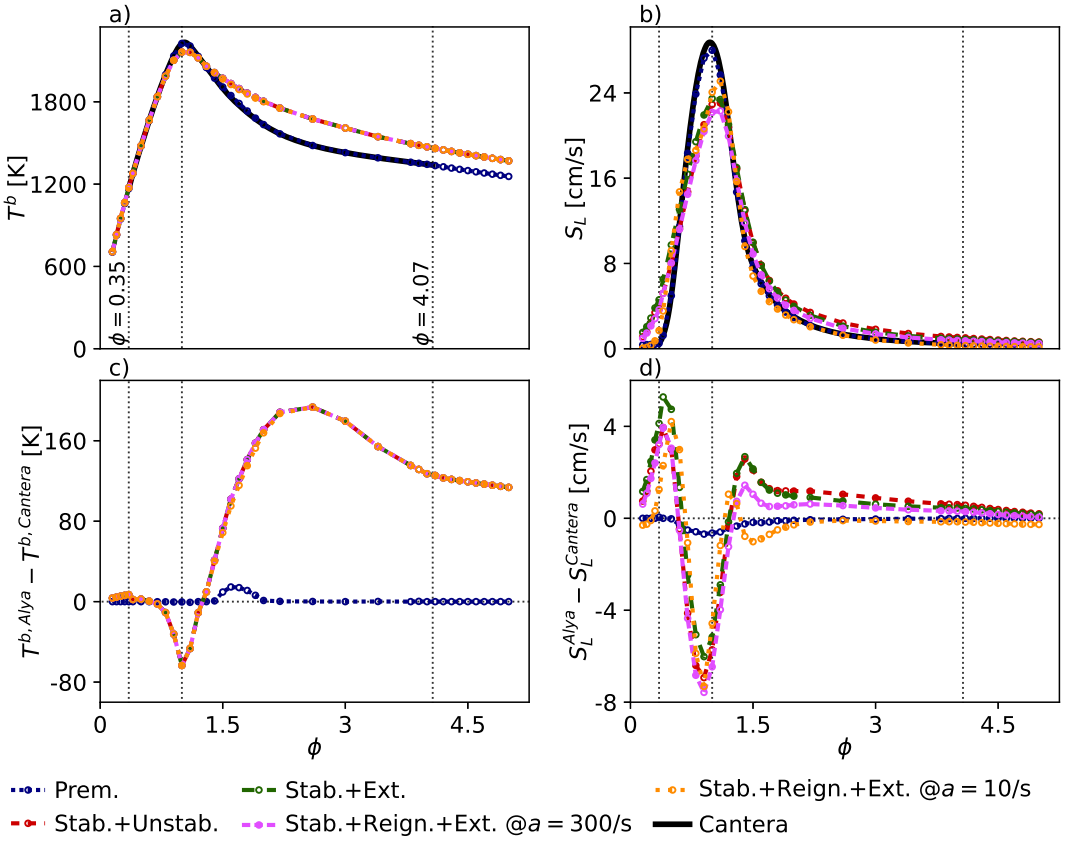

FIGURE 6.12: Effect of different manifolds on laminar premixed flame propagation using tabulated chemistry in Alya compared with the finite rate chemistry calculations of Cantera. The top row of plots shows the adiabatic flame temperature, and the flame speed calculated by Eq. (3.3). The bottom row shows the absolute error between the tabulated chemistry and finite-rate calculations. (Outside the flammability limits the premixed flamelet based manifold is used as reference.)

The flame speed and its difference from the finite rate chemistry solution are illustrated in Fig. 6.12b and d respectively. The discrepancies of the premixed flamelet manifold are discussed above in section 6.3.1, and repeated here for completeness. In general, the tables based on diffusion flamelets are characterized by lower propagation speed near stoichiometry, and relatively higher speed at leaner and richer conditions. This is well aligned with the behavior of the progress variable source term on the $Z - Y_c$ plane. In particular, on the lean side the "Stab.+Ext." strategy produces the highest flame speed, with a peak difference of ~ 5 cm/s between this manifold and the actual flame speed. The "Stab.+Unstab." and "Stab.+Reign.+Ext. @$a = 300$/s" manifolds behave very similarly on the lean side, with a peak difference of ~ 4 cm/s in flame speed. In these three cases the peak difference is located near the lean flammability limit and the flame speed remains significant down to the leanest assessed condition at $\phi = 0.15$. Meanwhile the manifold of "Stab.+Reign.+Ext. @$a = 10$/s" also shows significant differences compared to the finite rate flame speed but only within the flammability limit, since $\dot{\omega}_{Y_c}$ drops sharply to zero outside the lean flammability limit.

Near stoichiometry all diffusion flamelet based manifolds behave quite similarly, showing the most severe under-prediction of the flame speed of $\sim$ 6..8 cm/s at $\phi = 0.8$. The "Stab.+Ext." manifold is characterized by the lowest discrepancy here, since it contains the highest source terms, yet $\dot{\omega}_{Y_c}$ is not high enough to predict the premixed flame propagation. This negative peak is followed by another peak of S_L over-prediction on the rich side. Here "Stab.+Reign.+Ext. @$a = 10$/s" case stands out just as before, since it is characterized bt the lowest peak of difference, and at even richer conditions it again under-predicts the flame speed. This effect is related to the source term distribution of this manifold, as $\dot{\omega}_{Y_c}$ is highly concentrated near stoichiometry. Meanwhile, all the other diffusion flamelet based manifolds constantly over-predict the flame speed under these richer conditions. Note, that on the rich side a certain similarity is observed between the "Stab.+Unstab." and "Stab.+Ext." cases which is different from the lean side. These two manifolds produce the highest over-predictions of S_L on the rich side with a peak discrepancy of $\sim$ 3 cm/s, while the flame speeds in the case of "Stab.+Reign.+Ext. @$a = 300$/s" are somewhat lower.

Overall, the non-premixed manifolds consistently under-predict the flame speed near stoichiometry, while they produce over-predictions elsewhere. This may have sever consequences on the simulation results in complex cases, for instance by not capturing properly the stabilization of largely stoichiometric flames, or by predicting flame propagation in cases of overly lean mixtures.

6.3.4 Effect of sub-grid models on premixed flame propagation

The usage of β-functions to model the filter probability density function of the control variables is a major assumption of the present modeling strategy outlined in section 5.4.3. While other options are not explored in this work, it is of interest to explore the effect of the FPDF integrated tables on flame propagation. Here the laminar premixed flame configuration of section 6.3.1 is used for this purpose. The tables are replaced with their FPDF integrated counterparts, and the transported Z and Y_c are used as the $\widetilde{Z}$ and $\widetilde{Y}_c$ control variables of the integrated table. The joint FPDF is either $\widetilde{P}_{ZC} = \widetilde{P}_Z^{\beta}\widetilde{P}_C^{\delta}$ or $\widetilde{P}_{ZC} = \widetilde{P}_Z^{\delta}\widetilde{P}_C^{\beta}$, parametrized by a constant scaled variance: ζ_Z or ζ_C respectively. The manifold of premixed flamelets is used in this analysis. Note, that this configuration is non-physical, as the sub-grid variances cannot exist in laminar conditions on a well resolved grid. Furthermore, the scaled variance is likely to be non-constant across the flame. Nevertheless, the present analysis provides insight to the effect of the applied turbulence/chemistry interaction models.

Effect of mixture fraction variance

First the case of $\widetilde{P}_{ZC} = \widetilde{P}_Z^{\beta}\widetilde{P}_C^{\delta}$ is assessed in Fig. 6.13. The outlet temperature and the flame speed is calculated at different equivalence ratios and scaled mixture fraction variances. Figure 6.13a shows the outlet temperature of the system, while the other three plots show the flame speed, the relative difference of the flame speed and the $\zeta_Z = 0$ case, and the absolute difference of the flame speed and the finite rate solution. In general the increasing scaled variance decreases the outlet temperature, except in a small region around $\phi = 2.0$, where the adiabatic flame temperature is concave in Z, and small amounts of variance ($\zeta_Z \leq 0.05$) may cause outlet temperatures higher than the adiabatic one. A similar smoothing behavior is observed in the case of the flame speed in Fig. 6.13b, however, S_L does not approach zero as the variance increases. For instance a stoichiometric flame with $\zeta_Z = 0.8$ still propagates

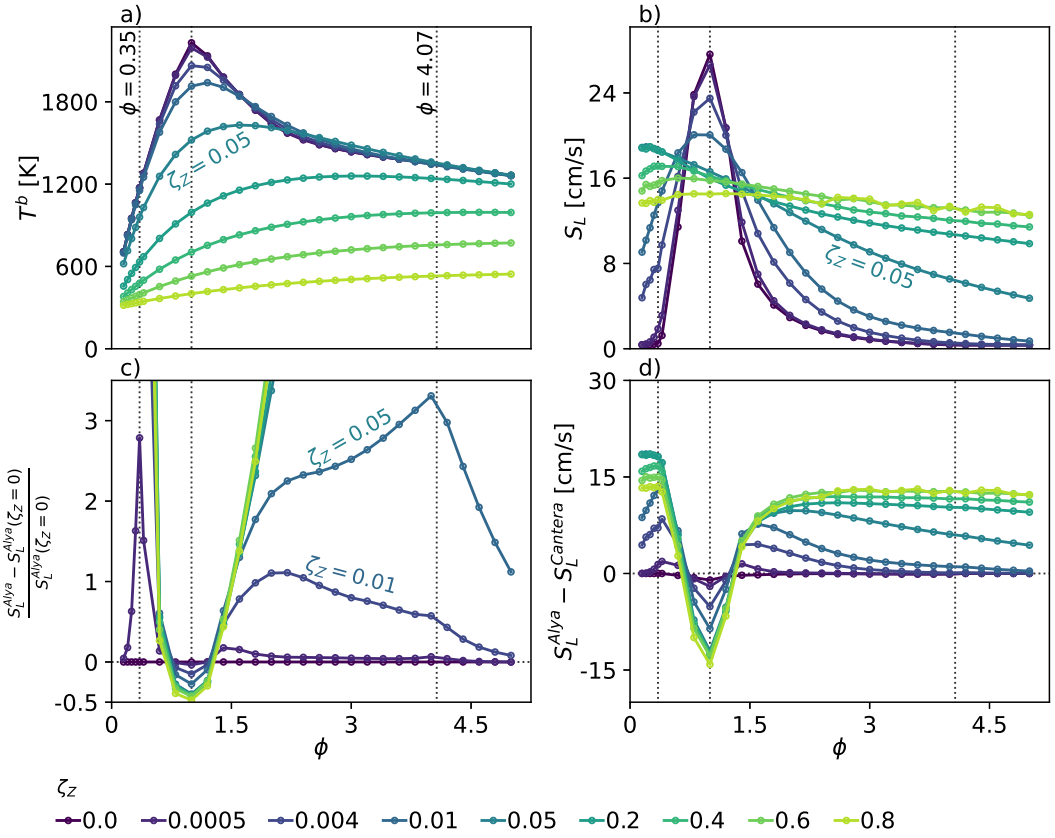

FIGURE 6.13: Effect of sub-grid mixture fraction variance on laminar premixed flame propagation using tabulated chemistry in Alya. The scaled sub-grid variance: ζ_Z is forced to take the indicated value. The figure shows the outlet temperature of the system (a), the flame speed (b) calculated by Eq. (3.3), the relative difference of the flame speed compared to the zero variance case (c), and the absolute difference of flame speed compared to the finite rate calculations of Cantera (d). (Outside the flammability limits the zero variance case is used as reference.)

with more than half of the real flame speed as Fig. 6.13c confirms. This is possible, because while the source term diminishes with increasing ζ_Z, the outlet value of the progress variable also diminishes, thus the reactive source only has to balance a smaller diffusive transport. As the mixture fraction variance limits the amount of progress variable, that can be produced in a propagating flame front, it may lead to flame extinction only if the variance varies in space. This is the case in realistic applications, where mixture fraction variance is produced in regions of high ∇Z.

The cases of $(\zeta_Z \leq 0.05)$ show significant variations compared to the zero variance limit, indicating, that the solution is highly susceptible to small mixture fraction variances. The only studied case, where the effect seems to be negligible is $\zeta_Z = 0.0005$. However, even this case becomes significantly different at lean conditions, where it extends the range of non-zero flame speeds as Fig. 6.13c shows. Such sensitivity highlights the importance of the ζ_Z discretization, which should be refined for small variances.

Effect of progress variable variance

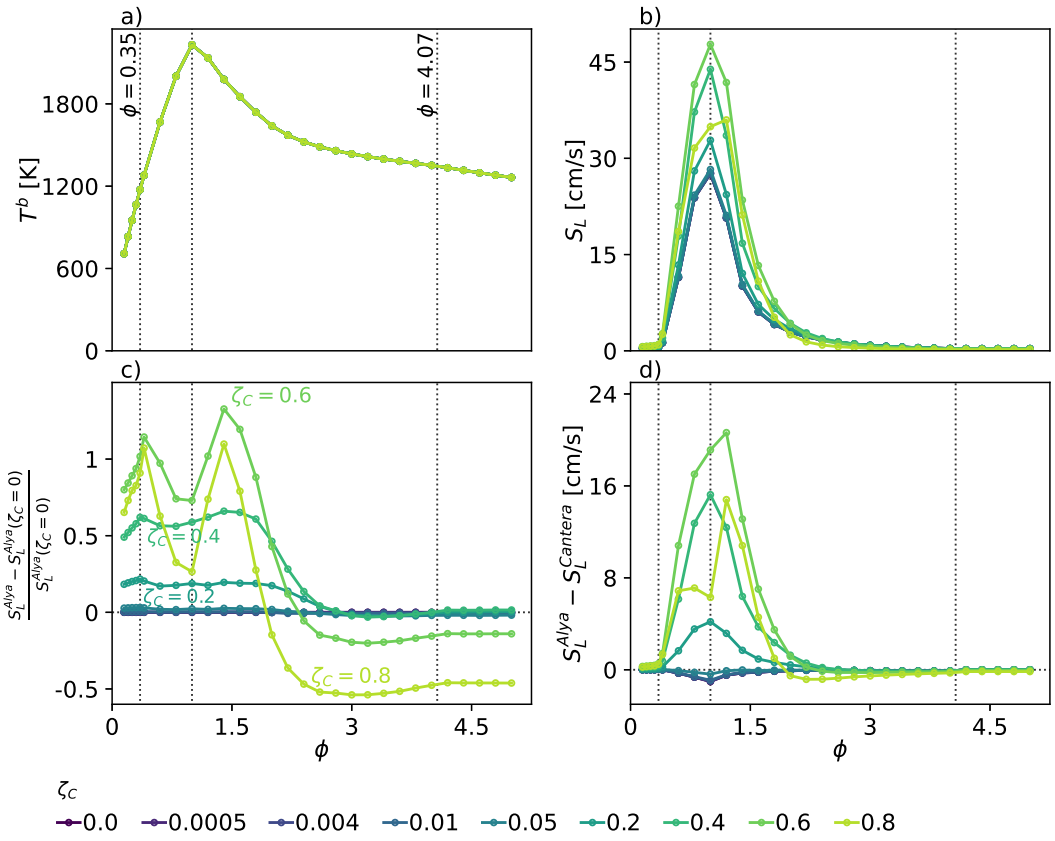

FIGURE 6.14: Effect of sub-grid progress variable variance on laminar premixed flame propagation using tabulated chemistry in Alya. The scaled sub-grid variance: ζ_C is forced to take the indicated value. The figure shows the outlet temperature of the system (a), the flame speed (b) calculated by Eq. (3.3), the relative difference of the flame speed compared to the zero variance case (c), and the absolute difference of flame speed compared to the finite rate calculations of Cantera (d). (Outside the flammability limits the zero variance case is used as reference.)

Next the case of $\widetilde{P}_{ZC} = \widetilde{P}_Z^{\delta}\widetilde{P}_C^{\beta}$ is assessed in Fig. 6.14 showing the same quantities as above. The 1D laminar flames are calculated assuming a constant scaled progress variable variance. The variance does not change the outlet condition, as the $C = 1$ state of the thermo-chemical manifolds is unaffected by the β-FPDF integration. In this case small variances have negligible effect, as only the $\zeta_C \geq 0.2$ cases show visible differences in S_L. The flame speed is affected differently depending on the equivalence ratio. This effect is best illustrated in Fig. 6.14c, by the relative change of flame speed between the given ζ_C and the zero variance case. On the leaner side of the assessed range, all ζ_C values increase the flame speed, while on the rich side a consistent decrease is observed. Note, that in the latter part the flame speed is already very low, but it may be reduced by 50% if the scaled variance reaches $\zeta_C = 0.8$. In the leaner part, the response of flame speed to the progress variable variance is not monotonous. The highest S_L is reached at $\zeta_C = 0.6$ where it is approximately doubled, but the further increase of the variance decreases the flame speed. This is

logical considering the trivial case of $\zeta_C = 1$, where S_L is zero, as the sub-grid state is an ensemble of fresh reactants and fully burnt gases, thus none of the filter volume is occupied by reacting intermediate states. Note the similarity of this assessment with the *a priori* study of Fiorina et al. (2010), where a comparable rise in the flame speed is predicted as an effect of the beta-FPDF, alas they used a more elaborate profile of ζ_C along the flame. Here, this change in flame speed is acknowledged and treated as a feature of the tabulated chemistry model.

Effect of sub-grid scalar transport

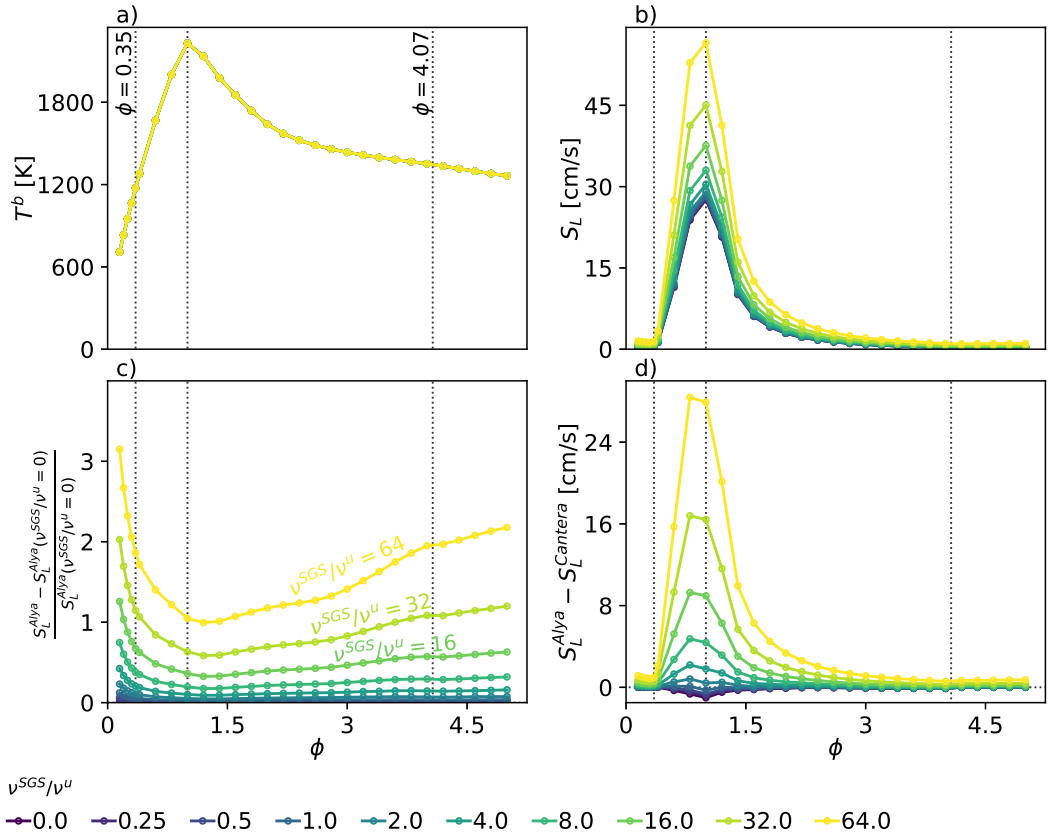

FIGURE 6.15: Effect of sub-grid diffusion on laminar premixed flame propagation using tabulated chemistry in Alya. The figure shows the outlet temperature of the system (a), the flame speed (b) calculated by Eq. (3.3), the relative difference of the flame speed compared to the zero sub-grid viscosity case (c), and the absolute difference of flame speed compared to the finite rate calculations of Cantera (d). (Outside the flammability limits the zero variance case is used as reference.)

The flame propagation is determined through the transport of control variables. While this is heavily affected by the presumed FPDF model through the source term and the properties, another significant effect is the sub-grid transport discussed in section 5.4.1. In practical LES simulations this is significant. The effect is studied by artificially increasing the diffusion terms in all governing equations of the 1D premixed flame problem, by mimicking the presence of a constant sub-grid viscosity. This parameter is defined proportionally to the kinematic viscosity of the unburnt

mixture, and the scalar equations consider a sub-grid Prandtl and Schmidt number of $Pr^{SGS} = Sc^{SGS} = 0.7$.

The characteristics of the premixed flame simulation with forced sub-grid transport are displayed in Fig. 6.15 using the same layout as above. This diffusive term cannot modify the equilibrium conditions, hence the outlet temperature stays constant irrespective of ν^{SGS}. The flame speed is affected uniformly across all equivalence ratios, showing an increase with increasing ν^{SGS}. As Fig. 6.15c demonstrates, in the studied range of sub-grid viscosities, this corresponds to doubling the propagation speed near stoichiometry. Meanwhile at conditions with lower flame temperature the effect is even more significant, as the relative importance of the constant ν^{SGS} increases compared to the temperature dependent molecular diffusion. Overall, the sub-grid transport may contribute significantly to the enhancement of flame speed.

6.3.5 Validation with counterflow diffusion flame

The other canonical flame configuration of this work: the counterflow diffusion flame of section 3.1.3 is also studied using tabulated chemistry in Alya. The case provides further reassurance on the implementation of the tabulation method and the low-dissipation scheme. The details of the tabulated chemistry method and the governing equations are the same as in section 6.3.1 in case of the premixed free flame. I.e.: the database is parameterized by mixture fraction and progress variable, and governing equations are solved for these control variables and for the enthalpy. In the present validation case the only difference is in the flamelets which constitute the manifold. Stable and unstable counterflow diffusion flamelets of methane and air are used here, appended with the pure mixing solution, as this manifold contains the exact thermo-chemical states that the test case aims to recreate. In fact, the tabulated chemistry simulations should only access the part of the manifold populated by the stable solutions, which is approximately the $C \in [0.8, 1]$ interval. (See Fig. 3.27.) Thus, using this manifold ("Stab.+Unstab.") is expected to produce identical results other manifolds which incorporate the stable branch.

Computational domain and grid

The computational domain is illustrated in Fig. 6.16. The problem is symmetric with respect to the y axis, and the solution on the symmetry line is equivalent to the Chem1D cases studied in section 3.1.3. The domain size is determined based on the studied strain rate to accommodate the changes in flame thickness. For this purpose the diffusive thickens is calculated as:

$$\delta_{diff} = \sqrt{\frac{2\mathcal{D}_{t,ox}}{a}} \tag{6.76}$$

which is a good measure of the flame scales, as appendix A illustrates. The selected domain is a $240\delta_{diff} \times 60\delta_{diff}$ rectangle, which is twice as large in the y direction as the domain used in the Chem1D calculations. The oxidizer and fuel inlets are situated on the bottom and the top edge of the domain centered in the x direction stretching from $x = -60\delta_{diff}$ to $x = 60\delta_{diff}$. The rest of these horizontal edges are modeled as slip walls, while the two vertical edges are outlets.

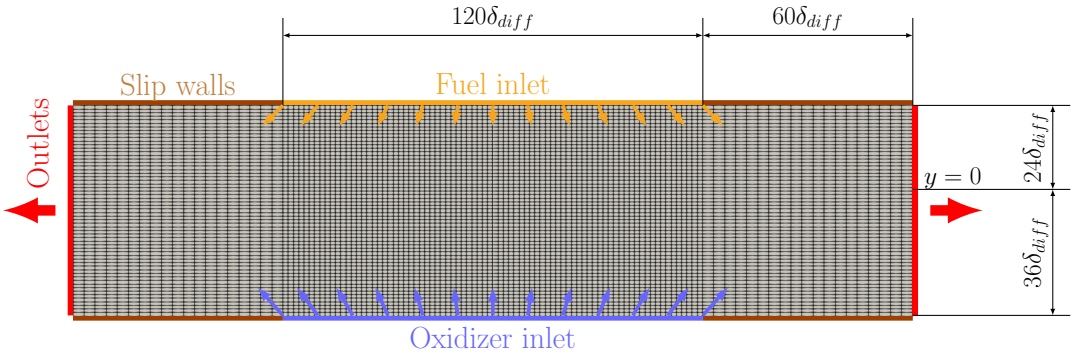

FIGURE 6.16: Computational domain and grid of counterflow diffusion flame simulations. For the sake of visibility, the grid displayed here is 10 times coarser than the actual grid.

The domain is discretized with equal element size in the vertical direction corresponding to one tenth of the diffusive thickness: $\Delta_y = 0.1\delta_{diff}$. A coarser non-uniform discretization is chosen in the horizontal direction, as the gradients are expected to be smoother in x. In the center of the domain an element size of $\Delta_x = 0.15\delta_{diff}$ is used in the $x \in [-60\delta_{diff}, 60\delta_{diff}]$ interval, while in the rest of the domain $\Delta_x = 0.3\delta_{diff}$ is applied. In total the grid is composed of 720000 quadrilateral elements.

Boundary conditions

The four horizontal wall segments are modeled as adiabatic non-permeable slip walls, using the boundary conditions:

$$\frac{\partial \xi_k}{\partial x} = 0, \qquad \frac{\partial u}{\partial x} = 0, \qquad \text{and} \qquad v = 0, \qquad \text{with } \xi_k \in \{Z, Y_c, h\}. \tag{6.77}$$

Meanwhile, on the outlets zero gradient boundary conditions are imposed for all unknowns. The two inlet conditions are critical for achieving a correspondence between the Chem1D simulations and the present 2D test case. The far-field flow has to be a purely strained potential flow. Furthermore, as shown in appendix A, the velocity at the oxidizer inlet has to be compensated for the effect of the thermal dilatation in the flame which creates an offset compared to the $v \propto -y$ behavior. (See Fig. A.3.) In the present cases, the flame-normal boundary velocity (v) is determined by extrapolating from the velocity field on the Chem1D simulation:

$$v_{ox} = v_{ox}^{Chem1D} - \left(y_{ox} - y_{ox}^{Chem1D}\right) a, \tag{6.78}$$

$$v_f = v_f^{Chem1D} - \left(y_f - y_f^{Chem1D}\right) \sqrt{\frac{\rho_{ox}}{\rho_f}} a, \tag{6.79}$$

where $y_{ox} = -36\delta_{diff}$ and $y_f = 24\delta_{diff}$ are the vertical location of the oxidizer and fuel inlets in Alya. Meanwhile, the velocity component tangential to the flame is calculated simply by using the strain rates:

$$u_{ox} = ax, \qquad \text{and} \qquad u_f = \sqrt{\frac{\rho_{ox}}{\rho_f}} ax. \tag{6.80}$$

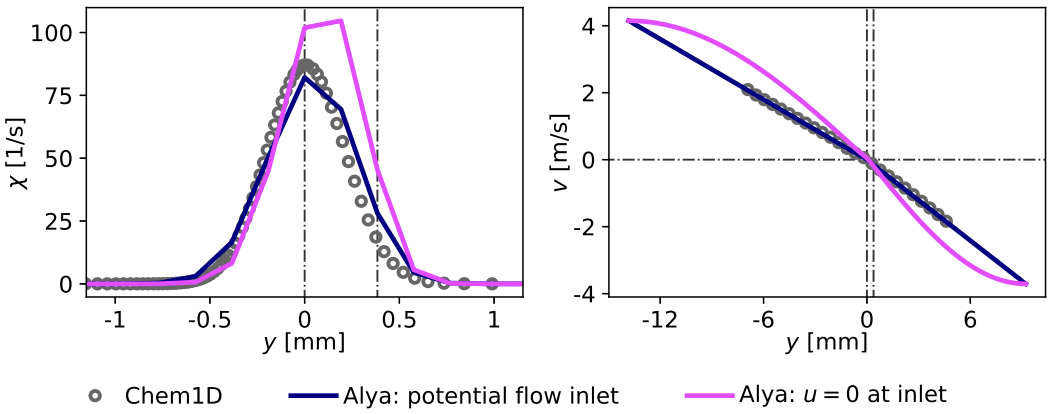

FIGURE 6.17: Cold mixing in counterflow configuration of air and methane using tabulated chemistry in Alya at a strain rate of $a = 300/\text{s}$. The profiles calculated with the potential flow inlet and the inlet with zero tangential velocity are compared with the finite rate chemistry solution of Chem1D (Somers, 1994).

The importance of imposing the tangential velocities of Eq. (6.80) is demonstrated in a case of cold mixing with a 5 times coarser mesh ($\Delta_y = 0.5\delta_{diff}$). Such a coarse mesh is adequate for capturing the velocity field, which is the focus of this example. Figure 6.17 shows these results at a strain rate of $a = 300/\text{s}$ comparing the Alya simulations with Chem1D (Somers, 1994). The left and right plots display the scalar dissipation rate, and the flame-normal velocity respectively. Two cases are assessed, one with the potential flow boundary conditions of Eq. (6.80) ("Alya: potential flow inlet"), and one with setting u_{ox} and u_f to zero and retaining only the flame-normal component ("Alya: $u = 0$ at inlet"). The former condition reproduces the velocity field well, and even the scalar dissipation rate is captured to some extent, despite the coarseness of the mesh. The latter condition has the same flame-normal velocity component on the inlets, however it takes a certain distance for the velocity to relax to a field resembling a pure straining flow. Consequently, the local strain rate in the mixing layer is significantly higher, and the sharper gradients result in a higher scalar dissipation rate.

Results

The outlined simulation strategy is used at various strain rates in stable reacting conditions. The unknown fields are initialized with the corresponding Chem1D solution. Figure 6.18 illustrates the solution in physical space. Note, that the present results are not shifted in physical space, their alignment with the Chem1D solution is purely a consequence of the well designed boundary conditions. The first row of plots show the velocity, which is heavily affected by the presence of the flame in the displayed region, inducing a local minimum and maximum in v. Both the location and magnitude of these local extrema are reproduced well. The subsequent three rows show the scalar fields of unscaled progress variable, its source term, and the tabulated mass fraction of the hydroxyl radical. Different discrepancies are revealed by these profiles. At $a = 1/\text{s}$ and $a = 10/\text{s}$ the manifold is deteriorated by the effects of non-injective progress variable behavior. In the former case this manifest in an overestimation of $\dot{\omega}_{Y_c}$ on the rich side (right) of the flame. Nevertheless the progress variable profile is reproduced well, as these source terms are fairly small.

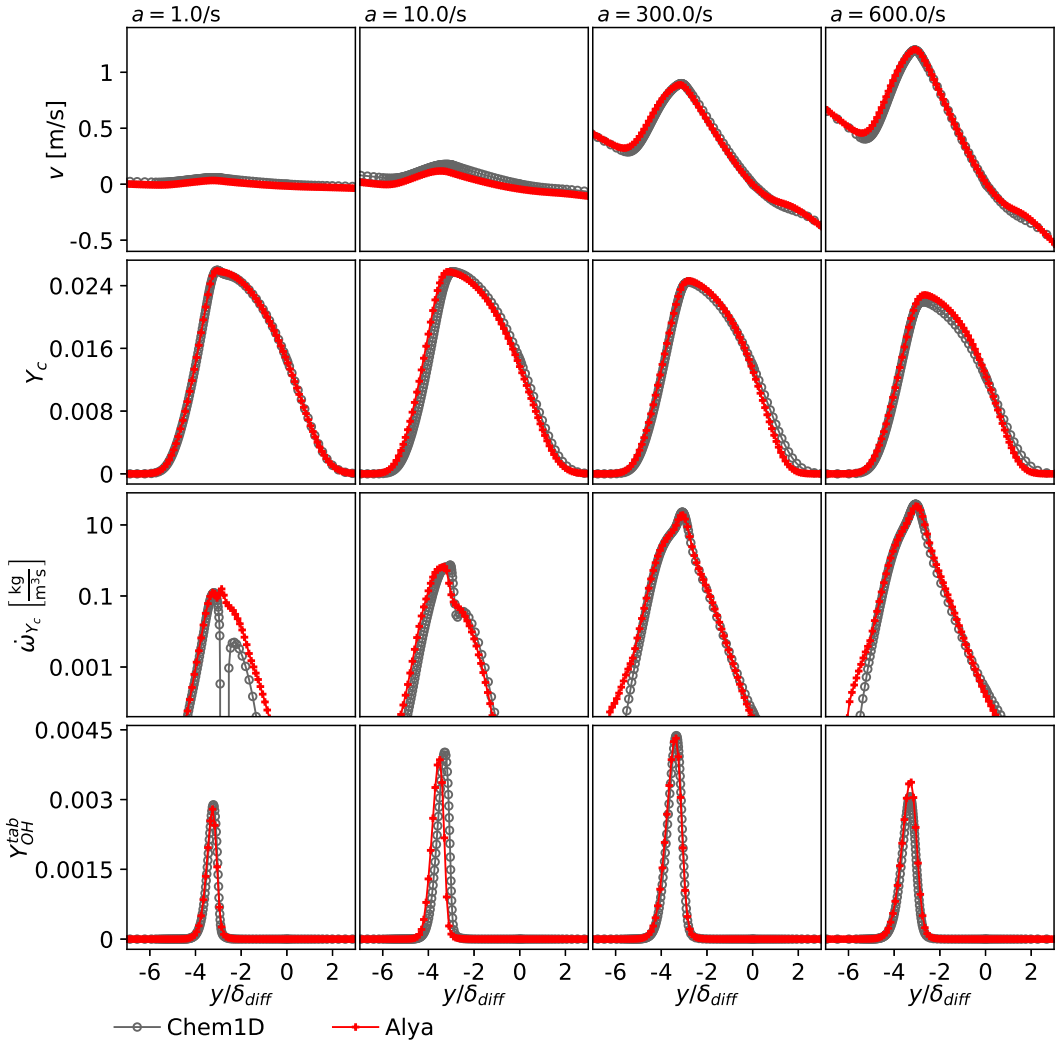

FIGURE 6.18: Stable burning solutions of methane/air flames in counterflow configuration using tabulated chemistry in Alya. The profiles of flame-normal velocity, progress variable, progress variable source term, and hydroxyl mass fraction are compared with the Chem1D (Somers, 1994) solution.

In the case of $a = 10/\text{s}$ the profiles are slightly shifted towards the oxidizer side (left), presumably also due to non-injective effects. At higher strain rates the results are generally better. In case of $a = 300/\text{s}$ the discrepancies are limited to a slight under-prediction of Y_c on the rich side, and negligible over-prediction of $\dot{\omega}_{Y_c}$ on the lean side. (Note the logarithmic scale.) By doubling the strain rate these discrepancies are still present, and additionally the peak progress variable and hydroxyl mass fraction are slightly over-predicted. Overall, the issues are similar to the ones observed in case of the premixed free flamelets, where small discrepancies arise due to numerical errors and the limitations of the manifold.

The performance of the tabulated chemistry method is further assessed in a more complete array of cases along the stable branch. The extinction point is identified as

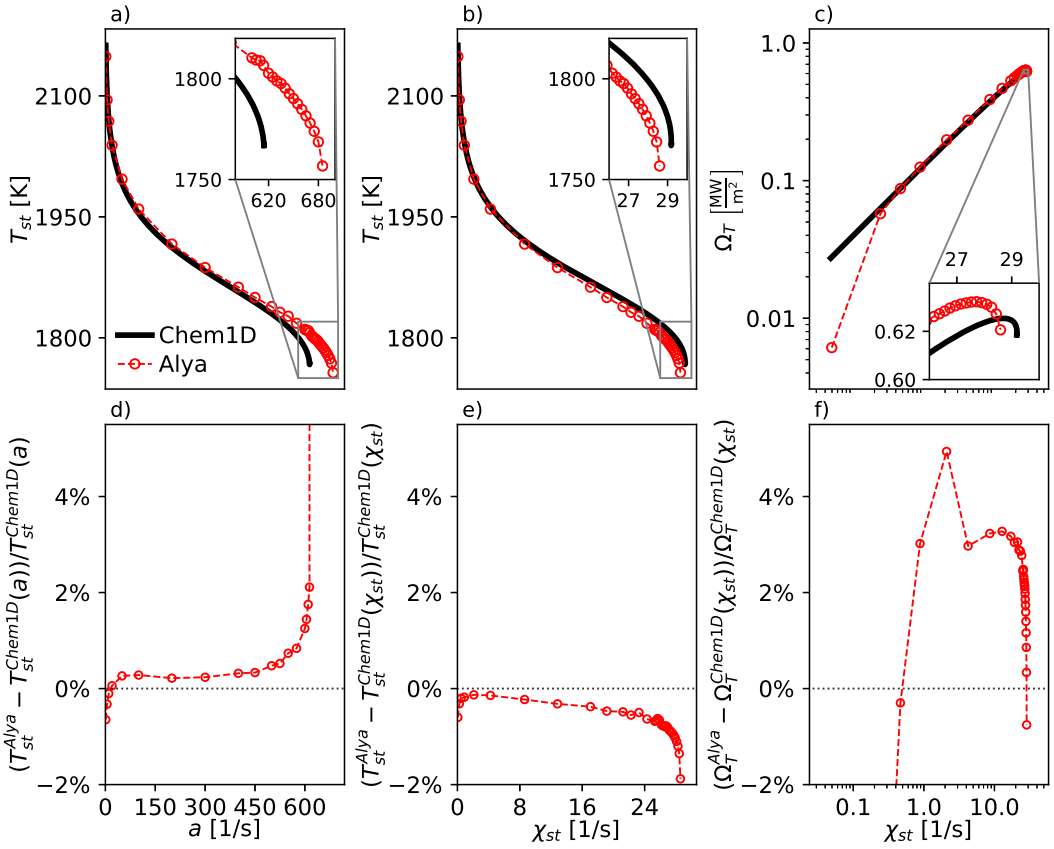

FIGURE 6.19: Properties of counterflow diffusion flames using tabulated chemistry in Alya compared with the finite rate chemistry calculations of Chem1D. The top row of plots shows the stoichiometric temperature as function of strain rate (a) and stoichiometric scalar dissipation rate (b), and the integral of heat release rate on the centerline (c) calculated by Eq. (3.21). The bottom row shows the relative error between the two methods.

$a^{ext}_{Alya} = 685/\text{s}$, which corresponds to a 11.5% over-prediction compared to the extinction point found using Chem1D at: $a^{ext}_{Chem1D} = 614.456/\text{s}$. Nevertheless, the stoichiometric scalar dissipation rate at the last reacting flame in Alya is: $\chi^{ext}_{st,Alya} = 28.593/\text{s}$, which is much closer to the finite rate value: $\chi^{ext}_{st,Chem1D} = 29.111/\text{s}$, corresponding to an under-prediction of -1.8%. Note, that the extinction point is found by simulating cases with $5/\text{s}$ increments in strain rate, and the next point ($a = 690/\text{s}$) undergoes extinction.

Such macroscopic properties of the counterflow diffusion flames are illustrated in Fig. 6.19, comparing them to the finite rate chemistry simulation of Chem1D. Figure 6.19a and b show the temperature of the stoichiometric mixture as function of strain rate and stoichiometric scalar dissipation rate. Meanwhile plots d and e correspond to the relative error, with taking the reference values of Chem1D at the same strain rate and the same stoichiometric scalar dissipation rate respectively. In most part of the stable branch the error in T_{st} is very low, well below 1%. Significant discrepancies arise only near the extinction point. In any case the error is related rather to the shift in a and χ_{st} than to the temperature differences. Figure 6.19c and f show

the integral of the tabulated heat release rate over the centerline, and its error compared to the Chem1D value calculated by Eq. (3.21). At the lowest studied strain rate ($a = 1/\mathrm{s}$) this quantity shows a significant error associated to the non-injective behavior of the manifold. The rest of the simulated cases follow the reference solution closely, and reproduce the approximate $\Omega_T \propto \sqrt{a} \propto \sqrt{\chi_{st}}$ trend discussed in section 3.1.4. The error is limited, but somewhat larger than in the case of T_{st}, as the integral heat release rate accumulates multiple effects of the manifold and the spatial distribution of the control variables.

6.3.6 Effect of different manifolds on counterflow diffusion flame

Similarly to section 6.3.3, it is of interest to assess the behavior of the counterflow diffusion flame configuration of section 6.3.5 simulated with a premixed flamelet based manifold. This is relevant in cases where the degree of fuel/oxidizer mixing before the flame is not certain, and it is *a priori* unknown which manifold is more suitable.

Figure 6.20 illustrates the difference between using a premixed flamelet based manifold ("Prem.") and one based on stable and unstable ("Stab.+Unstab.") diffusion flamelets. Other manifolds are not assessed here. The different columns correspond to four different strain rates, and the rows show progress variable, its source term, hydroxyl mass fraction, and temperature as function of the mixture fraction. The "Stab.+Unstab." solutions are identical to the cases presented in Fig. 6.18. Note, that the velocity profiles in the two simulations are nearly identical (not shown here). The vertical dash-dot lines indicate the lean flammability limit, the stoichiometric mixture, and the rich flammability limit. This representation provides further understanding of the behavior of the "Stab.+Unstab." manifold, which is expected to perform better under these conditions. The progress variable is reproduced well for $a \in \{1/\mathrm{s}, 10/\mathrm{s}, 300/\mathrm{s}\}$, and a slight overshoot is only present at $a = 600/\mathrm{s}$, related to the deviation of the s-curves. The progress variable source has deviations on the rich side at the lowest strain rate, and at $a = 10/\mathrm{s}$ near the local minimum of $\dot{\omega}_{Y_c}$, in the other two cases it is reproduced perfectly. The hydroxyl radical and the temperature show similar performance, with the temperature highlighting the non-injectivity issues at $a = 1/\mathrm{s}$.

The solutions obtained using the "Prem." database are notably different across all conditions. The progress variable is slightly lower in all the cases on the rich side. The largest deviations between the two manifolds are observed in the source term profiles. The "Prem." database tends to have lower source terms especially outside the flammability limit. For instance, it drops sharply across the lean flammability limit at $a = 300/\mathrm{s}$ and $a = 600/\mathrm{s}$. Nevertheless, the general flame behavior is reproduced even with the premixed flamelet based manifold, since the peak source term (displayed in the inset plots) is similar in the two tabulations. The hydroxyl mass fraction profile given by the "Prem." database shows slight differences from the "Stab.+Unstab." case. The oxidation layer of the counterflow diffusion flamelets becomes thicker with the increase of strain rate (Peters, 2001, §3.6), which is reflected in the widening of the Y_{OH} profiles in Fig. 6.20. The premixed flamelet based database can capture this effect to an extent, however the OH radical cannot be present below the lean flammability limit, and discrepancies arise at the higher strain rates. Finally, the temperature profiles only deviate between the two manifolds at rich conditions similar to the Y_c profiles. In rich mixtures the premixed flamelets relax to the equilibrium conditions directly without showing a significant local maximum, thus in the

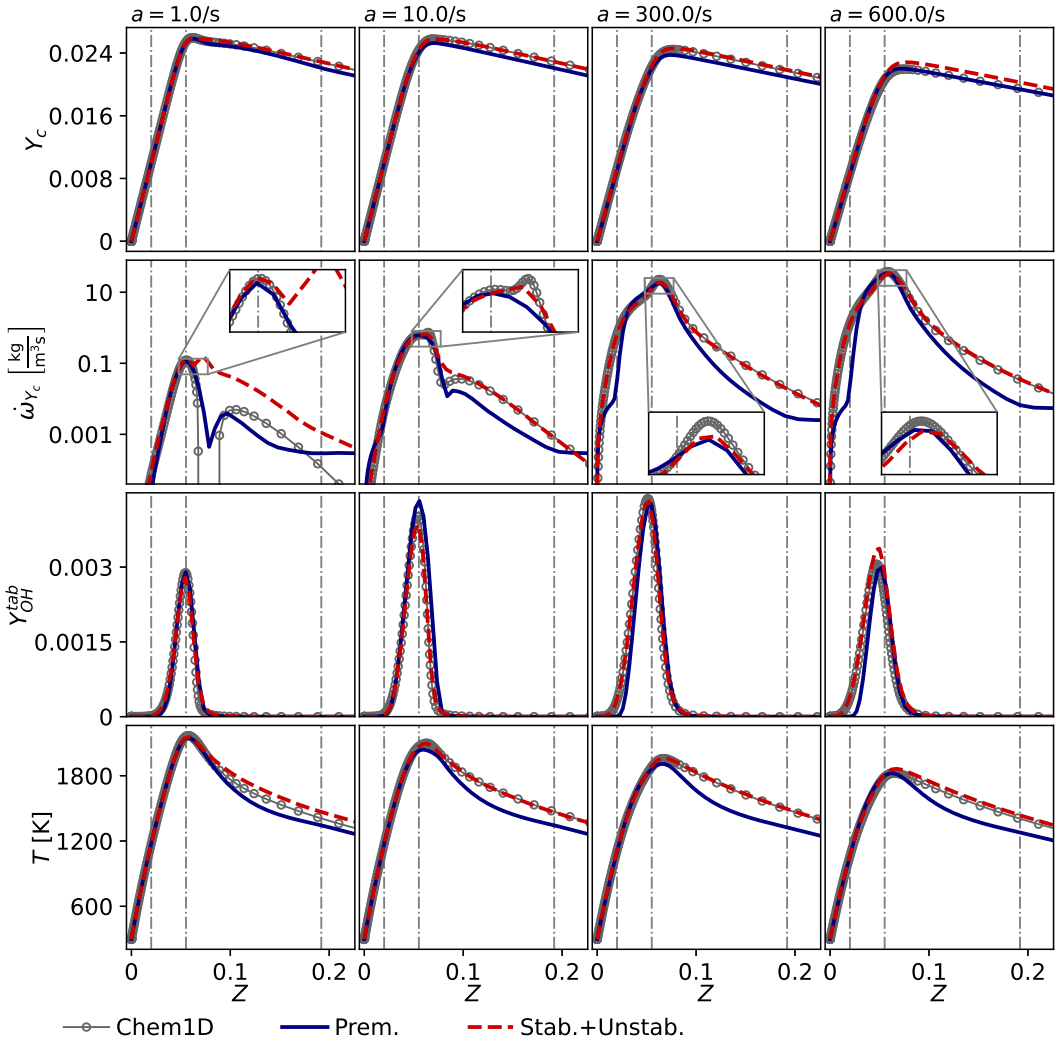

FIGURE 6.20: Stable burning solutions of methane/air flames in counterflow configuration using different manifolds in the tabulated chemistry model of Alya. The profiles of progress variable, progress variable source term, hydroxyl mass fraction, and temperature are compared with the Chem1D (Somers, 1994) finite rate chemistry solution in mixture fraction space.

"Prem." case the tabulated chemistry solution cannot access thermo-chemical states corresponding to such high temperatures.

The stoichiometric temperature, the temperature at a local mixture composition of $\phi = 1.5$, and the integral heat release rate are displayed in Fig. 6.21. The temperature values of Fig. 6.21b highlight the non-injectivity issues of the "Stab.+Unstab." manifold, since at low strain rates the equilibrium conditions are unattainable at this part of the flame. Across all conditions the premixed flamelet based manifold deviates significantly from the finite rate chemistry solution. It shows lower temperatures both at stoichiometry and especially at $\phi = 1.5$. In the latter case the temperature approaches equilibrium smoothly, thus it performs better at very low strain

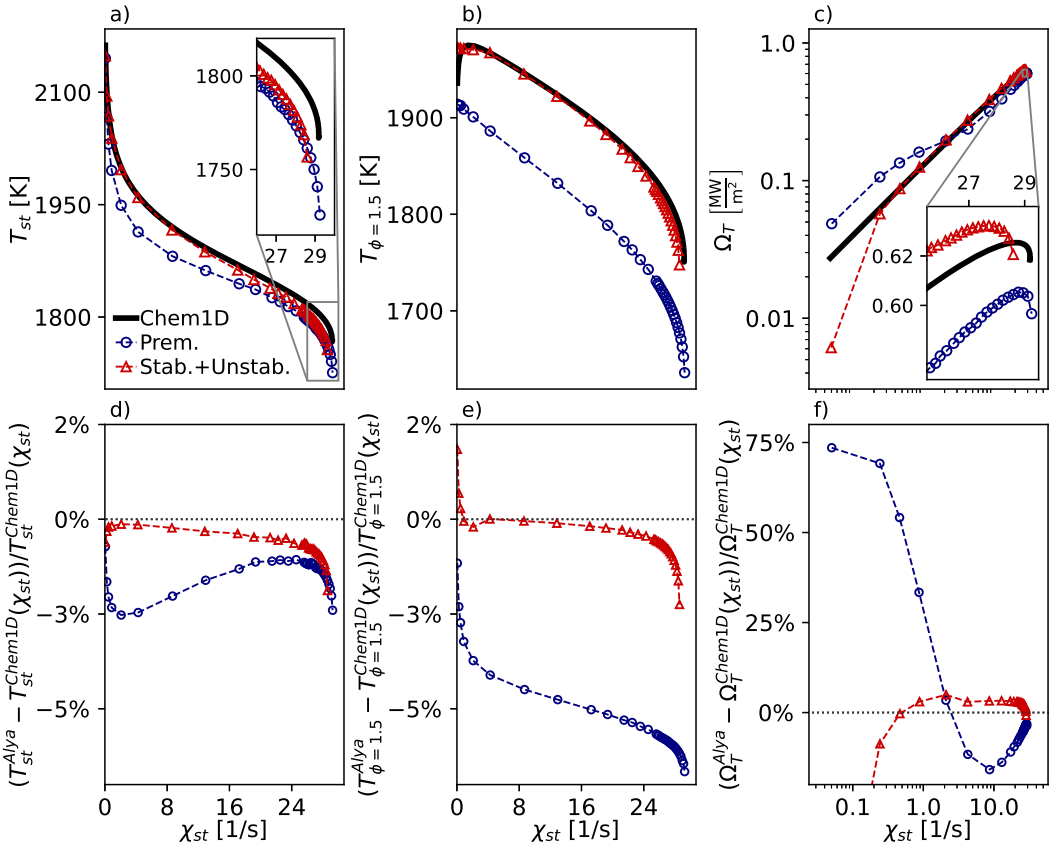

FIGURE 6.21: Effect of different manifolds on laminar counterflow diffusion flames using tabulated chemistry in Alya compared with the finite rate chemistry calculations of Chem1D. The top row of plots shows the stoichiometric temperature (a), the temperature at a local mixture composition of $\phi = 1.5$ (b), and the integral of heat release rate on the centerline (c) calculated by Eq. (3.21) as function of the stoichiometric scalar dissipation rate. The bottom row shows the relative difference between the tabulated and finite rate chemistry results.

rates. However, this also entails a significant over-prediction of the integral heat release rate as Fig. 6.21f illustrates. Interestingly, both approaches predict similar stoichiometric scalar dissipation rates at extinction. As reported above, the manifold based on stable and unstable counterflow diffusion flamelets places the extinction point at: $\chi_{st,Stab.+Unstab.}^{ext} = 28.593/\text{s}$. Meanwhile the "Prem." database shows extinction beyond: $\chi_{st,Prem.}^{ext} = 29.252/\text{s}$ ($a = 695/\text{s}$). Both solutions are fairly close to the finite rate chemistry value: $\chi_{st,Chem1D}^{ext} = 29.111/\text{s}$.

Overall, using a premixed flamelet based manifold for simulating diffusion flames seems to produce less significant errors, than using diffusion flamelet based manifolds in perfectly premixed conditions. (See section 6.3.3.) The extinction point is captured by the "Prem." table, and the discrepancies in the flame structure are significant but not particularly grave from the point of view of flame propagation.

6.4 Assessment of Lagrangian droplet models

This section evaluates the performance of the Lagrangian droplet models, focusing on the functionality added in this work, including the new model to obtain representative gas states in tabulated chemistry simulations outlined in section 4.3.2, and the two-way coupling of the liquid and gas phase presented in section 5.5.3. For the detailed assessment of the kinematic transport model see the work of Olivares Mañas (2018).

6.4.1 Validation of the TARES model

The tabulated average representative evaporation state (TARES) model of section 4.3.2 is assessed here. The model aspires to recreate the classical "1/3 law" of the droplet evaporation models, using a reduced set of tabulated parameters. A gas state is retrieved from the thermo-chemical tables, then the properties are adjusted in function of the temperature difference between this state and the T_m mean temperature of the "1/3 law", using linear approximations. If the manifold is composed of multiple enthalpy levels, then the closest temperature is found first and if T_m is still outside the manifold, then the aforementioned linear approximation is applied.

The TARES model is evaluated using Bird's correction at the experimental conditions of Chauveau et al. (2019) which is already discussed in section 4.5.2. The case concerns the evaporation of n-heptane droplets in molecular nitrogen gas atmosphere under micro-gravity conditions. The case is simulated using one-way coupling, thus the Eulerian transport is not simulated, and the seen conditions are imposed directly: $u_s = 0$ m/s, $Z_s = 0$, and the seen enthalpy is defined in function of the seen temperature: $h_s = f(T_s)$. Two different manifolds are used testing different aspects of the model. The first table is testing the linear approximation of λ_m, μ_m, and $\mathcal{D}_m$ in the TARES model in an adiabatic table, which represents mixing between N_2 at 298.15 K and n-heptane vapor at saturated conditions. This manifold is solely parameterized by mixture fraction, which is discretized by 101 equidistantly placed points. The second table is testing the iterative search of the closest enthalpy level in a non-adiabatic table. The manifold contains the mixing solutions of N_2 and n-heptane at various enthalpy levels, using the same discretization of Z, and 21 equidistant points in i, with the limiting enthalpy levels corresponding to the mixture at 250 K and 2000 K.

Figure 6.22 illustrates the equilibrium conditions of the outlined Alya simulation using the TARES model. The wet-bulb temperature and the evaporation rate constant are assessed in the left and right columns respectively. Even using the linear approximations in conjunction of the adiabatic table, the error in T_{wb} and K stays limited to single percent values at all assessed conditions. This relatively good performance is explained by the smooth change of λ, μ, and $\mathcal{D}$ in function of the temperature, and by the fact, that the mean specific heat and density correspond exactly to the classical "1/3 law" as detailed in section 4.3.2. By using a non-adiabatic table, the TARES model is able to find a closer state to the actual mean gas state, and the error is minimized at high temperature conditions. Note, the minor deterioration of evaporation rate constant in the low temperature cases. This is due to the high sensitivity of the relative error at very low values of K. In both cases the error between the classical "1/3 law" and the TARES model is significantly lower, than the error between any of the simulations and the experimental results of Chauveau et al. (2019).

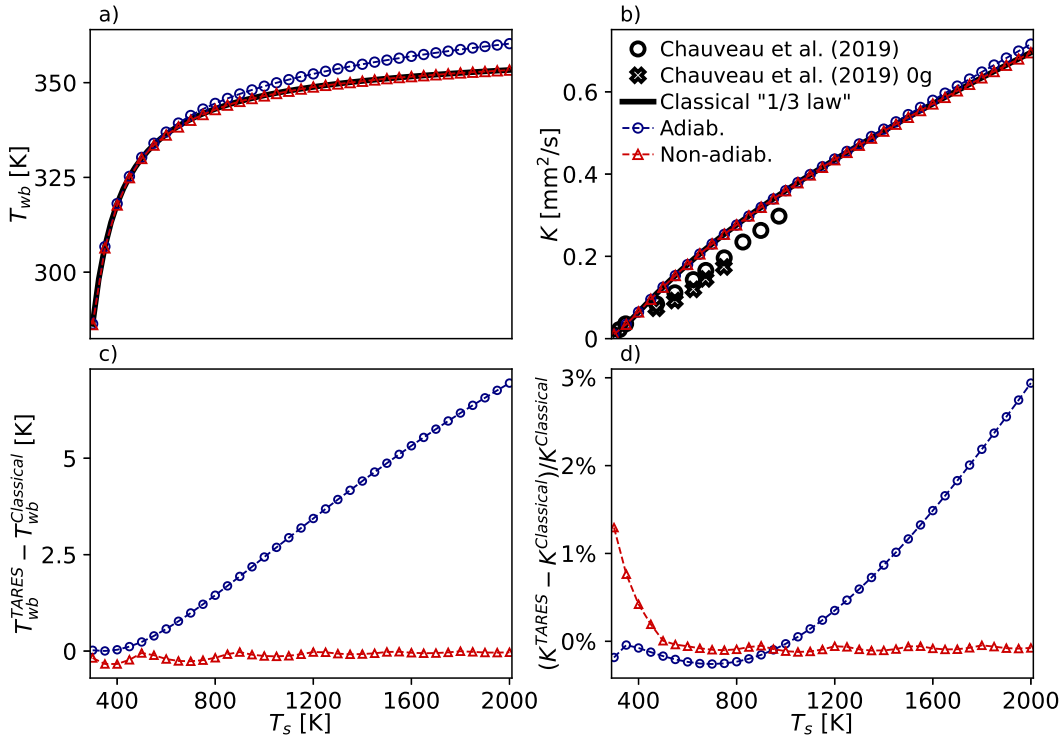

FIGURE 6.22: Wet-bulb conditions of n-heptane droplets with the TARES model using adiabatic (Adiab.) and non-adiabatic (Non-adiab.) manifolds compared to the the classical "1/3 law" at various seen gas temperatures. The top row of plots displays the wet-bulb temperature, and the evaporation rate constant. In the latter the experimental values of Chauveau et al. (2019) are also displayed. The bottom row shows the absolute error of the wet-bulb temperature, and the relative error of the evaporation rate constant in comparison to the classical "1/3 law".

6.4.2 Global conservation properties of Eulerian-Lagrangian coupling

The conservative coupling of the Eulerian and Lagrangian phases has a paramount importance is reacting flow simulations. The injected spray not only induces fluid flow through the momentum exchange, but it also creates the combustible mixture by evaporation. All mass change of the droplets must correspond to an equal mass increase in the gas phase in order to conserve the global equivalence ratio of the combustion system. This behavior is studied in a simple configuration of an n-heptane droplet in a cube shaped control volume of molecular nitrogen at 500 K. The droplet is initialized with a diameter of $d_{p,0} = 500$ μm. Furthermore, an initial temperature is imposed such, that it is 20 K below the wet-bulb temperature of stationary droplets in this atmosphere: $T_{p,0} = 310.05$ K. Finally an initial velocity is prescribed as $u_{p,0} = 1$ m/s in the x direction.

The solved Eulerian governing equations are those of non-adiabatic mixing in laminar flow, corresponding to Eq. (2.54), Eq. (2.55), Eq. (2.81), and Eq. (2.117), here

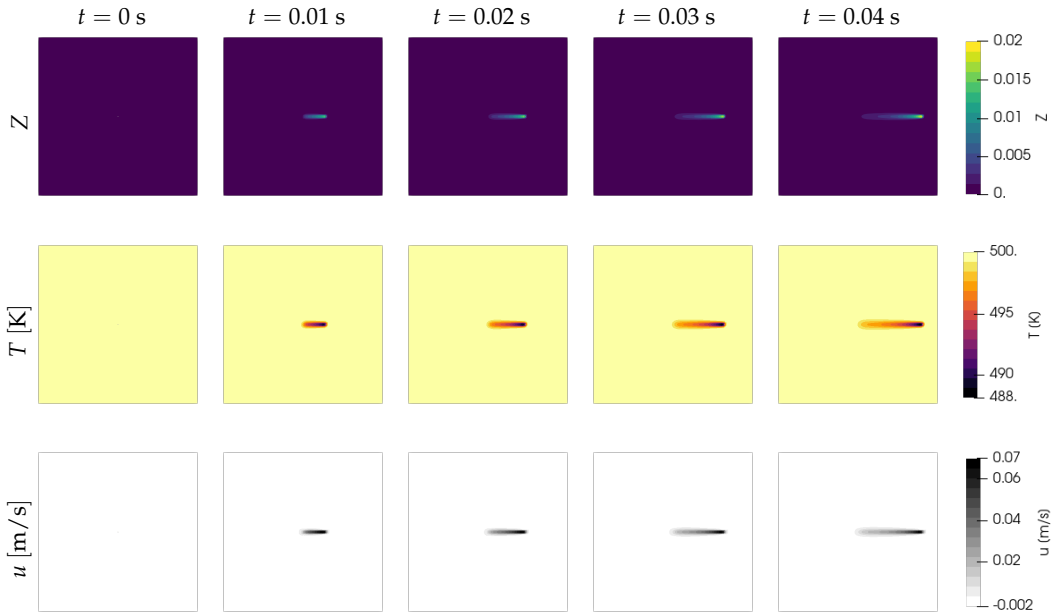

FIGURE 6.23: Illustration of Eulerian fields in single droplet simulation with two-way coupling. The three rows of contour plots indicate gas phase the mixture fraction, the temperature, and the velocity. The columns correspond to the indicated time instances.

repeated for the sake of completeness:

$$\partial_t \rho + \nabla \cdot (\rho \mathbf{u}) = S^e_\rho, \tag{6.81}$$

$$\partial_t (\rho \mathbf{u}) + \nabla \cdot (\rho \mathbf{u} \otimes \mathbf{u}) + \nabla p - \nabla \cdot \boldsymbol{\tau} (\mathbf{u}) = S^e_{\mathbf{u}}, \tag{6.82}$$

$$\partial_t (\rho h) + \nabla \cdot (\rho h \mathbf{u}) - \nabla \cdot (\rho \mathcal{D}_t \nabla h) = S^e_h, \tag{6.83}$$

$$\partial_t (\rho Z) + \nabla \cdot (\rho Z \mathbf{u}) - \nabla \cdot (\rho \mathcal{D}_t \nabla Z) = S^e_Z, \tag{6.84}$$

where the unity Lewis number assumption is used, and the evaporative sources are defined in section 5.5.3. This case corresponds to an open system, thus the thermodynamic pressure is constant 101325 Pa. All the equations are discretized in the non-conservative form, including the momentum equation. The material properties are retrieved from the non-adiabatic table used in section 6.4.1.

The simulation domain is a 0.1 m $\times$ 0.1 m $\times$ 0.1 m cube, centered around the droplet. It is discretized by regular hexahedra, with edge size of 1 mm, resulting in a grid of 1M elements. The case is simulated up to a physical time of 0.05 s, with a constant time step of $\delta t = 5$ μs. Figure 6.23 illustrates the case in the $x - y$ cross section of the cubic domain. The droplet moves towards the right of the domain, and affects the Eulerian fields in a streak. The mixture fraction in the vicinity of the droplet reaches a maximum of 0.02, meanwhile the gas is cooled notably as the liquid droplet is heated and cold vapor is added to the gas phase. Due to drag and the momentum carried by the vapor entering the gas phase, the droplet accelerates the initially quiescent flow field. By the end of the simulated time the droplet almost reaches the right boundary, but interactions with the boundary do not take place. Zero gradient condition for all unknowns is prescribed on these surfaces.

The mass, energy, and momentum conservation of the Eulerian-Lagrangian coupling is assessed by using the boundaries of this domain, as a control volume. (See

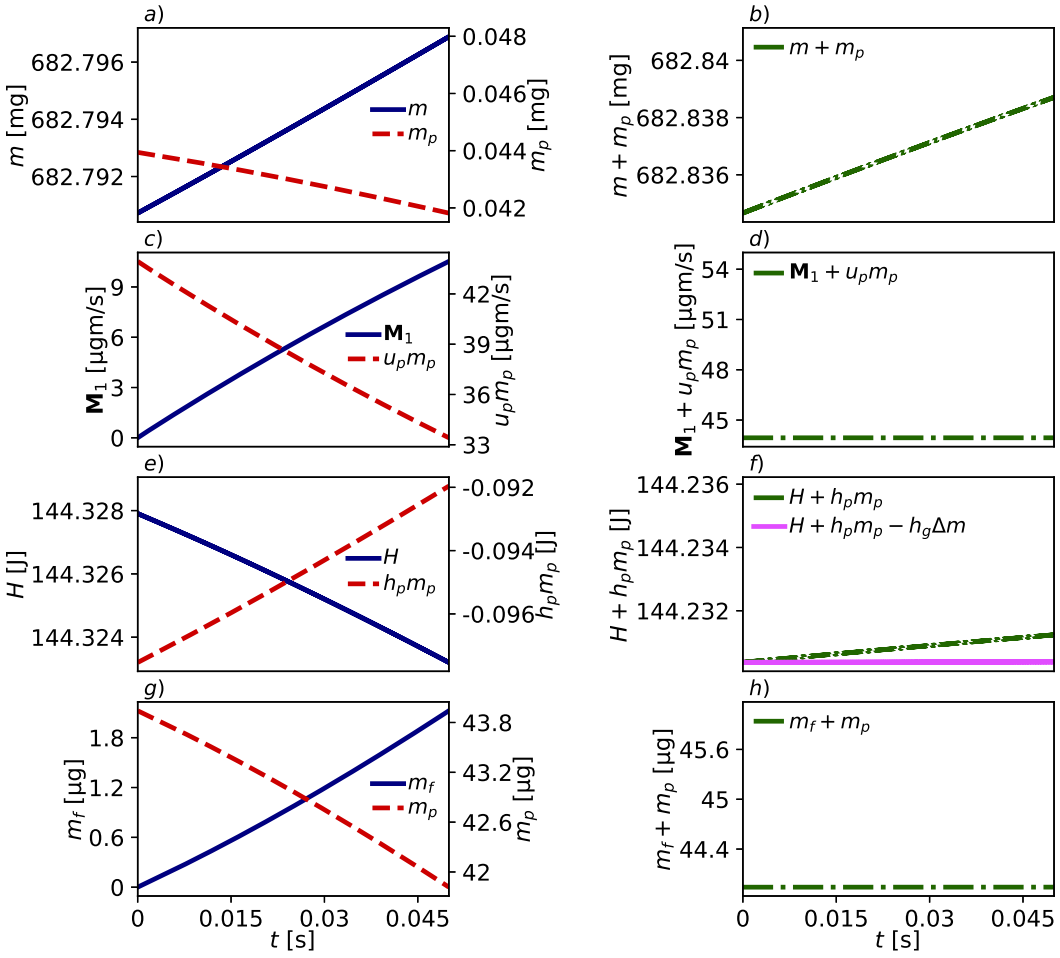

FIGURE 6.24: Total mass, momentum, enthalpy, and fuel mass in the liquid and gas phases in an open system. The left column of plots illustrates the individual contributions of the two phases, while on the right the sum of the two phases is displayed. The range of all vertical axes is identical in all rows.

a depiction in Fig. 5.16.) The overall mass (m), x momentum ($\mathbf{M}_1$), enthalpy (H) and fuel mass (m_f) contained in the gas phase is calculated as:

$$m = \int_\Omega \rho \mathrm{d}\Omega, \tag{6.85}$$

$$\mathbf{M}_1 = \int_\Omega \rho u \mathrm{d}\Omega, \tag{6.86}$$

$$H = \int_\Omega \rho h \mathrm{d}\Omega, \tag{6.87}$$

$$m_f = \int_\Omega \rho Z \mathrm{d}\Omega. \tag{6.88}$$

These integrals are evaluated within the finite element framework using the Gaussian quadrature method. The corresponding quantities of the droplets are straightforward to obtained from the solved unknowns, only the specific enthalpy of the liquid (h_p) needs a closure, which is calculated using the vapor enthalpy at the droplet

temperature (h_v) given by the NASA polynomials, and the heat of vaporization (L_v):

$$h_p = h_v(T_p) - L_v(T_p). \tag{6.89}$$

Figure 6.24 illustrates the temporal evolution of the conserved quantities in the two phases (left) and in the entire control volume (right). The presence of the droplet cools the domain, causing an increase of the average density. Consequently there is a notable influx of bath-gas through the boundaries. As Fig. 6.24a and b show, the mass of the gas phase increases more, than the decrease of the droplet mass. This influx of matter does not influence the momentum contained in the domain, as the net flux of $\mathbf{M}_1$ through the boundaries is negligible. Consequently the momentum is conserved exactly shown in Fig. 6.24d. The overall enthalpy in the domain is somewhat affected by the flow through the boundaries, as the far-field enthalpy (h_g) is non-zero. Figure 6.24f illustrates this, by subtracting $h_g \Delta m$ form the overall enthalpy of the two phases, where $\Delta m = m - m(0) + m_p - m_p(0)$ is the total mass change of the system since the initial condition, corresponding to the influx of far-field gases. Finally, the fuel mass is conserved precisely, since the far-field mixture fraction is zero. Not show here, the case is also studied in a closed domain with no-slip wall boundary conditions. In such a case the mass is conserved precisely, the enthalpy within the domain is only modified due to the $\frac{\mathrm{d}P_0}{\mathrm{d}t}$ term, and momentum is transferred to the no-slip walls due to friction. Overall, the two-way coupling strategy preserves accurately the conserved quantities.

6.5 Benchmarking under turbulent reacting conditions

The above assessments test some specific components of the low-dissipation scheme. Section 6.2 shows, that the implementation of the scheme is adequate to capture variable density flows under turbulent conditions, while the combustion models are assessed extensively in section 6.3. In this section, the low Mach number simulation strategy is finally tested under turbulent reacting conditions. Two configurations are studied, the technically premixed swirl flame of the PRECCINSTA burner (Meier et al., 2007), and the non-premixed DLR-A jet flame. (Meier et al., 2000)

6.5.1 PRECCINSTA turbulent premixed swirling flame

The first turbulent combustion test case of this work is a technically premixed flame in a swirl-stabilized bluff-body configuration known as the PRECCINSTA burner. The configuration is illustrated on Fig. 6.25. In the experimental setup, air enters the plenum (on the left of the figure) at ambient temperature and pressure. Subsequently the air flows into a radial swirler element, where methane is injected into the flow at high velocity through 12 different injection ports of ∅1mm. The reactants mix in the swirler, and a largely premixed mixture enters the combustion chamber. The degree of mixing depends on the operating condition, thus the flame may propagate either in well mixed or only partially premixed reactants.

The operating point to be investigated corresponds to an equivalence ratio of $\phi = 0.75$, which burns in stable operation at a Reynolds number of $Re = 35000$ based on the swirler outer diameter of $D_s = 27.85$ mm. Experimental measurements of this burner (Meier et al., 2007) and previous LES results of Alya with a different numerical scheme (Gövert et al., 2018) suggest, that the perfectly premixed assumption holds for this operating point and the burning of a homogeneous methane/air mixture can be considered to describe the reacting process. Under this assumption

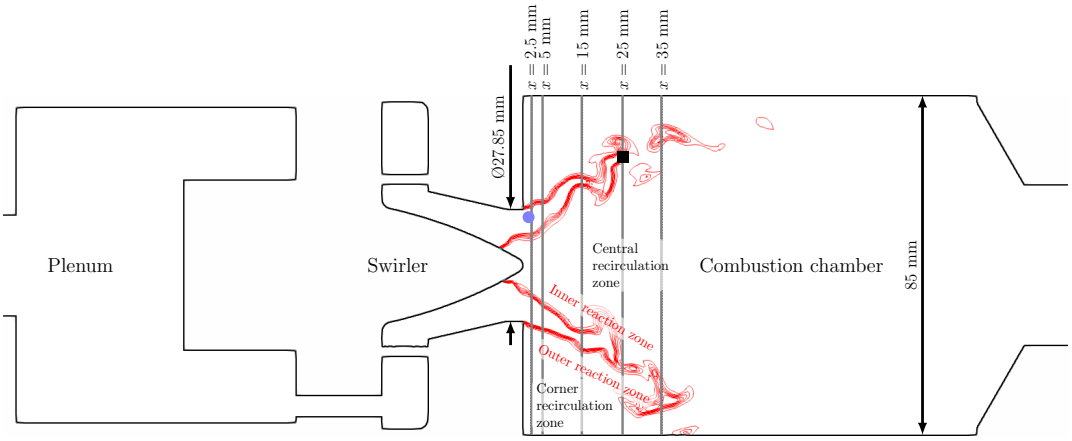

FIGURE 6.25: Illustration of the computational domain used for the PRECCINSTA burner simulation. The reference measurement locations are indicated with gray lines. For reference the flame location obtained in the LES is indicated by the red temperature iso-contours at $T \in \{800, 1000, 1200, 1600, 1800, 1900\}$K.

the flame exhibits a constant temperature ratio of $Tr \approx 6$, which is significantly more challenging task, than the $Tr = 2$ case of the anisothermal channel in section 6.2. Furthermore, the turbulent burning velocity, which is the key element to be predicted here, is influenced by all aspects of the simulation. The heat release in the reacting layer causes thermal dilatation, which effectively acts as a volumetric source of kinetic energy through the $\partial_t \Sigma$ term of Eq. (6.37). Meier et al. (2007) used laser Doppler velocimetry (LDV) in their experimental study to assess the mean and fluctuating components of the velocity field, which are taken as reference to assess the quality of the low dissipation scheme.

Note, that the goal of this section is to study the numerical method. The flame behavior itself is extensively studied in the literature using numerical methods. A non-exhaustive list of high-fidelity simulations is provided below. Roux et al. (2005) used the thickened flame model in a compressible LES to investigate the dynamic behavior of the flame. Moureau et al. (2007) investigated the case with a level-set based flame tracking method in LES applying the low-Mach number approximation, confirming the legitimacy of premixed combustion models in this configuration. Galpin et al. (2008) used a tabulated chemistry method with the presumed β-FPDF sub-grid closure in compressible LES, showing the potential of such modeling strategy. Fiorina et al. (2010) introduced the filtered tabulated chemistry for large-eddy simulation (F-TACLES) and studied this configuration, showing a good performance with the proposed sub-grid chemistry closure. Moureau, Domingo, and Vervisch (2011) executed a massively parallel DNS with perfectly premixed tabulated chemistry, to study turbulence/chemistry interactions in this case. Franzelli et al. (2012) found using the thickened flame model in compressible LES, that the perfectly premixed assumption may be valid for stable operating points, such as the one simulated here. Wang et al. (2014) used a Reaction–Diffusion Manifold (REDIM) to simulate the stable operating points of the flame using a the low Mach number approximation under the perfectly premixed assumption. Volpiani, Schmitt, and Veynante (2017) used the case to assess a new sub-grid frame wrinkling model. Gövert et al. (2018) simulated the flame using Alya with an implicit time stepping method using tabulated chemistry with and without the perfectly premixed assumption, and found negligible

effects on the velocity fields, which are also targeted here. More recently, Hosseini, Darabiha, and Thévenin (2022) simulated the case using a lattice Boltzmann method. Indeed, the case has become a standard benchmark in assessing combustion modelling strategies, and herein it is also used in this capacity.

Governing equations

The tabulated chemistry model used in this case is based on a single premixed flamelet at the global equivalence ratio ($\phi = 0.75$.) The thermo-chemical table is FPDF integrated, using a β-function in C. In perfectly premixed conditions, it is possible to choose the a_k weights of the progress variable such, that Y_c ranges from 0 to 1, thus it is identical to C. Furthermore, the enthalpy transport is retained for the modeling strategy, so the solved governing equations are the filtered Navier-Stokes equations (Eq. (5.30) and Eq. (5.47)), filtered equations for the enthalpy and progress variable (Eq. (5.117)), and a transport equation for the sub-grid progress variable variance (Eq. (5.123)). The PDEs are summarized below for completeness:

$$\partial_t \overline{\rho} + \nabla \cdot (\overline{\rho}\widetilde{\mathbf{u}}) = 0 \tag{6.90}$$

$$\partial_t (\overline{\rho}\widetilde{\mathbf{u}}) + \nabla \cdot (\overline{\rho}\widetilde{\mathbf{u}} \otimes \widetilde{\mathbf{u}}) + \nabla \overline{p} - \nabla \cdot \left(2\left(\overline{\mu} + \overline{\rho}\nu^{SGS}\right)\widetilde{\mathbf{S^D}(\mathbf{u})}\right) = 0 \tag{6.91}$$

$$\partial_t \left(\overline{\rho}\widetilde{h}\right) + \nabla \cdot \left(\overline{\rho}\widetilde{h}\widetilde{\mathbf{u}}\right) - \nabla \cdot \left(\overline{\rho}\left(\widetilde{\mathcal{D}_t} + \frac{\nu^{SGS}}{Pr^{SGS}}\right)\nabla \widetilde{h}\right) = 0 \tag{6.92}$$

$$\partial_t \left(\overline{\rho}\widetilde{C}\right) + \nabla \cdot \left(\overline{\rho}\widetilde{C}\widetilde{\mathbf{u}}\right) - \nabla \cdot \left(\overline{\rho}\left(\widetilde{\mathcal{D}_t} + \frac{\nu^{SGS}}{Sc^{SGS}}\right)\nabla \widetilde{C}\right) = \overline{\dot{\omega}_C} \tag{6.93}$$

$$\partial_t (\overline{\rho}C_v) + \nabla \cdot (\overline{\rho}C_v\widetilde{\mathbf{u}}) - \nabla \cdot \left(\overline{\rho}\left(\widetilde{\mathcal{D}_t} + \frac{\nu^{SGS}}{Sc^{SGS}}\right)\nabla C_v\right) = 2\frac{\overline{\rho}\nu^{SGS}}{Sc^{SGS}}\nabla \widetilde{C} \cdot \nabla \widetilde{C} + 2\left(\overline{C\dot{\omega}_C} - \widetilde{C}\overline{\dot{\omega}_C}\right) - \overline{\rho}\chi_C^{SGS}, \tag{6.94}$$

where the unity Lewis number assumption is used, all spray source terms and volumetric forces are zero, the sub-grid Prandtl and Schmidt numbers are 0.7, and Y_c is replaced by C in the notation, as they are equivalent in a perfectly premixed case. The sub-grid viscosity is closed using the model of Vreman (2004), using the constant $c = 0.1$ recommended for complex domains. All equations are discretized in the non-conservative form.

Computational grid

The computation domain and measurement locations are presented in Fig. 6.25. The domain includes the plenum, swirler and combustion chamber. A hybrid mesh of 16M elements and 4M degrees of freedom is applied with boundary layer refinement on the walls and tetrahedral mesh in the bulk flow. This grid is identical to one used by Gövert et al. (2018) in earlier perfectly premixed simulations in Alya.

The computational grid is illustrated in Fig. 6.26, using a cross-section of the swirler and the combustion chamber. The base element edge length is $h = 1.5$ mm with $h = 1$ mm refinement in the combustion chamber up to 70 mm from the swirler outlet. Another refinement region with mean element edge length of $h = 0.5$ mm is enclosing the reacting layers with the indicated dimensions. As the mesh sensitivity is already extensively studied by Gövert et al. (2018), here a single optimized grid is used to evaluate the low Mach discretization strategy. Note, that the volume of

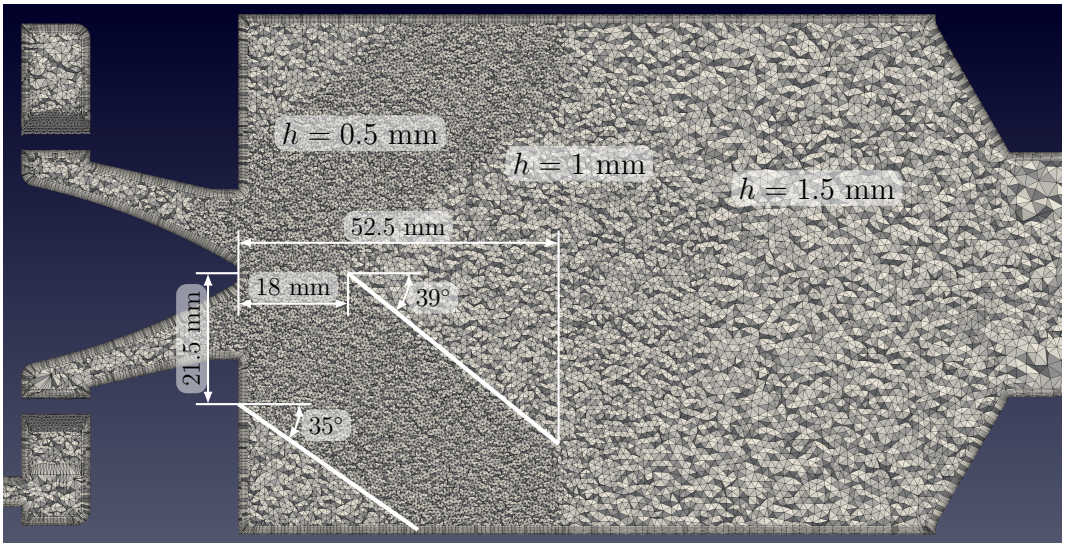

FIGURE 6.26: Computational grid of the PRECCINSTA burner.

these tetrahedral elements with edge length h is:

$$V_{element} = \frac{\sqrt{2}}{12} h^3, \tag{6.95}$$

thus the filter width applied in the sub-grid models is approximately half of the edge length:

$$\Delta_f = \sqrt[3]{V_{element}} \approx 0.4903h. \tag{6.96}$$

Tabulation strategy

The flamelet database is generated with the GRI3.0 mechanism (Smith et al., 2011) using a single unstretched adiabatic premixed flamelet at the global equivalence ratio of $\phi = 0.75$. In the flamelet calculation the pressure is a fixed constant at $P_0 = 101325.0$ Pa, while the temperature of the fresh reactants is given as 320 K, as the reactants are somewhat preheated by the high temperature burner components. The progress variable weights are taken following the work of Gövert et al. (2015), where the a_k weights are optimized using the CSP algorithm. (See section 3.2.1.) The β-FPDF was applied on the scaled progress variable to account for sub-grid turbulence/chemistry interaction.

The chemical scales and other properties of the studied perfectly premixed condition are summarized in Tab. 6.4. The filter size in the flame region (Eq. (6.96)) is approximately 2.5 times larger than the diffusive flame thickness. As section 6.3.2 illustrates, this would be the limit of feasibility for predicting laminar flame propagation using the present finite element framework, nevertheless here sub-grid closures are applied, which alleviate the numerical difficulties associated to the grid size. The flame speed is two orders of magnitude smaller than the mean velocities of the fresh reactants ($\mathcal{O}(10\ \mathrm{m/s})$), consequently the flame is highly elongated, as Fig. 6.25 illustrates.

Figure 6.27 illustrates the manifold used in the present case. Using this optimized progress variable, the temperature is nearly a linear function of C. Consequently, the

TABLE 6.4: Flamelet properties under the studied conditions of the PRECCINSTA burner using the unity Lewis number assumption and the GRI3.0 (Smith et al., 2011) chemical mechanism.

ϕ	0.75
Z	0.042
T^b	1936 K
S_L	0.246 m/s
δ_{diff}	0.102 mm
δ_{th}	0.549 mm
τ_{diff}	0.415 ms

convolution of the NASA polynomials (b_i) with the β-function does not affect significantly the temperature: $T^\star = T(\widetilde{h}, \widetilde{b_i})$. The filtered progress variable source term is displayed in Fig. 6.27b, indeed the CSP optimization promotes a quite distributed source term, which is advantageous in terms of numerical integration. As expected, the increasing variance distributes the source term in an even wider range, and finally at $\zeta_C = 1$ the source term becomes zero.

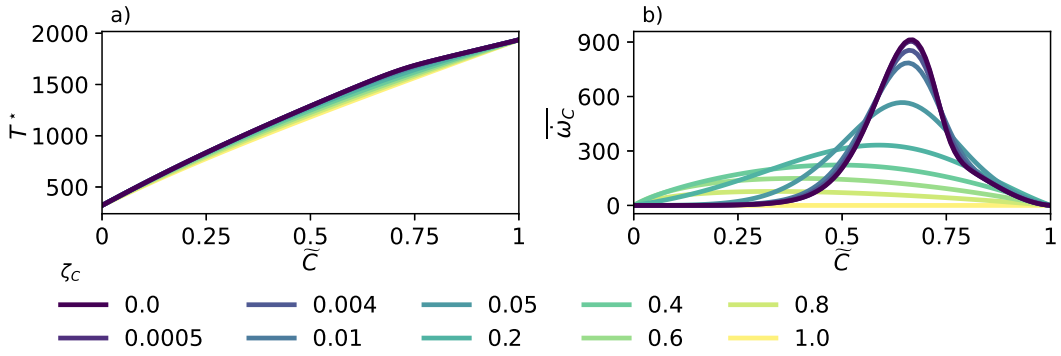

FIGURE 6.27: Temperature and filtered progress variable source term in the premixed thermo-chemical table for the PRECCINSTA simulation. The displayed temperature is calculated from the Favre-filtered enthalpy and NASA polynomials. Colors indicate various scaled variance levels.

Results

The numerical results are compared to the measurements of Meier et al. (2007) in Fig. 6.28 and Fig. 6.29. Generally, the velocity fields of the LES show a satisfactory agreement with the experimental results. The exact same tabulated chemistry method within the same numerical code and mesh was applied in the work of Gövert et al. (2018), thus the difference between the two approaches lies in the numerical scheme. The present low-dissipation scheme shows slight improvements compared to the implicit scheme applied in this earlier work. Namely, in the study of Gövert et al. (2018), this tabulation approach yields too strong recirculation in the downstream axial locations ($x \geq 25$ mm). As Fig. 6.28a and d indicate, in the present study $\langle \widetilde{u} \rangle$ shows good agreement with the experimental value. Some of the observed

minor discrepancies are also present in the literature. (Roux et al., 2005; Moureau et al., 2007; Galpin et al., 2008; Gövert et al., 2018) Such as the under-prediction of the velocity magnitude of the central reverse flow at $x \leq 5$ mm (Fig. 6.28j and m), or the under-prediction of $\langle \widetilde{u} \rangle$ and $\langle \widetilde{v} \rangle$ near the wall ($r > 30$ mm) at the more downstream locations (Fig. 6.28a and e.) These issues are not addressed here.

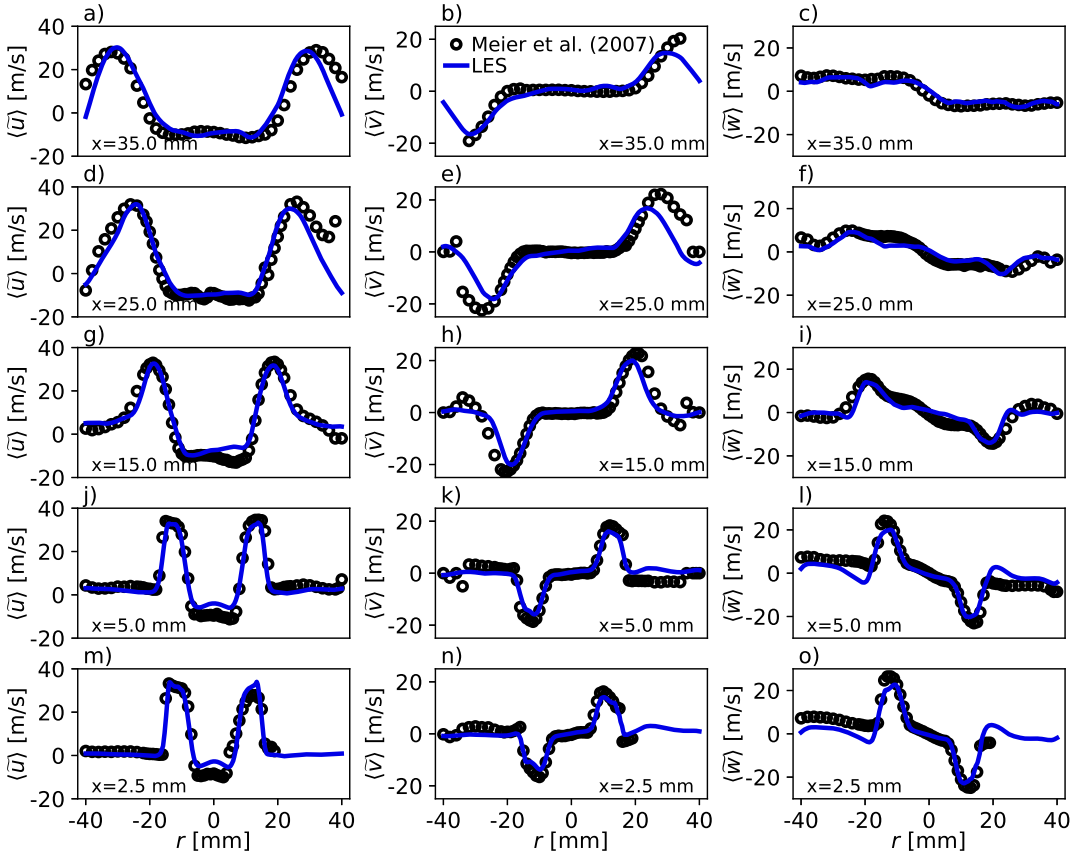

FIGURE 6.28: Comparison of mean velocity profiles in the PRECCINSTA burner at five axial locations: $x \in \{2.5, 5, 15, 25, 35\}$ mm. The three columns show the time averaged axial, radial, and tangential velocity components from left to right. Symbols indicate the measurement results of Meier et al. (2007), while the solid line shows the present LES results.

The flow in the first two measurement locations (Fig. 6.28j-o) is highly influenced by the flame anchoring location, which determines the behavior of the central and corner recirculation zones. The outer reaction zones indicated on Fig. 6.25 are attached to the corner of the swirler outlet, so this anchoring point is determined by the sharp change in the geometry. However, the inner reaction zone is attached to the conical central element of the swirler. The location of this attachment point varies during the simulation and affects the flow substantially. The relatively good agreement between the flow field and the experimental data indicate, that this feature of the PRECCINSTA flame is captured well by the simulation.

More downstream the swirling flow breaks down, creating a region of fresh gases in a conical shape, characterized by a half-angle of approximately 30°. The spreading angle is reproduced well, as the peak axial velocity component stays well aligned with the peak of the experiment in the left column of plots in Fig. 6.28. As the flame

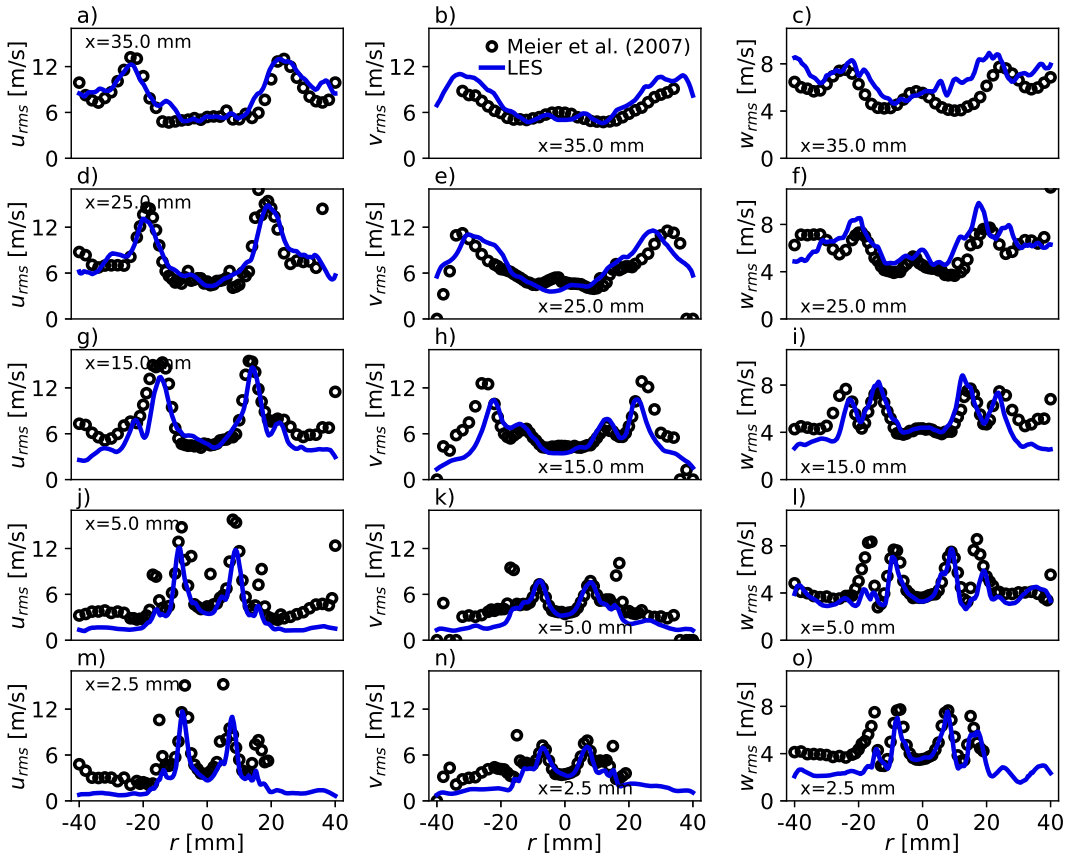

FIGURE 6.29: Comparison of RMS velocity profiles in the PRECCINSTA burner at five axial locations: $x \in \{2.5, 5, 15, 25, 35\}$ mm. The three columns show the time averaged axial, radial, and tangential velocity components from left to right. Symbols indicate the measurement results of Meier et al. (2007), while the solid line shows the present LES results.

propagates into the fresh reactants, thermal dilatation causes the flow to accelerate, consequently the axial velocity peak does not decay as severely as it would in a non-reacting flow. This acceleration also affects the radial velocity component, as v contributes significantly to the flame-normal velocity. The highest radial velocity is observed in Fig. 6.28h at $x = 15$ mm. The satisfactory prediction of this acceleration indicates, that the applied fractional step algorithm is appropriate for incorporating thermal dilatation effects which occur over short distances in the flame front at density ratios relevant for combustion systems. The circumferential velocity in the right column of Fig. 6.28 is not affected so significantly by the thermal dilatation. The swirling motion of the flame decays towards the outlet, but it stays significant throughout the combustion chamber.

The velocity fluctuations are presented in Fig. 6.29 using the same measurement locations. The displayed values are calculated from the resolved velocity filed, using Eq. (6.63). The flow enters the combustion chamber with substantial turbulent components generated by complex swirler geometry. At $x = 2.5$ mm the experimental profiles show two peaks associated to the shear layers in the inner and outer reaction zones. The former peak, located around $r \approx 7$ mm, is predicted well by the present LES method. Meanwhile the latter peak at $r \approx 15$ mm is consistently absent in LES,

except for the circumferential velocity component in Fig. 6.29o. These RMS profiles close to the inlet are comparable to the results of Gövert et al. (2018). Further downstream the fluctuating velocity components are augmented by the thermal dilation, and they stay significant at all measurement locations. At $x = 15$ mm the outer peak of v_{rms} becomes dominant (Fig. 6.29h) this peak is captured to some degree by the LES, however the remaining discrepancy corresponds to an under-prediction of radial turbulent transport. This shortcoming may be the cause of poor prediction of $\langle \widetilde{v} \rangle$ at high radii further downstream as Fig. 6.28e shows. At $x \geq 25$ mm the axial and radial velocity fluctuations are characterized by a single peak in the inner shear layer. The location and magnitude of these peaks are predicted adequately in the present work. Note, that this is a significant improvement compared to the implicit scheme used in the work of Gövert et al. (2018) which yielded nonphysical overshoots in the RMS velocity fluctuations at $x = 35$ mm.

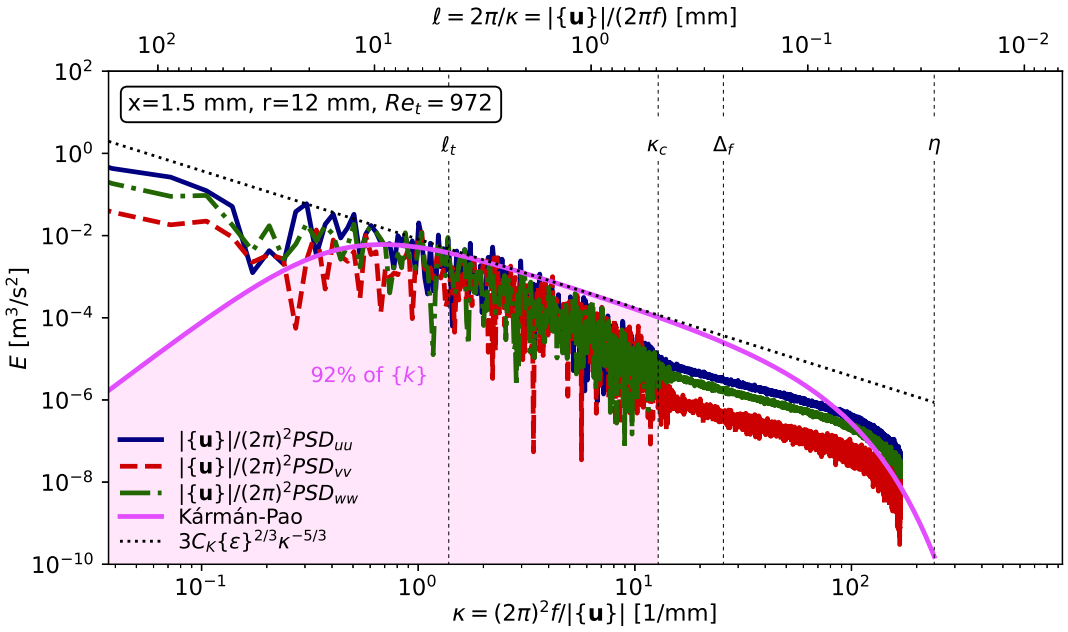

FIGURE 6.30: Velocity spectra at the inlet of the combustion chamber in the PRECCINSTA burner computed using the algorithm of Lomb (1976) and Scargle (1982). The power spectral density of the velocity components is scaled according to Taylor's hypothesis of frozen turbulence. For reference the turbulence scale estimates are displayed along with the corresponding von Kármán-Pao spectrum.

The LES results of the PRECCINSTA burner are used here, to demonstrate the scale estimation method outlined in section 5.1.6. Temporal data is collected at the axial locations of $x \in \{1.5, 2.5, 5, 15, 25, 35\}$ mm with 1 mm spacing in the radial direction. Among these points the minimum Kolmogorov length scale is identified as $\min(\eta) = 0.026$ mm, near the inlet of the combustion chamber at $r = 12$ mm. This point is located in the center of the high speed flow of fresh reactants, and is indicated by the blue circle in Fig. 6.25. The calculation agrees well with the one of Moureau, Domingo, and Vervisch (2011), who estimate $\min(\eta) = 0.029$ mm. In the same location the turbulence integral length scale is estimated to be: $\ell_t = 4.6$ mm using only the resolved turbulent kinetic energy. This estimate is reasonable, considering the geometrical scales in the swirler element. These length scales are displayed

in Fig. 6.30 using the corresponding wave number. For reference, the von Kármán-Pao spectrum defined in Eq. (5.28) parametrized by $\{\varepsilon\}$, $\{k\}$, and $\{\nu\}$ is also displayed. These estimates are compared to the velocity spectra, which is obtained by the Lomb-Scargle algorithm. (Lomb, 1976; Scargle, 1982) The cut-off length scale can be clearly identified by the transition in the spectrum, as beyond κ_c the PSD profiles only describe a noise associated to advecting a coarsely discretized signal with a fine time step. In the resolved part of the spectrum ($\kappa < \kappa_c$) the PSD shows high fluctuations, however the inertial sub-range can be identified to some extent. At low wave numbers the spectrum differs substantially from the model of Von Kármán (1948) and Pao (1965), as the latter aims to describe homogeneous isotropic turbulence with a clear dominant length scale, while the present LES is of an internal flow with substantial mean flow. Overall, a substantial part of the turbulent kinetic energy is resolved on the present grid, that is characterized by $\max\left(\frac{\Delta_f}{\eta}\right) \approx 10$ or $\max\left(\frac{h}{\eta}\right) \approx 20$.

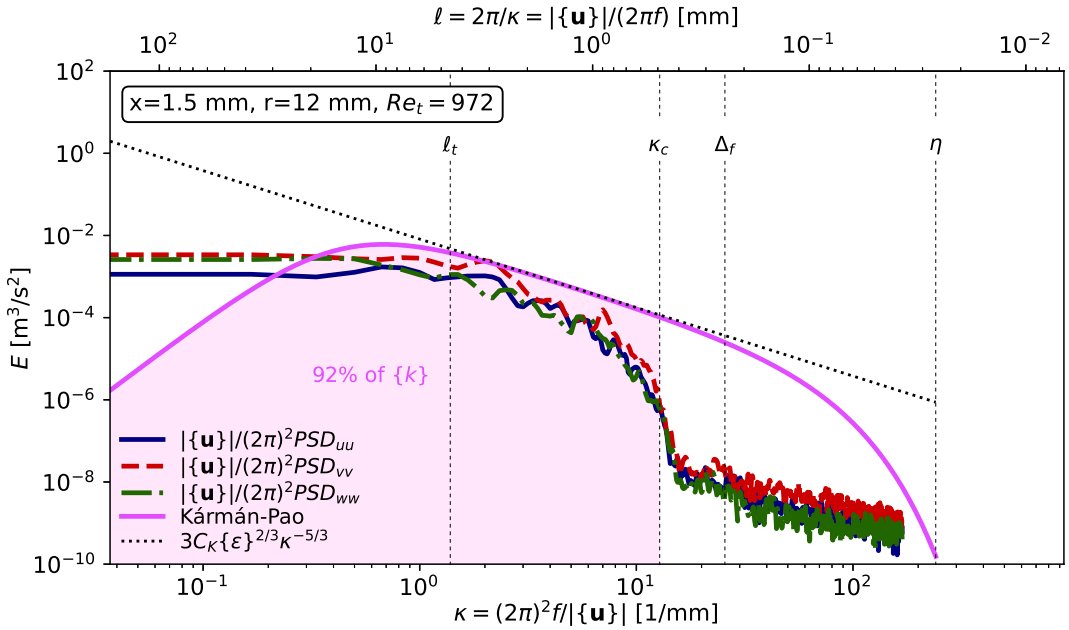

FIGURE 6.31: Velocity spectra at the inlet of the combustion chamber in the PRECCINSTA burner computed using the method of Welch (1967). The power spectral density of the velocity components is scaled according to Taylor's hypothesis of frozen turbulence. For reference the turbulence scale estimates are displayed along with the corresponding von Kármán-Pao spectrum.

The length sales are better represented using the algorithm of Welch (1967), which introduces a smoothing effect on the spectrum shown in Fig. 6.31. For this purpose, the signals are re-sampled equidistantly in time, and a 50% overlap is used between samples to remove the noise. In this case the cut-off is clearly identifiable and the noise beyond κ_c is suppressed by the method. The computed turbulence integral length scale is clearly associated to the onset of the inertial subrange. The slope of the spectra is somewhat different from the Kolmogorov spectrum of $E \propto \kappa^{-5/3}$, which may be associated to the numerical dissipation of the second order spacial discretization, as shown by Lele (1992). Note however, that the validity of Taylor's

hypothesis may be also questioned in this case, as the turbulence intensity in this location is approximately 9.6%, thus the smaller scales may be notably advected by the large-eddies. (Lumley, 1965) Nevertheless this analysis shows, that the scale estimation strategy outlined in section 5.1.6 is adequate under realistic conditions.

Based on the von Kármán-Pao model spectrum, the sub-grid kinetic energy is approximately 8% of the total turbulent kinetic energy in this point, corresponding to $e_K^{SGS} = \frac{0.08}{0.92} k^f \approx 1.32 \frac{\mathrm{m}^2}{\mathrm{s}^2}$. Meanwhile, the estimates of Yoshizawa (1986) or Bogey and Bailly (2006) discussed in section 5.1.5 give smaller sub-grid kinetic energy values: $0.77 \frac{\mathrm{m}^2}{\mathrm{s}^2}$ and $0.09 \frac{\mathrm{m}^2}{\mathrm{s}^2}$ respectively. Note, that using the scaling laws of the inertial subrange defined in Eq. (5.29), the velocity scale at the cut-off length is: $v_{2\Delta} = 1.85\ \mathrm{m/s}$, which gives a kinetic energy scale of $1.71\ \mathrm{m}^2/\mathrm{s}^2$. Indeed, the original constant of Yoshizawa (1986): $C_I = 0.0886$ appears to perform better overall.

While this witness point location is characterized by the lowest Kolmogorov scale estimates, it is located in the fresh reactant stream, thus it is not suitable to assess the variable density effects. A different witness point location is studied for this purpose, located at $x = 25$ mm and $r = 27$ mm indicated by the black square in Fig. 6.25. Here the density is indeed highly variable as the average progress variable is still below equilibrium: $\left\langle \widetilde{C} \right\rangle = 0.75$ due to the high intermittency of the flame. The Kolmogorov scale is estimated as $\eta = 92\ \mu$m, thus the LES models are active, although the Favre-averaged sub-grid turbulent kinetic energy dissipation is only one fourth of $\{\varepsilon\}$ since most of the spectrum is resolved. Using the Kolmogorov scale estimates based on Reynolds-averaging gives $\eta_{inco} = 101\ \mu$m according to Eq. (5.19), which is fairly close to the Favre-averaged value, thus this distinction appears to be less important. The point is ideal for assessing the difference between $\langle \widetilde{u} \rangle$ and $\langle \overline{u} \rangle$ according to section 5.1.5. The C_I constant of Yoshizawa (1986) is used to estimate the instantaneous sub-grid velocity scale: v^{SGS}, while the Favre-filtered density is taken from the thermo-chemical table to yield the instantaneous value of $\frac{\overline{\rho^2}}{\widetilde{\rho}^2} = \frac{\widetilde{\rho}}{\overline{\rho}}$. Taking these estimates, the Reynolds averaged error limit on the right hand side of Eq. (5.54) is $\langle \epsilon_{\overline{\mathbf{u}}=\widetilde{\mathbf{u}}} \rangle = 0.034$ m/s. Indeed, this is negligible in comparison to the mean velocity, suggesting, that the comparison of $\langle \widetilde{u} \rangle$ with the ensemble averaged measurement data is adequate in Fig. 6.28.

Finally, the turbulence integral scale estimates are used to locate the case in the regime diagrams discussed in section 5.3.2. Figure 6.32a presents the regime diagram of Peters (1999) relating the integral and Kolmogorov scales to length and velocity scales of the laminar premixed flamelet. Meanwhile, Fig. 6.32b shows the LES regime diagram introduced by Pitsch and De Lageneste (2002), which characterizes the resolution of the simulation with respect to the chemical and Kolmogorov scales. Note, that in both cases the regimes are only qualitative, as the displayed boundaries assume constant diffusivity, while the LES imposes more realistic material properties. The points are identified based on the coordinates of the figures according to Tab. 6.4 using $Ka = \frac{\tau_{diff}}{\tau_\eta}$ in Fig. 6.32b. The marker shapes identify the axial location of the point in the combustion chamber, while the color indicates the Reynolds-averaged scaled progress variable, highlighting the flame region with intermediate shades.

As Fig. 6.32a shows, the case is located in the regime of thin reaction zones. The inlet of fresh gases is characterized by $\frac{v'}{S_L} \approx 20$ as indicated by the dark circle markers. The turbulent velocity peaks around $\frac{v'}{S_L} \approx 50$ further downstream, as thermal dilatation and the breakdown of the swirling flow generates fluctuations. This point

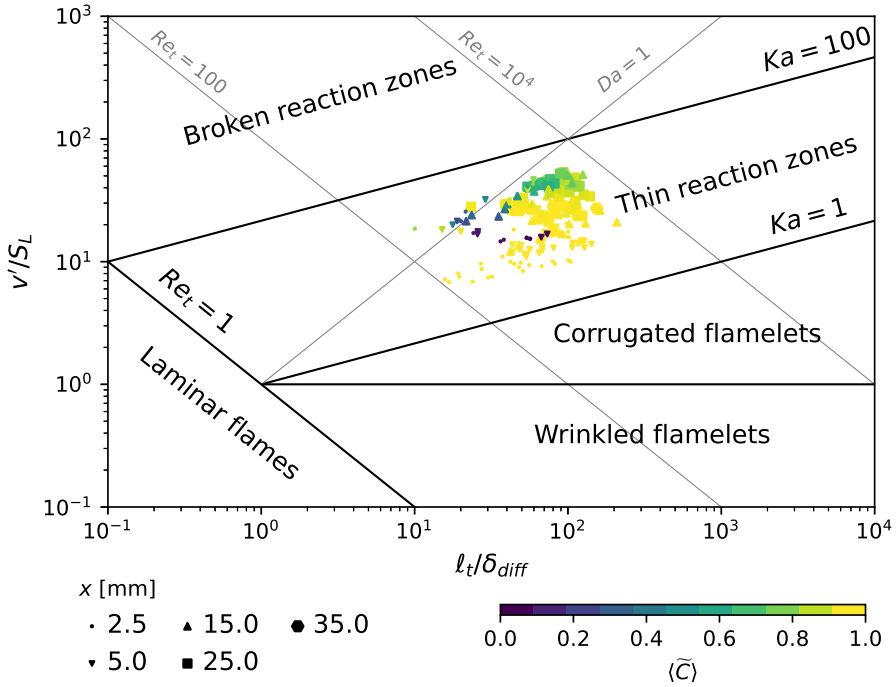

(A) Peters' regime diagram.

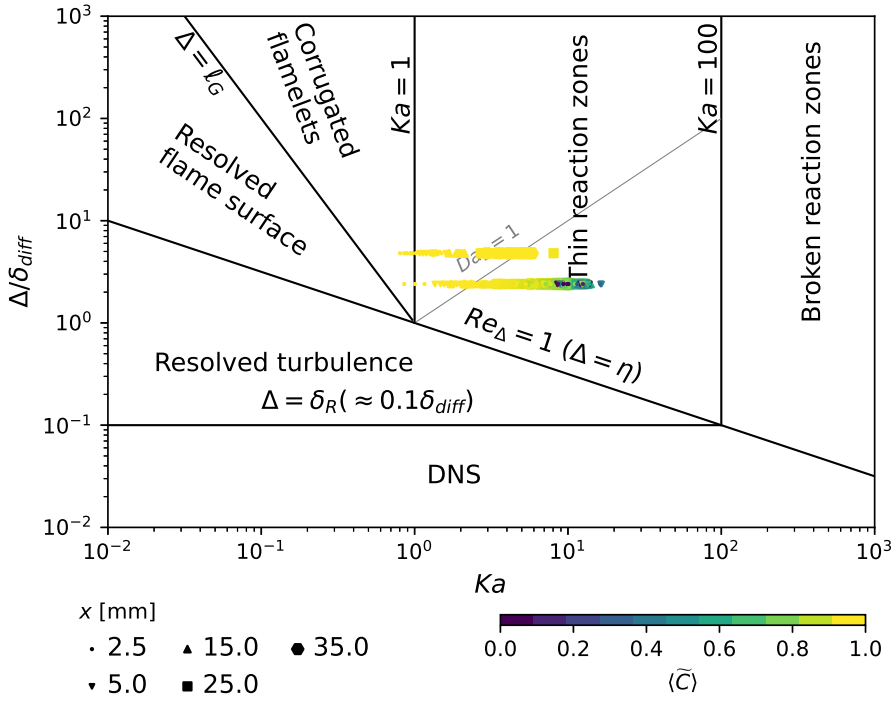

(B) LES regime diagram of Pitsch and De Lageneste (2002).

FIGURE 6.32: Regimes diagrams of the PRECCINSTA simulation.

also corresponds to the highest Karlovitz numbers. The fully reacted points indicated by the lightest colors correspond to the central and corner recirculation zones, where the turbulence tends to be less intense. Note, that the turbulence Reynolds number and the Karlovitz number are not as high as Fig. 6.32a insinuates, taking

into account the variable viscosity effects. The peak Reynolds number among the assessed points is 1546, located in the high speed fresh reactant flow at $x = 5$ mm and $r = 13$ mm.

The Karlovitz numbers do not exceed 20 according to the present estimates, as the LES regime diagram indicates in Fig. 6.32b. The points are characterized by two filter sizes corresponding to the different refinement regions. In the majority of the points the filter-scale Damköhler number is below unity, especially in the intermediate reaction progress states indicated by darker colors. This means, that part of the preheat zone broadening caused by the turbulent flow is resolved, which is well aligned with the instantaneous temperature field displayed in Fig. 6.25. Indeed in some locations the flame front is considerably broadened.

Note, that both Fiorina et al. (2010) and Moureau et al. (2007) presents different distributions of the Karlovitz number on the LES regime diagram of Pitsch and De Lageneste (2002). The former work suggests, that a substantial part of the flame lies within the regime of resolved flame surface. Meanwhile in the latter work they locate the flame on the limit of the regimes of thin reaction zones and broken reaction zones. The present work places the case between these two states. The differences are likely caused by the various definitions used to obtain the turbulent scales. More work is needed to identify the sources of these differences. An estimate of $Ka \approx 7.23$ is provided in the DNS study of Moureau, Domingo, and Vervisch (2011), which is more aligned with the present results. The Karlovitz numbers are clustered around the $\frac{\rho^u}{\rho^b} - 1 \approx 5$ value identified by MacArt, Grenga, and Mueller (2018) as the limit below which intense *back scatter* is affecting the turbulent energy cascade significantly. Indeed the thermal flame thickness of $\delta_{th} = 0.549$ mm lies between the identified integral and Kolmogorov scales, and overlaps with the cut-off scale of the mesh. As the present LES does not explicitly model the heat release effects on the unresolved spectrum, this shortcoming may cause some of the discrepancies observed in the velocity statistics in Fig. 6.28 and Fig. 6.29.

Overall, the present analysis of the PRECCINSTA flame illustrates, that the developed low-dissipation finite element scheme is coupled correctly with the turbulent combustion model. The predicted velocity fields are in good agreement with experimental results, and the observed minor discrepancies are in alignment with other computational studies in the literature. The overall modeling strategy of perfectly premixed combustion appears to be adequate in the thin reaction zones regime. The developed post-processing tools can identify the limitations of the models *a posteriori*.

6.5.2 DLR-A non-premixed jet flame

The final benchmark case is a turbulent jet diffusion flame experimentally studied by Meier et al. (2000), also known as the DLR-A jet. The case has quite a simple geometry, as the fuel jet is introduced into a low velocity co-flow through a pipe tapered to a thin edge. This case is similarly challenging as the premixed swirl flame discussed above, however the nature of the problem is completely different, as the combustion in diffusion flames is primarily governed by the mixing of reactants. The configuration is illustrated in Fig. 6.33. The fuel flow exhibits fully developed turbulence as it exits the tapered pipe of $D = 8$ mm inner diameter. This flow is characterized by a Reynolds number of 15200 based on the jet diameter. (The bulk velocity in the pipe is $U_0 = 42.2$ m/s.) The fuel reacts with the ambient air as they mix, and the flame is attached to the pipe. In the experiment the flame does not show

signs of localized extinction at any point. The fuel jet is composed of 22.1% CH_4, 33.2% H_2, and 44.7% N_2 by volume.

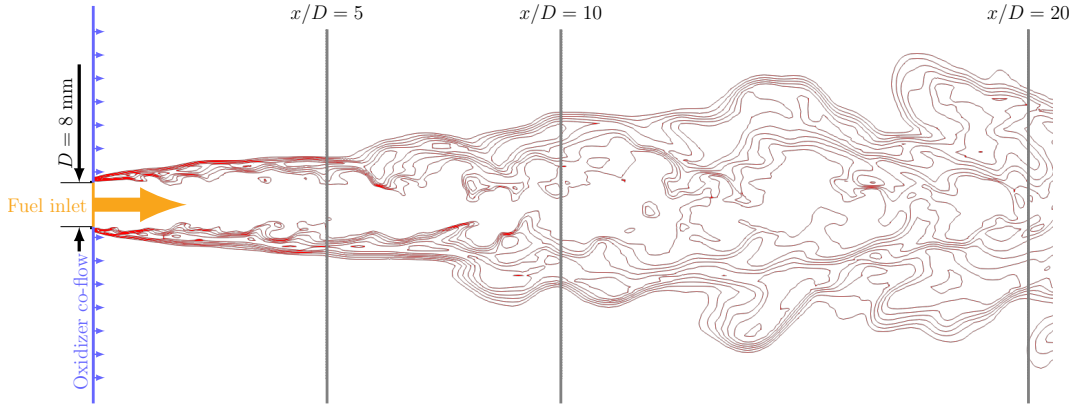

FIGURE 6.33: Illustration of the DLR-A jet flame. The relevant measurement locations are indicated with gray lines. For reference the flame location obtained in the LES on the finer mesh is indicated by the red temperature iso-contours at $T \in \{800, 1000, 1200, 1600, 1800, 2000\}$K.

The configuration was experimentally investigated in a series of studies, analyzing the thermo-chemical state of the jet with optical measurements (Bergmann et al., 1998; Meier et al., 2000), and obtaining the flow field using Laser Doppler Velocimetry (LDV) (Schneider et al., 2003). Subsequently the case has been the subject of various LES studies. Kempf et al. (2001) used a low Mach number LES with a tabulated chemistry model to study this configuration. Ihme, Bodony, and Pitsch (2006) also used tabulated chemistry to analyze the combustion noise. Frank, Kaiser, and Oefelein (2011) applied this test case, to study the effect of LES filtering on scalar transport. More recently Ventosa Molina et al. (2017) revisited the case, noting the difficulty to predict the flame anchoring using LES. As the focus of the present section is the assessment of the low-dissipation discretization strategy, the flame stabilization is forced here. This is achieved by including only the stable branch of counterflow diffusion flamelets in the thermo-chemical tables.

Governing equations

The present case is modeled with the flamelet/progress variable approach of Pierce and Moin (2004), however the gas states are limited to the stable branch. The thermo-chemical table is FPDF integrated in a pre-processing step using $\widetilde{P}_{ZC} = \widetilde{P}_Z^{\beta}\widetilde{P}_C^{\delta}$, as discussed in section 5.4.3. Thus besides the Navier-Stokes equations (Eq. (5.30) and Eq. (5.47)), filtered scalar equations are solved for enthalpy, mixture fraction, and progress variable (Eq. (5.117)), and the sub-grid variance of mixture fraction is likewise transported characterizing the sub-grid chemistry effects (Eq. (5.122)). The complete set of solved PDEs is:

$$\partial_t \overline{\rho} + \nabla \cdot (\overline{\rho}\widetilde{\mathbf{u}}) = 0 \tag{6.97}$$

$$\partial_t (\overline{\rho}\widetilde{\mathbf{u}}) + \nabla \cdot (\overline{\rho}\widetilde{\mathbf{u}} \otimes \widetilde{\mathbf{u}}) + \nabla \overline{p} - \nabla \cdot \left(2\left(\overline{\mu} + \overline{\rho}\nu^{SGS}\right)\widetilde{\mathbf{S}^{\mathbf{D}}(\mathbf{u})}\right) = 0 \tag{6.98}$$

$$\partial_t\left(\overline{\rho}\widetilde{h}\right)+\nabla\cdot\left(\overline{\rho}\widetilde{h}\widetilde{\mathbf{u}}\right)-\nabla\cdot\left(\overline{\rho}\left(\widetilde{\mathcal{D}_t}+\frac{\nu^{SGS}}{Pr^{SGS}}\right)\nabla\widetilde{h}\right)=0 \tag{6.99}$$

$$\partial_t\left(\overline{\rho}\widetilde{Z}\right)+\nabla\cdot\left(\overline{\rho}\widetilde{Z}\widetilde{\mathbf{u}}\right)-\nabla\cdot\left(\overline{\rho}\left(\widetilde{\mathcal{D}_t}+\frac{\nu^{SGS}}{Sc^{SGS}}\right)\nabla\widetilde{Z}\right)=0 \tag{6.100}$$

$$\partial_t\left(\overline{\rho}\widetilde{Y_c}\right)+\nabla\cdot\left(\overline{\rho}\widetilde{Y_c}\widetilde{\mathbf{u}}\right)-\nabla\cdot\left(\overline{\rho}\left(\widetilde{\mathcal{D}_t}+\frac{\nu^{SGS}}{Sc^{SGS}}\right)\nabla\widetilde{Y_c}\right)=\overline{\dot{\omega}_{Y_c}} \tag{6.101}$$

$$\partial_t\left(\overline{\rho}Z_v\right)+\nabla\cdot\left(\overline{\rho}Z_v\widetilde{\mathbf{u}}\right)-\nabla\cdot\left(\overline{\rho}\left(\widetilde{\mathcal{D}_t}+\frac{\nu^{SGS}}{Sc^{SGS}}\right)\nabla Z_v\right)= 2\frac{\overline{\rho}\nu^{SGS}}{Sc^{SGS}}\nabla\widetilde{Z}\cdot\nabla\widetilde{Z}-\overline{\rho}\chi_Z^{SGS}, \tag{6.102}$$

where the Vreman model is used for the sub-grid viscosity and diffusivity closure, and the unity Lewis number assumption is applied to all scalars. The model constants are selected as $Pr^{SGS}=Sc^{SGS}=0.7$, and $c=0.1$. (Vreman, 2004) The non-conservative form of these governing equations is discretized using the presented finite element scheme.

Computational grid

Two unstructured meshes are used to simulate this case, referred to as "coarse" and "fine". The jet axis is aligned with the x direction. The primary interest of the present analysis, is to assess the jet behavior up to the measurement location at $x=20D$ illustrated on Fig. 6.33. This region of interest corresponds to the refinement region in the two meshes. The main mesh properties are listed in Tab. 6.5. The coarse one is a rectangular domain, with a width of 1.4 m and a length of 2 m. A fully tetrahedral unstructured mesh is applied in this case with 5.7 million elements, and 970000 nodal degrees of freedom. An element size of 60 mm is set in the far field, the mesh around the jet is refined in 3 steps, with a mesh size of $h=4$ mm up to $x/D=125$, $h=2$ mm up to $x/D=45$, and $h=1$ mm up to $x/D=22.5$. The refinement regions are following the expected jet spreading angle. This mesh is illustrated in Fig. 6.34a, showing, that indeed this domain is suitable to capture the mesh over a long axial distance with certain accuracy.

TABLE 6.5: Grid properties of the DLR-A jet flame case.

	Δ_{axial}	Δ_{radial}	N_e	DoF
Coarse	1.0 mm	1.0 mm	5.7M	970k
Fine	0.5 mm	0.2 .. 1.0 mm	14M	6.9M

The fine mesh has a reduced domain size with a width of 0.24 m and a length of only 0.48 m, tailored to represent only the region of interest. A cross section of the domain is displayed in Fig. 6.34b, with the area highlighted by the solid rectangle corresponding to a section of $x/D=25$ length. Comparing the similar highlighted areas in Figs. 6.34a and b, indeed the fine mesh domain is significantly smaller, in order to accommodate the required resolution with only a moderate increase in the number of degrees of freedom. The fine grid consists of 14 million elements, most of which are prismatic, and 6.9 million nodal degrees of freedom. Up to $x/D=30$ the mesh is extruded from the plane of the inlet with a size of $\Delta_{axial}=0.5$ mm in the axial direction. The remaining part $(x/D>30)$ is a buffer region with unstructured tetrahedral mesh. The inlet plane is discretized with a base size of 5 mm in the far

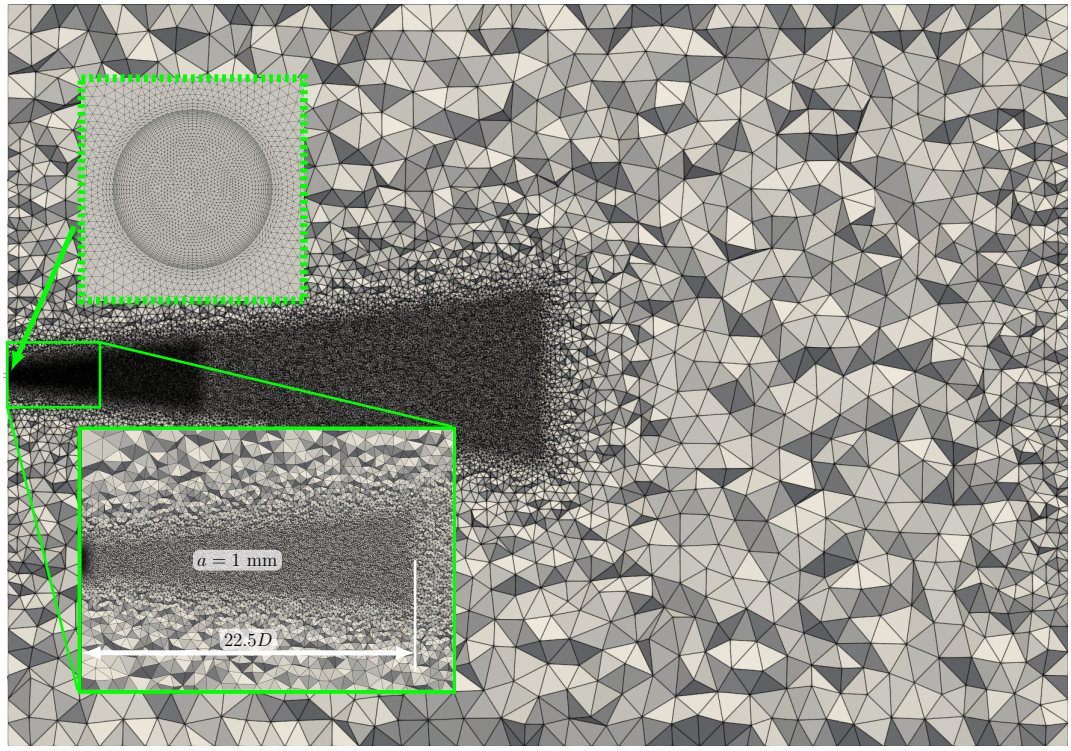

(A) Cross section of domain with coarse grid.

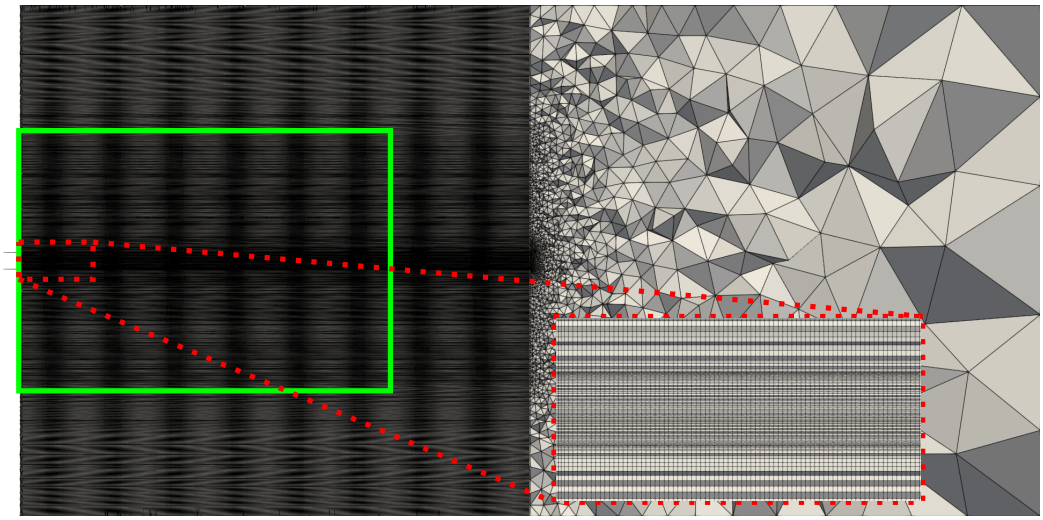

(B) Cross section of domain with fine grid.

FIGURE 6.34: Coarse and fine DLR-A jet grids. The solid green rectangle marks the region of interest with an axial length of $25D$.

field, it has a refinement region with a 0.06 m radius with a size of 1 mm, which decreases to 0.25 mm in the vicinity of the nozzle.

In order to ensure a consistency between the boundary conditions in the coarse and fine meshes, the same surface mesh is applied for the fuel inlet. The center of the inlet is meshed with triangles of 0.2 mm edge length, and the surface is further refined near the edge of the inlet, thus it is capable of representing the fully developed

boundary layer of the turbulent pipe flow to a sufficient degree. The inlet mesh is shown in Fig. 6.34a. A synthetic turbulent inlet velocity is imposed on this grid, the technique is further detailed below.

Tabulation strategy

The thermo-chemical states are represented by stable counterflow flamelets only, following the flamelet model of Peters (1984). Nevertheless, the laminar flamelets are parameterized by mixture fraction and progress variable as in the model of Pierce and Moin (2004). This ensures, that a single tabulation strategy is used here and in other cases where strain induced localized extinction is to be modeled. Counterflow diffusion flamelets are computed using the GRI3.0 mechanism (Smith et al., 2011) with imposing the pure fuel and oxidizer conditions on the boundaries. The progress variable is defined as:

$$Y_c = a_{CO_2} Y_{CO_2} + a_{CO} Y_{CO} + a_{H_2O} Y_{H_2O}, \tag{6.103}$$

with $a_{CO_2} = \frac{2}{W_{CO_2} \sum(a_k)}$, $a_{CO} = \frac{1}{W_{CO} \sum(a_k)}$, and $a_{H_2O} = \frac{2}{W_{H_2O} \sum(a_k)}$, where $\sum(a_k)$ is the sum of these weights prior to the division by this factor, thus the final a_k weights sum to 1. The turbulence-chemistry interaction is considered using a joint FPDF of: $\widetilde{P}_{ZC} = \widetilde{P}_Z^{\beta} \widetilde{P}_C^{\delta}$, where the β-function is only used for the mixture fraction. The necessary material properties, and the source term of the progress variable are integrated with the FPDF *a priori* and tabulated according to section 5.4.4.

TABLE 6.6: Flamelet properties under the studied conditions of the DLR-A jet flame using the unity Lewis number assumption and the GRI3.0 (Smith et al., 2011) chemical mechanism.

Z_{st}	0.167
a^{ext}	1178.8/s
χ_{st}^{ext}	294.6/s
δ_{diff}^{ext}	0.194 mm
$\tau_c^{ext,\chi}$	65.7 μs
τ_c^{ω}	104.0 μs

As discussed in section 5.3.1, the extinction point gives a good measure for the overall chemical behavior of the system. The main properties of the extinction point under the conditions of the DLR jet flames are summarized in Tab. 6.6. The gas mixture is somewhat more resistant to extinction than pure methane, which reflects in the higher extinguishing strain rate. The stoichiometric mixture fraction is quite high: $Z_{st} = 0.167$ compared to common pure fuels summarized in Tab. 2.2, since the fuel is considerably diluted by molecular nitrogen. Consequently, the stoichiometric scalar dissipation rate at the extinction point is significantly higher than in the case of methane. The diffusive thickness based on the thermal diffusivity of the oxidizer, as defined in Eq. (5.99), is approximately equal to the radial size of the smallest elements in the fine mesh, however with proper sub-grid modeling the applied grids are considered adequate. Note, that this is the smallest possible flame thickness and lower strain regions exhibit a significantly thicker flame, thus the grid resolution requirements are not as stringent as δ_{diff}^{ext} might suggest. The chemical time scales (Eq. (5.103) and Eq. (5.104)) are similar to those of methane, and they are captured

well by the explicit time marching scheme, which necessitates $\delta t = \mathcal{O}(1\ \mu s)$ to maintain numerical stability.

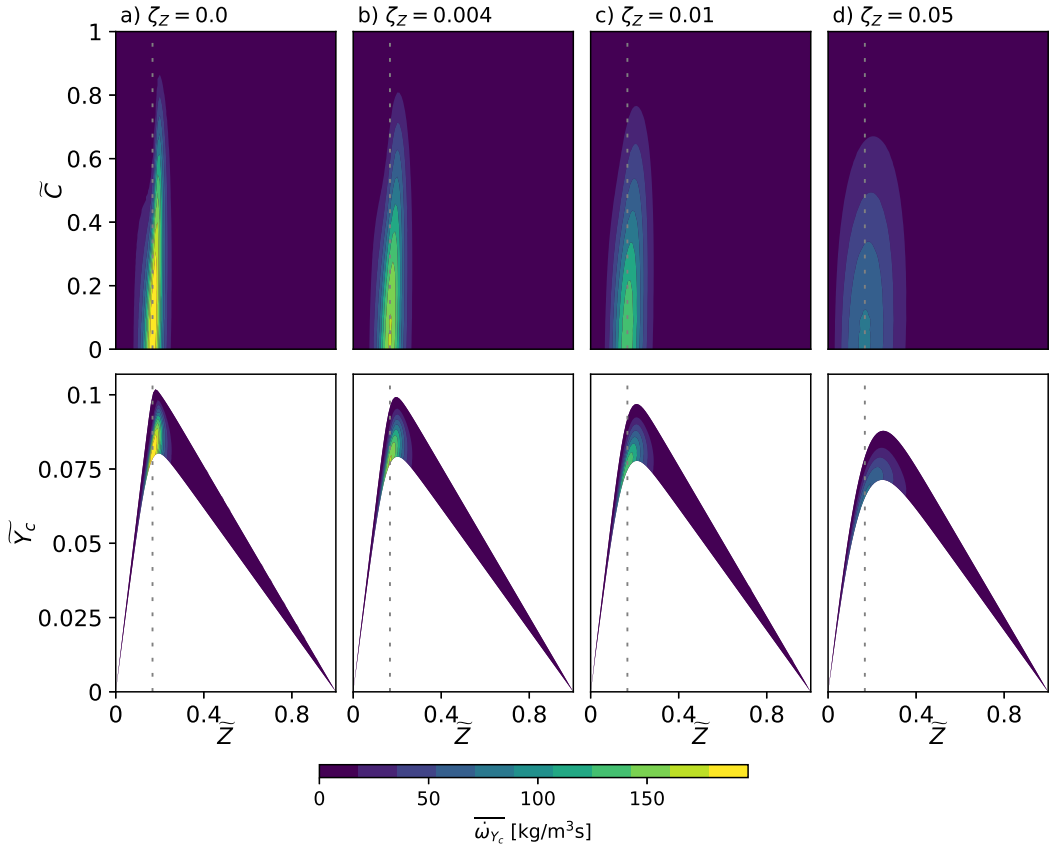

FIGURE 6.35: Illustration of the thermo-chemical table for the DLR-A jet simulation. The filtered progress variable source term contours are presented on the $\widetilde{Z} - \widetilde{C}$ and $\widetilde{Z} - \widetilde{Y_c}$ planes at various scaled mixture fraction variance values. The dashed line indicates the stoichiometric mixture fraction: $Z_{st} = 0.167$.

The FPDF-integrated thermo-chemical table is illustrated by the progress variable source term on the $\widetilde{Z} - \widetilde{C}$ and $\widetilde{Z} - \widetilde{Y_c}$ planes in Fig. 6.35 using various scaled mixture fraction variance levels. The reactions are concentrated to a small region around Z_{st}. As the scaled variance is increased, $\overline{\dot{\omega}_{Y_c}}$ drops significantly within the first 5% of the valid variance values, while the limits of progress variable decrease as well.

Turbulent inlet velocity profile

As the fuel inlet pipe is not included in the simulation domain, an inlet velocity profile with synthetic fluctuations is imposed in order to model the fully developed pipe flow. As discussed above, the same boundary condition is imposed on both the fine and coarse meshes, to mitigate the uncertainty of the present modeling decisions. The synthetic turbulent inlet model of Kempf, Klein, and Janicka (2005) was adapted in the work of Chrysokentis (2019) to use in Alya, and it is applied here as well. This method generates a spatially continuous mass conserving turbulent velocity field, with a single dominant length scale: ℓ_{in} and an RMS value of unity. This

turbulent filed has to be superimposed to a mean flow, with appropriate scaling to attain realistic RMS values. The mean profile is reconstructed from the log-law of wall bounded flows, using second order continuous polynomial interpolation in the core and buffer regions. (Pope, 2000, §7.1) Meanwhile, the RMS profiles are taken from the DNS data of El Khoury et al. (2013).

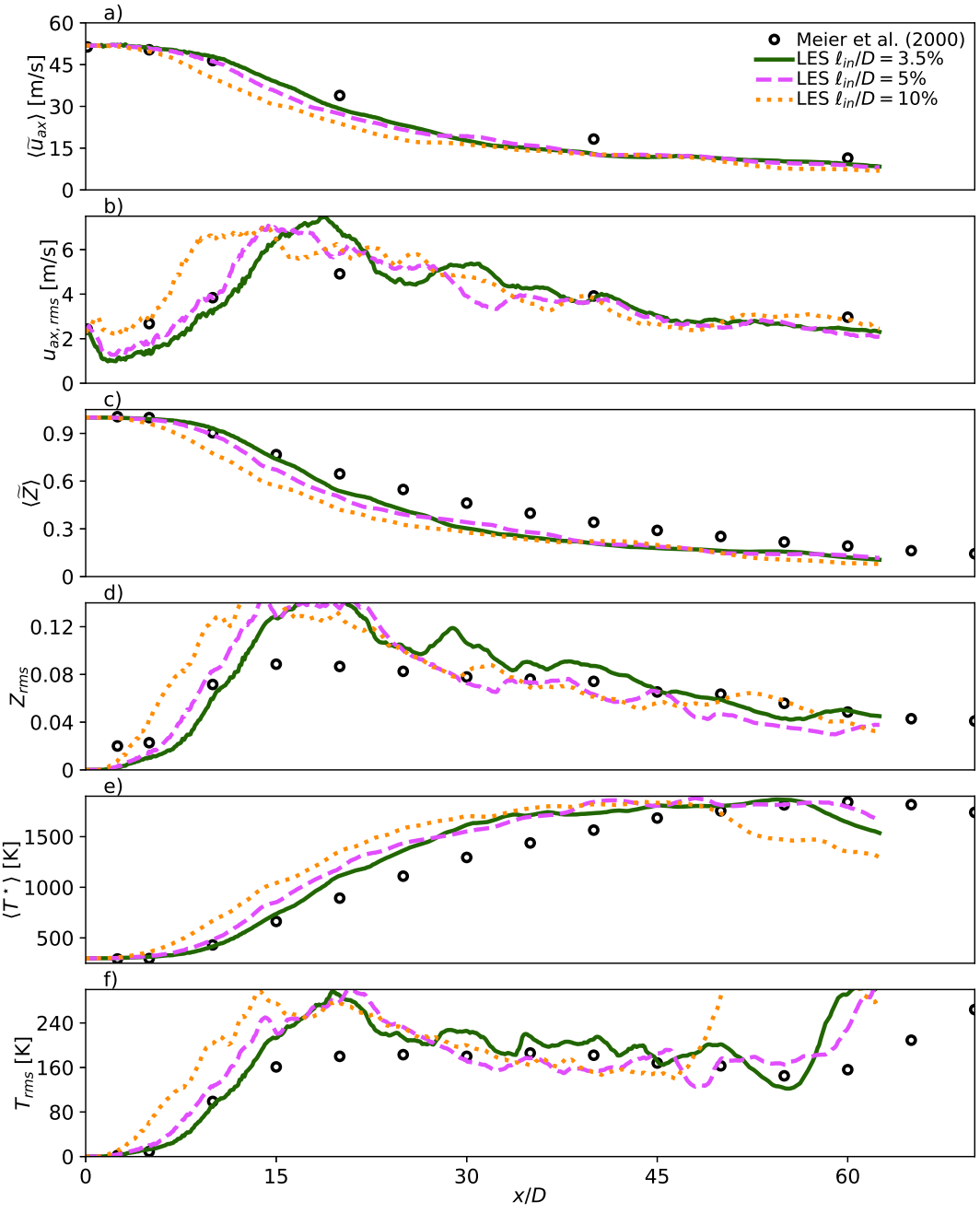

FIGURE 6.36: Sensitivity of velocity and scalar profiles to the turbulent boundary condition on the axis of the DLR-A jet flame using the coarse mesh.

The final, appropriately scaled turbulent database can be understood as an instantaneous turbulent field in space. The fluctuations have to be injected through the boundary at a rate consistent with Taylor's hypothesis of frozen turbulence. I.e.:

if the extruded coordinate in the database is discretized by steps of: Δ_x^{DB}, then this discretization corresponds to time steps of: $\delta t^{DB} = \frac{\Delta_x^{DB}}{U_0}$, where the bulk velocity of the pipe is used to establish the correspondence. There are various requirements on the parameters of the database. The length scale: ℓ_{in} shall be well represented both on the inlet mesh, and in the extruded dimension. Furthermore, the length of the extrusion shall be significantly larger than the length scales. Upon conversion to time by dividing with the bulk velocity, the total length of the domain shall be larger than characteristic time scales of the simulated system, to avoid spurious interference between the two inlet and the flame behavior.

Given that the discretization of the database is satisfactory, the only real degree of freedom in such an inlet strategy is the length scale: ℓ_{in}. The sensitivity to this parameter is explored in Fig. 6.36, where a slightly different numerical method is used affecting mainly the scalar transport, which manifest in overestimated scalar RMS values. Nevertheless, the comparison is sufficient to assess different inlet length scales. The figure presents the statistics of axial velocity, mixture fraction, and temperature along the axis of the jet. The mean profiles are calculated by time averaging the resolved velocity and mixture fraction, and the temperature recovered from the tabulated NASA polynomials with the resolved enthalpy. The RMS values are obtained analogously to Eq. (6.63). In this *a priori* sensitivity study the lowest assessed length scale: $\ell_{in} = 0.035D$ gives the best correspondence with the experimental data. Meanwhile the two larger assessed scales result in lower velocities and higher temperatures on the axis, as the jet starts to decay at a more upstream location. Note, that a fully laminar inlet profile is also testes, which result in severe over-prediction of the jet penetration with an intact jet core up to $x \approx 15D$ (not shown here.) In the final assessment, the $\ell_{in} = 0.035D$ turbulent inlet database is used, with $\delta t^{DB} = 3.7\ \mu$s, and 7500 steps. The selected time step is adequate to represent the length scale.

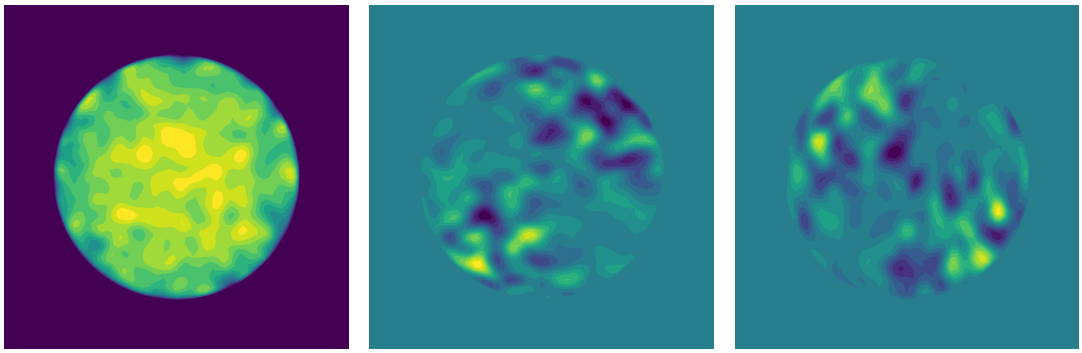

(A) Axial velocity. (B) First in-plane velocity. (C) Second in-plane velocity.

FIGURE 6.37: Illustration of instantaneous fields of the turbulent boundary condition in the DLR-A jet flame with $\ell_{in} = 0.035D$.

An instantaneous snapshot of this final inlet profile is presented in Fig. 6.37. The length scale of $\ell_{in} = 0.035D$ is among the smallest scales that can be represented on the applied inlet mesh. The axial inlet profile is dictated by the log-law, showing consistently higher velocities in the center of the inlet. Meanwhile the in-plane components have a mean value of zero.

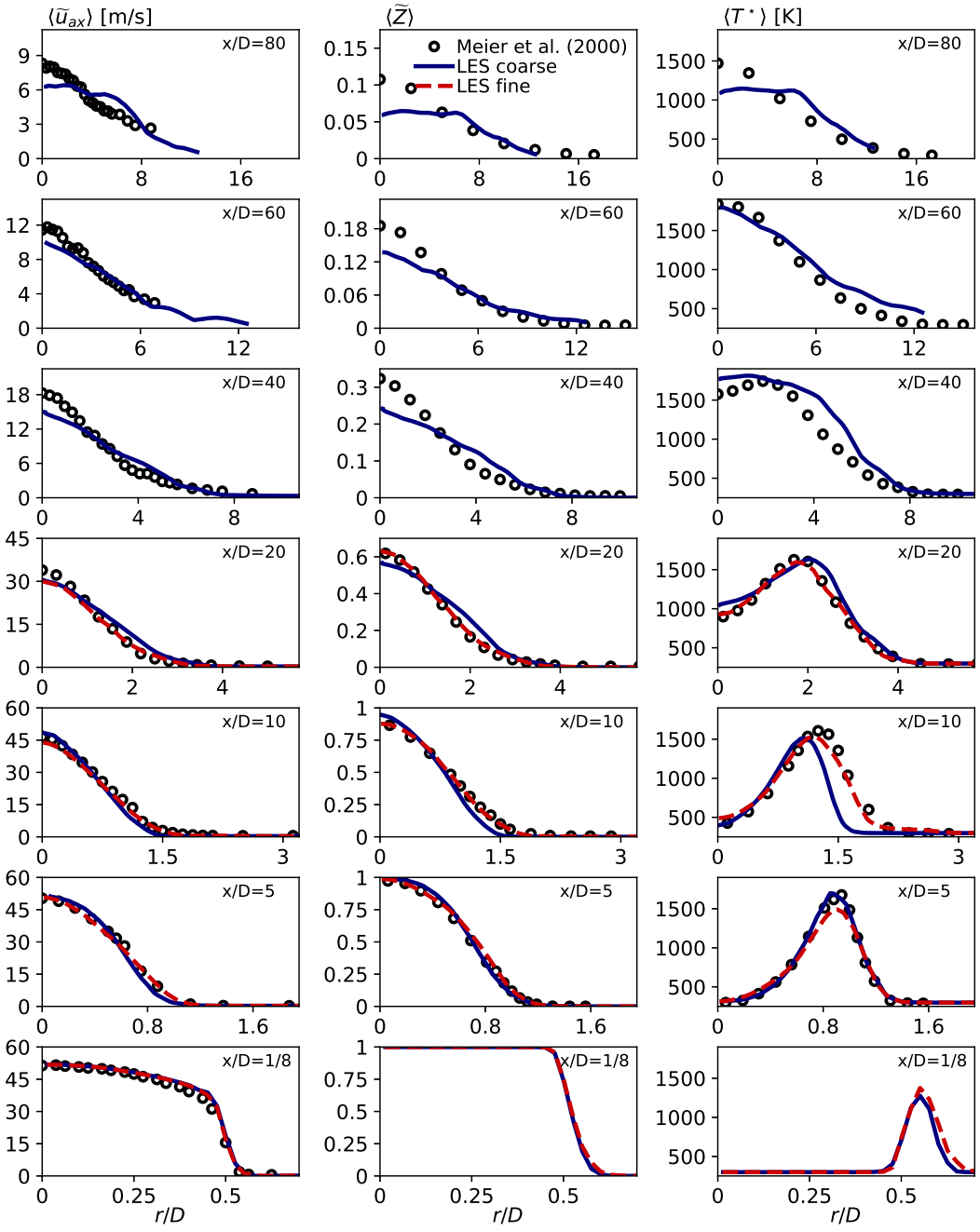

FIGURE 6.38: Comparison of mean profiles in the DLR A jet flame at various axial locations: $x \in \{1/8D, 5D, 10D, 20D, 40D, 60D, 80D\}$. The three columns show the time averaged axial velocity, mixture fraction, and temperature. Symbols indicate the measurement results of Meier et al. (2000), while the solid and dashed lines shows the present LES results on the coarse and fine grids respectively.

Results

The mean and RMS results of the present LES are compared to the measurements of Meier et al. (2000) and Schneider et al. (2003) to assess the quality of the numerical scheme. Figure 6.38 presents the radial profiles of time averaged quantities along different axial locations in the jet corresponding to the rows of plots. The results

of the coarse mesh are sampled at all available measurement locations, while the fine mesh is only evaluated at $x/D < 30$ where the refinement is sufficient. The displayed range of radii is varied along the jet according to $\max(r/D) = 0.7 + 0.25x/D$, in order to approximately follow the spreading of the flow. At the first axial location of $x = 1$ mm in the lowermost row of plots only the LDV flow field measurement data is available. This indicates, that using the log-law profile extended to the core and buffer regions with polynomial fits, is indeed an adequate representation of the flow. In the same location the mixture fraction field is undisturbed in nearly the entire inlet area, and shows a sharp gradient at the edge of the jet. The flame is located outside this jet core, at radii of $r/D > 0.5$. At this location the result of the two meshes is practically identical except for a slightly wider spreading of Z in the fine mesh, causing a wider flame profile.

As the flow progresses downstream, the jet spreads and exchanges mass and momentum with the oxidizer co-flow. The peaks of velocity and mixture fraction decrease. Meanwhile the peak temperature is approximately maintained, as long as stoichiometric mixtures are consistently present in the flame, which holds up to $x/D = 60$. The differences between the coarse and fine grid simulations accumulate with the height above the burner. The fine mesh shows a very good agreement with the measurement, with only minor discrepancies in the maximum of $\langle T^\star \rangle$ at $x \in \{5D, 10D\}$, and a small velocity deficit near the axis at $x/D = 20$. The results on the coarse mesh change in nature depending on the axial location. Up to $x/D = 10$, the coarse mesh simulations under-predict the jet spreading, while at higher locations the width is over-predicted with deficits in the peak $\langle \widetilde{u}_{ax} \rangle$ and $\left\langle \widetilde{Z} \right\rangle$. At higher axial locations outside the region of interest ($x/D \geq 40$), the quality of the coarse mesh simulation remains approximately constant, heavily affected by the initial discrepancies. Note, that this part is displayed for the sake of completeness, however, it is not the focus of the present evaluation.

The RMS profiles displayed in Fig. 6.39 further illustrate the jet behavior. In the locations of $x \in \{5D, 10D, 20D\}$ the peak RMS values are approximately constant. Furthermore, there is a clear increase in the axial velocity RMS from the inlet condition towards downstream. This inlet is captured to a satisfactory extent by the imposed turbulent inlet on both meshes. The fine mesh simulation is capable of predicting the initial increase of $u_{ax,rms}$, alas it somewhat over-predicts the mixture fraction fluctuations. In this case the temperature RMS is captured well, except a minor discrepancy at $x/D = 10$ at outer radii. Observing the instantaneous temperature contours in Fig. 6.33, this is likely related to the transition point where the turbulent motion becomes capable of deforming the outer edge of the flame. The dual behavior of the coarse mesh is likewise better explained by the RMS values. At $x/D = 5$ the coarse grid simulations consistently under predict all fluctuations. This initially less turbulent behavior delays the aforementioned turbulent transition of the outer edge of the flame to more downstream than $x/D = 10$. Interestingly, once this transition occurs, the quality of the coarse LES results slightly improves at $x/D = 20$, both in terms of mean (Fig. 6.38) and RMS (Fig. 6.39) values.

Finally, the statistics of axial velocity, mixture fraction, and temperature are also evaluated along the axis of the jet in Fig. 6.40. Up to a distance of approximately $5D$ the jet core appears to be intact, as all average quantities stay constant and the RMS values are minimal. Further downstream the effects of the jet decay reach the centerline. As the jet exchanges momentum and mass with the environment, the mean centerline velocity and mixture fraction decreases, meanwhile the corresponding RMS values reach a peak around $x \approx 15D$ and show a decay after this point. The

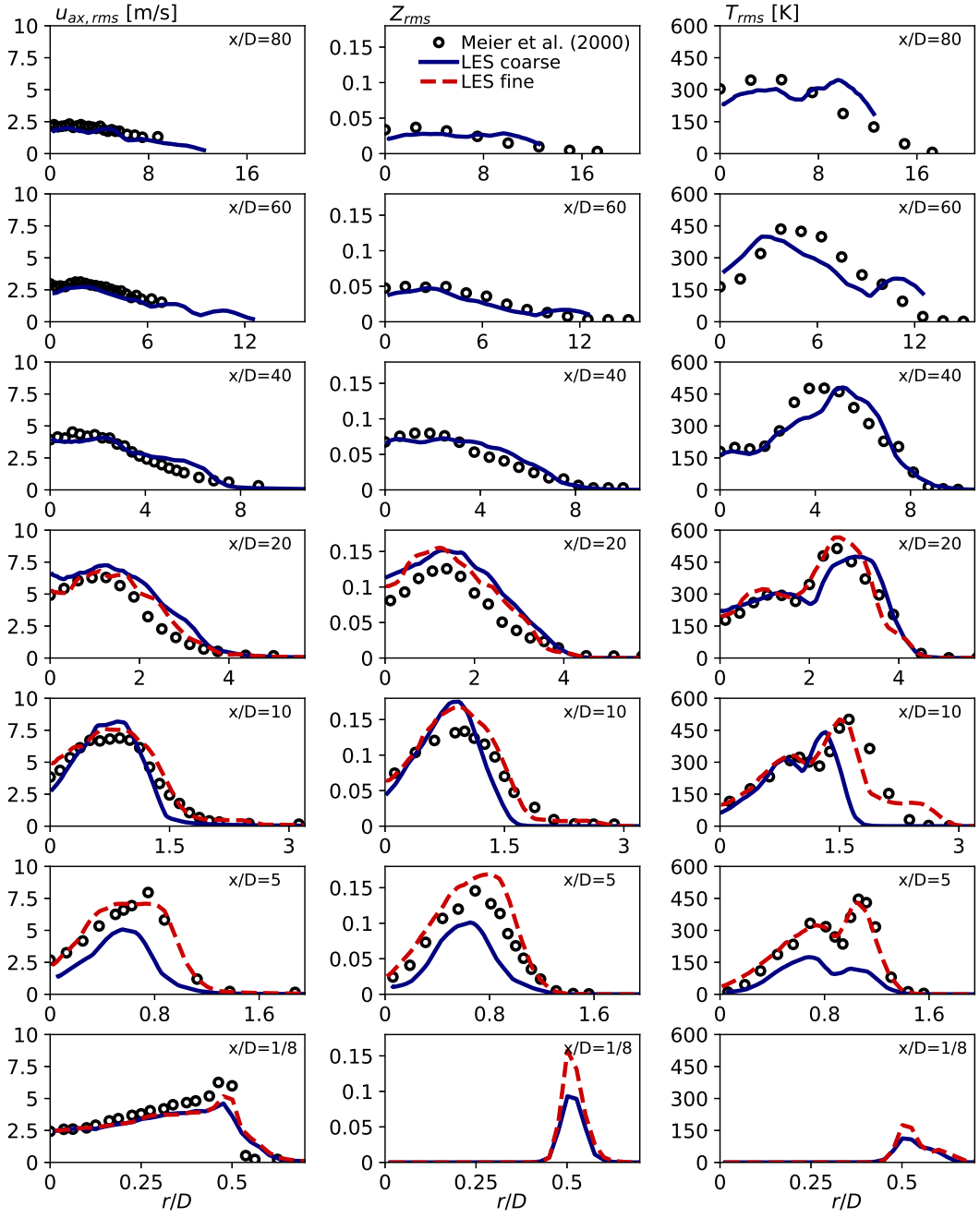

FIGURE 6.39: Comparison of RMS profiles in the DLR A jet flame at various axial locations: $x \in \{1/8D, 5D, 10D, 20D, 40D, 60D, 80D\}$. The three columns show the RMS of axial velocity, mixture fraction, and temperature. Symbols indicate the measurement results of Meier et al. (2000), while the solid and dashed lines shows the present LES results on the coarse and fine grids respectively.

decrease of the mixture fraction entails, that higher and higher temperature products can be present on the centerline. Consequently, the mean temperature increases along the axis until $x \approx 60D$, beyond which the mixture becomes lean and temperatures decrease again. The RMS of the temperature shows multiple peaks. The first one around $x \approx 20D$ is associated to the high fluctuations in mixture fraction. The

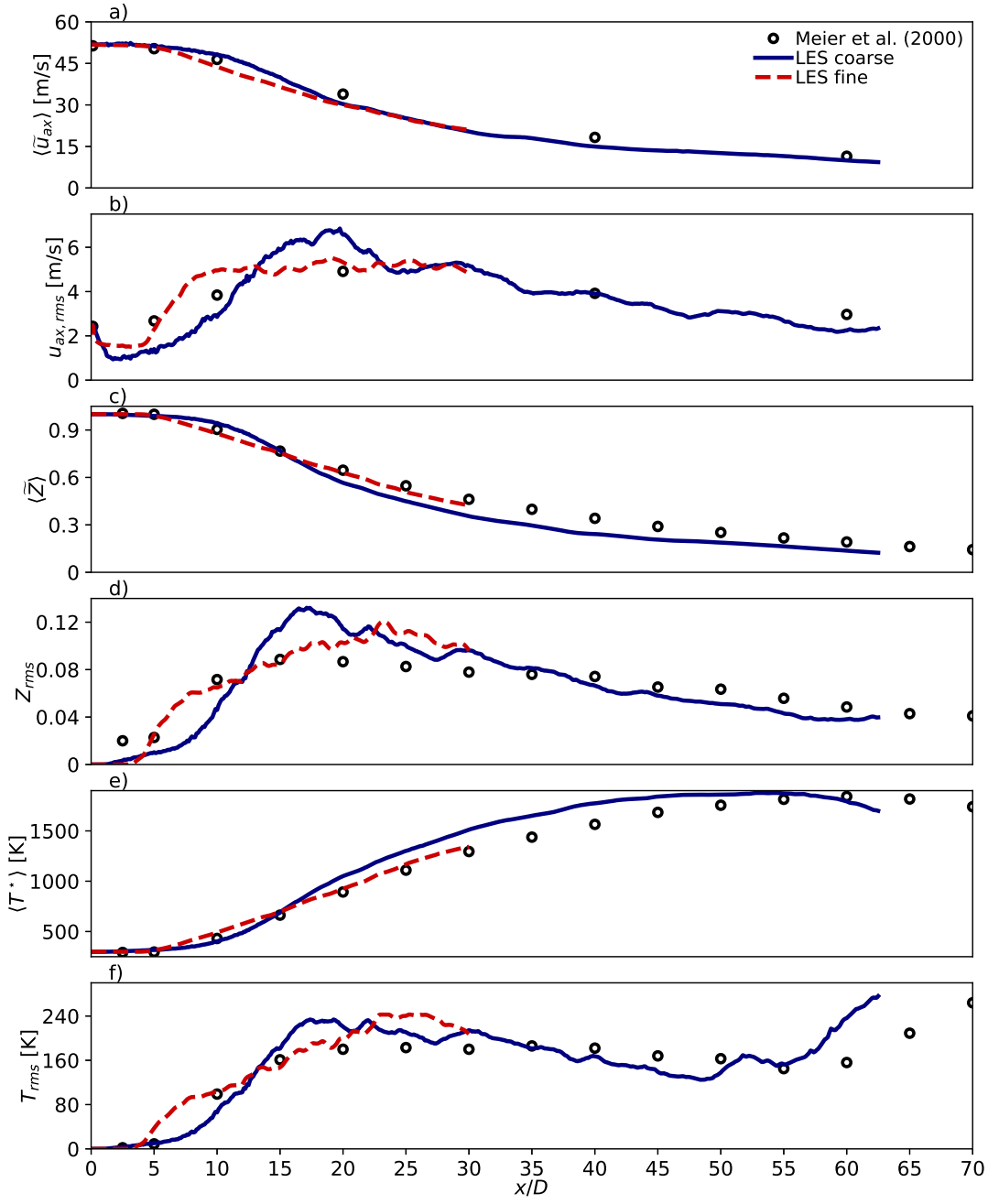

FIGURE 6.40: Comparison of mean and RMS profiles in the DLR-A jet flame on the jet axis. The rows show the mean and RMS of axial velocity, mixture fraction, and temperature. Symbols indicate the measurement results of Meier et al. (2000), while the solid and dashed lines shows the present LES results on the coarse and fine grids respectively.

second peak is beyond the displayed range, and corresponds to the higher sensitivity of temperature to mixture fraction fluctuations in lean mixtures. In a generic view, the same Z_{rms} corresponds to a higher T_{rms} if $\left\langle \widetilde{Z} \right\rangle$ is below the stoichiometric mixture fraction.

The LES results on the two meshes are displayed along the experimental values in Fig. 6.40. Note, that the coarse mesh results are only post-processed up to $x = 0.5$ m, while the fine mesh is restricted to the refinement region up to $x = 30D = 0.24$ m. Both simulations reproduce the general trends well, and the observed discrepancies are in alignment with the analysis of the radial profiles. In the coarse grid LES the mean velocity and mixture fraction are slightly over-predicted at $x = 10D$, where the corresponding RMS values are too low. Further downstream this case shows an over-prediction of the $u_{ax,rms}$ and Z_{rms} maxima, corresponding to the change of behavior of the case discussed above. Downstream of these two intense RMS peaks the mean values are under-predicted. The temperature is largely a consequence of the mixture fraction, where under-predictions of $\left\langle \widetilde{Z} \right\rangle$ correspond to over-predictions of $\langle T^{\star} \rangle$. Because of the too intense spreading, the coarse mesh under-predicts the flame length, with the temperature maximum along the axis located at $x = 53D$. The onset of the second increase in T_{rms} is linked to this maximum location, and it is likewise shifted upstream. The mesh refinement generally corresponds to an improvement in the region of interest. In this case the decay of the axial velocity starts slightly more upstream than the experiments predict. Indeed, the velocity RMS rises sharper in the $x \in [5D, 10D]$ interval, than it should. Further adjustments of the inlet boundary condition could potentially improve this behavior, however this is out of the scope of the present study. The mixture fraction profile shows similar tendencies, however in this case the correspondence with the measurements is significantly better, and it is improved compared to the coarse mesh LES. The mean and RMS of temperature also show a good agreement, as a consequence of improved Z predictions.

To gauge the grid quality, the Kolmogorov scale is assessed using the method outlined in section 5.1.6 based on the temporal data sampled at $x = 5D$ and $x = 10D$ on the jet axis. Interestingly, using both meshes $\eta \approx 35\mu$m is found in the former point, and $\eta \approx 26\mu$m in the latter, indicating that the Vreman sub-grid model is capable of predicting the sub-grid phenomena to a good degree. In fact, in the coarse mesh more than 90% of the turbulent kinetic energy dissipation is due to the sub-grid model, while in the fine mesh this figure is only $\sim 65\%$. In these studied locations, the coarse mesh is characterized by tetrahedral elements of edge length $h = 1$ mm corresponding to a filter size of $\Delta_f \approx 0.5$ mm. Meanwhile, the prismatic elements of the fine mesh feature edge lengths of $h = 0.2$ mm on the triangular face, with an element height of $\Delta_{axial} = 0.5$ mm, which corresponds to a filter length of $\Delta_f = \sqrt[3]{\Delta_{axial} \frac{\sqrt{3}}{4} h^2} \approx 0.21$ mm. In these points, the ratio of Δ_f to the Kolmogorov scale is similar in the present fine mesh and in the grid applied in the PRECCINSTA burner in section 6.5.1. This indicates, that the present numerical scheme performs well with $\Delta_f / \eta \approx 10$, while coarser grids are missing some of the key phenomena affecting the turbulent transition of the outer flame edge.

Overall, the low-dissipation finite element scheme of the present work behaves well in the DLR-A turbulent diffusion jet flame as well. This gives further confidence in the implementation of the framework, and in the coupling with tabulated chemistry method, in a case featuring large density ratios, and challenging turbulent behavior.

6.6 Overall performance of the numerical scheme

This chapter introduces a low-dissipation finite element scheme for low Mach number flows. The scheme is used with an explicit third order Runge-Kutta method in the simulation of laminar flows and in the context of large-eddy simulation. In the latter case appropriate sub-grid models are applied. The complete spatio-temporal discretization scheme using finite elements and explicit time integration is presented. The developed strategy exploits the stabilizing effect introduced by using an approximate Laplacian to stabilize the pressure equation. Otherwise no additional stabilization is introduced for the mass and momentum conservation. The error of kinetic energy conservation is of order $\mathcal{O}(\delta t\, h^{k+1})$, thus dissipation is limited given that the mesh is sufficiently fine. The finite element representation of the Eulerian gas phase is coupled to the Lagrangian phase in a conservative manner. This is particularly important is combustion simulation, where the spray injection can have a non-negligible effect on the velocity field, and the transfer of mass directly affects the local mixture fraction, which is a crucial property to predict. Only a minimal amount of model constants are associated to the used LES model. The present work refrains from tuning these constants, as this would hinder the universal applicability of the scheme in *a priori* unknown cases, although the theoretically correct values of these constants may be uncertain.

This numerical scheme is applied to various laminar and turbulent flow fields, in order to illustrate its performance. Firstly the canonical case of a turbulent channel flow is studied, at a wall Reynolds number of $\sim$ 400. The scheme preserves the advantageous behavior of its incompressible counterpart which provided the base of these developments, as a quasi-incompressible turbulent channel flow simulation demonstrates. Subsequently, the channel flow case is evaluated with a significant temperature gradient across the top and bottom walls. The general features of the turbulent heat transfer are captured well, with the LES predicting the macroscopic flow properties with an error below 2%, and recreating the mean and RMS fields to a good extent.

The coupling with tabulated chemistry methods is studied in canonical configurations of methane/air flames corresponding to the flamelets that are used to create the thermo-chemical tables: premixed free flames, and counterflow diffusion flames. In the latter case special care is taken to ensure the correspondence of boundary conditions between the Chem1D finite rate simulations and the tabulated chemistry simulations of Alya. The flame behavior is reproduced to a good extent with only 3% error in the flame speed of premixed flamelet, and 1.8% error in the stoichiometric scalar dissipation rate of the extinction point, given that in each case the thermo-chemical database is constructed from the corresponding flamelets. (I.e.: the exact solution is contained in the lookup table.) The premixed free flame case is used to assess the grid sensitivity of flame propagation. In the present finite element framework outstandingly coarse meshes are capable of reproducing the flame propagation with acceptable accuracy using only a few elements across the flame, as the Gaussian quadrature based numerical integration of the source term captures the progress variable production well. The sub-grid models are also assessed in this setup, giving valuable insight to the sub-grid turbulence chemistry interaction model. Small levels of mixture fraction variance are found to cause significant changes in flame propagation, enabling non-zero flame speeds outside the flammability limit, and decreasing the flame speed in near-stoichiometric mixtures significantly. The progress variable variance is found to cause notable differences above a threshold, as certain variance values may double the flame speed. The effect of the addition of a constant sub-grid

viscosity is also assessed, showing a consistent increase in flame propagation speed. While some of these effects may be viewed as an error, correcting them is out of the scope of the present work. Nevertheless, the presented assessment helps gauging the sub-grid effects on flame propagation. Finally, the effect of using manifolds of different flamelets on these canonical cases are assessed. Manifolds based on diffusion flamelets are found to produce large errors in premixed flame propagation, with significant under-prediction of flame speeds near stoichiometry, and the prediction of non-zero flame speeds outside the flammability limits. Meanwhile using a premixed flamelet based manifold in a counterflow diffusion flame seems to modify the flame structure notably, however the extinction point is recovered with good accuracy.

The Lagrangian droplet models are likewise assessed in isolated conditions. First, stand-alone Lagrangian particles are used with prescribing the seen conditions. As these simulations show, the tabulated average representative evaporation state (TARES) model of section 4.3.2 reproduces well the classical "1/3 law" results. Furthermore, the two-way coupling of mass, energy, and momentum exchange is also assessed in specifically designed cases of stand-alone droplets. Indeed, all the exchange of conserved properties is accounted for, both in open and closed domains.

Finally, two turbulent flames are simulated using tabulated chemistry in Alya. Both cases show excellent agreement with experimental results, illustrating the capabilities of the present simulation framework. In the PRECCINSTA confined premixed swirl flame the results of Alya are comparable to other LES studies, and in some aspects show improvement compared to previous Alya simulations using the variational multiscale method. This case is used for assessing the turbulent scale estimation strategy of section 5.1.6. The approximate Kolmogorov scales agree well with the literature, and the integral length scale is identified on the velocity spectra of single point samples using Taylor's hypothesis of frozen turbulence. In the DLR-A jet diffusion flame the results are similarly good quality. Key features of this rather large flame, such as the jet spreading or the flame length, are qualitatively reproduced with a considerably coarse mesh. The mesh is refined in a limited region, showing a clear improvement in the flame behavior.

In conclusion, the developed low Mach number solver behaves well in conjunction with tabulated chemistry methods. While there is room for improvement in accuracy across various sub-models, the overall approach is deemed suitable for the study of turbulent reacting flows with *a priori* unknown features.

Chapter 7

Swirl stabilized hydrogen flame

This chapter presents the analysis of a swirl stabilized hydrogen flame (Reichel, Terhaar, and Paschereit, 2015) using the developed low-dissipation scheme. The relevance of such configurations is highlighted by the widespread usage of swirl combustors in modern gas turbines, as the high enhancement of mixing and the resulting compact and low emissions flames are attractive to for practical applications. (Syred, 2006) The use of LES for the prediction of complex phenomena in gas turbine combustors has been successful in various scenarios. (Zhang and Mastorakos, 2016; Gövert et al., 2018) The present study analyses the inert and reacting conditions of this lab-scale burner operated with hydrogen in lean premixed conditions with a central air injection. Such designs are prone to flame stability problems such as lean blow out (LBO) or flashback. Both are severe risks regarding the operability and safety of the combustion device. Here the burner operation is studied under stable conditions and near the onset of flashback, providing insight to the flashback formation mechanism. Two different tabulated chemistry methods are applied, based on premixed flamelets. These represent different modeling complexity, which is reflected in the quality of the results. Note, that numerical work on this particular configuration is scarce, limited to the study of the mixing and cold flow by Tanneberger et al. (2015), and to the recent study of pollutant formation by Capurso et al. (2023).

The chapter is structured as follows. Section 7.1 introduces the characteristics of the lab-scale burner, including the burner geometry, the functionality of the components, the operating conditions, and the typical thermo-chemical states. The LES simulation of the inert flow are detailed in section 7.2, shortly discussing the computational approach, and assessing the dynamic and mean behavior of the flow. Finally the last two sections analyze the reacting conditions using two different combustion models. Section 7.3 uses a perfectly premixed combustion model based on a single premixed free flamelet corresponding to the global equivalence ratio, similar to the model applied in section 6.5.1. The model is described shortly, and the flame behavior is analyzed in detail in two different operating conditions. Meanwhile, in section 7.4 a more elaborate model is applied, accounting for mixture stratification and wall heat losses by tabulating free and burner-stabilized premixed flamelets at various equivalence ratios. The flame is further analyzed focusing on the non-homogeneity and thermal quenching effects.

Credit

This chapter presents the numerical results of a long term collaboration between the author's group and the experimental research group of Prof. Christian Oliver Paschereit at TU Berlin including Panagiotis Stathopoulos, Tom Tanneberger, and Thoralf Reichel. The applied computational meshes were created by Samuel Gómez González, the simulations were mainly conducted by Daniel Mira, with additional

studies executed by Jonathan Forck (2021) and the author. The present analysis is primarily the joint work of the author and Daniel Mira, with the POD calculations of section 7.2.3 executed by Tom Tanneberger. This work is partially published in Mira et al. (2018), Mira et al. (2020), and Mira, Both, and Surapaneni (2022).

7.1 Burner geometry and operating conditions

Below various details of the studied swirl stabilized hydrogen flame are discussed, including the details of burner geometry, the representative chemical scales of hydrogen combustion under preheated conditions at ambient pressure, and the specific behavior of the configuration in terms of flame stability.

7.1.1 General behavior of swirl flames

Introducing swirling motion in the combustion chamber is an effective way to promote the mixing of reactants prior to combustion, and to ensure flame stabilization in the combustion chamber. The concept is illustrated in a generic case in Fig. 7.1. This axisymmetric example features a mixing tube on the left, characterized by a strong swirling motion in addition to the axial flow. The mixing tube is connected by a sharp expansion to the combustion chamber on the right. The flame is stabilized at this sudden transition as the flow conditions change.

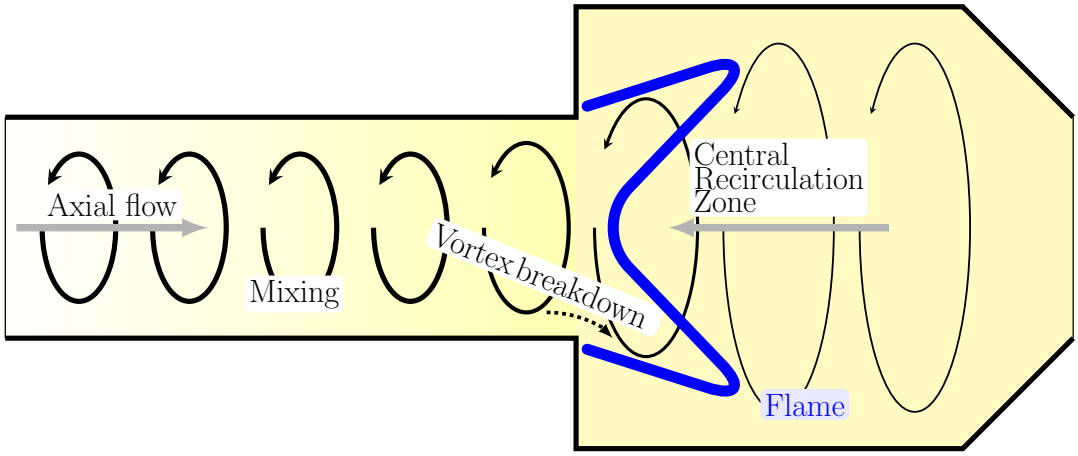

FIGURE 7.1: Illustration of vortex breakdown in a swirl stabilized flame.

As the swirling flow transitions to the combustion chamber, it faces an axial pressure gradient, which generates the *vortex breakdown*. I.e.: the main flow expands at an angle determined by the axial and swirling (circumferential) velocity components, and as a consequence recirculation occurs along the axis. This flow structure acts as a flame holding mechanism, as in the central region the turbulent flame propagation speed is able to match the axial velocities. Such flames are well-known to be stable for a wide range of operating conditions. (Fritz, Kröner, and Sattelmayer, 2004) Swirl-stabilized flames are commonly used in lean premixed burners, which aim to reduce nitrogen-oxide (NO_x) production by limiting the flame temperature. However, such flames are not exempt of technological challenges. (Kiesewetter, Konle,

and Sattelmayer, 2007; Seidel et al., 2013) One major issue is the existence of thermo-acoustic instabilities, since under lean conditions the global heat release rate is especially sensitive to the local mixture composition, and the long mixing sections introduce a time delay between the fuel inlet manifold and the flame, which promotes the unstable behavior of the system. (Taamallah et al., 2015a) Such features are not studied in this work, as the present hydrogen flame is acoustically stable under the examined conditions. Swirl-stabilization also promotes the existence of a *precessing vortex core* (PVC), which is a helical structure superimposed on the swirling motion, that breaks the symmetry of the flow. (Oberleithner et al., 2013) Such hydrodynamically generated self-excited oscillations can cause significant issues in terms of flame stability. Finally, the stable operation of the burner is also bounded by the limits of lean blow-out (LBO) and flashback. (Oberleithner et al., 2013; Huang and Yang, 2009) The former occurs when the flame is unable to stabilize due to excessively high gas velocities. Meanwhile the latter may happen, if the flame is able to propagate upstream into the mixing section.

These different instabilities ultimately contribute to reducing the operational flexibility of the burner under lean conditions. Instabilities can cause inefficient fuel consumption, high level of noise and eventually combustion hardware damage. There has been a substantial effort on the study of thermo-acoustic instabilities using experiments (Palies et al., 2009), numerical simulations (Noiray, Bothien, and Schuermans, 2011; Staffelbach et al., 2009) and more recently with a joint numerical and experimental approach. (Noh et al., 2019) Hydrodynamic instabilities such as the PVC are also encountered in many swirl-stabilized burners. In general, the PVC is synchronized with helical Kelvin-Helmholtz instabilities that are able to trap the fuel within the PVC leading to strong temporal fuel concentration fluctuations. (Galley et al., 2011) There has been many efforts dedicated to the study and the suppression of this instability. (Burmberger, Hirsch, and Sattelmayer, 2006; Jochmann et al., 2005; Juniper, 2012; Oberleithner et al., 2013) Several mechanisms can be identified as the root cause of damping in both isothermal and reacting flows. Those include a reduction of the circumferential velocities near the jet centerline (Syred, 2006), flame-induced dilatation and increased viscosity (Roux et al., 2005) or more recently density stratification. (Oberleithner et al., 2013) An even more hazardous dynamic phenomenon in premixed combustion is flashback, thus the flashback resistance of a design is of paramount importance. This is particularly relevant when combustors are operated with alternative fuels with varied compositions. (Xiao and Huang, 2016) The complexity of these dynamic phenomena makes the design of lean premixed combustion systems a difficult task, as the interaction of the fluid flow and heat release is hard to capture with elementary models. Thus, such cases provide an ideal use case for high-fidelity simulations, given that these are able to predict the dynamic behavior. This chapter sets out to apply the developed low-dissipation LES tool for the analysis of a premixed combustion system.

7.1.2 Burner configuration

The presently studied swirl stabilized hydrogen burner is designed and experimentally investigated in TU Berlin. For the details of the experimental analysis see the work of Reichel, Terhaar, and Paschereit (2015). (Reichel and Paschereit, 2017; Reichel, Terhaar, and Paschereit, 2018) As flashback is associated to the axial velocities in the mixing element, swirling combustors can benefit form additional axial air injection that reduces the velocity deficit along the centerline, thus providing

additional resistance against flashback. (Reichel, Terhaar, and Paschereit, 2015; Reichel and Paschereit, 2017). Axial air injection influences the location of the flame by displacing the stagnation point of the aerodynamically induced recirculation downstream in the combustion chamber, thus increasing burner stability. The studied configuration applies such an axial air injection mechanism. Burners operated with pure hydrogen require high fuel flow rates as hydrogen has a very low volumetric energy density. This provides the opportunity to introduce additional axial momentum in the system through the fuel jets, as it is done in the studied design.

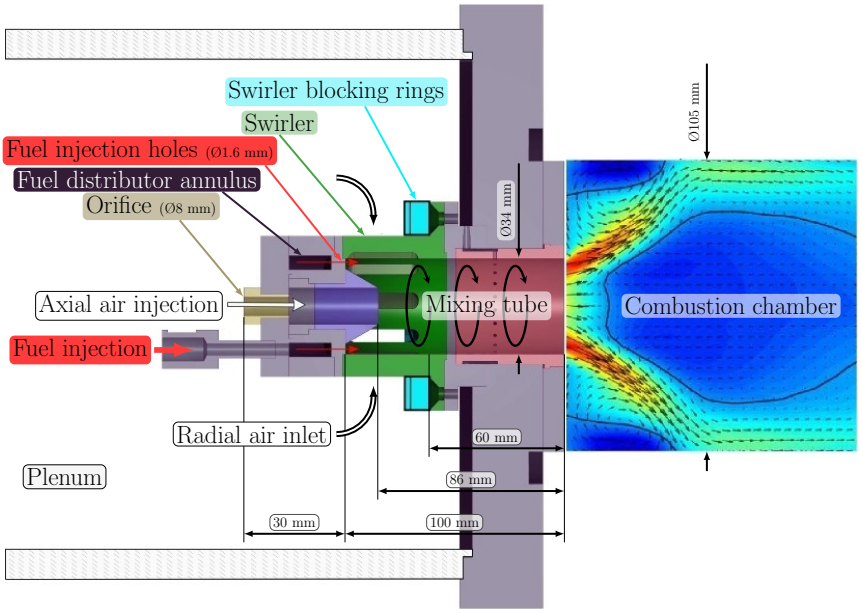

FIGURE 7.2: Illustration of the experimental configuration of the swirl stabilized hydrogen burner adapted from the work of Reichel and Paschereit (2017). (The mixing tube length is not to scale.)

The experimental configuration is depicted in Fig. 7.2. From left to right on the figure, the setup consists of a plenum, a fuel and axial air injection element, a swirler, a mixing tube, and a cylindrical combustion chamber of diameter $D_{CC} = 105$ mm. The preheated air flow is distributed from the plenum to the swirler and the axial air injection. The ratio of flow rates through these elements is determined by the pressure loss across the system. This modular burner design allows for the parametric study of different dimensions. The axial air injection is adjusted by the choice of orifice diameter, while the swirling motion can be adapted by introducing blocking rings on the swirler element, which obstruct part of the cross section. The orifice diameter studied here is $D_{or} = 8$ mm, while the blocking rings cover $h_{br} = 7$ mm of the total swirler inlet. Considering this reduced inlet surface, the swirler element may be characterized by a geometric swirl number of $Sn = 0.9$ following Gupta, Lilley, and Syred (1984).

Fuel injection pipes are passing through the plenum, supplying an annular distributor with hydrogen which injects the fuel into the mixing tube through 16 injection holes of $D_f = 1.6$ mm diameter. These fuel inlets are distributed in an annular pattern between the swirler inlets and the cone shaped central element of the axial air injection. The high speed fuel jets are mixed with the swirled air and the axial jet along a mixing tube, which has a total length of 100 mm from the fuel jets to the combustion chamber and a diameter of $D = 34$ mm. Note, that the mixing tube

length after the swirler element is only 60 mm. At the end of the mixing tube the reactant flow expands over a step change into a cylindrical combustion chamber, with a diameter ratio of 3.1. Further details of the configuration are published by Reichel and Paschereit (2017), and Tanneberger et al. (2015).

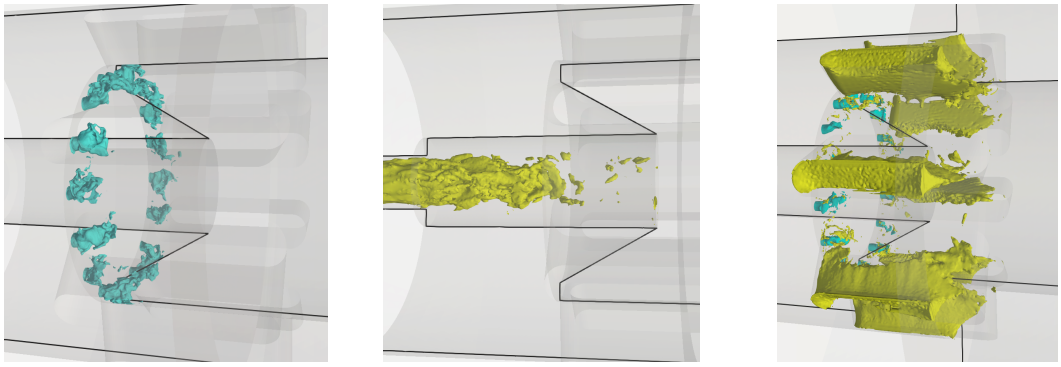

(A) Fuel jets. (B) Axial air jet. (C) Swirled air.

FIGURE 7.3: Illustration of fuel and oxidizer flows in the swirl stabilized hydrogen burner.

The behavior of the fuel and oxidizer inlets is qualitatively illustrated in Fig. 7.3 using the LES results of the present work. Note, that the aim here is to highlight the details of the burner configuration, the LES details are discussed in the remainder of this chapter. The 16 fuel jets are illustrated in Fig. 7.3a using the axial velocity isocontours. These are placed evenly around the conical element of the axial axial air injector. The axial air jet is shown in Fig. 7.3b similarly by an axial velocity contour. The jet flows through the orifice with $D_{or} = 8$ mm, then enters the central pipe of the conical axial air injection element, which has an inner diameter of 13.2 mm. As a result of this expansion the jet decelerates before entering the mixing tube. Finally Fig. 7.3c illustrates the radial flow of the swirler together with the fuel jets. The flow of the 8 swirler vanes is interacting with the hydrogen jets directly, as the axial location of the jets and the lower edge of the vanes is nearly in the same plane. The swirling flow interacts with the axial air jet and the hydrogen jets as they commence to blend along the mixing tube.

7.1.3 Thermo-chemical conditions

The combustor is operated at atmospheric pressure ($P_0 = 101325.0$ Pa) with preheated air at a temperature of $T_{air} = 453$ K. The pure hydrogen fuel is supplied at a lower temperature of $T_{H_2} = 320$ K. The adiabatic flame temperature, the flame speed, and flame thickness are illustrated in Fig. 7.4 at various equivalence ratios, using the San Diego mechanism UCSD (2018) with the unity Lewis number assumption. There are various outstanding differences between this case, and methane cases discussed in section 3.1.1 and section 6.5.1. The adiabatic flame temperature is higher near stoichiometry, however the lean flammability limit is outstandingly low ($\phi_L = 0.2$), where the adiabatic flame temperature predicted by this mechanism is only 1052 K. The rich flammability limit is not of interest here, as the modeled case achieves a good degree of mixing before combustion. A typical feature of hydrogen flames is the high flame speed, which is an order of magnitude higher near stoichiometry, than in than case of methane. Meanwhile the flame thickness is only

slightly smaller than in the previously presented methane cases, but remains the same order of magnitude.

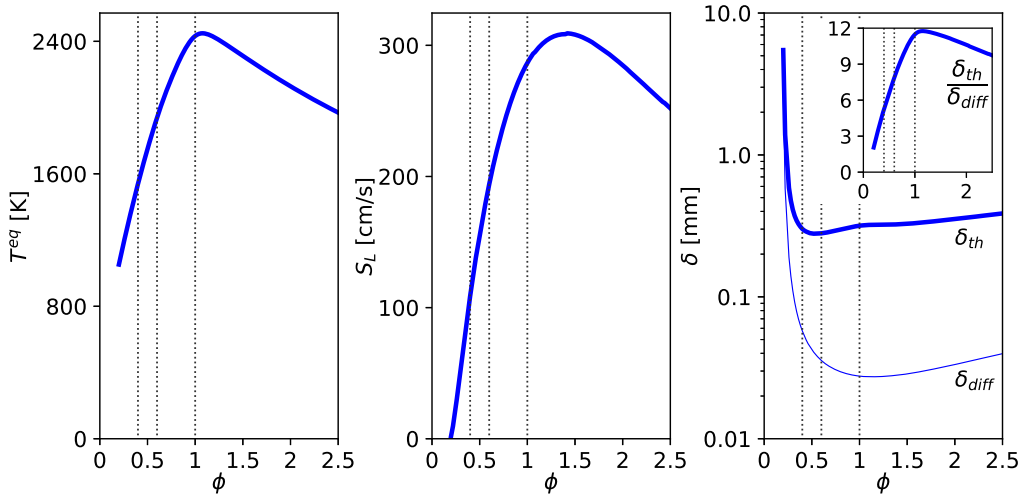

FIGURE 7.4: Properties of 1D premixed hydrogen/air flamelets as function of equivalence ratio at atmospheric pressure with an oxidizer temperature of $T_{air} = 453$ K and fuel temperature of $T_{H_2} = 320$ K, computed with the San Diego mechanism (UCSD, 2018) with the unity Lewis number assumption. From left to right: adiabatic flame temperature T^b, laminar flame speed S_L, flame thickness δ. The dashed lines indicate equivalence ratios of 0.4, 0.6, and 1.0.

A more quantitative illustration is given by Tab. 7.1, which presents the properties of four relevant flamelets, including the ones at the global equivalence ratios of the studied reacting cases (0.4 and 0.6). The two additional cases correspond to the global equivalence ratio at the limit of flashback (0.35) and to the stoichiometric conditions. With the exception of the thermal flame thickness, the properties are extremely sensitive to the mixture composition. The laminar flame speed nearly doubles between $\phi = 0.4$ and $\phi = 0.6$, while the adiabatic flame temperature increases by 26%. Most outstandingly, the chemical time scale decreases threefold. Assuming, that the fuel injection does not influence the turbulence scales significantly, this means, that the expected Karlovitz numbers are three times higher at $\phi = 0.4$ than at $\phi = 0.6$. (See section 5.3.2 for the definitions.) Another outstanding feature of this technically premixed case, lies in the density ratios. As the air is preheated, the density difference between unburnt and burnt mixtures is moderate despite the high flame temperatures. Meanwhile, the density ratio between the reactants: $\rho_{air}/\rho_{H_2} = 3.24$ is quite large, similar to the density ratios across the flame. Overall, these flamelet properties alone are capable of illustrating the extremely challenging conditions of hydrogen combustion.

7.1.4 Operational envelope

Combustors are subject to many constraints and requirements under which they are expected to operate safely and efficiently. Among other parameters this manifests in ranges of oxidizer and fuel mass flow rates. The latter may be expressed indirectly by the global mixture fraction or equivalence ratio discussed in section 2.2. Reichel,

TABLE 7.1: Flamelet properties under conditions relevant to the swirl stabilized hydrogen flame using the unity Lewis number assumption and the San Diego chemical mechanism (UCSD, 2018). The flamelets are computed using Cantera at atmospheric pressure at the specified equivalence ratios with an oxidizer temperature of $T_{air} = 453$ K and fuel temperature of $T_{H_2} = 320$ K.

			CTR3	CTR2		
ϕ [−]	0.0	0.35	0.4	0.6	1.0	∞
Z [kg/kg]	0.0	0.0102	0.0116	0.0173	0.0285	1.0
$X^u_{H_2}$ [kmol/kmol]	0.0	0.128	0.144	0.201	0.296	1.0
T^b [K]	453	1425	1539	1939	2432	320
ρ^u [kg/m^3]	0.781	0.714	0.706	0.674	0.619	0.241
ν^u [cm^2/s]	0.321	0.340	0.343	0.353	0.374	1.223
ν^b [cm^2/s]	0.321	2.294	2.622	3.966	6.273	1.223
ρ^u/ρ^b		3.08	3.31	4.11	5.10	
ν^b/ν^u		6.75	7.65	11.23	16.79	
S_L [m/s]		0.82	1.09	1.94	2.87	
δ_{diff} [mm]		0.0743	0.0575	0.0356	0.0276	
δ_{th} [mm]		0.3357	0.3010	0.2803	0.3172	
τ_{diff} [μs]		91.4	52.9	18.4	9.6	

Terhaar, and Paschereit (2015) investigated the burner experimentally, identifying stable burning conditions, flashback, and lean blow-out under various flow rates.

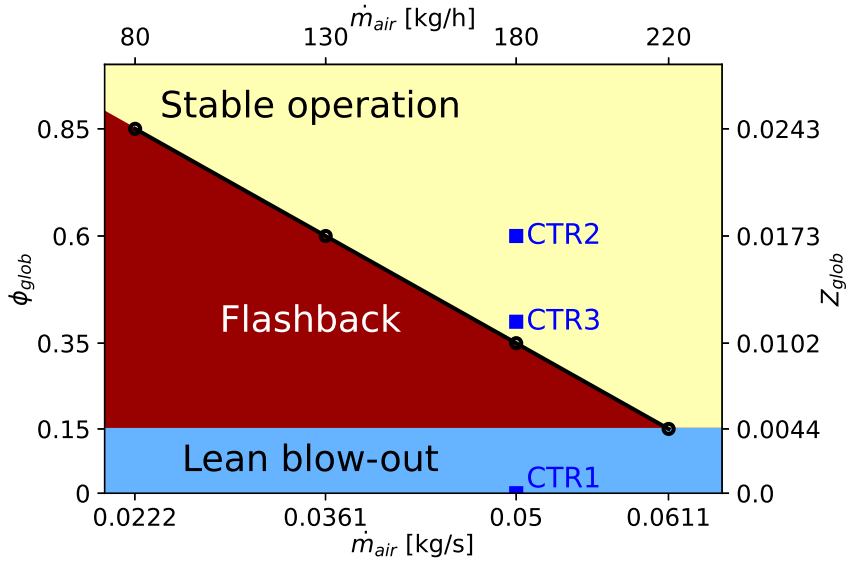

FIGURE 7.5: Operational envelope of the medium axial air injection case ($D_{or} = 8$ mm) of the swirl stabilized hydrogen burner experimentally determined by Reichel and Paschereit (2017).

As Reichel, Terhaar, and Paschereit (2015) found, higher axial air injection cases (higher D_{or}) are only limited by lean blow-out, and otherwise they produce a stable flame. This demonstrates the potential of such flashback-prevention techniques. The

presently studied $D_{or} = 8$ mm case is characterized by a medium strength axial air jet, where flashback is possible. While promoting flashback is not of industrial interest, it provides an excellent environment to study the instability, thus it is selected as the target of the present study. The experimental map of flame behavior on the $\dot{m}_{air} - \phi_{glob}$ plane is presented in Fig. 7.5. Logically, one would expect flashback to occur at higher equivalence ratios, where the mixture is more reactive and the flame propagates faster. Interestingly, in this burner flashback appears at low equivalence ratios. The experimental analysis of Reichel, Terhaar, and Paschereit (2015) attributes this behavior to the additional axial momentum introduced by the hydrogen jets at high equivalence ratios, which stabilizes the flame. Nevertheless, this unexpected result motivates a detailed computational analysis of the burner.

The experimental investigation ruled out boundary layer flashback as a possible explanation, as this phenomenon was not observed during the measurements. Furthermore, the axial velocity in the mixing tube is expected to exceed the laminar flame speed under all conditions. Other processes leading to flashback in lean premixed systems include flow instabilities and combustion induced vortex breakdown. (Fritz, Kröner, and Sattelmayer, 2004; Lieuwen et al., 2008). The latter is a phenomenon in which vortex breakdown occurs not due to the sudden expansion of the cross section as depicted in Fig. 7.1, but due to the presence of the flame in the vortex core. Since this phenomenon is not tied to the geometry, the flame may travel upstream, i.e.: flashback occurs. As pointed out by Fritz, Kröner, and Sattelmayer (2004), combustion induced vortex breakdown is very sensitive to the momentum distribution in the vortex core, and this mechanism is known to be responsible for flashback in many swirl-stabilized premixed combustors. (Kiesewetter, Konle, and Sattelmayer, 2007)

TABLE 7.2: Studied operating points of the swirl stabilized hydrogen flame.

Case	CTR1	CTR2	CTR3
ϕ_{glob} [−]	0.0	0.6	0.4
Z_{glob} [−]	0.0	0.0173	0.0116
T^{eq} [K]	453	1939	1539
ρ_{mix} [kg/m^3]	0.781	0.674	0.706
$\dot{m}_{air}$ [kg/h]	180	180	180
$\dot{V}_{air}$ [m^3/h]	230.4	230.4	230.4
$\dot{m}_{H_2}$ [kg/h]	0.0	3.17	2.11
$\dot{V}_{H_2}$ [m^3/h]	0.0	41.3	27.5
$u_{MT,air}$ [m/s]	70.5	70.5	70.5
u_{inj,H_2} [m/s]	0.0	356.5	237.7
$u_{MT,mix}$ [m/s]	70.5	83.1	78.9
$A_{MT}\rho_{air}u^2_{MT,air}$ [N]	3.52	3.52	3.52
$A_{fuel}\rho_{H_2}u^2_{inj,H_2}$ [N]	0.0	0.31	0.14
J	0.0	2.5	1.1
$Re_{MT,air}$	74800	74800	74800
$Re_{MT,mix}$	74800	80000	78300
Re_{inj,H_2}	0	4660	3110

The stable operating points investigated here are indicated by square markers on the stability map of Fig. 7.5. Three conditions are targeted at an air mass flow rate of $\dot{m}_{air} = 180$ kg/h: the inert air flow (CTR1), a case well withing the stable regime (CTR2), and a case approaching the flashback limit (CTR3). Experimental data is available at all three conditions. The oxidizer mass flow is kept constant corresponding to a roughly constant Reynolds number: $Re \approx 75000$ based on the flow conditions in the mixing tube. The key parameters of the cases are summarized in Tab 7.2. The density after prefect mixing (ρ_{mix}) is significantly affected by the fuel, as the density of hydrogen is very low. Consequently, while the mass flow rates of fuel ($\dot{m}_{H_2}$) are negligible compared to the oxidizer, the volume flow rate is significant, corresponding to $\sim$ 20% and $\sim$ 14% of the total volume flow rate in CTR2 and CTR3 respectively. Reference velocities are defined based on the mixing tube cross section ($A_{MT} = 9.08$ cm^2) and the total cross section of the fuel injection holes ($A_{fuel} = 0.322$ cm^2):

$$u_{MT,air} = \frac{\dot{V}_{air}}{A_{MT}}, \qquad u_{inj,H_2} = \frac{\dot{V}_{H_2}}{A_{fuel}}, \qquad u_{MT,mix} = \frac{\dot{V}_{air} + \dot{V}_{H_2}}{A_{MT}}. \tag{7.1}$$

The bulk velocity of the oxidizer ($u_{MT,air}$) is the one reported by Reichel, Terhaar, and Paschereit (2015) and Tanneberger et al. (2015), which is constant for all studied cases. As the fuel is injected through a relatively small cross section, the velocity of the fuel jets is significantly higher than this bulk velocity. Note, that the Mach number stays moderate, as the speed of sound in hydrogen is very large: $v_{sound,H2} = 1360$ m/s. The injected fuel corresponds to a significant volume flow, which is reflected in the increased bulk velocities considering the flow of the homogeneous mixture ($u_{MT,mix}$). As Reichel, Terhaar, and Paschereit (2015) point out, the axial momentum flow of the hydrogen jets may have a notable influence on the flow field. The momentum flow rates associated to the bulk flow of the air ($A_{MT}\rho_{air}u^2_{MT,air}$) and to the fuel jets ($A_{fuel}\rho_{H_2}u^2_{inj,H_2}$) in also included in Tab. 7.2. Indeed, the momentum addition from the fuel is notable. The momentum ratio: J is a measure of this effect, defined by Reichel, Terhaar, and Paschereit (2015) as:

$$J = \frac{\rho_{H_2}u^2_{inj,H_2}}{\rho_{air}u^2_{MT,air}}, \tag{7.2}$$

where the constants associated to the cross sectional areas are neglected. Finally, the table reports a set of representative Reynolds numbers as well. As mentioned above the Reynolds number based on the bulk air flow in the mixing tube is approximately 75000. This is somewhat increased by the addition of fuel, considering uniform flow. In comparison, the Reynolds number of the hydrogen jets is small ($\mathcal{O}(1000)$), since the injection hole diameters are small and the viscosity of pure hydrogen is considerably larger than that of air. As the fuel injection holes are only a few millimeters long between the fuel distributor annulus and the mixing tube, and the Reynolds numbers are considerably low, the fuel jets are not expected to be turbulent.

7.2 Inert flow

Firstly, the flow is assessed under non-reacting conditions. Simulations are executed under the conditions of CTR1, where flow measurement data is available under inert conditions. Furthermore, non-reacting simulations are also executed while injecting

material through the fuel injection ports, mimicking the presence of the fuel jets. These latter cases correspond to the momentum ratios (J) of CTR2 and CTR3, while the material properties are taken as the properties of perfectly premixed mixtures.

7.2.1 Computational aspects

To study the inert flow of the burner, the low-dissipation scheme of Lehmkuhl et al. (2019b) is used here. As discussed in section 6.2, the only difference between that method and the present low Mach number scheme, is the inclusion of additional terms that arise due to density fluctuations. Otherwise the exact same implementation of the fractional step algorithm is used here.

Computational domain and grid

An illustration of the computational domain is given by Fig. 7.6, showing the corresponding burner elements also displayed on Fig. 7.2. It is essential to consider the flow across the plenum and the air injection elements, as the flame dynamics are fundamentally influenced by the flow conditions in the mixing tube, especially the nature of the vortex breakdown. In the present inert flow simulations, the flow rates through the axial air injection orifice and the swirler element are determined by the pressure losses across both of these components. As mentioned before, the intensity of the axial jet is governed by the orifice diameter: $D_{or} = 8$ mm, and flame stability is specially sensitive to this parameter. Hence, these components need to be included in the simulation domain, to ensure the correct flow split between the axial air injection and the swirler. Following the computational study of Tanneberger et al. (2015), the length of the combustion chamber is shortened to $8.0D$ in the present simulations, which is a significant reduction of the original length of $17.6D$. Note, that this reduction is not expected to affect the upstream flow, while it reduces the computational cost substantially. This computational domain is characterized by two inlet boundary conditions marked BC_1 and BC_2 indicated on Fig. 7.6, corresponding to the upstream inlet of the fuel pipes and the large cross section of the plenum. Not shown here, the domain outlet is further downstream where the flow becomes uniform. The rest of the surfaces in the figure correspond to walls.

The numerical simulations are conducted on a hybrid unstructured mesh composed of prisms, pyramids, and tetrahedra. While several grid resolutions are assessed, here only the final one is presented featuring 64M elements and 13M nodal degrees of freedom. The key parts of this highly refined grid are displayed in Fig. 7.7, showing the resolution in the regions of interest: the mixing tube (MT) and two refinement regions in the combustion chamber (R1 and R2). Tetrahedral elements are applied in the bulk flow, while the wall boundaries are meshed with prismatic elements using a boundary layer refinement. The plenum is discretized coarsely, while mesh refinement is applied throughout the mixing tube and the combustion chamber. Not shown on the figure, the outlet of the combustion chamber also features coarse elements. The smallest element size is applied in the fuel injection holes.

A tetrahedral background mesh with average edge length of $h = 1$ mm is applied throughout the combustion chamber. The finer refinement region (R1) features elements of $h = 0.45$ mm up to $x = 30$ mm in a frustum following the expected flame spreading. Further downstream the second refinement region (R2) is discretized by tetrahedra of $a = 0.6$ mm up to $x = 70$ mm. The mesh throughout the mixing tube is even finer with tetrahedra of $h = 0.36$ mm. Finally the fuel injection is resolved with $h = 0.1$ mm elements in the tube, and $h = 0.2$ mm immediately downstream of the

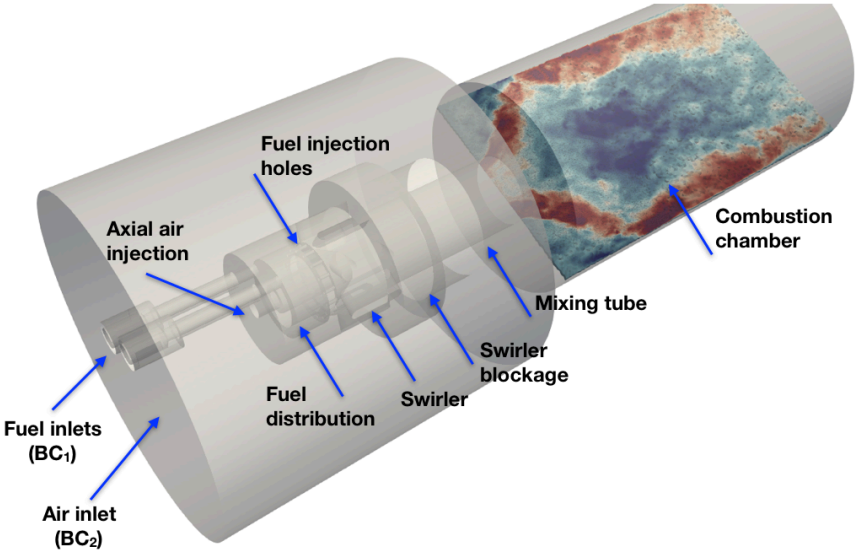

FIGURE 7.6: Illustration of the computational domain of the swirl stabilized hydrogen burner

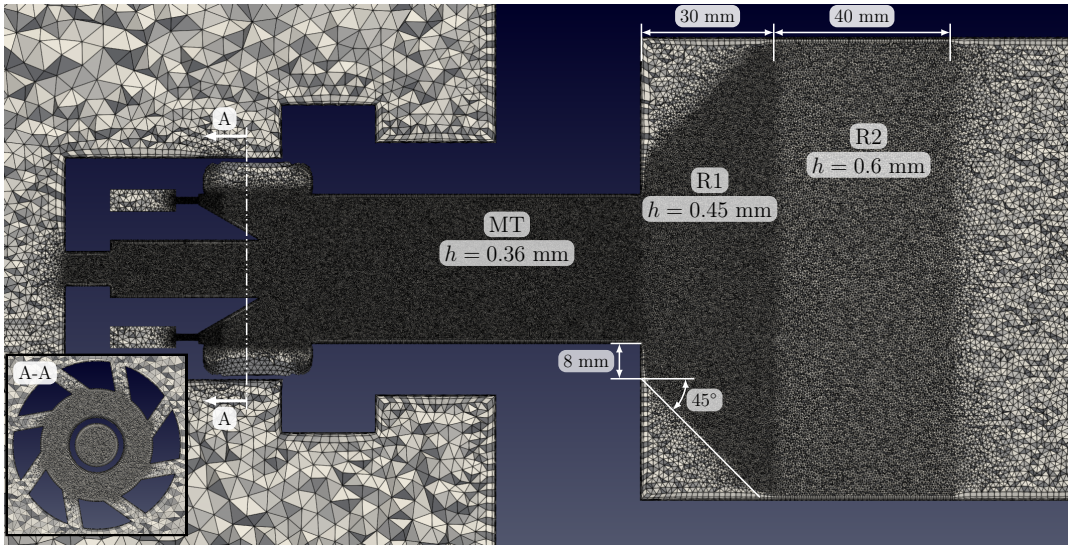

FIGURE 7.7: Illustration of the fine computational grid (M3) of the swirl stabilized hydrogen burner.

injectors to resolve the fuel jets, which gives $\sim$ 18 elements across the fuel injection pipes and $\sim$ 9 elements across the fuel jets. Such a jet resolution is similar to the coarse mesh applied on the DLR-A jet in section 6.5.2 shown in Fig. 6.34a. Note, that the present fuel jets are characterized by much lower Reynolds numbers than the DLR-A case, as Tab. 7.2 summarizes, thus this resolution is deemed adequate.

7.2.2 Mean flow

The mean flow fields are obtained by time averaging over a substantial physical time: $\Delta t \approx 210$ ms. This time scale may be compared to the flow through time of the

system based on the air volume flow rate: $\dot{V}_{air}$ reported in Tab. 7.2 and the approximate volume of the mixing tube and the combustion chamber: $V_{ref} = \frac{\pi}{4}(D^2 l_{MT} + D_{CC}^2 l_{CC}) = 0.00243 m^3$, with $l_{MT} = 86$ mm and $l_{CC} = 8D$. This time scale is: $\tau_{flowthroug} = \frac{V}{\dot{V}_{air}} = 38$ ms, thus the averaging time corresponds to ~ 5.5 flow through times. A better measure is to compare the averaging time to the typical time scales of the system, such as the dominant frequency of the precessing vortex core discussed below. This time scale is expressed in terms of the Strouhal number:

$$Sr = \frac{fD}{u_{MT,air}}, \tag{7.3}$$

with the experimental value being: $Sr = 0.5$, corresponding to a frequency of $f = 1038$ Hz. (Reichel, Terhaar, and Paschereit, 2013) I.e.: the time scale of this coherent structure is ~ 1 ms, thus the present averaging time captures this low frequency motion adequately. In order to have more statistically converged data, the LES results are azimuthally-averaged.

The mean flow field obtained through particle image velocimetry (PIV) in the experiments of Reichel, Terhaar, and Paschereit (2015), and the fields of the present LES are presented in Fig. 7.8. As the swirling flow exits the mixing tube, vortex breakdown occurs. The flow spreads radially as indicated by the mean radial velocity. Meanwhile the axial velocity component decays. On the axis of the burner a central recirculation zone is formed, while the geometry also promotes the formation of corner recirculation zones, both clearly identified by the negative axial velocities. The central recirculation zone is fairly close to the exit of the mixing tube, as in the studied case the amount of axial air injection is only moderate. The LES velocity fields agree qualitatively with the PIV measurements, capturing the location, length, and strength of the recirculation zones. The spreading angle of the high speed swirling flow is also reproduced well.

A more quantitative comparison is given by Fig. 7.9, which shows radial profiles of the mean and RMS fluctuations of the flow field at different axial distances. (See Fig. 7.8d for the indication of these locations.) The flow enters the combustion chamber with significant differences in the axial velocity between the axis and near the edge of the mixing tube, as most of the volume flow is concentrated on the outer edge of the tube. (See Fig. 7.9u.) Meanwhile the velocity on the axis is near zero already at the inlet of the combustion chamber, and a strong recirculation develops downstream, characteristic to the vortex breakdown. The location of the peak axial velocity follows the spreading angle of the high velocity layer, determined by the swirl number of the flow. The velocity fluctuations are already large at the entry of the combustion chamber, as the swirling flow is highly turbulent. Here the axial fluctuations have a peak associated to the highest $\langle \widetilde{u}_{ax} \rangle$ values, however they remain high even on the axis. Further downstream $u_{ax,rms}$ slightly decays on the centerline, meanwhile the peak follows the spreading angle of the flow and somewhat grows due to the highly sheared flow between the high velocity areas and the central recirculation zone. Subsequently the velocity fluctuations decay again when flow becomes more distributed as Fig. 7.9f shows. The radial velocity is moderate at the inlet, and it grows as the vortex breakdown converts the circumferential motion into radial motion. Initially $u_{rad,rms}$ is highest on the centerline, associated to the precessing vortex core, which is only present in the non-reacting case. (See the contrast compared to the reacting flow field in Fig. 7.17.) This peak is the highest throughout the assessed locations. A secondary peak of $u_{rad,rms}$ develops in the shear flow already at $x/D = 0.217$ as Fig. 7.9t shows. With the decay of the central peak this

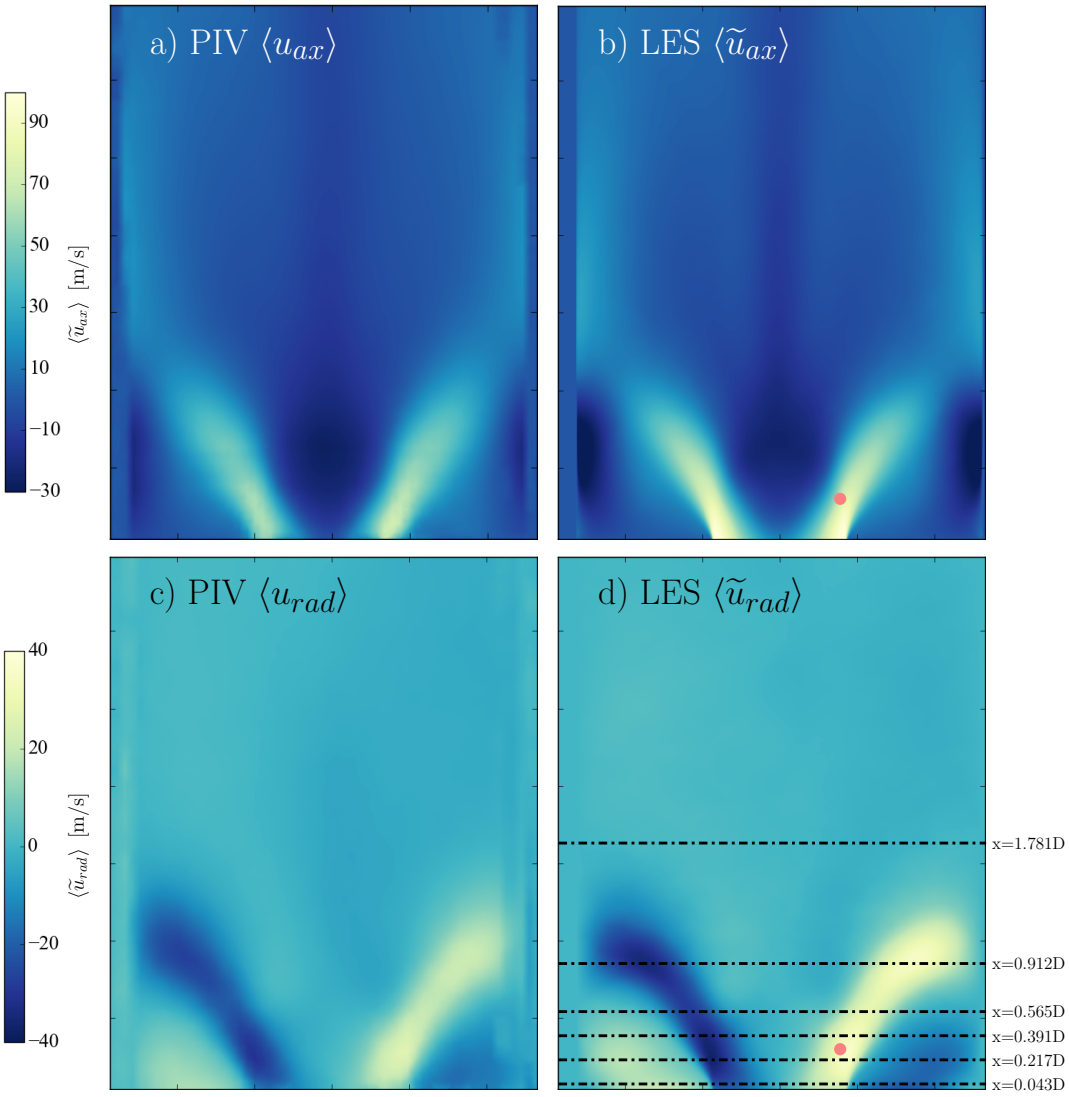

FIGURE 7.8: Comparison of inert flow field (CTR1) in the swirl stabilized hydrogen burner between the PIV measurements of Reichel, Terhaar, and Paschereit (2015) (left) and the LES (right) of the present work. The two rows of plots show the axial and radial velocity respectively.

second peak becomes the dominant one as at higher axial locations.

The first assessed location is very close to the burner surface, and the PIV data seems to be affected by this presence as Fig. 7.8a and c suggest, thus the bottom row in Fig. 7.9 is only indicative in the case of LES. In the rest of the assessed locations the mean axial and radial flow components in the first and third column of plots show a good degree of correlation with the experiment. The location of the peaks of $\langle \widetilde{u}_{ax} \rangle$ and $\langle \widetilde{u}_{rad} \rangle$ is reproduced accurately, indicating the correct spreading angle. The strength of the central recirculation is slightly under-predicted, similar to the case of the PRECCINSTA burner in section 6.5.1. Meanwhile the nature of the RMS values is also captured well, although $u_{ax,rms}$ is slightly over-predicted at higher axial locations. The nature of $u_{rad,rms}$ is also captured well, nevertheless the centerline value decays slower than the experiments suggest.

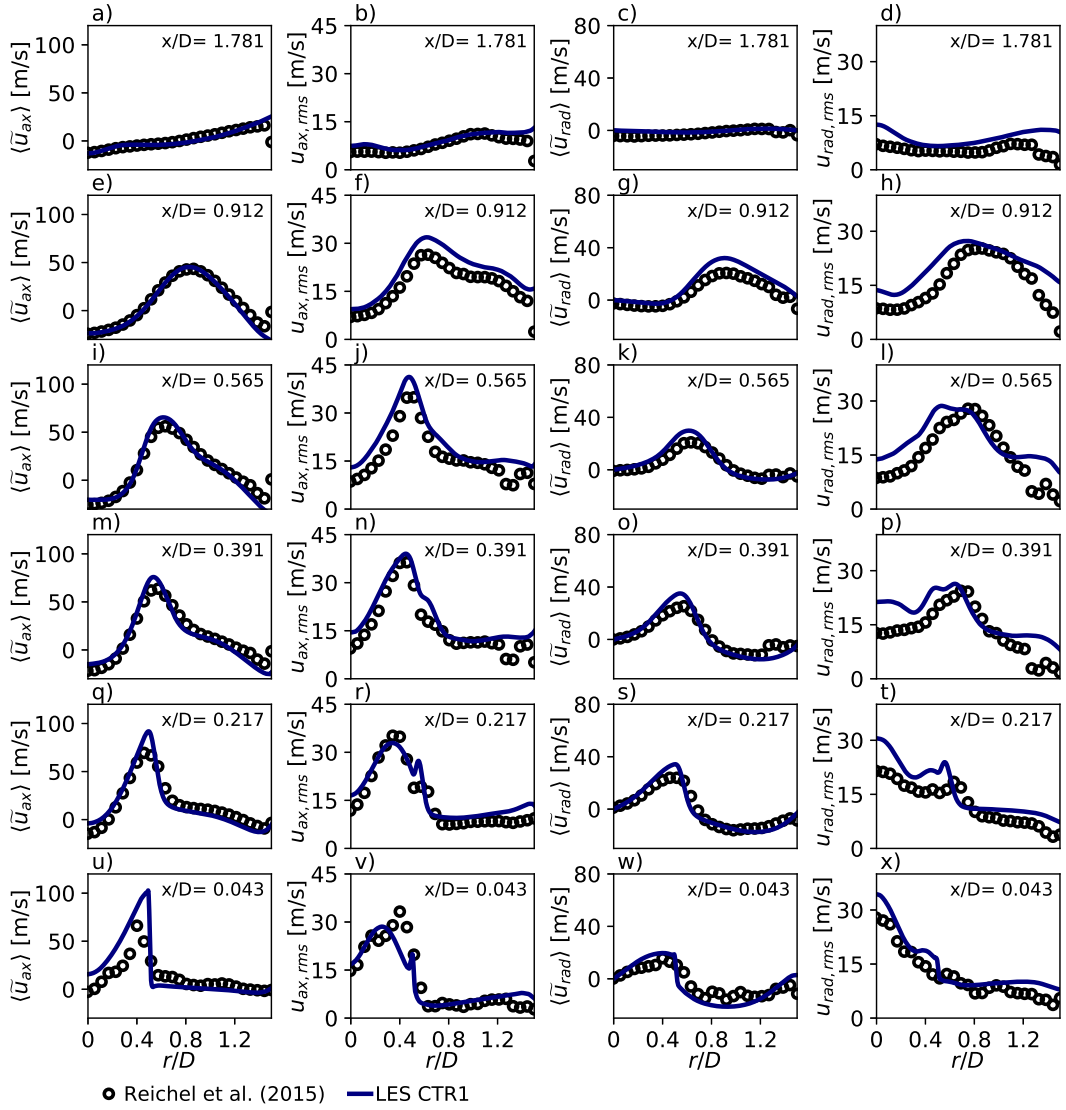

FIGURE 7.9: Comparison of inert (CTR1) velocity profiles in the swirl stabilized hydrogen burner between the PIV measurements of Reichel, Terhaar, and Paschereit (2015) and the LES of the present work. The rows of plots correspond to the indicated axial location, while the four columns show the mean and variance of the axial velocity, and the mean and variance of the radial velocity.

7.2.3 Flow dynamics

The non-reacting flow shows significant periodic behavior which is described by a characteristic Strouhal number of $Sr \approx 0.5$ corresponding to a frequency of $f = 1038$ Hz as discussed in section 7.2.2. Such phenomena is not present in the reacting experiments. While Kuenne, Ketelheun, and Janicka (2011) show, that the thermal dilation across flame fronts plays a role in suppressing oscillations, the addition of axial momentum is also known to attenuate the coherent fluctuations of swirling flows. (Terhaar et al., 2015) As Tab. 7.2 summarizes, the fuel jets have notable axial momentum upon entering the mixing tube. In this section the effect of these jets is assessed under constant density conditions, such that the momentum ratio: J is the same as in the reacting cases: CTR2 and CTR3. Note, that the mass flow rate through

the system is kept constant, thus the inlet flow rate through the plenum is slightly lower in these artificial cases.

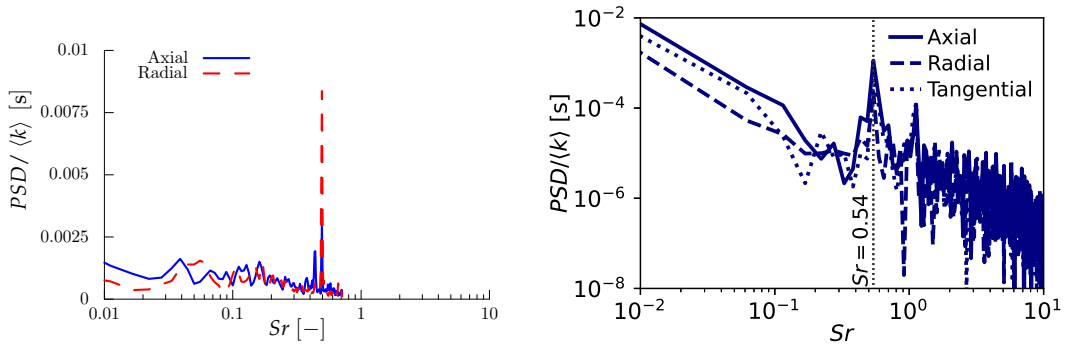

(A) Experimental power spectral density of (Reichel, Terhaar, and Paschereit, 2018).

(B) LES power spectral density using the method of Lomb (1976) and Scargle (1982).

FIGURE 7.10: Power spectral density of the velocity fluctuation at an observation point in the combustion chamber ($x = 10$ mm, $r = 15$ mm) of the swirl stabilized hydrogen flame under the CTR1 conditions.

First the flow dynamics is studied under the CTR1 conditions, where experimental data is available for comparison. (Reichel, Terhaar, and Paschereit, 2018) The power spectral density of different velocity components is presented in Fig. 7.10 at a single monitoring point marked in Fig. 7.8b and d by the red circle, which is located in the shear layer of the central recirculation zone shortly downstream of the mixing tube exit. In Fig. 7.10a the experimental power spectral density is reproduced for comparison. Both the axial and radial spectra clearly show a peak at $Sr \approx 0.5$. The characteristic frequency found in the LES simulations is very similar as Fig. 7.10b shows, where this local maximum of the PSD is located at $Sr = 0.54$, corresponding to a frequency of 1122 Hz. The peak is present in all three velocity components.

This characteristic frequency corresponds to the Precessing Vortex Core (PVC). As Syred (2006) elaborates, the PVC is a well-known global flow instability, which may develop in swirling flows undergoing vortex breakdown. The Kelvin-Helmholtz instabilities in the inner shear layer induce vorteces which are convected downstream. Due to the inverse axial velocities in the recirculation zone, these vorteces trigger a feed back loop and a precessing motion of the recirculation zone's stagnation point. Even though the flow field is highly turbulent, these instabilities form structures with a high degree of coherence. The phenomenon is illustrated in Fig. 7.11 using a cross section of the inert simulations. The point of zero in-plane velocity and zero axial velocity are off-center and differ from one another. These characteristic points of the flow rotate around the axis periodically.

The PVC may be well visualized by Proper Orthogonal Decomposition (POD), which expresses the spacio-temporal fields as a superposition of periodic modes. (Berkooz, Holmes, and Lumley, 1993) The POD modes are ordered by their contribution to the turbulent kinetic energy, thus a small set of modes may capture a large portion of the velocity fluctuations, especially in the presence of coherent instabilities like the precessing vortex core. Mira et al. (2018) have calculated the modes using the instantaneous fluctuations of the radial velocity in the combustion chamber. The first two modes of the inert CTR1 case are reproduced here for completeness in Fig. 7.12. In the experiments (left) and the LES likewise (right) one may identify

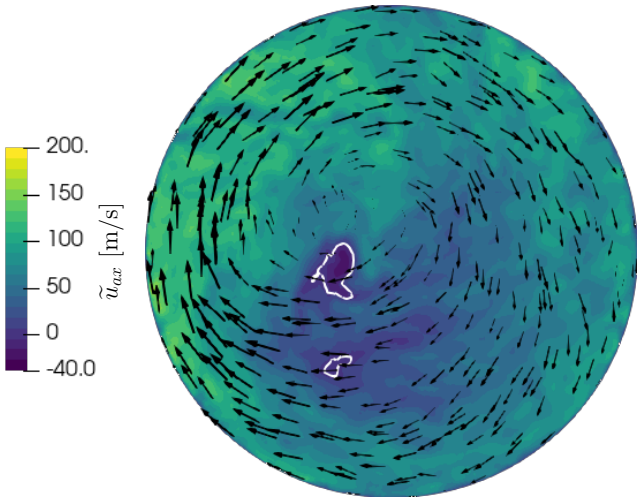

FIGURE 7.11: Illustration of precessing vortex core (PVC) in the mixing tube of the swirl stabilized hydrogen burner under inert conditions (CTR1). A cross section of the mixing tube at 5 mm upstream of the combustion chamber is shown, with the color scale showing the axial velocity, and the vector field representing the in-pane velocity components.

the dominant PVC behavior. The figure highlights the spatial scales of the structures, which corresponds to a period of $\sim 0.8D$ in the axial direction. As discussed before, the PVC has a scale of $Sr \approx 0.5$ in time. The first two modes are phase shifted compared to one another in both space and time by approximately quarter period ($0.2D$). The contours mark the local intensity or amplitude of the individual modes, thus the fact that they are symmetric does not correspond to an axisymmetric flow structure. In three dimensions the PVC is characterized by a single-helical co-rotating vortex structure, which is synchronized with the precession of the recirculation zone. The quarter period phase shift of the POD modes in Fig. 7.12 correspond to this helical structure along which the vortex core is located. The LES is able to reproduce the PVC structure, with the correct location and phase shift of the POD peaks.

The non-swirling fuel jets illustrated in Fig. 7.3a add a notable amount of axial momentum to the flow in the mixing tube. The air flow in the mixing tube is characterized by a certain axial and tangential momentum dictated by the geometry of the central axial air injection and the swirl generator. The flow passing through the 16 small injection holes modifies this distribution of momentum, and it modifies the swirl number. Such changes also affect the precessing vortex core, which is sensitive to the upstream flow conditions. (Reichel, Terhaar, and Paschereit, 2018) Here the swirl number definition of Terhaar et al. (2015) is used, to characterize the flow in the mixing tube:

$$Sn = \frac{2\pi \int_0^R \rho u_{ax} u_{tan} r^2 \mathrm{d}r}{2R\pi \int_0^R \rho \left(u_{ax}^2 - 0.5 u_{tan}^2\right) r \mathrm{d}r}, \tag{7.4}$$

where $R = 17$ mm is the radius of the mixing tube, u_{ax} is the axial velocity, and u_{tan} is the tangential velocity. By the addition of axial momentum through the fuel jets the swirl number decreases, as summarized in Tab. 7.3.

The swirl number at the inlet of the combustion chamber is significantly altered

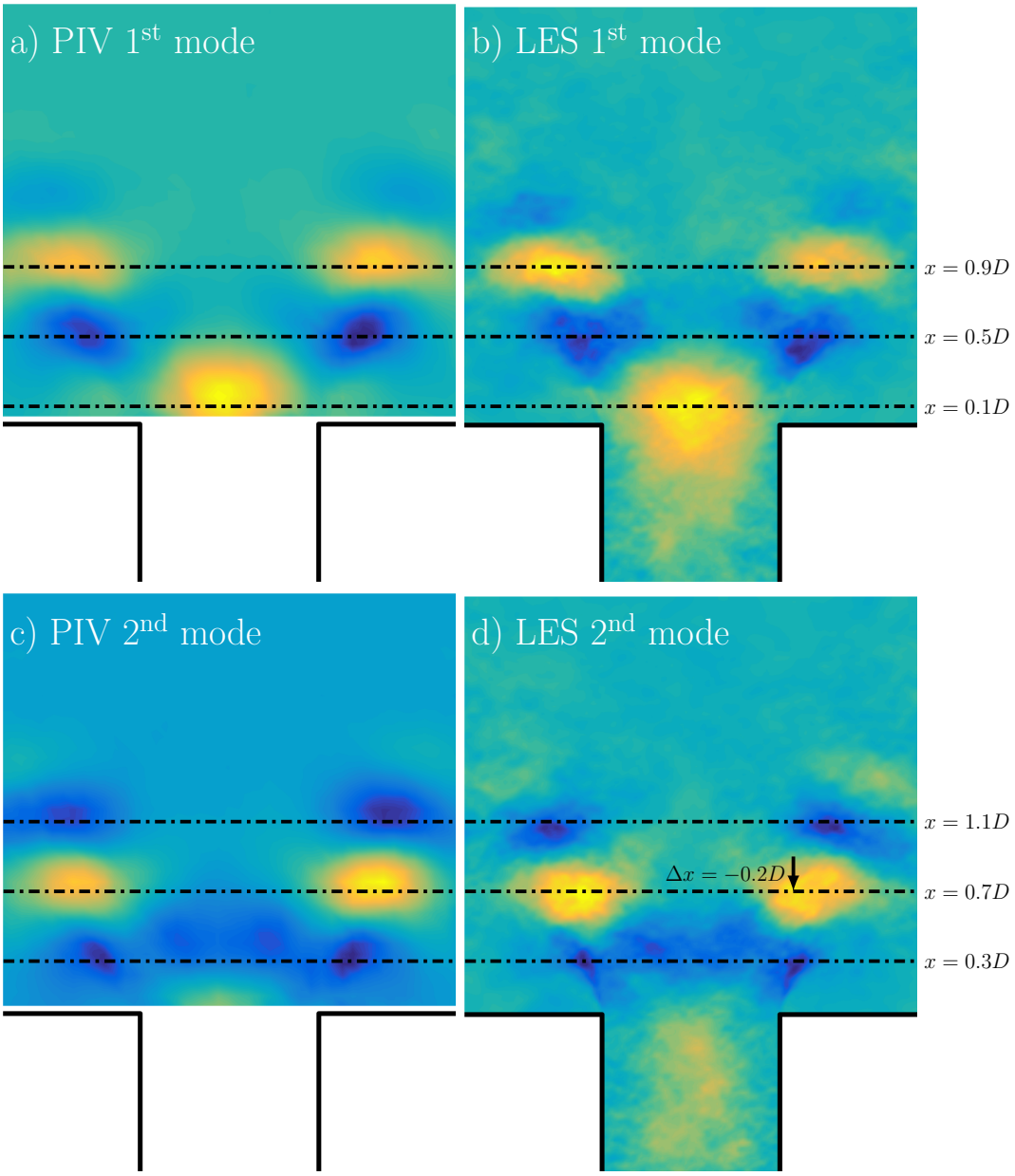

FIGURE 7.12: The first two modes of the proper orthogonal decomposition of the radial velocity fluctuation in the combustion chamber of the swirl stabilized hydrogen burner under inert conditions (CTR1). The PIV data of Reichel, Terhaar, and Paschereit (2015) is shown on the left, while the LES field of the present work are shown on the right.

by the additional fuel momentum. The fuel addition in the $J = 2.5$ case decreases the swirl number by more than 11% compared to the simple air flow. This change significantly affects the PVC, quantified by the velocity spectra presented in Fig. 7.13. As discussed above, the $J = 0.0$ case clearly shows a dominant frequency at $Sr = 0.54$ and a second peak at higher frequency. In the case of inert flow at $J = 1.1$ the dominant peak is still clearly identifiable, however in case of the radial velocity component, it is somewhat shifted to higher Strouhal numbers. Note, that the same velocity scale of $u_{MT,air} = 70.5$ m/s is used in all cases to compute Sr. Such a momentum

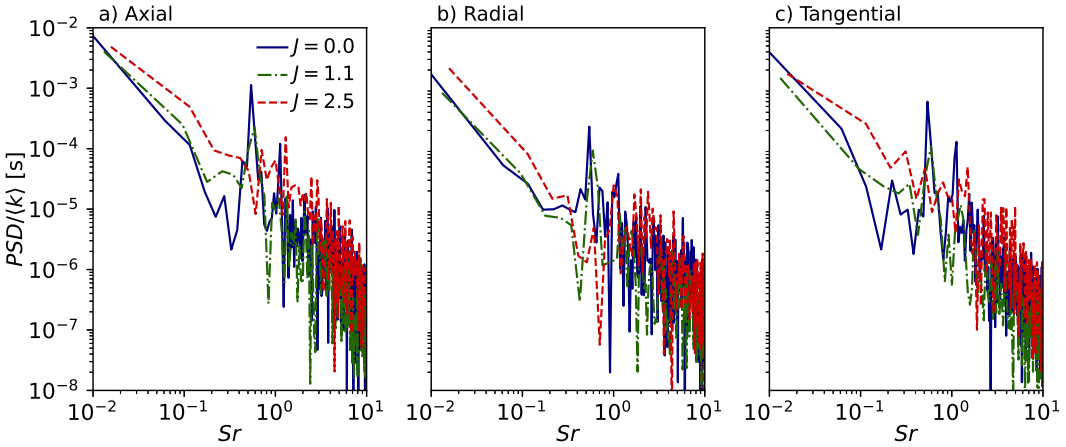

FIGURE 7.13: Power spectral density of the velocity fluctuation in the non-reacting LES cases with different flow rates through the fuel injector system of the swirl stabilized hydrogen flame at an observation point in the combustion chamber ($x = 10$ mm, $r = 15$ mm).

TABLE 7.3: Swirl numbers in inert flow simulations with various flow rates through the fuel injection system of the swirl stabilized hydrogen flame at the inlet of the combustion chamber.

J	Sn	$\frac{Sn-Sn_{CTR1}}{Sn_{CTR1}}$	
0.0	1.008		CTR1
1.1	0.918	-8.9%	$\sim$ CTR3
2.5	0.891	-11.6%	$\sim$ CTR2

ratio is characteristic to the CTR3 case of global equivalence ratio of $\phi = 0.4$. The presence of this characteristic frequency indicates, that the PVC stays active, which may contribute to the unusual onset of flashback at low equivalence ratios. In the $J = 2.5$ case the characteristic frequency vanishes, thus the momentum of the fuel jets alone is sufficient to suppress the hydrodynamic instability, and the the flow becomes more stable. Such an axial momentum addition corresponds to the $\phi = 0.6$ case of CTR2, which lies well within the stable operating range. Overall, the PVC is suppressed by the additional fuel momentum at high J. A similar effect is reported by Terhaar et al. (2015), who observed the attenuation of the PVC intensity by the addition of axial air injection.

7.3 Reacting flow with the perfectly premixed assumption

The reacting flow in the swirl stabilized hydrogen burner is analyzed without the effect of mixing, similarly to the case of the PRECCINSTA burner in section 6.5.1. The modeling details of this approach are described below, then the reacting flow simulations are assessed.

7.3.1 Perfectly premixed combustion model

Reichel, Terhaar, and Paschereit (2015) argue, that the flame stability is primarily dictated by the addition of axial momentum, and the mixing quality and local equivalence ratio fluctuations are secondary. For this reason, first the stable operation points are studied here using a perfectly premixed combustion model. Such a strategy is successfully applied in many studies of the stable operating conditions of the PRECCINSTA burner. (Moureau et al., 2007; Moureau, Domingo, and Vervisch, 2011; Franzelli et al., 2012) In fact, as Franzelli et al. (2012) shows, in the PRECCINSTA burner equivalence ratio fluctuations only become important in the highly unstable cases, which motivates the application of a perfectly premixed model on the swirl stabilized hydrogen flame.

Governing equations

The present perfectly premixed tabulation strategy is identical to the one applied in section 6.5.1 for the simulation of the PRECCINSTA burner. I.e.: the thermochemical conditions of a single premixed flamelet are mapped to the three-dimensional simulation domain after considering sub-grid effects. Thus, the PDE system consist of the Navier-Stokes equations and three transported scalars describing the thermochemical state: enthalpy, progress variable, and progress variable variance. The equations are reproduced here for completeness:

$$\partial_t \overline{\rho} + \nabla \cdot (\overline{\rho}\widetilde{\mathbf{u}}) = 0 \tag{7.5}$$

$$\partial_t (\overline{\rho}\widetilde{\mathbf{u}}) + \nabla \cdot (\overline{\rho}\widetilde{\mathbf{u}} \otimes \widetilde{\mathbf{u}}) + \nabla \overline{p} - \nabla \cdot \left(2\left(\overline{\mu} + \overline{\rho}\nu^{SGS}\right)\widetilde{\mathbf{S}^{\mathbf{D}}(\mathbf{u})}\right) = 0 \tag{7.6}$$

$$\partial_t \left(\overline{\rho}\widetilde{h}\right) + \nabla \cdot \left(\overline{\rho}\widetilde{h}\widetilde{\mathbf{u}}\right) - \nabla \cdot \left(\overline{\rho}\left(\widetilde{\mathcal{D}_t} + \frac{\nu^{SGS}}{Pr^{SGS}}\right)\nabla \widetilde{h}\right) = 0 \tag{7.7}$$

$$\partial_t \left(\overline{\rho}\widetilde{C}\right) + \nabla \cdot \left(\overline{\rho}\widetilde{C}\widetilde{\mathbf{u}}\right) - \nabla \cdot \left(\overline{\rho}\left(\widetilde{\mathcal{D}_t} + \frac{\nu^{SGS}}{Sc^{SGS}}\right)\nabla \widetilde{C}\right) = \overline{\dot{\omega}_C} \tag{7.8}$$

$$\partial_t (\overline{\rho}C_v) + \nabla \cdot (\overline{\rho}C_v\widetilde{\mathbf{u}}) - \nabla \cdot \left(\overline{\rho}\left(\widetilde{\mathcal{D}_t} + \frac{\nu^{SGS}}{Sc^{SGS}}\right)\nabla C_v\right) = 2\frac{\overline{\rho}\nu^{SGS}}{Sc^{SGS}}\nabla \widetilde{C} \cdot \nabla \widetilde{C} + 2\left(\overline{C\dot{\omega}_C} - \widetilde{C}\overline{\dot{\omega}_C}\right) - \overline{\rho}\chi_C^{SGS}. \tag{7.9}$$

Although non-unity Lewis number effects have a notable effect on laminar H_2 flames, here the diffusivities of the three scalars are taken equal to the thermal diffusivity. This unity Lewis number assumption may be justified by the importance of turbulent transport across the flame which entails a large sub-grid transport component. Furthermore, the experimental observations of Reichel, Terhaar, and Paschereit (2015) support, that the stabilization mechanism of the hydrogen flames is fundamentally dependent on the momentum distribution throughout the flow, and the preferential diffusion process is expected to have little influence on this. The model constants of the governing equations are also selected as before, using $Pr^{SGS} = Sc^{SGS} = 0.7$, and the sub-grid model of Vreman (2004) is used with a model constant of $c = 0.1$. The low-dissipation finite element strategy presented in chapter 6 does not need any additional tuning, and results in a second-order discretization in space, and third-order in time. Stabilization is kept to the minimum of feasibility, with only introducing a stabilizing effect to the Navier-Stokes equations through the application of an approximate discrete Laplacian. (See section 6.1.5.)

Tabulated chemistry model

The present modeling strategy represents the combustion of perfectly premixed hydrogen/air blends under preheated conditions in a turbulent flow field. Two equivalence ratios are analyzed as described in section 7.1.3: the case CTR2 at an equivalence ratio of $\phi = 0.6$, and the case CTR3 at $\phi = 0.4$. As shown in Tab. 7.1, the flame speed nearly doubles between the two cases, while the flame thickness remains roughly constant, thus the CTR2 case is significantly more reactive than CTR3. The combustion process is assumed to take place in the flamelet regime for all conditions tested in this study. I.e.: the chemical processes are expected to be significantly faster than turbulent mixing, thus the 1D structure of the reacting layer is preserved in the turbulent flow, and laminar flamelet solutions may be mapped onto the simulation domain. The assumption is reaffirmed *a posteriori* in section 7.3.6. The premixed flames computed using the full San Diego mechanism (UCSD, 2018) at these two equivalence ratios are tabulated for the two cases. This chemical mechanism is well validated, and demonstrated excellent performance in predicting hydrogen flame propagation under a variety of flow conditions. (Mira et al., 2013; Mira et al., 2014)

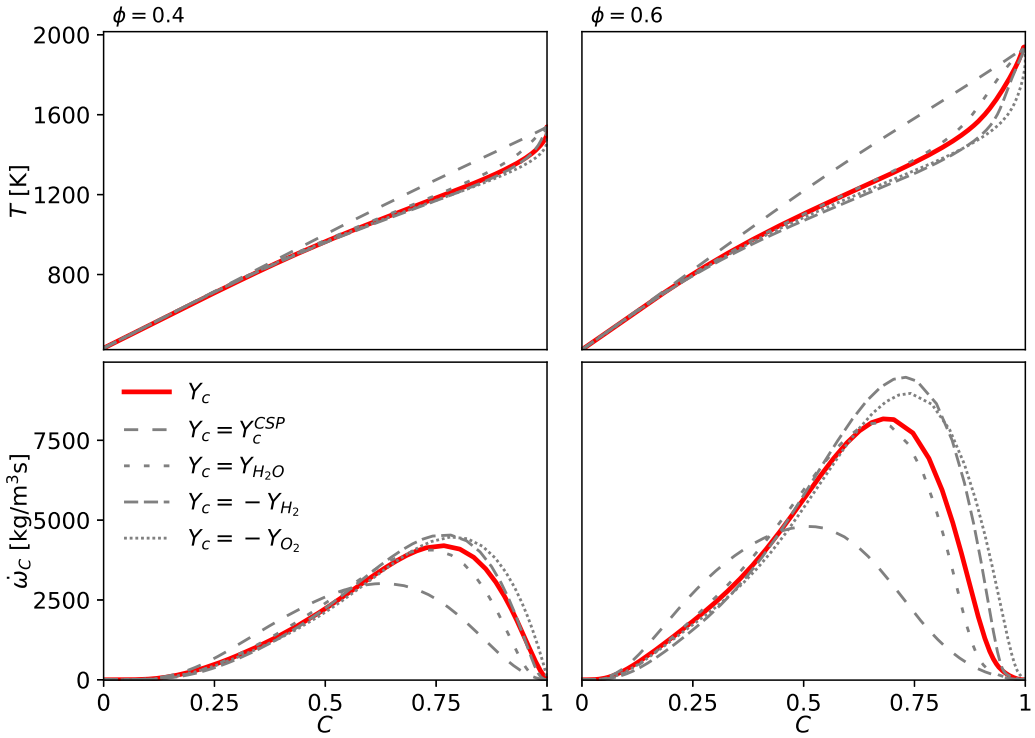

FIGURE 7.14: Progress variable definitions under the conditions of the swirl stabilized hydrogen burner.

As discussed in section 3.2.1 the progress variable parameterizing these flamelet solutions is *not* a result of optimization by the Computational Singular Perturbation method. (Lam, 1993; Massias et al., 1999) Nevertheless, the final Y_c definition is fairly close to using pure H_2O as progress variable, which is a viable solution in hydrogen flames. (Van Oijen and De Goey, 2000; Regele et al., 2013) Figure 7.14 illustrates different progress variable definitions by showing the temperature and the progress variable source terms under the perfectly premixed conditions of the CTR3

and CTR2 cases. Indeed, the presently used progress variable definition, marked by the solid line, is quite similar to using H_2O. Nevertheless, using the pure reactants also results in similar source terms. The real CSP-optimized linear combination, as defined in Tab. 3.7, distributes the evolution of reactions more evenly along C. (Gövert et al., 2015) In this case the temperature would be nearly a linear function of C, and the peak of $\dot{\omega}_C$ is significantly lower than in case of other definitions.

Although there exist alternatives to model the sub-grid turbulence/chemistry interaction, such as the method of Bray and Moss (1977) or Fiorina et al. (2010), here the β-FPDF sub-grid model is retained. The effect of sub-grid variance on the thermochemical manifold is the same as in case of the PRECCINSTA burner presented in Fig. 6.27. I.e.: the peak of progress variable source is decreased by increasing variance, however the more distributed $\dot{\omega}_C$ may increase the overall reactivity of the system, as discussed in section 6.3.4.

7.3.2 Adjustment of the axial momentum ratio for perfectly premixed conditions

As section 7.2.3 presents, the additional axial momentum of the jets introduced through the fuel ports has a significant effect on the flow dynamics even under inert conditions. The effect is also confirmed by the experimental studies of Reichel and Paschereit (2017). Consequently, in a perfectly premixed modeling approach it is of utmost importance to define the boundary conditions in a way, that respects the total mass flow rate, but also aims to reproduce the correct momentum fluxes. Note, that in the reacting cases only PIV measurements (Reichel, Terhaar, and Paschereit, 2018) are available at the entrance of the combustion chamber, which only provide information on the velocity field, thus the mixing quality is hard to assess *a priori*. Nevertheless, a scaled water tunnel experiment studied the mixing under quasi constant density conditions. (Reichel, Terhaar, and Paschereit, 2018) This study found rather low unmixedness levels in the studied geometry, however the real reacting case may behave differently due to the significant density ratio between the fuel and oxidizer. (See Tab. 7.1.) Here the perfectly premixed assumption is used as a simple modeling approach.

As Fig. 7.9 demonstrates, the flow field of the inert case (CTR1) exhibits a deficit in axial velocity toward the centerline across the mixing tube. This velocity deficit is partially eliminated by the addition of fuel injection in the cases of CTR2 and CTR3. The axial injection yields a more homogeneous radial distribution of axial velocity along the mixing tube and pushes the stagnation point further downstream.

Under the perfectly premixed modeling approach three parameters are kept constant, the global equivalence ratio, the total thermal power of the burner, and the ratio of the momentum of axial jets leaving the fuel ports and the momentum of the flow in the mixing tube. The first two conditions correspond to keeping the total mass flow rate of the perfectly premixed mixture equal to the sum of the fuel and oxidizer mass flow rates. Meanwhile, the last requirement helps in approaching the flow conditions of the mixing tube closely. The boundary conditions of the large-eddy simulations are determined by the constraints:

$$\dot{m}_{pp} = \dot{m}_{tp}, \qquad J_{pp} = J_{tp}, \tag{7.10}$$

where the "pp" and "tp" subscripts refer to the perfectly premixed and technically premixed cases respectively, and J is defined in Eq. (7.2). The total mass flow rate, is

given by the operating conditions as:

$$\dot{m}_{tp} = \dot{m}_{air} + \dot{m}_{H_2} = \frac{\dot{m}_{air}}{1 - Z_{glob}}, \tag{7.11}$$

where the parameters of the CTR2 and CTR3 cases are summarized in Tab. 7.2. The momentum ratio may be expressed from the mass flow rates using the cross sectional area of fuel injection holes (A_{fuel}) and that of the mixing tube (A_{MT}):

$$J_{tp} = \frac{\rho_{H_2} u_{inj,H_2}^2}{\rho_{air} u_{MT,air}^2} = \frac{\rho_{H_2} \left(\frac{\dot{m}_{H_2}}{A_{fuel}\rho_{H_2}}\right)^2}{\rho_{air} \left(\frac{\dot{m}_{air}}{A_{MT}\rho_{air}}\right)^2} = \frac{A_{MT}^2}{A_{fuel}^2} \frac{\rho_{air}}{\rho_{H_2}} \frac{\dot{m}_{H_2}^2}{\dot{m}_{air}^2} \tag{7.12}$$

In the perfectly premixed case the mass flow through the two inlets is determined such, that the same momentum ratio is achieved. As Tab. 7.2 illustrates, the mass flow rate of hydrogen is very small, thus the total mass flow rate barely depends on the case. The total mass flow is achieved as:

$$\dot{m}_{pp} = \dot{m}_{mix,1} + \dot{m}_{mix,2}, \tag{7.13}$$

where the subscripts "1" and "2" stand for the inlet through the plenum and the fuel injection system. Thus the momentum ratio in this case is:

$$J_{pp} = \frac{A_{MT}^2}{A_{fuel}^2} \frac{\rho_{mix}}{\rho_{mix}} \frac{\dot{m}_{mix,2}^2}{\dot{m}_{mix,1}^2}. \tag{7.14}$$

Finally, the mass flow through the plenum is determined by the following quadratic equation:

$$\underbrace{\left(1 - J_{pp}\frac{A_{fuel}^2}{A_{MT}^2}\right)}_{\alpha} \dot{m}_{mix,1}^2 \underbrace{-2\dot{m}_{pp}}_{\beta} \dot{m}_{mix,1} + \underbrace{\dot{m}_{pp}^2}_{\gamma} = 0, \tag{7.15}$$

where the mass flow through the plenum is given by the root: $\dot{m}_{mix,1} = \frac{-\beta - \sqrt{\beta^2 - 4\alpha\gamma}}{2\alpha}$. Note, that the other root is non-physical, as the definition of J disregards the direction of the flow.

The operating conditions of the perfectly premixed simulation cases are summarized in Tab. 7.4. The mass flow rate through the plenum ($\dot{m}_{mix,1}$) decreases by less than 4% compared to the technically-premixed cases of Tab. 7.2. Meanwhile, the volume flow rate through the same passages increases by $\sim$ 12% and $\sim$ 8% in the CTR2 and CTR3 cases respectively, as the density of the mixture is significantly lower than the density of pure air. These differences are not expected to cause significant change in the aerodynamic behavior of the central axial injection and swirler element. The mass flow rate through the fuel injection system is significantly higher than under technically-premixed conditions as the mixture is more dense than hydrogen. Alas, the flow rate through the injection holes is lower, and the resulting injection velocities ($u_{inj,mix}$) are moderate. The axial momentum flow through the injection holes is similar to the technically-premixed case, and even the Reynolds numbers are comparable, as the decreased injection velocities are paired with a likewise decreased viscosity. (See Tab. 7.1.) Note, that this equivalence assumes homogeneous flow

TABLE 7.4: Equivalent perfectly premixed operating conditions of the swirl stabilized hydrogen flame.

Case	CTR1	CTR2	CTR3
$\dot{m}_{mix,1}$ [kg/h]	180	173.43	175.54
$\dot{V}_{mix,1}$ [m^3/h]	230.38	257.41	248.74
$\dot{m}_{mix,2}$ [kg/h]	0	9.74	6.57
$\dot{V}_{mix,2}$ [m^3/h]	0	14.46	9.32
$u_{inj,mix}$ [m/s]	0	124.9	80.4
$A_{fuel}\rho_{mix}u^2_{inj,mix}$ [N]	0	0.34	0.15
J_{pp}	0	2.5	1.1
$Re_{inj,mix}$	0	5660	3760

through the fuel injection holes. While this not the case under the actual burner geometry, the effect of non-homogeneity is expected to be limited and to decay towards the combustion chamber.

7.3.3 Grid resolution

The computational grid presented in section 7.2.1 is applied in the perfectly premixed reacting simulations as well. As shown in Fig. 7.4, and further quantified in Tab. 7.1, the thermal flame thickness is approximately $\delta_{th} \approx 0.3$ mm throughout these operating conditions. This chemical length scale is significantly smaller than in the case of methane, putting a more stringent requirement on the sub-grid turbulence/chemistry interaction model, nevertheless the present modeling approach performs well. The same mesh is used in all perfectly premixed reacting cases, as the small changes in the chemical length scale do not justify further refinement.

The mesh resolution was assessed in the CTR3 ($\phi_{glob} = 0.4$) case using coarser meshes than the one presented in Fig. 7.7. Specifically, a coarse and an intermediate mesh are applied, with tetrahedral edge lengths of $a = 1.0$ mm and $a = 0.7$ mm in the R1 refinement zone respectively. The fine mesh applied in the rest of the perfectly premixed simulations is characterized by $a = 0.45$ mm in this zone. The mesh convergence analysis demonstrates the adequacy of the fine mesh. The grid quality is further assessed in Fig. 7.15, comparing the filter size to the estimated Kolmogorov scales (left) and displaying the local turbulence Reynolds number (right) along radial profiles at various axial locations in the simulations using the fine mesh. The scales are estimated following the strategy outlined in section 5.1.6. Indeed, using the fine mesh, the filter size remains moderate compared to the Kolmogorov scale, with $\max\left(\frac{\Delta_f}{\eta}\right) \approx 22$ in the mixing tube at $x/D = -2.5$, thus the LES of the fine mesh is deemed adequate. Note, that these monitoring points are located just 1 mm downstream ($x = -85$ mm) of the cone shaped element of the axial injection system, in the middle of the swirl generator. (See Fig. 7.2.) Further downstream the flow is more resolved as the high initial turbulence of the axial injection and the swirl generator decays to some extent. At the entrance of the combustion chamber at $x = 5$ mm the $\frac{\Delta_f}{\eta}$ ratio becomes comparable to the values observed in the PRECCINSTA case of section 6.5.1 as Fig. 7.15g illustrates. Further downstream this ratio decreases, as the flow becomes more uniform and the viscosity increases due to the

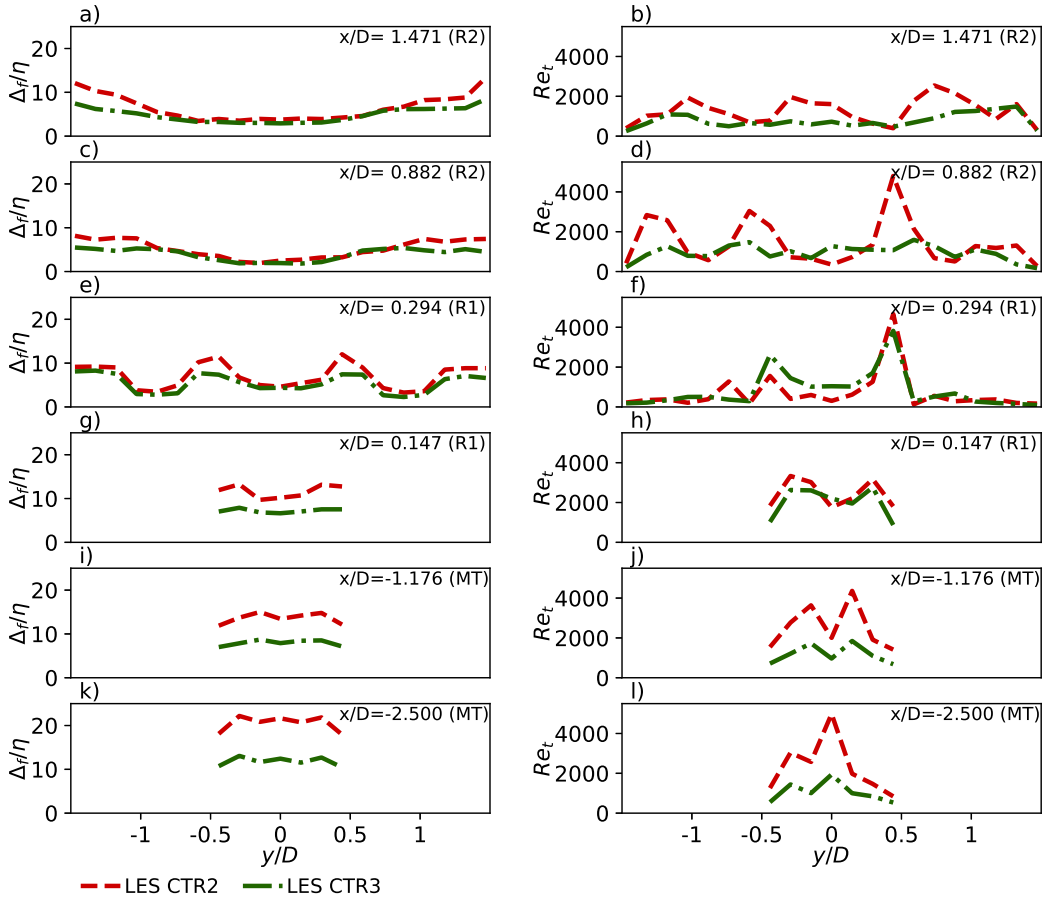

FIGURE 7.15: Turbulent scales of the swirl stabilized hydrogen flame in the reacting cases using the fine computational grid. Radial profiles along various axial locations of the filter size ($\Delta_f = \sqrt[3]{V_{element}} \approx 0.4903h$) compared to the Kolmogorov scale (left) and Reynolds number based on the turbulence integral scales (right) evaluated from temporal data at monitoring points.

heat release. Overall, the resolution of the fine grid is adequate for the LES of the swirl stabilized hydrogen flame. Moreover, the present analysis also highlights, that the coarser meshes would not only cause problems in terms of resolving the reacting front, but they would also pose a challenge for the LES model of the flow.

There is a clear difference between the two reacting cases displayed in Fig. 7.15. The jets entering through the fuel injection system not only increase the axial momentum in the mixing tube, but they also substantially increase the turbulence intensity of the flow. This manifests in lower Kolmogorov scales (Fig. 7.15k) and almost twice as high turbulence Reynolds numbers in CTR2 (Fig. 7.15l). By the entrance of the combustion chamber at $x/D = 0.147$ the two cases become more similar with nearly equal Re_t, however the difference in η persists even at $x/D = 0.294$. Further downstream there is a key difference in Re_t, as CTR2 appears to be more turbulent than CTR3. As demonstrated below, CTR2 is characterized by notably higher velocities, due to the $\sim 5\%$ higher flow rates (Tab. 7.2) and the significantly higher density ratios (Tab. 7.1) across the flame. These conditions result in significantly higher Re_t in the post-flame region of CTR2. Although the integral scales show a high turbulence intensity in the post flame region, the grid resolution stays adequate, as the

Kolmogorov scales are also affected by the increased viscosity of the flue gas.

TABLE 7.5: Grid resolution in the fine mesh of the swirl stabilized hydrogen flame simulations, with the peak y^+ values estimated *a posteriori* from the CTR3 simulation.

Case	Bulk element size: h [mm]	Boundary element quality: y^+
Fuel jets	0.20	< 100
Mixing tube	0.36	< 10
Combustion chamber	0.45	< 50

Finally, Tab. 7.5 summarizes the element sizes applied in different parts of the fine grid displayed in Fig. 7.7. The y^+ values of the first elements next to the boundary are estimated *a posteriori* form the simulations of the CTR3 case. While it is not feasible to ensure a fully wall-resolved simulation here, this is of lesser importance in the present burner than in the channel flow case of section 6.2, as the mass flow rate through the boundaries is prescribed using Dirichlet boundary conditions. I.e.: errors in the wall stresses do no lead to errors in the flow rate.

7.3.4 Mean flow

The statistically steady inert flow fields of section 7.2.2 are used as initial condition of the reacting perfectly premixed cases. The flame is ignited by imposing fully reacted conditions ($C = 1$) in the downstream parts of the domain. After the statistically steady state is established, the fields are time averaged over time intervals of $\Delta t \approx 11$ ms and $\Delta t \approx 23$ ms for CTR2 and CTR3 respectively. While these are lower, than the interval applied in the inert flow, the time frames are still sufficient to capture the relevant frequencies of the flame. (E.g.: the characteristic time scale in the inert flow is ~ 1 ms.) Note, that such strong low frequency fluctuations are not present in the reacting flow.

The field of mean axial velocity is illustrated in Fig. 7.16 for CTR2 ($\phi_{glob} = 0.6$) and CTR3 ($\phi_{glob} = 0.4$) on the top and bottom respectively. Compared to the inert case (CTR1) in Fig. 7.8, the reacting flow fields are fundamentally different. In the reacting cases the central recirculation zone is shifted downstream, furthermore, the spreading angle of the flow becomes wider. This axial displacement of the vortex breakdown is partially caused by the additional axial momentum introduced by the fuel jets. The thermal dilation in the reaction front also increases the axial flow and influences the vortex breakdown. As Billant, Chomaz, and Huerre (1998) identify, this influence may change the nature of the vortex breakdown altogether. In the present case the inert flow shows a narrower recirculation zone situated at the sudden change of the cross section, forming a *bubble-type* vortex breakdown, where positive axial velocities are recovered shortly downstream of the mixing tube's outlet. Contrarily, in the reacting cases discussed here, the heat release forces a wider opening angle and the stabilization mechanism transitions to a *cone-type* vortex breakdown, where the recirculation zone is extended to several diameters downstream of the mixing tube's outlet. As Reichel, Terhaar, and Paschereit (2015) shows experimentally, this shift in the vortex breakdown and the resulting increase in flashback resistance is as consequence of the increased axial momentum in the mixing tube, partly due to the axial air injection orifice, and partly due to the axial momentum of the fuel jets. The perfectly premixed simulation approach is capable of predicting

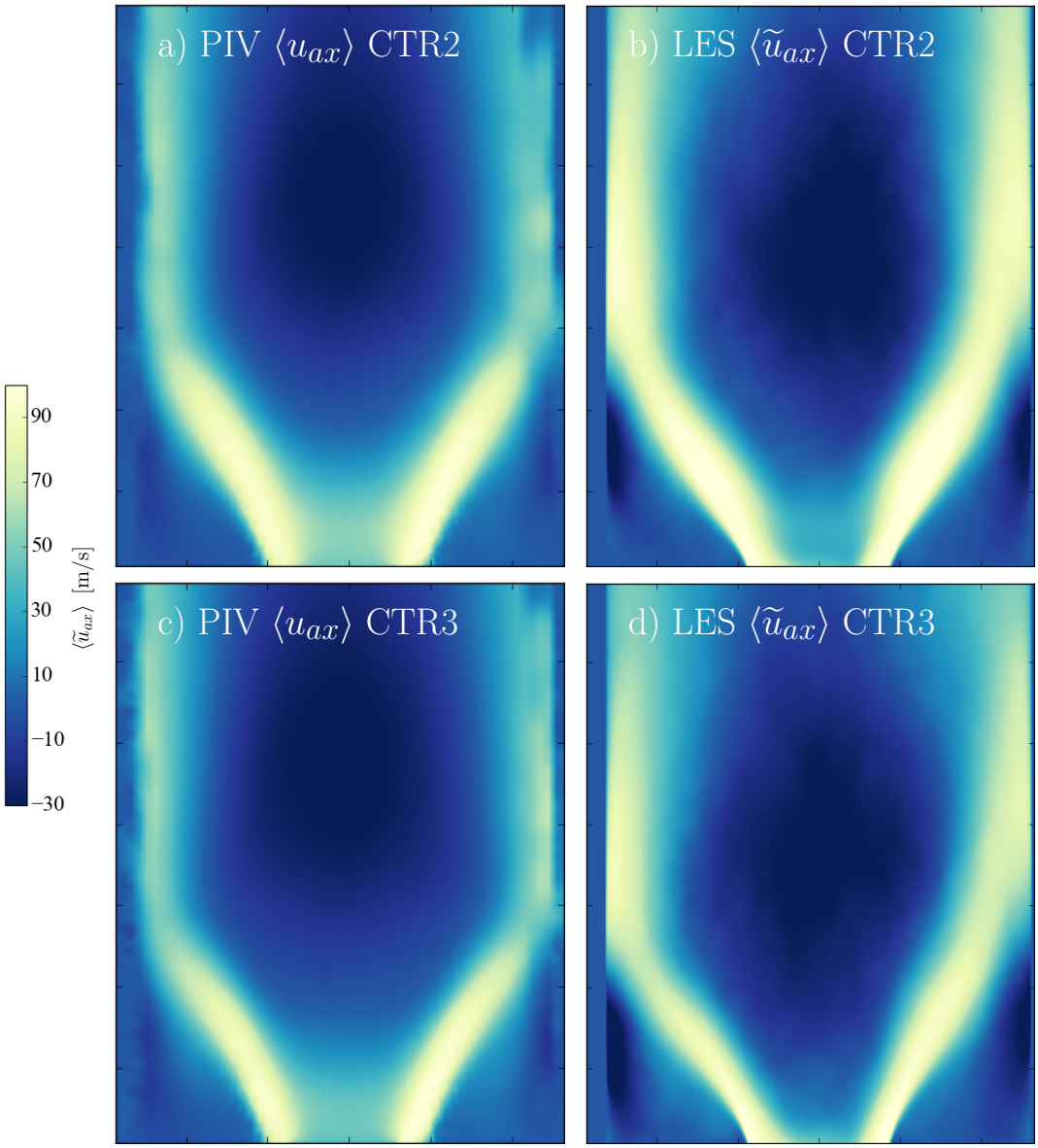

FIGURE 7.16: Comparison of axial velocity contours in the reacting flow fields of the swirl stabilized hydrogen burner between the PIV measurements of Reichel, Terhaar, and Paschereit (2015) (left) and the LES (right) of the present work using the perfectly premixed modeling approach. The two rows of plots show the cases of CTR2 ($\phi_{glob} = 0.6$) and CTR3 ($\phi_{glob} = 0.4$) respectively.

this transition from bubble-type to cone-type vortex breakdown, which is imperative in the flashback safety of this system. It is postulated, that under leaner conditions in the flashback regime of the burner (see Fig. 7.5) the vortex breakdown is capable of propagating into the mixing tube due to the thermal dilatation effects, i.e.: the flow field suffers *combustion-induced vortex breakdown*. (Oberleithner et al., 2015)

Despite the simplicity of the perfectly premixed model, the LES results of the stable cases agree reasonably well with the PIV measurements, indicating the adequacy of the inlet modeling presented in section 7.3.2. The size and location of the central

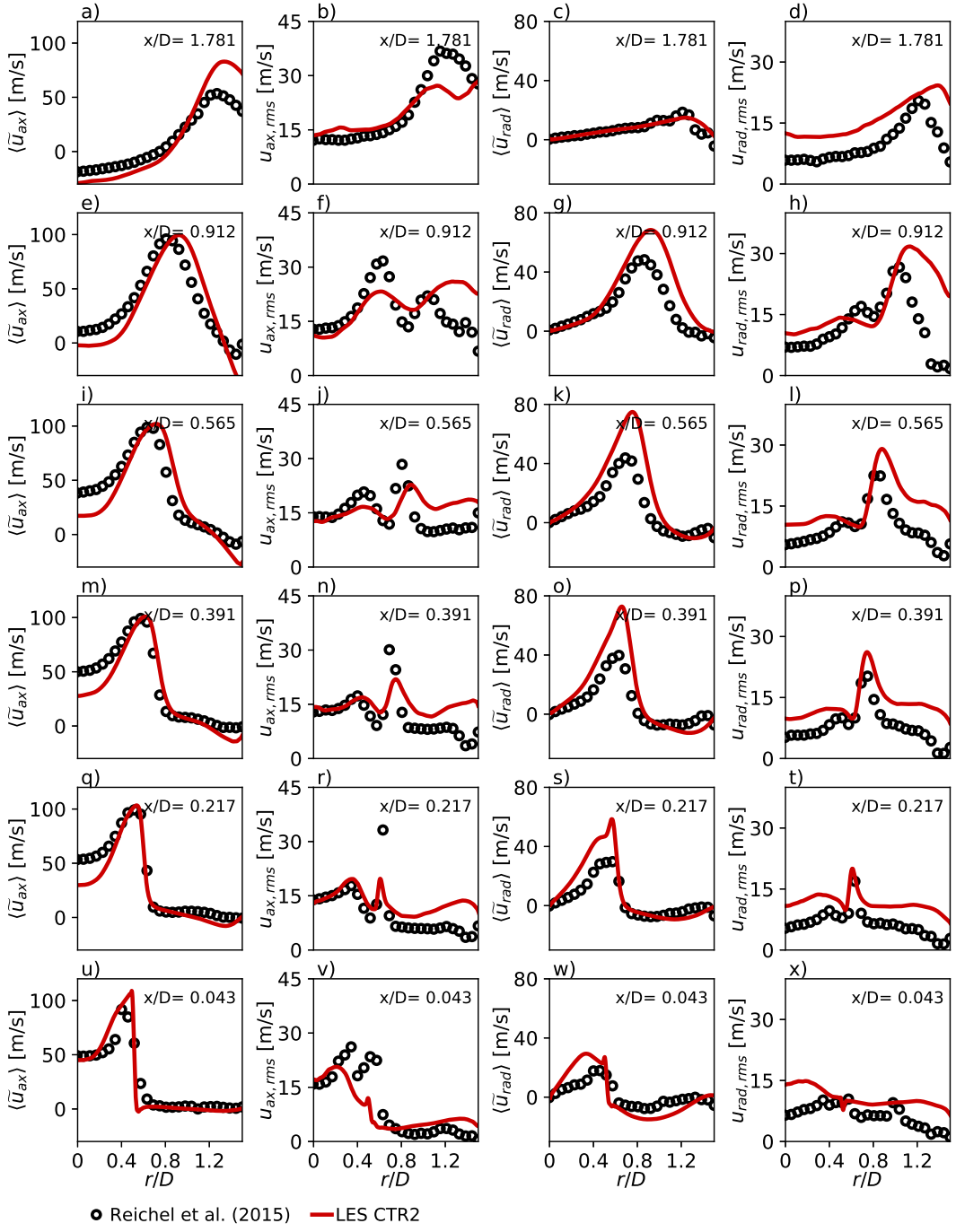

FIGURE 7.17: Comparison of velocity profiles in the CTR2 ($\phi_{glob} = 0.6$) case of the swirl stabilized hydrogen burner between the PIV measurements of Reichel, Terhaar, and Paschereit (2015) and the LES of the present work using the perfectly premixed combustion model. The rows of plots correspond to the indicated axial location, while the four columns show the mean and variance of the axial velocity, and the mean and variance of the radial velocity.

and corner recirculation zones are predicted well in both cases, and the LES also captures the spreading angle of the flow. There is a minor discrepancy in the location of the onset of the recirculation. The LES predicts the occurrence of these stagnation

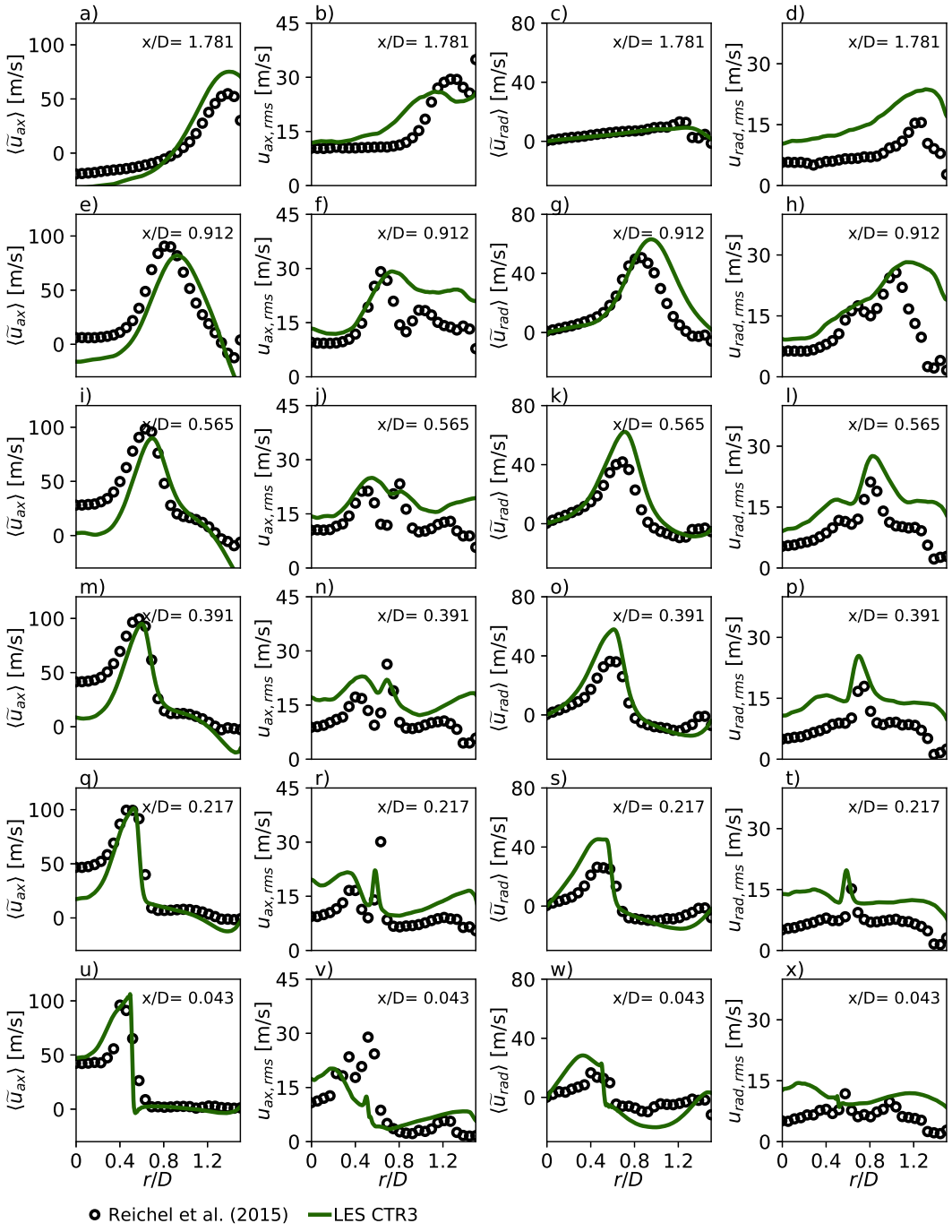

FIGURE 7.18: Comparison of velocity profiles in the CTR3 ($\phi_{glob} = 0.4$) case of the swirl stabilized hydrogen burner between the PIV measurements of Reichel, Terhaar, and Paschereit (2015) and the LES of the present work using the perfectly premixed combustion model. The rows of plots correspond to the indicated axial location, while the four columns show the mean and variance of the axial velocity, and the mean and variance of the radial velocity.

points too close to the mixing tube's outlet. This effect is better represented by the velocity profiles discussed below.

The axial and radial velocity field is compared quantitatively to the PIV data of

the corresponding reactive experiments in Fig. 7.17 and Fig. 7.18 using the velocity profiles along the radial direction at various axial locations. The figure shows the mean and RMS of the axial and radial velocity. Indeed, the flow is significantly different from the inert flow displayed in Fig. 7.9, since in the reacting cases the nature of the vortex breakdown changes. This is best represented by the profiles closest to the inlet at $x = 0.043D$: Fig. 7.17u-x and Fig. 7.18u-x. In the inert flow the mean axial velocity ($\langle \widetilde{u}_{ax} \rangle$) ranges approximately from 0 m/s at the centerline to 100 m/s near the edge of the mixing tube. In the reacting flow however, the vortex breakdown is not present at this location, and $\langle \widetilde{u}_{ax} \rangle$ ranges between 50 m/s in the center of the flow and 100 m/s near the edge. Further downstream the vortex breakdown develops gradually, as the axial velocity deficit on the centerline deepens and finally the central recirculation zone arises. According to the experiments of both CTR2 and CTR3, the recirculation is formed between the last two assessed locations: $0.912D < X < 1.781D$. Using the present perfectly premixed combustion model the axial velocity on the centerline deviates from the experiments significantly. This culminates in the upstream shift of the stagnation point ($\langle \widetilde{u}_{ax} \rangle = 0$ m/s), as the LES of CTR2 shows recirculation at $x = 0.912D$ (Fig. 7.17e) and the LES of CTR3 at $x = 0.565D$ (Fig. 7.18i). The location of the vortex breakdown is further analyzed in section 7.3.5. The discrepancies are likely caused by the simplicity of the combustion model, as the LES results only deviate from the PIV data significantly in the reacting cases. The flame exhibits certain behavior, that the perfectly premixed LES cannot predict accurately. Nevertheless, the different nature of the flow through the mixing tube may also affect the vortex breakdown. Other aspects of the mean flow are reproduced satisfactorily by the LES, such as the opening angle of the high speed conical flow and the trends in the velocity fluctuations. For instance, the RMS of both the axial and radial velocity fluctuations shows a double peak structure in the shear layers, which is not present in the inert simulations of CTR1. The LES correctly reproduces the location of these peaks, alas the magnitudes show a certain discrepancy.

The differences between the three LES simulations are highlighted in Fig. 7.19 showing the relation of the mean density and flow fields. As discussed before, the nature of the central recirculation zone changes due to the heat release rate and the increased axial momentum in the reacting cases. In the inert case the central recirculation zone is narrow and it is situated close to the exit of the mixing tube. Furthermore, it is characterized by rather low velocity magnitudes, and the region with significant recirculation is rather small. In the reacting cases recirculation becomes stronger, with the highest back-flow observed in the CTR3 case which is closer to flashback than CTR2. Comparing the two reacting cases, the most outstanding difference is the axial shift of the stagnation point. As Fig. 7.19b shows, in CTR2 significant positive axial velocity is present on the centerline above the flame brush, I.e.: the flow is able to penetrate the flame, thus the $\langle \widetilde{u}_{ax} \rangle$ line is further downstream than the flame. In the CTR3 case however, the axial velocity in the flame is very low on the centerline, and the stagnation point is situated closer to the flame. Quantitatively in CTR2 the recirculation starts at $x = 0.794D$ while in CTR3 this occurs at $x = 0.553D$. Interestingly, the flame is stabilized slightly more downstream in the CTR3 case as the dash-dot lines indicate. This is likely caused by the lower reactivity of the $\phi_{glob} = 0.4$ case. Indeed, as the equivalence ratio is decreased and the flashback conditions are approached, various phenomena are affecting the flow. On one hand the thermal dilatation becomes weaker, thus the flame suppresses less

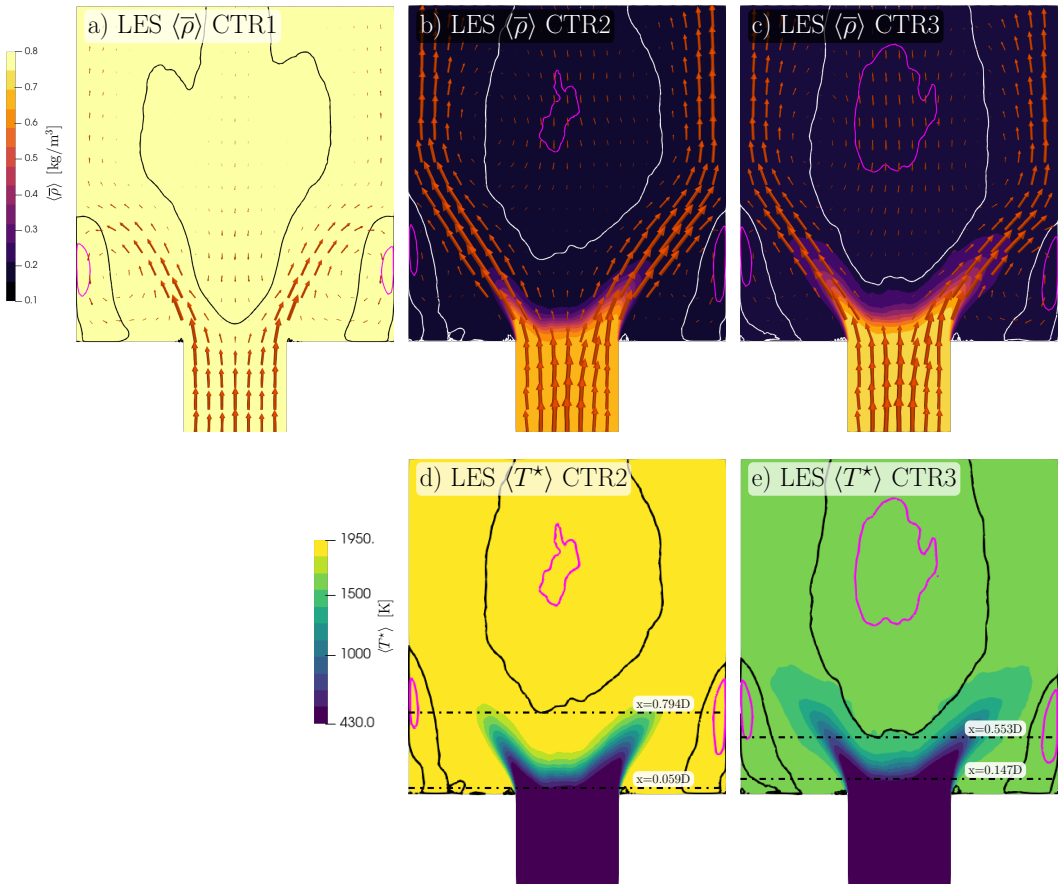

FIGURE 7.19: Comparison of simulated flow fields and flame shapes of the swirl stabilized hydrogen burner using the perfectly premixed combustion model. The columns correspond to the three cases CTR1 (inert, left), CTR2 ($\phi_{glob} = 0.6$, center) and CTR3 ($\phi_{glob} = 0.4$, right). The top row shows the density field with the in-plane velocity vector field, the bottom row shows the temperature distribution in the reacting cases. Contour lines mark the location of zero axial velocity (black/white) and an axial velocity of -30 m/s (magenta).

effectively the hydrodynamic instabilities and stronger recirculation becomes possible. Furthermore the axial momentum introduced through the fuel jets also decreases, favoring flashback conditions. On the other hand, the flame speed decreases nearly twofold, influencing the actual turbulent flame propagation speed substantially. (Sabel'nikov and Lipatnikov, 2011; Dong et al., 2013) This effect may impede the upstream propagation of the reacting front. The flashback event may happen under a very specific superposition of these counteracting effects. The satisfactory prediction of stable flames indicates, that the perfectly premixed LES model reproduced the turbulent flame speed to an acceptable extent despite its simplicity.

In conclusion, aligned with the experimental observations of Reichel, Terhaar, and Paschereit (2015), the axial momentum ratio (J) and the equivalence ratio (ϕ_{glob}) are the major controlling parameters of this burner. Adjusting the flow rates of the injection system such, that the axial momentum ratio is recovered is a viable approach for allowing the usage of perfectly premixed combustion models. A disagreement in the location of the vortex breakdown is observed between the present LES and the PIV measurements as the conditions approach flashback. This is possibly

linked to equivalence ratio fluctuations throughout the mixing tube. Nevertheless, the LES reproduces the mean flow behavior to a good extent.

7.3.5 Flow dynamics

As the previous section shows, the perfectly premixed LES model predicts various changes in the nature of the mean flow due to the heat release, and even between the reacting operating points there are significant differences. In this section the temporal behavior of the different cases is studied.

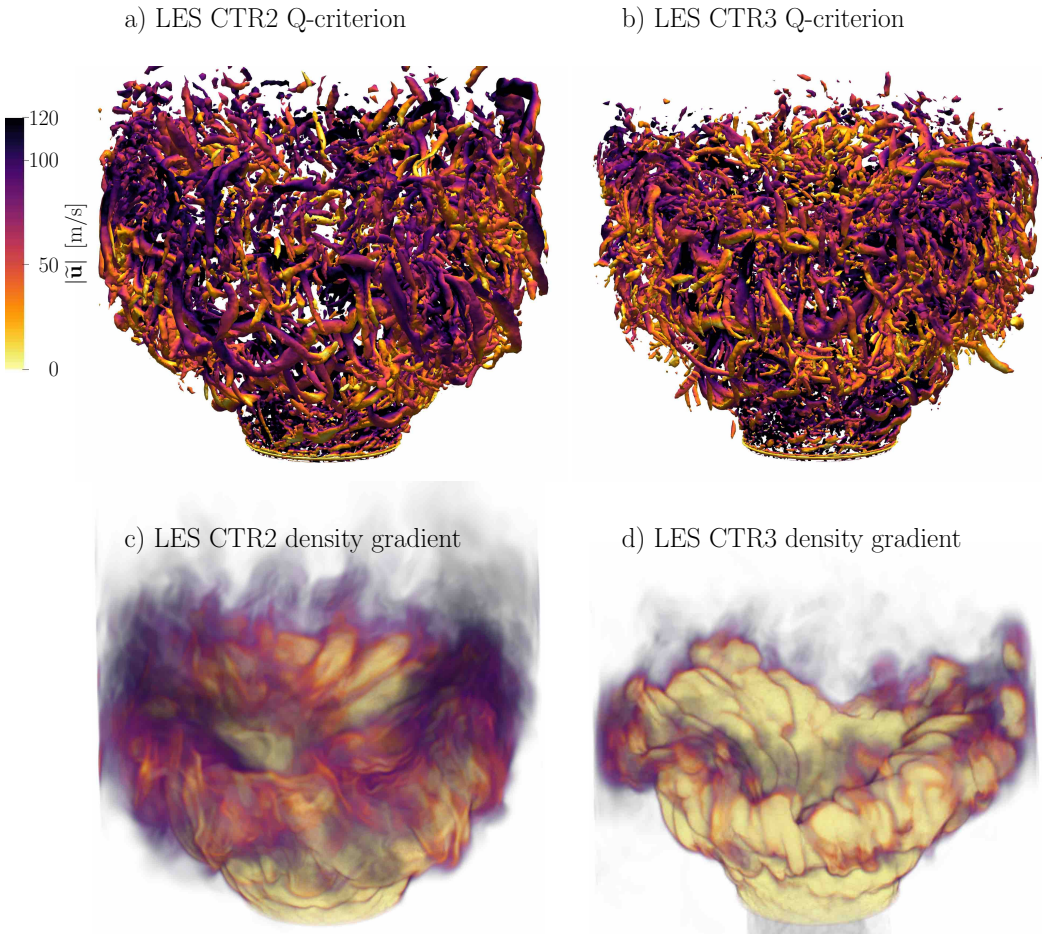

FIGURE 7.20: Instantaneous Q iso-surfaces (top) and the volumetric rendering of the density gradient (bottom) capturing the instantaneous flame shape in the swirl stabilized hydrogen burner. The columns correspond to the reacting cases CTR2 ($\phi_{glob} = 0.6$, left) and CTR3 ($\phi_{glob} = 0.4$, right).

Firstly, the instantaneous flow structures are analyzed. The Q-criterion of Hunt, Wray, and Moin (1988) is evaluated in the reacting cases, which captures coherent flow structures using the second scalar invariant of the velocity gradient tensor:

$$Q = \frac{1}{2}\left(\|\mathbf{\Omega}\|^2 - \|\mathbf{S}\|^2\right) \tag{7.16}$$

where $\mathbf{S}(\mathbf{u}) = \frac{1}{2}\left(\nabla\mathbf{u} + \nabla^{\mathrm{T}}\mathbf{u}\right)$ is the strain rate tensor, and $\mathbf{\Omega}(\mathbf{u}) = \frac{1}{2}\left(\nabla\mathbf{u} - \nabla^{\mathrm{T}}\mathbf{u}\right)$ is the rotation rate tensor. The Q-criterion defines an eddy structure as a region

with positive second invariant (Q), corresponding to zones where rotation dominates over strain. Figure 7.20 presents the iso-surfaces of Q in the CTR2 and CTR3 cases. The small structures detected by these iso-surfaces are attached to the mixing tube outlet, they are present throughout the shear layers of the high speed swirling flow, and they are fully absent in the corner recirculation zones. The figure also present a volume rendering of the instantaneous density gradient, that captures the flame shape and the resolved flame wrinkling. As the mean flow fields on Fig. 7.19 illustrate, the lower equivalence ratio CTR3 case is characterized by a somewhat wider spreading angle. Furthermore, the lower heat release rate in this case results in a lower burnt gas viscosity and density ratio (see Tab. 7.1), thus the structures of the flow remain smaller. The Q-contours show the formation of helicoidal-like structures, which develop in the outer shear layer and wrinkle the flame front. The higher density ratio in CTR2 enables the existence of high density gradients, which is reflected in Fig. 7.20c and d.

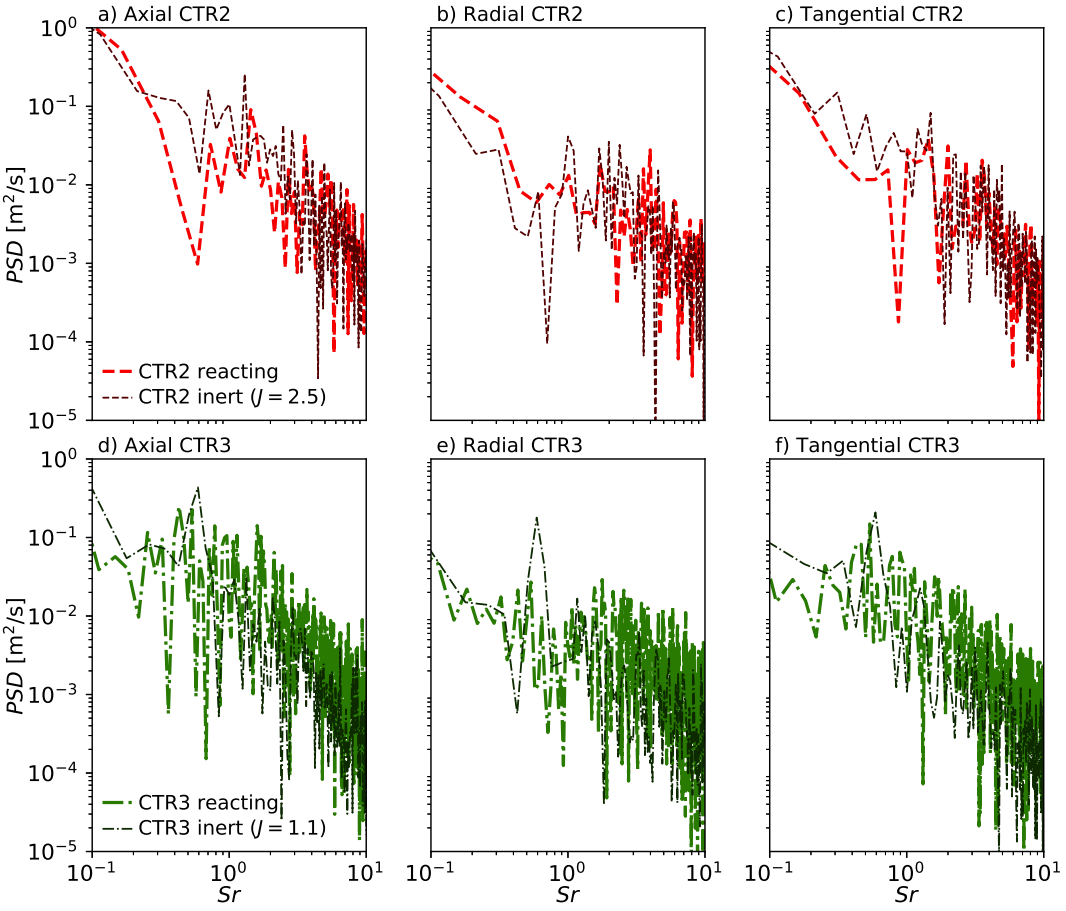

FIGURE 7.21: Power spectral density of the velocity fluctuation in the perfectly premixed reacting and inert LES cases of the swirl stabilized hydrogen flame at an observation point in the combustion chamber ($x = 10$ mm, $r = 15$ mm). The rows correspond to the flow conditions of CTR2 ($\phi_{glob} = 0.6$, top) and CTR3 ($\phi_{glob} = 0.4$, bottom), with the line style indicating the reacting and inert simulations.

As discussed in section 7.2.3, the inert flow shows the presence of a precessing vortex core. This coherent flow structure is diminished by the addition of axial momentum through the fuel injection ports, but under the conditions of CTR3 ($J = 1.1$)

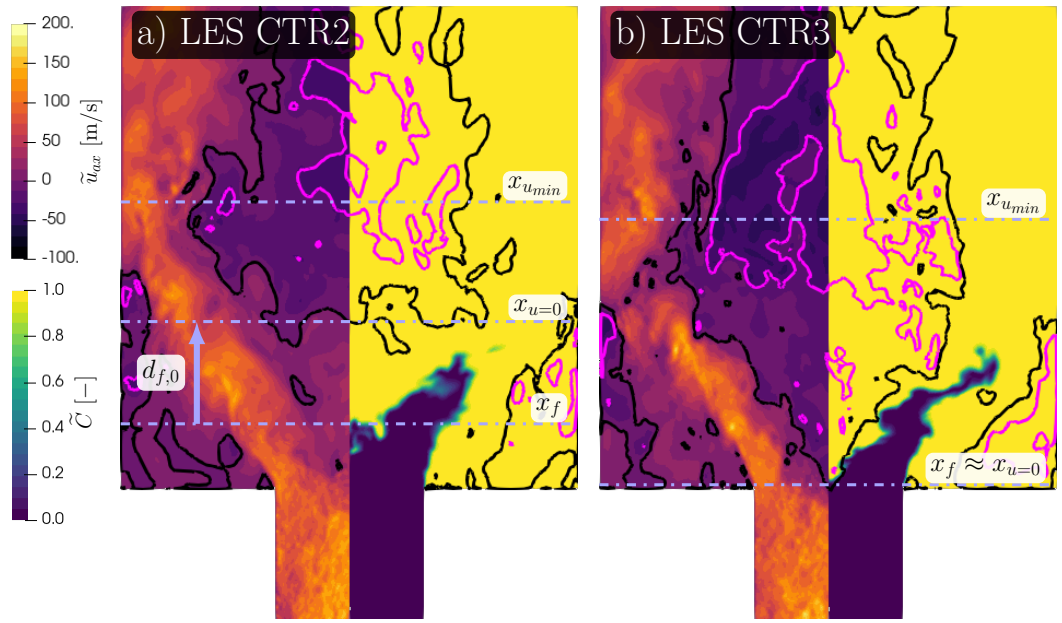

FIGURE 7.22: Instantaneous velocity and progress variable fields in the swirl stabilized hydrogen burner corresponding to the CTR2 ($\phi_{glob} = 0.6$, left) and CTR3 ($\phi_{glob} = 0.4$, right) conditions. Contour lines mark the location of zero axial velocity (black) and an axial velocity of -30 m/s (magenta). Axial distances are indicated, which mark specific points on the centerline of the domain: flame location (x_f), stagnation point ($x_{u=0}$), and the highest recirculation velocity ($x_{u_{min}}$).

it is still detectable in the velocity spectrum at its characteristic frequency, which corresponds to a Strouhal number of $Sr = 0.54$. Note, that the inert case (CTR1) also shows a strong secondary peak in the spectrum at $Sr \approx 1.1$. (See Fig. 7.10b.) The spectra of the velocity components is shown in Fig. 7.21 comparing the reactive and inert cases under the CTR2 ($\phi_{glob} = 0.6$) and CTR3 ($\phi_{glob} = 0.4$) conditions. In the case of CTR2 the fuel jets alone suppress the fluctuations at $Sr = 0.54$, however the $Sr \approx 1.1$ peak is present in the inert spectra. In the reacting case even this second peak is attenuated. Interestingly, the characteristic peaks of the axial and radial velocity components appear to be more affected than the peak in the tangential spectrum, possibly because the latter velocity component is mostly tangential to the flame front, while the others have significant flame-normal components. In the case of CTR3 the inert case still shows signs of the precessing vortex core at $Sr = 0.54$. This behavior is completely suppressed by the flame. Note, that in the analysis of Mira et al. (2018) the reacting cases were also assessed using POD, but no coherent structures are found. This effect of the heat release rate is extensively studied by Oberleithner et al. (2013) using linear stability analysis (LSA). By applying the LSA to different flow fields with stratified and with uniform density, they show that strong density gradients close to the origin of the global instability are the root cause of the suppression of the PVC instead of the altered velocity field or the change in viscosity. The latter is insignificant because turbulent transport outweighs the viscous one. Accordingly, the existence of the PVC does not only depend on the presence of heat release, but also on its position relative to the density gradients caused by heat release. As Oberleithner et al. (2013) show, the PVC is suppressed

in V-shape flame types, where the heat release takes place at the upstream part of the recirculation zone, i.e.: the gradients of the velocity and density field coincide locally. Indeed, this is the case of the present reacting cases, as the heat release alters the density field right in the the shear layers. (See Fig. 7.19 b and c.) The present perfectly premixed LES approach is capable of reproducing this phenomenon, confirming the theoretical findings of Oberleithner et al. (2013).

In order to further analyze the influence of the proximity of flashback and the dynamics of the flames under these conditions, a statistical distribution of the key parameters characterizing the flame evolution is evaluated. The studied parameters are locations of specific points along the centerline of the burner indicated on Fig. 7.22. The location of the flame (x_f) is identified by an intermediate progress variable value of $\widetilde{C} = 0.5$. The central recirculation zone is characterized by the location of the stagnation point at zero axial velocity ($x_{u=0}$), and the location of the minimal axial velocity ($x_{u_{min}}$). Furthermore, the distance of the flame and the stagnation point: $d_{f,0}$ is also evaluated. The figures indicate typical situations for the perfectly premixed LES cases of CTR2 and CTR3. Namely, in CTR2 the axial flow is able to penetrate the flame, as the mean flow also suggests in Fig. 7.19b, thus the stagnation point and the reaction zone are often separated. In CTR3 however, the flame and the stagnation point are typically closer to one another. This behavior of the simulation results is confirmed below, by evaluating the histogram of the indicated distances.

Figure 7.23 shows a comparison of the histograms of the recirculation zone parameters obtained for the experimental PIV data and present LES. In the CTR2 case the axial movement of these specific points is captured well by the LES, even if the mean location of stagnation point is not fully reproduced as readily discussed in relation to the mean flow. The CTR3 case shows larger discrepancies in the location of the stagnation point. In general, the LES tends to shift the locations upstream compared to the PIV, which is magnified as the flame approaches flashback. The center of the CRZ ($x_{u_{min}}$) shows a wider spatial distribution than the location of the stagnation point. This variation is reproduced well by the simulations, although an upstream shift is observed here as well. The PIV data shows a small upstream shift in the stagnation point location, which is magnified in the LES, as the stagnation point location is much more affected in the present perfectly premixed LES results than in the experiments.

The statistical analysis of the central recirculation zone is further complimented by the similar evaluation of the flame in Fig. 7.24. As Fig. 7.24a indicates, in the perfectly premixed LES cases the difference between the flame locations of CTR2 and CTR3 is subtle. In the CTR3 simulations, which are closer to flashback, the flame appears to be more lifted than in the CTR2 case. Nevertheless, as Fig. 7.24b shows, the significant difference between the two cases lies in the location of the stagnation point. In the more stable CTR2 case the axial flow is able to penetrate the flame front, causing a larger separation ($d_{f,0}$) between the flame and stagnation point. Meanwhile, in the CTR3 case, the stagnation point is more attached to the flame, shifting to most likely distance to zero. This change in behavior suggests the occurrence of combustion-induced vortex breakdown (Kiesewetter, Konle, and Sattelmayer, 2007), which is also observed by Tangermann and Pfitzner (2009) in a similar setup. In conclusion, the present analysis using the perfectly premixed model suggests, that the flashback is a consequence of an abrupt change in the flame behavior, as the flow dynamics are altered, ultimately leading to combustion-induced vortex breakdown. This is in agreement with the experimental observations of Reichel, Terhaar, and Paschereit (2015). Note, that the overall better correlation observed in CTR2 could indicate, that the assumption of perfectly premixed combustion near the stability

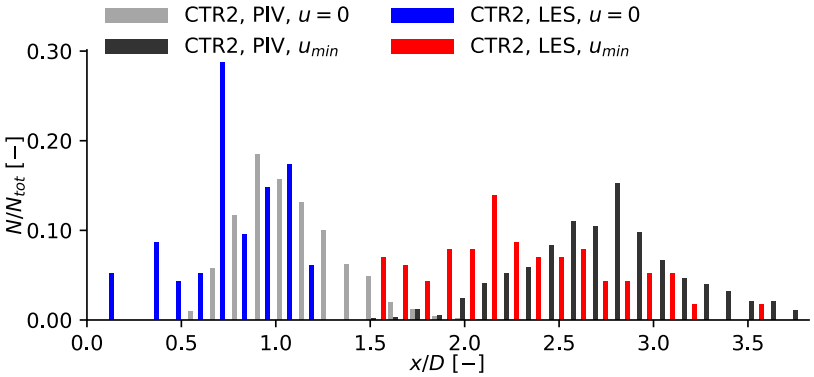

(A) Distribution of stagnation point location and peak recirculation in the CTR2 ($\phi_{glob} = 0.6$) case.

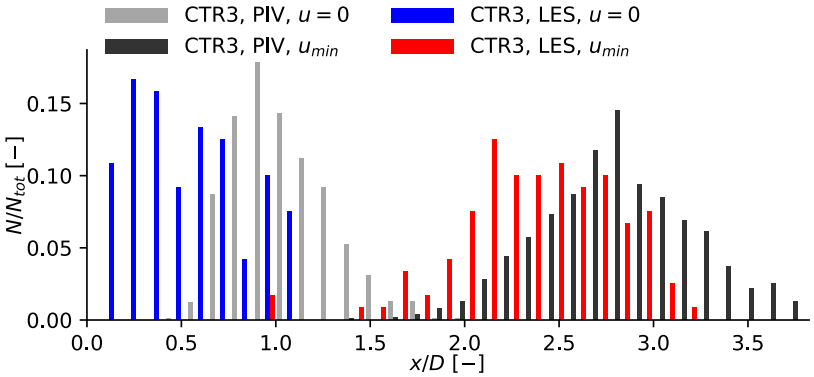

(B) Distribution of stagnation point location and peak recirculation in the CTR3 ($\phi_{glob} = 0.4$) case.

FIGURE 7.23: Distribution of stagnation point location and peak recirculation in the reacting cases of the swirl stabilized hydrogen burner.

limit, as the flashback phenomenon is highly sensitive to the upstream conditions of the mixing tube. (Reichel and Paschereit, 2017) The reacting flow is further analyzed in section 7.4, using a combustion model accounting for mixture stratification.

7.3.6 Scales of turbulence/chemistry interaction

Using the scale estimation strategy outlined in section 5.1.6, the reacting cases of the perfectly premixed LES are further analyzed in this section, with focus on the turbulence/chemistry interaction.

The location of various monitoring points on the regime diagram of Peters (1999) is identified in Fig. 7.25. The most upstream points are located in the mixing tube, 10 mm ahead of the entrance of the combustion chamber. The rest of the points are within the combustion chamber with the marker shape indicating the axial location, and the marker color the Reynolds-averaged scaled progress variable. As readily shown on Fig. 7.15 the distribution of turbulence Reynolds numbers is quite similar in the two reacting cases at $x = 0.147D$ corresponding to 5 mm downstream of the combustion chamber inlet. In the perfectly premixed simulations, the flame is often lifted above this location (see Fig. 7.24a), thus the mean progress variable at

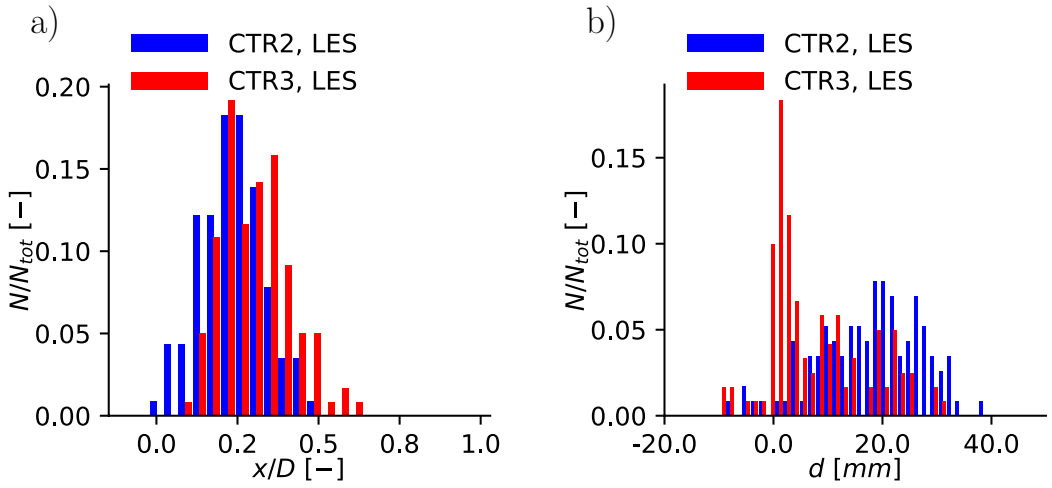

FIGURE 7.24: Distribution of the flame location (left) and the distance of the stagnation point form it (right) in the perfectly premixed reacting LES cases of the swirl stabilized hydrogen burner.

these points is low. As the flame is fairly compact, the turbulence of the fresh gas at this location is representative to the turbulence which interacts with the flame front. Since Re_t is similar in CTR2 and CTR3, the difference observed in Fig. 7.25 is largely due to the different scaling values: δ_{diff} and S_L. Consequently, the Karlovitz number of the two cases is different, with CTR2 characterized by $Ka \approx 2.4$, and CTR3 by $Ka \approx 4.6$. These values indicate, that the flamelet assumption holds in the swirl stabilized hydrogen flame across various premixed conditions, as the operating points are in the lower half of the thin reaction zones regime. Furthermore, even the more strict $Ka < 16$ condition identified by Poinsot, Veynante, and Candel (1991) holds in the present cases.

While these perfectly premixed cases are identified to both belong to the flamelet regime, the slight difference in the Karlovitz numbers may have an influence on the turbulent flame behavior. The two values are separated by the $\frac{\rho^u}{\rho^b} - 1$ limit of MacArt, Grenga, and Mueller (2018): 3.1 and 2.3 for CTR2 and CTR3 respectively. This limit indicates, that as the CTR2 case is closer to the corrugated flamelets regime, intense back scatter may affect the turbulent energy cascade. However, the CTR3 case is well within the thin reaction zones regime, and the effects of back scatter are expected to diminish for $Ka > \frac{\rho^u}{\rho^b} - 1$.

The other evaluated locations of Fig. 7.25 within the combustion chamber tend to be partially or fully reacted, showing the effect of the flame on the turbulence integral scales. These points are characterized by either higher or lower turbulent velocity fluctuations (v') compared to the incoming fresh gases. Not indicated in the figure, the lower v' values corresponds to the points located in the central recirculation zone. Meanwhile, the high velocity shear layer tends to become more turbulent in both CTR2 and CTR3.

The perfectly premixed simulation cases are also evaluated using the LES regime diagram of Pitsch and De Lageneste (2002) in Fig. 7.26 which incorporates both the

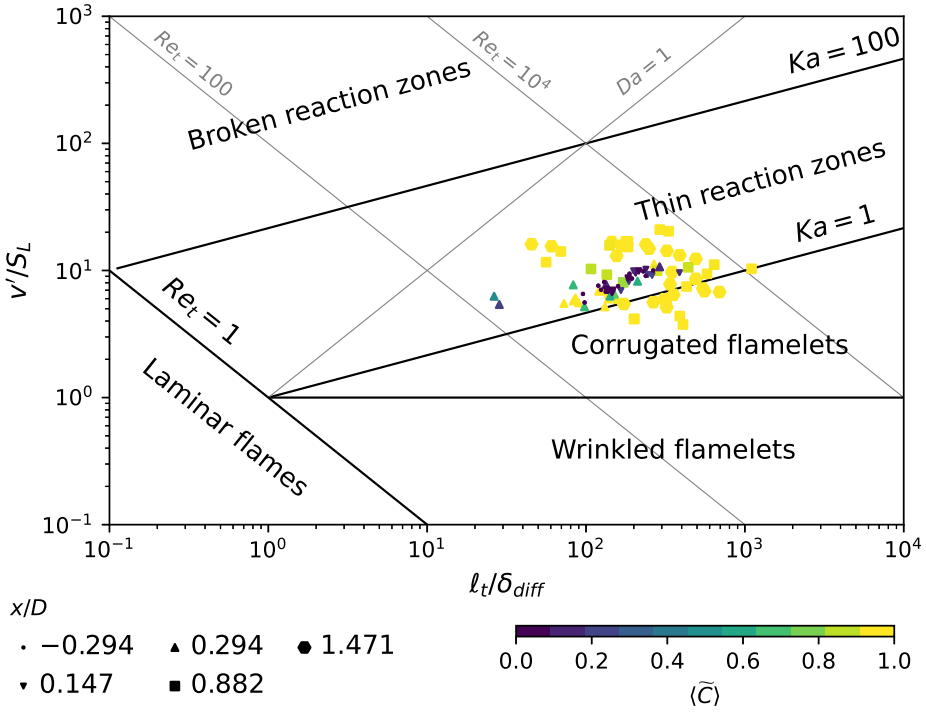

(A) Peters' regime diagram in the CTR2 case ($\phi_{glob} = 0.6$, $S_L = 1.94$ m/s, $\delta_{diff} = 35.6$ μm).

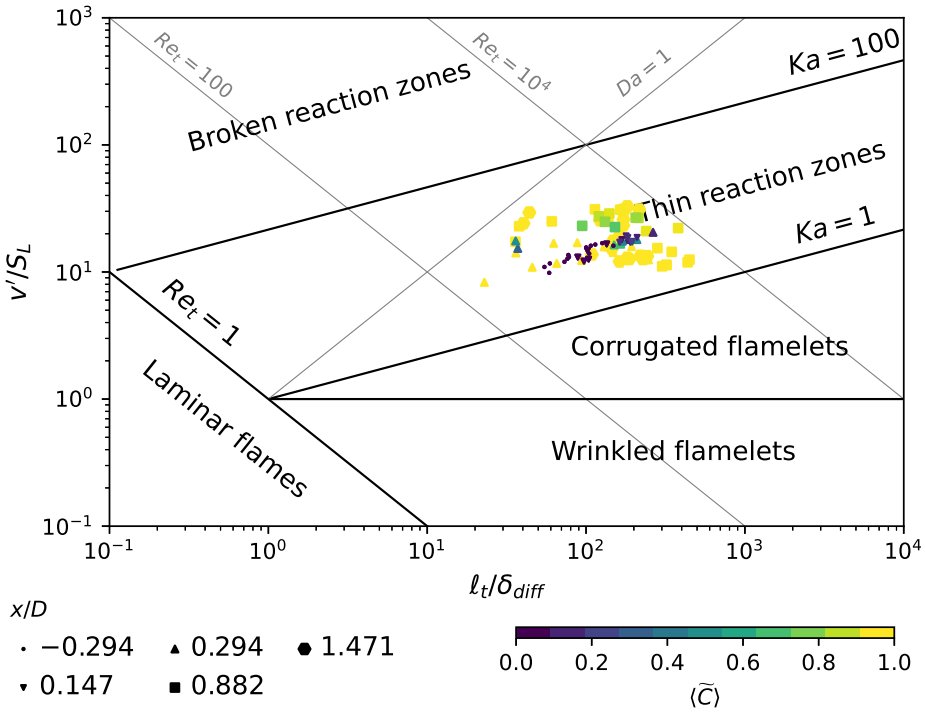

(B) Peters' regime diagram in the CTR3 case ($\phi_{glob} = 0.4$, $S_L = 1.09$ m/s, $\delta_{diff} = 57.5$ μm).

FIGURE 7.25: Peters' regime diagram in the reacting cases of the swirl stabilized hydrogen burner using the perfectly premixed combustion model.

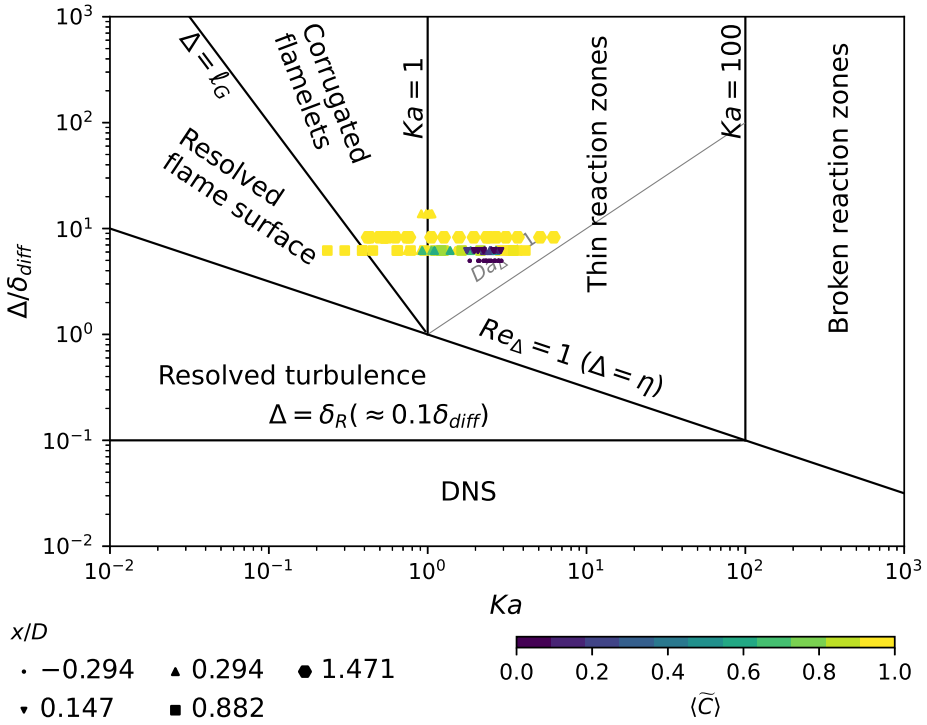

(A) LES regime diagram in the CTR2 case ($\phi_{glob} = 0.6$, $\delta_{diff} = 35.6\ \mu$m, $\tau_{diff} = 18.4\ \mu$s).

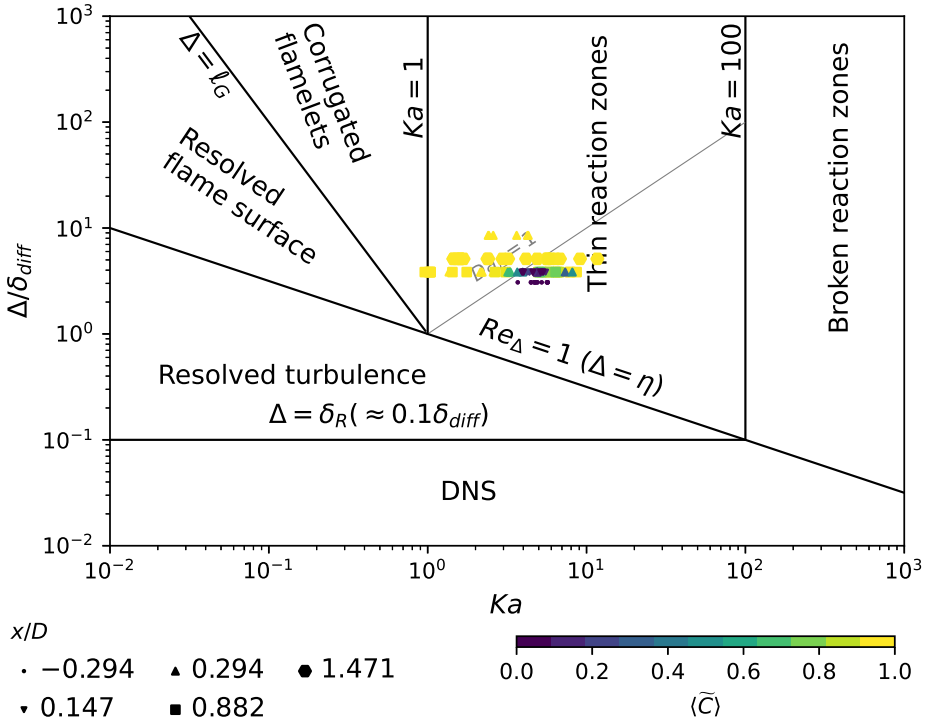

(B) LES regime diagram in the CTR3 case ($\phi_{glob} = 0.4$, $\delta_{diff} = 57.5\ \mu$m, $\tau_{diff} = 52.9\ \mu$s).

FIGURE 7.26: LES regime diagram of Pitsch and De Lageneste (2002) in the reacting cases of the swirl stabilized hydrogen burner using the perfectly premixed combustion model.

filtering effects and turbulent combustion regimes. The same marker stiles and coloring is applied as above in the regime diagram of Peters. This representation expresses the regimes better, as $Ka = \frac{\tau_{diff}}{\tau_\eta}$ is calculated directly, whereas on the diagram of Peters, the location of the limits assumes constant material properties and unity Schmidt numbers. Indeed, the fresh reactant flow is within the thin reaction zones regime. In the CTR2 case, the Karlovitz numbers are generally lower, as the chemical timescale is lower, thus certain witness points are characterized by $Ka < 1$, although most of these are in the post flame region. In comparison, in CTR3 the points are shifted downwards and to the right, as the flame becomes somewhat more resolved, and as the chemical time scale increases substantially. Mainly due to the slower chemistry, part of the assessed monitoring points are located at a filter-scale Damköhler number of $Da_\Delta < 1$, indicating that the part of he turbulent broadening of the preheat zone may be resolved in the CTR3 case. In comparison to the PRECCINSTA case in Fig. 6.32 the present H_2 cases are significantly more reactive, resulting in rather flamelet-like behavior. The level of resolution is somewhat lower here, placing a more stringent requirement on the performance of the sub-grid models.

7.4 Partially premixed reacting flow

The analysis using a perfectly premixed model presented in section 7.3 is capable of capturing the flame characteristics to an extent. However, the stratification of the fresh gas mixture may have an important effect on both the turbulent flow and the flame propagation. This section accounts for such mixture fraction variations, and analyses the effects on the swirl stabilized hydrogen flame.

7.4.1 Partially premixed combustion model

To extend the analysis to the effects of mixture fraction stratification, a more elaborate combustion model is used. The thermo-chemical tables are composed of arrays of premixed flamelets. Furthermore, to account for heat transfer to the burner walls, burner-stabilized flamelets are also included in the manifold.

Governing equations

In alignment with the extension of the modeling framework, additional control variables are needed to retrieve properties from the thermo-chemical manifolds. Firstly, the manifold is also parameterized by the filtered mixture fraction. Furthermore, the turbulence/chemistry interaction is considered following Domingo, Vervisch, and Veynante (2008), as it is *a priori* unknown, whether the sub-grid distribution of mixture fracton has a notable effect on the flame propagation. Thus, the sub-grid variances of both mixture fraction and progress variable are solved, giving the possibility to parameterize the joint FPDF of the control variables. Thus the final set of governing equations in this model consists of the Navier-Stokes equations (Eq. (5.30) and Eq. (5.47)), the equations of enthalpy, mixture fraction, and progress variable (Eq. (5.117)), and the transport equations of sub-grid variances of both mixture fraction (Eq. (5.122)) and progress variable (Eq. (5.123)). Here the equations are

reproduced for completeness:

$$\partial_t \overline{\rho} + \nabla \cdot (\overline{\rho}\widetilde{\mathbf{u}}) = 0 \tag{7.17}$$

$$\partial_t (\overline{\rho}\widetilde{\mathbf{u}}) + \nabla \cdot (\overline{\rho}\widetilde{\mathbf{u}} \otimes \widetilde{\mathbf{u}}) + \nabla \overline{p} - \nabla \cdot \left(2\left(\overline{\mu} + \overline{\rho}\nu^{SGS}\right)\widetilde{\mathbf{S^D}(\mathbf{u})}\right) = 0 \tag{7.18}$$

$$\partial_t \left(\overline{\rho}\widetilde{h}\right) + \nabla \cdot \left(\overline{\rho}\widetilde{h}\widetilde{\mathbf{u}}\right) - \nabla \cdot \left(\overline{\rho}\left(\widetilde{\mathcal{D}_t} + \frac{\nu^{SGS}}{Pr^{SGS}}\right)\nabla\widetilde{h}\right) = 0 \tag{7.19}$$

$$\partial_t \left(\overline{\rho}\widetilde{Z}\right) + \nabla \cdot \left(\overline{\rho}\widetilde{Z}\widetilde{\mathbf{u}}\right) - \nabla \cdot \left(\overline{\rho}\left(\widetilde{\mathcal{D}_t} + \frac{\nu^{SGS}}{Sc^{SGS}}\right)\nabla\widetilde{Z}\right) = 0 \tag{7.20}$$

$$\partial_t \left(\overline{\rho}\widetilde{Y_c}\right) + \nabla \cdot \left(\overline{\rho}\widetilde{Y_c}\widetilde{\mathbf{u}}\right) - \nabla \cdot \left(\overline{\rho}\left(\widetilde{\mathcal{D}_t} + \frac{\nu^{SGS}}{Sc^{SGS}}\right)\nabla\widetilde{Y_c}\right) = \overline{\dot{\omega}_{Y_c}} \tag{7.21}$$

$$\partial_t (\overline{\rho}Z_v) + \nabla \cdot (\overline{\rho}Z_v\widetilde{\mathbf{u}}) - \nabla \cdot \left(\overline{\rho}\left(\widetilde{\mathcal{D}_t} + \frac{\nu^{SGS}}{Sc^{SGS}}\right)\nabla Z_v\right) = 2\frac{\overline{\rho}\nu^{SGS}}{Sc^{SGS}}\nabla\widetilde{Z}\cdot\nabla\widetilde{Z} - \overline{\rho}\chi_Z^{SGS}, \tag{7.22}$$

$$\partial_t (\overline{\rho}Y_{c,v}) + \nabla \cdot (\overline{\rho}Y_{c,v}\widetilde{\mathbf{u}}) - \nabla \cdot \left(\overline{\rho}\left(\widetilde{\mathcal{D}_t} + \frac{\nu^{SGS}}{Sc^{SGS}}\right)\nabla Y_{c,v}\right) = 2\frac{\overline{\rho}\nu^{SGS}}{Sc^{SGS}}\nabla\widetilde{Y_c}\cdot\nabla\widetilde{Y_c} + 2\left(\overline{Y_c\dot{\omega}_{Y_c}} - \widetilde{Y_c}\overline{\dot{\omega}_{Y_c}}\right) - \overline{\rho}\chi_{Y_c}^{SGS}. \tag{7.23}$$

The model retains the unity Lewis number assumption, with the same rationale as in the perfectly premixed model of section 7.3.1. The rest of the modeling decisions are in alignment of the other turbulent simulations of this work. The sub-grid model of Vreman (2004) is applied with a model constant of $c = 0.1$ to ensure a robust method in this complex burner. Meanwhile the sub-grid diffusion of scalars is treated using $Pr^{SGS} = Sc^{SGS} = 0.7$. The equations are discretized in the non-conservative form.

Tabulated chemistry model

The thermo-chemical states are represented by free and burner-stabilized premixed flamelets depicted in Fig. 7.27 computed using the San Diego mechanism. (UCSD, 2018) Indeed, the laminar flame propagation is highly sensitive to both equivalence ratio and enthalpy variations. Thus it is expected, that the more elaborate modeling strategy of the present section may result in significantly different flow conditions, given that the flame is subjected to notable enthalpy deficit and mixture stratification. As discussed in section 7.1.3, the lean flammability limit is found at $\phi_L = 0.2$. The lean limit changes with enthalpy loss, e.g.: at $m/(\rho^u S_L) = 0.1$ the lowest flammable equivalence ratio is $\phi_L = 0.31$. A significant enthalpy loss can be realized before flame propagation becomes infeasible. As Fig. 7.27c illustrates, the enthalpy deficit of these last flammable states is approximately half of the maximum attainable enthalpy deficit, which shows similarity between the present H_2 flamelets and the methane cases of section 3.1.2.

The progress variable is chosen to be simply water vapor ($Y_c = Y_{H_2O}$) following the analysis of section 7.3.1, as it provides a reasonable representation across the assessed conditions. The same approach is taken by Van Oijen and De Goey (2000) and more recently Regele et al. (2013). Furthermore, following Gövert et al. (2018), the database is PDF integrated with the joint FPDF of mixture fraction, scaled progress variable, and scaled enthalpy. The former two control variables are modeled using statistically independent β-FPDFs while a δ-function is used for the enthalpy as: $\widetilde{P}_{ZCi} = \widetilde{P}_Z^{\beta}\widetilde{P}_C^{\beta}\widetilde{P}_i^{\delta}$. See Tab. 5.8 for other studies applying such sub-grid modeling.

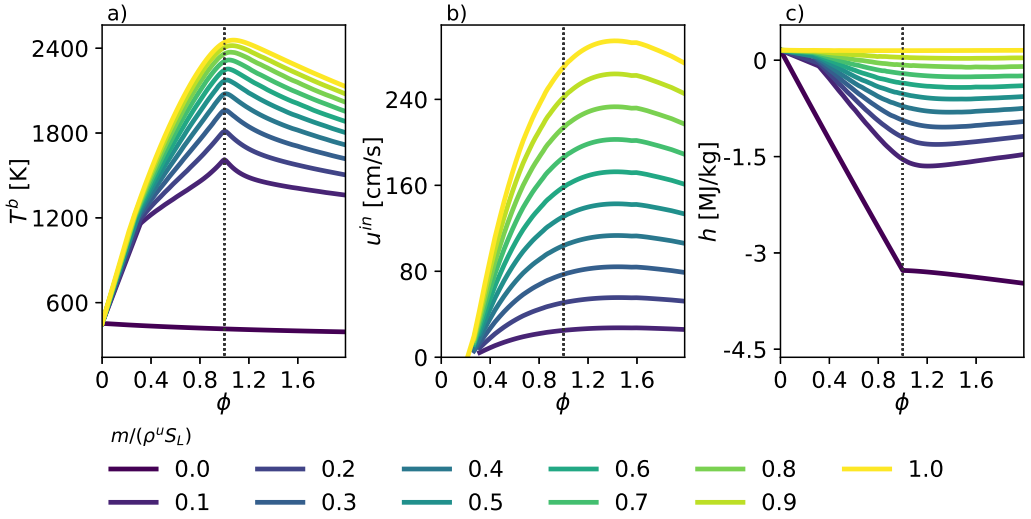

FIGURE 7.27: Properties of 1D premixed burner-stabilized flamelets of hydrogen/air mixtures as function of equivalence ratio under the conditions of the swirl stabilized hydrogen burner. From left to right: outlet flame temperature T^b, laminar flame speed S_L, enthalpy h. Different line correspond to different mass fluxes defined by $m/(\rho^u S_L)$ as indicated by the legend.

Figure 7.28 depicts the filtered progress variable source term in specific representative sections of the full database. As found *a posteriori*, the mixture fraction variance is negligible in the flame region, thus the figure depicts the effects of representative enthalpy deficit and sub-grid progress variable variance values. The source term is severely decreased by both increasing ζ_C and decreasing i. Nevertheless, as section 6.3.4 demonstrates, an elevated sub-grid progress variable variance does not necessarily decrease the overall reactivity of the system. Since the β-FPDF distributes the source term more uniformly along Y_c, the variance may cause an overall higher production of progress variable along the full width of the flame front. Contrarily, heat loss consistently decreases the flame speed, by decreasing the peak source term and shifting the progress variable production to higher values of Y_c. (See Fig. 3.35.)

Figure 7.28 also indicates two source term contour lines at $\overline{\dot{\omega}_{Y_c}} = 100$ kg/m^{3}s (red) and $\overline{\dot{\omega}_{Y_c}} = 200$ kg/m^{3}s (green). These limits are rather low in comparison to the peak of max $\left(\overline{\dot{\omega}_{Y_c}}\right) \approx 2500$ kg/m^{3}s. Furthermore, relevant constant equivalence ratio values are also indicated using dashed lines. The lean flammability limit is particularly relevant in the present cases, as the global equivalence ratio is rather low in both studied conditions. The red and green contour lines indicate, that both enthalpy deficit and progress variable variance can decrease the reactivity of the mixture significantly near the lean flammability limit. The contours also highlight the typical vertical shift with the decrease of i, and broadening with the increase of ζ_C.

7.4.2 Flame characteristics

The inclusion of partial premixing and heat loss effects has significant influence on the predicted flame behavior compared to the perfectly premixed model of section 7.3. This section present the LES simulation results using the partially premixed

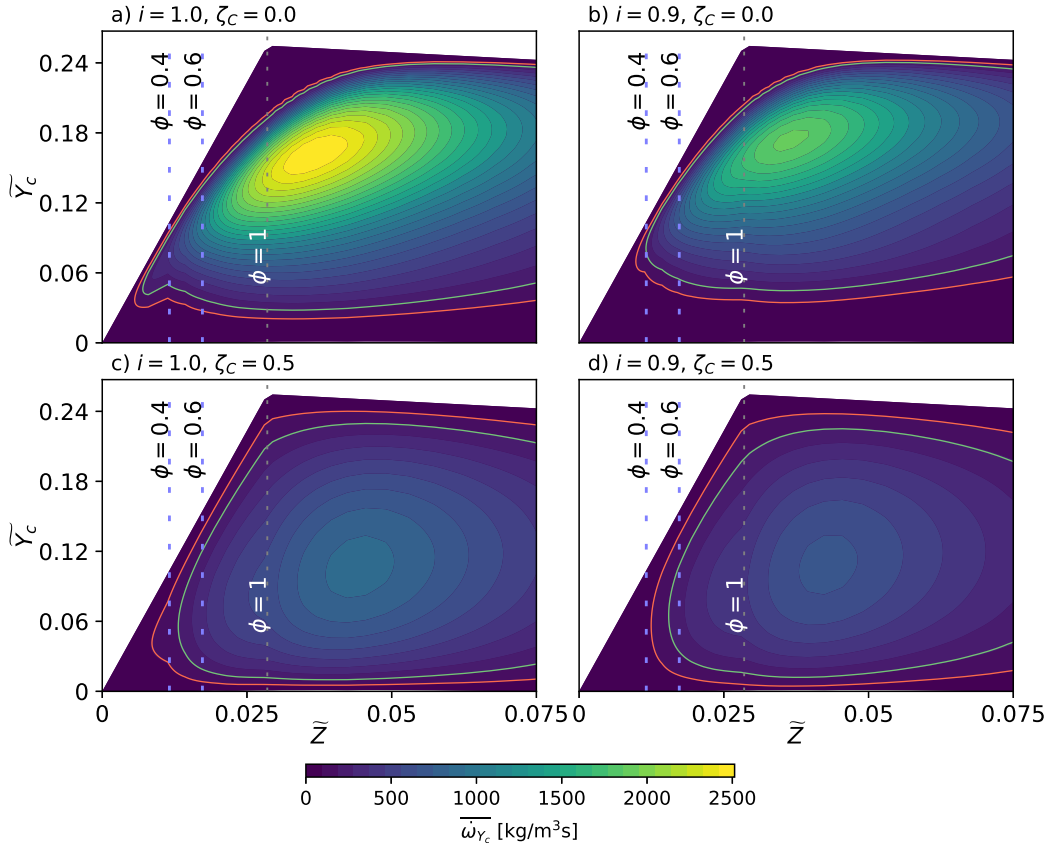

FIGURE 7.28: Illustration of the thermo-chemical table for the partially premixed simulations of the swirl stabilized hydrogen burner. The filtered progress variable source term contours are presented on the $\widetilde{Z} - \widetilde{Y}_c$ plane at various conditions. The dashed line indicates the stoichiometric mixture fraction: $Z_{st} = 0.0285$.

combustion model. In this case, the flow rates of air and hydrogen are prescribed directly on the boundaries according to Tab. 7.2. Furthermore, to model heat loss to the environment, the temperature is prescribed on the vertical and horizontal walls of the combustion chamber as the fresh oxidizer temperature (453 K). The characteristics of the simulated reacting flows under these conditions is discussed below.

Figure 7.29 presents various instantaneous scalar fields in the partially premixed simulations of the CTR2 and CTR3 cases. The location of the recirculation zone is indicated using contour lines of the axial velocity. Furthermore, to relate the fields to the flame location, the reaction zone is encompassed in a contour line of the heat release rate. As Fig. 7.29a and b illustrate, the encountered temperature values are radically different in the two cases. A high temperature zone is located in the center of the domain, while the corner recirculation zones are characterized by lower temperatures due to the heat exchange with the burner walls and the long residence time. In the CTR2 case the maximum instantaneous temperature is the maximum possible adiabatic flame temperature (~ 2400 K), while in the CTR3 case the peak temperature is well below it this value. The difference is explained by the instantaneous local equivalence ratio displayed in Fig. 7.29c and d. The fuel is distributed quite unevenly in the mixing tube, despite the relatively long mixing section and the highly turbulent flow. As Tab. 7.1 details, there is a 21% difference between the

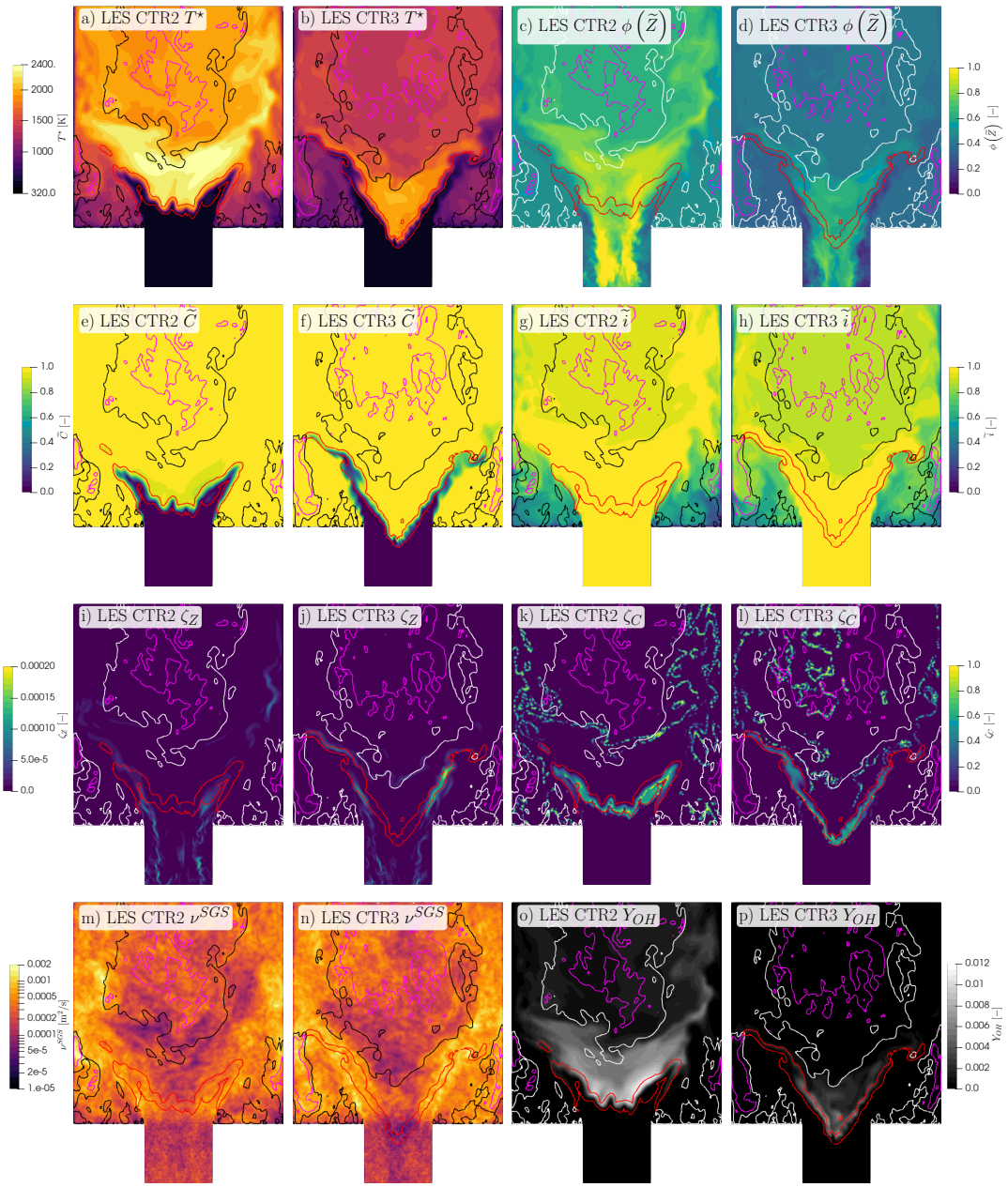

FIGURE 7.29: Instantaneous fields in the swirl stabilized hydrogen burner using the partially premixed combustion model corresponding to the CTR2 ($\phi_{glob} = 0.6$, first and third column) and CTR3 ($\phi_{glob} = 0.4$, second and fourth column) conditions. Contour lines mark the location of zero axial velocity (black/white), an axial velocity of -30 m/s (magenta), and a heat release rate of 0.5 GW/m^{3}s (red).

density of oxidizer and the stoichiometric mixture. This notable density difference hinders mixing as the inertial forces of the highly swirling flow promote the separation of the mixtures, forcing the lighter rich mixtures to the centerline of the flow. As the mixture enters the combustion chamber, it is characterized by an equivalence ratio peak on the centerline, and leaner mixtures on the edge of the mixing tube. In the CTR2 case this corresponds to stoichiometric conditions in the center of the flow,

and lean but flammable mixtures on the mixing tube edge. Meanwhile in CTR3, the core of the flow is lean as well, and the edge contains non-flammable gas pockets.

The equivalence ratio captures one dimension of the thermo-chemical tables, while the remaining table dimension are illustrated in Fig. 7.29e-l. The scaled progress variable $\widetilde{C}$ marks the transition to burnt state, however parts of this front are not reacting as the red contour line of heat release rate indicates. In the present simulations, the outer reaction zone is weakened by multiple effects. Firstly, the mixture on the edge of the mixing tube is leaner. And secondly, the fresh reactants interact with fully burnt cold combustion products in this area, which results in the local quenching of the flame. In the CTR2 case the outer reaction zone is partially quenched near the wall, while in the CTR3 it is fully absent due to the low reactivity of the lean mixtures on the edge of the flow. The figure also presents the scaled sub-grid variances (segregation factors) of mixture fraction and scaled progress variable. For the definition and of these quantities and their effect on 1D flame propagation see sections 5.4.3 and 6.3.4 respectively. Based on the latter section, the presently encountered sub-grid mixture fraction variance values are not expected to modify the flame propagation characteristics, as ζ_Z is very low in both the CTR2 and CTR3 case. Meanwhile the sub-grid progress variable variance reaches high values, especially in the reacting zone due to the reaction term in the variance transport (term "II" of Eq. 5.39). The instantaneous ζ_C values are higher in CTR2 than in CTR3, possibly because using the same mesh the flame front is resolved more coarsely in the former case. Nevertheless, the large ζ_C values of both cases may increase the flame propagation speed significantly. Figure 7.29m and n present the sub-grid viscosity field in logarithmic scale. The flame front is characterized by rather large sub-grid viscosity, as it is located in the shear layer of the vortex breakdown. In the present modeling strategy, the sub-grid transport modulates significantly the flame propagation, as discussed in section 6.3.4. The peak ν^{SGS} values are two orders of magnitude higher than the molecular viscosity in the unburnt mixtures, the turbulent flame front of the present cases propagates significantly faster than the laminar flame speed.

Finally, Fig. 7.29o and p present the OH radical mass fraction. The radical is produced in the flame front, and it is found in significant concentrations downstream of the flame. The area of large OH concentration is limited to the high equivalence ratio regions, thus Y_{OH} is relatively small in the central recirculation zone, which is characterized by decreased enthalpy levels and nearly homogeneous mixtures around the global equivalence ratio. As the richer CTR2 case is much more reactive, it shows significantly higher Y_{OH} values than CTR3. The instantaneous flame behavior is fairly similar between the CTR2 cases of the present partially premixed model, and the perfectly premixed fields of Fig. 7.22. However, significant differences are observed in CTR3 case. The perfectly premixed model predicted similar flame shapes and different velocity fields between CTR2 and CTR3. Meanwhile, using the more elaborate partially premixed model, the flame shapes between the two cases are radically different. The qualitative analysis of the present section is further elaborated below using the quantitative assessment of the mean fields.

7.4.3 Mean flow

The mean flow fields of the four reacting simulation cases of the present chapter are compared in Fig. 7.30, where the plots of Fig. 7.19 are repeated here for the sake of comparison. The figure illustrates the vortex breakdown phenomenon using isocontours of the average axial velocity and a vector filed of the in-plane velocity components. The flow field is related to the mean density gradients created by mixing

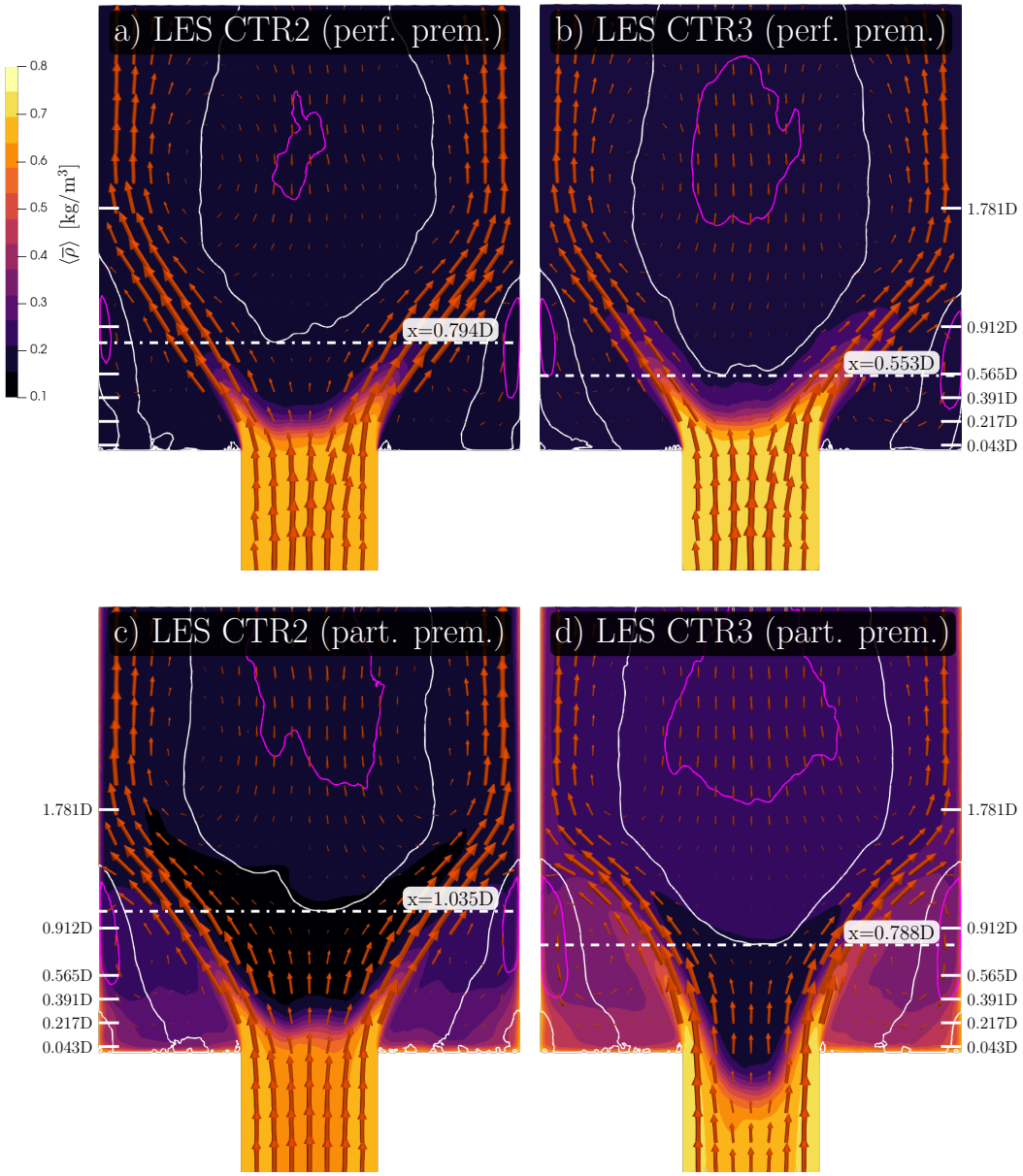

FIGURE 7.30: Comparison of simulated flow fields and flame shapes of the perfectly premixed (top) and partially premixed (bottom) LES of the swirl stabilized hydrogen burner, illustrated by the average density field and the in-plane velocity vector field. The columns correspond to the two reacting cases CTR2 ($\phi_{glob} = 0.6$, left) and CTR3 ($\phi_{glob} = 0.4$, right). Contour lines mark the location of zero average axial velocity (white) and an average axial velocity of -30 m/s (magenta).

and combustion. The nature of the flow is similar in all simulations, showing a cone-type vortex breakdown. The recirculation zone is extended to a large area, placing the positive axial flow to the edge of the combustion chamber. Nevertheless, differences are present between the perfectly premixed and partially simulation results. In both the CTR2 and CTR3 operating conditions, the more elaborate partially premixed model predicts a larger penetration of the axial flow, placing the stagnation

point more downstream than the previous results of section 7.3.4. Meanwhile the intensity of the recirculation zone is also larger in the partially premixed simulations, with the contour line of $\langle \widetilde{u}_{ax} \rangle = -30$ m/s covering a larger area. Furthermore, the relation of the flame location and the stagnation point is significantly different. In the more reactive CTR2 case the difference between the two simulation approaches is less outstanding. The flame is stabilized in a similar shape, but the axial flow is able to penetrate the flame front better in the partially premixed model. However, in the CTR3 case the differences are significant. While the perfectly premixed model suggests, that the flame shape remains largely constant, the present partially premixed model shows the flame entering the mixing tube. This large difference in flame behavior is linked to the nature of the reactant stratification. As presented in Fig. 7.29c and d, in CTR2 the incoming mixture is flammable across all locations while in CTR3 the flow is lined with a layer of very lean non-flammable mixtures on the edge of the mixing tube. Observing the vector field of Fig. 7.30d in the mixing tube, the presence of the flame has significant effect on the flow field, showing the onset of combustion induced vortex breakdown. I.e.: the velocity magnitude is the smallest at the flame tip, and there is a slight radial velocity component immediately upstream of the flame, as the flame front acts as an obstacle and disturbs the flow. Despite the shortcomings of the perfectly premixed model, an aspect that it predicts well is the axial shift in the stagnation point location transitioning from CTR2 to CTR3. In the perfectly premixed cases this difference is $-0.241D$, while in the partially premixed cases it is $-0.247D$.

A quantitative assessment of the partially premixed model predictions is given by the comparison of axial and radial velocity fields in Fig. 7.31 and Fig. 7.32 between the two simulation approaches and the experimental data of Reichel, Terhaar, and Paschereit (2015). As before, the figure shows the radial profiles of the average and RMS of axial and radial velocity components. In the CTR2 case of Fig. 7.31 the mean flow field is notably improved by the present modeling strategy, especially the axial velocity profiles. As the bottom row of the figure shows, the incoming velocity profile is very similar in the perfectly premixed and partially premixed simulations. This suggests, that the cold part of the flow is not influenced significantly by the density variations. At the second assessed location ($x = 0.217D$) the axial velocity of the partially premixed model agrees better with the experimental data, and the over-prediction of radial velocity is also less severe. This location coincides with the flame, in both the perfectly premixed and partially premixed cases, however in the latter the density ratio across the flame is approximately 5, as the composition on the centerline is nearly stoichiometric. Meanwhile, in the perfectly premixed case ρ^u/ρ^b is only 4.11. (See Tab. 7.1.) This increased density ratio leads to higher thermal dilatation and increased axial velocities on the centerline, which explains the better performance of the more elaborate partially premixed model. The axial velocity profiles of the CTR2 case continue to improve further downstream, although the strength of the corner recirculation zone is somewhat over-predicted. At the last assessed position of $x = 1.781D$ the recirculation is still predicted well, although the velocity near the wall is too high in both simulation cases. The latter discrepancy is likely due to the low grid resolution near the flow impingement on the burner wall. While the discrepancy is noted, it is not the focus of the present study. The radial velocity component also shows certain improvement compared to the perfectly premixed simulation, although the peak values of $\langle \widetilde{u}_{rad} \rangle$ are still higher than the experimental maxima. The RMS velocity profiles are somewhat changed in alignment with the changes of the mean flow.

The profiles of CTR3 case displayed in Fig. 7.32 also show certain improvement

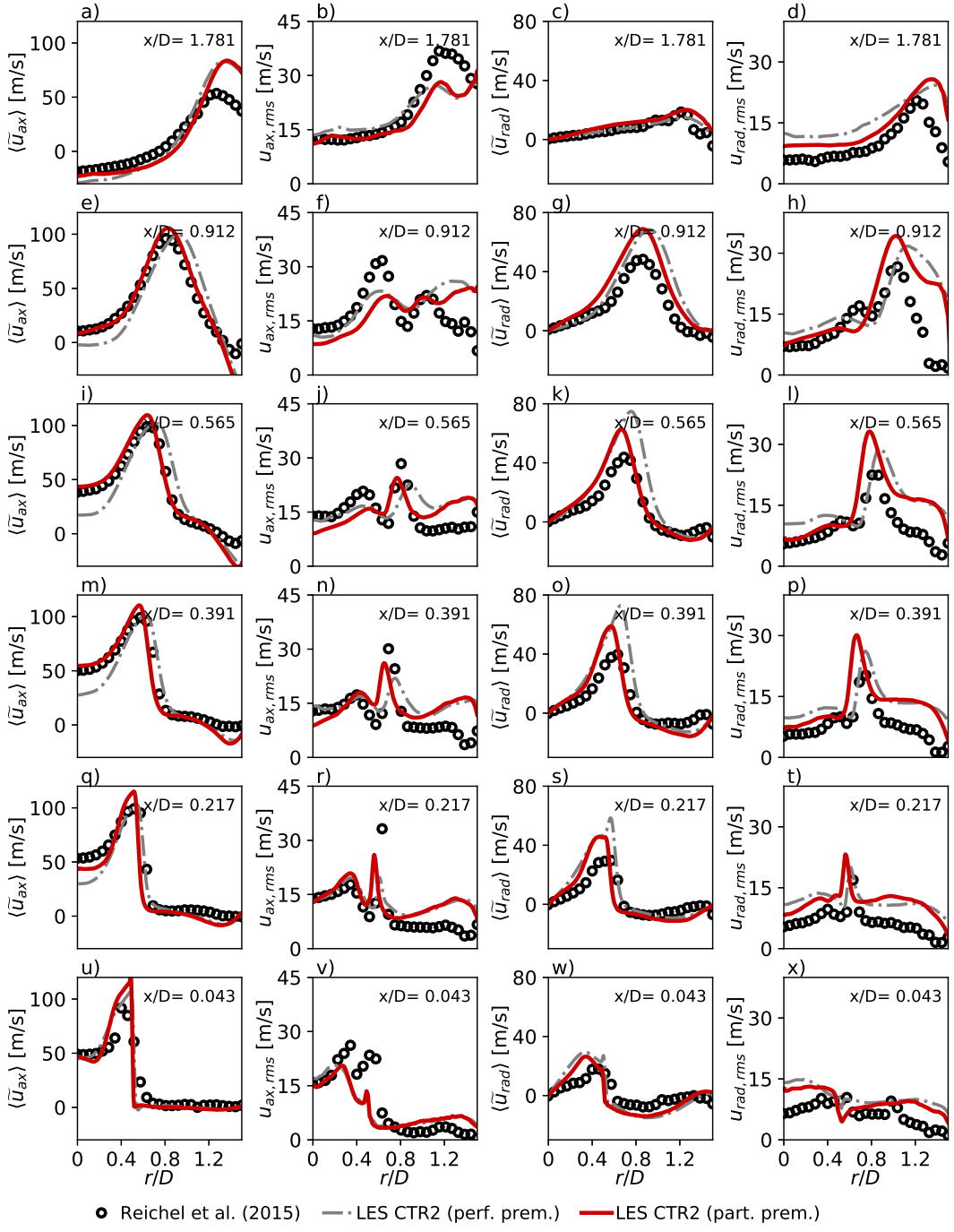

FIGURE 7.31: Comparison of velocity profiles in the CTR2 ($\phi_{glob} = 0.6$) case of the swirl stabilized hydrogen burner between the PIV measurements of Reichel, Terhaar, and Paschereit (2015) and the two LES methods of the present work with the solid lines and dash-dot lines indicating the partially premixed and perfectly premixed models respectively. The rows of plots correspond to the indicated axial location, while the four columns show the mean and variance of the axial velocity, and the mean and variance of the radial velocity.

using the partially premixed model of the present section. Nevertheless, the improvement is less clear. As the flame tip enters the mixing tube it obstructs part

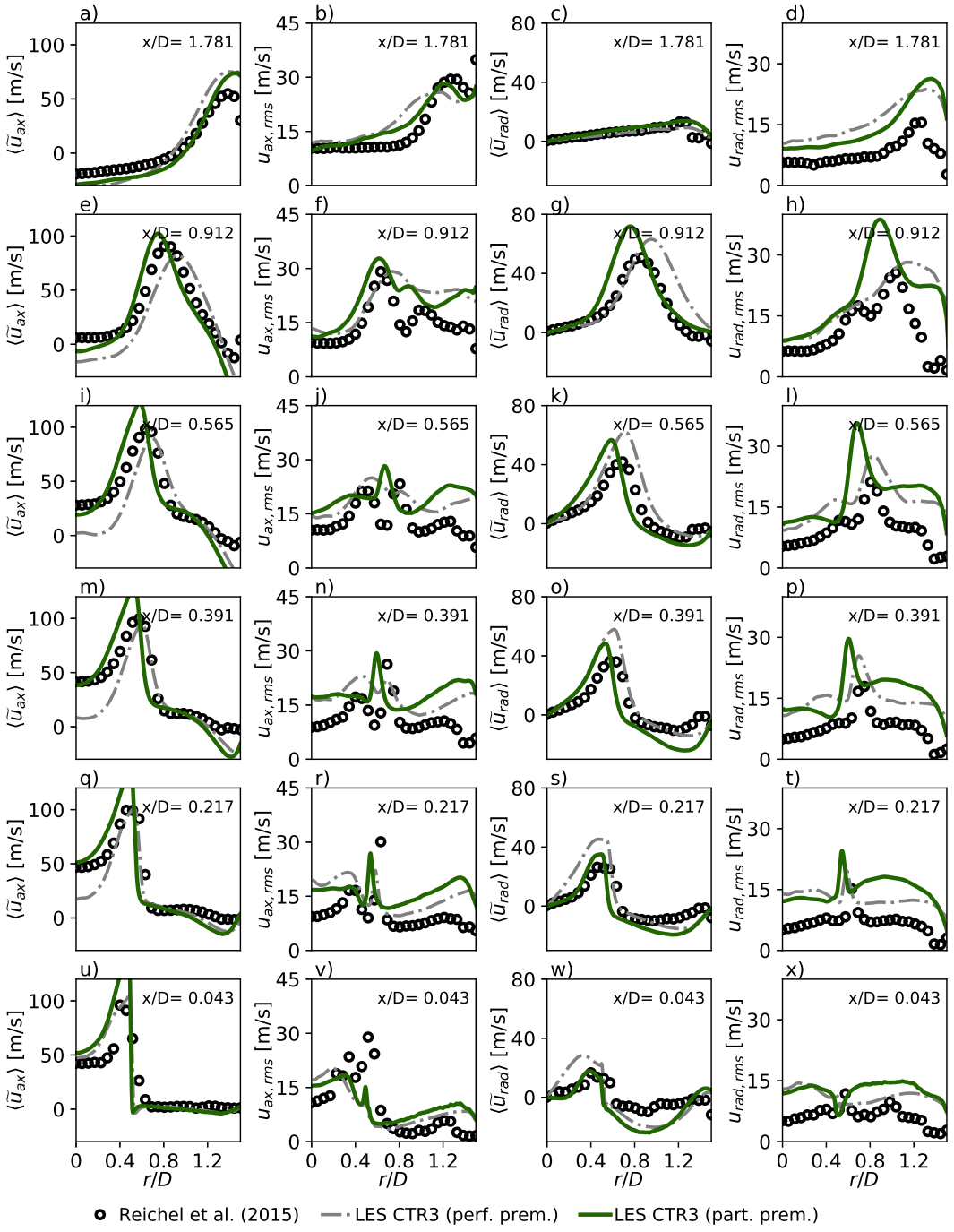

FIGURE 7.32: Comparison of velocity profiles in the CTR3 ($\phi_{glob} = 0.4$) case of the swirl stabilized hydrogen burner between the PIV measurements of Reichel, Terhaar, and Paschereit (2015) and the two LES methods of the present work with the solid lines and dash-dot lines indicating the partially premixed and perfectly premixed models respectively. The rows of plots correspond to the indicated axial location, while the four columns show the mean and variance of the axial velocity, and the mean and variance of the radial velocity.

of the cross section, leading to an increased axial velocity peak in Fig. 7.32u. This

velocity peak seems to significantly affect the spreading of the flow, with the spreading angle somewhat under-predicted, as the location of the velocity peaks indicate. However, just as in the case of CTR2, the prediction of the central recirculation zone is significantly improved. Overall, this highlights the delicate nature of this swirl stabilized hydrogen flame, as changes in the flame location have severe effects on the flow field.

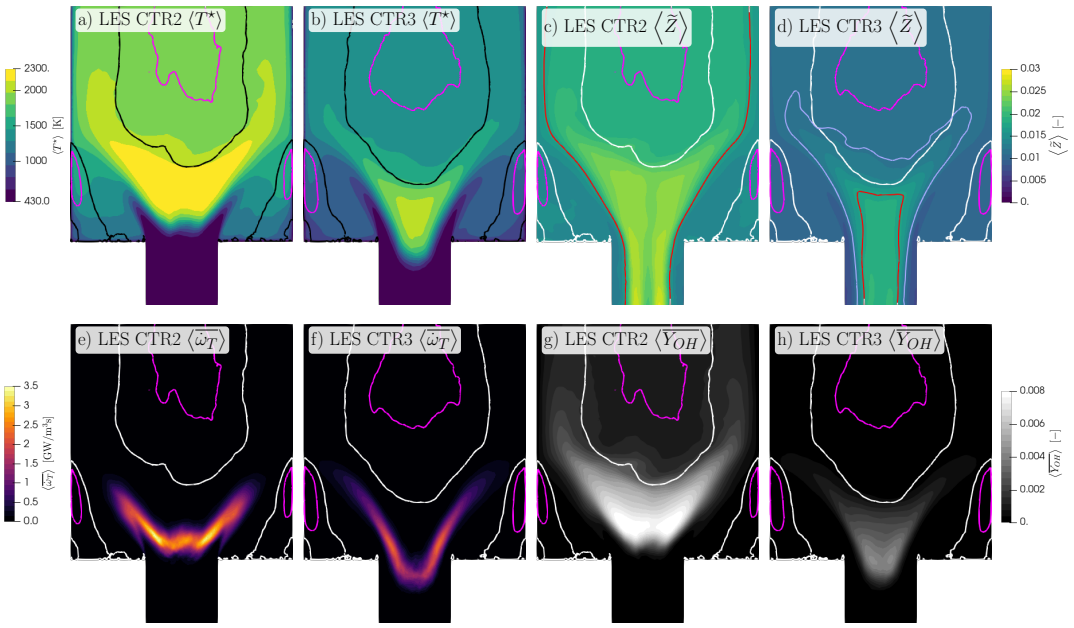

FIGURE 7.33: Comparison of mean simulated scalar fields of the partially premixed LES of the swirl stabilized hydrogen burner. The columns correspond to the two reacting cases CTR2 ($\phi_{glob} = 0.6$, first and third) and CTR3 ($\phi_{glob} = 0.4$, second and fourth). Contour lines mark the location of zero average axial velocity (black/white), an average axial velocity of -30 m/s (magenta), and the mixture fraction contours corresponding to $\phi = 0.6$ (red) and $\phi = 0.4$ (gray).

The mean flame state is further illustrated in Fig. 7.33, using the time averaged temperature (a and b), mixture fraction (c and d), heat release rate (e and f), and OH mass fraction (g and h). In contrast with the perfectly premixed temperature fields of Fig. 7.19, the present temperature distribution is highly affected by both the mixture stratification and the wall heat transfer in the corner recirculation zones. Both flames are characterized by a relatively richer adiabatic core, that can reach high temperatures. This core is limited by the flame front and the stagnation line of the central recirculation zone. As the average mixture fraction fields indicate, the composition in the central recirculation zone is rather uniform, however upstream of the stagnation line significant segregation is observed even on the mean fields. The core of the mixing tube is consistently richer than the edge. The contour lines indicate the global mixture fraction in the CTR2 (red) and CTR3 (gray) cases. The gray contour line is absent on Fig. 7.33c, since the average mixture fraction is above $Z = 0.0116$ ($\phi = 0.4$) throughout the displayed region. I.e.: in CTR2 the mean mixture fraction field is always within the flammability limit in the combustion chamber. Meanwhile, in the CTR3 case the lowest average mixture fraction value at the entrance of the combustion chamber is ~ 0.008 ($\phi \approx 0.27$). While these conditions are technically flammable, as Fig. 7.29 shows, this mean condition is a result of intermittent

flammable and non-flammable pockets. Furthermore, as the corner recirculation zone is characterized by significant heat loss, the flame is completely absent in the outer shear layers. (See Fig. 7.28 for the effect of heat loss on the flame propagation.) This effect is also captured by the mean heat release rate field, that shows an "M shape" in the CTR2 case with a very weak outer reaction zone, and a "V shape" in the CTR3 case where the outer reaction zone is absent. Finally, Fig. 7.33g an h show the OH radical mass fraction, further indicating the flame shape. This field is much more intense in the CTR2 case, where richer conditions are present in the core of the flame, yielding a higher equilibrium OH mass fraction.

7.5 Summary of swirl stabilized hydrogen flame simulations

This chapter details the numerical study of a swirl-stabilized hydrogen burner concept developed at TU Berlin. The burner mitigates the propensity of flashback, by introducing axial momentum through an axial air injection orifice and axially oriented fuel jets. The present analysis departs from the thorough assessment of the operating conditions, showing a remarkable complexity. Various key factors are identified such as the intense dependence of the flame speed and chemical time scale on the local equivalence ratio, or the high volume flow rate and axial momentum flow introduced by the fuel jets. An appropriate computational grid is presented for the study of this complex flow.

The low dissipation finite element approach is first used in the incompressible limit (Lehmkuhl et al., 2019b) to study the inert flow and the effect of the fuel jets under inert conditions. The mean flow fields of the LES show a bubble-type vortex breakdown, agreeing very well with the experimental observations of Reichel, Terhaar, and Paschereit (2015) using PIV. The LES also captures the precessing vortex core of the inert flow, characterized by a Strouhal number of ~ 0.5. Proper orthogonal decomposition (POD) is used to further analyze this coherent flow structure. The two most energetic POD modes are recovered by the LES, revealing a length scale of $0.8D$ associated with the precessing vortex core. As shown by additional inert simulations, this periodic behavior is readily attenuated and even suppressed solely by the addition of axial momentum though the fuel jets.

Subsequently the low Mach number extension of the method, detailed in chapter 6, is applied to study the reacting flow using two different chemistry models: one based on a single premixed flamelet (perfectly premixed), and a more elaborate one including various equivalence ratios and enthalpy levels (partially premixed). Additional modeling steps are taken to apply the perfectly premixed combustion model, where an equivalent flow condition is reached without explicitly simulating the mixing of hydrogen and air. This perfectly premixed model is used for an extensive study of the burner at two different flow conditions at a global equivalence ratio of $\phi_{glob} = 0.6$ (CTR2) and $\phi_{glob} = 0.4$ (CTR3). The results show a qualitatively good agreement with some aspects of the reacting flow. The vortex breakdown transitions to a cone-type in the presence of the flame, and the precessing vortex core is fully absent in both simulations. This model reproduces some quantitative properties of the flow as well, such as the opening angle of the vortex breakdown and the peak velocity magnitudes measured by Reichel, Terhaar, and Paschereit (2015). Nevertheless, a significant discrepancy is observed in the central recirculation zone, where the intensity of the recirculation is over-predicted and the location of the stagnation point is too close to the combustion chamber inlet. The validity of the flamelet assumption is supported by the *a posteriori* analysis of single point data, showing that

the Karlovitz number is reasonably low, and the applied grid resolution is adequate for the present LES modeling approach.

Finally, the partially premixed combustion model is applied on the same operating conditions. In the CTR2 case this more elaborate model significantly improves the flow field predictions, especially regarding the central recirculation zone. Nevertheless, the flame shape shows fairly similar behavior to the perfectly premixed case. This operating point is also investigated by Capurso et al. (2023). Their approach predicts a more homogeneous mixture at the combustion chamber inlet, with radial variations in the mean equivalence ratio in the range of $\langle \phi \rangle \in [0.55, 0.65]$. The same range in the present simulations is approximately $\phi\left(\langle Z \rangle\right) \in [0.5, 0.9]$. Meanwhile, in the work of Capurso et al. (2023) the central recirculation is very intense, similar to the perfectly premixed cases of the present work. This suggests, that the significant mixture stratification plays an important role in shaping the flow field and shifting the stagnation point downstream. The partially premixed approach is also used on the CTR3 case, where a radically different flame behavior is observed. While in the perfectly premixed approach the flame shape remains similar to the CTR2 case, in the partially premixed case the flame enters the mixing tube and shows signs of the formation of combustion induced vortex breakdown. This highlights the sensitivity of the case, as the flashback limit is approached.

Overall, the developed simulation approach provides valuable insight on the flame behavior in this challenging case without the *ad hoc* tuning of modeling constants. The perfectly premixed assumption seems to be overly simple to capture the flame stabilization mechanism, even though it provides reasonable predictions far from the unstable conditions (CTR2). The axial momentum of the fuel jets and the mixture stratification are both determining factors in the flow dynamics, influencing the nature of the vortex breakdown and determining the nature of the flashback phenomenon.

Chapter 8

Cambridge swirl bluff-body burner

This chapter presents the analysis of the Cambridge swirl bluff-body burner under various conditions. The configuration uses swirling air flow in combination with the recirculation zone formed over a bluff-body to promote flame stabilization. The relevance of this model aero-engine combustor is highlighted by its role as a target test case in various editions of the International Workshop on the Turbulent Combustion of Sprays. (TCS, 2023) The case focuses on finite rate chemistry effects in non-premixed gaseous and spray combustion, as shear induced localized extinction plays an important role in the combustion characteristics of the burner. (Cavaliere, Kariuki, and Mastorakos, 2013) Here the developed low-dissipation finite element scheme is applied together with tabulated chemistry methods and a Lagrangian treatment of the liquid fuel sprays. The analyzed conditions include an inert flow case (C1), an non-premixed methane case (F3A2), and two spray flames using n-heptane (H1S1) and n-dodecane (DD1S2) under similar flow conditions. The reacting cases correspond to stable burning conditions close to the blow-out limit showing intermittent flame lift-off due to shear induced localized extinction. The applicability of different tabulated chemistry methods is evaluated, and the flame behavior is analyzed comparing the different fuels.

The chapter is structured the following way. The properties of the combustor are extensively discussed *a priori* in section 8.1 introducing the burner geometry and flame behavior, and comparing the relevant thermo-chemical scales. The gas phase simulations are discussed in section 8.2, including the study of the inert flow field, and the detailed analysis of the non-premixed methane case. Finally, the Eulerian-Lagrangian spray flame simulations are presented in section 8.3. The focus is directed to the n-heptane case, which is used to evaluate the typical spray flame behavior in this combustor, and to assess the performance of different tabulated chemistry models. Finally, the difference between the n-heptane and n-dodecane flames is also investigated.

Credit

The work described in this chapter is primarily executed by the author, including the setup, execution, post-processing, and analysis of the different cases. The applied computational grids were created by Samuel Gómez González. Overall, the present modeling approach is unique, often showing improved results compared to other studies of the Cambridge swirl bluff-body burner, as discussed throughout the chapter. Novelty can be identified in some aspects of the modeling strategy. For instance, the methods to include heat loss in the tabulated chemistry simulations of Cambridge swirl bluff-body burner are discussed extensively, including the application of artificially scaled radiative source terms. Furthermore, to the knowledge of the author, this work presents the first application of manifolds

of unsteady extinguishing and reigniting flamelets at a single strain rate in non-autoigniting conditions. The analysis of the flame structure using the joint probability density functions of monitoring point data also provides novel insight. The presented work is partially published in Both, Mira, and Lehmkuhl (2021b), Both, Mira, and Lehmkuhl (2021a), and Both, Mira, and Lehmkuhl (2022a). The single point analysis and the estimation of droplet time scales are done using the libraries published at: `https://gitlab.com/BothAmbrus/KolmogorovAtWitness` and `https://gitlab.com/BothAmbrus/DropletEvaporation`

8.1 Burner characteristics

This section discusses the conditions and expected behavior of the Cambridge swirl bluff-body burner. This includes the burner geometry, the chemical characteristics of the burner operated with different fuels, and the operability of the system.

8.1.1 Geometry and flame behavior

The Cambridge swirl bluff-body burner is a model aero-engine combustor, designed to investigate the unsteady process of lean blow-out (LBO) or global extinction, furthermore, the high susceptibility to localized extinction leads to incomplete combustion. (Cavaliere, Kariuki, and Mastorakos, 2013) These finite rate chemistry effects pose a challenge to simulation methods.

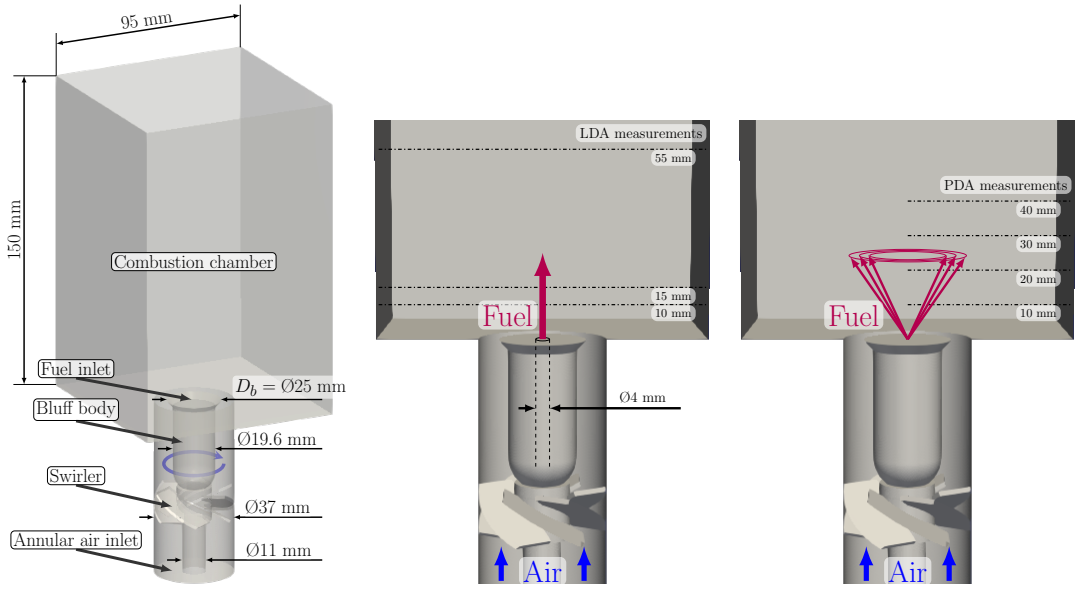

(A) Burner parts and dimensions. (B) Non-premixed gaseous flame configuration. (C) Hollow cone spray flame configuration.

FIGURE 8.1: Illustration of Cambridge swirl bluff-body burner geometry.

The burner configuration is illustrated in Fig. 8.1. Air is introduced to the burner through an annular duct of outer diameter of 37 mm and inner diameter of 11 mm. Guide vanes are placed in the air inlet at an angle of 60°, inducing swirling flow with a geometric swirl number: $S = 1.23$. Downstream of the swirler, the annular duct is narrowed in two sudden steps to a final width of 6 mm where it reaches the

combustion chamber. This is achieved by maintaining the outer duct diameter and increasing the inner one to $D_b = 25$ mm. The central part of this annular duct is a bluff-body of final diameter: D_b, which creates a strong central recirculation zone (CRZ) together with the effect of vortex breakdown stabilizing the flame. (Fritz, Kröner, and Sattelmayer, 2004) There are two different configurations analyzed in this study, the non-premixed gaseous flame, where fuel is injected through a pipe in the center of the bluff-body (Fig. 8.1b), and the spray flame, where the liquid fuel injector is placed in the same location (Fig. 8.1c). In the former case the fuel forms a turbulent gas jet with a diameter of 4 mm. Meanwhile, in the latter case the liquid fuel is introduced by a pressure swirl atomizer, creating a hollow-cone spray pattern of nominal spray angle: 60°. The swirling air flow and the fuel stream enter the rectangular combustion chamber of cross section: 95 mm $\times$ 95 mm and length: 150 mm.

The flame is stabilized on the bluff-body, as hot partially reacted gases are trapped in the central recirculation zone. In both the gaseous and spray flames the fuel stream interacts with this hot environment. The gas jet introduces a significant axial momentum, agitating the recirculation zone. The counteracting flow of unburnt fuel and hot flue gases promotes mixing, and finally the reactions occur in the shear layer on the edge of the bluff-body, where this partially reacted rich mixture interacts with the oxidizer flow. The flow acts differently in the spray flames, where the high density fuel droplets progress in a hollow cone pattern, with relatively less momentum transfer between the two phases. The flame consists of an inner reaction zone located near the hollow spray cone, and an outer reaction zone located in the shear layer that forms at the perimeter of the bluff-body. In all reacting cases the (outer) reaction zone shows high intermittency due to strain induced local extinction in the shear layer. The outlet of the combustion chamber is open to the atmosphere. For more information on the burner, see the experimental work of Cavaliere, Kariuki, and Mastorakos (2013) and Yuan, Kariuki, and Mastorakos (2018).

8.1.2 Thermo-chemical conditions

The combustor is operated with ambient air at atmospheric pressure here taken as $P_0 = 101325$ Pa and $T_{air} = 298.15$ K. The fuel inlet is also considered to be at this temperature in both the gaseous and liquid flames. Note, that a significant amount of heat is transferred to the spray droplets to facilitate evaporation, thus the gas phase reactions in the spray combustion cases typically take place at a decreased enthalpy level. Different chemical mechanisms are used in order to study the various fuels of this system. The gaseous methane flames are analyzed using the GRI3.0 (Smith et al., 2011). In fact, the present conditions are identical to ones used in the examples of chapter 3. Meanwhile n-heptane spray flames are studied using a skeletal mechanism of Lu and Law (2006), which has proved to perform well in n-heptane flame simulations. (Both, 2017; Benajes et al., 2022) Finally, n-dodecane is treated with the Jet A surrogate mechanism of Kathrotia et al. (2018) that includes n-dodecane as one of the primary fuels. The burner is studied using tabulated chemistry in section 8.2 and section 8.3. The flamelets involved in those manifolds, computed with the unity Lewis number assumption, are used here to illustrate the chemical scales and conditions of the different cases.

The adiabatic flame temperature, the flame speed, and flame thicknesses of premixed planar freely propagating flamelets are presented in Fig. 8.2 at various equivalence ratios for the three studied fuels: methane, n-heptane and n-dodecane. The

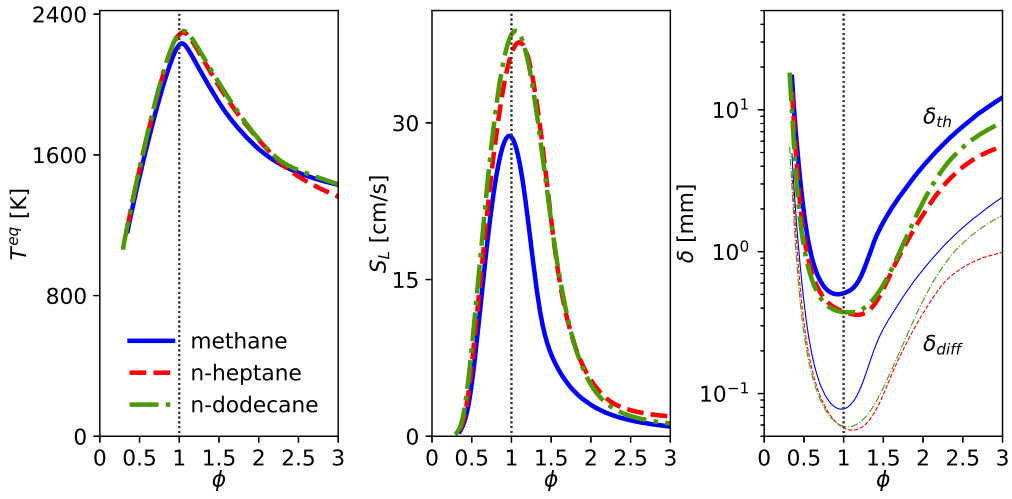

FIGURE 8.2: Properties of 1D premixed hydrocarbon flamelets as function of equivalence ratio at atmospheric pressure with an oxidizer temperature of $T_{air} = 298.15$ K and fuel temperatures of $T_f \in \{298.15, 371.54, 489.52\}$ K, for methane, n-heptane, and n-dodecane respectively. The unity Lewis number assumption is applied, using the chemical mechanisms of Smith et al. (2011), Lu and Law (2006), and Kathrotia et al. (2018). From left to right: adiabatic flame temperature T^b, laminar flame speed S_L, flame thickness δ.

solutions are obtained using Cantera (Goodwin, 2002). The adiabatic flame temperature of these fuels is fairly similar across all equivalence ratios, as the thermodynamic equilibrium is primarily modified by the stoichiometry of the problem (equivalence ratio), and the structure of these hydrocarbon fuels has only a secondary effect (e.g.: through the ratio of H and C content). The flame speed is fairly similar in the simulated n-heptane and n-dodecane flamelets, and it is notably lower in the methane flamelets. Note, that this trend would be similar using mixture-averaged transport as well. For instance, under stoichiometric conditions with mixture-averaged transport the calculated flame speeds would be 37.7 cm/s, 48.5 cm/s, and 43.4 cm/s for methane, n-heptane and n-dodecane respectively. Finally, the flame thickness is quite similar under these conditions, with slightly thicker fronts in the methane case, associated to the lower reactivity.

Further insight is provided by the counterflow diffusion flame behavior depicted in Fig. 8.3. Stable and unstable counterflow diffusion flamelets are calculated using the aforementioned conditions and chemical mechanisms with Chem1D (Somers, 1994) imposing unity Lewis numbers. The figure depicts the temperature of the stoichiometric point as a function of strain rate and stoichiometric scalar dissipation rate. Furthermore, the integrated heat release rate along the 1D flamelets is also displayed. In this case as well, the two liquid fuels show a lot of similarity, while the methane case is notably different. The stoichiometric temperatures are similar in a large portion of the stable branch, however the extinguishing strain rate of methane is much lower than that of the other two fuels. Consequently, the solutions deviate near the extinction point, and the unstable branch takes a very different course. The heat release rate is displayed in logarithmic scale, highlighting the approximate $\propto \sqrt{a}$ scaling described in section 3.1.4. This representation focuses on the lower strain

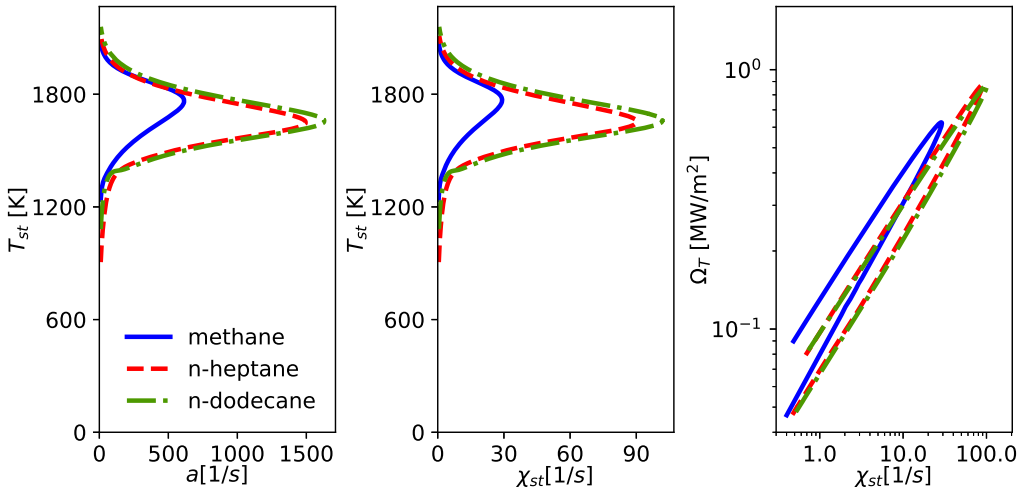

FIGURE 8.3: Properties of 1D counterflow diffusion hydrocarbon flamelets with an oxidizer temperature of $T_{air} = 298.15$ K and fuel temperatures of $T_f \in \{298.15, 371.54, 489.52\}$ K, for methane, n-heptane, and n-dodecane respectively. The unity Lewis number assumption is applied, using the chemical mechanisms of Smith et al. (2011), Lu and Law (2006), and Kathrotia et al. (2018). The left and middle plots show the temperature at the stoichiometric point: T_{st} as a function the strain rate: a and stoichiometric scalar dissipation rate: χ_{st}. The right plot illustrates the integral of heat release rate along the flamelet domain: Ω_T.

rates, where the three studied cases are rather similar. Indeed, here the heat release rate is governed by the mixing rate, explaining the similarity. The key difference of the fuels lies in the finite rate chemistry effects, which are more pronounced near the extinction point, and manifest in the different extinguishing strain rates.

The difference between the fuels is further highlighted by Tab. 8.1, summarizing the properties of the stoichiometric premixed flamelet, and the counterflow flamelet at the extinction point. The chemical scales of section 5.3.1, are also included for comparing the different behaviors. The stoichiometric mixture fraction (Z_{st}) of these fuels in ambient air are quite similar, with the differences arising from the different C/H ratio of the compounds. Meanwhile the fuel mole fraction ($X^u_{f,st}$) at stoichiometry shows drastic differences, as the molecular weight of these fuels varies on a broad range. Methane takes 9.5% of the volume in stoichiometric conditions. This is not as extreme as the case of hydrogen, where nearly a third of the volume flow is occupied by the fuel, however, it is still a significant portion. (See Tab. 7.1.) Meanwhile, in the case of n-heptane and n-dodecane, considering the vaporized fuels as ideal gases, the volume flow rate associated to the fuels under stoichiometric conditions is below 2%.

Table 8.1 also highlights the equilibrium conditions of stoichiometric mixtures. The difference in adiabatic flame temperature is only 69 K between the various fuels, and the cases are similar in other physical aspects as well. The density ratio across the stoichiometric flamelets is quite large ($\sim$ 8) compared to the swirl stabilized hydrogen flame discussed in section 7.1, since the oxidizer is not preheated in the Cambridge burner, and the contribution of the fuel in the mixture volume is less significant. The difference in kinematic viscosity between the unburnt and burnt

TABLE 8.1: Thermo-chemical properties under conditions relevant to the Cambridge swirl bluff-body burner calculated using the unity Lewis number assumption and the chemical mechanisms of Smith et al. (2011), Lu and Law (2006), and Kathrotia et al. (2018).

Stoichiometric premixed free flamelet			
	methane	n-heptane	n-dodecane
Z_{st} [kg/kg]	0.0552	0.0622	0.0628
$X^u_{f,st}$ [kmol/kmol]	0.0950	0.0187	0.0112
T^b_{st} [K]	2224	2286	2293
ρ^u_{st} [kg/m^3]	1.130	1.202	1.153
ν^u_{st} [cm^2/s]	0.159	0.150	0.162
ν^b_{st} [cm^2/s]	4.716	4.772	4.786
$\left(\rho^u/\rho^b\right)_{st}$	7.52	7.96	7.65
$\left(\nu^b/\nu^u\right)_{st}$	29.7	31.8	29.5
$S_{L,st}$ [cm/s]	28.6	36.6	38.5
$\delta_{diff,st}$ [mm]	0.0779	0.0572	0.0587
$\delta_{th,st}$ [mm]	0.5090	0.3778	0.3748
$\tau_{diff,st}$ [ms]	0.273	0.156	0.152
Counterflow diffusion flamelet at extinction point			
	methane	n-heptane	n-dodecane
a^{ext} [1/s]	614.5	1494.8	1629.6
χ^{ext}_{st} [1/s]	29.11	90.37	101.86
T^{ext}_{st} [K]	1760.7	1653.3	1661.5
δ^{ext}_{diff} [mm]	0.268	0.172	0.165
$\tau_c^{ext,\chi}$ [ms]	0.104	0.043	0.039
Counterflow diffusion manifold with $Y_c = Y_c^{ref}$			
	methane	n-heptane	n-dodecane
$\tau_c^{\dot{\omega}}$ [ms]	0.101	0.066	0.055

states is even more outstanding, with the mixture of combustion products being $\sim$ 30 times more viscous than the fresh mixture.

Finally, the table also presents the representative length, time, and velocity scales of the combustion process in the studied flamelets, as section 5.3.1 details. In the calculated flamelets the stoichiometric laminar flame speed is approximately 30% higher in the liquid fuel cases than in methane. Meanwhile the diffusive flame thickness: $\delta_{diff,st}$ is $\sim$ 25% smaller, resulting in more then 40% shorter chemical time scales. The table also summarizes properties of the extinction point in counterflow diffusion flamelets. The extinguishing strain rate is 2.4 and 2.7 times larger in the n-heptane and n-dodecane cases than in methane. Meanwhile the difference in stoichiometric scalar dissipation rate is even more outstanding: with ratios of 3.1 and 3.5 respectively, as the stoichiometric mixture fraction is larger for the two liquid fuels, and the $\chi(Z)$ profile is increasing in this range. As shown in Fig. 8.3, the stable branches of the three fuels exhibit similar behavior, thus the lower extinguishing

strain rate of the methane case corresponds to an approximately 100 K higher stoichiometric temperature at the extinction point. The length scale δ^{ext}_{diff} is only a function of the reference thermal diffusivity of the oxidizer and the extinguishing strain rate, as defined in Eq. (5.99). The present differences between the fuels are solely a consequence of the different a^{ext} values, as $\mathcal{D}_{t,ox}$ is the same in all three cases. As the extinguishing strain rate is heavily affected by the choice of fuel, δ^{ext}_{diff} shows more sensitivity than the $\delta_{diff,st}$ scale of premixed flamelets. Namely, the length scale of the diffusion flamelets is more then 40% smaller in the case of the two liquid fuels. This also indicates, that there is no clear relation of the $\delta^{ext}_{diff}/\delta_{diff,st}$ ratio, which is 3.4, 3.0, and 2.8 for methane, n-heptane, and n-dodecane respectively. The chemical time scale: $\tau_c^{ext,\chi}$ based on the stoichiometric scalar dissipation rate and mixture fraction shows even more variation, with the fuel. Note, that this difference is less severe, in case of the chemical time scale based on the progress variable source term: $\tau_c^{\dot{\omega}}$. This latter metric is more similar to the time scale of premixed flamelet, with the ratio of the two: $\tau_{diff,st}/\tau_c^{\dot{\omega}}$ being 2.7, 2.4, and 2.8 for the three fuels.

Overall, under similar conditions, the n-heptane and n-dodecane fuels are expected to be more reactive and less prone to finite rate chemistry effects, such as strain induced local extinction. Nevertheless, as shown below in section 8.3.5, similar conditions do not arise, and the different local extinction behavior is primarily governed by the way fuel is supplied to the reaction zone. For instance, the two liquid fuel cases result in radically different evaporation rates, due to the different volatility of the fuels.

8.1.3 Operational envelope

The stability characteristics of the Cambridge swirl bluff-body burner have been extensively studied by Cavaliere, Kariuki, and Mastorakos (2013), and Yuan, Kariuki, and Mastorakos (2018). The former work studies perfectly premixed and non-premixed gaseous methane flames along with an n-heptane spray flame. Meanwhile, the latter work focuses on the characterization of different spray flames.

The limit of global extinction in the case of methane, n-heptane, and n-dodecane fuels is depicted by Fig. 8.4, as determined by Cavaliere, Kariuki, and Mastorakos (2013) and Yuan, Kariuki, and Mastorakos (2018). This stability map represents the highest possible air flow rate where stable flames are observed as a function of the fuel flow rate. The limit is fairly similar in the three studied fuels, suggesting that convective transport plays a major role the extinction event, affecting all flames similarly. The remaining differences are caused be a range of factors. The methane jet acts significantly differently in the wake of the bluff-body than the two hollow cone spray flames. In the methane case, the fuel is readily available to mix with the oxidizer, and the incoming fuel jet yields a significant volume flow rate and momentum addition to the recirculation zone. Meanwhile the mixing ability of the spray flames is heavily affected by the volatility of the liquids, which is drastically different between n-heptane and n-dodecane. Furthermore, as Tab. 8.1 illustrates, even if these fuels would be added in a pre-vaporized form to the combustion chamber, they would correspond to a significantly lower volume flow rate. As further discussed in section 8.3.5, the difference in volatility is crucial in the two spray flames.

Figure 8.4 also highlights the studied operating conditions of the burner. Firstly, the inert flow is assessed with no fuel injection marked C1. The evaluated reacting cases are all fairly close to the blow-off condition. The non-premixed methane case (F3A2) features a slightly lower fuel mass flow rate and slightly higher air bulk velocity compared to the liquid cases of n-heptane (H1S1) and n-dodecane (DD1S2),

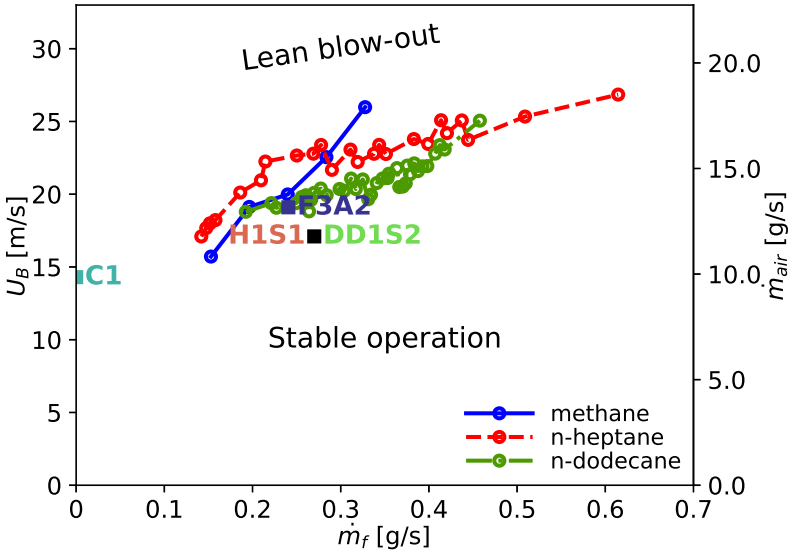

FIGURE 8.4: Operational envelope of the Cambridge swirl bluff-body burner experimentally determined by Cavaliere, Kariuki, and Mastorakos (2013) and Yuan, Kariuki, and Mastorakos (2018).

TABLE 8.2: Studied operating points of the Cambridge swirl bluff-body burner.

Case	C1	F3A2 (methane)	H1S1 (n-heptane)	DD1S2 (n-dodecane)
$\dot{m}_{air}$ [g/s]	9.85	13.16	11.78	11.78
$\dot{V}_{air}$ [cm^3/s]	8353	11160	9989	9989
$\dot{m}_f$ [g/s]	0	0.24	0.27	0.27
Z_{glob} [−]	0	0.0179	0.0224	0.0224
ϕ_{glob} [−]	0	0.312	0.346	0.342
P_{th} [kW]	0	12.0	12.0	11.9
U_B [m/s]	14.3	19.1	17.1	17.1
U_B/U_{BO} [−]		0.96	0.75	0.85
u_f [m/s]	0	29.2	12.6	11.5
$A_{in}\rho_{air}U_B^2$ [N]	0.141	0.251	0.201	0.201
$A_{fuel}\rho_f u_f^2$ [N]	0	0.0070	0.0034	0.0031
Re_B	22700	30400	27200	27200
$Re_{D_{hyd},1}$	14100	18800	16900	16900
$Re_{D_{hyd},in}$	10900	14600	13100	13100
Re_f	0	6700	4100	1200

which are the exact same in terms of $\dot{m}_f$ and U_B with the only difference associated to the liquid itself. Further details of the operating points are given in Tab. 8.2. The air/fuel ratio is larger in the methane case resulting in a slightly lower global equivalence ratio. The thermal power (P_{th}) is near 12 kW in all reacting cases. The different cases relate differently to the blow-out limit, as indicated by the U_B/U_{BO}

ratio, where U_{BO} is the average bulk velocity at blow-out. Considering central fuel pipe of diameter of 4 mm, methane fuel jet has a quite large bulk velocity (u_f) affecting the central recirculation zone. The bulk velocity of the liquid fuels is lower, calculated using an injector diameter of $D_f = 0.2$ mm, which is representative to the hollow cone atomizer. The table also presents the axial momentum input of the two streams at the entrance of the combustion chamber. The majority of the axial momentum is associated to the air stream ($A_{in}\rho_{air}U_B^2$), as the air mass flow rate is two orders of magnitude larger, than the fuel mass flow rates. The methane jet corresponds to only 2.7% of the axial momentum. The liquid inlet introduces even less axial momentum, furthermore the spray droplets exchange momentum with the gas of the combustion chamber slower than the methane jet, thus the spray affects the central recirculation zone less. Finally, the table also summarizes relevant Reynolds numbers. The Reynolds numbers related to the air flow are defined as:

$$Re_B = \frac{U_B D_b}{\nu_{air}}, \quad Re_{D_{hyd},1} = \frac{U_B A_{in} D_{hyd,1}}{A_1 \nu_{air}}, \quad Re_{D_{hyd},in} = \frac{U_B D_{hyd,in}}{\nu_{air}}, \tag{8.1}$$

where $\nu_{air} = 0.157$ cm^2/s is the viscosity of air at 298.15 K, $A_{in} = 5.84$ cm^2 is the cross section of the annulus right at the inlet of the combustion chamber, and $A_1 = 9.80$ cm^2 is the cross section of the annulus upstream of the swirler. Furthermore, $D_{hyd} = 4A/K = D_{outer} - D_{inner}$ is the hydraulic diameter of the annulus, where A is the cross section and K is the perimeter. Indeed, the studied conditions of the Cambridge swirl bluff-body burner are much less turbulent, that the case of the swirl stabilized hydrogen flame discussed in chapter 7, and resemble more the PRECCINSTA case of section 6.5.1. Finally, the fuel inlets are also characterized by a Reynolds number. In the case of the methane jet, this has important implications, as the incoming flow is mildly turbulent, which is modeled similarly to the DLR jet case of section 6.5.2. Nevertheless, the resolution requirements are less stringent as Re_f is significantly lower in the present case. The difference in the Reynolds numbers of the fuels highlights, that the atomization process is affected by the material properties of n-heptane and n-dodecane.

8.1.4 Computational grid

The computational domain corresponds to the volume illustrated in Fig. 8.1a, which contains a short portion of the upstream annulus, the swirler element, the sudden contractions of the air inlet annulus, and the combustion chamber. Furthermore, downstream of the combustion chamber, an outlet section is added, which is discretized coarsely and mitigates the problems associated with the outlet boundary conditions. The same domain is used in all presented simulations, with boundary conditions associated to the air inlet, the walls of the air duct and the bluff-body, the methane fuel inlet with $D_f = 4$ mm, the walls of the combustion chamber, and the outlet. In the spray combustion cases wall-like boundary conditions are imposed on the circular fuel inlet as well.

The numerical simulations are conducted on hybrid unstructured meshes consisting of prisms, pyramids, and tetrahedra. The coarse and fine grids are shown in Fig. 8.5a and 8.5b respectively. Both meshes have similar refinement regions, with a coarser level up to $x = 60$ mm and $x = 70$ mm in the two meshes, and a finer level in the reaction zone and the shear layers of the air inlet. The reaction zone is discretized by tetrahedral elements with an element edge length of $h = 1$ mm and $h = 0.5$ mm

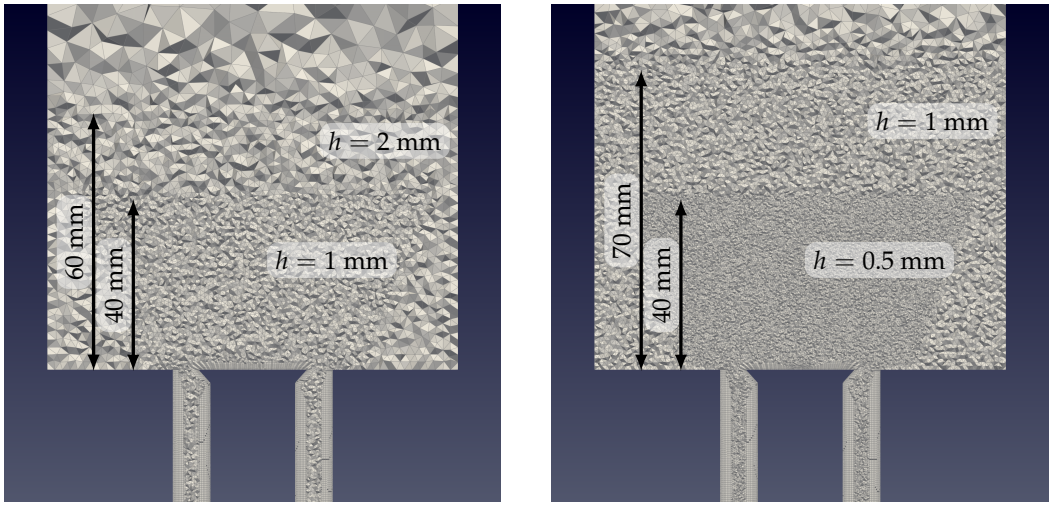

(A) Coarse mesh of 4M elements and 1.2M nodes. (B) Fine mesh of 17.2M elements and 3.4M nodes.

FIGURE 8.5: Illustration of computational grids applied for the Cambridge swirl bluff-body burner.

in the coarse and fine meshes respectively. This mesh refinement region is concentrated around the bluff-body, to capture the intermittent reacting layer. This yields a mesh of 1.2M and 3.4M degrees of freedom in the coarse and fine cases respectively. The resolution is similar to the previously studied cases of the present work in section 6.5. Note, that other studies applied different grid spacing in the flame region. Zhang et al. (2015) used tetrahedral elements of 0.4 mm in the combustion chamber. Elasrag and Li (2018) applied a polyhedral mesh without explicitly reporting the cell sizes, however their illustration resembles the presently used coarse mesh. Both Ma et al. (2019) and Foale (2022) discretized the flame region with a structured hexahedral mesh with the smallest element size being 0.1 mm. Paulhiac et al. (2020) applied a grid spacing of 0.2 mm to resolve the flame front in finite rate chemistry simulations.

Since the mesh is composed of tetrahedral elements in the bulk of the flow, the filter size Δ is approximately half of the element edge length h. (See Eq. (6.96).) Based on the thermal flame thickness $\delta_{th,st}$ of the stoichiometric premixed flamelets summarized in Tab. 8.1, in the coarse grid the filter size is approximately equal to the thermal flame thickness, while the fine mesh is twice as resolved. A similar comparison involving the counterflow diffusion flamelets has to consider, that the length scale δ_{diff} is ~ 4 times smaller than a flame thickness based on the mixture fraction gradient, since the heat release thickens the flame as appendix A demonstrates. Thus, the length scales of $\sim 4\delta^{ext}_{diff}$, which are typical to the extinguishing flame fronts, are resolved with a similar accuracy as the premixed flamelets. Furthermore, an *a posteriori* analysis of the single point statistics based on section 5.1.6 shows, that the minimum Kolmogorov scale encountered in the region of interest is: $\eta \approx 0.025$ mm near the annular air inlet of the combustion chamber. This indicates an η/h ratio of 40 in the coarse mesh and 20 in the fine mesh. Similar estimates are presented by Zhang and Mastorakos (2016) who use approximations of the integral scales, assuming a turbulence velocity scale of 20% of the bulk velocity, and an integral length scale of 5 mm based on the shear layer thickness. In conclusion, the fine mesh is acceptable for LES in terms of resolving the turbulent flow field,

while the coarse mesh poses more of a challenge for the sub-grid models. Finally, the Sauter mean diameter (SMD) of the droplets may also be used as a length scale to assess the mesh resolution. As further discussed in section 8.3.2, the SMD of the droplet injection model is $\sim$ 75 μm in alignment with the measurements of Yuan, Kariuki, and Mastorakos (2018). Meanwhile the highest initial droplet diameters are $\sim$ 125 μm. As section 5.5.2 details, the validity of the presently applied Lagrangian droplet models becomes questionable if the droplet size is comparable to the filter size. Specifically, the presently applied largest droplets of $d_p = 125$ μm occupy $\sim$ 7% of the host element volume in the fine grid. Even finer grids may affect the heat and mass transfer models of the droplets substantially, resulting in a different mixture field.

8.2 Gas phase behavior

In this section the Cambridge swirl bluff-body burner is studied without the added complexity of the multiphase flow. Simulations are executed under the C1 and F3A2 conditions, where quantitative measurement data is available for comparison. (Sidey et al., 2017)

8.2.1 Cold flow

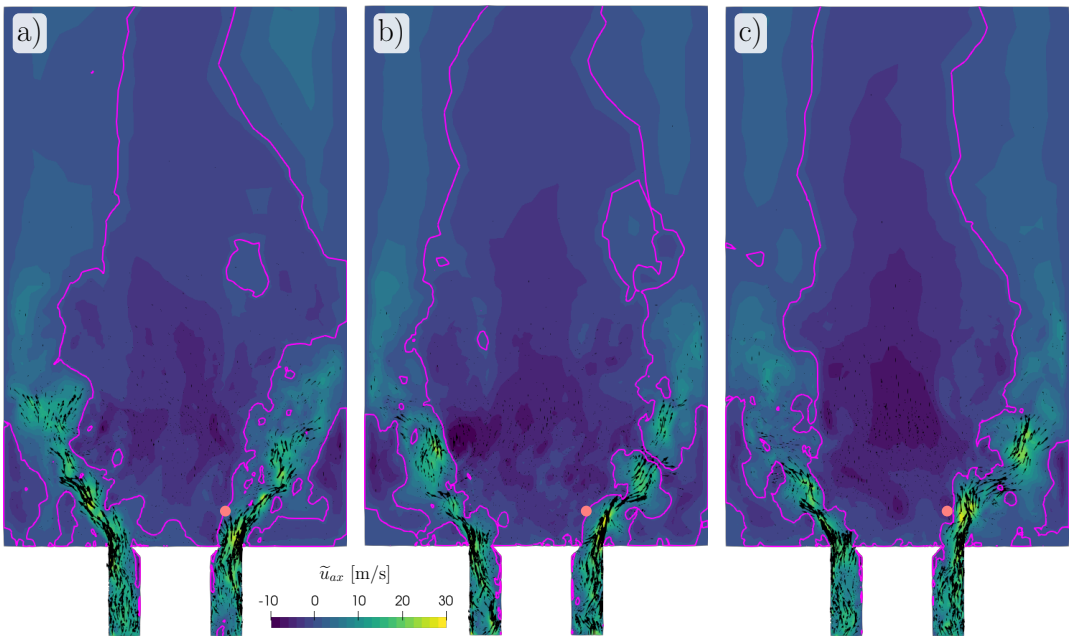

FIGURE 8.6: Examples of the instantaneous velocity fields of the inert flow (C1) in the Cambridge swirl bluff-body burner. The contour line (magenta) marks the position of zero axial velocity. The orange circle indicates the monitoring point at $x = 10$ mm and $r = 14$ mm.

The present simulation approach includes a non-swirling part of the annulus, the swirler, and the rest of the air inlet in the computational domain, thus LES is used to reproduce the turbulent swirling motion of the oxidizer. Such an approach removes the modeling uncertainty associated to imposing a complex inflow boundary condition further downstream, however it puts more emphasis on the correct

behavior of the Navier-Stokes solution method. The burner is simulated under inert conditions (without fuel flow) to assess the numerical scheme and the adequacy of the computational grid. The laser Doppler anemometry (LDA) measurement data of Tyliszczak, Cavaliere, and Mastorakos (2014) is used here as reference.

Figure 8.6 illustrates the instantaneous flow field, by the contour plot of the axial velocity component and a vector field of the in-plane velocity using LES results on the coarse grid. Note, that the plot is truncated at $x = -D_b$. The flow exits the air inlet annulus at an angle, as vortex breakdown takes place at the sudden expansion of the cross section. Recirculation zones are formed in the corners and in the center of the combustion chamber attached to the bluff-body. The high velocity air stream interacts with the central recirculation zone and creates a strong shear layer at the edge of the bluff-body. This shear layer is modulated by the incoming turbulence and the flow undergoes periodic shedding form the buff-body edge.

The LES results have been time averaged over 169 ms and 136 ms in the coarse and fine mesh respectively, which corresponds to approximately one flow-through time based on the volume of the combustion chamber and the flow rate of the air. Nevertheless, the simulation captures well the flow characteristics, since the typical time scales of the flow are much shorter, as further discussed below in relation to Fig. 8.11. Furthermore, this averaging time is also larger than the extinction time scales identified by Cavaliere, Kariuki, and Mastorakos (2013) and Yuan, Kariuki, and Mastorakos (2018). While these scales describe the reacting conditions, they are ultimately linked to the flow field in the system, thus they give a good indication of the burner's behavior. The time averaged velocity field is illustrated in Fig. 8.7. The swirling motion and the shape of the bluff-body directs the flow in a conical shape. The recirculation zones are pronounced both in the center of the chamber and in the corners, with both attached to the walls of the bluff-body and the combustion chamber. The intensity of the swirling motion decays relatively fast, as Fig. 8.7c indicates. The fluctuations of the axial (u_{rms}) and circumferential (w_{rms}) velocity components peak in the inner shear layer. Meanwhile, the peak of v_{rms} is located in the outer shear layer.

The flow field is further illustrated in Fig. 8.8, indicating the axial velocity by contours, and the in-plane components by vectors. As the axi-symmetric flow enters the rectangular combustion chamber, an asymmetry is formed. At $x = 8$ mm the most intense back-flow occurs in the corners, while there are parts with positive $\langle \widetilde{u} \rangle$, separating the corner recirculation zone into four parts. At this location material is carried towards the shear layer from both the corner and central recirculation zones. At $x = 13$ mm the corner recirculation zones are no longer disconnected, and the flow is more tangential in the outer parts of the domain. This trend is continued at $x = 18$ mm, with the in-plane velocity components being mostly tangential to the contour line separating the corner recirculation from the high speed axial flow. Finally, the phenomenon is reversed at $x \geq 23$ mm, where the radial velocity is positive and material enters the corner recirculation zones. At these higher axial locations the central recirculation zone has practically zero radial velocity component, and it rotates at a significantly slower rate, than the surrounding high speed flow. While the asymmetry is evident in the outer part of the domain, the contour lines of the central recirculation zone appear to be axi-symmetric, suggesting, that the flames stabilized on the bluff-body are likely to behave in an axi-symmetric manner close to the bluff-body.

The velocity fields obtained with the coarse and fine computational grids are compared to the measurement data of Tyliszczak, Cavaliere, and Mastorakos (2014) in Fig. 8.9 and Fig. 8.10, with the former figure showing the average velocity profiles,

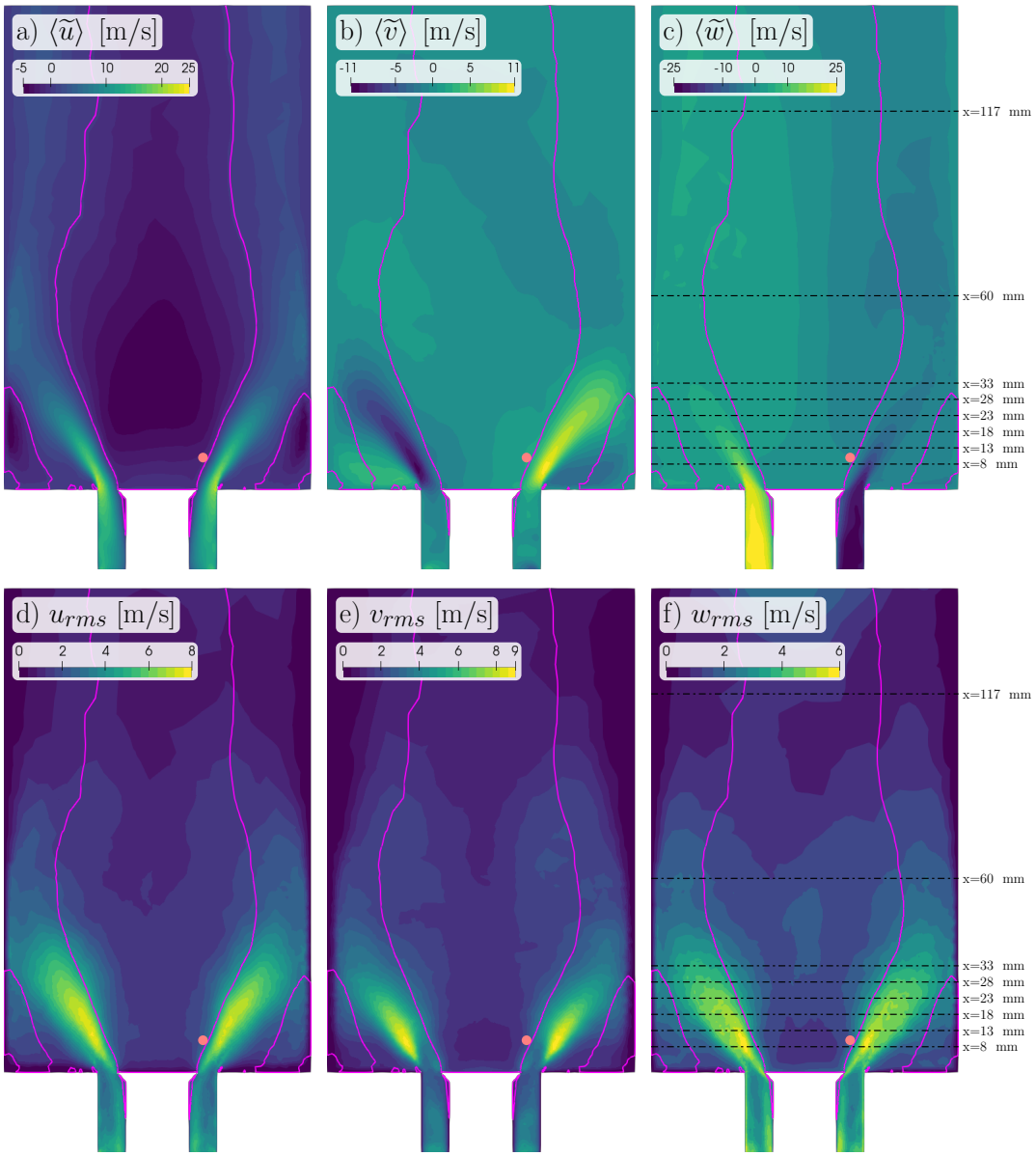

FIGURE 8.7: Mean and RMS velocity fields of the inert flow (C1) in the Cambridge swirl bluff-body burner. The top row shows the mean of the axial, radial, and circumferential velocity components, while the bottom row shows the corresponding RMS values. The contour line (magenta) marks the position of zero mean axial velocity. The orange circle indicates the monitoring point at $x = 10$ mm and $r = 14$ mm.

and later the RMS values. The studied locations are indicated on Fig. 8.7 by dash-dot lines. The mean profiles match very well with the experimental data. In particular the most upstream measurement location at $x = 8$ mm in Fig. 8.9v-x is reproduced adequately, indicating that the LES captures well the the flow inside the swirler and the air inlet annulus. At this location the central recirculation zone shows a high contrast compared to the peaks of the annular air stream, while the corner recirculation is weaker. As the radial velocity profile indicates, air flows towards the shear layers from both recirculation zones. Finally, the swirling motion is moderate in both recirculation regions, as it is concentrated to the high speed air inlet. More downstream

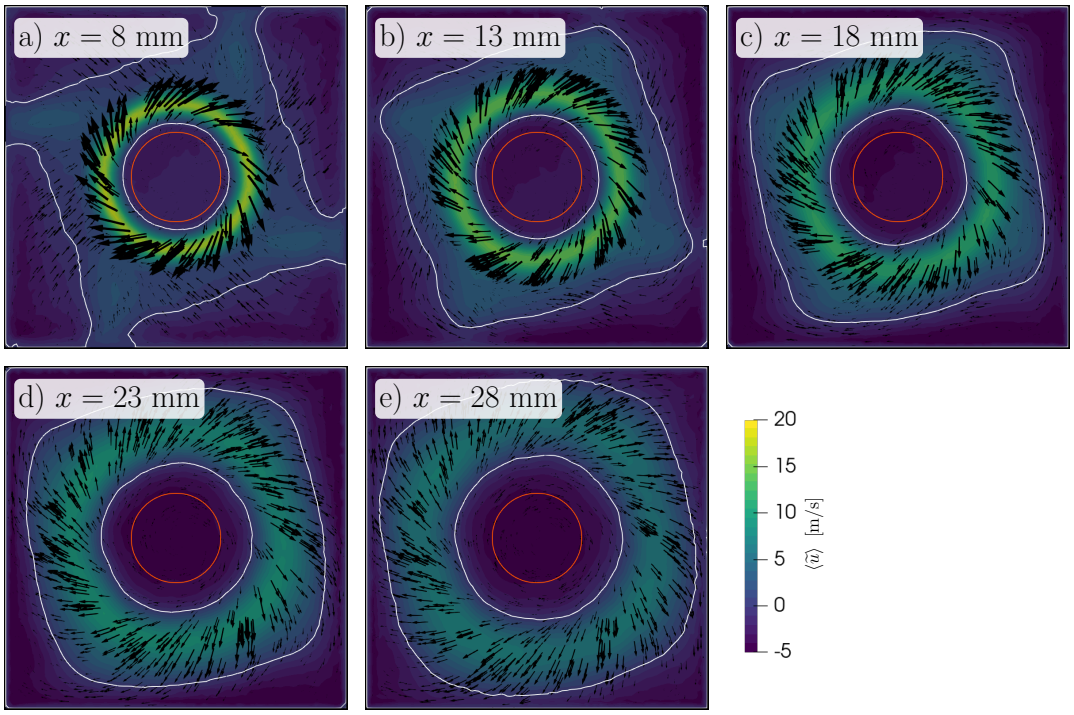

FIGURE 8.8: Mean swirling motion in the inert flow (C1) of the Cambridge swirl bluff-body burner at different axial locations in the combustion chamber. The contour line (white) marks the position of zero mean axial velocity, while the circle (orange) indicates the bluff-body diameter.

the shear layer spreads and the axial flow decelerates. The corner recirculation is the most pronounced at $x = 18$ mm. Here both the radial and circumferential velocities are uniformly positive for $r > 0$ mm, indicating that the high speed air flow feeds the corner recirculation zone, and that the entire flow rotates due to the swirling air inlet. This behavior is maintained up to $x = 33$ mm where the high speed air flow impinges on the vertical burner walls. Further downstream at $x = 60$ mm the radial flow is reversed, as Fig. 8.9e shows, where the main flow feeds central recirculation zone with air. Finally, at the last measurement location the flow becomes quite uniform, while a significant swirling motion is maintained.

The velocity fluctuation profiles of Fig. 8.10 also show a good level of correlation with the LDA measurements. The incoming airflow at $x = 8$ mm is highly turbulent. As mentioned before, the axial and circumferential velocity fluctuations peak in the inner shear layer, while the maximum of the radial velocity fluctuations is in the outer shear layer. The peak RMS values follow the high speed air flow, but significant fluctuations are observed in the recirculation regions as well, indicating, that these are highly mixed by the turbulent motion. The grid refinement has very little effect on the velocity statistics. The only notable difference is found in more downstream locations and in certain points of the RMS velocity profiles. Overall, the present low-dissipation flow solver preforms well in this domain, reproducing the statistical behavior of the flow to a good extent.

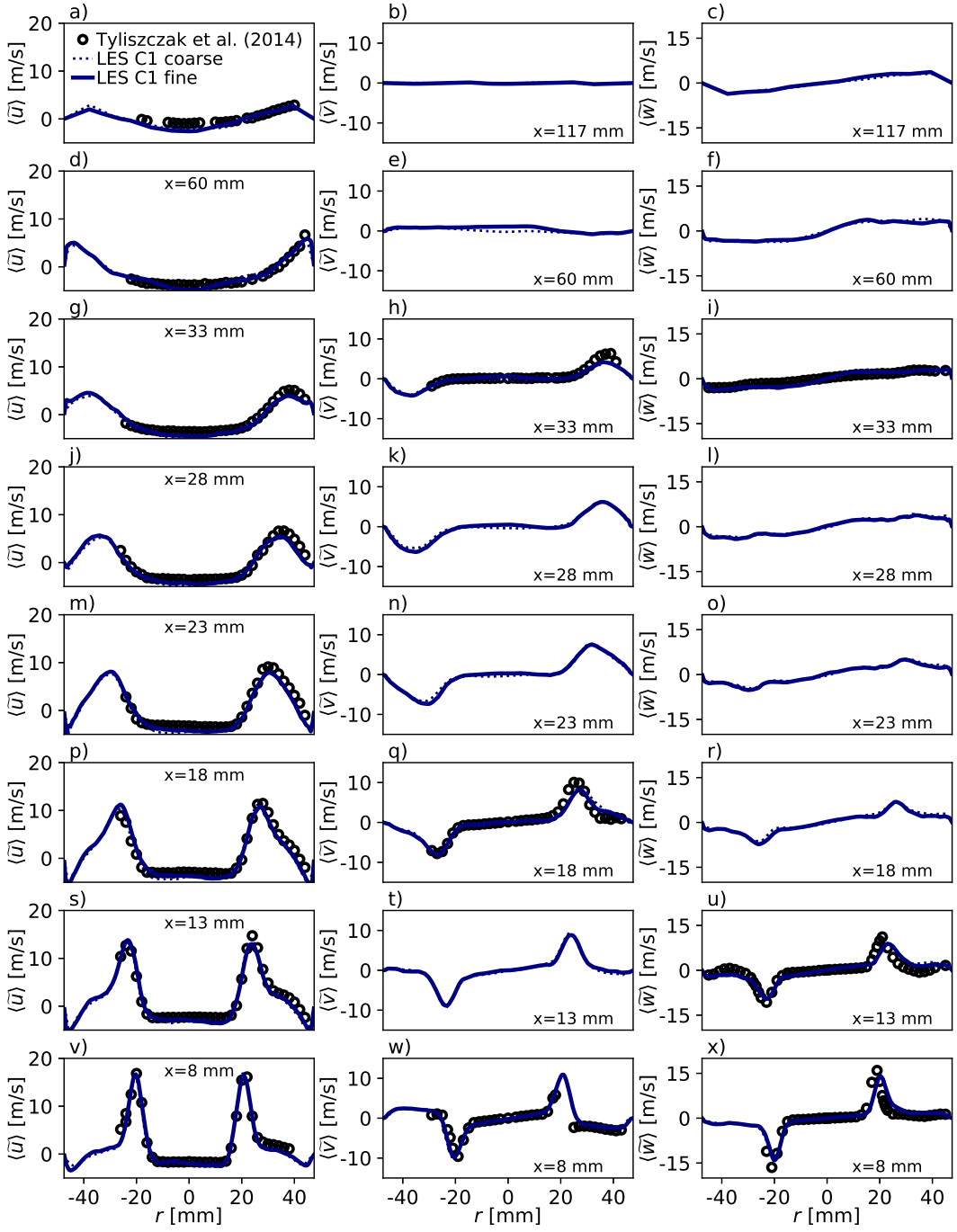

FIGURE 8.9: Comparison of mean inert (C1) velocity profiles in the Cambridge swirl bluff-body burner between the LDA measurements of Tyliszczak, Cavaliere, and Mastorakos (2014) and the LES of the present work. The rows of plots correspond to the indicated axial location, while the three columns show the mean of the axial, radial and tangential velocity.

Flow dynamics

The dynamic behavior of the incoming high speed swirling air flow has a great influence on the inner shear layer and the central recirculation zone, as the instantaneous

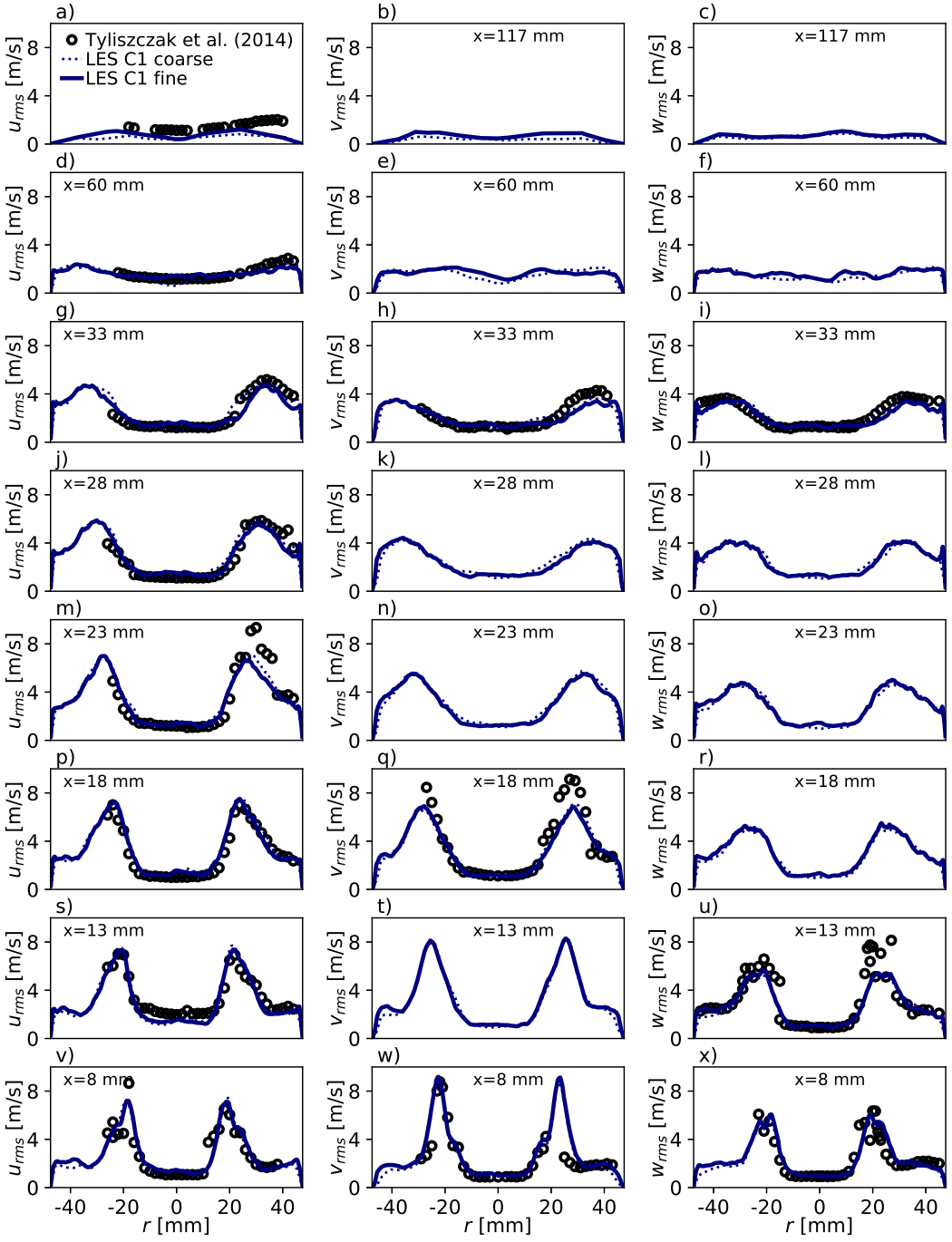

FIGURE 8.10: Comparison of RMS inert (C1) velocity profiles in the Cambridge swirl bluff-body burner between the LDA measurements of Tyliszczak, Cavaliere, and Mastorakos (2014) and the LES of the present work. The rows of plots correspond to the indicated axial location, while the three columns show the RMS of the axial, radial and tangential velocity.

flow fields of Fig. 8.6 readily suggest. The flow sheds periodically from the bluff-body edge, corrugating the shear layer and enhancing mixing between the fresh flow and the stagnant gases of the central recirculation zone. This periodic behavior

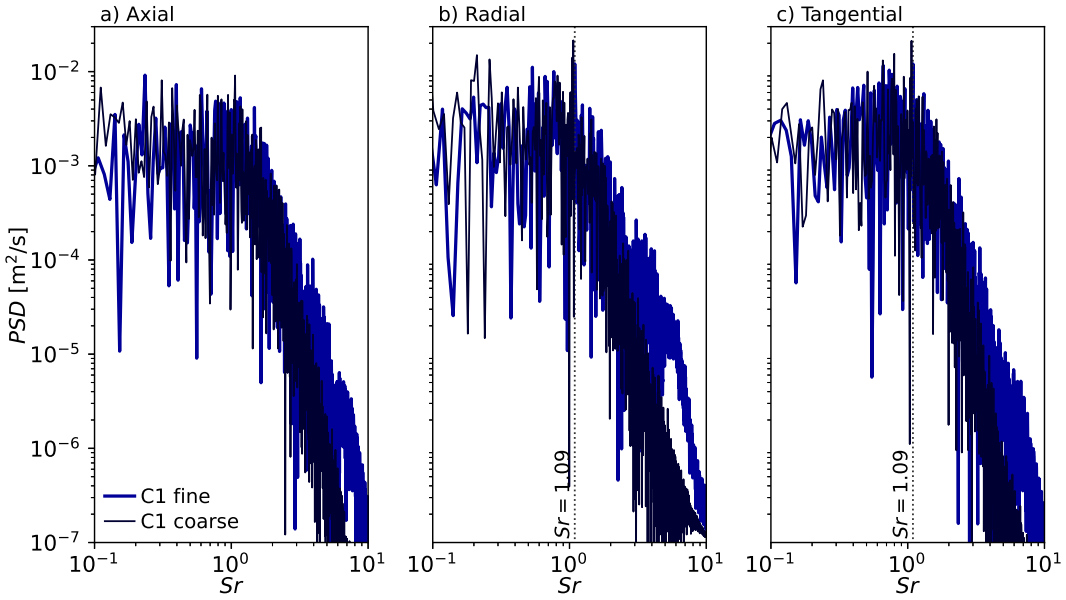

FIGURE 8.11: Power spectral density of the velocity fluctuation at an observation point in the combustion chamber ($x = 10$ mm, $r = 14$ mm) of the Cambridge swirl bluff-body burner under inert (C1) conditions. The single point data of the LES is analyzed using the method of Lomb (1976) and Scargle (1982).

is expressed in terms of the Strouhal number, defined as:

$$Sr = \frac{f D_b}{U_B}, \tag{8.2}$$

using the bluff-body diameter and the bulk velocity to scale the frequencies. The dominant frequency is identified on the Lomb-Scargle periodogram of the different velocity signals recorded in the shear layer displayed in Fig. 8.11. Indeed, the shedding creates a strong peak at a Strouhal number of $Sr = 1.09$ corresponding to a frequency of 625 Hz. The peak is especially pronounced in the spectrum of the radial and circumferential velocity, while it is weaker in the PSD of the axial velocity. This characteristic frequency if found using both the coarse and fine computational grids, underlining, that it is really significant in the flow dynamics of the inert case. This frequency corresponds to a time scale of 1.6 ms, which is well below the averaging time applied here.

8.2.2 Non-premixed methane flame

In this section the burner is analyzed under non-premixed gaseous reacting conditions. The F3A2 methane flame, experimentally studied by Cavaliere, Kariuki, and Mastorakos (2013), is simulated using the low-dissipation finite element approach of the present work. In this case a strong turbulent methane jet with a diameter of $D_f = 4$ mm is introduced directly into the central recirculation zone through the center of the bluff-body, as depicted in Fig. 8.1b. The jet mixes with the surrounding partially reacted rich gas mixture, and finally reactions occur predominantly in the inner shear layer between the central recirculation zone and the fresh oxidizer stream. This reacting layer is characterized by shear induced localized extinction.

This setup has been numerically studied by various authors. Zhang et al. (2015) applied the conditional moment closure in an LES solver based on the finite volume method to study the F3A2 operating point. Their study finds an excellent prediction of the local extinction associated to high scalar dissipation rates. Subsequently Zhang and Mastorakos (2016) applied the same method to study the transient behavior of the flame during the blow-off process. They identify the increased occurrence of localized extinction as an indicator of the vicinity of the blow-off. More recently Ma et al. (2019) applied the flamelet/progress variable model and the thickened flame model to study both the stable and blow-off conditions of the methane flames. They associate the blow-off event with the reduction of fuel-rich mixtures in the central recirculation zone, furthermore, their findings confirm the increased occurrence of localized extinction as the blow-off is approached.

Combustion model

In this case the thermo-chemical states are represented by stable and unsteady extinguishing counterflow diffusion flamelets following the approach of Chrigui et al. (2012). The flamelet solutions are obtained using Chem1D with the unity Lewis number assumption applying the GRI3.0 (Smith et al., 2011) chemical mechanism. As section 6.3.3 demonstrates, when the flamelets are adiabatic, this approach is fairly similar to the flamelet/progress variable model applied by Ma et al. (2019). In this work two tabulation strategies are tested, one applying adiabatic flamelets, and one incorporating heat loss effects through the artificial scaling of a radiative heat loss term. Both manifolds are discussed in detail in section 3.4.1 prior to the application of the presumed FPDF integration which is considered following Pierce and Moin (2004). I.e.: the sub-grid mixture fraction and scaled progress variable distributions are modeled with a beta and delta function respectively. Thus the LES solution of this flame necessitates governing equations representing mass and momentum conservation (Eq. (5.30) and Eq. (5.47)), enthalpy, mixture fraction, and progress variable transport (Eq. (5.117)), and the transport of sub-grid mixture fraction variance. (Eq. (5.122)) The equations are reproduced here for clarity:

$$\partial_t \overline{\rho} + \nabla \cdot (\overline{\rho}\widetilde{\mathbf{u}}) = 0 \tag{8.3}$$

$$\partial_t (\overline{\rho}\widetilde{\mathbf{u}}) + \nabla \cdot (\overline{\rho}\widetilde{\mathbf{u}} \otimes \widetilde{\mathbf{u}}) + \nabla \overline{p} - \nabla \cdot \left(2\left(\overline{\mu} + \overline{\rho}\nu^{SGS}\right)\widetilde{\mathbf{S}^{\mathbf{D}}(\mathbf{u})}\right) = 0 \tag{8.4}$$

$$\partial_t \left(\overline{\rho}\widetilde{h}\right) + \nabla \cdot \left(\overline{\rho}\widetilde{h}\widetilde{\mathbf{u}}\right) - \nabla \cdot \left(\overline{\rho}\left(\widetilde{\mathcal{D}_t} + \frac{\nu^{SGS}}{Pr^{SGS}}\right)\nabla \widetilde{h}\right) = 0 \tag{8.5}$$

$$\partial_t \left(\overline{\rho}\widetilde{Z}\right) + \nabla \cdot \left(\overline{\rho}\widetilde{Z}\widetilde{\mathbf{u}}\right) - \nabla \cdot \left(\overline{\rho}\left(\widetilde{\mathcal{D}_t} + \frac{\nu^{SGS}}{Sc^{SGS}}\right)\nabla \widetilde{Z}\right) = 0 \tag{8.6}$$

$$\partial_t \left(\overline{\rho}\widetilde{Y_c}\right) + \nabla \cdot \left(\overline{\rho}\widetilde{Y_c}\widetilde{\mathbf{u}}\right) - \nabla \cdot \left(\overline{\rho}\left(\widetilde{\mathcal{D}_t} + \frac{\nu^{SGS}}{Sc^{SGS}}\right)\nabla \widetilde{Y_c}\right) = \overline{\dot{\omega}_{Y_c}} \tag{8.7}$$

$$\partial_t (\overline{\rho}\widetilde{Z_v}) + \nabla \cdot (\overline{\rho}\widetilde{Z_v}\widetilde{\mathbf{u}}) - \nabla \cdot \left(\overline{\rho}\left(\widetilde{\mathcal{D}_t} + \frac{\nu^{SGS}}{Sc^{SGS}}\right)\nabla Z_v\right) = 2\frac{\overline{\rho}\nu^{SGS}}{Sc^{SGS}}\nabla \widetilde{Z} \cdot \nabla \widetilde{Z} - \overline{\rho}\chi_Z^{SGS}. \tag{8.8}$$

All scalar transport equations are treated with the unity Lewis number assumption, and the modeling constants are identical to the other turbulent cases simulated in this work. Specifically, the constant $c = 0.1$ is used in the eddy-viscosity model of Vreman (2004), and the sub-grid Schmidt and Prandtl numbers are set to $Pr^{SGS} =$

$Sc^{SGS} = 0.7$. Here, and throughout this chapter, the non-conservative discretization form of the governing equations is applied.

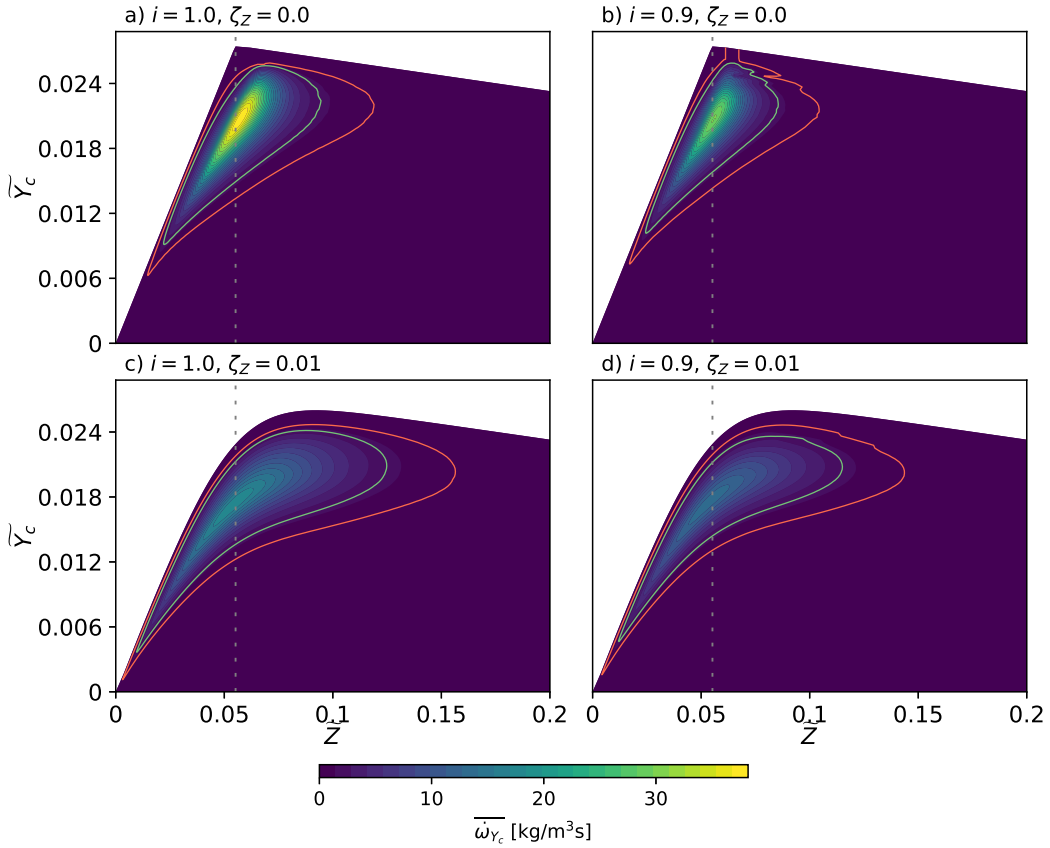

FIGURE 8.12: Illustration of the non-adiabatic thermo-chemical table applied in the methane (F3A2) case of the Cambridge swirl bluff-body burner. The filtered progress variable source term contours are presented on the $\widetilde{Z} - \widetilde{Y}_c$ plane at various conditions. The dashed line indicates the stoichiometric mixture fraction: $Z_{st} = 0.0552$. The red and green contour lines highlight the values of $\overline{\dot{\omega}_{Y_c}} = 0.5\,\mathrm{kg/m^3s}$ and $\overline{\dot{\omega}_{Y_c}} = 2\,\mathrm{kg/m^3s}$ respectively.

The progress variable definition of Ma (2016) is used here, taking a linear combination of the mass fractions of CO_2, CO, H_2O, and H_2:

$$Y_c = Y_c^{ref} = 4\frac{Y_{CO_2}}{W_{CO_2}} + \frac{Y_{CO}}{W_{CO}} + 2\frac{Y_{H_2O}}{W_{H_2O}} + 0.5\frac{Y_{H_2}}{W_{H_2}}. \tag{8.9}$$

The databases are PDF integrated by the joint FPDF of the control variables, which is taken as $\widetilde{P}_{ZC} = \widetilde{P}_Z^{\beta}\widetilde{P}_C^{\delta}$ and $\widetilde{P}_{ZCi} = \widetilde{P}_Z^{\beta}\widetilde{P}_C^{\delta}\widetilde{P}_i^{\delta}$ for the adiabatic and non-adiabatic manifolds respectively. Such approaches are applied for instance by Pierce and Moin (2004) for adiabatic manifolds, and Lamouroux et al. (2014) for non-adiabatic manifolds. For further examples of such sub-grid modeling strategies, see Tab. 5.8. The non-adiabatic thermo-chemical table is illustrated in Fig. 8.12 by the filtered progress variable source term on the $\widetilde{Z} - \widetilde{Y}_c$ plane. Note, that the non-adiabatic table applies the overall maximum progress variable at each mixture fraction as the limit of the Y_c coordinate, thus the shape of $\widetilde{Y_c^{end}}$ differs from the limit depicted in section 3.4.1. The peak source term is drastically decreased by both increasing mixture fraction

variance (ζ_Z) and decreasing scaled enthalpy (i). The increase of ζ_Z distributes the tabulated properties along the $\widetilde{Z}$ coordinate, resulting in the decrease of the peak $\widetilde{Y_c^{end}}$ and the widening of the region with significant source terms. The latter is well illustrated by the red and green contour lines corresponding to $\overline{\dot{\omega}_{Y_c}} = 0.5$ kg/m^{3}s and $\overline{\dot{\omega}_{Y_c}} = 2$ kg/m^{3}s. Meanwhile the decrease of enthalpy also has a profound effect on the source, decreasing the peak $\overline{\dot{\omega}_{Y_c}}$, and making the region of notable source terms narrower in the $\widetilde{Z}$ coordinate.

Flame characteristics

The methane case of F3A2 is simulated with the above outlined approaches. Following the methodology assessed in the DLR-A non-premixed jet flame in section 6.5.2, the velocity boundary conditions of the fuel jet contain a turbulent component based on the approach of Kempf, Klein, and Janicka (2005). The length scale of this injected turbulence is chosen as $\ell_{in} = 0.2D_f$ which is represented well on the inlet surface mesh of both the coarse and the fine grids. The mean velocity profile corresponds to that of a fully developed pipe flow, where the log-law of wall bounded flows is imposed, and polynomial interpolation is used in the core and buffer regions such that the profiles are second order continuous. (Pope, 2000, §7.1) The fluctuating components are superimposed on this mean flow such, that they correspond to the DNS data of El Khoury et al. (2013) at the Reynolds number of the fuel jet: $Re_f = 6700$. Both the air and fuel inlets have a constant temperature of 298.15 K. Furthermore, the heat transfer to the flat plate of the bluff-body and the walls of the combustion chamber are modeled by imposing a temperature of 700 K. Somewhat higher wall temperatures are imposed in the recent work of Meloni et al. (2023) for the simulation of premixed flames in this burner.

The flame behavior is demonstrated in Fig. 8.13, presenting three different instances of the velocity and scalar fields. The fuel jet penetrates into the central recirculation zone, creating a significant region with positive axial velocity. The length of the jet is limited, as it flows in opposition to the recirculating flue gases and the recirculation zone fully encompasses the jet. The fuel mixes with the surrounding material. At the base of the jet hot flue gases of $T^\star \geq 1500$ K are entrained into the methane flow. Meanwhile, the majority of the mixing occurs further downstream, where the methane jet slows down and lean equilibrium mixtures are carried towards the jet with $\phi \approx \phi_{glob} = 0.312$ and $T \approx T^b\left(\phi_{glob}\right) = 1091$ K. The resulting rich mixture ($\phi > 3.5$) forms a large accumulation at the tip of the jet. This rich mixture is carried towards the bluff body by the central recirculation zone. At these higher axial locations (near the tip of the fuel jet) the stoichiometric mixture fraction iso-contour is typically contained well within the recirculation zone, which indicates, that fresh oxidizer enters the recirculation and reaction fronts are formed within the $\widetilde{u} = 0$ m/s iso-contour. (See the top part of Fig. 8.13d, h, and l.) The mixing and reactions occur simultaneously, so the recirculating gases are heated up and their equivalence ratio decreases. At the base of the jet the mixture is near $\phi \approx 2$ with the occasional occurrence of richer and leaner pockets. This rich gas is either entrained into the methane jet or into the shear layer of the oxidizer flow. In the latter case reactions may occur near the stoichiometric mixture fraction iso-contour which is more aligned with the iso-contour of zero axial velocity at these axial locations. Local extinction occurs sporadically in this highly strained shear layer, as Fig. 8.13d illustrates, where the OH radical is fully absent in a large portion of the mixing layer.

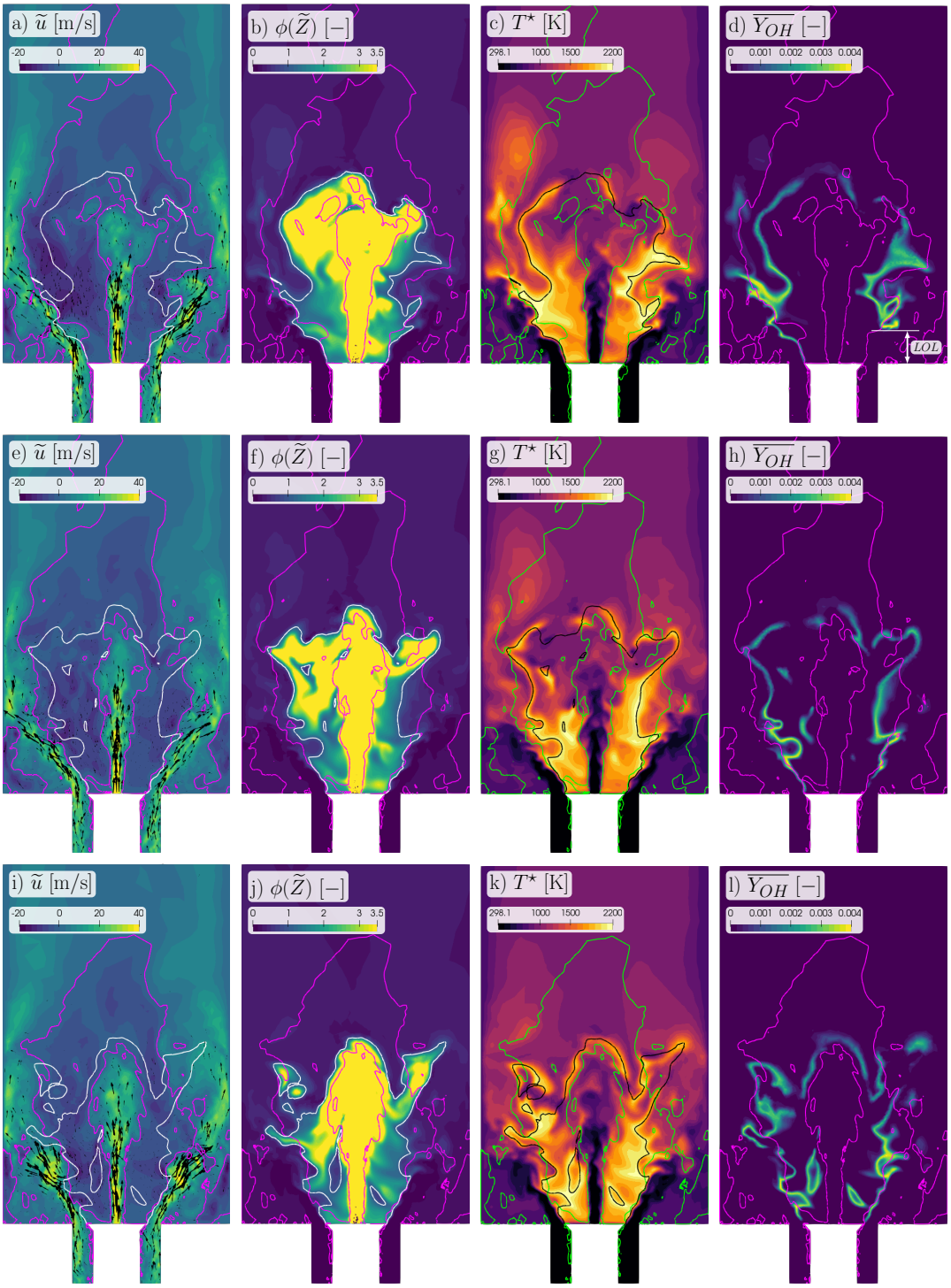

FIGURE 8.13: Examples of the instantaneous velocity and scalar fields of the non-premixed methane case (F3A2) in the Cambridge swirl bluff-body burner. The columns correspond to the velocity, equivalence ratio, temperature, and hydroxyl radical mass fraction fields, while the rows show different instantaneous snapshots. Contour lines mark the position of zero axial velocity (magenta/green) and stoichiometric mixture fraction (white/black).

Mean flow

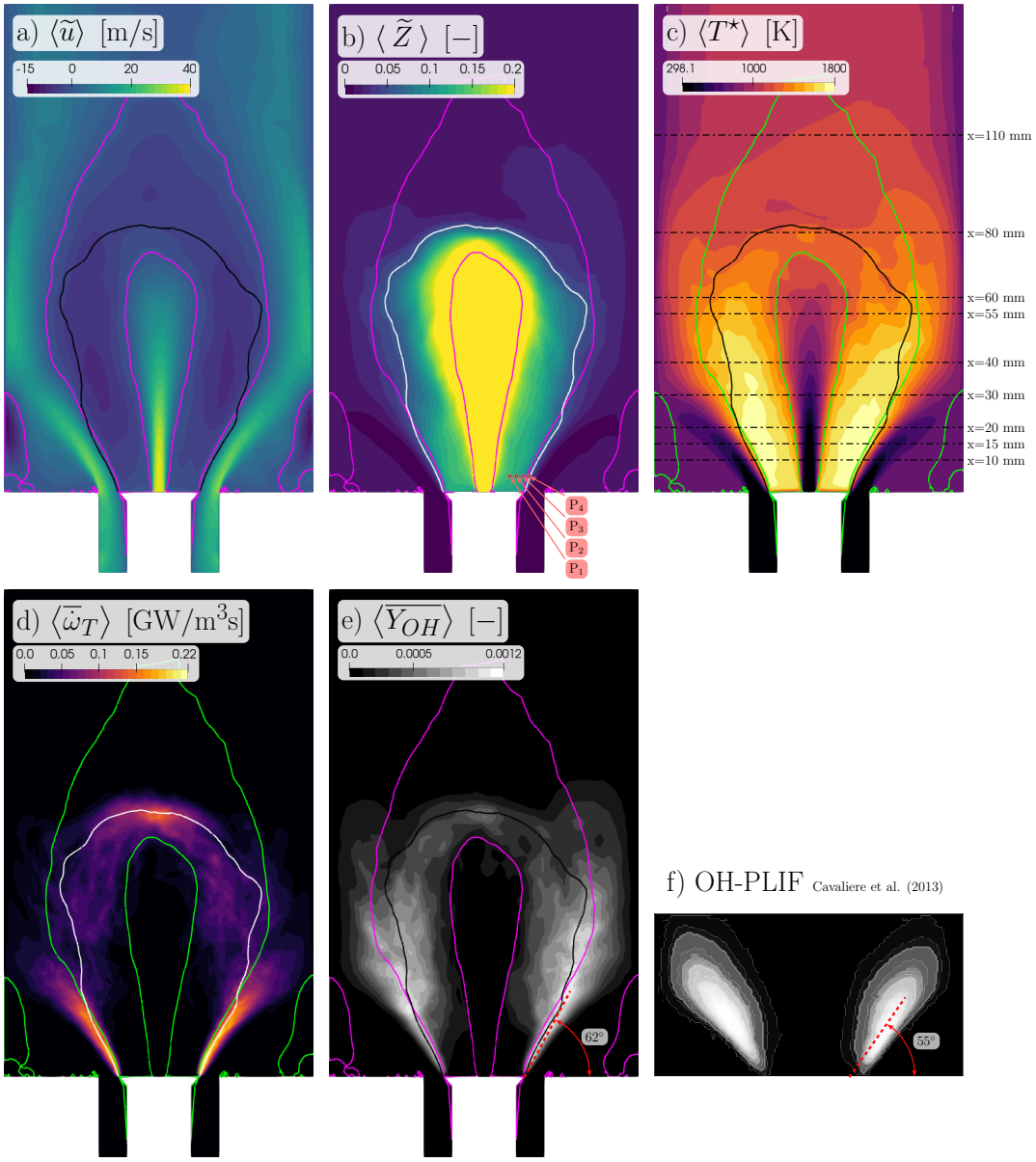

FIGURE 8.14: Mean velocity and scalar fields of the non-premixed methane case (F3A2) in the Cambridge swirl bluff-body burner, obtained by LES on the fine mesh using the non-adiabatic thermochemical manifold. The top row shows the mean of the axial velocity, mixture fraction, and temperature, while the bottom row shows the mean of heat release rate and hydroxyl radial mass fraction, and the average experimental OH-PLIF signal of Cavaliere, Kariuki, and Mastorakos (2013). Contour lines mark the position of zero mean axial velocity (magenta/green) and stoichiometric mixture fraction (black/white).

The reacting calculations are initialized from the inert flow of section 8.2.1, by introducing the methane jet, and imposing stoichiometric equilibrium conditions in part of the central recirculation zone. After the statistically steady conditions are reached, the LES fields are time averages over a period of $\Delta t \approx 150$ ms and

$\Delta t \approx 100$ ms on the coarse and fine meshes respectively. This is deemed adequate, considering the typical flow time scales of the burner identified in the cold flow simulations. The averaging is executed both with using the adiabatic and the non-adiabatic thermo-chemical manifolds. Figure 8.14 illustrates the time averaged LES results of the simulation using the non-adiabatic table with the fine computational grid. Despite the presence of the methane jet, the central recirculation zone stays strong. The jet penetrates more than 70 mm into the combustion chamber, as the contour line of zero mean axial velocity indicates. In this region the mean mixture fraction stays outside the flammability limit, however the fuel is mixed with the recirculating gases near equilibrium conditions, thus the jet is heated up substantially, with mean temperatures of $\langle T^\star \rangle \approx 1200$ K at the tip of the jet. The mean stoichiometric mixture fraction iso-contour is located above the jet tip at an axial distance of around 80 mm. Here a relatively stagnant point of heat release rate is formed. Nevertheless, the majority of heat release occurs in the shear layers attached to the bluff-body edge. Finally, in Fig. 8.14e and f the mean hydroxyl radical mass fraction is compared to the OH planar laser induced fluorescence measurements of Cavaliere, Kariuki, and Mastorakos (2013). In the present simulation the reaction zone spreads at 7° narrower angle than the measurements suggest. A similar tendency is also observed in the work of Ma et al. (2019), however with discrepancies of $\sim 20°$ and $\sim 13°$ for the flamelet/progress variable and the thickened flame model respectively.

A quantitative characterization of the F3A2 flow fields is given by Fig. 8.15 and Fig. 8.16, showing the mean and RMS velocity profiles obtained using the adiabatic and non-adiabatic tabulated chemistry models on the coarse and fine computational grids. The velocity statistics are compared to the laser Doppler anemometry (LDA) data of Cavaliere, Kariuki, and Mastorakos (2013). Note, that the inert flow profiles under the C1 condition are also included for comparison. The axial locations, where the velocity profiles are assessed, are indicated on Fig. 8.14c.

The mean velocity components of Fig. 8.15 do not show significant variation between cases of different grid resolution and different thermo-chemical manifolds. The highest mean axial velocities are associated to the methane jet. The axial velocity peaks of the air inlet at $x = 10$ mm are notably higher than in the C1 case, as Fig. 8.15s illustrates. At this location the difference between the C1 and F3A2 cases is primarily due to the 34% higher air flow rate in the latter case. The difference becomes more pronounced further downstream, as thermal dilation increases the volume flow rate in the reacting case. At $x = 110$ mm the positive axial flow is concentrated to the side of the domain, while the central recirculation zone is still significant. The radial velocity shows higher differences between the C1 and F3A2 cases. In the reacting flow the corner recirculation zone is filled with a very lean mixture near its equilibrium conditions. At $x = 10$ mm this zone shows a large inward radial velocity, as this lean mixture is entrained into the fresh oxidizer flow. Further downstream the radial velocity remains relatively large in the high speed oxidizer flow up to $x = 40$ mm where the flow impinges on the vertical burner walls. Finally, at $x = 110$ mm the direction of the radial velocity becomes reversed as the lean flue gases flow towards the central recirculation zone. The corner recirculation zones are the most intense at $x = 15$ mm. The swirling motion dominates throughout the combustion chamber, with the solid-body-like rotating flow characterizing most of the central recirculation zone. The mean LES profiles agree fairly well with the LDA measurements. The axial velocity peaks of the oxidizer flow are located at slightly higher radii in the LES than in the experiments, and the sudden change of the circumferential velocity in the centerline at $x = 10$ mm is not reproduced. Apart

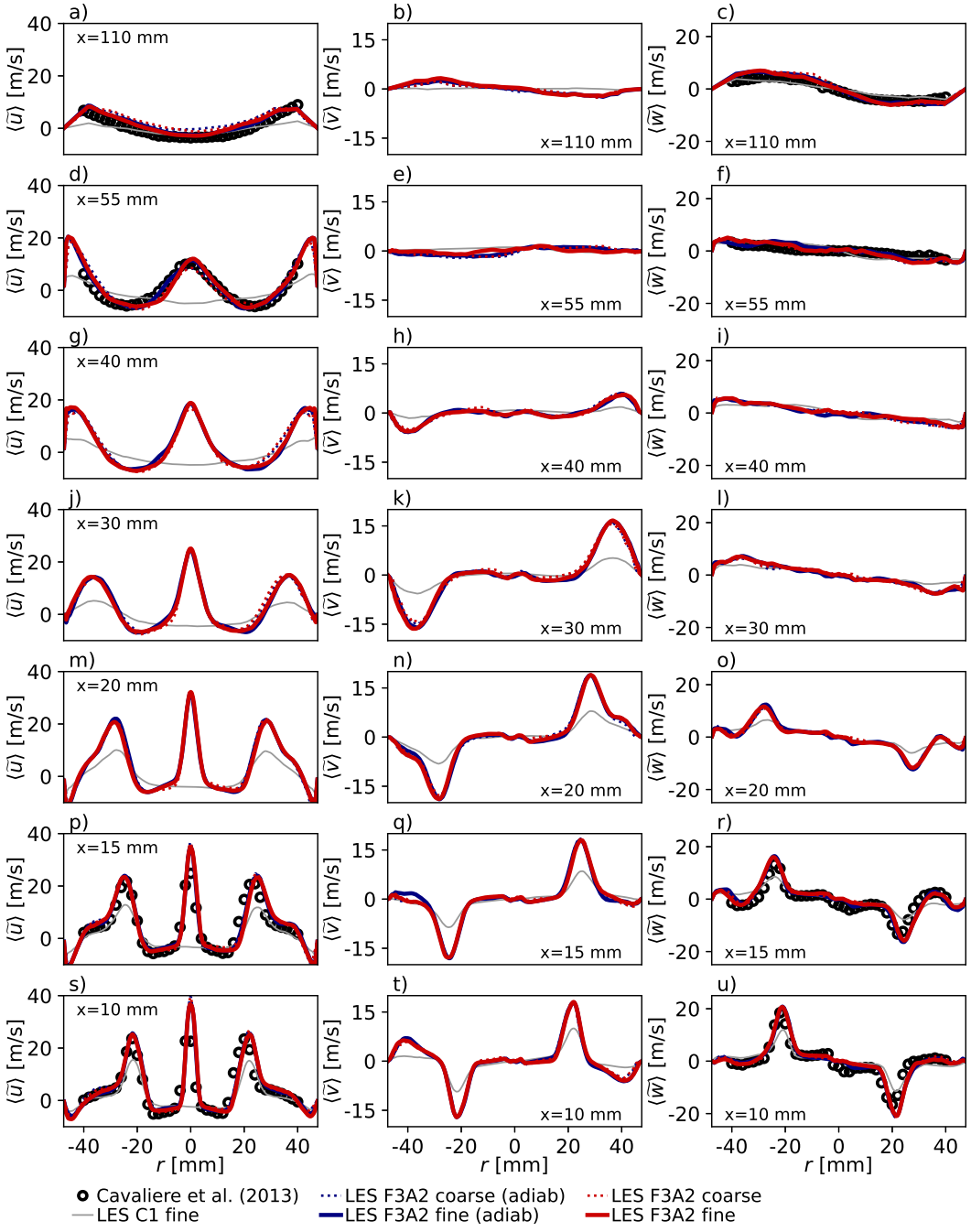

FIGURE 8.15: Comparison of mean velocity profiles in the non-premixed methane case (F3A2) of the Cambridge swirl bluff-body burner between the LDA measurements of Cavaliere, Kariuki, and Mastorakos (2013) and the LES of the present work. The rows of plots correspond to the indicated axial location, while the three columns show the mean of the axial, radial and tangential velocity.

of these discrepancies the velocity fields match well. The penetration length of the methane jet is captured especially well as Fig. 8.15d illustrates. Indeed, this aspect is quite challenging in the LES of the F3A2 flame, as both Zhang et al. (2015) and Ma et al. (2019) report shorter methane jets.

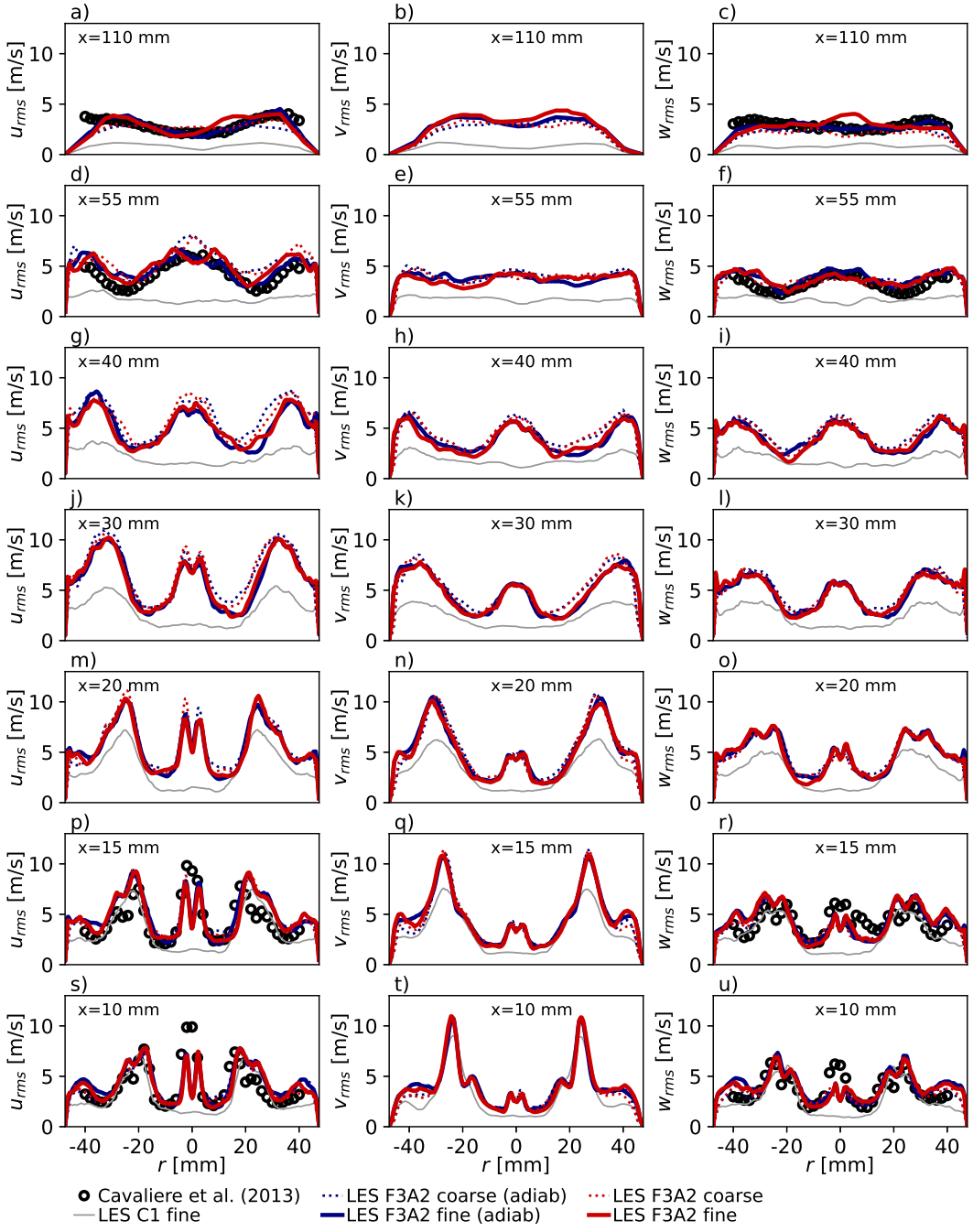

FIGURE 8.16: Comparison of RMS velocity profiles in the non-premixed methane case (F3A2) of the Cambridge swirl bluff-body burner between the LDA measurements of Cavaliere, Kariuki, and Mastorakos (2013) and the LES of the present work. The rows of plots correspond to the indicated axial location, while the three columns show the RMS of the axial, radial and tangential velocity.

The velocity fluctuations are compared with the measurement data in Fig. 8.16. The incoming turbulence of the oxidizer flow is generated within the simulation domain as the flow passes through the air inlet duct. As section 8.2.1 readily demonstrates, the present low-dissipation framework captures the inert flow well, thus the

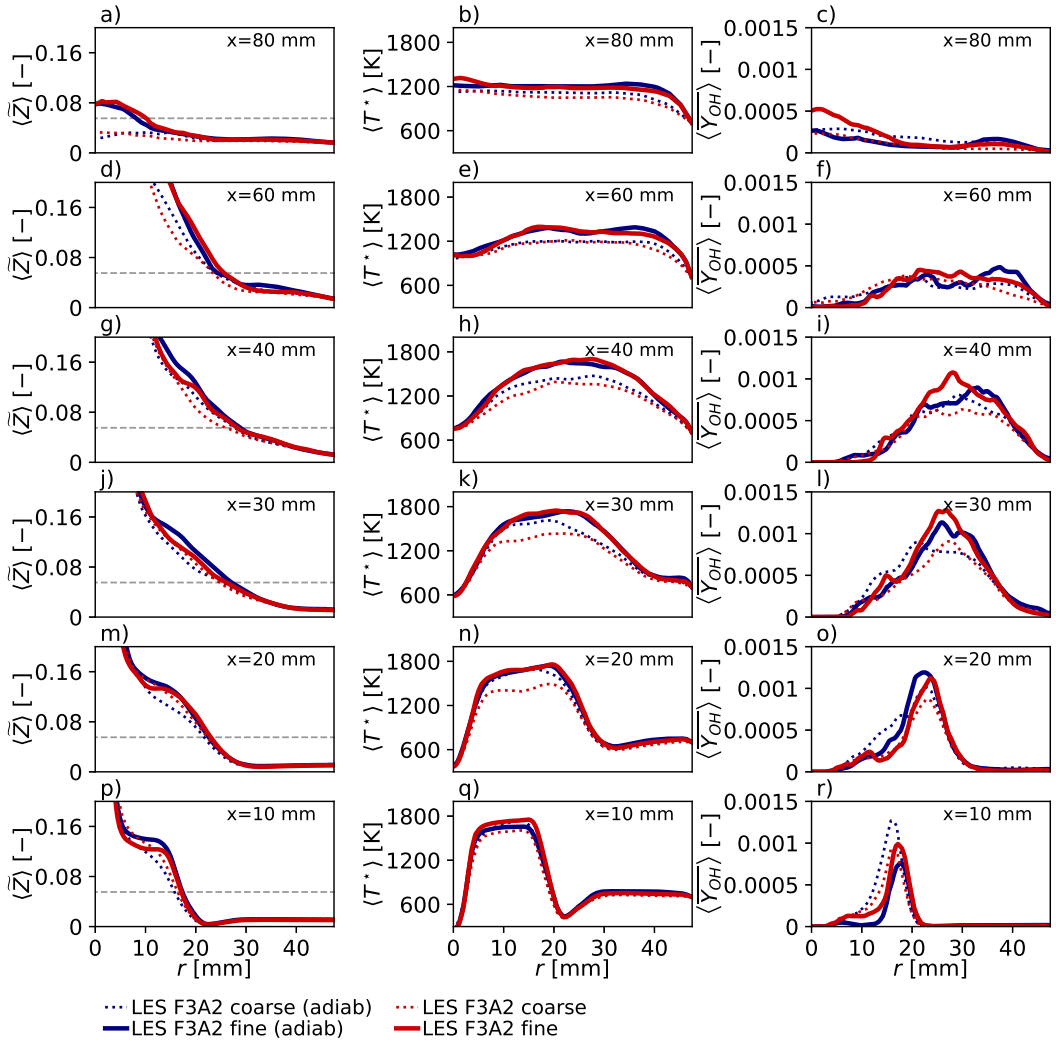

FIGURE 8.17: Mean scalar profiles in the non-premixed methane case (F3A2) of the Cambridge swirl bluff-body burner using the LES of the present work. The rows of plots correspond to the indicated axial location, while the three columns show the mean of the mixture fraction, temperature, and hydroxyl mass fraction.

velocity fluctuations of the oxidizer stream are correctly predicted at $x = 10$ mm. The fluctuations of the methane jet appear to be under-predicted in both the axial and tangential directions. In principle the synthetic turbulent inlet method of Kempf, Klein, and Janicka (2005) allows for the arbitrary tuning on the inlet RMS values, however in this work the incoming RMS magnitudes are based on the DNS data of El Khoury et al. (2013). It would reduce the generality of the developed framework, if it would be required to tune the inlet boundary conditions based on experimental data, thus the method of imposing the fluctuations from DNS pipe flow data is retained here. Note, that the discrepancies diminish further downstream, as the jet starts to spread and the fluctuating components develop. Similar behavior is observed in the DLR-A non-premixed jet flame of section 6.5.2, where the the initial RMS content diminishes close to the inlet, and takes ~ 10 or ~ 5 diameters to recover in the coarse and fine meshes respectively. More downstream the velocity

fluctuations increase and reach their maximum around $x = 20$ mm, then decrease again as the flow becomes more distributed in the chamber. At $x = 55$ mm the correlation with the LDA measurements is still adequate, although differences are observed between the coarse and fine grid results, with the former over-predicting the axial velocity fluctuations in certain locations.

The flame behavior is further analyzed quantitatively in Fig. 8.17 using the radial profiles of mean mixture fraction, temperature, and hydroxyl mass fraction at various axial locations. Note, that the mixture fraction scale is clipped at 0.2 to highlight the behavior near stoichiometry indicated by the dashed gray line. On the coarse computational grid the scalar fields behave differently using the adiabatic and non-adiabatic models. Meanwhile with mesh refinement the two models give more similar results. This suggests, that the finer grid is necessary for resolving the details of the flame, but the effect of heat loss on the thermo-chemical behavior is secondary. At $x = 10$ mm the mixture fraction and temperature show plateaus of $\left\langle \widetilde{Z} \right\rangle \approx 0.12$ and $\langle T^{\star} \rangle \approx 1700$ K. This is located in the recirculation zone in the $r \in [5, 15]$ mm range approximately. Observing the thermo-chemical table illustrated in Fig. 8.12, this plateau is around the rich flammability limit. Consequently, the reactions here are minimal, and the state is near equilibrium because it is a mixture of fuel and leaner fully reacted gases. Inwards from this range the fuel jet carries very rich mixtures. Meanwhile outwards the recirculation zone is limited by the shear layer, where this rich equilibrium mixture interacts with the fresh oxidizer, and the remaining unburnt hydrocarbons and radicals are oxidized. This reaction zone is marked by the peaks in the mean hydroxyl mass fraction. At around $r = 23$ mm the mean mixture fraction and temperature have a local minimum very close to the fresh oxidizer conditions, corresponding to the core of the oxidizer flow. At higher radii in the corner recirculation the mixture is very lean and it is characterized by a fairly low temperature. At higher axial locations the plateau of mean mixture fraction disappears, and the mean composition transitions more smoothly from rich to lean towards the edge of the chamber. The flame brush becomes more distributed radially indicated by the wider distribution of $\langle \overline{Y_{OH}} \rangle$, however the peak is slightly higher than at $x = 10$ mm due to the intermittency of the reacting zone when the flame is lifted. At $x = 80$ mm the fuel jet creates a very small rich region in the center of the domain, but otherwise the mixture is near the global mixture fraction $Z_{glob} = 0.0179$ and the temperature is fairly constant as well, except near the relatively colder burner wall.

Dynamic flame behavior

The flame is lifted from the bluff-body edge intermittently, as localized extinction happens due to the high strain in the shear layer. A lift-off length: LOL is defined, as the distance between the entrance of the combustion chamber, and the first location on the half-plane, where an instantaneous hydroxyl radical concentration of $\overline{Y_{OH}} = 0.0004$ is found, which corresponds to approximately 10% of the maximum possible value. The lift-off length of the right half-plane is illustrated in Fig. 8.13d. Cavaliere, Kariuki, and Mastorakos (2013) utilize the OH planar laser induced fluorescence (OH-PLIF) data to study a similarly defined lift-off length statistically. Such statistics is collected from the LES simulations as well, by evaluating the LOL at various time steps in four half-planes. (I.e.: the left and right half of the plane illustrated in Fig. 8.13, and the analogous half-planes normal to this plane.) The mean lift-off is summarized in Tab. 8.3. Cavaliere, Kariuki, and Mastorakos (2013) only assessed lift-off instances, where the LOL exceeds 0.2 mm. Under this condition, they found

TABLE 8.3: Mean flame lift-off length in methane case (F3A2) of the Cambridge swirl bluff-body burner.

	$\langle LOL \rangle$ [mm]	Sample count	
LES coarse (adiabatic)	3.3	404	
LES coarse	3.9	404	
LES fine (adiabatic)	4.9	253	
LES fine	4.8	225	
	$\langle LOL \vert LOL > 0.2 \text{ mm} \rangle$	Sample count	Lifted fraction
Cavaliere et al. (2013)	5.0		
LES coarse (adiabatic)	5.2 (+4%)	263	65%
LES coarse	5.0 (0%)	317	78%
LES fine (adiabatic)	6.1 (+22%)	204	81%
LES fine	5.6 (+12%)	191	85%

an average lift-off of: $\langle LOL|LOL > 0.2 \text{ mm} \rangle = 5$ mm. The simulations on the coarse mesh predict the mean lift-off values very closely. Nevertheless this is likely due to compensation of errors, as the refinement induces more lifted flames, with errors of 22% and 12% in $\langle LOL|LOL > 0.2 \text{ mm} \rangle$ for the adiabatic and non-adiabatic thermo-chemical manifolds respectively. Including heat loss consistently increases the fraction of samples with $LOL > 0.2$ mm, meanwhile it also decreases the mean lift-off thus the fraction of instances with shorter lift-off increases.

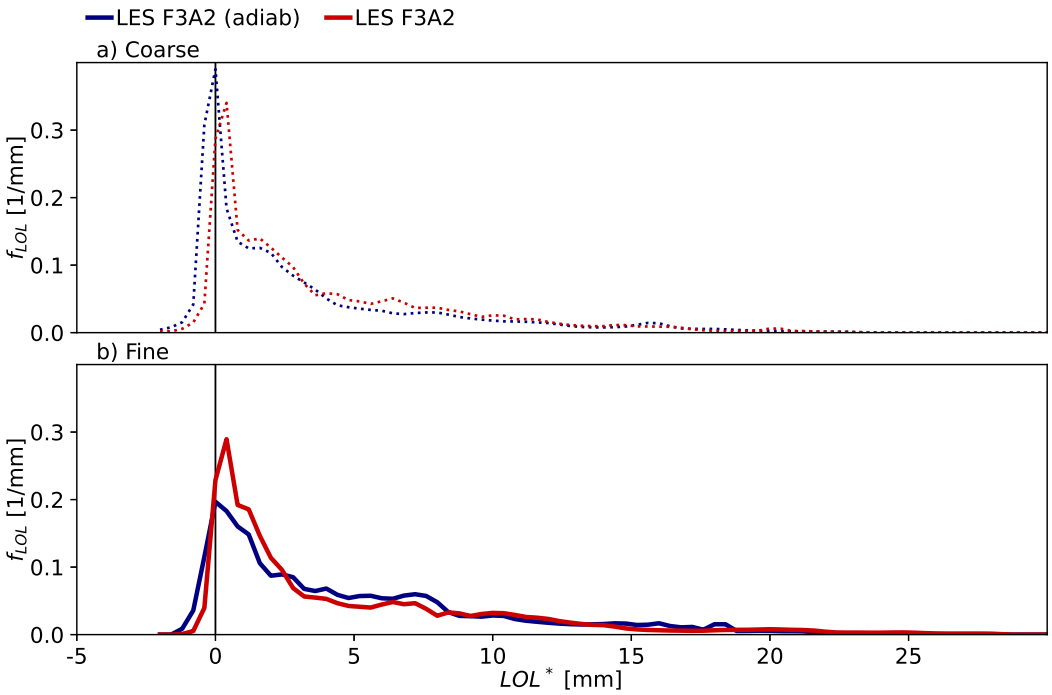

FIGURE 8.18: Probability density function of flame lift-off length in the methane case (F3A2) of the Cambridge swirl bluff-body burner.

The lift-off length statistics is further assessed in Fig. 8.18 using the probability

density function (PDF) of the computed heights. The tools used in appendix H are re-purposed for calculating the PDF. First the cumulative density function F_{LOL} is obtained as:

$$F_{LOL}\left(LOL^*\right) = \frac{1}{n}\sum_{i=1}^{n}\mathcal{H}\left(LOL^* - LOL_i\right), \tag{8.10}$$

where n is the sample count, $\mathcal{H}$ is the Heaviside function, and LOL_i is the i^{th} lift-off sample, thus $F_{LOL}\left(LOL^*\right)$ expresses the fraction of samples with a LOL_i smaller than LOL^*. Subsequently, the PDF is obtained by numerically differentiating the cumulative density function:

$$f_{LOL}\left(LOL^*\right) = \frac{\partial F_{LOL}\left(LOL^*\right)}{\partial LOL^*}. \tag{8.11}$$

The lift-off PDF curves show more nuances of the flame behavior than the simple arithmetic mean of the LOL values. Note, that in some instances the reaction zone is located below the inlet plane, thus the probability of negative LOL values is non-zero. Such states contribute to the fully attached conditions, which are excluded in the analysis of Cavaliere, Kariuki, and Mastorakos (2013). Indeed, the probability of fully attached flames is significantly higher in the coarse mesh, as Tab. 8.3 readily presents. Including heat loss in the thermo-chemical manifold tends to shift part of the distribution curve to higher LOL^* values, as the reaction zone is extinguished near the bluff-body due to to the lower mixture temperatures. Meanwhile, especially in the fine mesh, the probability of larger lift-offs decreases. Overall this results in a higher portion of lifted instances with relatively low lift-offs, which explains the improvement in the prediction of $\langle LOL|LOL > 0.2\text{ mm}\rangle$.

Cavaliere, Kariuki, and Mastorakos (2013) evaluated the lift-off PDF based on the reduced set of OH-PLIF images containing only reaction layers with at least 0.2 mm lift-off. This clipping of the sample is also executed with the LES data in order to compare with the experimental distribution in Fig. 8.19. The present simulations consistently over-predict the probability of shorter lift-off, while there is negative discrepancy in in the PDF near $LOL^* = 5$ mm. The probability of higher lift-offs is predicted well. This suggests, that the extinction events are occurring appropriately, reaching large instantaneous LOL conditions, however the flame returns to a more attached state without residing at the intermediate lift-off conditions for an appropriate time span. Similar behavior is observed in the simulations of Zhang et al. (2015), where highly lifted conditions are more probable than expected. Overall, the flame dynamics is reproduced with sufficient accuracy, considering the simplicity of the simulation method. Indeed, as Fig. 8.14 and Fig. 8.17 demonstrate, the reaction zone is located in the interaction of a highly reacted rich mixture and fresh oxidizer. This condition is not included explicitly in the thermo-chemical manifold, however the method still gives satisfactory results.

Single point analysis

The flame behavior is further analyzed using the monitoring points P_1 to P_4 marked on Fig. 8.14b. These are located at $x = 5$ mm coinciding with the mean lift-off height. The unknowns and other properties are recorded on these points within the averaging time spans applied above. Subsequently the data is processed using the tools of appendix H to obtain the joint probability density function of mixture fraction $\widetilde{Z}$ and temperature $T^\star$. In this case first the joint cumulative density function is computed

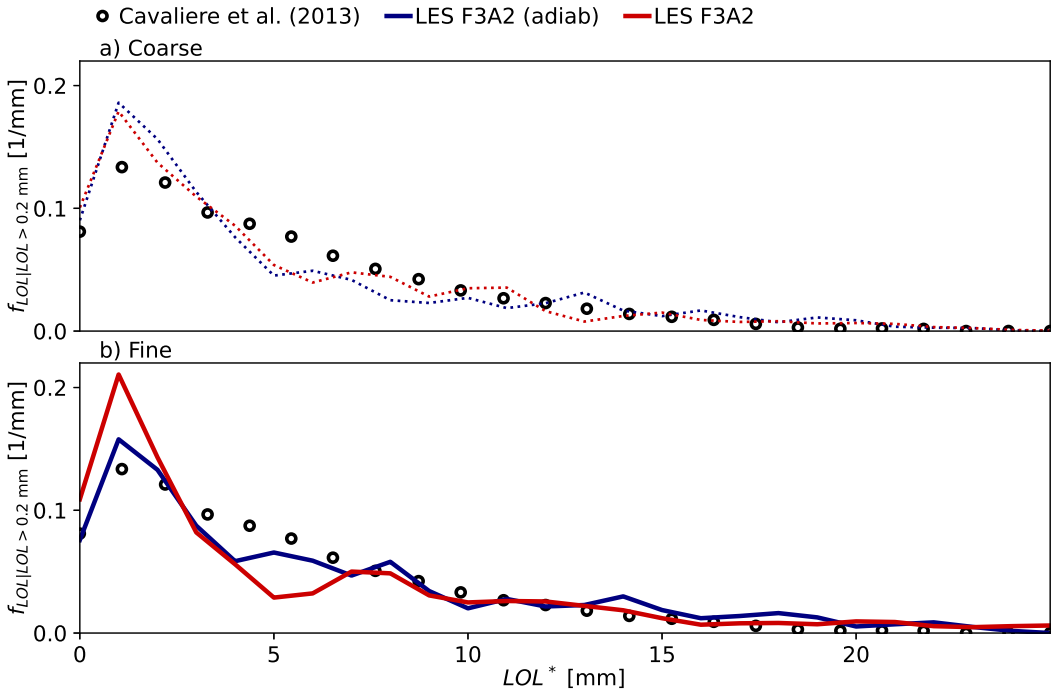

FIGURE 8.19: Probability density function of flame lift-off length conditioned to $LOL > 0.2$ mm in the methane case (F3A2) of the Cambridge swirl bluff-body burner.

as:

$$F_{\widetilde{Z}T^\star}\left(\widetilde{Z}^*, T^{\star,*}\right) = \frac{1}{t_{end} - t_{ini}} \int_{t_{ini}}^{t_{end}} \mathcal{H}\left(\widetilde{Z}^* - \widetilde{Z}\left(t\right)\right) \mathcal{H}\left(T^{\star,*} - T^\star\left(t\right)\right) \mathrm{d}t, \tag{8.12}$$

where $[t_{ini}, t_{end}]$ is the assessed time interval, $\mathcal{H}$ is the Heaviside function. Subsequently, the joint PDF of mixture fraction and temperature is obtained by the partial derivation of the joint CDF with respect to both coordinates:

$$f_{\widetilde{Z}T^\star}\left(\widetilde{Z}^*, T^{\star,*}\right) = \frac{\partial^2 F_{\widetilde{Z}T^\star}\left(\widetilde{Z}^*, T^{\star,*}\right)}{\partial \widetilde{Z}^* \partial T^{\star,*}}. \tag{8.13}$$

This joint PDF is displayed in Fig. 8.20 computed at the four different monitoring points, with green and red contour lines highlighting the levels of $f_{\widetilde{Z}T^\star} = 0.005/\mathrm{K}$ and $f_{\widetilde{Z}T^\star} = 0.0001/\mathrm{K}$. In the P_1 point the mixture is consistently rich, with the leanest encountered compositions located near stoichiometry, while in P_2 lean mixtures are found sporadically. In both points the states are limited to the stable branch, with little variation in the reaction progress. In the P_3 point the states become significantly more distributed on the $\widetilde{Z}^* - T^{\star,*}$ plane, with a notable portion of states located below the flamelet of the extinction point marked with the dotted line. The low temperature states are concentrated in two main areas as the red contour line indicates. One cluster is formed around the lean equilibrium states, and another cluster on the mixing line between fresh oxidizer: $\left(\widetilde{Z}^*, T^{\star,*}\right) = (0, 298.15\ \mathrm{K})$ and the mean state of P_3: $\left(\widetilde{Z}^*, T^{\star,*}\right) = (0.11, 1752\ \mathrm{K})$. As the thermo-chemical manifolds displayed in Fig. 8.12 illustrate, the latter cluster of mixing between rich equilibrium

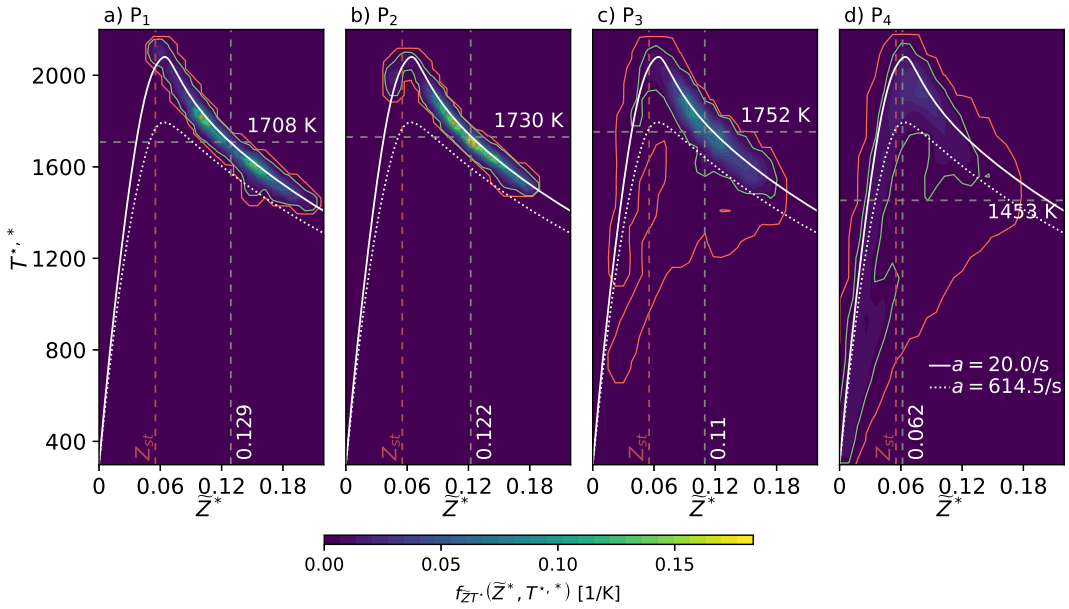

FIGURE 8.20: Joint probability density function of mixture fraction and temperature in monitoring points of the methane case (F3A2) of the Cambridge swirl bluff-body burner. The four points correspond to $r \in [8, 10, 12, 14]$ mm at an axial location of $x = 5$ mm. The dashed lines mark the temporal average of mixture fraction $\left\langle \widetilde{Z} \right\rangle$ and temperature $\langle T^\star \rangle$. The green and red contour lines indicate the levels of $f_{\widetilde{Z}T^\star} = 0.005$/K and $f_{\widetilde{Z}T^\star} = 0.0001$/K, while the solid and dotted white curves represent the adiabatic counterflow diffusion flamelets at a strain rate of $a = 20$/s and at the extinction point respectively.

mixtures and fresh oxidizer is characterized by very small source terms, indicating the presence of localized extinction. The outermost point: P_4 is very close to the stoichiometric mean mixture fraction iso-surface, with $\langle \widetilde{Z} \rangle = 0.062$. Here the states become very distributed on the $\widetilde{Z}^* - T^{\star,*}$ plane with an even higher fraction of extinguishing states. In this case the mixing line between rich equilibrium conditions and fresh oxidizer is partially highlighted by the green iso-contour of $f_{\widetilde{Z}T^\star} = 0.005$/K. The present statistical analysis provides further understanding of the local extinction phenomenon, highlighting the thermo-chemical states which are accessed in the manifold.

The scales of turbulence/chemistry interaction are assessed in various monitoring points of the F3A2 case using the scale estimation strategy outlined in section 5.1.6. Subsequently, the location of these monitoring points is identified on the regime diagram of Balakrishnan and Williams (1994) in $Da_t - Re_t$ plane, introduced in section 5.3.2, where the Damköhler number is defined using the chemical time scale: $\tau_c^{ext,\chi} = 104$ μs, which is obtained using the stoichiometric mixture fraction and the stoichiometric scalar dissipation rate at extinction. (See Tab. 8.1 for alternative time scales.) The points are located in the regimes of flamelets and broken flamelets, indicating that the present tabulated chemistry method is adequate in terms of the expected structures of the turbulence/chemistry interaction. In particular, the lowest observed integral Damköhler numbers are approximately 1.5 in the low temperature oxidizer flow. Meanwhile the smallest Kolmogorov-scale Damköhler number is 0.13, indicating, that the fastest turbulent scales are fast enough to

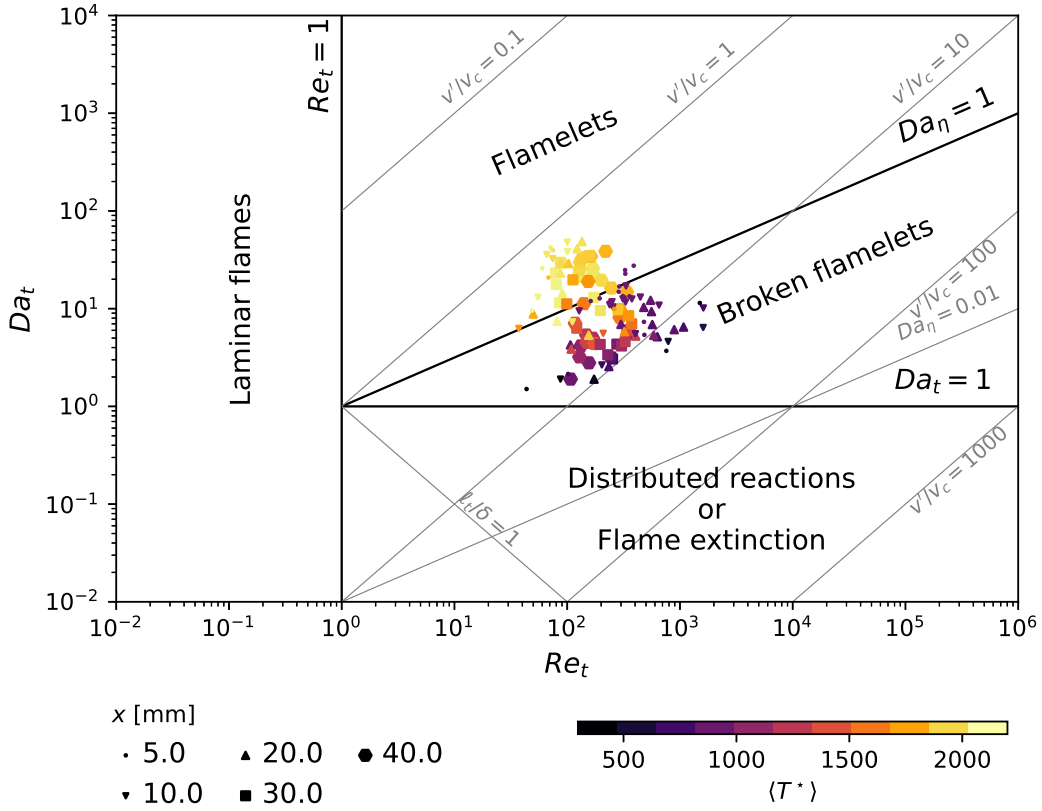

FIGURE 8.21: Turbulent non-premixed combustion regime diagram of Balakrishnan and Williams (1994) in the methane case (F3A2) of the Cambridge swirl bluff-body burner. The monitoring points correspond to $r \in [0, 2, 4, ..., 46]$ mm at five different axial location of $x \in [5, 10, 20, 30, 40]$ mm. The color scheme indicates the temporal mean temperature $\langle T^\star \rangle$.

disturb the combustion process. Nevertheless, as higher temperature states are approached, the Damköhler numbers increase, since the time scales of turbulence grow inside the more stagnant and higher viscosity flow (see Tab. 8.1) of the central recirculation zone.

Overall, the developed low-dissipation finite element scheme performs well in the non-premixed methane case (F3A2) of the Cambridge swirl bluff-body burner. The mean flow is reproduced to an adequate extent, with only 7° under-prediction of the flame spreading angle. The velocity fluctuations are also resolved adequately, indicating the good performance of the Navier-Stokes solver. In terms of combustion modeling, the case is identified to be in the flamelet regime based on the scales of turbulence, however the partial premixed nature of the reaction zones makes it a challenging problem for the tabulated chemistry model. Interactions are observed between rich equilibrium mixtures of the central recirculation zone and the fresh oxidizer. Such interactions are not represented directly by the counterflow diffusion flamelets constituting the thermo-chemical manifolds. Nonetheless, the flame dynamics are reproduced to a good extent, as indicated by the prediction of the dynamic lift-off behavior, with a mean lift-off height error of only 12%.

8.3 Spray flames

Finally, the spray flame cases of the Cambridge swirl bluff-body burner are studied using the Eulerian-Lagrangian approach developed in this study within the framework of the Alya code. (See chapter 6.) The n-heptane and n-dodecane flames studied here correspond to the H1S1 and DD1S2 operating conditions experimentally studied by Yuan et al. (2015) and Yuan, Kariuki, and Mastorakos (2018). As Fig. 8.4 readily illustrates, these are characterized by the same flow rate of both fuel and oxidizer with the only difference originating from the nature of the fuel. In fact the dodecane case is closer to the blow-off limit, as the lean blow-out happens at lower flow rates using this heavier hydrocarbon fuel. As Fig. 8.1c depicts, the liquid fuel is introduced directly into the combustion chamber at the center of the bluff-body by a hollow cone spray injector. The nominal spray half-angle of the injector is 30°. The fuel spray interacts with the hot flue gases of the central recirculation zone, where intense evaporation occurs and fuel vapor is introduced to this mixture. The reaction zones form an M shape stabilizing over the bluff body in the central recirculation zone, with the inner reaction zone located near the spray half angle, and the outer reaction zone over the bluff-body edge. The inner reaction layer interacts with the hollow cone spray, while the outer reaction layer is located in the shearing air flow at the edge of the bluff-body. The design of the burner and the carefully selected operating conditions promote unsteady effects, which results in the intermittent lift-off of the outer reaction zone, similarly to the methane flame of section 8.2.2. Although, the global equivalence ratio of the system is lean, a locally rich region tends to be formed over the bluff-body in the central recirculation zone, as experimentally demonstrated by Giusti, Kotzagianni, and Mastorakos (2016) using laser induced breakdown spectroscopy, and by Allison, Sidey, and Mastorakos (2017) and Sidey, Allison, and Mastorakos (2017) using planar laser induced fluorescence imaging of the fuel.

The Cambridge swirl spray flames have been the subject of various LES studies. Tyliszczak, Cavaliere, and Mastorakos (2014) studied the n-heptane flames of the earlier measurements of Cavaliere, Kariuki, and Mastorakos (2013) using Conditional Moment Closure (CMC). Note, that these flames correspond to a significantly different operating condition, with a fuel mass flow rate less than half of the presently studied cases: 0.12 g/s. Moreover a different pressure swirl atomizer is applied. The bulk air velocities in their study are also different: 14.3 m/s and 18.5 m/s. Tyliszczak, Cavaliere, and Mastorakos (2014) concluded, that the CMC approach is suitable for the qualitative characterization of the local extinction of the outer reaction zone, and the quantitative prediction of the global blow-out conditions. Subsequently, Giusti, Kotzagianni, and Mastorakos (2016) and Giusti and Mastorakos (2017) studied the stable ethanol flame of this configuration using the CMC model. They found a good performance of this simulation approach in case of this highly volatile fuel, as both the mean flow properties and the dynamic lift-off behavior is predicted quantitatively. Paulhiac et al. (2020) studied the flame structure of an n-heptane flame of the Cambridge swirl bluff-body burner, although also under the lower fuel flow rates of the measurement case of Cavaliere, Kariuki, and Mastorakos (2013). They used a 2-step chemistry mechanism in a highly refined computational grid, that allows for the omission of sub-grid chemistry modeling. Both Giusti and Mastorakos (2017) and Paulhiac et al. (2020) found, that high strain in the outer reaction zone is correlated with the lift-off events, even though the local strain rate does not exceed the extinguishing strain rate of the 1D flamelet configuration. This

suggests, that the present 3D lift-off phenomena is more complex, than the extinction event of the 1D counterflow diffusion flamelets, involving the convective transport of the radical pool. Elasrag and Li (2018) used a tabulated chemistry approach based on counterflow diffusion flamelets, similar to the F3A2 case studied above, to simulate the stable n-heptane flames. More recently, Foale, Giusti, and Mastorakos (2021) used CMC to investigate the behavior of various kerosene and synthetic jet fuel flames in the Cambridge swirl bluff-body burner. This study predicts the global extinction event with a $5\% - 20\%$ accuracy at various fuel flow rates. Fuel starvation is identified as the driving mechanism of global extinction in spray flames. I.e.: at the blow-out conditions the enhanced mixing of fresh oxidizer into the central recirculation zone cools the environment of the spray, which leads to lower evaporation rates.

8.3.1 Combustion model

Various tabulated chemistry methods are evaluated below in section 8.3.4, while this section defines the shared characteristics of the different modeling approaches. As throughout this work, the Navier-Stokes equations are solved under the low Mach number assumption using the developed low-dissipation finite element strategy. Besides mass and momentum conservation (Eq. (5.30) and Eq. (5.47)), a small number of transported scalars describe the gas state corresponding to enthalpy, mixture fraction, progress variable (Eq. (5.117)), and sub-grid mixture fraction variance (Eq. (5.122)). The relevant governing equations are reproduced here, including the source terms of the Eulerian-Lagrangian coupling with the spray cloud:

$$\partial_t \overline{\rho} + \nabla \cdot (\overline{\rho}\widetilde{\mathbf{u}}) = \overline{S_\rho^e} \tag{8.14}$$

$$\partial_t (\overline{\rho}\widetilde{\mathbf{u}}) + \nabla \cdot (\overline{\rho}\widetilde{\mathbf{u}} \otimes \widetilde{\mathbf{u}}) + \nabla \overline{p} - \nabla \cdot \left(2\left(\overline{\mu} + \overline{\rho}\nu^{SGS}\right)\widetilde{\mathbf{S^D}(\mathbf{u})}\right) = \overline{S_\mathbf{u}^e} \tag{8.15}$$

$$\partial_t \left(\overline{\rho}\widetilde{h}\right) + \nabla \cdot \left(\overline{\rho}\widetilde{h}\widetilde{\mathbf{u}}\right) - \nabla \cdot \left(\overline{\rho}\left(\widetilde{\mathcal{D}_t} + \frac{\nu^{SGS}}{Pr^{SGS}}\right)\nabla \widetilde{h}\right) = \overline{S_h^e} \tag{8.16}$$

$$\partial_t \left(\overline{\rho}\widetilde{Z}\right) + \nabla \cdot \left(\overline{\rho}\widetilde{Z}\widetilde{\mathbf{u}}\right) - \nabla \cdot \left(\overline{\rho}\left(\widetilde{\mathcal{D}_t} + \frac{\nu^{SGS}}{Sc^{SGS}}\right)\nabla \widetilde{Z}\right) = \overline{S_\rho^e} \tag{8.17}$$

$$\partial_t \left(\overline{\rho}\widetilde{Y_c}\right) + \nabla \cdot \left(\overline{\rho}\widetilde{Y_c}\widetilde{\mathbf{u}}\right) - \nabla \cdot \left(\overline{\rho}\left(\widetilde{\mathcal{D}_t} + \frac{\nu^{SGS}}{Sc^{SGS}}\right)\nabla \widetilde{Y_c}\right) = \overline{\dot{\omega}_{Y_c}} \tag{8.18}$$

$$\partial_t (\overline{\rho}Z_v) + \nabla \cdot (\overline{\rho}Z_v\widetilde{\mathbf{u}}) - \nabla \cdot \left(\overline{\rho}\left(\widetilde{\mathcal{D}_t} + \frac{\nu^{SGS}}{Sc^{SGS}}\right)\nabla Z_v\right) = 2\frac{\overline{\rho}\nu^{SGS}}{Sc^{SGS}}\nabla \widetilde{Z} \cdot \nabla \widetilde{Z} - \overline{\rho}\chi_Z^{SGS}, \tag{8.19}$$

where the filtered spray source terms are evaluated according to section 5.5.3. Note, that following Sitte and Mastorakos (2019) the spray source terms associated to the mixture fraction variance are neglected here, as the commonly used closure models entail substantial uncertainty. For further details of this neglected source term see section 5.4.2. Furthermore, the equations are discretized in the non-conservative form, where dilution terms appear associated to the mass source term of the continuity equation. In this case the right hand side of the momentum equation is appended with $-\widetilde{\mathbf{u}}\overline{S_\rho^e}$ according to section 5.2.1. The equivalent dilution terms of the scalar equations in the non-conservative form are: $-\widetilde{h}\overline{S_\rho^e}$, $-\widetilde{Z}\overline{S_\rho^e}$, $-\widetilde{Y_c}\overline{S_\rho^e}$ and $-Z_v\overline{S_\rho^e}$ as detailed in section 6.1.3. The progress variable is defined as: $Y_c = \frac{4Y_{CO_2}}{W_{CO_2}} + \frac{Y_{CO}}{W_{CO}} +$

$\frac{2Y_{H_2O}}{W_{H_2O}} + \frac{0.5Y_{H_2}}{W_{H_2}}$ following Ma (2016). This set of governing equations allows for the sub-grid chemistry closure considering a sub-grid beta distribution in Z and delta distribution in all other scalar quantities adapting the approach of Pierce and Moin (2004). As detailed in appendix K, this sub-grid modeling strategy provides the better results in terms of the flame dynamics. Nevertheless, the sub-grid turbulence/chemistry interaction modeling remains an open question.

8.3.2 Spray model

The evaporating spray cloud is represented by Lagrangian particles transported in the computational domain. As detailed in chapter 4, each numerical particle is characterized by a set of ordinary differential equations (ODE) that capture the evolution of their location, velocity, mass, and temperature. The droplet motion is tracked using a Newmark/Newton-Raphson time integration scheme developed by Houzeaux et al. (2016), with the drag determined by the correction of Naumann and Schiller (1935). Section 4.6.2 demonstrates, that the evaporation model of Abramzon and Sirignano (1989) may introduce significant modifications compared to Bird's correction. Especially in case of droplets with higher slip velocities interacting with flame-like gas states. Consequently, the Abramzon-Sirignano model is applied here. The ordinary differential equation system describing the droplet state (Eq. (4.2), Eq. (4.3), Tab. 4.4) is summarized here for completeness:

$$\frac{\mathrm{d}\mathbf{x}_p}{\mathrm{d}t} = \mathbf{u}_p, \tag{8.20}$$

$$m_p \frac{\mathrm{d}\mathbf{u}_p}{\mathrm{d}t} = \mathbf{F}_d, \tag{8.21}$$

$$\frac{\mathrm{d}T_p}{\mathrm{d}t} = \frac{\pi d_p \lambda_m N u_m^{*,AS}}{m_p c_{p,p}} \left(T_s - T_p\right) \frac{\ln\left(1+B_T\right)}{B_T} + \frac{L_v}{m_p c_{p,p}} \frac{\mathrm{d}m_p}{\mathrm{d}t}, \tag{8.22}$$

$$\frac{\mathrm{d}m_p}{\mathrm{d}t} = -\pi d_p \rho_m \mathcal{D}_m S h_m^{*,AS} \ln\left(1+B_M\right), \tag{8.23}$$

where only the drag force $\mathbf{F}_d$ is considered in the droplet kinematics. The droplet interface vapor mass fraction is evaluated assuming local thermodynamic equilibrium. The mean gas phase properties are evaluated in accordance with the TARES model developed in this work, which obtains the necessary quantities based on themo-chemical tables as discussed in section 4.3.2. Specifically, a first order Taylor-expansion of λ, μ and $\mathcal{D}$ is tabulated in terms of temperature, so close approximations can be provided, given the temperature of the "1/3-law". This temperature is used directly in conjunction with the NASA polynomials and the ideal gas law, to obtain the representative specific heat and density. The exact same approach is used irrespective of the utilized tables. As readily demonstrated in section 6.4.1, this approach approximates the evaporation rates of the classical "1/3-law" of Yuen and Chen (1976) closely. The liquid and phase change properties of the fuels are evaluated as a function of the droplet temperature following Daubert and Danner (1985). The Reynolds number dependence of the uncorrected Nusselt and Sherwood numbers are taken into account using the correlation of Ranz and Marshall (1952), with the final corrected values calculated according to section 4.4.6. Besides the extensive analysis presented in chapter 4, the validity of this evaporation model is further assessed in appendix L, which compares the Abramzon-Sirignano model to the Classical model. The latter, proves to be unsuitable for reproducing the spray evolution in the Cambridge swirl bluff-body burner.

The droplet injection is modeled empirically, in order to best represent the conditions of the pressure swirl atomizer creating the hollow cone spray. This model provides the initial condition of the individual Lagrangian particles in terms of location, velocity, temperature, and droplet size. The initial droplet temperature is kept constant, the same as the oxidizer inlet temperature: $T_{p,0} = 298.15$ K. The other four properties are determined stochastically. The computational droplets are introduced into the domain at the center of the bluff body, corresponding to the injection location. Specifically, the azimuthal location is selected uniformly in the $\varphi_0 \in [0°, 360°)$ range. Subsequently, the radial location is chosen on an annulus limited by a minimum and maximum diameter: $r_{min} = 90$ μm and $r_{max} = 150$ μm. This selection is done such, that the final spacial distribution of initial droplet locations is uniform, i.e.: larger radii are picked with higher probability, as a larger portion of the annulus surface is located at the outer edge. Thus the initial droplet location is determined as:

$$\varphi_0 = 2\pi U_1, \tag{8.24}$$

$$r_0 = \sqrt{r_{min}^2 + (r_{max}^2 - r_{min}^2)U_2}, \tag{8.25}$$

where U_1 and U_2 are independent pseudo-random numbers in the $[0, 1)$ interval. The polar angle determining the direction of the initial velocity vector is linked to the location along the annulus, thus the direction is parameterized by only one additional parameter: $\theta_{max} = 40°$, and the velocity direction is determined as:

$$\theta_0 = \theta_{max} \frac{r_0}{r_{max}}. \tag{8.26}$$

The minimum polar angle is a consequence of the applied minimum radius of the annulus: $\theta_{min} = \theta_{max} \frac{r_{min}}{r_{max}} = 24°$. This corresponds to a central spray half-angle of 32° with a variation of $\pm 8°$. The initial droplet velocity has no circumferential component. Finally, the complete velocity vector is determined by a given mean axial droplet velocity u_{ax}, which is modulated by a fluctuating component, that is normally distributed. A normally distributed pseudo-random number is obtained using the Box-Muller method (Box and Muller, 1958), using the uniformly distributed pseudo-random numbers:

$$u_{p,ax,0} = u_{ax} \left(1 + \frac{\sigma_{u,ax}}{u_{ax}} \sqrt{-2 \ln (U_3)} \cos (2\pi U_4) \right), \tag{8.27}$$

where $\frac{\sigma_{u,ax}}{u_{ax}}$ is the scaled standard deviation of the initial axial droplet velocity, and U_3 and U_4 are independent pseudo-random numbers in the $[0, 1)$ interval. The initial radial droplet velocity is determined such, that the velocity vector has a θ_0 polar angle. The outlined procedure provides the initial conditions of the kinematic behavior of the droplets.

Finally, the droplet size is also treated stochastically. A modified version of the Rosin-Rammler (Weibull) distribution is used following Ma (2016), where the distribution is shifted towards larger diameters to avoid numerical problems associated with small droplets. Furthermore, a clipping is applied at large diameters to avoid very large droplets, which would be theoretically possible to encounter, although with an infinitesimally small likelihood. The initial droplet diameter is obtained as:

$$d_{p,0} = d_{min} + (d_{RR} - d_{min}) \left(-\ln (1 - U_5 K_{RR}) \right)^{\frac{1}{q}}, \tag{8.28}$$

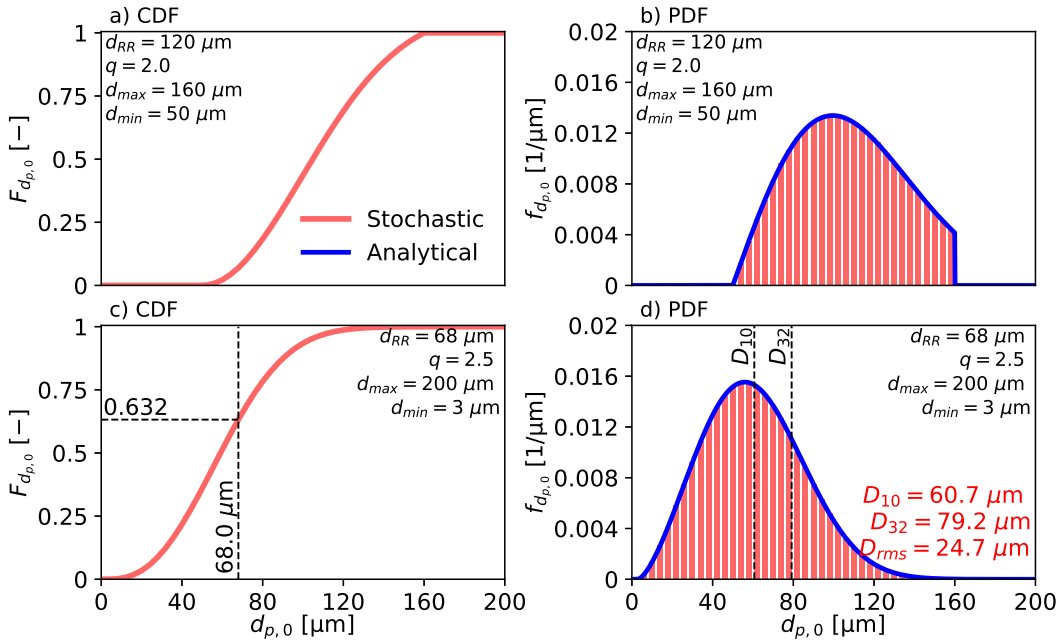

FIGURE 8.22: Modified Rosin-Rammler droplet size distributions, with the top row of plots illustrating an exaggerated use of the d_{min} and d_{max} parameters, and the bottom row showing the actual droplet size distribution used in the n-heptane (H1S1) and n-dodecane (DD1S2) cases of the Cambridge swirl bluff-body burner.

where d_{min} is the minimum droplet diameter, d_{RR} is a parameter controlling the mean diameter produced by the distribution, q is a parameter controlling the width of the distribution, and U_5 is a pseudo-random numbers in the $[0, 1)$ interval. Furthermore, the K_{RR} factor accounts for the clipping of the distribution at large diameters of d_{max}, corresponding to the cumulative density function (CDF) of the unmodified distribution up to a diameter of $d_{max} - d_{min}$:

$$K_{RR} = 1 - \exp\left(-\left(\frac{d_{max} - d_{min}}{d_{RR} - d_{min}}\right)^{q}\right). \tag{8.29}$$

The probability density function (PDF) of the initial droplet diameter in this modified Rosin-Rammler distribution in the $d_{p,0} \in [d_{min}, d_{max}]$ range is:

$$f_{d_{p,0}} = \frac{q}{K_{RR}\,(d_{RR} - d_{min})}\left(\frac{d - d_{min}}{d_{RR} - d_{min}}\right)^{q-1} \exp\left(-\left(\frac{d - d_{min}}{d_{RR} - d_{min}}\right)^{q}\right), \tag{8.30}$$

and for diameters outside the $[d_{min}, d_{max}]$ interval $f_{d_{p,0}}$ is zero. For further details on the classical Rosin-Rammler distribution see the work of Crowe et al. (2012, §3.4.2).

The droplet size distribution is demonstrated in Fig. 8.22 for a rather illustrative example (top) and for the actual parameters (bottom) used in the present simulations of the Cambridge swirl bluff-body burner. The stochastic diameter selection is tested by evaluating Eq. (8.28) using 10^6 different pseudo-random numbers. Subsequently, the cumulative density function (left) and the probability density function (right) is evaluated using these stochastic samples. The PDF plots also include the analytically derived distribution of Eq. (8.30). As the figure illustrates, the stochastic process approaches well the analytical distribution at such large sample sizes. The

example on top is significantly shifted to the right due to the large minimum diameter, furthermore the maximum limit also has a significant influence as the PDF is truncated. This truncation appears in the CDF as a discontinuity in the slope. While the presented diameter distribution function has many degrees of freedom, the parameters of d_{min} and d_{max} are much less influential in practical cases, such as in the presently applied droplet size distribution of Fig. 8.22c and d. The minimum diameter is very small, only serving the purpose of numerical feasibility. Likewise, the maximum diameter is placed well beyond the most significant parts of the distribution, thus K_{RR} is nearly 1. Consequently, the shape of the PDF is identical to the classical Rosin-Rammler distribution, with the only real difference being the 3 μm shift towards higher diameters. As Giusti (2013) details, it is possible to relate the d_{RR} parameter to a specific value of the CDF ($F_{d_{p,0}}$) under such conditions:

$$F_{d_{p,0}}\left(d_{RR}\right) = 1 - \frac{1}{e} \approx 0.632. \tag{8.31}$$

This relation is confirmed empirically in Fig. 8.22c using the stochastic samples, illustrating the effect of this parameter. The distribution may be further characterized by mean diameters:

$$D_{10} = \frac{\sum_{i=1}^{n} d_{p,0,i}^{1}}{\sum_{i=1}^{n} d_{p,0,i}^{0}} = \frac{\sum_{i=1}^{n} d_{p,0,i}}{n}, \qquad D_{32} = \frac{\sum_{i=1}^{n} d_{p,0,i}^{3}}{\sum_{i=1}^{n} d_{p,0,i}^{2}}, \tag{8.32}$$

where D_{10} is the simple arithmetic mean of the droplet diameters, while D_{32} is the Sauter mean diameter (SMD), which corresponds to the droplet size with the same volume to surface ratio as the entire sample. These two mean diameters are evaluated form the stochastic sample as: $D_{10} = 60.7$ μm and $D_{32} = 79.2$ μm for the presently applied parameters. Assuming, that the clipping is negligible and d_{min} is rather small, the mean diameter formula of the classical Rosin-Rammler distribution may be adapted as well: $D_{10} \approx d_{min} + (d_{RR} - d_{min})\,\Gamma\left(1 + \frac{1}{q}\right)$, which also gives 60.7 μm in this case, with the gamma function defined in Eq. (5.132). (Crowe et al., 2012, §3.4.2) Such estimates allow for a straightforward assessment of the parameters without a stochastic test.

The number of injected droplets in each time step is such, that the mean fuel mass flow rate: $\dot{m}_f = 0.27$ g/s is recovered. In each time step an array of of random droplet sizes is generated. Including the n^{th} droplet of this array would result in too large mass injection, thus the first $n-1$ droplets are injected, and the n^{th} droplet is saved as the first element of the array in the next time step. Thus it is possible to introduce large droplets with initial droplet mass larger than the product of the LES time step and the fuel mass flow rate. The mass to be injected is determined from the mass flow rate and the time elapsed since the last injection, with accounting for the difference due to the discrete droplet sizes. Each computational droplet carries the fuel mass corresponding to its volume, thus the concept of "parcels" is not used in this work.

The input parameters and some dependent quantities of the overall droplet injection model are summarized in Tab. 8.4. This injection strategy is the result of a sensitivity analysis, and subsequent manual tuning of the parameters in the H1S1 case, such that the resulting hollow cone spray agrees well with the experimental phase Doppler anemometry results. In this work the only difference between the n-heptane (H1S1) and n-dodecane (DD1S2) cases is the decreased droplet axial velocity in the latter case. The exact same parameters are used in other aspects in

TABLE 8.4: Droplet injection parameters in the simulations of the n-heptane (H1S1) and n-dodecane (DD1S2) cases of the Cambridge swirl bluff-body burner.

	H1S1	DD1S2
r_{min}	90 μm	
r_{max}	150 μm	
θ_{min}	24°	
θ_{max}	40°	
u_{ax}	18 m/s	14 m/s
$\frac{\sigma_{u,ax}}{u_{ax}}$	10%	
$T_{p,0}$	298.15 K	
d_{min}	3 μm	
d_{max}	200 μm	
d_{RR}	68 μm	
q	2.5	
D_{10}	60.7 μm	
D_{32}	79.2 μm	

all spray flame simulations. The droplet injection models reported in the literature show significantly different parameters. Note, that many of these studies involve a different pressure swirl atomizer, as the configuration has changed between the experimental study of Cavaliere, Kariuki, and Mastorakos (2013) and Yuan, Kariuki, and Mastorakos (2018). For instance Tyliszczak, Cavaliere, and Mastorakos (2014) impose a constant velocity magnitude of 9.9 m/s based on the flow rate and the injector geometry. Meanwhile, Giusti, Kotzagianni, and Mastorakos (2016) apply a tuning similar to the present study, and Paulhiac et al. (2020) base a more elaborate velocity model on previous studies. The presently used width parameter of $q = 2.5$ is the same as the one used by Paulhiac et al. (2020), while a narrower distribution with a value of 3 is used by Tyliszczak, Cavaliere, and Mastorakos (2014) and Giusti, Kotzagianni, and Mastorakos (2016), and an even larger value of 4.2 is used by Elasrag and Li (2018). The droplet diameter parameter: d_{RR} likewise varies significantly. This uncertainty highlights the need for highly resolved injection simulations such as the work of Janodet et al. (2022), which would allow simulations of spray combustion systems with *a priori* unknown spray characteristics.

8.3.3 Flame and spray characteristics

The studied spray flames are simulated with various approaches, presented in the rest of the chapter and in appendices K and L. As demonstrated subsequently in section 8.3.4, a thermo-chemical manifold based on premixed flamelets is found to be the most suitable to reproduce the dynamics of the H1S1 flame, along with the modeling strategy outlined in sections 8.3.1 and 8.3.2. The LES results of this n-heptane case are discussed here using the tabulation of premixed free and burner-stabilized flamelets, illustrating the general behavior of the Cambridge swirl spray flames.

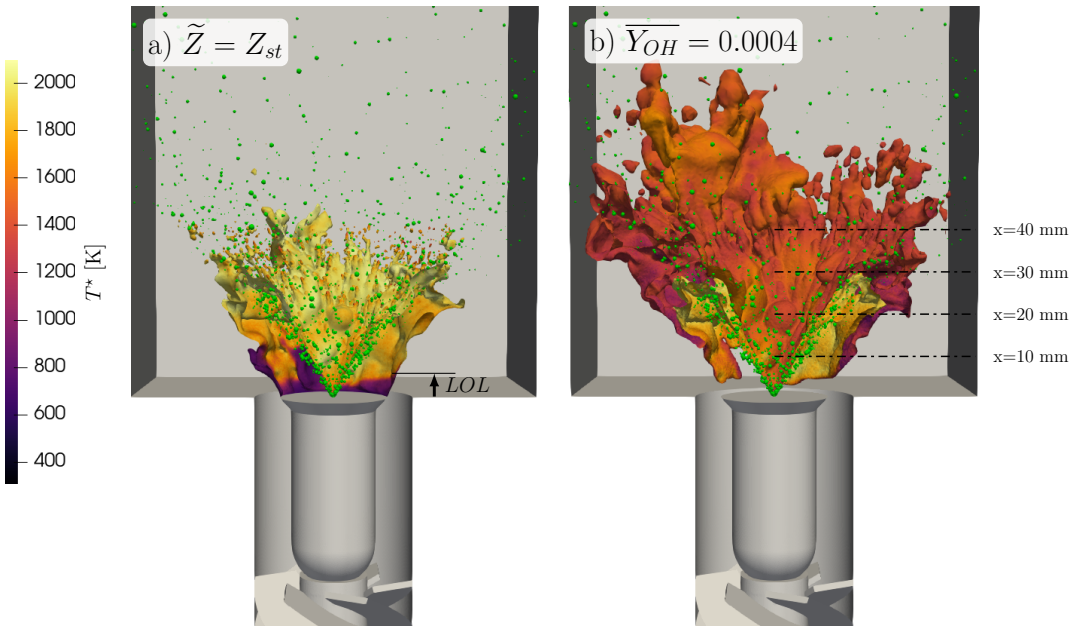

FIGURE 8.23: Instantaneous spray cloud (green) and stoichiometric mixture fraction (left) and hydroxyl mass fraction (right) iso-surfaces of the n-heptane simulation case (H1S1) in the Cambridge swirl bluff-body burner. The iso-surfaces are colored by temperature.

The instantaneous simulation results are illustrated in Fig. 8.23 using the stoichiometric mixture fraction iso-surface and the iso-surface of hydroxyl mass fraction at approximately 10% of the expected maximum. The hollow cone spray is also illustrated in the figure, by a sampling of the Lagrangian particles. Note, that the displayed diameters are proportional to the droplet diameter, but they are not to scale. The stoichiometric mixture fraction iso-surface forms an M shape, determining the position of the inner and outer reacting layers. As in the case of the non-premixed methane flame, an accumulation of rich gases is trapped over the bluff-body in the central recirculation zone. Reactions occur in the shear layer over the bluff-body edge, where this rich gas interacts with the fresh oxidizer forming the outer reaction layer. Furthermore, the inner reaction layer of the M shaped flame forms at the interaction of the rich mixture and the recirculating hot flue gases, which are near the global equivalence ratio of $\phi_{glob} = 0.346$. As Paulhiac et al. (2020) points out, the inner and outer reaction layers connect near the spray half angle, thus the flame tip is highly influenced by the interaction with the droplets that pass through it. This is reflected in Fig. 8.23a, where the stoichiometric mixture fraction iso-surface shows thin protrusions in the wake of the intensely evaporating droplets. As in the case of the methane flame, the outer reaction layer is intermittently lifted from the bluff-body edge. This is indicated by the low temperature regions along the stoichiometric iso-surface and by the absence of hydroxyl radicals.

The instantaneous flame behavior is further illustrated in Fig. 8.24 by the contours of the axial velocity and various scalar fields in three different time instances. The same scale is used as in the F3A2 case of Fig. 8.13 for better comparison. Near the bluff-body the velocity field resembles the cold flow (C1) case, except for a minor disturbance due to the presence of the Lagrangian fuel spray. The interaction with the spray creates a region of positive axial velocity in the area enclosed by the hollow cone spray, the bluff-body, and the shear layer. In some instances this flow structure

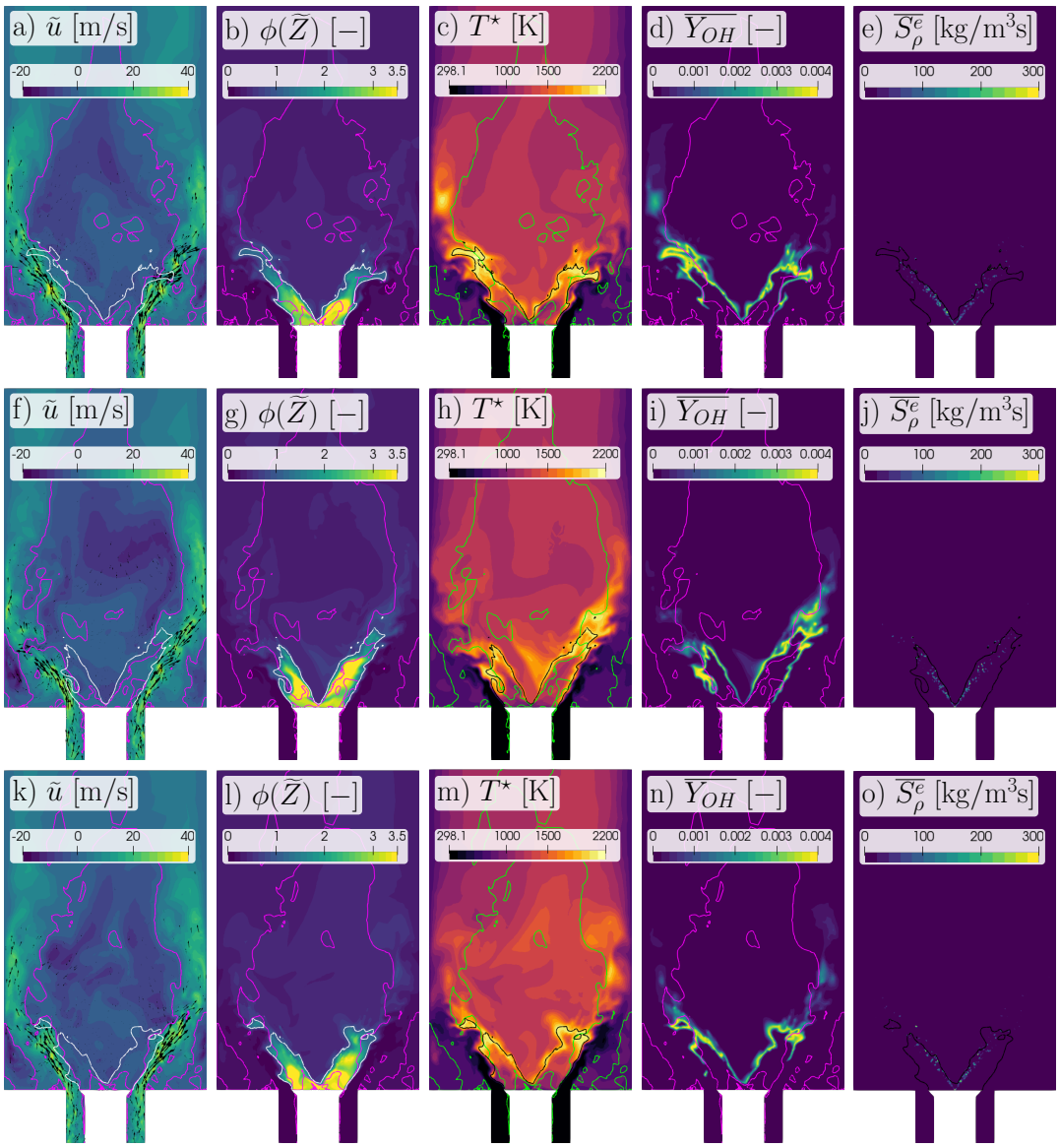

FIGURE 8.24: Examples of the instantaneous velocity and scalar fields of the n-heptane case (H1S1) in the Cambridge swirl bluff-body burner. The columns correspond to the velocity, equivalence ratio, temperature, hydroxyl radical mass fraction, and evaporative mass source term fields, while the rows show different instantaneous snapshots. Contour lines mark the position of zero axial velocity (magenta/green) and stoichiometric mixture fraction (white/black).

is enclosed in the central recirculation zone (Fig. 8.24a and k), while it can also be connected to the high speed oxidizer flow (Fig. 8.24f). The former case corresponds to a toroidal vortex, with upward movement in its center and downward on the edges. Paulhiac et al. (2020) postulates, that the growth and collapse of this vortical structure is related to the local extinction events of the outer reaction layer. The most intense evaporation occurs within the stoichiometric mixture fraction iso-contour as the $\overline{S^e_\rho}$ plots indicate. The hollow cone spray supplies fuel to the gas phase, which is convected towards the bluff-body by the central recirculation zone. Consequently the highest local equivalence ratios are encountered in the region enclosed by the

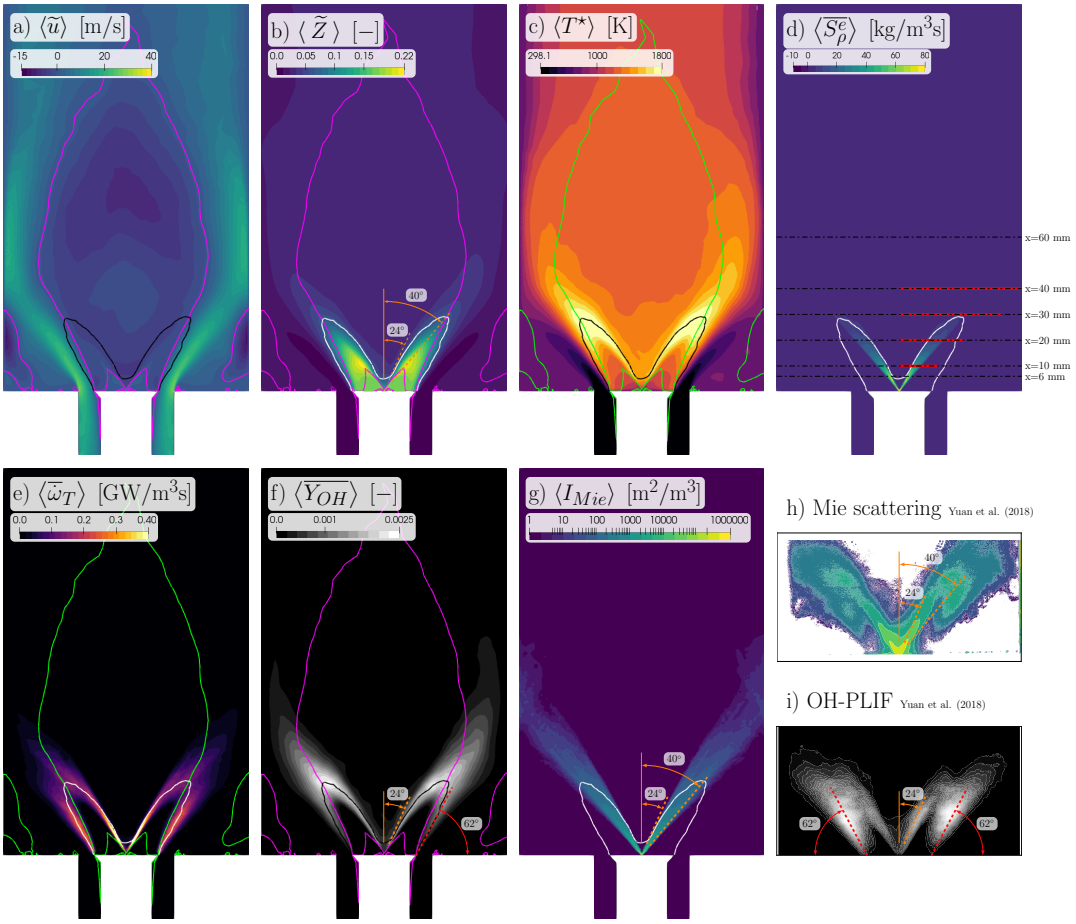

FIGURE 8.25: Mean velocity and scalar fields of the n-heptane case (H1S1) in the Cambridge swirl bluff-body burner, obtained by LES on the fine mesh using the premixed thermo-chemical manifold. The top row shows the mean of the axial velocity, mixture fraction, temperature, and evaporative mass source term, while the bottom row shows the mean of heat release rate, hydroxyl radial mass fraction, and equivalent Mie scattering field. For comparison the average experimental Mie scattering and OH-PLIF signals of Yuan, Kariuki, and Mastorakos (2018) are also included. Contour lines mark the position of zero mean axial velocity (magenta/green) and stoichiometric mixture fraction (black/white).

bluff-body and the spray, while most of the central recirculation zone at higher axial locations is characterized by the global equivalence ratio. The regions of rich mixture show high intermittency as the evaporation rate of the droplets vary and as the toroidal vortex interacts with the spray, advecting rich pockets to the flame base. The droplets which cross the stoichiometric mixture fraction iso-surface may continue the intense evaporation which creates small locally rich regions as shown in Fig. 8.24b and g. Compared to the fields of the methane case in Fig. 8.13, the mixtures immediately above the bluff-body are richer and consequently the temperatures here are lower. The thermal state of this region is also affected by the the latent heat of evaporation, and by the interaction with the colder bluff-body, where a Dirichlet boundary condition of 700 K is imposed. Higher temperatures are only present along the stoichiometric mixture fraction iso-surface, and in the intermittent

ejection of burnt gases near the flame tip as observed on the left side of Fig. 8.24c, and on the right of Fig. 8.24h and m. The direct interaction of the rich mixtures at the flame base with the fresh oxidizer flow creates the conditions necessary for local extinction. The instantaneous $\overline{Y_{OH}}$ field illustrate this intermittent lift-off, which occurs frequently in the H1S1 case.

Mean flame behavior

To further understand the flame behavior, the temporal average is discussed below. The presented data is collected over a statistically steady averaging period of $\Delta t \approx$ 125 ms on the fine mesh. As discussed in the cold flow analysis, a value of near-unity Strouhal number provides a typical time scale of the flow, which in this case is $D_b/U_B = 1.46$ ms. Considering other temporal scales of the burner, such as the blow-off time scale of $10 - 30$ ms experimentally determined by Yuan, Kariuki, and Mastorakos (2018), the present time averaging is considered adequate.

The mean flame behavior is illustrated in Fig. 8.25 by the average velocity and scalar fields. The mean length of the central recirculation zone is shorter than in the cold flow of Fig. 8.7, and it is rather similar to the non-premixed methane case of Fig. 8.14, despite the absence of the central fuel jet. The contour of stoichiometric mean mixture fraction forms an M shape, encompassing a volume much smaller than in the methane case. Rich conditions are found within this volume with a peak mean mixture fraction of ~ 0.22 along the outer edge of the hollow cone spray at a cone half-angle of 40°. Similarly to the non-premixed methane case, the iso-line of stoichiometric mean mixture fraction is located outside the iso-line of zero mean axial velocity. The peak of mean temperature is near the flame tip, as all other regions are affected by high intermittency in the reacting layer's location. Furthermore, the outer reacting layer is typically lifted resulting in low mean temperatures. The mean evaporative mass source is characterized by a peak shortly downstream the injection site around $x = 5$ mm, although the decay of $\left\langle \overline{S_\rho^e} \right\rangle$ further downstream is related more to the spreading of the hollow cone spray in space, as the instantaneous peaks shown in Fig. 8.24e, j, and o can be significant even beyond $x = 30$ mm. The average heat release rate is concentrated to the inner and outer reacting layers, with the former overlapping with the hollow cone spray near the innermost angle (24°), and the latter located in the shear layer over the bluff-body edge. The mean hydroxyl radical field of Fig. 8.25f is compared with the experimental OH-PLIF profile of Fig. 8.25i. The mean location of the inner reaction layer is predicted adequately, with both the LES and the experiments locating this layer at a somewhat higher cone half-angle than 24°. The LES predicts the direction of the outer reacting layer as 62° degrees from the bluff-body plate, which is also found in the F3A2 case, suggesting, that the mean reaction zone location is governed by aerodynamic effects. The experimental location of the outer reaction layer is significantly more distributed radially, nevertheless a mean angle of 62° seems plausible. Finally, the mean Mie scattering signal is analyzed. In the LES, the equivalent field is obtained by processing the Lagrangian particles contained in the elements of the computational grid following Giusti, Kotzagianni, and Mastorakos (2016), thus the displayed field is:

$$\langle I_{Mie} \rangle = \frac{\sum_k^N d_{p,k}^2}{V_{element}}, \tag{8.33}$$

where N is the total number of droplets that pass through the given element, $d_{p,k}$ is the droplet diameter and $V_{element}$ is the volume of the element. This equivalent

field is compared to the Mie scattering measurements in Fig. 8.25g and h displaying the fields in logarithmic scale. In the LES the spray departs from the injection site between the indicated half-angles of 24° and 40°. The droplet behavior is largely ballistic, showing only a little deviation from the initial spray angles as the Lagrangian particles interact with the central recirculation zone. Part of the spray reaches the burner walls, where a bounce-type boundary condition is applied, reversing the velocity component normal to the wall. The experimental image shows a much wider spatial distribution, although the most intense signal is concentrated near the spray half-angle. The presently applied variations in the angle seem reasonable. A significant Mie signal is observed throughout the entire axial length of the image (50 mm), which implies, that part of the spray exits the measurement region similarly to the LES results. For further details of the mean and RMS velocity fields see appendix M.

Mean spray behavior

The comparison of mean fields to the flame and spray imaging experiments of Yuan, Kariuki, and Mastorakos (2018) in Fig. 8.25 gives a qualitative validation of the present modeling approach. While the gas phase performance of the applied low-dissipation finite element scheme is assessed through the simulation of various turbulent flames in this work, the evaporating Lagrangian spray behavior needs further assessment. Here the mean droplet properties are compared to phase Doppler anemometry data. The averaging is done, by recording the droplet data over a time span of $\Delta t \approx 225$ ms and $\Delta t \approx 125$ ms in case of the coarse and fine mesh respectively. Furthermore, the data is azimuthally averaged by considering the droplets in an axi-symmetric control volume of $(x, r) \pm (0.5\text{ mm}, 0.5\text{ mm})$ at a given (x, r) location. Note, that to remove statistically uncertain points near the spray edge, the averaging is only done on points where at least 100000 droplets are recorded over the averaging period.

The mean and RMS droplet velocities are shown in Fig. 8.26 at the axial locations indicated in Fig. 8.25 by red lines. At $x = 10$ mm the mean axial droplet velocity is captured well at $r = 8$ mm, corresponding to a spray half-angle of 38.7°, which is towards the outer edge of the hollow cone spray. At locations closer to the center the mean axial velocity is consistently over-predicted, while on the outer edge an under-prediction is observed with no droplets detected at $r = 12$ mm. The present inlet strategy prescribes the expected value of the initial axial droplet velocity as 18 m/s, opposed to prescribing the velocity magnitude. This helps mitigating the over-prediction of $\langle u_p \rangle$ at low radii. Further downstream the spray starts to deviate from the inlet angles marked by the gray shading. This is also observed in the Mie scattering equivalent field of Fig. 8.25g. The mean droplet velocity becomes slightly under-predicted in the core of the spray, while the over and under-predictions persist on the inner and outer spray edge respectively. The RMS of the axial droplet velocity is consistently over-predicted in the core part of the spray, while better agreement is observed towards the edges. The root cause of these discrepancies is further analyzed below using the size-classified statistics. Compared to the mean values, large variations are present in both the axial and radial velocity component, as different droplet sizes are affected differently by drag.

The mean scalar properties of the droplet cloud are presented in Fig. 8.27. As summarized in Tab. 8.4, at the injection site the droplet cloud is characterized by a Sauter mean diameter of $D_{32} = 79.2\ \mu$m. The Sauter mean diameter in the spray core stays close to this value, showing a slight increase as the spray evolves downstream,

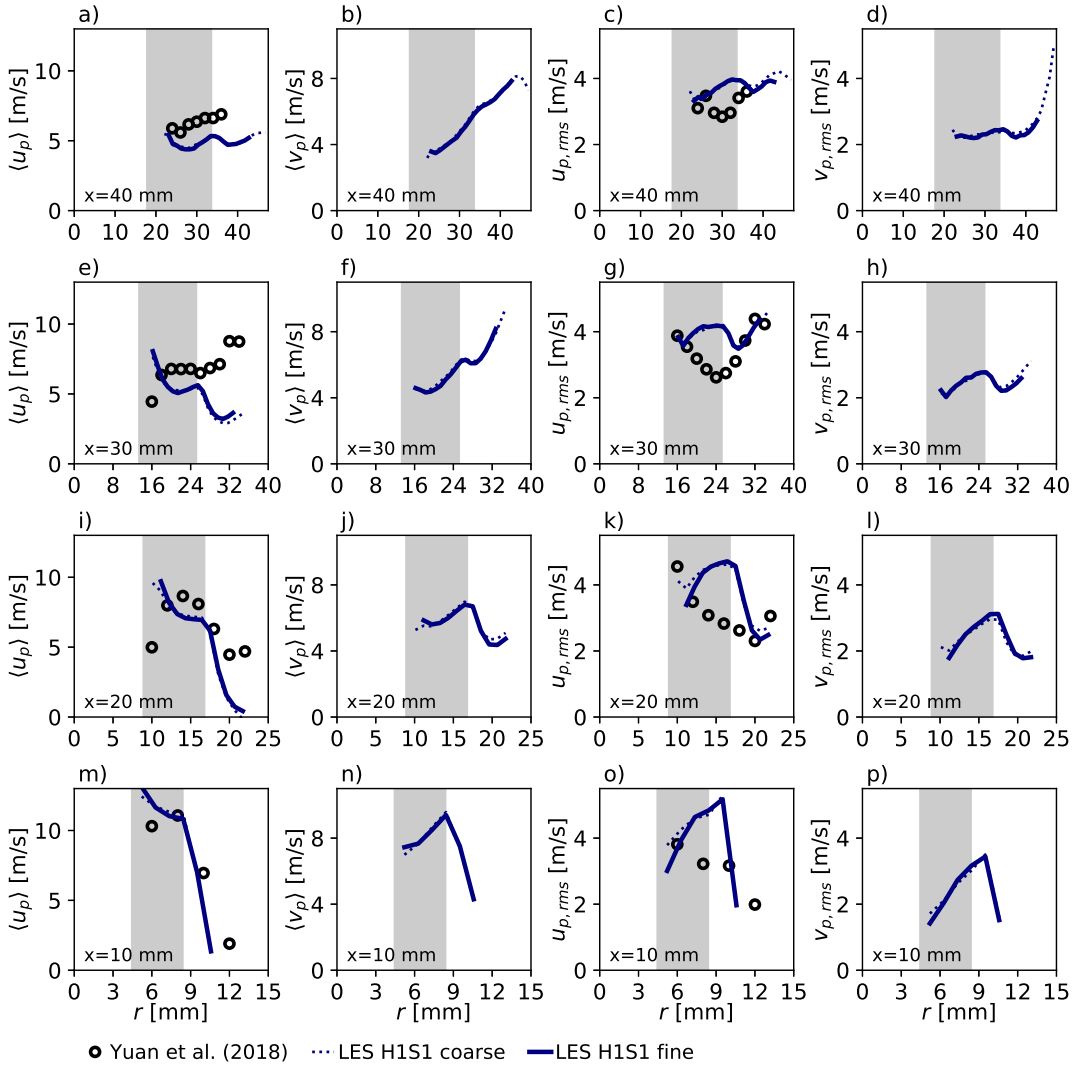

FIGURE 8.26: Comparison of mean and RMS droplet velocities in the n-heptane case (H1S1) of the Cambridge swirl bluff-body burner between the PDA measurements of Yuan, Kariuki, and Mastorakos (2018) and the LES of the present work. The rows of plots correspond to the indicated axial location, while the four columns show the mean of the axial and radial droplet velocity, and the corresponding RMS values. The gray shading represents the spray half-angle range of $[24°, 40°]$ with respect to the injector location.

since the evaporation affects smaller droplets more than larger ones. The diameter is predicted exceptionally well in the spray core throughout all axial locations, while an under-prediction is observed at the outer radii. The initial droplet temperature: $T_{p,0} = 298.15$ K is well below the boiling point of n-heptane: $T_{sat} = 371.54$ K. However, as the spray interacts with the hot flue gases of the central recirculation zone, the droplets rapidly approach an equilibrium temperature of approximately 15 K below the boiling point. The RMS of droplet diameter also remains close to the initial value of 24.7 μm. Meanwhile, the RMS of the droplet temperature indicates, that at $x = 10$ mm there is still substantial variation between droplets, since the larger droplets take longer to heat-up. Subsequently $T_{p,rms}$ drops as most droplets approach the equilibrium temperatures corresponding to their local environment.

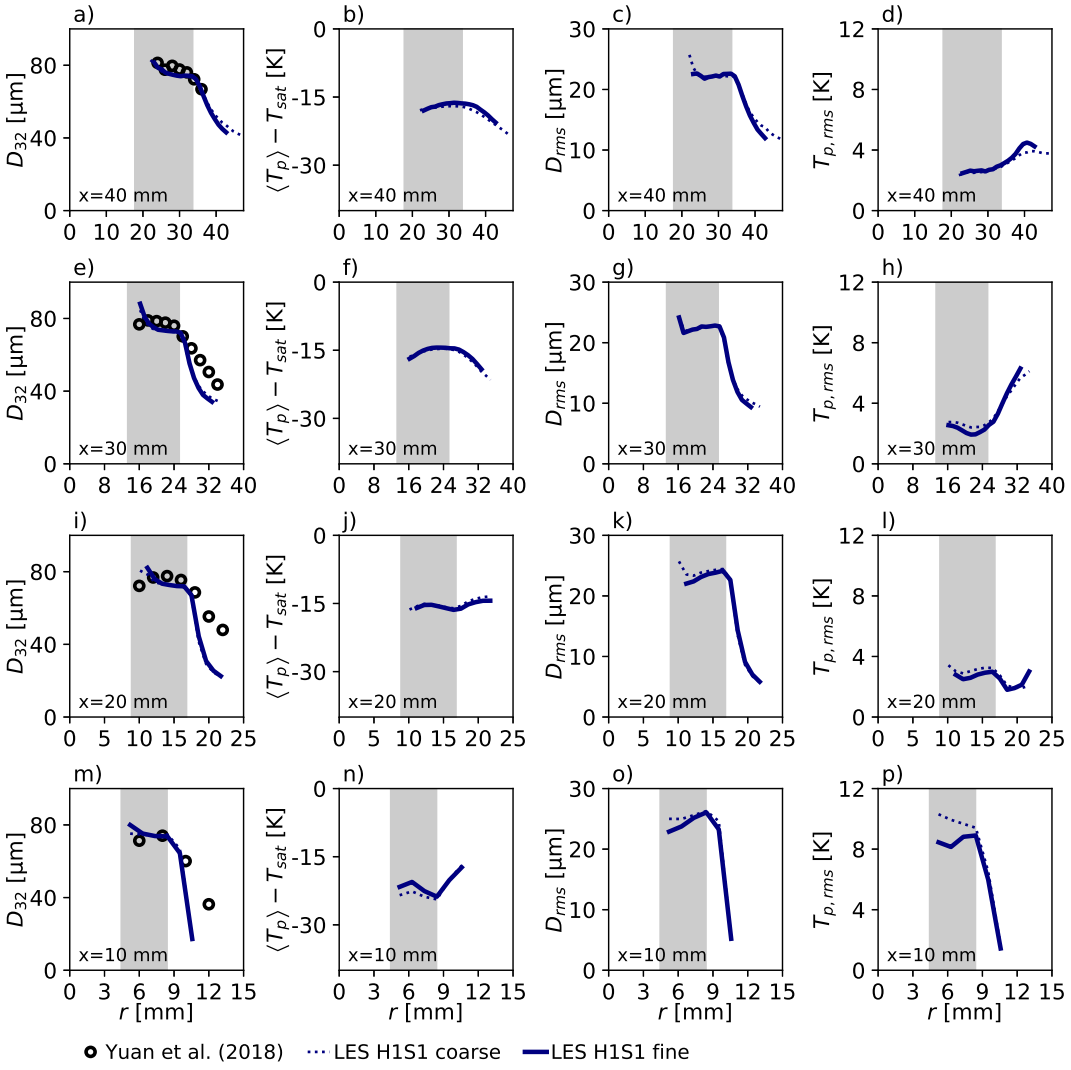

FIGURE 8.27: Comparison of mean and RMS droplet properties in the n-heptane case (H1S1) of the Cambridge swirl bluff-body burner between the PDA measurements of Yuan, Kariuki, and Mastorakos (2018) and the LES of the present work. The rows of plots correspond to the indicated axial location, while the four columns show the Sauter mean droplet diameter, the mean droplet temperature with respect to the boiling point (T_{sat} = 371.54 K), and the RMS of the droplet diameter and temperature. The gray shading represents the spray half-angle range of $[24°, 40°]$ with respect to the injector location.

The typical droplet behavior can be described by the time scale estimates of section 4.6. An example of these estimates are provided for droplets typical to the H1S1 case in Tab. 8.5, in a representative atmosphere of pure air at 1300 K. As demonstrated in Fig. 4.16, the heat-up process tends to be significantly faster, than the evaporation time scale. Furthermore, as Fig. 4.21 illustrates, the kinematic relaxation time tends to be smaller than the evaporation time at moderate seen temperatures. These observations corroborate the spray behavior in the LES: an equilibrium temperature is reached shortly after injection, while the mean droplet size and velocity remain large. Quantitatively, the time scales of Tab. 8.5 are compared here with the times

TABLE 8.5: Droplet time scale estimates in the n-heptane case (H1S1) of the Cambridge swirl bluff-body burner, assuming a seen gas state of hot air at 1300 K. The Reynolds number ($Re_{p,0}$) and the kinematic relaxation time ($\tau_{p,kin,0}$) are evaluated at the initial droplet temperature and velocity at a spray angle of 32°. The evaporation constant (K) and the related time scale ($\tau_{p,evap}$) is evaluated at the wet-bulb temperature of $T_p^{psy} = 350.0$ K assuming the initial droplet velocity. The heat-up time ($\tau_{p,heat}$) is estimated from the initial heat-up rate.

	$d_{p,0} = 10$ μm	$d_{p,0} = 79.2$ μm	$d_{p,0} = 120$ μm
$Re_{p,0}$	4.4	34.8	52.7
$\tau_{p,kin,0}$ [ms]	0.09	3.0	5.6
K [mm^2/s]	0.79	1.37	1.57
$\tau_{p,evap}$ [ms]	0.12	4.6	9.2
$\tau_{p,heat}$ [ms]	0.01	0.4	0.8

necessary to reach the axial locations: $x \in \{10, 20, 30, 40\}$ mm at a constant axial droplet velocity of 18 m/s: $\Delta t \in \{0.56, 1.11, 1.67, 2.22\}$ ms. The smallest injected droplets are expected to relax to the flow and evaporate before they could reach the first measurement location. The droplets initialized at the Sauter mean diameter of $d_{p,0} = 79.2$ μm have a heat-up time scale comparable of the time necessary to reach $x = 10$ mm, explaining why the mean temperatures in Fig. 8.27n can be lower than the droplet temperatures observed further downstream. The kinematic and evaporation time scales of these droplets are somewhat larger than the largest Δt estimate, thus such droplets may reach even the last measurement location, although their velocity and size are expected to decrease. Finally, the largest droplets of the initial size distribution characterized by times scales around twice as large than the droplets at the Sauter mean diameter. Note, that the wet-bulb temperature in this example is 21.54 K below the boiling point. In the LES higher equilibrium temperatures are possible, as the gas temperature can be locally higher, and the seen gas composition may contain fuel. The time scales may also be compared to the turbulent time scale estimates of section 5.1.6. For instance, in the point of $(x, r) = (10 \text{ mm}, 8 \text{ mm})$, the Kolmogorov time scale, the cut-off time scale, and the integral time scale are estimated as $\tau_\eta = 0.26$ ms, $\tau_\Delta = 0.46$ ms and $\tau_t = 1.14$ ms in the fine mesh simulation. Using the kinematic time scales of Tab. 8.5, these correspond to Stokes numbers of: $St_\eta \in [0.3, 11.5, 22.3]$, $St_\Delta \in [0.17, 6.5, 12.6]$ and $St_t \in [0.07, 2.6, 5.1]$. Note, that higher Stokes numbers correspond to ballistic behavior, while lower mean, that the droplets would relax to the turbulent motion of the flow quickly. The observed Stokes numbers suggest that the larger droplets, which carry most of the fuel mass, are not affected significantly by the turbulence. Nevertheless, the transport of small droplets may be improved by sub-grid models, although this is out of the scope of the present work.

Finally, the discrepancies observed in the mean droplet velocity are analyzed by comparing the droplet statistics obtained from the fine mesh simulation to the size-classified phase Doppler anemometry data of Yuan, Kariuki, and Mastorakos (2018) in Fig. 8.28. The criterion of including a data point is relaxed to minimum 100 droplets encountered at a given location within a given size class of small: $[10, 40)$ μm, intermediate: $[40, 80)$ μm, or large: $[80, 100)$ μm droplets. The droplets outside these intervals are disregarded. As Fig. 8.28g shows, at $x = 10$ mm in the LES the large

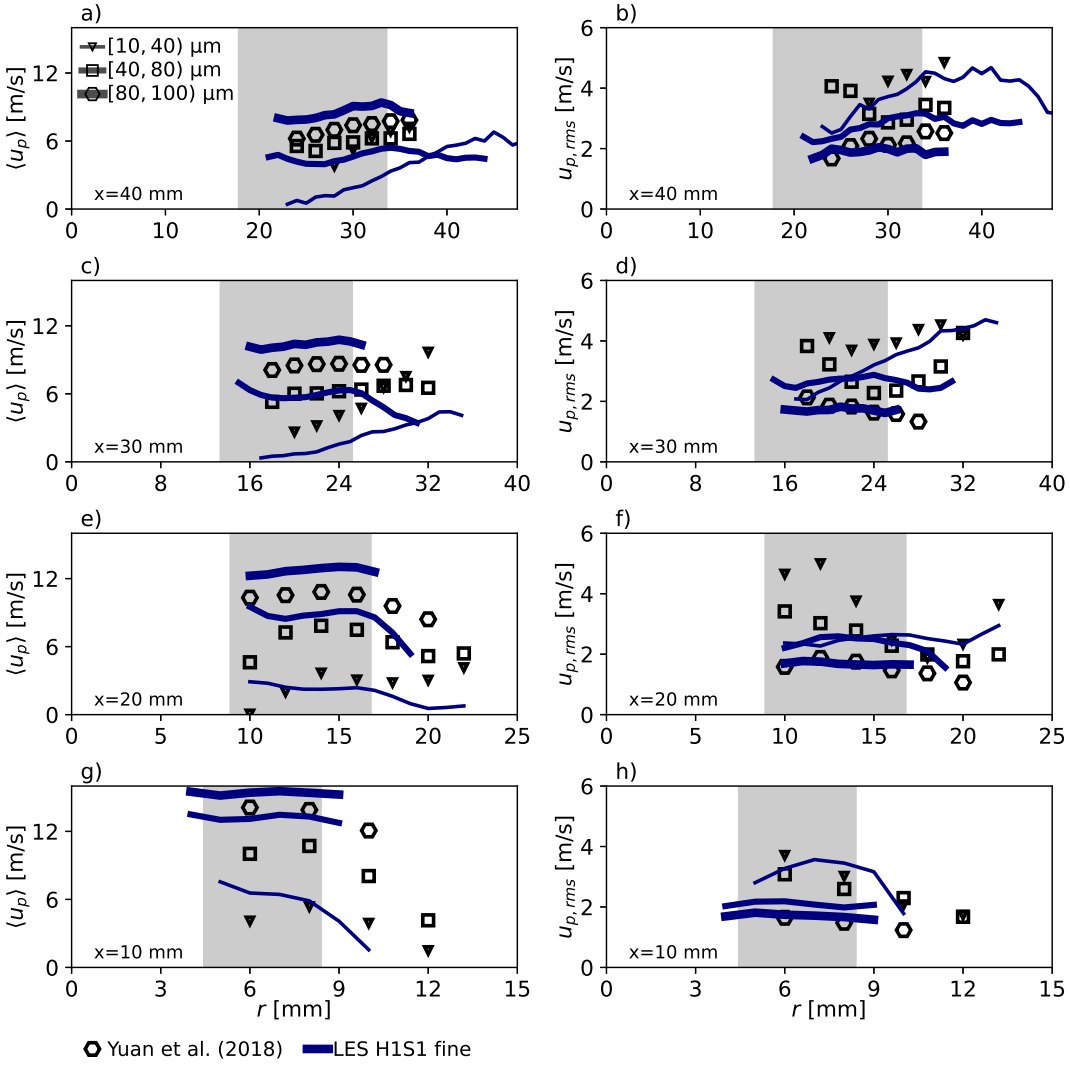

FIGURE 8.28: Comparison of mean and RMS axial droplet velocities per size class in the n-heptane case (H1S1) of the Cambridge swirl bluff-body burner between the PDA measurements of Yuan, Kariuki, and Mastorakos (2018) and the LES of the present work. The rows of plots correspond to the indicated axial location, while the two columns show the mean and RMS of the axial droplet velocity conditioned to the indicated size classes. The gray shading represents the spray half-angle range of $[24°, 40°]$ with respect to the injector location.

and intermediate droplets are concentrated within the initial half-angles of $[24°, 40°]$. Both of these size classes lose some momentum in this first part of the hollow cone, as the large droplets have a mean velocity around 16 m/s, and the intermediate ones around 14 m/s. The small droplets are significantly slower, and they are found even at a radius of $r = 10$ mm, as they are carried towards the bluff-body edge by positive radial gas phase velocities. The velocity magnitude of the large droplets is comparable to the PDA measurements, although the experiment suggest larger spray half-angles up to 45°. The mean velocity of the intermediate droplets is notably over-predicted. The discrepancies observed in the mean velocity of Fig. 8.26m are related to the over-prediction of the intermediate droplet velocity at lower radii,

and lack of large droplets at higher radii. Meanwhile, the RMS velocity of the small and large droplet classes is predicted rather well in Fig. 8.28h. The $u_{p,rms}$ of the small droplets are governed by the velocity fluctuations in the gas phase. Meanwhile, the good $u_{p,rms}$ predictions in the large size-class are due to the velocity fluctuations imposed by the spray boundary conditions ($\frac{\sigma_{u,ax}}{u_{ax}} = 10\%$). The intermediate droplets do not show sufficient variance in their axial velocity. At $x = 20$ mm the small droplets spread sufficiently, and the intermediate ones relax towards the expected mean and RMS values. The velocity RMS of the small droplets shows a deficit near $r = 12$ mm, suggesting, that the gas phase turbulence near the inner reacting layer is under-predicted. The lack of larger droplets at the outer radii continues to cause low overall mean velocities in Fig. 8.26i. Further downstream the outer edge of the spray starts to interact with the shear layer. In the experiments this causes elevated axial velocities in the small droplet class, and even the intermediate droplets are expected to accelerate due to this interaction. The droplet velocities of these two classes tend to be under-predicted in the shear layer. The over-prediction of the RMS axial velocity in Fig. 8.26 is rather curious, as RMS of the size classes tends to be under-predicted. It is rather a consequence of the different mean velocities in the three size classes, which causes a broader distribution of droplet velocities in the overall droplet population. In conclusion, the prediction of the droplet evolution may improve with more elaborate injection models, such as the size-conditional velocity model of Ma and Roekaerts (2016). Nevertheless, the evolution of the spray core is predicted to a satisfactory degree, especially considering that the majority of the fuel mass is carried by large droplets, thus these should be prioritized in terms of the spray flame simulation.

Flame dynamics

The intermittent lift-off of the outer reaction layer is studied statistically in the H1S1 case as well. The definitions of the lift-off length and the LOL probability density function are the same as in the non-premixed methane case of section 8.2.2. Below the flame lift-off is analyzed using the outlined simulation method applying a thermo-chemical manifold based on free and burner-stabilized premixed flamelets. As the methane case readily illustrates, the lift-off is sensitive to the applied computational grid. To assess the trends with grid refinement, an even finer grid is constructed using the uniform mesh multiplication method of Houzeaux et al. (2013). This case is labeled: "fine $\times 2$". The "fine" grid is transformed by dividing each edge in half and constructing new elements, thus the refined grid is characterized by tetrahedra of edge length of $a = 0.25$ mm in the region of interest. This grid has 138M linear elements, and 27M nodal degrees of freedom.

The mean lift-off length on the different grids is summarized in Tab. 8.6. As further discussed below in section 8.3.4, using a manifold based on premixed flamelets makes the probability of flame attachment ($LOL < 0.2$ mm) negligible. Thus the average lift-off and the average conditioned on only lifted instances is virtually the same. Similarly to the methane case, the coarse mesh shows a notably smaller mean lift-off than the fine mesh. However, the further refinement in the "fine $\times 2$" case does not modify the mean values notably. The lift-off behavior is further assessed using the probability density function of the lift-off in Fig. 8.29. Note, that since most of the instances are lifted, the two analyzed populations are virtually the same. Nevertheless, the curves of Fig. 8.29a and b are obtained with two different uniform discretizations of the LOL^* space: one using a spacing of 0.4 mm and one using 1 mm for the unconditioned and conditioned distributions respectively. The finer

TABLE 8.6: Mean flame lift-off length in n-heptane case (H1S1) of the Cambridge swirl bluff-body burner.

	$\langle LOL \rangle$ [mm]	Sample count	
LES coarse	3.08	480	
LES fine	5.26	268	
LES fine $\times 2$	5.24	272	
	$\langle LOL \vert LOL > 0.2 \text{ mm} \rangle$	Sample count	Lifted fraction
Yuan et al. (2018)	6.25		
LES coarse	3.13 (-50%)	475	99.0%
LES fine	5.26 (-16%)	268	100.0%
LES fine $\times 2$	5.28 (-16%)	271	99.6%

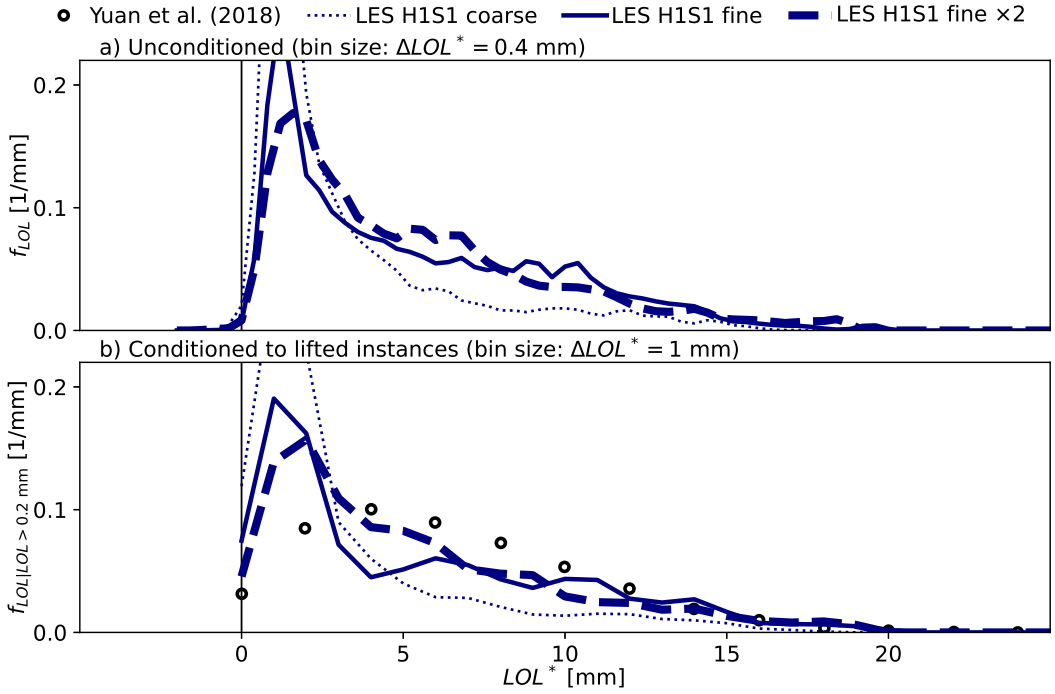

FIGURE 8.29: Probability density function of flame lift-off length in the n-heptane case (H1S1) of the Cambridge swirl bluff-body burner. The unconditioned statistics (top) uses all the time instances of the LES, while the conditioned one (bottom) only considers the lifted cases of $LOL > 0.2$ mm.

bin size in the LOL^* space resolves the sharp peaks of the lift-off PDF better, resulting in higher peak values. Similarly, the PDF values at $LOL^* = 0$ mm are likewise influenced by the finite bin size. The LES results on the coarse grid give a very sharp peak in the lift-off PDF at low LOL values, while the likelihood of $LOL > 5$ mm is greatly under-predicted. The mesh refinement consistently decreases the peak at low LOL, while the probability of higher lift-off approaches the experimental curve. A difference can be identified between the "fine" grid and the even more refined "fine $\times 2$" case on the well resolved distribution of Fig. 8.29a. The former appears

to have a secondary peak of f_{LOL} near a lift-off of 10 mm, although it is not strong enough to become a second mode of the distribution. Meanwhile, in the "fine $\times 2$" case, this secondary peak is shifted to lower lift-offs ($\sim$ 6 mm), making the PDF smoother. As Tab. 8.6 shows, this change does not modify the mean lift-off significantly, however the PDF resembles more the experimental curve. Overall, this small improvement comes at a great computational cost, as the "fine $\times 2$" grid contains nearly 8 times more nodal degrees of freedom. For the purposes of the rest of this study, the "coarse" and "fine" meshes provide sufficient detail.

8.3.4 Performance of tabulated chemistry models

Chapter 3 introduces various different tabulation strategies which are able to cover the $Z - Y_c$ plane with thermo-chemical states of predefined flamelet structures. As demonstrated in section 6.3.3 and section 6.3.6, these approaches are able to reproduce the propagation and structure of the simulated flames, given that the manifold already corresponds to the expected flame structure. Most spray flames are inherently partially premixed, as the droplets supply fuel vapor to the gas phase in a distributed manner. Nevertheless, the present work is confined to assuming either premixed or diffusion flamelet structure. In this section various tabulation strategies are assessed in the n-heptane case (H1S1) of the Cambridge swirl bluff-body burner in order to aid this modeling decision.

Paulhiac et al. (2020) identified the prevalence of a non-premixed flame structure in an n-heptane flame of the Cambridge swirl bluff-body burner using the flame index of Takeno, Murayama, and Tanida (1990), although this case corresponds to a different pressure swirl atomizer at a significantly different operating point. The existing LES studies based on CMC and tabulated chemistry models all inherently consider, that the flame structure is best represented by the counterflow diffusion flamelet configuration. However, the selection of premixed or diffusion flamelet structure is open to question in spray flames. To settle this argument Franzelli, Fiorina, and Darabiha (2013) and Olguin and Gutheil (2014) studied a counterflow configuration, with one of the streams corresponding to pure oxidizer and the other to a carrier oxidizer stream delivering a mono-disperse spray cloud. They found a unique behavior associated to the presence of evaporative source terms, which is not addressed by the classical tabulation methods. Nevertheless, as Franzelli et al. (2017) showed *a posteriori*, a tabulation method based on free premixed flamelets may provide adequate results in terms of flame propagation. They demonstrated the adequacy of the method on a model gas turbine combustor, that exhibits lean to stoichiometric mixture fractions throughout the domain. More recently Sacomano Filho et al. (2018) revisited the issue of laminar spray flame propagation in a plug-flow configuration, that decouples the strain effects from the evaporation. Their results confirm, that in such a configuration the application of free and burner stabilized premixed flamelets is justified, at least in terms of flame propagation speed.

As Paulhiac et al. (2020) shows, and as discussed above in section 8.3.3, the Cambridge swirl spray flames exhibit various regions with drastically different characteristics, and the droplet-flame interactions studied by Franzelli et al. (2017) and Olguin and Gutheil (2014) are more important in some regions than others. In particular, the the outer reaction zone does not interact with the spray at all. As shown in Fig. 8.24, the localized extinction of this reaction layer creates edge flames (triple flames) that propagate along the shear layer. Although, here the edge flame is situated between a rich mixture near equilibrium and the fresh oxidizer. As Illana, Mira, and Mura

(2021) show, the prediction of such triple flame structures is challenging for the classical tabulated chemistry methods if the mixture fraction profile ranges from very low to very high values. However, if the mixture fraction is well within the flammability limit, a tabulation based on premixed flamelets gives good predictions as Van Oijen and De Goey (2004) shows.

Thermo-chemical manifolds

In all flamelet calculations of the present section, the skeletal mechanism of Lu and Law (2006) is utilized, containing 188 species, and 939 reactions. The four different flamelet sets are illustrated in Fig. 8.30 by the adiabatic flame temperature (T^b) as function of the equivalence ratio in case of the premixed free flamelets, and by the temperature of the stoichiometric mixture (T_{st}) in case of the adiabatic counterflow diffusion flamelets. The premixed flamelets are calculated using the Cantera chemistry library. (Goodwin, 2002) The adiabatic enthalpy level, formed by the free flamelets, is established based on the oxidizer temperature of $T_{air} = 298.15$ K, and the boiling point of n-heptane at atmospheric pressure: $T_f = 371.54$ K. Decreased enthalpy states are introduced by using a burner-stabilized configuration besides free flamelets, as proposed by Van Oijen and De Goey (2000). The imposed mass flux is selected non-linearly as done in section 3.1.2: $m/(\rho^u S_L) \in \{1, 0.75, 0.5, 0.25, 0.15, 0.1, 0.05, 0.04, 0.03, 0.02, 0.01\}$. The applicability of this heat loss method for spray combustion is confirmed by the study of Sacomano Filho et al. (2018). Pure fuel and oxidizer are appended to the premixed manifold to cover all possible mixture states as discussed in section 3.2.2.

TABLE 8.7: Heat loss parameters in the counterflow diffusion flamelets of n-heptane case (H1S1) of the Cambridge swirl bluff-body burner.

T_f [K]	T_{air} [K]	c_{rad}	a_{ext} [1/s]	a_{uns} [1/s]
371.6	298.2	0	1495	1600
353.3	292.6	2	1443	1600
334.1	287.0	4	1396	1500
314.0	281.3	8	1344	1500
292.7	275.7	16	1280	1400
270.0	270.0	32	1193	1300

The one dimensional flamelet solver: Chem1D is used for the counterflow diffusion flamelets. (Ramaekers, 2011) In these cases two methods are applied simultaneously to account for enthalpy deficit: the inlet temperatures of the opposing diffusion flamelets are decreased, and a radiative heat loss term is included in the flamelet equations (Lammers and De Goey, 2004) multiplied with an artificial scaling coefficient c_{rad} ranging from 0 (adiabatic) to 32. As discussed in section 3.1.3, the latter scaled radiative method has different effects along different points of the flame, since the higher temperature gases suffer a higher radiative heat loss. Furthermore, the strain rate of the counterflow diffusion flame also affects the level of enthalpy deficit, as lower strains correspond to a higher residence time and thus allow higher amount of radiative heat loss. (See Fig.3.18 and Fig. 3.19.) The parameters applied in the counterflow cases are listed in Tab. 8.7. The radiative heat loss and the imposition of decreased inlet enthalpies results in a substantial decrease in

the extinguishing strain rate (a_{ext}). Note, that the lower limit of the included strain rates is 10/s, thus the equilibrium conditions are not included in the counterflow diffusion flamelet data sets. In both the premixed and counterflow diffusion cases, the manifolds are appended with a layer of cold reaction products and reactants as illustrated in section 3.3, thus the tables are capable of representing any states down to complete quenching due to heat loss.

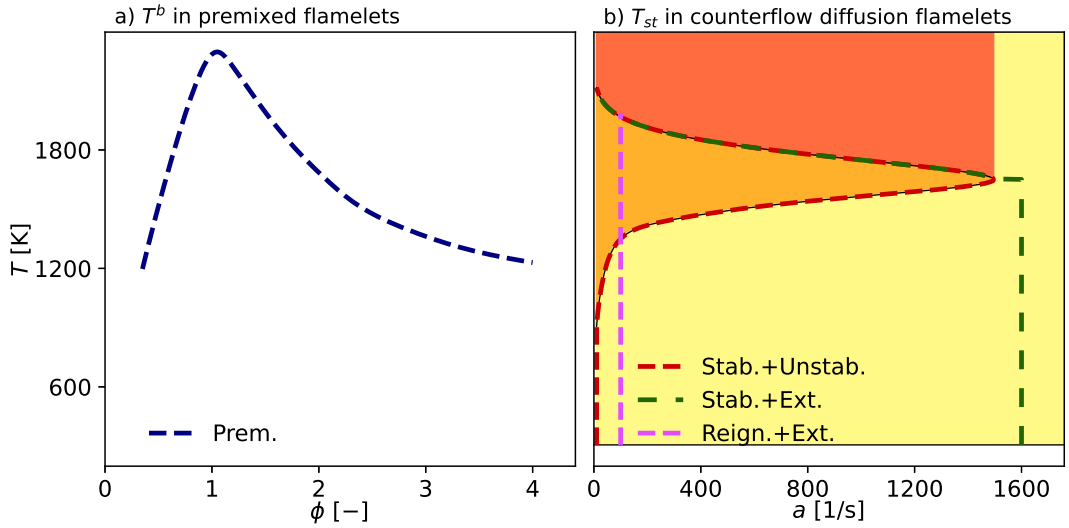

FIGURE 8.30: Illustration of the tabulated adiabatic premixed and counterflow diffusion flamelets in the n-heptane case (H1S1) of the Cambridge swirl bluff-body burner.

As Fig. 8.30 shows, the tabulation methods based on counterflow diffusion flamelets may cover the $Z - Y_c$ plane following different strategies. In this section three of these options are assessed. The "Stab.+Unstab." strategy combines the stable and unstable branches, following the classical Steady Flamelet Progress Variable approach of Pierce and Moin (2004). Note, that in this case it is imperative to use the "Central Unique (C.U.)" truncation method of section 3.3.2, as in case of higher c_{rad} values the stable and unstable branches form loops. The applied truncation keeps a uniquely parameterized set of states surrounding the extinction point. The "Stab.+Ext." strategy replaces the unstable branch with temporal samples taken from an unsteady extinguishing flamelet following Chrigui et al. (2012). The strain rates imposed in the unsteady calculations (a_{uns}) are summarized in Tab. 8.7. In this case the simpler "First Unique (F.U.)" truncation strategy is sufficient, as the extinguishing flamelets monotonously approach the pure mixing state. Finally, the last method assessed here, marked "Reign.+Ext.", is a subset of the Unsteady Flamelet/Progress Variable method of Ihme and See (2010). In this case a single strain rate: $a_{uns} = 100/\text{s}$ is selected to compute the reigniting and extinguishing flamelets initialized from the steady unstable solutions at $a_{IC} = 110/\text{s}$ and $a_{IC} = 90/\text{s}$ respectively. Such a simplification of imposing a single representative strain rate is often used in the modeling of autoigniting spray flames. (Bekdemir et al., 2013; Ma, 2016; Zhang et al., 2019; Mira et al., 2021a) As discussed in appendix K, in the present work the subgrid turbulence/chemistry interaction model of Pierce and Moin (2004) is preferred, which constructs the joint filter probability density function of mixture fraction (Z), scaled progress variable (C), and scaled enthalpy (i), assuming a beta-distribution

in Z and delta-distributions in the other two control variables. The final FPDF integrated thermo-chemical manifolds are parameterized by the $\widetilde{Z} \times \widetilde{C} \times \widetilde{i} \times \zeta_Z$ hypercube, with the dimensions discretized by 101, 101, 21, and 11 points respectively. An attractor-type non-linear refinement is applied in $\widetilde{Z}$, concentrating on $Z_{st} = 0.0622$ with a growth rate of $r = 1.05$, as defined in section 3.2.4. The scaled mixture fraction variance: ζ_Z is discretized more finely at low values with the coordinates given by a third order polynomial. The scaled progress variable and enthalpy are discretized uniformly.

The four non-adiabatic manifolds are illustrated in Fig. 8.31 by the distribution of the filtered progress variable source term on the $\widetilde{Z} - \widetilde{Y_c}$ plane. Compared to the manifold applied in the non-premixed methane flame (Fig. 8.12) the peak source terms in the n-heptane case are significantly higher, in line with the 28% higher stoichiometric flame speed. (See Tab. 8.1.) In all four tabulation strategies the peak source term is located on the rich side. The extent of notable source terms is indicated by the red and green contour lines corresponding to $\overline{\dot{\omega}_{Y_c}} = 0.5$ kg/m^{3}s and $\overline{\dot{\omega}_{Y_c}} = 2$ kg/m^{3}s respectively. The behavior of the adiabatic manifolds is similar to the one observed in the methane cases of section 3.4.1. In the premixed manifold the source terms are concentrated in a comparatively small range of mixture fractions, and the limit of notable source terms protrudes to low values of Y_c near stoichiometry. The manifolds containing the stable counterflow diffusion flamelets behave the same at high Y_c while there are slight differences between the unstable branch and the unsteady extinguishing flamelets as Fig. 8.31c and e illustrate. Finally, the manifold of reigniting and extinguishing counterflow diffusion flamelets in Fig. 8.31g show the lowest peak source terms and the extent of the $\overline{\dot{\omega}_{Y_c}} = 2$ kg/m^{3}s iso-line along mixture fraction is between that of the "Prem." manifold and the "Stab. + Unstab." and "Stab. + Ext." manifolds.

Figure 8.31 also illustrates the response of the four manifolds to heat loss. Note, that the constant scaled enthalpy level of 0.9 corresponds to the same enthalpy in all four cases, since all manifolds contain the adiabatic conditions and the minimal possible enthalpy states of "isothermal equilibrium" as discussed in section 3.1.2. Consequently, the enthalpy is scaled by the same $\widetilde{h^{min}}$ and $\widetilde{h_{ad}}$ values as defined in Eq. 5.142. All four manifolds show decreased source terms as a consequence of the enthalpy deficit. The most affected case is the manifold of premixed flamelets, where the peak decreases substantially, and the limits marked by the iso-lines also shrink. In the "Stab. + Unstab." manifold the effect of the "Central Unique (C.U.)" truncation strategy is clearly visible, as even with this tabulation method irregularities are observed at low $\widetilde{Y_c}$. These are absent in the "Stab. + Ext." case. Both of these cases show a slight shrinkage of the $\overline{\dot{\omega}_{Y_c}} = 2$ kg/m^{3}s iso-line in the $\widetilde{Z}$ direction, while in the "Stab. + Ext." manifold this iso-line also shifts upwards by a small amount. Out of the three counterflow diffusion manifolds the "Reign. + Ext." case shows the highest response to enthalpy deficit, as in this case the residence time is determined by the rather low constant strain rate of $a_{uns} = 100/\text{s}$, thus radiation may take higher effect than in the $a_{uns} > 1000/\text{s}$ flamelets of the "Stab. + Ext." manifold. As Fig. 8.31h shows, the peak source term decreases to a value similar to the premixed database at the same enthalpy level. Furthermore, iso-lines of low source terms show a shift both towards a narrower flammable range in $\widetilde{Z}$ and towards a higher values of $\widetilde{Y_c}$. Nevertheless, the extent of notable source terms in the $\widetilde{Z}$ direction is still significantly larger than in case of premixed flamelets.

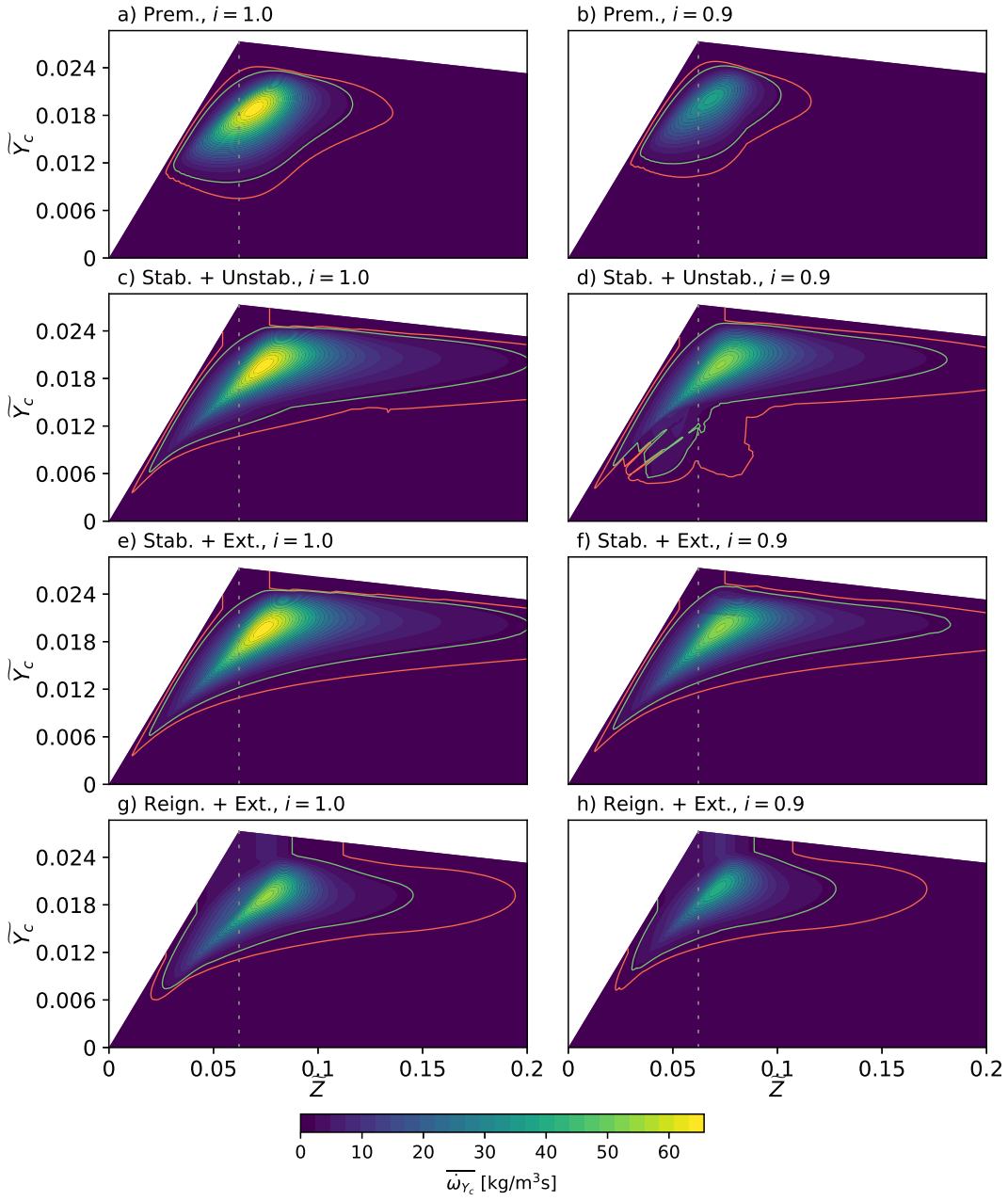

FIGURE 8.31: Comparison of the non-adiabatic thermo-chemical tables applied in the n-heptane (H1S1) case of the Cambridge swirl bluff-body burner. The filtered progress variable source term contours are presented on the $\widetilde{Z} - \widetilde{Y}_c$ plane at two different enthalpy levels. The dashed line indicates the stoichiometric mixture fraction: $Z_{st} = 0.0622$.

The principal difference between the thermo-chemical tables is indeed in the distribution of the progress variable source term $\dot{\omega}_{Y_c}$. The differences are further quantified Fig. 8.32 for the four databases at five different mixture fractions corresponding to the equivalence ratios: $\phi\left(\widetilde{Z}\right) \in \{0.3, 0.8, 1.0, 1.5, 3.0\}$. Concentrating first on the counterflow diffusion flames, the figure shows, that the source terms corresponding the unstable branch ("Stab.+Unstab.") and to the unsteady extinguishing

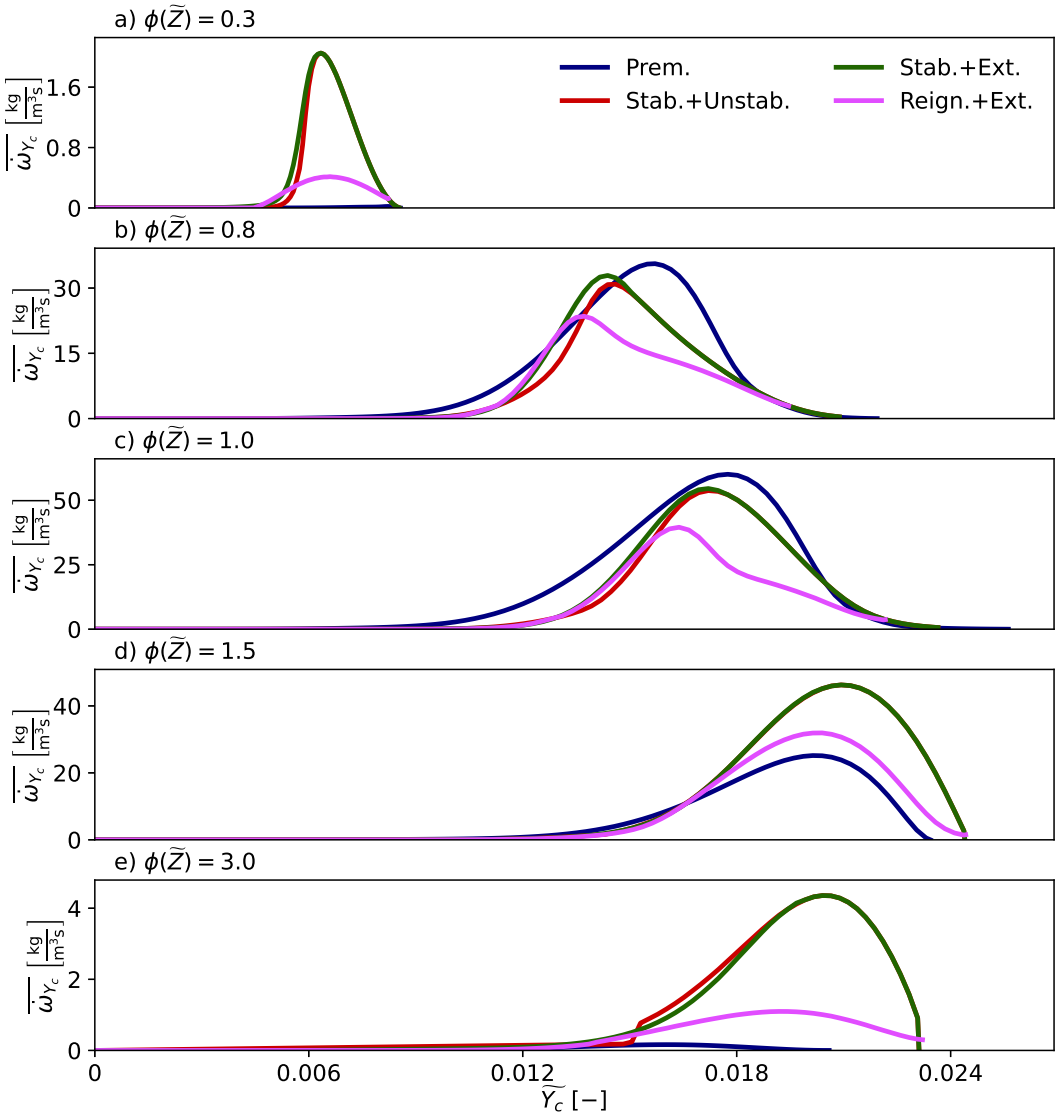

FIGURE 8.32: Comparison of progress variable source term ($\overline{\dot{\omega}_{Y_c}}$) in the manifolds applied for the n-heptane (H1S1) case of the Cambridge swirl bluff-body burner. The source term profiles are displayed along the progress variable ($\widetilde{Y_c}$) in slices of the applied tables at different mixture fractions (identified by the displayed equivalence ratios), the rest of the control variables are kept constant ($\widetilde{i} = 1$, $\zeta_Z = 0$).

flamelet ("Stab.+Ext.") are fairly close to each other, thus the method of Chrigui et al. (2012) appears to be a justified simplification of the Steady Flamelet Progress Variable model if the evaluation of the unstable branch is infeasible. The extinguishing flamelet produces slightly higher source terms on the lean side. Comparing these two manifolds to the unsteady flamelet reigniting and extinguishing at a constant strain rate of $a_{uns} = 100/\text{s}$ ("Reign.+Ext."), the source terms of this case are consistently lower, especially under very lean ($\phi = 0.3$) and very rich ($\phi = 3.0$) conditions. Finally, the premixed flamelet database ("Prem.") can be compared to the counterflow flamelets. As expected, outside the flammability limits, the premixed flamelets predict zero source term, and even at very rich but flammable mixtures ($\phi = 3.0$) the source term is negligible compared to the counterflow diffusion flames. However, at

the stoichiometric mixture fraction, and even at $\phi = 0.8$, the premixed flames are the most reactive. These differences in the source term profile are directly causing the differences in flame speed predictions of the different manifolds, as demonstrated in section 6.3.3.

Mean flame behavior

The LES simulations were executed using the four different thermo-chemical databases on the coarse and fine computational grids presented in Fig. 8.5. The main characteristics of the flame are not changed significantly by the choice of the manifold. For instance, the mean and RMS components of the velocity field are indistinguishable form the "Prem." case illustrated in Fig. 8.25 and appendix M, thus the velocity results are omitted here. Likewise, the velocity and size distribution of the droplet cloud is particularly insensitive both to the mesh size and to the tabulation strategy. As shown below, only the simulation using the premixed database shows significant lift-off. This behavior is extensively analyzed above in section 8.3.3. In the "Prem." case, the resulting edge flame seldom touches the bluff-body, and its location fluctuates as new extinct regions are created by the high shear rate, and as the large scale flow structures disturb the edge flame. The distinct dynamic flame behavior between the cases applying different manifolds causes slight differences in the mean scalar fields presented in Fig. 8.33. The evaporating hollow cone spray introduces mixture fraction into the domain, which is carried towards the bluff-body by the central recirculation zone, and towards the shear layer by the toroidal vortex structure near the injector. This is captured well in the left column of plots of Fig. 8.33, where the peak of $\left\langle \widetilde{Z} \right\rangle$ consistently coincides with the outer edge of the hollow cone spray. At $x = 6$ mm and $x = 10$ mm, a mean mixture fraction profile shows a plateau at $\left\langle \widetilde{Z} \right\rangle \approx 0.2$, corresponding to the rich core of the flame. Subsequently, the mixture fraction drops sharply in the shear layer as this rich mixture interacts with the fresh oxidizer. Note, that due to the higher bulk air velocity applied here and the differences in the spray injection, the present mixture fraction field is significantly leaner, than that reported by Paulhiac et al. (2020) showing values near 0.35 in the central recirculation zone. The mixture fraction shows certain sensitivity to the selection of the thermo-chemical manifold at $x = 6$ mm near the center of the domain. This region is particularly close to the tip of the hollow cone spray cloud, thus small differences in the behavior of the inner reaction layer can cause varied amounts of fluctuations, which lead to different mean mixture fractions. As Fig. 8.24 illustrates, near the axis of the burner the instantaneous stoichiometric iso-surface may get lifted from the immediate vicinity of the hollow cone spray. The sensitivity observed in Fig. 8.33p indicates, that this lift-off is the least pronounced in case of using the premixed flamelet database.

The central column of Fig. 8.33 presents the mean temperature field. Up to $x = 20$ mm the two reacting layers can be clearly distinguished by the temperature peaks, while more downstream there is only one single mean temperature maximum as the mean mixture fraction drops below the stoichiometric value at all radii, and the two reacting layers merge. The temperature profiles show a clear difference at $x = 6$ mm, associated to the variations in mixture fraction. Furthermore, the mean temperatures in the outer reacting layer show around 160 K difference between the "Prem." case and the "Stab.+Unstab." case, as localized extinction occurs with a significantly higher propensity with the former manifold. The differences in lift-off are

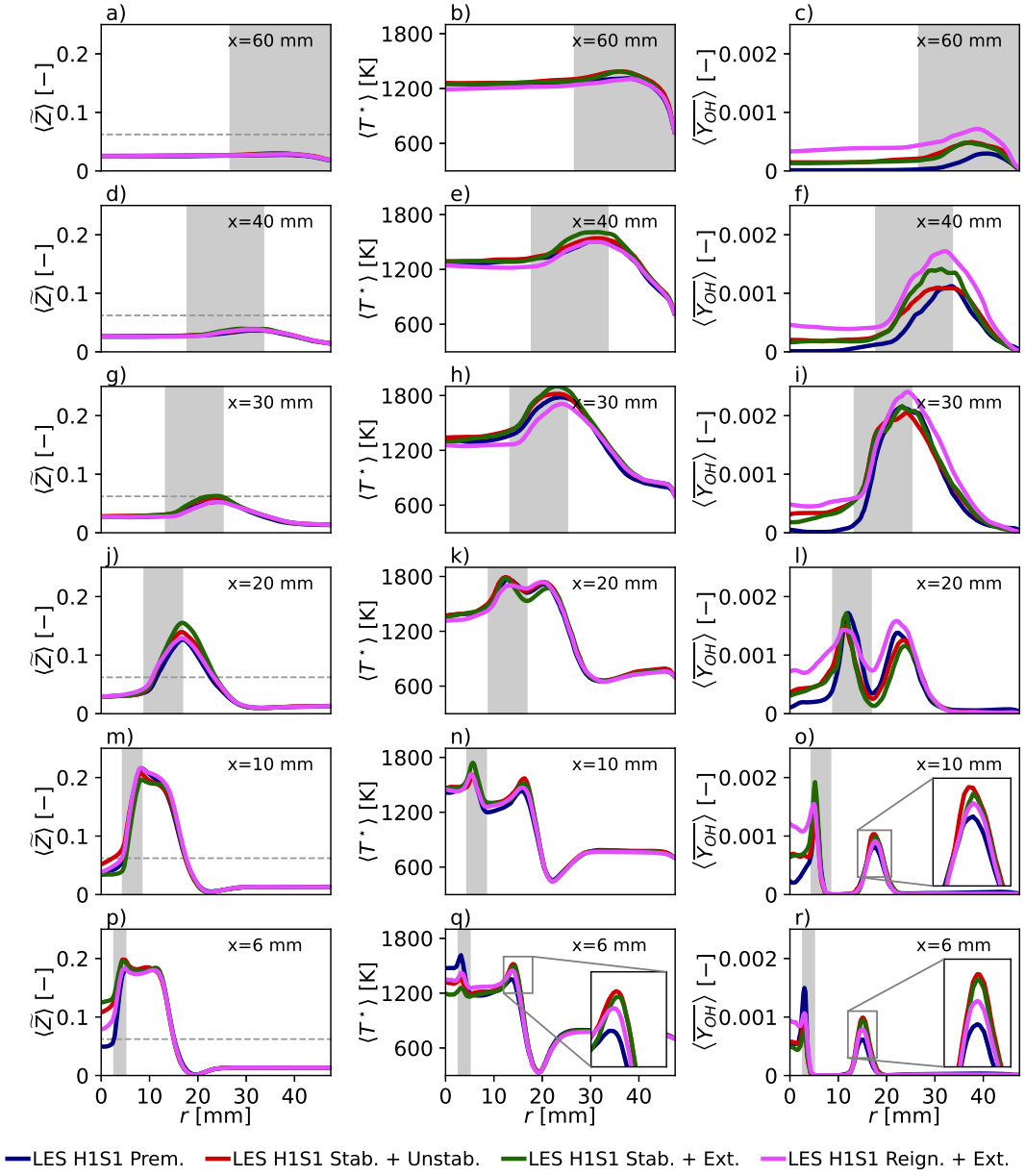

FIGURE 8.33: Mean scalar profiles in the n-heptane case (H1S1) of the Cambridge swirl bluff-body burner using different thermo-chemical manifolds on the fine grid. The rows of plots correspond to the indicated axial location, while the three columns show the mean of the mixture fraction, temperature, and hydroxyl mass fraction. The gray shading represents the spray half-angle range of $[24°, 40°]$ with respect to the injector location. The inset plot of temperature shows a range of $\langle T^{\star} \rangle \in [1200, 1600]$ K, while the ones of hydroxyl mass fraction show $\langle \overline{Y_{OH}} \rangle \in [0.0003, 0.0011]$.

also affecting the mean hydroxyl radical mass fraction. At $x = 6$ mm the $\langle \overline{Y_{OH}} \rangle$ profile shows significant differences in the outer reaction layer as a consequence of the intermittent lift-off. These differences diminish by $x = 10$ mm, as even in the case of the "Prem." manifold on the fine grid the flame only exhibits $LOL \geq 10$ mm in 19% of the studied instances, according to the results displayed in Fig. 8.29. Meanwhile the probability of $LOL \geq 6$ mm is 37%. Further downstream, and near the

centerline the hydroxyl radical mass fraction shows greater variations with different manifolds. The tables based on counterflow diffusion flamelets do not contain the equilibrium conditions, due to the non-zero lower limit of the strain rate and the truncation of solutions along $\widetilde{C}$. (See Fig. 3.26.) Consequently, the four manifolds converge to different final temperatures and OH mass fractions. Only the database of premixed flamelets imposes the equilibrium values at $\widetilde{C} = 1$.

Analysis of flame lift-off

TABLE 8.8: Mean flame lift-off length in the n-heptane case (H1S1) of the Cambridge swirl bluff-body burner using different thermo-chemical manifolds.

	$\langle LOL \rangle$ [mm]	Sample count	
LES Prem. coarse	3.08	480	
LES Stab. + Unstab. coarse	0.58	432	
LES Stab. + Ext. coarse	0.83	480	
LES Reign. + Ext. coarse	3.15	480	
LES Prem. fine	5.26	268	
LES Stab. + Unstab. fine	0.39	408	
LES Stab. + Ext. fine	0.42	304	
LES Reign. + Ext. fine	2.04	304	
	$\langle LOL \vert LOL > 0.2\text{ mm} \rangle$	Sample count	Lifted fraction
Yuan et al. (2018)	6.25		
LES Prem. coarse	3.13 (−50%)	475	99.0%
LES Stab. + Unstab. coarse	0.99 (−84%)	265	61%
LES Stab. + Ext. coarse	1.09 (−83%)	382	80%
LES Reign. + Ext. coarse	3.24 (−48%)	469	98%
LES Prem. fine	5.26 (−16%)	268	100.0%
LES Stab. + Unstab. fine	0.86 (−86%)	206	50%
LES Stab. + Ext. fine	0.77 (−88%)	186	61%
LES Reign. + Ext. fine	2.47 (−60%)	251	83%

While the mean properties of this spray flame are rather insensitive to the tabulation method, the local extinction of the outer reaction zone shows a great variability in function of applied manifold. As described in section 8.2.2, the lift-off is assessed in a similar manner to the experiments, using an iso-contour of the tabulated $\overline{Y_{OH}}$ field. The mean lift-off lengths are summarized in Tab. 8.8 both in terms of the simple arithmetic mean: $\langle LOL \rangle$, and in terms of the mean of lifted instances: $\langle LOL | LOL > 0.2\text{ mm} \rangle$. These are compared to the mean lift-off length experimentally determined by Yuan, Kariuki, and Mastorakos (2018) as: 6.25 mm using the hydroxyl planar laser induced fluorescence imaging of the flame. In general, all presented tabulated chemistry methods under-predict the lift-off. The "Stab. + Unstab." and "Stab. + Ext." manifolds shows very similar behavior, with a significant portion of the instances corresponding to fully attached reacting layers. The similarity of these methods is expected, as they share the stable branch, and show very similar behavior on the rest of the $Z - Y_c$ plane as well. The "Reign. + Ext." case

shows a higher mean lift-off due to the significantly lower progress variable source term. As the mesh is refined, the tabulation strategies based on counterflow diffusion flamelets tend to show lower lift-off, worsening the LES predictions. Meanwhile, the prediction of the premixed flamelet table is substantially improved by refinement. As discussed in section 8.3.3, further refinement does not change the mean lift-off substantially.

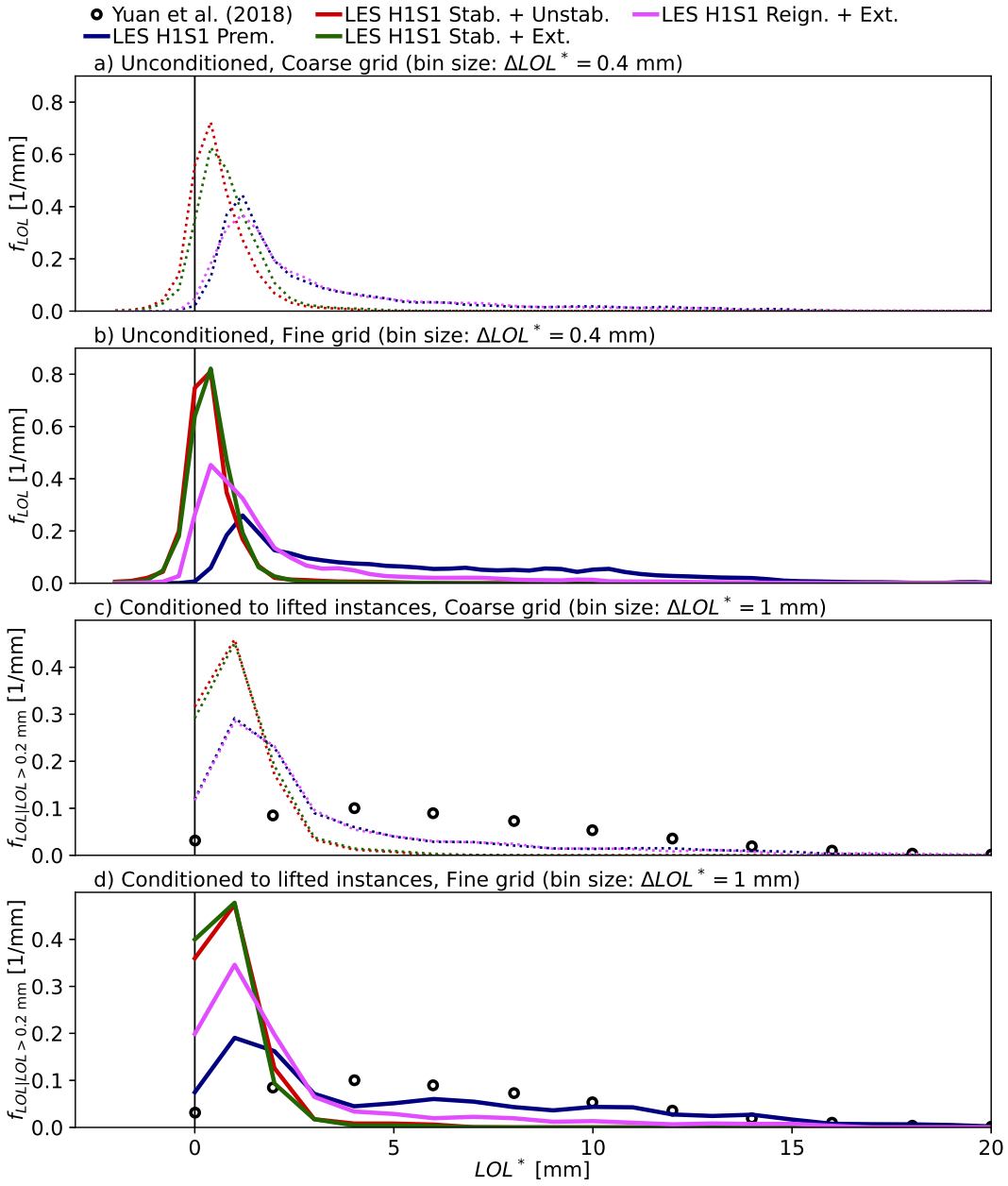

FIGURE 8.34: Effect of thermo-chemical manifolds on probability density function of flame lift-off length in the n-heptane case (H1S1) of the Cambridge swirl bluff-body burner. The unconditioned statistics (a,b) uses all the time instances of the LES, while the conditioned one (c,d) only considers the lifted cases of $LOL > 0.2$ mm.

The mean lift-off readily illustrates, that the manifold of premixed flamelets captures the dynamics of the outer reaction zone the best, with an error of only -16%

in the mean LOL. The lift-off statistics are further analyzed in Fig. 8.34 using the complete distribution of LOL values. The unconditioned PDFs of Fig. 8.34a and b readily illustrate, that most simulation methods show a substantial fraction of completely attached states. The only exceptions are the simulations using the "Prem." manifold, and the case of "Reign. + Ext." manifold in combination with the coarse mesh, which acts very similarly to the "Prem." case. Nevertheless, with mesh refinement even the "Reign. + Ext." case starts to show a notable fraction of attached instances. The "Stab. + Unstab." and "Stab. + Ext." cases show a particularly narrow LOL distribution without any instances of $LOL \geq 5$ mm. Such highly lifted flame states are scarce even using the "Reign. + Ext." case, as they are only observed in 19% and 14% of the instances in the coarse and fine grid LES respectively. Meanwhile, using the "Prem." manifold, a state of $LOL \geq 5$ mm occurs in 18% and 44% of the instances using the two grids.

The higher lift-off in the "Reign. + Ext." case is expected compared to the other two manifolds of counterflow diffusion flames ("Stab. + Unstab." and "Stab. + Ext."), as lower source terms are observed in the former thermo-chemical table throughout all equivalence ratios. The difference between the "Reign. + Ext." and the "Prem." manifold is less straightforward. As Fig. 8.32 presents, the premixed flamelets are more reactive on the lean side and near stoichiometry. In the presently studied configuration, such states are only observed in thin sheets within the turbulent shear layer. Meanwhile, the rich states, where the "Reign. + Ext." manifold is more reactive, are present in a larger volume of the low velocity recirculation zone. This difference likely causes the different lift-off dynamics, as the rich side of the reacting layer has higher local residence times, so the higher source terms in this part have more influence. Note, that as the results of Fig. 3.16 and the *a posteriori* analysis of section 6.3.3 show, the reactivity of the "Reign. + Ext." manifold could be further decreased by decreasing the applied strain rate. This suggests, that the Unsteady Flamelet/Progress Variable model of Ihme and See (2010) may improve the lift-off predictions, as it contains unsteady extinguishing and reigniting solutions at various strain rates. However, assessing this modeling strategy is out of the scope of the present study.

Summary of tabulation analysis

Different chemistry tabulation strategies are applied for the LES simulation of the H1S1 n-heptane case of the Cambridge swirl spray flames, including the strategy of Sacomano Filho et al. (2018) using free and burner-stabilized premixed flamelets, and three different strategies involving diffusion flamelets extended to non-adiabatic manifolds. The latter three manifolds are related to the tabulation strategies of Pierce and Moin (2004) and Chrigui et al., 2012, and a restricted subset of the manifold of Ihme and See (2010). The results are relatively insensitive to the choice of the table in terms of time averaged quantities, as the flame stabilization is hydro-dynamically driven in this configuration. I.e.: blow-out is prevented by the anchoring of high temperature flue gases on the bluff-body. Nevertheless, significant differences are observed in the finite rate chemistry effects displayed by the flame, that are quantified through the lift-off length statistics of the outer reaction layer. Namely, the tabulation strategy based on premixed flamelets provides the best lift-off prediction. As emphasized by many recent studies on the topic of tabulated chemistry methods for partially-premixed combustion, this result is not trivial. On one hand, this highlights the need to implement more sophisticated tabulated chemistry methods specifically in the LES context, such as the method proposed by Franzelli, Fiorina,

and Darabiha (2013) or Illana, Mira, and Mura (2021). On the other hand, more work is needed to identify the cases *a priori*, where classical models are indeed sufficient, especially in relation to the expected mixture fraction field.

8.3.5 Fuel effects

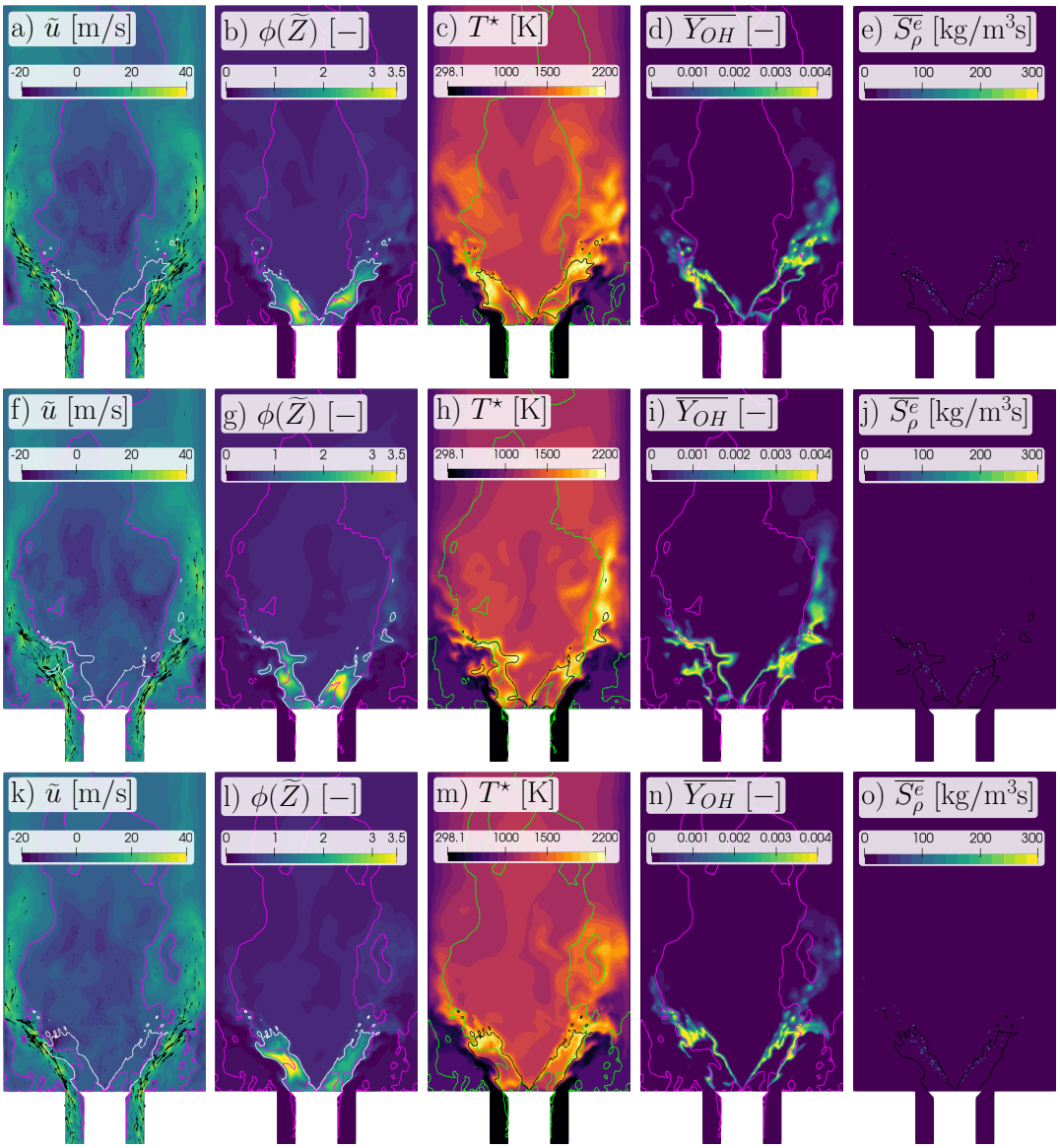

FIGURE 8.35: Examples of the instantaneous velocity and scalar fields of the n-dodecane case (DD1S2) in the Cambridge swirl bluff-body burner. The columns correspond to the velocity, equivalence ratio, temperature, hydroxyl radical mass fraction, and evaporative mass source term fields, while the rows show different instantaneous snapshots. Contour lines mark the position of zero axial velocity (magenta/green) and stoichiometric mixture fraction (white/black).

The change of fuel can affect various physical phenomena in the burner, and may lead to different flame behavior. The difference may originate from variations in the liquid properties, the change in the nature of the evaporation, or different

finite rate chemistry effects. In this section the n-heptane case (H1S1) of the Cambridge swirl bluff-body burner is compared to the n-dodecane case (DD1S2) using the LES model with a thermo-chemical table based on free and burner-stabilized premixed flamelets. The two manifolds are created using the chemical mechanisms of Lu and Law (2006) and Kathrotia et al. (2018) for n-heptane and n-dodecane respectively. As discussed in section 8.1.2, the n-heptane and n-dodecane flamelets behave quite similarly. The two flames are characterized by the same fuel and oxidizer flow rates, thus the observed differences are solely a consequence of the fuel effects. (See Tab. 8.2.) In the simulations the only difference in the spray boundary conditions is in the axial velocity magnitude, as Tab. 8.4 shows.

The instantaneous flame behavior of the n-dodecane flame is illustrated in Fig. 8.35. For the sake of comparison the same scaling is used as in the n-heptane case of Fig. 8.24, and the methane case of Fig. 8.13. The toroidal vortex created by the hollow cone spray is present in this case as well. Overall, the instantaneous velocity fields are very similar between the DD1S2 and H1S1 cases. The mixture fraction field shows significant rich peaks concentrated to the vicinity of the hollow cone spray. As these rich kernels are rather small, the stoichiometric mixture fraction iso-surface intermittently lifts off from the bluff-body when leaner mixtures are convected to the bluff-body surface. Such a situation is shown in Fig. 8.35b. Further downstream when the hollow cone spray interacts with the flame tip various locally rich pockets are formed. This indicates, that some isolated droplet combustion can occur in this region. High temperature states are found near the stoichiometric mixture fraction iso-line, although hot states often occur in the area limited by the hollow cone spray, the bluff-body surface, and the shear layer, when the the local composition becomes leaner. In such cases hydroxyl radical may be present right above the bluff-body. The outer reaction layer shows minor amounts of lift-off, although larger parts of the flame may suffer local extinction, as it is the case on the left of Fig. 8.35n. The presence of OH in the leaner mixtures right above the bluff-body surface contribute to the less lifted nature observed in these simulations. Even though high gas phase temperatures are observed along the entire hollow cone spray, the intense evaporation of the droplets starts with a certain delay from the spray injector. This is due to the relatively large heat-up time necessary in this fuel of lower volatility. Compared to the n-heptane case of Fig. 8.24, the DD1S2 flame appears to contain less amount of fuel in the central recirculation zone, and the presence of rich non-flammable pockets is more intermittent. Due to the leaner composition, the inner and outer reaction zone may become connected just above the bull-body, which behavior is not observed in the H1S1 simulations. The onset of significant evaporative mass source terms is significantly delayed in the n-dodecane case, while the n-heptane case shows notable values of $\overline{S_\rho^e}$ very close to the injection site.

Mean flame behavior

The comparison of the two flames is continued by the qualitative assessment of the time averaged fields in Fig. 8.36. Note, that the mean scalar fields are quantitatively compared in appendix M. In the case of the DD1S2 flame, the averaging is done over a time frame of $\Delta t \approx 208$ ms, which is sufficient to reach statistically converged results. As the iso-contour of $\langle \widetilde{u} \rangle = 0$ m/s indicates, the velocity field is fairly similar in the two cases both in the central and corner recirculation zones. However, the velocity contour in the toroidal vortex structure at the spray base shows notable differences. In the n-dodecane case this disturbance is significantly smaller partly due to the lower axial droplet velocity. Furthermore, in the H1S1 case part of the

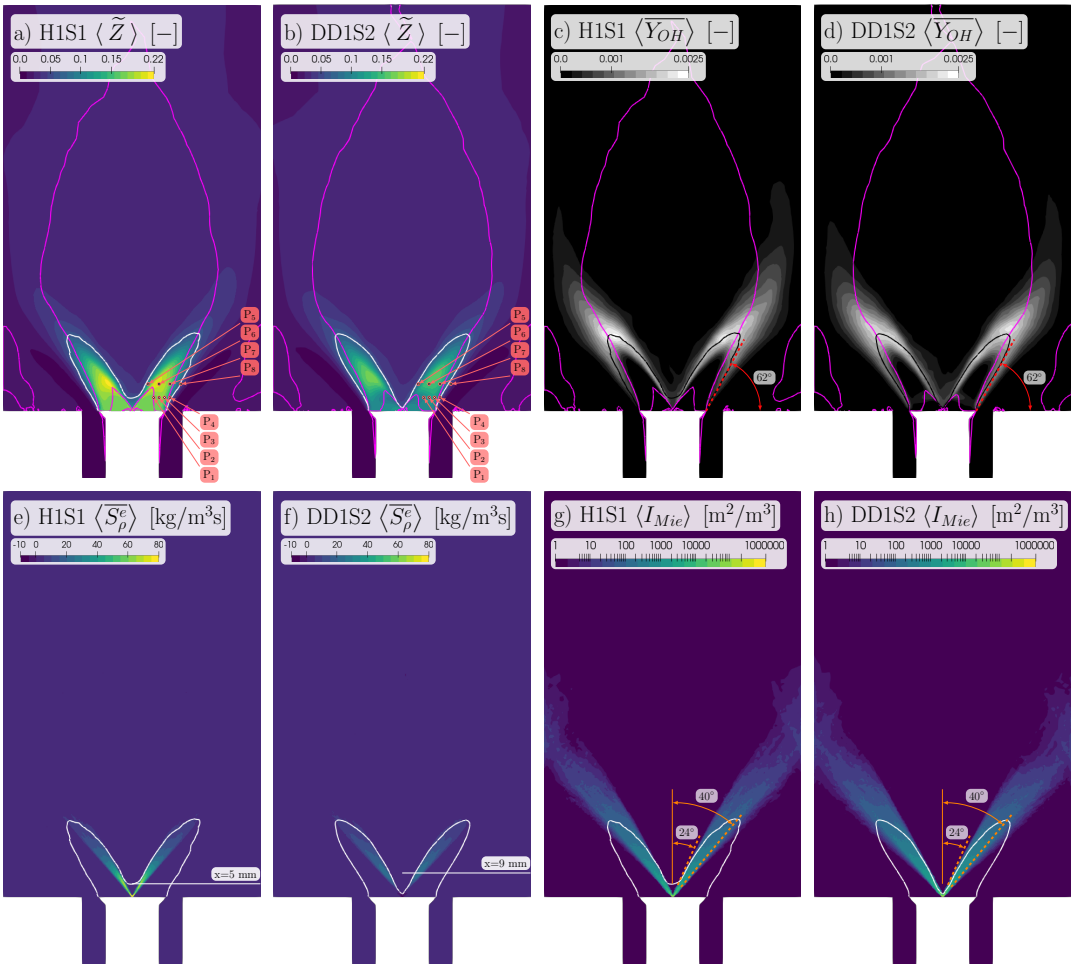

FIGURE 8.36: Comparison of mean scalar fields of the n-heptane (H1S1) and n-dodecane (DD1S2) cases of the Cambridge swirl bluff-body burner. The top row shows the mean mixture fraction, and hydroxyl radial mass fraction, while the bottom row shows the mean of evaporative mass source term, and equivalent Mie scattering field Contour lines mark the position of zero mean axial velocity (magenta) and stoichiometric mixture fraction (black/white).

momentum transfer between the gas and liquid phases is due to the incoming vapor. Meanwhile, the lower evaporation rates in the DD1S2 case eliminate this component and momentum is primarily transferred by drag between the two phases. (See Eq. (5.155) for the two components.) The mean mixture fraction field is very different in the two flames. The peak of mean mixture fraction is approximately $\left\langle \widetilde{Z} \right\rangle = 0.22$ in the n-heptane case while in the n-dodecane case it is 27% lower: only 0.16. Despite this difference in the peak, the stoichiometric mixture fraction iso-line is very similar in the two cases, as this limit is rather determined by the aerodynamic behavior of the shear layer and the central recirculation zone, than by the evaporation rates. The only difference is near the spray injection site, where the high evaporation rates in the n-heptane case create a rich region on the inside of the hollow cone spray. Meanwhile, in the n-dodecane flame the stoichiometric mixture fraction iso-line follows closely the hollow cone spray, even close to the bluff-body.

The mean hydroxyl mass fraction contours generally follow the stoichiometric mixture fraction iso-line. The outer reaction layer is oriented in the same direction in the two flames, as this is linked to the shear layer which is primarily influenced by the behavior of the swirling oxidizer flow. The same 62° angle is observed even in the non-premixed methane flame. The outer reaction layer shows notably higher $\langle \overline{Y_{OH}} \rangle$ values in the DD1S2 flame, since in the present simulations this case shows less lift-off. As illustrated by all the instances shown in Fig. 8.35, small hydroxyl layers tend to form just above the bluff-body, as leaner mixtures are observed near the injection point in the DD1S2 case. In the present simulations structures occur frequently enough to appear in the $\langle \overline{Y_{OH}} \rangle$ iso-contour of Fig. 8.36d. The mean evaporative mass source term further highlights the difference between heat and mass transfer in the two spray clouds. The n-heptane case shows positive $\left\langle \overline{S_\rho^e} \right\rangle$ throughout the entire domain. A peak of 80 kg/m^{3}s is observed near the injection site, due to the high density of droplets here, which commence the evaporation shortly after injection. Meanwhile, the evaporative source term peaks again near $x = 5$ mm. In the n-dodecane case $\left\langle \overline{S_\rho^e} \right\rangle$ is negative near the injection site, as the droplets are initially significantly colder than the wet-bulb conditions, thus fuel vapor condenses onto these cold droplets. The n-dodecane droplets need longer time to heat up to the wet-bulb conditions, which shifts the peak location of the evaporative source term to $x = 9$ mm. Note, that the region of notable evaporation rates is concluded in a similar axial distance since once the droplets reach the wet-bulb conditions, they evaporate at a similar rate, as discussed below. Finally, Fig. 8.36 also includes the average Mie scattering equivalent signal. Both the H1S1 and DD1S2 cases show a largely ballistic behavior, with the latter deviating more towards higher spray angles due to the lower initial axial velocity.

TABLE 8.9: Droplet time scale estimates in the n-heptane (H1S1) and n-dodecane (DD1S2) cases of the Cambridge swirl bluff-body burner, assuming a seen gas state of hot air at 1300 K. The Reynolds number ($Re_{p,0}$) and the kinematic relaxation time ($\tau_{p,kin,0}$) are evaluated at the initial droplet temperature and velocity at a spray angle of 32°. The evaporation constant (K) and the related time scale ($\tau_{p,evap}$) is evaluated at the wet-bulb temperature of $T_p^{psy,H} = 350.0$ K and $T_p^{psy,DD} = 457.9$ K assuming the initial droplet velocity. The heat-up time ($\tau_{p,heat}$) is estimated from the initial heat-up rate.

	$d_{p,0} = 10\ \mu$m		$d_{p,0} = 79.2\ \mu$m		$d_{p,0} = 120\ \mu$m	
	H1S1	DD1S2	H1S1	DD1S2	H1S1	DD1S2
$Re_{p,0}$	4.4	2.9	34.8	23.0	52.7	34.9
$\tau_{p,kin,0}$ [ms]	0.09	0.10	3.0	3.6	5.6	6.9
K [mm^2/s]	0.79	0.81	1.37	1.37	1.57	1.57
$\tau_{p,evap}$ [ms]	0.12	0.12	4.6	4.6	9.2	9.2
$\tau_{p,heat}$ [ms]	0.01	0.03	0.4	1.3	0.8	2.6

To further illustrate the differences in the two fuels, the droplet time scales of Tab. 8.5 are calculated for the DD1S2 case as well. The n-heptane case shows higher Reynolds numbers, as the droplet inlet velocity is 29% higher in the H1S1 case. Nevertheless, the kinematic relaxation time is fairly similar in the two fuels. Interestingly,

despite the difference in Reynolds number, once the droplets reach the wet-bulb conditions, the evaporation constant is nearly the same in the two fuels. The primary difference between these examples is in the heat-up time scale, which is more than three times higher in the n-dodecane case. For instance, if the droplets would not decelerate, in one $\tau_{p,heat}$ time span the droplet of $d_{p,0} = 79.2$ μm would reach an axial location of $x = 18.2$ mm in the DD1S2 case and $x = 7.2$ mm in the H1S1 case. This illustrates, why the resulting mixture fraction field is so different between the two cases.

Mean spray behavior

The difference between the n-heptane and n-dodecane flames is further studied by comparing the properties of the hollow cone spray. Figure 8.37 shows the differences in droplet velocity between the two cases at four different axial locations indicated in Fig. 8.25d. As the PDA measurement data shows, at $x = 10$ mm the axial droplet velocity in the spray core is significantly lower in the n-dodecane case, which is reproduced well by the changed droplet initial condition model. Subsequently, the n-dodecane droplets remain slower than the n-heptane ones at all measurement locations, although the difference between the two diminishes. The LES reproduces this trend, although $\langle u_p \rangle$ is under-predicted in the spray core. For the reason of this under-prediction see Fig. 8.28 and the related discussion. In the DD1S2 case the PDA measurements also provide the radial droplet velocity data, which is reproduced exceptionally well by the present simulation method. In line with the lower injection velocity, the radial droplet velocity is lower in the n-dodecane case than in the n-heptane case. As the droplets reach the shear layer at higher radii, their radial velocity increases substantially, which is captured by the LES at all measurement locations. According to the experimental data, the RMS components show less dependence on the fuel. Nevertheless, in the present LES simulations the velocity RMS appears to decrease together with the decreased velocity magnitude of the DD1S2 case.

The mean scalar properties of the droplet cloud are compared in Fig. 8.38. The PDA measurements detect slightly higher diameters in the n-dodecane case with a wider distribution in the radial direction. Since in the LES most of the injection parameters are unchanged between the H1S1 and DD1S2 case, the droplet size shows less differences. In particular, at $x = 10$ mm the two Sauter mean diameter curves of the LES cases practically overlap. Further downstream, differences arise between the fuels, as the droplet sizes are higher in the n-dodecane case. The key differences between the phase change behavior of the two fuels is the wet-bulb temperature and the time scale of reaching this temperature, as demonstrated in Tab. 8.9. The second column of plots in Fig. 8.38 shows the mean droplet temperature with respect to the boiling point of the fuels: $T_{sat}^{H} = 371.54$ K and $T_{sat}^{DD} = 489.52$ K. In the DD1S2 case the initial droplet temperature is significantly below the boiling point, and it gradually approaches a value about $T_{sat}^{DD} - 25$ K by the last measurement point. The heat-up is significantly faster in the H1S1 case, where the approximate equilibrium value of $T_{sat}^{H} - 15$ K is reached by $x = 20$ mm. These equilibrium temperatures are slightly higher than in the example of Tab. 8.9. As demonstrated in section 4.5, the wet-bulb conditions are mainly determined by the seen gas temperature and the seen vapor mass fraction, which differs between the LES and the single droplet example. Note, that the Reynolds number has little influence on the droplet temperature. The diameter RMS is very similar at $x = 10$ mm between the two cases and differences arise as the mean diameter starts to deviate. Meanwhile the temperature RMS shows great

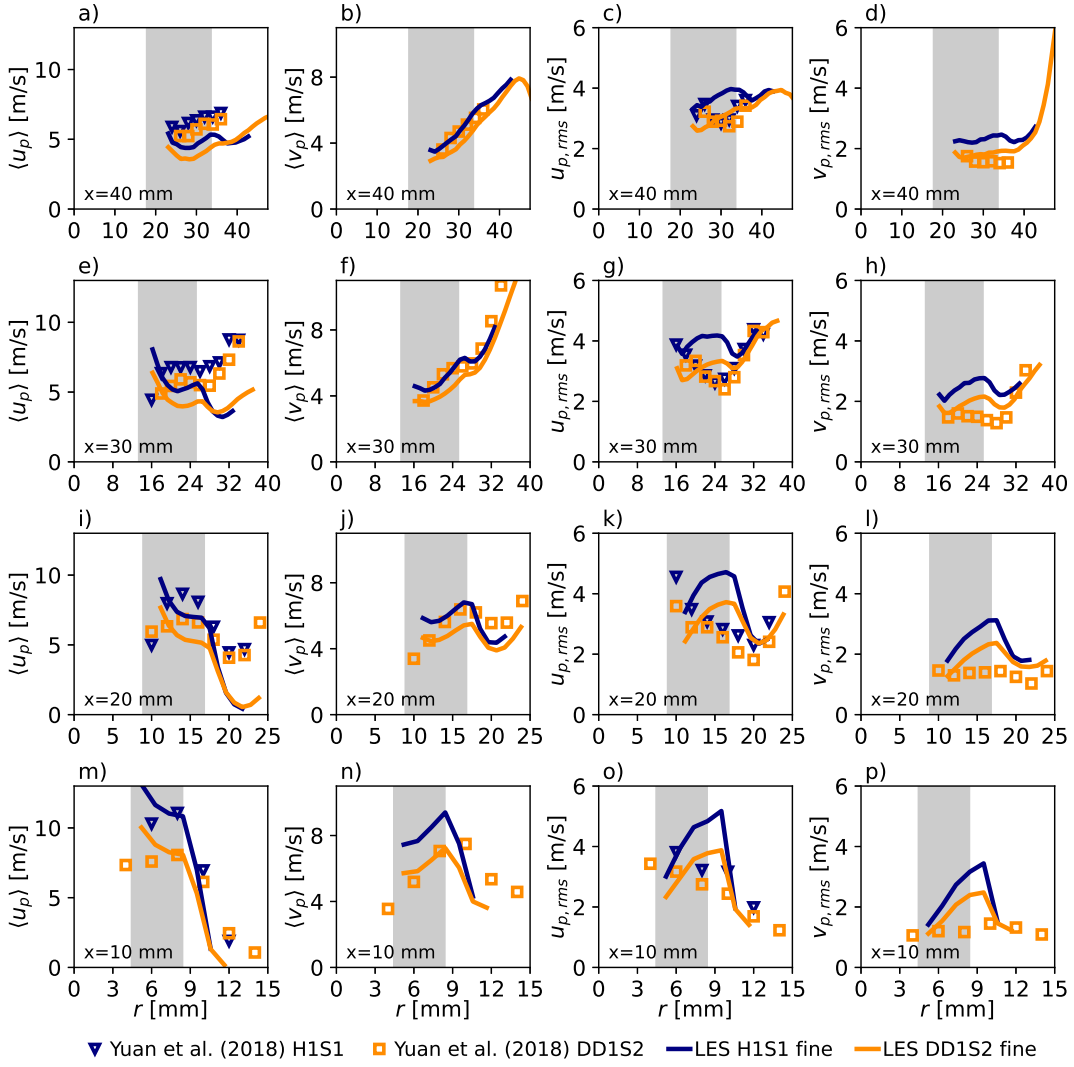

FIGURE 8.37: Comparison of mean and RMS droplet velocities in the n-heptane (H1S1) and n-dodecane (DD1S2) cases of the Cambridge swirl bluff-body burner between the PDA measurements of Yuan, Kariuki, and Mastorakos (2018) and the LES of the present work. The rows of plots correspond to the indicated axial location, while the four columns show the mean of the axial and radial droplet velocity, and the corresponding RMS values. The gray shading represents the spray half-angle range of $[24°, 40°]$ with respect to the injector location.

differences linked to the delayed heat-up in the n-dodecane case. At $x = 10$ mm the smallest n-dodecane droplets have already reached their equilibrium temperature as their heat-up timescale is of $\mathcal{O}(10\ \mu s)$. Meanwhile the larger droplets take significantly longer to reach high temperatures, which results in a temperature RMS of $\sim$ 40 K at this location. Further downstream $T_{p,rms}$ gradually decreases, with showing some signs of notable temperature differences even at $x = 30$ mm.

Overall, in the core of the spray the LES results compare well with the PDA measurements of Yuan, Kariuki, and Mastorakos (2018). This is achieved by only modifying the axial injection velocity in line with the observed decrease in experimental data. More elaborate injection models, such as the size-conditional model of

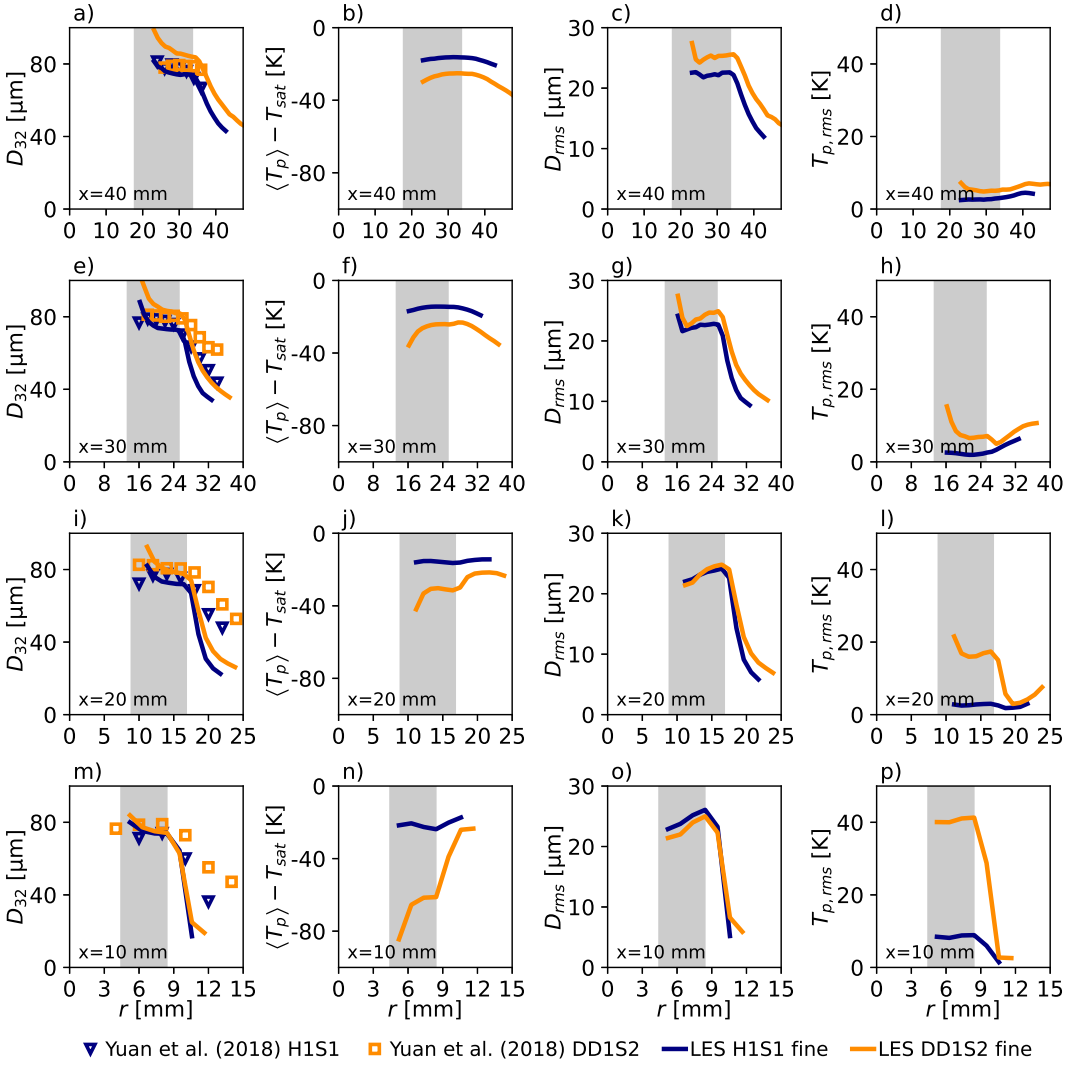

FIGURE 8.38: Comparison of mean and RMS droplet properties in the n-heptane (H1S1) and n-dodecane (DD1S2) cases of the Cambridge swirl bluff-body burner between the PDA measurements of Yuan, Kariuki, and Mastorakos (2018) and the LES of the present work. The rows of plots correspond to the indicated axial location, while the four columns show the Sauter mean droplet diameter, the mean droplet temperature, and the RMS of the droplet diameter and temperature. The gray shading represents the spray half-angle range of $[24°, 40°]$ with respect to the injector location.

Ma and Roekaerts (2016) could greatly improve the predictions near the spray edge. The results highlight the importance of droplet injection models. The presently applied empirical treatment extensively utilizes the measurement data, which is not possible under *a priori* unknown conditions.

Dynamic flame behavior

The difference between the two fuels is also reflected in the dynamic behavior of the flame. Here this is analyzed through the lift-off statistics. Using the OH-PLIF technique Yuan, Kariuki, and Mastorakos (2018) observe significantly higher lift-off

TABLE 8.10: Mean flame lift-off length in n-heptane (H1S1) and n-dodecane (DD1S2) cases of the Cambridge swirl bluff-body burner.

	$\langle LOL \rangle$ [mm]		Sample count			
	H1S1	DD1S2	H1S1	DD1S2		
LES coarse	3.08	1.61	480	376		
LES fine	5.26	1.40	268	440		
	$\langle LOL \vert LOL > 0.2$ mm$\rangle$		Sample count		Lifted fraction	
	H1S1	DD1S2	H1S1	DD1S2	H1S1	DD1S2
Yuan et al. (2018)	6.25	10.25				
LES coarse	3.13 (-50%)	1.64 (-84%)	475	370	99.0%	98.4%
LES fine	5.26 (-16%)	1.45 (-86%)	268	427	100.0%	97.0%

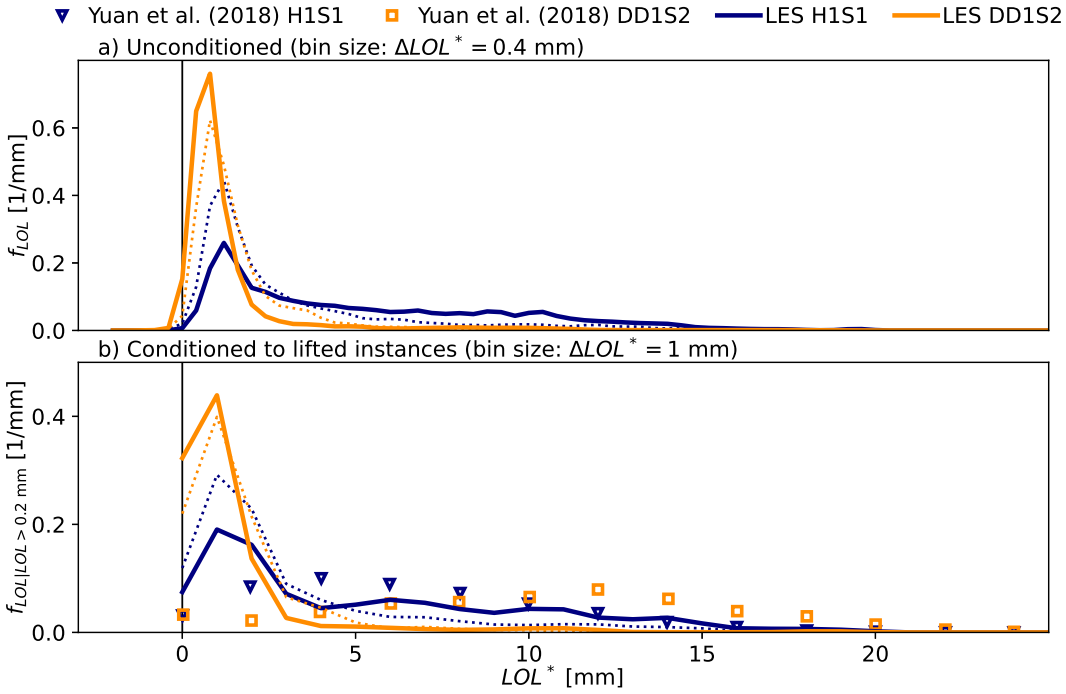

FIGURE 8.39: Probability density function of flame lift-off length in the n-heptane (H1S1) and n-dodecane (DD1S2) cases of the Cambridge swirl bluff-body burner. The unconditioned statistics (top) uses all the time instances of the LES, while the conditioned one (bottom) only considers the lifted cases of $LOL > 0.2$ mm. Dotted and solid lines mark the simulations on the coarse and fine grid respectively.

lengths in the n-dodecane case than in the n-heptane case. The mean value of lift-off is 6.25 mm in the H1S1 case, while it is 64% larger: 10.25 mm in the DD1S2 case. This increase in the mean lift-off is paired with a shift of the LOL probability density function as illustrated in Fig. 8.39b. The mode of the PDF in the H1S1 case is found at $LOL = 4$ mm while in the DD1S2 case the mode is near $LOL = 12$ mm. Figure 8.39 compares the probability density function of the experimentally determined lift-off

and the one obtained from the LES results on the coarse and fine grids. As discussed in section 8.3.3, the dynamics of the H1S1 case are reproduced well in the simulations, with only -16% error in the mean lift of length. Note, that in this case further mesh refinement can improve the shape of the lift-off PDF but the mean lift-off stays constant. In the n-dodecane case the predictions of the LES are significantly deteriorated. The mean lift-off is under-predicted by more than 80%, as the most common lift-off is near 0.8 mm in Fig. 8.39a. This discrepancy in the flame dynamics is likely related to the behavior of the mixture fraction field depicted in Fig. 8.35b, g, and, l. I.e.: the rich mixtures are located at higher axial locations, as evaporation is more delayed in the DD1S2 case because of the increased heat-up time of the droplets compared to the H1S1 case. In comparison, the n-heptane case tends to have quite rich mixtures on the bluff-body surface, which are outside the rich flammability limit as Fig. 8.24 illustrates. The different mixing field in the n-dodecane case allows for the presence of OH in the space enclosed by the bluff-body, the hollow cone spray, and the shear layer. Even though large scale local extinction is possible in this case as well, for instance in Fig. 8.35n, the lift-off predictions are affected by the phenomena near the bluff-body.

The effect is further illustrated by the statistical analysis of single point data presented in Fig. 8.40. The eight analyzed points are marked in Fig. 8.36a and b. The first two rows of plots show points P_1 to P_4 at an axial location of $x = 5$ mm, which is representative to the conditions near the bluff-body. Meanwhile, the third and fourth row show points P_5 to P_8, which are located near the plane of the peak of mean mixture fraction. In particular, P_4 and P_8 are near the stoichiometric iso-line of mean mixture fraction in the outer reaction zone, thus these points are capable of representing the effects of lift-off. Note, that in the fine grid H1S1 and DD1S2 simulations a state of $LOL \geq 5$ mm occurs in 44% and 6% of the instances respectively. Meanwhile, a state of $LOL \geq 10$ mm is observed in 19% of instances in the H1S1 flame and in only 2% of instances in the DD1S2 flame. The local mixture faction and temperature are recorded in time in the eight monitoring points, then the joint probability density function of these two quantities is evaluated using Eq. (8.12) and Eq. (8.13). Similarly to the non-premixed methane case (F3A2) in Fig. 8.20, the levels of $f_{\widetilde{Z}T^\star} = 0.005/\mathrm{K}$ and $f_{\widetilde{Z}T^\star} = 0.0001/\mathrm{K}$ are highlighted by green and red contour lines respectively. The stable counterflow diffusion flamelets at a strain rate of $a = 10/\mathrm{s}$ and at the extinction point are indicated by solid and dotted curves respectively.

At the P_1 and P_2 points shown in Fig. 8.40a and b the n-heptane flame shows very uniform states in both $\widetilde{Z}$ and $T^\star$. The temperature is near equilibrium, although a significant cooling effect can be attributed to the interaction with the spray and the 700 K bluff-body surface. Observing the structure of the thermo-chemical manifold presented in Fig. 8.31, these mixtures are outside the flammability limit. In P_3, closer to the bluff-body edge, the mean mixture fraction is still quite rich, however the joint PDF shows two arms connecting this rich mixture to the fresh oxidizer and to the equilibrium conditions near stoichiometry. Even closer to the shear layer in P_4 the effect of local extinction is fully visible in the H1S1 case, as the $f_{\widetilde{Z}T^\star} = 0.005/\mathrm{K}$ iso-contour shows two branches: one following the flamelets of the stable branch, and one connecting the rich mixtures of the central recirculation zone directly to the fresh oxidizer. The former states correspond to the reacting layer crossing the P_4 point, meanwhile the latter states correspond to local extinction. In comparison, the DD1S2 case of Fig. 8.40e-h shows a notably different behavior mainly because the central recirculation zone is characterized by lower mixture fractions at this axial location. The mean mixture fraction values are located within the flammability limit.

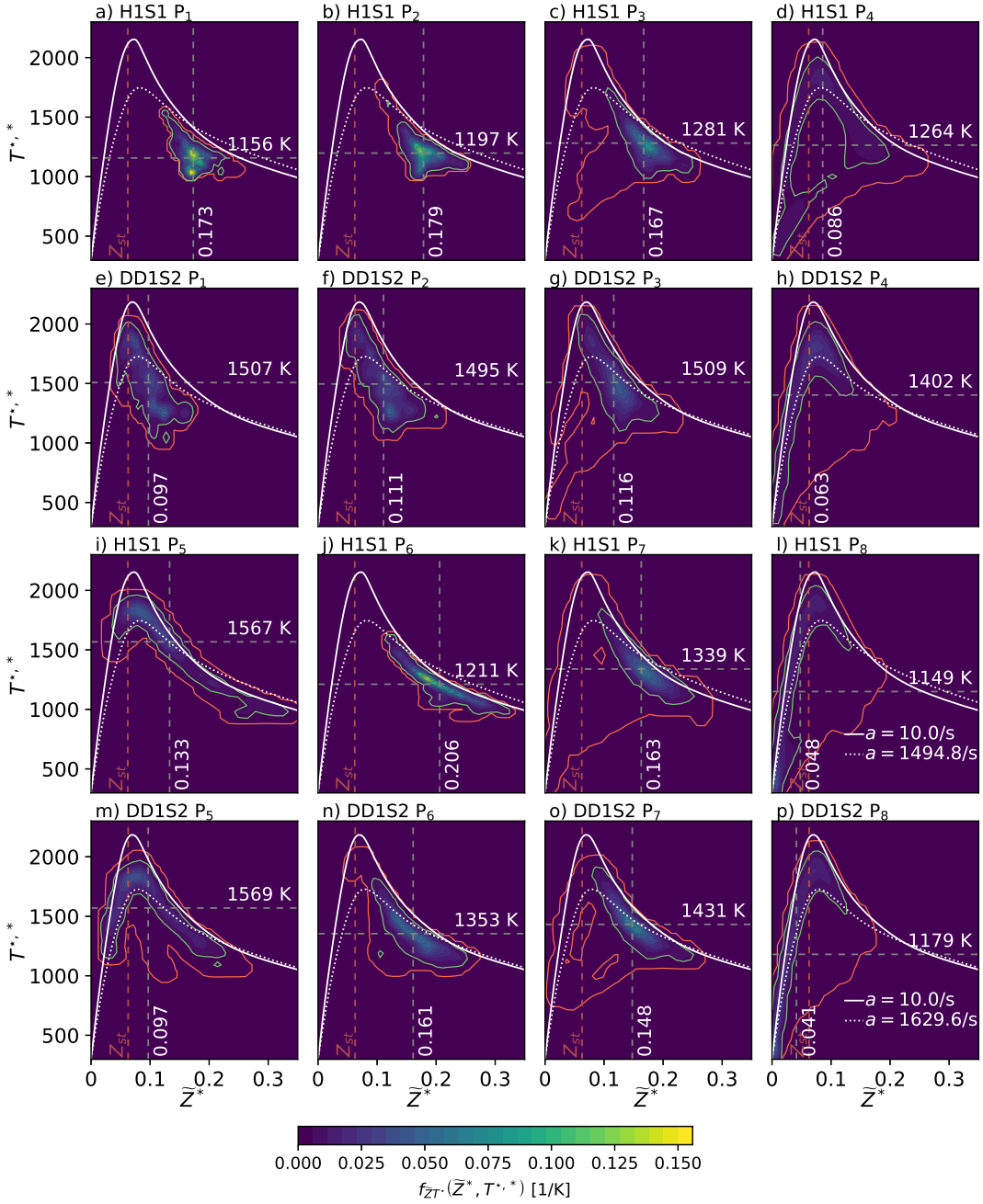

FIGURE 8.40: Joint probability density function of mixture fraction and temperature in monitoring points of the n-heptane (H1S1) and n-dodecane (DD1S2) cases of the Cambridge swirl bluff-body burner. The points P_1 to P_4 correspond to $r \in [8, 10, 12, 14]$ mm at an axial location of $x = 5$ mm, while the points P_5 to P_8 correspond to $r \in [6, 10, 14, 18]$ mm at an axial location of $x = 10$ mm, The dashed lines mark the temporal average of mixture fraction $\left\langle \widetilde{Z} \right\rangle$ and temperature $\langle T^\star \rangle$.

Lean mixtures may be observed in all four points, as opposed to the steadily rich conditions of P_1 and P_2 in the H1S1 flame. In these locations the n-dodecane flame shows significantly higher variability in both mixture fraction and temperature. The

states depart substantially from the equilibrium values, as the joint PDF shows a peak around the $(\widetilde{Z}^*, T^{\star,*}) \approx (0.12, 1100\ \mathrm{K})$ point. This most likely state of partially reacted gases is frequently mixed with near-equilibrium stoichiometric mixtures. At P_3 the behavior of the two flames is similar except that the n-dodecane flame shows munch lower mixture fractions and even pure oxidizer and lean equilibrium states can occur here. Finally, the PDF in the shear layer at P_4 indicates, that the mixing between rich equilibrium conditions and pure oxidizer is less likely in the DD1S2 case, corresponding to the lower probability of lift-off in this simulation.

The joint PDFs at a higher axial location ($x = 10$ mm) show similar trends as Fig. 8.40i-p displays. The average mixture fraction is consistently higher in the n-heptane case. The P_5 point is located near the inner reaction zone, which is heavily affected by the presence of the spray. The span of mixture fractions is very large here, ranging from the lean equilibrium conditions to the richest observed states. The n-heptane flame shows conditions near the stable branch with a smaller presence of lower temperature states around $\widetilde{Z}^* \approx 0.27$. Meanwhile, in the n-dodecane case larger deviations from equilibrium occur at two mixture fractions: $\widetilde{Z}^* \approx 0.12$ and $\widetilde{Z}^* \approx 0.22$. The states near $\widetilde{Z}^* \approx 0.12$ are related to the vertical movement of the mixture fraction field, when states of $(\widetilde{Z}^*, T^{\star,*}) \approx (0.12, 1100\ \mathrm{K})$ reach this higher axial location, which are abundant near P_1 and P_2. The deviation from equilibrium at very rich conditions is the effect of the most intensely evaporating droplets, which introduce fresh reactants to the gas phase at a faster rate than oxidation can occur. The P_6 point is characterized by the richest conditions among the assessed points, as it is located just below the hollow cone spray. In the H1S1 case the states are located near rich equilibrium with little variation in temperature, while in the DD1S2 simulation the a partially reacted mixtures are present at $\widetilde{Z}^* \approx 0.12$ due to the interaction with lean mixtures near the bluff-body. As the instantaneous contours of Fig. 8.24 and Fig. 8.35 show, the mixture field in n-dodecane case is more intermittent. At P_7 and P_8 the mean mixture fraction of the two cases becomes similar, and the differences are more nuanced. As the DD1S2 case produces a more attached flame, the shear layer fluctuates less due to the stabilizing effect of the flame. (Cocks, Soteriou, and Sankaran, 2015) Consequently, in the P_7 point only the more lifted H1S1 case shows the presence of pure oxidizer. In the P_8 point most states are observed near equilibrium as the $f_{\widetilde{Z}T^\star} = 0.005/\mathrm{K}$ iso-line indicates. Meanwhile, an indication of sporadic localized extinction is given by the $f_{\widetilde{Z}T^\star} = 0.0001/\mathrm{K}$ contour.

Overall, the sever under-prediction of the lift-off in the DD1S2 case is related to the observed mixture fraction field and the nature of the applied thermo-chemical manifolds. The outer reacting layer is situated between the fresh oxidizer and the rich equilibrium mixtures of the central recirculation zone. The different evaporation characteristics of the two fuels produces a significantly lower peak mixture fraction in the n-dodecane simulation. As Fig. 8.40d and h suggest, the n-heptane case shows higher localized extinction, because the mixing line between the rich equilibrium mixture and the oxidizer avoids the part of manifold characterized by high source terms. Meanwhile, in the n-dodecane case the same mixing line passes through a region with higher $\overline{\dot{\omega}_{Y_c}}$. Consequently, the mixing rate of the tow gases has to be more intense in the DD1S2 case to avoid approaching the equilibrium. The results may be improved by more elaborate thermo-chemical manifolds, which consider the interaction between fresh reactants and partially reacted mixtures, such as the model of Huang et al. (2022b). Nevertheless, this is out of the scope of the present work.

8.4 Summary of Cambridge swirl bluff-body burner simulations

This chapter presents the numerical study of the Cambridge swirl bluff-body burner. The burner is characterized by a high prevalence of finite rate chemistry effects such as localized extinction, which makes it a challenging case for tabulated chemistry methods. The present analysis departs from the *a priori* assessment of the burner characteristics. The chemical time scales are found to be in the order of magnitude: $\mathcal{O}\,(0.1\text{ ms})$ and $\mathcal{O}\,(0.01\text{ ms})$, with faster reactions observed in the liquid fuels. The simulated cases are characterized by moderate Reynolds numbers similar to the PRECCINSTA burner. Two computational grids are presented, corresponding to a coarse grid that can challenge the sub-grid models, and a fine grid which is more appropriate but entails a greater computational expense.

The simulation method is used in the incompressible limit to analyze the air flow in the burner. Strong recirculation is observed due to the combined effect of the bluff-body and the vortex breakdown in the highly swirling air flow. As the annular air flow is discharged into a combustion chamber of square cross section, asymmetries are observed in the corner recirculation zones, however this does not influence the flow over the bluff-body, that appears to remain axi-symmetric. The cold flow simulations show good agreement with the LDA measurement results indicating the adequacy of the computational grids to represent the turbulent flow. The temporal analysis of the flow reveals a weaker oscillation at a characteristic frequency corresponding to a Strouhal number of $Sr = 1.09$ based on the bluff-body diameter and the bulk air velocity.

The non-premixed methane flame is analyzed using manifolds of stable and unsteady extinguishing counterflow diffusion flamelets. The methane jet is modeled with a turbulent inlet database and the case shows an excellent jet penetration even on the coarse grid, illustrating the capabilities of the developed low-dissipation finite element method. While a slight misalignment is observed between the experimental reacting zone orientation and the present simulations, the flow field agrees well with LDA measurements. The dynamic behavior of the reaction zone is reproduced well, showing a lifted flame in 85% of the instances, with a mean lift-off height only 12% higher than the experimentally determined value. Two thermo-chemical manifolds are tested, one formed by adiabatic flamelets only, and one including heat loss through an artificially scaled radiative source term in the counterflow diffusion flame calculations. This modeling decision seems to have little influence on both the mean and dynamic behavior of the flame. A single point analysis in the central recirculation zone and in the intermittently lifted reaction zone reveals, that the local extinction occurs in mixing layers between the fresh oxidizer and rich equilibrium mixtures which are near the rich flammability limit. The quick mixing of these two states may occur without significant progress variable source terms in instances when the flame is lifted. Finally, the approximate turbulent scales of the single point analysis are used to evaluate the turbulent combustion regime of the case. The flame is identified to be in the "Flamelets" and "Broken flamelets" regime on the diagram of Balakrishnan and Williams (1994), thus the application of tabulated chemistry methods is appropriate based on the time scales of turbulence.

Subsequently the spray flames of the Cambridge swirl bluff-body burner are simulated using an Eulerian-Lagrangian representation of the multiphase flow. A detailed spray injection strategy is implemented, tuned on the experimental PDA and Mie scattering data of the n-heptane case. The behavior of the H1S1 n-heptane flame

is analyzed in detail using a thermo-chemical manifold based on free and burner-stabilized premixed flamelets, as this manifold is found to represent well the finite rate chemistry effects of the outer reaction zone. The mean location of the reaction layers compares well with the planar laser induced fluorescence measurements of the hydroxyl radical, and reasonable agreement is found between the experimental Mie scattering imaging of the spray cloud and the equivalent field in the LES. Comparing with the phase Doppler anemometry results of the fuel droplets, higher discrepancies are found. The origin of these differences is well explained by the size classified droplet data, and the discrepancy is considered to have a lesser influence on the flame behavior. The general temporal evolution of the droplet cloud can be estimated well by crude approximations based on single droplet simulations. I.e.: in the n-heptane case all droplets tend to heat up to the wet-bulb conditions quickly, thus intense evaporation takes place in the central recirculation zone. However, larger droplets may pass through the flame, as the kinematic relaxation to the flow and the evaporation takes significantly longer. In this case the dynamics of the outer reaction zone are predicted well with only -16% error in the mean lift-off. The grid refinement has a limited effect on the flame behavior, with the most affected metric being the lift-off dynamics.

The studied n-heptane flame is also used to assess the effect of different thermo-chemical manifolds. *A priori* there are large differences between the source terms of the different manifolds. The premixed flamelets tend to be more reactive on the lean side compared to diffusion flamelets. Furthermore they are more responsive to heat loss, as under the states of the same control variables the burner-stabilized flamelets are characterized by lower source terms than the counterflow diffusion flamelets with artificially scaled radiative heat loss. The manifold of unsteady extinguishing and reigniting counterflow diffusion flamelets at a single strain rate limits the source terms substantially. The mean flame behavior is only weakly affected by the choice of manifold, with slight differences observed in the mean mixture fraction and OH fields. The lift-off dynamics of the outer reaction layer shows larger differences, with the best predictions provided by the premixed flamelets, followed by the manifold of unsteady extinguishing and reigniting counterflow diffusion flamelets at a single strain rate. This behavior is directly related to the source terms encountered on the mixing line between the rich equilibrium mixtures of the central recirculation zone and the fresh oxidizer. The lowest source terms along this mixing line are found in the premixed manifold, thus the probability of reignition is the lowest and substantial lift-off can occur.

Finally, this configuration is used to analyze the effect of different liquid fuels using manifolds based on free and burner stabilized premixed flamelets. The n-heptane and n-dodecane flames are simulated under the same flow conditions. The PDA measurements suggest, that the spray breakup happens differently in the two cases. In the present LES only the initial axial droplet velocity is adjusted, however more detailed adjustments could further improve the simulation results. The orientation of the outer reaction layer is the same between all three studied reacting cases, including the non-premixed methane case. This suggests, that the flame shape is primarily governed by the flow conditions and the vortex breakdown, and the nature of the flame has a secondary influence. The most essential difference between the simulation cases of the two fuels, is that the n-dodecane flame shows significantly lower mixture fractions. According to the crude estimates of single droplet analysis, this is linked rather to the slower heat-up than to lower evaporation rates, as the wet-bulb temperature is expected to be more than 100 K higher in the n-dodecane case than in the n-heptane case. Injecting the droplets with the same initial temperature,

the n-dodecane case shows significantly lower evaporation rates near the injection site. Based on the experimental data, the n-dodecane flame is expected to be more lifted then the n-heptane case. The present simulation strategy cannot capture this trend, as the LES of the n-dodecane case produces a mostly attached flame. The lift-off characteristics is predicted significantly better in the n-heptane case than in the n-dodecane case. The cause of more attached flames in the n-dodecane case is found to be the lower mixture fraction in the central recirculation zone. Namely, in the n-dodecane case the mixing line between the recirculating rich equilibrium material and the fresh oxidizer passes through a state of higher tabulated source terms, which increases the probability of reignition. More elaborate chemistry models are needed to consistently predict the local extinction behavior of this mixing layer, irrespective of the composition of the recirculating gases.

Overall, the developed low-dissipation finite element scheme is suitable for the study of complex multiphase reacting flows. A substantial uncertainty is associated to the initial conditions of the Lagrangian droplets, which are tuned here based on measurement data. The spray models shall rely less on such *a priori* information, in order to make the present approach universally applicable in unknown situations. Despite this uncertainty, the present analysis highlights the behavior and applicability of various tabulated chemistry methods, including the root cause of their different performance in predicting finite rate chemistry effects. Such insight not only helps in the understanding of the Cambridge swirl bluff-body burner's behavior, but it is generally transferable to other similar configurations.

Chapter 9

Conclusions

Turbulent combustion is expected to retain an important role in key applications of the transportation, power, and industrial sectors in the transition to net-zero carbon emission technologies. The field is facing new challenges associated to the broad spectrum of novel sustainable fuel candidates. In particular, the aviation industry is projected to widely adapt the usage of biofuels and hydrogen-based fuels in the coming decades, while the regulations concerning non-CO_2 emissions are becoming more stringent. (IEA, 2021a; ICAO, 2023) The long standing technological challenges of gas turbine combustion related to the burner operability and pollutant emissions call for the continued study of these technologies. Large-eddy simulation of combustion systems provides valuable insight into these complex phenomena. This dissertation presents a framework for the study of turbulent flames using tabulated chemistry coupled with a low-dissipation LES solver implemented in the parallel multi-physics simulation code: Alya. (Vázquez et al., 2016) The approach aspires to be predictive in terms of the mean and dynamic flame behavior, while reducing the necessary modeling decisions and parameter tuning from the side of the user.

The main activities of this work are classified in two categories: development of computational tools and analysis of the combustion phenomena with said tools. The former encompasses the development of various new pre- and post-processing tools and the implementation of new functionalities within Alya, while the latter primarily concerns the detailed study of two model aero-engine combustors operated with hydrogen and normal alkanes respectively, with supporting studies in simplified configurations.

In particular, a unified framework is built for the calculation of various 1D flamelet solutions by interfacing with well established flamelet solvers: Cantera and Chem1D (Goodwin, 2002; Somers, 1994). The same framework also serves for processing the flamelet solutions and creating the thermo-chemical manifolds, with a precise treatment of the non-injectivity effects. As the present tabulated chemistry approach uses a polynomial representation of the thermal state, special care is taken regarding the application of presumed filter probability density functions in order to preserve consistency between the computation of temperature from enthalpy and its application in the ideal gas law. The tool is capable of recreating the chemistry tables shown throughout this work without the need for extensive programming background from the user, thus the learning-curve of using tabulated chemistry methods is flattened. A stand-alone single droplet model is implemented for the study of widely used evaporation models, allowing the straightforward evaluation of droplet behavior. Within this tool an implicit time integration scheme is devised based on a numerically evaluated Jacobian. The evaporation models are also implemented in Alya, using this numerical scheme. A new material property model is introduced in the framework of droplet transport, which exploits the information

contained in the thermo-chemical manifolds, simplifying the coupling of the Lagrangian droplets with the tabulated chemistry methods. Another standalone tool is built to analyze the monitoring point data produced by the LES simulations in Alya. This tool automates various tasks, including the estimation of Kolmogorov and turbulence integral scales, the identification of the monitoring points on various turbulent combustion regime diagrams, and the calculation of temporal spectra and joint probability density functions of properties. Finally, substantial developments are made within Alya. The incompressible low-dissipation finite element scheme is extended to variable density flows in the low Mach number limit. The flexibility of the tabulated chemistry models are improved in Alya, allowing for the solution an arbitrarily complex set of governing equations corresponding to the control variables of the thermo-chemical tables, and to post-processing variables. The manifolds are likewise treated in a flexible way. Furthermore, the Lagrangian particle transport method of Alya is equipped to represent evaporating particles, that are coupled to the gas phase field. The performance of the developed method is validated using various laminar and turbulent test cases under inert and reacting conditions. The continued development of all software is supported by automated unit and regression tests, ensuring the reproducibility of the presented results.

Throughout this dissertation various analyses are presented regarding phenomena in laminar and turbulent multiphase reacting flows. One dimensional flamelet calculations are used to assess different phenomena in a well controlled environment. Unsteady counterflow diffusion flamelets are simulated with different initial conditions to study the transient effects in extinction and reignition. The heat loss effects are studied by applying a burner-stabilized boundary condition on premixed flamelets, and an artificially scaled radiative heat loss term on counterflow diffusion flamelets. The performance of different progress variable definitions in representing the flamelet states is assessed. The developed single droplet tool is applied to thoroughly analyze various evaporation modeling approaches. Simulations are performed in simple configurations using Alya to asses the effect of sub-grid models and different thermo-chemical manifolds on flame propagation. The influence of the length scale parameter in the applied synthetic turbulent inlet approach is evaluated using the DLR-A turbulent jet. Finally, the developed simulation approach is applied for the analysis of the swirl stabilized hydrogen burner of TU Berlin, and the Cambridge swirl bluff-body burner. In the former case, two stable operating conditions are simulated gradually approaching the flashback limit. The flow instabilities are studied in detail, and the effect of mixture stratification is assessed by comparing a perfectly premixed and a technically premixed case. The Cambridge swirl bluff-body burner is studied under inert and stable reacting operating conditions, using methane, n-heptane, and n-dodecane as fuels. The cases are evaluated concentrating on the localized extinction phenomena in the outer reaction layer. The n-heptane flame is used to assess different tabulated chemistry strategies, and the n-heptane and n-dodecane flames are compared, analyzing the effect of the fuels. The findings of these analyses are summarized in detail after each chapter. Below the key conclusions are highlighted.

- Unsteady extinguishing and reigniting counterflow diffusion flamelets at a given strain rate tend to relax to very similar thermo-chemical states, except at low strain rates, where the initial condition influences the pathway of reignition.

- Heat loss limits the stable reacting flamelet solutions, with similar lower enthalpy limits observed in both premixed burner-stabilized flamelets and counterflow diffusion flamelets subjected to an artificially scaled radiative heat loss. Steady reactions become infeasible below certain temperatures.

- Thermo-chemical manifolds based on counterflow diffusion flames face notable problems regarding the injective definition of the progress variable. The shortcomings are concentrated on the description of rich mixtures near equilibrium.

- The Abramzon-Sirignano droplet evaporation considers the Stefan flow and the interaction of Stefan flow with the droplet motion, showing good performance under atmospheric pressure and flame-like gas phase conditions.

- Under the studied conditions, the non-equilibrium droplet interface effects considered by the Langmuir-Knudsen model are not expected to introduce significant changes in the evolution of sprays, compared to other models that also consider Stefan flow effects appropriately.

- At low seen gas temperatures the time scale of evaporation is significantly longer than the time scale of kinematic relaxation, however the two scales become comparable under flame-like conditions, meaning that relaxation to the gas phase velocity and droplet evaporation occurs simultaneously.

- The applied synthetic turbulent inlet model of pipe flows shows slight sensitivity to the selected length scale, however its applicability is also constrained by the scales representable on the inlet grid. Overall, turbulent mixing in the jet flow is induced by all tested length scales, with slight variations in the jet core evolution.

- Mixture stratification plays an important role in the turbulent flame stabilization mechanism of the swirl stabilized hydrogen flame of TU Berlin. Combustion-induced vortex breakdown is expected to be the driving mechanism of flashback, as parts of the flow become non-flammable with highly reactive mixtures concentrated in the center of the mixing tube.

- In the Cambridge swirl bluff-body burner tabulated chemistry methods are used to predict the shear induced localized extinction of the outer reaction zone. The extinction characteristics show strong sensitivity to the applied thermo-chemical manifold. The reacting layer is situated between the fresh oxidizer and rich equilibrium gases of the central recirculation zone, thus substantial extinction is possible if the mixing line between these two gas states has low reactivity. Good performance is found in cases, where this mixing line avoids the regions of the thermo-chemical manifold characterized by notable source terms. This is the case in the non-premixed methane flame using a manifold of counterflow diffusion flamelets, and in the n-heptane spray flame using premixed flamelets. However, in the n-dodecane spray flame the mixing line experiences notable source terms, and the probability of localized extinction is under-predicted. The evaluated tabulated chemistry methods do not explicitly consider the mixing between fresh oxidizer and rich equilibrium mixtures, and may over-predict the local concentration of radicals and the reaction rates.

- The two studied n-alkane liquid fuels of the Cambridge swirl bluff-body burner show similarities in their chemical behavior, while they differ substantially in terms of volatility. Consequently, the n-dodecane flame is characterized by a significantly leaner mixture field than the n-heptane flame. Single droplet simulations confirm, that the difference originates from the delayed heat-up time of the n-dodecane, while once the wet-bulb conditions are reached the two fuels evaporate at a similar rate.
- The developed low-dissipation finite element LES solver, coupled with tabulated chemistry methods and Lagrangian particle transport, is able to predict complex flame behavior without the need for case-by-case tuning of the modeling constants. Although uncertainties persist in terms of selecting the proper thermo-chemical tabulation strategy, and in the modeling of fuel spray injection.

9.1 Perspective

Overall, the objectives listed in section 1.3 are achieved, while various opportunities for further improvements are identified. Below, possible future model development and research activities are summarized.

- Computational optimizations are constantly needed to improve the performance of Alya.
  - The code needs to adapt to the ongoing paradigm shift in supercomputer architectures. More work is necessary to ensure that Alya simulations can be executed on future supercomputers.
  - A recent analysis of the code (POP, 2021) identified the potential of further optimizing the table lookup procedures. The tabulated chemistry algorithms need to be adapted to properly exploit the computational resources.
- While the present framework is capable of providing valuable insight into the complex flame behavior, the combustion LES capabilities of Alya may be further developed.
  - In this work the dissipative properties of the Navier-Stokes solver are examined, however there is room for improvement especially in terms of the scalar transport methods. Higher order finite element grids shall be explored for combustion phenomena, while new low-dissipation schemes may be developed as well.
  - The sub-grid combustion modeling strategy applied here is well established in the literature, however many recent works propose improvements. Such models shall be assessed within Alya.
  - Grid refinement may affect detrimentally the presently used Eulerian-Lagrangian representation of fuel sprays. Modeling approaches shall be explored to make the droplet evaporation grid-independent.
  - The most appropriate selection of thermo-chemical tables may vary from case-to-case or even between different regions of the flame. The method of Illana, Mira, and Mura (2021) shall be extended to LES in order to automate the local selection of the thermo-chemical manifold constructed from premixed and counterflow diffusion flamelets.

  - A major modeling uncertainty in simulating liquid fuels is associated to the spray atomization. Here phenomenological models are tuned based on detailed measurement data. Improvements are necessary in the treatment of atomization in Alya, to remove this uncertainty in *a priori* unknown cases.

- The simulation framework shall be consolidated and the presented results should be further analyzed including new applications in order to properly exploit the developments of this work.

  - The general observations regarding flamelet and droplet behavior shall be reiterated under high pressure conditions relevant to gas turbines.
  - While tabulated chemistry in combustion LES is a powerful tool, it assumes certain behavior of the combustion phenomena. The turbulent flames discussed in this study shall be simulated using alternative combustion models in order to gain more confidence in the conclusions. Such models shall be implemented in Alya, to avoid the influence of numerical methods.
  - The LES studies presented here generate a high amount of data, which may be further analyzed to fully exploit the computational effort.
  - The transient flashback conditions in the swirl stabilized hydrogen flame may be explored using the existing modeling setup.
  - Likewise, the transient blow-off conditions in the Cambridge swirl bluff-body burner at both gaseous and spray flame configurations may be studied.
  - Combustion systems of various fields can be readily analyzed without further development. The analysis of higher TRL systems would have a higher impact on the decarbonization efforts.
  - The structure of the tabulated chemistry solver allows for the straightforward coupling with emission models, which shall be further explored.

Appendix A

Mixture fraction and scalar dissipation rate in counterflow flames

The transport equation of mixture fraction in a counterflow diffusion flame configuration under the unity Lewis number assumption can be written as:

$$\frac{\partial \rho Z}{\partial t} + \frac{\partial \rho u Z}{\partial x} - \frac{\partial}{\partial x}\left(\rho \mathcal{D}_t \frac{\partial Z}{\partial x}\right) = -\rho G Z. \tag{A.1}$$

Under the assumptions of constant density and constant thermal diffusivity, this equation can be simplified to, using the continuity equation:

$$\frac{\partial Z}{\partial t} + u\frac{\partial Z}{\partial x} - \mathcal{D}_t \frac{\partial^2 Z}{\partial x^2} = 0. \tag{A.2}$$

Under the same constant density assumption, the velocity field of a purely straining flow is:

$$u = -xa, \tag{A.3}$$

so the steady-state mixture fraction equation is:

$$-xa\frac{\partial Z}{\partial x} - \mathcal{D}_t \frac{\partial^2 Z}{\partial x^2} = 0, \tag{A.4}$$

and the analytical solution of this equation is the one presented in Eq. (3.17):

$$Z = \tfrac{1}{2}\left[1 - \operatorname{erf}(\zeta)\right], \tag{A.5}$$

with $\zeta = x\sqrt{a/\left(2\mathcal{D}_t\right)} = x/\delta_{diff}$. (Peters, 1983)

This analytical solution is compared to the numerical solution of Chem1D in Fig. A.1, for mixing air: $X_{O_2} = 0.21$, $X_{N_2} = 0.79$, with air marked with an insignificant amount of methane: $X_{O_2} = 0.2095$, $X_{N_2} = 0.7895$, $X_{CH_4} = 0.001$ at a strain rate of $a = 300/\text{s}$. Both inlet streams are at room temperature: $T_f = T_o = 298.15$ K, and the pressure is set to $P = 101325$ Pa. The diffusivities are all taken equal according to the unity Lewis number assumption. The thermal diffusivity is taken in accordance with the GRI3.0 (Smith et al., 2011) chemical mechanism. The simulation domain is limited to $x \in [-6.912, 4.608]$ mm corresponding to $-18\delta_{diff}$ and $12\delta_{diff}$ respectively.

As Fig. A.1 shows, in the case of this quasi-constant composition and isothermal problem (corresponding to quasi-constant properties), the numerical solution given

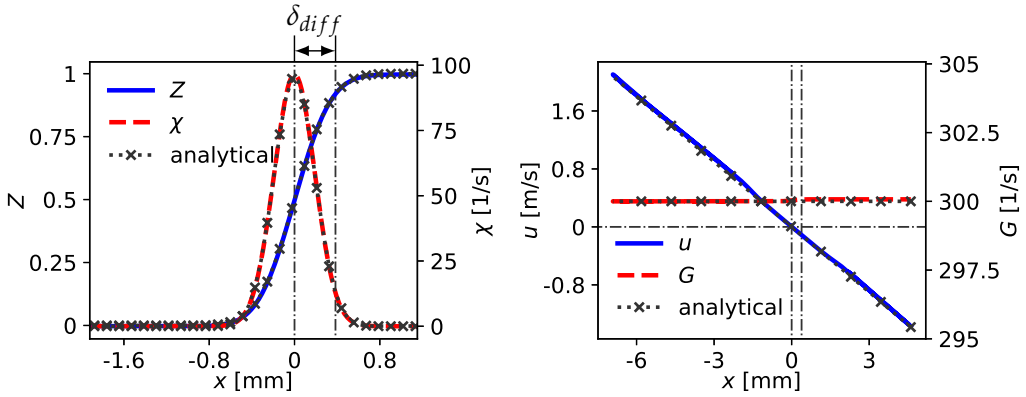

FIGURE A.1: Constant density mixing in 1D counterflow configuration of air and air marked with a trace amount of methane using the unity Lewis number assumption at a strain rate of $a = 300/\text{s}$. The profiles calculated with Chem1D (Somers, 1994) using the GRI3.0 (Smith et al., 2011) chemical mechanism are compared with the analytical solution. The illustrated quantities are, mixture fraction Z, scalar dissipation rate χ, velocity u, and stretch rate G.

by Chem1D completely reproduces the analytical solution. The mixture fraction follows the error-function profile, and consequently the scalar dissipation rate takes the form of a Gaussian function. Both profiles are characterized by a length scale of $\delta_{diff} = \sqrt{2\mathcal{D}_t/a} = 0.384$ mm, as the thermal diffusivity in air is $\mathcal{D}_t = 0.221$ cm^2/s. The maximum scalar dissipation rate is given by $a/\pi = 95.5/\text{s}$. The velocity profile follows the linear potential flow solution: Eq. (A.3), and the stretch rate is equal to the strain rate throughout the domain.

Variable density and diffusivity effects complicate the problem, and an analytical solution is no longer straightforward. Figure A.2 illustrates the non-reacting mixing between air and methane under the same conditions as described above. The far field on the fuel side still behaves as a potential flow, but characterized by a different strain rate, scaled with the square root of the density ratio $\sqrt{\rho_{ox}/\rho_f}$, as shown on Fig. 3.10. Thus the fuel side is characterized by higher velocities, since the densities are: $\rho_{ox} = 1.18$ kg/m^3 and $\rho_f = 0.65$ kg/m^3 for oxidizer and fuel respectively. Overall, the mixture fraction profile of air-methane mixing is slightly wider than the constant property solution mostly due to the density difference, and consequently the Z gradient is smaller, thus the scalar dissipation rate is slightly smaller as well, with a peak value of: 87.1/s.

The case further deviates from the constant property analytical solution in the presence of the flame. Figure A.3 illustrates mixture fraction and the flow field in the stable reacting flamelet of air and methane at a strain rate of $a = 300/\text{s}$ calculated with the unity Lewis number assumption. The main differences are related to the low density and high diffusivity characterizing the reacting layer. Under theses conditions, the stretch rate is much higher in the center of the domain than on any of the boundaries.

The velocity profile of the reacting case still resembles the potential flow conditions in the far field, although on the oxidizer side ($x < 0$) it is shifted compared to the constant property case, so $u^L = -ax^L$ is not valid on this domain. Note that this difference diminished by further increasing the domain size (not shown here),

however, since Chem1D represents the momentum conservation with the stretch equation Eq. (3.12) the domain is already sufficiently large, as G is smooth on both boundaries. Furthermore, the velocity profile is characterized by local extrema, as the flame is located on the oxidizer side, since $Z_{st} = 0.0552$ is below 0.5. On this part of the domain the velocity is positive, and local extrema can be created by thermal expansion, as the flow accelerates faster, than the stretch effects decelerate it.

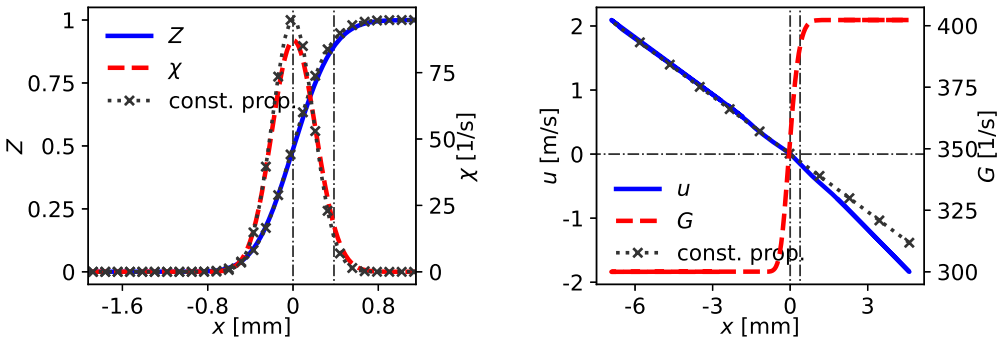

FIGURE A.2: Cold mixing in 1D counterflow configuration of air and methane using the unity Lewis number assumption at a strain rate of $a = 300/\text{s}$. The profiles calculated with Chem1D (Somers, 1994) are compared with the analytical solution of constant properties.

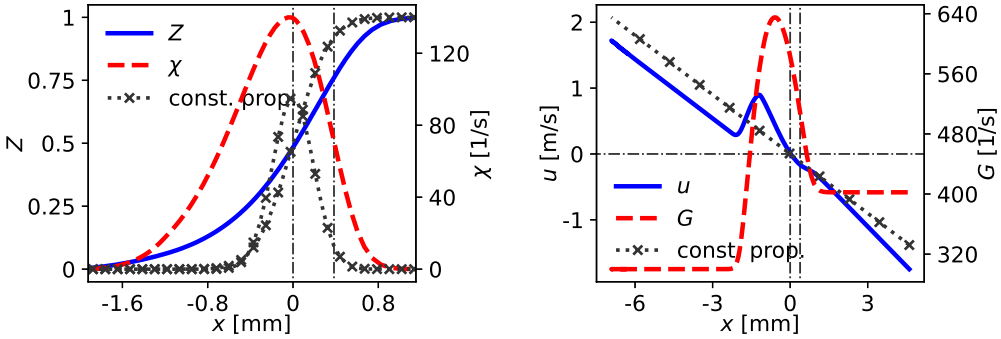

FIGURE A.3: Flow field in reacting 1D counterflow configuration of air and methane using the unity Lewis number assumption at a strain rate of $a = 300/\text{s}$. The profiles calculated with Chem1D (Somers, 1994) are compared with the analytical solution of constant properties.

In the reacting case the mixture fraction field is significantly wider, than in case of the constant property solution, as the flame front influences the mixing by the increase of the diffusivities and by thermal dilation. However, despite the lower mixture fraction gradient, the scalar dissipation rate is still higher than in case of the analytical solution, since the thermal diffusivity in the flamelet is very high. The temperature effect on thermal diffusivity is illustrated on Fig. 2.1, to further highlight, in the flame presented here, the maximum thermal diffusivity is 6.04 cm^2/s, which is ~ 27 times higher than the thermal diffusivity at the inlets.

Note, that if one would calculate the peak scalar dissipation rate $\max(\chi)$, or the stoichiometric scalar dissipation rate χ_{st}, and used the constant property solution: $\chi = \frac{a}{\pi} \exp\left(-2\left[\text{erf}^{-1}\left(1-2Z\right)\right]^2\right)$ to obtain an equivalent stain, then the strain rate would be significantly over-predicted. This effect is further illustrated on Fig. A.4, showing the scalar dissipation rate in mixture fraction space, comparing the analytical solution obtained with constant properties to the numerically obtained profiles of stable and unstable steady-state flamelets. In mixture fraction space, the error between the two solutions appears to be lower, as the effect of the different mixing thickness is not present because of the change of coordinates. The right plot shows, that the ratio of the two scalar dissipation rates is the highest near the stoichiometric mixture, and it decreases to 1 near the two inlets. The magnitude of the highest difference seems to increase with temperature, and it is around 2 for stable burning flamelets.

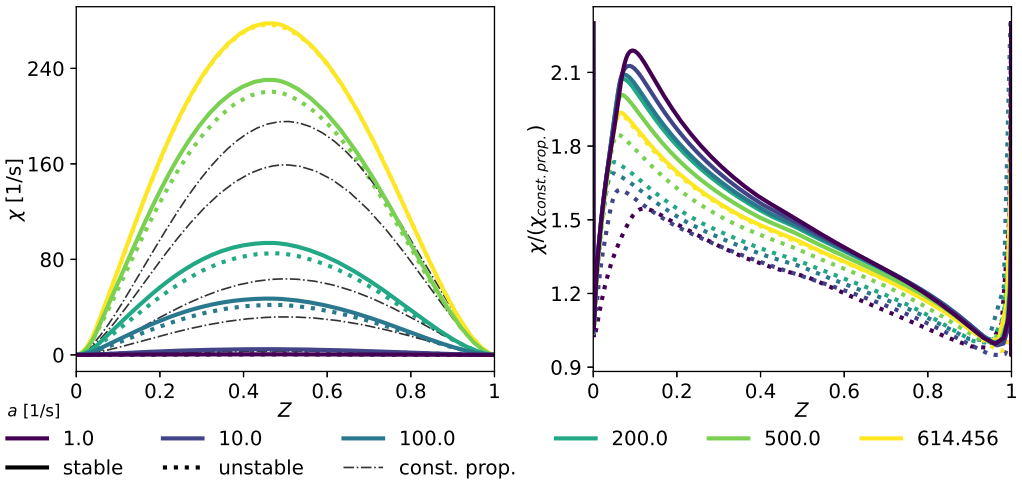

FIGURE A.4: Scalar dissipation rate in in mixture fraction space in 1D counterflow configuration of air and methane using the unity Lewis number assumption. The profiles calculated with Chem1D (Somers, 1994) are compared with the analytical solution of constant properties.

Overall, the analytical solution of scalar dissipation rate in constant property flows, represents a significant deviation compared to numerical solutions in reacting flows. This deviation is very large in physical space, but in mixture fraction space the general trends are reproduced with an maximum error of ~ 2 in mixture fraction space. The model function $\exp\left(-2\left[\text{erf}^{-1}\left(1-2Z\right)\right]^2\right)$ partially fits the numerical scalar dissipation rate profiles, provided that it is scaled appropriately. The χ profile has the most impact in the flame region, thus a scaling of $\sim 2a/\pi$ seems to be more appropriate. As stated above, in this case the strain rate can no longer be inferred from the analytical solution, but a parametrization based on stoichiometric scalar dissipation rate can provide the equivalence between solutions in physical space (Eq. (3.9), Eq. (3.10), Eq. (3.11), and Eq. (3.12)) and solutions in mixture fraction space (Eq. (3.15)), eliminating the need to know the most accurate scaling factor.

Appendix B

Functions of liquid and phase change properties

The phase change and liquid property calculations are based on the data of Daubert and Danner (1985). Five of the property functions defined by the National Standard Reference Data Series (NSRDS) are used in order to evaluate the temperature dependence of these properties:

$$f_0 = a + bT + cT^2 + dT^3 + eT^4 + fT^5, \tag{B.1}$$

$$f_1 = \exp\left(a + \frac{b}{T} + c\ln(T) + dT^e\right), \tag{B.2}$$

$$f_5 = \frac{a}{b\left[1+\left(1-\frac{T}{c}\right)^d\right]}, \tag{B.3}$$

$$f_6 = a\eta^{b+cT+dT^2+eT^3}, \tag{B.4}$$

$$f_{14} = \frac{a^2}{\eta} + b - 2ac\eta - ad\eta^2 - \frac{c^2}{3}\eta^3 - \frac{cd}{2}\eta^4 - \frac{d^2}{5}\eta^5, \tag{B.5}$$

where $\eta = 1 - \frac{T}{T_c}$ is one minus the reduced temperature with T_c being the critical temperature of the species. The coefficients and critical temperatures are summarized below in Tab. B.1, Tab. B.2, Tab. B.3, Tab. B.4, and Tab. B.5 for water, OME1 (dimethoxymethane, formerly methylal), n-heptane, n-decane, and n-dodecane respectively.

TABLE B.1: NSRDF functions and their coefficients for water properties according to Daubert and Danner (1985). ($W = 18.015$ kg/kmol, $T_c = 647.13$ K, $P_c = 219.4$ bar)

	L_v	P_{sat}	$c_{p,p}$	ρ_p
Function	f_6	f_1	f_0	f_5
a	2889425.47876769	73.649	15341.1046350264	98.343885
b	0.3199	−7258.2	−116.019983347211	0.30542
c	−0.212	−7.3037	0.451013044684985	647.13
d	0.25795	4.1653×10^{-6}	−0.000783569247849015	0.081
e		2	$5.20127671384957 \times 10^{-7}$	

TABLE B.2: NSRDF functions and their coefficients for OME1 properties (Enerxico, 2021).
($W = 76.095$ kg/kmol, $T_c = 480.6$ K, $P_c = 40.7$ bar)

	L_v	P_{sat}	$c_{p,p}$	ρ_p
Function	f_6	f_1	f_0	f_5
a	530000	14.0085839	1664.2	6.41848303
b	0.38795	−2920.0	−3.8936	0.07863948
c		1.18	0.0169	480.6
d				0.125224401
e				

TABLE B.3: NSRDF functions and their coefficients for n-heptane properties according to Daubert and Danner (1985).
($W = 100.20592$ kg/kmol, $T_c = 540.2$ K, $P_c = 27.19$ bar)

	L_v	P_{sat}	$c_{p,p}$	ρ_p
Function	f_6	f_1	f_{14}	f_5
a	499121.791545248	87.829	6.11976102401216	61.38396836
b	0.38795	−6996.4	3137.69909384855	0.26211
c		−9.8802	182.274175063868	540.2
d		7.2099×10^{-6}	−254.530511150515	0.28141
e		2		

TABLE B.4: NSRDF functions and their coefficients for n-decane properties according to Daubert and Danner (1985).
($W = 142.285$ kg/kmol, $T_c = 617.7$ K, $P_c = 20.91$ bar)

	L_v	P_{sat}	$c_{p,p}$	ρ_p
Function	f_6	f_1	f_0	f_5
a	464743.296904101	112.73	1958.18252099659	60.94208835
b	0.39797	−9749.6	−1.39094071757388	0.25745
c		−13.245	0.00754612221948905	617.7
d		7.1266×10^{-6}		0.28912
e		2		

TABLE B.5: NSRDF functions and their coefficients for n-dodecane properties according to Daubert and Danner (1985).
($W = 170.338$ kg/kmol, $T_c = 658.0$ K, $P_c = 18.22$ bar)

	L_v	P_{sat}	$c_{p,p}$	ρ_p
Function	f_6	f_1	f_0	f_5
a	454020.829174935	137.47	2983.53861146661	60.53982858
b	0.40681	−11976.0	−8.0352006011577	0.25511
c		−16.698	0.018207916025784	658.0
d		8.0906×10^{-6}		0.29368
e		2		

Examples of these functions are assessed in Fig. B.1. The liquid density, liquid specific heat, saturation pressure, and heat of vaporization are plotted according to the coefficients and template functions specified in Tab B.1, Tab B.3, and Tab B.5 for water, n-heptane, and n-dodecane respectively. At lower temperatures the density functions (Eq. (B.3)) behave rather linearly, however near the critical point of the fluid, the density abruptly drops. For reference, the vapor density is also plotted as function of temperature, assuming the pressure is the saturation pressure of the material, and further assuming, that the ideal gas law holds according to Eq. (2.5). The difference between the liquid and vapor densities correctly diminishes as the critical point is approached. The remaining difference might be a shortcoming of the ideal gas law applied to the saturated vapor, as pointed out by Ebrahimian and Habchi (2011).

Two distinct functions are used in case of the specific heat. For n-heptane a rather elaborate function f_{14} (Eq. (B.5)) is applied, while all other fluids used in this work are described using a simple polynomial: f_0 (Eq. (B.1)). As Fig. B.1 shows, the specific heat of the two hydrocarbons n-heptane and n-dodecane behave rather similarly at low temperatures. However, the elaborate specific heat function of n-heptane: f_{14} has a singularity near the critical point. This behavior is capturing the physical phenomenon more accurately, as in the vicinity of the critical point the isobaric heating of the fluid does not result in an increase of temperature. However, the presence of this singularity may cause numerical difficulties in high pressure applications. Although, such elevated pressures are out of the scope of this work, it is advised to apply these functions cautiously near the critical point of the materials.

The saturation pressure increases with temperature as expected. Upon closer inspection one may see, that the function f_1 (Eq. (B.2)) is an extension of the Clausius-Clapeyron relation, that describes the slope of saturation pressure curve as function of the temperature and other properties:

$$\frac{\mathrm{d}P_{sat}}{\mathrm{d}T} = \frac{L_v}{T\Delta\left(\frac{1}{\rho}\right)}, \tag{B.6}$$

where $\Delta\left(\frac{1}{\rho}\right)$ is the difference in specific volume between saturated vapor and saturated liquid and L_v is the latent heat of evaporation, all evaluated under the specific saturation conditions. Far from the critical point, one may neglect the specific volume of the liquid when calculating the change of specific volume: $\Delta\left(\frac{1}{\rho}\right) \approx \frac{1}{\rho_g}$, since the liquid is significantly more dense than its vapor: $\rho_p \gg \rho_g$. Furthermore the ideal gas law may be applied to calculate the vapor density. Thus, after integration along temperature, the Clausius-Clapeyron relation can be expressed as:

$$\ln\left(\frac{P_{sat,2}}{P_{sat,1}}\right) = -\frac{L_v W}{R_u}\left(\frac{1}{T_2} - \frac{1}{T_1}\right), \tag{B.7}$$

where $P_{sat,1}$ and T_1 have to be a known pair of saturation pressure and temperature.

Finally Fig. B.1 also shows the heat of vaporization. The function f_6 (Eq. (B.4)) inherently approaches 0 near the critical point as expected, since differences between the two phases are diminishing. At lower temperatures, the temperature dependence of L_v is fairly weak, however it is not negligible.

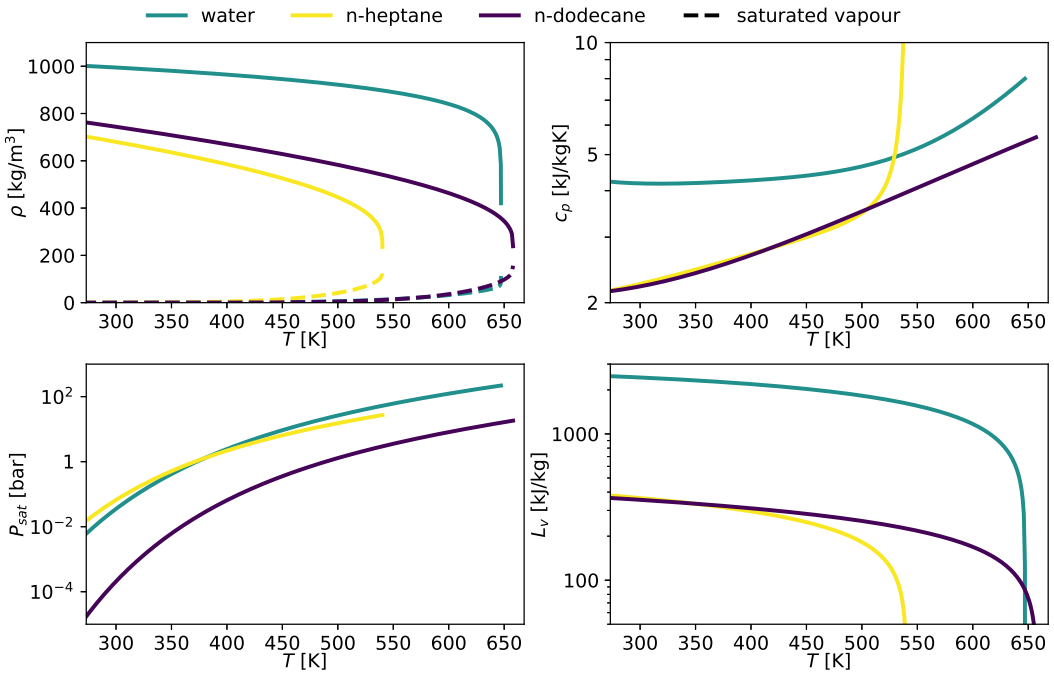

FIGURE B.1: Liquid and phase change properties of water, n-heptane, and n-dodecane as function of temperature. Upper left: density, upper right: specific heat, lower left: saturation pressure, lower right: heat of vaporization. The ideal gas density of saturated vapour is showed for comparison.

Appendix C

Validation of liquid and phase change property functions

This appendix presents a comparison between empirical data and the functions of Daubert and Danner (1985). The referenced sources of experimental liquid and phase change properties are summarized in Tab. C.1.

TABLE C.1: Reference data of liquid and phase change properties for water, n-heptane, and n-dodecane.

	water	n-heptane	n-dodecane
L_v	Schmidt and Grigull (1989)	Majer et al. (1979)	Viton, Chavret, and Jose (1996)
P_{sat}	Schmidt and Grigull (1989)	Willingham et al. (1945)	Morgan and Kobayashi (1994)
$c_{p,p}$	Schmidt and Grigull (1989)	Meijer et al. (1977)	Finke et al. (1954)
ρ_p	Schmidt and Grigull (1989)	Sagdeev et al. (2013)	Caudwell et al. (2004)

Figure C.1 illustrates the saturation pressure correlations of function f_1 of Daubert and Danner (1985), along with the reference data. The functions are presented in the commonly used $\log(P) - 1/T$ coordinates, where the Clausius-Clapeyron relation results in a linear behavior, given that it is evaluated using a constant latent heat. The functions of Daubert and Danner (1985) match the reference data perfectly, including the deviations from the Clausius-Clapeyron relation at low pressure. In general, even these deviations are relatively small, thus, using the assumption of ideal gas density, and constant heat of vaporization with the Clausius-Clapeyron relation would also be a fairly accurate representation of the saturation pressure.

The other liquid and phase change properties are shown in Fig. C.2 in more detail for atmospheric applications. The functions of Daubert and Danner (1985) are evaluated between 273.15 K and the saturation temperature of the fluids at $P = 1$ atm: 373.16 K, 371.54 K, 489.52 K for water, n-heptane, and n-dodecane respectively. The properties are normalized with their values at saturated conditions.

As Fig. C.2 illustrates, the hydrocarbons exhibit large changes ($> 10\%$) in all three properties on the selected temperature range. Thus the consideration of variable liquid properties is justified for the modeling of these fuels. For studies involving water, constant properties may be used as the variation of the properties is considerably smaller. Figure C.2 also shows a comparison with reference data from various sources listed in Tab. C.1. The functions of Daubert and Danner (1985) fit this reference data adequately for atmospheric applications.

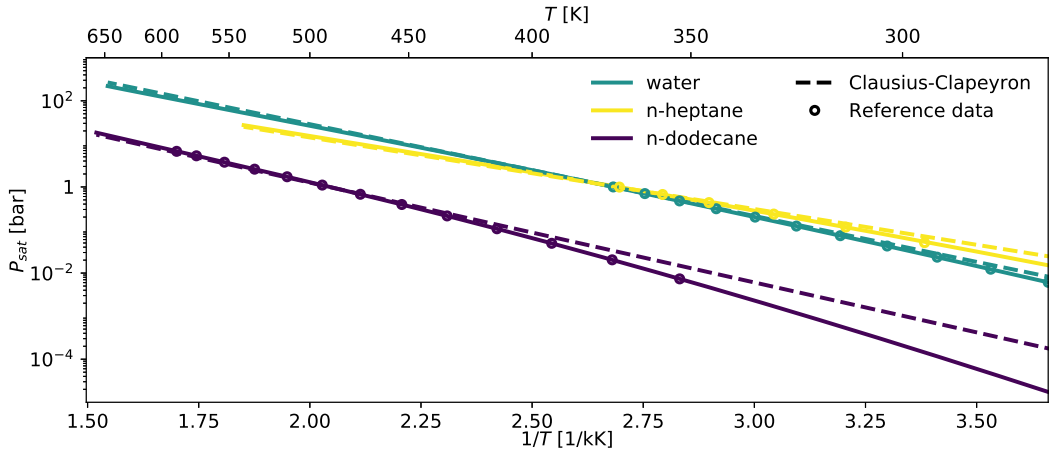

FIGURE C.1: Comparison of function f_1 of Daubert and Danner (1985) and the Clausius-Clapeyron relation (Eq. (B.7)) for water, n-heptane, and n-dodecane as function of temperature. L_v, $P_{sat,1}$, and T_1 of Eq. (B.7) are evaluated at 1 atm. Reference data from Schmidt and Grigull (1989), Willingham et al. (1945), and Morgan and Kobayashi (1994). Note, that the logarithmic scale magnifies the differences for n-dodecane.

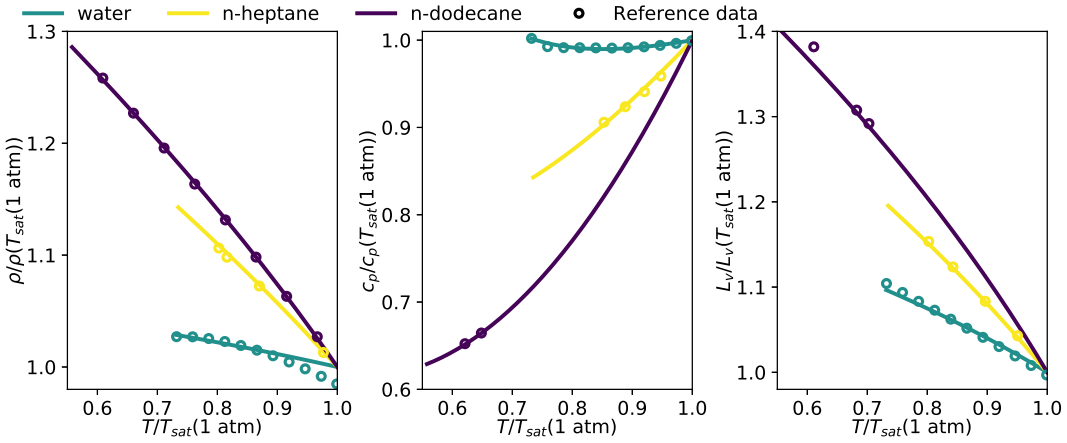

FIGURE C.2: Density, specific heat, and heat of vaporization of water, n-heptane, and n-dodecane as function of temperature according to Daubert and Danner (1985). The reference data sources are summarized in Tab. C.1.

Appendix D

Nusselt and Sherwood number of sphere in quiescent fluid

In this appendix it is shown that the Nusselt and Sherwood numbers of a spherical body in contact with quiescent fluid are 2. This follows directly from the film-thickness based interpretation of these non-dimensional numbers. However, it is worth to reinforce this relation by the derivations presented below.

D.1 Nusselt number

Take a sphere of radius r_p, with surface temperature T_p, immersed in a fluid with far-field temperature of T_s. Assume furthermore constant thermal conductivity λ_m throughout the fluid, and zero mass flux. Fourier's law of thermal conduction implies states, that the diffusive heat flux $\mathbf{\Phi}_T^{diff}$ is proportional to the temperature gradient, such that:

$$\mathbf{\Phi}_T^{diff} = -\lambda_m \nabla T. \tag{D.1}$$

This diffusive heat flux is the only mode of energy transport, since the mass flux around the sphere is zero: $\mathbf{\Phi}_{T,r} = \mathbf{\Phi}_T^{diff}$. If the sphere is centered on the origin, the azimuthal and polar symmetry implies, that only the radial component of the heat flux is non-zero:

$$\mathbf{\Phi}_{T,r} = -\lambda_m \frac{\mathrm{d}T}{\mathrm{d}r}, \tag{D.2}$$

and this heat flux is a function of only the radius. The surface integral of the heat flux over a sphere gives the total heat low rate between the sphere and the environment:

$$\dot{Q}_r = 4\pi r^2 \mathbf{\Phi}_{T,r}. \tag{D.3}$$

At steady state, the heat flux is constant across any surface encapsulating the isothermal sphere, thus:

$$\frac{\mathrm{d}\dot{Q}_r}{\mathrm{d}r} = 0, \tag{D.4}$$

and assuming a constant thermal conductivity:

$$\frac{\mathrm{d}}{\mathrm{d}r} r^2 \frac{\mathrm{d}T}{\mathrm{d}r} = 0. \tag{D.5}$$

By integrating Eq.(D.5) twice with respect to r, one attains its general solution:

$$T = \frac{C_{1,T}}{r} + C_{2,T}, \tag{D.6}$$

where $C_{1,T}$ and $C_{2,T}$ are integration constants subject to boundary conditions. By imposing the boundary conditions:

$$T(r_p) = T_p, \tag{D.7}$$
$$\lim_{r\to\infty} T(r) = T_s, \tag{D.8}$$

one achieves: $C_{1,T} = \left(T_p - T_s\right) r_p$ and $C_{2,T} = T_s$, thus the temperature profile in steady state is:

$$T = \left(T_p - T_s\right) \frac{r_p}{r} + T_s. \tag{D.9}$$

Substituting this solution into Eq. (D.2), the radial heat flux is:

$$\mathbf{\Phi}_{T,r} = \lambda_m \left(T_p - T_s\right) \frac{r_p}{r^2}, \tag{D.10}$$

and the heat flow rate between the sphere and the environment may be evaluated by integrating this heat flux on the sphere surface:

$$\dot{Q}_r = \pi \lambda_m 4 r_p \left(T_p - T_s\right). \tag{D.11}$$

Thus in accordance with Eq.(4.20) the Nusselt number of a sphere in quiescent fluid is indeed: $Nu_{m,0} = 2$ corresponding to an infinite thermal film thickness.

D.2 Sherwood number

Mass transfer can be studied in a similar manner. This model problem concerns the transport of species f dissolved in a bath gas b, each characterized by mass fractions: Y_f and $Y_b = 1 - Y_f$ respectively. Hirschfelder's law is used to define the diffusive mass flux of this species f:

$$\mathbf{\Phi}_{M,f}^{diff} = -\rho_m \mathcal{D}_m \nabla Y_f, \tag{D.12}$$

where ρ_m is the density of the mixture, and $\mathcal{D}_m$ is the mass diffusion coefficient of f in the mixture. An important distinction between section D.1 and this example, is that the differential diffusion of f and the bath gas creates a net mass flow: the Stefan flow. The resulting convective transport of f is characterized by the mass flux:

$$\mathbf{\Phi}_{M,f}^{conv} = Y_f \mathbf{\Phi}_M. \tag{D.13}$$

Thus the overall mass flux of species f is:

$$\mathbf{\Phi}_{M,f} = Y_f \mathbf{\Phi}_M - \rho_m \mathcal{D}_m \nabla Y_f. \tag{D.14}$$

In the following example, assume there is sphere of radius r_p with constant surface mass fraction of species f: $Y_{f,i}$ immersed in a mixture of f and b with the far-field mass fraction of f kept at $Y_{f,s}$. Furthermore the bath gas: b is insoluble in the sphere and the binary diffusion coefficient is constant throughout the domain. The

symmetry arguments of section D.1 still hold, thus radial the mass flux of f is:

$$\mathbf{\Phi}_{M,f,r} = Y_f \mathbf{\Phi}_{M,r} - \rho_m \mathcal{D}_m \frac{\mathrm{d}}{\mathrm{d}r} Y_f. \tag{D.15}$$

The insolubility of b in the sphere implies, that the mass flux of b across the surface of the sphere is 0, and in steady state the radial flux of b is 0 everywhere. Thus the flow exhibits unimolecular diffusion, when the only one component of a binary mixture has a net mass flux. In this case the total mass flux is the mass flux of species f: $\mathbf{\Phi}_{M,r} = \mathbf{\Phi}_{M,f,r}$, so Eq. (D.15) simplifies to:

$$\mathbf{\Phi}_{M,f,r} = -\frac{\rho_m \mathcal{D}_m}{1 - Y_f} \frac{\mathrm{d}}{\mathrm{d}r} Y_f, \tag{D.16}$$

and the total mass flow of f across a spherical surface of radius r is:

$$\dot{m}_f = 4\pi r^2 \mathbf{\Phi}_{M,f,r}. \tag{D.17}$$

Since in steady state, the mass flow of f is constant:

$$\frac{\mathrm{d}\dot{m}_f}{\mathrm{d}r} = 0. \tag{D.18}$$

Assuming, that the mass diffusion coefficient and density are constants throughout the domain, the above ODE takes the form:

$$\frac{\mathrm{d}}{\mathrm{d}r} \frac{r^2}{1 - Y_f} \frac{\mathrm{d}}{\mathrm{d}r} Y_f = 0. \tag{D.19}$$

In this case the integration yields:

$$\ln\left(1 - Y_f\right) = \frac{C_{1,M}}{r} + C_{2,M}, \tag{D.20}$$

with integration constants $C_{1,M}$ and $C_{2,M}$. By imposing the boundary conditions:

$$Y_f(r_p) = Y_{f,i}, \tag{D.21}$$

$$\lim_{r \to \infty} Y_f(r) = Y_{f,s}, \tag{D.22}$$

one achieves: $C_{1,M} = \ln\left(\frac{1-Y_{f,i}}{1-Y_{f,s}}\right) r_p$ and $C_{2,M} = \ln\left(1 - Y_{f,s}\right)$. Thus the mass fraction profile is described by:

$$\frac{1 - Y_f}{1 - Y_{f,s}} = \left(\frac{1 - Y_{f,i}}{1 - Y_{f,s}}\right)^{\frac{r_p}{r}}. \tag{D.23}$$

Consequently the radial mass flux is:

$$\mathbf{\Phi}_{M,f,r} = -\rho_m \mathcal{D}_m \ln\left(\frac{1 - Y_{f,i}}{1 - Y_{f,s}}\right) \frac{r_p}{r^2}, \tag{D.24}$$

and the mass flow through the surface of the sphere is:

$$\dot{m}_f = -4\pi r_p \rho_m \mathcal{D}_m \ln\left(\frac{1-Y_{f,i}}{1-Y_{f,s}}\right). \tag{D.25}$$

Thus, indeed the Sherwood number of the sphere without forced flow (only Stefan flow) is $Sh_{m,0} = 2$ in accordance with the MTS case of Tab. 4.3. This corresponds to an infinite film thickness as well.

Appendix E

Evaporating surfaces in film theory

The film theory of transport phenomena postulates that the differences between interface and bulk states diminish in a finite δ thickness, instead of the infinite distances of Appendix D. (Eq. (D.8), Eq. (D.22)) In this appendix the temperature and vapor mass fraction profiles are derived assuming individual and simultaneous heat and mass transfer through a finite film thickness for a flat plate and a sphere.

E.1 Flat plate

The configuration of transport in a half-space bounded by a plane of constant properties is peculiar in the sense, that steady state transport is not possible the way it is studied in Appendix D, since a temperature or mass fraction differences cannot coexist in this configuration in steady state. Nevertheless, the case may be studied in using film theory, by postulating, that potential gradients are concentrated in a film of finite thickness, beyond which the bulk temperature and mixture composition are constant. This bulk region absorbs all fluxes that cross the film, and the transfer rates are controlled by the film thickness. Thin films correspond to high gradients and consequently fast heat and mass transfer.

E.1.1 Mass transfer from a flat plate

In this setting mass conservation is characterized by a constant mass flux across the film. In particular, for unimolecular diffusion (i.e.: including Stefan flow) the mass flux of species f normal to the plane is:

$$\mathbf{\Phi}_{M,f,x} = -\frac{\rho_m \mathcal{D}_m}{1-Y_f}\frac{\mathrm{d}}{\mathrm{d}x}Y_f. \tag{E.1}$$

In steady state, this mass flux is constant throughout the film, giving the ordinary differential equation, that describes mass transfer:

$$\frac{\mathrm{d}\mathbf{\Phi}_{M,f,x}}{\mathrm{d}x} = 0, \tag{E.2}$$

$$\frac{\mathrm{d}}{\mathrm{d}x}\frac{1}{1-Y_f}\frac{\mathrm{d}}{\mathrm{d}x}Y_f = 0, \tag{E.3}$$

where the notion of Appendix D is adapted for Cartesian coordinates. Here the second equation assumes constant density and diffusivity throughout the The general solution of this ODE reads:

$$\ln\left(1-Y_f\right) = C_{1,M}x + C_{2,M}. \tag{E.4}$$

The problem is closed by imposing the boundary conditions at the plane surface and at the film thickness:

$$Y_f(0) = Y_{f,i}, \tag{E.5}$$
$$Y_f(\delta_M) = Y_{f,s}, \tag{E.6}$$

where δ_M is the thickness of the mass transfer film. In this case the integration constants are: $C_{1,M} = \ln\left(\frac{1-Y_{f,s}}{1-Y_{f,i}}\right)^{1/\delta_M}$ and $C_{2,M} = \ln\left(1 - Y_{f,i}\right)$, thus the fuel mass fraction profile is an exponential function:

$$\frac{1 - Y_f}{1 - Y_{f,i}} = \left(\frac{1 - Y_{f,s}}{1 - Y_{f,i}}\right)^{\frac{x}{\delta_M}}, \tag{E.7}$$

and the mass flux across the film is a constant given by:

$$\mathbf{\Phi}_{M,f,x} = -\rho_m \mathcal{D}_m \ln\left(\frac{1 - Y_{f,i}}{1 - Y_{f,s}}\right) \frac{1}{\delta_M}. \tag{E.8}$$

Considering that the unimolecular diffusion is intrinsically linked to the mass transfer in this configuration, a mass transfer coefficient may be defined, using $-\ln\left(\frac{1-Y_{f,i}}{1-Y_{f,s}}\right)$ as the characteristic potential difference driving the flow. Then a mass transfer coefficient can be defined as:

$$h_M^{plate} = \frac{\mathbf{\Phi}_{M,f,x}}{-\ln\left(\frac{1 - Y_{f,i}}{1 - Y_{f,s}}\right)} = \frac{\rho_m \mathcal{D}_m}{\delta_M}. \tag{E.9}$$

Provided that the problem can be characterized by a length scale L, a Sherwood number is the non-dimensional mass transfer coefficient:

$$Sh_{m,0}^{plate} = \frac{h_M^{plate} L}{\rho_m \mathcal{D}_m} = \frac{L}{\delta_M}. \tag{E.10}$$

E.1.2 Heat transfer from a flat plate

The mass flux of a unimolecular diffusion case (Eq. (E.1)) inherently considers the transport due to the net mass flux (Stefan flow). This consideration of Stefan flow is not obvious in the case of heat transfer, since in principle the two phenomena may be independent, and they are only linked through the assumptions of the modeled heat and mass transfer phenomena. For example in this work the interface temperature (T_p) and the interface mass fraction ($Y_{f,i}$) are related through the assumption of saturated vapor conditions on the interface. Nevertheless, the far-field temperature and composition are independent, thus various situations are possible depending on the far field conditions. Below, the heat transfer between a flat plate and the far field is studied both in the absence and presence of Stefan flow. The comparison of these cases yields in the classical Nusselt number correction of Bird, Stewart, and Lightfoot (1960, §19.4, §22.8) for flat plates.

Individual heat transfer

Without convective transport, the heat flux across the film is purely due to conduction according to Fourier's law of heat transfer. This $\mathbf{\Phi}_{T,x}^{diff}$ heat flux is constant through the film, giving a governing equation:

$$\mathbf{\Phi}_{T,x} = \mathbf{\Phi}_{T,x}^{diff} = -\lambda_m \frac{\mathrm{d}T}{\mathrm{d}x}, \tag{E.11}$$

$$\frac{\mathrm{d}\mathbf{\Phi}_{T,x}}{\mathrm{d}x} = 0. \tag{E.12}$$

Assuming constant thermal conductivity, the solution of this ODE is a linear temperature profile:

$$T = T_p + \left(T_s - T_p\right) \frac{x}{\delta_T}, \tag{E.13}$$

and the constant heat flux is simply proportional to the temperature gradient in this profile:

$$\mathbf{\Phi}_{T,x} = -\lambda_m \frac{T_s - T_p}{\delta_T}, \tag{E.14}$$

and a heat transfer coefficient can be defined as:

$$h_T^{plate} = \frac{\mathbf{\Phi}_{T,x}}{T_p - T_s} = \frac{\lambda_m}{\delta_T}, \tag{E.15}$$

where $T_p - T_s$ is the characteristic potential difference of the problem. Similarly to the case of mass transfer, the this heat transfer coefficient can be non-dimensionalized, yielding the Nusselt number:

$$Nu_{m,0}^{plate} = \frac{h_T L}{\lambda_m} = \frac{L}{\delta_T}. \tag{E.16}$$

Simultaneous heat and mass transfer

In the presence of mass transfer, the total energy flux is the sum of the diffusive and convective fluxes. In case of unimolecular diffusion the convection is caused by the mass flux of the fuel alone:

$$\mathbf{\Phi}_{T,x} = \mathbf{\Phi}_{T,x}^{diff} + \mathbf{\Phi}_{T,x}^{conv} = -\lambda_m \frac{\mathrm{d}T}{\mathrm{d}x} + c_{p,vap,m} \mathbf{\Phi}_{M,f,x} \left(T - T_0\right), \tag{E.17}$$

where $c_{p,vap,m}$ is the specific heat of the vapour of species f, and T_0 is an arbitrary reference temperature. The convective part of the heat transfer takes this form, since in unimolecular diffusion only species f is transported, thus the associated heat flux is due to the enthalpy of species f alone, estimated as $h_f = c_{p,vap,m}\left(T - T_0\right)$. (See Eq. (2.78) for further explanation on heat transfer due to simultaneous temperature and mass fraction gradients.) The heat transfer is described by the ODE:

$$\frac{\mathrm{d}\mathbf{\Phi}_{T,x}}{\mathrm{d}x} = 0, \tag{E.18}$$

that can be transformed to:

$$\frac{\mathrm{d}}{\mathrm{d}x}\left(\frac{\mathrm{d}T}{\mathrm{d}x}+\Xi_{1,x}T\right)=0, \tag{E.19}$$

with the factor $\Xi_{1,x}$ is defined as: $\Xi_{1,x} = -\frac{c_{p,vap,m}\mathbf{\Phi}_{M,f,x}}{\lambda_m} = \frac{c_{p,vap,m}}{c_{p,m}}\frac{1}{Le_m}\ln\left(\frac{1-Y_{f,i}}{1-Y_{f,s}}\right)\frac{1}{\delta_M}$, where $Le_m = \frac{\lambda_m}{c_{p,m}\rho_m\mathcal{D}_m}$ is the Lewis number of species f in the film. If $\Xi_{1,x}$ is considered constant across the film, then the general solution is:

$$T = C_{1,T}e^{-\Xi_{1,x}x} + C_{2,T}, \tag{E.20}$$

where $C_{1,T}$ and $C_{2,T}$ are integration constants subject to boundary conditions. By imposing the boundary conditions:

$$T(0) = T_p, \tag{E.21}$$
$$T(\delta_T) = T_s, \tag{E.22}$$

where δ_T is the thermal film thickness, the temperature profile is:

$$T = T_p + \left(T_s - T_p\right)\frac{e^{-\Xi_{1,x}x}-1}{e^{-\Xi_{1,x}\delta_T}-1}. \tag{E.23}$$

Equation (E.17) is evaluated using this temperature profile and taking T_0 as the liquid temperature, yielding the total heat flux between the interface and the bulk fluid, which is constant throughout the entire film:

$$\begin{aligned}\mathbf{\Phi}_{T,x} &= -\lambda_m\left(T_s-T_p\right)\frac{-\Xi_{1,x}e^{-\Xi_{1,x}x}}{e^{-\Xi_{1,x}\delta_T}-1} - \lambda_m\left(T_s-T_p\right)\frac{\Xi_{1,x}e^{-\Xi_{1,x}x}-\Xi_{1,x}}{e^{-\Xi_{1,x}\delta_T}-1} \\ &= -\lambda_m\left(T_s-T_p\right)\frac{-\Xi_{1,x}}{e^{-\Xi_{1,x}\delta_T}-1}.\end{aligned} \tag{E.24}$$

The correction method of Bird uses the Nusselt and Sherwood numbers of individual heat and mass transfer: $Nu_{m,0}^{plate}$ and $Sh_{m,0}^{plate}$ defined in Eq. (E.16) and Eq. (E.10) respectively. Furthermore, the effective Nusselt number of the present case modified by the Stefan flow is:

$$Nu_m^{plate,*,B} = \frac{\mathbf{\Phi}_{T,x}L}{\lambda_m\left(T_p-T_s\right)} = \frac{-\Xi_{1,x}L}{e^{-\Xi_{1,x}\delta_T}-1}. \tag{E.25}$$

The ratio of the two Nusselt numbers is:

$$\frac{Nu_m^{plate,*,B}}{Nu_{m,0}^{plate}} = \frac{-\Xi_{1,x}\delta_T}{e^{-\Xi_{1,x}\delta_T}-1} = \frac{\beta}{e^{\beta}-1}, \tag{E.26}$$

with the parameter $\beta = -\Xi_{1,x}\delta_T = \frac{c_{p,vap,m}}{c_{p,m}}\frac{1}{Le_m}\ln\left(1+B_M\right)\frac{\delta_T}{\delta_M}$, where $B_M = \frac{Y_{f,i}-Y_{f,s}}{1-Y_{f,i}}$ is the Spalding mass transfer number. Bird, Stewart, and Lightfoot argue, that the ratio of the layer thicknesses can be expressed as the ratio of layer thicknesses in the individual heat and mass transfer cases, postulating that the thermal film thickness is unchanged by the presence of Stefan flow. In this case the β factor may be expressed

using the Nusselt and Sherwood numbers of individual heat and mass transfer:

$$\beta = \frac{c_{p,vap,m}}{c_{p,m}} \frac{1}{Le_m} \frac{Sh^{plate}_{m,0}}{Nu^{plate}_{m,0}} \ln\left(1 + B_M\right). \tag{E.27}$$

Bird, Stewart, and Lightfoot (1960) propose, that if empirical correlations are available for evaluating $Nu^{case}_{m,0}$ and $Sh^{case}_{m,0}$ for an arbitrary problem that differs from the flat plate, then the effective Nusselt number may still be determined as:

$$Nu^{case,*,B}_{m} = Nu^{case}_{m,0} \frac{\beta}{e^{\beta} - 1}, \tag{E.28}$$

where β is evaluated using $Nu^{case}_{m,0}$ and $Sh^{case}_{m,0}$. Subsequently a mean heat transfer coefficient of this problem can be determined by un-scaling this effective Nusselt number using a representative thermal conductivity and length scale:

$$h^{case}_{T} = \frac{Nu^{case,*,B}_{m} \lambda_m}{L^{case}}. \tag{E.29}$$

E.2 Sphere

The case of a sphere is radically different from the flat plate. The problem is inherently characterized by a length scale: the diameter d_p. Furthermore fluxes of conserved properties diminish as $\mathbf{\Phi} \propto r^{-2}$, that allows the existence of infinite boundary layers as presented in Appendix D. Below film theory is applied to the heat and mass transfer around a sphere under the conditions studied in Appendix D. It is shown, that despite the differences Bird's correction indeed holds for spheres as well.

E.2.1 Mass transfer around a sphere

In this work the conservation of species f is characterized by the same governing equation irrespective whether or not there is simultaneous heat transfer. Thus the general solution of fuel mass fraction takes the form presented in Eq. (D.20). However, instead of the boundary condition in Eq. (D.22), the seen fuel mass fraction is reached at $r_{BL,M} = r_p + \delta_M$:

$$Y_f(r_{BL,M}) = Y_{f,s}, \tag{E.30}$$

where δ_M is the film thickness of the mass transfer boundary layer, and r_p is the radius of the sphere. In this case the integration constants of Eq. (D.20) are: $C_{1,M} = \ln\left(\frac{1-Y_{f,s}}{1-Y_{f,i}}\right) \frac{1}{1/r_{BL,M} - 1/r_p}$ and $C_{2,M} = \ln\left(1 - Y_{f,i}\right) + \ln\left(\frac{1-Y_{f,s}}{1-Y_{f,i}}\right) \frac{1/r_p}{1/r_{BL,M} - 1/r_p}$, thus the mass fraction profile takes the form:

$$\frac{1 - Y_f}{1 - Y_{f,i}} = \left(\frac{1 - Y_{f,s}}{1 - Y_{f,i}}\right)^{\frac{1/r_p - 1/r}{1/r_p - 1/r_{BL,M}}}. \tag{E.31}$$

Consequently the mass flux is:

$$\mathbf{\Phi}_{M,f,r} = -\rho_m \mathcal{D}_m \ln\left(\frac{1 - Y_{f,i}}{1 - Y_{f,s}}\right) \frac{1}{\left(\frac{1}{r_p} - \frac{1}{r_{BL,M}}\right) r^2}, \tag{E.32}$$

and the mass flow leaving the sphere according to Eq. (D.17) is:

$$\dot{m}_f = -\pi \rho_m \mathcal{D}_m \frac{4}{1/r_p - 1/r_{BL,M}} \ln\left(\frac{1-Y_{f,i}}{1-Y_{f,s}}\right), \tag{E.33}$$

thus the Sherwood number analogously to Eq. (E.10) can be related to the layer thickness as:

$$Sh_{m,0} = \frac{2}{1-\frac{r_p}{r_p+\delta_M}} = 2 + \frac{d_p}{\delta_M}. \tag{E.34}$$

E.2.2 Heat transfer around a sphere

As in the case of the flat plate, heat transfer from a sphere may be radically affected by the presence of Stefan flow. Applying film theory, the bulk temperature is reached at a radius of $r_{BL,T} = r_p + \delta_T$:

$$T(r_{BL,T}) = T_s. \tag{E.35}$$

Individual heat transfer

In the absence of a net mass flow, the general solution of Eq. (D.6) still holds. The integration constants take the form: $C_{1,T} = (T_s - T_p)\frac{1}{1/r_{BL,T}-1/r_p}$ and $C_{2,T} = T_p - (T_s - T_p)\frac{1/r_p}{1/r_{BL,T}-1/r_p}$, thus the temperature is given by:

$$T = T_p + (T_s - T_p)\frac{\frac{1}{r}-\frac{1}{r_p}}{\frac{1}{r_{BL,T}}-\frac{1}{r_p}}. \tag{E.36}$$

The conductive heat flux in this case is:

$$\mathbf{\Phi}_{T,r} = \lambda_m (T_p - T_s)\frac{1}{\left(\frac{1}{r_p}-\frac{1}{r_{BL,T}}\right)r^2}, \tag{E.37}$$

resulting in a heat transfer rate of:

$$\dot{Q}_r = \pi \lambda_m d_p (T_p - T_s)\frac{2}{1-\frac{r_p}{r_{BL,T}}}, \tag{E.38}$$

thus, in the absence of net mass transfer, the relation between the Nusselt number and the thermal film thickness is analogous to the relation derived for the Sherwood number above:

$$Nu_{m,0} = \frac{2}{1-\frac{r_p}{r_p+\delta_T}} = 2 + \frac{d_p}{\delta_T}. \tag{E.39}$$

Simultaneous heat and mass transfer

In the presence of the unimolecular diffusion of species f, the radial energy flux of Eq. (D.2) is complemented by the contribution of convective transfer:

$$\mathbf{\Phi}_{T,r} = \mathbf{\Phi}_{T,r}^{diff} + \mathbf{\Phi}_{T,r}^{conv} = -\lambda_m \frac{\mathrm{d}T}{\mathrm{d}r} + c_{p,vap,m}\mathbf{\Phi}_{M,f,r}(T - T_0), \tag{E.40}$$

where $c_{p,vap,m}$ is the specific heat of the vapour of species f, and T_0 is an arbitrary reference temperature. Thus energy conservation is described by the following ordinary differential equation:

$$\frac{\mathrm{d}}{\mathrm{d}r}r^2\left(-\frac{c_{p,vap,m}\mathbf{\Phi}_{M,f}(r)}{\lambda_m}\left(T-T_0\right)+\frac{\mathrm{d}T}{\mathrm{d}r}\right)=0, \tag{E.41}$$

$$\frac{\mathrm{d}}{\mathrm{d}r}\left(r^2\frac{\mathrm{d}T}{\mathrm{d}r}+\Xi_1 T+\Xi_2\right)=0, \tag{E.42}$$

where using Eq. (E.32) one reaches the coefficients: $\Xi_1=\frac{c_{p,vap,m}}{c_{p,m}Le_m}\frac{1}{1/r_p-1/r_{BL,M}}\ln\left(\frac{1-Y_{f,i}}{1-Y_{f,s}}\right)$, and $\Xi_2=-\frac{c_{p,vap,m}}{c_{p,m}Le_m}\frac{1}{1/r_p-1/r_{BL,M}}\ln\left(\frac{1-Y_{f,i}}{1-Y_{f,s}}\right)T_0$. Using a scaled temperature: $\theta=\frac{T-T_p}{T_s-T_p}$, the temperature and its derivative are may be expressed as: $T=T_p+\theta\left(T_s-T_p\right)$, and $\frac{\mathrm{d}T}{\mathrm{d}r}=\left(T_s-T_p\right)\frac{\mathrm{d}\theta}{\mathrm{d}r}$. Eq. (E.42) can be reformulated as:

$$\frac{\mathrm{d}}{\mathrm{d}r}\left(r^2\left(T_s-T_p\right)\frac{\mathrm{d}\theta}{\mathrm{d}r}+\Xi_1\left(T_s-T_p\right)\theta+\Xi_1 T_p+\Xi_2\right)=0, \tag{E.43}$$

$$\frac{\mathrm{d}}{\mathrm{d}r}\left(r^2\frac{\mathrm{d}\theta}{\mathrm{d}r}+\Xi_1\theta+\Xi_2^*\right)=0, \tag{E.44}$$

where additional constants are absorbed in Ξ_2^*. Eq. (E.44) is a separable differential equation, with the general solution:

$$\theta=C_{1,T}e^{\frac{\Xi_1}{r}}+C_{2,T}, \tag{E.45}$$

where $C_{1,T}$ and $C_{2,T}$ are integration constants subject to boundary conditions. By imposing the boundary conditions:

$$\theta(r_p)=0, \tag{E.46}$$

$$\theta(r_{BL,T})=1, \tag{E.47}$$

one achieves: $C_{1,T}=\left(e^{\Xi_1/r_{BL,T}}-e^{\Xi_1/r_p}\right)^{-1}$ and $C_{2,T}=-C_{1,T}e^{\Xi_1/r_p}$, thus the temperature profile in steady state is:

$$T=T_p+\left(T_s-T_p\right)\frac{e^{\frac{\Xi_1}{r}}-e^{\frac{\Xi_1}{r_p}}}{e^{\frac{\Xi_1}{r_{BL,T}}}-e^{\frac{\Xi_1}{r_p}}}. \tag{E.48}$$

Taking T_0 to be equal to the droplet temperature, the radial heat flux is proportional to $\frac{1}{r^2}$, as expected:

$$\mathbf{\Phi}_{T,r}=-\lambda_m\left(\frac{\mathrm{d}T}{\mathrm{d}r}+\frac{\Xi_1}{r^2}\left(T-T_0\right)\right) \tag{E.49}$$

$$=-\lambda_m\left(T_s-T_p\right)\frac{-\frac{\Xi_1}{r^2}e^{\frac{\Xi_1}{r}}}{e^{\frac{\Xi_1}{r_{BL,T}}}-e^{\frac{\Xi_1}{r_p}}}-\lambda_m\left(T_s-T_p\right)\frac{\frac{\Xi_1}{r^2}\left(e^{\frac{\Xi_1}{r}}-e^{\frac{\Xi_1}{r_p}}\right)}{e^{\frac{\Xi_1}{r_{BL,T}}}-e^{\frac{\Xi_1}{r_p}}} \tag{E.50}$$

$$=-\lambda_m\left(T_s-T_p\right)\frac{1}{r^2}\frac{-\Xi_1 e^{\frac{\Xi_1}{r_p}}}{e^{\frac{\Xi_1}{r_{BL,T}}}-e^{\frac{\Xi_1}{r_p}}}. \tag{E.51}$$

Consequently, the heat transfer rate between the sphere and the far field is:

$$\dot{Q}_r = \pi \lambda_m d_p \left(T_p - T_s\right) \frac{2\frac{\Xi_1}{r_p}}{1 - e^{\frac{\Xi_1}{r_{BL,T}} - \frac{\Xi_1}{r_p}}}. \tag{E.52}$$

The numerator and exponent in the denominator of the last term can be reformulated as:

$$2\frac{\Xi_1}{r_p} = 2\frac{c_{p,vap,m}}{c_{p,m} Le_m} \frac{1/r_p}{1/r_p - 1/r_{BL,M}} \ln\left(\frac{1 - Y_{f,i}}{1 - Y_{f,s}}\right) \tag{E.53}$$

$$= \frac{c_{p,vap,m}}{c_{p,m} Le_m} Sh_{m,0} \ln\left(\frac{1 - Y_{f,i}}{1 - Y_{f,s}}\right) = -\beta Nu_{m,0}, \tag{E.54}$$

$$\frac{\Xi_1}{r_{BL,T}} - \frac{\Xi_1}{r_p} = -\frac{c_{p,vap,m}}{c_{p,m} Le_m} \frac{1/r_p - 1/r_{BL,T}}{1/r_p - 1/r_{BL,M}} \ln\left(\frac{1 - Y_{f,i}}{1 - Y_{f,s}}\right) \tag{E.55}$$

$$= -\frac{c_{p,vap,m}}{c_{p,m} Le_m} \frac{Sh_{m,0}}{Nu_{m,0}} \ln\left(\frac{1 - Y_{f,i}}{1 - Y_{f,s}}\right) = \beta. \tag{E.56}$$

Hence, despite the different nature of the temperature and mass fraction profiles in the films surrounding the sphere, the correction proposed by Bird, Stewart, and Lightfoot (1960) still holds for spheres as well:

$$\frac{Nu_m^{*,B}}{Nu_{m,0}} = \frac{2\frac{\Xi_1}{r_p} \Big/ Nu_{m,0}}{1 - e^{\frac{\Xi_1}{r_{BL,T}} - \frac{\Xi_1}{r_p}}} = \frac{\beta}{e^{\beta} - 1}. \tag{E.57}$$

Note, that choosing the reference temperature as $T_0 = T_p$ has certain implications on the enthalpy flux defined in Eq. (E.40). Evaluating $\mathbf{\Phi}_{T,r}$ on the droplet surface, the second term of the equation is zero. Consequently, this choice of reference temperature means, that $\mathbf{\Phi}_{T,r}$ represents only the conductive heat flux on the sphere's interface. In the rest of the film the heat flux is no longer purely conductive, as T differs from T_0. From the perspective of coupling spherical Lagrangian droplets with the Eulerian gas phase, all energy flows have to be accounted for. According to the above arguments, on the gaseous side of the interface $\dot{Q}_r$ is only the conductive energy flow. To reach the total energy flow Eq. (E.40) has to be evaluated with $T_0 = 0\,\mathrm{K}$, which gives the correct form of heat flow through the interface: $\dot{Q}_r + \dot{m}_r h_f(T_p)$. (Xia et al., 2013)

Appendix F

Wet-bulb conditions of the diffusion only evaporation model (D/D)

For the diffusion only model (D/D) defined in section 4.4, the psychrometric wet-bulb conditions are given by:

$$c_{p,m}\left(T_s - T_p^{psy,D/D}\right) = \frac{1}{Le_m}\frac{Sh_{m,0}}{Nu_{m,0}}\left(Y_{f,i}^{psy,D/D} - Y_{f,s}\right)L_v. \tag{F.1}$$

The far-field temperature T_s, and vapor mass fraction $Y_{f,s}$ are boundary conditions of the problem, while the wet-bulb temperature $T_p^{psy,D/D}$ is the unknown, and the interface vapor mass fraction $Y_{f,i}^{psy,D/D}$ is a monotonous increasing function in temperature up to the boiling point of the liquid. At atmospheric pressure, far from the critical point, the latent heat of vaporization L_v is only weakly dependent on the droplet temperature. The other coefficients: $c_{p,vap,m}$ and ϕ_m are also constrained to a range of finite values. Thus, Eq. (F.1) only has a solution for a constrained range of far-field temperatures, unlike in the case of thermodynamic wet-bulb conditions. (Tab. 4.5) This highlights the limitation of neglecting Stefan flow in the evaporation model.

Figure F.1 shows the difference between the thermodynamic wet-bulb conditions and the wet-bulb conditions given by Eq. (F.1) for the diffusion only model where the differences in wet-bulb temperatures and the corresponding vapor mass fractions are $\Delta T_p^{D/D} = T_p^{psy,D/D} - T_p^{th}$, and $\Delta Y_{f,i}^{D/D} = Y_{f,i}^{psy,D/D} - Y_{f,i}^{th}$ respectively. (See Fig. 4.13 for the thermodynamic wet-bulb conditions.) The curves corresponding to equilibrium states are presented as a function of the seen gas temperature T_s, and parametrized by the seen gas vapor mass fraction $Y_{f,s}$, and the Reynolds number Re_m. This latter dependence corresponds to Reynolds numbers of $Re_m \in \{0, 1, 10, 100, 1000\}$, the legend omits this dependence for simplicity, as the equilibrium conditions are rather insensitive to the Reynolds number in this exhaustive range. Nonetheless to interpret the variation: lighter colors correspond to higher Reynolds numbers.

The vicinity of the saturation condition is illustrated best by the Spalding mass transfer number $B_M = \frac{Y_{f,i}^{psy,D/D} - Y_{f,s}}{1 - Y_{f,i}^{psy,D/D}}$. It is evident, that in case of the diffusion only model (D/D), the wet-bulb conditions are only found below a certain seen gas temperature. In Fig. F.1, the wet-bulb calculations are arbitrarily cut-off where $B_M = 20$, thus the maximum displayed seen temperature is: $\max\left(T_s\right)^{D/D} = T_{p|B_M=20}$

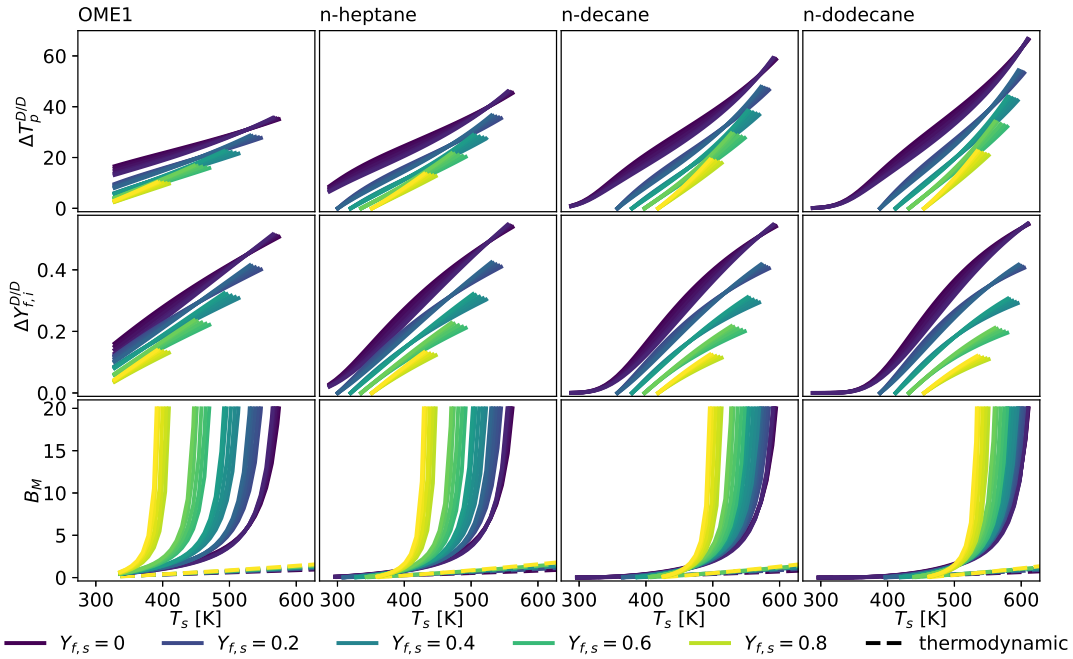

FIGURE F.1: Comparison of psychrometric and thermodynamic wet-bulb conditions of OME1, n-heptane, n-decane, and n-dodecane at atmospheric pressure with air as bath gas according to the diffusion only model (D/D): Eq. (F.1). The difference in wet-bulb temperatures and the corresponding vapor mass fractions are $\Delta T_p^{D/D} = T_p^{psy,D/D} - T_p^{th}$, and $\Delta Y_{f,i}^{D/D} = Y_{f,i}^{psy,D/D} - Y_{f,i}^{th}$.

$+ \frac{\phi_m}{c_{p,vap,m}} L_v \left(Y_{f,i|B_M=20} - Y_{f,s} \right)$. After this limit, the Spalding transfer number keeps approaching infinity, while the change in $\max\left(T_s\right)^{D/D}$ is small.

Table F.1 illustrates, how setting a higher limiting Spalding number at the web-bulb conditions affects the corresponding maximum seen temperature. The the limiting values on Fig. F.1 for $Y_{f,s} = 0$ and $Re_m = 0$ are: 574.0 K, 561.9 K, 594.7 K, 610.9 K, for OME1, n-heptane, n-decane, and n-dodecane respectively. However, if a cut-off point of $B_M = 200$ is chosen instead, the limiting seen temperatures would be only ~ 20 K higher.

TABLE F.1: Limiting cases where the web-bulb conditions of the diffusion only model ($Y_{f,i}^{psy,D/D}$ and $T_p^{psy,D/D}$) are evaluated for $Y_{f,s} = 0$ and $Re_m = 0$.

	water	OME1	n-heptane	n-decane	n-dodecane
T_{sat} (1 atm) [K]	373.2	315.0	371.5	447.5	489.5
$T_{p\|B_M=200}$ [K]	373.1	314.6	371.0	446.5	488.3
$\max\left(T_s\right)^{D/D}_{\|B_M=200}$ [K]	1647.2	595.9	581.3	614.2	630.7
$T_{p\|B_M=20}$ [K]	372.3	311.3	366.2	439.0	478.9
$\max\left(T_s\right)^{D/D}_{\|B_M=20}$ [K]	1624.8	574.0	561.9	594.7	610.9

For reference, the corresponding values of water are also shown in Tab. F.1. Water

is characterized by a significantly higher latent heat than the hydrocarbons studied here as shown in appendix B. Consequently, the limiting temperature is significantly higher, where the application of the diffusion only model (D/D) is numerically possible. This justifies the success of such simplistic models in specific low-volatility applications, such as Inthavong et al. (2022).

The fact that Eq. (F.1) can produce an equilibrium (wet-bulb) droplet temperature under specific conditions does not imply, that it is a valid model. The effect of Stefan flow shall not be neglected even below the limits of Tab. F.1. The application of this model should be limited to fluids with low volatility interacting with a low temperature environment, however choosing this model over the other models presented in section 4.4 is only justified by its computational simplicity. Considering the operations needed to evaluate the mean gas properties, the material properties of the liquid, and the phase change properties, this advantage is negligible compared to Bird's correction (B) (that do not need iterative methods to determine the rate of evaporation). Thus it is recommended to avoid the usage of the diffusion only model (D/D) altogether, especially in combustion applications.

Appendix G

Wet-bulb conditions of the classical evaporation model (S/D)

In case of the classical evaporation model (S/D) defined in section 4.4, the wet-bulb conditions are given by:

$$c_{p,vap,m}\left(T_s - T_p^{psy,S/D}\right) = \ln\left(1 + B_T^{psy,S/D}\right) L_v. \tag{G.1}$$

The differences between the psychrometric and thermodynamic wet-bulb conditions are illustrated in Fig. G.1 through the difference in wet-bulb temperature and vapor mass fraction: $\Delta T_p^{S/D} = T_p^{psy,S/D} - T_p^{th}$, and $\Delta Y_{f,i}^{S/D} = Y_{f,i}^{psy,S/D} - Y_{f,i}^{th}$ respectively. (See Fig. 4.13 for the thermodynamic wet-bulb conditions.)

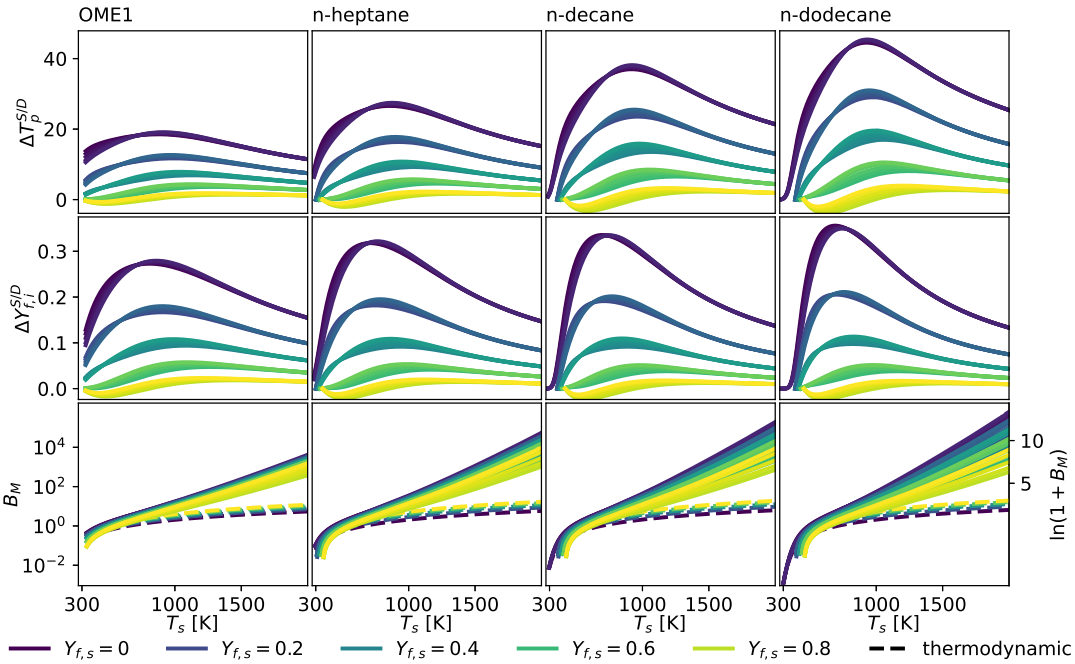

FIGURE G.1: Comparison of psychrometric and thermodynamic wet-bulb conditions of OME1, n-heptane, n-decane, and n-dodecane at atmospheric pressure with air as bath gas according to the classical evaporation model (S/D): Eq. (G.1). The difference in wet-bulb temperatures and the corresponding vapor mass fractions are $\Delta T_p^{S/D} = T_p^{psy,S/D} - T_p^{th}$, and $\Delta Y_{f,i}^{S/D} = Y_{f,i}^{psy,S/D} - Y_{f,i}^{th}$.

The classical model yields an equilibrium state at all studied conditions, since $\ln\left(1 + B_T^{psy,S/D}\right)$ is *not* limited as the droplet temperature approaches the boiling

point. As Fig. G.1 shows, the equilibrium conditions are rather insensitive to the Reynolds number. The difference between the thermodynamic and psychrometric conditions both in terms of temperature and vapor mass fraction is attained when the droplets interact with dry air ($Y_{f,s} = 0$)

The presence of the logarithmic term in the web-bulb equation Eq. (G.1) causes the main difference between this model and the others presented in Tab. 4.5. To illustrate this, $\ln(1 + B_M)$ is shown on the right axis of Fig. G.1. To maintain equilibrium temperatures, $\ln\left(1 + B_M^{psy}\right)$ has to be in the same order of magnitude as B_M^{th} in Fig. 4.13 for high temperature seen gas. This results in significantly higher droplet temperatures, and surface vapor mass fractions, although not as high as with the diffusion only model. This over-prediction entails an unrealistically high evaporation rate. Indeed, the main issue with the classical model (S/D) is the disparity caused by considering Stefan flow in the mass transfer, but not in the heat transfer. As chapter 4 concludes, it is best to avoid this inconsistency irrespective of the flow conditions, and use Bird's correction, or the Abramzon-Sirignano model, even if the classical model can give reasonable results under certain conditions. (Miller, Harstad, and Bellan, 1998; Noh et al., 2018)

Appendix H

Filter density function and Favre filtering

This appendix defines and illustrates the filter density function (FDF) in the context of large-eddy simulation. Subsequently, the concept is used to illustrate the differences between non-density-weighted filtering and Favre-filtering. The filter density function simply takes the weight by which various unfiltered states contribute to the filtered value, formally defined as:

$$h_\psi(\psi^*;\mathbf{x},t) = \int_\Omega \delta\left(\psi(\mathbf{x}^*,t) - \psi^*\right) G(\Delta,\mathbf{x},\mathbf{x}^*)\mathrm{d}\mathbf{x}^*, \tag{H.1}$$

where h_ψ is the FDF of variable ψ, δ is the Dirac delta function, and G is the filter function of the numerical method. (Fox, 2003) Although the filter function corresponding the numerical discretization is generally unknown (Rogallo and Moin, 1984), this appendix uses the box filter defined in Eq. (5.2) for illustration purposes. In case of the box filter, $h_\psi(\psi^*;\mathbf{x},t)\mathrm{d}\psi^*$ corresponds to the portion of volume occupied by states of $\psi \in [\psi^* - \frac{1}{2}\mathrm{d}\psi^*, \psi^* + \frac{1}{2}\mathrm{d}\psi^*]$ within the filter volume.

Numerically evaluating the FDF from a discretized field can prove to be difficult, as the Dirac delta function is hard to handle in relation with a finite sample space. (Pope, 1985) Instead, the cumulative filter density function (CFDF) is better suited for numerical computation:

$$H_\psi(\psi^*;\mathbf{x},t) = \int_{-\infty}^{\psi^*} h_\psi(\psi^\bullet;\mathbf{x},t)\mathrm{d}\psi^\bullet. \tag{H.2}$$

Since only the Dirac delta term is dependent on ψ^* in Eq. (H.1), the CFDF can be expressed as:

$$H_\psi(\psi^*;\mathbf{x},t) = \int_\Omega \mathcal{H}\left(\psi^* - \psi(\mathbf{x}^*,t)\right) G(\Delta,\mathbf{x},\mathbf{x}^*)\mathrm{d}\mathbf{x}^*, \tag{H.3}$$

where $\mathcal{H}$ is the Heaviside step function. Now H_ψ may be evaluated in a smooth manner, with an appropriate discretization of ψ^*, and the filter density function can be calculated as: $h_\psi(\psi^*;\mathbf{x},t) = \frac{\partial H_\psi(\psi^*;\mathbf{x},t)}{\partial \psi^*}$.

The concept of the CFDF and FDF are demonstrated in Fig. H.1 using the box filter. The first row of plots show the 1D field in space (same as in Fig. 5.1), while the second and third rows are the CFDF and the FDF respectively. The different columns correspond to different filter sizes. Indeed, the simplicity of the box filter allows to illustrate the CFDF in a geometric way, as displayed in the first row of plots. Here $H_\psi = 0.6$ is reached at a ψ^* value such, that in 60% of the filter volume the field is below ψ^*. As the filter size increases, the CFDF and FDF become wider

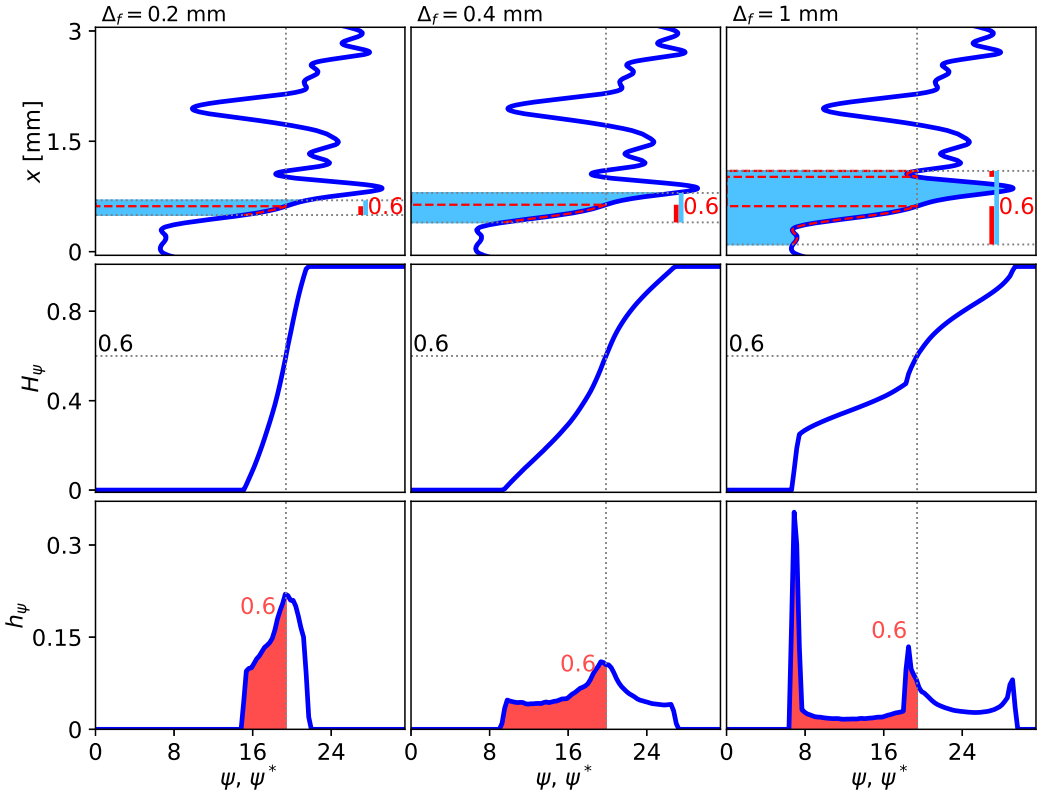

FIGURE H.1: Illustration of filter density function of a 1D field evaluated at one specific point using the box filter with different filter lengths. The different columns correspond to filter widths of $\Delta_f \in \{0.2, 0.4, 1.0\}$mm respectively, while the rows show the spatial field, its cumulative filter density function, and the filter density function.

and wider. Meanwhile they begin to show less regular structures such as multiple modes in the FDF, corresponding to high slopes of the CFDF. In fact, if the filter width approaches zero, the filter density function approaches a delta function and the cumulative counterpart a Heaviside function.

Based on the requirements of suitable filter function (Pope, 2000), the filter density function has the following properties:

$$1 = \int_{-\infty}^{\infty} h_\psi(\psi^*; \mathbf{x}, t) \mathrm{d}\psi^*, \quad \text{and} \quad \overline{\psi}(\mathbf{x}, t) = \int_{-\infty}^{\infty} \psi^* h_\psi(\psi^*; \mathbf{x}, t) \mathrm{d}\psi^*. \tag{H.4}$$

I.e.: once h_ψ is known at a specific location and time instance, the filtered field can also be evaluated without the knowledge of the fully resolved field. Furthermore, the FDF also provides a tool to evaluate the filtering of higher moments of the unknown (see section 2.3.3):

$$\overline{\psi^n}(\mathbf{x}, t) = \int_{-\infty}^{\infty} \psi^{*n} h_\psi(\psi^*; \mathbf{x}, t) \mathrm{d}\psi^*, \quad n \in \mathbb{N}. \tag{H.5}$$

The FDF is useful to describe the state of a single variable, however, to get the sub-grid cross correlation between more fields, one needs to know their joint filter

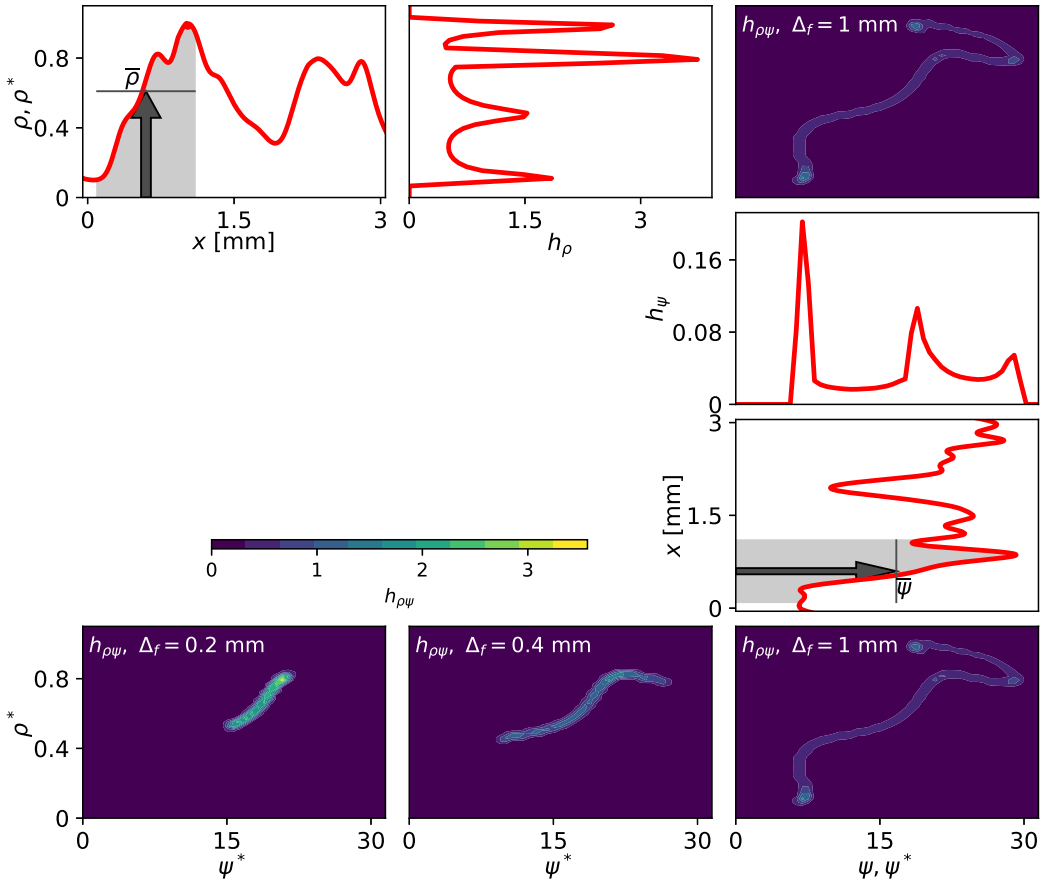

FIGURE H.2: Illustration of joint filter density function of two 1D fields: ρ and ψ evaluated at one specific point using the box filter with different filter lengths.

density function. Here, the joint FDF of N different fields is defined as:

$$h_{\psi_1\psi_2\ldots\,\psi_N}(\psi_1^*, \psi_2^*, \ldots \psi_N^*; \mathbf{x}, t) = \int_\Omega \delta\left(\psi_1(\mathbf{x}^*, t) - \psi_1^*\right) \delta\left(\psi_2(\mathbf{x}^*, t) - \psi_2^*\right) \ldots \delta\left(\psi_N(\mathbf{x}^*, t) - \psi_N^*\right) G(\Delta, \mathbf{x}, \mathbf{x}^*) \mathrm{d}\mathbf{x}^*, \tag{H.6}$$

Similar to the FDF, for numerical reasons it is advantageous to define the joint cumulative density function:

$$H_\psi(\psi_1^*, \psi_2^*, \ldots \psi_N^*; \mathbf{x}, t) = \int_{-\infty}^{\psi_1^*} \int_{-\infty}^{\psi_2^*} \ldots \int_{-\infty}^{\psi_N^*} h_{\psi_1\psi_2\ldots\,\psi_N}(\psi_1^\bullet, \psi_2^\bullet, \ldots \psi_N^\bullet; \mathbf{x}, t) \mathrm{d}\psi_1^\bullet \mathrm{d}\psi_2^\bullet \ldots \mathrm{d}\psi_N^\bullet, \tag{H.7}$$

where the order of the integrals is again interchangeable as in Eq. (H.3), thus the joint CFDF is the filtered value of the product of N Heaviside functions, where this product identifies the volume where all the unfiltered ψ_i fields are simultaneously lower than the corresponding ψ_i^*. Subsequently, the joint FDF may be calculated as the partial derivative of the joint CFDF:

$$h_{\psi_1\psi_2\ldots\,\psi_N}(\psi_1^*, \psi_2^*, \ldots \psi_N^*; \mathbf{x}, t) = \frac{\partial^N H_\psi(\psi_1^*, \psi_2^*, \ldots \psi_N^*; \mathbf{x}, t)}{\partial\psi_1^* \partial\psi_2^* \ldots \partial\psi_N^*}. \tag{H.8}$$

The marginal FDF of a single variable may be obtained by integrating the joint FDF along all other fields:

$$h_{\psi_1}(\psi_1^*;\mathbf{x},t) = \int_{-\infty}^{\infty} \dots \int_{-\infty}^{\infty} h_{\psi_1\psi_2\dots\,\psi_N}(\psi_1^*,\psi_2^\bullet,\dots\,\psi_N^\bullet;\mathbf{x},t)\mathrm{d}\psi_2^\bullet\dots\,\mathrm{d}\psi_N^\bullet. \tag{H.9}$$

Finally, the conditional FDF of a variable ψ_1, conditioned to a given value of $\psi_2^*,\dots\,\psi_N^*$ is:

$$h_{\psi_1|\psi_2\dots\,\psi_N}(\psi_1^*|\psi_2^*,\dots\,\psi_N^*;\mathbf{x},t) = \frac{h_{\psi_1\psi_2\dots\,\psi_N}(\psi_1^*,\psi_2^*,\dots\,\psi_N^*;\mathbf{x},t)}{h_{\psi_2\dots\,\psi_N}(\psi_2^*,\dots\,\psi_N^*;\mathbf{x},t)}, \tag{H.10}$$

with $h_{\psi_2\dots\,\psi_N}(\psi_2^*,\dots\,\psi_N^*;\mathbf{x},t) = \int_{-\infty}^{\infty} h_{\psi_1\psi_2\dots\,\psi_N}(\psi_1^\bullet,\psi_2^*,\dots\,\psi_N^*;\mathbf{x},t)\mathrm{d}\psi_1^\bullet$, that essentially corresponds to a re-normalization of $h_{\psi_1\psi_2\dots\,\psi_N}$ at a given array of conditions: $\psi_2^*,\dots\,\psi_N^*$.

Figure H.2 demonstrates the relationship of the marginal and joint filter density function of ρ and ψ using the same fields as in Fig. 5.2. The top right part of the figure shows the relation of the FDFs using the largest filter size of the example at a specific point, where large differences are observed between $\overline{\psi}$ and $\widetilde{\psi}$. As Eq. (H.9) suggests, the marginal FDFs: h_ρ and h_ψ are a "projection" of the joint FDF to the ρ^* and ψ^* axes respectively. Note, that the discretization of ψ^* is different in the case of Fig. H.1 and Fig. H.2, thus h_ψ has different magnitudes but it is characterized by the same shape.

The bottom row of plots in Fig. H.2 displays the joint FDF using different filter sizes. In all cases the correlation between ρ and ψ stays positive, i.e.: higher values of ψ occur at higher densities. However, the joint FDF becomes more and more spread with the increase of the filter size, resulting in larger and larger differences between non-density-weighted and Favre-filtering. The relationship is further examined below.

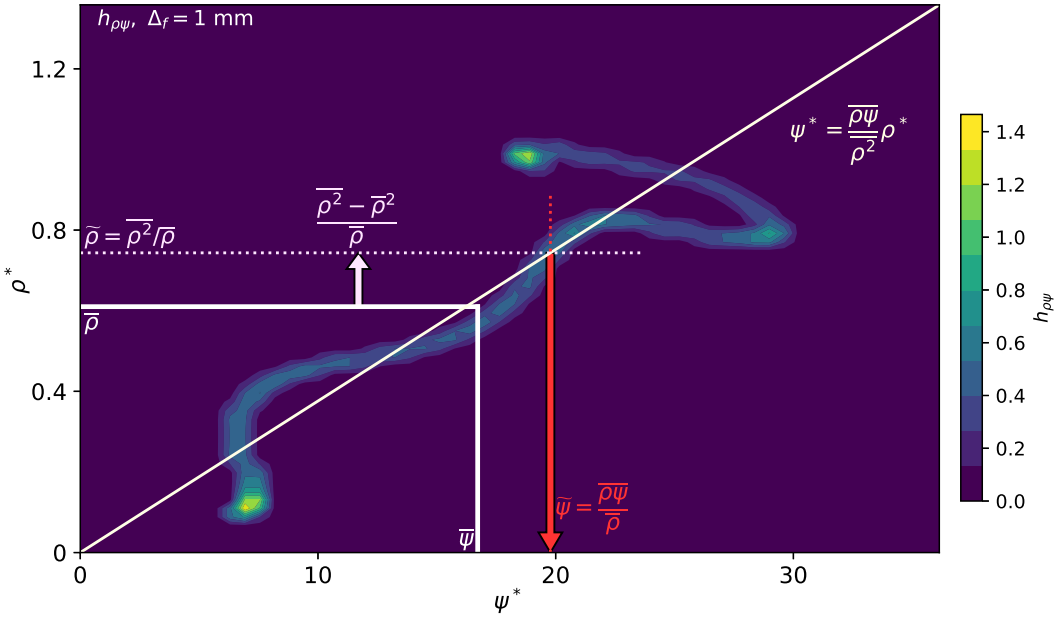

FIGURE H.3: Illustration of Favre-filtering with a known joint filter density function of density and a field: ψ.

Figure H.3 uses the same spatial data as above, and it illustrates the filtered values geometrically on the $\rho^* - \psi^*$ plane. In this context, the $(\overline{\psi}, \overline{\rho})$ point is the "center of gravity" of the joint FDF, while the linear function given by: $\psi^* = \left(\overline{\rho\psi}/\overline{\rho^2}\right)\rho^*$ is the lest square fit of the joint FDF with a forced zero intercept. (Pettit and Peers, 1991) Note, that this fitted line does not necessarily pass through the $(\overline{\psi}, \overline{\rho})$ point. By definition this fitted line goes through the $(\widetilde{\psi}, \widetilde{\rho})$ point of the $\rho^* - \psi^*$ plane, where $\widetilde{\rho} = \overline{\rho^2}/\overline{\rho}$ is the Favre-filtered density.

As described in section 5.4, $\overline{\rho}$ and $\overline{\rho^2}$ can be inferred from the presumed sub-grid state of the gas in this study, and $\widetilde{\psi}$ is given by the numerical solution of the PDEs. Thus, in general only the slope of the least square fit $\left(\overline{\rho\psi}/\overline{\rho^2}\right)$ and sub-grid variance of the density $\left(\overline{\rho^2} - \overline{\rho}^2\right)$ may be obtained. To quantify the difference between $\overline{\psi}$ and $\widetilde{\psi}$ one needs additional information about the relation of ψ and ρ. In case of the fields describing the local gas state this problem is closed using the assumptions of section 5.4. However, in case of the velocity field it is difficult to determine $\overline{\mathbf{u}}$. In this case one may estimate the range of possible filtered quantities using an upper bound of the sub-grid covariance (Pearson, 1895) as:

$$\widetilde{\psi} - \frac{\sqrt{\overline{\psi^2} - \overline{\psi}^2}\sqrt{\overline{\rho^2} - \overline{\rho}^2}}{\overline{\rho}} \quad \leq \quad \overline{\psi} \quad \leq \quad \widetilde{\psi} + \frac{\sqrt{\overline{\psi^2} - \overline{\psi}^2}\sqrt{\overline{\rho^2} - \overline{\rho}^2}}{\overline{\rho}}, \tag{H.11}$$

where obtaining an estimate of the sub-grid variance of the field $\left(\overline{\psi^2} - \overline{\psi}^2\right)$ is an easier task, than determining the sub-grid correlation of ψ and ρ. The bounds given in Eq. (H.11) are correctly approaching the Faver-filtered quantity as the sub-grid variance of either density or the unknown approach zero. Furthermore, it also reveals that as the filtered density increases the influence of the sub-grid variances diminishes.

The maximum estimated deviation between $\overline{\psi}$ and $\widetilde{\psi}$ according to Eq. (H.11) is shown in Fig. H.4 using artificial model FDFs. The plot shows the contour of the FDFs using contour lines, the points of non-density-weighed filtered quantities and Favre filtered quantities using symbols, and the estimated range of possible $\overline{\psi}$ values using the shading of the background. The model FDF in the first column is constructed as the product of two Gaussian distributions, thus by construction it represents uncorrelated fields. The other two columns show positively and negatively correlated FDFs constructed from the sum of two similar Gaussian distributions with different modus in ψ^* and ρ^*. Each of these model functions is rescaled to obtain a prescribed value of $\overline{\psi}$, $\overline{\rho}$, $\sqrt{\overline{\psi^2} - \overline{\psi}^2}$, and $\sqrt{\overline{\rho^2} - \overline{\rho}^2}$, in the first row these are set to 0.7, 20, 0.3, and 10 respectively. Such high variances are chosen, to achieve two very distinct peaks in the bimodal cases. The figure also shows Pearson's (1895) coefficient of correlation:

$$r = \frac{\overline{\rho\psi} - \overline{\rho}\,\overline{\psi}}{\sqrt{\overline{\psi^2} - \overline{\psi}^2}\sqrt{\overline{\rho^2} - \overline{\rho}^2}}, \tag{H.12}$$

that quantifies the sub-grid covariance of ψ and ρ in a normalized way. ($r \in [0, 1]$)

Figure H.4 illustrates the effect of the different terms in Eq. (H.11). In the second row of plots the filtered density is shifted to $\overline{\rho} = 1.5$, and consequently, the interval of possible non-density-weighted values decreases significantly. Similarly in the third row, the distributions are shifted across ψ^* such, that $\overline{\psi} = 0$. As expected, this does

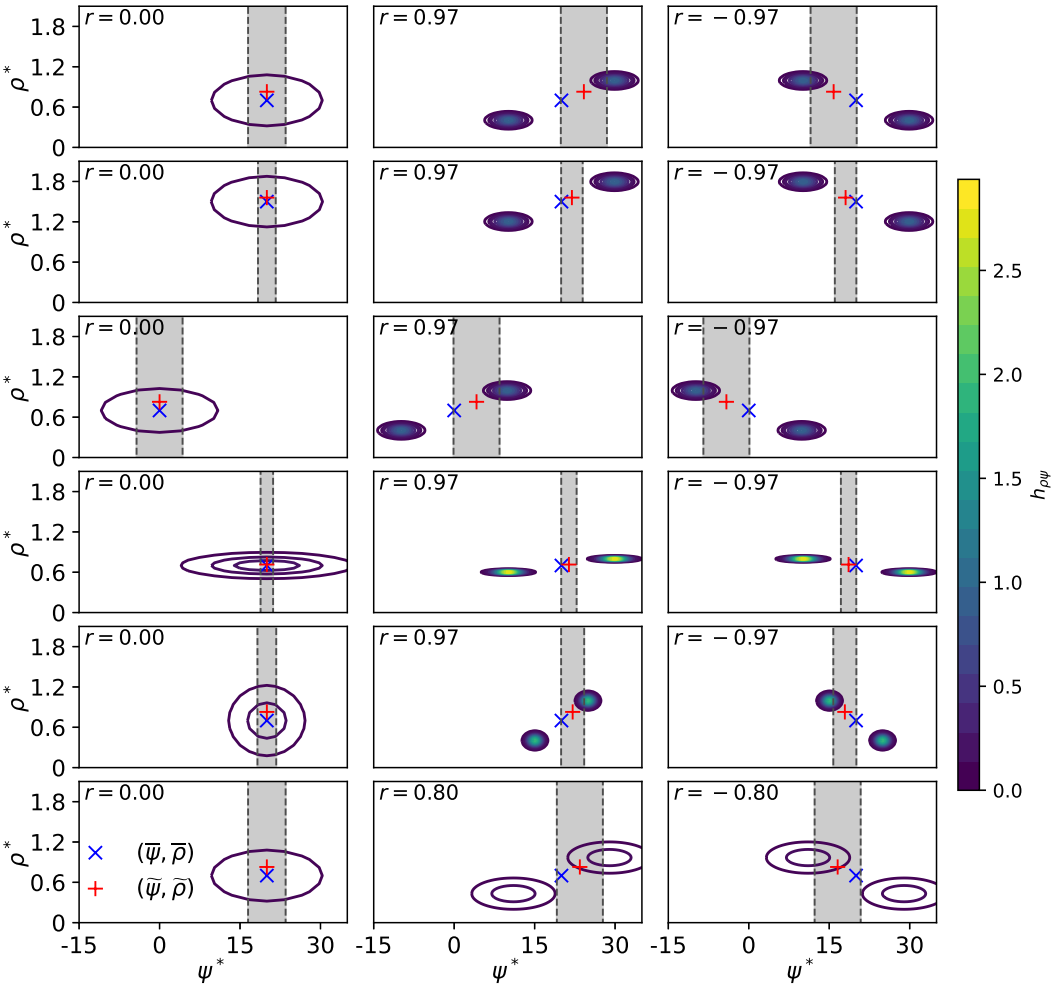

FIGURE H.4: Estimation of difference between non-density-weighted and Favre filtering on model functions. The different columns show an uncorrelated, and positively correlated, and a negatively correlated field. The $(\overline{\psi}, \overline{\rho})$ and $(\widetilde{\psi}, \widetilde{\rho})$ points are marked with "X" and "+" respectively. The first row of plots is taken as reference, then the consecutive rows show the sensitivity to: row 2: $\overline{\rho}$, row 3: $\overline{\psi}$, row 4: $\overline{\rho^2} - \overline{\rho}^2$, row 5: $\overline{\psi^2} - \overline{\psi}^2$, row 6: coefficient of correlation. Each plot displays Pearson's (1895) coefficient of correlation: $r = \frac{\overline{\rho\psi} - \overline{\rho}\,\overline{\psi}}{\sqrt{\overline{\psi^2} - \overline{\psi}^2}\sqrt{\overline{\rho^2} - \overline{\rho}^2}}$

not affect the width of the range. In rows four and five $\sqrt{\overline{\psi^2} - \overline{\psi}^2}$ and $\sqrt{\overline{\rho^2} - \overline{\rho}^2}$ are narrowed to 0.1 and 5.0 respectively, narrowing the range of possible filtered values. Finally, in row six the correlated distributions are constructed from wider peaks, that result in a more moderate coefficient of correlation. In this case the estimated range is the exact same as in the first row, but the actual filtered unknown is closer to the Favre-filtered value, since r is decreased to 0.8.

As shown above, it is possible to give an upper bound of $|\widetilde{\psi} - \overline{\psi}|$, given a good estimate of $\sqrt{\overline{\psi^2} - \overline{\psi}^2}$ and using the sub-grid closure methods of section 5.4 for otaining $\overline{\rho^2}$. If the difference shows to be small, then the numerical solution: $\widetilde{\psi}$ may be

used directly in comparisons with time averaged measurements, or in the calculation of other temporal statistical quantities.

Appendix I

Reynolds-averaged kinetic energy equation

The Reynolds-averaging operator: $\langle\cdot\rangle$ introduced in section 5.1.1 may be applied on the transport equation of kinetic energy: Eq. (2.74) in order to gain further understanding on the behavior of turbulent motion. The application of the operator transforms the equation to:

$$\begin{aligned}\partial_t\left(\langle\rho e_K\rangle\right)+\nabla\cdot\left(\langle\rho e_K\mathbf{u}\rangle\right)+\nabla\cdot\left(\langle p\mathbf{u}\rangle\right)-\nabla\cdot\left(\langle\mathbf{u}\cdot\boldsymbol{\tau}\left(\mathbf{u}\right)\rangle\right)=\\ \langle\mathbf{u}\cdot S_{\mathbf{u}}\rangle+\langle P\nabla\cdot\mathbf{u}\rangle-\underbrace{\langle\mathbf{S}:\boldsymbol{\tau}\left(\mathbf{u}\right)\rangle}_{\langle\rho\varepsilon^{tot}\rangle}-\left\langle e_K S_\rho\right\rangle,\end{aligned}\tag{I.1}$$

where properties of the Reynolds-averaging operator are exploited, such as linearity, and its commutability with derivative operators. This equation expresses the transport of mean kinetic energy per unit volume: $\langle\rho e_K\rangle$. Here the mean viscous dissipation rate of kinetic energy: $\left\langle\rho\varepsilon^{tot}\right\rangle$ is of particular interest.

The term can be transformed using the Favre-averaging operator:

$$\left\langle\rho\varepsilon^{tot}\right\rangle=\langle\rho\rangle\left\{\varepsilon^{tot}\right\}.\tag{I.2}$$

thus, following Knaus and Pantano (2009) and substituting the expression of $\boldsymbol{\tau}\left(\mathbf{u}\right)$ into the equation, the Favre-averaged kinetic energy dissipation rate is:

$$\left\{\varepsilon^{tot}\right\}=\frac{\left\langle\mathbf{S}:\left(2\rho\nu\mathbf{S^D}\right)\right\rangle}{\langle\rho\rangle}.\tag{I.3}$$

The numerator of this expression may be further transformed as:

$$\left\langle\mathbf{S}:\left(2\rho\nu\mathbf{S^D}\right)\right\rangle=\underbrace{\langle\mathbf{S}\rangle:\left\langle2\rho\nu\mathbf{S^D}\right\rangle}_{\langle\rho\rangle\varepsilon^{mean}}+\underbrace{\left\langle\mathbf{S}^{\dagger}:\left(2\rho\nu\mathbf{S^D}\right)^{\dagger}\right\rangle}_{\langle\rho\rangle\{\varepsilon\}},\tag{I.4}$$

where the first term gives ε^{mean}: the kinetic energy dissipation rate due to velocity gradients in the mean flow, while the second term: $\{\varepsilon\}$ is the mean kinetic energy dissipation rate due to strain rate fluctuations.

Similarly, the kinetic energy may be decomposed as:

$$\langle\rho e_K\rangle=\langle\rho\rangle\left\{e_K\right\}=\langle\rho\rangle\frac{1}{2}\left\{\mathbf{u}\right\}\cdot\left\{\mathbf{u}\right\}+\langle\rho\rangle\underbrace{\frac{1}{2}\left\{\mathbf{u}^{\dagger\dagger}\cdot\mathbf{u}^{\dagger\dagger}\right\}}_{\{k\}},\tag{I.5}$$

where $\{k\} = \frac{1}{2}\left(\left\{u^{\dagger\dagger\,2}\right\} + \left\{v^{\dagger\dagger\,2}\right\} + \left\{w^{\dagger\dagger\,2}\right\}\right)$ is the Favre-averaged turbulent kinetic energy. Through analysis similar to the one of section 5.1.3 one may show, that the viscous dissipation rate of the mean turbulent kinetic energy: $\{k\}$ is $\{\varepsilon\}$. (Launder and Spalding, 1974)

In conclusion, the Favre-averaged turbulent kinetic energy dissipation rate is:

$$\{\varepsilon\} = \frac{\left\langle \mathbf{S}^{\dagger} : \left(2\rho\nu\mathbf{S}^{\mathbf{D}}\right)^{\dagger} \right\rangle}{\langle\rho\rangle}, \tag{I.6}$$

where $\mathbf{S}^{\dagger} = \mathbf{S} - \langle\mathbf{S}\rangle$ is the fluctuating component of the strain rate, and $\left(2\rho\nu\mathbf{S}^{\mathbf{D}}\right)^{\dagger} = 2\rho\nu\mathbf{S}^{\mathbf{D}} - \left\langle 2\rho\nu\mathbf{S}^{\mathbf{D}}\right\rangle$ is the fluctuating part of the viscous stress tensor. Note, that the expression is significantly simpler in the field of incompressible flow simulations, where the velocity field is divergence free, and the material properties are typically taken constant.

Appendix J

EMAC formulation

The temporal and convective terms of the momentum equation may be cast in various forms. As discussed in section 5.2 while these forms are completely equivalent on the continuous level, once they are discretized using finite elements they exhibit different intrinsic conservative properties. In particular, in the formulations studied in section 5.2, the strict conservation of kinetic energy, momentum, and angular momentum can depend on the strict local conservation of mass. To mitigate the consequences of non-conservative behavior Charnyi et al. (2017) introduced a discretization strategy for this term, which ensures the simultaneous conservation of linear and angular momentum besides kinetic energy. Their method is developed for incompressible flows using mixed finite elements to stabilize pressure. This method has been extended to equal order finite elements by Lehmkuhl et al. (2019b) and it has been tested in fully turbulent incompressible flows with success. Recently Coppola et al. (2019) classified a family of commonly used discretization strategies that stem from the splitting of the convective term. However a different approach is explored by Ortega (2018), extending the approach of Lehmkuhl et al. (2019b) to compressible flows. Below this extension is detailed.

In this work the kinetic energy, momentum, and angular momentum conserving (EMAC) scheme of Charnyi et al. (2017) is reformulated for the low Mach regime. The incompressible implementation exploits the symmetry properties of $C(\rho, \mathbf{u})$. The underlying idea of the present extension is to use a change of variables to preserve the fundamental behavior of the original method. In this case $\mathbb{A} \equiv \sqrt{\rho}\mathbf{u}$ is used in order to express the momentum flux as a vector product of two equal terms: $\rho\mathbf{u} \otimes \mathbf{u} = \mathbb{A} \otimes \mathbb{A}$. Such $\sqrt{\rho}$ formalism, appears in many studies related to variable density flows. Van Driest (1951) introduced a scaling law for turbulent thermal boundary layers applying this transformation. Various studies used the formalism to study the effects of compressibility on forced and decaying turbulence in ideal gas (Yih, 1960; Kida and Orszag, 1992; Cook and Zhou, 2002). More recently Rozema et al. (2018) developed a conservative discretization scheme for compressible flows using finite volume method by using a $\sqrt{\rho}$ formalism in the vector of unknowns. In the present study a scheme is developed, where the transport of $\mathbb{A}$ is not required, as it is only used in the assembly of the individual terms of the Navier-Stokes equations.

For arbitrary vector fields of: $\mathbf{u}, \mathbf{v}, \mathbf{w} \in \mathbf{H}^1(\Omega)$ the trilinear form is defined using the notation introduced in section 2.3.2. The trilinear form is $b : \mathbf{H}^1(\Omega) \times \mathbf{H}^1(\Omega) \times \mathbf{H}^1(\Omega) \rightarrow \mathbb{R}$ with:

$$b(\mathbf{u}, \mathbf{v}, \mathbf{w}) = (\mathbf{u} \cdot \nabla \mathbf{v}, \mathbf{w}). \tag{J.1}$$

Note, that parentheses are used to denote the L^2 inner product operator on the entire control volume Ω as: $(\mathbf{a}, \mathbf{b}) = \int_\Omega \mathbf{a} \cdot \mathbf{b} \mathrm{d}V$, where $\mathbf{a}$ and $\mathbf{b}$ are arbitrary vectors. By

definition, the trilinear form may be transformed as:

$$b\left(\mathbf{u},\mathbf{v},\mathbf{w}\right)=\left(\left(\nabla\mathbf{v}\right)\mathbf{u},\mathbf{w}\right)=\left(\left(\nabla\mathbf{v}\right)^{T}\mathbf{w},\mathbf{u}\right). \tag{J.2}$$

Furthermore, restricting $\mathbf{u}$ to: $\mathbf{u}\in\mathbf{H}_{0}^{1}\left(\Omega\right)$, i.e.: the subspace of $\mathbf{H}^{1}\left(\Omega\right)$ that is constant zero on the boundary Γ, further identities can be derived. In such a case, the following may be derived using integration by parts:

$$b\left(\mathbf{u},\mathbf{v},\mathbf{w}\right)=-b\left(\mathbf{u},\mathbf{w},\mathbf{v}\right)-\left(\left(\nabla\cdot\mathbf{u}\right)\mathbf{v},\mathbf{w}\right), \tag{J.3}$$

$$b\left(\mathbf{u},\mathbf{w},\mathbf{w}\right)=-\frac{1}{2}\left(\left(\nabla\cdot\mathbf{u}\right)\mathbf{w},\mathbf{w}\right). \tag{J.4}$$

Additionally the symmetric part of the gradient is denoted as $\nabla_{s}\mathbf{u}\equiv\mathbf{D}\left(\mathbf{u}\right)=\frac{\nabla\mathbf{u}+\left(\nabla\mathbf{u}\right)^{T}}{2}$, while the skew-symmetric part is: $\nabla_{n}\mathbf{u}\equiv\frac{\nabla\mathbf{u}-\left(\nabla\mathbf{u}\right)^{T}}{2}$. For $\mathbf{u},\mathbf{v}\in\mathbf{H}^{1}\left(\Omega\right)$ the following holds,

$$\left(\nabla_{n}\mathbf{u}\right)\mathbf{v}=\frac{1}{2}\left(\nabla\times\mathbf{u}\right)\times\mathbf{v}, \tag{J.5}$$

$$\left(\mathbf{u}\cdot\nabla\right)\mathbf{u}=\left(\nabla\times\mathbf{u}\right)\times\mathbf{u}+\frac{1}{2}\nabla\left|\mathbf{u}\right|^{2}, \tag{J.6}$$

$$\left(\nabla\mathbf{u}\right)\mathbf{u}=\left(\nabla_{s}\mathbf{u}\right)\mathbf{u}+\left(\nabla_{n}\mathbf{u}\right)\mathbf{u}=\mathbf{D}\left(\mathbf{u}\right)\mathbf{u}+\frac{1}{2}\left(\nabla\times\mathbf{u}\right)\times\mathbf{u}. \tag{J.7}$$

The last expression is connected to the trilinear form as:

$$\left(\mathbf{D}\left(\mathbf{u}\right)\mathbf{u},\mathbf{u}\right)=\left(\left(\nabla\mathbf{u}\right)\mathbf{u},\mathbf{u}\right)=b\left(\mathbf{u},\mathbf{u},\mathbf{u}\right). \tag{J.8}$$

Using Eq. (J.5), Eq. (J.6), and Eq. (J.7) one gets:

$$\left(\mathbf{u}\cdot\nabla\right)\mathbf{u}=2\mathbf{D}\left(\mathbf{u}\right)\mathbf{u}-\frac{1}{2}\nabla\left|\mathbf{u}\right|^{2}. \tag{J.9}$$

Introducing the notation: $\mathbb{A}\equiv\sqrt{\rho}\mathbf{u}$, allows the preservation of the symmetric properties used in the incompressible formulation of Charnyi et al. (2017). The nonlinear term of the momentum equation can be written as:

$$\nabla\cdot\left(\rho\mathbf{u}\otimes\mathbf{u}\right)=\nabla\cdot\left(\mathbb{A}\otimes\mathbb{A}\right)=\left(\nabla\cdot\mathbb{A}\right)\mathbb{A}+\left(\mathbb{A}\cdot\nabla\right)\mathbb{A}. \tag{J.10}$$

Using Eq. (J.9) yields the proposed EMAC formulation of the convective term for variable density flows:

$$C_{emac}\left(\rho,\mathbf{u}\right)\equiv2\mathbf{D}\left(\mathbb{A}\right)\mathbb{A}+\left(\nabla\cdot\mathbb{A}\right)\mathbb{A}-\tfrac{1}{2}\nabla\left|\mathbb{A}\right|^{2}. \tag{J.11}$$

Note, that the above derivation does not take advantage of the continuity equation, thus the temporal term may be kept in its conservative form: $\partial_{t}\left(\rho\mathbf{u}\right)$, or may be transformed as: $\rho\partial_{t}\mathbf{u}+\left(\partial_{t}\rho\right)\mathbf{u}$.

Appendix K

Sub-grid chemistry models in the Cambridge spray burner

The Cambridge swirl bluff-body burner provides a uniquely responsive test case for the evaluation of chemical modeling effects, as a combination of very stable and very sensitive characteristics. On one hand, the spray cloud and the mean flow field are barely affected by changes in the thermo-chemical manifolds, and even the mixture fraction and temperature fields are fairly insensitive to these modeling choices. On the other hand, the statistical analysis of the flame lift-off length (LOL) is sensitive enough to capture differences between chemistry models. (See section 8.3.4.) In this appendix two sub-grid turbulence/chemistry interaction models are compared in the n-heptane (H1S1) case of the Cambridge swirl bluff-body burner.

The modeling strategy applied in this work uses the density-weighted joint filter probability density function (joint FPDF) of the thermo-chemical manifold's control variables to describe the sub-grid state. The unfiltered control variables in the spray flames of the present case are the mixture fraction (Z), the scaled progress variable (C), and the scaled enthalpy (i). Statistical independence is assumed between these variables, thus the joint FPDF is constructed as a product of marginal FPDFs, which are modeled either as beta or delta distributions. Here two combinations are tested following the reasoning of Pierce and Moin (2004) and Domingo, Vervisch, and Veynante (2008). The former approach considers, that the sub-grid distribution of mixture fraction is the single determining factor in sub-grid chemical effects, thus the density-weighted joint FPDF is constructed as: $\widetilde{P}_{ZCi} = \widetilde{P}_Z^{\beta}\widetilde{P}_C^{\delta}\widetilde{P}_i^{\delta}$, where only the mixture fraction is modeled with a beta distribution. In the present work this method is applied by default for the analysis of the Cambridge swirl bluff-body burner. Meanwhile the latter approach assumes, that both the mixture fraction and the scaled progress variable are characterized by independent beta distributions on the sub-grid scale: $\widetilde{P}_{ZCi} = \widetilde{P}_Z^{\beta}\widetilde{P}_C^{\beta}\widetilde{P}_i^{\delta}$. In this case the sub-grid variance of the progress variable is also transported using the following governing equation:

$$\partial_t\left(\overline{\rho}Y_{c,v}\right) + \nabla\cdot\left(\overline{\rho}Y_{c,v}\widetilde{\mathbf{u}}\right) - \nabla\cdot\left(\overline{\rho}\left(\widetilde{\mathcal{D}_t} + \frac{\nu^{SGS}}{Sc^{SGS}}\right)\nabla Y_{c,v}\right) = 2\frac{\overline{\rho}\nu^{SGS}}{Sc^{SGS}}\nabla\widetilde{Y}_c\cdot\nabla\widetilde{Y}_c + 2\left(\overline{Y_c\dot{\omega}_{Y_c}} - \widetilde{Y}_c\overline{\dot{\omega}_{Y_c}}\right) - \overline{\rho}\chi_{Y_c}^{SGS}, \tag{K.1}$$

which provides the parameters of the $\widetilde{P}_C^{\beta}$ distribution together with $\widetilde{Y}_c$. The remaining modeling strategy is the same as outlined in section 8.3, thus premixed flamelets are used to construct the thermo-chemical databases.

The effect of the two sub-grid strategies is illustrated in Fig. K.1 by the probability density function of flame lift-off length along the outer reaction layer. On the coarse

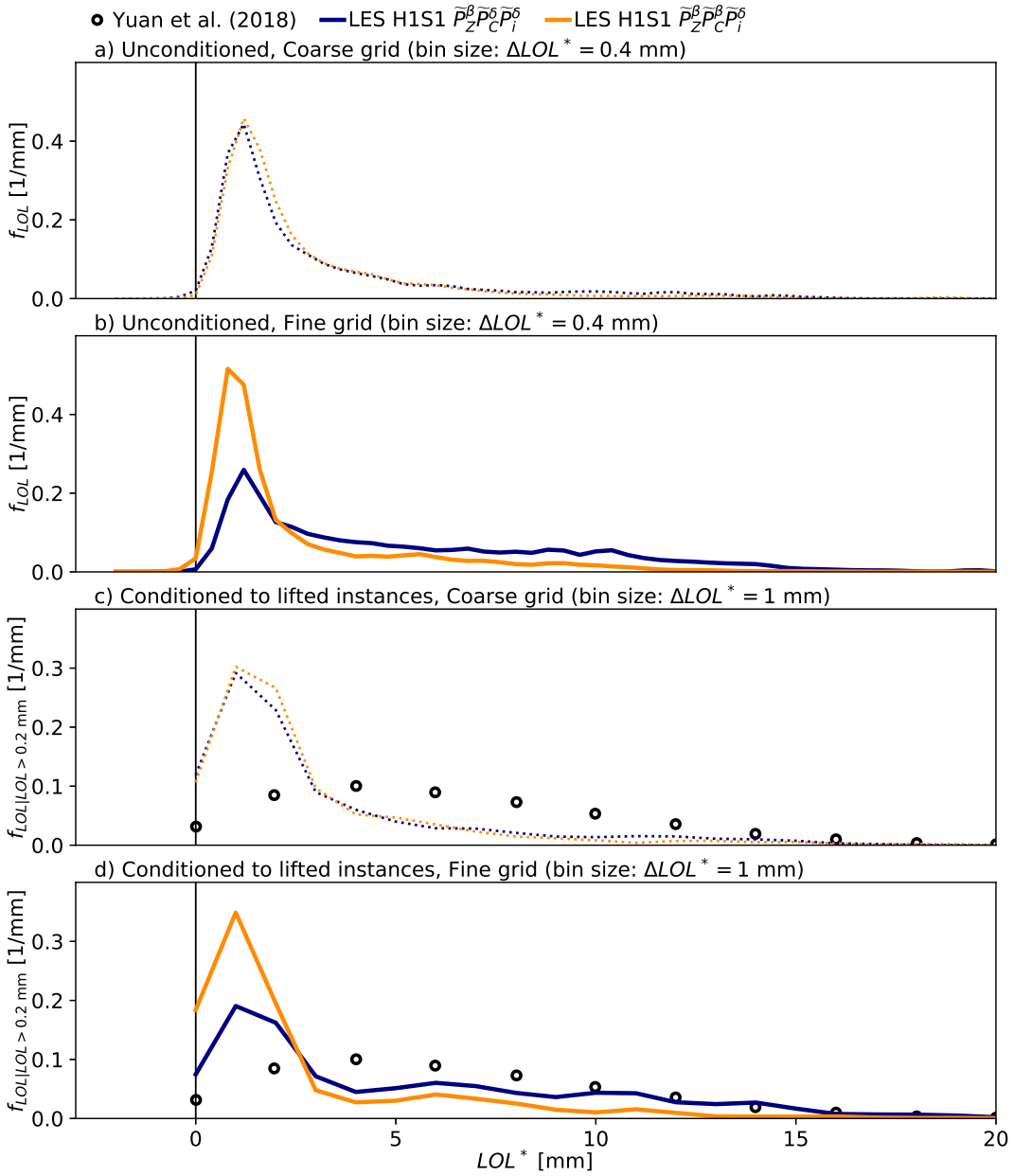

FIGURE K.1: Effect of sub-grid turbulence/chemistry interaction models on probability density function of flame lift-off length in the n-heptane case (H1S1) of the Cambridge swirl bluff-body burner. The unconditioned statistics (a,b) uses all the time instances of the LES, while the conditioned one (c,d) only considers the lifted cases of $LOL > 0.2$ mm.

mesh the lift-off is only slightly affected by this modeling decision. In the base case of $\widetilde{P}_Z^{\beta}\widetilde{P}_C^{\delta}\widetilde{P}_i^{\delta}$ on the coarse mesh the mean lift-off is $\langle LOL \rangle = 3.1$ mm, and the same mean value is reached by conditioning the cases to lifted instances, as only 1% of the cases are qualified as attached according to the criterion of Cavaliere, Kariuki, and Mastorakos (2013): $LOL \leq 0.2$ mm. In the case following Domingo, Vervisch, and Veynante (2008): $\widetilde{P}_Z^{\beta}\widetilde{P}_C^{\beta}\widetilde{P}_i^{\delta}$ on the coarse mesh, the mean lift-off is $\langle LOL \rangle = 2.8$ mm

in both the unconditioned and conditioned cases. This nearly 10% difference is not outstanding on the PDF curves, note however, that the $\widetilde{P}_Z^{\beta}\widetilde{P}_C^{\beta}\widetilde{P}_i^{\delta}$ case has consistently lower likelihood to show lift-off states of $LOL > 7$ mm and higher likelihood of $LOL \approx 2$ mm.

The differences are more pronounced on the fine mesh. As discussed in section 8.3.3 the mesh refinement improves the lift-off predictions in the base case of $\widetilde{P}_Z^{\beta}\widetilde{P}_C^{\delta}\widetilde{P}_i^{\delta}$ using the premixed flamelet based manifold. In this case the mean lift-off length is $\langle LOL|LOL > 0.2\,\text{mm}\rangle = 5.3$ mm, which compares fairly well with the experimental value of 6.25 mm determined by Yuan, Kariuki, and Mastorakos (2018). Meanwhile, using the strategy of $\widetilde{P}_Z^{\beta}\widetilde{P}_C^{\beta}\widetilde{P}_i^{\delta}$ on the fine mesh, the mean lift-off is the lowest among the cases presented here: $\langle LOL|LOL > 0.2\,\text{mm}\rangle = 2.7$ mm, as the flame becomes more likely to have a small lift-off. These results are aligned well with the 1D analysis of section 6.3.4 which showed, that higher sub-grid progress variable variances may result in increased flame propagation speeds. This can ultimately lead to a more attached flame.

Overall, as Floyd et al. (2009) identifies, the actual prediction of the correct sub-grid progress variable variance value has a greater influence on the results, than the selection of the sub-grid model which uses this variance. The validity of Eq. K.1 is uncertain. For instance Nilsson et al. (2019) found, that the variance production with the gradient diffusion assumption may be inadequate, as this term can become negative to balance the reactive production of $Y_{c,v}$. In light of this uncertainty and the observed deterioration of the lift-off results in the H1S1 case, it is not recommended to use the $\widetilde{P}_Z^{\beta}\widetilde{P}_C^{\beta}\widetilde{P}_i^{\delta}$ sub-grid modeling strategy for the Cambridge swirl bluff-body burner in its present form. More work is needed to establish a reliable sub-grid turbulence/chemistry interaction model in the developed low-dissipation finite element framework.

Appendix L

Evaporation models in the Cambridge spray burner

The Cambridge swirl bluff-body burner is especially challenging for the Lagrangian droplet evaporation models, as the spray is injected directly into the partially reacted rich gases of the central recirculation zone. Under these conditions the droplets interact with very high temperature mixtures. As chapter 4 demonstrates, different heat and mass transfer models show a great variability with such seen gas states. This appendix compares the performance of two evaporation models: the classical one of section 4.4.4, and the presently recommended model of Abramzon and Sirignano (1989) detailed in section 4.4.6. The classical evaporation model only considers Stefan flow in the mass transfer and neglects it in the heat transfer, which results in unrealistically high evaporation rates. While this behavior is readily demonstrated in chapter 4 and appendix G, the inferiority of the classical evaporation model is not straightforward. For instance Noh et al. (2018) studied the CORIA Rouen spray burner (CRSB), which exhibits a flame lift-off due to high oxidizer velocities near the spray injector. In such a situation the interaction of the flame and the spray is of lesser importance, and even the classical evaporation model can predict a reasonable flame behavior. Nevertheless, as Noh et al. (2018) found, the performance of models considering Stefan flow is superior. The present appendix illustrates the severe consequences of applying the classical evaporation model in a case, where the flame interacts directly with the fuel spray in the n-heptane case (H1S1) of the Cambridge swirl bluff-body burner.

The basic modeling strategy of the Cambridge swirl spray flames is the one outlined in section 8.3. Here this is labeled "AS" as the evaporation model of Abramzon and Sirignano (1989) is used, which describes the droplet mass and temperature evolution as:

$$\frac{\mathrm{d}T_p}{\mathrm{d}t} = \frac{\pi d_p \lambda_m Nu_m^{*,AS}}{m_p c_{p,p}} \left(T_s - T_p\right) \frac{\ln\left(1+B_T\right)}{B_T} + \frac{L_v}{m_p c_{p,p}} \frac{\mathrm{d}m_p}{\mathrm{d}t}, \tag{L.1}$$

$$\frac{\mathrm{d}m_p}{\mathrm{d}t} = -\pi d_p \rho_m \mathcal{D}_m Sh_m^{*,AS} \ln\left(1+B_M\right). \tag{L.2}$$

Meanwhile, the classical evaporation model, marked "S/D", changes the droplet ODEs to:

$$\frac{\mathrm{d}T_p}{\mathrm{d}t} = \frac{\pi d_p \lambda_m Nu_{m,0}}{m_p c_{p,p}} \left(T_s - T_p\right) + \frac{L_v}{m_p c_{p,p}} \frac{\mathrm{d}m_p}{\mathrm{d}t}, \tag{L.3}$$

$$\frac{\mathrm{d}m_p}{\mathrm{d}t} = -\pi d_p \rho_m \mathcal{D}_m Sh_{m,0} \ln\left(1+B_M\right). \tag{L.4}$$

For further details of the evaporation models see section 4.4. This comparison is executed on the coarse mesh of the Cambridge swirl bluff-body burner, characterized by tetrahedral elements of edge length $a = 1$ mm. Note, that here a thermo-chemical manifold of stable and unsteady extinguishing counterflow diffusion flamelets is applied, which is a notable difference between the present results and the base case of section 8.3. Nevertheless, as section 8.3.4 demonstrates, the tabulation strategy only has a minimal effect on the mixture fraction and temperature fields, thus the conclusions of the present comparison are generally valid.

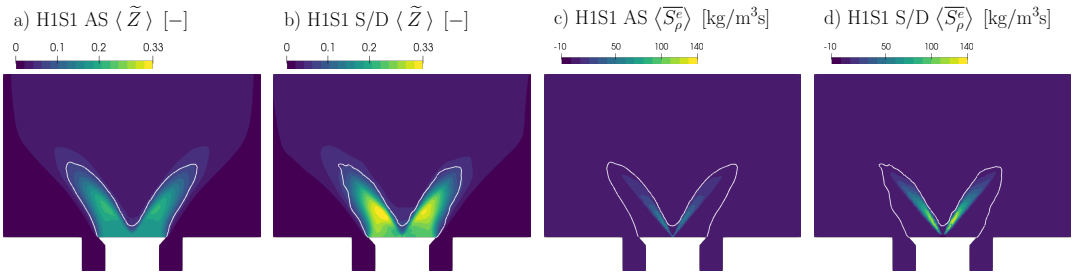

FIGURE L.1: Comparison of mean scalar fields of the n-heptane case (H1S1) of the Cambridge swirl bluff-body burner using the Abramzon-Sirignano (AS) evaporation model and the Classical evaporation model (S/D) which neglects Stefan flow. The plots show the mean mixture fraction (a,b), and evaporative mass source term (c,d). The contour line marks the position of stoichiometric mixture fraction (white).

The mixture fraction fields are illustrated in Fig. L.1a and b. Indeed, the classical evaporation model shows approximately 50% higher peak values of the time averaged mixture fraction. The location of the peak mixture fraction is the same, linked to the spray location. This higher mixture fraction peak modifies the flame characteristics significantly, as the outer reaction zone is characterized by higher scalar dissipation rates, and the typical mixtures are further away from the flammable range. Figure L.1c and d shows the time averaged evaporative mass source term. Indeed, the droplet heat-up and evaporation is much slower in the Abramzon-Sirignano model, showing a maximum $\left\langle \overline{S_\rho^e} \right\rangle$ of approximately 80 [kg/m^{3}s], while this peak is near 140 [kg/m^{3}s] in the case of the classical model.

The effects are further illustrated in Fig. L.2 using the averaged droplet data. Using the classical model the droplets evaporate before the last measurement location of $x = 40$ mm is reached, thus the "S/D" curves are absent in Fig. L.2a-c. Interestingly, the Sauter mean diameter is not affected significantly, as the fast evaporation removes the smaller droplets while the larger droplets are also evaporating at a high rate. In the Abramzon-Sirignano model the mean droplet temperature remains around 15 K below the boiling point of n-heptane. Using the classical model the mean droplet temperature approaches the boiling point at $x = 20$ mm as very high Spalding mass transfer numbers are necessary to maintain equilibrium (wet-bulb) conditions. (See appendix G.) As the fast evaporation filters out the smaller droplets in the classical model, the mean droplet velocity becomes significantly higher, since the larger droplets are initially less affected by drag. Overall, the classical model is not suitable to reproduce the spray flame behavior in the Cambridge swirl bluff-body burner.

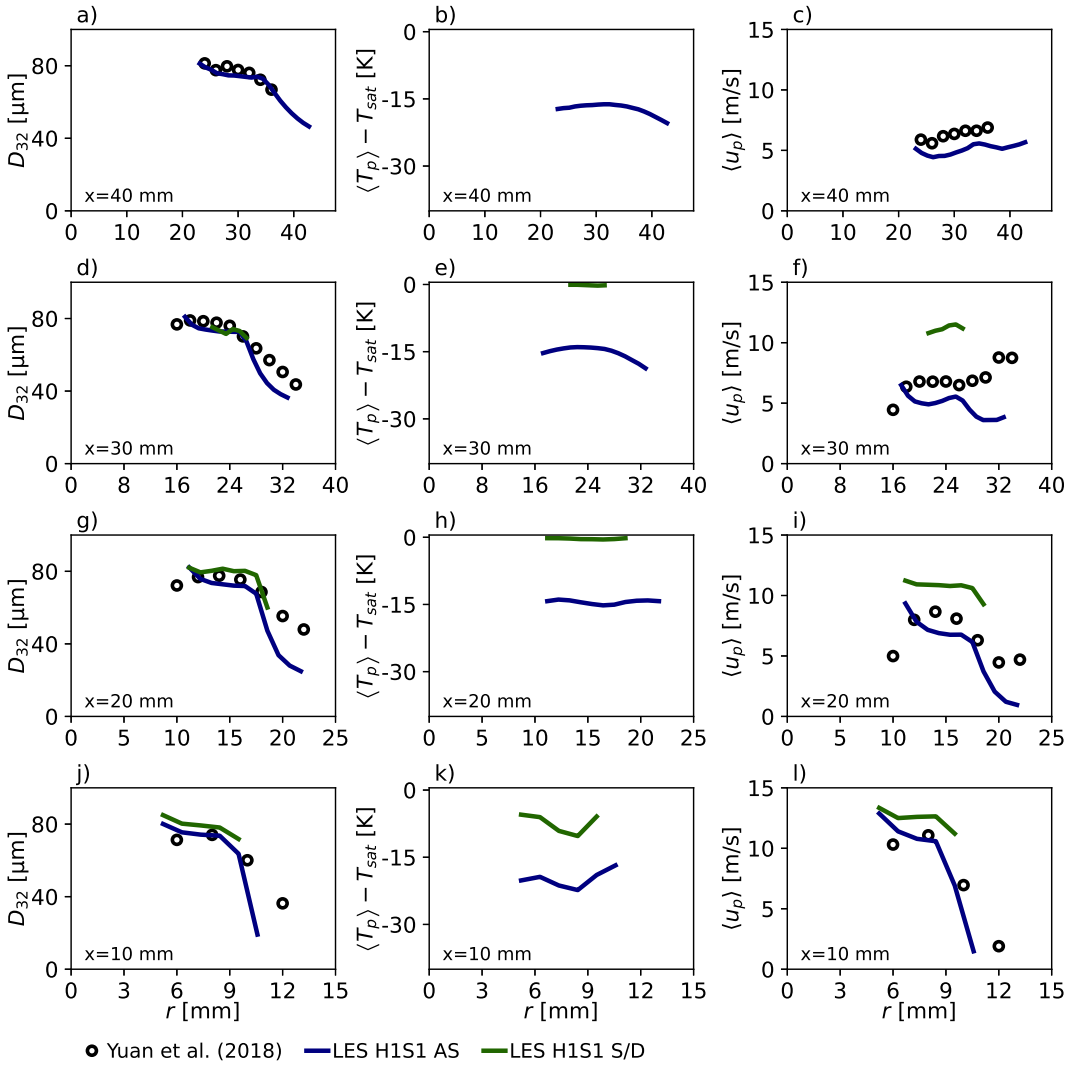

FIGURE L.2: Comparison of mean droplet properties in the n-heptane case (H1S1) of the Cambridge swirl bluff-body burner using the Abramzon-Sirignano (AS) evaporation model and the Classical evaporation model (S/D) which neglects Stefan flow. The PDA measurements of Yuan, Kariuki, and Mastorakos (2018) are indicated by symbols and the LES results of the present work by lines. The rows of plots correspond to the indicated axial location, while the three columns show the Sauter mean diameter, and the mean droplet temperature and axial droplet velocity.

Appendix M

Additional results of the Cambridge spray burner

This appendix provides additional results on the n-heptane (H1S1) and n-dodecane (DD1S2) cases of the Cambridge swirl bluff-body burner which does not form an integral part of the discussion in section 8.3. These results are produced with the same modeling strategy as outlined in section 8.3.1 for the gas phase, and section 8.3.2 for the liquid injection. The thermo-chemical manifold is constructed from free and burner-stabilized premixed flamelets.

The mean and RMS velocity components of the H1S1 case are compared to the cold flow case (C1) and the non-premixed methane case (F3A2) in Fig. M.1 and Fig. M.2 respectively. In general the high speed oxidizer flow is very similar in the methane and n-heptane cases both in terms of mean and RMS values, as the air flow rate is only $\sim$ 10% lower in the latter case. The central recirculation zone is perturbed by the momentum introduced by the fuel spray. As Fig. M.1m, n, p and q show, this creates a very concentrated region with positive axial velocity with likewise positive radial velocity. In the same location there is a small impact on the velocity fluctuations. The effect of the spray on the mean velocity field vanishes at $x = 20$ mm, and the central recirculation zone becomes similar to the cold flow case. Overall, the flow field of the H1S1 case resembles the non-premixed methane case except for the effect of the gaseous fuel jet.

The scalar fields of the reacting flow simulations using different fuels: methane (F3A2), n-heptane (H1S1) and n-dodecane (DD1S2), are also compared here quantitatively. Figure M.3 shows the mean profiles of mixture fraction, temperature, and hydroxyl mass fraction. While, Fig. M.4 shows the RMS of mixture fraction and temperature. The mean mixture fraction fields show significant differences in the central recirculation zone, while these differences decrease towards the outer edge of the flame. Similar trends are observed in the mean temperature. All cases show a rich plateau of mixture fraction at the flame base, where the interaction of this partially reacted mixture and the fresh oxidizer creates the intermittently lifted outer reaction zone. The flames are similar in the outer reaction layer even in terms of the RMS values, and differences are mostly observed in the central recirculation zone. For instance the temperature RMS is nearly identical in the outer reaction zone in Fig. M.4l, as this is mostly created by the radial movement of the reaction layer, and the effect of flame lift-off is secondary.

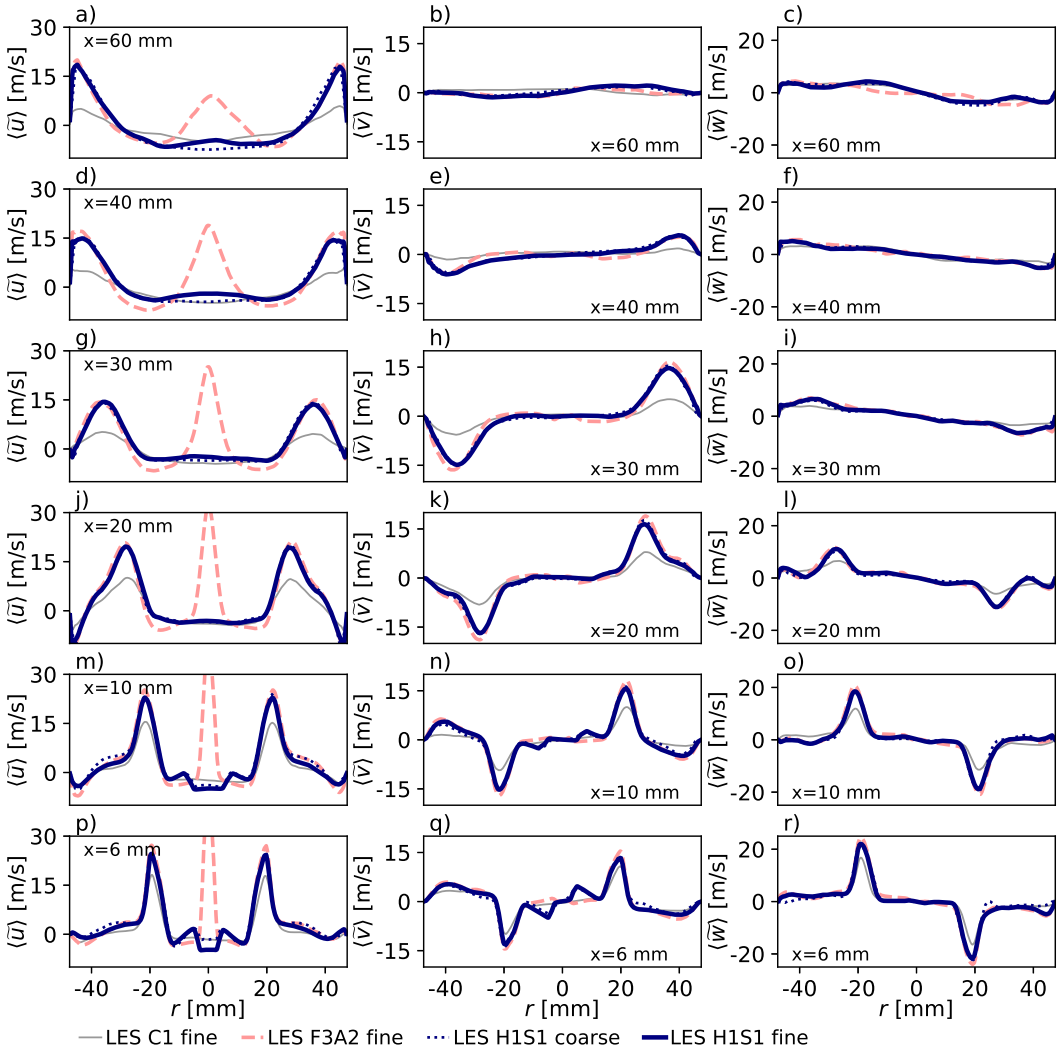

FIGURE M.1: Mean velocity profiles in the n-heptane case (H1S1) of the Cambridge swirl bluff-body burner using the LES of the present work. The rows of plots correspond to the indicated axial location, while the three columns show the mean of the axial, radial and tangential velocity.

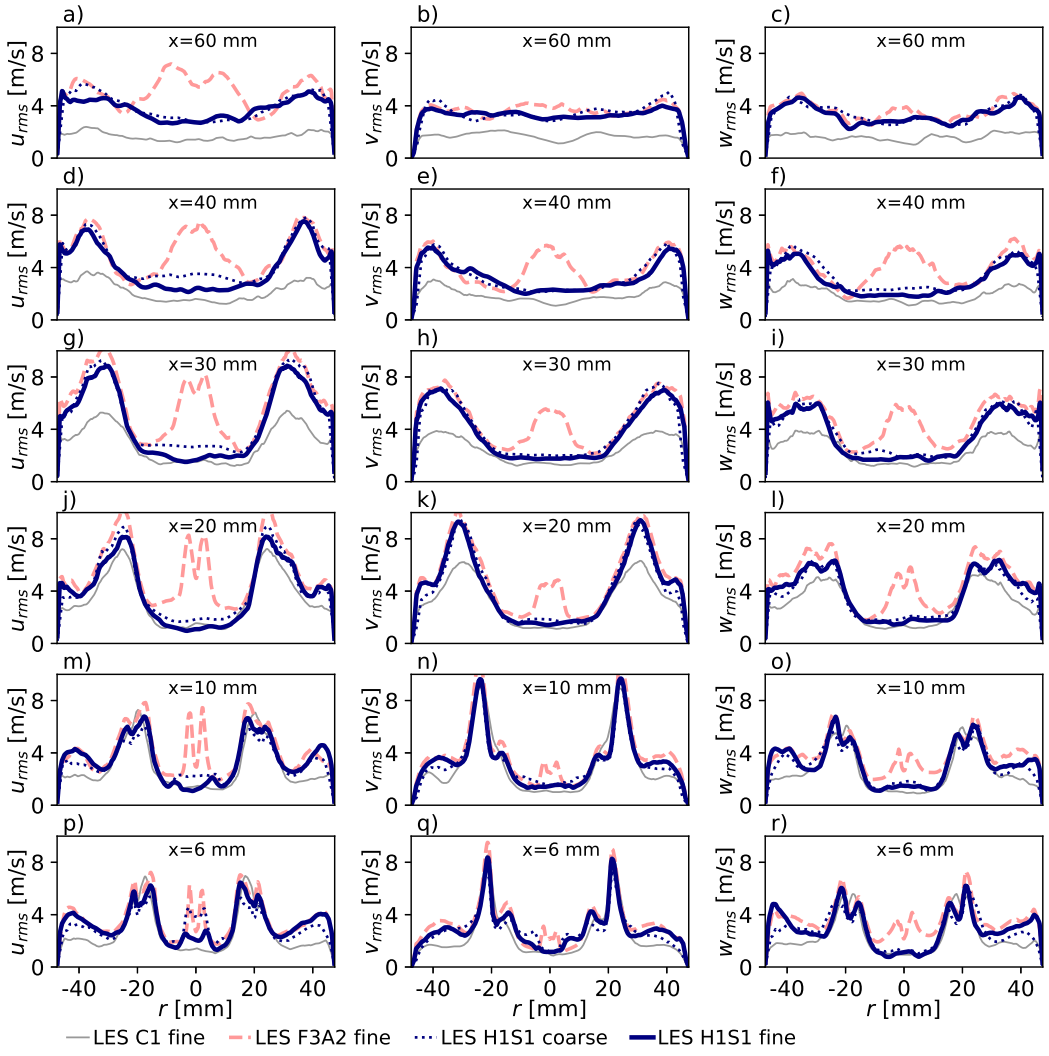

FIGURE M.2: RMS velocity profiles in the n-heptane case (H1S1) of the Cambridge swirl bluff-body burner using the LES of the present work. The rows of plots correspond to the indicated axial location, while the three columns show the RMS of the axial, radial and tangential velocity.

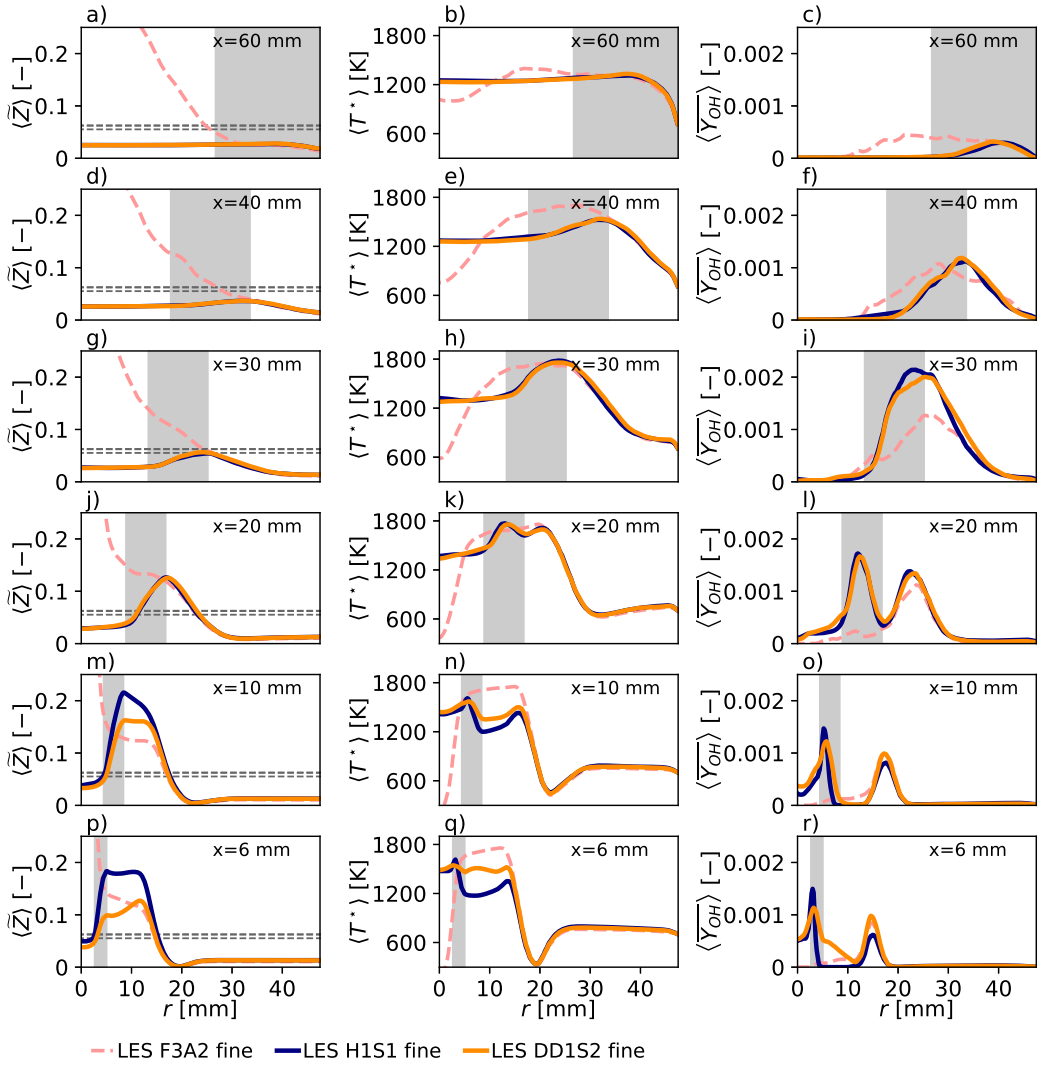

FIGURE M.3: Mean scalar profiles in the n-heptane (H1S1) and n-dodecane (DD1S2) cases of the Cambridge swirl bluff-body burner using the LES of the present work. The rows of plots correspond to the indicated axial location, while the three columns show the mean of the mixture fraction, temperature, and hydroxyl mass fraction. The gray shading represents the spray half-angle range of $[24°, 40°]$ with respect to the injector location. The horizontal dashed gray lines shows the stoichiometric mixture fraction of the three fuels.

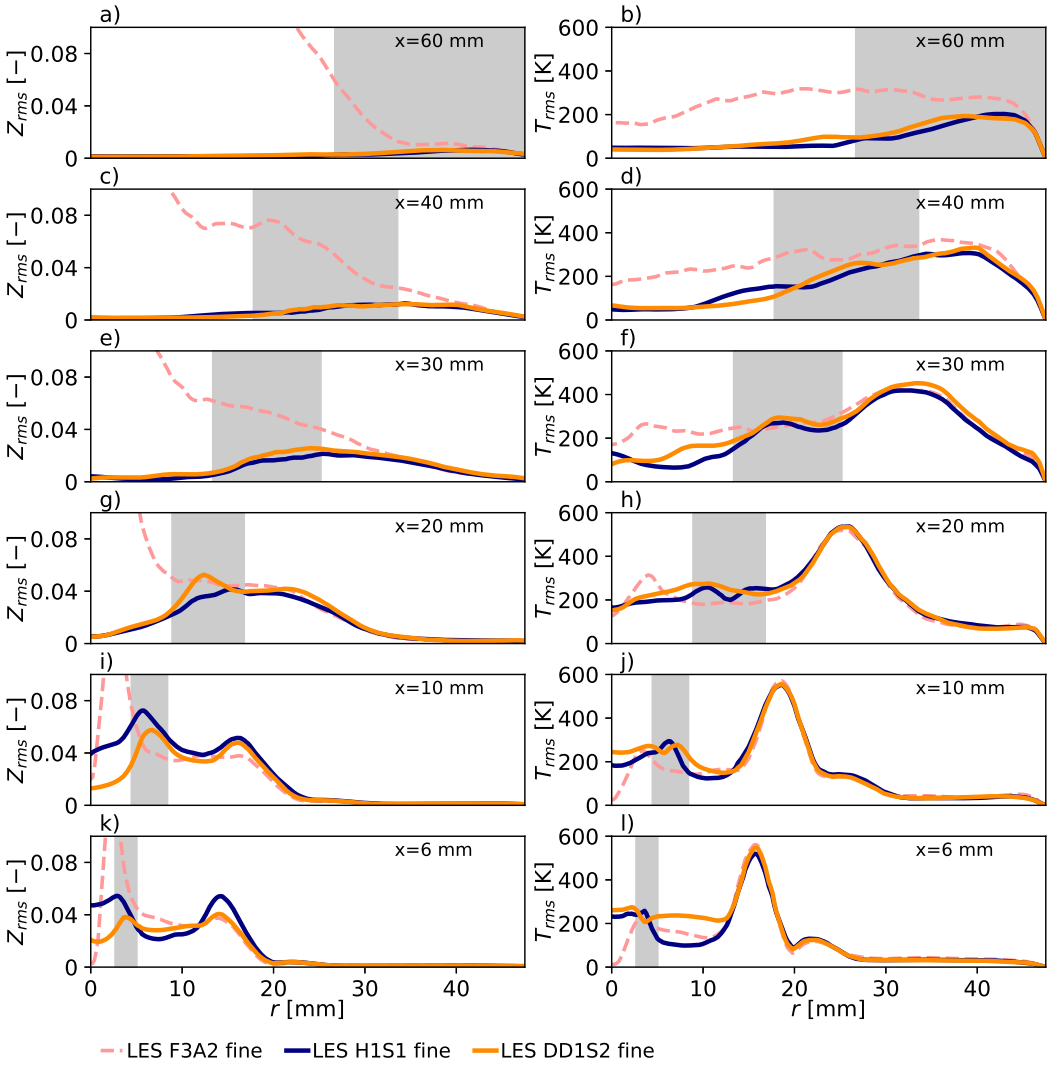

FIGURE M.4: RMS scalar profiles in the n-heptane (H1S1) and n-dodecane (DD1S2) cases of the Cambridge swirl bluff-body burner using the LES of the present work. The rows of plots correspond to the indicated axial location, while the three columns show the RMS of the mixture fraction, temperature. The gray shading represents the spray half-angle range of $[24°, 40°]$ with respect to the injector location.

Bibliography

Abramzon, B and W A Sirignano (1989). "Droplet vaporization model for spray combustion calculations". In: *International journal of heat and mass transfer* 32.9, pp. 1605–1618.

ACARE (2023). *Fly the green deal*. Ed. by Advisory Council of Aeronautic Research in Europe. URL: https://www.acare4europe.org/news/fly-the-green-deal/.

Albrecht, BA, S Zahirovic, RJM Bastiaans, JA Van Oijen, and LPH De Goey (2008). "A premixed flamelet- PDF model for biomass combustion in a grate furnace". In: *Energy & fuels* 22.3, pp. 1570–1580.

Alessandro, D'Ausilio, Ivana Stankovic, and Bart Merci (2019). "LES study of a turbulent spray jet: mesh sensitivity, mesh-parcels interaction and injection methodology". In: *Flow, Turbulence and Combustion* 103.2, pp. 537–564.

Allison, Patton M, Jennifer A Sidey, and Epaminondas Mastorakos (2017). "Transient Behavior of Kerosene Flames in a Bluff-Body Stabilized Swirl Combustor". In: *55th AIAA Aerospace Sciences Meeting*, p. 1569.

Ames, research staff (1953). *Equations, tables, and charts for compressible flow*. NACA report. National Advisory Committee for Aeronautics (NACA).

ATAG (2023). *Waypoint 2050*. Ed. by Air Transport Action Group. URL: https://aviationbenefits.org/environmental-efficiency/climate-action/waypoint-2050/.

Aulery, Frederic, Dorian Dupuy, Adrien Toutant, Françoise Bataille, and Ye Zhou (2017). "Spectral analysis of turbulence in anisothermal channel flows". In: *Computers & Fluids* 151, pp. 115–131.

Avdić, Amer, Guido Kuenne, Francesca di Mare, and Johannes Janicka (2017). "LES combustion modeling using the Eulerian stochastic field method coupled with tabulated chemistry". In: *Combustion and Flame* 175, pp. 201–219.

Avila, Matias, Javier Principe, and Ramon Codina (2011). "A finite element dynamical nonlinear subscale approximation for the low Mach number flow equations". In: *Journal of Computational Physics* 230.22, pp. 7988–8009.

Bailly, Christophe and Daniel Juve (1999). "A stochastic approach to compute subsonic noise using linearized Euler's equations". In: *5th AIAA/CEAS aeroacoustics conference and exhibit*, p. 1872.

Bajaj, Chetan, Muhsin Ameen, and John Abraham (2013). "Evaluation of an unsteady flamelet progress variable model for autoignition and flame lift-off in diesel jets". In: *Combustion Science and Technology* 185.3, pp. 454–472.

Balakrishnan, G and FA Williams (1994). "Turbulent combustion regimes for hypersonic propulsion employing hydrogen-air diffusion flames". In: *Journal of Propulsion and Power* 10.3, pp. 434–437.

Banchelli, Fabio, Marta Garcia-Gasulla, Guillaume Houzeaux, and Filippo Mantovani (2020). "Benchmarking of state-of-the-art HPC Clusters with a Production CFD Code". In: *Proceedings of the Platform for Advanced Scientific Computing Conference*, pp. 1–11.

Banchelli, Fabio, Guillermo Oyarzun, Marta Garcia-Gasulla, Filippo Mantovani, Ambrus Both, Guillaume Houzeaux, and Daniel Mira (2022). "A portable coding

strategy to exploit vectorization on combustion simulations". In: *arXiv preprint arXiv:2210.11917*.

Bejan, Adrian (2006). *Advanced engineering thermodynamics*. John Wiley & Sons.

Bekdemir, C, LMT Somers, and LPH De Goey (2011). "Modeling diesel engine combustion using pressure dependent flamelet generated manifolds". In: *Proceedings of the Combustion Institute* 33.2, pp. 2887–2894.

Bekdemir, C, LMT Somers, LPH De Goey, J Tillou, and C Angelberger (2013). "Predicting diesel combustion characteristics with large-eddy simulations including tabulated chemical kinetics". In: *Proceedings of the Combustion Institute* 34.2, pp. 3067–3074.

Benajes, J, José M García-Oliver, José Manuel Pastor, I Olmeda, Ambrus Both, and Daniel Mira (2022). "Analysis of local extinction of a n-heptane spray flame using large-eddy simulation with tabulated chemistry". In: *Combustion and Flame* 235, p. 111730.

Bergmann, V, W Meier, D Wolff, and W Stricker (1998). "Application of spontaneous Raman and Rayleigh scattering and 2D LIF for the characterization of a turbulent CH4/H2/N2 jet diffusion flame". In: *Applied Physics B* 66.4, pp. 489–502.

Berkooz, Gal, Philip Holmes, and John L Lumley (1993). "The proper orthogonal decomposition in the analysis of turbulent flows". In: *Annual review of fluid mechanics* 25.1, pp. 539–575.

Bilger, RW (1975). "A note on Favre averaging in variable density flows". In: *Combustion Science and Technology* 11.5-6, pp. 215–217.

— (1980). "Turbulent flows with nonpremixed reactants". In: *Turbulent reacting flows*, pp. 65–113.

— (2004). "Some aspects of scalar dissipation". In: *Flow, turbulence and combustion* 72.2, pp. 93–114.

Bilger, RW, SH Stårner, and RJ Kee (1990). "On reduced mechanisms for methane/air combustion in nonpremixed flames". In: *Combustion and Flame* 80.2, pp. 135–149.

Billant, Paul, Jean-Marc Chomaz, and Patrick Huerre (1998). "Experimental study of vortex breakdown in swirling jets". In: *Journal of Fluid Mechanics* 376, pp. 183–219.

Bird, R Byron, Warren E Stewart, and Edwin N Lightfoot (1960). *Transport phenomena. 1960*.

Bogey, Christophe and Christophe Bailly (2006). "Large eddy simulations of round free jets using explicit filtering with/without dynamic Smagorinsky model". In: *International journal of heat and fluid flow* 27.4, pp. 603–610.

Borghi, R (1985). "On the structure and morphology of turbulent premixed flames". In: *Recent advances in the Aerospace Sciences*. Springer, pp. 117–138.

Borrell, Ricard, Juan Carlos Cajas, Daniel Mira, Ahmed Taha, Seid Koric, Mariano Vázquez, and Guillaume Houzeaux (2018). "Parallel mesh partitioning based on space filling curves". In: *Computers & Fluids* 173, pp. 264–272.

Borrell, Ricard, Damien Dosimont, Marta Garcia-Gasulla, Guillaume Houzeaux, Oriol Lehmkuhl, Vishal Mehta, Herbert Owen, Mariano Vázquez, and Guillermo Oyarzun (2020). "Heterogeneous CPU/GPU co-execution of CFD simulations on the POWER9 architecture: Application to airplane aerodynamics". In: *Future Generation Computer Systems* 107, pp. 31–48.

Both, Ambrus (2017). "RANS-FGM simulation of n-heptane spray flame in OpenFOAM: A new implementation of flamelet generated manifold to account for enthalpy loss with detailed reaction mechanisms". In:

Both, Ambrus, Oriol Lehmkuhl, Daniel Mira, and Marc Ortega (2020). "Low-dissipation finite element strategy for low Mach number reacting flows". In: *Computers & Fluids* 200, p. 104436.

Both, Ambrus, Daniel Mira, and Oriol Lehmkuhl (2021a). "LES study of the impact of fuel composition on a swirl spray flame approaching blow-off". In: *13th International ERCOFTAC Symposium on Engineering Turbulence Modelling and Measurements*, pp. 527–532.

— (2021b). "Optimization of the progress variable definition using a genetic algorithm for the combustion of complex fuels". In: *10th European Combustion Meeting: April 14-15, 2021, virtual edition: proceedings volume*. MCM, pp. 1145–1151.

— (2022a). "Assessment of tabulated chemistry models for the LES of a model aeroengine combustor". In: *Global Power and Propulsion Society Technical Conference Chania22: September 11-14, 2022, Chania, Greece*. GPPS, pp. 1–10.

— (2022b). "Evaporation of volatile droplets subjected to flame-like conditions". In: *International Journal of Heat and Mass Transfer* 187, p. 122521.

Boussinesq, Joseph (1877). *Essai sur la théorie des eaux courantes*. Impr. nationale.

Box, George EP and Mervin E Muller (1958). "A note on the generation of random normal deviates". In: *The annals of mathematical statistics* 29.2, pp. 610–611.

Bradley, Derek, LK Kwa, AKC Lau, M Missaghi, and SB Chin (1988). "Laminar flamelet modeling of recirculating premixed methane and propane-air combustion". In: *Combustion and flame* 71.2, pp. 109–122.

Branley, N and WP Jones (2001). "Large eddy simulation of a turbulent non-premixed flame". In: *Combustion and flame* 127.1-2, pp. 1914–1934.

Braun-Unkhoff, Marina, Uwe Riedel, and Claus Wahl (2017). "About the emissions of alternative jet fuels". In: *CEAS Aeronautical Journal* 8, pp. 167–180.

Bray, Ken, Pascale Domingo, and Luc Vervisch (2005). "Role of the progress variable in models for partially premixed turbulent combustion". In: *Combustion and flame* 141.4, pp. 431–437.

Bray, KNC and J Barrie Moss (1977). "A unified statistical model of the premixed turbulent flame". In: *Acta Astronautica* 4.3-4, pp. 291–319.

Brouwer, J, J Reiss, and J Sesterhenn (2014). "Conservative time integrators of arbitrary order for finite-difference discretization of compressible flow". In: *Computers & Fluids* 100, pp. 1–12.

BSC (2021). *MareNostrum4 User's Guide*. URL: https://www.bsc.es/user-support/mn4.php.

Buckmaster, J, Paul Clavin, A Linan, M Matalon, N Peters, G Sivashinsky, and Forman A Williams (2005). "Combustion theory and modeling". In: *Proceedings of the Combustion Institute* 30.1, pp. 1–19.

Buckmaster, John D (1985). *The mathematics of combustion*. SIAM.

Burmberger, Stephan, Christoph Hirsch, and Thomas Sattelmayer (2006). "Designing a radial swirler vortex breakdown burner". In: *Turbo Expo: Power for Land, Sea, and Air*. Vol. 42363, pp. 423–431.

Calmet, Hadrien, Kiao Inthavong, Ambrus Both, Anurag Surapaneni, Daniel Mira, Beatriz Egukitza, and Guillaume Houzeaux (2021). "Large eddy simulation of cough jet dynamics, droplet transport, and inhalability over a ten minute exposure". In: *Physics of Fluids* 33.12, p. 125122.

Calmet, Hadrien, C Kleinstreuer, Guillaume Houzeaux, AV Kolanjiyil, Oriol Lehmkuhl, Edgar Olivares, and Mariano Vázquez (2018). "Subject-variability effects on micron particle deposition in human nasal cavities". In: *Journal of Aerosol Science* 115, pp. 12–28.

Calmet, Hadrien, David Oks, Alfonso Santiago, Guillaume Houzeaux, Antoine Le Corfec, Laura Deruyver, Clement Rigaut, Pierre Lambert, Benoit Haut, and Jonathan Goole (2022). "Validation and Sensitivity analysis for a nasal spray deposition computational model". In: *International journal of pharmaceutics* 626, p. 122118.

Calmet, Hadrien, T Yamamoto, B Eguzkitza, O Lehmkuhl, E Olivares, Y Kobayashi, K Tomoda, G Houzeaux, and M Vázquez (2019). "Numerical evaluation of aerosol exhalation through nose treatment". In: *Journal of Aerosol Science* 128, pp. 1–13.

Capecelatro, Jesse and Olivier Desjardins (2013). "An Euler–Lagrange strategy for simulating particle-laden flows". In: *Journal of Computational Physics* 238, pp. 1–31.

Capuano, Francesco, Gennaro Coppola, Matteo Chiatto, and Luigi de Luca (2016). "Approximate projection method for the incompressible Navier–Stokes equations". In: *AIAA Journal* 54.7, pp. 2179–2182.

Capurso, T, D Laera, E Riber, and B Cuenot (2023). "NOx pathways in lean partially premixed swirling H2-air turbulent flame". In: *Combustion and Flame* 248, p. 112581.

Castanet, Guillaume, Lionel Perrin, Ophélie Caballina, and Fabrice Lemoine (2016). "Evaporation of closely-spaced interacting droplets arranged in a single row". In: *International Journal of Heat and Mass Transfer* 93, pp. 788–802.

Caudwell, DR, JPM Trusler, V Vesovic, and WA Wakeham (2004). "The viscosity and density of n-dodecane and n-octadecane at pressures up to 200 MPa and temperatures up to 473 K". In: *International Journal of Thermophysics* 25.5, pp. 1339–1352.

Cavaliere, Davide E, James Kariuki, and Epaminondas Mastorakos (2013). "A comparison of the blow-off behaviour of swirl-stabilized premixed, non-premixed and spray flames". In: *Flow, turbulence and combustion* 91.2, pp. 347–372.

Cecere, Donato, Eugenio Giacomazzi, Franca R Picchia, Nunzio Arcidiacono, Filippo Donato, and Roberto Verzicco (2011). "A non-adiabatic flamelet progress–variable approach for LES of turbulent premixed flames". In: *Flow, turbulence and combustion* 86.3, pp. 667–688.

Ceriello, Giuseppe, Giancarlo Sorrentino, Antonio Cavaliere, Pino Sabia, Mara de Joannon, and Raffaele Ragucci (2020). "The role of dilution level and canonical configuration in the modeling of MILD combustion systems with internal recirculation". In: *Fuel* 264, p. 116840.

Charnyi, Sergey, Timo Heister, Maxim A Olshanskii, and Leo G Rebholz (2017). "On conservation laws of Navier–Stokes Galerkin discretizations". In: *Journal of Computational Physics* 337, pp. 289–308.

Chatelain, Alexandre, Frederic Ducros, and Olivier Metais (2004). "LES of turbulent heat transfer: proper convection numerical schemes for temperature transport". In: *International journal for numerical methods in fluids* 44.9, pp. 1017–1044.

Chatelier, Adrien, Benoit Fiorina, Vincent Moureau, and Nicolas Bertier (2020). "Large Eddy simulation of a turbulent spray jet flame using filtered tabulated chemistry". In: *Journal of Combustion* 2020.

Chauveau, Christian, Madjid Birouk, Fabien Halter, and Iskender Gökalp (2019). "An analysis of the droplet support fiber effect on the evaporation process". In: *International Journal of Heat and Mass Transfer* 128, pp. 885–891.

Chen, Jacqueline H (2011). "Petascale direct numerical simulation of turbulent combustion—fundamental insights towards predictive models". In: *Proceedings of the Combustion Institute* 33.1, pp. 99–123.

Chen, Zhi, Shaohong Ruan, and Nedunchezhian Swaminathan (2015). "Simulation of turbulent lifted methane jet flames: Effects of air-dilution and transient flame propagation". In: *Combustion and Flame* 162.3, pp. 703–716.

— (2016). "Numerical study of transient evolution of lifted jet flames: partially premixed flame propagation and influence of physical dimensions". In: *Combustion Theory and Modelling* 20.4, pp. 592–612.

Chrigui, Mouldi, James Gounder, Amsini Sadiki, Assaad R Masri, and Johannes Janicka (2012). "Partially premixed reacting acetone spray using LES and FGM tabulated chemistry". In: *Combustion and flame* 159.8, pp. 2718–2741.

Chrysokentis, Georgios (2019). "Development of a Large-Eddy simulation framework for engineering applications using the finite element method". PhD thesis. Universitat Politècnica de Catalunya.

Cocks, Peter AT, Marios C Soteriou, and Vaidyanathan Sankaran (2015). "Impact of numerics on the predictive capabilities of reacting flow LES". In: *Combustion and Flame* 162.9, pp. 3394–3411.

Codina, Ramon and Jordi Blasco (1997). "A finite element formulation for the Stokes problem allowing equal velocity-pressure interpolation". In: *Computer Methods in Applied Mechanics and Engineering* 143.3-4, pp. 373–391.

Codina, Ramon, Javier Principe, and Matías Ávila (2010). "Finite element approximation of turbulent thermally coupled incompressible flows with numerical subgrid scale modelling". In: *International Journal of Numerical Methods for Heat & Fluid Flow* 20.5, pp. 492–516.

Colin, Olivier and Jean-Baptiste Michel (2016). "A two-dimensional tabulated flamelet combustion model for furnace applications". In: *Flow, Turbulence and Combustion* 97.2, pp. 631–662.

Colucci, PJ, FA Jaberi, P Givi, and SB Pope (1998). "Filtered density function for large eddy simulation of turbulent reacting flows". In: *Physics of Fluids* 10.2, pp. 499–515.

Cook, Andrew W and James J Riley (1994). "A subgrid model for equilibrium chemistry in turbulent flows". In: *Physics of fluids* 6.8, pp. 2868–2870.

Cook, Andrew W and Ye Zhou (2002). "Energy transfer in Rayleigh-Taylor instability". In: *Physical Review E* 66.2, p. 026312.

Coppola, Gennaro, Francesco Capuano, Sergio Pirozzoli, and Luigi de Luca (2019). "Numerically stable formulations of convective terms for turbulent compressible flows". In: *Journal of Computational Physics* 382, pp. 86–104.

Crowe, Clayton T, John D Schwartzkopf, Martin Sommerfeld, and Yutaka Tsuji (2012). *Multiphase Flows with droplets and particles*. Taylor & Francis.

Cuenot, B and T Poinsot (1994). "Effects of curvature and unsteadiness in diffusion flames. Implications for turbulent diffusion combustion". In: *Symposium (International) on Combustion*. Vol. 25. 1. Elsevier, pp. 1383–1390.

Cuenot, Benedicte, Fokion N Egolfopoulos, and Thierry Poinsot (2000). "An unsteady laminar flamelet model for non-premixed combustion". In: *Combustion Theory and Modelling* 4.1, p. 77.

Darbyshire, OR and N Swaminathan (2012). "A presumed joint PDF model for turbulent combustion with varying equivalence ratio". In: *Combustion science and technology* 184.12, pp. 2036–2067.

Daubert, Thomas E and Ronald P Danner (1985). *Data compilation tables of properties of pure compounds*. Design Institute for Physical Property Data, American Institute of Chemical Engineers.

De, Santanu and Seung Hyun Kim (2013). "Large eddy simulation of dilute reacting sprays: Droplet evaporation and scalar mixing". In: *Combustion and flame* 160.10, pp. 2048–2066.

Delhaye, S, LMT Somers, JA Van Oijen, and LPH De Goey (2008). "Incorporating unsteady flow-effects in flamelet-generated manifolds". In: *Combustion and Flame* 155.1-2, pp. 133–144.

Denker, D, K Niemietz, A Attili, M Korkmaz, and H Pitsch (2019). "Prediction of non-premixed combustion regimes in a DI diesel engine in various operation points". In: *Proceedings of the 9th European Combustion Meeting*, pp. 14–17.

Deprédurand, Valérie, Guillaume Castanet, and Fabrice Lemoine (2010). "Heat and mass transfer in evaporating droplets in interaction: influence of the fuel". In: *International journal of heat and mass transfer* 53.17-18, pp. 3495–3502.

Dhuchakallaya, Isares, Phadungsak Rattanadecho, and Paul Watkins (2013). "Auto-ignition and combustion of diesel spray using unsteady laminar flamelet model". In: *Applied thermal engineering* 52.2, pp. 420–427.

Dianat, M, Z Yang, D Jiang, and JJ McGuirk (2006). "Large eddy simulation of scalar mixing in a coaxial confined jet". In: *Flow, turbulence and combustion* 77.1, pp. 205–227.

Domingo, Pascale and Luc Vervisch (2015). "Large eddy simulation of premixed turbulent combustion using approximate deconvolution and explicit flame filtering". In: *Proceedings of the Combustion Institute* 35.2, pp. 1349–1357.

Domingo, Pascale, Luc Vervisch, Sandra Payet, and Raphael Hauguel (2005). "DNS of a premixed turbulent V flame and LES of a ducted flame using a FSD-PDF subgrid scale closure with FPI-tabulated chemistry". In: *Combustion and Flame* 143.4, pp. 566–586.

Domingo, Pascale, Luc Vervisch, and Denis Veynante (2008). "Large-eddy simulation of a lifted methane jet flame in a vitiated coflow". In: *Combustion and Flame* 152.3, pp. 415–432.

Domingo-Alvarez, Patricia, Pierre Bénard, Vincent Moureau, Ghislain Lartigue, and Frederic Grisch (2020). "Impact of spray droplet distribution on the performances of a kerosene lean/premixed injector". In: *Flow, Turbulence and Combustion* 104.2, pp. 421–450.

Donea, J, S Giuliani, H Laval, and L Quartapelle (1982). "Finite element solution of the unsteady Navier-Stokes equations by a fractional step method". In: *Computer Methods in Applied Mechanics and Engineering* 30.1, pp. 53–73.

Dong, Huy Quang, Vincent Robin, Arnaud Mura, and Michel Champion (2013). "Analysis of algebraic closures of the mean scalar dissipation rate of the progress variable applied to stagnating turbulent flames". In: *Flow, turbulence and combustion* 90.2, pp. 301–323.

Doost, AS, Anja Ketelheun, Amsini Sadiki, and Johannes Ja-nicka (2015). "Differential diffusion effects in FGM context for premixed LES of hydrogen blended fuels". In: *7th European Combustion Meeting, Budapest, Hungary*.

Dressler, L, FL Sacomano Filho, A Sadiki, and J Janicka (2021). "Influence of thickening factor treatment on predictions of spray flame properties using the atf model and tabulated chemistry". In: *Flow, Turbulence and Combustion* 106.2, pp. 419–451.

Ebrahimian, V and C Habchi (2011). "Towards a predictive evaporation model for multi-component hydrocarbon droplets at all pressure conditions". In: *International Journal of Heat and Mass Transfer* 54.15-16, pp. 3552–3565.

Egüz, Ulaş, Niels Leermakers, Bart Somers, and Philip De Goey (2014). "Modeling of PCCI combustion with FGM tabulated chemistry". In: *Fuel* 118, pp. 91–99.

El-Asrag, Hossam A, Markus Braun, and Assaad R Masri (2016). "Large eddy simulations of partially premixed ethanol dilute spray flames using the flamelet generated manifold model". In: *Combustion Theory and Modelling* 20.4, pp. 567–591.

El Khoury, George K, Philipp Schlatter, Azad Noorani, Paul F Fischer, Geert Brethouwer, and Arne V Johansson (2013). "Direct numerical simulation of turbulent pipe flow at moderately high Reynolds numbers". In: *Flow, turbulence and combustion* 91.3, pp. 475–495.

Elasrag, Hossam and Shaoping Li (2018). "Investigation of extinction and reignition events using the flamelet generated manifold model". In: *Turbo Expo: Power for Land, Sea, and Air*. Vol. 51050. American Society of Mechanical Engineers, V04AT04A023.

Enerxico (2021). *Report on the characterization of the physico-chemical properties of the fuels under investigation*. Deliverable. Enerxico project.

Favre, AJ (1965). *The equations of compressible turbulent gases*. Tech. rep. AIX-MARSEILLE UNIV (FRANCE) INST DE MECANIQUE STATISTIQUE DE LA TURBULENCE.

Ferraris, SA and JX Wen (2007). "Large eddy simulation of a lifted turbulent jet flame". In: *Combustion and Flame* 150.4, pp. 320–339.

Fiala, Thomas and Thomas Sattelmayer (2014). "Nonpremixed counterflow flames: scaling rules for batch simulations". In: *Journal of Combustion* 2014.

Fick, A. (1855). "Über Diffusion". In: *Annalen der Physik* 94, pp. 59–86.

Finke, HL, ME Gross, Guy Waddington, and HM Huffman (1954). "Low-temperature thermal data for the nine normal paraffin hydrocarbons from octane to hexadecane". In: *Journal of the American Chemical Society* 76.2, pp. 333–341.

Finneran, J (2021). "On the evaluation of transport properties for droplet evaporation problems". In: *International Journal of Heat and Mass Transfer* 181, p. 121858.

Finneran, Joshua, Colin P Garner, and François Nadal (2021). "Deviations from classical droplet evaporation theory". In: *Proceedings of the Royal Society A* 477.2251, p. 20210078.

Fiorina, Benoit, Romain Baron, Olivier Gicquel, D Thevenin, Stéphane Carpentier, and Nasser Darabiha (2003). "Modelling non-adiabatic partially premixed flames using flame-prolongation of ILDM". In: *Combustion Theory and Modelling* 7.3, p. 449.

Fiorina, Benoit, O Gicquel, L Vervisch, S Carpentier, and N Darabiha (2005a). "Approximating the chemical structure of partially premixed and diffusion counterflow flames using FPI flamelet tabulation". In: *Combustion and flame* 140.3, pp. 147–160.

— (2005b). "Premixed turbulent combustion modeling using tabulated detailed chemistry and PDF". In: *Proceedings of the Combustion Institute* 30.1, pp. 867–874.

Fiorina, Benoit, Denis Veynante, and Sébastien Candel (2015). "Modeling combustion chemistry in large eddy simulation of turbulent flames". In: *Flow, Turbulence and Combustion* 93.1, pp. 3–42.

Fiorina, Benoit, Ronan Vicquelin, Pierre Auzillon, Nasser Darabiha, Olivier Gicquel, and Denis Veynante (2010). "A filtered tabulated chemistry model for LES of premixed combustion". In: *Combustion and Flame* 157.3, pp. 465–475.

Flammang, Brooke E, Simone Marras, Erik J Anderson, Oriol Lehmkuhl, Abhishek Mukherjee, David E Cade, Michael Beckert, Jason H Nadler, Guillaume Houzeaux, Mariano Vázquez, et al. (2020). "Remoras pick where they stick on blue whales". In: *Journal of Experimental Biology* 223.20, jeb226654.

Floyd, J, Andreas Markus Kempf, A Kronenburg 1, and RH Ram (2009). "A simple model for the filtered density function for passive scalar combustion LES". In: *Combustion Theory and Modelling* 13.4, pp. 559–588.

Foale, Jenna M (2022). "Simulating Extinction and Blow-off in Kerosene Swirl Spray Flames". PhD thesis. University of Cambridge.

Foale, Jenna M, Andrea Giusti, and Epaminondas Mastorakos (2021). "Simulating the blowoff transient of a swirling, bluff body-stabilized kerosene spray flame using detailed chemistry". In: *AIAA Scitech 2021 Forum*, p. 0187.

Forck, Jonathan (2021). "Numerical investigation of the mixing and combustion in a partially premixed swirl-stabilized hydrogen flame". MSc thesis. Universitat Politècnica de Catalunya.

Fossi, Alain, Alain DeChamplain, Benjamin Akih-Kumgeh, and Jeffrey Bergthorson (2020). "Large eddy simulation of an ignition sequence and the resulting steady combustion in a swirl-stabilized combustor using FGM-based tabulated chemistry". In: *International Journal of Numerical Methods for Heat & Fluid Flow*.

Fox, Rodney O (2003). *Computational models for turbulent reacting flows*. Cambridge university press.

Frank, Jonathan H, Sebastian A Kaiser, and Joseph C Oefelein (2011). "Analysis of scalar mixing dynamics in LES using high-resolution imaging of laser Rayleigh scattering in turbulent non-reacting jets and non-premixed jet flames". In: *Proceedings of the Combustion Institute* 33.1, pp. 1373–1381.

Franzelli, B, B Fiorina, and N Darabiha (2013). "A tabulated chemistry method for spray combustion". In: *Proceedings of the Combustion Institute* 34.1, pp. 1659–1666.

Franzelli, B, A Vié, M Boileau, B Fiorina, and N Darabiha (2017). "Large eddy simulation of swirled spray flame using detailed and tabulated chemical descriptions". In: *Flow, Turbulence and Combustion* 98.2, pp. 633–661.

Franzelli, Benedetta, Eleonore Riber, Laurent YM Gicquel, and Thierry Poinsot (2012). "Large eddy simulation of combustion instabilities in a lean partially premixed swirled flame". In: *Combustion and flame* 159.2, pp. 621–637.

Fritz, Jassin, Martin Kröner, and Thomas Sattelmayer (2004). "Flashback in a swirl burner with cylindrical premixing zone". In: *J. Eng. Gas Turbines Power* 126.2, pp. 276–283.

Frössling, Nils (1938). "Über die verdunstung fallernder tropfen". In: *Gerlands Beiträge zur Geophysik* 52, pp. 170–216.

Fureby, Christer (2017). "On the Supersonic Flame Structure in the HyShot II Scramjet Combustor". In: *26th International Colloquium on the Dynamics of Explosions and Reactive Systems (ICDERS)," Boston, Massachusetts*.

Galley, David, Sébastien Ducruix, François Lacas, and Denis Veynante (2011). "Mixing and stabilization study of a partially premixed swirling flame using laser induced fluorescence". In: *Combustion and Flame* 158.1, pp. 155–171.

Galpin, Jéremy, Alexandre Naudin, Luc Vervisch, Christian Angelberger, Olivier Colin, and Pascale Domingo (2008). "Large-eddy simulation of a fuel-lean premixed turbulent swirl-burner". In: *Combustion and Flame* 155.1-2, pp. 247–266.

Ganter, Sebastian, Arne Heinrich, Thorsten Meier, Guido Kuenne, Christopher Jainski, Martin C Rißmann, Andreas Dreizler, and Johannes Janicka (2017). "Numerical analysis of laminar methane–air side-wall-quenching". In: *Combustion and Flame* 186, pp. 299–310.

Garmory, Andrew and Epaminondas Mastorakos (2011). "Capturing localised extinction in Sandia Flame F with LES–CMC". In: *Proceedings of the Combustion Institute* 33.1, pp. 1673–1680.

Gatley, Donald P et al. (2005). *Understanding psychrometrics*.

Germano, Massimo (1992). "Turbulence: the filtering approach". In: *Journal of Fluid Mechanics* 238, pp. 325–336.

Gibbs, Josiah Willard (1879). "On the equilibrium of heterogeneous substances". In: *Transactions of the Connecticut Academy of Arts and Sciences* 3, pp. 343–527.

Gicquel, Olivier, Nasser Darabiha, and Dominique Thévenin (2000). "Liminar premixed hydrogen/air counterflow flame simulations using flame prolongation of ILDM with differential diffusion". In: *Proceedings of the Combustion Institute* 28.2, pp. 1901–1908.

Giusti, Andrea (2013). "Development of numerical tools for the analysis of advanced airblast injection systems for lean burn aero-engine combustors". PhD thesis. Università degli Studi di Firenze.

Giusti, Andrea, Maria Kotzagianni, and Epaminondas Mastorakos (2016). "LES/CMC simulations of swirl-stabilised ethanol spray flames approaching blow-off". In: *Flow, Turbulence and Combustion* 97.4, pp. 1165–1184.

Giusti, Andrea and Epaminondas Mastorakos (2017). "Detailed chemistry LES/CMC simulation of a swirling ethanol spray flame approaching blow-off". In: *Proceedings of the Combustion Institute* 36.2, pp. 2625–2632.

Gkantonas, Savvas, Mariano Sirignano, Andrea Giusti, Andrea D'Anna, and Epaminondas Mastorakos (2020). "Comprehensive soot particle size distribution modelling of a model Rich-Quench-Lean burner". In: *Fuel* 270, p. 117483.

Godsave, GAE (1953). "Studies of the combustion of drops in a fuel spray—the burning of single drops of fuel". In: *Symposium (international) on combustion*. Vol. 4. 1. Elsevier, pp. 818–830.

Goodwin, ARH, JV Sangers, and CJ Peters (2010). *Applied thermodynamics of fluids*. The Royal Society of Chemistry.

Goodwin, David G (2002). "Cantera C++ user's guide". In: *California Institute of Technology*.

Gordon, Sanford and Bonnie J McBride (1994). *Computer program for calculation of complex chemical equilibrium compositions and applications. Part 1: Analysis*. Tech. rep.

Gövert, Simon (2016). "Modelling the effects of heat loss and fuel/air mixing on turbulent combustion in gas turbine combustion systems". PhD thesis. TU Twente.

Gövert, Simon, Daniel Mira, Jim BW Kok, Mariano Vázquez, and Guillaume Houzeaux (2015). "Turbulent combustion modelling of a confined premixed jet flame including heat loss effects using tabulated chemistry". In: *Applied energy* 156, pp. 804–815.

— (2018). "The effect of partial premixing and heat loss on the reacting flow field prediction of a swirl stabilized gas turbine model combustor". In: *Flow, turbulence and combustion* 100.2, pp. 503–534.

Gravemeier, Volker and Wolfgang A Wall (2010). "An algebraic variational multiscale–multigrid method for large-eddy simulation of turbulent variable-density flow at low Mach number". In: *Journal of Computational Physics* 229.17, pp. 6047–6070.

Green, Don W and James O Maloney (1999). *Perry's chemical engineers' handbook*. McGraw-Hill.

Grenga, Temistocle, Ludovico Nista, Christoph Schumann, Amir Noughabi Karimi, Gandolfo Scialabba, Antonio Attili, and Heinz Pitsch (2022). "Predictive data-driven model based on generative adversarial network for premixed turbulence-combustion regimes". In: *Combustion Science and Technology*, pp. 1–24.

Grinstein, Fernando F, Len G Margolin, and William J Rider (2007). *Implicit large eddy simulation*. Vol. 10. Cambridge university press Cambridge.

Gubernov, VV, V Bykov, and U Maas (2017). "Hydrogen/air burner-stabilized flames at elevated pressures". In: *Combustion and Flame* 185, pp. 44–52.

Guermond, Jean-Luc, Richard Pasquetti, and Bojan Popov (2011). "Entropy viscosity method for nonlinear conservation laws". In: *Journal of Computational Physics* 230.11, pp. 4248–4267.

Gupta, Ashwani K, David G Lilley, and Nick Syred (1984). *Swirl flows*. Tunbridge Wells.

Hansinger, Maximilian, Yipeng Ge, and Michael Pfitzner (2020). "Deep residual networks for flamelet/progress variable tabulation with application to a piloted flame with inhomogeneous inlet". In: *Combustion Science and Technology*, pp. 1–27.

Hawkes, Evatt R, Obulesu Chatakonda, Hemanth Kolla, Alan R Kerstein, and Jacqueline H Chen (2012). "A petascale direct numerical simulation study of the modelling of flame wrinkling for large-eddy simulations in intense turbulence". In: *Combustion and flame* 159.8, pp. 2690–2703.

Héder, Mihály (2017). "From NASA to EU: the evolution of the TRL scale in Public Sector Innovation". In: *The Innovation Journal* 22.2, pp. 1–23.

Hirschfelder, Joseph O, Charles F Curtiss, Robert Byron Bird, and Maria Goeppert Mayer (1964). *Molecular theory of gases and liquids*. Vol. 165. Wiley New York.

Hollmann, C and E Gutheil (1996). "Modeling of turbulent spray diffusion flames including detailed chemistry". In: *Symposium (international) on combustion*. Vol. 26. 1. Elsevier, pp. 1731–1738.

Hossain, Mamdud, JC Jones, and Weeratunge Malalasekera (2001). "Modelling of a bluff-body nonpremixed flame using a coupled radiation/flamelet combustion model". In: *Flow, Turbulence and Combustion* 67.3, pp. 217–234.

Hosseini, Seyed Ali, Nasser Darabiha, and Dominique Thévenin (2022). "Low Mach number lattice Boltzmann model for turbulent combustion: flow in confined geometries". In: *Proceedings of the Combustion Institute*.

Houzeaux, Guillaume, Rosa Maria Badia, Ricard Borrell, Damien Dosimont, Jorge Ejarque, Marta Garcia-Gasulla, and V López (2022). "Dynamic resource allocation for efficient parallel CFD simulations". In: *Computers & Fluids* 245, p. 105577.

Houzeaux, Guillaume and Ramon Codina (2003). "A Chimera method based on a Dirichlet/Neumann (Robin) coupling for the Navier–Stokes equations". In: *Computer Methods in Applied Mechanics and Engineering* 192.31-32, pp. 3343–3377.

Houzeaux, Guillaume, Raúl de la Cruz, Herbert Owen, and Mariano Vázquez (2013). "Parallel uniform mesh multiplication applied to a Navier–Stokes solver". In: *Computers & Fluids* 80, pp. 142–151.

Houzeaux, Guillaume, Marta Garcia, Juan Carlos Cajas, Antoni Artigues, Edgar Olivares, Jesús Labarta, and Mariano Vázquez (2016). "Dynamic load balance applied to particle transport in fluids". In: *International Journal of Computational Fluid Dynamics* 30.6, pp. 408–418.

Hu, Yong and Ryoichi Kurose (2019). "Large-eddy simulation of turbulent autoigniting hydrogen lifted jet flame with a multi-regime flamelet approach". In: *International Journal of Hydrogen Energy* 44.12, pp. 6313–6324.

Hu, Yong, Hernan Olguin, and Eva Gutheil (2017). "A spray flamelet/progress variable approach combined with a transported joint PDF model for turbulent spray flames". In: *Combustion Theory and Modelling* 21.3, pp. 575–602.

Huang, Chih-Chia, Jeroen A van Oijen, Niels G Deen, and Yali Tang (2022a). "Incorporation of flamelets generated manifold method in coarse-grained Euler-Lagrange simulations of pulverized coal combustion". In: *Chemical Engineering Science* 260, p. 117838.

Huang, Xu, Mark J Tummers, Eric H van Veen, and Dirk JEM Roekaerts (2022b). "Modelling of MILD combustion in a lab-scale furnace with an extended FGM model including turbulence–radiation interaction". In: *Combustion and Flame* 237, p. 111634.

Huang, Ying and Vigor Yang (2009). "Dynamics and stability of lean-premixed swirl-stabilized combustion". In: *Progress in energy and combustion science* 35.4, pp. 293–364.

Hunt, J.C.R., A.A. Wray, and P. Moin (1988). "Eddies, stream and convergence zones in turbulent flows". In: *Proceedings of Summer Program, Center for Turbulence Research, Stanford University*, pp. 193–208.

ICAO (2023). *Committee on Aviation Environmental Protection Report (Doc 10126)*. Ed. by International Civil Aviation Organization. URL: https://store.icao.int/en/committee-on-aviation-environmental-protection-report-doc-10126.

IEA (2000). *World energy outlook 2000*. International Energy Agency, Paris.

— (2021a). *Net Zero by 2050: A Roadmap for the Global Energy Sector*. International Energy Agency, Paris.

— (2021b). *World energy outlook 2021*. International Energy Agency, Paris.

— (2022). *World energy outlook 2022*. International Energy Agency, Paris.

Ihme, M, D Bodony, and H Pitsch (2005). "Towards the prediction of combustion-generated noise in non-premixed turbulent flames using large-eddy simulation". In: *CTR Annual Research Briefs*, pp. 311–323.

Ihme, Matthias, Daniel Bodony, and Heinz Pitsch (2006). "Prediction of Combustion-Generated Noise in Non-Premixed Turbulent Jet Flames Using LES". In: *12th AIAA/CEAS Aeroacoustics Conference (27th AIAA Aeroacoustics Conference)*, p. 2614.

Ihme, Matthias and Heinz Pitsch (2008a). "Modeling of radiation and nitric oxide formation in turbulent nonpremixed flames using a flamelet/progress variable formulation". In: *Physics of Fluids* 20.5, p. 055110.

— (2008b). "Prediction of extinction and reignition in nonpremixed turbulent flames using a flamelet/progress variable model: 2. Application in LES of Sandia flames D and E". In: *Combustion and flame* 155.1-2, pp. 90–107.

Ihme, Matthias and Yee Chee See (2010). "Prediction of autoignition in a lifted methane/air flame using an unsteady flamelet/progress variable model". In: *Combustion and Flame* 157.10, pp. 1850–1862.

Ihme, Matthias, Lee Shunn, and Jian Zhang (2012). "Regularization of reaction progress variable for application to flamelet-based combustion models". In: *Journal of Computational Physics* 231.23, pp. 7715–7721.

Illana, Enric, Daniel Mira, and Arnaud Mura (2021). "An extended flame index partitioning for partially premixed combustion". In: *Combustion Theory and Modelling* 25.1, pp. 121–157.

Ingenito, Antonella and Claudio Bruno (2010). "Physics and regimes of supersonic combustion". In: *AIAA journal* 48.3, pp. 515–525.

Inthavong, Kiao, David F Fletcher, Mehrdad Khamooshi, Sara Vahaji, and Hana Salati (2022). "Wet surface wall model for latent heat exchange during evaporation". In: *International Journal for Numerical Methods in Biomedical Engineering* 38.4, e3581.

Jacob, SD and T Rindlisbacher (2019). "The Landing and Take-Off Particulate Matter Standards for Aircraft Gas Turbine Engines". In: *ICAO 2019 Environmental Report*, pp. 100–105.

Janicka, J and AJPotCI Sadiki (2005). "Large eddy simulation of turbulent combustion systems". In: *Proceedings of the Combustion Institute* 30.1, pp. 537–547.

Janodet, Romain, Carlos Guillamón, Vincent Moureau, Renaud Mercier, Ghislain Lartigue, Pierre Bénard, Thibaut Ménard, and Alain Berlemont (2022). "A massively parallel accurate conservative level set algorithm for simulating turbulent atomization on adaptive unstructured grids". In: *Journal of Computational Physics* 458, p. 111075.

Jasper, Ahren W, C Melania Oana, and James A Miller (2015). ""Third-body" collision efficiencies for combustion modeling: Hydrocarbons in atomic and diatomic baths". In: *Proceedings of the combustion Institute* 35.1, pp. 197–204.

Jenny, Patrick, Dirk Roekaerts, and Nijso Beishuizen (2012). "Modeling of turbulent dilute spray combustion". In: *Progress in Energy and Combustion Science* 38.6, pp. 846–887.

Jin, Guodong, Guo-Wei He, and Lian-Ping Wang (2010). "Large-eddy simulation of turbulent collision of heavy particles in isotropic turbulence". In: *Physics of Fluids* 22.5, p. 055106.

Jochmann, P, A Sinigersky, R Koch, and H-J Bauer (2005). "URANS prediction of flow instabilities of a novel atomizer combustor configuration". In: *Turbo Expo: Power for Land, Sea, and Air*. Vol. 4725, pp. 19–27.

Juniper, Matthew P (2012). "Absolute and convective instability in gas turbine fuel injectors". In: *Turbo Expo: Power for Land, Sea, and Air*. Vol. 44687. American Society of Mechanical Engineers, pp. 189–198.

Kader, BA (1981). "Temperature and concentration profiles in fully turbulent boundary layers". In: *International journal of heat and mass transfer* 24.9, pp. 1541–1544.

Kalbhor, Abhijit and Jeroen A Van Oijen (2023). "Modeling soot formation in normal and inverse diffusion flames using FGM chemistry and sectional method". In: *12th Mediterranean Combustion Symposium*.

Kathrotia, Trupti, Sandra Richter, Clemens Naumann, Nadezhda Slavinskaya, Torsten Methling, Marina Braun-Unkhoff, and Uwe Riedel (2018). "Reaction model development for synthetic jet fuels: surrogate fuels as a flexible tool to predict their performance". In: *Turbo Expo: Power for Land, Sea, and Air*. Vol. 51043. American Society of Mechanical Engineers, V003T03A008.

Kee, R J, G Dixon-Lewis, J Warnatz, M E Coltrin, J A Miller, and H K Moffat (1999). "Transport: a software package for the evaluation of gas-phase, multicomponent transport properties". In: *Chemkin Collection*.

Kemenov, Konstantin A, Haifeng Wang, and Stephen B Pope (2012). "Modelling effects of subgrid-scale mixture fraction variance in LES of a piloted diffusion flame". In: *Combustion Theory and Modelling* 16.4, pp. 611–638.

Kempf, Andreas, Markus Klein, and Johannes Janicka (2005). "Efficient generation of initial-and inflow-conditions for transient turbulent flows in arbitrary geometries". In: *Flow, Turbulence and combustion* 74.1, pp. 67–84.

Kempf, Andreas M, Christoph Schneider, Amsini Sadiki, and Johannes Janicka (2001). "Large eddy simulation of a highly turbulent methane flame: application to the DLR standard flame". In: *Second Symposium on Turbulence and Shear Flow Phenomena*. Begel House Inc.

Keshtiban, IJ, F Belblidia, and MF Webster (2004). "Compressible flow solvers for low Mach number flows-a review". In: *Int. J. Numer. Methods Fluids* 23, pp. 77–103.

Ketelheun, Anja, Guido Kuenne, and Johannes Janicka (2013). "Heat transfer modeling in the context of large eddy simulation of premixed combustion with tabulated chemistry". In: *Flow, turbulence and combustion* 91.4, pp. 867–893.

Kheirkhah, Sina and Ömer L Gülder (2022). "A revisit to the validity of flamelet assumptions in turbulent premixed combustion and implications for future research". In: *Combustion and Flame* 239, p. 111635.

Kida, Shigeo and Steven A Orszag (1992). "Energy and spectral dynamics in decaying compressible turbulence". In: *Journal of Scientific Computing* 7.1, pp. 1–34.

Kiesewetter, F., M. Konle, and T. Sattelmayer (2007). "Analysis of Combustion Induced Vortex Breakdown Driven Flame Flashback in a Premix Burner With Cylindrical Mixing Zone". In: *J. Eng. Gas Turbines Power* 129, pp. 929–936.

Klapdor, EV, F Di Mare, W Kollmann, and J Janicka (2013). "A compressible pressure-based solution algorithm for gas turbine combustion chambers using the PDF/FGM model". In: *Flow, turbulence and combustion* 91.2, pp. 209–247.

Knaus, R and C Pantano (2009). "On the effect of heat release in turbulence spectra of non-premixed reacting shear layers". In: *Journal of Fluid Mechanics* 626, pp. 67–109.

Knudsen, E and H Pitsch (2010). "Large-eddy simulation for combustion systems: modeling approaches for partially premixed flows". In: *The Open Thermodynamics Journal* 4.1.

Kolla, H, ER Hawkes, AR Kerstein, N Swaminathan, and JH Chen (2014). "On velocity and reactive scalar spectra in turbulent premixed flames". In: *Journal of fluid mechanics* 754, pp. 456–487.

Kolmogorov, Andrey Nikolaevich (1941). "The local structure of turbulence in incompressible viscous fluid for very large Reynolds numbers". In: *Cr Acad. Sci. URSS* 30, pp. 301–305.

Kronenburg, A (2007). "Spray Combustion–A Fresh Perspective". In: *Proc. Aust. Combust. Symp., Sydney: University of Sydney*.

Kuenne, G, A Ketelheun, and J Janicka (2011). "LES modeling of premixed combustion using a thickened flame approach coupled with FGM tabulated chemistry". In: *Combustion and Flame* 158.9, pp. 1750–1767.

Kulkarni, Sagar, Camilo F Silva, and Wolfgang Polifke (2022). "Response of spray number density and evaporation rate to velocity oscillations". In: *International Journal of Spray and Combustion Dynamics*, p. 17568277221085957.

Kundu, Pijush K, Ira M Cohen, and David R Dowling (2015). *Fluid mechanics*. Academic press.

Kuo, Kenneth K (1986). *Principles of combustion*. John Wiley & Sins, Inc.

Lam, Sau-Hai and Dimitris A Goussis (1989). "Understanding complex chemical kinetics with computational singular perturbation". In: *Symposium (International) on Combustion*. Vol. 22. 1. Elsevier, pp. 931–941.

Lam, SH (1993). "Using CSP to understand complex chemical kinetics". In: *Combustion Science and Technology* 89.5-6, pp. 375–404.

Lammers, FA and LPH De Goey (2004). "The influence of gas radiation on the temperature decrease above a burner with a flat porous inert surface". In: *Combustion and flame* 136.4, pp. 533–547.

Lamouroux, Jean, Matthias Ihme, Benoit Fiorina, and Olivier Gicquel (2014). "Tabulated chemistry approach for diluted combustion regimes with internal recirculation and heat losses". In: *Combustion and flame* 161.8, pp. 2120–2136.

Langella, Ivan, Nedunchezhian Swaminathan, and Robert W Pitz (2016). "Application of unstrained flamelet SGS closure for multi-regime premixed combustion". In: *Combustion and Flame* 173, pp. 161–178.

Lanzafame, R and M Messina (2000). "A new method for the calculation of gases enthalpy". In: *Collection of Technical Papers. 35th Intersociety Energy Conversion Engineering Conference and Exhibit (IECEC)(Cat. No. 00CH37022)*. Vol. 1. IEEE, pp. 318–328.

Lapointe, Simon and Guillaume Blanquart (2017). "A priori filtered chemical source term modeling for LES of high Karlovitz number premixed flames". In: *Combustion and Flame* 176, pp. 500–510.

Launder, BE and DB Spalding (1974). "The numerical computation of turbulent flows". In: *Computer Methods in Applied Mechanics and Engineering* 3, pp. 269–289.

Law, Chung K (2007). "Combustion at a crossroads: Status and prospects". In: *Proceedings of the Combustion Institute* 31.1, pp. 1–29.

Lefebvre, Arthur H and Dilip R Ballal (2010). *Gas turbine combustion: alternative fuels and emissions*. CRC press.

Lehmkuhl, O, D Mira, L Gasparino, H Owen, and G Houzeaux (2019a). "Large-Eddy Simulation of Primary Atomization Using an Entropy Stable Conservative Level Set". In: *ERCOFTAC Workshop Direct and Large Eddy Simulation*. Springer, pp. 207–213.

Lehmkuhl, Oriol, Guillaume Houzeaux, Herbert Owen, Giorgios Chrysokentis, and Ivette Rodríguez (2019b). "A low-dissipation finite element scheme for scale resolving simulations of turbulent flows". In: *Journal of Computational Physics* 390, pp. 51–65.

Lehmkuhl, Oriol, Adrián Lozano-Durán, and Ivette Rodriguez (2020). "Active flow control for external aerodynamics: from micro air vehicles to a full aircraft in stall". In: *Journal of Physics: Conference Series*. Vol. 1522. 1. IOP Publishing, p. 012017.

Lele, Sanjiva K (1992). "Compact finite difference schemes with spectral-like resolution". In: *Journal of computational physics* 103.1, pp. 16–42.

Lessani, Bamdad and Miltiadis V Papalexandris (2006). "Time-accurate calculation of variable density flows with strong temperature gradients and combustion". In: *Journal of Computational Physics* 212.1, pp. 218–246.

Libby, PA and FA Williams (1980). *Turbulent reacting flows*. Springer.

Lieuwen, Tim, Vince McDonell, Domenic Santavicca, and Thomas Sattelmayer (2008). "Burner development and operability issues associated with steady flowing syngas fired combustors". In: *Combustion Science and Technology* 180.6, pp. 1169–1192.

Liñan, Amable (1974). "The asymptotic structure of counterflow diffusion flames for large activation energies". In: *Acta Astronautica* 1.7-8, pp. 1007–1039.

Locci, Carlo, Olivier Colin, Damien Poitou, and Fabian Mauss (2015). "A tabulated, flamelet based no model for large eddy simulations of non premixed turbulent jets with enthalpy loss". In: *Flow, Turbulence and Combustion* 94.4, pp. 691–729.

Löhner, Rainald, Fernando Mut, Juan Raul Cebral, Romain Aubry, and Guillaume Houzeaux (2011). "Deflated preconditioned conjugate gradient solvers for the pressure-Poisson equation: Extensions and improvements". In: *International Journal for Numerical Methods in Engineering* 87.1-5, pp. 2–14.

Lomb, Nicholas R (1976). "Least-squares frequency analysis of unequally spaced data". In: *Astrophysics and space science* 39.2, pp. 447–462.

Lu, Tianfeng and Chung K Law (2006). "Linear time reduction of large kinetic mechanisms with directed relation graph: n-Heptane and iso-octane". In: *Combustion and Flame* 144.1, pp. 24–36.

— (2009). "Toward accommodating realistic fuel chemistry in large-scale computations". In: *Progress in Energy and Combustion Science* 35.2, pp. 192–215.

Lumley, JL (1965). "Interpretation of time spectra measured in high-intensity shear flows". In: *The physics of fluids* 8.6, pp. 1056–1062.

Luo, Yujuan, Xu Wen, Haiou Wang, Kun Luo, and Jianren Fan (2018). "Evaluation of different flamelet tabulation methods for laminar spray combustion". In: *Physics of Fluids* 30.5, p. 053603.

Ma, Likun (2016). "Computational modeling of turbulent spray combustion". PhD thesis. TU Delft.

Ma, Likun, Xu Huang, and Dirk Roekaerts (2017). "Large Eddy Simulation of CO2 diluted oxy-fuel spray flames". In: *Fuel* 201, pp. 165–175.

Ma, Likun, Bertrand Naud, and Dirk Roekaerts (2016). "Transported PDF modeling of ethanol spray in hot-diluted coflow flame". In: *Flow, Turbulence and Combustion* 96.2, pp. 469–502.

Ma, Likun and Dirk Roekaerts (2016). "Modeling of spray jet flame under MILD condition with non-adiabatic FGM and a new conditional droplet injection model". In: *Combustion and Flame* 165, pp. 402–423.

— (2017). "Numerical study of the multi-flame structure in spray combustion". In: *Proceedings of the Combustion Institute* 36.2, pp. 2603–2613.

Ma, Peter C, Hao Wu, Matthias Ihme, and Jean-Pierre Hickey (2018). "Nonadiabatic flamelet formulation for predicting wall heat transfer in rocket engines". In: *AIAA Journal* 56.6, pp. 2336–2349.

Ma, Peter C, Hao Wu, Jeffrey W Labahn, Thomas Jaravel, and Matthias Ihme (2019). "Analysis of transient blow-out dynamics in a swirl-stabilized combustor using large-eddy simulations". In: *Proceedings of the Combustion Institute* 37.4, pp. 5073–5082.

MacArt, Jonathan F, Temistocle Grenga, and Michael E Mueller (2018). "Effects of combustion heat release on velocity and scalar statistics in turbulent premixed jet flames at low and high Karlovitz numbers". In: *Combustion and Flame* 191, pp. 468–485.

Majer, Vladimír, Václav Svoboda, Slavoj Hála, and Jiří Pick (1979). "Temperature dependence of heats of vaporization of saturated hydrocarbons C5-C8; Experimental data and an estimation method". In: *Collection of Czechoslovak Chemical Communications* 44.3, pp. 637–651.

Martin, Rocio, Manel Soria, Oriol Lehmkuhl, Andrey Gorobets, and Alexey Duben (2019). "Noise radiated by an open cavity at low Mach number: Effect of the cavity oscillation mode". In: *International Journal of Aeroacoustics* 18.6-7, pp. 647–668.

Massey, James C, Zhi X Chen, and Nedunchezhian Swaminathan (2021). "Modelling heat loss effects in the Large Eddy Simulation of a lean swirl-stabilised flame". In: *Flow, Turbulence and Combustion* 106.4, pp. 1355–1378.

Massias, An, D Diamantis, E Mastorakos, and DA Goussis (1999). "An algorithm for the construction of global reduced mechanisms with CSP data". In: *Combustion and Flame* 117.4, pp. 685–708.

Meier, W, P Weigand, XR Duan, and R Giezendanner-Thoben (2007). "Detailed characterization of the dynamics of thermoacoustic pulsations in a lean premixed swirl flame". In: *Combustion and Flame* 150.1-2, pp. 2–26.

Meier, Wolfgang, Robert S Barlow, Y-L Chen, and J-Y Chen (2000). "Raman/Rayleigh/LIF measurements in a turbulent CH4/H2/N2 jet diffusion flame: experimental techniques and turbulence–chemistry interaction". In: *Combustion and Flame* 123.3, pp. 326–343.

Meijer, EL, JG Blok, J Kroon, and HAJ Oonk (1977). "The carvoxime system: IV. heat capacities and enthalpies of melting of dl-carvoxime, l-carvoxime and standard n-heptane". In: *Thermochimica Acta* 20.3, pp. 325–334.

Meloni, Roberto, Nicola Chiarizia, Pier Carlo Nassini, and Antonio Andreini (2023). "E-POD investigations of turbulent premixed flame dynamics approaching lean blow-out conditions". In: *International Journal of Spray and Combustion Dynamics*, p. 17568277221151141.

Mercier, Renaud, Pierre Auzillon, Vincent Moureau, Nasser Darabiha, Olivier Gicquel, Denis Veynante, and Benoit Fiorina (2014). "Les modeling of the impact of heat losses and differential diffusion on turbulent stratified flame propagation:

Application to the tu darmstadt stratified flame". In: *Flow, turbulence and combustion* 93.2, pp. 349–381.

Michel, Jean-Baptiste, Olivier Colin, Christian Angelberger, and Denis Veynante (2009). "Using the tabulated diffusion flamelet model ADF-PCM to simulate a lifted methane–air jet flame". In: *Combustion and Flame* 156.7, pp. 1318–1331.

Miller, RS, K Harstad, and J Bellan (1998). "Evaluation of equilibrium and non-equilibrium evaporation models for many-droplet gas-liquid flow simulations". In: *International Journal of Multiphase Flow* 24.6, pp. 1025–1055.

Mira, D., X. Jiang, C. Moulinec, and D.R. Emerson (2013). "Numerical simulations of turbulent jet flames with non-premixed combustion of hydrogen-enriched fuels". In: *Computers & Fluids* 88, pp. 688–701.

— (2014). "Numerical assessment of subgrid scale models for scalar transport in large-eddy simulations of hydrogen-enriched fuels". In: *Int. J. Hydrogen Energy* 39, pp. 7173–7189.

Mira, D, O Lehmkuhl, P Stathopoulos, T Tanneberger, TG Reichel, CO Paschereit, M Vázquez, and G Houzeaux (2018). "Numerical investigation of a lean premixed swirl-stabilized hydrogen combustor and operational conditions close to flashback". In: *Turbo Expo: Power for Land, Sea, and Air*. Vol. 51067. American Society of Mechanical Engineers, V04BT04A009.

Mira, D, Oriol Lehmkuhl, Ambrus Both, Panagiotis Stathopoulos, Tom Tanneberger, Thoralf G Reichel, Christian Oliver Paschereit, Mariano Vázquez, and Guillaume Houzeaux (2020). "Numerical characterization of a premixed hydrogen flame under conditions close to flashback". In: *Flow, Turbulence and Combustion* 104.2, pp. 479–507.

Mira, Daniel, Ambrus Both, and Anurag Surapaneni (2022). "Influence of axial air injection on the flame stability of a technically premixed hydrogen flame". In: *Proceedings of Global Power and Propulsion Society, GPPS Chania22*. Global Power and Propulsion Society.

Mira, Daniel, Eduardo Pérez, Ricard Borrell, and Guillaume Houzeaux (2022). "HPC-enabling technologies for high-fidelity combustion simulations". In: *Proceedings of the Combustion Institute*. ISSN: 1540-7489. DOI: https://doi.org/10.1016/j.proci.2022.07.222.

Mira, Daniel, Eduardo J Pérez-Sánchez, Anurag Surapaneni, Jesús Benajes, José M García-Oliver, José M Pastor, and Daiana De León (2021a). "LES Study on Spray Combustion With Renewable Fuels Under ECN Spray-A Conditions". In: *Internal Combustion Engine Division Fall Technical Conference*. Vol. 85512. American Society of Mechanical Engineers, V001T06A004.

Mira, Daniel, Anurag Surapaneni, Eduardo Pérez, Ambrus Both, Oriol Lehmkuhl Barba, and Guillaume Houzeaux (2021b). "Assessment of chemistry reduction in high-pressure spray flames of oxymethylene ethers using large-eddy simulations". In: *ETMM13 Rhodes, Greece 15-17 September, 2021: conference proceedings*, pp. 396–401.

Miró, A, M Soria, JC Cajas, I Rodríguez, and Charles Moulinec (2021). "Flow topology and heat transfer analysis of slotted and axisymmetric synthetic impinging jets". In: *International Journal of Thermal Sciences* 164, p. 106847.

Modest, Michael F and Sandip Mazumder (2013). *Radiative heat transfer*. Academic press.

Morgan, David L and Riki Kobayashi (1994). "Direct vapor pressure measurements of ten n-alkanes m the 10-C28 range". In: *Fluid Phase Equilibria* 97, pp. 211–242.

Morinishi, Yohei (2010). "Skew-symmetric form of convective terms and fully conservative finite difference schemes for variable density low-Mach number flows". In: *Journal of Computational Physics* 229.2, pp. 276–300.

Moser, Robert D, John Kim, and Nagi N Mansour (1999). "Direct numerical simulation of turbulent channel flow up to Re τ= 590". In: *Physics of fluids* 11.4, pp. 943–945.

Moureau, Vincent, P Domingo, and Luc Vervisch (2011). "From large-eddy simulation to direct numerical simulation of a lean premixed swirl flame: Filtered laminar flame-pdf modeling". In: *Combustion and Flame* 158.7, pp. 1340–1357.

Moureau, Vincent, Philippe Minot, Heinz Pitsch, and Claude Bérat (2007). "A ghost-fluid method for large-eddy simulations of premixed combustion in complex geometries". In: *Journal of Computational Physics* 221.2, pp. 600–614.

Mukundakumar, Nithin, Denis Efimov, Nijso Beishuizen, and Jeroen van Oijen (2021). "A new preferential diffusion model applied to FGM simulations of hydrogen flames". In: *Combustion Theory and Modelling* 25.7, pp. 1245–1267.

Mura, Arnaud, Anthony Techer, and Guillaume Lehnasch (2022). "Analysis of high-speed combustion regimes of hydrogen jet in supersonic vitiated airstream". In: *Combustion and Flame* 239, p. 111552.

Mustata, Radu, Luis Valiño, Carmen Jiménez, WP Jones, and S Bondi (2006). "A probability density function Eulerian Monte Carlo field method for large eddy simulations: Application to a turbulent piloted methane/air diffusion flame (Sandia D)". In: *Combustion and Flame* 145.1-2, pp. 88–104.

Najafi-Yazdi, Alireza, Benedicte Cuenot, and Luc Mongeau (2012). "Systematic definition of progress variables and intrinsically low-dimensional, flamelet generated manifolds for chemistry tabulation". In: *Combustion and Flame* 159.3, pp. 1197–1204.

Naud, Bertrand, Ricardo Novella, José Manuel Pastor, and Johannes F Winklinger (2015). "RANS modelling of a lifted H2/N2 flame using an unsteady flamelet progress variable approach with presumed PDF". In: *Combustion and Flame* 162.4, pp. 893–906.

Naumann, Z and L Schiller (1935). "A drag coefficient correlation". In: *Zeitschrift Verein Deutscher Ingenieure* 77, pp. 318–323.

Navarro-Martinez, S and A Kronenburg (2009). "LES–CMC simulations of a lifted methane flame". In: *Proceedings of the Combustion Institute* 32.1, pp. 1509–1516.

Newmark, Nathan M (1959). "A method of computation for structural dynamics". In: *Journal of the engineering mechanics division* 85.3, pp. 67–94.

Nguyen, Phuc-Danh, Luc Vervisch, Vallinayagam Subramanian, and Pascale Domingo (2010). "Multidimensional flamelet-generated manifolds for partially premixed combustion". In: *Combustion and Flame* 157.1, pp. 43–61.

Nguyen, Tuan M and William A Sirignano (2018). "The impacts of three flamelet burning regimes in nonlinear combustion dynamics". In: *Combustion and Flame* 195, pp. 170–182.

Nicoud, FC (1998). "Numerical study of a channel flow with variable properties". In: *CTR Annual Research Briefs*, pp. 289–310.

Nicoud, Franck (2000). "Conservative high-order finite-difference schemes for low-Mach number flows". In: *Journal of Computational Physics* 158.1, pp. 71–97.

Nilsson, Thommie, Ivan Langella, Nguyen Anh Khoa Doan, Nedunchezhian Swaminathan, Rixin Yu, and Xue-Song Bai (2019). "A priori analysis of sub-grid variance of a reactive scalar using DNS data of high Ka flames". In: *Combustion Theory and Modelling* 23.5, pp. 885–906.

Noh, D, E Karlis, S Navarro-Martinez, Y Hardalupas, AMKP Taylor, D Fredrich, and WP Jones (2019). "Azimuthally-driven subharmonic thermoacoustic instabilities in a swirl-stabilised combustor". In: *Proceedings of the Combustion Institute* 37.4, pp. 5333–5341.

Noh, Dongwon, Simon Gallot-Lavallée, William P Jones, and Salvador Navarro-Martinez (2018). "Comparison of droplet evaporation models for a turbulent, non-swirling jet flame with a polydisperse droplet distribution". In: *Combustion and Flame* 194, pp. 135–151.

Noiray, Nicolas, Mirko Bothien, and Bruno Schuermans (2011). "Investigation of azimuthal staging concepts in annular gas turbines". In: *Combustion Theory and Modelling* 15.5, pp. 585–606.

Nomura, Hiroshi, Yasushige Ujiie, Hans J Rath, Jun'ich Sato, and Michikata Kono (1996). "Experimental study on high-pressure droplet evaporation using microgravity conditions". In: *Symposium (International) on Combustion*. Vol. 26. 1. Elsevier, pp. 1267–1273.

Novoselov, Alex G, Cristian E Lacey, Bruce A Perry, and Michael E Mueller (2021). "Large Eddy Simulation of a turbulent lifted flame using multi-modal manifold-based models: Feasibility and interpretability". In: *Proceedings of the Combustion Institute* 38.2, pp. 2581–2588.

Oberleithner, Kilian, Michael Stöhr, Seong Ho Im, Christoph M Arndt, and Adam M Steinberg (2015). "Formation and flame-induced suppression of the precessing vortex core in a swirl combustor: experiments and linear stability analysis". In: *Combustion and Flame* 162.8, pp. 3100–3114.

Oberleithner, Kilian, Steffen Terhaar, Lothar Rukes, and Christian Oliver Paschereit (2013). "Why nonuniform density suppresses the Precessing Vortex Core". In: *Journal of Engineering for Gas Turbines and Power* 135.12.

Oks, David, Mariano Vázquez, Guillaume Houzeaux, Constantine Butakoff, and Cristóbal Samaniego (2022). "Fluid-structure interaction analysis of eccentricity and leaflet rigidity on thrombosis biomarkers in bioprosthetic aortic valve replacements". In: *bioRxiv*.

Olbricht, Clemens, Anja Ketelheun, Frederik Hahn, and Johannes Janicka (2010). "Assessing the predictive capabilities of combustion LES as applied to the Sydney flame series". In: *Flow, turbulence and combustion* 85.3, pp. 513–547.

Olguin, Hernan and Eva Gutheil (2014). "Influence of evaporation on spray flamelet structures". In: *Combustion and Flame* 161.4, pp. 987–996.

Olivares Mañas, Edgar (2018). "Parallel Lagrangian particle transport: application to respiratory system airways". PhD thesis. Universitat Politècnica de Catalunya.

Oran, Elaine S and Jay P Boris (1991). *Numerical approaches to combustion modeling*. American Institute Aeronautics and Astronautics, New York, United States.

Ortega, Marc (2018). "Study of compressible flows using Galerkin methods". BSc thesis. Universitat Politècnica de Catalunya (UPC).

Owen, Herbert, Georgios Chrysokentis, Matias Avila, Daniel Mira, Guillaume Houzeaux, Ricard Borrell, Juan Carlos Cajas, and Oriol Lehmkuhl (2020). "Wall-modeled large-eddy simulation in a finite element framework". In: *International Journal for Numerical Methods in Fluids* 92.1, pp. 20–37.

Oyarzun, Guillermo, Daniel Mira, and Guillaume Houzeaux (2021). "Performance assessment of cuda and openacc in large scale combustion simulations". In: *arXiv preprint arXiv:2107.11541*.

Palies, Paul, Daniel Durox, Thierry Schuller, Pascal Morenton, and Sébastien Candel (2009). "Dynamics of premixed confined swirling flames". In: *Comptes Rendus Mecanique* 337.6-7, pp. 395–405.

Pantangi, Pradeep, Amsini Sadiki, Johannes Janicka, Markus Mann, and Andreas Dreizler (2014). "LES of premixed methane flame impinging on the wall using non-adiabatic flamelet generated manifold (FGM) approach". In: *Flow, turbulence and combustion* 92.4, pp. 805–836.

Pao, Yih-Ho (1965). "Structure of turbulent velocity and scalar fields at large wavenumbers". In: *The Physics of Fluids* 8.6, pp. 1063–1075.

Pastor, José V, José M García-Oliver, Carlos Micó, Alba A García-Carrero, and Arantzazu Gómez (2020). "Experimental study of the effect of hydrotreated vegetable oil and oxymethylene ethers on main spray and combustion characteristics under engine combustion network spray a conditions". In: *Applied Sciences* 10.16, p. 5460.

Paulhiac, Damien, Bénédicte Cuenot, Eleonore Riber, Lucas Esclapez, and Stéphane Richard (2020). "Analysis of the spray flame structure in a lab-scale burner using large eddy simulation and discrete particle simulation". In: *Combustion and Flame* 212, pp. 25–38.

Pearson, Karl (1895). "Correlation coefficient". In: *Royal Society Proceedings*. Vol. 58, p. 214.

Pecquery, François, Vincent Moureau, Ghislain Lartigue, Luc Vervisch, and Anthony Roux (2014). "Modelling nitrogen oxide emissions in turbulent flames with air dilution: Application to LES of a non-premixed jet-flame". In: *Combustion and flame* 161.2, pp. 496–509.

Pera, Cécile, Julien Réveillon, Luc Vervisch, and Pascale Domingo (2006). "Modeling subgrid scale mixture fraction variance in LES of evaporating spray". In: *Combustion and Flame* 146.4, pp. 635–648.

Perot, J Blair (1993). "An analysis of the fractional step method". In: *Journal of Computational Physics* 108.1, pp. 51–58.

Peters, Norbert (1983). "Local quenching due to flame stretch and non-premixed turbulent combustion". In: *Combustion Science and Technology* 30.1-6, pp. 1–17.

— (1984). "Laminar diffusion flamelet models in non-premixed turbulent combustion". In: *Progress in energy and combustion science* 10.3, pp. 319–339.

— (1988). "Laminar flamelet concepts in turbulent combustion". In: *Symposium (international) on combustion*. Vol. 21. 1. Elsevier, pp. 1231–1250.

— (1999). "The turbulent burning velocity for large-scale and small-scale turbulence". In: *Journal of Fluid mechanics* 384, pp. 107–132.

— (2001). *Turbulent combustion*. IOP Publishing.

Pettit, LI and HW Peers (1991). "An Example not to be Followed?" In: *Teaching Statistics* 13.1, pp. 8–8.

Pierce, Charles D and Parviz Moin (2004). "Progress-variable approach for large-eddy simulation of non-premixed turbulent combustion". In: *Journal of fluid Mechanics* 504, pp. 73–97.

Piomelli, Ugo (1997). *Large-eddy and direct simulation of turbulent flows*. Citeseer.

Pitsch, Heinz (2005). "A consistent level set formulation for large-eddy simulation of premixed turbulent combustion". In: *Combustion and Flame* 143.4, pp. 587–598.

— (2006). "Large eddy simulation of turbulent combustion". In: *Annual Review of Fluid Mechanics* 38.1, pp. 453–482. DOI: 10.1146/annurev.fluid.38.050304.092133.

Pitsch, Heinz and L Duchamp De Lageneste (2002). "Large-eddy simulation of premixed turbulent combustion using a level-set approach". In: *Proceedings of the Combustion Institute* 29.2, pp. 2001–2008.

Pitsch, Heinz and Sergei Fedotov (2001). "Investigation of scalar dissipation rate fluctuations in non-premixed turbulent combustion using a stochastic approach". In: *Combustion Theory and Modelling* 5.1, p. 41.

Pitsch, Heinz and Matthias Ihme (2005). "An unsteady/flamelet progress variable method for LES of nonpremixed turbulent combustion". In: *43rd AIAA Aerospace Sciences Meeting and Exhibit*, p. 557.

Pitsch, Heinz and Helfried Steiner (2000). "Large-eddy simulation of a turbulent piloted methane/air diffusion flame (Sandia flame D)". In: *Physics of fluids* 12.10, pp. 2541–2554.

Poinsot, T, D Veynante, and S Candel (1991). "Diagrams of premixed turbulent combustion based on direct simulation". In: *Symposium (international) on combustion*. Vol. 23. 1. Elsevier, pp. 613–619.

Poinsot, Thierry and Denis Veynante (2005). *Theoretical and numerical combustion*. RT Edwards, Inc.

POP (2021). *Report on co-design of Alya for combustion*. URL: https://co-design.pop-coe.eu/reports/POP2-AR-130-Alya-CoEC.html.

Pope, Stephen B (1985). "PDF methods for turbulent reactive flows". In: *Progress in energy and combustion science* 11.2, pp. 119–192.

— (2000). *Turbulent flows*. Cambridge university press.

Popp, Sebastian, Franziska Hunger, Sandra Hartl, Danny Messig, Bruno Coriton, Jonathan H Frank, Frederik Fuest, and Christian Hasse (2015). "LES flamelet-progress variable modeling and measurements of a turbulent partially-premixed dimethyl ether jet flame". In: *Combustion and Flame* 162.8, pp. 3016–3029.

Prakash, R Surya, Hrishikesh Gadgil, and BN Raghunandan (2014). "Breakup processes of pressure swirl spray in gaseous cross-flow". In: *International journal of multiphase flow* 66, pp. 79–91.

Proch, F and AM Kempf (2015). "Modeling heat loss effects in the large eddy simulation of a model gas turbine combustor with premixed flamelet generated manifolds". In: *Proceedings of the combustion institute* 35.3, pp. 3337–3345.

Proch, Fabian and Andreas M Kempf (2014). "Numerical analysis of the Cambridge stratified flame series using artificial thickened flame LES with tabulated premixed flame chemistry". In: *Combustion and Flame* 161.10, pp. 2627–2646.

Radl, Stefan, Begona C Gonzales, Christoph Goniva, and Stefan Pirker (2015). "State of the art in mapping schemes for dilute and dense Euler-Lagrange simulations". In:

Ramaekers, WJS (2011). "Development of flamelet generated manifolds for partially-premixed flame simulations". PhD thesis. Technische Universiteit Eindhoven.

Raman, Venkatramanan, Heinz Pitsch, and Rodney O Fox (2006). "Eulerian transported probability density function sub-filter model for large-eddy simulations of turbulent combustion". In: *Combustion Theory and Modelling* 10.3, pp. 439–458.

Ranz, W E and W R Marshall (1952). "Evaporation from drops: Part 1". In: *Chem. eng. prog* 48.3, pp. 141–146.

Regele, Jonathan D, Edward Knudsen, Heinz Pitsch, and Guillaume Blanquart (2013). "A two-equation model for non-unity Lewis number differential diffusion in lean premixed laminar flames". In: *Combustion and flame* 160.2, pp. 240–250.

Reichel, Thoralf G, Katharina Goeckeler, and Oliver Paschereit (2015). "Investigation of lean premixed swirl-stabilized hydrogen burner with axial air injection using oh-plif imaging". In: *Journal of Engineering for Gas Turbines and Power* 137.11.

Reichel, Thoralf G and Christian Oliver Paschereit (2017). "Interaction mechanisms of fuel momentum with flashback limits in lean-premixed combustion of hydrogen". In: *International Journal of Hydrogen Energy* 42.7, pp. 4518–4529.

Reichel, Thoralf G, Steffen Terhaar, and Christian O Paschereit (2013). "Flow field manipulation by axial air injection to achieve flashback resistance and its impact on mixing quality". In: *43rd AIAA Fluid Dynamics Conference*, p. 2603.

Reichel, Thoralf G, Steffen Terhaar, and Christian Oliver Paschereit (2018). "Flashback Resistance and Fuel–Air Mixing in Lean Premixed Hydrogen Combustion". In: *Journal of Propulsion and Power* 34.3, pp. 690–701.

Reichel, Thoralf G, Steffen Terhaar, and Oliver Paschereit (2015). "Increasing flashback resistance in lean premixed swirl-stabilized hydrogen combustion by axial air injection". In: *Journal of Engineering for Gas Turbines and Power* 137.7, p. 071503.

Reiss, Julius (2015). "A family of energy stable, skew-symmetric finite difference schemes on collocated grids". In: *Journal of Scientific Computing* 65.2, pp. 821–838.

Reveillon, J and L Vervisch (2000). "Spray vaporization in nonpremixed turbulent combustion modeling: a single droplet model". In: *Combustion and flame* 121.1-2, pp. 75–90.

Rieth, Martin, Andreas M Kempf, Oliver T Stein, Andreas Kronenburg, Christian Hasse, and Michele Vascellari (2019). "Evaluation of a flamelet/progress variable approach for pulverized coal combustion in a turbulent mixing layer". In: *Proceedings of the Combustion Institute* 37.3, pp. 2927–2934.

Rittler, Andreas, Fabian Proch, and Andreas M Kempf (2015). "LES of the Sydney piloted spray flame series with the PFGM/ATF approach and different sub-filter models". In: *Combustion and Flame* 162.4, pp. 1575–1598.

Rodriguez, I, O Lehmkuhl, and M Soria (2021). "On the effects of the free-stream turbulence on the heat transfer from a sphere". In: *International Journal of Heat and Mass Transfer* 164, p. 120579.

Rodriguez, Ivette, Oriol Lehmkuhl, and Ricard Borrell (2020). "Effects of the actuation on the boundary layer of an airfoil at Reynolds number Re= 60000". In: *Flow, Turbulence and Combustion* 105.2, pp. 607–626.

Rogallo, Robert S and Parviz Moin (1984). "Numerical simulation of turbulent flows". In: *Annual review of fluid mechanics* 16, pp. 99–137.

Roux, Sebastién, G Lartigue, Thierry Poinsot, Ulrich Meier, and Claude Bérat (2005). "Studies of mean and unsteady flow in a swirled combustor using experiments, acoustic analysis, and large eddy simulations". In: *Combustion and Flame* 141.1-2, pp. 40–54.

Rowlinson, JS (2005). "The Maxwell–Boltzmann distribution". In: *Molecular Physics* 103.21-23, pp. 2821–2828.

Rozema, Wybe, Roel WCP Verstappen, Arthur EP Veldman, and Johan C Kok (2018). "Low-Dissipation Simulation Methods and Models for Turbulent Subsonic Flow". In: *Archives of Computational Methods in Engineering*, pp. 1–32.

Sabel'nikov, VA and AN Lipatnikov (2011). "A simple model for evaluating conditioned velocities in premixed turbulent flames". In: *Combustion Science and Technology* 183.6, pp. 588–613.

Sacomano Filho, Fernando Luiz, Guenther Carlos Krieger Filho, Jeroen Adrianus van Oijen, Amsini Sadiki, and Johannes Janicka (2019). "A novel strategy to accurately represent the carrier gas properties of droplets evaporating in a combustion environment". In: *International Journal of Heat and Mass Transfer* 137, pp. 1141–1153.

Sacomano Filho, Fernando Luiz, Guido Kuenne, Mouldi Chrigui, Amsini Sadiki, and Johannes Janicka (2017). "A consistent Artificially Thickened Flame approach for spray combustion using LES and the FGM chemistry reduction method: Validation in Lean Partially Pre-Vaporized flames". In: *Combustion and Flame* 184, pp. 68–89.

Sacomano Filho, Fernando Luiz, Nico Speelman, Jeroen Adrianus van Oijen, Laurentius Philippus Hendrika de Goey, Amsini Sadiki, and Johannes Janicka (2018).

"Numerical analyses of laminar flames propagating in droplet mists using detailed and tabulated chemistry". In: *Combustion Theory and Modelling* 22.5, pp. 998–1032.

Sagaut, Pierre (2006). *Large eddy simulation for incompressible flows: an introduction*. Springer Science & Business Media.

Sagdeev, DI, MG Fomina, G Kh Mukhamedzyanov, and IM Abdulagatov (2013). "Experimental Study of the Density and Viscosity of n-Heptane at Temperatures from 298 K to 470 K and Pressure upto 245 MPa". In: *International Journal of Thermophysics* 34.1, pp. 1–33.

Saghafian, Amirreza, Lee Shunn, David A Philips, and Frank Ham (2015). "Large eddy simulations of the HIFiRE scramjet using a compressible flamelet/progress variable approach". In: *Proceedings of the Combustion Institute* 35.2, pp. 2163–2172.

Sanderson, Benjamin M and Brian C O'Neill (2020). "Assessing the costs of historical inaction on climate change". In: *Scientific reports* 10.1, p. 9173.

Sanjosé, M, JM Senoner, F Jaegle, B Cuenot, S Moreau, and Thierry Poinsot (2011). "Fuel injection model for Euler–Euler and Euler–Lagrange large-eddy simulations of an evaporating spray inside an aeronautical combustor". In: *International Journal of Multiphase Flow* 37.5, pp. 514–529.

Sazhin, Sergei (2014). *Droplets and sprays*. Vol. 345. Springer.

Sazhin, Sergei S (2017). "Modelling of fuel droplet heating and evaporation: Recent results and unsolved problems". In: *Fuel* 196, pp. 69–101.

Scargle, Jeffrey D (1982). "Studies in astronomical time series analysis. II-Statistical aspects of spectral analysis of unevenly spaced data". In: *The Astrophysical Journal* 263, pp. 835–853.

Schmidt, Ernst and Ulrich Grigull (1989). "Properties of water and steam in SI-units. 4". In:

Schneider, Ch, Andreas Dreizler, J Janicka, and EP Hassel (2003). "Flow field measurements of stable and locally extinguishing hydrocarbon-fuelled jet flames". In: *Combustion and Flame* 135.1-2, pp. 185–190.

Scholtissek, Arne, Wai Lee Chan, Hongbin Xu, Franziska Hunger, Hemanth Kolla, Jacqueline H Chen, Matthias Ihme, and Christian Hasse (2015). "A multi-scale asymptotic scaling and regime analysis of flamelet equations including tangential diffusion effects for laminar and turbulent flames". In: *Combustion and Flame* 162.4, pp. 1507–1529.

Seidel, V, A Marosky, C Hirsch, T Sattelmayer, W Geng, and F Magni (2013). "Influence of the inflow confinement on the flashback limits of a premixed swirl burner". In: *Turbo Expo: Power for Land, Sea, and Air*. Vol. 55102. American Society of Mechanical Engineers, V01AT04A068.

Seshadri, Ko and N Peters (1988). "Asymptotic structure and extinction of methane-air diffusion flames". In: *Combustion and Flame* 73.1, pp. 23–44.

Shashank, E Knudsen, E Knudsen, and H Pitsch (2011). "Spray evaporation model sensitivities". In: *Annual Research Briefs* 2011, pp. 213–224.

Shu, Chi-Wang and Stanley Osher (1988). "Efficient implementation of essentially non-oscillatory shock-capturing schemes". In: *Journal of computational physics* 77.2, pp. 439–471.

Shum-Kivan, F, J Marrero Santiago, A Verdier, E Riber, B Renou, G Cabot, and B Cuenot (2017). "Experimental and numerical analysis of a turbulent spray flame structure". In: *Proceedings of the Combustion Institute* 36.2, pp. 2567–2575.

Sidey, J. A. M., A. Giusti, P. Benie, and E. Mastorakos (2017). *The Swirl Flames Data Repository*. URL: http://swirl-flame.eng.cam.ac.uk.

Sidey, Jennifer A, Patton M Allison, and Epaminondas Mastorakos (2017). "The effect of fuel composition on swirling kerosene flames". In: *55th AIAA Aerospace Sciences Meeting*, p. 0383.

Sitte, Michael Philip (2019). "Modelling of Spray Combustion with Doubly Conditional Moment Closure". PhD thesis. University of Cambridge.

Sitte, Michael Philip and Epaminondas Mastorakos (2019). "Large eddy simulation of a spray jet flame using doubly conditional moment closure". In: *Combustion and flame* 199, pp. 309–323.

Slotnick, Jeffrey P, Abdollah Khodadoust, Juan Alonso, David Darmofal, William Gropp, Elizabeth Lurie, and Dimitri J Mavriplis (2014). *CFD vision 2030 study: a path to revolutionary computational aerosciences*. Tech. rep.

Smagorinsky, Joseph (1963). "General circulation experiments with the primitive equations: I. The basic experiment". In: *Monthly weather review* 91.3, pp. 99–164.

Smith, Gregory P, David M Golden, Michael Frenklach, Nigel W Moriarty, Boris Eiteneer, Mikhail Goldenberg, C Thomas Bowman, Ronald K Hanson, Soonho Song, WC Gardiner Jr, et al. (2011). "GRI-Mech 3.0, 1999". In: *URL http://www. me. berkeley. edu/gri_mech*.

Somers, Bart (1994). "The simulation of flat flames with detailed and reduced chemical models". PhD thesis. Gastec NV NL.

Sreenivasan, Katepalli R (1995). "On the universality of the Kolmogorov constant". In: *Physics of Fluids* 7.11, pp. 2778–2784.

Staffelbach, Gicquel, LYM Gicquel, G Boudier, and Thierry Poinsot (2009). "Large Eddy Simulation of self excited azimuthal modes in annular combustors". In: *Proceedings of the Combustion Institute* 32.2, pp. 2909–2916.

Stokes, G. G. (1851). "On the effect of internal friction of fluids on the motion of pendulums". In: *Transactions of the Cambridge Philosophical Society* 9, part ii, pp. 8–106.

Sun, Rui and Heng Xiao (2015). "Diffusion-based coarse graining in hybrid continuum–discrete solvers: theoretical formulation and a priori tests". In: *International Journal of Multiphase Flow* 77, pp. 142–157.

Surapaneni, A and D Mira (2023). "Assessment of dynamic adaptive chemistry with tabulated reactions for the simulation of unsteady multiregime combustion phenomena". In: *Combustion and Flame* 251, p. 112715.

Surapaneni, Anurag (2019). "Development of a finite rate chemistry solver with tabulated dynamic adaptive chemistry". MSc thesis. TU Delft.

Surapaneni, Anurag and Daniel Mira (2021). "Semi implicit solver for high fidelity LES/DNS solutions of reacting flows". In: *10th European Combustion Meeting: April 14-15, 2021, virtual edition: proceedings volume*. MCM, pp. 30–34.

Swaminathan, N (2002). "Flamelet regime in non-premixed combustion". In: *Combustion and flame* 129.1-2, pp. 217–219.

Syred, Nicholas (2006). "A review of oscillation mechanisms and the role of the precessing vortex core (PVC) in swirl combustion systems". In: *Progress in Energy and Combustion Science* 32.2, pp. 93–161.

Taamallah, Soufien, Zachary A LaBry, Santosh J Shanbhogue, and Ahmed F Ghoniem (2015a). "Thermo-acoustic instabilities in lean premixed swirl-stabilized combustion and their link to acoustically coupled and decoupled flame macrostructures". In: *Proceedings of the combustion institute* 35.3, pp. 3273–3282.

Taamallah, Soufien, Konstantina Vogiatzaki, Fahad M Alzahrani, Esmail MA Mokheimer, MA Habib, and Ahmed F Ghoniem (2015b). "Fuel flexibility, stability and emissions in premixed hydrogen-rich gas turbine combustion: Technology, fundamentals, and numerical simulations". In: *Applied energy* 154, pp. 1020–1047.

Takeno, T, M Murayama, and Y Tanida (1990). "Fractal analysis of turbulent premixed flame surface". In: *Experiments in fluids* 10.2-3, pp. 61–70.

Tang, Yihao and Venkat Raman (2021). "Large eddy simulation of premixed turbulent combustion using a non-adiabatic, strain-sensitive flamelet approach". In: *Combustion and Flame* 234, p. 111655.

Tangermann, E, M Pfitzner, M Konle, and TJCS Sattelmayer (2010). "Large-eddy simulation and experimental observation of combustion-induced vortex breakdown". In: *Combustion science and technology* 182.4-6, pp. 505–516.

Tangermann, Eike and Michael Pfitzner (2009). "Evaluation of combustion models for combustion-induced vortex breakdown". In: *Journal of Turbulence* 10, N7.

Tanneberger, Tom, Thoralf G Reichel, Oliver Krüger, Steffen Terhaar, and Christian Oliver Paschereit (2015). "Numerical investigation of the flow field and mixing in a swirl-stabilized burner with a non-swirling axial jet". In: *Turbo Expo: Power for Land, Sea, and Air*. Vol. 56697. American Society of Mechanical Engineers, V04BT04A026.

Taylor, Geoffrey Ingram (1938). "The spectrum of turbulence". In: *Proceedings of the Royal Society of London. Series A-Mathematical and Physical Sciences* 164.919, pp. 476–490.

TCS (2023). *International Workshop on the Turbulent Combustion of Sprays*. URL: www.tcs-workshop.org.

Terhaar, Steffen, Thoralf G Reichel, Christina Schrödinger, Lothar Rukes, Christian Oliver Paschereit, and Kilian Oberleithner (2015). "Vortex breakdown types and global modes in swirling combustor flows with axial injection". In: *Journal of propulsion and power* 31.1, pp. 219–229.

Toutant, Adrien and Francoise Bataille (2013). "Turbulence statistics in a fully developed channel flow submitted to a high temperature gradient". In: *International Journal of Thermal Sciences* 74, pp. 104–118.

Trias, FX and O Lehmkuhl (2011). "A self-adaptive strategy for the time integration of Navier-Stokes equations". In: *Numerical Heat Transfer, Part B: Fundamentals* 60.2, pp. 116–134.

Tsuji, Hiroshi (1982). "Counterflow diffusion flames". In: *Progress in energy and combustion science* 8.2, pp. 93–119.

Tyliszczak, Artur, Davide E Cavaliere, and Epaminondas Mastorakos (2014). "LES/CMC of blow-off in a liquid fueled swirl burner". In: *Flow, Turbulence and Combustion* 92.1, pp. 237–267.

UCSD (2018). *Chemical-Kinetic Mechanisms for Combustion Applications*. San Diego Mechanism web page, Mechanical and Aerospace Engineering (Combustion Research), University of California at San Diego. URL: http://combustion.ucsd.edu.

Urzay, J, M Bassenne, GI Park, and P Moin (2014). "Characteristic regimes of subgrid-scale coupling in LES of particle-laden turbulent flows". In: *Proceedings of Summer Program, Center for Turbulence Research, Stanford University*, pp. 3–13.

Van Driest, Edward R (1951). "Turbulent boundary layer in compressible fluids". In: *Journal of Aeronautical Sciences* 18.3, pp. 145–160.

Van Oijen, JA and LPH De Goey (2000). "Modelling of premixed laminar flames using flamelet-generated manifolds". In: *Combustion Science and Technology* 161.1, pp. 113–137.

— (2004). "A numerical study of confined triple flames using a flamelet-generated manifold". In: *Combustion Theory and Modelling* 8.1, p. 141.

Van Oijen, JA, A Donini, RJM Bastiaans, JHM ten Thije Boonkkamp, and LPH De Goey (2016). "State-of-the-art in premixed combustion modeling using flamelet generated manifolds". In: *Progress in Energy and Combustion Science* 57, pp. 30–74.

Van Oijen, JA, FA Lammers, and LPH De Goey (2001). "Modeling of complex premixed burner systems by using flamelet-generated manifolds". In: *Combustion and Flame* 127.3, pp. 2124–2134.

Vascellari, M, GL Tufano, OT Stein, A Kronenburg, AM Kempf, A Scholtissek, and C Hasse (2017). "A flamelet/progress variable approach for modeling coal particle ignition". In: *Fuel* 201, pp. 29–38.

Vázquez, Mariano, Guillaume Houzeaux, Seid Koric, Antoni Artigues, Jazmin Aguado-Sierra, Ruth Arís, Daniel Mira, Hadrien Calmet, Fernando Cucchietti, Herbert Owen, et al. (2016). "Alya: Multiphysics engineering simulation toward exascale". In: *Journal of computational science* 14, pp. 15–27.

Ventosa Molina, Jordi (2015). "Numerical simulation of turbulent diffusion flames using flamelet models on unstructured meshes". PhD thesis. Universitat Politècnica de Catalunya (UPC).

Ventosa-Molina, Jordi, J Chiva, Oriol Lehmkuhl, J Muela, Carlos David Pérez-Segarra, and A Oliva (2017). "Numerical analysis of conservative unstructured discretisations for low Mach flows". In: *International Journal for Numerical Methods in Fluids* 84.6, pp. 309–334.

Ventosa Molina, Jordi, Oriol Lehmkuhl, Carlos David Pérez-Segarra, and A Oliva (2017). "Large Eddy Simulation of a Turbulent Diffusion Flame: Some Aspects of Subgrid Modelling Consistency". In: *Flow, Turbulence and Combustion* 99.1, pp. 209–238.

Verdier, Antoine, Javier Marrero Santiago, Alexis Vandel, Sawitree Saengkaew, Gilles Cabot, Gerard Grehan, and Bruno Renou (2017). "Experimental study of local flame structures and fuel droplet properties of a spray jet flame". In: *Proceedings of the Combustion Institute* 36.2, pp. 2595–2602.

Verstappen, RWCP and AEP Veldman (2003). "Symmetry-preserving discretization of turbulent flow". In: *Journal of Computational Physics* 187.1, pp. 343–368.

Vervisch, Luc and Thierry Poinsot (1998). "Direct numerical simulation of non-premixed turbulent flames". In: *Annual review of fluid mechanics* 30.1, pp. 655–691.

Veynante, Denis and Ronnie Knikker (2006). "Comparison between LES results and experimental data in reacting flows". In: *Journal of turbulence* 7, N35.

Vié, Aymeric, Stéphane Jay, Bénédicte Cuenot, and Marc Massot (2013). "Accounting for polydispersion in the eulerian large eddy simulation of the two-phase flow in an aeronautical-type burner". In: *Flow, turbulence and combustion* 90.3, pp. 545–581.

Viton, C, M Chavret, and J Jose (1996). "Enthalpies of Vaporization of Normal Alkanes from Nonane to Pentadecane at Temperatures from 298 to 359 K". In: *ELDATA: Int. Electron. J. Phys. Chem. Data* 2, p. 103.

Volpiani, Pedro S, Thomas Schmitt, and Denis Veynante (2017). "Large eddy simulation of a turbulent swirling premixed flame coupling the TFLES model with a dynamic wrinkling formulation". In: *Combustion and Flame* 180, pp. 124–135.

Von Kármán, Theodore (1948). "Progress in the statistical theory of turbulence". In: *Proceedings of the National Academy of Sciences* 34.11, pp. 530–539.

Vreman, AW (2004). "An eddy-viscosity subgrid-scale model for turbulent shear flow: Algebraic theory and applications". In: *Physics of fluids* 16.10, pp. 3670–3681.

Vreman, AW, BA Albrecht, JA Van Oijen, LPH De Goey, and RJM Bastiaans (2008). "Premixed and nonpremixed generated manifolds in large-eddy simulation of Sandia flame D and F". In: *Combustion and Flame* 153.3, pp. 394–416.

Vreman, AW, RJM Bastiaans, and BJ Geurts (2009). "A similarity subgrid model for premixed turbulent combustion". In: *Flow, turbulence and combustion* 82.2, pp. 233–248.

Vreman, Bert, Bernard Geurts, and Hans Kuerten (1994). "Realizability conditions for the turbulent stress tensor in large-eddy simulation". In: *Journal of Fluid Mechanics* 278, pp. 351–362.

Wang, P, NA Platova, J Fröhlich, and U Maas (2014). "Large eddy simulation of the PRECCINSTA burner". In: *International Journal of Heat and Mass Transfer* 70, pp. 486–495.

Wehrfritz, Armin, Ossi Kaario, Ville Vuorinen, and Bart Somers (2016). "Large eddy simulation of n-dodecane spray flames using flamelet generated manifolds". In: *Combustion and Flame* 167, pp. 113–131.

Welch, Peter (1967). "The use of fast Fourier transform for the estimation of power spectra: a method based on time averaging over short, modified periodograms". In: *IEEE Transactions on audio and electroacoustics* 15.2, pp. 70–73.

Wen, Xu, Xue-Song Bai, Kun Luo, Haiou Wang, Yujuan Luo, and Jianren Fan (2018). "A generalized flamelet tabulation method for partially premixed combustion". In: *Combustion and Flame* 198, pp. 54–68.

Wilke, CR (1950). "A viscosity equation for gas mixtures". In: *The journal of chemical physics* 18.4, pp. 517–519.

Williams, Forman (2006). "Descriptions of nonpremixed turbulent combustion". In: *44th AIAA Aerospace Sciences Meeting and Exhibit*, p. 1505.

Willingham, Charles B, William J Taylor, Joan M Pignocco, and Frederick D Rossini (1945). "Vapor pressures and boiling points of some paraffin, alkylcyclopentane, alkylcyclohexane, and alkylbenzene hydrocarbons". In: *Journal of Research of the National Bureau of Standards* 35.3, pp. 219–244.

Wollny, P, B Rogg, and A Kempf (2018). "Modelling heat loss effects in high temperature oxy-fuel flames with an efficient and robust non-premixed flamelet approach". In: *Fuel* 216, pp. 44–52.

Wu, Hao, Yee Chee See, Qing Wang, and Matthias Ihme (2015). "A Pareto-efficient combustion framework with submodel assignment for predicting complex flame configurations". In: *Combustion and Flame* 162.11, pp. 4208–4230.

Xia, Jun, Hua Zhao, Athanasios Megaritis, Kai H Luo, Alasdair Cairns, and Lionel C Ganippa (2013). "Inert-droplet and combustion effects on turbulence in a diluted diffusion flame". In: *Combustion and Flame* 160.2, pp. 366–383.

Xiao, Heng and Paola Cinnella (2019). "Quantification of model uncertainty in RANS simulations: A review". In: *Progress in Aerospace Sciences* 108, pp. 1–31.

Xiao, Wei and Yong Huang (2016). "Lean blowout limits of a gas turbine combustor operated with aviation fuel and methane". In: *Heat and Mass Transfer* 52.5, pp. 1015–1024.

Yih, Chia-Shun (1960). "A transformation for non-homentropic flows, with an application to large-amplitude motion in the atmosphere". In: *Journal of Fluid Mechanics* 9.1, pp. 68–80.

Yoshizawa, Akira (1986). "Statistical theory for compressible turbulent shear flows, with the application to subgrid modeling". In: *The Physics of fluids* 29.7, pp. 2152–2164.

Yuan, R, J Kariuki, A Dowlut, R Balachandran, and E Mastorakos (2015). "Reaction zone visualisation in swirling spray n-heptane flames". In: *Proceedings of the Combustion Institute* 35.2, pp. 1649–1656.

Yuan, Ruoyang, James Kariuki, and Epaminondas Mastorakos (2018). "Measurements in swirling spray flames at blow-off". In: *International Journal of Spray and Combustion Dynamics* 10.3, pp. 185–210.

Yuen, M. C. and L. W. Chen (1976). "On drag of evaporating liquid droplets". In: *Combustion Science and Technology* 14.4-6, pp. 147–154. DOI: 10.1080/00102207608547524.

Zhang, Hongda, Chao Han, Taohong Ye, and Zhuyin Ren (2016). "Large eddy simulation of turbulent premixed combustion using tabulated detailed chemistry and presumed probability density function". In: *Journal of Turbulence* 17.3, pp. 327–355.

Zhang, Huangwei, Andrew Garmory, Davide E Cavaliere, and Epaminondas Mastorakos (2015). "Large eddy simulation/conditional moment closure modeling of swirl-stabilized non-premixed flames with local extinction". In: *Proceedings of the Combustion Institute* 35.2, pp. 1167–1174.

Zhang, Huangwei and Epaminondas Mastorakos (2016). "Prediction of global extinction conditions and dynamics in swirling non-premixed flames using LES/CMC modelling". In: *Flow, Turbulence and Combustion* 96.4, pp. 863–889.

Zhang, Jingyuan, Tian Li, Henrik Ström, and Terese Løvås (2020a). "Grid-independent Eulerian-Lagrangian approaches for simulations of solid fuel particle combustion". In: *Chemical Engineering Journal* 387, p. 123964.

Zhang, Yan, Hu Wang, Ambrus Both, Likun Ma, and Mingfa Yao (2019). "Effects of turbulence-chemistry interactions on auto-ignition and flame structure for n-dodecane spray combustion". In: *Combustion Theory and Modelling* 23.5, pp. 907–934.

Zhang, Yan, Shijie Xu, Shenghui Zhong, Xue-Song Bai, Hu Wang, and Mingfa Yao (2020b). "Large eddy simulation of spray combustion using flamelet generated manifolds combined with artificial neural networks". In: *Energy and AI* 2, p. 100021.